

R. A. Evarestov

# **Quantum Chemistry of Solids**

**The LCAO  
First Principles  
Treatment  
of Crystals**



**Springer**



# Springer Series in SOLID-STATE SCIENCES

---

## *Series Editors:*

M. Cardona P. Fulde K. von Klitzing R. Merlin H.-J. Queisser H. Störmer

The Springer Series in Solid-State Sciences consists of fundamental scientific books prepared by leading researchers in the field. They strive to communicate, in a systematic and comprehensive way, the basic principles as well as new developments in theoretical and experimental solid-state physics.

- |   |  |
|---|--|
| 138 <b>Phase Separation<br/>in Soft Matter Physics</b><br>Micellar Solutions, Microemulsions,<br>Critical Phenomena<br>By P.K. Khabibullaev and A.A. Saidov | 147 <b>Electron Scattering in Solid Matter</b><br>A Theoretical<br>and Computational Treatise<br>By J. Zabloudil, R. Hammerling,<br>L. Szunyogh, and P. Weinberger |
| 139 <b>Optical Response of Nanostructures</b><br>Microscopic Nonlocal Theory<br>By K. Cho   | 148 <b>Physical Acoustics in the Solid State</b><br>By B. Lüthi  |
| 140 <b>Fractal Concepts<br/>in Condensed Matter Physics</b><br>By T. Nakayama and K. Yakubo   | 149 <b>Solitary Waves<br/>in Complex Dispersive Media</b><br>Theory · Simulation · Applications<br>By V.Yu. Belashov and S.V. Vladimirov                           |
| 141 <b>Excitons in Low-Dimensional<br/>Semiconductors</b><br>Theory, Numerical Methods,<br>Applications By S. Glutsch                                       | 150 <b>Topology in Condensed Matter</b><br>Editor: M.I. Monastyrsky  |
| 142 <b>Two-Dimensional Coulomb Liquids<br/>and Solids</b><br>By Y. Monarkha and K. Kono   | 151 <b>Particle Penetration and Radiation<br/>Effects</b><br>By P. Sigmund   |
| 143 <b>X-Ray Multiple-Wave Diffraction</b><br>Theory and Application<br>By S.-L. Chang  | 152 <b>Magnetism</b><br>From Fundamentals<br>to Nanoscale Dynamics<br>By H.C. Siegmann and J. Stöhr  |
| 144 <b>Physics of Transition Metal Oxides</b><br>By S. Maekawa, T. Tohyama,<br>S.E. Barnes, S. Ishihara,<br>W. Koshiba, and G. Khaliullin                   | 153 <b>Quantum Chemistry of Solids</b><br>The LCAO First Principles<br>Treatment of Crystals<br>By R.A. Evarestov  |
| 145 <b>Point-Contact Spectroscopy</b><br>By Y.G. Naidyuk and I.K. Yanson  | 154 <b>Low-Dimensional Molecular Metals</b><br>By N. Toyota, M. Lang and J. Müller   |
| 146 <b>Optics of Semiconductors<br/>and Their Nanostructures</b><br>Editors: H. Kalt and M. Hetterich   |  |

---

Volumes 91–137 are listed at the end of the book.

Robert A. Evarestov

# Quantum Chemistry of Solids

The LCAO First Principles Treatment of Crystals

With 78 Figures and 126 Tables

**Professor Dr. Robert A. Evarestov**  
St. Petersburg State University  
Chemistry Department  
Stary Peterhof University Prospect 26  
198504 St. Petersburg, Russia  
E-mail: evarest@hm.csa.ru

*Series Editors:*

**Professor Dr., Dres. h. c. Manuel Cardona**  
**Professor Dr., Dres. h. c. Peter Fulde\***  
**Professor Dr., Dres. h. c. Klaus von Klitzing**  
**Professor Dr., Dres. h. c. Hans-Joachim Queisser**  
Max-Planck-Institut für Festkörperforschung, Heisenbergstrasse 1, 70569 Stuttgart, Germany  
\* Max-Planck-Institut für Physik komplexer Systeme, Nöthnitzer Strasse 38  
01187 Dresden, Germany

**Professor Dr. Roberto Merlin**  
Department of Physics, 5000 East University, University of Michigan  
Ann Arbor, MI 48109-1120, USA

**Professor Dr. Horst Störmer**  
Dept. Phys. and Dept. Appl. Physics, Columbia University, New York, NY 10027 and  
Bell Labs., Lucent Technologies, Murray Hill, NJ 07974, USA

Library of Congress Control Number: 2006936622

ISBN 978-3-540-48746-3 Springer Berlin Heidelberg New York

This work is subject to copyright. All rights are reserved, whether the whole or part of the material is concerned, specifically the rights of translation, reprinting, reuse of illustrations, recitation, broadcasting, reproduction on microfilm or in any other way, and storage in data banks. Duplication of this publication or parts thereof is permitted only under the provisions of the German Copyright Law of September 9, 1965, in its current version, and permission for use must always be obtained from Springer. Violations are liable to prosecution under the German Copyright Law.

Springer is a part of Springer Science+Business Media  
[springer.com](http://springer.com)

© Springer-Verlag Berlin Heidelberg 2007

The use of general descriptive names, registered names, trademarks, etc. in this publication does not imply, even in the absence of a specific statement, that such names are exempt from the relevant protective laws and regulations and therefore free for general use.

Typesetting: Digital data supplied by authors  
Production: LE-TeX Jelonek, Schmidt & Vöckler GbR, Leipzig  
Cover production: Manfred Bender, WMX Design GmbH, Heidelberg  
SPIN 11555100 Printed on acid-free paper 57/3100/YL - 5 4 3 2 1 0

This book is dedicated to my teacher and friend  
Professor Marija I. Petrashen

---

## Preface

Nobel Prize Winner Prof. Roald Hoffmann forwarding a recently published book by Dronskowski [1] on computational chemistry of solid-state materials wrote that one is unlikely to understand new materials with novel properties if one is wearing purely chemical or physical blinkers. He prefers a coupled approach – a chemical understanding of bonding merged with a deep physical description. The quantum chemistry of solids can be considered as a realization of such a coupled approach.

It is traditional for quantum theory of molecular systems (molecular quantum chemistry) to describe the properties of a many-atom system on the grounds of interatomic interactions applying the linear combination of atomic orbitals (LCAO) approximation in the electronic-structure calculations. The basis of the theory of the electronic structure of solids is the periodicity of the crystalline potential and Bloch-type one-electron states, in the majority of cases approximated by a linear combination of plane waves (LCPW). In a quantum chemistry of solids the LCAO approach is extended to periodic systems and modified in such a way that the periodicity of the potential is correctly taken into account, but the language traditional for chemistry is used when the interatomic interaction is analyzed to explain the properties of the crystalline solids. At first, the quantum chemistry of solids was considered simply as the energy-band theory [2] or the theory of the chemical bond in tetrahedral semiconductors [3]. From the beginning of the 1970s the use of powerful computer codes has become a common practice in molecular quantum chemistry to predict many properties of molecules in the first-principles LCAO calculations. In the condensed-matter studies the accurate description of the system at an atomic scale was much less advanced [4].

During the last 10 years this gap between molecular quantum chemistry and the theory of the crystalline electronic structure has become smaller. The concepts of standard solid-state theory are now compatible with an atomic-scale description of crystals. There are now a number of general-purpose computer codes allowing prediction from the first-principles LCAO calculations of the properties of crystals. These codes are listed in Appendix C. Nowadays, the quantum chemistry of solids can be considered as the original field of solid-state theory that uses the methods of molecular quantum chemistry and molecular models to describe the different properties of solid materials including surface and point-defect modeling.

## VIII Preface

In this book we have made an attempt to describe the basic theory and practical methods of modern quantum chemistry of solids.

This book would not have appeared without the help of Prof. M. Cardona who supported the idea of its writing and gave me useful advice.

I am grateful to Prof. C. Pisani and members of the Torino group of Theoretical Chemistry, Prof. R. Dovesi, Prof. C. Roetti, for many years of fruitful cooperation. Being a physicist-theoretician by education, I would never have correctly estimated of the role of quantum chemistry approaches to the solids without this cooperation. I am grateful to all my colleagues who took part in our common research (Prof. V. Smirnov, Prof. K. Jug, Prof. T. Bredow, Prof. J. Maier, Prof. E. Kotomin, Prof. Ju. Zhukovskii, Prof. J. Choisnet, Prof. G. Borstel, Prof. F. Illas, Dr. A. Dobrotvorsky, Dr. V. Lovchikov, Dr. V. Veryazov, Dr. I. Tupitsyn, Dr. A. Panin, Dr. A. Bandura, Dr. D. Usvyat, Dr. D. Gryaznov, V. Alexandrov) or sent me the recent results of their research ( Prof. C. Pisani, Prof. R. Dovesi, Prof. C. Roetti, Prof. P. Deak, Prof. P. Fulde, Prof. G. Stoll, Prof. M. Schütz, Prof. A. Schluger, Prof. L. Kantorovich, Prof. C. Minot, Prof. G. Scuseria, Prof. R. Dronskowski, Prof. A. Titov). I am grateful to Prof. I. Abarenkov, head of the Prof. M.I. Petrashen named seminar for helpful discussions and friendly support. I would like to express my thanks to the members of the Quantum Chemistry Department of St. Petersburg State University, Dr. A. Panin and Dr. A. Bandura, for help in preparing the manuscript – without their help this book would not be here.

I am especially indebted to Dr. C. Ascheron, Mrs. A. Lahee and Dr. P. Capper of Springer-Verlag for encouragement and cooperation.

St. Petersburg,

*Robert Evarestov*

August, 2006

---

# Contents

---

## Part I Theory

---

<b>1</b>	<b>Introduction</b>	<b>3</b>
<b>2</b>	<b>Space Groups and Crystalline Structures</b>	<b>7</b>
2.1	Translation and Point Symmetry of Crystals	7
2.1.1	Symmetry of Molecules and Crystals: Similarities and Differences	7
2.1.2	Translation Symmetry of Crystals. Point Symmetry of Bravais Lattices. Crystal Class	11
2.2	Space Groups	16
2.2.1	Space Groups of Bravais Lattices. Symmorphic and Nonsymmorphic Space Groups	16
2.2.2	Three-periodic Space Groups	18
2.2.3	Site Symmetry in Crystals. Wyckoff Positions	22
2.3	Crystalline Structures	26
2.3.1	Crystal-structure Types. Structure Information for Computer Codes	26
2.3.2	Cubic Structures: Diamond, Rocksalt, Fluorite, Zincblende, Cesium Chloride, Cubic Perovskite	28
2.3.3	Tetragonal Structures: Rutile, Anatase and $\text{La}_2\text{CuO}_4$	34
2.3.4	Orthorhombic Structures: $\text{LaMnO}_3$ and $\text{YBa}_2\text{Cu}_3\text{O}_7$	37
2.3.5	Hexagonal and Trigonal Structures: Graphite, Wurtzite, Corundum and $\text{ScMnO}_3$	42
<b>3</b>	<b>Symmetry and Localization of Crystalline Orbitals</b>	<b>47</b>
3.1	Translation and Space Symmetry of Crystalline Orbitals. Bloch Functions	47
3.1.1	Symmetry of Molecular and Crystalline Orbitals	47
3.1.2	Irreducible Representations of Translation Group. Brillouin Zone	51
3.1.3	Stars of Wavevectors. Little Groups. Full Representations of Space Groups	58

3.1.4	Small Representations of a Little Group. Projective Representations of Point Groups . . . . .	61
3.2	Site Symmetry and Induced Representations of Space Groups . . . . .	66
3.2.1	Induced Representations of Point Groups. Localized Molecular Orbitals . . . . .	66
3.2.2	Induced Representations of Space Groups in $\mathbf{q}$ -basis . . . . .	71
3.2.3	Induced Representations of Space Groups in $\mathbf{k}$ -basis. Band Representations . . . . .	73
3.2.4	Simple and Composite Induced Representations . . . . .	76
3.2.5	Simple Induced Representations for Cubic Space Groups $O_h^1$ , $O_h^5$ and $O_h^7$ . . . . .	78
3.2.6	Symmetry of Atomic and Crystalline Orbitals in $\text{MgO}$ , $\text{Si}$ and $\text{SrZrO}_3$ Crystals . . . . .	83
3.3	Symmetry of Localized Crystalline Orbitals. Wannier Functions . . . . .	86
3.3.1	Symmetry of Localized Orbitals and Band Representations of Space Groups . . . . .	86
3.3.2	Localization Criteria in Wannier-function Generation . . . . .	90
3.3.3	Localized Orbitals for Valence Bands: LCAO approximation . . . . .	94
3.3.4	Variational Method of Localized Wannier-function Generation on the Base of Bloch Functions . . . . .	96
<b>4</b>	<b>Hartree–Fock LCAO Method for Periodic Systems . . . . .</b>	<b>105</b>
4.1	One-electron Approximation for Crystals . . . . .	105
4.1.1	One-electron and One-determinant Approximations for Molecules and Crystals . . . . .	105
4.1.2	Symmetry of the One-electron Approximation Hamiltonian . . . . .	109
4.1.3	Restricted and Unrestricted Hartree–Fock LCAO Methods for Molecules . . . . .	111
4.1.4	Specific Features of the Hartree–Fock Method for a Cyclic Model of a Crystal . . . . .	116
4.1.5	Restricted Hartree–Fock LCAO Method for Crystals . . . . .	119
4.1.6	Unrestricted and Restricted Open-shell Hartree–Fock Methods for Crystals . . . . .	122
4.2	Special Points of Brillouin Zone . . . . .	124
4.2.1	Supercells of Three-dimensional Bravais Lattices . . . . .	124
4.2.2	Special Points of Brillouin-zone Generating . . . . .	125
4.2.3	Modification of the Monkhorst–Pack Special-points Meshes . . . . .	128
4.3	Density Matrix of Crystals in the Hartree–Fock Method . . . . .	132
4.3.1	Properties of the One-electron Density Matrix of a Crystal . . . . .	132
4.3.2	The One-electron Density Matrix of the Crystal in the LCAO Approximation . . . . .	137
4.3.3	Interpolation Procedure for Constructing an Approximate Density Matrix for Periodic Systems . . . . .	140
<b>5</b>	<b>Electron Correlations in Molecules and Crystals . . . . .</b>	<b>147</b>
5.1	Electron Correlations in Molecules: Post-Hartree–Fock Methods . . . . .	147
5.1.1	What is the Electron Correlation ? . . . . .	147

5.1.2	Configuration Interaction and Multi-configuration Self-consistent Field Methods .....	150
5.1.3	Coupled-cluster Methods .....	154
5.1.4	Many-electron Perturbation Theory .....	155
5.1.5	Local Electron-correlation Methods .....	158
5.2	Incremental Scheme for Local Correlation in Periodic Systems .....	163
5.2.1	Weak and Strong Electron-correlation .....	163
5.2.2	Method of Increments: Ground State .....	166
5.2.3	Method of Increments: Valence-band Structure and Bandgap .....	169
5.3	Atomic Orbital Laplace-transformed MP2 Theory for Periodic Systems .....	174
5.3.1	Laplace MP2 for Periodic Systems: Unit-cell Correlation Energy .....	174
5.3.2	Laplace MP2 for Periodic Systems: Bandgap .....	177
5.4	Local MP2 Electron-correlation Method for Nonconducting Crystals .....	180
5.4.1	Local MP2 Equations for Periodic Systems .....	180
5.4.2	Fitted Wannier Functions for Periodic Local Correlation Methods .....	184
5.4.3	Symmetry Exploitation in Local MP2 Method for Periodic Systems .....	188
6	<b>Semiempirical LCAO Methods for Molecules and Periodic Systems .....</b>	193
6.1	Extended Hückel and Mulliken–Rüdenberg Approximations .....	193
6.1.1	Nonself-consistent Extended Hückel–Tight-binding Method .....	193
6.1.2	Iterative Mulliken–Rüdenberg Method for Crystals .....	199
6.2	Zero-differential Overlap Approximations for Molecules and Crystals .....	203
6.2.1	Zero-differential Overlap Approximations for Molecules .....	203
6.2.2	Complete and Intermediate Neglect of Differential Overlap for Crystals .....	208
6.3	Zero-differential overlap Approximation in Cyclic-cluster Model .....	211
6.3.1	Symmetry of Cyclic-cluster Model of Perfect Crystal .....	211
6.3.2	Semiempirical LCAO Methods in Cyclic-cluster Model .....	215
6.3.3	Implementation of the Cyclic-cluster Model in MSINDO and Hartree–Fock LCAO Methods .....	220
7	<b>Kohn–Sham LCAO Method for Periodic Systems .....</b>	231
7.1	Foundations of the Density-functional Theory .....	231
7.1.1	The Basic Formulation of the Density-functional Theory .....	231
7.1.2	The Kohn–Sham Single-particle Equations .....	234
7.1.3	Exchange and Correlation Functionals in the Local Density Approximation .....	237
7.1.4	Beyond the Local Density Approximation .....	240
7.1.5	The Pair Density. Orbital-dependent Exchange-correlation Functionals .....	244

7.2	Density-functional LCAO Methods for Solids . . . . .	249
7.2.1	Implementation of Kohn–Sham LCAO Method in Crystals Calculations . . . . .	249
7.2.2	Linear-scaling DFT LCAO Methods for Solids . . . . .	253
7.2.3	Heyd–Scuseria–Ernzerhof Screened Coulomb Hybrid Functional . . . . .	259
7.2.4	Are Molecular Exchange-correlation Functionals Transferable to Crystals? . . . . .	263
7.2.5	Density-functional Methods for Strongly Correlated Systems: SIC DFT and DFT+U Approaches . . . . .	270

---

## Part II Applications

---

8	<b>Basis Sets and Pseudopotentials in Periodic LCAO Calculations</b> . . . . .	281
8.1	Basis Sets in the Electron-structure Calculations of Crystals . . . . .	281
8.1.1	Plane Waves and Atomic-like Basis Sets. Slater-type Functions	281
8.1.2	Molecular Basis Sets of Gaussian-type Functions . . . . .	285
8.1.3	Molecular Basis Sets Adaptation for Periodic Systems . . . . .	291
8.2	Nonrelativistic Effective Core Potentials and Valence Basis Sets . . . . .	298
8.2.1	Effective Core Potentials: Theoretical Grounds . . . . .	298
8.2.2	Gaussian Form of Effective Core Potentials and Valence Basis Sets in Periodic LCAO Calculations . . . . .	302
8.2.3	Separable Embedding Potential . . . . .	304
8.3	Relativistic Effective Core Potentials and Valence Basis Sets . . . . .	310
8.3.1	Relativistic Electronic Structure Theory: Dirac–Hartree–Fock and Dirac–Kohn–Sham Methods for Molecules . . . . .	310
8.3.2	Relativistic Effective Core Potentials . . . . .	314
8.3.3	One-center Restoration of Electronic Structure in the Core Region . . . . .	316
8.3.4	Basis Sets for Relativistic Calculations of Molecules . . . . .	318
8.3.5	Relativistic LCAO Methods for Periodic Systems . . . . .	320
9	<b>LCAO Calculations of Perfect-crystal Properties</b> . . . . .	327
9.1	Theoretical Analysis of Chemical Bonding in Crystals . . . . .	328
9.1.1	Local Properties of Electronic Structure in LCAO HF and DFT Methods for Crystals and Post-HF Methods for Molecules . . . . .	328
9.1.2	Chemical Bonding in Cyclic-cluster Model: Local Properties of Composite Crystalline Oxides . . . . .	333
9.1.3	Chemical Bonding in Titanium Oxides: Periodic and Molecular-crystalline Approaches . . . . .	342
9.1.4	Wannier-type Atomic Functions and Chemical Bonding in Crystals . . . . .	350
9.1.5	The Localized Wannier Functions for Valence Bands: Chemical Bonding in Crystalline Oxides . . . . .	358

9.1.6	Projection Technique for Population Analysis of Atomic Orbitals. Comparison of Different Methods of the Chemical-bonding Description in Crystals . . . . .	369
9.2	Electron Properties of Crystals in LCAO Methods . . . . .	375
9.2.1	One-electron Properties: Band Structure, Density of States, Electron Momentum Density . . . . .	375
9.2.2	Magnetic Structure of Metal Oxides in LCAO Methods: Magnetic Phases of $\text{LaMnO}_3$ and $\text{ScMnO}_3$ Crystals . . . . .	383
9.3	Total Energy and Related Observables in LCAO Methods for Solids . . . . .	393
9.3.1	Equilibrium Structure and Cohesive Energy . . . . .	393
9.3.2	Bulk Modulus, Elastic Constants and Phase Stability of Solids: LCAO ab-initio Calculations . . . . .	398
9.3.3	Lattice Dynamics and LCAO Calculations of Vibrational Frequencies . . . . .	403
<b>10</b>	<b>Modeling and LCAO Calculations of Point Defects in Crystals . . . . .</b>	<b>409</b>
10.1	Symmetry and Models of Defective Crystals . . . . .	409
10.1.1	Point Defects in Solids and Their Models . . . . .	409
10.1.2	Symmetry of Supercell Model of Defective Crystals . . . . .	413
10.1.3	Supercell and Cyclic-cluster Models of Neutral and Charged Point Defects . . . . .	417
10.1.4	Molecular-cluster Models of Defective Solids . . . . .	421
10.2	Point Defects in Binary Oxides . . . . .	426
10.2.1	Oxygen Interstitials in Magnesium Oxide: Supercell LCAO Calculations . . . . .	426
10.2.2	Neutral and Charged Oxygen Vacancy in $\text{Al}_2\text{O}_3$ Crystal: Supercell and Cyclic-cluster Calculations . . . . .	429
10.2.3	Supercell Modeling of Metal-doped Rutile $\text{TiO}_2$ . . . . .	435
10.3	Point Defects in Perovskites . . . . .	438
10.3.1	Oxygen Vacancy in $\text{SrTiO}_3$ . . . . .	438
10.3.2	Supercell Model of Fe-doped $\text{SrTiO}_3$ . . . . .	445
10.3.3	Modeling of Solid Solutions of $\text{La}_c\text{Sr}_{1-c}\text{MnO}_3$ . . . . .	452
<b>11</b>	<b>Surface Modeling in LCAO Calculations of Metal Oxides . . . . .</b>	<b>459</b>
11.1	Diperiodic Space Groups and Slab Models of Surfaces . . . . .	459
11.1.1	Diperiodic (Layer) Space Groups . . . . .	459
11.1.2	Oxide-surface Types and Stability . . . . .	466
11.1.3	Single- and Periodic-slab Models of $\text{MgO}$ and $\text{TiO}_2$ Surfaces . . . . .	470
11.2	Surface LCAO Calculations on $\text{TiO}_2$ and $\text{SnO}_2$ . . . . .	482
11.2.1	Cluster Models of (110) $\text{TiO}_2$ . . . . .	482
11.2.2	Adsorption of Water on the $\text{TiO}_2$ (Rutile) (110) Surface: Comparison of Periodic LCAO-PW and Embedded-cluster LCAO Calculations . . . . .	487
11.2.3	Single-slab LCAO Calculations of Bare and Hydroxylated $\text{SnO}_2$ Surfaces . . . . .	495
11.3	Slab Models of $\text{SrTiO}_3$ , $\text{SrZrO}_3$ and $\text{LaMnO}_3$ Surfaces . . . . .	507

11.3.1 Hybrid HF-DFT Comparative Study of SrZrO <sub>3</sub> and SrTiO <sub>3</sub> (001) Surface Properties .....	507
11.3.2 F Center on the SrTiO <sub>3</sub> (001) Surface .....	513
11.3.3 Slab Models of LaMnO <sub>3</sub> Surfaces .....	515
<b>A Matrices of the Symmetrical Supercell Transformations of 14 Three-dimensional Bravais Lattices .....</b>	<b>521</b>
<b>B Reciprocal Matrices of the Symmetric Supercell Transformations of the Three Cubic Bravais Lattices .....</b>	<b>525</b>
<b>C Computer Programs for Periodic Calculations in Basis of Localized Orbitals .....</b>	<b>527</b>
<b>References .....</b>	<b>531</b>
<b>Index .....</b>	<b>553</b>

## **Part I**

---

### **Theory**

## Introduction

Prof. P. Fulde wrote in the preface to the first edition of his book [5]: Monographs are required that emphasize the features common to quantum chemistry and solid-state physics. The book by Fulde presented the problem of electron correlations in molecules and solids in a unified form. The common feature of these fields is also the use of the LCAO (linear combination of atomic orbitals) approximation: being from the very beginning the fundamental principle of molecular quantum chemistry LCAO only recently became the basis of the first-principles calculations for periodic systems. The LCAO methods allow one to use wavefunction-based (Hartree–Fock), density-based (DFT) and hybrid Hamiltonians for electronic- structure calculations of crystals. Compared to the conventional plane-waves (PW) or muffin-tin orbitals (MTO) approximations the LCAO approach has proven to be more flexible. To analyze the local properties of the electronic structure the LCAO treatment may be applied to both periodic- and molecular-cluster (nonperiodic) models of solid. Furthermore, post-Hartree–Fock methods can be extended to periodic systems exhibiting electron correlation. LCAO methods are able to avoid an artificial periodicity typically introduced in PW or MTO for a slab model of crystalline surfaces. The LCAO approach is a natural way to extend to solid-state procedures of the chemical bonding analysis developed for molecules. With recent advances in computing power LCAO first-principles calculations are possible for systems containing many (hundreds) atoms per unit cell. The LCAO results are comparable with the traditional PW or MTO calculations in terms of accuracy and variety of accessible physical properties. More than 30 years ago, it was well understood that the quantum theory of solids based on LCAO enabled solid-state and surface chemists to follow the theoretically based papers that appeared ( [2]). As an introduction to the theory of the chemical bond in tetrahedral semiconductors the book [3](translation from the Russian edition of 1973) appeared. Later other books [6] and [7] appeared. These books brought together views on crystalline solids held by physicists and chemists. The important step in the computational realization of the LCAO approach to periodic systems was made by scientists from the Theoretical Chemistry Group of Turin University (C. Pisani, R. Dovesi, C. Roetti) and the Daresbury Computation Science Department in England (N.M. Harrison, V.R. Saunders) with their coworkers from different countries who developed several versions of the CRYSTAL computer code—(88, 92, 95, 98, 03, 06) for the first- principles LCAO calculations of periodic systems. This code is now

used by more than 200 scientific groups all over the world. Many results applying the above code can be found in the book published about ten years ago by Springer: [4]. The publication includes review articles on the Hartree–Fock LCAO approach for application to solids written by scientists actively working in this field. The book by Fulde mentioned earlier takes the next step to bridge the gap between quantum chemistry and solid-state theory by addressing the problem of electron correlations. During the next ten years many new LCAO applications were developed for crystals, including the hybrid Hartree–Fock–DFT method, full usage of the point and translational symmetry of periodic system, new structure optimization procedures, applications to research related to optical and magnetic properties, study of point defects and surface phenomena, generation of the localized orbitals in crystals with application to the correlation effects study. Also, LCAO allowed the development of  $O(N)$  methods that are efficient for large-size many-atom periodic systems. Recently published books including [8–11] may be considered as the high-quality modern text books. The texts provide the necessary background for the existing approaches used in the electronic-structure calculations of solids for students and researchers. Published in the Springer Series in Solid State Sciences (vol. 129) a monograph [12] introduces all the existing theoretical techniques in materials research (which is confirmed by the subtitle of this book: *From Ab initio to Monte Carlo Methods*). This book is written primarily for materials scientists and offers to materials scientists access to a whole variety of existing approaches. However, to our best knowledge a comprehensive account of the main features and possibilities of LCAO methods for the first-principles calculations of crystals is still lacking. We intend to fill this gap and suggest a book reflecting the state of the art of LCAO methods with applications to the electronic-structure theory of periodic systems. Our book is written not only for the solid-state and surface physicists, but also for solid-state chemists and material scientists. Also, we hope that graduate students (both physicists and chemists) will be able to use it as an introduction to the symmetry of solids and for comparison of LCAO methods for solids and molecules. All readers will find the description of models used for perfect and defective solids (the molecular-cluster, cyclic-cluster and supercell models, models of the single and repeating slabs for surfaces, the local properties of the electronic-structure calculations in the theory of the chemical bonding in crystals). We hope that the given examples of the first-principles LCAO calculations of different solid-state properties will illustrate the efficiency of LCAO methods and will be useful for researchers in their own work. This book consists of two parts: theory and applications. In the first part (theory) we give the basic theory underlying the LCAO methods applied to periodic systems. The translation symmetry of solids and its consequence is discussed in connection with a so-called cyclic (with periodical boundary conditions) model of an infinite crystal. For chemists it allows clarification of why the  $\mathbf{k}$ -space introduction is necessary in the electronic-structure calculations of solids. The site-symmetry approach is considered briefly (it is given in more detail in [13]). The analysis of site symmetry in crystals is important for understanding the connection between one-particle states (electron and phonon) in free atoms and in a periodic solid. To make easier the practical LCAO calculations for specific crystalline structures we explain how to use the data provided on the Internet sites for crystal structures of inorganic crystals and irreducible representations of space groups. In the next chapters of Part I we give the basics of Hartree–Fock and Kohn–Sham methods

for crystals in the LCAO representation of crystalline orbitals. It allows the main differences between the LCAO approach realization for molecules and periodic systems to be seen. The hybrid Hartree–Fock–DFT methods were only recently extended from molecules to solids, and their advantages are demonstrated by the LCAO results on bandgap and atomic structure for crystals.

In the second part (applications) we discuss some recent applications of LCAO methods to calculations of various crystalline properties. We consider, as is traditional for such books the results of some recent band-structure calculations and also the ways of local properties of electronic- structure description with the use of LCAO or Wannier-type orbitals. This approach allows chemical bonds in periodic systems to be analyzed, using the well-known concepts developed for molecules (atomic charge, bond order, atomic covalency and total valency). The analysis of models used in LCAO calculations for crystals with point defects and surfaces and illustrations of their applications for actual systems demonstrate the efficiency of LCAO approach in the solid-state theory. A brief discussion about the existing LCAO computer codes is given in Appendix C.

## Space Groups and Crystalline Structures

### 2.1 Translation and Point Symmetry of Crystals

#### 2.1.1 Symmetry of Molecules and Crystals: Similarities and Differences

Molecules consist of positively charged nuclei and negatively charged electrons moving around them. If the translations and rotations of a molecule as a whole are excluded, then the motion of the nuclei, except for some special cases, consists of small vibrations about their equilibrium positions. Orthogonal operations (rotations through symmetry axes, reflections in symmetry planes and their combinations) that transform the equilibrium configuration of the nuclei of a molecule into itself are called the symmetry operations of the molecule. They form a group  $F$  of molecular symmetry. Molecules represent systems from finite (sometimes very large) numbers of atoms, and their symmetry is described by so-called point groups of symmetry. In a molecule it is always possible to so choose the origin of coordinates that it remains fixed under all operations of symmetry. All the symmetry elements (axes, planes, inversion center) are supposed to intersect in the origin chosen. The point symmetry of a molecule is defined by the symmetry of an arrangement of atoms forming it but the origin of coordinates chosen is not necessarily occupied by an atom.

In modern computer codes for quantum-chemical calculations of molecules the point group of symmetry is found automatically when the atomic coordinates are given. In this case, the point group of symmetry is only used for the classification of electronic states of a molecule, particularly for knowledge of the degeneracy of the one-electron energy levels. To make this classification one needs to use tables of irreducible representations of point groups. The latter are given both in books [13–15] and on an Internet site [16]. Calculation of the electronic structure of a crystal (for which a macroscopic sample contains  $10^{23}$  atoms) is practically impossible without the knowledge of at least the translation symmetry group. The latter allows the smallest possible set of atoms included in the so-called primitive unit cell to be considered. However, the classification of the crystalline electron and phonon states requires knowledge of the full symmetry group of a crystal (space group). The structure of the irreducible representations of the space groups is essentially more complicated and use of existing tables [17] or the site [16] requires knowledge of at least the basics of space-group theory.

Discussions of the symmetry of molecules and crystals are often limited to the indication that under operations of symmetry the configuration of the nuclei is transformed to itself. The symmetry group is known when the coordinates of all atoms in a molecule are given. Certainly, the symmetry of a system is defined by a geometrical arrangement of atomic nuclei, but operations of symmetry translate all equivalent points of space to each other. In equivalent points the properties of a molecule or a crystal (electrostatic potential, electronic density, etc.) are all identical. It is necessary to remember that the application of symmetry transformations means splitting all space into systems of equivalent points irrespective of whether there are atoms in these points or not. In both molecules and in crystals the symmetry group is the set of transformations in three dimensional space that transforms any point of the space into an equivalent point. The systems of equivalent points are called orbits of points (This has nothing to do with the orbitals – the one-electron functions in many-electron systems). In particular, the orbits of equivalent atoms in a molecule can be defined as follows. Atoms in a molecule occupy the positions  $\mathbf{q}$  with a certain site symmetry described by some subgroups  $F_{\mathbf{q}}$  of the full point symmetry group  $F$  of a molecule. The central atom (if one exists) has a site-symmetry group  $F_{\mathbf{q}} = F$ . Any atom on the principal symmetry axis of a molecule with the symmetry groups  $C_n$ ,  $C_{nv}$ ,  $S_n$  also has the full symmetry of the molecule ( $F_{\mathbf{q}} = F$ ). Finally,  $F_{\mathbf{q}} = F$  for any atom lying in the symmetry plane of a molecule with the symmetry group  $F = C_s$ . In other cases  $F_{\mathbf{q}}$  is a subgroup of  $F$  and includes those elements  $R$  of point group  $F$  that satisfy the condition  $R\mathbf{q} = \mathbf{q}$ . Let  $F_1$  be a site-symmetry group of a point  $\mathbf{q}_1$  in the molecular space. This point may not be occupied by an atom. Let the symmetry group of a molecule be decomposed into left cosets with respect to its site-symmetry subgroup  $F_{\mathbf{q}}$ :

$$F = \sum_j R_j F_1, \quad R_1 = E, \quad j=1,2,\dots,t \quad (2.1)$$

The set of points  $\mathbf{q}_j = R_j \mathbf{q}_1$ ,  $j=1,2,\dots,t$ , forms an orbit of the point  $\mathbf{q}_1$ .

The point  $\mathbf{q}_j$  of the orbit has a site-symmetry group  $F_j = R_j F R_j^{-1}$  isomorphic to  $F_1$ . Thus, an orbit may be characterized by a site group  $F_1$ , (or any other from the set of groups  $F_j$ ). The number of points in an orbit is equal to the index  $t = n_F / n_{F_j}$  of the group  $F_j$  in  $F$ .

If the elements  $R_j$  in (2.1) form a group  $P$  then the group  $F$  may be factorized in the form  $F = P F_j$ . The group  $P$  is called the permutation symmetry group of an orbit with a site-symmetry group  $F_j$  (or orbital group).

In a molecule, all points of an orbit may be either occupied by atoms of the same chemical element or vacant. Only the groups  $C_n$ ,  $C_{nv}$ ,  $C_s$  may be site-symmetry groups in molecules. A molecule with a symmetry group  $F$  may have  $F$  as a site-symmetry group only for one point of the space (for the central atom, for example). For any point-symmetry group a list of possible orbits (and corresponding site groups) can be given. In this list some groups may be repeated more than once. This occurs if in  $F$  there are several isomorphic site-symmetry subgroups differing from each other by the principal symmetry axes  $C_n$ , two-fold rotation axes  $U$  perpendicular to the principal symmetry axis or reflection planes. All the atoms in a molecule may be partitioned into orbits.

Example. The list of orbits in the group  $F = C_{4v}$  is

$$F_q = C_{4v}(1), C_s(4), C_1(8) \quad (2.2)$$

The number of atoms in an orbit is given in brackets. For example, in a molecule  $XY_4Z$  (see Fig. 2.1) the atoms are distributed over three orbits: atoms X and Z occupy

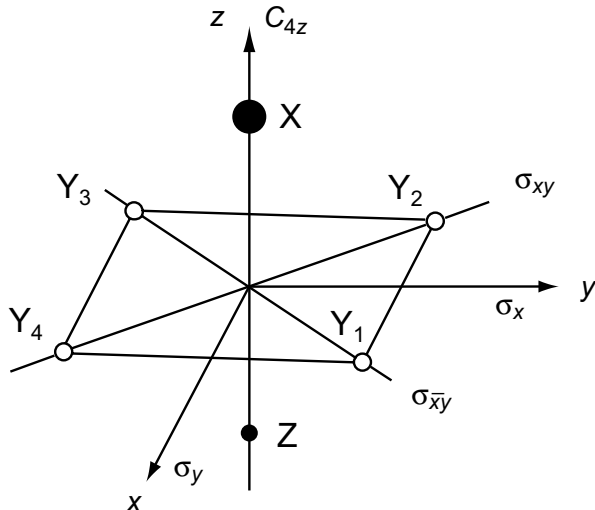


Fig. 2.1. Tetrahedral molecule  $XY_4Z$

positions on the main axis with site-symmetry  $F=C_{4v}$  and four Y atoms occupy one of the orbits with site-symmetry group  $C_s$ . The symmetry information about this molecule may be given by the following formula:

$$C_{4v}[C_{4v}(X,Z), C_s(Y)] \quad (2.3)$$

which indicates both the full symmetry of the molecule (in front of the brackets) and the distribution of atoms over the orbits. For molecules  $IF_5$  and  $XeF_4O$  (having the same symmetry  $C_{4v}$ ) this formula becomes

$$C_{4v}[C_{4v}(I,F), C_s(F)] \text{ and } C_{4v}[C_{4v}(Xe,O), C_s(F)] \quad (2.4)$$

As we can see, atoms of the same chemical element may occupy different orbits, *i.e.* may be nonequivalent with regard to symmetry.

In crystals, systems of equivalent points (orbits) are called Wyckoff positions. As we shall see, the total number of possible splittings of space of a crystal on systems of equivalent points is finite and for the three-dimensional periodicity case equals 230 (number of space groups of crystals). The various ways of filling of equivalent points by atoms generate a huge (hundreds of thousands) number of real crystalline structures.

As well as molecules, crystals possess point symmetry, *i.e.* equivalent points of space are connected by the point-symmetry transformations. But in a crystal the

number of the point-symmetry elements (the rotation axis or reflection planes) is formally infinite. Therefore, it is impossible to find such a point of space where all the point-symmetry elements intersect. It is connected by the fact that, unlike molecules, in crystals among operations of symmetry there are translations of a group of rather small number of atoms to space. The presence of translation symmetry means the periodicity of the perfect crystals structure: translations of the primitive unit cell reproduce the whole crystal.

In real crystals of macroscopic sizes translation symmetry, strictly speaking, is absent because of the presence of borders. If, however, we consider the so-called bulk properties of a crystal (for example, distribution of electronic density in the volume of the crystal, determining the nature of a chemical bond) the influence of borders can not be taken into account (number of atoms near to the border is small, in comparison with the total number of atoms in a crystal) and we consider a crystal as a boundless system, [13].

In the theory of electronic structure two symmetric models of a boundless crystal are used: or it is supposed that the crystal fills all the space (model of an infinite crystal), or the fragment of a crystal of finite size (for example, in the form of a parallelepiped) with the identified opposite sides is considered. In the second case we say, that the crystal is modeled by a cyclic cluster which translations as a whole are equivalent to zero translation (Born–von Karman Periodic Boundary Conditions – PBC). Between these two models of a boundless crystal there exists a connection: the infinite crystal can be considered as a limit of the sequence of cyclic clusters with increasing volume. In a molecule, the number of electrons is fixed as the number of atoms is fixed. In the cyclic model of a crystal the number of atoms (and thus the number of electrons) depends on the cyclic-cluster size and becomes infinite in the model of an infinite crystal. It makes changes, in comparison with molecules, to a one-electron density matrix of a crystal that now depends on the sizes of the cyclic cluster chosen (see Chap. 4). As a consequence, in calculations of the electronic structure of crystals it is necessary to investigate convergence of results with an increase of the cyclic cluster that models the crystal. For this purpose, the features of the symmetry of the crystal, connected with the presence of translations also are used.

In the theory of electronic structure of crystals, we also use the molecular-cluster model: being based on physical reasons we choose a molecular fragment of a crystal and somehow try to model the influence of the rest of a crystal on the cluster chosen (for example, by means of the potential of point charges or a field of atomic cores). From the point of view of symmetry such a model possesses only the symmetry of point group due to which it becomes impossible to establish a connection of molecular-cluster electronic states with those of a boundless crystal. At the same time, with a reasonable molecular-cluster choice it is possible to describe well enough the local properties of a crystal (for example, the electronic structure of impurity or crystal imperfections). As an advantage of this model it may also be mentioned an opportunity of application to crystals of those methods of the account of electronic correlation that are developed for molecules (see Chap. 5).

The set of operations of symmetry of a crystal forms its group of symmetry  $G$  called a space group of symmetry. Group  $G$  includes both translations, operations from point groups of symmetry, and also the combined operations. The structure of space groups of symmetry of crystals and their irreducible representations is much

more complex than in the case of point groups of symmetry of molecules. Without knowledge of some basic data from the theory of space groups it is impossible even to prepare inputs for computer codes to calculate the electronic structure of a crystal. These data will be briefly stated in the following sections.

### 2.1.2 Translation Symmetry of Crystals. Point Symmetry of Bravais Lattices. Crystal Class

Translation symmetry of a perfect crystal can be defined with the aid of three non-coplanar vectors:  $\mathbf{a}_1, \mathbf{a}_2, \mathbf{a}_3$  basic translation vectors. Translation  $t_{\mathbf{a}}$  through the lattice vector

$$\mathbf{a} = n_1 \mathbf{a}_1 + n_2 \mathbf{a}_2 + n_3 \mathbf{a}_3 \quad (2.5)$$

where  $n_1, n_2, n_3$  are integers, relates the equivalent points  $\mathbf{r}$  and  $\mathbf{r}'$  of the crystal:

$$\mathbf{r}' = \mathbf{r} + \mathbf{a} \quad (2.6)$$

Translations  $t_{\mathbf{a}}$  are elements of the translation group  $T$ . If we draw all the vectors  $\mathbf{a}$  from a given point (the origin), then their endpoints will form the Bravais lattice, or “empty” lattice, corresponding to the given crystal. The endpoints of the vectors in this construction are the lattice points (lattice nodes). Three of the basic translation vectors define the elementary parallelepiped called the primitive unit cell (PUC). The PUC contains lattice points only at the eight corners of the parallelepiped. Each corner belongs to eight PUC, so that by fixing the PUC by one lattice point at the corner we refer the remaining of the corners to the nearest seven PUC’s. We note that the basic translation vectors cannot be chosen uniquely. However, whatever the choice of these vectors, the volume of the PUC is always the same. The PUC defines the smallest volume whose translations form the whole Bravais lattice (direct lattice). Usually, the basic vectors are chosen to be the shortest of all those possible. Atoms of a crystal are not necessarily located in the direct lattice points. In the simplest case when all the crystal is obtained by translations of one atom (such crystals are termed monoatomic, many metals belong to this type) all atoms can be placed in direct lattice points.

As a set of points, the direct lattice possesses not only translation but also point symmetry, *i.e.* lattice points are interchanged when rotations around one of the axes of symmetry, reflections in planes of symmetry and their combinations are applied. All the point-symmetry operations of the Bravais lattice are defined when the origin of the coordinate system is chosen in one of the lattice points. The corresponding PUC can be defined as the reference unit cell (it is obtained by a zeroth translation ( $n_1 = n_2 = n_3 = 0$  in (2.5))). Among point-symmetry operations of a direct lattice it is obligatory to include inversion  $I$  in the origin of coordinates since, together with translation on a vector  $\mathbf{a}$  the group of translations  $T$  also includes translation on a vector  $-\mathbf{a}$ . The identity element of group  $T$  is  $t_0$  – a zeroth translation. Elements  $R$  of point group  $F^0$  transform each lattice vector into a lattice vector:  $R\mathbf{a} = \mathbf{a}'$ . The point group  $F^0$  of symmetry of the direct lattice determines the crystal system (or syngony). There are seven systems (syngonies) of direct lattices. It turns out that not all point groups can be lattice symmetry groups  $F^0$ . The requirement that both  $\mathbf{a}$  and  $R\mathbf{a}$  can simultaneously be lattice vectors restricts the number of possible point groups. Let us now establish these limitations [18].

To establish the rotations of the group  $F^0$ , let us take the basic lattice vectors  $\mathbf{a}_1, \mathbf{a}_2, \mathbf{a}_3$  as the basis unit vectors in the space of the lattice vectors  $\mathbf{a}$ , and write down the matrix  $D(R)$  of the transformation  $R$  in the new basis, in which all the lattice vectors have integer components. If the matrix of the orthogonal transformation  $R$  in this basis is denoted by  $D'(R)$ , then  $D'(R) = U^{-1}D(R)U$ , where  $U$  is a matrix of the transformation from the initial orthonormal basis to the basis  $\mathbf{a}_1, \mathbf{a}_2, \mathbf{a}_3$ . If  $R$  is a rotation (or mirror rotation) through an angle  $\varphi$  the traces of the matrices  $D(R)$  and  $D'(R)$  are equal:

$$\text{Sp}D'(R) = \text{Sp}D(R) = \pm 1 + 2 \cos(\varphi) \quad (2.7)$$

Since, however,  $R$  should transform the lattice vector  $\mathbf{a}$  into the lattice vector  $\mathbf{a}' = R\mathbf{a}$  it follows that all the elements of  $D'(R)$  and hence its trace, must be integers. It follows that  $\cos(\varphi) = \cos(2\pi \frac{m}{n}) = \pm 1, \pm 2, 0$ . Consequently, the group  $F^0$  can contain only two-, three-, four- and sixfold axes. Finally, it can be shown that if the group  $F^0$  contains the subgroup  $C_n$ ,  $n > 2$ , it will also contain the subgroup  $C_{nv}$ . The above three limitations ensure that the point group of the lattice can only be one of the seven point groups:  $S_2, C_{2h}, D_{2h}, D_{3h}, D_{4h}, D_{6h}, O_h$ . This is why there are only seven syngonies: namely, triclinic, monoclinic, orthorhombic, rhombohedral, tetragonal, hexagonal and cubic. It is seen that, unlike molecules, in point groups of symmetry of crystals there is no axis of symmetry of the fifth order (rotations around such axes are incompatible with the presence of translations).

Two Bravais lattices with the same group of point symmetry  $F^0$  fall into one type if they can be transferred to each other by the continuous deformation that is not decreasing the point symmetry of a lattice. In three-dimensional space there are 14 types of direct lattices whose distribution on syngonies is shown in Table 2.1. In addition to the translational subgroup  $T$ , the space group contains other transformations whose form depends on the symmetry of the Bravais lattice and the symmetry of the components of the crystal, *i.e.* on the symmetry of the PUC as the periodically repeating set of particles forming the crystal. This last fact frequently ensures that not all the transformations in the point group  $F^0$  are included in the symmetry group of the crystal. Not all transformations that map the sites on each other need result in a corresponding mapping of the crystal components. It is therefore possible that the point group of a crystal  $F$  (crystal class) will only be a subgroup of a point group of an empty lattice. So the real crystal structure point-symmetry group  $F$  may coincide with the lattice point symmetry group  $F^0$  or be its subgroup. The distribution of crystal classes  $F$  and Bravais lattices on syngonies is given in Table 2.1.

The lattice types are labeled by  $P$  (simple or primitive),  $F$  (face-centered),  $I$  (body-centered) and  $A(B, C)$  (base-centered). Cartesian coordinates of basic translation vectors written in units of Bravais lattice parameters are given in the third column of Table 2.1. It is seen that the lattice parameters (column 4 in Table 2.1) are defined only by syngony, *i.e.* are the same for all types of Bravais lattices with the point symmetry  $F^0$  and all the crystal classes  $F$  of a given syngony.

The point symmetry group of a *triclinic* lattice  $\Gamma_t$  (Fig. 2.2) consists of only inversion in the coordinates origin.

Therefore this lattice is defined by 6 parameters – lengths  $a, b, c$  of basic translation vectors and angles  $\alpha, \beta, \gamma$  between their pairs  $\mathbf{a}_2 - \mathbf{a}_3, \mathbf{a}_1 - \mathbf{a}_3$  and  $\mathbf{a}_1 - \mathbf{a}_2$ , respectively.

In simple  $\Gamma_m$  and base-centered  $\Gamma_m^b$  *monoclinic* lattices one of the vectors (with length  $c$ , for example) is orthogonal to the plane defined by two vectors with length

**Table 2.1.** Distribution of crystal classes  $F$  and Bravais lattices on singonies  $F^0$ 

Syngony $F^0$ : crystal classes $F$ :	Direct lattice types	Basic translation vectors	Bravais lattice param.
Triclinic $S_2$ : $C_1, S_2(C_i)$	$P$	Any noncoplanar	$a, b, c,$ $\alpha, \beta, \gamma$
Monoclinic $C_{2h}$ : $C_s, C_2, C_{2h}$	$P$ $A, B, C$	$(0, -b, 0), (a \sin \gamma, -a \cos \gamma, 0), (0, 0, c)$ $(0, -b, 0), (1/2)(a \sin \gamma, -a \cos \gamma, -c),$ $(1/2)(a \sin \gamma, -a \cos \gamma, c)$	$a, b, c, \gamma$
Orthorhombic $D_{2h}$ : $C_{2v}, D_2, D_{2h}$	$P$ $A, B, C$ $F$ $I$	$(0, -b, 0), (a, 0, 0), (0, 0, c)$ $(1/2)(a, -b, 0), (1/2)(a, b, 0), (0, 0, c)$ $(1/2)(a, 0, c), (1/2)(0, -b, c), (1/2)(a, -b, 0)$ $(1/2)(a, b, c), (1/2)(-a, -b, c), (1/2)(a, -b, -c)$	$a, b, c$
Tetragonal $D_{4h}$ : $S_4, D_{2d}, C_4, C_{4v},$ $C_{4h}, D_4, D_{4h}$	$P$ $I$	$(a, 0, 0), (0, a, 0), (0, 0, c)$ $(l/2)(-a, a, c), (1/2)(a, -a, c), (1/2)(a, a, -c)$	$a, c$
Hexagonal $D_{6h}$ : $C_3, S_6, C_{3v}, C_{3h}, D_3,$ $D_{3d}, D_{3h}, C_6, C_{6h},$ $C_{6v}, D_6, D_{6h}$	$H$	$(a/2, -a/2, 0), (0, a, 0), (0, 0, c)$	$a, c$
Rhombohedral $D_{3d}$ : $C_3, S_6, C_{3v}, D_3, D_{3d}$	$R$	$(a, 0, c), (-a/2, a/2, c), (-a/2, -a/2, c)$	$a, c$
Cubic $O_h$ : $T, T_d, T_h, O, O_h$	$P$ $F$ $I$	$(a, 0, 0), (0, a, 0), (0, 0, a)$ $(1/2)(0, a, a), (1/2)(a, 0, a), (1/2)(a, a, 0)$ $(1/2)(-a, a, a), (1/2)(a, -a, a), (1/2)(a, a, -a)$	$a$

$a$  and  $b$  ( $\gamma$  is the angle between these vectors not equal to 90 or 120 degrees). In lattice  $\Gamma_m^b$  the centered face can be formed by a pair of nonorthogonal lattice vectors. For example, in a  $C$  centered monoclinic lattice the lattice point appears on the face formed by  $\mathbf{a}_1$  and  $\mathbf{a}_2$  basic translation vectors. In the base-centered lattice one can consider so-called conventional unit cell – the parallelepiped, reflecting the monoclinic symmetry of the lattice. For a simple monoclinic lattice  $\Gamma_m$  the conventional and primitive unit cells coincide, for a base-centered monoclinic lattice  $\Gamma_m^b$  the conventional unit cell contains 2 primitive unit cells (see Fig. 2.2).

All the three translation vectors of a simple *orthorhombic* lattice  $\Gamma_o$  are orthogonal to each other, so that the conventional cell coincides with the primitive cell and is defined by three parameters – lengths of the basic translation vectors. For base-centered  $\Gamma_o^b$ , face-centered  $\Gamma_o^f$  and body-centered  $\Gamma_o^v$  lattices the conventional unit cell contains two, four and two primitive cells, respectively (see Fig. 2.2).

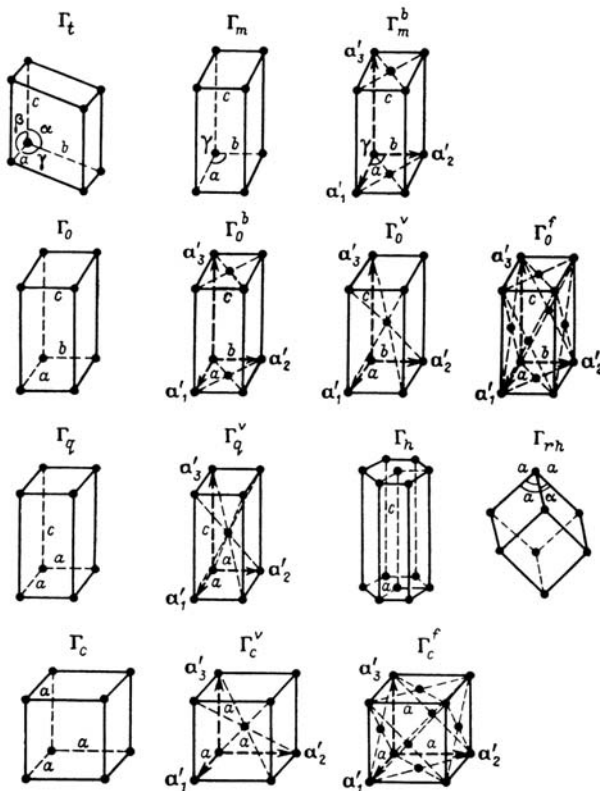


Fig. 2.2. Three-dimensional Bravais lattices

The *tetragonal* lattices  $\Gamma_q$  (simple) and  $\Gamma_q^v$  (body-centered) are defined by two parameters, as two of the three orthogonal translation vectors of a conventional unit cell have the same length  $a$ .

The *hexagonal* lattice is defined by two parameters:  $a$  – length of two equal basic translation vectors (with the angle 120 degree between them) and  $c$  – length of the third basic translation vector orthogonal two the plane of first two vectors.

In a *rhombohedral(triclinic)* lattice all three translation vectors have the same length  $a$ , all three angles  $\alpha$  between them are equal (but differ from 90 degree), so this lattice is defined by two parameters. There are two possibilities to define the rhombohedral lattice parameters. In the first case the parameters  $a$  and  $\gamma$  are given directly. In the second case the lengths  $a$  and  $c$  of the hexagonal unit-cell translation vectors are given: this cell consists of three primitive rhombohedral cells (so-called hexagonal setting for rhombohedral Bravais lattice).

Three *cubic* lattices (simple  $\Gamma_c$ , face-centered  $\Gamma_c^f$  and body-centered  $\Gamma_c^v$ ) are defined by one lattice parameter  $a$  – the length of conventional cubic cell edge (see Table 2.1 and Fig. 2.2).

The unit cell of a crystal is defined as that volume of space that its translations allow all the space without intervals and superpositions to be covered. The PUC is the minimal volume  $V_{\mathbf{a}} = \mathbf{a}_1[\mathbf{a}_2 \times \mathbf{a}_3]$  unit cell connected with one Bravais lattice point. Conventional unit cells are defined by two, four and two lattice points, for the base-, face- and body-centered lattices, respectively.

The 32 point groups, enumerated in Table 2.2, are known as crystallographic point groups and are given in Schönflies (Sch) notation. The Sch notation is used for molecules. In describing crystal symmetry the international notation (or Hermann–Mauguin notation) is also of use. In the latter, the point-group notation is determined from the principal symmetry elements: an  $n$  fold axis is denoted by the symbol  $n$ , a reflection mirror plane by symbol  $m$ . The symbols  $n/m$  and  $nm$  are used for the combinations of an  $n$  fold axis with the reflection plane perpendicular to the axis or containing the axis, respectively. Instead of mirror rotation axes, the international system uses inversion axes  $\bar{n}$  when a rotation through an angle  $2\pi/n$  is followed by the inversion operation. The full international notation of a point group consists of the symbols of group generators. Abbreviated international notations are also used. The Schönflies and international full and abbreviated notations of crystallographic point groups are given in Table 2.2.

**Table 2.2.** Crystallographic point groups: Schönflies and International notations

International			International		
Schoenflies	Full	Abbreviated	Schoenflies	Full	Abbreviated
$C_n$	$n$	$n$	$D_2$	32	32
$C_s(C_{1h})$	$m$	$m$	$D_4$	422	422
$C_i(S_2)$	$I$	$T$	$D_6$	622	622
$S_4$	4	4	$D_{2h}$	$2/m\ 2/m\ 2/m$	mmm
$S_6$	3	3	$D_{3h}$	$6m2$	$6m2$
$C_{2h}$	$2/m$	$2/m$	$D_{4h}$	$4/m\ 2/m\ 2/m$	$4/mmm$
$C_{ih}$	6	6	$D_{6h}$	$6/m\ 2/m\ 2/m$	$6/mmm$
$C_{4h}$	$4/m$	$4/m$	$D_{2d}$	42m	42m
$C_{6h}$	$6/m$	$6/m$	$D_{3d}$	$32/m$	$3m$
$C_{2v}$	$2mm$	$2mm$	$T$	23	23
$C_{3v}$	$3m$	$3m$	$T_h$	$2/m3$	$m3$
$C_{4v}$	$4mm$	$4mm$	$T_d$	43m	43m
$C_{6v}$	$6mm$	$6mm$	$O$	432	432
$D_2$	222	222	$O_h$	$4/m\ 3\ 2/m$	$m3m$

Let us make a linear transformation of PUC translation vectors:

$$\mathbf{A}_j = \sum_{i=1}^3 l_{ji} \mathbf{a}_i, \quad |\det \mathbf{l}| = L \quad (2.8)$$

where the integer coefficients  $l_{ji}$  form the matrix  $\mathbf{l}$ . Vectors  $\mathbf{A}_j$  and their integer linear combinations

$$\mathbf{A}_n = \sum_{j=1}^3 n_j \mathbf{A}_j \quad (2.9)$$

define for  $L > 1$  new, “rare” Bravais lattice for which it is possible to consider various unit cells also. The primitive cell of a new lattice with volume  $V_A = L \times V_a$  will be the so-called large unit cell (supercell), in relation to an initial primitive unit cell. At  $L = 1$  transformation (2.8) means transferring to other vectors of the basic translations, to another under the form, but not on the volume primitive cell (see Fig. 2.3).

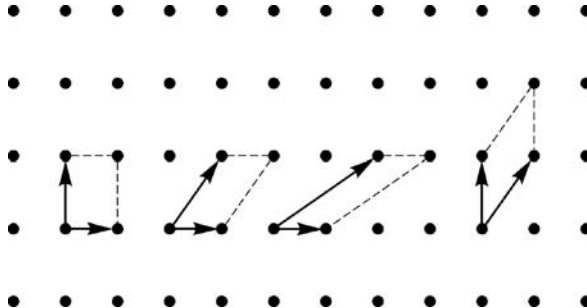


Fig. 2.3. Different primitive unit cell choices

The crystallographic (conventional) unit cell is defined as the minimal volume unit cell in the form of a parallelepiped constructed on vectors of translations and possessing the point symmetry of the lattice. For simple lattices  $P$  of all symmetries, except for hexagonal ( $H$ ), the vectors of the basic translations can be chosen in such a manner that the primitive cell constructed on them is crystallographic. For the centered lattices the crystallographic unit cells consist of 2, 4 and 2 primitive cells for base-, face- and body-centered lattices, respectively (Fig. 2.2). In the description of symmetry of a trigonal crystal both rhombohedral and hexagonal cells are used. The latter is defined by transformation (2.8) with a matrix

$$l = \begin{pmatrix} 2 & 1 & 0 \\ -1 & 1 & 0 \\ 1 & 1 & 1 \end{pmatrix} \quad (2.10)$$

and  $L = 3$ . As  $L = 3$  for this matrix the hexagonal unit cell contains 3 rhombohedral unit cells.

## 2.2 Space Groups

### 2.2.1 Space Groups of Bravais Lattices. Symmorphic and Nonsymmorphic Space Groups

As considered in the previous section Bravais lattices define the group  $T$  of lattice translations. The general symmetry transformation of a Bravais lattice “empty” lat-

tice) can be written in the form  $t_{\mathbf{a}}R$ . Operations  $R$  transform any translation vector  $\mathbf{a}$  to another translation vector  $R\mathbf{a}$  and form point group  $F^0$  (holohedric point group). The combined operation  $t_{\mathbf{a}}R$  transforms the point of space with radius-vector  $\mathbf{r}$  to an equivalent point  $\mathbf{r}' = R\mathbf{r} + \mathbf{a}$ . The identity element of the Bravais lattice symmetry group is  $t_0E$ . The multiplication law for operations  $t_{\mathbf{a}}R$  is:

$$t_{\mathbf{a}_1}R_1t_{\mathbf{a}_2}R_2\mathbf{r} = R_1R_2\mathbf{r} + \mathbf{a}_1 + R_1\mathbf{a}_2 = t_{\mathbf{a}_1+R_1\mathbf{a}_2}R_1R_2\mathbf{r} \quad (2.11)$$

so that

$$(t_{\mathbf{a}}R)^{-1}\mathbf{r} = R^{-1}\mathbf{r} - R^{-1}\mathbf{a} = t_{-R^{-1}\mathbf{a}}R^{-1}\mathbf{r} \quad (2.12)$$

The operations  $t_{\mathbf{a}}$  and  $R$  do not commute. Indeed

$$t_{\mathbf{a}}R\mathbf{r} = R\mathbf{r} + \mathbf{a}; \quad R t_{\mathbf{a}}\mathbf{r} = R(\mathbf{r} + \mathbf{a}) = R\mathbf{r} + t_{R\mathbf{a}}\mathbf{r} = t_{R\mathbf{a}}R\mathbf{r} \quad (2.13)$$

so that

$$t_{\mathbf{a}}R = R t_{R^{-1}\mathbf{a}} \quad (2.14)$$

Operations  $t_{\mathbf{a}}R$  form the space group  $G^0$  of an “empty” Bravais lattice. As lattice translations (also called proper translations)  $t_{\mathbf{a}}$  and point-symmetry operations  $R$  do not commute the space groups  $G^0 = T \wedge F^0$  are a semidirect product of the translation and point groups of lattice symmetry. The point symmetry operations  $R$  form subgroup  $F^0$  of space group  $G^0$  (such space groups are termed *symmorphic* space groups). The group  $T$  of pure translations forms an invariant subgroup of  $G^0$ . As  $t_{\mathbf{a}}^{-1} = t_{-\mathbf{a}}$  we have  $(t_{\mathbf{a}}R)^{-1}t_{\mathbf{a}'}t_{\mathbf{a}}R = (t_{\mathbf{a}}R)^{-1}t_{\mathbf{a}+\mathbf{a}'}R = t_{R\mathbf{a}'}$ .

The group of translations  $T$  is a subgroup of the full group symmetry  $G$  that also contains operations of point group  $F$  and their combinations with translations. Groups of symmetry of crystals are called space groups. The space groups do not necessarily contain translations in three-dimensional space. In two-periodic space groups translations only in a plane appear (such groups are used, for example, in the crystalline surface modeling, see Chap. 11). One-periodic space-group elements include translations only along an axis (for example, symmetry groups of polymers). There is difference between two-periodic and plane groups: in the former, the symmetry operations are transformations in a whole three-dimensional space, in the latter – only in plane (there are known 80 two-periodic groups, and 17 plane groups [19]).

Any symmetry operation  $g$  of a crystal with space group  $G$  can be written in the form of  $g_i = t_{\mathbf{v}_i+\mathbf{a}}R_i$  where  $\mathbf{v}_i$  is the so-called improper (fractional) translation, depending on element  $R_i$  of a point group of a crystal and satisfying the requirements described below. The operation  $g_i$  transforms the point of space with radius-vector  $\mathbf{r}$  to an equivalent point  $\mathbf{r}' = g_i\mathbf{r} = R_i\mathbf{r} + \mathbf{v}_i$ . The operations  $t_{\mathbf{a}}$  are elements of the group of translations  $T$  – translations on the corresponding vector of the Bravais lattice.

In crystals, unlike molecules, together with rotations through axes of symmetry and reflections in planes there exist rotations through screw axes (rotation followed by translation along a rotation axis on a part of a vector of translation) and reflections in planes with partial translation in a plane (such planes are termed glide planes). Translation along a screw axis of symmetry cannot be arbitrary and depends on the order of this axis. Let the order of an axis be equal to  $n$  ( $n$  rotations through axis are equivalent to an identity operation). Thus,  $n$  translations along an axis should

give a vector of translation of a lattice, *i.e.* an element of group  $T$  that forms a subgroup of a space group of a crystal. Otherwise, rotation through a screw axis will not be an operation of symmetry. For example, rotation through an axis of the fourth order can be accompanied by translation along this axis on a quarter or half of the vector of translation. A similar requirement is imposed on the operation of sliding reflection: two sequential reflections in a glide plane should be equivalent to translation on a vector of a lattice. By definition, any symmetry operation  $g$  of a space group transforms any atom of a crystal to equivalent atom. The equivalent atoms are always the atoms of the same chemical identity but the latter can be nonequivalent (see Chap. 3). Therefore, fractional (improper) translations can appear only in those crystals that contain several equivalent atoms in the primitive unit cell. The presence of identical atoms in a primitive cell – a condition necessary, but insufficient for the occurrence of fractional translations in the space-group elements. As an example, we consider in Sect. 2.3 the perovskite  $\text{CaTiO}_3$  structure with three equivalent oxygen atoms in a primitive unit cell and symmorphic space group  $O_h^1$ .

The set of fractional translations  $\mathbf{v}$  in the space-group elements  $g = t_{\mathbf{v}}R$  depends on the choice of origin (with respect to which the space-group elements are written) and on the labeling of axes (choice of setting) [19].

By definition, the symmorphic space groups contain, together with each element  $t_{\mathbf{a}}R$ , the elements  $R$  and  $t_{\mathbf{a}}$  of the point group  $F$  and translation group  $T$ , respectively. This means that for a symmorphic space group the origin of the coordinate system may be chosen in such a way that the local (site) symmetry group of origin coincides with the point group of the crystal  $F$ . This means that all fractional translations  $\mathbf{v}$  are zero. Such a choice of origin is accepted for symmorphic space groups in the International tables [19]. For nonsymmorphic space groups some fractional translations will be nonzero for any choice of origin.

In the next subsection we discuss 73 symmorphic and 157 nonsymmorphic space groups.

### 2.2.2 Three-periodic Space Groups

The full information on space groups is given in the International Tables for Crystallography [19] and presented on a site [16]. The knowledge of general principles of the space-group designations is necessary to use the crystal-structure databases correctly.

Table 2.3 gives the list of 230 three-periodic space groups (two-periodic space groups are considered in Chap. 11). The point-group  $F$  symbols are underlined for the space groups that appear as the first ones in the list of a given crystal class.

The seven holohedric point groups  $F^0$  and all their subgroups form 32 crystallographic point groups (32 crystalline classes). By combining these 32 point groups with the translation groups of 14 Bravais lattices, 73 symmorphic space groups are obtained, including 14 space groups of the symmetry of empty Bravais lattices (see Table 2.3). The remaining 157 space groups include point-symmetry operations with improper (partial) translations, *i.e.* rotations through screw axes and reflections in glide planes.

There are three systems of designations of space groups. First, all groups are numbered from 1 up to 230 in order of increasing point symmetry of the corresponding Bravais lattice (syngonies from triclinic to cubic). For fixed syngony the ordering is

**Table 2.3.** 230 three-periodic space groups

$N_G$	$G$	$IG$	$N_G$	$G$	$IG$	$N_G$	$G$	$IG$
Triclinic:								
1	$C_1^1$	$P\underline{1}$	2	$C_i^1$	$P\bar{1}$			
Monoclinic:								
3	$C_2^1$	$P\underline{2}$	4	$C_2^2$	$P2_1$	5	$C_2^3$	$C2$
6	$C_s^1$	$P\underline{m}$	7	$C_s^2$	$Pc$	8	$C_s^3$	$Cm$
9	$C_s^4$	$Cc$	10	$C_{2h}^1$	$P2/m$	11	$C_{2h}^2$	$P2_1/m$
12	$C_{2h}^3$	$C2/m$	13	$C_{2h}^4$	$P2/c$	14	$C_{2h}^5$	$P2_1/c$
15	$C_{2h}^6$	$C2/c$						
Orthorhombic:								
16	$D_2^1$	$P\underline{222}$	17	$D_2^2$	$P222_1$	18	$D_2^3$	$P2_12_12$
19	$D_2^4$	$P2_12_12_1$	20	$D_2^5$	$C222_1$	21	$D_2^6$	$C222$
22	$D_2^7$	$F222$	23	$D_2^8$	$I222$	24	$D_2^9$	$I2_12_12_1$
25	$C_{2v}^1$	$Pmm2$	26	$C_{2v}^2$	$Pmc2_1$	27	$C_{2v}^3$	$Pcc2$
28	$C_{2v}^4$	$Pma2$	29	$C_{2v}^5$	$Pca2_1$	30	$C_{2v}^6$	$Pnc2$
31	$C_{2v}^7$	$Pmn2_1$	32	$C_{2v}^8$	$Pba2$	33	$C_{2v}^9$	$Pna2_1$
34	$C_{2v}^{10}$	$Pnn2$	35	$C_{2v}^{11}$	$Cmm2$	36	$C_{2v}^{12}$	$Cmc2_1$
37	$C_{2v}^{13}$	$Ccc2$	38	$C_{2v}^{14}$	$Amm2$	39	$C_{2v}^{15}$	$Abm2$
40	$C_{2v}^{16}$	$Ama2$	41	$C_{2v}^{17}$	$Aba2$	42	$C_{2v}^{18}$	$Fmm2$
43	$C_{2v}^{19}$	$Fdd2$	44	$C_{2v}^{20}$	$Imm2$	45	$C_{2v}^{21}$	$Iba2$
46	$C_{2v}^{22}$	$Ima2$	47	$D_{2h}^1$	$Pmmm$	48	$D_{2h}^2$	$Pnnn$
49	$D_{2h}^3$	$Pccm$	50	$D_{2h}^4$	$Pban$	51	$D_{2h}^5$	$Pmma$
52	$D_{2h}^6$	$Pnna$	53	$D_{2h}^7$	$Pmna$	54	$D_{2h}^8$	$Pcca$
55	$D_{2h}^9$	$Pbam$	56	$D_{2h}^{10}$	$Pccn$	57	$D_{2h}^{11}$	$Pbcm$
58	$D_{2h}^{12}$	$Pnnm$	59	$D_{2h}^{13}$	$Pmmn$	60	$D_{2h}^{14}$	$Pbcn$
61	$D_{2h}^{15}$	$Pbca$	62	$D_{2h}^{16}$	$Pnma$	63	$D_{2h}^{17}$	$Cmcm$
64	$D_{2h}^{18}$	$Cmca$	65	$D_{2h}^{19}$	$Cmmm$	66	$D_{2h}^{20}$	$Cccm$
67	$D_{2h}^{21}$	$Cmma$	68	$D_{2h}^{22}$	$Ccca$	69	$D_{2h}^{23}$	$Fmmm$
70	$D_{2h}^{24}$	$Fddd$	71	$D_{2h}^{25}$	$Immm$	72	$D_{2h}^{26}$	$Ibam$
73	$D_{2h}^{27}$	$Ibca$	74	$D_{2h}^{28}$	$Imma$			
Tetragonal:								
75	$C_4^1$	$P\underline{4}$	76	$C_4^2$	$P4_1$	77	$C_4^3$	$P4_2$
78	$C_4^4$	$P4_3$	79	$C_4^5$	$I4$	80	$C_4^6$	$I4_1$
81	$S_4^1$	$P\bar{4}$	82	$S_4^2$	$I\bar{4}$	83	$C_{4h}^1$	$P4/m$
84	$C_{4h}^2$	$P4_2/m$	85	$C_{4h}^3$	$P4/n$	86	$C_{4h}^4$	$P4_2/n$
87	$C_{4h}^5$	$I\bar{4}/m$	88	$C_{4h}^6$	$I4_1/a$	89	$D_4^1$	$P422$
90	$D_4^2$	$P42_12$	91	$D_4^3$	$P4_122$	92	$D_4^4$	$P4_12_12$

to be continued

$N_G$	$G$	$IG$	$N_G$	$G$	$IG$	$N_G$	$G$	$IG$
Tetragonal:								
93	$D_4^5$	$P4_222$	94	$D_4^6$	$P4_22_12$	95	$D_4^7$	$P4_322$
96	$D_4^8$	$P4_32_12$	97	$D_4^9$	$I422$	98	$D_4^{10}$	$I4_122$
99	$C_{4v}^1$	$P4mm$	100	$C_{4v}^2$	$P4bm$	101	$C_{4v}^3$	$P4cm$
102	$C_{4v}^4$	$P4_2nm$	103	$C_{4v}^5$	$P4cc$	104	$C_{4v}^6$	$P4nc$
105	$C_{4v}^7$	$P4_2mc$	106	$C_{4v}^8$	$P4_2bc$	107	$C_{4v}^9$	$I4mm$
108	$C_{4v}^{10}$	$I4cm$	109	$C_{4v}^{11}$	$I4_1md$	110	$C_{4v}^{12}$	$I4_1cd$
111	$D_{2d}^1$	$P\bar{4}2m$	112	$D_{2d}^2$	$P4_2c$	113	$D_{2d}^3$	$P\bar{4}2_1m$
117	$D_{2d}^7$	$P\bar{4}b2$	118	$D_{2d}^8$	$P\bar{4}n2$	119	$D_{2d}^9$	$I\bar{4}m2$
120	$D_{2d}^{10}$	$I\bar{4}c2$	121	$D_{2d}^{11}$	$I\bar{4}2m$	122	$D_{2d}^{12}$	$I\bar{4}2d$
123	$D_{4h}^1$	$P4/mmm$	124	$D_{4h}^2$	$P4/mcc$	125	$D_{4h}^3$	$P4/nbm$
126	$D_{4h}^4$	$P4/nnc$	127	$D_{4h}^5$	$P4/mbm$	128	$D_{4h}^6$	$P4/mnc$
129	$D_{4h}^7$	$P4/nmm$	130	$D_{4h}^8$	$P4/ncc$	131	$D_{4h}^9$	$P4_2/mmc$
132	$D_{4h}^{10}$	$P4_2/mcm$	133	$D_{4h}^{11}$	$P4_2/nbc$	134	$D_{4h}^{12}$	$P4_2/nnm$
135	$D_{4h}^{13}$	$P4_2/mbc$	136	$D_{4h}^{14}$	$P4_2/mnm$	137	$D_{4h}^{15}$	$P4_2/nmc$
138	$D_{4h}^{16}$	$P4_2/ncm$	139	$D_{4h}^{17}$	$I4/mmm$	140	$D_{4h}^{18}$	$I4/mcm$
141	$D_{4h}^{19}$	$I4_1/amd$	142	$D_{4h}^{20}$	$I4_1/acd$			
Rhombohedral:								
143	$C_3^1$	$P\bar{3}$	144	$C_3^2$	$P3_1$	145	$C_3^3$	$P3_2$
146	$C_3^4$	$R3$	147	$C_{3i}^1$	$P\bar{3}$	148	$C_{3i}^2$	$R\bar{3}$
149	$D_3^1$	$P3_12$	150	$D_3^2$	$P321$	151	$D_3^3$	$P3_112$
152	$D_3^4$	$P3_121$	153	$D_3^5$	$P3_212$	154	$D_3^6$	$P3_221$
155	$D_3^7$	$R32$	156	$C_{3v}^1$	$P3m1$	157	$C_{3v}^2$	$P31m$
158	$C_{3v}^3$	$P3c1$	159	$C_{3v}^4$	$P31c$	160	$C_{3v}^5$	$R3m$
161	$C_{3v}^6$	$R3c$	162	$D_{3d}^1$	$P\bar{3}1m$	163	$D_{3d}^2$	$P\bar{3}1c$
164	$D_{3d}^3$	$P\bar{3}m1$	165	$D_{3d}^4$	$P\bar{3}c1$	166	$D_{3d}^5$	$R\bar{3}m$
167	$D_{3d}^6$	$R\bar{3}c$						
Hexagonal:								
168	$C_6^1$	$P\bar{6}$	169	$C_6^2$	$P6_1$	170	$C_6^3$	$P6_5$
171	$C_6^4$	$P6_2$	172	$C_6^5$	$P6_4$	173	$C_6^6$	$P6_3$
174	$C_{3h}^1$	$P\bar{6}$	175	$C_{6h}^1$	$P6/m$	176	$C_{6h}^2$	$P6_3/m$
177	$D_6^1$	$P662$	178	$D_6^2$	$P6_122$	179	$D_6^3$	$P6_522$
180	$D_6^4$	$P6_222$	181	$D_6^5$	$P6_422$	182	$D_6^6$	$P6_322$
183	$C_{6v}^1$	$P6mm$	184	$C_{6v}^2$	$P6cc$	185	$C_{6v}^3$	$P6_3cm$
186	$C_{6v}^4$	$P6_3mc$	187	$D_{3h}^1$	$P\bar{6}m2$	188	$D_{3h}^2$	$P\bar{6}c2$
189	$D_{3h}^3$	$P\bar{6}2m$	190	$D_{3h}^4$	$P\bar{6}2c$	191	$D_{6h}^1$	$P6/mmm$
192	$D_{6h}^2$	$P6/mcc$	193	$D_{6h}^3$	$P6_3/mcm$	194	$D_{6h}^4$	$P6_3/mmc$

to be continued

$N_G$	$G$	$IG$	$N_G$	$G$	$IG$	$N_G$	$G$	$IG$
Cubic:								
195	$T^1$	<u><math>P23</math></u>	196	$T^2$	$F23$	197	$T^3$	$I23$
198	$T^4$	$P2_13$	199	$T^5$	$I2_13$	200	$T_h^1$	$Pm\bar{3}$
201	$T_h^2$	$Pn\bar{3}$	202	$T_h^3$	$Fm\bar{3}$	203	$T_h^4$	$Fd\bar{3}$
204	$T_h^5$	$Im\bar{3}$	205	$T_h^6$	$Pa\bar{3}$	206	$T_h^7$	$Ia\bar{3}$
207	$O^1$	<u><math>P432</math></u>	208	$O^2$	$P4_232$	209	$O^3$	$F432$
210	$O^4$	$F4_132$	211	$O^5$	$I432$	212	$O^6$	$P4_332$
213	$O^7$	$P4_132$	214	$O^8$	$I4_132$	215	$T_d^1$	<u><math>P\bar{4}3m</math></u>
216	$T_d^2$	$F\bar{4}3m$	217	$T_d^3$	$I\bar{4}3m$	218	$T_d^4$	<u><math>P\bar{4}3n</math></u>
219	$T_d^5$	$F\bar{4}3c$	220	$T_d^6$	$I\bar{4}3d$	221	$O_h^1$	<u><math>Pm\bar{3}m</math></u>
222	$O_h^2$	$Pn\bar{3}n$	223	$O_h^3$	$Pm\bar{3}n$	224	$O_h^4$	$Pn\bar{3}m$
225	$O_h^5$	$Fm\bar{3}m$	226	$O_h^6$	$Fm\bar{3}c$	227	$O_h^7$	$Fd\bar{3}m$
228	$O_h^8$	$Fd\bar{3}c$	229	$O_h^9$	$Im\bar{3}m$	230	$O_h^{10}$	$Ia\bar{3}d$

made over Bravais lattice types and for the fixed Bravais lattice type – over crystal classes (point group  $F$ ) beginning from the symmorphic space group. In this list, the space groups of “empty” lattices appear as the first ones for fixed type of the lattice. Secondly, the more informative Schönflies symbol is used for space groups. This contains the Schönflies symbol of point group  $F$  of a crystal class and the upper numerical index distinguishing space groups within the limits of one crystal class.

Thirdly, the most detailed information on a space group is contained in so-called international designations. In these is there both a symbol of the Bravais lattice type, and a symbol of a crystal class with the indication of the elements of symmetry (axes and planes). For a designation of types of Bravais lattices the following symbols (see Table 2.3) are used:  $P$  simple (or primitive);  $A$ ,  $B$ ,  $C$  – one face (base-) centered;  $F$  – face-centered;  $I$  – body-centered. For hexagonal and trigonal (rhombohedral) lattices symbols  $H$  and  $R$  are accepted. The letter is followed by a set of characters indicating the symmetry elements. These sets are organized in the following way.

There exist only two triclinic space groups (1, 2) with symbols  $P1$  (no point-symmetry operations) and  $P\bar{1}$  (the inversion operation appears, this is the symmetry group of triclinic Bravais lattice). For monoclinic space groups (3 – 15) one symbol is needed that gives the nature of the twofold axis (rotation axis 2 or screw axis  $2_1$ ) or reflection plane (mirror plane  $m$  or glide plane  $c$ ). Two settings are used for monoclinic space groups:  $y$ -axis unique, or, used in Table 2.3,  $z$ -axis unique. Primitive and base-centered ( $z$ -axis unique) monoclinic Bravais lattices symmetry groups are  $P2/m$  (10) and  $C2/m$  (11), respectively.

The symbols of orthorhombic space groups (16 – 74) contain the three sets. For symmorphic groups as a symbol of a crystal class the international designation of point groups corresponding to it serves. In Table 2.3 conformity of Schönflies’s symbols (applied for molecules) and international symbols for point groups of symmetry of crystals is given. For example,  $N225$ ,  $O_h^5$  and  $Fm\bar{3}m$  – three symbols of the same space groups of symmetry of a crystal with NaCl structure.

For nonsymmorphic groups in a symbol of the point group it is underlined also, which axes are screw and which planes are planes of the sliding reflections. For example, for the group of symmetry of rutile structure it is possible to use designations  $N136$ ,  $D_{4h}^{14}$  or  $P4_2/mnm$ , where the symbol  $4_2$  means that an axis of the fourth order is a screw axis, with translation on half a period along this axis on rotation by angle  $\pi/2$ , and a symbol  $n$  means that two of the four vertical planes are planes of sliding reflection. A more detailed explanation of the principles of international designations can be found in [19]. In Table 2.3 are given the list of 230 space groups with the indication of all three mentioned designations for each of them.

### 2.2.3 Site Symmetry in Crystals. Wyckoff Positions

To characterize a space group  $G$  an analytical description may be employed, which states for a space group the coordinates of all points that are equivalent to a chosen point  $\mathbf{q}$  with coordinates  $(xyz)$ . An analytical description of all 230 space groups is given in the International Tables for Crystallography [19] and is based on the fact that for a given space group  $G$  all points of a three-dimensional space are subdivided into sets of symmetrically equivalent points called crystallographic orbits.

All the points of a given crystallographic orbit may be obtained from one (arbitrary) crystallographic orbit point  $\mathbf{q}$  (generating point) by applying to the latter all the operations of space group  $G$ . Due to the infinite number of translations (in the model of an infinite crystal) there is an infinite number of points in each space group crystallographic orbit. Any one of the crystallographic orbit points may represent the whole crystallographic orbit, *i.e.* may be a generating point  $\mathbf{q}$  of the crystallographic orbit.

All symmetry operations  $t_{\mathbf{v}_i+\mathbf{a}}R_i = (R_i|\mathbf{v}_i + \mathbf{a})$ ,  $i = 1, 2, \dots, n_{\mathbf{q}}$  of a space group  $G$  that satisfy the condition  $t_{\mathbf{v}+\mathbf{a}}R\mathbf{q} = \mathbf{q}$  form a finite site-symmetry group  $G_{\mathbf{q}}$  of  $\mathbf{q}$  with respect to  $G$ . The site-symmetry group  $G_{\mathbf{q}}$  is isomorphic to one of the 32 crystallographic point groups. If the origin of the space group is at the position  $\mathbf{q}$ , the elements of the site-symmetry group  $G_{\mathbf{q}}$  will be of the form  $t_0R$ .

The site-symmetry groups  $G_j$  of different points  $\mathbf{q}_j$  of the same crystallographic orbit are conjugate groups of  $G_1 = G_{\mathbf{q}}$ , *i.e.* the site-symmetry groups  $G_1$  and  $G_j$  of points  $\mathbf{q}_1 = \mathbf{q}$  and  $\mathbf{q}_j$  of the same orbit are related by  $g_jG_1g_j^{-1} = G_j$  ( $g_j \in G$ ,  $g_j \notin G_j$ ,  $g_j\mathbf{q}_1 = \mathbf{q}_j$ ). For a point  $\mathbf{q}$  at a general position the site-symmetry group  $G_{\mathbf{q}}$  consists of only the identity operation  $t_0E = (E|\mathbf{0})$ ; the site-symmetry group of a point at a special position includes at least one other symmetry operation in addition to the identity operation.

An infinite number of crystallographic orbits for a given space group  $G$  can be subdivided into sets of so-called Wyckoff positions of  $G$ . All the crystallographic orbits that have the same (not only isomorphic but the same) site-symmetry group belong to the same Wyckoff position. If the coordinates of the generating point of a crystallographic orbit do not contain free parameters, the corresponding Wyckoff position consists of only one crystallographic orbit; in other cases an infinite number of crystallographic orbits belongs to the same Wyckoff position with variable parameters.

The different Wyckoff positions are labeled by small Roman letters. The maximum number of different Wyckoff positions of a space group is 27 (in the group  $D_{2h}^1 - Pmmm$ ). The various possible sets of Wyckoff positions for all the space

groups are given in the International Tables for Crystallography [19] and reproduced on an Internet site [16]. As an example, Table 2.4 lists those for the space group  $D_{4h}^{14}(P4_2/m2_l/n2/m)$ , the symmetry group of a rutile structure (see Sect. 2.3.3)

**Table 2.4.** Wyckoff Positions of Space Group 136 ( $P4_2/mnm$ ) \*

Multipl.	Wyck. letter	Site symm.	Coordinates
16	k	1	$(x, y, z)(-x, -y, z)(-y + 1/2, x + 1/2, z + 1/2)$ $(y + 1/2, -x + 1/2, z + 1/2)(-x + 1/2, y + 1/2, -z + 1/2)$ $(x + 1/2, -y + 1/2, -z + 1/2)(y, x, -z)(-y, -x, -z)$ $(-x, -y, -z)(x, y, -z)(y + 1/2, -x + 1/2, -z + 1/2)$ $(-y + 1/2, x + 1/2, -z + 1/2)(x + 1/2, -y + 1/2, z + 1/2)$ $(-x + 1/2, y + 1/2, z + 1/2)(-y, -x, z)(y, x, z)$
8	j	..m	$(x, x, z)(-x, -x, z)(-x + 1/2, x + 1/2, z + 1/2)$ $(x + 1/2, -x + 1/2, z + 1/2)(-x + 1/2, x + 1/2, -z + 1/2)$ $(x + 1/2, -x + 1/2, -z + 1/2)(x, x, -z)(-x, -x, -z)$
8	i	m..	$(x, y, 0)(-x, -y, 0)(-y + 1/2, x + 1/2, 1/2)$ $(y + 1/2, -x + 1/2, 1/2)(-x + 1/2, y + 1/2, 1/2)$ $(x + 1/2, -y + 1/2, 1/2)(y, x, 0)(-y, -x, 0)$
8	h	2..	$(0, 1/2, z)(0, 1/2, z + 1/2)(1/2, 0, -z + 1/2)$ $(1/2, 0, -z)(0, 1/2, -z)(0, 1/2, -z + 1/2)$ $(1/2, 0, z + 1/2)(1/2, 0, z)$
4	g	m.2 m	$(x, -x, 0)(-x, x, 0)(x + 1/2, x + 1/2, 1/2)$ $(-x + 1/2, -x + 1/2, 1/2)$
4	f	2.m m	$(x, x, 0)(-x, -x, 0)(-x + 1/2, x + 1/2, 1/2)$ $(x + 1/2, -x + 1/2, 1/2)$
4	e	2.m m	$(0, 0, z)(1/2, 1/2, z + 1/2)(1/2, 1/2, -z + 1/2)$ $(0, 0, -z)$
4	d	$\bar{4}..$	$(0, 1/2, 1/4)(0, 1/2, 3/4)(1/2, 0, 1/4)$ $(1/2, 0, 3/4)$
4	c	2/m..	$(0, 1/2, 0)(0, 1/2, 1/2)(1/2, 0, 1/2)(1/2, 0, 0)$
2	b	m.m m	$(0, 0, 1/2)(1/2, 1/2, 0)$
2	a	m.m m	$(0, 0, 0)(1/2, 1/2, 1/2)$

\*Equivalent sets of Wyckoff positions

(ab)(c)(d)(e)(fg)(h)(i)(j)(k)

For this group there are 11 different Wyckoff positions denoted by letters from a to k. The number of crystallographic orbit points in the primitive unit cell (multiplicity) equals  $n_F/n_q$  where  $n_F = 16$  is the order of the point group  $D_{4h}$  and  $n_q$  is the order of the site symmetry group  $G_q$ . The number of points in a Wyckoff position and their coordinates are given in the International Tables with respect to the conventional unit cell of the lattice (for the space group  $D_{4h}^{14}$  with a simple Bravais lattice, the

conventional unit cell coincides with the primitive unit cell). Use of the Wyckoff general position  $k(xyz)$  points allows one to determine the appropriate Seitz space-group symbols for the coset representatives in the decomposition

$$G = \sum_{i=1}^{n_F} (R_i | \mathbf{v}_i) T = \sum_{i=1}^{n_F} t_{\mathbf{v}_i} R_i T \quad (2.15)$$

of space group  $G$  with respect to the translation group  $T$ . In Table 2.4 these symbols are written under the coordinates of the points obtained from the point  $\mathbf{r}(x, y, z)$  by performing the space-group operation  $t_{\mathbf{v}_i} R_i$ . The orientation of the symmetry elements with respect to the tetragonal lattice translation vectors  $\mathbf{a}_1(a, 0, 0)$ ,  $\mathbf{a}_2(0, a, 0)$  and  $\mathbf{a}_3(0, 0, c)$  is shown in Fig. 2.4. In the point group  $D_{4h}$  there are four rotations around

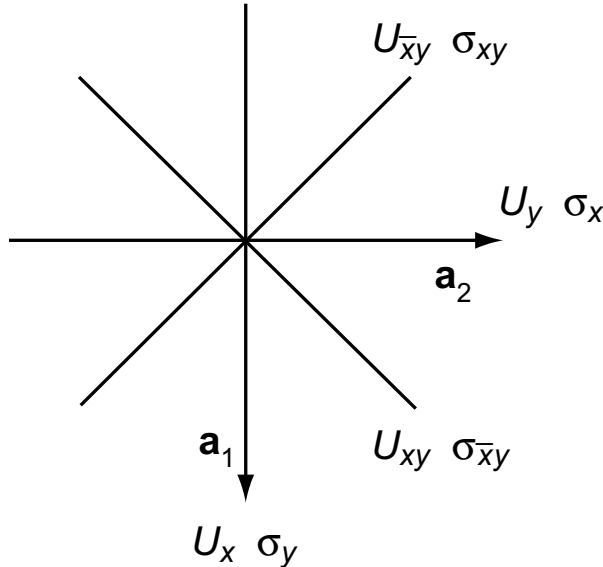


**Fig. 2.4.** Orientation of the symmetry elements with respect to the tetragonal lattice translations

twofold axes ( $U_x$ ,  $U_y$ ,  $U_{xy}$ ,  $U_{\bar{xy}}$ ) and four rotations (including the identity operation) around the main fourfold  $z$ -axis ( $E$ ,  $C_{4z}$ ,  $C_{4z}^2 = C_{2z}$ ,  $C_{4z}^3 = C_{4z}^{-1}$ ).

The remaining 8 symmetry operations are all products of inversion  $I$  with rotations:  $I$ , reflections  $\sigma_x$ ,  $\sigma_y$ ,  $\sigma_{xy}$ ,  $\sigma_{\bar{xy}}$ ,  $\sigma_z$  in the planes perpendicular to the corresponding twofold axes and  $z$ -axis; mirror rotations  $S_{4z}^{-1}$ ,  $S_{4z}$ . It is seen from Table 2.4 that the elements of the point group  $D_{2h}(E, C_{2z}, U_{xy}, U_{\bar{xy}}, I, \sigma_z, \sigma_{xy}, \sigma_{\bar{xy}})$  appear in the cosets decomposition (2.15) without fractional translations. These elements form the site symmetry group of the coordinate system origin placed at the point of Wyckoff position  $a(0, 0, 0)$ . The second point of this position  $(1/2, 1/2, 1/2)$  is obtained from the first one by application of any symmetry operation from these eight

$(C_{4z}, C_{4z}^{-1}, S_{4z}, S_{4z}^{-1}, U_x, U_y, \sigma_x, \sigma_y)$  that come into the coset representatives in (2.15) with fractional translation  $\mathbf{v} = (1/2, 1/2, 1/2)$ . We therefore write the space group  $D_{4h}^{14}$  (for the case when the Wyckoff position a is taken as the origin) as

$$D_{4h}^{14} = \sum_{R \in D_{2h}} \left[ (R|0)\mathbf{T} + (U_x | \frac{1}{2} \frac{1}{2} \frac{1}{2})(R|0)\mathbf{T} \right] \quad (2.16)$$

Considering the full international symbol  $P4_2/m2_1/n2/m$  of the space group  $D_{4h}^{14}$ , we see that the coset representatives in the decomposition of (2.15) with respect to the translation group  $\mathbf{T}$  correspond to this symbol. Indeed, in our example of a tetragonal lattice the three positions in this symbol correspond to the symmetry directions [001]; [100], [010]; and [110], [110], respectively. Rotation through the angle  $\pi/2$  about the  $z$ -axis is followed by translation along this axis by one-half of the translation vector  $\mathbf{a}_3$  as is seen from the symbol for the element  $(C_{4z}|l/2, 1/2, 1/2)$ . The notations  $2_l$  and 2 for twofold  $x$ - and  $xy$ -rotation axes agree with the fourfold symbols for  $(U_x | \frac{1}{2} \frac{1}{2} \frac{1}{2})$  and  $(U_{xy}|000)$ . Finally, the notations m, n, m for the reflection planes perpendicular to the corresponding symmetry directions in the international symbol for the space group agree with the Seitz symbols  $\sigma_z|000$ ,  $(\sigma_x | \frac{1}{2} \frac{1}{2} \frac{1}{2})$ , and  $(\sigma_{xy}|000)$ , respectively. The space group  $D_{4h}^{14}$  may also be described by its six generators: three primitive translations  $t_{\mathbf{a}_i} = (E|\mathbf{a}_i)$  ( $i = 1, 2, 3$ ) of the simple tetragonal lattice and three generating elements  $(C_{4z}|l/2, 1/2, 1/2)$ ,  $(U_x | l/2, 1/2, 1/2)$ ,  $(I|0, 0, 0)$ .

The coordinates of Wyckoff positions a, b, c, d do not contain free parameters (Table 2.4); those of e, f, g, h positions contain one free parameter; the coordinates of the positions  $i$  and  $j$  contain two free parameters. This means that an infinite number of Wyckoff sets e – f exists in the crystal but the sets a, b, c, d consist of only one crystallographic orbit. Pairs of Wyckoff positions a – b, f – g, and i – j have isomorphic site symmetry groups ( $D_{2h}$ ,  $C_{2v}$  and  $C_s$ , respectively). As is seen from the Table pairs of points a – b and f – g not only have isomorphic but also equivalent Wyckoff positions. The equivalent sites have the same point-group symmetry and the same orientations of symmetry elements with respect to the lattice. The equivalent sets of Wyckoff positions for all the space groups can be found on the Internet site [16]. This information will be used in the next section for the description of different crystal lattice structures. This means that if equivalent points are occupied by atoms in the crystal lattice there are possible equivalent descriptions of this structure. For example, rutile  $\text{TiO}_2$  structure with two formula units in the primitive cell can be given in two equivalent descriptions:  $\text{Ti}(2a)\text{O}(4f)$  or  $\text{Ti}(2b)\text{O}(4g)$ . For  $\text{NbOCl}_3$  structure ( $Z = 4$ ) with the same space group two equivalent descriptions can be given:  $\text{Nb}(4f)\text{O}(4g)\text{Cl}(4g)\text{Cl}(8i)$  and  $\text{Nb}(4g)\text{O}(4f)\text{Cl}(4f)\text{Cl}(8i)$ . In this case, the  $\text{Cl}(8i)$  position is the same but  $\text{Cl}(4f)$  and  $\text{Cl}(4g)$  positions interchange.

The difference between oriented site-symmetry groups of different Wyckoff positions is due to different orientations of the elements of the site-symmetry group  $G_q$  with respect to the lattice. The difference arises when similar symmetry elements (reflections in planes and rotations about twofold axes of symmetry) occur in more than one class of elements of the point group F. Only eleven site groups [ $C_2(2)$ ,  $C_s(m)$ ,  $C_{2h}(2/m)$ ,  $C_{2v}(2mm)$ ,  $C_{3v}(3mm)$ ,  $D_2(222)$ ,  $D_3(322)$ ,  $D_{2d}(42m)$ ,  $D_{3d}(32m)$ ,  $D_{2h}(mmm)$ , and  $D_{3A}(62m)$ ] can have different orientations with respect to the Bravais lattice. Oriented site-symmetry symbols show how the symmetry elements at a site are related to the symmetry elements of a space group. The site-symmetry

symbols display the same sequence of symmetry directions as the space-group international symbol. Sets of equivalent symmetry directions that do not contribute any element to the site-symmetry group  $G_q$  are represented by a dot. In our example of the space group  $D_{4h}^{14}$  the site-symmetry groups  $G_a, G_b$  do not contain reflection in the planes  $\sigma_x, \sigma_y$  (the dot is at the second position) and the site group  $G_e = 2.m\bar{m}$  does not contain reflection in the plane  $\sigma_z$  (a dot is at the first position, Table 2.3).

In the next section we consider 15 types of crystal structures belonging to different space groups. As will be seen, the different crystal structures can be considered as one or another means of the distribution of the atoms between the Wyckoff positions of the corresponding space group.

## 2.3 Crystalline Structures

### 2.3.1 Crystal-structure Types. Structure Information for Computer Codes

The *Bravais lattice* is an infinite set of points generated by three nonparallel basic translation vectors, such that each point is identical in itself and its surroundings, see Sect. 2.1.2. With each Bravais lattice point may be associated a number of atoms (so-called basis). If atomic coordinates relative to the lattice point are given, together with the lengths and directions of the lattice vectors chosen to define the axes of reference, the complete structure (crystal lattice) is defined. The Internet page [20] currently contains links to about 300 structures in more than 90 of the 230 space groups. A graphical representation as well as useful information about these crystal lattices can be obtained. Other sources of information can be found at various sites linked with [21]. The crystal-structure type is specified when one states which sets of Wyckoff positions for the corresponding space group are occupied by atoms. To distinguish different structures of the same type one needs the numerical values of lattice parameters and additional data if Wyckoff positions with free parameters in the coordinates are occupied. When describing the crystal-structure type one also gives the value of  $Z$  (the number of formula units in the conventional unit cell). This information is, in principle, not necessary as  $Z$  is defined by the chemical formula of the compound and the multiplicity of Wyckoff positions in the unit cell occupied by atoms. It is also necessary to take into account that the primitive unit cell of any crystal contains half the number of atoms in a body-centered cell, one-quarter the number in a face-centered, and half the number in an  $A, B$ , or  $C$  base-centered cell. Trigonal cells contain one-third the number of atoms in the corresponding hexagonal cell. The Wyckoff-site description of a crystal-structure type is also origin dependent (see Sect. 2.2.3). It was shown that equivalent alternatives often arise if two or more sets of sites are physically equivalent (see Sect. 2.2.3). The crystal lattice structure types can be indexed in different ways [20]. In *Strukturbericht* designation symbols  $A$  and  $B$  are used for monoatomic and diatomic (with equal numbers of atoms of each type) crystal types, symbols  $C$  and  $D$  – for  $AB_2$  and  $A_nB_m$  compounds, respectively. Symbols  $E, F, G, \dots, K$  specify more complex compounds, symbols  $L, O$ , and  $S$  specify alloys, organic compounds and silicates. The *The Pearson symbol* indicates the crystal symmetry and the number of atoms in the conventional unit cell. For example, rocksalt NaCl structure has a face-centered (F) cubic (c) structure with 8

atoms in the cubic (nonprimitive!) unit cell, so it is designated *cF8*. The letters m, o, t, h, c are used in Pearson symbols for monoclinic, orthorhombic, tetragonal, hexagonal, trigonal and cubic Bravais lattice-types, respectively. Pearson symbols do not necessarily specify a unique structure: diamond, NaCl and zincblende *cF8* structures differ by symbols *A*, *B1* and *B3* (numbers in symbols *B1* and *B3* were assigned in roughly the historical order of the study of crystal lattices). The *prototype index* is an index of the various crystal structures by prototype compound (diamond, rocksalt, zincblende structures). Some compounds can be associated with more than one prototype: ZnS compound can be found in zincblende and wurtzite structure. Finally, the *space group index* of a structure can be used. Space groups are listed in the order they appear in the International Tables [19]. As space groups refer to one of seven syngonies the structures are ordered as triclinic (space groups 1 and 2), monoclinic (3–15), orthorhombic (16–74), tetragonal (75–142), trigonal (143–167), hexagonal (168–194) and cubic (195–230). For example, cubic structures correspond to the three Pearson symbols *cPn*, *cFn* and *cIn*. In the next subsections we give short descriptions of 15 types of crystal structures. We use space-group and prototype indexes in subsection titles. In the corresponding tables we give for each structure all the mentioned indexes. These tables show that the same compound can be found in different structures (*C* – diamond, graphite, ZnS – sphalerite, wurtzite, CaTiO<sub>3</sub> – cubic perovskite, distorted (orthorhombic) perovskite, TiO<sub>2</sub> – rutile, anatase). Different structures can have the same Bravais lattice (diamond, NaCl, fluorite, sphalerite) or even the same space group (rocksalt NaCl – fluorite CaF<sub>2</sub>). For any structure type we give the prototype, space group (number and international symbol), number of formula units in the primitive and conventional unit cells, the occupation of Wyckoff positions by atoms and the equivalent Wyckoff-site description.

This possibility of different equivalent descriptions of the crystal-structure types has to be taken into account when the symmetry of electron and phonon states in crystals is analyzed. Furthermore, when preparing the input data for modern computer codes (see Appendix C) one usually takes crystal-structure data from the database or original papers. These data often contain information about the structure in the form accepted in ICSD (Inorganic Crystal Structure Database), see site [22].

As an example, we take the data for rutile structure given in this database (in brackets some clarifications are given).

COL ICSD Collection Code 82656

DATE Recorded June 26, 1998; updated Nov 30, 1999

NAME Titanium dioxide

MINERAL Rutile – synthetic at 1573 K

REFERENCE Journal of Solid State Chemistry 127 (1996) 240 – 247

CELL (lattice parameters for simple tetragonal lattice, unit cell volume and number of formula units in conventional cell):  $a = 4.594(0)$   $b = 4.594(0)$   $c = 2.959(0)$   $\alpha = 90.0$   $\beta = 90.0$   $\gamma = 90.0$   $V = 62.4$   $Z = 2$

SGR (space group) *P 4<sub>2</sub>/m n m* (136) – tetragonal

CLAS (point symmetry group *F* of crystal) *4/mmm* (Hermann–Mauguin) – *D<sub>4h</sub>* (Schoenflies)

PRS (Pearson symbol) tP6

PARM (Wyckoff positions occupied by atoms and their parameters)

Atom	No	OxStat	Wyck	---	X	---	---	Y	---	---	Z	---
Ti	1	4.000	2a		0.			0.			0.	
O	1	-2.000	4f		0.3047(2)			0.3047(2)			0.	

As  $Z = 2$  (two formula units in primitive unit cell, the conventional unit cell coincides with the primitive one as the Bravais lattice is simple tetragonal) one needs 2 sets of coordinates for Ti atom (2a) and four sets for O atom (4f). As is seen for each Wyckoff position occupied by an atom there are given coordinates of only one representative. The others can be found on the site [16] for space group 136:

$$2a : (0, 0, 0) \left( \frac{1}{2}, \frac{1}{2}, \frac{1}{2} \right); 4f : (x, x, 0) (-x, -x, 0) \left( -x + \frac{1}{2}, x + \frac{1}{2}, \frac{1}{2} \right) \left( x + \frac{1}{2}, -x + \frac{1}{2}, \frac{1}{2} \right)$$

In this case,  $x = 0.3047$  as follows from the structure data. To the best of our knowledge only computer code CRYSTAL [23] allows one to include the space-group information in input data so that any occupied Wyckoff position can be presented by one representative. In the other computer codes the coordinates of all atoms in the PUC are introduced and the point symmetry of the structure is found by the code itself and used in calculations. From this example it is seen that the necessary information for structures requires the use not only of the database but also IT.

Obviously, atoms of different chemical elements are always nonequivalent in a crystal, *i.e.* cannot be connected by operations of symmetry. But atoms of one chemical element in a crystal can not to be connected by operations of symmetry. These atoms are not equivalent in a crystal structure even when they occupy the same Wyckoff position with different free parameters (examples of such the structures can be found in the next sections).

In the next sections we briefly discuss the 15 crystal structures ordered by space-group index. There are included structures with both symmorphic and nonsymmorphic space groups, the structures with the same Bravais lattice and crystal class but different space groups, structures described by only lattice parameters or by the lattice parameters and free parameters of the Wyckoff positions occupied by atoms.

A nonmathematical introduction to the key elements of the crystal-structure description can be found in the recently published book by Tilley [24]. As well as covering the basics this book contains an introduction to areas of crystallography, such as modulated structures, quasicrystals, protein crystallography, which are the subject of important and active research.

### 2.3.2 Cubic Structures: Diamond, Rocksalt, Fluorite, Zincblende, Cesium Chloride, Cubic Perovskite

In Table 2.5 we give general information about all the cubic structures under consideration: prototype name, Pearson and strukturbericht designations, space group and Wyckoff positions occupations, and possible equivalent description of the structure. All these structures contain one formula unit in the primitive unit cell ( $Z=1$ ). For the structures cF with a face-centered cubic lattice the number of atoms is given for the cubic unit cell consisting of four primitive unit cells (this is traditional for crystal-structure databases). In computer calculations only the atoms inside the primitive unit cell have to be included: two atoms for diamond, rocksalt, zincblende and cesium

Table 2.5. Cubic structures\*

Prototype	Pearsons symbol	Strukturbericht designation	Space group	Wyckoff positions	Equivalent description
<b>Diamond</b> (C)	cF8	A4	Fd3m(227)	C(8a)	C(8b)
<b>Rocksalt</b> (NaCl)	cF8	B1	<i>Fm</i> $\bar{3}m$ (225)	Na(4a) Cl(4b)	Na(4b) Cl(4a)
<b>Fluorite</b> (CaF <sub>2</sub> )	cF12	C1	<i>Fm</i> $\bar{3}m$ (225)	Ca(4a) F(8c)	Ca(4b) F(8c)
<b>Zincblende</b> (ZnS)	cF8	B3	F43m(216)	Zn(4a) S(4c)	Zn(4b) S(4d)
<b>Cesium</b>	cP2	B2	<i>Pm</i> $\bar{3}m$ (221)	Cs(1a)	Cs(1b)
<b>Chloride</b> (CsCl)				Cl(1b)	Cl(1a)
<b>Perovskite</b> (cubic) (CaTiO <sub>3</sub> )	cP5	E21	<i>Pm</i> $\bar{3}m$ (221)	Ca(1a) Ti(1b) O(3c)	Ti(1a) Ca(1b) O(3d)

\*Equivalent sets of Wyckoff positions for space groups [16]

216 (abcd)(e)(fg)(h)(i)

221 (ab)(cd)(ef)(g)(h)(ij)(kl)(m)(n)

225 (ab)(c)(d)(e)(f)(g)(hi)(j)(k)(l)

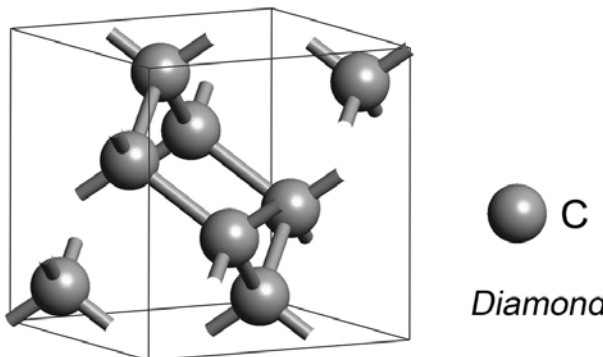
227 (ab)(cd)(e)(f)(g)(h)(i)

chloride structures, three and five atoms for fluorite and cubic perovskite structures, respectively.

*Diamond structure*(Fig. 2.5) is described by nonsymmorphic space group N227 with the face-centered cubic lattice: the macroscopic cubic symmetry of this crystal appears as the direct product of the first carbon atom site symmetry group  $T_d$  and inversion I at the center of C–C bond moving the first carbon to the equivalent second carbon atom in the primitive unit cell.

The coordinates of the carbon atoms can be given in fractions of primitive lattice vectors (these vectors are nonorthogonal for a face-centered cubic lattice) or in Cartesian coordinates. The primitive vectors themselves are usually given in Cartesian coordinates that for cubic lattices are directed along the translation vectors of the conventional (cubic) unit cell (see Fig. 2.2). To describe the diamond structure it is enough to give the numerical value of one parameter – the length of the cubic unit-cell translation vector (cubic lattice parameter  $a$ ). One can find [20] the following numerical data for diamond structure (for an experimental value of 3.57 Å of the lattice parameter) in the form:

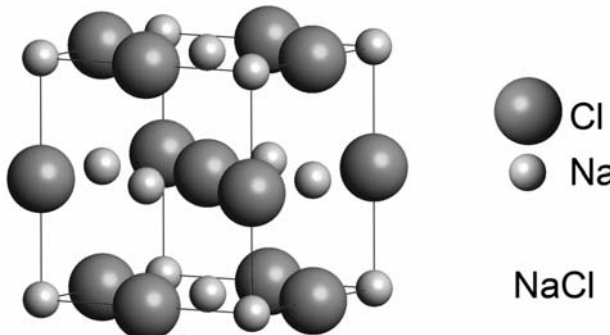
Primitive vectors  $\mathbf{a}_1 = (0.000, 1.785, 1.785)$   $\mathbf{a}_2 = (1.785, 0.000, 1.785)$   $\mathbf{a}_3 = (1.785, 1.785, 0.000)$  Volume = 11.37482325

**Fig. 2.5.** Diamond structure

Atom	Lattice coordinates			Cartesian coordinates		
C	0.12500	0.12500	0.12500	0.44625	0.44625	0.44625
C	-0.12500	-0.12500	-0.12500	-0.44625	-0.44625	-0.44625

These numerical data correspond to the origin choice 2 for the space group N227 in [19] and the diamond structure description C(8a) with the shifted origin.

*Rocksalt* NaCl structure (see Fig. 2.6) has the symmetry of symmorphic space group N225 and is typical of alkali halide crystals (Li, Na, K fluorides, chlorides and bromides) and some oxides (MgO, CaO, SrO).

**Fig. 2.6.** NaCl structure

The structure is defined also by only the face-centered cubic lattice parameter  $a$  (for NaCl crystal the experimental value of  $a=5.63$  Å):

Primitive vectors

$$\mathbf{a}_1 = (0.000, 2.815, 2.815)$$

$$\mathbf{a}_2 = (2.815, 0.000, 2.815)$$

$$\mathbf{a}_3 = (2.815, 2.815, 0.000)$$

Volume = 44.61338675

Atom	Lattice coordinates			Cartesian coordinates	
Na	0.000	0.000	0.000	0.000	0.000
Cl	0.500	0.500	0.500	2.815	2.815

This description  $\text{Na}(4\text{a})\text{Cl}(4\text{b})$  is equivalent to the description in which the coordinates of atoms are interchanged.

The same space group N225 is the symmetry group of the *fluorite*  $\text{CaF}_2$  structure (Fig. 2.7).

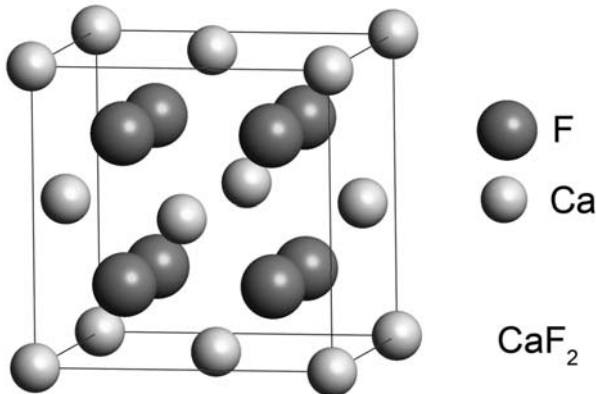


Fig. 2.7. Fluorite structure

Some compounds with this structure are the following:  $\text{CO}_2$ ,  $\text{CdF}_2$ ,  $\text{CeO}_2$ ,  $\text{SrCl}_2$ ,  $\text{SrF}_2$ ,  $\text{TiO}_2$ ,  $\text{ZrO}_2$ . For the experimental lattice parameter  $a=5.46295 \text{ \AA}$  the structure data are the following ( $\text{Ca}(4\text{a})\text{F}(8\text{c})$ ):

Primitive vectors

$$\mathbf{a}_1 = (0.000000, 2.731475, 2.731475)$$

$$\mathbf{a}_2 = (2.731475, 0.000000, 2.731475)$$

$$\mathbf{a}_3 = (2.731475, 2.731475, 0.000000)$$

Volume = 40.75882781

Atom	Lattice coordinates			Cartesian coordinates		
Ca	0.0000000	0.0000000	0.0000000	0.0000000	0.0000000	0.0000000
F	0.2500000	0.2500000	0.2500000	1.3657375	1.3657375	1.3657375
F	0.7500000	0.7500000	0.7500000	4.0972125	4.09721250	4.09721250

The Ca atom in the fluorite structure can be placed also in Wyckoff position b (0.5,0.5,0.5). The same space group describes the symmetry of crystals ( $\text{Li}_2\text{O}$ ,  $\text{Na}_2\text{O}$ ) with so-called antifluorite structure: two cations occupy the Wyckoff position c and oxygen – the Wyckoff position a. The symmorphic space group N225 is given in [19] for one origin choice (in Wyckoff position a with the site symmetry group  $O_h$ ).

The point symmetry of the *zincblende*  $\text{ZnS}$  (Fig. 2.8) structure is tetrahedral, but the lattice is cubic face-centered.

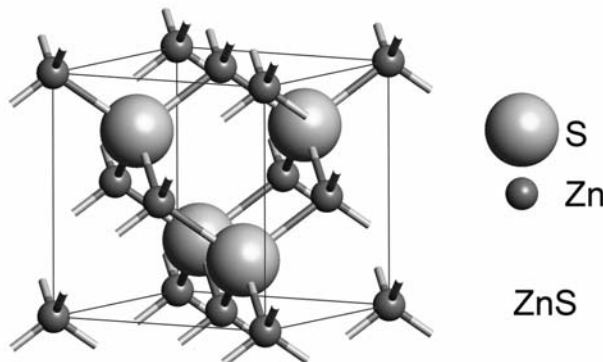


Fig. 2.8. Zincblende structure

This structure can be obtained from the diamond structure by exchanging two carbon atoms with Zn and S atoms, so that the operation of interchange of two atoms in the primitive unit cell disappears. The zincblende structure is known for different compounds (AgI, AlAs, AlP, AlSb, BAs, BN, BP, BeS, BeSe, BeTe, CdS, CuBr, CuCl, CuF, CuI, GaAs, GaP, GaSb, HgS, HgSe, HgTe, INAs, InP, MnS, MnSe, SiC, ZnSe, ZnTe). For  $a=5.4093$  Å the ZnS structure data are the following:

Primitive vectors

$$\mathbf{a}_1 = (0.00000, 2.70465, 2.70465)$$

$$\mathbf{a}_2 = (2.70465, 0.00000, 2.70465)$$

$$\mathbf{a}_3 = (2.70465, 2.70465, 0.00000)$$

$$\text{Volume} = 39.56974149$$

Atom	Lattice coordinates	Cartesian coordinates
Zn	0.000000 0.000000 0.000000	0.000000 0.000000 0.000000
S	0.250000 0.250000 0.250000	1.352325 1.352325 1.352325

For an equivalent description of the structure the Zn and S atoms can be interchanged.

For the next two structures the Bravais lattice is simple cubic.

*Cesium chloride* CsCl structure (Fig. 2.9) has the symmetry of symmorphic space group N221 and two equivalent descriptions Cs(1a)Cl(1b) and Cs(1b)Cl(1a). This structure was found for crystals CsBr, CsI, RbCl, AlCo, AgZn, BeCu, MgCe, RuAl, SrTl.

For a simple cubic lattice parameter  $a=4.11$  Å the CsCl crystal data are the following:

Primitive vectors

$$\mathbf{a}_1 = (4.11, 0.00, 0.00)$$

$$\mathbf{a}_2 = (0.00, 4.11, 0.00)$$

$$\mathbf{a}_3 = (0.00, 0.00, 4.11)$$

$$\text{Volume} = 69.42653100$$

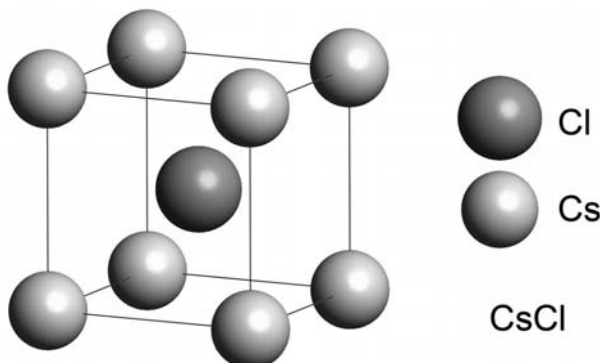


Fig. 2.9. CsCl structure

Atom	Lattice coordinates			Cartesian coordinates	
Cs	0.000	0.000	0.000	0.000	0.000
Cl	0.500	0.500	0.500	2.055	2.055

In the equivalent description of this structure the Cs and Cl atoms can be interchanged.

The *cubic perovskite*  $\text{CaTiO}_3$  structure (Fig. 2.10) is more complicated and found as the high-temperature modification of different crystals ( $\text{SrTiO}_3$ ,  $\text{BaTiO}_3$ ,  $\text{PbTiO}_3$ ,  $\text{SrZrO}_3$ ,  $\text{PbZrO}_3$ ).

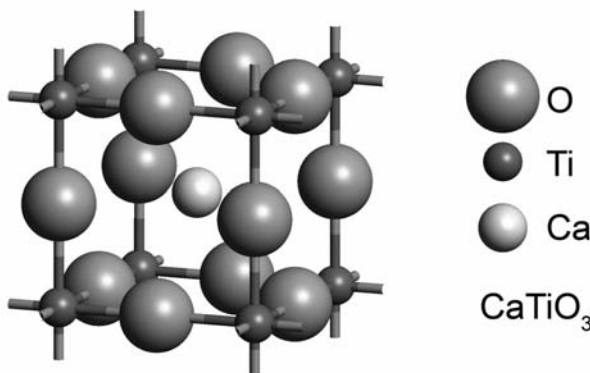


Fig. 2.10. Perovskite structure

The structure is defined by one simple cubic lattice parameter and for  $a=3.795 \text{ \AA}$  five atoms in the  $\text{CaTiO}_3$  unit cell have the coordinates:

Primitive vectors

$$\mathbf{a}_1 = (3.795, 0.000, 0.000)$$

$$\mathbf{a}_2 = (0.000, 3.795, 0.000)$$

$$\mathbf{a}_3 = (0.000, 0.000, 3.795)$$

Volume =54.65568

Atom	Lattice coordinates	Cartesian coordinates
Ca	0.0000 0.0000 0.0000	0.0000 0.0000 0.0000
Ti	0.5000 0.5000 0.5000	1.8975 1.8975 1.8975
O	0.5000 0.0000 0.0000	1.8975 0.0000 0.0000
O	0.0000 0.5000 0.0000	0.0000 1.8975 0.0000
O	0.0000 0.0000 0.5000	0.0000 0.0000 1.8975

In the cubic perovskite structure the Ti–O distance is equal to one half of the translation vector length. In the equivalent structure description (when Ca and Ti atoms are interchanged) the three oxygen atoms positions need to be taken as (0.5 0.5 0), (0.5,0,0.5) and (0,0.5,0.5).

The considered different cubic structures are defined by one numerical parameter – the cubic lattice constant. This is due to the fact that in these structures atoms occupy Wyckoff positions that have no free parameters. The definition of the more complicated structures requires the knowledge of both the lattice constants and the numerical values of the free parameters for the free-parameter-dependent Wyckoff positions occupied by atoms.

### 2.3.3 Tetragonal Structures: Rutile, Anatase and $\text{La}_2\text{CuO}_4$

In Table 2.6 we give general information about three tetragonal structures: two modifications (rutile and anatase) of titanium dioxide  $\text{TiO}_2$  and lanthanum cuprate  $\text{La}_2\text{CuO}_4$ .

**Table 2.6.** Tetragonal structures\*

Prototype	Pearsons symbol	Strukturbericht designation	Space group	Wyckoff positions	Equivalent description
<b>Rutile</b> ( $\text{TiO}_2$ )	tP6	C4	$P4_2/mnm(136)$	Ti(2a) O(4f)	Ti(2b) O(4g)
<b>Anatase</b> ( $\text{TiO}_2$ )	tI12	C5	$I4_1/amd(141)$	Ti(2a) O(4e)	Ti(2b) O(4e)
<b>Lanthanum cuprate</b> ( $\text{La}_2\text{CuO}_4$ )	tI14	-	$I4/mmm(139)$	La(2e) Cu(1a) O <sub>1</sub> (2c) O <sub>2</sub> (2e)	La(2e) Cu(1b) O <sub>1</sub> (2c) O <sub>2</sub> (2e)

\*Equivalent sets of Wyckoff positions for space groups [16]

136 (ab)(c)(d)(e)(fg)(h)(i)(j)(k)

141 (ab)(cd)(e)(f)(g)(h)(i)

139 (ab)(c)(d)(f)(e)(g)(h)(ij)(k)(l)(m)(n)(o)

The rutile and anatase phases of titanium dioxide have been widely studied in recent years. The rutile form is used as a white pigment and opacifier, the anatase phase finds applications in photo catalysts and nanostructured solar cells.  $\text{La}_2\text{CuO}_4$  has attracted considerable research efforts as it was found to become a high- $T_c$  superconductor ( $T_c = 35$  K) when properly doped with Sr or Ba atoms. Both  $\text{TiO}_2$  modifications contain 6 atoms (two formula units) in the primitive cell.

The *rutile structure* (Fig. 2.11) belongs to the  $P4_2/mnm$  nonsymmorphic space group.

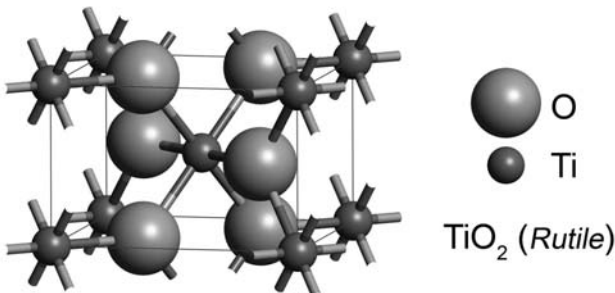


Fig. 2.11. Rutile structure

The unit cell of the primitive tetragonal lattice is defined by the lattice vectors  $\mathbf{a}_1 = \mathbf{a}_2$  (in the  $xy$ -plane) and  $\mathbf{c}$  (along  $z$ -axis). The rotations through a fourth-order axis are followed by the improper translations along the  $z$ -axis of one half of the  $\mathbf{c}$ -vector length to ensure transformation of any of the oxygen atoms to another one, see Table 2.4. As is seen from Table 2.6 two Ti atoms of the primitive cell occupy Wyckoff position  $a(000; 1/2, 1/2, 1/2)$ , four oxygen atoms occupy Wyckoff position  $f$  with one free parameter  $u$ :  $(\pm(u, u, 0); \pm(u+1/2, 1/2-u, 1/2))$ . The Wyckoff positions coordinates are given in units of  $a$ ,  $a$ ,  $c$ . Thus, the rutile structure is defined by three parameters:  $a$ ,  $c$  and  $u$ . The following numerical data for rutile structure are given in [20]:

Primitive vectors

$$\mathbf{a}_1 = (4.59373, 0.00000, 0.00000)$$

$$\mathbf{a}_2 = (0.00000, 4.59373, 0.00000)$$

$$\mathbf{a}_3 = (0.00000, 0.00000, 2.95812)$$

Volume = 62.42329930

Atom	Lattice coordinates			Cartesian coordinates		
Ti	0.0000	0.0000	0.0000	0.00000000	0.00000000	0.00000
Ti	0.5000	0.5000	0.5000	2.29686500	2.29686500	1.47906
O	0.3053	0.3053	0.0000	1.40246577	1.40246577	0.00000
O	-0.3053	-0.3053	0.0000	-1.40246577	-1.40246577	0.00000
O	0.8053	0.1947	0.5000	3.69933077	0.89439923	1.47906
O	0.1947	0.8053	0.5000	0.89439923	3.69933077	1.47906

The *anatase* structure (Fig. 2.12) belongs to the I4/amd nonsymmorphic space group.

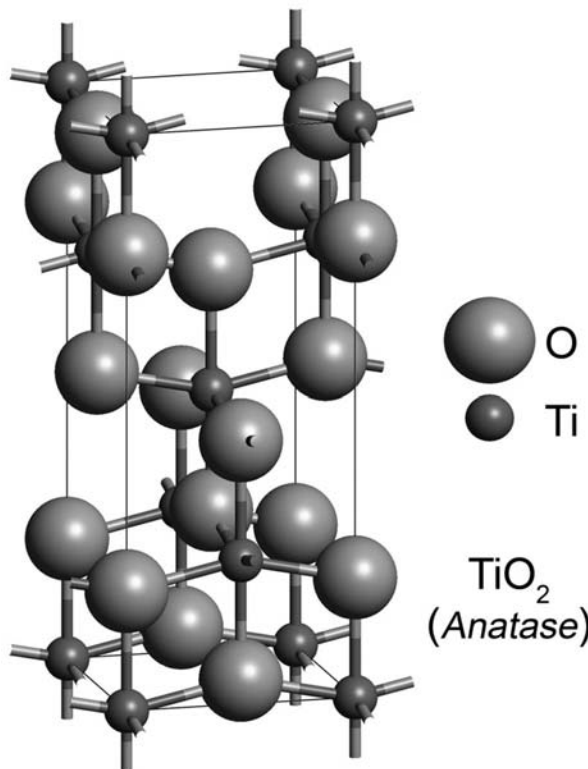


**Fig. 2.12.** Anatase structure

The tetragonal unit cell of a body-centered tetragonal lattice is defined by the lattice vectors  $\mathbf{a}_1 = \mathbf{a}_2$  (in the  $xy$ -plane) and  $\mathbf{c}$  (along the  $z$ -axis) and contains 2 primitive unit cells (see Fig. 2.2). To describe the primitive unit cell the translation vectors  $\mathbf{a}_1(a, 0, 0)$ ,  $\mathbf{a}_2(0, a, 0)$ ,  $\mathbf{a}_3(1/2a, 1/2a, 1/2c)$  are used. As is seen from Table 2.6. two Ti atoms of the primitive cell occupy Wyckoff position 2a( $0, 0, 0$ ;  $0, 1/2, 1/4$ ), four oxygen atoms occupy Wyckoff position 4e ( $0, 0, u$ ;  $1/2, 0, -u + 1/2$ ;  $0, 1/2, u + 1/4$ ;  $1/2, 1/2, -u + 1/2$ ). The anatase structure is defined by three parameters:  $a$ ,  $c$ ,  $u$ . The numerical data for anatase structure, given in [20] are the following:

Primitive vectors

$$\mathbf{a}_1 = (3.7850, 0.0000, 0.0000)$$

$$\mathbf{a}_2 = (0.0000, 3.7850, 0.0000)$$

$$\mathbf{a}_3 = (1.8925, 1.8925, 4.7570)$$

Volume = 68.14985232

Atom	Lattice coordinates			Cartesian coordinates		
Ti	0.125	-0.125	-0.25	0.0000	-0.94625	-1.18925
Ti	0.125	0.125	0.25	0.0000	0.94625	1.18925
O	0.08159975	0.33159975	-0.16319950	0.0000	0.94625	-0.77634
O	-0.08159975	-0.33159975	0.16319950	0.0000	-0.94625	0.77634
O	0.33159975	0.08159975	0.33680050	1.8925	0.94625	1.602160
O	-0.33159975	-0.08159975	-0.33680050	-1.8925	-0.94625	-1.60216

These data correspond to the coordinate system origin shifted by  $(1/8, -1/8, -1/4)$  (in the units of primitive translations), in comparison with the origin choice made in [19].

The *lanthanum cuprate* structure (Fig. 2.13) belongs to the symmorphic space group I4/mmm with the body-centered tetragonal lattice and contains 7 atoms in the primitive unit cell.

The Cu atom occupies Wyckoff position 1a(000), two La atoms and two oxygen atoms  $O_2$  occupy Wyckoff position 2e  $\pm(0, 0, z)$  with different numerical values of the  $z$ -parameter for La and oxygen atoms; the two remaining oxygen atoms occupy Wyckoff position 2c(0, 1/2, 0; 1/2, 0, 0). The structure is defined by two tetragonal lattice parameters (lengths of  $\mathbf{a}_1 = \mathbf{a}_2$  primitive translations and  $\mathbf{c}$  – translation vector of the tetragonal unit cell containing two primitive cells) and two  $z$ -parameters defining the positions of the La and  $O_2$  atoms. The numerical data for this structure are taken from [20]. The primitive translation vector  $\mathbf{a}_3(1/2, 1/2, 1/2)$  is given in units of  $a, a, c$ .

Primitive vectors

$$\mathbf{a}_1 = (3.78730, 0.00000, 0.00000)$$

$$\mathbf{a}_2 = (0.00000, 3.78730, 0.00000)$$

$$\mathbf{a}_3 = (1.89365, 1.89365, 6.64415)$$

Volume = 95.30130

Atom	Cartesian coordinates			Free parameter z
Cu	0.00000000	0.00000000	0.00000000	
La	0.00000000	0.00000000	4.79176098	0.3606
La	0.00000000	0.00000000	8.49653902	
$O_1$	1.89365000	0.00000000	0.00000000	
$O_1$	0.00000000	1.89365000	0.00000000	
$O_2$	0.00000000	0.00000000	2.42910124	0.1828
$O_2$	0.00000000	0.00000000	10.85919876	

The  $La_2CuO_4$  structure (see Fig. 2.13) consists of  $CuO_2$ –La–O–O–La planes repeated along the  $z$ -axis (translation vector  $\mathbf{c}$ ).

The electronic structure calculations show (see Chap. 9): the highest occupied band states in the lanthanum cuprate are  $O_1 - 2p_x, 2p_y$  states strongly mixed with Cu –  $3d_{x^2-y^2}$  states. This result agrees with the hypothesis that the high- $T_c$  conductivity can be explained by  $CuO_2$ -plane consideration as is done in most theoretical models.

### 2.3.4 Orthorhombic Structures: $LaMnO_3$ and $YBa_2Cu_3O_7$

In Table 2.7 we give the information about two orthorhombic structures: lanthanum manganite  $LaMnO_3$  (Fig. 2.14) and yttrium cuprate  $YBa_2Cu_3O_7$  (Fig. 2.15).

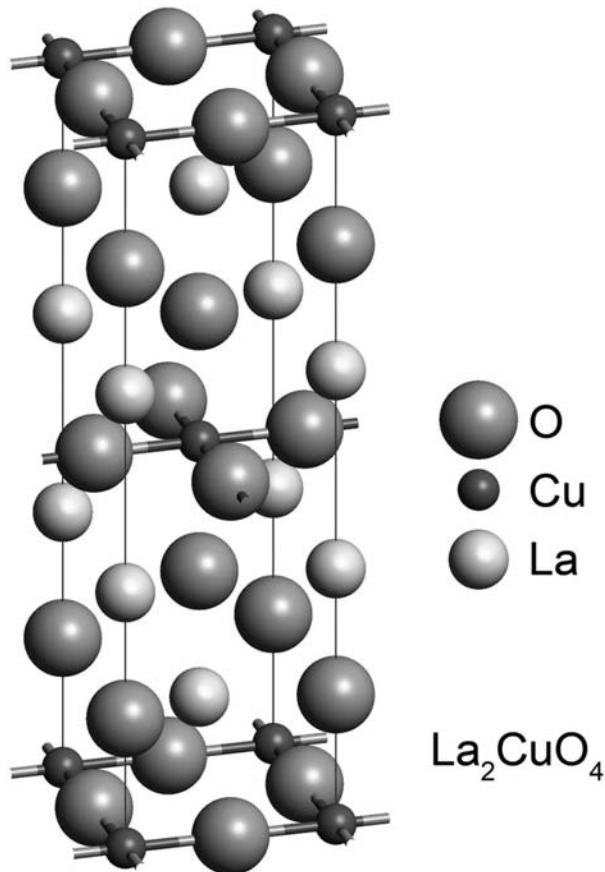


Fig. 2.13.  $\text{La}_2\text{CuO}_4$  structure

Among the manganese oxides,  $\text{LaMnO}_3$  is important as it is the parent system in the family of manganites, that show colossal magneto resistance effects. In the low-temperature phase this crystal belongs to the nonsymmorphic space group N62 with the simple orthorhombic lattice. There are four formula units (20 atoms) in the primitive unit cell. The structure parameters can be found in the literature in two different settings used for the nonsymmorphic space group N62 description. In the standard setting Pnma (accepted in [19]) the primitive orthorhombic lattice vectors  $\mathbf{a}, \mathbf{b}, \mathbf{c}$  define the following Wyckoff positions occupied by atoms: La 4c( $x, 1/4, z$ ), Mn 4a( $0, 0, 0; 1/2, 0, 1/2; 0, 1/2, 0; 1/2, 1/2, 1/2$ ), O<sub>1</sub> 4c( $x, 1/4, z; 1/2 - x, -1/4, 1/2 + z; -x, -1/4, -z; x + 1/2, 1/4, 1/2 - z$ ) and O<sub>2</sub> 8d ( $x, y, z$ ). The Pbnm setting means the cyclic transposition of basic translation vectors  $\mathbf{a}, \mathbf{b}, \mathbf{c}$  to  $\mathbf{c}, \mathbf{a}, \mathbf{b}$  and the corresponding changes in the Wyckoff positions coordinates: c( $z, x, 1/4$ ) and

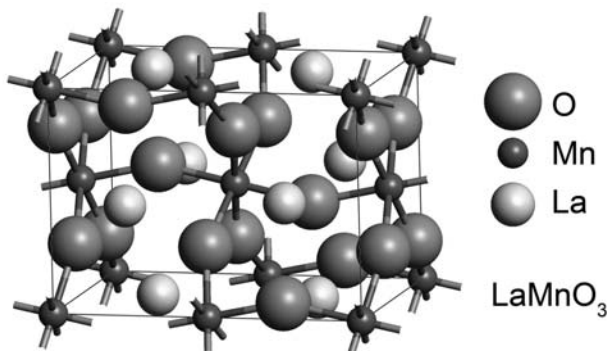


Fig. 2.14. Orthorhombic  $\text{LaMnO}_3$  structure

Table 2.7. Orthorhombic structures.\*

Prototype	Space group	Wyckoff positions	Equivalent description
$\text{LaMnO}_3$	$\text{Pnma}(62)$	$\text{La}(4c)$ $\text{Mn}(4a)$ $\text{O}1(4c)$ $\text{O}2(8d)$	$\text{La}(4c)$ $\text{Mn}(4b)$ $\text{O}1(4c)$ $\text{O}2(8d)$
$\text{YBa}_2\text{Cu}_3\text{O}_7$	$\text{Pmmm}(47)$	$\text{Y}(1h)$ $\text{Ba}(2t)$ $\text{Cu}_1(1a)$ $\text{Cu}_2(2q)$ $\text{O}_1(1e)$ $\text{O}_2(2r)$ $\text{O}_3(2s)$ $\text{O}_4(2q)$	$\text{Y}(1a)$ $\text{Ba}(2q)$ $\text{Cu}_1(1h)$ $\text{Cu}_2(2t)$ $\text{O}_1(1d)$ $\text{O}_2(2s)$ $\text{O}_3(2r)$ $\text{O}_4(2t)$

\*Equivalent sets of Wyckoff positions for space groups [16]

62  $\text{Pnma}$  (ab)(c)(d)

47  $\text{Pmmm}$  (abcdefg)(ijklmnopqrst)(uvwxyz)

$\text{d}(z, x, y)$ . When using the structure data from the literature one has to take into account the setting chosen. The structure is defined by three orthorhombic lattice parameters and 7 internal parameters: two parameters  $x, z$  for La and  $\text{O}_1$  atoms and 3 parameters for  $\text{O}_2$  atoms. The equivalent description of LMO structure given in Table 2.7 for the fixed setting means in fact the change of the coordinate system origin - moving the Mn atom position from  $\text{a}(000)$  to  $\text{b}(001/2)$ . The coordinates of c and d points has to be also changed to  $(x, 1/4, z + 1/2)$ ,  $d(x, y, z + 1/2)$ . In this case, the structure parameters do not change.

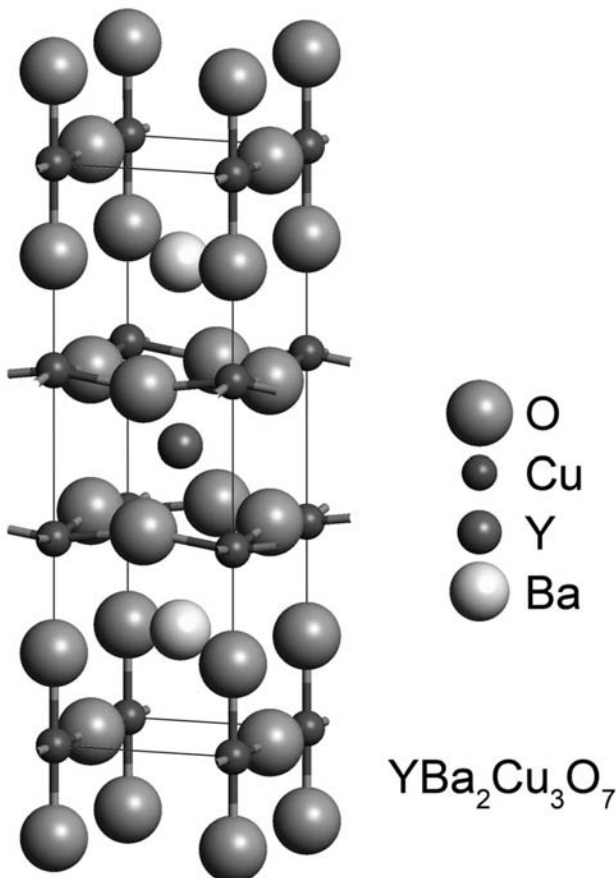


Fig. 2.15.  $\text{YBa}_2\text{Cu}_3\text{O}_7$  structure

Taken from [20] the structure data are given in the Pnma setting.  
Primitive vectors

$$\mathbf{a}_1 = (5.6991, 0.0000, 0.0000)$$

$$\mathbf{a}_2 = (0.0000, 7.7175, 0.0000)$$

$$\mathbf{a}_3 = (0.0000, 0.0000, 5.5392)$$

Volume = 243.62954930

Atom	Lattice coordinates			Cartesian coordinates		
Mn	0.00000000	0.00000000	0.00000000	0.00000000	0.00000000	0.00000000
Mn	0.50000000	0.00000000	0.50000000	2.84955000	0.00000000	2.76960000
Mn	0.00000000	0.50000000	0.00000000	0.00000000	3.85875000	0.00000000
Mn	0.50000000	0.50000000	0.50000000	2.84955000	3.85875000	2.76960000
La	0.54349985	0.25	0.00636915	3.09746000	1.92938000	0.03528000
La	-0.04349985	0.75	0.50636915	-0.24791000	5.78812000	2.80488000
La	-0.54349985	0.75	-0.00636915	-3.09746000	5.78812000	-0.03528000
La	1.04349985	0.25	0.49363085	5.94701000	1.92938000	2.73432000
O <sub>1</sub>	-0.01069994	0.25	-0.07329939	-0.06098000	1.92938000	-0.40602000
O <sub>1</sub>	0.51069994	0.75	0.42670061	2.91053000	5.78812000	2.36358000
O <sub>1</sub>	0.01069994	0.75	0.07329939	0.06098000	5.78812000	0.40602000
O <sub>1</sub>	0.48930006	0.25	0.57329939	2.78857000	1.92938000	3.17562000
O <sub>2</sub>	0.30140022	0.03849951	0.22570046	1.71771000	0.29712000	1.25020000
O <sub>2</sub>	0.19859978	-0.03849951	0.72570046	1.13184000	-0.29712000	4.01980000
O <sub>2</sub>	-0.30140022	0.53849951	-0.22570046	-1.71771000	4.15587000	-1.25020000
O <sub>2</sub>	0.80140022	0.46150049	0.27429954	4.56726000	3.56163000	1.51940000
O <sub>2</sub>	-0.30140022	-0.03849951	-0.22570046	-1.71771000	-0.29712000	-1.25020000
O <sub>2</sub>	0.80140022	0.03849951	0.27429954	4.56726000	0.29712000	1.51940000
O <sub>2</sub>	0.30140022	0.46150049	0.22570046	1.71771000	3.56163000	1.25020000
O <sub>2</sub>	0.19859978	0.53849951	0.72570046	1.13184000	4.15587000	4.01980000

The Y–Ba–Cu–O systems are known as high- $T_c$  superconductors ( $T_c = 93$  K) when oxygen atoms in the  $\text{YBa}_2\text{Cu}_3\text{O}_7$  system are partly replaced by vacancies or fluorine atoms to synthesize ceramic oxides  $\text{YBa}_2\text{Cu}_3\text{O}_{7-x}$ . The atomic structure of this compound is described by symmorphic space group Pmmm, the primitive unit cell of the orthorhombic lattice consists of one formula unit with the atoms distributed over several planes (see Fig. 2.15). The three copper atoms form two nonequivalent groups:  $\text{Cu}_1$  atom occupies Wyckoff position 1a(0,0,0), forming Cu–O chains and two  $\text{Cu}_2$  atoms – Wyckoff position 2q(0,0, $\pm z$ ) (see Table 2.7), forming  $\text{CuO}_2$  planes. Two Ba atoms occupy 2t(1/2,1/2, $\pm z$ ) position. The seven oxygens form four nonequivalent atomic systems:  $O_1$  – 1e(0,1/2,0),  $O_2$  – 2r(0,1/2, $\pm z$ ),  $O_3$  – 2s(1/2,0, $\pm z$ ) and  $O_4$  – 2q(0,0, $\pm z$ ). The structure requires 8 parameters for its definition: three orthorhombic lattice parameters and five internal parameters of Ba,  $\text{Cu}_2$  and  $O_2$ ,  $O_3$ ,  $O_4$  atomic positions. All the structural data from [20] are the following.

Primitive vectors

$$\mathbf{a}_1 = (3.8227, 0.0000, 0.0000)$$

$$\mathbf{a}_2 = (0.0000, 3.8872, 0.0000)$$

$$\mathbf{a}_3 = (0.0000, 0.0000, 11.6802)$$

Volume = 173.56308

Atom	Cartesian coordinates	Free parameter z (in $ \alpha_3 $ units)
Cu <sub>1</sub>	0.00000000 0.00000000 0.00000000	
Cu <sub>2</sub>	0.00000000 0.00000000 4.15347912	0.3556
Cu <sub>2</sub>	0.00000000 0.00000000 7.52672088	
O <sub>1</sub>	0.00000000 1.94360000 0.00000000	
O <sub>2</sub>	0.00000000 1.94360000 4.42679580	0.3790
O <sub>2</sub>	0.00000000 1.94360000 7.25340420	
O <sub>3</sub>	1.91135000 0.00000000 4.41394758	0.3779
O <sub>3</sub>	1.91135000 0.00000000 7.26625242	
O <sub>4</sub>	0.00000000 0.00000000 1.85715180	0.1590
O <sub>4</sub>	0.00000000 0.00000000 9.82304820	
Ba	1.91135000 1.94360000 2.15266086	0.1843
Ba	1.91135000 1.94360000 9.52753914	

### 2.3.5 Hexagonal and Trigonal Structures: Graphite, Wurtzite, Corundum and ScMnO<sub>3</sub>

In this section we consider three hexagonal (graphite, wurtzite and ScMnO<sub>3</sub>, see Figures 2.16–2.18, respectively) and one trigonal (corundum) structure, see Fig. 2.19

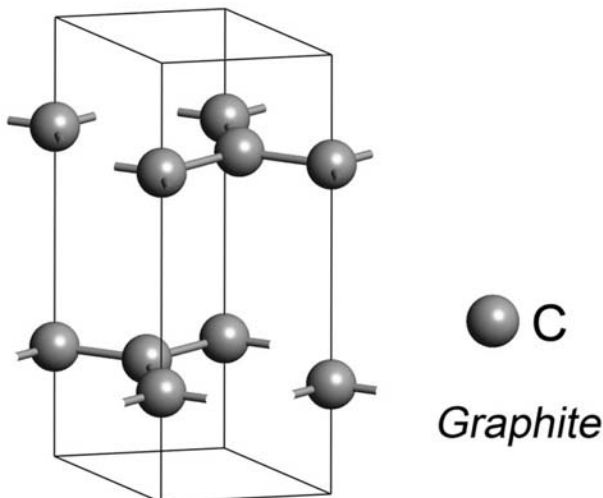


**Fig. 2.16.** Graphite structure

The latter structure can also be described in hexagonal axes.

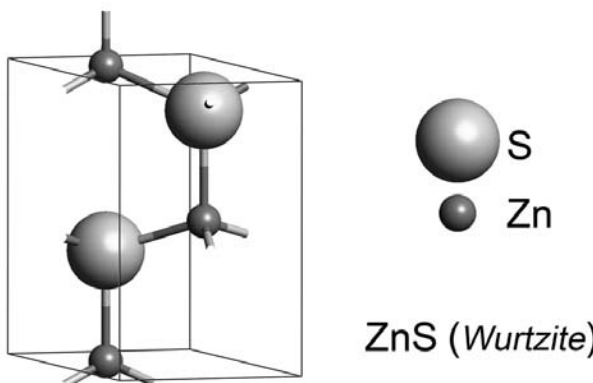
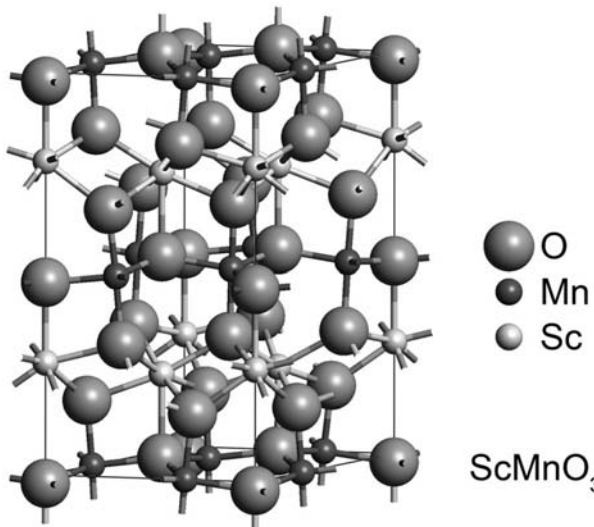


Fig. 2.17. Wurtzite structure

Fig. 2.18.  $\text{ScMnO}_3$  structure

The graphite structure belongs to the nonsymmorphic space group  $\text{P}6_3/\text{mmc}$ , the primitive unit cell of the hexagonal lattice contains 4 carbon atoms occupying two nonequivalent Wyckoff positions: 2a (0,0,0;0,0,1/2) and 2b(0,0,1/4;0,0,-1/4). The structure is described by two hexagonal lattice parameters  $a$  and  $c$ . The graphite structure consists of atomic layers separated by a distance larger than the interatomic distance in one layer. Therefore, the one-layer approximation is in some cases used for graphite: only two carbon atoms in the primitive cell of the plane hexagonal lattice are included in the structure.

The numerical values of the graphite structure data from [20] are the following:

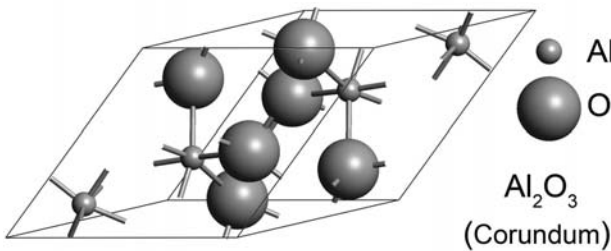


Fig. 2.19. Corundum structure

Table 2.8. Hexagonal structures\*

Prototype	Pearson symbol	Strukturbericht designation	Space group	Wyckoff positions	Equivalent description
<b>Graphite</b> C	hP4	A9	$P6_3/mmc$ (194)	C(2a) C(2b)	-
<b>Wurtzite</b> (ZnS)	hP4	B4	$P6_3mc$ (186)	Zn(2b) S(2b)	-
<b>ScMnO<sub>3</sub></b>	hP30	-	$P6_3cm$ (185)	Sc <sub>1</sub> (2a) Sc <sub>2</sub> (4b) Mn(6c) O <sub>1</sub> , O <sub>2</sub> (6c) O <sub>3</sub> (2a) O <sub>4</sub> (4b)	-
<b>Corundum</b> (Al <sub>2</sub> O <sub>3</sub> )	hR10	D <sub>5</sub> <sub>1</sub>	$R\bar{3}c$ (167)	Al(4c) O(6e)	-

\*Equivalent sets of Wyckoff positions for space groups [16]

194 (a)(b)(cd)(e)(f)(g)(h)(i)(j)(k)(l)

186 (a)(b)(c)(d)

185 (a)(b)(c)(d)

167 (a)(b)(c)(d)(e)(f)

Primitive vectors

$$\mathbf{a}_1 = (1.22800000, -2.12695839, 0.00000000)$$

$$\mathbf{a}_2 = (1.22800000, 2.12695839, 0.00000000)$$

$$\mathbf{a}_3 = (0.00000000, 0.00000000, 6.69600000)$$

$$\text{Volume} = 34.97863049$$

Atom	Lattice coordinates			Cartesian coordinates		
C	0.00000000	0.00000000	0.25000000	0.00000000	0.00000000	1.67400000
C	0.00000000	0.00000000	0.75000000	0.00000000	0.00000000	5.02200000
C	0.33333333	0.66666667	0.25000000	1.22800000	0.70898613	1.67400000
C	0.66666667	0.33333333	0.75000000	1.22800000	-0.70898613	5.02200000

The *wurtzite* structure of ZnS is the hexagonal analog of the zincblende structure of ZnS (see Sect. 3.2.2) and belongs to the nonsymmorphic space group P63mc with a hexagonal lattice. The primitive unit cell contains two formula units, both Zn and S atoms occupy the same Wyckoff position 2b( $1/3, 2/3, z$ ;  $2/3, 1/3, z + 1/2$ ) with the different values of internal parameter  $z$ . Thus, the wurtzite structure is defined by 4 parameters – two lattice and two internal ones. The numerical values of the structure data from [20] are the following:

Primitive vectors

$$\mathbf{a}_1 = (1.91135000, -3.31055531, 0.00000000)$$

$$\mathbf{a}_2 = (1.91135000, 3.31055531, 0.00000000)$$

$$\mathbf{a}_3 = (0.00000000, 0.00000000, 6.26070000)$$

Volume = 79.23078495

Atom	Lattice coordinates			Cartesian coordinates		
Zn	0.33333333	0.66666667	0.00000000	1.91135000	1.10351844	0.00000000
Zn	0.66666667	0.33333333	0.50000000	1.91135000	-1.10351844	3.13035000
S	0.33333333	0.66666667	0.37480000	1.91135000	1.10351844	2.34651036
S	0.66666667	0.33333333	-0.12520000	1.91135000	-1.10351844	-0.78383964

RMnO<sub>3</sub> rare-earth *manganites* show a wide variety of physical properties. For R<sup>3+</sup> cations with large ionic size RMnO<sub>3</sub> oxides crystallize in a perovskite-type structure, with orthorhombic symmetry, as was illustrated in Sect. 2.3.4 by the example of LaMnO<sub>3</sub> manganite. For R = Y, Sc, Ho–Lu the perovskite structure becomes metastable and a new hexagonal polytype stabilizes. The hexagonal manganites are an interesting group of compounds because of their unusual combination of electrical and magnetic properties: at low temperatures they show coexistence of ferroelectric and magnetic orderings. ScMnO<sub>3</sub> plays a prominent role in this series. It has the highest Neel temperature and the smallest distance between magnetic ions Mn<sup>3+</sup> along the hexagonal axis direction. At temperatures below 1200 K ScMnO<sub>3</sub> structure belongs to space group P63cm with hexagonal lattice and six formula units (30 atoms) per cell. The six Mn atoms occupy Wyckoff position 6c( $x, 0, z; 0, x, z; -x, -x, z; -x, 0, z + 1/2; 0, -x, z + 1/2; x, x, z + 1/2$ ). The six Mn atoms are distributed in the  $z = 0$  and  $z = 1/2$  planes. Each Mn atom occupies the center of a triangular bipyramidal whose vertices are oxygen atoms (see Fig. 2.18). As a result, each Mn atom is coordinated by five oxygen atoms in a bipyramidal configuration. The same Wyckoff position 6c is occupied by nonequivalent (with the different internal parameters  $x, z$ ) oxygens O<sub>1</sub>, O<sub>2</sub>. Sc<sub>1</sub> and O<sub>3</sub> atoms occupy Wyckoff position 2a ( $0, 0, z; 0, 0, z + 1/2$ ), Sc<sub>2</sub> and O<sub>4</sub> atoms – Wyckoff position 4b( $1/3, 2/3, z; 2/3, 1/3, z + 1/2; 1/3, 2/3, z + 1/2; 2/3, 1/3, z$ ). One O<sub>3</sub> atom and two O<sub>4</sub> atoms are in the equatorial plane of the bipyramid, whereas the O<sub>1</sub> and O<sub>2</sub> atoms are at the apices. Sc atoms occupy two crystallographic positions Sc<sub>1</sub> and Sc<sub>2</sub>, both of them bonded to seven oxygen atoms. Both RO<sub>7</sub> polyhedra can be described as monocapped octahedra. The capping oxygens are O<sub>3</sub> for Sc<sub>1</sub> and O<sub>4</sub> for Sc<sub>2</sub>. Along the axis  $z$ , the structure consists of layers of corner-sharing MnO<sub>5</sub> bipyramids separated by layers of edge-sharing RO<sub>7</sub> polyhedra. The structure is defined by two hexagonal lattice parameters and 10 internal parameters – two for each type of atoms Mn, O<sub>1</sub>, O<sub>2</sub>, and one for each type of atoms Sc<sub>1</sub>, Sc<sub>2</sub>, O<sub>3</sub> and O<sub>4</sub>. The numerical values of all the structure parameters can be found, for example in [25]. The description of the ScMnO<sub>3</sub> shows it as a very complicated one with many atoms in the primitive cell.

Nevertheless, the first-principles LCAO calculations of  $\text{ScMnO}_3$  were recently made (see Chap. 9).

*Aluminum oxide* ( $\alpha - \text{Al}_2\text{O}_3$ , *corundum*) has a large number of technological applications. Due to its hardness, its chemical and mechanical stability at high temperatures and its electronic properties as a widegap insulator it is used for the fabrication of abrasives, as a carrier for thin metal films in heterogeneous catalysis and in optical and electronic devices.  $\alpha - \text{Al}_2\text{O}_3$  crystallizes in a rhombohedral structure with the space group  $R\bar{3}c$ . The primitive rhombohedral unit cell consists of two  $\text{Al}_2\text{O}_3$  units with experimental lattice parameters  $a = 5.128 \text{ \AA}$  and  $\alpha = 55.333 \text{ \AA}$ . Four Al atoms occupy Wyckoff position 4c:  $\pm(x, x, x; -x+1/2, -x+1/2, -x+1/2)$ . Six oxygen atoms occupy Wyckoff position 6e:  $\pm(x, -x+1/2, 1/4; 1/4, x, -x+1/2; -x+1/2, 1/4, x)$ . Using the transformation of the rhombohedral lattice vectors with the matrix (2.10) one obtains the hexagonal setting of the  $\alpha - \text{Al}_2\text{O}_3$  structure. Its unit cell consists of 3 primitive unit cells (the determinant of the transformation matrix equals 3). The lattice parameters in this hexagonal setting are  $a = 4.763 \text{ \AA}$ ,  $c = 13.003 \text{ \AA}$ . In hexagonal axes the positions occupied by atoms are written in the form  $4c \pm(0, 0, z; 0, 0, -z+1/2)$  and  $6e \pm(x, 0, 1/4; 0, x, 1/4; -x, -x, 1/4)$ . The two internal parameters of the corundum structure define the Al and O atoms positions; in terms of the hexagonal lattice,  $x_{\text{Al}}(\text{hex}) = 0.35228$  and  $x_{\text{O}}(\text{hex}) = 0.306$ . On the rhombohedral lattice this translates to  $z_1 = x_{\text{Al}}(\text{hex}) = 0.35228$  and  $x_1 = 1/4 - x_{\text{O}}(\text{hex}) = -0.0564$ . In rhombohedral axes the numerical data for corundum structure are given, for example, in [20]:

Primitive rhombohedral vectors

$$\mathbf{a}_1 = (0.256984, 3.621398, 3.621398)$$

$$\mathbf{a}_2 = (3.621398, 0.256984, 3.621398)$$

$$\mathbf{a}_3 = (3.621398, 3.621398, 0.256984)$$

Volume = 84.89212148

Atom	Lattice coordinates			Cartesian coordinates		
Al	0.35228000	0.35228000	0.35228000	2.64202250	2.64202250	2.64202250
Al	-0.35228000	-0.35228000	-0.35228000	-2.64202250	-2.64202250	-2.64202250
Al	0.14772000	0.14772000	0.14772000	1.10786750	1.10786750	1.10786750
Al	-0.14772000	-0.14772000	-0.14772000	-1.10786750	-1.10786750	-1.10786750
O	-0.05640000	0.55640000	0.25000000	2.90580145	0.84408855	1.87494500
O	0.05640000	-0.55640000	-0.25000000	-2.90580145	-0.84408855	-1.87494500
O	0.55640000	0.25000000	-0.05640000	0.84408855	1.87494500	2.90580145
O	-0.55640000	-0.25000000	0.05640000	-0.84408855	-1.87494500	-2.90580145
O	0.25000000	-0.05640000	0.55640000	1.87494500	2.90580145	0.84408855
O	-0.25000000	0.05640000	-0.55640000	-1.87494500	-2.90580145	-0.84408855

By consideration of the hexagonal and trigonal structures we conclude the discussion of the structure definitions by space groups and Wyckoff positions. In the next chapter we consider the symmetry of crystalline orbitals, both canonical and localized.

## Symmetry and Localization of Crystalline Orbitals

### 3.1 Translation and Space Symmetry of Crystalline Orbitals. Bloch Functions

#### 3.1.1 Symmetry of Molecular and Crystalline Orbitals

In a previous chapter we considered the symmetry of a crystalline structure for fixed nuclei positions. The aim of the first-principles approaches in quantum chemistry is to calculate the properties of molecules and crystals without the use of empirical parameters. In principle, all the particles—electrons and nuclei—should be involved in such calculations. In fact, the solution of this complicated task is simplified in the Born–Oppenheimer approximation (also called the adiabatic approximation). In the first stage the electronic subsystem is studied for different nuclear configurations to calculate the potential-energy surface and to find the optimized atomic positions corresponding to the minimal total energy per primitive cell. The nuclear motion can be studied *a posteriori*, by considering the electronic energy surface as an external potential. Quantum chemistry of solids concerns mainly those physical and chemical properties of solids that depend on the electronic structure. The problem of nuclear motion is solved in approaches using molecular-dynamics methods [26]. These approaches (not considered in this book) allow the study of thermodynamic and transport properties of solids and deserve a separate monograph. The calculations of the electronic subsystem in the adiabatic approximation are always connected with the choice of the electronic Hamiltonian. Formally, the symmetry of the electronic Hamiltonian may differ from the symmetry of the nuclear configuration. However, in the case of crystalline solids the approximate electronic Hamiltonians are usually chosen in such a way that the translational and point symmetry of a crystal is maintained. In Chapters 4–6 we consider in more detail two of the mostly popular approximate methods of many-electron systems description – Hartree–Fock method and the density-functional theory. In both approaches the approximate many-electron function is introduced in such a way that the electron subsystem calculations are made for one-electron wavefunctions. The latter are known as molecular orbitals in molecules and crystalline orbitals in crystals. The symmetry of the electronic Hamiltonian ensures that orbitals (one-electron functions for many-electron systems) transform according to the irreducible representations of point groups for molecules and space groups for crystals.

Let the wavefunction  $\varphi(\mathbf{r})$  depend on the coordinates of only one electron,  $\hat{H}$  is a Hamiltonian operator and  $E$  the energy of the eigenstate  $\varphi(\mathbf{r})$ . The function  $\varphi(\mathbf{r})$  satisfies the time-independent equation

$$\hat{H}(\mathbf{r})\varphi(\mathbf{r}) = E\varphi(\mathbf{r}) \quad (3.1)$$

The transformation  $g$  is said to be a symmetry operation of the Hamiltonian  $\hat{H}$  if  $\hat{H}(g^{-1}\mathbf{r}) = \hat{H}(g\mathbf{r})$ , *i.e.* if  $\hat{H}$  is invariant under  $g$ . Symmetry operations  $g$  that leave  $\hat{H}$  invariant form a group. This group is called the symmetry group of the Hamiltonian or of the Schrodinger equation (3.1).

We introduce in the linear vector space  $L$  of functions  $\varphi(\mathbf{r})$  the operators  $\hat{g} = \hat{D}(g)$  as

$$\hat{D}(g)\varphi(\mathbf{r}) = \hat{g}\varphi(\mathbf{r}) = \varphi(g^{-1}\mathbf{r}) \quad (3.2)$$

The operators  $\hat{g}$  are linear and the correspondence  $g \rightarrow \hat{g}$  is preserved in the composition law:

$$\hat{g}_2\hat{g}_1\varphi(\mathbf{r}) = \hat{g}_2\varphi(g_1^{-1}\mathbf{r}) = \varphi(g_1^{-1}g_2^{-1}\mathbf{r}) = \varphi((g_2g_1)^{-1}\mathbf{r}) \quad (3.3)$$

Hence, the set of operators  $\hat{D}(g) = \hat{g}(g \in G)$  is a rep of  $G$  and  $L$  is the space of this rep. If  $g \in G$  is a symmetry operation of the Hamiltonian operator  $\hat{H}$  then

$$\hat{H}(\mathbf{r})\hat{g}\varphi(\mathbf{r}) = \hat{H}(\mathbf{r})\varphi(g^{-1}\mathbf{r}) = E\varphi(g^{-1}\mathbf{r}) = \hat{g}E\varphi(\mathbf{r}) = \hat{g}\hat{H}\varphi(\mathbf{r}) \quad (3.4)$$

This relation holds for any eigenfunction of  $\hat{H}$  and for all linear combinations of the eigenfunctions, *i.e.* for any function in the linear vector space  $L$ . Therefore, the following operator relation may be written:

$$\hat{g}\hat{H} = \hat{H}\hat{g}, \quad \hat{D}(g)\hat{H} = \hat{H}\hat{D}(g), \quad g \in G \quad (3.5)$$

This expresses in mathematical form the symmetry properties of the Hamiltonian of a quantum mechanical system.

We choose in the space  $L$  a symmetry-adapted basis  $\varphi_{i\mu}^\alpha(\mathbf{r})$ , where the index  $i = 1, 2, \dots, n$  labels the basis functions of the irrep  $\alpha$  and the index  $\mu$  distinguishes independent basis functions of equivalent irreps. The matrices of the operators  $\hat{D}(g)$  have in this basis a quasidiagonal structure

$$D_{i\alpha\mu;j\beta\nu}(g) = D_{ij}^{(\alpha)}\delta_{\alpha\beta}\delta_{\mu\nu} \quad (3.6)$$

We write the operator relation (3.5) in the chosen basis using the quasidiagonal form (3.6) of matrices

$$\sum_{i'} H_{i\alpha\mu,i'\beta\nu} D_{i'j}^{(\beta)}(g) = \sum_{i'} D_{ii'}^{(\alpha)}(g) H_{i'\alpha\mu,j\beta\nu} \quad (3.7)$$

or

$$H_{\alpha\mu,\beta\nu} D^{(\beta)}(g) = D^{(\alpha)}(g) H_{\alpha\mu,\beta\nu} \quad (3.8)$$

where the notation  $H_{\alpha\mu,\beta\nu}$  is introduced for matrices with matrix elements  $(H_{\alpha\mu,\beta\nu})_{ii'} = H_{i\alpha\mu,i'\beta\nu}$ .

In accordance with Schur's Lemmas for irreducible representations

$$H_{\alpha\mu,\beta\nu} = H_{\mu\nu}^{(\alpha)} E \text{ for } \beta = \alpha \quad (3.9)$$

and

$$H_{\alpha\mu,\beta\nu} = 0 \text{ for } \beta \neq \alpha \quad (3.10)$$

where  $E$  is an  $n_\alpha \times n_\alpha$  unit matrix. Hence, in the symmetry-adapted basis the matrix  $H$  of the Hamiltonian has quasidiagonal structure (Wigner's theorem)

$$H_{i\alpha\mu,j\beta\nu} = H_{\mu\nu}^{(\alpha)} \delta_{ij} \delta_{\alpha\beta} \quad (3.11)$$

The block  $H^{(\alpha)}$  is composed of matrix elements

$$H_{\mu\nu}^{(\alpha)} = \int (\varphi_{i\mu}^\alpha(\mathbf{r}))^* \hat{H} \varphi_{i\nu}^\alpha(\mathbf{r}) d\mathbf{r} \quad (3.12)$$

does not depend on the index  $i = 1, 2, \dots, n_\alpha$  and is repeated  $n_\alpha$  times in the matrix  $H$  of the Hamiltonian  $\hat{H}$ .

In the symmetry-adapted basis the diagonalizing of the matrix  $H$  is reduced to the diagonalizing of its diagonal blocks. Every eigenvalue of the matrix  $H^{(\alpha)}$  is repeated  $n_\alpha$  times in the total list of the eigenvalues of the operator  $\hat{H}$ . From the above discussion it also follows that the eigenfunctions of the Hamiltonian  $\hat{H}$  corresponding to the same eigenvalue are the basis functions of an irrep of the symmetry group  $G$  of  $\hat{H}$  (in the absence of accidental degeneracy that is not due to the symmetry) and the degeneracies of eigenvalues are equal to dimensions of the irreps of  $G$  (also in the absence of accidental degeneracy). Thus, the eigenstates  $\varphi(\mathbf{r})$  and their eigenvalues may be labeled by the irreps of the symmetry group  $G$  of the Hamiltonian  $\hat{H}$ .

The symmetry properties of molecular orbitals and the degeneracy of the corresponding eigenvalues are defined by the irreducible representations of the point groups. The tables of these irreps characters are published in many books [13, 27] and their notations are well known and as a rule unambiguous. The energy-level degeneracy is usually 1 (a, b irreps), 2 (e irreps) and 3 (t irreps). As an exclusion, the icosahedral point symmetry group of the fullerene molecule  $C_{60}$  has 4- and 5-dimensional representations (g and h irreps, respectively). The first-principles LCAO calculations of the molecular systems are usually made directly without the application of the Wigner theorem, the symmetry of molecular orbitals is used mainly for their classification and interpretation of the results obtained. However for a large number of basis functions the diagonalizing of the matrix  $H$  becomes difficult, time-consuming work. Use of a symmetry-adapted basis in such a case can be useful even for molecular systems.

For crystalline solids the translation symmetry of the Hamiltonian is taken into account in any electronic-structure calculations as it allows calculations to be made for the basis connected only with the primitive unit cell. In the translation-symmetry-adapted basis the matrix  $H$  has a quasidiagonal structure with identical blocks related to an irrep  $\mathbf{k}$  of the translation symmetry group  $T$ . As the latter is Abelian its irreps are one-dimensional. The translation symmetry adapted functions are known as Bloch functions and numbered by wavevector  $\mathbf{k}$ . Use of the point symmetry of a crystal allows the number of Bloch functions calculated to be decreased and further block-diagonalization of Hamiltonian of a crystal to be made.

The space symmetry of crystalline orbitals is defined by irreducible representations of space groups. As will be shown in the next sections the structure of these irreps is

more complicated than in the case of point groups. The dimensions of the space-group irreps and the corresponding degeneracy of energy levels are also different from those for point groups. In versions CRYSTASL-98,03,06 computer codes the automatic full space group symmetry adaptation of LCAO is included [28]. It is particularly efficient for crystals with high symmetry containing many atoms in the primitive unit cell, for example, a cubic crystal of pyrope with 80 atoms in the cell [29].

The time-reversal symmetry of the crystalline Hamiltonian introduces an additional energy-level degeneracy. Let the Hamiltonian operator  $\hat{H}$  be real. The transition in the time-dependent Schrodinger equation to a complex-conjugate equation with simultaneous time-inversion substitution

$$i \frac{\partial \varphi(\mathbf{r}, t)}{\partial t} = \hat{H}\varphi(\mathbf{r}, t), \quad i \frac{\partial \varphi^*(\mathbf{r}, -t)}{\partial t} = \hat{H}\varphi^*(\mathbf{r}, -t) \quad (3.13)$$

shows that the functions  $\varphi(\mathbf{r}, t)$  and  $\varphi^*(\mathbf{r}, -t)$  are solutions of the same time-dependent Schrodinger equation. This combined operation (complex conjugation + time inversion) is called the time-reversal transformation. Applying this operation to the time-independent Schrödinger equation for the time-independent part of stationary-state wavefunctions

$$\hat{H}\varphi(\mathbf{r}) = E\varphi(\mathbf{r}), \quad \hat{H}\varphi^*(\mathbf{r}) = E\varphi^*(\mathbf{r}) \quad (3.14)$$

we see that  $\varphi(\mathbf{r})$  and  $\varphi^*(\mathbf{r})$  are the eigenfunctions of the same real operator  $\hat{H}$  belonging to the same eigenvalue  $E$ . So with respect to the time-independent part of stationary states  $\varphi(\mathbf{r})$  the time-reversal operator reduces to a simple complex conjugation

$$\hat{K}\varphi(\mathbf{r}) = \varphi^*(\mathbf{r}) \quad (3.15)$$

Let  $\varphi_i$  ( $i = 1, 2, \dots, n$ ) be eigenfunctions of a real Hamiltonian  $\hat{H}$  belonging to an eigenvalue  $E$  and also be the basis of a unitary irrep  $D(g)$  of its symmetry group  $G$  ( $g \in G$ ). The functions  $\hat{K}\varphi_i = \varphi_i^*$  are also eigenfunctions of  $\hat{H}$  belonging to the same eigenvalue  $E$ , but transforming according to the irrep  $D^*(g)$  [13]. The irreps  $D(g)$  and  $D^*(g)$  may be either equivalent or inequivalent. The functions  $\varphi_i$  and  $\varphi_i^*$  may be linearly dependent or linearly independent. There are three cases: 1) the functions  $\varphi_i$  and  $\varphi_i^*$  are linearly dependent and are bases of equivalent irreps; 2) the functions  $\varphi_i$  and  $\varphi_i^*$  are linearly independent and transform according to inequivalent irreps; 3) the functions  $\varphi_i$  and  $\varphi_i^*$  are linearly independent and are bases of equivalent irreps. In cases 2 and 3 the eigenvalue  $E$  belongs to  $2n$  states  $\varphi_i$  and  $\varphi_i^*$ . They form a basis of the rep of the group  $G$  that is the sum of two irreps  $D(g)$  and  $D^*(g)$  of the same dimension  $n$ . Thus, the degeneracy of the eigenvalue  $E$  doubles with respect to that caused by the symmetry group in the space. In case 1, there is no additional degeneracy. In tables of irreps of space groups the complex conjugate irreps are usually united in one so-called physically irreducible rep. When analyzing the degeneracy of one-electron energy levels in crystals it is necessary to take into account the time-reversal symmetry. In particular, even in the case when the point-symmetry group  $F$  of a crystal does not include inversion the complex conjugated crystalline orbitals with wavevectors  $\mathbf{k}$  and  $-\mathbf{k}$  correspond to the same energy eigenvalue.

### 3.1.2 Irreducible Representations of Translation Group. Brillouin Zone

The group  $T$  of pure translations  $t_{\mathbf{a}}$  of an infinite lattice is a group of infinite order. By introducing cyclic boundary conditions one assumes that the infinite crystal consists of equivalent blocks in the form of parallelepipeds having sides  $\mathbf{A}_1 = N_1 \mathbf{a}_1, \mathbf{A}_2 = N_2 \mathbf{a}_2, \mathbf{A}_3 = N_3 \mathbf{a}_3$ . It is assumed that the points of different blocks connected by translations are physically equivalent, *i.e.*  $t_{\mathbf{A}_j}^{N_j} = \mathbf{t}_0$ . The large positive number  $N = N_1 N_2 N_3$  defines the size of each block, also called the main region of a crystal (this block contains  $N$  primitive unit cells in the cyclic model of a crystal). Only the finite-order group  $T^{(N)}$  (modulo translations  $\mathbf{A}_1, \mathbf{A}_2, \mathbf{A}_3$ ) of  $N$  translations  $\mathbf{a}_n = \sum_{i=1}^3 n_i \mathbf{a}_i$  inside the main region is considered when generating the irreps of the translation group. Because this group is Abelian all its irreps are one-dimensional. Moreover, the group  $T^{(N)}$  is a direct product of groups  $T^{(N_1)}, T^{(N_2)}$  and  $T^{(N_3)}$ , as all the translations  $t_{\mathbf{a}_n}$  commute. Each group  $T^{(N_i)}$  of  $N_i$  translations  $t_{n_i \mathbf{a}_i}$  has  $N_i$  one-dimensional irreps  $D^j(t_{n_i \mathbf{a}_i}), j = 1, 2, \dots, N_i$ , satisfying the condition  $[D^j(t_{\mathbf{a}_n})]^{N_j} = D^j(t_{N_j \mathbf{a}_n}) = D^j(\mathbf{t}_0) = 1$ . Taking  $D^j(t_{\mathbf{a}_i}) = \exp(-2\pi i p_j/N_j)$  (where  $p_j$  is an integer) one satisfies this condition. The integer  $p_j = 0, 1, \dots, N_j - 1 (i = 1, 2, 3)$  denotes different irreps of the translation group  $T^{(N_i)}$ . The irrep  $D^{(p_1 p_2 p_3)}(t_{\mathbf{a}_n})$  of the translation group  $T^{(N)}$  can be written as

$$D^{(p_1 p_2 p_3)}(t_{\mathbf{a}_n}) = \exp[-2\pi i(p_1 n_1/N_1 + p_2 n_2/N_2 + p_3 n_3/N_3)] \quad (3.16)$$

There are  $N = N_1 N_2 N_3$  sets of integers  $p_1, p_2, p_3$  ( $p_i = 0, 1, \dots, N_i - 1$ ) that are used to label  $N$  different irreps of the translation group  $T^{(N)}$ .

Introducing the primitive translation vectors  $\mathbf{B}_1, \mathbf{B}_2, \mathbf{B}_3$  of the reciprocal lattice by

$$(\mathbf{a}_i \cdot \mathbf{B}_j) = 2\pi \delta_{ij}, \quad (i, j = 1, 2, 3) \quad (3.17)$$

one may define allowed  $\mathbf{k}$  vectors (wavevectors) by  $\mathbf{k} = \kappa_1 \mathbf{B}_1 + \kappa_2 \mathbf{B}_2 + \kappa_3 \mathbf{B}_3$ , where  $\kappa_i = p_i/N_i (i = 1, 2, 3)$ . Thus

$$(\mathbf{k} \cdot \mathbf{a}_n) = 2\pi(n_1 p_1/N_1 + n_2 p_2/N_2 + n_3 p_3/N_3) \quad (3.18)$$

so that

$$D^{(\mathbf{k})}(t_{\mathbf{a}_n}) = \exp(-i\mathbf{k} \cdot \mathbf{a}_n) \quad (3.19)$$

The  $N$  irreps of  $T^{(N)}$  are now labeled by the  $N$  allowed  $\mathbf{k}$  vectors. The point symmetry of reciprocal lattice coincides with that of the direct one. However, the type of reciprocal lattice may differ from that of the direct lattice.

Adding the reciprocal lattice vector

$$\mathbf{B}_m = \sum_i m_i \mathbf{B}_i \quad (3.20)$$

to the allowed  $\mathbf{k}$  vector we have

$$\begin{aligned} \exp(-i(\mathbf{k} + \mathbf{B}_m) \cdot \mathbf{a}_n) &= \exp(-i\mathbf{k} \cdot \mathbf{a}_n) \exp(-i\mathbf{B}_m \cdot \mathbf{a}_n) \\ &= \exp(-i\mathbf{k} \cdot \mathbf{a}_n) \end{aligned} \quad (3.21)$$

A pair of vectors  $\mathbf{k}$  and  $\mathbf{k}' = \mathbf{k} + \mathbf{B}_m$  is said to be equivalent since the irrep of  $T^{(N)}$  described by  $\mathbf{k}$  can be equally well described by  $\mathbf{k}'$ . Therefore, the label  $\mathbf{k}$  is

determined up to within a reciprocal lattice vector and can be changed by vectors  $\mathbf{B}_m$  of the reciprocal lattice.

The basis functions for the irreps of the translation group  $T^{(N)}$  are known as Bloch functions  $\varphi(\mathbf{k}, \mathbf{r})$  and may be written in the form

$$\varphi(\mathbf{k}, \mathbf{r}) = \exp(i\mathbf{k} \cdot \mathbf{r})U(\mathbf{k}, \mathbf{r}) \quad (3.22)$$

where  $U(\mathbf{k}, \mathbf{r}) = U(\mathbf{k}, \mathbf{r} + \mathbf{a}_n)$ . Indeed

$$\begin{aligned} t_n \varphi(\mathbf{k}, \mathbf{r}) &= \exp(-i\mathbf{k} \cdot \mathbf{a}_n) \exp(i\mathbf{k} \cdot \mathbf{r})U(\mathbf{k}, \mathbf{r} - \mathbf{a}_n) \\ &= \exp(-i\mathbf{k} \cdot \mathbf{a}_n)\varphi(\mathbf{k}, \mathbf{r}). \end{aligned} \quad (3.23)$$

The Bloch functions are also called the  $\mathbf{k}$  basis.

Applying a space group operator  $g \equiv t_v R (g \in G)$  to the Bloch function  $\varphi(\mathbf{k}, \mathbf{r})$  we obtain a Bloch function  $\tilde{\varphi}(\mathbf{k}, \mathbf{r})$ . Indeed

$$\begin{aligned} t_{\mathbf{a}_n} t_v R \varphi(\mathbf{k}, \mathbf{r}) &= t_v R t_{R^{-1}\mathbf{a}_n} \varphi(\mathbf{k}, \mathbf{r}) \\ &= \exp(-i\mathbf{k} \cdot R^{-1}\mathbf{a}_n) t_v R \varphi(\mathbf{k}, \mathbf{r}) \\ &= \exp(-iR\mathbf{k} \cdot \mathbf{a}_n) t_v R \varphi(\mathbf{k}, \mathbf{r}) \end{aligned} \quad (3.24)$$

i.e.

$$t_v R \varphi(\mathbf{k}, \mathbf{r}) = \tilde{\varphi}(R\mathbf{k}, \mathbf{r}) \quad (3.25)$$

As follows from (3.21) from the point of view of determining all the irreducible representations of a space group it is only necessary to consider the wavevectors in one unit cell of reciprocal space ( $\mathbf{k}$  space) and the unit cell that is chosen is referred to as the first Brillouin zone (BZ). For most space groups it is not a primitive unit cell in  $\mathbf{k}$  space. Instead, the unit cell of  $\mathbf{k}$  space is the Wigner–Seitz unit cell. The latter is defined as consisting of all those points of  $\mathbf{k}$  space that lie closer to  $\mathbf{k} = \mathbf{0}$  than to any other reciprocal lattice point. Its boundaries are therefore the planes that are the perpendicular bisectors of the lines joining the point  $\mathbf{k} = \mathbf{0}$  to the nearest and sometimes to the next-nearest reciprocal lattice nodes (the planes bisecting the line from  $\mathbf{k} = \mathbf{0}$  to  $\mathbf{k} = \mathbf{B}_m$  have the equation  $\mathbf{k}\mathbf{B}_m = |\mathbf{B}_m|^2/2$ ). For some direct lattices (simple cubic, for example, see Fig. 3.1) only nearest-neighbor reciprocal lattice points are involved in the construction of the Brillouin zone but for others (face-centered cubic for example, see Fig. 3.2) next-nearest neighbors are involved as well.

The advantage of this choice is that the Wigner–Seitz unit cell manifests the point-group symmetry  $F^0$  of the appropriate crystal system. The disadvantage is that for certain Bravais lattices the appearance of BZ may be different for different values of lattice parameters. For all Bravais lattices except those of extremely low symmetry the advantage of this definition outweighs the disadvantage [17]. For monoclinic and triclinic space groups the problem of drawing of Brillouin zones for all possible relative values of lattice parameters is so complicated that the primitive unit cell of the reciprocal lattice is used for the Brillouin zone. In [30] one can find Brillouin zones representations for all the Bravais lattices and for each set of possible restrictions on the lattice parameters. For cubic, hexagonal, simple tetragonal and simple orthorhombic lattices the shape of the Brillouin zone is unique, while for trigonal, body-centered tetragonal, body-, base- and face-centered orthorhombic lattices there are two or more

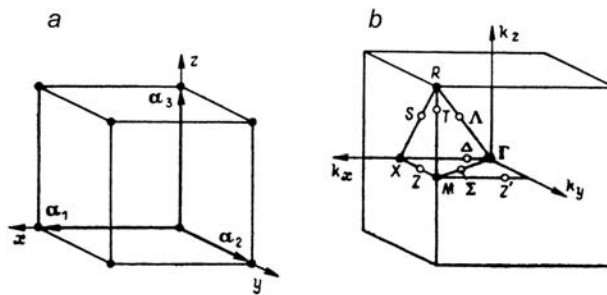


Fig. 3.1. Primitive unit cell and Brillouin zone for simple cubic lattice

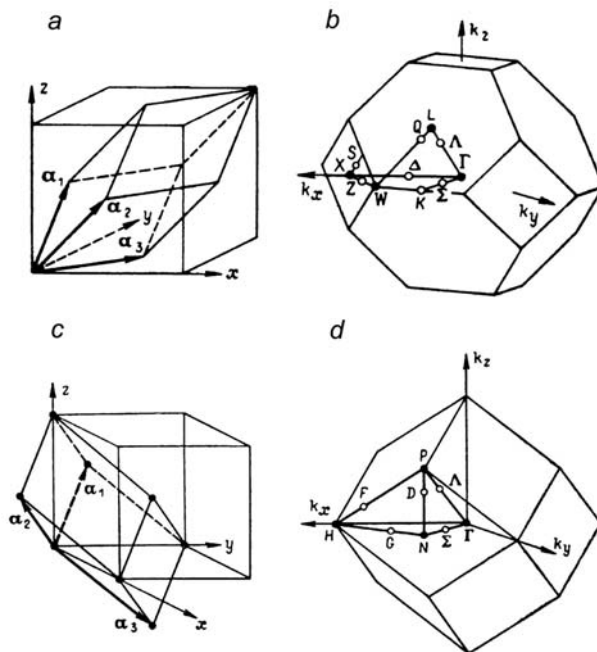
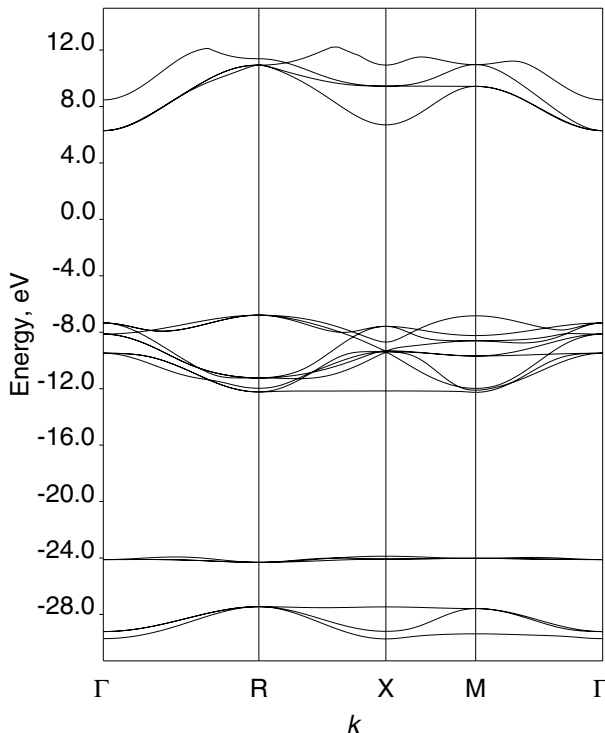


Fig. 3.2. Primitive unit cells (a, c) and Brillouin zones (b, d) for face-centered and body-centered cubic lattices

possible shapes depending on the relative lengths of the primitive translations and the angles between them.

By construction, the BZ contains  $N$  allowed  $\mathbf{k}$  vectors when  $N$  primitive unit cells are included in the main region of a crystal. As the number  $N$  is assumed to be arbitrarily large, in the limiting case of  $N = \infty$  the allowed  $\mathbf{k}$  vectors take all values inside the BZ. In the electronic-structure calculations of crystals finite (and relatively small) numbers of  $\mathbf{k}$  points are considered. However, the interpolation procedure used after calculation allows the one-electron energies to be shown as continuous functions of wavevectors (see, for example, Figures 3.3 – 3.5 for band structures of  $\text{SrZrO}_3$ ,  $\text{MgO}$  and  $\text{Si}$  crystals, respectively).



**Fig. 3.3.** Hartree–Fock energy bands for  $\text{SrZrO}_3$  crystal

Two vectors  $\mathbf{k}$  and  $\mathbf{k}'$  are said to be equivalent if  $\mathbf{k}' = \mathbf{k} + \mathbf{B}_m$ . By definition, no two interior points of a Brillouin zone can be equivalent; but every point on the surface of the Brillouin zone has at least one equivalent also on the surface of the Brillouin zone. For each BZ there is a basic domain  $\Omega$  such that  $\sum_R R\Omega$  is equal to the whole BZ, where  $R$  are the elements of the holosymmetric point group  $F^0$  ( $F^0$  is the point-symmetry group of the Bravais lattice and defines the appropriate crystal system).

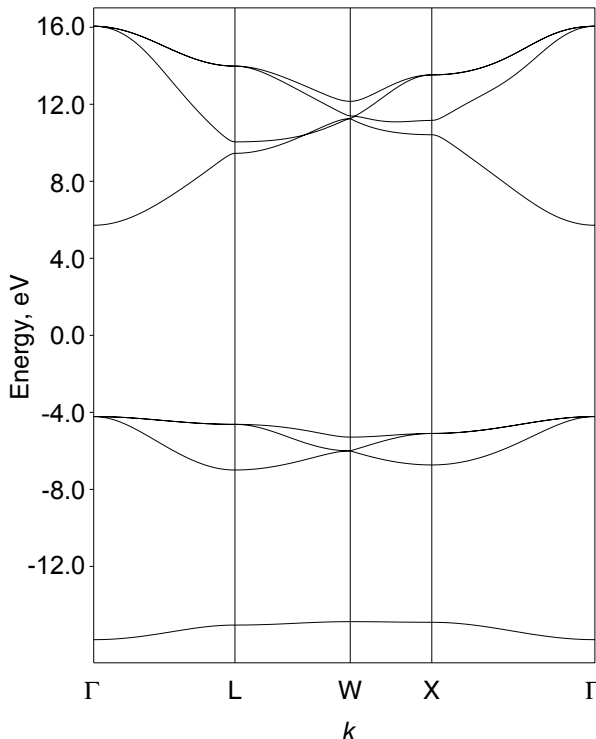


Fig. 3.4. Hartree-Fock energy bands for MgO crystal

For each space group there is a representation domain  $\Phi$  of the appropriate BZ (it is also called the irreducible part of the Brillouin zone), such that  $\sum_R R\Phi$  is equal to the whole BZ, where the sum over  $R$  runs through the elements of the point-symmetry group  $F \subseteq F^0$  ( $F$  is also called the isogonal point group and is obtained by taking all the distinct elements  $R$  that are found in the elements  $t_v R$  of space group  $G$ ). For each holosymmetric space group (for which the set of all the distinct rotational parts of the space-group symmetry operations forms the holosymmetric point group  $F^0$  of the appropriate crystal system)  $\Phi$  can be taken to be identical with  $\Omega$ . But for the remaining space groups the volume of  $\Phi$  is some small-integer multiple of the volume of  $\Omega$ . This multiple is equal to  $n_{F^0}/n_F$ , *i.e.* is defined by orders  $n_{F^0}$  and  $n_F$  of the holosymmetric point group  $n_{F^0}$  and crystal structure point group  $F$ . The majority of crystal structures considered in Sect. 2.3 have holosymmetric point groups. The exclusions refer to the structures of sphalerite and wurtzite with point groups  $T_d$  and  $C_{6v}$  being subgroups of cubic and hexagonal lattices point groups  $O_h$  and  $D_{6h}$ . In two cases under consideration (BZ for face-centered and hexagonal lattices, Figures 3.2 and 3.6) the basic domain volumes are equal to  $1/48$  and  $1/24$  of the Brillouin-zone volume, the representation domains are two times larger.

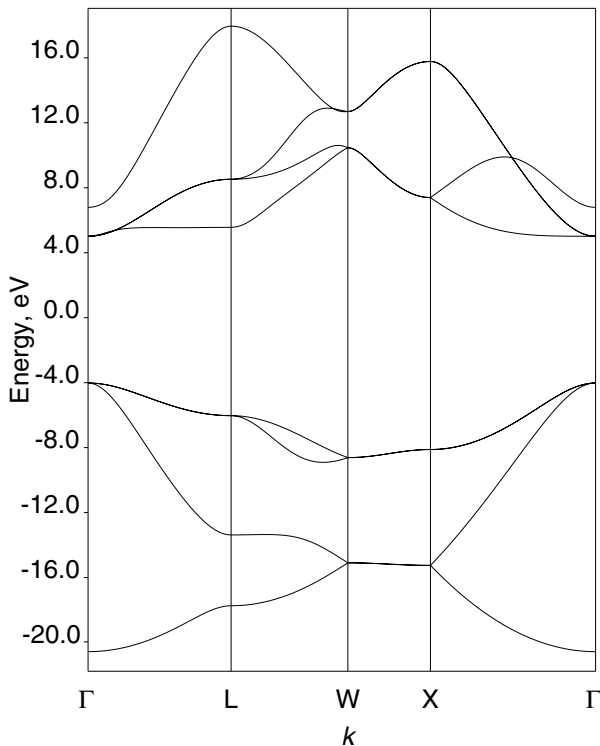


Fig. 3.5. Hartree-Fock energy bands for silicon crystal

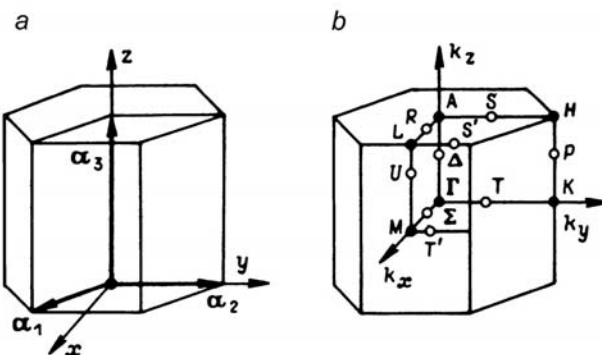


Fig. 3.6. Primitive unit cell and Brillouin zone for hexagonal lattice

Those elements of the point-symmetry group  $F^0$  of the reciprocal lattice that transform a point  $\mathbf{k}$  into itself or into some equivalent  $\mathbf{k}$  point form the wavevector point-symmetry group  $F_{\mathbf{k}} \subset F^0$ . For example, for the direct face-centered cubic lattice ( $F^0 = O_h$ ) BZ points  $\Gamma(0,0,0)$ ,  $X(1/2,1/2,0)$ ,  $L(1/2,1/2,1/2)$ ,  $W(1/4,1/2,3/4)$  (see Fig. 3.2) have point symmetry groups  $O_h$ ,  $D_{4h}$ ,  $D_{3d}$ ,  $D_{2d}$ , respectively. The point group  $F_{\mathbf{k}}$  of the  $\mathbf{k}$  vectors  $F, Z, M, A$  (Fig. 3.7) for a simple tetragonal lattice coincides with the  $D_{4h}$  point group of the tetragonal lattice itself; the point group  $D_{2h}$  of the  $\mathbf{k}$  vectors  $X$  and  $R$  is a subgroup of  $D_{4h}$ .

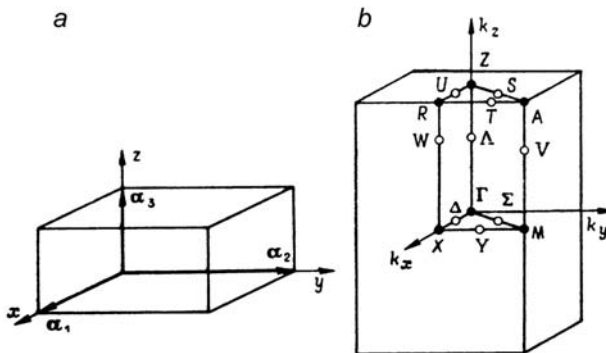


Fig. 3.7. Primitive unit cell and Brillouin zone for simple tetragonal lattice

All the mentioned points of the BZ are called points of symmetry. By definition,  $\mathbf{k}$  is a point of symmetry if there exists a neighborhood of  $\mathbf{k}$  in which no point  $\mathbf{k}'$  has the same symmetry group  $F_{\mathbf{k}}$  and  $F_{\mathbf{k}'} \subset F_{\mathbf{k}}$ . The  $\Gamma(\mathbf{k} = \mathbf{0})$  point of the Brillouin zone is usually a symmetry point; exceptions here are the space groups of the crystallographic classes  $C_s, C_{nv}, C_n$ . All the other symmetry points are situated on the surface of the Brillouin zone and are usually denoted in a more or less unique way by capital Roman letters as in Fig. 3.7 for a simple tetragonal lattice. Kovalev [31], however, used ordinal numbers to denote  $\mathbf{k}$  vectors.

If, in any sufficiently small neighborhood of  $\mathbf{k}$ , there is a line (plane) of points passing through  $\mathbf{k}$  and having the same point group  $F_{\mathbf{k}}$  then  $\mathbf{k}$  is said to be on a line (plane) of symmetry. The lines of symmetry are denoted both by Roman (on the surface of the Brillouin zone) and Greek (inside the Brillouin zone) capital letters. A symmetry line may be denoted by two symmetry points at the ends of this line:  $\Lambda - \Gamma L(C_{3v})$ ,  $\Sigma - \Gamma M(C_{2v})$ ,  $\Delta - \Gamma X(C_{2v})$  (Fig. 3.2a); the corresponding  $F_{\mathbf{k}}$  groups are in parentheses. It is evident that the point groups  $C_{2v}$  of different wavevectors, being isomorphic to each other, do not coincide for all symmetry lines. For example, the second-order symmetry axis  $C_2$  is along the  $X$ -coordinate axis for the  $\Gamma X$  line and along the  $XY$  symmetry axis for the  $\Gamma M$  line.

Tables 3.1, 3.2 and 3.3 of  $\mathbf{k}$  vector types for BZ symmetry points and symmetry lines (space groups 221, 225 and 136) are taken from the site [16]. In fact, for all the space groups referring to the same crystal class and the same lattice type the  $\mathbf{k}$  vector

types are the same (groups 221 – 224 with simple cubic lattice, groups 225 – 228 with face-centered cubic lattice and groups 123 – 138 for a simple tetragonal lattice). This follows from the fact that in reciprocal space only the point-symmetry operations  $R$  transform the  $\mathbf{k}$  vectors. In the space-group sets mentioned the difference in symmetry operations appears only in the direct lattice where the improper translations are different. The columns labeled CDML and ITA in Tables 3.1–3.3 mean the  $\mathbf{k}$  points notations used in [17] (accepted in solid-state theory) and in [16] as Wyckoff positions of the reciprocal lattice space group. The latter notations are practically not used as the  $\mathbf{k}$  points labels. In the next section we discuss the generation of the space-group irreps from those of translation group.

**Table 3.1.** The  $\mathbf{k}$ -vector types of group 221 [Pm $\bar{3}$ m] (Table for arithmetic crystal class m $\bar{3}$ mP, Pm $\bar{3}$ m- $O_h^1$  (221) to Pn $\bar{3}$ m- $O_h^4$  (224)). Reciprocal-space group (Pm $\bar{3}$ m)- $O_h^1$  (221)

k-vector label	Wyckoff position			Parameters
	CDML		ITA	
$\Gamma$ 0,0,0	1	a	m $\bar{3}$ m	0,0,0
R 1/2,1/2,1/2	1	b	m $\bar{3}$ m	1/2,1/2,1/2
M 1/2,1/2,0	3	c	4/mm.m	1/2,1/2,0
X 0,1/2,0	3	d	4/mm.m	0,1/2,0
$\Delta$ 0,u,0	6	e	4m.m	0,y,0 : 0 < y < 1/2
T 1/2,1/2,u	6	f	4m.m	1/2,1/2,z : 0 < z < 1/2
$\Lambda$ u,u,u	8	g	.3m	x,x,x : 0 < x < 1/2
Z u,1/2,0	12	h	mm2..	x,1/2,0 : 0 < x < 1/2
$\Sigma$ u,u,0	12	i	m.m2	x,x,0 : 0 < x < 1/2
S u,1/2,u	12	j	m.m2	x,1/2,x : 0 < x < 1/2

### 3.1.3 Stars of Wavevectors. Little Groups. Full Representations of Space Groups

The representation theory of space groups uses a theorem that the translation group  $T$  is an invariant subgroup of  $G$  ( $T \triangleleft G$  see Sect. 2.1.2). Therefore, the little-group method [13] may be used for the generation of irreps of space group  $G$  from irreps of translation subgroup  $T$ . As was shown in Sect. 3.1.2, the one-dimensional irreps of translation group  $T$  transform under point-symmetry operations  $R$  of space group  $G$  according to relation (3.25) *i.e.* the Bloch function with wave vector  $\mathbf{k}$  transforms to a Bloch function with wavevector  $R\mathbf{k}$ .

Let us suppose that  $D(g)$  is an irrep of  $G$  acting in a space  $L$  of dimension  $n$ . The operators  $D(g)$  for  $g = t_a \in T$  form a rep of  $T$  that is in general reducible. Let it contain irreps of  $T$  characterized by the vectors  $\mathbf{k} = \mathbf{k}_1, \mathbf{k}_2, \dots, \mathbf{k}_n$ . Therefore a basis can be found in space  $L$  that consists of Bloch functions  $\varphi(\mathbf{k}_1, \mathbf{r}), \dots, \varphi(\mathbf{k}_n, \mathbf{r})$ . With respect to this basis, the elements of  $T$  are represented in the irrep  $D(g)$  by diagonal matrices with elements  $\exp(-i\mathbf{k}_p \cdot \mathbf{a})$ ,  $p = 1, 2, \dots, n$ . The fact that  $D(g)$  is a rep of  $G$  implies that if we start with  $\varphi(\mathbf{k}, \mathbf{r})$  and generate the Bloch functions

**Table 3.2.** The  $\mathbf{k}$ -vector types of group 225 [Fm $\bar{3}$ m] (Table for arithmetic crystal class m $\bar{3}$ mF, Fm $\bar{3}$ m- $O_h^5$ (225) to Fd $\bar{3}$ c- $O_h^8$ (228)). Reciprocal-space group (Im $\bar{3}$ m)- $O_h^9$ (229)

k-vector label		Wyckoff position			Parameters	
CDML		ITA			ITA	
$\Gamma$	0, 0, 0	2	a	m $\bar{3}$ m	0, 0, 0	
X	1/2, 0, 1/2	6	b	4/mm.m	0, 1/2, 0	
L	1/2, 1/2, 1/2	8	c	. $\bar{3}$ m	1/4, 1/4, 1/4	
W	1/2, 1/4, 3/4	12	d	$\bar{4}$ m.2	1/4, 1/2, 0	
$\Delta$	$u, 0, u$	12	e	4m.m	$x, 0, 0 : 0 < x < 1/2$	
$\Lambda$	$u, u, u$	16	f	.3m	$x, x, x : 0 < x < 1/4$	
V	$1/2, u, 1/2 + u$	24	g	mm2..	$x, 1/2, 0 : 0 < x < 1/4$	
$\Sigma$	$u, u, 2u$	24	h	m.m2	$x, x, 0 : 0 < x < 3/8$	
S	$1/2 + u, 2u, 1/2 + u$	24	h	m.m2	$x, 1/2, x : 0 < x < 1/8$	
$S \sim S_1$ [KM]		24	h	m.m2	$x, x, 0 : 3/8 < x < 1/2$	
SM + $S_1$ [GMM]		24	h	m.m2	$x, x, 0 : 0 < x < 1/2$	
Q	$1/2, 1/4 + u, 3/4 - u$	48	i	..2	$1/4, 1/2 - y, y : 0 < y < 1/4$	

**Table 3.3.** The  $\mathbf{k}$ -vector types of group 136 [P42/mmm] (Table for arithmetic crystal class 4/mmmP, P4/mmm- $D_{4h}^1$ (123) to P42/ncm- $D_{4h}^{16}$ (138)). Reciprocal-space group (P4/mmm)- $D_{4h}^1$ (123)

k-vector label		Wyckoff position			Parameters	
CDML		ITA			ITA	
$\Gamma$	0, 0, 0	1	a	4/mmm	0, 0, 0	
Z	0, 0, 1/2	1	b	4/mmm	0, 0, 1/2	
M	1/2, 1/2, 0	1	c	4/mmm	1/2, 1/2, 0	
A	1/2, 1/2, 1/2	1	d	4/mmm	1/2, 1/2, 1/2	
R	0, 1/2, 1/2	2	e	mmm.	0, 1/2, 1/2	
X	0, 1/2, 0	2	f	mmm.	0, 1/2, 0	
$\Delta$	$0, 0, u$	2	g	4mm	$0, 0, z : 0 < z < 1/2$	
V	$1/2, 1/2, u$	2	h	4mm	$1/2, 1/2, z : 0 < z < 1/2$	
W	$0, 1/2, u$	4	i	2mm.	$0, 1/2, z : 0 < z < 1/2$	
$\Sigma$	$u, u, 0$	4	j	m.2m	$x, x, 0 : 0 < x < 1/2$	
S	$u, u, 1/2$	4	k	m.2m	$x, x, 1/2 : 0 < x < 1/2$	
$\Delta$	$0, u, 0$	4	l	m2m.	$0, y, 0 : 0 < y < 1/2$	
U	$0, u, 1/2$	4	m	m2m.	$0, y, 1/2 : 0 < y < 1/2$	
Y	$u, 1/2, 0$	4	n	m2m.	$x, 1/2, 0 : 0 < x < 1/2$	
T	$u, 1/2, 1/2$	4	o	m2m.	$x, 1/2, 1/2 : 0 < x < 1/2$	

$t_{\mathbf{v}}R\varphi(\mathbf{k}, \mathbf{r}) = \tilde{\varphi}(R\mathbf{k}, \mathbf{r})$ , where  $t_{\mathbf{v}}R \in G$  then we obtain some linear combination of  $n$  Bloch functions of the initial basis. This means that  $R\mathbf{k}$  is one of the vectors  $\mathbf{k}, \mathbf{k}_2, \dots, \mathbf{k}_n$ .

In  $n$ -dimensional space  $L$  there are no nonzero subspaces invariant with respect to  $D(g)$  for all  $g \in G$ .

Therefore, as we run over all elements of  $G$  operating on  $\varphi(\mathbf{k}, \mathbf{r})$  by  $D(g)$ , we generate the entire space  $L$ , *i.e.* each of the vectors  $\mathbf{k}_1, \dots, \mathbf{k}_n$  appears as the transform of  $\mathbf{k}$  under some element of the point group  $F$  (point group of the space group  $G$ ). It may be that the vectors  $\mathbf{k}_1, \dots, \mathbf{k}_n$  are not all different. A set of  $n_s$  distinct (nonequivalent)  $k$  vectors chosen from the set  $\mathbf{k}_1, \dots, \mathbf{k}_n$  is called the star of wavevector  $\mathbf{k}$  and is denoted as  ${}^*\mathbf{k}$ . A star can be generated from one of its members by operating on it by elements of point group  $F$ . The  $\Gamma$  point of BZ forms one-ray star for any space group as it is a coordinate system origin for all the point-symmetry group  $F$  transformations in reciprocal space. The stars  ${}^*X$ ,  ${}^*L$  and  ${}^*W$  (see Fig. 3.2 of the Brillouin zone for the fcc direct lattice) consist of 3, 4 and 6 rays, respectively.

The point group of the wavevector  $\mathbf{k}$  (little cogroup of  $\mathbf{k}$ )  $F_{\mathbf{k}} \subseteq F$ , by definition, consists of all the rotations or reflections  $R\mathbf{k}$  ( $i = 1, 2, \dots, n_k$ ) that rotate  $\mathbf{k}$  into itself or an equivalent vector  $R\mathbf{k} = \mathbf{k} + \mathbf{B}_m$ .

In Sect. 3.1.2 points and lines of symmetry in the Brillouin zone were defined for the case when  $F = F^0$  (holosymmetric space groups, in particular  $O_h^5$  and  $D_{4h}^{14}$ ). In the same manner the points and lines of symmetry may be defined for the point group  $F \subseteq F^0$ . Then, instead of the basic domain of the Brillouin zone the representation domain is introduced.

We can write  $F$  as a sum of left cosets with respect to the subgroup  $F_{\mathbf{k}}$ :

$$F = \sum_{i=1}^{n_s} R_i F_{\mathbf{k}} \quad (3.26)$$

where  $n_s = n_F/n_{\mathbf{k}}$  is the number of  $\mathbf{k}$ -vectors in the star  ${}^*\mathbf{k}$ . If  $R_i \mathbf{k} = \mathbf{k}_i$  then all elements of the left coset  $R_i F_{\mathbf{k}}$  transform  $\mathbf{k}$  into  $\mathbf{k}_i$ .

By definition, the little group  $G_{\mathbf{k}}$  of wavevector  $\mathbf{k}$  consists of all elements  $g_j^{\mathbf{k}} = t_{\mathbf{v}_j^{(\mathbf{k})} + \mathbf{a}} R_j^{(\mathbf{k})}$ ,  $j = 1, 2, \dots, n_k$ , where  $R_j^{(\mathbf{k})} \in F_{\mathbf{k}}$ . The group  $G_{\mathbf{k}} \subseteq G$  is a space group of order  $N \cdot n_{\mathbf{k}}^j$  so that we can write  $G$  as a sum of left cosets with respect to the subgroup  $G_{\mathbf{k}}$ :

$$G = \sum_{j=1}^{n_s} g_j G_{\mathbf{k}}, \quad g_j = t_{\mathbf{v}_j} R_j \notin G_{\mathbf{k}} \quad (3.27)$$

Any element of coset  $g_j G_{\mathbf{k}}$  transforms a Bloch function  $\varphi(\mathbf{k}, \mathbf{r})$  into a Bloch function  $\varphi(\mathbf{k}_j, \mathbf{r})$ . Thus, if the vectors  $\mathbf{k}, \mathbf{k}_2, \dots, \mathbf{k}_n$  characterizing the rep  $D(g)$  of dimension  $n = n_{\alpha} n_s$  are not all unique, then the star  $\mathbf{k}, \mathbf{k}_2, \dots, \mathbf{k}_{n_s}$  is repeated exactly  $n_{\alpha}$  times in the set  $\mathbf{k}_1, \mathbf{k}_2, \dots, \mathbf{k}_n$ .

Let the basis set of space  $L^{(1)}$  be formed by Bloch functions  $\varphi_i^{(\alpha)}(\mathbf{k}, \mathbf{r})$ , ( $i = 1, 2, \dots, n_{\alpha}$ ).

These functions form a basis of the so-called small (allowed) irrep of the space group  $G_{\mathbf{k}}$ :

$$D(g)\varphi_i^{(\alpha)}(\mathbf{k}, \mathbf{r}) = \sum_{i=1}^{n_{\alpha}} D_{ii'}^{(\mathbf{k}, \alpha)}(g)\varphi_{i'}^{(\alpha)}(\mathbf{k}, \mathbf{r}), \quad g \in G_{\mathbf{k}} \quad (3.28)$$

The wavevector  $\mathbf{k}$  is called a canonical wavevector.

Not all the irreps of space group  $G_{\mathbf{k}}$  are small irreps of this group since the small irrep basis functions  $\varphi_i^{(\alpha)}(\mathbf{k}, \mathbf{r}), (i = 1, 2, \dots, n_{\alpha})$  have an additional property: they are Bloch functions with the same vector  $\mathbf{k}$ , *i.e.* the matrices of the small irrep are diagonal for the pure translations  $t_{\mathbf{a}}$  and have  $n_{\alpha}$  equal diagonal elements  $\exp(-i\mathbf{k}\cdot\mathbf{a})$ . The Bloch functions  $\varphi_i(\mathbf{k}_j, \mathbf{r}) = t_{\mathbf{v}_j} R_j \varphi_i(\mathbf{k}, \mathbf{r})$  form the basis set of irrep  $\mathbf{k}_j = R_j \mathbf{k}$  of the translation group  $T$ . The space group elements  $g^{(\mathbf{k}_j)} = g_j g^{(\mathbf{k})} g_j^{-1}$  form the group  $G_{\mathbf{k}}$  of the wavevector  $\mathbf{k}_j$ . The point group  $F_{\mathbf{k}}^j$  consists of elements  $R^{(\mathbf{k}_j)} = R_j R^{(\mathbf{k})} R_j^{-1}$ . The basis functions  $\varphi_i^{(\alpha)}(\mathbf{k}_j, \mathbf{r}), (i = 1, 2, \dots, n_{\alpha})$  of a space  $L^{(j)}$  transform over the irrep  $D^{(\mathbf{k}, \alpha)}(g_j^{-1} g^{(\mathbf{k}_j)} g_j)$

$$\begin{aligned} \hat{g}^{(\mathbf{k}_j)} \varphi_i(\mathbf{k}_j, \mathbf{r}) &= \hat{g}_j \hat{g}^{(\mathbf{k})} \varphi_i(\mathbf{k}, \mathbf{r}) = \sum_{i'} D_{ii'}^{(\mathbf{k}, \alpha)} \left( g^{(\mathbf{k})} \right) \varphi_{i'}(\mathbf{k}_j, \mathbf{r}) \\ &= \sum_{i'} D_{ii'}^{(\mathbf{k}, \alpha)} \left( g^{-1} g^{(\mathbf{k})} g_j \right) \varphi_{i'}(\mathbf{k}_j, \mathbf{r}) \end{aligned} \quad (3.29)$$

The space  $L = \sum_j L^{(j)}$  of  $n_s n_{\alpha}$  functions  $\varphi_i(\mathbf{k}_j, \mathbf{r}), (i = 1, \dots, n_{\alpha}, j = 1, \dots, n_s)$  is irreducible under  $G$ . These functions form a basis of the so-called full irrep  $D^{(*\mathbf{k}, \alpha)}(g)$  of the space group. The full irrep  $D^{(*\mathbf{k}, \alpha)}(g)$  of  $G$  is induced by the small irrep  $D^{(\mathbf{k}, \alpha)}(g)$  of the little group  $G_{\mathbf{k}} \subseteq G$ :  $D^{(*\mathbf{k}, \alpha)}(g) = D^{(\mathbf{k}, \alpha)}(g) \uparrow G$ ,

$$D_{i'j',ij}^{(*\mathbf{k}, \alpha)}(g) = D_{ii'}^{(\mathbf{k}, \alpha)} \left( g_{j'}^{-1} g g_j \right) \delta_{j'j} \quad (3.30)$$

The little group  $G_{\mathbf{k}}$  is itself a space group. The small irreps of  $G_{\mathbf{k}}$  can be found if projective irreps of the point group  $F_{\mathbf{k}}$  are known.

### 3.1.4 Small Representations of a Little Group. Projective Representations of Point Groups

The small reps of little groups are sufficient for many purposes in solid-state theory, such as classifying states within electron energy bands and vibration frequencies within phonon band spectra, and for generating the symmetry-adapted wavefunctions.

The little group  $G_{\mathbf{k}}$  is itself a space group. Whereas in the reps of  $G$  the translation  $t_{\mathbf{a}}$  is represented by a diagonal matrix, in the small irreps  $D^{(\mathbf{k}, \alpha)}$  of  $G_{\mathbf{k}}$  that we are looking for  $t_{\mathbf{a}}$  is represented by a scalar matrix

$$D^{(\mathbf{k}, \alpha)}(t_{\mathbf{a}}) = \exp(-i\mathbf{k} \cdot \mathbf{a}) E_{n_{k\alpha}} \quad (3.31)$$

where  $n_{k\alpha}$  is the dimension of the small irrep  $D^{(\mathbf{k}, \alpha)}$  and  $E_{n_{k\alpha}}$  is the unit matrix of order  $n_{k\alpha}$ .

We decompose  $G_{\mathbf{k}}$  into left cosets with respect to the translation group  $T$ :

$$G_{\mathbf{k}} = \sum_j g_j T, \quad g_j = t_{\mathbf{v}_j} R_j \quad (3.32)$$

The coset representatives in (3.32) obey the multiplication rule

$$t_{\mathbf{v}_i} R_i t_{\mathbf{v}_j} R_j = R_i R_j t_{\mathbf{v}_i + R_i \mathbf{v}_j} = t_{\mathbf{a}_{ij} + \mathbf{v}_s} R_s \quad (3.33)$$

where

$$t_{\mathbf{a}_{ij}} \in T \text{ and } \mathbf{a}_{ij} = \mathbf{v}_i + R_i \mathbf{v}_j - \mathbf{v}_s \quad (3.34)$$

Because  $\mathbf{a}_{ij}$  is a translation it follows that

$$D^{(\mathbf{k}, \alpha)}(g_i) D^{(\mathbf{k}, \alpha)}(g_j) = \exp(-i\mathbf{k} \cdot \mathbf{a}_{ij}) D^{(\mathbf{k}, \alpha)}(g_s) \quad (3.35)$$

If we now set for all  $g \in G_k$

$$D^{(\mathbf{k}, \alpha)}(g) = \exp(-i\mathbf{k} \cdot \mathbf{v}) \tilde{D}^{(\mathbf{k}, \alpha)}(R) \quad (3.36)$$

then from (3.35) we obtain

$$\tilde{D}^{(\mathbf{k}, \alpha)}(R_i) \tilde{D}^{(\mathbf{k}, \alpha)}(R_j) = \exp(-i\mathbf{B}_i \cdot \mathbf{v}_j) \tilde{D}^{(\mathbf{k}, \alpha)}(R_s) \quad (3.37)$$

where the reciprocal lattice vector  $B_i$  is defined by the relation

$$R_i^{-1} \mathbf{k} = \mathbf{k} + \mathbf{B}_i \quad (3.38)$$

Equations (3.36) together imply that the matrices  $\tilde{D}^{(\mathbf{k}, \alpha)}(R)$  are the same for all members of any fixed coset in (3.32), *i.e.* these matrices are in correspondence with the elements of the factor group  $G_k/T$ . The factor group  $G_k/T$  is isomorphic with the little cogroup  $F_k$  so that  $\tilde{D}^{(\mathbf{k}, \alpha)}$  is a matrix-valued function on the elements of the point group of wavevector  $\mathbf{k}$  with the multiplication law

$$\tilde{D}^{(\mathbf{k}, \alpha)}(R_i) \tilde{D}^{(\mathbf{k}, \alpha)}(R_j) = \exp(-i\mathbf{B}_i \cdot \mathbf{v}_j) \tilde{D}^{(\mathbf{k}, \alpha)}(R_i R_j) \quad (3.39)$$

Matrices  $\tilde{D}^{(\mathbf{k}, \alpha)}$  form a so-called projective rep of the point group  $F_{\mathbf{k}}$  with the factor system

$$\omega(R_i, R_j) = \exp(-i\mathbf{B}_i \cdot \mathbf{v}_j) \quad (3.40)$$

where  $\mathbf{B}_i$  is defined by (3.38).

We see from (3.36) that the small irreps  $D^{(\mathbf{k}, \alpha)}$  of a little group are found if the projective irreps  $\tilde{D}^{(\mathbf{k}, \alpha)}(R)$  of the point group  $F_{\mathbf{k}}$  with the factor system (3.40) are known.

A factor system is specified by  $n_{F_{\mathbf{k}}}^2$  coefficients  $\omega(R_i, R_j)$ , where  $n_{F_{\mathbf{k}}}$  is the order of the point group of wave vector  $F_{\mathbf{k}}$ . These coefficients must satisfy the following identities for any  $R_i, R_j, R_k$ :

$$(R_i, R_j R_k)(R_j, R_k) = (R_i R_j, R_k)(R_i, R_j) \quad (3.41)$$

implied by the associative law of group multiplication  $R_i(R_j R_k) = (R_i R_j) R_k$ . However, conditions (3.41) do not define a factor system uniquely [27]. If  $D(R)$  is a projective representation of the group belonging to the factor system  $\omega(R_i, R_j)$  then any other representation  $D'(R) = D(R)/u(R)$  where  $u(R)$  is an arbitrary single-valued function on the group,  $|u(R)| = 1$ , also defines a projective representation of the group, but with factor system  $\omega'(R_i, R_j) = \omega(R_i, R_j)u(R_i, R_j)/u(R_i)u(R_j)$ . The factor systems  $\omega(R_i, R_j)$  and  $\omega'(R_i, R_j)$  representations satisfying (3.41) are said to be projectively equivalent or  $p$  equivalent. The set of all  $p$  equivalent factor systems is called a class of factor systems. Note that two different  $p$  equivalent

representations may belong to the same factor system. For this to occur it is necessary that  $u(R_i)u(R_j) = u(R_iR_j)$ , *i.e.* function  $u(R)$  defines some ordinary (with all  $\omega(R_i, R_j) = 1$ ) one-dimensional representation of the group. The group may have several classes of factor systems. It can be shown [27] that if  $\omega(R_i, R_j) = \omega(R_j, R_i)$  for any pair of commuting elements ( $R_iR_j = R_jR_i$ ) the factor system  $\omega(R_i, R_j)$  is  $p$  equivalent to identity factor system  $\omega(R_i, R_j) = 1$  and the corresponding representation is  $p$  equivalent to ordinary representation. Although the total number of possible factor systems is infinite, it can be shown that for a finite group the number of classes  $K$  of factor systems is finite [27]. For every group there is class  $K_0$  with all  $\omega(R_i, R_j) = 1$ , which is called vector or ordinary representation. The other representations of the class  $K_0$  with  $\omega(R_i, R_j) \neq 1$  are projectively equivalent to vector representations. The dimensions of all  $p$  equivalent representations are the same, the factor systems may differ. If a group has several classes of factor systems then only the class  $K_0$  may correspond to one-dimensional representations and there will be no one-dimensional representations for classes  $K_0 \neq K_p$ .

Projective representations were first introduced by Shur [32], who developed a general theory of projective representations and worked out methods for constructing projective representations of finite groups. The connection between projective representations of point groups and representations of space groups was demonstrated by Lyubarskii, Kovalev, Bir [27, 31, 33]. To find  $D^{(\mathbf{k}, \alpha)}$  with the factor system (3.40) Herring's approach [34] may be useful. In this approach the problem is reduced to finding ordinary irreps of abstract groups with order greater than that of  $F_{\mathbf{k}}$  but not very large.

In [30] it is shown that these groups for different wavevectors in the Brillouin zone of one space group or for the same wavevector in the Brillouin zone of different space groups may be isomorphic. In [30] all the irreps of all the abstract groups that occur among reps of space groups are completely identified. In [17] the small irreps of little groups are found from those of the translation group by successive augmentations, each augmenting operator being chosen so that the augmented group contains the unaugmented one as an invariant subgroup.

The classes of all factor systems and the corresponding projective representations characters can be found in [27] for all 32 crystallographic point groups. Ten groups ( $C_1, S_2, C_s, C_2, S_4, C_4, C_3, S_6, C_6, C_{3h}$ ) are cyclic, only one factor system  $K_0$  belongs to these groups, *i.e.* for these groups all the projective representations are  $p$  equivalent to ordinary representations.

This short description of projective representations of point groups allows us to understand information given in different tables and on the site [16]. When using different existing tables for small representations of little groups one has to remember that the projective representations of point groups can be ordered in different ways and may appear to be  $p$  equivalent to each other.

When the space group  $G$  is isomorphic all the fractional translations  $\mathbf{v}_i$  may be chosen to be zero (Sect. 3.3) so that all the factors  $\omega(R_i, R_j) = 1$  and  $\check{D}^{(\mathbf{k}, \alpha)}(R_i)$  coincide with the  $\alpha$ th irrep of the point group  $F_k$ . When  $\mathbf{k}$  is an interior point of the Brillouin zone ( $R_i^{-1}\mathbf{k} - \mathbf{k} = 0$  for all  $R_i$  in the group  $F_{\mathbf{k}}$ ) it can also be that at some points of the Brillouin zone on its surface ( $R_i^{-1}\mathbf{k} - \mathbf{k} \mathbf{v}_j = 0$  for all  $R_i$  and  $\mathbf{v}_j$  in the group  $G_k$ ). In both these cases the projective irreps  $D^{(\mathbf{k}, \alpha)}(R)$  also coincide with the usual irreps of the point group of a wavevector. However, for some points

on the surface of the Brillouin zone in the case of nonsymmorphic space groups the projective irreps  $D^{k,\alpha}(R)$  are not the usual irreps of the point group  $F_k$ .

As an example, we consider nonsymmorphic space group  $O_h^7$  – the symmetry group of diamond structure. The Brillouin zone for the face-centered-cubic lattice and the symmetry points and the symmetry directions are shown in Fig. 3.2. The small representations of little groups  $G_\Gamma$  and  $G_L$  are  $p$  equivalent to the ordinary irreducible representations of the corresponding wavevector point groups  $O_h$  and  $D_{3d}$ . For the  $\Gamma$  point it is evident as this point is inside (at the center) of the Brillouin zone. For the  $L$  point it can be easily shown. Indeed the point group of  $L(1/2, 1/2, 1/2)$  consists of rotations  $C_{31}$ ,  $C_{31}^{-1}$  through one of four third-order rotation axes, three rotations through second-order axes  $U_{xy}^-, U_{yz}^-$  and  $U_{xz}^-$  (these operations and identity operation form point group  $D_3$ ). All the remaining operations of the  $D_{3d}$  point group are obtained from relation  $D_{3d} = D_3 \times C_i$  (direct product of  $D_3$  and inversion group  $C_i$ ). As can be seen from [16] these point-symmetry operations are included in space group  $O_h^7$  (origin choice 2) with proper translations, so that for any two elements  $R_i$  and  $R_j$  of point group  $D_{3d}$  the multipliers  $\omega(R_i, R_j) = 1$ . For  $X$  and  $W$  points the small representations are not  $p$  equivalent to ordinary representations of wavevector point groups  $D_{4h}$  and  $D_{2d}$ , respectively. To show this it is enough to find in the corresponding little cogroups at least one pair of commuting elements for which  $\omega(R_i, R_j) \neq \omega(R_j, R_i)$ . The point group  $D_{4h} = D_4 \times C_i$  of  $X(1/2, 1/2, 0)$  includes rotations  $C_{4z}$ ,  $C_{2z}$  and  $C_{4z}^{-1}$  through fourth-order  $z$  axis, rotations  $C_{2x}$  and  $C_{2y}$  through  $x$ - and  $y$ -coordinate axes and rotations  $U_{x-y}^-, U_{xy}^-$  through second-order axes. The space group  $O_h^7$  includes commuting elements  $C_{2y}$  and  $IC_{2y} = \sigma_y$  with improper translations  $(1/4, 1/2, /3/4)$  and  $(1/2, 3/4, 1/4)$ , respectively, given in basic translation vectors  $\mathbf{a}_1, \mathbf{a}_2, \mathbf{a}_3$  (see [16, 19]). For the transformation  $C_{2y}$  and  $\mathbf{k} = X$  we have  $C_{2y}\mathbf{k} - \mathbf{k} = \mathbf{b}_1 + \mathbf{b}_2$  (sum of two basic reciprocal lattice vectors), for the transformation  $IC_{2y} = \sigma_y$  we have  $\sigma_y\mathbf{k} - \mathbf{k} = 0$ . Therefore  $\omega(C_{2y}, \sigma_y) = \exp(i\pi/2) = i$  and  $\omega(\sigma_y, C_{2y}) = 1$ . Considering the commuting elements  $C_{2y}$  and  $\sigma_x = IC_{2x}$  from point group  $D_{2d}$  of wavevector  $W$  it is easy to show that  $\omega(C_{2y}, \sigma_x) = -i$  and  $\omega(\sigma_x, C_{2y}) = i$ . In Table 3.4 are given for space group  $O_h^7$  labels of the corresponding projective irreducible representations of point groups  $F_X$  and  $F_W$  and their dimensions. The point-symmetry group  $F_Z$  of the symmetry direction  $XW$  (12 rays in the star) on the surface of the Brillouin zone (see Fig. 3.2) consists of elements being common for both point groups  $F_X$  and  $F_W : E, C_{2y}, \sigma_x, \sigma_z$ . It was seen that  $\omega(C_{2y}, \sigma_x) \neq \omega(\sigma_x, C_{2y})$  so that the only wavevector point group  $C_{2v}$  two-dimensional irreducible representation is not  $p$  equivalent to any of the four ordinary one-dimensional representations of point group  $C_{2v}$  (see Table 3.4).

The numbering of some small representations of space groups is different in different tables. For example, four small two-dimensional representations at the  $X$  point are ordered in different ways on the site [16] and in tables [17]. The ray of stars  $L, X$  and  $W$  chosen for the small-representation generation can also be different, as can the origin choice for space-group description. All these differences do not change the full representations of space groups.

The dimension of a space-group full representation (degeneracy of energy levels in a crystal) for a given  $\mathbf{k}$  is equal to the product of the number of rays in the star  $\mathbf{k}^*$  and the dimension of the point group  $F_\mathbf{k}$  irreducible representation (ordinary or projective). In particular, for the space group under consideration at the  $X$  point the dimensions of full representations are 6 and at the  $W$  point – 12. As to each of the

Table 3-4. Characters of projective representations of point groups  $D_{4h}$  and  $D_{2d}$  for  $X$  and  $W$  points (space group  $O_h^7$ )

degenerated states corresponds the same one-electron energy it is enough to identify energy levels only for one ray of the wavevector star as it is made in the figures showing the electronic band structure. The degeneracy of levels at the symmetry points of the  $BZ$  is defined by the dimensions of wavevector point-group representations (ordinary or projective). To identify the one-electron energies at the symmetry lines the compatibility relations are used. In Sect. 3.2.6 we discuss the band structure of some crystals using the considered information.

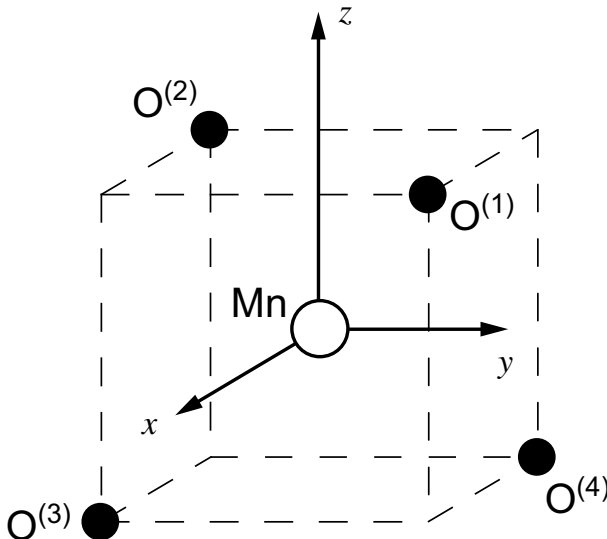
When the space group is realized in a crystalline structure the atomic states included in the LCAO basis define the symmetry of crystalline orbitals appearing in the electronic-structure calculations. The symmetry connection of atomic and crystalline orbitals is given by induced representations of space groups considered in the next subsection.

## 3.2 Site Symmetry and Induced Representations of Space Groups

### 3.2.1 Induced Representations of Point Groups. Localized Molecular Orbitals

In the previous section we examined the use of space-group irreducible representations for the classification of the delocalized (Bloch-type) crystalline states. In this traditional approach the crystal is considered as a whole system and the symmetry properties of the environment of constituent atoms are ignored. This results in a loss of information about the connection between the atomic and crystalline states. This information is widely used in the quantum chemistry of solids as it allows the crystalline properties to be explained from the knowledge of the chemical nature of the constituent atoms and their interactions. In the plane-waves methods of electronic-structure calculations the Bloch-type delocalized states are not directly connected with the states of the separate atoms. However, in the LCAO methods the Bloch-type delocalized functions are represented as the linear combination of the functions of separate atoms. Therefore, the symmetry connection between the delocalized Bloch and localized atomic states appears to be important. If we use not only the space symmetry of a crystal as a whole but also the site symmetry of different groups of constituent atoms we can considerably extend the possibilities of the group-theory applications. To study this in more detail the reader is referred to our previous book [13] where we examined the theory and the applications of the site-symmetry approach to the electron, phonon, magnetic properties of crystals and in the theory of phase transitions. In this section, we examine only those theoretical aspects of the site-symmetry approach that concern the electron states and allow analysis of the symmetry connection between the delocalized Bloch-type and localized Wannier-type electron states in crystals. We begin from the short description of the site (local) symmetry approach in molecular quantum chemistry.

In the molecular systems with the point symmetry group  $G$  the site-symmetry subgroup  $H_q$  includes those symmetry operations that keep the point  $q$  fixed:  $hq = q$ . As an example, we consider a tetrahedral molecular ion  $[\text{MnO}_4]^-$  (see Fig. 3.8). The Mn atom site-symmetry group coincides with the whole symmetry group  $T_d$ . The site-symmetry group of any of the four oxygens is  $C_{3v} \subset T_d$ .

Fig. 3.8.  $\text{MnO}_4^-$  ion

Let  $\hat{D}(g)$  be a rep of a group  $G$  ( $g \in G$ ). A set of operators  $\hat{D}(h)$  ( $h \in H \subset G$ ) is a rep of  $H$  subduced by rep  $\hat{D}(g)$  of  $G$ . The subduced irrep is denoted as  $\hat{D} \downarrow H$ . Even if  $\hat{D}(g) = \hat{D}^{(\alpha)}(g)$ ,  $g \in G$  is an irrep of  $G$  the subduced rep is, in general, reducible and may be decomposed into irreps  $d^{(\gamma)}$  of  $H$ :

$$\hat{D}^{(\alpha)} \downarrow H = \sum_{\gamma} r_{\gamma}^{(\alpha)} d^{(\gamma)}(h) \quad (3.42)$$

The multiplicities are equal to

$$r_{\gamma}^{(\alpha)} = n_H^{-1} \sum_h \chi^{(\alpha)}(h) \left[ X^{(\gamma)}(h) \right]^* \quad (3.43)$$

where  $\chi^{(\alpha)}(h)$  and  $\chi^{(\gamma)}(h)$  are the characters of irreps  $D^{\alpha}(h)$  and  $d^{(\gamma)}(h)$  of the groups  $G$  and  $H \subset G$  respectively.

Subducing the irreps of the group  $G$  with respect to its subgroup  $H$  and decomposing the subduced rep over the irreps of a subgroup one obtains a correlation table. The rows of this table are labeled by irreps of a group  $G$ ; the columns denote different subgroups  $H$  of this group  $G$ . The frequencies of subduction by each irrep of  $G$  for the irreps of these subgroups are listed in the body of the table. One also has to take into account the possibility of different orientations of isomorphic subgroups with respect to the group  $G$ .

As an example we consider the correlation table for the point group  $T_d$  (Table 3.5).

The subduction of the subgroup irreps by the group irrep can be considered as the reciprocal operation to the induction of the group reps by the irreps of the subgroup

**Table 3.5.** Correlation table for the point group  $T_d$ 

$T_d$	$C_{2v}$	$C_{3v}$
$a_1$	$a_1$	$a_1$
$a_2$	$a_2$	$a_2$
$e$	$a_1 \ a_2$	$e$
$t_1$	$a_2 \ b_1 \ b_2$	$a_2 \ e$
$t_2$	$a_1 \ b_1 \ b_2$	$a_1 \ e$

H. Let group G be decomposed into left cosets with respect to H:

$$G = \sum_{j''}^t g_{j''} H, \quad g_1 = E, \quad t = n_G/n_H \quad (3.44)$$

and L be a basis space of some rep of a group G. It is also a rep of its subgroup H. Let  $L^{(1)}$  be a subspace of L with the basis  $e_{i1}^{(\gamma)}$ , ( $i = 1, 2, \dots, n_\gamma$ ) transforming according to an irrep  $d^\gamma(h)$  of H:

$$D(h)e_{i1}^{(\gamma)} = \sum_{i'} d_{ii'}(h)e_{i'i}^{(\gamma)}, \quad i = 1, 2, \dots, n_\gamma \quad (3.45)$$

To express the invariance of  $L^{(1)}$  under  $\hat{D}(h)$  ( $h \in H$ ) independently of a particular choice of basis we write

$$\hat{D}(h)L^{(1)} = L^{(1)} \quad (3.46)$$

The linearly independent basis set

$$e_{ij}^{(\gamma)} = \hat{D}(g_j)e_{i1}^{(\gamma)}, \quad j = 1, \dots, t; \quad i = 1, 2, \dots, n_\gamma \quad (3.47)$$

spans a space  $L^{(n)}$  of the dimension  $n = t \cdot n_\gamma$ . This space is invariant under the operators  $\hat{D}(g)$ ,  $g \in G$  and is defined as the space of the group G induced by the irrep  $d^{(\gamma)}$  of its subgroup H and is written as  $d^{(\gamma)} \uparrow G$ . The matrices  $D^{[\gamma]}(g)$  of the induced rep  $d^{(\gamma)} \uparrow G$  have a block structure. Nonzero blocks are matrices of the irrep  $d^{(\gamma)}$  of H. Every row and every column of  $D^{[\gamma]}(g)$  has only one nonzero block. In the general case, a rep  $d^{(\gamma)} \uparrow G$  is reducible

$$d^{(\gamma)} \uparrow G = \sum_{\alpha} r_{\alpha}^{[\gamma]} D^{(\alpha)}(g) \quad (3.48)$$

The Frobenius reciprocity theorem is proved [13]: the multiplicity of an irrep  $D^{(\alpha)}(g)$  of G in a rep  $d^{[\gamma]} \uparrow G$  induced by an irrep  $d^{(\gamma)}$  of  $H \subset G$  is equal to the multiplicity of an irrep  $d^{(\gamma)}$  of H in the rep  $D^{(\alpha)} \downarrow H$  subduced by  $D^{(\alpha)}$  of H.

Using the Frobenius theorem one can also write the reciprocal correlation table in which the irreps of the point group induced by irreps of its different point subgroups are given. Representations of the point group  $T_d$  induced by irreps of its point subgroups  $C_{2v}$  and  $C_{3v}$  are given in Table 3.6. The latter subgroup may be considered as the site-symmetry group of the oxygen atom in the molecular ion  $(\text{MnO}_4)^-$ .

**Table 3.6.** Induced irreps of the point group  $T_d$ 

$C_{2v}$	$T_d$	$C_{3v}$	$T_d$
$a_1$	$a_1$ $e$ $t_2$	$a_1$	$a_1$ $t_2$
$a_2$	$a_2$ $e$ $t_1$	$a_1$	$a_2$ $t_1$
$b_1$	$t_1$ $t_2$	$e$	$e$ $t_1$ $t_2$
$b_2$	$t_1$ $t_2$		

The first and third columns in Table 3.6 contain the symbols of the point subgroups  $C_{2v}$  and  $C_{3v}$  and their irreps. The rest of the columns give the symbols of the induced representations of point group  $T_d$  decomposed over the irreps of this group.

The comparison of Tables 3.5 and 3.6 allows the Frobenius theorem to be checked. The tables of induced representations of the point groups are given in [13] and are the reciprocal correlation tables. The latter are given in [14]. In MO LCAO calculations the canonical MO (delocalized over the whole space) are found. Their symmetry is defined by the irreps of the symmetry group of the whole molecule induced by the irreps of the site-symmetry groups of the constituent atoms. Use of the induced representations of point groups allows the canonical MO to be divided into sets, connected with the localized MO (LMO) and find the possible center of localization. In many cases this procedure can be done in several ways. Let us examine MO and LMO in the  $(\text{MnO}_4)^-$  molecular ion. The  $4s$ -,  $4p$ - and  $3d$ -functions of the Mn atom span the space of the irreps  $a_1, t_2, e + t_2$  of the molecular symmetry group  $T_d$ . The site symmetry group of the O atom is  $C_{3v}$ . As follows from Table 3.6 the  $2s$  and  $2p_z$  functions of the oxygen atom contribute to the canonical orbitals of  $a_1$  and  $t_2$  symmetry, and oxygen  $2p_x, 2p_y$  functions contribute to functions with the symmetries  $e, t_1, t_2$ . The site group  $C_{3v}$  may correspond to localized functions centered on oxygen atoms as well as on the Mn–O bond axis. The site group  $C_{2v}$  may be related to a two-centered O–O bond or to a three-centered O–Mn–O bond. The latter may also have  $C_s$  symmetry. Table 3.7 lists one-electron energies of the  $(\text{MnO}_4)^-$  ion valence orbitals calculated by a) the nonempirical MO LCAO method, b) the SWX $_\alpha$  method, c) a semiempirical CNDO method (see Chap. 6). The weights of valence atomic orbitals in molecular orbitals are also given in cases a) and c) (in parentheses).

The valence canonical MO given in Table 3.7 may be distributed over sets according to their symmetry. There are three possible variants of distribution compatible with the symmetry requirements:

- 1 )  $C_{3v}(a_1) - 5a_1, 4t_2; C_{3v}(a_1) - 6a_1, 6t_2; C_{3v}(e) - 1e, 1t_1, 5t_2$
- 2 )  $C_{3v}(a_1) - 5a_1, 4t_2; C_{2v}(a_1) - 6a_1, 1e, 5t_2; C_{2v}(b_1) - 1t_1, 6t_2$  (3.49)
- 3 )  $C_{3v}(a_1) - 5a_1, 4t_2; C_s(a') - 6a_1, 1e, 5t_2, 6t_2, 1t_1$

The first variant is the most preferable as it corresponds to two-centered bonds, whereas the second and the third possibilities contain sets with bonds of more than two centers. The greater the number of centers participating in a bond, the less localized it seems to be. Table 3.7 shows that the sets  $C_{3v}(a_1)$  correspond to orbitals localized near the oxygen atoms, the  $s$ -type is the lowest in energy and the  $2p_z$ -type (directed along the O–Mn line) is higher. The localized functions of symmetry contain

**Table 3.7.** Electronic structure of  $(\text{MnO}_4)^-$ 

State symmetry	One-electron energies [eV]			Atomic contributions [%]				
	$SWX_\alpha$	CNDO	HF LCAO	3d	4s	4p	2s	2p
1	-9.28	-7.01	-7.62		-			100 (100)
$6a_1$	-10.53	-8.95	-8.03		8 (5)	4 (2)	88 (93)	
$6t_2$	-10.37	-9.68	-9.06	3 (17)	7 (2)	2 (5)	88 (76)	
$1e$	-12.24	-10.15	-11.48	29 (23)				72 (77)
$5t_2$	-12.43	-11.26	-12.82	53 (18)	2 (2)	6 (4)	39 (72)	
$4t_2$	-24.30	-32.68	-29.44	7 (2)	4 (17)	87.5 (79)	15 (2)	
$5a_1$	-24.65	-36.43	-30.01		7.5 (21)	91.5 (78)	- (1)	

a considerable admixture of Mn  $3d$  states. So the center of localization is apparently displaced along the bond line towards the Mn atom.

Each of the three sets (3.50) contains states of  $t_2$  symmetry and in two sets there are states of  $a_1$  symmetry. When generating localized orbitals it is possible to take the linear combinations of initial canonical functions of the same symmetry and to vary the coefficients to get the orbitals with the best spatial localization. However, in the case of  $(\text{MnO}_4)^-$  the orbitals  $5a_1$  and  $6a_1$  have considerably different energies. Therefore, the linear combinations must be used only for orbitals of  $t_2$  symmetry (especially  $5t_2$  and  $6t_2$ ).

The analysis of the calculated one electron-states is often made only according to the weights of the atomic functions, and symmetry considerations are not taken into account. As a result, the  $6t_2, 6a_1, 1t_1$  states can be treated as being in the set corresponding to the localized functions of  $2p$ -type centered on oxygen atoms. As follows from Table 3.7, these states do not span the space of the rep induced by some irrep of the site group of the oxygen atom. Therefore, it is impossible to generate any function localized on the oxygen atom. Hence, simply the analysis of the atomic orbital contributions in molecular states with close energies does not permit one to correctly relate the canonical orbitals to the localized ones.

As we can see, induced reps of point groups, in combination with an analysis of the atomic contributions in molecular eigenfunctions, are a good tool to find the regions of localization of electron density on atoms and bonds in a molecule. Of course the energy criterion must also be taken into consideration: a set is chosen so as to unite states with close energies.

Table 3.7 shows that the symmetry of localized orbitals does not depend in practice on the method of calculation of electronic structure. In particular, the method described here is equally applicable to results of  $SWX_\alpha$  calculations where the atomic basis is not used at all. The change in energy ordering of the  $6a_1$  and  $6t_2$  levels from that of the nonempirical method does not change the symmetry found for the localized orbitals.

The localized orbitals generation from the set of canonical MO allowed by symmetry requires additional choice of the localization criteria. The different orbital localization methods are implemented in molecular computer codes [35]. All of them are connected with the search for the coefficients connecting LMO with the canonical MO to satisfy the localization criteria.

The method due to Edmiston and Ruedenberg [36] works by maximizing the sum of the localized orbitals two-electron self-repulsion integrals. The method requires the two-electron integrals, transformed into the MO basis. Because only the orbitals to be localized are needed, the integral transformation is actually not very time consuming. However, the extension of this method to crystals is practically difficult as this requires the transformations of lattice sums of two electron integrals.

The population method due to Pipek and Mezey [37] maximizes a certain sum of gross atomic Mulliken populations. The latter are not realistic when the LCAO basis includes diffuse atomic orbitals as is necessary for crystalline solids.

The most appropriate for the extension to crystal appears to be the Boys method. The Boys method [38] minimizes the sum of spreads of the localized orbitals  $\phi_i(\mathbf{r})$

$$\min I = \sum_{i=1}^N [\langle \mathbf{r}^2 \rangle_i - \langle \mathbf{r} \rangle_i^2], \left( \langle \mathbf{r}^m \rangle_i \equiv \int \mathbf{r}^m |\phi_i(\mathbf{r})|^2 d\mathbf{r} \right) \quad (3.50)$$

The summation in (3.50) is made over  $N$  occupied canonical MO found in LCAO self-consistent calculations.

$\sum_{i=1}^N \langle \mathbf{r}^2 \rangle_i$  is invariant with respect to any unitary transformation among functions  $\phi_i$ :

$$\phi_i' = \sum_{i'}^N U_{i'i} \phi_{i'} \quad (3.51)$$

The minimum of the functional  $I$  corresponds to the maximum of the functionals:

$$\tilde{I} = \sum_{i=1}^N \langle \mathbf{r}^2 \rangle_i, \quad \text{or} \quad \tilde{\tilde{I}} = \sum_{i>j=1}^N [\langle \mathbf{r} \rangle_i - \langle \mathbf{r} \rangle_j]^2 \quad (3.52)$$

Thus, the Boys method can also be considered as maximization of the sum of distances between the orbital centroids  $\tilde{\tilde{I}}$ . The modifications of the Boys method are necessary to extend it for the localized crystalline orbitals generation. These modifications are considered in Sect. 3.3

### 3.2.2 Induced Representations of Space Groups in $\mathbf{q}$ -basis

Any subgroup rep can generate some induced rep of a group (see Sect. 3.2.1). In the particular case of a space group  $G$  the small irreps of the little group  $G_k \subset G$  induce its full irreps.

In this and the next subsections we consider induced reps of space groups generated by the irreps  $\beta$  of the site-symmetry subgroup  $G_{\mathbf{q}}$  of point  $\mathbf{q}$  in the direct lattice space ( $\beta \uparrow G$ ). This type of induced rep of space groups was considered in [13]. In [39] a more general concept of band reps was introduced. All elements of the space group  $G$  can be written in the form  $t_{\mathbf{v}_R + \mathbf{a}_n} R$ , where  $\mathbf{v}_R$  is a fractional lattice translation associated with the F point-group element  $R$  and  $\mathbf{a}_n$  is a direct lattice translation vector.

The elements of the site-symmetry group  $G_{\mathbf{q}} \subseteq G$  of the point  $\mathbf{q}$  in the direct lattice space are those elements of  $G$  for which  $g_{\mathbf{q}}\mathbf{q} = t_{\mathbf{v}_R + \mathbf{a}_n} R_{\mathbf{q}}\mathbf{q} = \mathbf{q}$ . The space-group elements  $g_{\mathbf{q}}$  are supposed to be given in the coordinate system whose origin is at one of the Wyckoff positions. The site-symmetry group elements for the other Wyckoff positions are mapped by the space-group elements with the point-symmetry operators  $R$ . Thus the site-symmetry group  $G_{\mathbf{q}} \subseteq G$  is isomorphic with the point group  $F_{\mathbf{q}}$  formed by  $R_{\mathbf{q}}$ . When the coordinate system origin is moved to the other Wyckoff position  $\mathbf{q}_1$  the site-symmetry group elements of this new origin are elements of the point group  $F_{\mathbf{q}_1}$  but the site-symmetry group elements  $g_{\mathbf{q}}$  of the former origin  $\mathbf{q}$  contain translations. As an example we consider the space group  $O_h^7$  for the two origin choices given in the International Tables for Crystallography [19]. The site-symmetry group of Wyckoff position a(000) is mapped to the pure point-symmetry operations of the group for the first origin choice and to the set of operations with the translational part for the second origin choice.

Let the representatives  $g_{jn}$  ( $j = 1, 2, \dots, n_q = n_G/n_F$ ) in the decomposition

$$G = \sum_{j,n} g_{jn} G_{\mathbf{q}}, \quad g_{jn} = t_{\mathbf{v}_j + \mathbf{a}_n} R_j \quad (3.53)$$

be chosen so that the points

$$\mathbf{q}_j = t_{\mathbf{v}_j} R_j \mathbf{q} \quad (3.54)$$

occupy the positions within the smallest unit cell (primitive or Wigner–Seitz). The operations  $g_{jn}$  generate from the point  $\mathbf{q}$  sublattices  $\mathbf{q}_j + \mathbf{a}_n$  ( $j = 1, 2, \dots, n_q$ ).

Let the local functions  $W_{i1}^{(\beta)}(\mathbf{r}) \equiv W_i(\mathbf{r} - \mathbf{q})$ , ( $i = 1, 2, \dots, n_{\beta}$ ) be centered at point  $\mathbf{q}$  of the direct lattice and span the space of the irrep  $\beta$  of the site-symmetry group  $G_{\mathbf{q}} \subset G$  with matrices  $d^{(\beta)}(g_{\mathbf{q}})$  and characters  $\chi^{(\beta)}(g_{\mathbf{q}})$  ( $g_{\mathbf{q}} \in G_{\mathbf{q}}$ ). The nature of these functions depends on the physical problem under consideration. In the electron-band theory of crystals  $W_i^{(\beta)}(\mathbf{r} - \mathbf{q}_A)$  are atomic functions of atom A. In phonon spectroscopy applications  $W_i^{(\beta)}(\mathbf{r} - \mathbf{q}_A)$  mean the components of atomic displacements of an atom A, in magnetically ordered crystals these functions are the magnetic moments of atoms [13].

Functions  $W_{i1}^{(\beta)}(\mathbf{r})$  transform as

$$\begin{aligned} \hat{g}_{\mathbf{q}} W_{i1}^{(\beta)}(\mathbf{r}) &= W_i^{(\beta)}(R_{\mathbf{q}}^{-1}(\mathbf{r} - \mathbf{v}_{\mathbf{q}} - \mathbf{a}_n - R_{\mathbf{q}}\mathbf{q})) \\ &= W_i^{(\beta)}(R_{\mathbf{q}}^{-1}(\mathbf{r} - \mathbf{q})) = \sum_{i'=1}^{n_{\beta}} d_{i'i}^{(\beta)}(R_{\mathbf{q}}) W_{i'1}^{(\beta)}(\mathbf{r}) \end{aligned} \quad (3.55)$$

since the vector  $\mathbf{q}$  remains invariant under the operations of the site group  $G_{\mathbf{q}}$ . All the functions  $W_{i1}^{(\beta)}(\mathbf{r})$  ( $i = 1, 2, \dots, n_{\beta}$ ) are associated with the site  $\mathbf{q}$ .

The local functions associated with the smallest unit cell are obtained from local functions  $W_{i1}^{(\beta)}(\mathbf{r})$  through

$$W_{ij}^{(\beta)}(\mathbf{r}) = \hat{t}_{\mathbf{v}_j} R_j W_{i1}^{(\beta)}(\mathbf{r}) = \mathbf{W}_i^{(\beta)} \left( \mathbf{R}_j^{-1}(\mathbf{r} - \mathbf{q}) \right), \quad (3.56)$$

$$i = 1, 2, \dots, n_\beta; \quad j = 1, 2, \dots, n_{\mathbf{q}}$$

Functions in other unit cells are obtained through

$$W_{ij}^{(\beta)}(\mathbf{r} - \mathbf{a}_n) = \hat{t}_{\mathbf{a}_n} W_{ij}^{(\beta)}(\mathbf{r}) = W_{ij}^{(\beta)} \left( R_j^{-1}(\mathbf{r} - \mathbf{q}_j - \mathbf{a}_n) \right) \quad (3.57)$$

The local functions  $W_{ij}^{(\beta)}(\mathbf{r} - \mathbf{a}_n)$  form the basis of an induced rep  $\beta \uparrow G$  of space group  $G$ . Indeed, let the element  $t_{\mathbf{v}_R} R$  transform the  $j$ th sublattice into the  $j'$ th one and be written in the form

$$t_{\mathbf{v}_R} R = t_{\mathbf{a}_{jj'}} t_{\mathbf{v}_{j'}} R_{j'} t_{\mathbf{v}_q} R_q (t_{\mathbf{v}_j} R_j)^{-1} \quad (3.58)$$

where  $R = R_{j'} R_q R_j^{-1}$  ( $R_q \in F_q$ ) and  $\mathbf{a}_{jj'}$  is the lattice vector. Equation (3.58) may be checked directly. From (4.2.6) we get for the local functions

$$t_{\mathbf{v}_R} R W_{ij}^{(\beta)}(\mathbf{r} - \mathbf{a}_n) = \sum_{i'} \left( R_{j'}^{-1} R R_j \right) W_{i'j'}^{(\beta)}(\mathbf{r} - R\mathbf{a}_n - \mathbf{a}_{j'j}) \quad (3.59)$$

The dimension of the rep  $\beta \uparrow G$  is infinite for the model of an infinite crystal. In a cyclic model, the infinite crystal is replaced by a main region consisting of  $N$  smallest unit cells and periodic boundary conditions are introduced. The total number of local functions  $W_{ij}^{(\beta)}(\mathbf{r} - \mathbf{a}_n)$  becomes finite and equals  $n_\beta n_{\mathbf{q}} N$  ( $i = 1, 2, \dots, n_\beta, j = 1, 2, \dots, n_{\mathbf{q}}$ ;  $n$  takes  $N$  values). These functions form an  $n_\beta n_{\mathbf{q}} N$ -dimensional space of the rep of the space group  $G$ . This rep matrix consists of  $n_\beta n_{\mathbf{q}}$  blocks arising from  $d^{(\beta)}$ .

To specify the induced rep  $\beta \uparrow G$  in the basis of local functions  $W_{ij}^{(\beta)}(\mathbf{r} - \mathbf{a}_n)$  one has to indicate the symmetry center  $\mathbf{q}$  of local functions by its Wyckoff position and the irrep  $\beta$  of the site-symmetry point group  $G_{\mathbf{q}}$ . Thus, in the  $\mathbf{q}$  basis the induced rep  $\beta \uparrow G$  is specified by the index  $(\mathbf{q}, \beta)$ .

As an example, we consider oxygen atom  $2s$  functions in the perovskite  $\text{CaTiO}_3$  structure. The oxygen atoms occupy Wyckoff position  $c$  of the space group  $O_h^1$  with the site-symmetry  $D_{4h}$ . The  $2s$ -functions of an oxygen atom transform over  $a_{1g}$  irrep of the point group  $D_{4h}$ . Thus, the induced representation in  $\mathbf{q}$  basis  $(c, a_{1g})$  is three-dimensional at each  $\mathbf{k}$  point ( $d^{(\beta)} = a_{1g}, n_\beta = 1, n_{\mathbf{q}} = 3$ ).

### 3.2.3 Induced Representations of Space Groups in $\mathbf{k}$ -basis.

#### Band Representations

In Sect. 3.1 we have considered the space-group irreps  $D^{(\mathbf{k}, \alpha)}(g)$  defined by stars  ${}^* \mathbf{k}$  of wavevectors  $\mathbf{k}$  from the first Brillouin zone and by irreps  $D^{(\alpha)}$  of little groups  $G_{\mathbf{k}}$ . Let us construct in the space of induced rep  $(\mathbf{q}, \beta)$  new basis functions that span the space of irreps of the translation group  $T$  (Bloch functions)

$$\Psi_{ij}^{(\beta)}(\mathbf{k}, \mathbf{r}) = \sum_n \exp(i\mathbf{k}\mathbf{a}_n) W_{ij}^{(\beta)}(\mathbf{r} - \mathbf{a}_n), \quad (i = 1, 2, \dots, n_\beta; \quad j = 1, 2, \dots, n_{\mathbf{q}}) \quad (3.60)$$

and *vice versa*

$$\begin{aligned} W_{ij}^{(\beta)}(\mathbf{r} - \mathbf{a}_n) &= \frac{V_a}{(2\pi)^3} \int \exp(-i\mathbf{k}\cdot\mathbf{a}_n) \Psi_{ij}^{(\beta)}(\mathbf{k}, \mathbf{r}) d\mathbf{k} \\ W_{ij}^{(\beta)}(\mathbf{r} - \mathbf{a}_n) &= N^{-1} \sum_{\mathbf{k}} \exp(-i\mathbf{k}\cdot\mathbf{a}_n) \Psi_{ij}^{(\beta)}(\mathbf{k}, \mathbf{r}) \end{aligned} \quad (3.61)$$

for infinite and cyclic models of a crystal, respectively. Using (3.24), (3.28) and (3.59) one obtains

$$t_{\mathbf{v}_R} R \Psi_{ij}^{(\beta)}(\mathbf{k}, \mathbf{r}) = \exp(-iR\mathbf{k} \cdot \mathbf{a}_{jj'}) \sum_{i'} d_{i'i}^{(\beta)} \left( R_j^{-1} R R_j \right) \Psi_{i'j'}(R\mathbf{k}, \mathbf{r}) \quad (3.62)$$

Let the wavevector  $\mathbf{k}$  be fixed and  $t_{\mathbf{V}_R} R \in G_{\mathbf{k}}$ . Then  $p = n_{\beta} n_q$  functions  $\Psi_{ij}^{(\beta)}(\mathbf{k}, \mathbf{r})$  span the space of the small representation of the little group  $G_{\mathbf{k}}$  with the character

$$\chi_{\mathbf{k}}^{(\beta)}(g) = \sum_{j=1}^{n_q} \exp(-i\mathbf{k} \cdot \mathbf{a}_{jj'}) \tilde{\chi}^{(\beta)}(R_j^{-1} R R_j) \quad (3.63)$$

where

$$\tilde{\chi}^{(\beta)}(R_j^{-1} R R_j) = \begin{cases} 0, & \text{if } R_j^{-1} R R_j \neq R_q \\ \chi^{(\beta)}(R_q), & \text{if } R_j^{-1} R R_j = R_q \end{cases} \quad (3.64)$$

Knowing the characters (3.63) of the induced rep one can easily calculate the number of times the small irrep  $D^{(\mathbf{k}, \gamma)}$  of the group  $G_{\mathbf{k}}$  with characters  $\chi^{(\mathbf{k}, \gamma)}(g), g \in G_{\mathbf{k}}$  is contained in the induced rep  $(\mathbf{q}, \beta)$ .

This procedure gives the labels of the induced rep  $(\mathbf{q}, \beta)$  in the  $\mathbf{k}$  basis corresponding to those in the  $\mathbf{q}$  basis, *i.e.* the results of the reduction of the induced rep over irreps of the group  $G_{\mathbf{k}}$ . All the information obtained can be specified by listing the symmetry (the labels of irreps) of the Bloch states with wavevectors  $\mathbf{k}$  corresponding only to a relatively small number of  $\mathbf{k}$  points in the Brillouin zone forming a set  $K$ . The set  $K$  contains the inequivalent symmetry points of the Brillouin zone and one representative point from each inequivalent symmetry element (symmetry line or symmetry plane) if the latter does not contain the points of higher symmetry.

The symmetry properties of basis functions with other vectors  $\mathbf{k}$  can be determined with the use of the compatibility relations.

The set  $K$  for the space groups with high-symmetry classes consists only of the symmetry points. For instance, the set  $K$  for the space groups  $O_h^5, O_h^7$  contains the points  $\Gamma, X, L, W$  (Fig. 3.2); for the space group  $O_h^4$  - the points  $\Gamma, X, M, R$  (Fig. 3.2). The symmetry points can be absent in the Brillouin zone of space groups with low symmetry classes.

The symmetry properties of basis functions of an induced rep are described by the full group irreps  $(^*\mathbf{k}, \gamma)$  or by the small irreps  $(\mathbf{k}, \gamma)$  of the wavevector groups  $G_{\mathbf{k}}$  unambiguously related to them. Thus, as an index of an induced rep we shall use the symbols of those small irreps of the little groups  $G_{\mathbf{k}}$  with wavevectors from the set  $K$  that correspond to basis functions of a given induced rep

$$\mathbf{k}_1(\gamma_1^{(1)}, \gamma_2^{(1)}, \dots), \mathbf{k}_2(\gamma_1^{(2)}, \gamma_2^{(2)}, \dots), \dots, \mathbf{k}_i \in K \quad (3.65)$$

The index of the induced rep (3.65) can also be considered as the set of so-called subduction frequencies  $r_{(\mathbf{k},\gamma)}^{(\mathbf{q},\beta)}$ . The latter give the number of times the irrep  $(\mathbf{k},\gamma)$  of  $G$  is contained in the induced rep  $(\mathbf{q},\beta)$ . From the Frobenius theorem the subduction frequencies  $r_{(\mathbf{k},\gamma)}^{(\mathbf{q},\beta)}$  are equal to the number of times the irrep  $(\mathbf{k},\gamma)$  subduces the irrep  $\beta$  of  $G_{\mathbf{k}}$

$$r_{\beta}^{(\mathbf{k},\gamma)} = r_{(\mathbf{k},\gamma)}^{(\mathbf{q},\beta)} = \sum_{g \in G_{\mathbf{q}}} \left( \chi^{(\beta)*}(g) \right) \chi^{(\mathbf{k},\gamma)}(g) \quad (3.66)$$

where  $\chi^{(\mathbf{k},\gamma)}(g)$  and  $\chi^{(\beta)}(g)$  are the characters of the irreps  $(\mathbf{k},\gamma)$  of  $G$  and  $\beta$  of  $G_{\mathbf{q}}$ , respectively.

To calculate the subduction frequencies (3.66) one may use different procedures [13]. The first uses (3.63) and does not require knowledge of the full irrep  $(\mathbf{k},\gamma)$  characters. Indeed, one obtains, according to (3.63), the characters  $\chi_{\mathbf{k}}^{(\beta)}(g)$  of the rep of a little group  $G_{\mathbf{k}}$ . Reducing this rep requires the characters of the irreps of the little group  $G_{\mathbf{k}}$  (tabulated in [17] and on site [16]) and gives the induced rep index (3.66) in the  $\mathbf{k}$ -basis. The second procedure for calculating subduction frequencies uses (3.66) and requires the character  $\chi^{(\mathbf{k},\gamma)}$  of full irreps of space groups.

Comparing the two ways of finding the induced rep index in the  $\mathbf{k}$  basis one may conclude:

1. the first one is more appropriate for  $\mathbf{q}$  sets consisting of only one Wyckoff position in the unit cell (this is possible only in symmorphic space groups);
2. the second one is more appropriate for those wavevector stars that consist of one ray so that the full and small irreps coincide.

In [39] the concept of a band rep of a space group, which may be an induced rep, was introduced. Band reps were used to define the symmetry of an electron energy band as a whole entity.

From the group-theoretical point of view a band rep of a space group is a direct sum of its irreps that have the following properties:

- 1) the space of the band rep contains the basis vectors with all the  $\mathbf{k}$  vector stars in the Brillouin zone;
- 2) the compatibility relations are fulfilled throughout the Brillouin zone in the model of an infinite crystal or for  $N$  points in the cyclic model.

It is obvious that at every  $\mathbf{k}$  point there is the same number  $p$  of Bloch-type basis states.

In a cyclic model of a crystal with  $N$  primitive cells in the main region a band rep is an  $Np$  dimensional reducible rep of a space group. An induced rep is a particular case of a band rep as it satisfies both properties 1 and 2 with  $p = n_{\mathbf{q}} n_{\beta}$  ( $n_{\beta}$  is the dimension of the site-symmetry group irrep for a point  $\mathbf{q}$  belonging to the set of  $n_{\mathbf{q}}$  points in the unit cell).

The index of a band rep in the  $\mathbf{k}$  basis has the form given by (3.65). By analogy with the same index for an induced rep, all information about the band rep can be given by specifying the symmetry (the labels of irreps) of the basis vectors with wavevectors  $\mathbf{k} \in K$ .

It is seen now that band reps (induced reps included) of space groups can be specified by the index (3.65) in the  $\mathbf{k}$  basis, and only those band reps that are induced ones can also be specified in the  $\mathbf{q}$  basis in the form  $(\mathbf{q},\beta)$ .

Let us return to our example of the induced representation  $(c, a_{1g})$  of the space group  $O_h^1$  formed by  $2s$  functions of oxygen atoms in the perovskite structure. Using the full group irreps from the site [16] we calculate the subduction frequencies (3.66) for belonging to  $K$  set points of Brillouin zone and write the induced band representation  $(c, a_{1g})$  in the  $\mathbf{k}$  basis in the form  $\Gamma(1^+3^+)R(5^+)M(4^+5^-)X(1^+3^-4^-)$ . The labels of the small irreps of the little groups are taken from [17].

### 3.2.4 Simple and Composite Induced Representations

The use of the  $\mathbf{q}$  basis of induced reps allows one to introduce the concept of simple induced reps, that facilitates the analysis of all possible types of induced reps for a given space group. An induced rep is called simple if it is impossible to split up the space of this rep into subspaces that are invariant under operators  $\hat{g}$  ( $g \in G$ ) and are also the spaces of some induced reps.

By definition, a composite induced rep is a direct sum of the simple ones. As a group rep, a simple induced rep is reducible, so we prefer to avoid the expression “irreducible induced rep” used in [39]. The term introduced in [40], “elementary induced rep”, is equivalent to the term simple induced rep used in this book.

All simple induced reps may be generated by induction from the irreps of site-symmetry groups  $G_{\mathbf{q}'}$ , of a relatively small number of  $\mathbf{q}'$  points forming the set  $Q$  in the Wigner–Seitz unit cell of the direct lattice. The set  $Q$  consists of

- 1) all the inequivalent symmetry points of the Wigner–Seitz unit cell;
- 2) one representative point from all the inequivalent symmetry lines and symmetry planes that do not contain the symmetry points.

The site groups  $G_{\mathbf{q}}$  for all  $\mathbf{q} \in Q$  are called maximal isotropy subgroups in [40]. The set  $Q$  in the Wigner–Seitz unit cell is determined in the same way as the set  $K$  in the Brillouin zone. However, the action of symmetry operations in the direct and reciprocal spaces is different.

A reducible rep  $d(g) = \sum_{\beta} r_{\beta} d^{(\beta)}(g)$  of the site group  $G_{\mathbf{q}}$  induces a composite induced rep that is the direct sum of reps induced by the irreps  $d^{(\beta)}(g)$ . As an example, we can consider a composite rep induced by  $d$  functions of a transition metal atom (Wyckoff position a) in the perovskite structure: these functions span the reducible 5-dimensional rep of the the site-symmetry group  $O_h$  subducing  $t_{2g}$  and  $e_{2g}$  irreps. Therefore the induced irrep in  $\mathbf{q}$  basis is composite:  $b(e_g) + b(t_{2g})$ .

Now let us show that if the  $\mathbf{q}$ -point does not belong to the set  $Q$ , the rep  $(\mathbf{q}, \beta)$  induced from the irrep of the site group  $G_{\mathbf{q}}$  is composite.

Let  $\mathbf{q}'$  be one of the points in the set  $Q$  for which the site group  $G_{\mathbf{q}'}$  contains  $G_{\mathbf{q}}$  as a subgroup ( $G_{\mathbf{q}} \subset G_{\mathbf{q}'}$ ).

This condition may be satisfied for several points  $\mathbf{q}'$  of the set  $Q$ . The decomposition of the site group  $G_{\mathbf{q}'}$  into left cosets with respect to the subgroup  $G_{\mathbf{q}}$  has the form

$$G_{\mathbf{q}'} = \sum_{j=1}^n t_{\mathbf{v}_j} R_j G_{\mathbf{q}} \quad (3.67)$$

If the functions  $W_{i1}^{(\beta)}(\mathbf{r})$  ( $i = 1, 2, \dots, n_{\beta}$ ) span the space of an irrep  $\beta$  of the group  $G_{\mathbf{q}}$  then  $n \cdot n_{\beta}$  functions

$$W_{ij}^{(\beta)}(\mathbf{r}) = t_{\mathbf{v}_j} R_j W_{il}^{(\beta)}(\mathbf{r}) \quad (3.68)$$

form the space of the site group  $G_{\mathbf{q}}$  rep  $\beta \uparrow G_{\mathbf{q}}$  induced from the irrep  $\beta$  of its subgroup  $G_{\mathbf{q}'}$ . Let us decompose the rep  $\beta \uparrow G_{\mathbf{q}'}$  into the irreps  $\alpha'$  of the group  $G_{\mathbf{q}'}$

$$\beta \uparrow G_{\mathbf{q}'} = \sum_{\alpha'} r_{\alpha'} \alpha' \quad (3.69)$$

The irrep  $\beta$  of the group  $G_{\mathbf{q}'}$  and rep  $\beta \uparrow G_{\mathbf{q}'}$  of the group  $G_{\mathbf{q}'}$  generate the same induced rep

$$(\mathbf{q}, \beta) = (\mathbf{q}', \beta \uparrow G_{\mathbf{q}'}) = \sum_{\alpha'} r_{\alpha'} (\mathbf{q}', \alpha') \quad (3.70)$$

which is obviously composite. Thus, we have proved that all the possible simple induced reps of a given space group  $G$  may be generated by induction from the irreps of the subgroups  $G_{\mathbf{q}'}$  for  $\mathbf{q}' \in Q$ .

In [40] a complete classification of the inequivalent simple induced reps is given and all the cases when the reps induced from the irreps of maximal isotropy subgroups can be equivalent to one another are considered. First, equivalent induced reps at the same site  $\mathbf{q}' \in Q$  arise.

- 1) by induction from one-dimensional irreps forming an orbit of the normalizer  $N_G(G_{\mathbf{q}'})$ ; there are 23 pairs of them belonging to 15 space groups; and
- 2) four types of isotropy subgroups ( $C_{2v}, D_2, D_{2h}, T$ ) may generate reps induced by irreps that do not form an orbit of  $N_G(G_{\mathbf{q}'})$ . There are 34 pairs of them belonging to 25 space groups.

Second, there are 17 pairs of different maximal isotropy subgroups (belonging to 14 space groups) yielding 63 pairs of equivalent induced reps by induction from one-dimensional irreps. When inducing from two-dimensional irreps of isotropy subgroups, 33 pairs of equivalent induced reps are obtained, belonging to 23 space groups. In total, there are 153 pairs of equivalent induced reps (57 at the same site and 96 at different sites) induced from different irreps of maximal isotropy subgroups. In [40] it was also shown that 40 reps belonging to 25 space groups and induced from irreps of maximal isotropy groups are composite.

There is a formal analogy between simple induced reps and reps irreducible in the usual group-theoretical sense. However, this analogy is not complete. Indeed, the composite induced rep decomposition into simple ones is not always unique. This occurs whenever the site-symmetry group  $G_{\mathbf{q}}$  is not the maximal isotropy one ( $\mathbf{q} \notin Q$ ). In this case, the group  $G_{\mathbf{q}}$  is a subgroup of several maximal isotropy groups  $G_{\mathbf{q}'} (\mathbf{q}' \in Q)$ . Consequently, the induced rep decomposition (3.70) will be different for different points.

The theory of induced representations of space groups gives the answer to the question of whether it is possible to generate in the space of states of a given energy band the basis of localized functions? The answer to this question allows the symmetry connection between delocalized Bloch-type and localized Wannier-type crystalline orbitals to be obtained. This point is discussed in Sect. 3.3.

The following qualitative discussion should explain some features of band reps corresponding to real energy bands in crystals. Let a crystal be formed from isolated constituent atoms by decreasing the interatomic distances from very large ones to those corresponding to real crystalline structure. The crystal field may split the degenerate one-electron atomic levels due to symmetry requirements, leading to quite

narrow energy bands, because of the interatomic interactions. The interatomic distances are sufficiently large that the crystalline orbitals corresponding to these bands are localized quite well at the atomic sites and are close to atomic functions. The Bloch states of these narrow energy bands span the spaces of some band reps that certainly have  $\mathbf{q}$  basis, *i.e.* are induced representations. These reps are induced by those irreps of site-symmetry groups of atoms that describe the transformation properties of atomic states generating the energy bands. The further decrease of the interatomic distances may considerably transform the energy bands (join them together into more complicated ones and later split them up again into other simple ones) but a new electronic state of arbitrary symmetry cannot arise nor can any state disappear. At the same time, the wavefunctions of all possible symmetry types may change and corresponding one-electron energies may shift along the energy scale. Thus, an energy band corresponding to a band rep without a  $\mathbf{q}$  basis (*i.e.* that is not an induced rep) may arise. However, this band, in joining with one or several neighboring ones, forms an energy band corresponding to a composite induced rep with  $\mathbf{q}$  basis. In the joint space of these band states one can generate the basis of localized functions. Thus, the calculated one-electron energy band spectra of crystals may always be divided into bands connected with some simple or composite induced reps. When the interatomic distances are decreased to those in a real crystal the atomic functions undergo more or less extensive modifications and become the Wannier functions of a crystal (see Sect. 3.3). When the latter arise directly from atomic functions one can use for them the same notation ( $s, p, d$  and so on). Let the atoms be at Wyckoff positions with the site symmetry group  $G_q$ . Localized functions transforming according to irreps of the group  $G_q$  correspond to the bands arising from atomic levels split by a crystalline field. If these Wyckoff positions belong to the set  $Q$ , the band states usually form the space of a simple induced rep. When atoms are at positions that do not belong to the set  $Q$  the band states form the basis of a composite induced rep. If, when the interatomic distances are decreased, the energy bands cross one another then the states of the resultant composite band also span the space of a composite induced rep. However, it may happen that this new band splits into several subbands related to localized functions that have centers of localization somewhat displaced from the atomic positions for further decreases in the interatomic distances. This case is typical for the electronic structure of crystals with covalent chemical bonding.

The information about the simple induced representations of the space groups can be given in the form of tables, shown in the next section for the space groups  $O_h^5$ ,  $O_h^7$  and  $O_h^1$ .

### 3.2.5 Simple Induced Representations for Cubic Space Groups $O_h^1$ , $O_h^5$ and $O_h^7$

The correspondence between symbols of simple induced reps in  $\mathbf{q}$ - and  $\mathbf{k}$ -basis for  $\mathbf{q} \in Q$  and  $\mathbf{k} \in K$  is usually given in tables of simple induced reps having the following structure (*e.g.* Tables 3.8–3.10 for the space groups  $O_h^1$ ,  $O_h^5$  and  $O_h^7$ , respectively).

The first two columns of the table contain the labels of the induced reps in the  $\mathbf{q}$ -basis (these labels number the rows of the table): the international symbols (Roman letters  $a, b, c$  and so on) of the Wyckoff positions (sites in direct space) and the Mulliken symbols of the irreps of the site-symmetry groups for these Wyckoff positions. For example,  $d(a_{2u})$  and  $d(e_u)$  are the labels of induced reps in  $\mathbf{q}$ -basis for space

**Table 3.8.** Simple induced representations of the  $O_h^1$  -  $Pm\bar{3}m$  space group

$q$	$\beta$	$\Gamma$	$R$		$M$		$X$	
			$a$	$b$	$a$	$b$	$a$	$b$
$a$	$a_{1g}$	$1^+$	$1^+$	$2^-$	$1^+$	$4^+$	$1^+$	$3^-$
	$a_{1u}$	$1^-$	$1^-$	$2^+$	$1^-$	$4^-$	$1^-$	$3^+$
	$a_{2g}$	$2^+$	$2^+$	$1^-$	$2^+$	$3^+$	$2^+$	$4^-$
	$a_{2u}$	$2^-$	$2^-$	$1^+$	$2^-$	$3^-$	$2^-$	$4^+$
	$e_g$	$3^+$	$3^+$	$3^-$	$1^+2^+$	$3^+4^+$	$1^+2^+$	$3^-4^-$
	$e_u$	$3^-$	$3^-$	$3^+$	$1^-2^-$	$3^-4^-$	$1^-2^-$	$3^+4^+$
	$t_{1g}$	$4^+$	$4^+$	$5^-$	$3^+5^+$	$2^+5^+$	$3^+5^+$	$1^-5^-$
$b$	$t_{1u}$	$4^-$	$4^-$	$5^+$	$3^-5^-$	$2^-5^-$	$3^-5^-$	$1^+5^+$
	$t_{2g}$	$5^+$	$5^+$	$4^-$	$4^+5^+$	$1^+5^+$	$4^+5^+$	$2^-5^-$
	$t_{2u}$	$5^-$	$5^-$	$4^+$	$4^-5^-$	$1^-5^-$	$4^-5^-$	$2^+5^+$
			$c$	$d$	$c$	$d$	$c$	$d$
$c$	$a_{1g}$	$1^+3^+$	$5^+$	$4^-$	$4^+5^-$	$1^+5^-$	$1^+3^-4^-$	$1^+2^+3^-$
	$a_{1u}$	$1^-3^-$	$5^-$	$4^+$	$4^-5^+$	$1^-5^+$	$1^-3^+4^+$	$1^-2^-3^+$
	$b_{1g}$	$2^+3^+$	$4^+$	$5^-$	$3^+5^-$	$2^+5^-$	$2^+3^-4^-$	$1^+2^+4^-$
	$b_{1u}$	$2^-3^-$	$4^-$	$5^+$	$3^-5^+$	$2^-5^+$	$2^-3^+4^+$	$1^-2^-4^+$
$d$	$a_{2g}$	$4^+$	$2^+3^+$	$1^-3^-$	$2^+3^-4^-$	$1^-2^-3^+$	$3^+5^-$	$1^-5^+$
	$a_{2u}$	$4^-$	$2^-3^-$	$1^+3^+$	$2^-3^+4^+$	$1^+2^+3^-$	$3^-5^+$	$1^+5^-$
	$b_{2g}$	$5^+$	$1^+3^+$	$2^-3^-$	$1^+3^-4^-$	$1^-2^-4^+$	$4^+5^-$	$2^-5^+$
	$b_{2u}$	$5^-$	$1^-3^-$	$2^+3^+$	$1^-3^+4^+$	$1^+2^+4^-$	$4^-5^+$	$2^+5^-$
$e_g$	$4^+5^+$	$4^+5^+$	$4^-5^-$		$1^-2^-5^+5^-$	$3^-4^-5^+5^-$	$1^-2^-5^+5^-$	$3^+4^-5^+5^-$
	$e_u$	$4^-5^-$	$4^-5^-$	$4^+5^+$	$1^+2^+5^-5^+$	$3^+4^-5^-5^+$	$1^+2^+5^-5^+$	$3^-4^-5^-5^+$

In  $(aaa)$  units:  $\mathbf{a}_1(100)$ ,  $\mathbf{a}_2(010)$ ,  $\mathbf{a}_3(001)$  $Q: O_h(m\bar{3}m) - a(000)$ ,  $b(1/2, 1/2, 1/2)$ ; $D_{4h}(4/mmm) - c(1/2, 1/2, 0)$ ,  $d(1/2, 0, 0)$ In  $(2\pi/a, 2\pi/a, 2\pi/a)$  units:  $\mathbf{b}_1(100)$ ,  $\mathbf{b}_2(010)$ ,  $\mathbf{b}_3(001)$  $K: O_h - \Gamma(000)$ ,  $R(1/2, 1/2, 1/2)$ ;  $D_{4h} - M(1/2, 1/2, 0)$ ,  $X(1/2, 0, 0)$ 

group  $O_h^1$  (Table 3.8). The remaining columns give the labels of induced reps in the  $\mathbf{k}$ -basis, with the symbols of  $\mathbf{k}$ -points (wavevectors) in the first row of the table and the indices of small irreps of little groups in subsequent rows. For example,  $4^-$  in the column  $\Gamma$  means small irrep  $\Gamma_{4^-}$ . Below the table supplementary information is given – the primitive translations, the coordinates and site-symmetry groups of Wyckoff positions in the direct lattice and the analogous data for the reciprocal lattice. The correspondence between small representations of little groups for symmetry points in BZ is given in Table 3.11 (space group  $O_h^1$ ) and in Table 3.12 (space group  $O_h^5$ ).

In Tables 3.8–3.10 of simple induced reps the labeling of the space-group irreps is that of [17], the labeling of the point group irreps is that of [30] and the site points  $\mathbf{q}$  are indexed as Wyckoff positions from [19].

**Table 3.9.** Simple induced representations of the  $O_h^5 - Fm\bar{3}m$  space group

$q$	$\beta$	$\Gamma$	$L$	$X$	$W$
$a$	$a_{1g}$	$1^+$	$1^+$ $2^-$	$1^+$	$1$ $2$
	$a_{1u}$	$1^-$	$1^-$ $2^+$	$1^-$	$1$ $2$
	$a_{2g}$	$2^+$	$2^+$ $1^-$	$2^+$	$2$ $1$
	$a_{2u}$	$2^-$	$2^-$ $1^+$	$2^-$	$2$ $1$
	$e_g$	$3^+$	$3^+$ $3^-$	$1^+2^+$	$1\ 2$ $1\ 2$
	$e_u$	$3^-$	$3^-$ $3^+$	$1^-2^-$	$3\ 4$ $3\ 4$
	$t_{1g}$	$4^+$	$2^+3^+$ $1^-3^-$	$3^+5^+$	$3\ 5$ $4\ 5$
	$t_{1u}$	$4^-$	$2^-3^-$ $1^+3^+$	$3^-5^-$	$2\ 5$ $1\ 5$
$b$	$t_{2g}$	$5^+$	$1^+3^+$ $2^-3^-$	$4^+5^+$	$4\ 5$ $3\ 5$
	$t_{2u}$	$5^-$	$1^-3^-$ $2^+3^+$	$4^-5^-$	$1\ 5$ $2\ 5$
$c$	$a_1$	$1^+2^-$	$1^+2^-$	$4^+3^-$	$5$
	$a_2$	$2^+1^-$	$2^+1^-$	$3^+4^-$	$5$
	$e$	$3^+3^-$	$3^+3^-$	$3^+4^+3^-4^-$	$5\ 5$
	$t_1$	$4^+5^-$	$2^+3^+1^-3^-$	$2^+5^+1^-5^-$	$1\ 2\ 3\ 4\ 5$
	$t_2$	$5^+4^-$	$1^+3^+2^-3^-$	$1^+5^+2^-5^-$	$1\ 2\ 3\ 4\ 5$
$d$	$a_g$	$1^+3^+5^+$	$1^+3^+2^-3^-$	$1^+4^+3^-4^-5^-$	$1\ 2\ 5\ 5$
	$a_u$	$1^-3^-5^-$	$1^-3^-2^+3^+$	$1^-4^-3^+4^+5^+$	$3\ 4\ 5\ 5$
	$b_{1g}$	$2^+3^+4^+$	$2^+3^+1^-3^-$	$2^+3^+3^-4^-5^-$	$1\ 2\ 5\ 5$
	$b_{1u}$	$2^-3^-4^-$	$2^-3^-1^+3^+$	$2^-3^-3^+4^+5^+$	$3\ 4\ 5\ 5$
	$b_{2g}$	$4^+5^+$	$1^+3^+1^-3^-$	$1^-2^-5^+5^-$	$1\ 3\ 4\ 4\ 5$
	$b_{2u}$	$4^-5^-$	$1^-3^-1^+3^+$	$1^+2^+5^-5^+$	$1\ 1\ 2\ 4\ 5$
	$b_{3g}$	$4^+5^+$	$2^+3^+2^-3^-$	$5^+1^-2^-5^-$	$2\ 3\ 3\ 4\ 5$
	$b_{3u}$	$4^-5^-$	$2^-3^-2^+3^+$	$5^-1^+2^+5^+$	$1\ 2\ 2\ 3\ 5$

In  $(aaa)$  units:  $\mathbf{a}_1(0, 1/2, 1/2)$ ,  $\mathbf{a}_2(1/2, 0, 1/2)$ ,  $\mathbf{a}_3(1/2, 1/2, 0)$

$Q: O_h(m\bar{3}m) - a(000)$ ,  $b(1/2, 1/2, -1/2)$ ;

$T_d(\bar{4}3m) - c(1/4, 1/4, 1/4)$ ;  $D_{4h}(mmm) - d(1/2, 0, 0)$ .

In  $(2\pi/a, 2\pi/a, 2\pi/a)$  units:  $\mathbf{b}_1(-111)$ ,  $\mathbf{b}_2(1-11)$ ,  $\mathbf{b}_3(11-1)$

$K: O_h - \Gamma(000)$ ;  $D_{4h} - X(0, 1/2, 1/2)$

$D_{3d} - L(1/2, 1/2, 1/2)$ ;  $D_{2d} - W(1/4, 1/2, 3/4)$ .

According to the theory developed in previous sections, all the information about the induced reps of a given space group is contained in the table of its simple induced reps. Using these tables one can solve the following two purely mathematical problems:

1) Finding the irreducible components of the space-group reps induced by the irreps of all the possible site-symmetry subgroups for a given space group.

2) Finding the irreducible components of the site-symmetry group reps subduced by the irreps of the corresponding space group.

To solve these two problems one also needs:

a) the compatibility relation tables for the irreps of space groups [17];

b) tables of induced reps of crystallographic point groups [13].

**Table 3.10.** Simple induced representations of the  $O_h^7 - Fd\bar{3}m$  space group

$q$	$\beta$	$\Gamma$	$X$	$L$		$W$	
						$a$	$b$
$a$	$a_1$	$1^+2^-$	1		$1^+2^-$	1	2
	$a_2$	$1^-2^+$	2		$1^-2^+$	2	1
	$e$	$3^+3^-$	1 2		$3^+3^-$	1 2	1 2
$b$	$t_1$	$4^+5^-$	2 3 4		$1^-2^+3^+3^-$	1 1 2	1 2 2
	$t_2$	$4^-5^+$	1 3 4		$1^+2^-3^+3^-$	1 2 2	1 1 2
				$c$	$d$		
$c$	$a_{1g}$	$1^+5^+$	1 3	$1^+2^-3^-$	$1^+2^-3^+$	1 2	
	$a_{1u}$	$1^-5^-$	2 3	$1^-2^+3^+$	$1^-2^+3^-$	1 2	
	$a_{2g}$	$2^+4^+$	2 4	$1^-2^-3^-$	$1^-2^+3^+$	1 2	
$d$	$a_{2u}$	$2^-4^-$	1 4	$1^+2^-3^+$	$1^+2^-3^-$	1 2	
	$e_g$	$3^+4^+4^+$	1 2 3 4	$1^-2^-3^+3^-3^-$	$1^-2^+3^+3^-3^+$	1 1 2 2	
	$e_u$	$3^-4^-4^-$	1 2 3 4	$1^+2^+3^-3^+3^+$	$1^+2^-3^-3^-3^+$	1 1 2 2	

For the direct and reciprocal lattice translation vectors and coordinates of  $K$ -set points see Table 3.9.

$Q$ :  $T_d(\bar{4}3m) - a(000)$ ,  $b(1/2, 1/2, -1/2)$ ;  
 $D_{3d}(\bar{3}m - c(1/8, 1/8, 1/8)$ ,  $d(-3/8, -3/8, 5/8)$ .

**Table 3.11.** Space group  $O_h^1$ : correspondence between small representations of little groups  $G_\Gamma$ ,  $G_R$ ,  $G_X$  and  $G_M$  and irreducible representations of point groups  $O_h$  and  $D_{4h}$ 

$\Gamma, R$	$O_h$	$X, M$	$D_{4h}$
$1^+$	$a_{1g}$	$1^+$	$a_{1g}$
$1^-$	$a_{1u}$	$1^-$	$a_{1u}$
$2^+$	$a_{2g}$	$2^+$	$a_{2g}$
$2^-$	$a_{2u}$	$2^-$	$a_{2u}$
$3^+$	$e_g$	$3^+$	$b_{1g}$
$3^-$	$e_u$	$3^-$	$b_{1u}$
$4^+$	$t_{1g}$	$4^+$	$b_{2g}$
$4^-$	$t_{1u}$	$4^-$	$b_{2u}$
$5^+$	$t_{2g}$	$5^+$	$e_g$
$5^-$	$t_{2u}$	$5^-$	$e_u$

We consider now in more detail the application of the tables of simple induced reps for the solution of the two problems mentioned above. Suppose one needs to find, for a given space-group, the irreducible components of the space group reps induced by some irrep of the site-symmetry subgroup  $G_q \subset G$ . One has to consider four cases.

la)  $\mathbf{q} \in Q$  and  $\mathbf{k} \in K$ . All the irreps in question can be found immediately from the table of simple induced reps. For example, all the irreps  $(^*\mathbf{k}, \beta)$  of the space group  $O_h^1$  with  $\mathbf{k} \in K$  contained in the simple induced rep  $d(a_{1g})$  are enumerated in the row  $d(a_{1g})$  of Table 3.8:  $\Gamma(1^+3^+)R(4^-)M(1^+5^-)X(1^+2^+3^-)$ .

**Table 3.12.** Space group  $O_h^5$ : correspondence between small representations of little groups  $G\Gamma, G_x, G_L, G_w$  and irreducible representations of point groups  $O_h, D_{4h}, D_{3d}$  and  $D_{2d}$ 

$\Gamma$	$O_h$	$X$	$D_{4h}$	$L$	$D_{3d}$	$W$	$D_{2d}$
1 <sup>+</sup>	$a_{1g}$	1 <sup>+</sup>	$a_{1g}$	1 <sup>+</sup>	$a_{1g}$	1	$a$
1 <sup>-</sup>	$a_{1u}$	1 <sup>-</sup>	$a_{1u}$	1 <sup>-</sup>	$a_{1u}$	2	$b$
2 <sup>+</sup>	$a_{2g}$	2 <sup>+</sup>	$a_{2g}$	2 <sup>+</sup>	$a_{2g}$	3,4	$e$
2 <sup>-</sup>	$a_{2u}$	2 <sup>-</sup>	$a_{2u}$	2 <sup>-</sup>	$a_{2u}$		
3 <sup>+</sup>	$e_g$	3 <sup>+</sup>	$b_{1g}$	3 <sup>+</sup>	$e_g$		
3 <sup>-</sup>	$e_u$	3 <sup>-</sup>	$b_{1u}$	3 <sup>-</sup>	$e_u$		
4 <sup>+</sup>	$t_{1g}$	4 <sup>+</sup>	$b_{2g}$				
4 <sup>-</sup>	$t_{1u}$	4 <sup>-</sup>	$b_{2u}$				
5 <sup>+</sup>	$t_{2g}$	5 <sup>+</sup>	$e_g$				
5 <sup>-</sup>	$t_{2u}$	5 <sup>-</sup>	$e_u$				

lb)  $\mathbf{q} \in Q$  and  $\mathbf{k} \notin K$ . After using the table of simple induced reps it is necessary to use the tables of compatibility relations. As an example the latter are given in Table 3.13 for the  $R$  and  $M$  points of the BZ. For example, the simple induced rep  $d(a_{1g})$  of the group  $O_h^1$  contains the irreps  $R_{4-}$  and, according to Table 3.13 of compatibility relations, the irreps  $\Lambda_1, \Lambda_2$  with  $\mathbf{k} \notin K$  since  $R_{4-} \downarrow G_d = \Lambda_1 + \Lambda_2$ .

**Table 3.13.** Compatibility relations for space group  $O_h^1$ . For the  $\Gamma$  and  $X$  points the compatibility relations for the space group  $O_h^1$  coincide with those for the space group  $O_h^5$  (see Table 3.12)

$R$	1 <sup>+</sup>	1 <sup>-</sup>	2 <sup>+</sup>	2 <sup>-</sup>	3 <sup>+</sup>	3 <sup>-</sup>	4 <sup>+</sup>	4 <sup>-</sup>	5 <sup>+</sup>	5 <sup>-</sup>
$\Lambda(\Gamma L)$	1	2	2	1	3	3	2,3	1,3	1,3	2,3
$S(R X)$	1	2	4	3	1,4	2,3	2,3,4	1,3,4	1,2,3	1,2,4
$T(R M)$	1	2	4	1,3	2,4	2,5	1,5	4,5	3,5	
$M$	1 <sup>+</sup>	1 <sup>-</sup>	2 <sup>+</sup>	2 <sup>-</sup>	3 <sup>+</sup>	3 <sup>-</sup>	4 <sup>+</sup>	4 <sup>-</sup>	5 <sup>+</sup>	5 <sup>-</sup>
$\Sigma(\Gamma M)$	1	2	4	3	4	3	1	2	2,3	1,4
$Z(X M)$	1	2	4	3	1	2	3	4	2,4	1,3
$T(R M)$	1	2	2	1	3	4	4	3	5	5

1c)  $\mathbf{q} \notin Q$  and  $\mathbf{k} \in K$ . First, the table of induced representations of point groups is used to obtain the decomposition (3.75) and then the table of simple induced reps may be used.

1d)  $\mathbf{q} \notin Q$  and  $\mathbf{k} \notin K$ . All three tables (simple induced reps of a space group, induced representations of point groups and compatibility relations) are necessary. All the four cases are considered in detail in [13] on the example of the space group  $D_{4h}^{14}$  (symmetry group of rutile structure). If we now seek the irreducible components of the site-symmetry group reps subduced by a given space group irrep  $(^*\mathbf{k}, \gamma)$  (problem 2) we also have four cases to consider.

2a)  $\mathbf{k} \in K$  and  $\mathbf{q} \in Q$ . One finds the irrep  $(^*\mathbf{k}, \gamma)$  in question in the rows of the table of simple induced reps corresponding to the irreps of the site group. According to the Frobenius reciprocity theorem the irrep  $\beta$  is contained in the reducible rep of the group  $G_q$  subduced by the irrep  $(^*\mathbf{k}, \gamma)$  of the space group  $G$  as many times as the symbol  $(^*\mathbf{k}, \gamma)$  is repeated in the corresponding row of the table of simple induced reps. For example, the rep of the site group  $G_d=D_{4h}$  subduced by the irrep  $M_{5-}$  of the space group  $O_h^1$  consists of the irreps  $a_{1g}$  and  $e_u$  (Table 3.13).

2b)  $\mathbf{k} \in K$  and  $\mathbf{q} \notin Q$ . First one finds the irreps  $\alpha'$  contained in the decomposition of the rep of the group  $G_{\bar{g}'}$  ( $G_q \subset G_{\bar{g}'}$  subduced by the irrep  $(^*\mathbf{k}, \gamma)$ ) (as is done in 2a). Then, using the table of induced representations of point groups one decomposes the reps of the group  $G_{\bar{g}}$  subduced by the irreps  $\alpha'$  of the group  $G_{\bar{g}'}$ .

2c)  $\mathbf{k} \notin K$  and  $\mathbf{q} \in Q$ . Using the compatibility-relations perovskite table one completes the simple induced reps table by one additional column only in the rows corresponding to the irreps of the group  $G_{\bar{g}}$ . Then one proceeds as in case 2a.

2d)  $\mathbf{k} \notin K$  and  $\mathbf{q} \notin Q$ . The irreducible components of the subduced rep can be found in two steps: first, the compatibility-relations table is used as in case 2c, and then the table of induced representations of point groups as in case 2b.

Unfortunately simple induced reps for 230 space groups can not be found on any Internet site. One can find them in the book by Kovalev [31], but the irreps notations in this book sometimes differ from those used by Miller and Love [17] and on the site [16]. The latter notations are introduced in tables of simple induced reps of 25 frequently used space groups given in [13]. In this section we reproduce from [13] the simple induced tables for three cubic space groups belonging to the crystal class  $O_h$ :  $O_h^1$  (simple cubic lattice, see the Brillouin zone in Fig. 3.1) and  $O_h^5$ ,  $O_h^7$  (face-centered cubic lattices, the Brillouin zone in Fig. 3.2). The symmetry of the perovskite form of  $\text{SrZrO}_3$ ,  $\text{MgO}$  and silicon crystals is described by the groups  $O_h^1$ ,  $O_h^5$  and  $O_h^7$ , respectively. These crystals are examples of systems with different types of chemical bonding: the mixed ionic-covalent bonding (in  $\text{SrZrO}_3$  the Sr atom is in the  $\text{Sr}^{2+}$  state, the Zr–O bonding is essentially covalent), ionic bonding ( $\text{MgO}$ ) and covalent bonding (Si). In the next subsection we illustrate the use of the simple induced representations in the electronic-structure theory for these relatively simple structures.

### 3.2.6 Symmetry of Atomic and Crystalline Orbitals in $\text{MgO}$ , $\text{Si}$ and $\text{SrZrO}_3$ Crystals

The space symmetry of crystalline orbitals generated by atomic orbitals of the LCAO basis can be found from the tables of induced representations of space groups considered in previous section. The knowledge of space symmetry of crystalline orbitals allows the pictures of electronic bands given as a result of electronic-structure calculations to be understood. It is also useful in localized crystalline orbitals generation (see Sect. 3.3). As an example, we show the energy bands for  $\text{MgO}$  (Fig. 3.4), silicon (Si) (Fig. 3.5) and  $\text{SrZrO}_3$  crystals (Fig. 3.3). The LCAO calculations of these crystals were made using the Hartree–Fock LCAO method (see Chap. 4).  $\text{MgO}$  crystal has rocksalt structure with symmorphic space group  $O_h^5$ , Si crystal has diamond structure with nonsymmorphic space group  $O_h^7$  and  $\text{SrZrO}_3$  crystal has perovskite structure with symmorphic space group  $O_h^1$ , see Sect. 2.3.2. The translation symmetry of the first two crystals is described by the same face-centered cubic lattice, of

the third one – by the simple cubic lattice. The point group  $F = O_h$  of all the three crystals is holosymmetric (coincides with point group  $F^0$  of the cubic lattice). For the first two crystals the wavevector belongs to the same Brillouin zone (Fig. 3.2), the representation domain coincides with the basic domain, the symmetry points of BZ are the same:  $\Gamma(0, 0, 0)$ ,  $X(1/2, 1/2, 0)$ ,  $L(1/2, 1/2, 1/2)$  and  $W(1/4, 1/2, 3/4)$  with the wavevector point groups  $O_h$ ,  $D_{4h}$ ,  $D_{3d}$  and  $D_{2d}$ , respectively. For the third crystal, the wavevector belongs to the simple cubic lattice Brillouin zone (Fig. 3.1), the representation domain also coincides with basic domain, the symmetry points of BZ are:  $\Gamma(0, 0, 0)$ ,  $R(1/2, 1/2, 1/2)$ ,  $X(1/2, 0, 0)$  and  $M(1/2, 1/2, 0)$  with the wavevector point groups  $O_h$ ,  $O_h$ ,  $D_{4h}$  and  $D_{4h}$ , respectively. For the symmorphic space groups  $O_h^5$  and  $O_h^1$  the small representations of little groups of symmetry points of BZ coincide with the ordinary (vector) irreducible representations of the corresponding wavevector point groups. For nonsymmorphic space group  $O_h^7$  the small representations of little groups  $G_\Gamma$ ,  $G_X$ ,  $G_L$  and  $G_W$  were considered in Sect. 3.1.4. For the  $\Gamma$  and  $L$  points the notations given in Table 3.12 are used as the corresponding small representations are  $p$ -equivalent to ordinary representations of point groups  $O_h$  and  $D_{3d}$ . For the  $X$  and  $W$  points the small representations are not  $p$ -equivalent to ordinary irreducible representations of point groups  $D_{4h}$  and  $D_{2d}$ , respectively. The notations for these representations were given in Sect. 3.4.

Let us connect the pictures of the calculated band structures with the symmetry of crystalline orbitals. As for MgO and silicon crystals the dimensions of the corresponding small representations are different at the  $X$  and  $W$  points, the splitting of the valence band to one-sheet and three-sheet subbands takes place for MgO, but for *Si* crystal the valence band is not split. In the symmetry directions of the Brillouin zone the compatibility relations are used to explain the energy-level splittings. The compatibility relations for space groups  $O_h^5$  and  $O_h^7$  are given in Table 3.14 and in Table 3.13 for space group  $O_h^1$ .

For the symmetry directions in the Brillouin zone  $\Delta(\Gamma X)$ ,  $\Delta(\Gamma L)$ ,  $\Sigma$  (see Fig. 3.2) the small representations of both space groups are  $p$ -equivalent to ordinary irreducible representations of point groups  $C_{4v}$ ,  $C_{3v}$  and  $C_{2v}$ . The notations of these representations are taken from [17]. For symmetry directions on the surface of the Brillouin zone  $Z(XW)$ ,  $S$  small representations of space group  $O_h^5$  are  $p$ -equivalent to ordinary irreducible representations of point group  $C_{2v}$ , for the symmetry direction  $Q$  – to ordinary irreducible representations of group  $C_s$ . For the nonsymmorphic space group  $O_h^7$  small representations in the symmetry direction  $Z$  are not  $p$ -equivalent to ordinary irreducible representations of point group  $C_{2v}$  (see Sect. 3.2.2).

In Tables 3.15 and 3.16 we give the notations of induced representations in  $\mathbf{k}$ -basis for symmetry points of the Brillouin zone. We include only the band representations for upper valence bands of all the crystals under consideration.

These bands are induced by the oxygen atom  $2s$ ,  $2p$  states in MgO, by the silicon atom  $3s$ ,  $3p$  states in silicon, by the strontium atom  $4p$  states and oxygen atom  $2s$ ,  $2p$  states in  $\text{SrZrO}_3$ . The symmetry of the corresponding crystalline orbitals is given in Figures 3.3–3.5 and was extracted directly from the tables of the simple induced representations of the corresponding space groups given in Sect. 3.2.5 as the Wyckoff positions occupied by atoms belong to the  $Q$  sets in all three structures under consideration. For all three crystals the short symbol of the BR in  $\mathbf{k}$ -basis contains only the indices of the small IRs for the most symmetrical points of the BZ, because the

**Table 3.14.** Compatibility relations for space groups  $O_h^5$  and  $O_h^7$ 

$\Gamma(O_h^5, O_h^7)$	1 <sup>+</sup>	1 <sup>-</sup>	2 <sup>+</sup>	2 <sup>-</sup>	3 <sup>+</sup>	3 <sup>-</sup>	4 <sup>+</sup>	4 <sup>-</sup>	5 <sup>+</sup>	5 <sup>-</sup>
$\Delta(\Gamma X)$	1	2	3	4	1,3	2,4	2,5	4,5	1,5	3,5
$\Delta(\Gamma L)$	1	2	2	1	3	3	2,3	1,3	1, 3	2,3
$\Sigma$	1	2	4	3	1,4	2,3	2,3,4	1,3,4	1,2,3	1,2,4
$X(O_h^5)$	1 <sup>+</sup>	1 <sup>-</sup>	2 <sup>+</sup>	2 <sup>-</sup>	3 <sup>+</sup>	3 <sup>-</sup>	4 <sup>+</sup>	4 <sup>-</sup>	5 <sup>+</sup>	5 <sup>-</sup>
$\Delta$	1	2	2	1	3	4	4	3	5	5
$Z(XW)$	1	2	3	4	1	2	4	3	2,3	1,4
$S$	1	2	4	3	4	3	1	2	2,3	1,4
$X(O_h^7)$	1	2	3	4						
$\Delta$	1,4	2,3	5	5						
$Z(XW)$	1	1	1	1						
$S$	1,3	2,4	3,4	1,2						
$L(O_h^5, O_h^7)$	1 <sup>+</sup>	1 <sup>-</sup>	2 <sup>+</sup>	2 <sup>-</sup>	3 <sup>+</sup>	3 <sup>-</sup>				
$\Lambda$	1	2	2	1	3	3				
$Q$	1	1	2	2	1,2	1,2				
$W(O_h^5)$	1	2	3	4	5		$W(O_h^7)$	1	2	
$Z$	1	2	2	1	3,4			1	1	
$Q$	1	2	1	2	1,2			1,2	1,2	

**Table 3.15.** Band representations of space groups  $O_h^5$  and  $O_h^7$  for upper valence bands of MgO and Si crystals

	$\Gamma$	X	L	W
MgO - $O_h^5$				
$b(1/2, 1/2, 1/2)$	$a_{1g}$	1 <sup>+</sup>	1 <sup>+</sup>	2 <sup>-</sup>
	$t_{1u}$	5 <sup>-</sup>	2 <sup>-</sup> 5 <sup>-</sup>	1 <sup>+</sup> 3 <sup>+</sup>
Si - $O_h^7$				
$a(0\ 0\ 0)$	$a_1$	1 <sup>+</sup> 2 <sup>-</sup>	1	1 <sup>+</sup> 2 <sup>-</sup>
	$t_2$	4 <sup>-</sup> 5 <sup>+</sup>	1 3 4	1 <sup>+</sup> 2 <sup>-</sup> 3 <sup>+</sup> 3 <sup>-</sup>
				1 2 2

**Table 3.16.** Band representations of upper valence bands in SrZrO<sub>3</sub> crystal induced from Sr 4p-, O 2s- and O 2p- atom-like states

Atom states	q-basis	$\Gamma$	R	M	X
Sr 4p-	( $b, t_{1u}$ )	4 <sup>-</sup>	5 <sup>+</sup>	2 <sup>-</sup> 5 <sup>-</sup>	1 <sup>+</sup> 5 <sup>+</sup>
O 2s-	( $d, a_{1g}$ )	1 <sup>+</sup> 3 <sup>+</sup>	4 <sup>-</sup>	1 <sup>+</sup> 5 <sup>-</sup>	1 <sup>+</sup> 2 <sup>+</sup> 3 <sup>-</sup>
O 2p <sub>z</sub> -	( $d, a_{2u}$ )	4 <sup>-</sup>	1 <sup>+</sup> 3 <sup>+</sup>	1 <sup>+</sup> 2 <sup>+</sup> 3 <sup>-</sup>	1 <sup>+</sup> 5 <sup>-</sup>
O 2p <sub>x,y</sub> -	( $d, e_u$ )	4 <sup>-</sup> 5 <sup>-</sup>	4 <sup>+</sup> 5 <sup>+</sup>	3 <sup>+</sup> 4 <sup>+</sup> 5 <sup>±</sup>	3 <sup>-</sup> 4 <sup>-</sup> 5 <sup>±</sup>

indices for all other IRs contained in the BR are determined with the help of compatibility relations. These are the states responsible for four-sheet valence bands in the first two crystals (Fig. 3.4 and Fig. 3.5) and for the 6- and 9-sheet valence bands in  $SrZrO_3$  crystal (Fig. 3.3)

Due to the considered symmetry difference of crystalline orbitals in  $MgO$  and  $Si$  crystals the nature of chemical bonding in these crystals is also different. Indeed, in ionic  $MgO$  crystal the splitting of the valence band allows the crystalline orbitals localized on an oxygen atom to be generated and transformed over  $a_{1g}$  and  $t_{1u}$  irreducible representations of the oxygen site-symmetry group  $O_h$ . In covalent  $Si$  crystal all four sheets of the valence band have to be included in localization so that the localized orbitals found are centered at the middle of the  $Si - Si$  bond.

In  $SrZrO_3$  crystal oxygen  $2s$  functions transform according to  $\beta = a_{1g}$  IR of the oxygen site-symmetry group  $G_{\mathbf{q}} = D_{4h}$  and generate a 3-sheeted BR. The symmetry of states in this band is fully determined by the  $2s$  function of one of three oxygens in the primitive cell and may be labeled by the symbol  $(d, a_{1g})$  as oxygen atoms occupy Wyckoff position  $d$  in space group  $O_h^1$ . In Table 3.16 this band, with the symbol of the BR  $(d, a_{1g})$ , is given in  $\mathbf{k}$ -basis ( $\Gamma, R, M, X$  are the symmetry points of the BZ).

In Sect. 3.2.4 we defined simple and composite BRs. A BR is simple if it does not consist of two or more BRs of a smaller dimension. All simple BRs for a given space group are generated by the IRs of site-symmetry groups of just a few points in the Wigner–Seitz cell of the direct lattice.

In our examples, all the induced irreps are simple, excluding the BR corresponding to the 6-sheeted lower valence subband (see Fig. 3.3). This band representation is a composite one as it is formed by two simple band representations  $(d, a_{1g})$  and  $(b, t_{1u})$  induced by O  $2s$ - and Sr  $4p$ states, respectively. Analysis of the space symmetry of crystalline orbitals is used to consider the possible centers of localization of chemical bonding in crystals. This task requires the Wannier-function definition and is considered in the next section.

### 3.3 Symmetry of Localized Crystalline Orbitals.

#### Wannier Functions

##### 3.3.1 Symmetry of Localized Orbitals and Band Representations of Space Groups

The localized molecular orbitals (LMO) are extensively used not only for the chemical-bonding analysis in molecules but also in the local correlation methods [41] (we consider the problem of electron correlation in molecules and crystals in Chap. 5). The LMO are generated from the canonical MO occupied by electrons and found in the Hartree–Fock or DFT calculations. This generation is based on one or other localization criteria [42].

Localized crystalline orbitals (LCO) are generated from a canonical delocalized Bloch functions (CO). As in the case of the molecules one or other localization criteria is used. The orthonormalized LCO in crystals are known as Wannier functions. Wannier functions (WFs) have attracted much attention in solid-state physics since their first introduction in 1937 [43] and up to now. The analytical behavior of Bloch

functions of energy bands in  $\mathbf{k}$ -space determines the degree of localization of the corresponding Wannier functions in  $\mathbf{r}$ -space [44, 45]. A useful concept of band (induced) representations has been introduced in the theory of crystals, according to which the position of symmetry localization and the symmetry properties of Wannier functions for a given energy band define unambiguously the symmetry properties of the corresponding Bloch functions [13]. But the last decade has been marked by an outburst of interest in WFs, owing to the development of new theories related to them, and effective methods for their generation [5, 46–48].

Due to their high localization, WFs are especially beneficial when applied in the following areas of solid-state theory.

1. Linear scaling (so-called  $O(N)$ ) algorithms for calculation of crystalline electronic structure are based on the concept of WFs [50].

2. WFs play an important role in the theory of electronic polarization in insulators [51]. The electronic polarization itself and related properties can be expressed simply via the centroids of WFs, connected with the valence-band states.

3. Wannier functions are often used as a convenient basis for describing the local phenomena in solids, such as point defects, excitons, surfaces, *etc.* [52].

4. They can serve as a useful tool in the solution of the problem of electron correlation in crystals [41].

5. WFs, being spatially localized combinations of Bloch functions, thus form a natural basis for analysis of chemical bonding in crystals [47, 53, 54].

The background of LOs symmetry analysis is the theory of BRs of space groups  $G$ . This analysis is equally applicable to localized Wannier orbitals (LWOs) *i.e.* to an orthonormal set of LOs. We describe the main principles of this theory related to the examined problem.

The LOs  $V_{i1p}^{(\beta)}(\mathbf{r}) \equiv V_i^{(\beta)}(\mathbf{r} - \mathbf{q}_1^{(p)})$  are the basis functions of the irreducible representation (IR)  $\beta$  of the site-symmetry group  $G_{\mathbf{q}^{(p)}} \subset G$  corresponding to their centering point (centroid)  $\mathbf{q}_1^{(p)}$  (index  $p$  distinguishes the symmetry nonequivalent points in the space of the crystal):

$$(\hat{R}|\mathbf{v}_R)V_{i1p}^{(\beta)}(\mathbf{r}) = \sum_{i'} d_{i'i}^{(\beta)}(R)V_{i'1p}^{(\beta)}(\mathbf{r}) \quad (3.71)$$

where  $(\hat{R}|\mathbf{v}_R) \in G_{\mathbf{q}^{(p)}}$ ,  $d^{(\beta)}(R)$  is the matrix mapping the element  $(\hat{R}|\mathbf{v}_R)$  in the IR  $\beta$ . For example, in crystal  $\text{SrZrO}_3$  index  $p = 1, 2, 3$  numbers symmetry nonequivalent Sr, Zr and one of the three oxygen atoms. Applying symmetry operations from the decomposition of the group  $G$  into the left cosets with respect to the site group  $G_{\mathbf{q}^{(p)}}$

$$G = \sum_j (R_j|\mathbf{v}_j + \mathbf{a}_n) \cdot G_{\mathbf{q}^{(p)}} \quad (3.72)$$

to the functions  $V_{i1p}^{(\beta)}(\mathbf{r})$

$$V_{ijp}^{(\beta)}(\mathbf{r} - \mathbf{a}_n) \equiv (R_j|\mathbf{v}_j + \mathbf{a}_n)V_{i1p}^{(\beta)}(\mathbf{r}) \quad (3.73)$$

one can obtain the complete basis in the space  $\Omega_p^{(\beta)}$  of the reducible representation of the group  $G$  induced from the IR  $\beta$  of the group  $L_{\mathbf{q}^{(p)}}$ . The functions  $V_{ijp}^{(\beta)}(\mathbf{r} - \mathbf{a}_n) \equiv$

$V_i^{(\beta)}(\mathbf{r} - \mathbf{q}_{j,\mathbf{n}}^{(p)} - \mathbf{a}_\mathbf{n})$  are centered at the points  $\mathbf{q}_{j,\mathbf{n}}^{(p)} \equiv (R_j|\mathbf{v}_j + \mathbf{a}_\mathbf{n})\mathbf{q}_1^{(p)} = R_j\mathbf{q}_1^{(p)} + \mathbf{v}_j + \mathbf{a}_\mathbf{n}$ . Such a basis consisting of the LOs  $V_{ijp}^{(\beta)}(\mathbf{r} - \mathbf{a}_\mathbf{n}) \equiv V_\tau(\mathbf{r} - \mathbf{a}_\mathbf{n}) \equiv V_t(\mathbf{r})$  is called the  $\mathbf{q}$ -basis (Sect. 3.2.2). The index  $\tau$  replaces  $i, j, \beta, p$ , and the index  $t$  replaces  $\tau, \mathbf{n}$  to simplify a traditional group-theoretical notation. This basis is fully determined by its single representative (for example,  $V_{11p}^{(\beta)}(\mathbf{r})$ ). All the other basis functions of the same BR can be obtained from it by the symmetry operations, (3.73). A BR is characterized in  $\mathbf{q}$ -basis by the site  $\mathbf{q}^{(p)}$  (the centroid of  $V_{11p}^{(\beta)}(\mathbf{r})$ ) and the IR  $\beta$  of the site group  $G_{\mathbf{q}^{(p)}} : (\mathbf{q}^{(p)}, \beta)$  is a symbol of the BR in  $\mathbf{q}$ -basis. For example, in MgO crystal oxygen  $2s$ -functions transform according to  $\beta = a_{1g}$  IR of the site-symmetry group  $G_{\mathbf{q}^{(1)}} = O_h$  and decomposition (3.72) consists of 1 term as the point group of the crystal is  $O_h$ . The functions  $V_{i1p}^{(a_{1g})}(\mathbf{r} - \mathbf{a}_\mathbf{n})$  are centered at the oxygens in a whole direct lattice. Silicon crystal has space group  $O_h^7$ , diamond-type lattice with two atoms per unit cell, occupying the Wyckoff position  $a$  with the site-symmetry group  $G_a = T_d$ . The calculated upper valence and lower conduction bands shown in Fig. 3.5 are composite (for each wavevector value there are  $4 + 4 = 8$  Bloch states). The corresponding induced representation is engendered by  $a_1, t_2$  irreps of the point group  $G_a$ , corresponding by symmetry to the  $s, p$  states of Si atom. The upper valence band in silicon crystal is connected with the one-electron states localized not on the Si atom but on the Si–Si bond middle (Wyckoff position  $c$  with the site-symmetry group  $D_{3d}$ ). This can be found by inducing the four-sheet upper valence band states from the identity representation  $a_{1g}$  of the point group  $D_{3d}$ . The lower conduction-band states symmetry is defined by the induction from the irrep  $a_{2u}$  of the same point group. Therefore, these two band representations may be labeled by the symbols  $(c, a_{1g}), (c, a_{2u})$ .

As the third example of the band representations generated we consider  $\text{SrZrO}_3$  crystal. The configurations of valence electrons in free atoms are:

$$\text{O} - 2s^2 2p^4, \quad \text{Sr} - 4p^6 5s^2, \quad \text{Zr} - 4d^2 5s^2 \quad (3.74)$$

The semicore  $4p$ -states of Sr atom are included in (3.74) as they take part in the valence-band structure. The cubic phase of  $\text{SrZrO}_3$  with the space group

$$Pm\bar{3}m$$

( $O_h^1$ , a simple cubic lattice) consists of one formula unit (5 atoms) in the primitive unit cell. Atoms Sr, Zr and O occupy Wyckoff positions (Cartesian coordinates are given in units of lattice constant of the crystal)  $b$  ( $1/2, 1/2, 1/2$ ),  $a$  ( $0, 0, 0$ ) (site group  $O_h$  for both), and  $d$  ( $0, 0, 1/2$ ) (site group  $D_{4h}$ ), respectively. Fig. 3.3 shows the valence energy bands of this crystal calculated by HF LCAO method with the help of CRYSTAL03 code [23]. 30 electrons per primitive unit cell of  $\text{SrZrO}_3$  crystal occupy 15 one-electron levels for each  $\mathbf{k}$ -point in the BZ. The 15-sheeted valence band consists of two subbands (6 and 9 sheets). The analysis of the projected densities of states shows that the lower 6-sheeted subband is formed by Sr  $4p$ - and O  $2s$ -states, the upper 9-sheeted band is connected mainly with O  $2p$ -states. These free-atom electron states are transformed by the interatomic interaction in crystalline LOs. The latter basis (just as the basis of canonical Bloch one-electron states) may be used to describe the electronic structure of the crystal and calculate its properties. In the  $\text{SrZrO}_3$  crystal, two induced BRs

correspond to six- and nine-sheeted bands. As is seen from Table 3.16, the states of six-sheeted band are induced by LO of the symmetry  $a_{1g}$  of oxygen site-symmetry group  $D_{4h}$  (Wyckoff position  $d$ ) and by LOs of the symmetry  $t_{1u}$  of Sr-atom site-symmetry group  $O_h$  (Wyckoff position  $b$ ), *i.e.* by O 2s- and Sr 4p-atomic-like states. The states of the nine-sheeted band are induced by LOs of the symmetry  $a_{2u}$  and  $e_u$  of oxygen site-symmetry group  $D_{4h}$ , *i.e.* by O 2p-atomic-like states. In  $\text{SrZrO}_3$  crystal oxygen 2s-functions transform according to  $\beta = a_{1g}$  IR of the site-symmetry group  $G_{\mathbf{q}} = D_{4h}$  and decomposition consists of 3 terms as the point group of the crystal is  $O_h$ . The functions  $V_{ijp}^{(a_{1g})}(\mathbf{r} - \mathbf{a}_n)$  are centered on the oxygens in a whole direct lattice ( $j = 1, 2, 3$  numbers oxygens in one primitive cell). This is an example of the  $\mathbf{q}$ -basis corresponding to a 3-sheeted BR, induced by O 2s-type atomic states. This basis is fully determined by a 2s-function of one of the three oxygens in the primitive cell and may be labeled by the symbol  $(d, a_{1g})$  as oxygen atoms occupy Wyckoff position  $d$  in space group  $O_h^1$ .

Resolving this BR into IRs of the space group  $G$ , one gets the indices of the BR in  $\mathbf{k}$ -basis (Bloch basis). The short symbol of the BR in  $\mathbf{k}$ -basis contains only the indices of the small IRs for the most symmetrical points of the BZ, because the indices for all other IRs contained in the BR are determined with the help of compatibility relations. For example, in Table 3.16 the BR  $(d, a_{1g})$  is given in  $\mathbf{k}$ -basis ( $\Gamma, R, M, X$  are the symmetry points of the BZ).

In our example, the BR corresponding to the 6-sheeted valence band is a composite one as it is formed by two simple band representations  $(d, a_{1g})$  and  $(b, t_{1u})$  induced by O 2s- and Sr 4p-states, respectively.

From the theory of the band representations of space groups, it follows that the generation of LOs corresponding to a given simple or composite energy band is possible only if the canonical (Bloch) orbitals of this band form the basis of some simple or composite BR. This analysis permits not only to establish the principal possibility to construct LOs, but also to define the possible positions of their centroids  $\mathbf{q}^{(p)}$  and their symmetry with respect to the site-symmetry group  $G_{\mathbf{q}^{(p)}}$ . The latter is not always unambiguous due to the fact that there are the BRs that have different symbols in  $\mathbf{q}$ -basis, but the same index in  $\mathbf{k}$ -basis or there are the composite BRs that can be decomposed into simple ones by several ways (see Sect. 3.2.4).

Thus, the symmetry analysis consists of a procedure of identifying the localized-orbitals symmetry from the symmetry of the canonical orbitals of the energy band under consideration, or of establishing the fact that the construction of LOs from the canonical orbitals chosen is impossible for the reasons of symmetry.

When calculating the electronic structure of a crystal its cyclic model is used *i.e.* the model of a finite crystal with periodic boundary conditions – a supercell, consisting of  $N$  unit cells. Generally, when a numerical integration over the BZ is carried out as a summation over a set of special points of the BZ, it means that a cyclic model of a certain size is introduced for the crystal. The relation between the symmetry group  $G$  of the model of an infinite crystal and the symmetry group  $G^{(N)}$  of a corresponding cyclic model and their IRs and BRs has been studied in detail in [55]. The localized orbitals of the model of an infinite crystal are well approximated by the localized orbitals of a cyclic models with a size slightly exceeding the region of their localization.

We assume that the canonical delocalized orbitals  $\varphi_{m\mu}^{(\gamma)}(\mathbf{k}, \mathbf{r}) \equiv \varphi_\sigma(\mathbf{k}, \mathbf{r}) \equiv \varphi_s(\mathbf{r})$  (the index  $m$  numbers the basis vectors of IR  $\gamma$  with wavevector  $\mathbf{k}$ ,  $\mu$  discriminates between the independent bases of equivalent IRs; the index  $\sigma$  replaces  $\gamma, m, \mu$ , and  $s$  replaces  $\sigma, \mathbf{k}$ ) of an energy band under consideration form a basis in the space  $\Omega$  of some simple BR of the group  $G^{(N)}$  of a crystal (index  $p$  is omitted for simplicity). The same space  $\Omega$  is spanned also by the set of LOs  $V_{ij}^{(\beta)}(\mathbf{r} - \mathbf{a}_n) \equiv V_t(\mathbf{r})$ . The delocalized and localized bases are bounded by a linear transformation in the space  $\Omega$ :

$$V_\tau(\mathbf{r} - \mathbf{a}_n) = \sum_{\mathbf{k}} \exp(-i\mathbf{k}\mathbf{a}_n) \sum_{\sigma} U_{\sigma,\tau}(\mathbf{k}) \varphi_{\sigma}(\mathbf{k}, \mathbf{r}), \quad \text{or} \quad (3.75)$$

$$V_t(\mathbf{r}) = \sum_s U_{st} \cdot \varphi_s(\mathbf{r}) \quad \text{with} \quad U_{st} = U_{\sigma,\tau}(\mathbf{k}) \cdot \exp(-i\mathbf{k}\mathbf{a}_n) \quad (3.76)$$

If the matrix  $U$  is unitary and the functions  $\varphi_s(\mathbf{r})$  are orthonormalized, the functions  $V_t(\mathbf{r})$  form an orthonormal system of LWOs  $V_t(\mathbf{r}) = W_t(\mathbf{r})$ .

Their localization extent depends on the choice of the matrix  $U_{\sigma,\tau}(\mathbf{k})$  in (3.76). The existence of Wannier functions decreasing exponentially at infinity (for the model of an infinite crystal) is established in many cases. The different localization criteria used for the generation of localized orbitals in crystals are considered in the next subsection.

### 3.3.2 Localization Criteria in Wannier-function Generation

The *general method* of the most localized Wannier-function (WF) generation exists only for the one-dimensional case and was offered by Kohn [57].

It is a variational method based on the first-principles approach, *i.e.* without preliminary knowledge of Bloch-type delocalized functions. The localized functions with the symmetry of Wannier functions and depending on some number of parameters are used.

If spin variables are ignored the one determinant wavefunction for the system of  $M$  electrons occupying  $M$  Bloch-type states can be written as

$$\Psi_0 = (M!)^{-1/2} \det \left| \left( \Phi^{(\varphi)} \right)_{\tau\mathbf{k},i} \right| = (M!)^{-1/2} \det \left| \left( \Phi^W \right)_{s\mathbf{n},i} \right| \quad (3.77)$$

where  $\Phi^{(\varphi)}$  and  $\Phi^W$  are Bloch and Wannier functions, respectively

$$\left( \Phi^{(\varphi)} \right)_{\tau\mathbf{k},i} = \varphi_{\tau\mathbf{k},i}(\mathbf{r}_i) \quad (3.78)$$

$$\left( \Phi^W \right)_{s\mathbf{n},i} = W_s(\mathbf{r}_i - \mathbf{a}_n) \quad (3.79)$$

and  $\mathbf{r}_i$  – coordinate of the  $i$ th electron ( $i = 1, 2, \dots, M$ ).

The total energy  $E_0$  per cell, is

$$E_0 = M^{-1} \left( \Psi_0, \sum_{i=1}^M H_i \Psi_0 \right) = M^{-1} \sum_{\tau, \mathbf{k}} E_{\tau, \mathbf{k}} = \sum_s (W_s(\mathbf{r}), H W_s(\mathbf{r})) \quad (3.80)$$

The better the initial modeling localized functions approximate WF  $W_s(\mathbf{r})$ , the closer to the minimal value  $E_0$  is the value of the total energy calculated on these

modeling functions. Thus, the variational principle assuming a variation of parameters of modeling functions is used to minimize the value of the total energy calculated on such functions.

Before calculation of the total energy on the basis of the trial localized functions  $f_s(\mathbf{r}, \alpha, \beta, \dots)$  (where  $\alpha, \beta, \dots$  are variational parameters), their orthonormalization is made. Functions  $f_s(\mathbf{r} - \mathbf{a}_n)$  are orthogonalized by means of a procedure suggested by Des Cloizeaux [56]. This procedure consists of construction of the orthonormalized trial Bloch functions  $\psi_s(\mathbf{r}, \mathbf{k})$ :

$$\psi_s(\mathbf{r}, \mathbf{k}) = M^{-1/2} \sum_n \exp(i\mathbf{k}\mathbf{a}_n) \left\{ \sum_{s'} f_{s'}(\mathbf{r} - \mathbf{a}_n) \left[ S^{(\psi)^{-1/2}}(\mathbf{k}) \right]_{s's} \right\} \quad (3.81)$$

where  $S^{(\psi)}(\mathbf{k})$  is an overlap matrix of trial Bloch functions, directly constructed of trial localized functions  $f_s(\mathbf{r} - \mathbf{a}_n)$ :

$$\left[ S^{(\psi)}(\mathbf{k}) \right]_{s's} = \sum_n (f_{s'}(\mathbf{r}), f_s(\mathbf{r} - \mathbf{a}_n)) \exp(i\mathbf{k}\mathbf{a}_n) \quad (3.82)$$

Then the modeling localized functions  $W_s^{(m)}(\mathbf{r}) = W_s^{(m)}(\mathbf{r}, \alpha, \beta, \dots)$  are defined. These functions depend on the same parameters as function  $f_s(\mathbf{r}, \alpha, \beta, \dots)$  does:

$$W_s^{(m)}(\mathbf{r}) = M^{-1/2} \sum_{\mathbf{k}} \psi_s(\mathbf{r}, \mathbf{k}) \quad (3.83)$$

and are substituted in (3.83) with the purpose of minimization of the total energy  $E_0$ .

The advantages of the method are the following: WF generation does not require preliminary Bloch-function calculation, the WF symmetry is taken into account at a stage of choice of trial modeling functions. Disadvantages of the method: the procedure is laborconsuming in realization; the WF obtained are approximate and their differences from the exact WF depend on the choice of the trial modeling functions; there is no universal procedure of a choice of basis of trial functions for different crystals; use of the one-determinant approximation for vacant states WF is not quite correct.

The method of WF generation using the *Slater-Koster interpolation procedure* was suggested in [58]. In this method a group of one-electron energy bands is chosen and described by model Hamiltonian matrices  $H(\mathbf{k})$ :

$$\sum_{\mu} H_{\nu\mu}(\mathbf{k}) e_{\mu\tau}(\mathbf{k}) = E_{\tau\mathbf{k}} e_{\nu\tau}(\mathbf{k}) \quad (3.84)$$

where  $e(\mathbf{k})$  and  $E_{\tau\mathbf{k}}$  are eigenvectors and eigenvalues of a matrix model Hamiltonian  $H(\mathbf{k})$  that should coincide with the eigenvalues of the exact Hamiltonian matrix in the given point  $\mathbf{k}$ . For the model Hamiltonian Fourier decomposition is used

$$H(\mathbf{k}) = \sum_n \varepsilon(\mathbf{a}_n) \exp(-i\mathbf{k}\mathbf{a}_n) \quad (3.85)$$

The WF is defined as

$$W_s(\mathbf{r}\mathbf{a}_n) = \frac{V_a}{(2\pi)^3} \int d\mathbf{k} \exp(-i\mathbf{k}\mathbf{a}_n) \sum_{\tau} e_{\tau s}(\mathbf{k}) \varphi_{\tau}(\mathbf{r}, \mathbf{k}) \quad (3.86)$$

so that Fourier coefficients  $\varepsilon_{s's}(\mathbf{a}_n)$  (Slater–Koster parameters) are elements of a Hamiltonian matrix in the basis of WF:

$$\varepsilon_{s's}(\mathbf{a}_n) = \int W_{s'}^*(\mathbf{r} - \mathbf{a}_n) H W_s(\mathbf{r}) d\mathbf{r} \quad (3.87)$$

For well-localized WF values  $\varepsilon_{s's}(\mathbf{a}_n)$  quickly decrease with increase of  $|\mathbf{a}_n|$ . Therefore, in this case in decomposition (3.90) it is enough to consider a small amount of the matrices  $\varepsilon(\mathbf{a}_n)$  corresponding to small values of translation vectors. Additional reduction of the number of independent Slater–Koster parameters is possible when the symmetry is taken into account. The remaining independent elements of matrices  $\varepsilon(\mathbf{a}_n)$  can be found by means of a least squares method, adjusting eigenvalues of a matrix  $H(\mathbf{k})$  to the calculated band structure. Matrices of eigenvectors  $e(\mathbf{k})$  for well-adjusted modeling Hamiltonian are matrices of the unitary transformation  $U(\mathbf{k})$  connecting Bloch functions with localized WF.

There is still an uncertainty in the choice of relative phase multipliers for matrices  $U(\mathbf{k})$  (or)  $e(\mathbf{k})$  at different  $\mathbf{k}$  (this problem can be solved only in crystals with inversion symmetry [59]). Let  $u_s(\mathbf{r}, \mathbf{k})$  be periodic parts of Bloch functions  $\psi_s(\mathbf{r}, \mathbf{k})$ :

$$u_s(\mathbf{r}, \mathbf{k}) = \exp(-i\mathbf{k} \cdot \mathbf{r}) \psi_s(\mathbf{r}, \mathbf{k}) \quad (3.88)$$

Phase multipliers at matrices  $U(\mathbf{k})$  need to be chosen so that decomposition coefficients  $V_j(s, \mathbf{k})$  of functions  $u_s(\mathbf{r}, \mathbf{k})$  on plane waves:

$$u_s(\mathbf{r}, \mathbf{k}) = \sum_j V_j(s, \mathbf{k}) \exp(i\mathbf{K}_j \cdot \mathbf{r}) \quad (3.89)$$

remained real (this is possible if the space group of symmetry of a crystal contains an inversion).

Advantages of the method: for WF generation it is possible to choose any groups of energy band – occupied, vacant or both; the use of expected WF symmetry reduces the number of independent Slater–Koster parameters.

Disadvantages of the method: an efficient procedure for the case when the lattice has no the center of inversion it is not developed; the WF maximal localization criteria is not formulated; the method is complex enough in realization.

The recently developed WF generation method of Marzari and Vanderbilt [46, 60] extends to crystalline solids the Boys [38] criteria of localized MO generation (see Sect. 3.3.1). The localized WF (let their number be  $N$  for the primitive unit cell) are found by the minimization of the functional

$$I = \sum_{s=1}^N \left[ \langle \mathbf{r}^2 \rangle_s - \langle \mathbf{r} \rangle_s^2 \right] \quad (3.90)$$

where

$$\langle \mathbf{r}^2 \rangle_s = \int \mathbf{r}^2 |W_s(\mathbf{r})|^2 d\mathbf{r} \quad (3.91)$$

$$\langle \mathbf{r} \rangle_s = \int \mathbf{r} |W_s(\mathbf{r})|^2 d\mathbf{r} \quad (3.92)$$

Minimization of (3.90) is made in reciprocal space, for which expressions (3.91) and (3.92) can be rewritten in the form:

$$\langle \mathbf{r} \rangle_s = i \frac{V_a}{(2\pi)^3} \int d\mathbf{k} \langle u_s(\mathbf{r}, \mathbf{k}) | \nabla_{\mathbf{k}} | u_s(\mathbf{r}, \mathbf{k}) \rangle \quad (3.93)$$

$$\langle \mathbf{r}^2 \rangle_s = - \frac{V_a}{(2\pi)^3} \int d\mathbf{k} \langle u_s(\mathbf{r}, \mathbf{k}) | \nabla_{\mathbf{k}}^2 | u_s(\mathbf{r}, \mathbf{k}) \rangle \quad (3.94)$$

where  $u_s(\mathbf{r}, \mathbf{k})$  are periodic parts of the Bloch functions defined by (3.89).

The gradient in  $\mathbf{k}$ -space, used in (3.93) and (3.94) is correctly defined only in the model of an infinite crystal when a variable  $\mathbf{k}$  is continuous. In a cyclic model of a crystal the gradient of the function is replaced with the approximate finite-differences expressions, and integration on the Brillouin zone is made by summation over a discrete set of wavevectors  $\mathbf{k}$ . Let  $M_{mn}^{(\mathbf{k}, \mathbf{b})}$  be defined as the scalar product:

$$M_{s's}^{(\mathbf{k}, \mathbf{b})} = \langle u_{s'}(\mathbf{r}, \mathbf{k}) | u_s(\mathbf{r}, \mathbf{k} + \mathbf{b}) \rangle \quad (3.95)$$

where  $\mathbf{b}$  is a vector connecting each  $\mathbf{k}$ -point from a discrete set, corresponding to the considered cyclic model, with one of its nearest neighbors. Then  $\langle \mathbf{r}^2 \rangle_s$  and  $\langle \mathbf{r} \rangle_s$  can be approximately calculated using (3.93) and (3.94):

$$\langle \mathbf{r} \rangle_s = - \frac{1}{L} \sum_{\mathbf{k}, \mathbf{b}} w_b \mathbf{b} \operatorname{Im} \ln M_{ss}^{(\mathbf{k}, \mathbf{b})} \quad (3.96)$$

$$\langle \mathbf{r}^2 \rangle_s = \frac{1}{L} \sum_{\mathbf{k}, \mathbf{b}} w_b \left\{ \left[ 1 - \left| M_{ss}^{(\mathbf{k}, \mathbf{b})} \right|^2 \right] + \left[ \operatorname{Im} \ln M_{ss}^{(\mathbf{k}, \mathbf{b})} \right]^2 \right\} \quad (3.97)$$

The multiplier  $w_b$  depends on the type of Bravais lattice.

Let  $\delta U_{rs}$  be the changes of functional (3.90) value at infinitesimal transformation  $\delta U(\mathbf{k})$  of matrices  $U(\mathbf{k})$ :

$$\delta U_{rs}(\mathbf{k}) = \delta_{rs} + d\Delta_{rs}(\mathbf{k}) \quad (3.98)$$

Here,  $d\Delta(\mathbf{k})$  is the antihermitian matrix of infinitesimal transformation. It is possible to show that the gradient of functional (3.91) in the space of matrices  $U$  is expressed by the following formula:

$$G(\mathbf{k}) = \frac{dI}{d\Delta(\mathbf{k})} = 4 \sum_{\mathbf{b}} w_{\mathbf{b}} \left( A \left\{ R^{(\mathbf{k}, \mathbf{b})} \right\} - S \left\{ T^{(\mathbf{k}, \mathbf{b})} \right\} \right) \quad (3.99)$$

where

$$R_{s's}^{(\mathbf{k}, \mathbf{b})} = M_{s's}^{(\mathbf{k}, \mathbf{b})} \left[ M_{ss}^{(\mathbf{k}, \mathbf{b})} \right]^* \quad (3.100)$$

$$T_{s's}^{(\mathbf{k}, \mathbf{b})} = \frac{M_{s's}^{(\mathbf{k}, \mathbf{b})}}{M_{ss}^{(\mathbf{k}, \mathbf{b})}} \left( \operatorname{Im} \ln M_{ss}^{(\mathbf{k}, \mathbf{b})} + \mathbf{b} \langle \mathbf{r} \rangle \right) \quad (3.101)$$

and  $A$  and  $S$  are superoperators:

$$A\{B\} \equiv \frac{B - B^{\dagger}}{2} \quad (3.102)$$

$$S\{B\} \equiv \frac{B + B^{\dagger}}{2i}$$

The algorithm of functional (3.90) minimization is based on expression (3.99) and consists in an iterative procedure of the steepest descent. For this purpose, on each iteration the matrix  $d\Delta(\mathbf{k})$  is chosen in the form of:

$$d\Delta(\mathbf{k}) = \varepsilon G(\mathbf{k}) \quad (3.103)$$

where  $\varepsilon$  is a positive small constant. As is seen from (3.99), a matrix  $G(\mathbf{k})$  is anti-hermitian ( $G^\dagger = -G$ ), and for this choice the functional change:

$$dI = -\varepsilon \sum_{\mathbf{k}} \sum_{ss'} |G_{ss'}(\mathbf{k})|^2 \quad (3.104)$$

is less than zero. Hence, on each step of the iterative procedure the value of the sum of WF dispersions (3.90) decreases.

Thus, the method consists in a choice of initial approximation to WF and the subsequent iterative procedure of construction as much as possible localized WF (in sense of a minimality of the sum of their dispersions). Subsequently, this method has been advanced and generalized to the case of entangled energy bands [61].

Advantages of the method: the method is universal and can practically be applied for any system; the method is efficient and can be automated to apply in computer code [62]. Disadvantages of the method: in the method the criterion of localization is fixed as the Boys localization criterion, therefore there is no opportunity to receive WF as much as possible localized concerning any another criterion; the symmetry use is not included, in some cases the number of iterations strongly depends on the initial approximation; the use of a sufficiently dense grid of wavevectors is necessary to obtain a good accuracy in the gradient calculation.

This method of WF generation is now widely used in PW DFT calculations of Bloch functions. In the next two sections we consider the LCAO approach to maximally localized WF generation.

### 3.3.3 Localized Orbitals for Valence Bands: LCAO approximation

The method of the localized WF generation for occupied energy bands was suggested in [53, 63, 64] and implemented with the CRYSTAL code for LCAO calculations of periodic systems. In this method, WFs are sought in the form of a linear combination of atomic orbitals (AO):

$$W_s(\mathbf{r}) = \sum_{\mu} \sum_{\mathbf{n}} c_{\mu s}^{\mathbf{n}} \phi_{\mu}(\mathbf{r} - \mathbf{s}_{\mu} - \mathbf{a}_{\mathbf{n}}) \quad (3.105)$$

where  $\phi_{\mu}(\mathbf{r} - \mathbf{s}_{\mu} - \mathbf{a}_{\mathbf{n}})$  is the  $\mu$ th AO, centered in a point  $\mathbf{s}_{\mu} + \mathbf{a}_{\mathbf{n}}$ , the index  $s$  numbers the localized functions in one primitive cell, and  $c_{\mu s}^{\mathbf{n}}$  are the coefficients connecting WF and AO. Construction of the localized functions is made by means of an iterative procedure where each step consists of two basic stages.

Let us designate WF after the  $(n - 1)$ th step through  $W_s^{(n-1)}(\mathbf{r})$ . At the first stage, named by authors “Wannierization”, the localized functions  $\bar{W}_s^{(n-1)}(\mathbf{r})$  that maximize the functional are sought

$$I_W^{(n)} = \sum_{s=1}^N \left\langle \bar{W}_s^{(n)}(\mathbf{r}) \left| V_s^{(n-1)} \right| W_s^{(n-1)}(\mathbf{r}) \right\rangle \quad (3.106)$$

where the operator  $V_s^{(n-1)}$  cuts off the tails of functions  $W_s^{(n-1)}(\mathbf{r})$ :

$$V_s W_s(\mathbf{r}) = \sum_A p_{A,s} \sum_{\mu \in A} c_{\mu s}^{G_{A,s}} \quad (3.107)$$

Here, index  $A$  runs over atoms in a cell, multipliers  $p_{A,s}$  are equal to unity only for those atoms on which the Mulliken populations of WF  $W_s(\mathbf{r})$  are more than the, fixed in advance, chosen threshold (for other atoms they are supposed to be equal to zero), and the vector  $\mathbf{G}_{A,s}$  defines a cell in which this population is maximal. Thus, the application of the operator  $V_s^{(n-1)}$  leaves in the sum (3.107) only the members corresponding to atomic functions of one cell and not necessarily over all the atoms of this cell. The renormalization of functions  $V_s^{(n-1)} \left| W_s^{(n-1)}(\mathbf{r}) \right\rangle$  makes them, and, hence, the functions  $\bar{W}_s^{(n)}(\mathbf{r})$ , more localized. To carry out the Wannierization step at the first cycle of the iterative procedure an initial guess built up from  $\Gamma$  point coefficients in Bloch functions is used in (3.106)

At the second stage termed by “localization”, the linear combination of WF, belonging to one cell is searched:

$$W_s^{(n)}(\mathbf{r}) = \sum_{s' s} O_{s' s} \bar{W}_{s'}^{(n)}(\mathbf{r}) \quad (3.108)$$

to maximize the functional (similar to that offered by Boys for molecules)

$$I_B^{(n)} = \sum_{s < t} \left[ \langle \mathbf{r} \rangle_s^{(n)} - \langle \mathbf{r} \rangle_t^{(n)} \right]^2 \quad (3.109)$$

Here  $\langle \mathbf{r} \rangle_s^{(n)}$  is a point of  $W_s^{(n)}(\mathbf{r})$  centering (centroid position). In other words, this procedure as much as possible “moves apart” WF centroids positions that promotes greater efficiency on the following step of the iterative procedure.

Advantages of the method: the algorithm is efficient and universal, it allows one to construct quickly well localized WF; the procedure is completely automated and included in the computer code CRYSTAL. The applications of this method to actual crystals are discussed in Chap. 9. Disadvantages of the method: in this method it is possible to use only Bloch functions calculated in LCAO approximation (PW-based Bloch functions can not be used); there is no possibility to apply different localization criteria in WF generation; the Mulliken atomic populations used in the iteration procedure are essentially dependent on the AO basis chosen and for diffuse AO are sometimes unrealistic.

The analysis of the basic methods of WF generation shows that though these methods are effective enough, all of them possess those or other disadvantages. It is possible to specify three basic types of these disadvantages:

i) WF symmetry is not considered at all, or if it is considered, it is not formulated in the mechanism of definition of this symmetry. It leads, first, to an increase in time of calculations, and, secondly, to loss of the control over properties of WF symmetry during their construction.

ii) The criterion of WF localization ensuring the generation of maximally localized WF is fixed or not defined. In the framework of the same method it is impossible to compare WF generated for different localization criteria.

An attempt to overcome the disadvantages mentioned was made in [42] where a variational method of Wannier-type function generation was suggested. This method is applicable with the different localization criteria, the Bloch functions can be calculated both in LCAO and in PW basis, the full symmetry is taken into account. In the next section we consider it in more detail.

### 3.3.4 Variational Method of Localized Wannier-function Generation on the Base of Bloch Functions

The background of Wannier-function symmetry analysis is the theory of representations (reps) of a space group  $G$  induced from the irreducible representations (irreps) of its site subgroup  $G_{\mathbf{q}} \subset G$  called, for brevity, induced representations (indreps). From the theory of indreps of space groups it follows that the construction of localized functions corresponding to a given simple or composite energy band is possible only if canonical orbitals of this band form the basis of some simple or composite indrep. This analysis permits us not only to establish the principle possibility to construct localized orbitals but also to define the possible positions of their symmetry localization center  $\mathbf{q}$  and their symmetry with respect to site-symmetry group  $G_{\mathbf{q}}$ .

Thus, the symmetry analysis consists of a procedure of identifying localized functions symmetry from the symmetry of the canonical orbitals of the considered energy band, or of establishing the fact that the construction of localized functions is impossible for the reasons of symmetry.

We assume that the canonical orbitals  $\varphi_{m\mu}^{(\gamma)}(\mathbf{k}, \mathbf{r}) \equiv \varphi_{\sigma}(\mathbf{k}, \mathbf{r}) \equiv \varphi_s(\mathbf{r})$  (the index  $m$  numbers the basis vectors of irrep  $\gamma$  with wavevector  $\mathbf{k}$ ,  $\mu$  discriminates between the independent bases of equivalent irreps; the index  $\sigma$  replaces  $\gamma, m, \mu$  and  $s$  replaces  $\sigma, \mathbf{k}$ ) of an energy band under consideration form a basis in the space  $Q_{(\mathbf{q}, \beta)}$  of some indrep of the group  $G^{(N)}$  of a crystal. The localized functions are defined by a unitary transformation in the space of indrep:

$$W_{ij}^{(\beta)}(\mathbf{r} - \mathbf{a}_n) = N^{-\frac{1}{2}} \sum_{\mathbf{k}} \exp(-i\mathbf{k}\mathbf{a}_n) \psi_{ij}^{(\beta)}(\mathbf{k}, \mathbf{r}) \quad (3.110)$$

or

$$W_{\tau}^{(\beta)}(\mathbf{r} - \mathbf{a}_n) = N^{-\frac{1}{2}} \sum_{\mathbf{k}} \exp(-i\mathbf{k}\mathbf{a}_n) \psi_{\tau}^{(\beta)}(\mathbf{k}, \mathbf{r}) \quad (3.110a)$$

In (3.110, 3.110a) the summation is over the set of  $N$  special points in the BZ, which corresponds to the cyclic model considered [55], and the quasi-Bloch functions  $\psi_{ij}^{(\beta)}(\mathbf{k}, \mathbf{r}) \equiv \psi_{\tau}^{(\beta)}(\mathbf{k}, \mathbf{r})$  are linear combinations of the canonical orbitals  $\varphi_{m\mu}^{(\gamma)}(\mathbf{k}, \mathbf{r}) \equiv \varphi_{\sigma}(\mathbf{k}, \mathbf{r})$  with the same  $\mathbf{k}$  belonging to the considered energy band:

$$\psi_{ij}^{(\beta)}(\mathbf{k}, \mathbf{r}) = \sum_{\gamma m \mu} U_{\gamma m \mu, ij}(\mathbf{k}) \varphi_{m\mu}^{(\gamma)}(\mathbf{k}, \mathbf{r}) \quad (3.111)$$

or

$$\psi_{\tau}^{(\beta)}(\mathbf{k}, \mathbf{r}) = \sum_{\sigma} U_{\sigma, \tau}(\mathbf{k}) \varphi_{\sigma}(\mathbf{k}, \mathbf{r}) \quad (3.111a)$$

where  $U_{\gamma m\mu, ij}(\mathbf{k}) \equiv U_{\sigma, \tau}(\mathbf{k})$  is a unitary matrix, which in the case of a nondegenerate band is reduced to a phase factor  $\exp(i\alpha(\mathbf{k}))$ . It follows from (3.110) and (3.111)

$$W_{ij}^{(\beta)}(\mathbf{r} - \mathbf{a}_n) = N^{-\frac{1}{2}} \sum_{\mathbf{k}} \sum_{\gamma m\mu} U_{\gamma m\mu, ij}(\mathbf{k}) \cdot \exp(-i\mathbf{k}\mathbf{a}_n) \cdot \varphi_{m\mu}^{(\gamma)}(\mathbf{k}, \mathbf{r}) \quad (3.112)$$

or

$$W_t(\mathbf{r}) = N^{-\frac{1}{2}} \sum_s U_{st} \cdot \varphi_s(\mathbf{r}) \quad \text{with} \quad U_{st} = U_{\gamma m\mu, ij}(\mathbf{k}) \cdot \exp(-i\mathbf{k}\mathbf{a}_n) \quad (3.112a)$$

If the functions  $\psi_{ij}^{(\beta)}(\mathbf{k}, \mathbf{r})$  satisfy the conditions of orthonormality

$$\frac{V_a}{(2\pi)^3} \int (\psi_{ij}^{(\beta)}(\mathbf{k}, \mathbf{r}))^* \psi_{i'j'}^{(\beta)}(\mathbf{k}', \mathbf{r}) d\mathbf{r} = \delta_{ii'} \delta_{jj'} \delta(\mathbf{k} - \mathbf{k}') \quad (3.113)$$

the functions  $W_{ij}^{(\beta)}(\mathbf{r} - \mathbf{a}_n)$  form an orthonormal system:

$$(W_{ij}^{(\beta)}(\mathbf{r} - \mathbf{a}_n), W_{i'j'}^{(\beta)}(\mathbf{r} - \mathbf{a}_{n'})) = \delta_{ii'} \delta_{jj'} \delta_{nn'} \quad \text{or} \quad (W_t(\mathbf{r}), W_{t'}(\mathbf{r})) = \delta_{tt'} \quad (3.114)$$

Let  $Q_{(\mathbf{q}, \beta)}$  be the space of a simple indrep  $(\mathbf{q}, \beta)$  (for simplicity). The space  $Q_{(\mathbf{q}, \beta)}$  is spanned by both the set of orthonormal functions  $W_{ij}^{(\beta)}(\mathbf{r} - \mathbf{a}_n) \equiv W_t^{(\beta)}(\mathbf{r})$  and the set of Bloch functions  $\varphi_{m\mu}^{(\gamma)}(\mathbf{k}, \mathbf{r}) = \varphi_s(\mathbf{r})$ , see (3.112). The orthonormal functions  $W_t^{(\beta)}(\mathbf{r})$  in (3.112) can be chosen real (if irrep  $\beta$  is real) and transform according to the irrep  $\beta$  of the site groups  $L_{\mathbf{q}_j, n}$  of the points  $\mathbf{q}_j, n$ . Their localization depends on the choice of the matrix  $U_{\gamma m\mu, ij}(\mathbf{k})$  in (3.112). The existence of Wannier functions decreasing exponentially at infinity (for the model of an infinite crystal) is established in many cases. The uniqueness of these functions for nondegenerate bands in crystals with centers of inversion was proved [44,57]. In this case Wannier functions correspond to a special choice of phase factors  $U_{\gamma m\mu, ij}(\mathbf{k}) = \exp(i\alpha(\mathbf{k}))$  of Bloch orbitals  $\varphi_{m\mu}^{(\gamma)}(\mathbf{k}, \mathbf{r}) = \varphi_s(\mathbf{r})$  in (3.112). Any other choice of phase factors destroys either the symmetry properties of the Wannier functions, or their reality, or both [42]. Obviously these functions are as well localized as possible (fall off exponentially in the model of infinite crystal). If the choice of phase factors is not correct the Wannier functions lose the exponential character of their decrease and, therefore, are not maximally localized according to any reasonable criterion of localization. Unfortunately, the uniqueness of Wannier functions is not yet proved for the more general case of the degenerate bands in crystals with centers of inversion, where it apparently exists.

As a criterion of localization for a localized function  $W(\mathbf{r})$  one uses the value of the integral over the whole space of the crystal [42]

$$\mathbf{I} = \int \rho(\mathbf{r}) |W(\mathbf{r})|^2 d\mathbf{r} \quad (3.115)$$

with the weight function  $\rho(\mathbf{r}) \geq 0$ , which is supposed to be invariant under the operations from the site-symmetry group  $G_{\mathbf{q}}$ . Particular choices of the weight function are:

1.

$$\rho(\mathbf{r}) = (\mathbf{r} - \mathbf{q})^2 \quad \text{Boys localization criteria} \quad (3.115a)$$

2.

$$\rho(\mathbf{r}) = \begin{cases} 1, & \text{if } \mathbf{r} \in \Delta; \\ 0, & \text{if } \mathbf{r} \notin \Delta \end{cases} \quad (3.115b)$$

where  $\Delta$  is some region surrounding the point  $\mathbf{q}$  of symmetry localization of the function  $W_0^{(\beta)}(\mathbf{r})$ ;

3.

$$\rho(\mathbf{r}) = (\pi r_o^2)^{-3/2} \exp\left(-\frac{(\mathbf{r} - \mathbf{q})^2}{r_o^2}\right) \quad (3.115c)$$

which underlines the contribution in (3.115) of the values of the function  $|W_0^{(\beta)}(\mathbf{r})|^2$  inside the sphere of radius  $r_o$ . As a special case of (3.115c) for  $r_o \rightarrow 0$  one has  $\rho(\mathbf{r}) = \delta(\mathbf{r} - \mathbf{q})$ .

One searches for the set of nonorthogonal localized functions  $V_{ij}^{(\beta)}(\mathbf{r} - \mathbf{a}_n)$  in the form

$$V_{ij}^{(\beta)}(\mathbf{r} - \mathbf{a}_n) = N^{-\frac{1}{2}} \sum_{\mathbf{k}} \sum_{\gamma m \mu} C_{\gamma m \mu, ij}(\mathbf{k}) \cdot \exp(-i\mathbf{k}\mathbf{a}_n) \cdot \varphi_{m \mu}^{(\gamma)}(\mathbf{k}, \mathbf{r}) \quad (3.116)$$

or

$$V_t^{(\beta)}(\mathbf{r}) = N^{-\frac{1}{2}} \sum_s C_{st} \cdot \varphi_s(\mathbf{r}) \quad (3.116a)$$

The system of functions  $V_t^{(\beta)}(\mathbf{r}) \equiv V_{ij}^{(\beta)}(\mathbf{r} - \mathbf{a}_n)$  can be obtained from the function  $V_{11}^{(\beta)}(\mathbf{r}) \equiv V_0^{(\beta)}(\mathbf{r})$  in the same way as the functions  $W_{ij}^{(\beta)}(\mathbf{r} - \mathbf{a}_n)$  from the function  $W_{11}^{(\beta)}(\mathbf{r})$  (see above). Therefore, it is sufficient to find only one function, for example

$$V_0^{(\beta)}(\mathbf{r}) = N^{-\frac{1}{2}} \sum_s C_{s0} \cdot \varphi_s(\mathbf{r}) \quad (3.117)$$

The coefficients  $C_{s0}$  can be found from the following variational problem: to find the coefficients  $C_{s0}$  in (3.117), maximizing (or minimizing) the functional (3.115) and satisfying the supplementary condition:

$$\int |V_0^{(\beta)}(\mathbf{r})|^2 d\mathbf{r} = 1 \quad (3.118)$$

This variational problem is equivalent to the eigenvalues and eigenvectors problem for the matrix:

$$A_{ss'} = \frac{1}{N} \int \rho(\mathbf{r}) \varphi_s^*(\mathbf{r}) \varphi_{s'}(\mathbf{r}) d\mathbf{r} \quad (3.119)$$

The eigenvalues of the matrix  $A$  are stationary values of the localization criterion (3.115), and the eigenvectors corresponding to these values are required coefficients of the expansion (3.117). In our case, it is necessary to search for the eigenvector corresponding to the highest eigenvalue for the choices (3.115b) and (3.115c) of the weight function  $\rho(\mathbf{r})$  and to the lowest one for the case (3.115a). Let us note that it is sufficient to use the variational procedure in the subspace of the first basis vectors of

the irrep  $\beta$  of the site group  $L_{\mathbf{q}}$  instead of the whole space of the canonical orbitals of the energy band under consideration.

Though the set of the functions  $V_t(\mathbf{r})$  is not orthogonal, these functions are close to the accurate localized Wannier functions  $W_t^{(\beta)}(\mathbf{r}) \equiv W_{ij}^{(\beta)}(\mathbf{r} - \mathbf{a}_n)$ . They can be chosen real (for real irrep  $\beta$  of the site group  $L_{\mathbf{q}}$ ) and satisfy all the symmetry requirements for the functions  $W_t^{(\beta)}(\mathbf{r})$ . The orthonormal system  $\widetilde{W}_t^{(\beta)}(\mathbf{r})$  is generated from the functions  $V_t^{(\beta)}(\mathbf{r})$  by a suitable symmetrical orthogonalization procedure for periodic systems:

$$\widetilde{W}_t^{(\beta)}(\mathbf{r}) = \sum_{t'} (S^{-\frac{1}{2}})_{t't} V_{t'}^{(\beta)}(\mathbf{r}) \quad (3.120)$$

where  $S$  is the overlapping matrix of the functions  $V_t^{(\beta)}(\mathbf{r})$ :

$$S_{tt'} \equiv (V_t^{(\beta)}(\mathbf{r}), V_{t'}^{(\beta)}(\mathbf{r})) \quad (3.121)$$

Combining (3.116a) and (3.120) we get

$$\widetilde{W}_t^{(\beta)}(\mathbf{r}) = N^{-\frac{1}{2}} \sum_{t's} C_{st'} \cdot (S^{-\frac{1}{2}})_{t't} \varphi_s(\mathbf{r}) \quad (3.122)$$

As the symmetrical orthogonalization procedure (3.122) leaves unchanged the reality and symmetry properties of the functions, the set of orthonormalized functions  $\widetilde{W}_t^{(\beta)}(\mathbf{r})$  satisfy all the requirements to the localized Wannier functions (reality, symmetry requirements and orthonormality) and (in the case when this set of functions is unique) has to coincide with the latter:

$$\widetilde{W}_t^{(\beta)}(\mathbf{r}) = W_t^{(\beta)}(\mathbf{r}) \quad (3.123)$$

The weight function  $\rho(\mathbf{r})$  in the functional **I**, see (3.115), can be varied. In particular, one can choose for the region  $\Delta$  in (3.115b) a muffin-tin sphere, some part of a Wigner–Seitz cell (even very small), etc. The functions  $V_t(\mathbf{r})$  depend on the choice of  $\rho(\mathbf{r})$ , but, according to calculations, after the procedure of symmetric orthogonalization we always have the same result even for degenerated bands in crystals with a center of inversion. Apparently, the proposed method gives, in these cases, the orthonormal set of maximally localized Wannier functions. Thus, the numerical calculations imply constructing matrix  $A_{ss'}$  (3.119), diagonalization of this matrix, then obtaining the overlap matrix  $S_{tt'}$  (3.121), taking the matrix square root of it and other operations of linear algebra.

To demonstrate the reliability of the proposed variational method let us consider two examples of its applications given in [42] – the Wannier-function generation in silicon and MgO crystals.

In accordance with the theory of induced (band) representations the corresponding Wannier functions in the silicon crystal (four per unit cell) are centered at the middle of the bonds between the nearest Si atoms (Wyckoff position  $c$  with site group  $G_c = D_{3d}$ ) and transform according to the irrep  $a_{1g}$  of the site group  $D_{3d}$ , see Sect. 3.3.1.

For the variational procedure two sets of Bloch functions were used (both obtained with the help of CRYSTAL code [23]). The first set ( $S_1$ ) corresponds to the full electron Hartree–Fock LCAO calculations, the second one ( $S_2$ ) – to the pseudopotential

Hartree–Fock LCAO method. A model of a finite crystal with periodical boundary conditions (cyclic model) with the main region composed of  $4 \times 4 \times 4 = 64$  primitive cells was adopted. The first basis consists of 13  $s$ - and  $p$ - atomic-like functions per atom, the pseudopotential basis consists of 2  $s$ -, 6  $p$ - and 5  $d$ -functions per atom. The weight function  $\rho(\mathbf{r}) = \delta(\mathbf{r} - \mathbf{q})$  has been taken in (3.115).

**Table 3.17.** Localized states for the upper valence band of Si crystal along [1,1,1] direction (the origin is taken in the middle of the bond,  $x$  in  $a\sqrt{3}/96$  units,  $a$  being the conventional lattice constant), [42]

x	$W_1(x)$	$W_8(x)$	$W_{64}(x)$	$W_{64}^{(no)}(x)$
0	-0.2300	-0.2036	-0.1982	-0.1988
3	-0.2190	-0.1975	-0.1926	-0.1930
6	-0.1566	-0.1465	-0.1436	-0.1437
9	0.1204	0.1216	0.1199	0.1196
11	0.4116	0.3840	0.3725	0.3747
12	-0.5831	-0.7333	-0.7579	-0.7406
15	-0.0596	-0.0401	-0.0354	-0.0373
18	0.0497	0.0336	0.0288	0.0307
22	0.0620	0.0501	0.0453	0.0471
27	0.0250	0.0327	0.0317	0.0321
33	-0.0099	0.0097	0.0127	0.0121
39	-0.0098	-0.0002	0.0040	0.0030
45	0.0045	-0.0017	0.0011	0.0004
51	0.0045	-0.0002	0.0006	0.0003
57	-0.0098	0.0005	0.0003	0.0003
63	-0.0099	0.0000	0.0000	-0.0001
69	0.0250	-0.0006	-0.0002	-0.0002
75	0.0649	-0.0015	-0.0002	-0.0001
81	-0.0596	0.0008	0.0000	-0.0001
84	-0.5831	-0.0082	-0.0005	0.0000
87	0.1204	-0.0001	0.0000	0.0000
90	-0.1566	-0.0002	-0.0001	-0.0002
93	-0.2190	-0.0006	-0.0002	-0.0004
96	-0.2300	-0.0008	-0.0003	-0.0006

The bigger the cyclic model of a crystal, the closer are its Wannier functions to those of the model of an infinite crystal. In [42] the convergence of the Wannier functions  $W(\mathbf{r})$  (for the set  $S_1$ ) for different sizes of cubic cells defining the cyclic model of a crystal was studied. The smallest cubic cell consists of four primitive cells, the larger ones consist of 8 and 64 smallest cubic cells. The total number of wavevectors used in BZ summation is four times larger than the number of smallest cubic cells in the supercell. The localized functions  $W_1(x)$ ,  $W_8(x)$ ,  $W_{64}(x)$  were calculated according to (3.112) as a linear combinations of 4 (supercell coincides with a smallest cubic

cell), 32 ( $2 \times 2 \times 2 = 8$  cubic cells in a supercell) and 256 ( $4 \times 4 \times 4 = 64$  cubic cells in a supercell) Bloch states. Table 3.17 gives the values of the Wannier functions  $W_1(x)$ ,  $W_8(x)$ ,  $W_{64}(x)$  and  $W_{64}^{(no)}(x)$  (the latter is nonorthogonalized) in some points along the  $[1, 1, 1]$  direction. As is seen from the table the function  $W_{64}^{(no)}(x)$  is very close to  $W_{64}(x)$ . So the orthogonalization procedure changes the Wannier function insignificantly. When comparing the functions  $W_1(x)$ ,  $W_8(x)$ ,  $W_{64}(x)$  it is necessary to take into account that these functions are normalized differently, in the volume of 1, 8 and 64 cubic cells, respectively. The fact that their values are relatively close to each other from  $x = 0$  to  $x = 48$  (in units of  $a\sqrt{3}/96$ , the translational period in the  $[1, 1, 1]$  direction is equal to  $a\sqrt{3}$ ) shows a good localization of the Wannier function under consideration.

Figure 3.9 gives the  $W_{64}(x)$  and pseudopotential(pp) Wannier function  $W_{64}^{(pp)}(x)$  in the  $[111]$  direction.

The functions differ significantly at the atom cores. Outside the cores the behavior of the functions is alike. This is quite natural, since the pseudopotential Wannier functions are constructed from smooth pseudowave Bloch functions, that are nonorthogonal to the core states. Orthogonalization of these smooth Wannier functions to the localized core functions would lead to an increase of oscillations at atom cores observed in the Wannier functions  $W_{64}(x)$ . The differences between the Wannier functions in the interatomic space are due to the normalization.

In this case, the method reveals a very good stability with respect to the choice of the weight function  $\rho(\mathbf{r})$  form. The computations give the same resulting orthogonalized Wannier functions, whereas the intermediate nonorthogonalized functions  $V_t(\mathbf{r})$  turn out to be different. An amazing feature was noted. Even if one uses the weight functions  $\rho(\mathbf{r})$  centered at any point in the localization region of the Wannier function and so the functions  $V_t(\mathbf{r})$  do not have the symmetry compatible with the site group  $G_{\mathbf{q}}$ , the same orthogonalized Wannier functions arise after the symmetrical orthogonalization procedure. The latter not only conserves the symmetry of the localized orbitals, but reconstructs(!) it up to an appropriate level. The cause of such flexibility is the fact that the most localized Wannier functions corresponding to a certain energy band are unique and just these functions arise without fail as the result of the proposed variational procedure [42]).

To construct the Wannier functions for the upper valence bands of the perfect MgO crystal a set of MgO Bloch functions has been applied [42], that were obtained in pseudopotential Hartree–Fock LCAO calculations with the CRYSTAL code [23]. The  $4 \times 4 \times 4$  cyclic system has been used in the calculations. The valence band of MgO represents two separated bands, and thus it is possible to construct two independent sets of Wannier functions (for each of the bands). The method of induced representations gives all the Wannier functions being centered on O atoms (Wyckoff position  $b$  with site group  $G_c = O_h$ ) and transforming – according to the irrep  $a_g$  of the site group  $O_h$  for the lower band (one Wannier function per unit cell) and according to the irrep  $t_{1u}$  – for the upper band (three Wannier functions per unit cell). The weight function  $\rho(\mathbf{r}) = \delta(\mathbf{r} - \mathbf{q})$  was taken in (3.115) located some distance away from the centering point of the corresponding Wannier function – as the Wannier functions of the upper band are antisymmetric and thus equal zero in their centering points, while, as stated above, the symmetrical centering of  $\rho(\mathbf{r})$  function is not necessarily needed.

Figure 3.10 shows the Wannier functions for both the bands in the  $[111]$  direction.

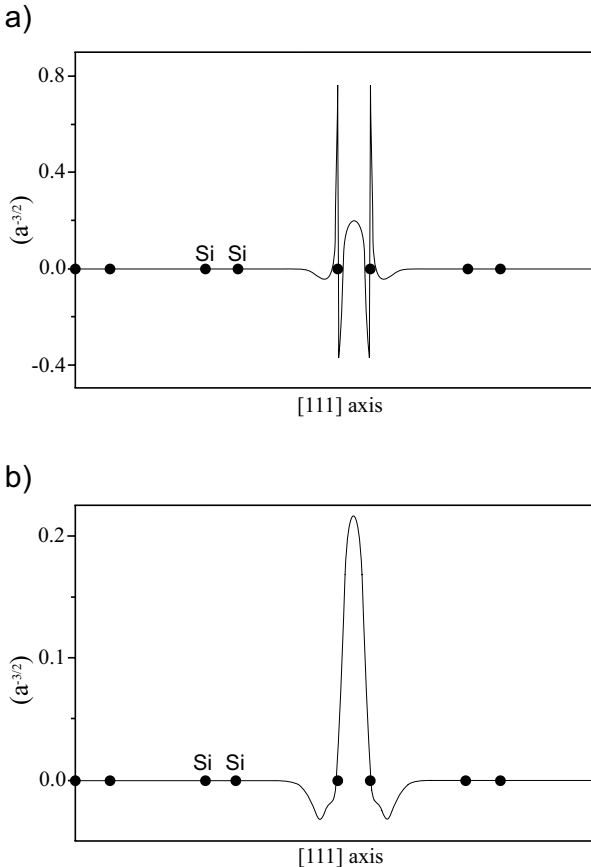


**Fig. 3.9.** Wannier functions for the silicon upper valence band along the [111] direction: a) full electron calculation; b) pseudopotential calculation

The function corresponding to the upper band (dashed curve) is determined up to a linear combination of the three functions transforming via  $t_{1u}$  irrep. One can see that both Wannier functions are almost completely localized around one of the oxygen atoms, which confirms the ionic character of MgO compound.

The character of the localization of Wannier functions depends on the analytical properties of Bloch states (as a function of the wavevector) that are essentially determined by the nature of the system under consideration. One can arbitrary change only the form of an unitary transformation of Bloch functions. It is just this arbitrariness that is used in the variational approach [42] to assure the best localization of Wannier functions. The accuracy of the Wannier functions obtained by the proposed method is determined solely by the accuracy of the Bloch functions and the size of the supercell used. As the calculations have shown, the proposed method is reliable and useful in the problem of generation of the localized Wannier functions. In the two examples

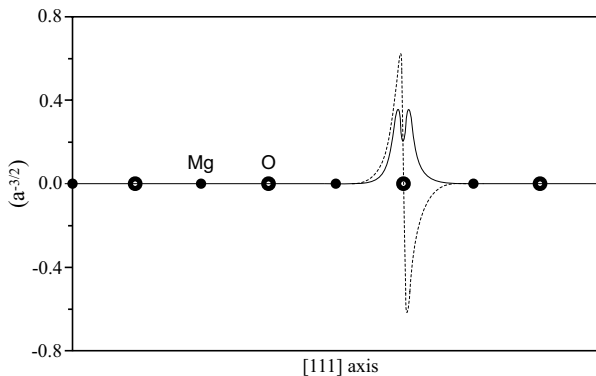


**Fig. 3.10.** Wannier functions for the MgO upper valence band along [111] direction: solid line for WF of  $a_{1g}$  symmetry, dotted line – for one of the three WFs of  $t_{1u}$  symmetry

considered the Bloch states of only occupied bands were used for WF generation. Inclusion of the vacant band states of the appropriate symmetry allows Wannier-type atomic orbitals (WTAO) to be generated. WTAO are used for the chemical-bonding analysis in crystals. We consider WTAO applications in Chap. 9.

---

## Hartree–Fock LCAO Method for Periodic Systems

### 4.1 One-electron Approximation for Crystals

#### 4.1.1 One-electron and One-determinant Approximations for Molecules and Crystals

The complex quantum-mechanical systems that are molecules and crystals, consisting of a great number of atomic nuclei and electrons, can in many cases be modeled by the nonrelativistic Hamiltonian having the form

$$\hat{H} = -\frac{1}{2} \sum_{i=1}^{2N_e} \Delta_{\mathbf{r}_i} - \frac{1}{2} \sum_{j=1}^{N_a} \frac{1}{M_j} \Delta_{\mathbf{R}_j} + V(\mathbf{r}, \mathbf{R}) \quad (4.1)$$

where  $\mathbf{r}_i$  are the coordinates of electrons ( $i = 1, 2, \dots, 2N_e$ ),  $\mathbf{R}_j$  are the coordinates of nuclei ( $j = 1, 2, \dots, N_a$ ) and  $V(\mathbf{r}, \mathbf{R})$  is the energy of the Coulomb interaction of electrons and nuclei:

$$V(\mathbf{r}, \mathbf{R}) = \sum_{j < j'} \frac{Z_j Z_{j'}}{|\mathbf{R}_j - \mathbf{R}_{j'}|} + \sum_{i < i'} \frac{1}{|\mathbf{r}_i - \mathbf{r}_{i'}|} - \sum_{ij} \frac{Z_j}{|\mathbf{r}_i - \mathbf{R}_j|} \quad (4.2)$$

The Hamiltonian (4.1) is approximate as it does not take into account the spin-orbit interaction and other relativistic effects. The calculation of eigenfunctions and eigenvalues of the operator (4.1), *i.e.* the solution of the time-independent Schrodinger equation

$$\hat{H}\Phi = E\Phi \quad (4.3)$$

is possible only after applying some approximations. The first of them is the adiabatic approximation. It permits the motion of electrons and nuclei to be considered separately and is based on the large difference in electron and nuclear masses ( $m_e \ll M_j$ ).

In the adiabatic approximation, first the problem of electronic motion is solved for fixed positions of nuclei

$$\left[ -\frac{1}{2} \sum_{i=1}^{2N_e} \Delta_{\mathbf{r}_i} + V(\mathbf{r}, \mathbf{R}) \right] \psi(\mathbf{r}, \mathbf{R}) = W(\mathbf{R})\psi(\mathbf{r}, \mathbf{R}) \quad (4.4)$$

The wavefunctions  $\psi(\mathbf{r}, \mathbf{R})$  and the eigenvalues  $W(\mathbf{R})$  in (4.4) depend on the nuclear coordinates  $\mathbf{R}$  as parameters. Then, the found eigenvalues  $W(\mathbf{R})$  are used as the operators of potential energy in the equation determining the nuclear motion:

$$\left[ -\frac{1}{2} \sum_{j=1} \frac{1}{M_j} \Delta_{\mathbf{R}_j} + W(\mathbf{R}) \right] \chi(\mathbf{R}) = \varepsilon \chi(\mathbf{R}) \quad (4.5)$$

This way of solving (4.3) is equivalent to the representation of the wavefunction  $\Phi$  in the form of the product

$$\Phi(\mathbf{r}, \mathbf{R}) = \psi(\mathbf{r}, \mathbf{R}) \chi(\mathbf{R}) \quad (4.6)$$

Further corrections of this reasonable approximation may be obtained from adiabatic perturbation theory by using, as the small parameter, the value  $(\frac{1}{M})^{1/4}$  where  $M$  is the average mass of the nuclei. Equation (4.4) is often considered as an independent problem without any relation to the more general problem (4.3). This is motivated by the following reasoning. If the temperature is not very high, the nuclei vibrate about some equilibrium positions  $\mathbf{R}^{(0)}$ . Thus, in calculating the electronic structure, only the configuration with the nuclei fixed at their equilibrium positions  $\mathbf{R}^{(0)}$  is considered. The latter are typically known from experimental data (*e.g.*, from X-ray or neutron-scattering crystallographic data). This means of electronic-structure calculation without using any other experimental data (except the equilibrium positions of nuclei) is often considered as made from first-principles. Often, the first-principle calculations are made with the geometry optimization when the positions of nuclei are found from the total-energy minimization. Formally, the results of such calculations correspond to zeroth temperature. We write the equation for the electronic function of the system in the form

$$\hat{H}_e \psi = \left[ \sum_i \hat{H}_0(\mathbf{r}_i) + \sum_{i,i'} \frac{1}{|\mathbf{r}_i - \mathbf{r}_{i'}|} \right] \psi = E \psi \quad (4.7)$$

where

$$\hat{H}_0(\mathbf{r}_i) = -\frac{1}{2} \Delta_{\mathbf{r}_i} - \sum_j \frac{Z_j}{|\mathbf{r}_i - \mathbf{R}_j^{(0)}|} + \sum_{j < j'} \frac{Z_j Z_{j'}}{|\mathbf{R}_j^{(0)} - \mathbf{R}_{j'}^{(0)}|} \quad (4.8)$$

We assume here that there is a finite number of electrons in the system. This is certainly true for molecules, but for crystals it implies that we are using the model of a finite but boundless crystal (cyclic model), *i.e.* we consider the bulk of a crystal with cyclic boundary conditions imposed on opposite sides. The Hamiltonian  $\hat{H}_e$ , being an operator acting on the functions depending on the electron coordinates  $\mathbf{r}_i$  is invariant under symmetry operations transforming the nuclear equilibrium configuration into itself. Later, we call it the symmetry group of a crystal.

Equation (4.7) is still very complex. Its solution is not yet possible without further simplifying approximations. The variables (electron coordinates) cannot be separated in (4.7) because of the terms describing the mutual Coulomb repulsion between electrons. This is why the exact many-electron wavefunction  $\psi$  may not be represented as a product (or the finite sum of products) of one-electron functions. However, the approximate wavefunction  $\tilde{\psi}$  may be taken as a sum of the products of one-electron

functions, which have to be chosen so that the approximate function  $\tilde{\psi}$  is as close as possible to the exact solution  $\psi$ .

The Hamiltonian  $\hat{H}_e$  does not contain the spin operators. Therefore the one-electron functions may be expressed in the form of the product  $\varphi(\mathbf{r}_i)\alpha_{\pm}(\sigma_i)$  of functions  $\varphi(\mathbf{r}_i)$  depending on the spatial coordinates of electrons and functions  $\alpha_{\pm}(\sigma_i)$  depending on spin variables only ( $\alpha, \beta$  notations are also used for  $\alpha_{\pm}(\sigma_i)$ ). The function  $\psi$  has to be antisymmetric under the exchange of any pair of electrons. This requirement is satisfied by the antisymmetric product of one-electron functions

$$\psi = [(2N_e)!]^{-1/2} \det [\varphi_1(\mathbf{r}_1)\alpha_+(\sigma_1) \dots \varphi_{N_e}(\mathbf{r}_{N_e})\alpha_-(\sigma_{N_e})] \quad (4.9)$$

The function  $\psi$  has to transform according to one of the irreps of the symmetry group  $G$  (point group for molecules or space group for crystals). We restrict ourselves to calculation of the ground state of the system. The latter is assumed to be invariant under the elements of the symmetry group  $G$  and to correspond to a total spin equal to zero. In this case, the wavefunction may be written in the form of a single determinant (one-determinant approximation).

In the Hartree–Fock method (also known as the one-electron approximation or self-consistent field (SCF) method) the system of equations for one-electron functions is obtained from the variational principle minimizing the functional

$$E = \int \psi^* \hat{H}_e \psi d\tau \quad (4.10)$$

provided

$$\int \varphi_i^*(\mathbf{r}) \varphi_{i'}(\mathbf{r}) d\mathbf{r} = \delta_{ii'} \quad (4.11)$$

The supplementary conditions (4.11) are not the primary restriction of generality. Indeed, the orthogonalization procedure of one-electron functions may be fulfilled directly in the determinant (4.9) without any change in its value. The same condition (4.11) assures the normalization of the function to 1. The one-electron functions satisfy the following system of Hartree–Fock equations:

$$\hat{F}\varphi_i(\mathbf{r}) = \sum_{i'} \varepsilon_{i'i} \varphi_{i'}(\mathbf{r}) \quad (4.12)$$

or

$$\hat{F}\varphi_i = \varphi_i \varepsilon \quad (4.13)$$

where the Hartree–Fock operator

$$\hat{F} = \hat{H}_0 + \hat{J} - \hat{K} \quad (4.14)$$

is defined below,  $\varphi$  is a row of functions  $\varphi_i$  and  $\varepsilon$  is the matrix of coefficients  $\varepsilon_{i'i}$ .

In the Hartree–Fock operator  $\hat{F}$  the term  $\hat{H}_0$  is the one-electron operator (4.8). The action on the function  $\varphi_i(\mathbf{r})$  of the Coulomb operator  $\hat{J}$  and exchange operator  $\hat{K}$  is determined in the following way. Denote by  $\rho(\mathbf{r}, \mathbf{r}')$  the mixed electron density with fixed spin (spinless electron-density matrix)

$$\rho(\mathbf{r}, \mathbf{r}') = \sum_{i=1}^{N_e} \varphi_i(\mathbf{r}) \varphi_i^*(\mathbf{r}') = \varphi(\mathbf{r}) \varphi^\dagger \quad (4.15)$$

where  $\varphi^\dagger$  is the column of functions  $\varphi_i^*(\mathbf{r}')$ . Then

$$\hat{J}\varphi_i(\mathbf{r}) = 2 \int \frac{\rho(\mathbf{r}', \mathbf{r}')}{|\mathbf{r} - \mathbf{r}'|} d\mathbf{r}' \varphi_i(\mathbf{r}') \quad (4.16)$$

$$\hat{K}\varphi_i(\mathbf{r}) = \int \frac{\rho(\mathbf{r}, \mathbf{r}')}{|\mathbf{r} - \mathbf{r}'|} \varphi_i(\mathbf{r}') d\mathbf{r}' \quad (4.17)$$

The operator  $\hat{J}$  is the potential energy operator of an electron in the Coulomb field created by all the electrons of the system, with the electron in question included. This is a normal multiplication operator. It acts on the functions depending on the space coordinates of an electron. The Coulomb operator is determined if the electron density  $\rho(\mathbf{r}', \mathbf{r}')$  is known. The operator  $\hat{K}$  is an integral nonlocal operator with the nucleus  $\rho(\mathbf{r}, \mathbf{r}')/|\mathbf{r} - \mathbf{r}'|$ . To calculate the function  $\hat{K}\varphi_i$  it is necessary to know the function values in the entire domain of its determination. The operator  $\hat{F}$  (4.14) is self-adjoint, as  $\rho(\mathbf{r}, \mathbf{r}') = \rho^*(\mathbf{r}', \mathbf{r})$ .

Multiplying both sides of (4.12) by  $\varphi_j^*(\mathbf{r})$ , integrating over  $d\mathbf{r}$  and using the orthonormality of the functions  $\varphi_i^*(\mathbf{r})$ , we obtain

$$\varepsilon_{ji} = \int \varphi_j^* \hat{F} \varphi_i d\mathbf{r} = \left( \int \varphi_j^* \hat{F} \varphi_i d\mathbf{r} \right)^* = \varepsilon_{ij}^* \quad (4.18)$$

The matrix  $\varepsilon$  in (4.18) is Hermitian. It may be diagonalized with the help of a unitary transformation  $U$ :

$$\hat{F}(\varphi U) = \varphi \varepsilon U = (\varphi U)(U^{-1} \varepsilon U), \quad (4.19)$$

where  $U^{-1} \varepsilon U$  is a diagonal matrix. The unitary transformation  $U$  ( $UU^\dagger = 1$ ) does not change the electron-density matrix

$$\rho(\mathbf{r}, \mathbf{r}') = \varphi(\mathbf{r}) \varphi^\dagger(\mathbf{r}') = \varphi U U^\dagger \varphi^\dagger = (\varphi U)(\varphi U)^\dagger \quad (4.20)$$

Then, this transformation keeps the Coulomb  $\hat{J}$  and exchange  $\hat{K}$  operators invariant (and the total  $\hat{F}$ ). Therefore, without any restriction on the generality the matrix  $\varepsilon$  in the right-hand side of (4.13) may be considered as diagonal

$$\hat{F}\varphi_i = \varepsilon_i \varphi_i \quad (4.21)$$

The system of Hartree–Fock equations (4.21) is nonlinear. To solve it, an iterative method is usually used. In the course of the  $p$ th iteration the electron-density matrix  $\rho^{(p)}(\mathbf{r}, \mathbf{r}')$  and hence the operators  $\hat{J}$  and  $\hat{K}$  are considered to be fixed. The system (4.21) then transforms into one linear equation with a fixed self-adjoint operator

$$\hat{F}^{(p)} = \hat{H}_0 + \hat{J}^{(p)} - \hat{K}^{(p)} \quad (4.22)$$

The eigenstates of this operator corresponding to the lower eigenvalues are populated with electrons. The occupied states are used to construct  $\rho^{(p+1)}(\mathbf{r}, \mathbf{r}')$  according to (4.20) and then  $\hat{J}^{(p+1)}$  and  $\hat{K}^{(p+1)}$  according to (4.16) and (4.17). Then, the subsequent iteration is performed. The procedure of solution is stopped when the functions  $\varphi_j^{(p)}$  approach  $\varphi_j^{(p-1)}(\mathbf{r})$  (within the desired accuracy). In practice, other criteria are also

used to estimate the accuracy of the obtained solution (total energy, electron-density convergence criteria).

Thus, by an iterative method a self-consistent solution of the nonlinear equations (4.21) may be obtained. The rate of convergence of the iterative procedure depends on the nature of the physical system as well as on the choice of the initial approximation.

The calculation of the eigenfunctions of the operator  $\hat{F}$  during the  $p$ th iteration is itself a difficult problem that may be solved only approximately. To simplify it, the nonlocal exchange potential  $\hat{K}$  is often replaced by a local potential. The one possible form of the local exchange potential is (especially for crystals)

$$\hat{K}\varphi_i = -3\alpha \left[ (3/4\pi)\rho(\mathbf{r}, \mathbf{r})^{1/3} \right] \varphi_i \quad (4.23)$$

proposed by Slater. The constant  $\alpha$  in crystal electronic-structure calculations is an adjustable parameter. The widely used local density approximation (LDA) is considered in Chap. 7. If no iterative procedure is performed the electron structure obtained is said to be nonself-consistent. This kind of calculation is justified only when the one-electron Hamiltonian  $\hat{F}^{(0)}$  correctly reflects the main features of the exact (self-consistent) energy operator. It is very difficult to guess such a potential without involving some empirical data. The sum of atomic (or ionic) potentials is the simplest and most natural form of the molecular or crystal potential in nonself-consistent calculations. It is also used as an initial approximation in self-consistent electronic-structure calculations. The one-electron Hamiltonian approximation using the LCAO form of crystalline orbitals is known as the tight-binding (TB) method. This nonself-consistent approach was popular in the 1970s when the self-consistent Hartree–Fock calculations were possible only for simple crystals. At the present time the TB scheme is mainly used as the interpolation scheme: LCAO Hamiltonian parameters are found by fitting to the band structure calculated self-consistently, for example, using a plane-waves basis. Comparing calculation schemes of molecular quantum chemistry with those of quantum chemistry of solids one can say that the TB scheme is a semiempirical extended Hückel theory with periodical boundary conditions. The considered one-electron and one-determinant approximations are applied both for molecules and crystals. The symmetry of the one-electron Hamiltonian in both cases coincides with the symmetry of the nuclei configuration only for the case of closed-shell molecules or nonconducting crystalline solids. This is shown in next section.

#### 4.1.2 Symmetry of the One-electron Approximation Hamiltonian

The many-electron Hamiltonian  $\hat{H}_e$  in (4.7), acting in the space of functions depending on the coordinates of all the electrons, is invariant under the operators  $\hat{g}$  of the equilibrium nuclear configuration symmetry group  $G$ . The operators of electron kinetic energy in (4.8) and the Coulomb repulsion between electrons in (4.7) remain unchanged under any transformation belonging to the point- or space-group operations since, according to the definition, the elements of these groups are the transformations that do not change the distances between any two points of the space. As to the operators of electron–nuclear interaction in (4.8), the operations  $\hat{g}$  permute the members of the sum, leaving the sum as a whole invariant. Indeed, the coordinate  $\mathbf{r}_i$  transforms under  $g$  in

$$\mathbf{r}'_i = g\mathbf{r}_i \quad (4.24)$$

and the denominator in (4.8) becomes equal to

$$|\mathbf{r}'_i - \mathbf{R}_j^{(0)}| = |g\mathbf{r}_i - \mathbf{R}_j^{(0)}| = |g(\mathbf{r}_i - g^{-1}\mathbf{R}_j^{(0)})| = |\mathbf{r}_i - g^{-1}\mathbf{R}_j^{(0)}| \quad (4.25)$$

i.e. to the denominator of other members in the sum in (4.8). This reasoning also proves the invariance of the one-electron operator  $\hat{H}_0$  (4.8) under the transformations  $g$  from the group  $G$ .

The set of one-electron functions transforming according to the  $n_\beta$ -dimensional irrep  $D^{(\beta)}$  is called the shell. For molecules, these shells are connected with irreps of the point-symmetry group. For a crystal,  $\beta = (*\mathbf{k}, \gamma)$  – full irreducible representation of space group  $G$ , defined by the star of wavevector  $*\mathbf{k}$  and irrep  $\gamma$  of the point group of this vector. Taking into consideration the spin states  $\alpha_\pm(\sigma)$  we have  $2n_\beta$  one-electron states in the shell. The functions  $\varphi_i^{(\beta)}(\mathbf{r})\alpha_\pm(\sigma)$  span the space of the rep  $D^{(\beta)} \times D^{1/2}$ , where  $D^{1/2}$  is the rep according to which the spin functions transform. For the systems with closed shells (molecules in the ground state and nonconducting crystals) the determinant (4.9) consisting of the functions of filled shells describes the state invariant under the operations of the group  $G$  (transforms over unity irrep of  $G$ ). In fact any transformation of  $G$  replaces the columns of the determinant by their linear combinations, which does not change the value of the determinant, i.e. does not change the many-electron wave function  $\psi$ . In the case of open-shell systems (molecular radicals or metallic solids) the ground state of the system is described by a linear combination of determinants, appearing under the symmetrization over the identity irrep of group  $G$ . For crystals, the one-determinant approximation is practically the only way to make the electronic-structure calculations.

Now we check that for the closed-shell systems the group  $G$  is a symmetry group of the Hartree–Fock equations (4.21). First we note that the sum

$$\sum_{i=1}^{n_\beta} [\varphi_i^{(\beta)}(\mathbf{r}')]^* \varphi_i^{(\beta)}(\mathbf{r}) \quad (4.26)$$

is invariant under the group  $G$ , i.e. transforms over identity irrep of  $G$ . This follows from the well-known property for finite groups of the direct product of irreps  $D^{(\beta)} \times [D^{(\beta)}]^*$ . The electron-density matrix  $\rho(\mathbf{r}, \mathbf{r}')$  is also invariant under  $G$  because for filled shells it is the sum of terms like (4.26)

$$\rho(g\mathbf{r}, g\mathbf{r}') = \rho(\mathbf{r}, \mathbf{r}') \quad (4.27)$$

The operators  $\hat{F}$  (4.21) and  $\hat{F}^{(p)}$ , (4.22) are one-electron, i.e. they are determined in the space of functions depending on the coordinates of one electron.

The invariance of the operator  $\hat{H}$  is already proved. For Coulomb  $\hat{J}$  and exchange  $\hat{K}$  operators and for an arbitrary function  $\varphi(\mathbf{r})$  we have

$$\begin{aligned} \hat{g}\hat{J}\varphi(\mathbf{r}) &= 2 \int \frac{\rho(\mathbf{r}', \mathbf{r}')}{|g^{-1}\mathbf{r} - \mathbf{r}'|} d\mathbf{r}' \varphi(g^{-1}\mathbf{r}) \\ &= 2 \int \frac{\rho(g^{-1}\mathbf{r}', g^{-1}\mathbf{r}')}{|g^{-1}\mathbf{r} - g^{-1}\mathbf{r}'|} d(g^{-1}\mathbf{r}') \varphi(g^{-1}\mathbf{r}) \\ &= 2 \int \frac{\rho(\mathbf{r}', \mathbf{r}')}{|\mathbf{r} - \mathbf{r}'|} d\mathbf{r}' \varphi(g^{-1}\mathbf{r}) = \hat{J}\hat{g}\varphi(\mathbf{r}) \end{aligned} \quad (4.28)$$

$$\begin{aligned}\hat{g}\hat{K}\varphi(\mathbf{r}) &= \int \frac{\rho(\mathbf{g}^{-1}\mathbf{r}, \mathbf{r}')}{|\mathbf{g}^{-1}\mathbf{r} - \mathbf{r}'|} \varphi(\mathbf{r}') d\mathbf{r}' \\ &= \int \frac{\rho(\mathbf{r}', \mathbf{r}')}{|\mathbf{r} - \mathbf{r}'|} \varphi(\mathbf{g}^{-1}\mathbf{r}') d\mathbf{r}' = \hat{K}\hat{g}\varphi(\mathbf{r})\end{aligned}\quad (4.29)$$

The relation (4.27) and the equality  $|\mathbf{g}^{-1}\mathbf{r} - \mathbf{g}^{-1}\mathbf{r}'| = |\mathbf{r} - \mathbf{r}'|$  and  $d(\mathbf{g}^{-1}\mathbf{r}') = d\mathbf{r}'$  are used to prove the invariance of  $\hat{F}$ . As (4.28) and (4.29) hold for an arbitrary function  $\varphi(\mathbf{r})$

$$\hat{g}\hat{J} = \hat{J}\hat{g}, \quad \hat{g}\hat{K} = \hat{K}\hat{g} \quad (4.30)$$

and therefore

$$\hat{g}\hat{F} = \hat{F}\hat{g}, \quad \hat{g}\hat{F}^{(p)} = \hat{F}^{(p)}\hat{g} \quad (4.31)$$

Thus, the operator  $\hat{F}(\hat{F}^{(p)})$  in the electron equation (4.21) has the symmetry group  $G$  of the equilibrium nuclear configuration if the electron-density matrix  $\rho(\mathbf{r}, \mathbf{r}')[\rho^{(p)}(\mathbf{r}, \mathbf{r}')]$  is invariant under  $G$ . The eigenfunctions of the operator  $\hat{F}(\hat{F}^{(p)})$  form the bases of irreps of  $G$ . The invariance of  $\rho(\mathbf{r}, \mathbf{r}')[\rho^{(p)}(\mathbf{r}, \mathbf{r}')]$  is assured for the system with closed shells.

Thus, taking as the initial approximation that the electron density  $\rho^{(0)}(\mathbf{r}, \mathbf{r}')$  is invariant under the group  $G$  we have, during any iteration step and in the self-consistent limit, the one-electron functions classified according to the irreps of the group  $G$  – the symmetry group of the equilibrium nuclear configuration.

In the absence of external fields the realness of the one-electron approximation Hamiltonian is assured at all stages of the self-consistent calculations, at least for a system with closed shells. The realness of the Hamiltonian  $\hat{F}^{(p)}$  leads to the real electron-density matrix  $\rho^{(p+1)}(\mathbf{r}, \mathbf{r}')$  generated by the eigenfunctions of  $\hat{F}^{(p)}$ . Indeed, let the functions  $\varphi_i^{(\beta)}(\mathbf{r})$  and  $(\varphi_i^{(\beta)}(\mathbf{r}))^*$  belong to the same one-electron energy and describe the occupied electron states. If they span the space of the same irrep  $D^{(\beta)}$  of  $G$  ( $D^{(\beta)}$  is real) then the partial sum (4.26) formed by these functions and involved in  $\rho^{(p+1)}(\mathbf{r}, \mathbf{r}')$  is obviously real. If they are the independent bases of the irreps  $D^{(\beta)}$  and  $(D^{(\beta)})^*$  (equivalent or inequivalent) then the sum of two terms of the type (4.26) is also real. This is the case of additional degeneracy due to the Hamiltonian being real. Thus, the electron-density matrix is the sum of real members and is real itself. The real density matrix  $\rho^{(p+1)}(\mathbf{r}, \mathbf{r}')$  generates the real Coulomb  $\hat{J}^{(p+1)}$  and exchange  $\hat{K}^{(p+1)}$  operators and therefore the real one-electron Hamiltonian  $\hat{F}^{(p+1)}$  for the  $(p+1)$ th iteration of the self-consistent calculations. The realness of the one-electron approximation Hamiltonian of molecular systems causes additional degeneracy of the energy levels in cyclic point-symmetry groups  $C_n$ . In the case of crystals degenerated energy levels appear corresponding to  $\mathbf{k}$  and  $-\mathbf{k}$  even for the case when the inversion is absent in the point group  $F_k$ . In the next sections we consider the Hartree–Fock LCAO approach for periodic systems in comparison with that for molecular systems.

#### 4.1.3 Restricted and Unrestricted Hartree–Fock LCAO Methods for Molecules

The solution of Hartree–Fock equations without any additional approximations is practically possible only for atoms. Due to the high symmetry of atomic systems these equations can be solved numerically or by using analytical representation of

atomic orbitals (AO). The tables of Roothaan–Hartree–Fock atomic wavefunctions by Clementi and Roetti [65] give atomic functions expanded in terms of Slater-type orbitals with integer quantum numbers. In molecular quantum chemistry the molecular orbital (MO) is expanded in terms of Gaussian-type orbitals (GTO). Different atomic functions used in calculations of molecules and crystals are considered in Chap. 8. For the moment, we restrict ourselves by representation of MO  $\varphi_i(\mathbf{r})$  as a linear combination of atomic orbitals  $\chi_{\mu A}(\mathbf{r})$  (MO LCAO approximation):

$$\varphi_i(\mathbf{r}) = \sum_{\mu A} C_{i\mu} \chi_{\mu A}(\mathbf{r}) \quad (4.32)$$

where  $\mu$  numbers all basis functions centered on atom A and summation is made over all the atoms in the molecular system. The MO LCAO approximation (also known as the Hartree–Fock–Roothaan approximation [66]) is practically the only way to make first-principles calculations for molecular systems. In the standard derivation of the Hartree–Fock equations relative to a closed-shell system, the constraint that each molecular orbital is populated by two electrons or vacant is introduced (Restricted Hartree–Fock theory – RHF).

In the MO LCAO approximation RHF method (4.21) transform to the matrix equations

$$\mathbf{FC} = \mathbf{SCE} \quad (4.33)$$

where  $\mathbf{F}$  and  $\mathbf{S}$  are the Fock and the overlap matrices,  $\mathbf{C}$  and  $\mathbf{E}$  are the matrices of eigenvectors and eigenvalues. The dimension M of square matrices  $\mathbf{F}, \mathbf{S}, \mathbf{C}$  is equal to the number of items in the sum (4.32), *i.e.* the total number of AO used in the calculation.

The Fock matrix  $\mathbf{F}$  is the sum of one-electron  $\mathbf{H}$  and two-electron  $\mathbf{G}$  parts. The former includes the kinetic (T) and nuclear attraction (Z) energy, the latter is connected with the electron–electron interactions. The matrix elements  $H_{\mu\nu}$  are written in the form

$$H_{\mu\nu} = -1/2 \int \chi_{\mu}^*(\mathbf{r}) \nabla_{\mathbf{r}}^2 \chi_{\nu}(\mathbf{r}) dV + \sum_{\mathbf{A}} \int \chi_{\mu}^*(\mathbf{r}) \frac{Z_{\mathbf{A}}}{|\mathbf{r} - \mathbf{R}_{\mathbf{A}}|} \chi_{\nu}(\mathbf{r}) dV = T_{\mu\nu} + Z_{\mu\nu} \quad (4.34)$$

The one-electron matrix  $\mathbf{H}$  is independent of the density matrix and therefore does not change during the self-consistent solution of Hartree–Fock–Roothaan equations. The two-electron matrix  $\mathbf{G}$  includes Coulomb ( $\mathbf{C}$ ) and exchange ( $\mathbf{X}$ ) parts of interelectron interaction:

$$G_{\mu\nu} = C_{\mu\nu} + X_{\mu\nu} = \sum_{\lambda\sigma} P_{\lambda\sigma}(\mu\nu|\lambda\sigma) - \frac{1}{2} \sum_{\lambda\sigma} P_{\lambda\sigma}(\mu\lambda|\nu\sigma) \quad (4.35)$$

where

$$(\mu\nu|\lambda\sigma) = \int \int \chi_{\mu}^*(\mathbf{r}) \chi_{\nu}^*(\mathbf{r}) |\mathbf{r} - \mathbf{r}'|^{-1} \chi_{\lambda}(\mathbf{r}') \chi_{\sigma}(\mathbf{r}') dV dV' \quad (4.36)$$

are two-electron integrals calculated with basis atomic orbitals. The one-electron kinetic energy and nuclear attraction integrals and two-electron integrals can be calculated at the beginning of solution of these equations and stored in the external memory of a computer. In some cases, this integrals calculation is more efficient at each step of the self-consistent process.

The two-electron part (4.35) contains one-electron density matrix elements

$$P_{\lambda\sigma} = 2 \sum_i C_{i\mu}^* C_{i\nu} \quad (4.37)$$

The one-electron density matrix  $\mathbf{P}$  in AO basis is calculated self-consistently after the initial set of coefficients  $\mathbf{C}$  is known. The simple one-electron Hamiltonian of Huckel type is often used as an initial approximation to the Hartree–Fock Hamiltonian. It is important to remember that the one-electron approximation is made when the many-electron wavefunction is written as the Slater determinant or their linear combination. For bound states, precise solution of Schrödinger equation can be expressed as a (in general infinite) linear combination of Slater determinants.

The approximation of the one-electron Hamiltonian is the next step in the framework of the one-electron approximation – the electron–electron interactions are excluded from the Hamiltonian. In solid-state theory the LCAO one-electron Hamiltonian approximation is known as the tight binding method. In molecular quantum chemistry the one-electron Hamiltonians of Hückel or Mulliken–Rüdenberg types (see Chap. 6) were popular in the 1950s and the beginning of the 1960s when the first-principles, Hartree–Fock LCAO calculations were practically impossible.

The total electron energy  $E_e$  in the Hartree–Fock LCAO method is calculated from the relation

$$E_e = \frac{1}{2} \sum_{\mu\nu} P_{\mu\nu} (F_{\mu\nu} + T_{\mu\nu} + Z_{\mu\nu}) \quad (4.38)$$

The total energy  $E = E_e + E_N$  is the sum of electron energy and nuclear repulsion energy

$$E_N = \sum_{j < j'} \frac{Z_j Z_{j'}}{|\mathbf{R}_j - \mathbf{R}_{j'}|} \quad (4.39)$$

The energy  $E_N$  is fixed for fixed nuclei configuration  $\{\mathbf{R}_1, \dots, \mathbf{R}_j, \dots, \mathbf{R}_N\}$ . When the optimization of molecular atomic configuration is made, the different nuclei configurations are considered to find that which gives the total energy minima. For each such configuration the self-consistent electron-energy calculation is made. By definition, in the molecular states with closed shells all MO are fully occupied by electrons (by 2, 4 and 6 electrons for nondegenerated, two- and three-times degenerated irreps of point groups, respectively) or empty. The corresponding many-electron wavefunction can be written as a single Slater determinant, each MO is occupied by an equal number of electrons with  $\alpha$  and  $\beta$  spins. Such a function describes the ground state of a molecule with total spin  $S=0$  and with the symmetry of identity representation of the point-symmetry group.

In the case of open-shell molecular systems a single Slater determinant describes a state with the fixed spin-projection (equal to the difference of  $n_\alpha$  and  $n_\beta$  electrons) but is not the correct spin eigenfunction. Indeed, let in the open-shell configuration the highest one-electron energy level be occupied by one electron with  $\alpha$  spin. As there are no spin interactions in the Hartree–Fock Hamiltonian the same electron energy corresponds to the function with  $\beta$ -spin electrons on the highest occupied level. This means that in order to get the correct total spin eigenfunction transforming over the identity representation of the point group it is necessary to use a sum of Slater

determinants. The molecules with an odd number of electrons, the radicals and the magnetic systems have the open shells in the ground state.

The restricted open-shell Hartree–Fock (ROHF) and the unrestricted Hartree–Fock Method (UHF) approximations permit, however, open-shell systems to be described, while maintaining the simplicity of the single-determinant approximation. This is made at the stage of self-consistent electronic-structure calculations. Afterwards, the obtained spin-orbitals can be used to get the correct total spin many-determinant wavefunction and to calculate the corresponding electron energy.

The ROHF [67] many-electron wavefunction is, in the general case, a sum of Slater determinants; each determinant contains a closed-shell subset, with doubly occupied orbitals and an open-shell subset, formed by orbitals occupied by a single electron.

In one particular case, the ROHF wavefunction reduces to a single determinant: this is the so-called half-closed- shell cases, where it is possible to define two sets of orbitals, the first  $n_d$  occupied by paired electrons and the second  $n_s$ , by electrons with parallel spins. The total number of electrons  $n = n_d + n_s$ . In all molecular programs ROHF means a single-determinant wavefunction with maximal spin projection that is automatically eigenfunctions of  $S^2$  with the maximal spin projector value  $S = n_s/2$ . So, for the ROHF method projection on a pure spin state is not required. The space symmetry of the Hamiltonian in the ROHF method remains the same as in the RHF method, *i.e.* coincides with the space symmetry of nuclei configuration. The double-occupancy constraint allows the ROHF approach to obtain solutions that are eigenfunctions of the total spin operator. The molecular orbitals diagram for the ROHF half-closed shell is given in Fig. 4.1, (left).

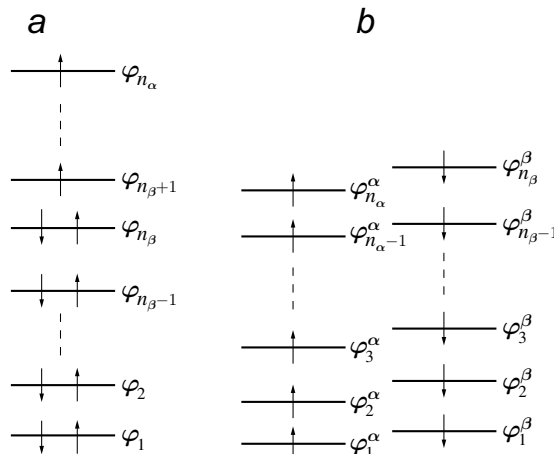


**Fig. 4.1.** The one-electron levels filling in (a) ROHF and (b) UHF methods

In the UHF method, keeping a single-determinant description, the constraint of double occupancy of molecular orbitals is absent as  $\alpha$  electrons are allowed to occupy orbitals other than those occupied by the  $\beta$  electrons, see Fig. 4.1 (right). The

greater variational freedom allows the UHF method to produce wavefunctions that are energetically more stable, *i.e.* give lower electron energy. Another advantage of the UHF method is that it allows solutions with locally nonzero negative or positive spin density (*i.e.* ferromagnetic or antiferromagnetic systems). However, UHF solutions are formed by a mixture of spin states and are eigenfunctions only of the total spin-projection operator  $S_z$ .

In the UHF approach, the single-determinant wavefunction is computed using  $n_\alpha$  MOs  $\varphi^\alpha(\mathbf{r})$  and  $n_\beta$  MOs  $\varphi^\beta(\mathbf{r})$ , corresponding to the electrons with  $\alpha$  and  $\beta$  spin, respectively. The wavefunction of the system with  $n$  electrons ( $n = n_\alpha + n_\beta$ ) has the following form:

$$\Psi = (N!)^{-1/2} \det \left\{ \varphi_1^\alpha(\mathbf{r}_1) \alpha(1) \dots \varphi_{n_\alpha}^\alpha(\mathbf{r}_{n_\alpha}) \alpha(n_\alpha) \right. \\ \left. \varphi_1^\beta(\mathbf{r}_{n_\alpha+1}) \beta(n_\alpha + 1) \dots \varphi_{n_\beta}^\beta(\mathbf{r}_n) \beta(n) \right\} \quad (4.40)$$

The energy expression is given by the following formula:

$$E = \langle \Psi | \hat{H} | \Psi \rangle = \sum_i \langle \varphi_i^\alpha | \hat{H} + 1/2(\hat{J} - \hat{K}^\alpha) | \varphi_i^\alpha \rangle + \sum_j \langle \varphi_j^\beta | \hat{H} - 1/2(\hat{J} - \hat{K}^\beta) | \varphi_j^\beta \rangle \quad (4.41)$$

where the Coulomb  $\hat{J}$  and the exchange  $\hat{K}^\alpha, \hat{K}^\beta$  operators are defined as in the standard RHF equations, that is:

$$\hat{J}(\mathbf{r})\varphi(\mathbf{r}) = \sum_i \left( \int d\mathbf{r}' \varphi_i^*(\mathbf{r}') |\mathbf{r} - \mathbf{r}'|^{-1} \varphi_i(\mathbf{r}') \right) \varphi(\mathbf{r}) \quad (4.42)$$

$$\hat{K}^\alpha(\mathbf{r})\varphi(\mathbf{r}) = \sum_i \left( \int d\mathbf{r}' (\varphi_i^\alpha)^*(\mathbf{r}') |\mathbf{r} - \mathbf{r}'|^{-1} \varphi_i(\mathbf{r}') \right) \varphi_i^\alpha(\mathbf{r}) \quad (4.43)$$

$$\hat{K}^\beta(\mathbf{r})\varphi(\mathbf{r}) = \sum_i \left( \int d\mathbf{r}' (\varphi_i^\beta)^*(\mathbf{r}') |\mathbf{r} - \mathbf{r}'|^{-1} \varphi_i(\mathbf{r}') \right) \varphi_i^\beta(\mathbf{r}) \quad (4.44)$$

In the LCAO approximation we write now MO for  $\alpha$ - and  $\beta$ -spins with different coefficients

$$\varphi_i^\alpha(\mathbf{r}) = \sum_{\mu A} C_{i\mu}^\alpha \chi_{\mu A}(\mathbf{r}); \quad \varphi_i^\beta(\mathbf{r}) = \sum_{\mu A} C_{i\mu}^\beta \chi_{\mu A}(\mathbf{r}) \quad (4.45)$$

and introduce the total density  $\mathbf{P}^{tot}$  and spin density matrices  $\mathbf{P}^{spin}$

$$\mathbf{P}^{tot} = \mathbf{P}^\alpha + \mathbf{P}^\beta, \quad \mathbf{P}^{spin} = \mathbf{P}^\alpha - \mathbf{P}^\beta \\ P_{\lambda\sigma}^\alpha = \sum_i C_{i\lambda}^{\alpha*} C_{i\sigma}^\alpha, \quad P_{\lambda\sigma}^\beta = \sum_j C_{j\lambda}^{\beta*} C_{j\sigma}^\beta \quad (4.46)$$

The total density matrix is used to get the expectation value of one-electron operators that are spin independent

$$\langle \hat{O} \rangle = \sum_\mu \sum_\nu P_{\mu\nu}^{tot} \langle \chi_\mu | \hat{O} | \chi_\nu \rangle \quad (4.47)$$

To get the equations for the optimal UHF orbitals we proceed as in the standard RHF case: we compute the first energy variation, then we introduce the orthonormality

constraint of the basis set by means of the Lagrange multipliers method [68]. The Pople–Nesbet equations

$$\mathbf{F}^\alpha \mathbf{C}^\alpha = \mathbf{S} \mathbf{C}^\alpha \mathbf{E}^\alpha \quad (4.48)$$

$$\mathbf{F}^\beta \mathbf{C}^\beta = \mathbf{S} \mathbf{C}^\beta \mathbf{E}^\beta \quad (4.49)$$

of the UHF LCAO method can be considered as the extension of the RHF LCAO method equations (4.33) to the case when MO occupied by  $\alpha$  and  $\beta$  spins are varied independently. However, (4.48) and (4.49) can not be solved independently as the Fock matrix depends not only on the total density  $\mathbf{P}^{\text{tot}}$  and has the form:

$$\mathbf{F}^\alpha = \mathbf{F} - \frac{1}{2} \mathbf{K}[\mathbf{P}^{\text{spin}}], \quad \mathbf{F}^\beta = \mathbf{F} + \frac{1}{2} \mathbf{K}[\mathbf{P}^{\text{spin}}] \quad (4.50)$$

where the matrices  $\mathbf{F}$  and  $\mathbf{G}$  are defined as

$$\mathbf{F} = \mathbf{H} + \mathbf{G}; \quad \mathbf{G} = \mathbf{J}[\mathbf{P}^{\text{tot}}] - \frac{1}{2} \mathbf{K}[\mathbf{P}^{\text{tot}}] \quad (4.51)$$

The total electron energy expression now has the form

$$E = Sp \mathbf{P}^{\text{tot}} \mathbf{H} + \frac{1}{2} Sp \mathbf{P}^{\text{tot}} \mathbf{G} - \frac{1}{4} Sp \mathbf{P}^{\text{spin}} \mathbf{K}[\mathbf{P}^{\text{spin}}] \quad (4.52)$$

To solve the UHF method equations the iterative procedure is necessary as was already discussed for the RHF method. At first, an initial guess at the density matrices  $\mathbf{P}^\alpha$  and  $\mathbf{P}^\beta$  is made. Then, the Fock matrices  $\mathbf{F}^\alpha$  and  $\mathbf{F}^\beta$  are calculated from (4.46). The matrices of coefficients  $\mathbf{C}^\alpha$  and  $\mathbf{C}^\beta$  are determined by diagonalization of the Fock matrices for  $\alpha$ - and  $\beta$ -spins and the density matrix for the next iteration is built. The whole process must be repeated to self-consistency; the convergence criteria consider either the density matrix or the total electron energy. In order to get spin-polarized solutions from an UHF calculation, it is necessary that the initial density matrices  $\mathbf{P}^\alpha$  and  $\mathbf{P}^\beta$  are chosen to be different and this difference maintained during the whole SCF process [69]. The RHF closed-shell solution can be considered as a special case of the UHF method, where the number of  $\alpha$  electrons coincide with the number of  $\beta$  electrons ( $n_\alpha = n_\beta$ ). In the RHF method  $\mathbf{P}^\alpha = \mathbf{P}^\beta$  for the whole SCF process. In the UHF method (when initial matrices  $\mathbf{P}^\alpha \neq \mathbf{P}^\beta$ ) we could have either spin-polarized solutions at the end of the SCF cycle or the spin polarization will vanish in the course of the SCF process. Reaching a closed-shell solution from a spin-polarized starting point is favored when the latter solution has lower energy.

The extension of the RHF, ROHF and UHF LCAO methods to periodic systems is considered in the next sections. We begin this consideration from the discussion of specific features of these methods when instead of a molecular system the cyclic model of a crystal is introduced.

#### 4.1.4 Specific Features of the Hartree–Fock Method for a Cyclic Model of a Crystal

The extension of the HF method to a model of an infinite crystal leads to difficulties connected with the one-electron Bloch functions (BF) behavior since they do not fall

off to zero at infinity and therefore can not be normalized to unity in a space [70]. To overcome this difficulty, periodic boundary conditions (PBC) are introduced for the BF normalized in the main region of volume of the crystal containing a large number  $N$  of primitive unit cells of volume.

In the HF method for molecular systems a many-electron wavefunction in the form of a Slater determinant is written for the system containing a fixed number of electrons. PBC introduction for the infinite crystal allows the system of infinite number of electrons to be replaced by the system of a finite number of electrons (a cyclic cluster). But, in a cyclic cluster containing a large number  $N$  of primitive unit cells the number of electrons remains huge and from the very beginning it is necessary to take into account the translation symmetry that is an opportunity to generate a whole cyclic cluster by translations of a primitive unit cell. The concept of the cyclic cluster helps to understand why, on calculation of the Fock matrix for a crystal, it is necessary to make summations on a direct lattice and on the Brillouin zone. Thus, the dimension of the Fock matrix is determined by the number of the basis atomic functions referring not to an infinite crystal or its main region but to its small part – the primitive unit cell.

Let the infinite crystal be replaced with a cyclic system (cyclic cluster) from  $N = N_1 \times N_2 \times N_3$  primitive cells, *i.e.* replaced with a parallelepiped with edges  $N_i \mathbf{a}_i (i = 1, 2, 3)$ . Periodic boundary conditions mean that opposite sides of a parallelepiped are identified, *i.e.* translations on vectors  $N_i \mathbf{a}_i (i = 1, 2, 3)$  are equivalent to zero translation. The number of electrons in a cyclic system is equal  $N \times n$ , where  $n$  is the number of electrons on a primitive unit cell. In the HF method the cyclic system under consideration can be considered as a huge molecular system with periodical boundary conditions imposed on molecular orbitals. The matrix elements of the Fock operator for the cyclic cluster in the LCAO basis have to include the summation on all atoms in the cyclic cluster. To calculate the one-electron density matrix elements the summation has to be performed on all the molecular orbitals occupied by  $N \times n$  electrons. We shall notice that for essentially ionic systems the cyclic cluster under consideration should be placed in a Madelung field of the rest of an infinite crystal. This means that in the diagonal elements of the Fock matrix contributions should be added from the field of point charges of those atoms that are not included in the cyclic cluster. With such an approach interatomic interactions in a crystal are actually separated into short-range and long-range ones. The former are taken into account directly in the cyclic-cluster calculation, the latter are approximated by inclusion of the Madelung field acting on every atom of the cyclic cluster under consideration. The efficient techniques of the Madelung field calculation are developed in the solid-state theory [71] and we do not discuss them here. In [55] the symmetry group of the cyclic model of a crystal was examined and the connection of this group with the symmetry group of an infinite crystal was discussed. In particular, it was shown that the inner translations of a cyclic system form a subgroup of the translation group of an infinite crystal. This allows calculation of the electronic structure of the cyclic system using the atomic basis symmetrized over the operations of this translation subgroup. This means use of LCAO Bloch functions for those wavevectors that are connected with the group  $T^{(N)}$  of inner translations of cyclic system. By this the Fock matrix is split up into blocks whose dimension is determined by number of different one-dimensional representations of the translation group  $T^{(N)}$ , *i.e.* those nonequivalent wavevectors

in the Brillouin zone that correspond to these representations. These wavevectors are defined by the relation  $\exp(-ik\mathbf{A}) = 1$ , where  $\mathbf{A}$  is the translation vector of the cyclic system as a whole. Comparing the HF method for crystals with that for molecules we conclude that instead of one the system of HF equations the separate equations for any of nonequivalent wavevectors is necessary to solve at each iteration of the self-consistent procedure. The preliminary atomic basis symmetrization in the Hartree–Fock calculations of molecular systems can also be carried out to split up the Fock matrix into blocks of smaller dimensions. However, the gain of such a splitting, as a rule, is insignificant especially for those point groups that have many dimensional irreducible representations. For a crystal, the direct account of translation symmetry is a unique way to calculate the electronic structure. The summation over a direct lattice in the Fock matrix appears as the sum over atoms included in the cyclic cluster. The use of the translation symmetry allows one to calculate only those matrix elements of the Fock matrix that are connected with the AOs of the reference primitive unit cell (the zero translation vector corresponds to the reference primitive cell). In the density-matrix calculation for a cyclic system the summation over wavevector appears. This summation means the use of an atomic basis symmetrized over the translation subgroup of a cyclic system symmetry group and replaces the summation over the occupied MO of a cyclic system by summation over occupied crystalline orbitals for different wavevectors. Their number is determined by the number of electrons in a primitive unit cell. The further splitting of the Fock matrix can be made using the connection between the irreducible representations of the symmetry group of a cyclic system and those of an infinite-crystal symmetry group. For each wavevector only the one ray of its star can be considered, and summation on a star is carried out by application of operations of the point group of a crystal to that crystalline orbital calculated for this ray. The full space group symmetry inclusion in the HF LCAO method is considered in [28, 29] and realized in the CRYSTAL code [23].

Naturally, there is a question: what size is it possible to be limited to in cyclic system modeling of each an actual crystal? This depends on the character of localization of electronic density in a crystal: in ionic crystals and semiconductors with a large energy gap (5–10 eV) the electronic density is well-enough localized on ions or interatomic bonds so the cyclic system of rather small sizes describes a short-range part of the interatomic interactions. This means that on calculation of the one-electron density for such crystals it is possible to be limited to summation on a rather small number of points of the Brillouin zone. In crystals with a small energy gap, or metals, the size of the needed cyclic system becomes essentially larger as the one-electron states are more delocalized (in metals these states are practically delocalized over the whole infinite crystal). Therefore, the summation over the Brillouin zone in calculations of crystals with a small energy gap requires many  $\mathbf{k}$ -points to be included. We see that one-to-one correspondence between the cyclic system size in direct lattice and the finite set of wavevectors in the Brillouin zone allows an investigation of the convergence of the results of electronic-structure calculations on the size of the cyclic system sufficient to describe short-range interatomic interactions in a crystal. Nevertheless, such an investigation is made by the primitive unit cell calculations.

In the next sections we consider in more detail the HF LCAO method for periodic systems.

### 4.1.5 Restricted Hartree–Fock LCAO Method for Crystals

The reformulation of Hartree–Fock LCAO molecular equations (4.33) to make them suitable for periodic systems was proposed in [74] about forty years ago. However, the first HF LCAO calculations were made mainly for the simple solids [72] or for one-periodic systems (polymers) [73, 74] in which the direct lattice summations are essentially simpler than in the two- or three-periodic systems. The periodic HF LCAO method for the systems with any periodicity (polymers, surfaces, bulk crystals) was implemented in the CRYSTAL code [23] after the detailed theoretical study of the exact-(nonlocal) exchange Hamiltonian for the periodic systems. The following main aspects were examined [75]: (i) the point and translational symmetry properties of the HF LCAO Hamiltonian and the transformation of all relevant monoelectronic and bielectronic terms under the symmetry operators, (ii) the use of general yet powerful criteria for the truncation of infinite sums of Coulomb and exchange integrals, (iii) the use of a procedure for performing integrals over wavevector  $\mathbf{k}$  as needed in the reconstruction of the Fock matrix in the SCF calculation. The first successful applications of the CRYSTAL code to the calculations of the ground-state properties of the two-periodic [76] (hexagonal boron nitride) and three-periodic [77] (cubic boron nitride and silicon) have opened a more than 25-year *ab-initio* HF LCAO study of the bulk electronic properties of crystals, both perfect and defective, the extension of the method to the surface modeling and magnetic systems. The density functional theory (DFT) LCAO and hybrid (HF-DFT) calculation schemes were implemented in the later versions of the CRYSTAL code [78]. The next step was made when the EMBED code [79] appeared with the implementation of the perturbed cluster model of point defects in crystals. The detailed discussion of many results obtained by HF and DFT LCAO methods we postpone until Chapters 9–11. The reader interested in the list of the actual systems calculations is referred to the Internet sites [80] and [81]. Recently, periodic boundary conditions were included in the molecular code Gaussian [82] and the first-principles HF and DFT calculations were made with the use of this code [83]. In Appendix C we give brief information about these two and some other HF and DFT LCAO computer codes for crystals.

In this section, we examine the main modifications in the Hartree–Fock–Roothaan equations (4.33), it being necessary to take into account the translation symmetry of periodic systems. The first most important difference appears in the LCAO representation of the crystalline orbitals (CO) compared to the molecular orbitals (MO).

For the periodic system the AO symmetrization over the translation subgroup of the space group is made giving the Bloch sums of AOs:

$$\chi_{\mu\mathbf{k}}(\mathbf{r}) = \frac{1}{\sqrt{N}} \sum_{\mathbf{R}_n} \exp(i\mathbf{k}\mathbf{R}_n) \chi_{\mu}(\mathbf{r} - \mathbf{R}_n) \quad (4.53)$$

In (4.53), the index  $\mu$  labels all AOs in the reference primitive unit cell ( $\mu = 1, 2, \dots, M$ ) and  $\mathbf{R}_n$  is the translation vector of the direct lattice (for the reference primitive cell  $\mathbf{R}_n = 0$ ). The summation in (4.53) is supposed to be made over the infinite direct lattice (in the model of the infinite crystal) or over the inner primitive translations  $\mathbf{R}_n^0$  of the cyclic cluster (in the cyclic model of a crystal). In the latter case, the sum of the two inner translation vectors  $\mathbf{R}_n^0 + \mathbf{R}_m^0 = \mathbf{R}_l$  may appear not to be the inner translation of the cyclic cluster. However, the subtraction of the translation vector  $\mathbf{A}$  of the cyclic cluster as a whole (in the cyclic model the vector  $\mathbf{A}$  is

supposed to be equivalent to the zero translation) gives the inner translation again:  $\mathbf{R}_l^0 = \mathbf{R}_l - \mathbf{A}$ .

The Bloch sum of AO (4.53) satisfies the Bloch theorem. To check this let us apply the translation operator  $\hat{t}_{\mathbf{R}_m}$  (for the fixed translation  $\mathbf{R}_m$ ) to the sum (4.53)

$$\begin{aligned} \hat{t}_{\mathbf{R}_m} \chi_{\mu\mathbf{k}}(\mathbf{r}) &= \chi_{\mu\mathbf{k}}(\mathbf{r} - \mathbf{R}_m) \\ &= \exp(-i\mathbf{k}\mathbf{R}_m) \frac{1}{\sqrt{N}} \sum_{\mathbf{R}_n} \exp(i\mathbf{k}(\mathbf{R}_n + \mathbf{R}_m)) \chi_{\mu}(\mathbf{r} - \mathbf{R}_m - \mathbf{R}_n) \\ &= \exp(-i\mathbf{k}\mathbf{R}_m) \sum_{\mathbf{R}_{n'}=\mathbf{R}_n+\mathbf{R}_m} \exp(i\mathbf{k}\mathbf{R}_{n'}) \chi_{\mu}(\mathbf{r} - \mathbf{R}_{n'}) = \exp(-i\mathbf{k}\mathbf{R}_m) \chi_{\mu}(\mathbf{r}) \end{aligned} \quad (4.54)$$

The replacing of the sum over translation vectors ( $\mathbf{R}_n + \mathbf{R}_m$ ) by the sum over translation vectors  $\mathbf{R}_{n'}$  is evidently possible for the infinite crystal. In the cyclic cluster this replacement means the subtraction of the translation vector  $\mathbf{A}$ .

In the LCAO approximation CO is the Bloch function as it is expanded over the Bloch sums of AOs:

$$\varphi_{i\mathbf{k}}(\mathbf{r}) = \sum_{\mu} C_{i\mu}(\mathbf{k}) \chi_{\mu\mathbf{k}}(\mathbf{r}) \quad (4.55)$$

In the MO LCAO approximation the index  $i$  in the expansion (4.32) numbers the MOs (their total number  $M$  is equal to the number of atomic orbitals used in the expansion (4.32)). In the case of closed shells the  $N_e$  electrons of the molecule occupy  $N_e/2$  MOs and  $(M - N_e/2)$  MOs are empty. The total number of COs of the cyclic cluster equals  $M \times N$  ( $N$  is the number of the primitive unit cells in the cyclic cluster;  $M$  is the number of AO basis functions per primitive unit cell). For the cyclic cluster containing  $N_e = N \times n$  electrons ( $n$  is the number of electrons per primitive unit cell)  $N_e/2$  crystalline orbitals are occupied by electrons and  $(M \times N - N_e/2)$  orbitals are empty. The numbering of crystalline orbitals is made by two indices  $i$  and  $\mathbf{k}$ : the one-electron states of a crystal form the energy bands numbered by index  $i$  and joining the  $N$  states with the same  $i$ . The closed-shell case (the nonconducting crystals) means that all the energy bands are filled or empty (there are no partly filled energy bands). For  $N \rightarrow \infty$  the total number of COs also becomes infinite, the one-electron energy levels form the continuous energy bands, but the total number of energy bands remains finite and is equal to  $M$ . For the closed-shell case  $n/2$  electrons occupy the lowest-energy bands for each  $\mathbf{k}$ -vector. As discussed in Sect. 3.2.5 MgO and Si crystals are examples of nonconducting systems with different values of the forbidden energy gap (Figs. 3.4–3.5). The latter is the crystalline analog of the HOMO (highest-occupied MO)–LUMO (lowest-unoccupied MO) one-electron energies difference. In both cases,  $n = 8$  (there are 8 valence electrons per primitive cell), 8 electrons occupy 4 valence energy bands (for MgO crystal the whole valence band is split into two subbands).

On the basis of Bloch functions, the Fock and overlap matrices  $F$  and  $S$  become

$$F_{\mu\nu}(\mathbf{k}) = \sum_{\mathbf{R}_n} \exp(i\mathbf{k}\mathbf{R}_n) F_{\mu\nu}(\mathbf{R}_n); \quad S_{\mu\nu}(\mathbf{k}) = \sum_{\mathbf{R}_n} \exp(i\mathbf{k}\mathbf{R}_n) S_{\mu\nu}(\mathbf{R}_n) \quad (4.56)$$

where  $F_{\mu\nu}(\mathbf{R}_n)$  is the matrix element of the Fock operator between the  $\mu$ th AO located in the reference (zero) cell and the  $\nu$ -th AO located in the  $\mathbf{R}_n$  cell. The matrix element  $S_{\mu\nu}(\mathbf{R}_n)$  is the overlap integral of the same AOs. The row index can be limited to the

reference cell for translational symmetry. Matrices represented on the Bloch basis (or in  $\mathbf{k}$ -space) take a block-diagonal form, as Bloch functions are bases for irreducible representations of the translation group  $T$  ( $T^{(N)}$  for the cyclic cluster of  $N$  primitive cells); each block has the dimensions of the AO basis in the primitive cell,  $M$ ,

$$F(\mathbf{k})C(\mathbf{k}) = S(\mathbf{k})C(\mathbf{k})E(\mathbf{k}) \quad (4.57)$$

In the HF LCAO method, (4.57) for the periodic systems replaces (4.33) written for the molecular systems. In principle, the above equation should be solved at each SCF procedure step for all the (infinite)  $\mathbf{k}$ -points of the Brillouin zone. Usually, a finite set  $\{\mathbf{k}_j\}$  ( $j = 1, 2, \dots, L$ ) of  $\mathbf{k}$ -points is taken (this means the replacing the infinite crystal by the cyclic cluster of  $L$  primitive cells). The convergence of the results relative to the increase of the  $\mathbf{k}$ -points set is examined in real calculations, for the convergent results the interpolation techniques are used for eigenvalues and eigenvectors as these are both continuous functions of  $\mathbf{k}$  [84]. The convergence of the SCF calculation results is connected with the density matrix properties considered in Sect. 4.3

The overlap matrix elements in the AO basis are the lattice sums of the overlap integrals between AOs, numbered now by indices of AO in the zero cell and of the cell defined by the translation vector  $\mathbf{R}_n$ :

$$S_{\mu\nu}(\mathbf{R}_n) = \int \chi_{\mu}^{*}(\mathbf{r}) \chi_{\nu}(\mathbf{r} - \mathbf{R}_n) d^3\mathbf{r} \quad (4.58)$$

The Fock matrix elements (as in the case of molecules) are the sums of one-electron (the kinetic energy  $T$  and the nuclear attraction energy  $Z$ ) and two-electron (Coulomb  $J$  and exchange energies) parts. The difference of these matrices from the molecular analogs is the appearance of the sums over a direct lattice, containing one-electron (kinetic energy and nuclear attraction) and two-electron integrals:

$$F_{\mu\nu}(\mathbf{R}_n) = T_{\mu\nu}(\mathbf{R}_n) + Z_{\mu\nu}(\mathbf{R}_n) + J_{\mu\nu}(\mathbf{R}_n) + X_{\mu\nu}(\mathbf{R}_n) \quad (4.59)$$

$$T_{\mu\nu}(\mathbf{R}_n) = -\frac{1}{2} \int \chi_{\mu}^{*}(\mathbf{r}) \nabla_{\mathbf{r}}^2 \chi_{\nu}(\mathbf{r} - \mathbf{R}_n) d^3\mathbf{r} \quad (4.60)$$

$$Z_{\mu\nu}(\mathbf{R}_n) = \sum_{A=1}^{N_A} \sum_{\mathbf{R}_m} \int \chi_{\mu}^{*}(\mathbf{r}) \frac{Z_A}{|\mathbf{r} - \mathbf{A} - \mathbf{R}_m|} \chi_{\nu}(\mathbf{r} - \mathbf{R}_n) d^3\mathbf{r} \quad (4.61)$$

(A numbers atoms in the primitive cell)

$$J_{\mu\nu}(\mathbf{R}_n) = \sum_{\lambda\sigma}^M \sum_{\mathbf{R}_{m'}} P_{\lambda\sigma}(\mathbf{R}_{m'}) \sum_{\mathbf{R}_m} (\mu 0 \nu \mathbf{R}_n | \lambda \mathbf{R}_m \sigma(\mathbf{R}_m + \mathbf{R}_{m'}) ) \quad (4.62)$$

$$X_{\mu\nu}(\mathbf{R}_n) = -\frac{1}{2} \sum_{\lambda\sigma}^M \sum_{\mathbf{R}_{m'}} P_{\lambda\sigma}(\mathbf{R}_{m'}) \sum_{\mathbf{R}_m} (\mu 0 \lambda \mathbf{R}_m | \nu \mathbf{R}_n \sigma(\mathbf{R}_m + \mathbf{R}_{m'}) ) \quad (4.63)$$

The two-electron integrals in (4.62) and (4.63) are defined as

$$(\mu 0 \nu \mathbf{R}_n | \lambda \mathbf{R}_m \sigma(\mathbf{R}_m + \mathbf{R}_{m'})) = \int \int \chi_{\mu}^{*}(\mathbf{r}) \chi_{\nu}(\mathbf{r} - \mathbf{R}_n) |\mathbf{r} - \mathbf{r}'|^{-1} \chi_{\lambda}^{*}(\mathbf{r}' - \mathbf{R}_m) \chi_{\sigma}(\mathbf{r} - \mathbf{R}_m - \mathbf{R}_{m'}) d^3\mathbf{r} d^3\mathbf{r}' \quad (4.64)$$

The comparison of (4.36) and (4.64) shows the difference in the two-electron integrals definitions for crystals and molecules.

The spinless one-electron density matrix (DM) elements are defined in the LCAO approximation as

$$P_{\lambda\sigma}(\mathbf{R}_{m'}) = 2 \int d\mathbf{k} e^{i\mathbf{k}\mathbf{R}_{m'}} \sum_i C_{i\lambda}^*(\mathbf{k}) C_{i\sigma}(\mathbf{k}) \theta(\epsilon_F - \epsilon_i(\mathbf{k})) \quad (4.65)$$

where  $\epsilon_F$  is the Fermi energy, the integration in (4.65) extends to the first Brillouin zone and corresponds to the model of the infinite crystal. In the cyclic-cluster model the integration is replaced by the summation over  $\mathbf{k}$ -points numbering the irreps of the group of the inner cyclic-cluster translations. The DM elements depend on the eigenvectors  $C_i(\mathbf{k})$  of the  $F(\mathbf{k})$  matrix. The integration or summation over  $\mathbf{k}$  in DM elements makes it impossible to solve (4.57) for different  $\mathbf{k}$  independently.

The electron energy of the crystal (per primitive unit cell) as calculated within the HF LCAO approximation can be expressed in terms of the one-electron density matrix (DM) and includes the lattice sums

$$E_e = \frac{1}{2} \sum_{\mu\nu}^M \sum_{\mathbf{R}_n} P_{\mu\nu}(\mathbf{R}_n) (F_{\mu\nu}(\mathbf{R}_n) + T_{\mu\nu}(\mathbf{R}_n) + Z_{\mu\nu}(\mathbf{R}_n)) \quad (4.66)$$

The direct lattice summations in the Fock matrix elements and the  $\mathbf{k}$  dependence of the one-electron DM, energy levels and COs are the main difficulties of the HF LCAO method for periodic systems, compared with molecules. A special strategy must be specified for the treatment of the infinite Coulomb and exchange series as well as for the substitution of the integral that appears in DM with a weighted sum extended to a finite set of  $\mathbf{k}$ -points. The efficient solution of these problems has been implemented in the CRYSTAL code [23]. These problems are also valid for UHF and ROHF LCAO methods for periodic systems considered in the next subsection.

#### 4.1.6 Unrestricted and Restricted Open-shell Hartree–Fock Methods for Crystals

The unrestricted and restricted open-shell Hartree–Fock Methods (UHF and ROHF) for crystals use a single-determinant wavefunction of type (4.40) introduced for molecules. The differences appearing are common with those examined for the RHF LCAO method: use of Bloch functions for crystalline orbitals, the dependence of the Fock matrix elements on the lattice sums over the direct lattice and the Brillouin-zone summation in the density matrix calculation. The use of one-determinant approaches is the only possibility of the first-principles wavefunction-based calculations for crystals as the many-determinant wavefunction approach (used for molecules) is practically unrealizable for the periodic systems. The UHF LCAO method allowed calculation of the bulk properties of different transition-metal compounds (oxides, perovskites) – the systems with open shells due to the transition-metal atom. We discuss the results of these calculations in Chap. 9. The point defects in crystals in many cases form the open-shell systems and also are interesting objects for UHF LCAO calculations (see Chap. 10).

In the UHF or ROHF cases two sets of matrix equations are solved self-consistently for  $\alpha$  and  $\beta$  spins [69]:

$$F^\alpha(\mathbf{k})C^\alpha(\mathbf{k}) = S(\mathbf{k})C^\alpha(\mathbf{k})E^\alpha(\mathbf{k}) \quad (4.67)$$

$$F^\beta(\mathbf{k})C^\beta(\mathbf{k}) = S(\mathbf{k})C^\beta(\mathbf{k})E^\beta(\mathbf{k}) \quad (4.68)$$

where the  $F^\alpha(\mathbf{k})$ ,  $F^\beta(\mathbf{k})$  and  $S(\mathbf{k})$  matrices are obtained by Fourier transform from the corresponding direct space equivalent quantities as in (4.56).

The Fourier components of the density matrix for  $\alpha$  and  $\beta$  spins are different as they are obtained by using the  $C^\alpha(\mathbf{k})$  and  $C^\beta(\mathbf{k})$  eigenvectors obtained from (4.67) and (4.68), respectively:

$$P_{\lambda\sigma}^\alpha(\mathbf{R}_m) = \int d\mathbf{k} e^{i\mathbf{k}\mathbf{R}_m} \sum_i n_i^\alpha C_{i\lambda}^{*\alpha}(\mathbf{k}) C_{i\sigma}^\alpha(\mathbf{k}) \quad (4.69)$$

$$P_{\lambda\sigma}^\beta(\mathbf{R}_m) = \int d\mathbf{k} e^{i\mathbf{k}\mathbf{R}_m} \sum_i n_i^\beta C_{i\lambda}^{*\beta}(\mathbf{k}) C_{i\sigma}^\beta(\mathbf{k}) \quad (4.70)$$

where  $n_i^{\alpha,\beta}$  are the occupations of CO by electrons with  $\alpha$  and  $\beta$  spins.

The total density  $P(\mathbf{R}_m)$  and spin density  $P^{spin}(\mathbf{R}_m)$  Fourier components are defined as

$$P(\mathbf{R}_m) = P^\alpha(\mathbf{R}_m) + P^\beta(\mathbf{R}_m) \quad (4.71)$$

$$P^{spin}(\mathbf{R}_m) = P^\alpha(\mathbf{R}_m) - P^\beta(\mathbf{R}_m) \quad (4.72)$$

The  $F^\alpha(\mathbf{R}_m)$  and  $F^\beta(\mathbf{R}_m)$  matrices are defined as follows:

$$F_{\mu\nu}^\alpha(\mathbf{R}_m) = F_{\mu\nu}(\mathbf{R}_m) + X_{\mu\nu}^{spin}(\mathbf{R}_m) \quad (4.73)$$

$$F_{\mu\nu}^\beta(\mathbf{R}_m) = F_{\mu\nu}(\mathbf{R}_m) - X_{\mu\nu}^{spin}(\mathbf{R}_m) \quad (4.74)$$

The  $F(\mathbf{R}_m)$  matrix is defined as in (4.59), where the total density matrix  $P(\mathbf{R}_m)$  defined in (4.71) is used in the Coulomb and exchange terms;  $X_{\mu\nu}^{spin}(\mathbf{R}_m)$  is defined as  $X_{\mu\nu}(\mathbf{R}_m)$  in (4.63), where, however, the spin density matrix  $P^{spin}(\mathbf{R}_m)$  is used instead of the total density matrix  $P(\mathbf{R}_m)$ .

The ROHF LCAO method for crystals differs from the UHF method in the equations defining the CO. Let  $n = n_\alpha + n_\beta$  electrons per primitive unit cell be considered ( $n_\alpha > n_\beta$ ). For the  $n_\beta$  CO the closed-shell RHF LCAO equations are solved, the CO of  $n_\alpha + n_\beta$  electrons with  $\alpha$  spin are found from the equation analogous to (4.57). In the ROHF method the total density  $P(\mathbf{R}_m)$  and spin density  $P^{spin}(\mathbf{R}_m)$  matrices are defined as

$$P(\mathbf{R}_m) = P^{\alpha,\beta}(\mathbf{R}_m) + P^\alpha(\mathbf{R}_m) \quad (4.75)$$

$$P^{spin}(\mathbf{R}_m) = P^{(\alpha-\beta)}(\mathbf{R}_m) \quad (4.76)$$

In (4.75)  $P^{\alpha,\beta}$  is the DM calculated with the doubly occupied COs and in (4.76)  $P^{(\alpha-\beta)}$  is DM calculated for COs with  $\alpha$  spin.

The UHF method many-electron wavefunction is the eigenfunction of the spin projection operator  $\hat{S}_z$  with zero eigenvalue, the ROHF method many-electron function

describes the spin state with the maximally possible spin projection  $S_z = \frac{1}{2}(n_\alpha - n_\beta)$ . If we compare the UHF scheme with the RHF scheme for the closed-shell case, we see that the most relevant quantities (Fock and density matrices, eigenvalues and eigenvectors) are duplicated, so that it is possible to differentiate  $\alpha$  orbitals from  $\beta$  orbitals. As in the case of molecules it is important that at the starting guess  $P^\alpha$  and  $P^\beta$  density matrices are different. In the CRYSTAL code there exists an option to construct a DM formed by the superposition of atomic solutions, where it is possible to assign a specific polarization (or no polarization) to each atom of the system [69]. Once the SCF process is started, it is often useful to introduce some constraints on the populations of the  $\alpha$  and  $\beta$  orbitals. This is performed in the CRYSTAL code by *ad-hoc* translations of the eigenvalues spectrum in such a way that the difference between the number of  $\alpha$  and  $\beta$  electrons is equal to the value introduced in the input.

It is well known from Hartree–Fock studies of molecular systems, that it is very common to have problems of SCF convergence when studying open-shell systems; similarly, convergence problems are not rare in the Hartree–Fock treatment of spin-polarized crystals. A well-known technique for the solution of convergence problems, in the case of open-shell molecules, is the so-called level-shifting method [85]; this approach has shown its effectiveness in the periodic HF context also, especially in the case of crystals containing transition elements.

## 4.2 Special Points of Brillouin Zone

### 4.2.1 Supercells of Three-dimensional Bravais Lattices

Let  $\mathbf{a}_i(\Gamma_1)$  ( $i=1,2,3$ ) be the basic translation vectors of the initial direct lattice of type  $\Gamma_1$  and  $\mathbf{a}_j(\Gamma_2)$  ( $j = 1, 2, 3$ ) be the basic translation vectors of a new lattice of type  $\Gamma_2$  with the same point symmetry (symmetrical transformation) but composed of supercells. Then

$$\mathbf{a}_j(\Gamma_2) = \sum_i l_{ji}(\Gamma_2\Gamma_1) \mathbf{a}_i(\Gamma_1) \quad |\det l| = L, j = 1, 2, 3 \quad (4.77)$$

where  $l_{ji}(\Gamma_2\Gamma_1)$  are integer elements of the matrix  $l(\Gamma_2\Gamma_1)$  defining the transition from the lattice of type  $\Gamma_1$  to the lattice of type  $\Gamma_2$ .

The vectors  $\mathbf{a}_j(\Gamma_2)$  have well-defined orientation with respect to point-symmetry elements of the lattices that are the same for both lattices because of the symmetrical character of the transformation (4.77). Let us define the components of the vectors  $\mathbf{a}_j(\Gamma_2)$  by the parameters  $s_k$  assuring their correct orientation relative to the lattice symmetry elements and the correct relations between their lengths (if there are any). Then three vector relations (4.77) give nine linear nonhomogeneous equations to determine nine matrix elements  $l_{ij}(\Gamma_2\Gamma_1)$  as functions of the parameters  $s_k$ . The requirements that these matrix elements must be integers define the possible values of the parameters  $s_k$  giving the solution of the problem.

Let us demonstrate the procedure of finding the matrix of a symmetrical transformation (4.77) by the example of the rhombohedral crystal system where there is only one lattice type (R). The basic translation vectors of the initial lattice are the following:

$$\mathbf{a}_1 = (a, 0, c) \quad \mathbf{a}_{2,3} = (-a/2, \pm a\sqrt{3}/2, c)$$

The basic translation vectors of the new lattice composed of supercells for symmetrical transformation (4.77) have the same form (the parameters  $a$  and  $c$  of the initial lattice are replaced with the parameters  $s_1a$ ,  $s_2c$ )

$$\mathbf{a}_1 = (s_1a, 0, s_2c) \quad \mathbf{a}_{2,3} = (-s_1a/2, \pm s_1a\sqrt{3}/2, s_2c)$$

Inserting them in (4.77) one obtains nine equations for nine elements of the matrix  $l$ . The solution of this system is

$$l_{ij} = \frac{s_2 + 2s_1}{3} \delta_{ij} + \frac{s_2 - s_1}{3} (1 - \delta_{ij})$$

where  $i,j=1,2,3$ . As the matrix elements  $l_{ij}$  must be integers let us assign  $(s_2 - s_1)/3 = n_2$  and  $(s_2 + 2s_1)/3 = n_1 + n_2$ . The matrix of the symmetrical transformation for a rhombohedral lattice with the corresponding value of  $L$  may be found in Appendix A and [86] where the matrices of the symmetrical transformations for all three-dimensional crystal lattices are given. Let us explain the peculiarities of the consideration made for each of the seven possible crystal systems.

In the triclinic crystal system an arbitrary matrix with integer elements defines a symmetrical transformation (any transformation seems to be symmetrical because of the low point symmetry of the lattice).

In the monoclinic crystal system there are two lattices: simple (P) and base-centered (A) each of which is defined by five parameters. Therefore the matrices of symmetrical transformations are determined by five integers.

In the hexagonal crystal system there is only one lattice type (P), but the basic translation vectors may be oriented in two different ways relative to the basic translation vectors of the initial lattice: either parallel to them or rotated through an angle of  $\pi/6$  about the  $z$ -axis. Therefore, two types of symmetrical transformation are possible in this case (with two parameters for each).

In the orthorhombic crystal system the base-centered lattice merits special attention because of different possible settings. Let the initial base-centered lattice have the setting C. The transition to base-centered lattices with settings C and A (or B) gives different results (see Appendix A). The change of setting for the transition to other types of lattice does not give new supercells.

In the tetragonal crystal system there are two types of Bravais lattice (P and I). All their symmetrical transformations may be obtained from the symmetrical transformations for orthorhombic lattices if one sets  $n_1 = n_2$  and takes into account that base-centered and face-centered orthorhombic lattices become simple and body-centered tetragonal ones, respectively.

The matrices of symmetrical transformations for all the types (P, F, I) of cubic lattices may also be obtained from the matrices of symmetrical transformations for orthorhombic lattices if one sets  $n_1 = n_2 = n_3 = n$ .

#### 4.2.2 Special Points of Brillouin-zone Generating

In self-consistent calculations of the electronic structure of crystals both in the basis of plane waves and in the basis of localized atomic-type functions, one needs in every

stage of the self-consistent procedure to evaluate an approximate electron-density matrix by integration over the Brillouin zone (BZ):

$$\rho(\mathbf{r}, \mathbf{r}') = \int_{BZ} Q_{\mathbf{r}, \mathbf{r}'}(\mathbf{k}) d\mathbf{k}, \quad Q_{\mathbf{r}, \mathbf{r}'}(\mathbf{k}) = \sum_v \psi_v^*(\mathbf{k}, \mathbf{r}') \psi_v(\mathbf{k}, \mathbf{r}) \quad (4.78)$$

where the sum is over occupied electronic states of the crystal. In practice,  $\psi(\mathbf{k}, \mathbf{r})$  (and  $\varphi(\mathbf{k}) \equiv Q_{\mathbf{r}, \mathbf{r}'}(\mathbf{k})$ ) are calculated in some finite meshes of  $\mathbf{k}$ -points. Therefore, one needs for the evaluation of the integral (4.78) to construct the interpolation formula of the numerical integration based on an interpolation procedure by means of some set of interpolation functions.

The functions  $\varphi(\mathbf{k}) \equiv Q_{\mathbf{r}, \mathbf{r}'}(\mathbf{k})$  are periodic in the reciprocal space with periods determined by the basic translation vectors  $\mathbf{b}_i$  of the reciprocal lattice and having the full point symmetry of the crystal ( $F$  is a point group of order  $n_F$  of the crystal).

$$\varphi(\mathbf{k} + \mathbf{b}_m) = \varphi(\mathbf{k}) = \varphi(f\mathbf{k}), \quad f \in F, \quad \mathbf{b}_m = \sum_{i=1}^3 m_i \mathbf{b}_i \quad (4.79)$$

The plane waves  $\exp(i\mathbf{k} \cdot \mathbf{a}_n)$  seem to be the most convenient as interpolation functions for the integrand in the BZ integration, where  $\mathbf{a}_n = \sum_{i=1}^3 n_i \mathbf{a}_i$  are direct lattice translation vectors and  $\mathbf{a}_i$  are primitive translations. It is easy with plane waves to take into account the translational and point symmetry of the crystal.

In the problem of BZ integration, nodes for the interpolation ( $\mathbf{k}$ -points of the BZ) were called special points (SP).

Many procedures for special points generation have been proposed [87–90]. The supercell (large unit cell–small Brillouin zone) method appears to be the most general and fruitful in practical applications [86, 87] as it gives as a rule the most efficient sets of special points.

Let  $\mathbf{B}_i(\Gamma_1)$  ( $i = 1, 2, 3$ ) and  $\mathbf{b}_j(\tilde{\Gamma}_2)$  ( $j = 1, 2, 3$ ) be basic translation vectors of the reciprocal lattices corresponding to direct ones determined by basic translation vectors  $\mathbf{a}_i(\Gamma_1)$  and  $\mathbf{a}_j(\Gamma_2)$ , respectively. The transformation (4.77) of the direct lattices is accompanied by the following transformation of reciprocal lattices:

$$\mathbf{b}_j(\tilde{\Gamma}_2) = \sum_i (l^{-1}(\Gamma_2 \Gamma_1))_{ij} \mathbf{B}_i(\tilde{\Gamma}_1) \quad (4.80)$$

For the symmetrical transformation (4.77) the transformation (4.80) is also symmetrical as it does not change the point symmetry of the reciprocal lattice. The symmetrical transformation is compatible with the change of the reciprocal-lattice type in the limits of the same crystal system too. The vectors  $\mathbf{b}_j$  defining the small Brillouin zone are very important in the theory of special points [86]. Let  $f(\mathbf{K})$  be the function with a point symmetry  $F$  to be integrated over the initial Brillouin zone where the wavevector  $\mathbf{K}$  varies. Usually, the point-symmetry group  $F$  either coincides with the crystal class  $\tilde{F}$  of the crystal (if  $\tilde{F}$  contains the inversion  $I$ ) or  $F = \tilde{F} \times C_i$  (otherwise) [86]. The function  $f(\mathbf{K})$  may be expanded in Fourier series over symmetrized plane waves  $P_m(\mathbf{K})$

$$f(\mathbf{K}) = \sum_m f_m P_m(\mathbf{K}) \quad (4.81)$$

$$P_m(\mathbf{K}) = \frac{1}{n_G} \sum_{g \in G} \exp(i\mathbf{K} \cdot g\mathbf{a}_m) \quad (4.82)$$

where  $\mathbf{a}_m = \sum_{i=1}^3 m_i \mathbf{a}_i$  is some translation vector of the direct lattice, the integer  $m = 0, 1, 2, \dots$  numerates the stars of vectors  $g\mathbf{a}_m$  ( $g \in F$ ) in order of increasing length. The functions  $P_m(\mathbf{K})$  have the properties [88]

$$\frac{1}{V_{BZ}} \int_{BZ} P_m(\mathbf{K}) d\mathbf{K} = \delta_{m0}, \quad m = 0, 1, 2, \dots \quad (4.83)$$

Let  $\bar{m}$  be a subset of  $m$  corresponding to the stars of vectors  $g\mathbf{a}_m$  ( $g \in F$ ). As is proved in [86], for symmetrical transformation (4.77)  $L$  points in the initial Brillouin zone (related to the initial basic translation vectors  $\mathbf{a}_i$ )

$$\mathbf{K}_t^{(\mathbf{k})} = \mathbf{k} + \sum_j q_{tj} \mathbf{b}_j \quad (4.84)$$

where  $q_{tj}$  are integers and  $\mathbf{k}$  is an arbitrary vector in the small Brillouin zone (related to the basic translation vectors  $\mathbf{a}_j$ ), satisfy the relation:

$$\sum_{t=1}^L P_m(\mathbf{K}_t^{(\mathbf{k})}) = L \sum_{\bar{m}} P_{\bar{m}}(\mathbf{k}) \delta_{m\bar{m}} \quad (4.85)$$

or

$$\sum_{s=1}^N w_s P_m(\mathbf{K}_s^{(\mathbf{k})}) = \sum_{\bar{m}} P_{\bar{m}}(\mathbf{k}) \delta_{m\bar{m}} \quad (4.86)$$

In the latter relation  $s$  numbers the different irreducible wavevector  $\mathbf{K}$  stars that contain the points (4.84) and  $w_s = L_s/L$  ( $L_s$  is the number of points (4.84) belonging to the  $s$ th star,  $\sum_{s=1}^N L_s = L$ ). The points  $\mathbf{K}_s^{(\mathbf{k})}$  are usually chosen in the irreducible part of the Brillouin zone.

Relations (4.81)–(4.83) give the following formula of the approximative numerical integration:

$$\frac{1}{V_{BZ}} \int_{BZ} f(\mathbf{K}) d\mathbf{K} \approx \sum_{s=1}^N w_s f(\mathbf{K}_s^{(\mathbf{k})}) \quad (4.87)$$

Let  $M = s_o$  be the number denoting the set of vectors  $g\mathbf{a}_m$  with the smallest (nonzero) lengths. If  $f(\mathbf{K})$  is some linear combination of  $P_m(\mathbf{K})$  with  $m < M$ , then the formula (4.87) appears to be exact. The number  $M$  characterizes the accuracy of the numerical integration formula. The special choice of  $\mathbf{k}$  can either increase the accuracy  $M$ , or change the number  $N$  of points  $\mathbf{K}_s^{(\mathbf{k})}$  (or both), [89].

To generate the set of points  $\mathbf{K}_s^{(\mathbf{k})}$  for any of the 14 Bravais lattices it is sufficient to find the inverse of the corresponding matrix from Appendix A, to pick out according to (4.84)  $L$  points in the Brillouin zone related to basic translation vectors  $\mathbf{a}_i$  and to distribute them over stars. The distribution of these points over stars depends on the symmetry group  $F$  of the function  $f(\mathbf{K})$  and can not be made in general form.

The sets of special points for numerical integration over the Brillouin zone of cubic crystals are given in Tables 4.1–4.3. They are obtained by symmetrical increasing of

the unit cells of cubic lattices for  $L \leq 32$ . The tables contain the sets (4.84) with  $\mathbf{k} = 0$  and some efficient sets with  $\mathbf{k} \neq 0$ . Some sets were found earlier in [87,89]. The types of lattices (TL) composed of supercells are indicated in the second columns. The symbols of the matrices  $Q = l^{-1}$  of the transformation of basic vectors of reciprocal lattices are given in the third column. The matrices  $Q_i$  themselves are given in Appendix B.

The system of symmetrized plane waves  $P_m(\mathbf{K})$  depends on the crystal class. Therefore, the number  $M$  that characterizes the efficiency of the set of special points may be different for different crystal classes [86]. In Tables 4.1–4.3 the numbers  $M$  are given for crystal classes  $T_d$ ,  $O$ ,  $O_h$  and  $T$ ,  $T_h$  (in parentheses).

In addition, in Table 4.1 for  $L = 4$  two special points  $(1/2, 0, 1/4)$  and  $(1/2, 1/4, 0)$  are related to different stars in crystal classes  $T$ ,  $T_h$  and each of them is a special point with the weight 1/4; in crystal classes  $T_d$ ,  $O$ ,  $O_h$  they are related to the same star and this three-special-point set contains only one of these points with the weight 1/2.

**Table 4.1.** Special points of the Brillouin zone for the simple cubic lattice generated by the symmetrical transformation;  $\mathbf{B}_1 = \frac{2\pi}{a}(1, 0, 0)$ ,  $\mathbf{B}_2 = \frac{2\pi}{a}(0, 1, 0)$ ,  $\mathbf{B}_3 = \frac{2\pi}{a}(0, 0, 1)$ ;  $\mathbf{K}_s = \alpha_1 \mathbf{B}_1 + \alpha_2 \mathbf{B}_2 + \alpha_3 \mathbf{B}_3 \equiv (\alpha_1, \alpha_2, \alpha_3)$

$L$	$TL$	$l^{(-1)}$	$M$	Special points $\mathbf{K}_s$ and weights $w_s$ in {}
2	$F$	$\frac{1}{2}Q_2$	2	$(0, 0, 0) \{ \frac{1}{2} \}$ $(\frac{1}{2}, \frac{1}{2}, \frac{1}{2}) \{ \frac{1}{2} \}$
4	$I$	$\frac{1}{2}Q_3$	3	$(0, 0, 0) \{ \frac{1}{4} \}$ $(\frac{1}{2}, \frac{1}{2}, 0) \{ \frac{3}{4} \}$
			4	$(\frac{1}{4}, 0, 0) \{ \frac{1}{4} \}$ $[(\frac{1}{2}, 0, \frac{1}{4}) \{ \frac{1}{4} \} (\frac{1}{2}, \frac{1}{4}, 0) \{ \frac{1}{4} \}]$ $(\frac{1}{2}, \frac{1}{2}, \frac{1}{4}) \{ \frac{1}{4} \}$
8	$P$	$\frac{1}{2}Q_1$	4	$(0, 0, 0) \{ \frac{1}{8} \}$ $(\frac{1}{2}, 0, 0) \{ \frac{3}{8} \}$ $(\frac{1}{2}, \frac{1}{2}, 0) \{ \frac{3}{8} \}$ $(\frac{1}{2}, \frac{1}{2}, \frac{1}{2}) \{ \frac{1}{8} \}$
			15(19)	$(\frac{1}{8}, \frac{1}{8}, \frac{1}{8}) \{ \frac{1}{8} \}$ $(\frac{3}{8}, \frac{1}{8}, \frac{1}{8}) \{ \frac{3}{8} \}$ $(\frac{3}{8}, \frac{3}{8}, \frac{1}{8}) \{ \frac{3}{8} \}$ $(\frac{3}{8}, \frac{3}{8}, \frac{3}{8}) \{ \frac{1}{8} \}$
16	$F$	$\frac{1}{4}Q_2$	7	$(0, 0, 0) \{ \frac{1}{16} \}$ $(\frac{1}{4}, \frac{1}{4}, \frac{1}{4}) \{ \frac{1}{2} \}$ $(\frac{1}{2}, 0, 0) \{ \frac{3}{16} \}$ $(\frac{1}{2}, \frac{1}{2}, 0) \{ \frac{3}{16} \}$ $(1, 1, 1) \{ \frac{1}{16} \}$
27	$P$	$\frac{1}{3}Q_1$	9	$(0, 0, 0) \{ \frac{1}{27} \}$ $(\frac{1}{3}, 0, 0) \{ \frac{2}{9} \}$ $(\frac{1}{3}, \frac{1}{3}, 0) \{ \frac{4}{9} \}$ $(\frac{1}{3}, \frac{1}{3}, \frac{1}{3}) \{ \frac{8}{27} \}$
32	$I$	$\frac{1}{4}Q_3$	12	$(0, 0, 0) \{ \frac{1}{32} \}$ $(\frac{1}{4}, \frac{1}{4}, 0) \{ \frac{3}{8} \}$ $(\frac{1}{2}, 0, 0) \{ \frac{3}{32} \}$ $(\frac{1}{2}, \frac{1}{4}, \frac{1}{4}) \{ \frac{3}{8} \}$ $(\frac{1}{2}, \frac{1}{2}, 0) \{ \frac{3}{32} \}$ $(\frac{1}{2}, \frac{1}{2}, \frac{1}{2}) \{ \frac{1}{32} \}$

#### 4.2.3 Modification of the Monkhorst–Pack Special-points Meshes

The most popular special-points (SP) sets are meshes obtained by a very simple algorithm proposed by Monkhorst and Pack (MP) in [90]:

$$\mathbf{k}_p^{(n)} = \sum_{i=1}^3 u_{p_i}^{(n)} \mathbf{b}_i, n = 1, 2, \dots, p_i = 1, 2, \dots, n, \quad u_{p_i}^{(n)} = \frac{2p_i - n - 1}{2n} \quad (4.88)$$

**Table 4.2.** Special points of the Brillouin zone for the face-centered cubic lattice \*) generated by the symmetrical transformation

$L$	$TL$	$l^{(-1)}$	$M$	Special points $\mathbf{K}_s$ and weights $w_s$ in {}
4	$P$	$\frac{1}{2}Q_3$	2	$(0, 0, 0) \{ \frac{1}{4} \}$ $(0, \frac{1}{2}, \frac{1}{2}) \{ \frac{3}{4} \}$
			2	$(\frac{1}{4}, \frac{1}{4}, \frac{1}{2}) \{ 1 \}$
			2	$(\frac{1}{2}, \frac{1}{2}, \frac{1}{2}) \{ 1 \}$
8	$F$	$\frac{1}{2}Q_1$	4	$(0, 0, 0) \{ \frac{1}{8} \}$ $(\frac{1}{2}, \frac{1}{2}, \frac{1}{2}) \{ \frac{1}{2} \}$ $(0, \frac{1}{2}, \frac{1}{2}) \{ \frac{3}{8} \}$
			4	$(0, \frac{1}{4}, \frac{1}{4}) \{ \frac{1}{4} \}$ $(\frac{1}{4}, \frac{1}{4}, \frac{1}{2}) \{ \frac{1}{2} \}$ $(\frac{1}{4}, \frac{1}{4}, \frac{1}{2}) \{ \frac{1}{4} \}$
			8(10)	$(\frac{1}{4}, \frac{1}{4}, \frac{1}{4}) \{ \frac{1}{4} \}$ $(\frac{1}{2}, \frac{1}{2}, \frac{1}{4}) \{ \frac{3}{4} \}$
16	$I$	$\frac{1}{4}Q_4$	6(7)	$(0, 0, 0) \{ \frac{1}{16} \}$ $(\frac{1}{4}, \frac{1}{4}, \frac{1}{2}) \{ \frac{3}{4} \}$ $(0, \frac{1}{2}, \frac{1}{2}) \{ \frac{3}{16} \}$
			6(7)	$(0, \frac{1}{4}, \frac{1}{4}) \{ \frac{3}{8} \}$ $(\frac{1}{2}, \frac{1}{2}, \frac{1}{2}) \{ \frac{1}{4} \}$ $(\frac{1}{4}, \frac{1}{4}, \frac{1}{2}) \{ \frac{3}{8} \}$
27	$F$	$\frac{1}{3}Q_1$	9	$(0, 0, 0) \{ \frac{1}{27} \}$ $(\frac{1}{3}, \frac{1}{3}, \frac{1}{3}) \{ \frac{8}{27} \}$ $(0, \frac{1}{3}, \frac{1}{3}) \{ \frac{2}{9} \}$ $(\frac{1}{3}, \frac{1}{3}, \frac{2}{3}) \{ \frac{4}{9} \}$
32	$P$	$\frac{1}{4}Q_3$	8	$(0, 0, 0) \{ \frac{1}{32} \}$ $(0, \frac{1}{4}, \frac{1}{4}) \{ \frac{3}{16} \}$ $(\frac{1}{4}, \frac{1}{4}, \frac{1}{2}) \{ \frac{3}{8} \}$ $(\frac{1}{2}, \frac{1}{2}, \frac{1}{2}) \{ \frac{1}{8} \}$
				$(0, \frac{1}{2}, \frac{1}{2}) \{ \frac{3}{32} \}$ $(\frac{1}{4}, \frac{1}{2}, \frac{3}{4}) \{ \frac{3}{16} \}$
			8	$(\frac{1}{4}, \frac{1}{4}, \frac{1}{4}) \{ \frac{1}{4} \}$ $(\frac{1}{2}, \frac{1}{2}, \frac{1}{4}) \{ \frac{3}{4} \}$

$$*) \mathbf{B}_1 = \frac{2\pi}{a}(-1, 1, 1), \mathbf{B}_2 = \frac{2\pi}{a}(1, -1, 1), \mathbf{B}_3 = \frac{2\pi}{a}(1, 1, -1)$$

$$\mathbf{K}_s = \alpha_1 \mathbf{B}_1 + \alpha_2 \mathbf{B}_2 + \alpha_3 \mathbf{B}_3 \equiv (\alpha_1, \alpha_2, \alpha_3)$$

These meshes are widespread in modern Hartree–Fock and density-functional theory calculations of crystals and are automatically generated in the corresponding computer codes. But MP meshes of SP have at least one shortcoming, which may be understood if one oversees the problem from the point of view of the more general large unit cell–small Brillouin zone (LUC–SBZ) method of SP generation. The MP method is a particular case of the LUC–SBZ method. In [91] the modification of the MP meshes was suggested that makes faster and more regular convergence of the results of the self-consistent calculations of the electronic structure of crystals.

MP meshes (4.88) are a particular case of the meshes (4.84), which corresponds to the transformation (4.77) with the diagonal matrices

$$l_{ji}^{(n)} = n\delta_{ji}, \quad L = n^3, \quad n = 1, 2, \dots, \quad i, j = 1, 2, 3 \quad (4.89)$$

and a special choice of  $\mathbf{k}$  in (4.84):

$$\mathbf{k} = \begin{cases} \frac{1}{2n}(\mathbf{b}_1 + \mathbf{b}_2 + \mathbf{b}_3) & \text{for even } n \\ 0 & \text{for odd } n \end{cases} = \begin{cases} \left( \frac{1}{2n}(1, 1, 1) \right) & \text{for even } n \\ 0 & \text{for odd } n \end{cases} \quad (4.90)$$

The  $\mathbf{k}$ -vector choice (4.90) is not the best one. As an example, we demonstrate this for cubic crystals. In this case, transformation (4.89) assures at least the cutoff

**Table 4.3.** Special points of the Brillouin zone for the body-centered cubic lattice \*) generated by the symmetrical transformation

$L$	$TL$	$l^{(-1)}$	$M$	Special points $\mathbf{K}_s$ and weights $w_s$ in $\{\}$
2	$P$	$\frac{1}{2}Q_2$	2	$(0, 0, 0) \{\frac{1}{2}\}$ $(\frac{1}{2}, \frac{1}{2}, \frac{1}{2}) \{\frac{1}{2}\}$
			2	$(\frac{1}{4}, \frac{1}{4}, \frac{1}{4}) \{1\}$
			2	$(0, 0, \frac{1}{2}) \{1\}$
			2	$(\frac{1}{4}, \frac{1}{4}, \frac{1}{4}) \{1\}$
			3	$(\frac{1}{12}, \frac{1}{4}, \frac{1}{4}) \{1\}$
4	$F$	$\frac{1}{4}Q_5$	3	$(0, 0, 0) \{\frac{1}{4}\}$ $(\frac{1}{4}, \frac{1}{4}, \frac{1}{4}) \{\frac{1}{2}\}$ $(\frac{1}{2}, \frac{1}{2}, \frac{1}{2}) \{\frac{1}{4}\}$
			3	$(\frac{1}{4}, \frac{1}{4}, \frac{1}{4}) \{\frac{1}{2}\}$ $(0, 0, \frac{1}{2}) \{\frac{1}{2}\}$
			6	$(\frac{1}{8}, \frac{1}{8}, \frac{1}{8}) \{\frac{1}{2}\}$ $(\frac{3}{8}, \frac{3}{8}, \frac{3}{8}) \{\frac{1}{2}\}$
8	$I$	$\frac{1}{2}Q_1$	5	$(0, 0, 0) \{\frac{1}{8}\}$ $(0, 0, \frac{1}{2}) \{\frac{3}{4}\}$ $(\frac{1}{2}, \frac{1}{2}, \frac{1}{2}) \{\frac{1}{8}\}$
			5	$(\frac{1}{4}, \frac{1}{4}, \frac{1}{4}) \{\frac{3}{4}\}$ $(\frac{1}{4}, \frac{1}{4}, \frac{1}{4}) \{\frac{1}{4}\}$
			6	$(0, 0, \frac{1}{4}) \{\frac{1}{4}\}$ $(0, \frac{1}{4}, \frac{1}{4}) \{\frac{1}{2}\}$ $(\frac{1}{4}, \frac{1}{4}, \frac{1}{2}) \{\frac{1}{4}\}$
16	$P$	$\frac{1}{4}Q_2$	6	$(0, 0, 0) \{\frac{1}{16}\}$ $(\frac{1}{4}, \frac{1}{4}, \frac{1}{4}) \{\frac{3}{8}\}$ $(0, 0, \frac{1}{2}) \{\frac{3}{8}\}$ $(\frac{1}{4}, \frac{1}{4}, \frac{1}{4}) \{\frac{1}{8}\}$
			6	$(\frac{1}{2}, \frac{1}{2}, \frac{1}{2}) \{\frac{1}{16}\}$
			6	$(\frac{1}{8}, \frac{1}{8}, \frac{1}{8}) \{\frac{1}{8}\}$ $(\frac{1}{8}, \frac{1}{8}, \frac{3}{8}) \{\frac{1}{2}\}$ $(\frac{5}{8}, \frac{3}{8}, \frac{3}{8}) \{\frac{1}{8}\}$ $(\frac{3}{8}, \frac{1}{8}, \frac{1}{8}) \{\frac{1}{4}\}$
27	$I$	$\frac{1}{3}Q_1$	10(11)	$(0, 0, 0) \{\frac{1}{27}\}$ $(0, 0, \frac{1}{3}) \{\frac{4}{9}\}$ $(\frac{1}{3}, \frac{1}{3}, \frac{1}{3}) \{\frac{2}{9}\}$ $(0, \frac{1}{3}, \frac{1}{3}) \{\frac{8}{27}\}$
32	$F$	$\frac{1}{8}Q_5$	12	$(0, 0, 0) \{\frac{1}{32}\}$ $(\frac{1}{8}, \frac{1}{8}, \frac{1}{8}) \{\frac{1}{4}\}$ $(\frac{1}{4}, \frac{1}{4}, \frac{1}{4}) \{\frac{3}{16}\}$ $(0, 0, \frac{1}{2}) \{\frac{3}{16}\}$
				$(\frac{1}{8}, \frac{3}{8}, \frac{3}{8}) \{\frac{1}{4}\}$ $(\frac{1}{4}, \frac{1}{4}, \frac{1}{4}) \{\frac{1}{16}\}$ $(\frac{1}{2}, \frac{1}{2}, \frac{1}{2}) \{\frac{1}{32}\}$

\*)  $\mathbf{B}_1 = \frac{2\pi}{a}(0, 1, 1)$ ,  $\mathbf{B}_2 = \frac{2\pi}{a}(1, 0, 1)$ ,  $\mathbf{B}_3 = \frac{2\pi}{a}(1, 1, 0)$ 

$$\mathbf{K}_s = \alpha_1 \mathbf{B}_1 + \alpha_2 \mathbf{B}_2 + \alpha_3 \mathbf{B}_3 \equiv (\alpha_1, \alpha_2, \alpha_3)$$

length  $R_{\text{cut}} = n \cdot |\mathbf{a}_i|$  whatever the  $\mathbf{k}$ . The  $\mathbf{k}$ -vector choice (4.90) increases slightly the cutoff length  $R_{\text{cut}}$  for even  $n$  in an fcc lattice (see Table 4.4).

In all the other cases of cubic crystals (in bcc and sc lattices and for odd  $n$  in fcc lattice) the meshes MP (4.88) do not increase the standard cut-off length  $R_{\text{cut}} = n \cdot |\mathbf{a}_i|$  and are equivalent to the meshes with  $\mathbf{k}=0$  that contain the point  $\Gamma$  and consist of the whole  $\mathbf{k}$ -stars.

In [91] another choice of the  $\mathbf{k}$ -point in (4.88) was proposed and the corresponding SP sets were called modified MP (MMP) meshes. They depend on the type of cubic crystal lattice.

$$1. \tilde{\mathbf{k}} = \frac{1}{4n}(1, 1, 1) \text{ for sc lattice (MMP1=MMP2);}$$

**Table 4.4.** Characteristics of MP, MMP1 and MMP2  $\mathbf{k}$ -points meshes for sc and bcc cubic lattices ( $R_{\text{cut}}$  and  $M$  are the cutoff length and the precision of the meshes,  $N$  is the number of  $\mathbf{k}$ -points in the IBZ;  $R_{\text{cut}}$  is in  $a$  units,  $a$  is a cubic lattice constant)

$n$	$4R_{\text{cut}}^2$ (in $a^2$ ), $M, N$											
	sc						bcc					
	$\Gamma M = \text{MP}$	$\text{MMP1} = \text{MMP2}$	$\Gamma M = \text{MP}$	$\text{MMP1}$	$\text{MMP2}$							
1	4 1 1	16 4 1	3 1 1	4 2 1	8 3 1							
2	16 4 4	64 15 4	12 5 3	16 6 2	32 12 6							
3	36 9 4	144 40 10	27 10 4	36 14 5	72 30 18							
4	64 15 10	256 79 20	48 19 8	64 26 8	128 59 40							
5	100 25 10	400 141 35	75 32 10	100 45 14	200 104 75							
6	144 40 20	576 224 56	108 51 16	144 70 20	288 163 126							
7	196 56 20	784 341 84	147 72 20	196 102 30	392 221 196							
8	256 79 35	1024 488 120	192 99 29	256 143 40	512 265 288							

2.  $\tilde{\mathbf{k}} = \frac{1}{4n}(1, 1, 1)$  (MMP1) and  $\tilde{\mathbf{k}} = \frac{1}{4n}(-1/3, 1, 1)$  (MMP2) for bcc lattice;

3.  $\tilde{\mathbf{k}} = \frac{1}{2n}(1, 1, 1)$  (MMP1) and  $\tilde{\mathbf{k}} = \frac{1}{2n}(0.4588, 0.3112, 0.1477)$  (MMP2) for fcc lattice.

The main characteristics of the proposed meshes for sc and bcc lattices are given in Table 4.4 and for fcc lattice in Table 4.5.

**Table 4.5.** Characteristics of  $\Gamma M$ , MP, MMP1 and MMP2  $\mathbf{k}$ -points meshes for fcc cubic lattice and convergence of PW DFT binding energy  $E$  per unit cell (in ev) for SiC crystal for  $\Gamma M$ , MP and MMP2  $\mathbf{k}$ -points meshes, [91] ( $R_{\text{cut}}$  and  $M$  are the cutoff length and the precision of the meshes,  $N$  is the number of  $\mathbf{k}$ -points in the IBZ;  $R_{\text{cut}}$  is in  $a$  units,  $a$  is a cubic lattice constant).

$n$	$\Gamma M$				MP				MMP1				MMP2			
	$4R_{\text{cut}}^2$	$M$	$N$	$E$	$4R_{\text{cut}}^2$	$M$	$N$	$E$	$4R_{\text{cut}}^2$	$M$	$N$	$E$	$4R_{\text{cut}}^2$	$M$	$N$	
1	2	1	1	-2.931	2	1	1	-2.931	4	2	1	12.843	6	3	1	
2	8	4	3	12.236	16	8	2	14.990	16	8	2	14.990	24	13	6	
3	18	9	4	14.615	18	9	4	14.615	36	20	6	15.100	54	33	18	
4	32	17	8	14.987	64	40	10	15.110	64	40	10	15.110	96	67	40	
5	50	29	10	15.076	50	29	10	15.076	100	71	19	15.111	150	121	75	
6	72	47	16	15.100	144	113	28	15.111	144	113	28	15.111	216	180	126	
7	98	68	20	15.108	98	68	20	15.108	196	163	44	15.111	294	227	196	
8	128	98	29	15.110	256	207	60	15.111	256	207	60	15.111	384	253	288	

MMP2 meshes are the best ones as they give the maximal value of the cutoff length  $R_{\text{cut}}$  and the precision  $M$  for the given transformation (4.89). MMP1 meshes for bcc and fcc lattices give the smaller value of the cutoff length and the precision, but at the same time consist of the smaller number of points in the IBZ. The one-SP meshes MMP2 (for  $n = 1$ ) are mean value points of Baldereschi, [92].

The idea of the proposed modification of the MP meshes can be also used to generate MMP meshes for all noncubic lattices.

The efficiency of MMP  $\mathbf{k}$ -points meshes is demonstrated for an fcc lattice in Table 4.5, where PW DFT binding energies  $E$  per unit cell (in eV) for SiC crystal (fcc lattice) are given for different choices of  $\mathbf{k}$ -meshes.

DFT-PW calculations [91] were performed on a SiC crystal for different SP meshes to investigate which one corresponds to the best convergence of the results for the total energy per unit cell. The experimental value  $a = 4.35 \text{ \AA}$  was taken for the fcc lattice constant of SiC, the electron–ion interaction was described by ultrasoft, Vanderbilt-type pseudopotentials [93], the cutoff energy for the plane-wave basis set was taken to be 1000 eV. The generalized gradient corrections (GGA) DFT method was used (see Chap. 7).

In Table 4.5 are given the calculated binding energy values (defined as the difference between the sum of Si and C atomic energies with Vanderbilt-type pseudopotentials and the total energy per primitive unit cell) for three types of meshes mentioned above and used in calculations.

As is seen, the faster convergence takes place for the modified Monkhorst–Pack schemes. For comparison, the experimental 13.0 eV and Hartree–Fock 9.0 eV may be found in [94].

The suggested modification of Monkhorst–Pack special-points meshes for Brillouin-zone integration is essentially useful for crystals with many atoms in a primitive unit cell or for point-defect calculations in a supercell model. In these cases each step of the self-consistent procedure in Hartree–Fock or DFT calculations is time consuming, so that the higher efficiency of  $\mathbf{k}$ -point meshes shortens the computing time. It is also important for the lattice parameters or atom-position optimization in crystals, when the self-consistent procedure is repeated for different atomic structures. The special point set generation considered can be applied both in LCAO and plane-wave calculations to approximate the DM of a crystal.

## 4.3 Density Matrix of Crystals in the Hartree–Fock Method

### 4.3.1 Properites of the One-electron Density Matrix of a Crystal

As is well known, the energy of a system within the single-determinant Hartree–Fock approximation can be expressed in terms of the one-electron density matrix (DM). The one-electron spinless DM  $\rho(\mathbf{R}, \mathbf{R}')$  is defined as

$$\rho(\mathbf{R}, \mathbf{R}') = \int_{V_N} \psi(\mathbf{R}, \mathbf{R}_2, \dots, \mathbf{R}_M) \psi^*(\mathbf{R}', \mathbf{R}_2, \dots, \mathbf{R}_M) d^3 \mathbf{R}_2 d^3 \mathbf{R}_3 \dots d^3 \mathbf{R}_M \quad (4.91)$$

where the electron position vectors  $\mathbf{R}$  and  $\mathbf{R}'$  vary within the basic domain of a crystal of volume  $V_N$ , *i.e.* a cyclic cluster consisting of  $N$  primitive unit cells. The DM of

the infinite crystal is obtained from the DM of the basic domain by taking the limit  $N \rightarrow \infty$ . In its translational symmetry, the DM is periodic on the direct lattice:

$$\rho(\mathbf{R}, \mathbf{R}') = \rho(\mathbf{R} + \mathbf{R}_n, \mathbf{R}' + \mathbf{R}_n) \quad (4.92)$$

where  $\mathbf{R}_n$  is an arbitrary translation vector of the Bravais lattice.

We will represent the electron position vector  $\mathbf{R}$  in the form  $(\mathbf{r}, \mathbf{R}_n)$ , where  $\mathbf{R}_n$  specifies the primitive cell within which the end of the vector  $\mathbf{R}$  lies and  $\mathbf{r}$  is the position vector of an electron within this primitive cell. Therefore, we have  $\mathbf{R} = \mathbf{r} + \mathbf{R}_n$ . Using (4.92), the density matrix can be written in the form

$$\rho(\mathbf{R}, \mathbf{R}') = \rho(\mathbf{r} + \mathbf{R}_n, \mathbf{r}' + \mathbf{R}_{n'}) = \rho(\mathbf{r}, \mathbf{r}' + \mathbf{R}_{n'} - \mathbf{R}_n) = \rho_{\mathbf{r}, \mathbf{r}'}(\mathbf{R}_{n'} - \mathbf{R}_n) \quad (4.93)$$

The notation  $\rho_{\mathbf{r}, \mathbf{r}'}(\mathbf{R}_n)$  for the one-electron DM in the coordinate representation implies that the indices  $\mathbf{r}$  and  $\mathbf{r}'$  of the matrix vary continuously only within the primitive cell. Therefore, there is an analogy between the properties of the DM in the coordinate representation and the properties of the DM represented in terms of a set of basis functions, for example, in terms of Bloch sums of atomic orbitals (AOs) or plane waves.

As is known, the diagonal elements of the one-electron DM in the coordinate representation are equal to the electron density:

$$\rho(\mathbf{R}) = \rho(\mathbf{R}, \mathbf{R}) = \rho_{\mathbf{r}, \mathbf{r}}(0) \quad (4.94)$$

From the normalization condition for the many-electron wavefunction within the basic domain, it follows that

$$\int_{V_N} \rho(\mathbf{R}, \mathbf{R}) d^3 \mathbf{R} = N n = \sum_{\mathbf{R}_n} \int_{V_a} \rho_{\mathbf{r}, \mathbf{r}}(0) d^3 \mathbf{r} = N \int_{V_a} \rho_{\mathbf{r}, \mathbf{r}}(0) d^3 \mathbf{r} \quad (4.95)$$

Therefore, the electron density is normalized to the number of electrons per primitive cell,

$$\int_{V_a} \rho_{\mathbf{r}, \mathbf{r}}(0) d^3 \mathbf{r} = n \quad (4.96)$$

By using the single-determinant approximation to the many-electron wavefunction, the DM can be expressed through the one-electron wavefunctions (crystalline orbitals):

$$\rho(\mathbf{R}, \mathbf{R}') = \sum_i \sum_{\mathbf{k}} n_i(\mathbf{k}) \varphi_{i\mathbf{k}}(\mathbf{R}) \varphi_{i\mathbf{k}}^*(\mathbf{R}') \quad (4.97)$$

where the index  $i$  specifies the energy bands and  $n_i(\mathbf{k})$  are the occupation numbers. In nonconducting crystals, the energy bands are either completely filled or empty; therefore,  $n_i(\mathbf{k})$  are independent of  $\mathbf{k}$  and  $n_i = 0, 2$ .

The one-electron DM is invariant under any orthogonal transformation in the space of occupied states. In particular, in nonconducting crystals, we can go over from the orthonormal set of extended Bloch states  $\varphi_{i\mathbf{k}}(\mathbf{R})$  to the orthonormal set of localized Wannier functions (see Chap. 3):

$$W_i(\mathbf{R} - \mathbf{R}_n) = \sqrt{\frac{1}{N}} \sum_{\mathbf{k}} \exp(i\mathbf{k}\mathbf{R}_n) \varphi_{i\mathbf{k}}(\mathbf{R}) \quad (4.98)$$

In this case, (4.97) for the DM takes the form

$$\rho(\mathbf{R}, \mathbf{R}') = \sum_i n_i \sum_{\mathbf{R}_m} W_i(\mathbf{R} - \mathbf{R}_m) W_i^*(\mathbf{R}' - \mathbf{R}_m) \quad (4.99)$$

or

$$\rho_{\mathbf{r}, \mathbf{r}'}(\mathbf{R}_n) = \sum_i n_i \sum_{\mathbf{R}_m} W_i(\mathbf{r} - \mathbf{R}_m) W_i^*(\mathbf{r}' - \mathbf{R}_m + \mathbf{R}_n) \quad (4.100)$$

It is well known that the Wannier functions  $W_i(\mathbf{R})$  vanish exponentially as  $|\mathbf{R}| \rightarrow \infty$  in crystals with completely filled bands. Since the vectors  $\mathbf{r}$  and  $\mathbf{r}'$  lie in the reference (zeroth) primitive unit cell, the products of the Wannier functions on the right-hand side of (4.100) fall off exponentially with increasing  $|\mathbf{R}_n|$ . Therefore, we may expect the total lattice sum in (4.100) for the offdiagonal elements  $\rho_{\mathbf{r}, \mathbf{r}'}(\mathbf{R}_n)$  of the DM to also vanish exponentially with increasing  $|\mathbf{R}_n|$ . It should be noted that in metals, the DM decays according to a power law.

Under translation through a lattice vector, according to Bloch's theorem, the crystal orbitals transform according to irreducible representations of the translation group

$$\varphi_{i\mathbf{k}}(\mathbf{R} + \mathbf{R}_n) = \exp(-i\mathbf{k}\mathbf{R}_n) \varphi_{i\mathbf{k}}(\mathbf{R}) \quad (4.101)$$

This condition is satisfied for both the infinite crystal and the basic domain; only the sets of values of the wavevector  $\mathbf{k}$  for which (4.101) is satisfied are different in these two cases. By applying Bloch's theorem (4.101) to the wavefunctions in (4.97) for the one-electron DM of the basic domain, we obtain

$$\rho_{\mathbf{r}, \mathbf{r}'}(\mathbf{R}_n) = \sum_i \sum_{\mathbf{k}} n_i(\mathbf{k}) \varphi_{i\mathbf{k}}(\mathbf{r}) \varphi_{i\mathbf{k}}^*(\mathbf{r}' + \mathbf{R}_n) = \frac{1}{N} \sum_{\mathbf{k}} \exp(-i\mathbf{k}\mathbf{R}_n) P_{\mathbf{r}, \mathbf{r}'}(\mathbf{k}) \quad (4.102)$$

where  $P_{\mathbf{r}, \mathbf{r}'}(\mathbf{k})$  is the density matrix in  $\mathbf{k}$ -space, which is defined as

$$P_{\mathbf{r}, \mathbf{r}'}(\mathbf{k}) = N \sum_i n_i(\mathbf{k}) \varphi_{i\mathbf{k}}(\mathbf{r}) \varphi_{i\mathbf{k}}^*(\mathbf{r}') \quad (4.103)$$

From the familiar orthogonality relations for columns and rows of the matrices in the irreducible representations of the Abelian translation group, it follows that

$$\frac{1}{N} \sum_{\mathbf{R}_n} \exp(i\mathbf{k}\mathbf{R}_n) = \delta_{\mathbf{k}, \mathbf{b}}; \quad \frac{1}{N} \sum_{\mathbf{k}} \exp(i\mathbf{k}\mathbf{R}_n) = \delta_{\mathbf{R}_n, \mathbf{A}} \quad (4.104)$$

where  $\mathbf{b}$  is a reciprocal lattice vector and  $\mathbf{A}$  is a primitive translation of the basic domain as a whole. Using (4.104), it is easy to derive an inverse relation of (4.102)

$$P_{\mathbf{r}, \mathbf{r}'}(\mathbf{k}) = \sum_{\mathbf{R}_n} \exp(i\mathbf{k}\mathbf{R}_n) \rho_{\mathbf{r}, \mathbf{r}'}(\mathbf{R}_n) \quad (4.105)$$

It follows from (4.105) that  $P_{\mathbf{r}, \mathbf{r}'}(\mathbf{k})$  is a periodic function in the reciprocal space

$$P_{\mathbf{r},\mathbf{r}'}(\mathbf{k} + \mathbf{b}_m) = P_{\mathbf{r},\mathbf{r}'}(\mathbf{k}) \quad (4.106)$$

Using the hermiticity of the DM

$$\rho(\mathbf{R}, \mathbf{R}') = \rho^*(\mathbf{R}', \mathbf{R}) \quad (4.107)$$

we find that

$$\rho_{\mathbf{r},\mathbf{r}'}(\mathbf{R}_n) = \rho_{\mathbf{r}',\mathbf{r}}^*(-\mathbf{R}_n); \quad P_{\mathbf{r},\mathbf{r}'}(\mathbf{k}) = P_{\mathbf{r}',\mathbf{r}}^*(-\mathbf{k}) \quad (4.108)$$

From (4.96), the normalization condition for the DM in  $\mathbf{k}$ -space can easily be found to be

$$\int_{V_a} P_{\mathbf{r},\mathbf{r}}(\mathbf{k}) d^3\mathbf{r} = n \quad (4.109)$$

Here, the integration is performed over a primitive cell of volume  $V_a$ .

In the case where the many-electron wavefunction is calculated in the single-determinant approximation, the spinless DM is duodempotent:

$$\int_{V_N} \rho(\mathbf{R}, \mathbf{R}'') \rho(\mathbf{R}'', \mathbf{R}') d^3\mathbf{R}'' = 2\rho(\mathbf{R}, \mathbf{R}') \quad (4.110)$$

Similar relations also hold for the matrices  $\rho_{\mathbf{r},\mathbf{r}'}(\mathbf{R}_n)$  and  $P_{\mathbf{r},\mathbf{r}'}(\mathbf{k})$

$$\sum_{\mathbf{R}_m} \int_{V_a} d^3\mathbf{r}'' \rho_{\mathbf{r},\mathbf{r}''}(\mathbf{R}_m) \rho_{\mathbf{r}'',\mathbf{r}'}(\mathbf{R}_n - \mathbf{R}_m) = 2\rho_{\mathbf{r},\mathbf{r}'}(\mathbf{R}_n) \quad (4.111)$$

$$\int_{V_a} d^3\mathbf{r}'' P_{\mathbf{r},\mathbf{r}''}(\mathbf{k}) P_{\mathbf{r}'',\mathbf{r}'}(\mathbf{k}) = 2P_{\mathbf{r},\mathbf{r}'}(\mathbf{k}) \quad (4.112)$$

The one-electron density matrix has the same point-symmetry group  $F$  as the crystal structure.

Let operator  $\hat{g} = t_{\mathbf{v}}R$  correspond to the coset representative  $t_{\mathbf{v}}R$  in the coset decomposition of the crystal structure space group  $G$  over translation subgroup  $T$  (see (2.15)). In this notation the density matrix point symmetry can be written in the form

$$\hat{g}\rho(\mathbf{R}, \mathbf{R}') = \rho(\hat{g}^{-1}\mathbf{R}, \hat{g}^{-1}\mathbf{R}') = \rho(\mathbf{R}, \mathbf{R}') \quad (4.113)$$

For the density matrix  $\rho_{\mathbf{r}\mathbf{r}'}(\mathbf{R}_n)$  in the direct space, we can write

$$\hat{g}\rho_{\mathbf{r}\mathbf{r}'}(\mathbf{R}_n) = \rho_{\hat{g}^{-1}\mathbf{r} + \mathbf{R}_n, \hat{g}^{-1}\mathbf{r}' + \mathbf{R}'_n}(R^{-1}\mathbf{R}_n + \mathbf{R}_m - \mathbf{R}'_n) = \rho_{\mathbf{r}\mathbf{r}'}(\mathbf{R}_n) \quad (4.114)$$

where  $\mathbf{R}_m$  is the translation vector that returns  $\hat{g}^{-1}\mathbf{r}$  back to the reference unit cell. In a similar manner, the  $\mathbf{R}'_n$  vector returns  $R^{-1}\mathbf{r}'$  back to the reference cell. Using relation (4.105) for the DM in the reciprocal space, we obtain

$$\hat{g}P_{\mathbf{r}\mathbf{r}'}(\mathbf{k}) = \exp [iR^{-1}\mathbf{k}(\mathbf{r}' - \mathbf{R}_n)] P_{R^{-1}\mathbf{r} + \mathbf{R}_n, R^{-1}\mathbf{r}' + \mathbf{R}'_n}(R^{-1}\mathbf{k}) = P_{\mathbf{r}\mathbf{r}'}(\mathbf{k}) \quad (4.115)$$

Hence, we have a useful relation between matrix elements of the DM for the star of the wavevector  $\mathbf{k}$ :

$$P_{rr'}(R\mathbf{k}) = \exp [i\mathbf{k}(\mathbf{R}'_n - \mathbf{R})] P_{R^{-1}\mathbf{r}+\mathbf{R}_n, R^{-1}\mathbf{r}'+\mathbf{R}'_n} \quad (4.116)$$

In practical calculations of the band structure of crystals by the Hartree–Fock method, the one-electron density matrix  $P_{rr'}(\mathbf{k})$  in the reciprocal space can be calculated only for a rather small finite set of special points (see Sect. 4.2). Let us consider such a set of special points  $\{\mathbf{k}_j\}, j = 1, 2, \dots, N_0$ . Then, in the calculation of the density matrix of the infinite crystal the integration over the Brillouin-zone volume  $V_B$  is changed by the sum over the special points chosen

$$\frac{1}{V_B} \int_{V_B} d^3\mathbf{k} P_{rr'}(\mathbf{k}) \cong \frac{1}{N_0} \sum_{\mathbf{k}_j} P_{rr'}(\mathbf{k}_j) \quad (4.117)$$

Thus the the approximate density matrix  $\tilde{\rho}(\mathbf{R}, \mathbf{R}')$  is introduced

$$\begin{aligned} \tilde{\rho}(\mathbf{R}, \mathbf{R}') &= \frac{1}{N_0} \sum_{\mathbf{k}_j} P_{rr'}(\mathbf{k}_j) \\ \tilde{\rho}_{r,r'}(\mathbf{R}_n) &= \frac{1}{N_0} \sum_{\mathbf{k}_j} \exp(-i\mathbf{k}\mathbf{R}_n) P_{r,r'}(\mathbf{k}_j) \end{aligned} \quad (4.118)$$

The approximate density matrix  $\tilde{\rho}(\mathbf{R}, \mathbf{R}')$  satisfies the translation-symmetry conditions. This matrix also satisfies the point-symmetry condition, provided that the whole star of each vector  $\mathbf{k}_j$  is included in the set of special points  $\{\mathbf{k}_j\}$ . However, the approximate density matrix  $\tilde{\rho}(\mathbf{R}, \mathbf{R}')$  does not satisfy other properties of the exact DM. It is easy to see that an arbitrary finite sum over vectors  $\mathbf{k}_j$ , of delocalized Bloch functions  $\varphi_{i\mathbf{k}_j}(\mathbf{r})$  does not decrease with  $|\mathbf{r}| \rightarrow \infty$ . Therefore, provided that the  $\mathbf{R}$  vector in expression (4.97) for the DM is fixed, the approximate density matrix  $\tilde{\rho}$  does not decrease and does not approach zero as  $|\mathbf{R} - \mathbf{R}'| \rightarrow \infty$ . This incorrect asymptotics of the approximate DM is the reason for the divergence in the calculation of  $\rho^2$  and for the violation of the idempotency conditions. Indeed, using the orthonormality of the set of Bloch functions  $\varphi_{i\mathbf{k}}$ , it is easy to verify [95] that

$$\hat{\rho}^2 = 2 \frac{N}{N_0} \hat{\rho} \rightarrow \infty \text{ at } N \rightarrow \infty \quad (4.119)$$

The incorrect asymptotic behavior of the approximate density matrix  $\tilde{\rho}$  gives rise to divergences in calculations of the average values of some physical quantities. In particular, for the exchange energy per unit cell  $K_{ex}$ , we obtain the divergence

$$K_{ex} = \frac{1}{N} \int_{V_N} d^3\mathbf{R} \int_{V_N} d^3\mathbf{R}' \frac{|\tilde{\rho}(\mathbf{R}, \mathbf{R}')|^2}{|\mathbf{R} - \mathbf{R}'|} \rightarrow \infty \text{ at } N \rightarrow \infty \quad (4.120)$$

It was empirically found that, in a calculation of the electron structure of crystals with nonlocal exchange, the integration of the Hartree–Fock exchange potential over the direct lattice requires a so-called exchange-interaction radius to be introduced. The exchange-interaction radius cannot be arbitrarily large but must correspond to the used number of points  $\mathbf{k}$  in the Brillouin zone.

This fact was explained in [95]. It was shown that the use of a finite number of special points and simple cubature formulas for integration over the Brillouin zone

leads to an incorrect behavior of the offdiagonal matrix elements of the DM at large distances. This leads to nonphysical divergences in the calculation of the Hartree–Fock nonlocal exchange potential and the Hartree–Fock exchange energy of a crystal. Similar divergences take place in the calculation of the square of the DM. This naturally violates the idempotency of the exact one-electron matrix required of the Hartree–Fock one-determinant method. In the theory of special points, the divergence problem arises only in the cases where the total exchange energy and the exchange potential of the crystal depend on offdiagonal elements of the DM. Thus, in contrast to the Hartree–Fock method, this problem is nonexistent in methods based on density-functional theory; it is precisely the approximation where the theory of special points was first applied. In calculations of the electron structure with nonlocal exchange, this theory must be modified to avoid the above-mentioned divergences (see Sect. 4.3.3). The considered properties of DM (translation and point symmetry, duodempotency and normalization properties) do not depend on the basis choice (LCAO or plane waves). In the next section we consider the density matrix of a crystal in the LCAO approximation.

### 4.3.2 The One-electron Density Matrix of the Crystal in the LCAO Approximation

In Sect. 4.1.5 the Hartree–Fock LCAO approximation for periodic systems was considered. The main difference of the CO LCAO method (crystalline orbitals as linear combination of atomic orbitals) from that used in molecular quantum chemistry, the MO LCAO (molecular orbitals as linear combination of atomic orbitals) method was explained. In the CO LCAO approximation the one-electron wavefunction of a crystal (CO -  $\varphi_{ik}(\mathbf{R})$ ) is expanded in Bloch sums  $\chi_{\mu k}(\mathbf{R})$  of AOs:

$$\varphi_{ik}(\mathbf{R}) = \sum_{\mu} C_{i\mu}(\mathbf{k}) \chi_{\mu k}(\mathbf{R}) \quad (4.121)$$

where

$$\chi_{\mu k}(\mathbf{R}) = \frac{1}{\sqrt{N}} \sum_{\mathbf{R}_n} \exp(i\mathbf{k}\mathbf{R}_n) \chi_{\mu}(\mathbf{R} - \mathbf{R}_n) \quad (4.122)$$

In (4.121) and (4.122), the index  $\mu$  labels all AOs in the reference primitive cell ( $\mu = 1, 2, \dots, M$ ) and the index  $i$  numbers the energy bands ( $i = 1, 2, \dots, M$ ). The appearance of energy bands for periodic systems is the result of translation repeating of the primitive unit cells AO over the infinite crystal of the cyclic system modeling the infinite crystal. In the calculation of the molecular electronic structure the MOs are filled by electrons, taking into account the degeneracy of levels due to the point-symmetry group. In crystals, COs are filled by electrons and the degeneracy of one-electron states is defined by irreps of the space-symmetry group of a crystal. This means that the one-electron energy bands are filled by electrons and for nonconducting crystals the valence bands are filled and the conduction bands are empty.

The Bloch sums (4.121) of AOs, as well as the AOs, do not constitute an orthonormal basis; that is, the overlap integrals

$$\begin{aligned} S_{\mu\nu}(\mathbf{k}) &= \int d^3\mathbf{R} \chi_{\mu\mathbf{k}}^*(\mathbf{R}) \chi_{\nu\mathbf{k}}(\mathbf{R}) \\ s_{\mu\nu}(\mathbf{R}_n) &= \int d^3\mathbf{R} \chi_{\mu}^*(\mathbf{R}) \chi_{\nu}(\mathbf{R} - \mathbf{R}_n) \end{aligned} \quad (4.123)$$

are not equal to  $\delta_{\mu\nu}$ .

The crystalline orbitals  $\varphi_{i\mathbf{k}}(\mathbf{r})$  compose an orthonormal set from which the following orthonormality relations can be derived for the elements of the matrix  $\mathbf{C}(\mathbf{k})$  involved in (4.57):

$$\{\mathbf{C}(\mathbf{k})\mathbf{S}(\mathbf{k})\mathbf{C}(\mathbf{k})\}_{ij} = \delta_{ij} \quad (4.124)$$

In terms of the Bloch sums of AOs, the DM elements  $P_{\mu\nu}(\mathbf{k})$  can be expressed as

$$P_{\mu\nu}(\mathbf{k}) = \sum_i n_i(\mathbf{k}) C_{i\mu}(\mathbf{k}) C_{i\nu}^*(\mathbf{k}) \quad (4.125)$$

Within the LCAO approximation, the DM elements in the coordinate space are given by an expression similar to (4.101),

$$\rho_{\mu\nu}(\mathbf{R}_n) = \frac{1}{N} \sum_{\mathbf{k}} \exp(-i\mathbf{k}\mathbf{R}_n) P_{\mu\nu}(\mathbf{k}) \quad (4.126)$$

and the DM in the reciprocal space is related to the DM in the direct (coordinate) space through a relation similar to (4.105)

$$P_{\mu\nu}(\mathbf{k}) = \sum_{\mathbf{R}_n} \exp(i\mathbf{k}\mathbf{R}_n) \rho_{\mu\nu}(\mathbf{R}_n) \quad (4.127)$$

In the reciprocal space, the analog of the normalization condition (4.109) for the DM in the AO representation is the relation

$$Sp(\mathbf{P}(\mathbf{k})\mathbf{S}(\mathbf{k})) = \sum_{\mu\nu} P_{\mu\nu}(\mathbf{k}) S_{\mu\nu}(\mathbf{k}) = n \quad (4.128)$$

The normalization condition for the DM in the coordinate space (analog of (4.95)) is

$$\sum_{\mathbf{R}_n} Sp[\rho(\mathbf{R}_n)s(-\mathbf{R}_n)] = n \quad (4.129)$$

The idempotency relation for the density matrix  $\mathbf{P}(\mathbf{k})$  in the reciprocal space (with allowance for the nonorthogonality of the basis) has the form ( $n_i(\mathbf{k}) = 0, 2$ )

$$\mathbf{P}(\mathbf{k})\mathbf{S}(\mathbf{k})\mathbf{P}(\mathbf{k}) = 2\mathbf{P}(\mathbf{k}) \quad (4.130)$$

In the coordinate space, the idempotency relation for the DM is written as

$$\sum_{\mathbf{R}_m, \mathbf{R}'_m} \rho(\mathbf{R}_m)\mathbf{S}(\mathbf{R}'_m - \mathbf{R}_m)\rho(\mathbf{R}_n - \mathbf{R}'_m) = 2\rho(\mathbf{R}_n) \quad (4.131)$$

In various semiempirical versions of the Hartree–Fock approximation (see Chap. 6), the orthonormal set of Löwdin atomic orbitals (LAOs) rather than the nonorthogonal AO basis is used; the LAOs are defined as

$$\chi_{\mu\mathbf{k}}^L(\mathbf{R}) = \sum_{\nu} S_{\mu\nu}^{-1/2}(\mathbf{k}) \chi_{\nu\mathbf{k}}(\mathbf{R}) \quad (4.132)$$

In this basis, the normalization condition for the density matrix  $P^L(\mathbf{k})$  is simplified; instead of (4.129) we have

$$Sp P^L(\mathbf{k}) = n, \quad Sp \rho^L(0) = n \quad (4.133)$$

In the LCAO basis, the idempotency relations for the DM in the coordinate and reciprocal spaces are similar to (4.128) and (4.129) for the DM in the coordinate representation; in the reciprocal space, we have

$$P^L(\mathbf{k})P^L(\mathbf{k}) = 2P^L(\mathbf{k}) \quad (4.134)$$

and in the coordinate space, the relation has the form

$$\sum_{\mathbf{R}_m} \rho^L(\mathbf{R}_m) \rho^L(\mathbf{R}_n - \mathbf{R}_m) = 2\rho^L(\mathbf{R}_n) \quad (4.135)$$

In particular, for the reference primitive cell ( $\mathbf{R}_n = 0$ ), with allowance for the hermiticity of the DM, we have

$$\sum_{\mathbf{R}_n} \rho^L(\mathbf{R}_n) \rho^{L*}(\mathbf{R}_n) = 2\rho^L(0) \quad (4.136)$$

The offdiagonal elements of the DM in the AO basis determine the quantities

$$W_{AB}(\mathbf{R}_n) = \sum_{\mu \in A, \nu \in B} |\rho_{\mu\nu}^L(\mathbf{R}_n)|^2 \quad (4.137)$$

that can be considered as the extension to the crystals of the Wiberg indices introduced for molecules [96]. The Wiberg indices  $W_{AB}(\mathbf{R}_n)$  can be interpreted as chemical-bond indices (orders) between atoms A and B, belonging to the reference and  $\mathbf{R}_n$ th primitive cells, respectively [97, 98]. These indices are subject to a relation that is a consequence of the idempotency of the DM. To derive this relation, we consider the diagonal matrix elements of (4.136) and carry out summation over all AO indices of atom A. The result is

$$\sum_{B \neq A} \sum_{\mathbf{R}_n} W_{AB}(\mathbf{R}_n) = 2\rho_A^L - \sum_{\mu \in A} \rho_{\mu\mu}^L(0) \quad (4.138)$$

Here,  $\rho_A^L$  is the total electron population (in Lowdin's sense) of atom A,

$$\rho_A^L = \sum_{\mu} \rho_{\mu\mu}^L(0) \quad (4.139)$$

Let us define the covalence  $C_A$  of atom A as the sum of the chemical-bond orders (Wiberg indices) between atom A and all other atoms of the crystal. Using the idempotency relation (4.138), we have

$$C_A = \sum_{B, \mathbf{R}_n \neq A, 0} W_{AB}(\mathbf{R}_n) = 2\rho_A^L - \sum_{\mu \in A} \rho_{\mu\mu}^L(0) \quad (4.140)$$

It follows from (4.140) that the covalence of atom  $A$  in the crystal can be calculated either by summing the bond indices between atom  $A$  and all other atoms of the crystal or by using only single-center DM elements related to atom  $A$ . This property of the covalence is a consequence of the idempotency of the DM.

The Wiberg indices (4.137) and atomic covalence (4.140) are called the local properties of the electronic structure of periodic systems. These properties also include AO populations, atomic charges (electrovalencies) and total atomic valences [97]. The analysis of the local properties of the electronic structure in molecular quantum chemistry is very popular as it gives useful information about the chemical bonding. The local properties of the electronic structure of crystals are considered in more detail in Chap. 9. The above consideration holds for the density matrix of the basic domain of the crystal; that is, it is assumed that the number  $N$  of primitive cells in this domain is so large that the introduction of cyclic boundary conditions virtually does not affect the density matrix of the infinite crystal.

In actual practice, the SCF calculations of periodic systems are made with the approximate DM  $\tilde{\rho}(\mathbf{R}, \mathbf{R}')$ , which is calculated by summation in (4.102) over a finite (relatively small) number of  $\mathbf{k}$ -points. As a result, the divergence of the summation in the direct lattice can appear in the nonlocal exchange part of the Fock matrix. This problem is considered in the next section.

### 4.3.3 Interpolation Procedure for Constructing an Approximate Density Matrix for Periodic Systems

Let the electronic structure of a crystal be calculated using the one-electron wavefunctions found at a finite number  $L$  of points  $\{\mathbf{k}_j\}$  in the BZ ( $j = 1, 2, \dots, L$ ). This raises the question of how the sum over  $\mathbf{k}$  points in the BZ should be approximately calculated in (4.102) for the one-electron DM of the crystal.

We consider a set of points  $\{\mathbf{k}_j\}$  generated by the large- unit- cell (LUC) – small brillouin zone (SBZ) method, see Sect. 4.2.2. In this method, the primitive lattice vectors  $\mathbf{a}_i$  ( $i = 1, 2, 3$ ) are transformed with the aid of a matrix  $\mathbf{l}$  whose elements are integers (see (4.77)):

$$\mathbf{A}_j^L = \sum_{i=1}^3 l_{ji} \mathbf{a}_i, \quad L = |\det \mathbf{l}| \quad (4.141)$$

The basis vectors  $\mathbf{A}_j^L$  determine an LUC and a new Bravais superlattice. The LUC thus constructed has volume  $V_L = L V_{\mathbf{a}}$  and consists of  $L$  primitive cells. The superlattice vectors  $\mathbf{A}$  are linear combinations (with integral-valued coefficients) of the basis vectors  $\mathbf{A}_j^L$ . The matrix  $\mathbf{l}$  in (4.141) is chosen such that the point symmetry of the new superlattice is identical to that of the original lattice (the corresponding transformation (4.141) is called a symmetric transformation, see Sect. 4.2.1). The type of direct lattice can be changed if there are several types of lattice with the given point symmetry. The LUC is conveniently chosen in the form of a Wigner–Seitz (WS) cell, which possesses the point symmetry of the lattice.

We introduce the periodic boundary conditions for the crystal domain coinciding with the LUC; that is, we assume that all translations through the superlattice vectors  $\mathbf{A}$  are equivalent to the identity translation. Thus, we have a system of finite size, *i.e.* a cyclic cluster belonging to the symmetry group  $\mathbf{G}^L = \mathbf{T}^L \mathbf{F}$ , see Sect. 2.2.3

(we consider only symmetric transformations). Here, the subgroup  $T^L$  includes  $L$  translations through the vectors  $\mathbf{R}_n^0$  of inner translations of the original direct lattice that lie within the LUC or fall on its boundary. The lattice sites lying on the boundary of the LUC are connected by superlattice vectors  $\mathbf{A}$ . These lattice sites should be counted only once, because they belong simultaneously to several LUCs.

For the cyclic cluster thus constructed, the following orthogonality relations hold:

$$\frac{1}{L} \sum_{\mathbf{R}_n^0} \exp(i\mathbf{k}_j \mathbf{R}_n^0) = \delta_{\mathbf{k}, \mathbf{b}} \quad (4.142)$$

$$\frac{1}{L} \sum_{\mathbf{k}_j} \exp(-i\mathbf{k}_j \mathbf{R}_n^0) = \delta_{\mathbf{R}_n^0, \mathbf{A}} \quad (4.143)$$

These relations are a generalization of the analogous equations for the basic domain of the crystal because the cyclic cluster is obtained with the help of transformation (4.141), in which the matrix  $l$  can be nondiagonal. The vectors  $\mathbf{k}_j$  in (4.142) and (4.143) label  $L$  different irreducible representations of the group  $T^L$  and can be found from the relation

$$\exp(i\mathbf{k}_j \mathbf{A}) = 1, \quad (j = 1, 2, \dots, L) \quad (4.144)$$

Equation (4.142) is a consequence of the orthogonality of the characters of irreducible representations of the translation group to the character of the unit representation ( $\mathbf{k} = 0$ ), while (4.143) means that the characters of a regular representation of the group are equal to zero for all elements of the group except for the identity element (*i.e.* except for the identity translation and equivalent translations through the superlattice vectors  $\mathbf{A}$ ).

Let the density matrix  $P(\mathbf{k})$  be known at a finite set of points determined by the LUC-SBZ method and, therefore, satisfying (4.144). Our aim is to approximate the DM at an arbitrary point  $\mathbf{k}$  in the BZ. The interpolation procedure suggested in [70] and discussed in this subsection is appropriate for calculations in both the coordinate representation and the AO basis. For this reason, we drop the indices on the DM, keeping in mind that these indices are  $\mathbf{r}$  and  $\mathbf{r}'$  in the coordinate representation and  $\mu$  and  $\nu$  in the AO or orthogonalized-AO representation.

The expansions of the density matrix  $P(\mathbf{k})$  given by (4.105) and (4.127) can be rewritten in the form

$$P(\mathbf{k}) = \sum_{\mathbf{R}_n^0} \exp(i\mathbf{k} \mathbf{R}_n^0) \rho(\mathbf{R}_n^0) + \sum_{\mathbf{A} \neq 0} \sum_{\mathbf{R}_n^0} \exp(i\mathbf{k}(\mathbf{R}_n^0 + \mathbf{A})) \rho(\mathbf{R}_n^0 + \mathbf{A}) \quad (4.145)$$

where the translations  $(\mathbf{R}_n^0 + \mathbf{A})$  lie in the basic domain of the crystal. As mentioned in Sect. 4.3.2, the offdiagonal elements of the density matrix  $\rho(\mathbf{R}_n^0 + \mathbf{A})$  fall off with distance as Wannier functions (exponentially in the case of insulators). Therefore, as the LUC grows in size and the values of  $|\mathbf{A}|$  become sufficiently large, the second term in (4.145) will be small in magnitude. With this in mind we will approximate the density matrix  $\tilde{P}(\mathbf{k})$  of the crystal as follows [70]. In the expansion given by (4.145), we drop the sum over the superlattice sites with  $\mathbf{A} \neq 0$  and take the remaining expression as an interpolation formula for determining the DM at any  $\mathbf{k}$  point in the BZ; we rewrite this expression in the form

$$\tilde{P}(\mathbf{k}) = \sum_{\mathbf{R}_n^0} \exp(i\mathbf{k}\mathbf{R}_n^0) \rho^0(\mathbf{R}_n^0) \quad (4.146)$$

This formula was proposed in [70] for the interpolation of an arbitrary periodic function  $f(\mathbf{k})$ . The interpolation coefficients  $\rho^0(\mathbf{R}_n^0)$  (the number of which is  $L$ ) can be found from the condition

$$\tilde{P}(\mathbf{k}_j) = \sum_{\mathbf{R}_n^0} \exp(i\mathbf{k}_j \mathbf{R}_n^0) \rho^0(\mathbf{R}_n^0) = P(\mathbf{k}_j) \quad (4.147)$$

Using the orthogonality relation (4.143), the interpolation coefficients can be found to be

$$\rho^0(\mathbf{R}_n^0) = \frac{1}{L} \sum_{\mathbf{k}_j} \exp(-i\mathbf{k}_j \mathbf{R}_n^0) P(\mathbf{k}_j) \quad (4.148)$$

The coefficients  $\rho^0(\mathbf{R}_n^0)$  can also be represented as a sum of the DM elements  $\rho(\mathbf{R}_n^0)$  over the superlattice sites. Indeed, substituting (4.146) for  $P(\mathbf{k}_j)$  into (4.148) and using (4.143), we have

$$\rho^0(\mathbf{R}_n^0) = \sum_{\mathbf{A}} \rho(\mathbf{R}_n^0 + \mathbf{A}) \quad (4.149)$$

It should be noted that the matrix  $\rho^0(\mathbf{R}_n^0)$  can be defined for all vectors  $\mathbf{R}_n$  of the Bravais lattice by using the appropriate extensions of (4.148) and (4.149). It is easy to see that  $\rho^0(\mathbf{R}_n^0)$  is a periodic function of period  $\mathbf{A}$ . Substituting (4.148) for the coefficients  $\rho^0(\mathbf{R}_n^0)$  into (4.149), we obtain an interpolation formula for the DM in the reciprocal space,

$$\tilde{P}(\mathbf{k}) = \sum_{\mathbf{k}_j} P(\mathbf{k}_j) \Omega_j(\mathbf{k}) \quad (4.150)$$

$$\Omega_j(\mathbf{k}) = \frac{1}{L} \sum_{\mathbf{R}_n^0} \exp(i(\mathbf{k} - \mathbf{k}_j) \mathbf{R}_n^0) \quad (4.151)$$

Here,  $\Omega_j(\mathbf{k})$  are interpolation weights, the sum of which is equal to unity (the normalization natural for weighting factors). Indeed, using (4.143), we find

$$\sum_{\mathbf{k}_j} \Omega_j(\mathbf{k}) = \sum_{\mathbf{R}_n^0} \exp(i\mathbf{k}\mathbf{R}_n^0) \left[ \frac{1}{L} \sum_{\mathbf{k}_j} \exp(-i\mathbf{k}_j \mathbf{R}_n^0) \right] = \sum_{\mathbf{R}_n^0} \exp(i\mathbf{k}\mathbf{R}_n^0) \delta_{\mathbf{R}_n^0, 0} = 1 \quad (4.152)$$

For the appropriate DM in the coordinate space, one can write equations similar to (4.118) and (4.133):

$$\tilde{\rho}(\mathbf{R}_n) = \frac{1}{N} \sum_{\mathbf{k}} \exp(-i\mathbf{k}\mathbf{R}_n) \tilde{P}(\mathbf{k}) = \sum_{\mathbf{R}_n^0} \rho^0(\mathbf{R}_n^0) \left[ \frac{1}{N} \sum_{\mathbf{k}} \exp(i\mathbf{k}(\mathbf{R}_n^0 - \mathbf{R}_n)) \right] \quad (4.153)$$

According to (4.143), the expression in the square brackets on the right-hand side of (4.153) is equal to unity if the vector  $\mathbf{R}_n$  belongs to the set of vectors  $\{\mathbf{R}_n^0\}$  (*i.e.* if this vector lies within the LUC or on its boundary) and vanishes otherwise. Therefore, the appropriate DM can be represented in the form

$$\tilde{\rho}(\mathbf{R}_n) = \omega(\mathbf{R}_n) \rho^0(\mathbf{R}_n) \quad (4.154)$$

where  $\omega(\mathbf{R}_n)$  is the so-called weighting function,

$$\omega(\mathbf{R}_n) = \frac{1}{N} \sum_{\mathbf{k}} \exp(i\mathbf{k}(\mathbf{R}_n^0 - \mathbf{R}_n)) = \begin{cases} 1, & \text{if } \mathbf{R}_n \in \{\mathbf{R}_n^0\} \\ 0, & \text{if } \mathbf{R}_n \notin \{\mathbf{R}_n^0\} \end{cases} \quad (4.155)$$

We note that the procedure described above for interpolating the DM in the BZ is not uniquely determined, because the LUC (*i.e.* the set of vectors  $\{\mathbf{R}_n^0\}$ ) can be variously chosen for the same superlattice. Furthermore, the LUC can be chosen differently for the pairs of DM indices  $\mathbf{r}, \mathbf{r}'$  and  $\mu, \nu$ . In this book, the LUC is taken to be the Wigner–Seitz cell, because only this cell has a symmetry identical to the point symmetry of the superlattice in all cases. In order to correlate the LUC with a cyclic cluster, we choose the LUC to be dependent on the pair of DM indices as follows. In the coordinate representation, the LUC ( $V_{\mathbf{A}}$ -region) is centered at the point  $(\mathbf{r} - \mathbf{r}')$ ; therefore, we have

$$\omega_{\mathbf{r}\mathbf{r}'}(\mathbf{R}_n) = \omega(\mathbf{R}_n + \mathbf{r}' - \mathbf{r}) = \begin{cases} 1, & \text{if } \mathbf{R}_n + \mathbf{r}' - \mathbf{r} \in V_{\mathbf{A}} \\ 0, & \text{if } \mathbf{R}_n + \mathbf{r}' - \mathbf{r} \notin V_{\mathbf{A}} \end{cases} \quad (4.156)$$

In the AO representation, the LUC is centered at the point  $\mathbf{d}_{\mu} - \mathbf{d}_{\nu}$  where  $\mathbf{d}_{\mu}$  and  $\mathbf{d}_{\nu}$  are the position vectors of the two atoms to which the AOs with indices  $\mu$  and  $\nu$  belong, respectively. Thus, we have

$$\omega_{\mu\nu}(\mathbf{R}_n) = \omega(\mathbf{R}_n + \mathbf{d}_{\nu} - \mathbf{d}_{\mu}) = \begin{cases} 1, & \text{if } \mathbf{R}_n + \mathbf{d}_{\nu} - \mathbf{d}_{\mu} \in V_{\mathbf{A}} \\ 0, & \text{if } \mathbf{R}_n + \mathbf{d}_{\nu} - \mathbf{d}_{\mu} \notin V_{\mathbf{A}} \end{cases} \quad (4.157)$$

The weighting function  $\omega_{\mu\nu}(\mathbf{R}_n)$  of (4.157) introduced into expressions for the DM specifies the cyclic boundary conditions and the cyclic cluster. Indeed, let an arbitrarily chosen LUC be fixed and let us consider the orbitals of atoms A and B in this LUC ( $\mu \in A, \nu \in B$ ). Out of all matrix elements  $\tilde{\rho}_{\mu\nu}(\mathbf{R}_n + \mathbf{A})$  with indices  $\mu$  and  $\nu$  kept fixed and the vector  $\mathbf{A}$  running over the superlattice, only one matrix element is nonzero. For this matrix element, the vector  $(\mathbf{d}_{\nu} + \mathbf{R}_n + \mathbf{A})$  (the position vector of atom B) falls into the Wigner–Seitz cell centered at atom A site. This matrix element exactly equals the matrix element  $\rho_{\mu\nu}^0(\mathbf{R}_n)$ .

According to (4.154), the approximate density matrix  $\tilde{\rho}(\mathbf{R}_n)$  found by interpolation in the BZ contains the weighting function of (4.155)–(4.157) as a factor. This function ensures the proper behavior of the offdiagonal elements of the approximate DM as  $|\mathbf{R}_n| \rightarrow \infty$ . As already mentioned, the matrix without a weighting factor is a periodic (not vanishing at infinity) function

$$\rho^0(\mathbf{R}_n + \mathbf{A}) = \rho^0(\mathbf{R}_n) \quad (4.158)$$

However, this DM is frequently used in many calculations based on the Hartree–Fock approximation or its semiempirical (with nonlocal exchange) versions for crystals (the CNDO and INDO methods, see Chap. 6). In those calculations, all summations over the lattice sites are usually truncated by introducing artificially interaction ranges. The non decaying density matrix  $\rho^0(\mathbf{R}_n)$  gives rise to a divergent exchange term in

the Fock matrix. In other words, as the corresponding interaction range increases in size at a fixed number of involved  $\mathbf{k}$  points, the results do not converge to a certain limit and the total energy of the system sharply decreases.

In order to avoid these divergences, *the exchange interaction range should be chosen such that the corresponding sphere differs only slightly from the Wigner–Seitz cell of the superlattice*, which generates precisely the set of  $\mathbf{k}$  points used in the calculations. In this case, the size of the summation domain in the coordinate space is in accord with the number of  $\mathbf{k}$  points used in the calculations and the exchange term in the HF operator does not diverge. The approximate density matrix  $\tilde{\rho}^0(\mathbf{R}_n)$  is not subject to these drawbacks, and the balance between the size of the summation domain in the coordinate space and the number of  $\{\mathbf{k}_j\}$  points involved occurs automatically.

It should be noted that in the versions of the density-functional theory in which the exchange-correlation term depends on the electron density alone, both approaches are equivalent. Indeed, the electron density  $\rho(\mathbf{R}, \mathbf{R}) = \rho_{rr}(0)$  depends only on the diagonal elements of the DM; therefore, the weighting function of (4.155) and (4.156) is equal to unity in this case.

In general, the approximate DM does not satisfy all the conditions to which the exact DM is subject. Let us elucidate which of the relations presented in Sect. 4.2.2 holds for the approximate DM and which do not.

The normalization conditions (4.95), (4.128), and (4.129) are very important. The approximate DM in the coordinate representation and in the LAO basis meets these conditions because the weighting function for the diagonal elements of the DM is equal to unity. In the nonorthogonal basis, a modified normalization condition is satisfied,

$$\sum_{\mathbf{R}_n} \text{Sp} [\tilde{\rho}(\mathbf{R}_n) \tilde{s}(-\mathbf{R}_n)] = n \quad (4.159)$$

where  $\tilde{s}(\mathbf{R}_n)$  is an approximate overlap-integral matrix, which is obtained by interpolating in the BZ in much the same way as the approximate DM was obtained and has the form

$$\tilde{s}_{\mu\nu}(\mathbf{R}_n) = \omega(\mathbf{R}_n + \mathbf{d}_\nu - \mathbf{d}_\mu) s_{\mu\nu}^0(\mathbf{R}_n) \quad (4.160)$$

$$s_{\mu\nu}^0(\mathbf{R}_n) = \frac{1}{L} \sum_{\mathbf{k}_j} \exp(-\mathbf{k}_j \mathbf{R}_n) S(\mathbf{k}_j) = \sum_{\mathbf{A}} s(\mathbf{R}_n + \mathbf{A}) \quad (4.161)$$

It is easy to verify that in all cases the approximate DM is Hermitian, *i.e.* it obeys relations identical to (4.107) and (4.108).

In general, the approximate DM is not idempotent, because (4.112) holds only at points  $\mathbf{k} = \mathbf{k}_j$  ( $j = 1, 2, \dots, L$ ) and is not satisfied at other points of the BZ. For this reason, (4.111) and (4.136) in the coordinate space do not generally hold. However, in the important particular case where the vector  $\mathbf{R}_n$  in these equations is zero, the idempotency relation is satisfied. In the coordinate space and in the LAO representation, we have

$$\sum_{\mathbf{R}_m} \tilde{\rho}(\mathbf{R}_m) \tilde{\rho}(-\mathbf{R}_m) = 2\tilde{\rho}(0) \quad (4.162)$$

Therefore, the important relation for the Wiberg indices (4.140) is also satisfied. We note that the matrix  $\rho^0(\mathbf{R}_n)$  obeys the relation

$$\sum_{\mathbf{R}_m^0} \rho^0(\mathbf{R}_m^0) \rho^0(\mathbf{R}_n^0 - \mathbf{R}_m^0) = 2\rho^0(\mathbf{R}_n^0) \quad (4.163)$$

In the strict sense, (4.162) is not an idempotency relation, because summation is carried out only over the vectors  $\mathbf{R}_m^0$ , lying within the LUC, whereas the vector difference  $(\mathbf{R}_n^0 - \mathbf{R}_m^0)$  can lie outside the LUC. If we perform summation over all Bravais lattice vectors, the right-hand side of (4.162) will diverge, because  $\rho^0(\mathbf{R}_n^0)$  does not vanish at infinity.

For the approximate DM to have the proper point symmetry, the LUC should be taken to be the Wigner–Seitz (WS) cell. In this case, however, the symmetry can be broken if on the boundary of the WS cell, there are atoms of the crystal. Indeed, if an atom lies on the WS cell boundary, then there is one or several equivalent atoms that also lie on the boundary of the cell and their position vectors differ from that of the former atom by a superlattice vector  $\mathbf{A}$ . When constructing the approximate density matrix  $\tilde{\rho}$  we assigned only one of several equivalent atoms to the WS cell. In other words, in the set  $\{\mathbf{R}_n^0\}$ , there are no two vectors that differ from each other by a superlattice vector  $\mathbf{A}$ . In this case, if a point-symmetry operation takes one boundary atom into another atom assigned to another WS cell, then the point symmetry of the density matrix  $\tilde{\rho}$  is broken, because the symmetry of the weighting function  $\omega_{\mu\nu}(\mathbf{R}_n)$  of (4.157) is broken.

Since it is desirable to preserve the point symmetry when calculating the electronic structure, the approximate DM can be replaced by an averaged density matrix (see also [99, 100]):

$$\rho^s = \frac{1}{N_s} \sum_{\alpha=1}^{N_s} \tilde{\rho}^\alpha(\mathbf{R}_n) = \omega^s(\mathbf{R}_n) \rho^0(\mathbf{R}_n) \quad (4.164)$$

Here, the index  $\alpha = 1, 2, \dots, N_s$  labels all  $N_s$  possible ways in which one of the equivalent boundary atoms can be assigned to a given WS cell and the symmetrical weighting function is defined as

$$\omega_{\mu\nu}^s(\mathbf{R}_n) = \frac{1}{N_s} \sum_{\alpha=1}^{N_s} \omega_{\mu\nu}^\alpha(\mathbf{R}_n) = \begin{cases} \frac{1}{n_{\mu\nu}^s}, & \text{if } \mathbf{R}_n + \mathbf{d}_\nu - \mathbf{d}_\mu \in V_A \\ 0, & \text{if } \mathbf{R}_n + \mathbf{d}_\nu - \mathbf{d}_\mu \notin V_A \end{cases} \quad (4.165)$$

where  $n_{\mu\nu}^s$  is the number of atoms in the WS cell (including its boundary) that are translationally equivalent to atom  $B$  ( $\nu \in B$ ) in the case where the WS cell is centered at the atom- $A$  site ( $\mu \in A$ ). In other words,  $n_{\mu\nu}^s$  is the number of WS cells that have atom  $B$  in common. If atom  $B$  is strictly inside the WS cell, then  $n_{\mu\nu}^s = 1$  and (4.165) is identical to (4.157). We note that the density matrix  $\rho^s(\mathbf{R}_n)$  does not satisfy idempotency relation (4.162) and corresponds to a mixed state of the system. However, as the LUC enlarges, the effect of the boundary atoms decreases and the density matrix  $\rho^s(\mathbf{R}_n)$  approaches the idempotent density matrix  $\rho(\mathbf{R}_n)$ .

*The above consideration can be interpreted as deduction of the cyclic cluster model of the infinite crystal when the Hartree–Fock LCAO method (or its semiempirical version with nonlocal exchange) is applied.*

The study of the approximate density matrix properties allowed the implementation of the cyclic cluster model in the Hartree–Fock LCAO calculations of crystalline systems [100] based on the idempotency relations of the density matrix. The results

obtained for cyclic-cluster modeling the rutile  $\text{TiO}_2$  structure are discussed in Chap. 9.

The consideration presented allows one to better understand the features of Hartree–Fock self-consistent calculations of the electronic structure of an infinite crystal with a nonlocal exchange potential determined by the offdiagonal elements of the one-electron density matrix. It has been shown that the number of  $\mathbf{k}$  points chosen in the BZ for calculations should be in accord with the size of the interaction range in the coordinate space. In other words, there should be *a correlation between summations over the Bravais lattice in the coordinate space and over the BZ in the reciprocal space*. It was also shown that when the Fock operator (or the Kohn–Sham operator in hybrid DFT methods, see Chap. 7) contains offdiagonal DM elements, the BZ special-point technique should be modified: weighting-function introduction in the direct-lattice sums entering the exchange term establishes the necessary balance and removes the artificial divergences. The HF LCAO method is a well-defined starting point for more sophisticated techniques allowing inclusion of the electron correlation. We consider this problem in the next chapter.

---

## Electron Correlations in Molecules and Crystals

### 5.1 Electron Correlations in Molecules: Post-Hartree–Fock Methods

#### 5.1.1 What is the Electron Correlation ?

Electrons in molecules and crystals repel each other according to Coulomb's law, with the repulsion energy depending on the interelectron distance as  $r_{12}^{-1}$ . This interaction creates a correlation hole around any electron, *i.e.* the probability to find any pair of electrons at the same point of spin-coordinate space is zero. From this point of view only the Hartree product  $\Psi_H$  of molecular or crystalline spin-orbitals  $\psi_i(\mathbf{x})$ :

$$\Psi_H(\mathbf{x}_1, \mathbf{x}_2, \dots, \mathbf{x}_{N_e}) = \psi_1(\mathbf{x}_1)\psi_2(\mathbf{x}_2)\dots\psi_{N_e}(\mathbf{x}_{N_e}) \quad (5.1)$$

is a completely uncorrelated function. The Hartree product (5.1) describes the system of  $N_e$  electrons in an independent particle model. This independence means that the probability of simultaneously finding electron 1 at  $\mathbf{x}_1$ , electron 2 at  $\mathbf{x}_2$ , *etc.* ( $\mathbf{x}$  means the set of coordinate  $\mathbf{r}$  and spin  $\sigma$  variables) is given by

$$\begin{aligned} & |\Psi_H(\mathbf{x}_1, \mathbf{x}_2, \dots, \mathbf{x}_{N_e})|^2 d\mathbf{x}_1 d\mathbf{x}_2 \dots d\mathbf{x}_{N_e} \\ &= |\psi_1(\mathbf{x}_1)|^2 d\mathbf{x}_1 |\psi_2(\mathbf{x}_2)|^2 d\mathbf{x}_2 \dots |\psi_{N_e}(\mathbf{x}_{N_e})|^2 d\mathbf{x}_{N_e} \end{aligned} \quad (5.2)$$

which is the probability of finding electron 1 at  $\mathbf{x}_1$  times the probability of finding electron 2 at  $\mathbf{x}_2$ , *etc.*, *i.e.* product of probabilities.

The well-known Extended Hückel semiempirical method for molecules and the tight-binding approach to crystals are examples of the models with full absence of electron correlation in the wavefunction. The Hamiltonian in these methods does not include explicitly electron–electron interactions (such a Hamiltonian was defined in Chap. 4 as the one-electron Hamiltonian) so that the total many-electron wavefunction is a simple product (5.1) of the one-electron functions and the total electron energy is a sum of one-electron energies. The semiempirical parameters used in these methods allow one to take the correlation into account at least partly. The difference between the one-electron Hamiltonian and the Hamiltonian of the one-electron approximation (HF method) is the following. The former does not include electron–electron interaction so that the calculation of its eigenvalues and eigenvectors does not

require a self-consistent procedure. The Hamiltonian of the one-electron approximation includes explicitly the interelectron interactions, the one-electron approximation is made only in the many-electron wavefunction. The one-electron approximation Hamiltonian depends on the one-electron wavefunctions unknown at the beginning of the calculation (for example, the Coulomb and exchange parts of the Hamiltonian in the Hartree–Fock method, see Chap. 4) and the self-consistent calculation is required.

As considered in Chap. 4 the Hartree–Fock (SCF) method replaces the instantaneous electron–electron repulsion with the repulsion of each electron with an average electron charge cloud. The HF method assumes that the many-electron wavefunction can be written as one Slater determinant (4.9). The Hartree–Fock method is usually defined as “uncorrelated”. However, the electron motions are no longer completely independent.

For two electrons with different spins,  $|\varphi_1(\mathbf{r}_1)\alpha(\sigma_1)\varphi_2(\mathbf{r}_2)\beta(\sigma_2)|$  the probability of finding electron 1 at  $\mathbf{r}_1$  and electron 2 at  $\mathbf{r}_2$  is

$$\begin{aligned} P(\mathbf{r}_1, \mathbf{r}_2) d\mathbf{r}_1 d\mathbf{r}_2 &= d\mathbf{r}_1 d\mathbf{r}_2 \int d\sigma_1 \int d\sigma_2 |\Psi|^2 \\ &= \frac{1}{2} [| \varphi_1(\mathbf{r}_1) |^2 | \varphi_2(\mathbf{r}_2) |^2 + | \varphi_1(\mathbf{r}_2) |^2 | \varphi_2(\mathbf{r}_1) |^2] d\mathbf{r}_1 d\mathbf{r}_2 \end{aligned} \quad (5.3)$$

The electrons are uncorrelated.

For two electrons with the same spin  $|\varphi_1(\mathbf{r}_1)\alpha(\sigma_1)\varphi_2(\mathbf{r}_2)\alpha(\sigma_2)|$  the probability of finding electron 1 at  $\mathbf{r}_1$  and electron 2 at  $\mathbf{r}_2$  is

$$\begin{aligned} P(\mathbf{r}_1, \mathbf{r}_2) d\mathbf{r}_1 d\mathbf{r}_2 &= \frac{1}{2} (| \varphi_1(\mathbf{r}_1) |^2 | \varphi_2(\mathbf{r}_2) |^2 + | \varphi_1(\mathbf{r}_2) |^2 | \varphi_2(\mathbf{r}_1) |^2) \\ &\quad - [ \varphi_1^*(\mathbf{r}_1) \varphi_2(\mathbf{r}_1) \varphi_2^*(\mathbf{r}_2) \varphi_1(\mathbf{r}_2) + \varphi_1(\mathbf{r}_1) \varphi_2^*(\mathbf{r}_1) \varphi_2(\mathbf{r}_2) \varphi_1^*(\mathbf{r}_2) ] d\mathbf{r}_1 d\mathbf{r}_2 \end{aligned} \quad (5.4)$$

Now,  $P(\mathbf{r}_1, \mathbf{r}_2) = 0$ . No two electrons with the same spin can be at the same place. This is called the Fermi hole. Thus, *same-spin electrons are correlated in Hartree–Fock, different-spin electrons are not*. Sometimes, it is said that HF methods take into account the so-called spin correlation.

The HF methods are also called by the independent electrons approximation [5] but this independence is restricted by the Pauli principle.

The exact solution of Hartree–Fock–Roothaan equations (4.33) for molecular systems means use of a complete set of basis functions (such a solution corresponds to the Hartree–Fock limit and in practice can be achieved mainly for the simple molecules).

In modern molecular quantum chemistry the correlation energy is defined as the difference between the exact energy and the HF energy in a complete basis (Hartree–Fock limit). As one does not know the exact energy one uses the experimental total energy (the sum of the experimental cohesive energy and free-atom energies) or calculates the exact energy for a given one-electron basis set and defines the basis set correlation energy as the difference between the exact and HF energies calculated for the same one-electron basis set. In molecular systems, the correlation energy is about 1 eV per electron pair in a bond or lone pair.

The HF method is usually defined as uncorrelated, however, as we see, the electron motions are no longer completely independent. One of the first attempts to include the electron-correlation in calculations was made by Fock *et al.* [101], who suggested the incomplete separation of variables for two-valent atoms.

The key distinction between the Hamiltonian operator and the Fock operator is the following, [102]: the former returns the electronic energy for the many-electron system, the latter is really not a single operator, but the set of all of the interdependent one-electron operators that are used to find the one-electron functions (molecular or crystalline orbitals) from which the HF wavefunction is constructed as a Slater determinant (4.9). The HF wavefunction corresponds to the lowest possible energy for a single-determinant many-electron wavefunction formed from the chosen basis set.

Including electron-correlation in MO theory means an attempt to modify the HF wavefunction to obtain a lower electronic energy when we operate on that modified wavefunction with the Hamiltonian. This is why the name post-Hartree–Fock methods is traditionally used for the methods including the electron-correlation.

As was mentioned in Sect. 4.1.3 in the unrestricted Hartree–Fock approximation (where the coordinate dependence of spin-up and spin-down MOs was allowed to differ) the one-determinant many-electron wavefunction is, in the general case, not an eigenfunction of the total spin operator  $S^2$ . To repair that deficiency the technique of projection is used [103] so that the resulting wavefunction becomes a sum of several Slater determinants and therefore partly takes into account electron-correlation, *i.e.* goes beyond the one-determinant HF approximation. However, the coefficients in the sum of Slater determinants are defined only by the projection procedure, *i.e.* the total spin-symmetry requirements introduced for the many-electron wavefunction.

The sum of Slater determinants

$$\Psi = C_0 \Psi_{HF} + C_1 \Psi_1 + C_2 \Psi_2 + \dots \quad (5.5)$$

is used also in other post-HF approaches: configuration interaction (CI), multiple-configuration SCF (MCSCF) and coupled-cluster (CC) methods applied to include the electron-correlation in molecules.

Often, the HF approximation provides an accurate description of the system and the effects of the inclusion of correlations with CI or MCSCF methods are of secondary importance. In this case, the correlation effects may be considered as a smaller perturbation and as such treated using the perturbation theory. This is the approach of Möller–Plesset [104] or many-body perturbation theory for the inclusion of correlation effects. In the MP2 approximation only the second-order many-body perturbations are taken into account.

The above-mentioned quantum-chemical approaches to electron-correlations in molecules (also called wavefunction-based correlation methods) are described in detail in monographs [5, 102], recent review articles [105, 106] and are implemented in modern computer codes [35, 107, 108]. The main disadvantage of the wavefunction-based correlation methods is the high scaling of the computational cost with the number of atoms  $N$  in a molecule [109], at least when the canonical MOs are used. The scaling of the computational complexity is  $O(N^5)$  for the simplest and cheapest method – second-order perturbation theory MP2. For the CC theory the computational cost scales are  $O(N^6)$  and even  $O(N^7)$  for the truncated beyond doubles and triples substitutions, respectively. Such a high “scaling wall” [109] restricts the application range of the wavefunction-based correlation methods to molecules of rather modest size. For this reason the density-functional-based correlation methods (see Chap. 7) remain until now the main way to treat large molecular systems. The main disadvantages

of the latter methods are the principal impossibility for systematic improvements, the underestimation of transition-state energies, and the inability to describe weak interactions (dispersive forces).

The essential progress in the correlation effects inclusion was achieved in the so-called local correlation methods [109,110] taking into account the short-range nature of the correlation. In these methods, the localized MOs are generated from the occupied canonical MOs using different localization criteria, see Sect. 3.3.1. For the virtual space the atomic-orbital basis is projected out of the occupied MO space.

As compared to the molecules the wavefunction-based correlation methods for periodic systems are practically reliable only when the molecular cluster model is used. Unfortunately, the well-known problems of the cluster choice and the influence of the dangling bonds on the numerical results restricts the application range of the molecular cluster model to the essentially ionic systems.

The more sophisticated incremental scheme [111–114] maintains the infinite nature of periodic systems but the correlation effects are calculated incrementally using standard quantum-chemical codes.

Only recently was the MP2 theory applied to the periodic systems based on the local correlation methods and use of Wannier functions [109,115].

While for the molecules the local correlation methods are already implemented in the MOLPRO code [116] the implementation of this approach to the periodic systems is the main goal of the new CRYSCOR project [117].

In the next sections we briefly discuss the basic ideas of CI, MCSCF and CC post-HF methods for molecules as they are directly extended to the crystalline solids in the framework of the molecular cluster model. In more detail, the local correlation and MP2 methods are considered both for the molecules and the periodic systems.

### 5.1.2 Configuration Interaction and Multi-configuration Self-consistent Field Methods

Methods designed to account for electron correlation in molecules are divided into two classes: wavefunction(WF)-based methods and density-functional (DF)-based methods. The former use, in one or another way, the HF(noncorrelated) orthonormal MOs and therefore are also called post-HF (PHF) methods. In the majority of cases RHF orbitals are used. The latter are based on the density-functional theory (DFT), considered in Chap. 7.

PHF methods can, in turn, be classified as the variational and nonvariational ones. In the former group of methods the coefficients in linear combination of Slater determinants and in some cases LCAO coefficients in HF MOs are optimized in the PHF calculations, in the latter such an optimization is absent. To the former group of PHF methods one refers different versions of the configuration interaction (CI) method, the multi-configuration self-consistent field (MCSCF) method, the variational coupled cluster (CC) approach and the rarely used valence bond (VB) and generalized VB methods. The nonvariational PHF methods include the majority of CC realizations and many-body perturbation theory (MBPT), called in its molecular realization the Möller-Plessett (MP) method. In MP calculations not only RHF but UHF MOs are also used [107].

In this section, we discuss CI and MCSCF methods, CC and MP approaches are considered in the next sections.

The concept of the electron configuration has sense only when the one-electron functions of space and spin coordinates are used to approximate the corresponding many-electron wavefunction. The latter is called the configuration-state function (CSF) when the basis of spin-adapted many-electron functions is used. The configuration is specified by fixing the occupation numbers of the molecular spin-orbitals (MSO) and the molecular spin state. For the closed-shell singlets (the ground-state configuration) CSF can always be represented as a single determinant and transforms over identity representation of the molecular point-symmetry group. As the degeneracy of the molecular one-electron states is defined by the dimensions of the irreps of the corresponding point-symmetry group the closed-shell configuration occupation numbers are zero or twice these dimensions ( $\alpha$  and  $\beta$  electron-spin projections are allowed). In the majority of open-shell systems (excited-states configurations or ground states of radicals) proper CSFs can only be represented by a combination of two or more Slater determinants. Let the Hartree–Fock–Roothaan (MO LCAO) equations (4.33) be solved and the Slater determinant  $\Phi_0 = \Psi_{HF} = |\psi_1, \psi_2, \dots, \psi_N|$  in (5.5) is obtained. Solving MO LCAO equations will give  $M > N$  orthonormal MSOs ( $M$  is the total number of AOs used in the calculation and  $N$  is the number of electrons). For the ground state the  $N$  energetically lowest MSOs are occupied, which results in the HF determinant. To construct Slater determinants for excited states we may also use energetically higher orbitals, being vacant in the HF solution. It should be added that all MSOs (both those that for the ground state are occupied and those that are empty) are orthonormal as the eigenfunctions to the same Hartree–Fock operator. This represents an important simplification in the calculations.

In the full CI (FCI) method (precise with respect to the basis chosen)  $M$  HF MOs  $\varphi_i$  ( $i = 1, 2, \dots, M$ ) generate  $N_{CI} = C_M^{\frac{1}{2}N+M_S} C_M^{\frac{1}{2}N-M_S}$  determinants for the system with  $N$  electrons and fixed total spin projection  $M_S$ .

Let us rewrite the many-determinant wavefunction (5.5) in the form

$$\Phi = \sum_{I=0}^{N_{CI}-1} C_I \Phi_I \quad (5.6)$$

where index  $I$  numbers different configurations. The HF approximation corresponds to  $I = 0$  and  $C_0 = 1$  and  $C_I = 0$  for  $I > 0$  in (5.6).

In the FCI method all MSOs are usually supposed to be fixed as the solutions of HF MO LCAO equations but the parameters CI are varied in the expression

$$L = \langle \Phi | \hat{H}_e | \Phi \rangle - \lambda [\langle \Phi | \Phi \rangle - 1] \quad (5.7)$$

We find [8]

$$\begin{aligned} \frac{\partial}{\partial C_K^*} & \left[ \langle \sum_I C_I \Phi_I | \hat{H}_e | \sum_J C_J \Phi_J \rangle - \lambda \langle \sum_I C_I \Phi_I | \sum_J C_J \Phi_J \rangle \right] \\ &= \frac{\partial}{\partial C_K^*} \sum_{I,J} C_I^* C_J \left[ \langle \Phi_I | \hat{H}_e | \Phi_J \rangle - \lambda \langle \Phi_I | \Phi_J \rangle \right] \\ &= \sum_J C_J \left[ \langle \Phi_K | \hat{H}_e | \Phi_J \rangle - \lambda \langle \Phi_K | \Phi_J \rangle \right] = 0 \end{aligned} \quad (5.8)$$

This gives the matrix eigenvalue problem

$$HC = \lambda SC \quad (5.9)$$

where

$$H_{KJ} = \langle \Phi_K | \hat{H}_e | \Phi_J \rangle, \quad S_{KJ} = \langle \Phi_K | \Phi_J \rangle \quad (5.10)$$

and the eigenvalue in (5.9) is equal to

$$\lambda = \frac{\langle \Phi | \hat{H}_e | \Phi \rangle}{\langle \Phi | \Phi \rangle} \quad (5.11)$$

The Hamiltonian operator  $\hat{H} = \hat{h} + \hat{g}$  consists of the single-electron  $\hat{h} = \sum_{i=1}^N \hat{h}(\mathbf{r}_i)$  and two-electron  $\hat{g} = \frac{1}{2} \sum_{i \neq j=1}^N \frac{1}{|\mathbf{r}_i - \mathbf{r}_j|}$  parts. Calculating for operators  $\hat{h}$  and  $\hat{g}$  the matrix elements  $\langle \Phi | \hat{h} | \Phi \rangle$ ,  $\langle \Phi | \hat{g} | \Phi \rangle$  and taking into account the orthonormality of MSOs it can be shown [8] that:

1. Different configurations are orthonormal;
2. For any single-electron operator  $\hat{h}$  there will be nonvanishing matrix elements only between configurations that differ at most in one MSO;
3. For any two-electron operator  $\hat{g}$  there will be nonvanishing matrix elements only between configurations that differ at most in two MSOs. The MOs  $\varphi_i$  are solutions to the HF equations

$$\hat{F}\varphi_i = \epsilon_i \varphi_i \quad (5.12)$$

where

$$\hat{F} = \hat{h} + \sum_{j=1}^N \left( \hat{J}_j - \hat{K}_j \right) \quad (5.13)$$

The  $j$  summation in (5.13) runs over all those orbitals that for the ground-state configuration  $\Phi_0$  are occupied. The Coulomb  $\hat{J}_j$  and exchange  $\hat{K}_j$  operators were defined in (4.16) and (4.17).

Let now the matrix elements  $\langle \Phi_J | \hat{H}_e | \Phi_I \rangle$  be calculated, where  $\Phi_I = \Phi_0$  and  $\Phi_J = \Phi'_n$  (in the  $\Phi'_n$  configuration one electron has been excited from the  $n$ th occupied spin-orbital to the  $\nu$ th empty spin-orbital). It can be shown [8] that both overlap and Hamiltonian matrix elements vanish between the ground-state configuration  $\Phi_0$  and any single-excited one. Having determined all the relevant matrix elements of (5.9) one may obtain the wavefunction (5.6) as well as the corresponding total electron energy of the FCI method. Notice that in contrast to the HF calculations, the FCI calculations do not require any self-consistency with respect to MOs. Diagonalization of the  $N$ -electron Hamiltonian in the basis of Slater determinants gives us energies and WFs of the ground and excited states of the system. It is pertinent to note that for the FCI method the choice of MO basis is not important because any unitary transformation of the MO basis induces unitary transformation of the determinant basis.

The FCI method is the most general of several theories for treating electron correlations. As a variational method it provides upper bounds for the correlation energy. By definition the FCI calculation means that all  $N_{CI}$  configurations (possible for a

given number of electrons  $N$  and  $M$  AO basis functions) are included in the sum (5.6). FCI calculations can be practically realized only for small molecules and small basis sets as the number of possible configurations drastically increases with increasing number of atoms in a molecule and large-scale CI calculations become very expensive.

As an example, the  $\text{CH}_4$  molecule with 10 electrons can be taken [5]. Using a minimal basis set of 9 AOs (1s, 2s, 2p for the C atom and 1s for each of four H atoms) one can construct  $N_{CI} = 43758$  Slater determinants (configurations). When the tetrahedral point-symmetry restrictions are taken into account this number considerably reduces ( $N_{CI} = 5292$  for singlet states). Enlarging the basis set to 35 functions (double-zeta plus polarization basis, see Chap. 8) increases the number of singlets to  $2 \times 10^{10}$ . When larger molecules are considered and larger basis sets are used, the restriction of the chosen configurations is required. There are several ways of achieving this restriction.

1. Develop some procedure for selection of the most important configurations. In its most general form this method is called GenCI. Frequently used are CIS, CID, CISD, CISDT *etc.* methods where 1-electron, 2-electron, 1+2-electron, 1+2+3-electron excitations of electrons from occupied HF states to virtual ones are taken into account. These methods can be called restricted CI (RCI) methods. In some computer codes for molecular calculations automatic selection of the most important configurations is performed [119].

2. Subdivide one-electron MOs into several groups. The most primitive subdivision is in three groups: inactive MOs, active MOs, and virtual MOs. Inactive MOs have occupancy 2 in all determinants in CI expansion, virtual MOs have occupancy 0 in all determinants in CI expansion, and occupancies of active MOs are between 0 and 2. It is supposed that in CI wavefunction only excitations within active MOs are taken into account.

3. Combination of 1 and 2, that is subdivision of MOs into groups and use of RCI in the active space.

If RCI expansions are used or orbitals are subdivided into inactive and active groups, or both, then variation of the orbitals themselves may lead to an essential energy decrease (in contrast to the FCI method where it does not happen). Such combined methods that require both optimization of CI coefficients and LCAO coefficients in MOs are called MCSCF methods. Compared with the CI method, the calculation of the various expansion coefficients is significantly more complicated, and, as for the Hartree–Fock–Roothaan approximation, one has to obtain these using an iterative approach, *i.e.* the solution has to be self-consistent (this gives the label SCF).

One of the most popular methods of MCSCF class is the complete active space SCF (CASSCF) method by Roos [118] where FCI is performed in active space and optimization of MOs is also done. Note that active–active orbital rotations are irrelevant in the framework of this method.

The most popular version of the RCI method application is to restrict by only single- and double-excited configurations (CISD method). It is well known that the CI single (CIS) method finds no use for ground states as the ground-state HF energy is unaffected by inclusion of single excitations (Brillouin theorem, [102]). In the CISD method the singly excited determinants mix with doubles and thus can have some influence on the lowest eigenvalue [102]. What about triple excitations? While there are

no nonzero matrix elements between the ground state and triply excited states, the triplets do mix with the doubles, and can through them influence the lowest-energy eigenvalue (CISDT method). So, here is some motivation for including them. On the other hand, there are a lot of triples, making their inclusion difficult in a practical sense. As a result, triples and higher-level excitations, are usually not accounted for in the RCI methods so that the CISD approximation dominates in CI calculations. The scaling for CISD with respect to system size, in the large-basis limit, is on the order of  $N^6$ . It poses a limit on the sizes of systems that can be practically addressed. Fortunately, the symmetry restrictions allow significant reduction in the computational effort. Similarly, the core orbitals can be frozen in the generation of the excited state.

### 5.1.3 Coupled-cluster Methods

The CC method [120] is one of the mathematically elegant techniques for estimating the electron correlation [102, 121]. In this method, the FCI wavefunction is represented as

$$\Psi_{CC} = \exp(\hat{T})\Psi_{HF} \quad (5.14)$$

The cluster operator  $\hat{T}$  is defined in terms of standard creation–annihilation operators as

$$\hat{T} = \sum_j^{\leq N} \sum_i^{>N} t_j^i a_i^\dagger a_j + \sum_{j_1 < j_2}^{\leq N} \sum_{i_1 < i_2}^{>N} t_{j_1 j_2}^{i_1 i_2} a_{i_1}^\dagger a_{i_2}^\dagger a_{j_1} a_{j_2} + \dots \quad (5.15)$$

Coefficients  $t$  in the last expansion are called the CC amplitudes and they can be defined either variationally or by solving a system of linear equations. The total number of items in (5.15) equals the number of electrons  $N$  because no more than  $N$  excitations are possible. In most computer codes the nonvariational CC method is implemented since the variational one is technically very complicated. Formally operating on the  $\Psi_{HF}$  with  $(1 + \hat{T})$  gives, in essence, the FCI wavefunction. However, the advantage of the CC representation (5.14) lies in the consequences associated with truncation of  $\hat{T}$  [102]. When, in (5.15), only single or double excitations are involved, the method is called CCS or CCD, respectively, when single and double excitations – then CCSD, *etc.* Let us consider as an example the CCD approximation when  $\hat{T} = \hat{T}_2$  and the expansion (5.15) has the form

$$\Psi_{CCD} = \exp(\hat{T}_2)\Psi_{HF} = (1 + \hat{T}_2 + \frac{\hat{T}_2^2}{2!} + \frac{\hat{T}_2^3}{3!} + \dots)\Psi_{HF} \quad (5.16)$$

Note that the first two terms in parentheses of (5.16) define the CID method. However, the remaining terms involve products of excitation operators. Each application of  $\hat{T}_2$  generates double excitations, so the product of two applications generates quadruple excitations. Similarly, the cube of  $\hat{T}_2$  generates hexuple substitutions, *etc.* Such high-level excitations can not be practically included in CI calculations (in this sense the RCI method is called nonsize consistent).

The computational problem of the CC method is determination of the cluster amplitudes  $t$  for all of the operators included in the particular approximation. In the standard implementation, this task follows the usual procedure of left-multiplying the Schrodinger equation by trial wavefunctions expressed as determinants of the HF

orbitals. This generates a set of coupled, nonlinear equations in the amplitudes that must be solved, usually by some iterative technique. With the amplitudes in hand, the coupled-cluster energy is computed as

$$E_{CC} = \langle \Psi_{HF} | \hat{H} | \exp(\hat{T}) \Psi_{HF} \rangle \quad (5.17)$$

In practice, the cost of including single excitations  $\hat{T}_1$  in addition to doubles is worth the increase in accuracy, and this defines the CCSD model. The scaling behavior of CCSD is on the order of  $N^6$ . Inclusion of connected triple excitations (*i.e.* those arising with their own unique amplitudes from  $\hat{T}_3$ , not the disconnected triples arising as products of  $\hat{T}_1$  and  $\hat{T}_2$ ) defines CCSDT, but this is very computationally costly scaling as  $N^8$ , and making it intractable for all but the smallest of molecules. Various approaches to estimating the effects of the connected triples using perturbation theory have been proposed (each with its own acronym). Of these, the most robust, and thus most commonly used, is that in the so-called CCSD(T) method, which also includes a singles/triples coupling term [122]. The (T) approach, in general, slightly overestimates the triples correction, and does so by an amount about equal to the ignored quadruples, *i.e.* there is a favorable cancelation of errors [123]. This makes the CCSD(T) model extremely effective in most instances. Analytic gradients [124] and second derivatives [125] are available for CCSD and CCSD(T), which further increases the utility of these methods. Note, however, that truncated coupled-cluster theory is not variational.

#### 5.1.4 Many-electron Perturbation Theory

We follow in this subsection the many-electron perturbation theory description given in [8]. Often, the Hartree–Fock approximation provides an accurate description of the system and the effects of the inclusion of correlations as, *e.g.*, with the CI or MCSCF methods, may be considered as important but small corrections. Accordingly, the correlation effects may be considered as a small perturbation and as such treated using the perturbation theory. This is the approach of [126] for the inclusion of correlation effects.

For the sake of simplification we shall here consider the ground state but mention that the method in principle can be applied for any state, *i.e.* also for an excited state.

Our starting point is the Hartree–Fock equations (4.13) where the HF operator  $\hat{F}$ , (4.14) is a single-electron operator, being a sum of the one-electron operator  $\hat{h}$ , (4.8), local Coulomb  $\hat{J}$ , (4.16) and nonlocal exchange  $\hat{K}$ , (4.17) operators.

Solving HF equations (4.13) gives not only the  $N$  occupied orbitals, but – in principle – a complete set of  $M$  (total number of AO basis functions) orbitals, since  $\hat{F}$  is a Hermitian operator.

The operator  $\hat{F}$  is a single-electron operator, which we formally wrote as  $\hat{F}(i)$ , where  $i$  numbers electrons. We define now first the  $N$ -electron operator

$$\hat{G}' = \sum_{i=1}^N \hat{F}(i) \quad (5.18)$$

This is also a Hermitian operator, and the  $N$ -electron Slater determinants

$$|\psi_{i_1}, \psi_{i_2}, \dots, \psi_{i_N}| \quad (5.19)$$

define a complete set of eigenfunctions with

$$\hat{G}'|\psi_{i_1}, \psi_{i_2}, \dots, \psi_{i_N}| = (\varepsilon_{i_1} + \varepsilon_{i_2} + \dots + \varepsilon_{i_N})|\psi_{i_1}, \psi_{i_2}, \dots, \psi_{i_N}| \quad (5.20)$$

In particular, for the ground state we have

$$\hat{G}'|\psi_1, \psi_2, \dots, \psi_N| = \left[ \sum_{i=1}^N \varepsilon_i \right] |\psi_1, \psi_2, \dots, \psi_N| \quad (5.21)$$

It follows from (4.38) that

$$\sum_{i=1}^N \varepsilon_i = E_{HF} + \frac{1}{2} \sum_{i,j=1}^N \left[ \langle \psi_i \psi_j | \frac{1}{|\mathbf{r}_1 - \mathbf{r}_2|} | \psi_i \psi_j \rangle - \langle \psi_j \psi_i | \frac{1}{|\mathbf{r}_1 - \mathbf{r}_2|} | \psi_i \psi_j \rangle \right] = E_{HF} + E' \quad (5.22)$$

where

$$E' = \frac{1}{2} \sum_{i,j=1}^N \left[ \langle \psi_i \psi_j | \frac{1}{|\mathbf{r}_1 - \mathbf{r}_2|} | \psi_i \psi_j \rangle - \langle \psi_j \psi_i | \frac{1}{|\mathbf{r}_1 - \mathbf{r}_2|} | \psi_i \psi_j \rangle \right] \quad (5.23)$$

Since the total electronic energy from the Hartree–Fock approximation is the starting point in the perturbation calculation, we see from (5.22) that it is convenient to consider the operator

$$\hat{G} = \hat{G}' - E' \quad (5.24)$$

Operator  $\hat{G}$  has the same eigenfunctions as  $\hat{G}'$  but the eigenvalues have been shifted by  $E'$ . The precise form of  $\hat{G}$  is

$$\hat{G} = \sum_{i=1}^N \hat{F}(i) - E' = \sum_{i=1}^N \hat{h}(i) + \sum_{i,j=1}^N \left[ \hat{J}_j(i) - \hat{K}_j(i) \right] - E' \quad (5.25)$$

This can be compared with the true  $N$ -electron Hamilton operator,

$$\hat{H}_e = \sum_{i=1}^N \hat{h}(i) + \frac{1}{2} \sum_{i \neq j} \frac{1}{|\mathbf{r}_i - \mathbf{r}_j|} \quad (5.26)$$

In order to apply perturbation theory we write

$$\hat{H}_e = \hat{G} + \Delta \hat{H} \quad (5.27)$$

with

$$\Delta \hat{H} = \frac{1}{2} \sum_{i \neq j} \frac{1}{|\mathbf{r}_i - \mathbf{r}_j|} - \sum_{i,j=1}^N \left[ \hat{J}_j(i) - \hat{K}_j(i) \right] + E' \quad (5.28)$$

First-order perturbation theory gives that the ground-state energy changes by

$$\langle \Phi_0 | \Delta \hat{H} | \Phi_0 \rangle \quad (5.29)$$

By using the precise form of the operators in (5.28) one may now show that this term vanishes. The proof of this is very similar to the one showing that the Hamiltonian

matrix elements between the ground state and any single-excited configuration vanish [8]. First, the second-order term is nonvanishing. This term is

$$\sum_{i,j} \sum_{\alpha,\beta} \frac{\langle \Phi_0 | \Delta \hat{H} | \Phi_{i,j}^{\alpha,\beta} \rangle \langle \Phi_{i,j}^{\alpha,\beta} | \Delta \hat{H} | \Phi_0 \rangle}{E_0 - E_{i,j}^{\alpha,\beta}} \quad (5.30)$$

where we have used the fact that only those configurations  $\Phi_{i,j}^{\alpha,\beta}$  where exactly two electrons have been excited from the ground state  $\Phi_0$  have nonvanishing matrix elements in the denominator. To prove this, one uses the fact that  $\Delta \hat{H}$  consists of two-electron operators and that there will be nonvanishing elements only when the two determinants differ by at most two orbitals. It can also be proved that there is no contribution from single-excited configurations. Furthermore,

$$E_0 = \sum_{i=1}^N \epsilon_i - E' = E_{HF} \quad (5.31)$$

and

$$E_{i,j}^{\alpha,\beta} = E_{HF} + \epsilon_\alpha + \epsilon_\beta - \epsilon_i - \epsilon_j \quad (5.32)$$

are the eigenvalues of  $G'$ . The most important aspect is now that the denominator in (5.30) equals

$$-\epsilon_\alpha - \epsilon_\beta + \epsilon_i + \epsilon_j \quad (5.33)$$

due to (5.32). The two first energies are energies of orbitals that for the ground state are vacant, whereas the last two are those of occupied orbitals. This means that the denominator is small (and, hence, the correlation effects are large) when there is a small energy difference between occupied and unoccupied orbitals. This partly explains the results for the H + H system where the correlation is important for large interatomic distances, when the energies of the occupied and unoccupied orbitals approach each other. The result tells us also that, *e.g.*, for compounds containing transition-metal atoms, where there are many (empty and occupied)  $d$  orbitals close to each other, we will expect that correlation effects are important, or, alternatively, that the Hartree–Fock approximation (*i.e.* the single-Slater-determinant approximation) is not a very good one. Turning to the cyclic model of a crystalline solid we conclude that the smaller the bandgap the larger the correlation effects on the ground-state energy.

The higher-order terms to the perturbation series can also be calculated. These will become increasingly complex, but already second-order MP2 perturbation theory provides a very important improvement over the pure Hartree–Fock approximation, and in very many cases results from this method are highly accurate. The higher-order calculations are given the labels MP3, MP4. We do not discuss here many numerical results for the ground state of molecular systems obtained in CI, MCSCF, CC or perturbation theory calculations, rather we refer the reader to monographs [5, 8, 102]. Meanwhile it is clear that direct extension of CI or CC methods to the molecular cluster models of periodic systems is a difficult task. The molecular cluster reasonably models the periodic system when it is chosen sufficiently large to suppress the dangling bonds influence. Even for ionic crystals such a cluster can consist of up to 50–100 atoms. The one possibility of the calculation efforts decreasing is connected with the use of localized MOs in the Slater determinants. The local electron correlation methods are considered in the next subsection.

### 5.1.5 Local Electron-correlation Methods

In the wavefunction-based improvements upon mean-field HF method to account for electron correlation (CI, CC, MP) the demands on the computational resources (CPU time, memory or disk space) exhibit a strong dependence on the system size. Let the system consist of  $N$  atoms. If we assume a given basis set, the cost of MP2 calculations scales between  $N^3$  and  $N^5$  (asymptotic limit) [127]. Higher correlation methods CCSD and CCSD(T) scale as  $N^6$  and  $N^7$ , respectively. The latter means that doubling the size of the molecular system increases the computational costs by a factor of 64 and 128! This high scaling behavior restricts the application range for these accurate and reliable methods to only small molecules, a traditional dilemma in quantum chemistry for a long time (especially, since density-functional theory became available).

Local electron-correlation methods are *ab-initio* wavefunction-based electronic-structure methods that exploit the short-range nature of dynamic correlation effects and in this way allow linear scaling  $O(N)$  in the electron-correlation calculations [128, 129, 131–135] to be attained.  $O(N)$  methods are applied to the treatment of extended molecular systems at a very high level of accuracy and reliability as CPU time, memory and disk requirements scale linearly with increasing molecular size  $N$ .

Linear-scaling electron-correlation methods were developed by: 1) combining the Pulay–Saebo local correlation variant [136] with integral-direct techniques [131] and consequently exploiting the spatial locality of the electron-correlation effect; 2) Laplace-transform techniques suggested in [137] and applied in [129].

In a first step, a linear-scaling local MP2 (LMP2) algorithm was implemented [129, 131, 132]. With this algorithm, MP2 calculations on spatially extended molecular systems including more than 200 atoms and 2000 basis functions can easily be performed on a current low-cost Pentium PC. The linear-scaling approach was also developed for high-level correlation methods, *i.e.* linear-scaling, local CCSD with (T) correction ([133, 134, 142, 143]). In particular, for the CCSD(T) method, reductions in required CPU time were obtained by more than a factor of 1000 compared to the conventional (T) method.

The chemical systems well beyond 1000 basis functions, 100 atoms and some hundred correlated electrons are now within reach of the local electron-correlation methods. It is clear that these methods still are considerably more expensive than modern, linear-scaling DFT algorithms (see Chap. 7), but this now is just due to a higher prefactor, and no longer due to less favorable scaling behavior. Thus, the long-standing scaling problem of *ab-initio* electronic-structure theory clearly is defeated. On the other hand, local correlation methods combine all the well-known advantages of wavefunction-based methods over DFT, like reliability, possibilities for systematic improvements, *etc.*

At first, all these methods were developed for closed-shell systems only. Later research in this area was directed towards local methods for open-shell systems and excited states, local triples corrections beyond (T) (triples included in coupled cluster iterations), [138], local energy gradients for geometry optimizations of large molecules [139], combination of the local correlation method with explicitly correlated wavefunctions. It is evident from the discussion that these local  $O(N)$  methods open the applications of coupled-cluster theory to entirely new classes of molecules, which were far out-of-scope for such an accurate treatment before. Possible applications lie, for example, in the determination of the thermochemistry of reactions involving

large closed-shell (or singlet biradiaclic) organic molecules including the computation of accurate barrier heights (which is an area, where DFT often fails badly). Furthermore, once local MP2 NMR shifts become available, NMR spectra of extended organic molecules could reliably be predicted, which might be helpful in the determination of the structure of such molecules.

Another potential application field are intermolecular complexes and clusters [140]. Here, the local correlation method has some conceptual advantages, insofar that it eliminates the notorious basis-set superposition error (BSSE) [141]. This allows for the BSSE-free calculation of interaction energies structures of large molecular clusters (*i.e.* involving many monomers) without the expensive counterpoise correction that is required in conjunction with canonical methods. There are many more application areas one could think of.

One of the most impressive applications of the local correlation methods is their extension to the periodic systems. Having in mind to discuss this extension on the MP2 level in the next section we restrict the discussion here to the consideration of local MP2 methods for molecular systems with closed shells, referring the reader to the papers discussing local CC methods [128, 133, 134, 142, 143].

In the local MP2 method [131] the occupied canonical MOs of the preceding HF calculation are localized using the Pipek–Mezey [37] localization procedure and keeping the localized orbitals orthonormal. Even though the localization is formally an  $O(N^3)$  step, the localization time is negligible for all the local MP2 calculations.

The use of local orbital bases opens the way for two distinct approximations. First, for the correlation of each electron pair  $ij$  an individual subset (domain) of the virtual orbitals that is independent of the molecular size can be selected. This reduces the scaling of the number of configuration-state functions (CSFs) and corresponding amplitudes from  $O(N^4)$  to  $O(N^2)$ . Secondly, a hierarchical treatment of different electron pairs depending on the minimum distance  $R$  of the two correlated localized occupied MOs (LMOs)  $i$  and  $j$  can be devised. In implementation [131], a subset of atoms is assigned to each LMO according to the procedure of [144]. The pairs  $(ij)$  are then classified according to the minimum distance between any atoms in the two different subsets. *Strong pairs* ( $R \leq 1$  Bohr) are treated at the highest level, *e.g.*, local CCSD. These involve pairs of local orbitals that share at least one atom and typically account for more than 90% of the correlation energy. *Weak pairs* ( $1 < R \leq 8$  Bohr) and *distant pairs* ( $8 < R \leq 15$  Bohr) are (optionally) treated by local MP2, while *very distant pairs* ( $R > 15$  Bohr) can be entirely neglected (in [131], strong and weak pairs are both treated by LMP2). For the distant pairs, the required two-electron integrals can be obtained using multipole approximations [145] leading to substantial savings. The numbers of strong, weak, and distant pairs scale only linearly with molecular size  $N$  whereas the number of very distant pairs scales quadratically with  $N$ . The neglect of very distant pairs leads to an overall linear dependence of the number of CSFs and of the corresponding transformed integrals. The multipole treatment of distant pairs further reduces the number of integrals that must be constructed via the four-index integral transformation; this fact can be exploited to devise an integral transformation algorithm for which all computational resources (CPU, memory, and disk) scale only linearly with  $N$  [131].

In the basis  $\{\chi_\mu\}$  with overlap matrix  $S_{\mu\nu} = \langle \chi_\mu | \chi_\nu \rangle$  the localized occupied orbitals  $|\phi_i\rangle$  are represented by a coefficient matrix  $L$

$$|\phi_i\rangle = \sum_{\mu} |\chi_{\mu}\rangle L_{\mu i} \quad (5.34)$$

The virtual space is spanned by a set of nonorthogonal functions  $\{\tilde{\phi}_r\}$  that are obtained directly from the AOs  $\{\chi_{\mu}\}$  by projecting out the occupied space, *i.e.*

$$|\tilde{\phi}_r\rangle = \left(1 - \sum_{i=1}^m |\phi_i\rangle\langle\phi_i|\right) |\chi_{\mu}\rangle = \sum_{\mu} |\chi_{\mu}\rangle P_{\mu\nu} \quad (5.35)$$

where the projection matrix is defined as

$$P = I - LL^{\dagger}S \quad (5.36)$$

Here indices  $i, j, \dots$ , are used for the occupied LMOs,  $r, s, \dots$ , for projected AOs, and  $\mu, \nu, \rho, \sigma$  for AOs. Quantities in the projected basis are capped by a tilde.

To each LMO  $|\phi_i\rangle$ , a subset  $[i]$  (orbital domain) of the projected AOs  $|\tilde{\phi}_r\rangle$  is assigned. The orbital domains are selected in [131] as described by Boughton–Pulay [144] using a threshold of 0.02, but in addition discarding centers with a Mulliken gross charge below 0.01 (0.03 for H atoms). The electron pairs  $(ij)$  were classified as strong, weak or distant and very distant pairs ( $R > 15$  Bohr) were neglected. The correlation space for the strong and weak electron pairs  $(ij)$  was spanned by pair domains  $[ij] = [i] \cup [j]$ , which are the union of the two related orbital domains. Distant pairs were treated by a multipole approximation, as described in [145]. This requires the use of asymmetric pair domains  $r \in [i]$ ,  $s \in [j]$  for this class of configurations, *i.e.* long-range ionic excitations are neglected. The error of this approximation is negligible if the cutoff distance is chosen to be  $R > 8$  Bohr. The linear dependencies are removed for each individual pair domain separately, as described in detail in [128].

In the local basis, the first-order wavefunction takes the form

$$|\Psi^{(1)}\rangle = \frac{1}{2} \sum_{ij \in P} \sum_{rs \in [ij]} \tilde{T}_{rs}^{ij} |\Phi_{ij}^{rs}\rangle \text{ with } \tilde{T}_{rs}^{ij} = \tilde{T}_{sr}^{ji} \quad (5.37)$$

where  $P$  represents the pair list and it is implicitly assumed that the pair domains  $[ij]$  are defined as described above. Note that the number of projected functions  $r, s \in [ij]$  for a given pair  $(ij)$  is independent of the molecular size. Therefore, the individual amplitude matrices  $\tilde{T}_{rs}^{ij}$  are very compact and their sizes are independent of the molecular size. The total number of amplitudes  $\tilde{T}_{rs}^{ij}$  depends linearly on the molecular size and it is assumed that they can be stored in high-speed memory.

Since the local orbital basis does not diagonalize the zeroth-order HF Hamiltonian, an iterative procedure is required to determine the amplitudes  $\tilde{T}^{ij}$ . By minimizing the Hylleraas functional, one obtains the linear equations [130]

$$\tilde{R}^{ij} = \tilde{K}^{ij} + \tilde{F} \tilde{T}^{ij} \tilde{S} + \tilde{S} \tilde{T}^{ij} \tilde{F} - \sum_k \tilde{S} \left[ F_{ik} \tilde{T}^{kj} + F_{kj} \tilde{T}^{ik} \right] \tilde{S} \quad (5.38)$$

For the desired solution, the residuals  $(\tilde{R}^{ij})_{rs}$  must vanish for  $r, s \in [ij]$ . The quantities  $\tilde{S}$  and  $\tilde{F}$  are the overlap and Fock matrices in the projected basis, respectively,

and the exchange matrices  $\left(\tilde{K}^{ij}\right)_{rs} = (ri|sj)$  represent a small subset of the transformed two-electron integrals. For a given pair  $(ij)$ , only the local blocks  $\left(\tilde{K}^{ij}\right)_{rs}$ ,  $\tilde{F}_{rs}$ , and  $\tilde{T}_{rs}$  for  $r, s \in [ij]$  are needed in the first three terms, while for the overlap matrices in the sum only the blocks connecting the domain  $[ij]$  with  $[ik]$  or  $[jk]$  are required. The sizes of all these matrix blocks are independent of the molecular size. Taking further into account that for a given pair  $(ij)$  the number of terms  $k$  in the summation becomes asymptotically independent of the molecular size if very distant pairs are neglected, it follows that the computational effort scales linearly with molecular size. Further savings are possible by skipping terms with coupling matrix elements  $F_{ik}$  or  $F_{kj}$  falling below a certain threshold, which can be progressively reduced as the iteration proceeds. In the calculations [131] the initial threshold was set to  $10^{-2}$ , and reduced in each iteration by a constant factor until the final value of  $10^{-5}$  was reached. This threshold yields the energy to an accuracy better than  $10^{-7}$  Hartree. This screening reduces the iteration time, but is not essential for achieving linear-scaling. There are two possible algorithms to compute the terms in the sum. In the first algorithm (I) the matrix multiplications  $\tilde{S} \times \tilde{T}^{kj} \times \tilde{S}$  are performed inside the summation, which seems wasteful at first glance but has the advantage that all matrix multiplications are over small local blocks only. Alternatively, in the second algorithm (II) the matrix multiplications are performed outside the summation, but then the accumulated matrix in the square brackets has a much larger dimension, which is the union of all pair domains having either the orbital  $i$  or  $j$  in common. If very distant pairs are neglected, these united-pair domains (UP2) also become independent of molecular size, and therefore algorithm II scales linearly with molecular size as well. A comparison of the measured CPU times for both algorithms for linear chains of polyglycine peptides as a function of the number of monomers [131] shows that both algorithms closely approach linear-scaling. It was found that Algorithm I has a significantly lower prefactor than Algorithm II, and has therefore been chosen as the default in the MOLPRO program [116]. Note that both algorithms would lead to  $O(N^3)$  scaling if the very distant pairs were not neglected. Typically, 5–7 iterations are needed to converge the energy to better than  $10^{-7}$  Hartree, the number of iterations has been found to be essentially independent of the molecular size.

The potential bottleneck is the following: the overlap and Fock matrices are stored in memory as full  $M \times M$  matrices, where  $M$  is the number of AOs. The subblocks needed for a given matrix multiplication are extracted on the fly from these matrices. Full square matrices are also needed for computing and storing the projected orbitals. Thus, the memory requirement formally scales with  $O(M^2)$  but since only very few full matrices are needed, the prefactor is so small that this causes no bottleneck in practice for up to 2000–3000 basis functions. In principle, this bottleneck could be avoided by storing for each pair only the local subblocks needed. This would lead to strict linear-scaling of the memory (or disk) requirements.

Once the amplitudes have converged, the second-order correlation energy is obtained by tracing the amplitudes with the exchange matrices, *i.e.*

$$E_2 = \sum_{ij \in P} \sum_{rs \in [ij]} \left( 2\tilde{T}_{rs}^{ij} - \tilde{T}_{sr}^{ij} \right) \tilde{K}_{rs}^{ij} \quad (5.39)$$

The overall cost to solve the linear equations (5.38) and to compute the second-order energy (5.39) depends linearly on the molecular size and does not constitute any computational or storage bottleneck, once the necessary quantities are available. As in the canonical case, the computational effort of a local MP2 calculation is entirely dominated by the integral transformation required to construct the exchange matrices  $\tilde{K}^{ij}$ . The linear scaling integral transformation is considered in detail in [131, 132].

The optimization of atomic structures requires the availability of analytic energy gradients. In the LMP2 method, the bottleneck is the calculation of the 4-index electron-repulsion integrals (ERIs) and their transformation from the atomic orbitals into the local orbital basis. The computational effort for this step scales with the fourth power of the basis-set size (for fixed molecular size), and therefore the cost quickly increases with basis-set quality. The same is true for the computation of LMP2 (or MP2) energy gradients, which requires a reverse transformation of the amplitudes from the molecular orbitals into the atomic orbital basis. It has been demonstrated for LMP2 [146] and LCCSD [147] that the computational effort for ERI evaluation and transformation can be reduced by 1–2 orders of magnitude using density-fitting (DF) methods. In the DF approach the one-electron charge densities in the ERIs, which are binary products of orbitals, are approximated by linear expansions in an auxiliary basis set. This leads to a decomposition of the 4-index ERIs in terms of 2- and 3-index ERIs, and the  $O(M^4)$  AO dependence of the computational cost is reduced to  $O(M^3)$ . Linear-scaling of the computational cost with molecular size in the context of DF can be achieved by employing the concept of locality also for the fitting functions. The key here is the use of local fitting domains, as discussed in [146, 147]. Furthermore, local-density fitting can be used to speed up the calculation of the exchange part to the Fock matrix in Hartree–Fock calculations [146]. The fitting errors introduced by the DF approximation are systematic and substantially smaller than any other typical errors of the calculation (like basis-set truncation or the error due to the local approximation), provided that a suitable auxiliary basis set is employed. Energy gradients for canonical DF-MP2 on top of an ordinary Hartree–Fock (HF) reference function, *i.e.* without invoking the DF approximation already at the HF level, were first implemented in [148]. An efficient method to compute analytical energy derivatives for the local MP2 approach was presented in [139] where the advantages of the local and density-fitting approximations in the calculation of analytic energy gradients were combined. All 4-index integrals and their derivatives were replaced by products of 2-index and 3-index quantities, which can be manipulated very efficiently. Moreover, the expensive backtransformation of the effective second-order density matrix into the basis was avoided. As a consequence, the method has a much lower prefactor than conventional MP2 gradient programs, and the effort scales only cubically with the basis-set size for a given molecule.

Many applications of local MP2 and local CCSD methods to molecular systems can be found in [132–134, 139, 142, 149].

Another linear-scaling MP2 algorithm was proposed in [129] that is based on the atomic-orbitals Laplace-transform (LT) MP2 method [137]. In this method, the energy denominators (5.32) in (5.30) are eliminated by Laplace-transformation, which paves the way to express the MP2 energy directly in the basis. The price to pay is the additional Laplace integration, which is carried out by quadrature over a few (8–10) points. For each of the quadrature points an integral transformation has to

be performed, but the transformation matrices are much sparser than the canonical MO coefficients; therefore, more efficient prescreening is possible. In this respect, the algorithm [137] is related to the local MP2 method. It appears, however, that due to the multiple transformations the LT-MP2 method has a higher prefactor than the LMP2 method, which requires only a single transformation. On the other hand, the LT-MP2 method does not involve any truncation of the virtual space and therefore yields the exact canonical MP2 energy within a certain accuracy, which is primarily determined by the number of quadrature points and the prescreening thresholds used [131]. An LT linear-scaling coupled-cluster (LTCC) method was also developed and implemented for closed [143] and open [138] shells.

In Sections 5.3 and 5.4 we consider Laplace-transform MP2 (LTMP2) and local MP2 (LMP2) methods extensions to periodic systems, implemented in computer codes GAUSSIAN03 [107] and CRYSCOR [117], respectively. These two extensions are similar to their molecular counterparts in the preliminary calculation of delocalized canonical orbitals (Bloch functions for periodic systems) and further construction of localized crystalline orbitals (Wannier functions for periodic systems). However the correlation effects for periodic systems may be taken into account in another way when the SCF calculations are made in Wannier-functions basis. Such an approach was named the incremental scheme [5, 49, 110] and is considered in the next section.

## 5.2 Incremental Scheme for Local Correlation in Periodic Systems

### 5.2.1 Weak and Strong Electron-correlation

In both molecules and solids the electron-correlation effects may be strong or weak. Let us consider an example of a H<sub>2</sub> molecule. For the two electrons involved, Heitler and London [150] suggested the following correlated ground-state wavefunction

$$\Psi_{HL}(\mathbf{r}_1\sigma, \mathbf{r}_2\sigma) = \frac{1}{N} [\chi_a(\mathbf{r}_1)\chi_b(\mathbf{r}_2) + \chi_b(\mathbf{r}_1)\chi_a(\mathbf{r}_2)] [\alpha_1\beta_2 - \alpha_2\beta_1] \quad (5.40)$$

where the AOs  $\chi_a(\mathbf{r})$  and  $\chi_b(\mathbf{r})$  are centered on atoms  $a$  and  $b$  of the molecule, and the spin functions  $\alpha$  and  $\beta$  denote spin-up and spin-down states, respectively. One notes that this wavefunction does not contain ionic configurations in which two electrons are in the same atomic orbital  $\chi_a(\mathbf{r})$  or  $\chi_b(\mathbf{r})$ . Therefore, their mutual Coulomb repulsion is minimal at the expense of the kinetic energy. The Heitler–London ansatz should work well when the Coulomb repulsion completely dominates the kinetic-energy gain caused by spreading an electron over both atoms. In this case we speak of the strong correlation limit and we expect it to be applicable, *e.g.* when we stretch the H–H bond length to large values.

A very different ansatz applies when the opposite limit holds, *i.e.* when the kinetic-energy gain due to spreading an electron over both atoms dominates the mutual electron repulsions. The molecular-orbital theory describes the two electrons within the independent electron approximation and the bonding molecular orbital of an H<sub>2</sub> molecule is

$$\varphi(\mathbf{r}) = \frac{1}{N} [\chi_a(\mathbf{r}) + \chi_b(\mathbf{r})] \quad (5.41)$$

and it is occupied by the two electrons with opposite spins. Thus, the antisymmetric wavefunction is

$$\begin{aligned}\Psi_{MO}(\mathbf{r}_1, \sigma, \mathbf{r}_2, \sigma) = & \frac{1}{N} [\chi_a(\mathbf{r}_1)\chi_a(\mathbf{r}_2) + \chi_b(\mathbf{r}_1)\chi_b(\mathbf{r}_2) \\ & + \chi_a(\mathbf{r}_1)\chi_b(\mathbf{r}_2) + \chi_b(\mathbf{r}_1)\chi_a(\mathbf{r}_2)] [\alpha_1\beta_2 - \alpha_2\beta_1]\end{aligned}\quad (5.42)$$

Contrary to (5.40), the wavefunction (5.42) contains, with considerable weight, ionic configurations in which both electrons are at one H site. These configurations imply a large Coulomb repulsion between the two electrons. Therefore, the MO LCAO approximation will be a reasonable description of the true or exact wavefunction only when the energy gain due to hybridization of the atomic wavefunction is large as compared with the Coulomb repulsions. In reality, the ground-state wavefunction of H<sub>2</sub> has a form between (5.40) and (5.42). There are ionic configurations present, but their weight is partially suppressed as compared with (5.42). The partial suppression of charge fluctuations, *i.e.* a reduction of the mean-square deviations of the electronic charges is a hallmark of electronic correlations. Charge fluctuations imply configurations in which the electronic charges deviate from the average charge distribution. When in a configuration of the H<sub>2</sub> molecule both electrons are on one atomic site so that the other site is empty, the deviation from the average charge is as large as possible. In fact, we may use the degree of suppression of charge fluctuations as a measure of the strength of electron correlations. A complete suppression of charge fluctuations, as in the Heitler–London wavefunction, implies the strong correlation limit. From the above it is obvious that we can learn much about electron correlations and their influence by studying the wavefunction of a system.

The solids with weak and with strong correlations require different methods of treatment. For example, when the correlations are weak, a wavefunction of independent electrons, *i.e.* a self-consistent field (SCF) or Hartree–Fock (HF) wavefunction seems a good starting point for the implementation of correlation corrections. In a solid, the molecular orbitals are replaced by crystalline (Bloch) orbitals. The latter are solutions of the SCF(HF) equations (4.57).

As we have pointed out above, a possible measure of the strength of electronic correlations is the degree of suppression of charge fluctuations in the true or correlated ground-state wavefunction as compared with those in a corresponding SCF or HF wavefunction. In order to obtain a feeling of how strong those suppressions are, we can calculate them for different chemical bonds [110]. Let  $\Sigma$  denote the ratio

$$\Sigma = \frac{\langle \Phi_{SCF} | \delta n^2 | \Phi_{SCF} \rangle - \langle \Psi_0 | \delta n^2 | \Psi_0 \rangle}{\langle \Phi_{SCF} | \delta n^2 | \Phi_{SCF} \rangle - \langle \Psi_{PC} | \delta n^2 | \Psi_{PC} \rangle} \quad (5.43)$$

where  $\delta n^2 = n^2 - \bar{n}^2$  and  $\bar{n}$  is the average electron number in an orbital being part of a bond, *e.g.*  $\bar{n} = 1$  in a carbon  $sp^3$  orbital of a C–C  $\sigma$ -bond. The wavefunctions  $|\Phi_{SCF}\rangle$ ,  $|\Psi_0\rangle$  and  $|\Psi_{PC}\rangle$  denote the HF ground state, the correlated or true ground state and the ground state we would have if the energy gain due to delocalization, *i.e.* moving an electron from atom to atom, were arbitrarily small. In  $|\Psi_{PC}\rangle$  the charge fluctuations are reduced by the largest amount that is compatible with the charge distribution, *i.e.* with the one-particle density matrix. A value of  $\Sigma = 0$  implies no suppression of charge fluctuations and hence the limit of uncorrelated electrons, while  $\Sigma = 1$  corresponds to the limit of strong electron correlations. For the H<sub>2</sub>

molecule  $\Sigma = 0.15$ , while for a C–C  $\sigma$ -bond  $\Sigma \sim 0.2$ , indicating that electrons in diamond are weakly correlated. The same holds true for silicon. For a C–C  $\pi$ -bond instead one finds  $\Sigma \sim 0.5$  and correlations, *e.g.* in polyacetylene are fairly strong. When we consider the Cu–O planes of the perovskite-like  $\text{La}_2\text{CuO}_4$ , we find that for a Cu site  $\Sigma_{\text{Cu}} = 0.8$ , while for an O site  $\Sigma_{\text{O}} = 0.7$ . Therefore, all Cu configurations different from  $3d^{10}$  and  $3d^9$  are essentially suppressed in  $|\Psi_0\rangle$ , while they still have an appreciable weight in  $|\Psi_{\text{SCF}}\rangle$ . More examples can be found in [5]. Reductions of electronic charge fluctuations as quantified by  $\Sigma$  can be described within a minimal basis set, *e.g.* a set of  $s$  and  $p$  functions for the valence electrons of atoms of the second row. They are caused by interatomic correlations, and we refer to the latter when we speak of weakly or strongly correlated electrons. They should be distinguished from intraatomic correlations that influence electrons on a given atomic site. They require a larger basis set for their description. At least one set of polarization functions must be included in this set, *e.g.* a set of  $d$  functions in the case of atoms of the second row. For more details on these different types of correlations we refer to reference [5]. In order to determine the correlated ground-state wavefunction  $|\Psi_0\rangle$  for the solids with relatively weak correlations one may start from the HF wavefunction  $|\Psi_{\text{SCF}}\rangle$ .

The wavefunction-based (post-Hartree–Fock) methods have received little attention in the electron-correlation theory for crystals compared with those for molecular systems [110]. The progress in the electron-correlation study in solids is connected mainly with density-functional theory (DFT), determining directly various physical properties of a system without a knowledge of the many-electron wavefunction. This feature makes DFT theory simpler and more attractive in the calculations of the electronic structure of crystals. Unfortunately, for the density-functional-based methods there is no procedure for systematic improvement of the calculated results when a higher accuracy is desired. Although often ground-state properties of unexpected accuracy are obtained, this is not always the case, in particular when electron correlations in a crystal are strong. Various improvements that have been applied, like self-interaction corrections (SIC) or LDA + U [151–153], show that they remain essentially uncontrolled. On the other hand, today we can calculate electronic ground-state wavefunctions for small molecules with high precision and there are controlled approximation schemes available for various degrees of accuracy. There is no reason why similar calculations cannot be done for solids; in fact it has been demonstrated that they can [110]. It was already mentioned in Chap. 4, that accurate HF solutions for a variety of crystalline systems have been available for many years now [4, 154]. The clever exploitation of the full symmetry of the crystal and implementation of special algorithms for the exact or approximate estimate of infinite lattice sums, permit the solution of big systems like faujasite (144 atoms, 1728 AOs per unit cell) [155] to be obtained at quite low computational cost. However, the limitations of the HF approximation are well known, essentially due to its neglecting dynamical electron-correlation.

The practical methods of post-HF calculations for solids were discussed during the workshop “Local correlation methods: from molecules to crystals” [156]. Computational strategies were considered and new developments suggested in this area of research (the texts of invited speaker talks are published on an Internet site [156]). In particular, it was stated that the development of post-HF methods for crystals is essentially connected with the progress in the localized Wannier-function (LWF)

generation. In the last decade, LWF have been very intensively used in practical calculations of solids, see [157] and references therein. LWF for correlation calculations can be derived from Bloch states by a localization method as long as one does not have to deal with partially filled bands as in metals. There is also the possibility to generate LWFs directly from HF calculations, as is done in the computer code WANNIER [158].

In order to calculate the correlated ground state  $|\Psi_0\rangle$  and its energy  $\mathcal{E}_0$ , we split the many-electron Hamiltonian  $H$  into

$$H = H_{SCF} + H_{res} \quad (5.44)$$

where  $H_{SCF}$  is the SCF part of the Hamiltonian and  $H_{res}$  is the residual interaction part. We may write

$$\mathcal{E}_0 = \frac{\langle \Phi_{SCF} | H | \Psi_0 \rangle}{\langle \Phi_{SCF} | \Psi_0 \rangle} \quad (5.45)$$

provided  $\langle \Phi_{SCF} | \Psi_0 \rangle \neq 0$ . This will be the case as long as we deal with finite systems.

It is worth mentioning that instead of dividing  $H$  as in (5.44) we could have split it also into a one-electron part  $H_{KS}$  corresponding to the Kohn-Sham equation in density-functional theory (see Chap. 7) and a remaining part. This has the advantage that the energy of the related ground state  $\Psi_{KS}$ , a Slater determinant constructed from solutions of the Kohn-Sham equation, is much closer to the true ground-state energy than is  $\mathcal{E}_0$ . Such a scheme may appear useful for the solids with the strong electron correlations and is used, for example, in the SIC and LDA+U approaches mentioned above. But, treating the remaining part  $H_{res}$  would not be interpretative as an correlation-energy calculation in the sense that is traditional for molecular systems.

Treating a solid implies dealing with essentially infinitely many-electrons. However, in practice, we can correlate only a relatively small number of them. Therefore, we first have to reduce the calculations to a small number of electrons. This can be done by means of the method of increments considered in the next section.

### 5.2.2 Method of Increments: Ground State

A method of increments [111, 159, 160] is a wavefunction-based ab-initio correlation method for solids. This method is closely related to the ideas of the local ansatz (LA), [5] where local operators acting on the SCF wavefunction are used to admix suitable one- and two-particle excitations to the mean-field HF ground state. The many-electron Hamiltonian is split according to (5.44) and the ground-state Hamiltonian  $H_{SCF}$  and the corresponding wavefunction  $\Phi_{SCF} = \Phi_0$  are assumed to be known.

A product of two operators  $A$  and  $B$  in the Liouville space is defined as follows:

$$(A|B) = \langle \Phi_0 | A^\dagger B | \Phi_0 \rangle^c = (A^\dagger B)^c \quad (5.46)$$

The superscript  $c$  indicates that the cumulant of the expectation value is taken, which is given by

$$(A)^c = \langle A \rangle \quad (5.47)$$

$$\langle AB \rangle^c = (AB) - \langle A \rangle \langle B \rangle \quad (5.48)$$

⋮

By using (5.46) the exact ground-state energy  $E$  is written in the following way:

$$E = (H|\Omega) = E_{HF} + (H_I|\Omega) \quad (5.49)$$

where  $\Omega$  plays the role of the wave operator that describes the transformation from the HF ground-state to the exact ground-state. For a solid with well-defined bonds, one can express the HF ground-state  $\Phi_0$  in terms of localized orbitals and label those orbitals by a bond index  $i$ . For ionic systems this index numbers the ions whose states form the occupied bands (for example, oxygen ions in MgO crystal).

The following operators are defined:  $A_i$ , where  $i$  should be considered as a compact index that includes the bond  $i$  as well as the one- and two-particle excitations of bond  $i$ , and  $A_{ij}$ , which describes the two-particle excitations where one excitation is out of bond  $i$  while the other is out of bond  $j$ . Within the restricted operator subspace spanned by  $A_i$  and  $A_{ij}$  the operator  $\Omega$  can be written in the form

$$|\Omega\rangle = \left| 1 + \sum_i n_i A_i + \sum_{\substack{ij \\ (i \neq j)}} n_{ij} A_{ij} \right\rangle \quad (5.50)$$

The parameters  $n_i$  and  $n_{ij}$  in (5.50) are determined from the set of equations

$$\begin{aligned} 0 &= (A_k|H) + \sum_i n_i (A_k|H A_i) + \sum_{\substack{ij \\ (i \neq j)}} n_{ij} (A_k|H A_{ij}) \\ 0 &= (A_{kl}|H) + \sum_i n_i (A_{kl}|H A_i) + \sum_{\substack{ij \\ (i \neq j)}} n_{ij} (A_{kl}|H A_{ij}) \end{aligned} \quad (5.51)$$

where (5.50) was used.

The method of increments provides a scheme in which the set of equations (5.51) and hence the correlation energy is evaluated in a hierarchical order [159].

(a) First, all electrons are kept frozen except for those, *e.g.*, in bond  $i$ . The operators  $A_i$  describe the corresponding excitations of these two electrons and (5.51) reduces to

$$0 = (A_i|H) + n_i^{(1)} (A_i|H A_i) \quad (5.52)$$

Within this approximation, the  $n_i^{(1)}$  are independent of each other and the correlation energy becomes

$$E_{corr}^{(1)} = \sum_i \epsilon_i \quad (5.53)$$

with

$$\epsilon_i = n_i^{(1)} (H_I|A_i) \quad (5.54)$$

(b) In the next step the electrons in two bonds, *e.g.*,  $i$  and  $j$  are correlated. The corresponding  $n^{(2)}$  parameters are determined from the coupled equations

$$\begin{aligned} 0 &= (A_i|H) + n_i^{(2)} (A_i|H A_i) + n_j^{(2)} (A_i|H A_j) + n_{ij}^{(2)} (A_i|H A_{ij}) \\ 0 &= (A_j|H) + n_i^{(2)} (A_j|H A_i) + n_j^{(2)} (A_j|H A_j) + n_{ij}^{(2)} (A_j|H A_{ij}) \\ 0 &= (A_{ij}|H) + n_i^{(2)} (A_{ij}|H A_i) + n_j^{(2)} (A_{ij}|H A_j) + n_{ij}^{(2)} (A_{ij}|H A_{ij}) \end{aligned} \quad (5.55)$$

Again, the increments  $\delta n_i = n_i^{(2)} - n_i^{(1)}$  and  $\delta n_j = n_j^{(2)} - n_j^{(1)}$  are treated as independent of each other in this approximation, and we have

$$E_{corr}^{(2)} = \sum_i \epsilon_i + \frac{1}{2} \sum_{\substack{ij \\ (i \neq j)}} \Delta \epsilon_{ij} \quad (5.56)$$

where

$$\Delta \epsilon_{ij} = \epsilon_{ij} - (\epsilon_i + \epsilon_j) \quad (5.57)$$

and

$$\epsilon_{ij} = (H_I | n_i^{(2)} A_i + n_j^{(2)} A_j + n_{ij}^{(2)} A_{ij} ) \quad (5.58)$$

(c) Analogously, one calculates the three-bond energy increment, which is defined as

$$\Delta \epsilon_{ijk} = \epsilon_{ijk} - (\Delta \epsilon_i + \Delta \epsilon_j + \Delta \epsilon_k) + (\Delta \epsilon_{ij} + \Delta \epsilon_{jk} + \Delta \epsilon_{ik}) \quad (5.59)$$

The correlation energy  $\epsilon_{ijk}$  is that obtained when all electrons are kept frozen except those in bonds  $i$ ,  $j$ , and  $k$ . Again, the increments  $\Delta \epsilon_{ijk}$  are treated as being independent of each other.

The total correlation energy within this approximation is the sum of all increments,

$$E_{corr}^{solid} = \sum_i \epsilon_i + \frac{1}{2} \sum_{\substack{ij \\ (i \neq j)}} \Delta \epsilon_{ij} + \frac{1}{6} \sum_{\substack{ijk \\ (i \neq j \neq k)}} \Delta \epsilon_{ijk} + \dots \quad (5.60)$$

It is obvious that by calculating higher and higher increments the exact correlation energy within the coupled electron-pair approximation at level zero [161] is obtained.

The method of increments is useful only if the incremental expansion is well convergent, *i.e.* if increments up to, say, triples are sufficient, and if increments become rapidly small with increasing distance between localized orbitals. These conditions were shown to be well met in the case of different solids [110, 162]. Ideally, the increments should be local entities not sensitive to the surroundings.

The theory described above has been applied to a great variety of materials, thus demonstrating the feasibility of calculations of that kind. They include the elemental semiconductors [159], III-V [163] and II-VI compounds [164], ionic crystals like MgO [165], CaO [166], NiO [167], alkali halides [168], TiO<sub>2</sub> (with a sizeable amount of covalency) [169], rare-gas crystals [170, 171], solid mercury [172, 173] and the rare-earth compound GdN [174] with the 4f electrons kept within the core. The method of increments allows the CCSD local correlation scheme to be extended from molecules to solids. *In most cases* the program package CRYSTAL [23] was used for the SCF part including a localization procedure for determining the Wannier functions.

*An alternative approach* to CRYSTAL is an embedded-cluster approach called WANNIER, where the localization procedure is part of the SCF calculations. Thereby, the solid is modeled by a central cluster embedded in a field created by the remaining part of the infinite solid [158]. Test calculations at the SCF level for LiH agree very well with those obtained from CRYSTAL. For example, the difference in the SCF ground-state energy is only 0.05 eV per Li when a Li Wannier function extending over four and over three nearest-neighbors is used. Embedded-cluster calculations seem to be a very promising scheme for the future in order to perform high-quality

electronic-structure calculations not only for solids, but also for very large molecules. In the  $\text{CeO}_2$  coupled-cluster calculations [175] several embeddings were tested: from purely point charges up to pseudopotential – surrounding of oxygens to imitate the Ce ions. Embedded large nearly neutral clusters ( $\text{Ce}_4\text{O}_7$ ) as well as several individual clusters, each of which consists of only correlated parts of the solid, were used in the calculations. Analysis of the obtained results allowed the conclusion that all tested embedding schemes should result in the same value of correlation energy. At the same time a large neutral cluster seems to be the best choice for the embedding.

*A third way* of obtaining the SCF ground-state wavefunction is by means of an ordinary cluster calculation. In this case, a fragment of the crystal lattice is used. Its dangling bonds are saturated with hydrogen atoms when dealing with covalent solids and it is surrounded by a large number of point charges when an ionic solid is treated. The wavefunction of the innermost bond or ion can be used to a good approximation for every bond or ion of the solid. An example is  $\text{X}_{35}\text{H}_{36}$  ( $\text{X} = \text{C}, \text{Si}, \text{Ge}, \text{Sn}$ ), where the localized orbital for the central bond agrees with that obtained from CRYSTAL, after a localization procedure has been applied [110].

### 5.2.3 Method of Increments: Valence-band Structure and Bandgap

The valence-band energies for solids can be regarded as energy differences between the  $N$  electron ground-state and a state with  $(N - 1)$  electrons, where one delocalized Bloch electron has been removed. The bandgap can be regarded as the energy difference between the  $N$ -electron ground state and the state with  $(N + 1)$  electrons, where one delocalized Bloch electron has been added. Fixing the number of electrons  $N$  in the ground-state means that PBC are introduced for the main region of a crystal, *i.e.* that the finite size system is considered.

At the SCF level, Koopmans' theorem holds, and the task of determining the band energies and energy gap can be reduced to finding the one-electron energies of the respective Bloch states. It is well known that SCF (HF) calculations tend to overestimate the energy gap, giving too low an energy for the top of the upper valence band and too high an energy of the conduction-band bottom. DFT, on the other hand, yields gaps that are far too small when using the common functionals such as LDA or GGA. To overcome this problem, several DFT-based or hybrid HF-DFT approaches were developed (see Chap. 7). As was already mentioned, DFT-based approaches do not provide clear concepts of systematically improving accuracy and the numerical results essentially depend on the density-functional chosen.

The incremental scheme based on the wavefunction HF method was extended to the calculation of valence-band energies when the electron-correlation is taken into account. In [176, 177] an effective Hamiltonian for the  $(N - 1)$ -electron system was set up in terms of local matrix elements derived from multireference configuration-interaction (MRCI) calculations for finite clusters. This allowed correlation corrections to a HF band structure to be expressed and reliable results obtained for the valence-band structure of covalent semiconductors. A related method based on an effective Hamiltonian in localized Wannier-type orbitals has also been proposed and applied to polymers [178, 179]. Later, the incremental scheme was used to estimate the relative energies of valence-band states and also yield absolute positions of such states [180].

This is important as a prerequisite for the determination of bandgaps. Unfortunately, a further extension of the formalism to also cover conduction-band states (which would complete the information on bandgaps) is not possible along the same lines.

This is because an effective Hamiltonian for  $(N+1)$ -particle states cannot be extracted from finite-cluster calculations (which do not lead to stable states for the extra electron). Instead, a scheme for the calculation of localized states in infinite periodic surroundings is necessary [112, 181]. However, the information on the correlation-induced shift of the absolute position of the upper valence-band edge, already allows for an estimate of correlation effects on bandgaps. In a reasonable approximation, one can assume that correlation effects for the process of removing one electron, and the inverse process of adding an extra electron, are almost symmetric. This approximation seems plausible in view of the fact that the dominant effect of correlations caused by an added electron (hole) is the generation of a long-ranged polarization cloud. The latter moves with the added particle and together with it forms a quasiparticle. A simple estimate of the corresponding gap correction is obtained by calculating the classical polarization-energy gain in a continuum approximation. This is given in [5]:

$$\delta E = \frac{1}{2} \int d^3 \mathbf{r} \mathbf{P} \cdot \mathbf{E} = -\frac{\epsilon_0 - 1}{2\epsilon_0} \frac{e^2}{l_c} \quad (5.61)$$

where  $\mathbf{P}$  is the macroscopic polarization,  $\mathbf{E}$  is the electric field generated by the extra particle and  $\epsilon_0$  is the dielectric constant of the medium. The cutoff  $l_c$  is approximately equal to the length at which the dielectric function,  $\epsilon(r)$ , reaches its asymptotic value,  $\epsilon_0$ , as a function of the distance,  $r$ , from the extra particle. The contribution,  $\delta E$  is approximately the same for an added electron and an added hole because  $l_c$  should be nearly equal in both cases. Therefore, this assumption can be considered as physically justified, and indeed final estimates for the correlation-induced reduction of bandgaps compare reasonably well with experiment [180].

The incremental scheme for the valence band rests on the observation that a HF-hole can be either described in reciprocal or in direct space. In reciprocal space, the  $(N-1)$ -electron states are introduced

$$|\mathbf{k}\nu\sigma\rangle = a_{\mathbf{k}\nu\sigma} |\Phi_{scf}\rangle \quad (5.62)$$

where  $a_{\mathbf{k}\nu\sigma}$  annihilates an electron with wave vector  $\mathbf{k}$  and spin  $\sigma$  in band  $\nu$  of the HF-determinant  $|\Phi_{scf}\rangle$  of the neutral system in the ground state (the spin index will be suppressed as the spinless HF Hamiltonian is supposed to be considered). According to Koopmans' Theorem, its HF one-electron energies can be written in the form

$$\varepsilon_{\mathbf{k}\nu}^{scf} = E_0^{scf} - \langle \mathbf{k}\nu | H | \mathbf{k}\nu \rangle \quad (5.63)$$

where  $E_0^{scf}$  is the HF-ground-state energy.

The states  $|\mathbf{k}\nu\rangle$  can be approximated in terms of basis functions adapted to translational symmetry, with creation – annihilation operators  $b_{\mathbf{k}n}^\dagger, b_{\mathbf{k}n}$ :

$$a_{\mathbf{k}\nu} = \sum_n d_{\nu n} b_{\mathbf{k}n} \quad (5.64)$$

The coefficients,  $d_{\nu n}$  are found by diagonalizing the matrix

$$H_{nn'}^{scf}(\mathbf{k}) = \langle \mathbf{k}n | E_0^{scf} - H | \mathbf{k}n' \rangle \quad (5.65)$$

where  $|\mathbf{k}n\rangle = b_{\mathbf{k}n}|\Phi_{scf}\rangle$  are assumed to be orthogonal, for simplicity.

To base considerations on states with localized extra electrons or holes, the Wannier-type transformation is introduced, yielding localized states within each unit cell. The number of these states equals the number of bands included in the Wannier transformation. In the case of elemental semiconductors such as diamond or silicon these are one-electron states localized at the middle of the nearest atoms bonds so that  $n=1,2,3,4$  (see Chap. 3 for the discussion of the connection between Bloch and Wannier states). A local description arises through the decomposition of the  $b_{\mathbf{k}n}$  into a sum of local operators marked with a cell index  $\mathbf{R}$  (translation vector of the direct lattice):

$$b_{\mathbf{k}n} = \frac{1}{\sqrt{N}} \sum_{\mathbf{R}} \exp(-i\mathbf{k}\mathbf{R}) c_{\mathbf{R}n} \quad (5.66)$$

The operator  $c_{\mathbf{R}n}$  annihilates an electron in a local basis function centered in cell  $\mathbf{R}$ . The sum in (5.66) is precisely the projector onto the irreducible representation  $\mathbf{k}$  of the translation group. In this basis the matrix (5.65) becomes

$$H_{nn'}^{scf}(\mathbf{k}) = \sum_{\mathbf{R}} \exp(-i\mathbf{k}\mathbf{R}) \langle \mathbf{0}n | E_0^{scf} - H | \mathbf{R}n' \rangle \quad (5.67)$$

which can be obtained by the direct-space quantities  $\langle \mathbf{0}n | H | \mathbf{R}n' \rangle$ . Without loss of generality, the functions annihilated by the  $c_{\mathbf{R}n}$  can be chosen as localized orbitals spanning the occupied HF space of the neutral system, *i.e.* as localized two-center bond orbitals for covalent semiconductors. In this case,  $\langle \mathbf{0}n | H | \mathbf{R}n' \rangle$  represents the hopping matrix element between a HF-hole located in the central cell in bond  $n$  to a bond  $n'$  in cell  $\mathbf{R}$ . The direct lattice formalism allows for inclusion of local correlation effects. Such effects are obtained when the HF states  $|\mathbf{R}n'\rangle$  are replaced by their correlated counterparts  $|\mathbf{R}n'\rangle$ , and  $E_0^{scf}$  is replaced by the true ground-state energy,  $E_0$ .

An incremental scheme application to valence bands requires computing the correlated nondiagonal matrix elements  $\langle \mathbf{0}n | H | \mathbf{R}n' \rangle$  in terms of a rapidly converging series of approximations. Figure (5.1) shows the correlated valence-band structure for Si with and without correlation, taken from [177]. The energy at the top of the valence band in both cases has been set to zero. The local matrix elements were extracted from calculations of a set of small molecules  $X_n H_m$  and used to set up an incremental expansion of the bulk band structure.

For computing the absolute shift of the valence bands one needs to consider also the diagonal matrix element

$$\langle \mathbf{0}n | H | \mathbf{0}n' \rangle \quad (5.68)$$

Such a calculation is discussed in detail in [180]. First, a HF-hole is considered in a specific localized bond orbital  $B_i$  of a finite cluster simulating the crystalline semiconductor, with  $B_i$  representing  $|\mathbf{0}i\rangle$ .

Let  $\epsilon_i^{scf}$  denote the HF-value of a hole in this particular bond  $B_i$ :

$$\epsilon_i^{scf} = \langle B_i | E_0^{scf} - H | B_i \rangle \quad (5.69)$$

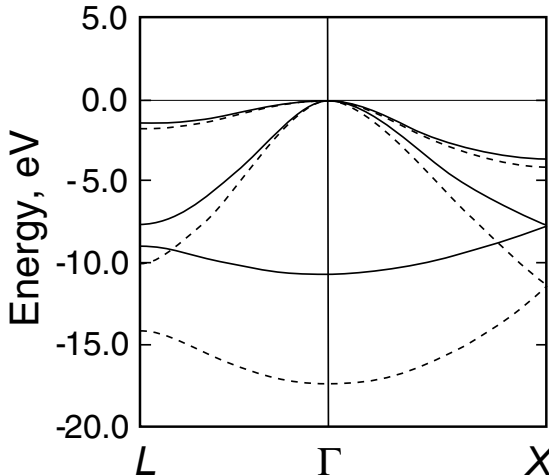


**Fig. 5.1.** The SCF (dashed lines) and correlated (solid lines) band structure for silicon, [177].

As a first step correlation calculations are performed both for the neutral cluster and for the cluster with a hole in bond  $B_i$  by restricting electron excitations to excitations out of this bond only. The energy difference,  $\epsilon_i^{intra}$  between the correlated energies of the neutral and the charged cluster is then an excitation energy improved with respect to the HF-value (5.69) by the inclusion of correlation effects. The difference,

$$\Delta_i^{in} = \epsilon_i^{intra} - \epsilon_i^{scf} \quad (5.70)$$

constitutes the “intrabond” increment of the correlation corrections to the diagonal element. In the next step, correlations are taken into account by releasing electrons out of two bonds, namely the one that contains the hole,  $B_i$ , and one additional bond  $B_j$ . Again, a reference calculation is needed for the neutral cluster, where electrons are excited out of these two bonds. Let us denote the corresponding energy with  $E_{i;j}^0$ . For the case with a hole, a multireference configuration-interaction (MRCI) calculation is performed where the two HF-determinants that contain the HF-hole in bond  $B_i$  and bond  $B_j$ , respectively, are the reference functions forming the model space. The calculation results in a diagonal  $(2 \times 2)$ -eigenenergy matrix with eigenvalues  $\lambda_1$  and  $\lambda_2$  and corresponding eigenvectors  $|\Psi_1\rangle$  and  $|\Psi_2\rangle$ . Due to the diagonalization in the course of the correlation treatment the two eigenvectors are delocalized over the region spanned by the two bonds considered. To get the matrix element of the Hamiltonian between the local states, as in (5.69), the diagonal representation of  $H$  given by the eigenenergies is rotated back into a local matrix representation. To do so, the eigenvectors are projected onto the model space to give the reduced eigenvector matrix,  $\underline{\mathbf{D}}$ :

$$\underline{\mathbf{D}} = \begin{pmatrix} \langle B_i | \Psi_1 \rangle & \langle B_i | \Psi_2 \rangle \\ \langle B_j | \Psi_1 \rangle & \langle B_j | \Psi_2 \rangle \end{pmatrix} \quad (5.71)$$

Due to this projection, the two eigenvectors contained in (5.71) are not strictly orthonormal, but can be made so by means of Löwdin symmetric orthonormalization ( $\underline{\mathbf{D}} \rightarrow \widetilde{\underline{\mathbf{D}}}$ ). The matrix

$$\underline{\mathbf{M}} = \widetilde{\underline{\mathbf{D}}} \begin{pmatrix} E_{i;j}^0 - \lambda_1 & 0 \\ 0 & E_{i;j}^0 - \lambda_2 \end{pmatrix} \widetilde{\underline{\mathbf{D}}}^\dagger \quad (5.72)$$

gives the matrix representation of  $H$  in local states. The diagonal element of this matrix corresponding to the bond  $B_i$  is the correlated value of one-electron energy (5.69) taking into account the effect of correlation of one additional bond  $B_j$ . The procedure can be extended to include further increments. Double-bond increments contain the effect of considering two additional bonds  $B_j, B_k$ , while the triple-bond increments include three further bonds and  $B_j, B_k, B_l$ .

The mainly local character of the correlation effects manifests itself in a rapid decrease of the magnitude of the increments, both with regard to the number of bonds and distances between them. This allows the numerical effort for the calculation to be reduced to just a few increments, which can be evaluated for a finite (embedded) cluster. In [180] it is demonstrated that for diamond and silicon crystals the largest correlation correction comes from the single excitations of the increment called SB1 that takes into account 66% and 64% of the overall correlation effect, respectively. Thus the polarization of the first coordination sphere, stabilizing the ionized system, gives by far the most important separate correlation effect.

The bonds  $B_i$  used in the formulation of the incremental scheme above, can be obtained by a HF-calculation for such a finite cluster with an *a-posteriori* Boys localization [38], which directly yields the bonds as localized HF-orbitals. All increments were derived in [180] from the cluster calculations. C and Si clusters dangling bonds were suppressed by the introduction of hydrogen atoms. The electron correlations dramatically reduce the diagonal elements from their HF eigenvalues  $-0.68$ ,  $-0.51$  hartree to  $-0.45$ ,  $-0.34$  Hartree, for C and Si, respectively. When these values of the diagonal matrix element are fed into a band-structure calculation the absolute shift of the valence bands due to electronic correlations is obtained. The above results lead to a shift of the upper valence band at the  $\Gamma$ -point of 3.90 eV for C and 2.63 eV for Si. To compare these results with experiment, we note that in diamond the HF-gap at the  $\Gamma$ -point has been calculated as 13.8 eV [182], while the experimental one is 7.3 eV. If one attributes the reduction of 6.5 eV in equal parts to the shift of the conduction and the valence band, each shift should amount to 3.3 eV, so we overestimate the shift by 0.6 eV. In the case of Si the (direct) HF-gap at the  $\Gamma$ -point of 8.4 eV [182], is too large by 5.0 eV, as compared to the corresponding experimental value of 3.4 eV, which would attribute a share of 2.5 eV to the valence band shift. The result obtained in [180] of 2.6 eV nearly coincides with this shift. The deviation of these estimates for diamond from the experimental value can be explained by the crude assumption of a symmetric contribution, both for the valence and for the conduction band, to the closing of the direct HF-gap.

Different approaches to the problem of excitations in correlated electron systems are considered in [183]. They are based on a quasiparticle description when electron correlations are weak and on a Green's function or projection operator approach when they are strong. In both cases, intersite correlation contributions to the energy bands require special attention.

It is shown that for both small and large correlation-energy contributions the method of increments reduces the amount of computations decisively.

In [162] a critical review of the incremental scheme of obtaining the energetic properties of extended systems from wavefunction-based *ab-initio* calculations of small (embedded) building blocks is given, which has been applied to a variety of van der Waals-bound (solid Xe), ionic (MgO), and covalent (C and Si) solids in the past few years. Its accuracy is assessed by means of model calculations for finite systems, and the prospects for applying it to delocalized systems are given. The individual determination of the increments of the many-body expansion leads, on the other hand, to the possibility of determining these increments in small finite model systems where a suitable embedding makes the orbitals of a given building block (or pairs, triples, *etc.* of building blocks) similar to those of the extended one. This efficiently reduces the computational effort and obviates the necessity of restricting excitations to the virtual space (by introducing a domain structure) as in the local-correlation methods. This also means that the many-body expansion approach can be used with every quantum-chemical program package.

The correlated band structure of the one-periodic systems (polymers) was efficiently studied using the AO Laplace-transformed MP2 theory discussed in next section.

## 5.3 Atomic Orbital Laplace-transformed MP2 Theory for Periodic Systems

### 5.3.1 Laplace MP2 for Periodic Systems: Unit-cell Correlation Energy

In [184] explicit expressions were presented for electron-correlation at the MP2 level and implemented for the total energy per unit cell and for the band structure of extended systems. Using MP2 for  $E^N$ ,  $E^{N-1}$ ,  $E^{N+1}$  (the total energies of one determinant states for  $N$ ,  $(N-1)$ - and  $(N+1)$ -electron systems) a formula was presented for a direct evaluation of the bandgap rather than obtaining it as a difference of two large numbers. The formulation was given in the conventional crystalline orbitals delocalized over the whole extended system. Later [185] this theory for periodic systems was reformulated. The unit cell MP2 energy was evaluated by Laplace transforming the energy denominator and heavily screening negligible contributions in the AO formulation. This is the extension to periodic systems of the AO Laplace-transformed formulation applied earlier for molecules in [186, 187]. This Laplace MP2 real-space approach avoids the high computational cost of multidimensional wavevector  $\mathbf{k}$  integrations that is critical in order to obtain accurate estimates. It is efficient to treat one-, two and three-periodic crystals (1D, 2D, and 3D systems, respectively). The benchmark calculations [185, 188] were carried out for polymers (1D) and hexagonal BN plane (2D) as well as stacked 1D polymers. The HF portion of calculations was carried out using a PBC option of the molecular computer code Gaussian03 [107].

Here, we briefly present the main points of Laplace MP2 theory for periodic systems.

Equation (5.30) for the correlation energy in the MP2 approximation for molecules can be written in the form

$$E_2 = - \sum_{ij,ab}^{Occ, Vir} \frac{(ia|jb)[2(ia|jb) - (ib|ja)]^*}{\epsilon_a + \epsilon_b - \epsilon_i - \epsilon_j} \quad (5.73)$$

where  $\epsilon_i$  and  $\epsilon_a$  are HF energies of the canonical occupied and virtual MOs, respectively. The two-electron integrals in the canonical MO basis,  $(ia|jb)$ , are obtained by transformation of the Coulomb two-electron integrals in the atom-centered Gaussian-type orbital basis,

$$\begin{aligned} (ia|jb) &= \int i(1)j(2) \frac{1}{r_{12}} a(1)b(2) d\mathbf{r}_1 d\mathbf{r}_2 \\ &= \sum_{\mu\nu\lambda\sigma} (\mu\nu|\lambda\sigma) C_{\mu i}^* C_{\nu a} C_{\lambda j}^* C_{\sigma b} \end{aligned} \quad (5.74)$$

For periodic systems the MP2 correlation energy correction is given by an expression very similar to the molecular case [184]; the only difference is the use of the crystalline Bloch (canonical) orbitals instead of MOs:

$$\begin{aligned} E_2 = -Re \left[ \frac{1}{V_{\mathbf{k}}^4} \int d\mathbf{k}_1 d\mathbf{k}_2 d\mathbf{k}_3 d\mathbf{k}_4 \sum (i(\mathbf{k}_1)a(\mathbf{k}_3)|j(\mathbf{k}_2)b(\mathbf{k}_4)) \right. \\ \left. \times \frac{2(i(\mathbf{k}_1)a(\mathbf{k}_3)|j(\mathbf{k}_2)b(\mathbf{k}_4)) - (i(\mathbf{k}_1)b(\mathbf{k}_4)|j(\mathbf{k}_2)b(\mathbf{k}_3))^*}{\epsilon_a(\mathbf{k}_3) + \epsilon_b(\mathbf{k}_4) - \epsilon_i(\mathbf{k}_1) - \epsilon_j(\mathbf{k}_2)} \right] \end{aligned} \quad (5.75)$$

The generalization to a spin unrestricted formalism is done in a similar fashion as in the molecular case.

The two-electron integrals in the energy formula are now complex and given by

$$\begin{aligned} (i(\mathbf{k}_1)a(\mathbf{k}_3)|j(\mathbf{k}_2)b(\mathbf{k}_4)) = \sum_{pqrs} \sum_{\mu\nu\lambda\sigma} (\mu_p\nu_q|\lambda_r\sigma_s) C_{\mu i}^* C_{\nu a} C_{\lambda j}^* C_{\sigma b} \\ \times \exp[i(-\mathbf{k}_1 p + \mathbf{k}_3 q - \mathbf{k}_2 r + \mathbf{k}_4 s) \cdot \mathbf{g}] \end{aligned} \quad (5.76)$$

Here, the subscripts  $p, q, r, s$  indicate which cell the particular AO belongs to.

Provided that the energy denominator is a strictly positive quantity, the Laplace-transform can be used to write

$$\begin{aligned} &\frac{1}{\epsilon_a(\mathbf{k}_3) + \epsilon_b(\mathbf{k}_4) - \epsilon_i(\mathbf{k}_1) - \epsilon_j(\mathbf{k}_2)} \\ &= \int \exp[(-\epsilon_a(\mathbf{k}_3) - \epsilon_b(\mathbf{k}_4))t] \exp[(\epsilon_i(\mathbf{k}_1) + \epsilon_j(\mathbf{k}_2))t] dt \end{aligned} \quad (5.77)$$

The central feature of the transformed energy denominator is that the indices and attached quantities that were coupled by the denominator are now decoupled, allowing a reordering of the summations. In particular, the four different  $\mathbf{k}$ -integrations can be carried out independently of each other, yielding the following unit-cell MP2 correlation energy formula (where repeated greek indices are contracted):

$$\begin{aligned} E_2 &= \int \sum_{prs} T_{\mu_0\lambda_r}^{\nu_p\sigma_s}(t) [2(\mu_0\nu_p|\lambda_r\sigma_s) - (\mu_0\sigma_s|\lambda_r\nu_p)] dt \\ &= \int \sum_{prs} T_{\mu_0\lambda_r}^{\nu_p\sigma_s}(t) v_{\nu_p\sigma_s}^{\mu_0\lambda_r} dt \end{aligned} \quad (5.78)$$

where the amplitudes  $T$  of the Coulomb integrals transformed by the Fourier-transformed weighted density and complimentary matrices  $X$  and  $Y$ , respectively:

$$T_{\mu_0 \lambda_r}^{\nu_p \sigma_s}(t) = X_{\mu_0 \gamma_t} Y_{\nu_p \delta_u} (\gamma_t \delta_u | \kappa_v \epsilon_w) X_{\lambda_r \kappa_v} Y_{\sigma_s \epsilon_w} = (\underline{\mu}_0 \bar{\nu}_p | \underline{\lambda}_r \bar{\sigma}_s) \quad (5.79)$$

where

$$\begin{aligned} X_{\mu_p \gamma_s} &= \frac{1}{V_k} \int \sum_j C(\mathbf{k})_{\mu j} \exp(-\epsilon_j(\mathbf{k})t) C(\mathbf{k})_{\gamma j} \\ &\quad \times \exp[i\mathbf{k} \cdot (\mathbf{p} - \mathbf{s})] d\mathbf{k}, \\ Y_{\mu_p \gamma_s} &= \frac{1}{V_k} \int \sum_a C(\mathbf{k})_{\mu a} \exp(\epsilon_a(\mathbf{k})t) C(\mathbf{k})_{\gamma a} \\ &\quad \times \exp[i\mathbf{k} \cdot (\mathbf{p} - \mathbf{s})] d\mathbf{k} \end{aligned} \quad (5.80)$$

In matrix elements (5.80) the summation runs over the occupied states ( $j$ ) and virtual states ( $a$ ), respectively.  $C(\mathbf{k})_{\mu j}$  and  $C(\mathbf{k})_{\mu a}$  are the expansion coefficients on the atomic basis for states  $j$  and  $a$  at point  $\mathbf{k}$ .  $V_k$  is the volume of the first Brillouin zone, where integration over  $\mathbf{k}$  is performed.

By comparing the expression (5.78) for the MP2 correlation energy to the canonical reciprocal-space expression (5.75), it becomes clear that the multidimensional quasi-momentum integration has been reduced to a series of independent Fourier transforms (5.80). For all practical purposes, the computational cost of calculating the MP2 correlation energy in the AO basis is independent of the number of  $\mathbf{k}$ -points used in the Brillouin-zone integration. Very dense  $\mathbf{k}$ -point meshes can be used at little extra cost and thus, convergence issues found in earlier [184] reciprocal-space MP2 implementations are avoided. As was shown in [189] the interactions between atoms in the central cell (cell 0) and atoms in the neighboring cells can be quantified by considering the atoms the basis functions in (5.78) are centered on. In the case of periodic MP2 theory, it is particularly interesting to consider a cell-pair partitioning,

$$E_2 = \sum_r e_2^{\mathbf{0}r} \quad (5.81)$$

$$e_2^{\mathbf{0}r} = \int \sum_{ps} T_{\mu_0 \lambda_r}^{\nu_p \sigma_s}(t) [2(\mu_0 \nu_p | \lambda_r \sigma_s) - (\mu_0 \sigma_s | \lambda_r \nu_p)] dt \quad (5.82)$$

Whereas for  $e_2^{\mathbf{0}r}$  the contributions from cells  $\mathbf{p}$  and  $\mathbf{s}$  decay exponentially with intercell distance between  $\mathbf{0}$  and  $\mathbf{r}$ , the correlation contribution from  $e_2^{\mathbf{0}r}$  itself decays quickly, with respect to  $|\mathbf{o} - \mathbf{r}|$  distance.

It has been shown for molecules [189] that the expected  $1/R^6$  decay of distant correlation contributions is closely modeled by the atom-pair partitioning. The same type of decay is also observed in the periodic case and  $e_2^{\mathbf{0}r}$  decays as  $1/|\mathbf{o} - \mathbf{r}|^6$ . Of course, the extent of the lattice summations over  $\mathbf{p}, \mathbf{s}$  in (5.78) greatly affects both the computational cost and the accuracy of the calculation. By taking advantage of the spatial decay properties mentioned above, the energy contraction can be carried out only for cells such that  $|\mathbf{o} - \mathbf{r}| \leq r_{max}$ , while the  $\mathbf{p}$  and  $\mathbf{s}$  lattice summation truncations must be controlled [185].

The smooth decay of the energy contributions in the contraction can, of course, be used to safely truncate the lattice summation. For example, the central cell energy contribution  $e_2^{\mathbf{0}\mathbf{r}}$  provides a good estimate for the contribution from distant cells. In most cases, the magnitude  $e_2^{\mathbf{0}\mathbf{r}}$  is reasonably well approximated by  $e_2^{\mathbf{0}\mathbf{0}}/|\mathbf{o} - \mathbf{r}|^6$ . A system with a unit-cell translation length of 2.5 Å can, thus, be expected to have no significant contribution to the correlation energy contraction beyond approximately the fifth or sixth neighboring cell. However, although relatively few cells need to be considered in the energy contraction ( $r_{max}=4\text{--}6$  cells for 1D systems such as polyacetylene, typically), the spatial framework of duplicated cells needs to be large enough so that all significant charge distributions, including the ones centered near the edge, are properly expanded.

### 5.3.2 Laplace MP2 for Periodic Systems: Bandgap

To correct the HF bandgap at the MP2 level the quasiparticle energy formalism was applied [185, 188]. The quasiparticle (MP2) energies for a given state  $g$  is given by (closed-shell case):

$$\epsilon_g^{MP2} = \epsilon_g + U(g) + V(g) = \epsilon_g + \Delta\epsilon_g^{MP2} \quad (5.83)$$

$$U(g) = - \sum_{i,ab} \frac{(ia|gb)[2(ia|gb) - (ib|ga)]}{\epsilon_a + \epsilon_b - \epsilon_i - \epsilon_g} \quad (5.84)$$

$$V(g) = \sum_{ij,a} \frac{(ia|jb)[2(ia|jb) - (ig|ja)]}{\epsilon_a + \epsilon_g - \epsilon_i - \epsilon_j} \quad (5.85)$$

where  $i$  and  $j$  are occupied, and  $a$  and  $b$  are unoccupied HF orbitals of the system. Consequently,  $\epsilon_i, \epsilon_j$  and  $\epsilon_a, \epsilon_b$  are occupied and unoccupied HF orbital energies, respectively. In a finite-basis calculation, the number of virtual orbitals is finite and determined by the basis set. The Laplace-transform of the energy denominators is applied to Eqs.(5.84) and (5.85) and using an AO-basis formulation one obtains

$$\Delta\epsilon_g^{MP2} = \int_0^\infty dt \sum_{\mu_0 \lambda_r \nu_p \sigma_s} G_{\mu_0 \lambda_r}^{\nu_p \sigma_s}(t) v_{\mu_0 \lambda_r}^{\nu_p \sigma_s} \quad (5.86)$$

where

$$\begin{aligned} v_{\mu_0 \lambda_r}^{\nu_p \sigma_s} &= 2(\mu_0 \lambda_r | \nu_p \sigma_s) - (\mu_0 \sigma_s | \nu_p \lambda_r) \\ (\mu_0 \lambda_r | \nu_p \sigma_s) &= \int dr_1 dr_2 |r_1 - r_2|^{-1} \mu_0(r_1) \lambda_r(r_1) | \nu_p(r_2) \sigma_s(r_2) \end{aligned} \quad (5.87)$$

are two-electron integrals of AOs, for orbitals centered on cells with real-space coordinates  $\mathbf{0}, \mathbf{r}, \mathbf{p}$ , and  $\mathbf{s}$ , respectively. All real-space integrations are performed over all space.  $\Delta\epsilon_g^{MP2}$  is the MP2 correction to the HF eigenvalue as defined in (5.83). The other required quantity in (5.86) is

$$\begin{aligned} G_{\mu_0 \lambda_r}^{\nu_p \sigma_s}(t) &= \sum_{\gamma_t \delta_u \kappa_v \varepsilon_w} X_{\mu_0 \gamma_t}^t Y_{\nu_p \delta_u}^t (\gamma_t \delta_u | \kappa_v \varepsilon_w) \\ &\times [W_{\lambda_r \kappa_v}^t Y_{\sigma_s \varepsilon_w}^t + X_{\lambda_r \kappa_v}^t Z_{\sigma_s \varepsilon_w}^t] \end{aligned} \quad (5.88)$$

The elements of the X and Y matrices are given in (5.80). The elements of the W and Z matrices are defined by

$$W_{\mu_p \gamma_s}^t = C(\mathbf{k}^\dagger)_{\mu g} \exp[-\epsilon_g(\mathbf{k}^\dagger)t] C(\mathbf{k}^\dagger)_{\gamma g} \exp[\mathbf{k}^\dagger(\mathbf{p} - \mathbf{s})] \quad (5.89)$$

$$Z_{\mu_p \gamma_s}^t = -C(\mathbf{k}^\dagger)_{\mu g} \exp[\epsilon_g(\mathbf{k}^\dagger)t] C(\mathbf{k}^\dagger)_{\gamma g} \exp[\mathbf{k}^\dagger(\mathbf{p} - \mathbf{s})] \quad (5.90)$$

where for evaluating the correction to the bandgap, W and Z are constructed from the highest-occupied crystal orbitals (HOCO) and lowest-unoccupied crystal orbitals (LUCO) at point  $\mathbf{k}$  at which the bandgap is minimum. Note that adding a constant value (*e.g.*, the Fermi energy) to all occupied orbital energies, and subtracting the same value from all virtual orbital energies does not affect the denominators of (5.84) and (5.85) nor the MP2 corrections, but they guarantee that all the integrals containing terms such as  $\exp[-\epsilon_i(\mathbf{k})t]$  and  $\exp[-\epsilon_a(\mathbf{k})t]$  are finite. Depending on whether  $g$  is the HOCO or the LUO,  $U(g(\mathbf{k})) + V(g(\mathbf{k}))(g(\mathbf{k}))$  corresponds to the MP2 correction to the ionization potential or the electron affinity. The subtraction of these two corrections, in the spirit of Koopman's theorem, yields the correction to the bandgap. Indirect bandgaps are obtained in a similar fashion by considering two different  $\mathbf{k}$  points.

Finally, (5.86) is approximated by numerical Gauss-Legendre quadrature after a logarithmic transform of the  $t$  variable

$$\Delta\epsilon_g^{MP2} \approx \sum_n \omega_n \sum_{\mu_0 \lambda_r \nu_p \sigma_s} G_{\mu_0 \lambda_r}^{\nu_p \sigma_s}(t_n) v_{\mu_0 \lambda_r}^{\nu_p \sigma_s} \quad (5.91)$$

where  $t_n$  and  $\omega_n$  are the quadrature points and weights, respectively. Usually 3–5 points are enough to evaluate the gap corrections, although more are necessary for the energy [188].

The Laplace MP2 method is applied in [185] for the calculation of the correlation corrections to the bandgap in 1D and 2D systems. Let us consider the results for a 2D system – hexagonal boron nitride in a one-layer model. Like graphite, BN can exist in the form of nanotubes. Because these nanotubes can be viewed as hexagonal BN sheets rolled onto themselves, hexagonal boron nitride has been the object of renewed interest. The main absorption of a thin film of hexagonal BN is found at 6.2 eV and a sharp fall at about 5.8 eV was attributed to the direct bandgap on the basis of semiempirical calculations [190]. The quasiparticle band energy structure at both the Hartree-Fock and the correlated level was calculated in [191] using a method very similar to MP2, the second-order many-body Green-function approach. Hexagonal BN was shown to have a rather complex band structure. Points P and Q are two high-symmetry points within a Brillouin zone with hexagonal symmetry – the hexagon corner and center of edge, respectively. The HF bandgap is minimum at  $\mathbf{k}$ -point P and was evaluated to be 12.46 eV and the quasiparticle gap to be 2.88 eV. At point Q, the HF gap is 16.45 eV and correlation was said to decrease it to 6.48 eV.

PBC MP2 calculations [185] have been unable to corroborate these results. In these calculations, the HF band structure was shown to have a minimum bandgap of 13.73 eV at a point that is neither P nor Q, but rather in between, at a point of higher symmetry still. After examination of the phases of the Bloch orbitals at these points, one can say that point P is best characterized as corresponding to a trans alternation,

whereas  $Q$  corresponds to a *cis* alternation. Laplace MP2 calculation, thus, seems to indicate first, that the Hartree–Fock method favors a form that is a mixture of these two distinct alternations, and second, that for a meaningful calculation, great care should be taken in the convergence of the HF density by using an appropriate  $\mathbf{k}$ -mesh and spatial framework. The correlation correction to the bandgap is very important, as suggested by the MP2 studies. Using 5 Laplace quadrature points and 49 cells to carry out the final contraction, the MP2 gap correction is  $-6.25$  eV. The direct MP2 bandgap can be thus estimated to be at most 7.5 eV, approximately 1.5 eV above the experimental absorption peak. This constitutes a rather good agreement given that much larger basis sets would be needed to properly describe the conduction band that is thought to have a very large extent into the vacuum region.

The Laplace MP2 algorithm of a correlated band-structure calculation is discussed in [188] and applied to trans-polyacetylene.

The post-HF methods for periodic systems were discussed in Sections 5.2 and 5.3. The incremental technique and the Laplace MP2 approach can be mentioned as the most successful approaches to the correlation in solids [5, 192]. The former uses standard molecular codes with clusters of various shapes and sizes to calculate the correlation energy, the latter adopts a formulation of correlation directly in AO basis.

The incremental scheme can be realized using the different post-Hartree–Fock methods (MP2, coupled-cluster CCSD(T)). This scheme is applicable both for non-conducting crystals and metals. The use of finite clusters allows modern sophisticated molecular codes to be applied (like MOLPRO code [116]). The incremental scheme can be used not only for calculation of the energy but also for the energy gradients necessary in the atomic-structure optimization. Unfortunately, the application of the incremental scheme requires some “hand” work when choosing the cluster size and shape for any new system. To the best of our knowledge the code WANNIER (for crystals) [158] allows consideration only of the crystals with a small number of atoms in the unit cell. If clusters are used instead of crystals – the finite nature of the system under consideration affects the results. It is not so easy to set a reasonable cluster to approximate a crystal, especially when there are many atoms in the unit cell. We do not think that these disadvantages are intrinsic features of the incremental scheme, but are mainly connected with the necessity of some standard code generation.

The essential advantage of the Laplace MP2 method is its incorporation in publicly available Gaussian03 [107] computer code with PBC introduction for HF calculations. Due to the Laplace-transform the dense grids of  $\mathbf{k}$ -points can be afforded, the virtual space is not truncated so the method gives the true MP2 energy. The Laplace MP2 band structure can be calculated, including the correlation correction to the bandgap. As no results of its application to 3D systems were published it is difficult to judge how reliable this method is for three-dimensional crystals.

In the next section we consider a local MP2 scheme for periodic systems that is now incorporated in more or less “standard” CRYSCOR correlation computer code for nonconducting crystals [109].

## 5.4 Local MP2 Electron-correlation Method for Nonconducting Crystals

### 5.4.1 Local MP2 Equations for Periodic Systems

The local MP2 electron-correlation method for nonconducting crystals [109] is an extension to crystalline solids of the local correlation MP2 method for molecules (see Sect. 5.1.5), starting from a local representation of the occupied and virtual HF subspaces. The localized HF crystalline orbitals of the occupied states are provided in the LCAO approximation by the CRYSTAL program [23] and based on a Boys localization criterion. The localization technique was considered in Sect. 3.3.3. The label  $im$  of the occupied localized Wannier functions (LWF)  $W_{im} = W_i(\mathbf{r} - \mathbf{R}_m)$  includes the type of LWF and translation vector  $\mathbf{R}_m$ , indicating the primitive unit cell, in which the LWF is centered ( $m = 0$  for the reference cell). The index  $i$  runs from 1 to  $N_b$ , the number of filled electron bands used for the localization procedure; the correlation calculation is restricted usually to valence bands LWFs. The latter are expressed as a linear combination of the Gaussian-type atomic orbitals (AOs)  $\chi_\mu(\mathbf{r} - \mathbf{R}_n) = \chi_{\mu n}$  numbered by index  $\mu = 1, \dots, M$  ( $M$  is the number of AOs in the reference cell) and the cell  $n$  translation vector  $\mathbf{R}_n$ :

$$W_{im}(\mathbf{r}) = \sum_{\mu n} l_{\mu n,im} \chi_{\mu n}(\mathbf{r}) \quad (5.92)$$

AOs constitute the nonorthogonal basis set used for the solution of the HF crystalline equations. To exploit the translation invariance property of LWFs the matrix  $L_{\mu n}^i = l_{\mu n,i0}$  has been introduced.

As in the molecular case (Sect. 5.1.5) for the virtual space the projected AOs (PAOs) are used. To generate PAOs the projector  $\hat{P} = \sum_l^{occ} |l\rangle\langle l|$  onto the occupied HF space is expressed in terms of the density matrix in an AO representation,  $P$ , which is calculated very accurately by the CRYSTAL program via Brillouin-zone integration over all canonical occupied crystalline orbitals  $|l\rangle$ :

$$\hat{P} = \sum_{\mu\nu} |\nu\rangle P_{\mu\nu} \langle\mu| \quad (5.93)$$

The projector onto the virtual space is hence obtained:  $\hat{Q} = 1 - \hat{P}$ . By acting with  $\hat{Q}$  on any one of the local functions  $\chi_{\mu n} \equiv \chi_\beta$  of the original AO set, a Q-projected AO is obtained, or simply PAO:

$$\hat{Q}\chi_\beta(\mathbf{r}) = \sum_{\mu n} Q_{\nu\mu} \chi_{\mu n} = \tilde{\chi}_\beta(\mathbf{r}) \quad (5.94)$$

In what follows, PAOs are identified with the Latin letter corresponding to the Greek letter labeling the AOs from which they are generated,  $\tilde{\chi}_\beta(\mathbf{r}) \leftrightarrow |b\rangle \equiv |bn\rangle$ .

The set of all PAOs so generated (the standard PAO set) constitutes a nonorthogonal, linearly dependent, incomplete set of local functions, strictly orthogonal to all WFs. The problem of the adequacy of the standard set to describe excitations is a delicate issue, because the basis sets usually adopted to solve the HF problem for

crystals are calibrated so as to describe accurately only the occupied subspace. Indications from molecular experience could not be easily transferable to the periodic case, especially in the case of dense crystals.

An essential feature of  $O(N)$  local techniques is the introduction of some metric expressing the “distance” between local functions, and the approximate treatment or total neglect of terms entering the exact equations, according to the distance between the functions on which they depend. The wealth of experience gained in molecular studies can be exploited to this end.

A preliminary step is the definition of WF domains. According to the standard convention, the domain of the  $i$ th WF,  $\mathbf{D}_i \equiv \{\chi_\alpha\}_i$  is the set of all AOs associated with the smallest and most compact set of atoms such that  $\mathbf{D}_i$  “spans”  $W_i$ , it is clearly sufficient to define this set for WFs in the reference cell ( $im = i0$ ). The criterion adopted to select the spanning set is based on the one proposed by Boughton and Pulay [193]. Briefly, one includes in the set, step by step, all AOs belonging to a group of symmetry-equivalent atoms (that is, atoms that are carried into each other by a symmetry operation that reproduces the LWF into itself). At each step, the norm  $N^{BP}$  of the difference between  $W_i$  and the best possible linear combination of AOs in the set is determined. The process is stopped when  $N^{BP}$  is below a certain threshold  $T^{BP}$ , for instance, 0.02;  $T^{BP}$  will be called the Boughton-Pulay (BP) parameter. The sequence according to which atoms are introduced in the domain is as follows. First, a “kernel” is selected including atoms  $A$  that contribute a Mulliken population  $Q_i^A$  larger than a certain threshold, *e.g.*, 0.2 ( $Q_i^A = |\sum_{\beta \in A} \sum_{\alpha} P_{i,\beta}^n P_{i,\alpha}^n (\nu n | \mu m)|; \beta \equiv \nu m|$ );

next, groups of symmetry-related atoms are introduced in order of increasing distance from the kernel (if the distance is the same, atoms with larger  $Q_i^A$  are included first).

After defining the domains, it is expedient to introduce, for any two WFs,  $i$  and  $j$ , a measure  $d_{ij}$  of the distance between them: the standard definition was adopted, namely, the minimum distance between any two atoms belonging to the respective kernels. A classification of LWF pairs by distance is then possible, based on the idea (strongly supported by the results of molecular calculations) that excitations from two local occupied orbitals become progressively less important with increasing distance  $d$  between the two centers. Strong ( $d = 0$ ), weak ( $0 < d \leq d_1$ ), distant ( $d_1 < d < d_2$ ) and very distant ( $d_2 < d$ ) pairs can be so termed, and the respective excitations are treated in a progressively less accurate way; in molecular calculations a standard choice is  $d_1 = 8$  Bohr,  $d_2 = 15$  Bohr (see Sect. 5.1.5). The *total neglect* of contributions from very distant pairs is crucial to the realization of  $O(N)$  computational schemes. In the following, two WFs will be said to be “close-by” each other, if they do *not* form a very distant pair. For each WF pair, a pair-excitation domain or simply, “pair domain”, can be defined, which is the union of the respective domains ( $\mathbf{D}_{i,j} \in \mathbf{D}_i \cup \mathbf{D}_j$ ). Given the biunivocal correspondence between AOs and PAOs (see (5.94)),  $\tilde{\chi}_\beta$  will be said to “belong to”  $\mathbf{D}_{i,j}$  (briefly,  $|\beta\rangle \in \mathbf{D}_{i,j}$ ), if  $\chi_\beta$  does. Excitations from  $i,j$  are usually restricted to PAOs belonging to  $\mathbf{D}_{i,j}$ .

The use of distance criteria in the definition of the shape of the LWF domains and for controlling the level of the approximation is certainly not the only possibility, even if it is the simplest one; for instance, some “topological” index might be used instead, as is already possible in the MOLPRO program [116].

Definitions and conventions introduced are not specific of any given level of local correlation theory and can be used both in CC and MP theory. In [109] the MP2, the simplest local correlation method, was considered.

The first-order perturbative correction to the HF wavefunction (5.37) is written as a combination of contravariant doubly excited configurations

$$|\Psi^{(1)}\rangle = \sum_{ij} |\Psi\rangle_{(ij)} \quad (5.95)$$

where

$$|\Psi\rangle_{(ij)} = \sum_{ab} T_{ab}^{ij} |\Phi_{ab}^{ij}\rangle \quad (5.96)$$

The exact equations that determine the excitation amplitudes  $T_{ab}^{ij}$  are

$$\begin{aligned} 0 = R_{ab}^{ij} = K_{ab}^{ij} + \sum_{cd} \left\{ F_{ac} T_{cd}^{ij} S_{db} + S_{ac} T_{cd}^{ij} F_{db} \right. \\ \left. - S_{ac} \left[ \sum_l \left( F_{il} T_{cd}^{lj} + T_{cd}^{il} F_{lj} \right) \right] S_{db} \right\} \end{aligned} \quad (5.97)$$

Here,  $K_{ab}^{ij}$  is the two-electron “exchange” integral,

$$K_{ab}^{ij} = (ia|jb) \quad (5.98)$$

$F_{il}$  and  $F_{db}$  are elements of the WF or PAO representation of the Fock operator, respectively, and  $S_{ab}$  is the overlap between PAOs. Equation (5.97) must be solved iteratively in the unknown amplitudes until all residuals  $R_{ab}^{ij}$  are zero. For any given set of amplitudes, the Hylleraas functional can be calculated:

$$E_2 = \sum_{(ij)} E_2^{ij} = \sum_{ij} \sum_{ab} (K_{ab}^{ij} + R_{ab}^{ij})(2T_{ab}^{ij} - T_{ba}^{ij}) \quad (5.99)$$

It is easily shown that  $E_2 \geq E^{(2)}$  (the MP2 estimate of the correlation energy), the equality sign holding true only at convergence, when all residuals are zero. In the above equations, the locality assumption is introduced according to the vicinity criteria, by restricting the sums over  $(ij)$  to close-by WF pairs, and those over  $(ab)$  to PAOs  $\in \mathbf{D}_{ij}$ .

For the case of a crystalline application, the fact that all two-index quantities (Fock matrix in the PAO and in the WF representation, overlap matrix in the PAO representation) and all four-index quantities (amplitudes, residuals, two-electron integrals) are translationally invariant was used. For instance,

$$T_{an'+m, bm'+n}^{im, j(n+m)} = T_{an', bm'}^{0, jn} \quad (5.100)$$

Furthermore, the total correction energy can be written as a sum of *correction energies per cell*:  $E_2 = LE_2^{cell}$ , where  $L$  is the total number of cells in the crystal with periodic boundary conditions, and the expression for  $E_2^{cell}$  is the same as in (5.99), but with the sum restricted to “zero-cell” WF pairs, that is, with the first WF in the reference zero cell:

$$E_2^{cell} = \sum_{ijn} E_2^{i0,jn}$$

So, finally, it is confined to a *local* problem, *in the vicinity of the zero cell*. The computation becomes  $O(0)$  with respect to the size  $L$  of the macroscopic crystal and (asymptotically)  $O(N)$  with respect to the size  $N$  of its unit cell.

In order to reformulate (5.97) for a given zero-cell WF pair  $(i0, jn)$  in the periodic case, the following notation is introduced,

$$R_{ab} = K_{ab} + A_{ab} + B_{ab} \quad (5.101)$$

where  $a, b \equiv |am\rangle, |bn\rangle$  and the apex  $i0, jn$  is implicit in all four terms. This allows an “internal” contribution,  $A_{ab}$  (second and third terms in (5.97), which depends on the amplitudes referring to the same  $i0, jn$  pair, and an “external”  $B_{ab}$  contribution (last two terms in (5.97)), which depends on amplitudes involving other WF pairs, to be distinguished.

The most computationally demanding step in the implementation of the local MP2 method is the evaluation of the two-electron integrals  $K_{12} = \langle i_1 a_1 | i_2 a_2 \rangle$ . The straightforward solution is to express them as a linear combination of analytical  $K^A$  integrals over AOs, with coefficients depending on the four local functions. Other techniques are possible, however. In [157] the technique of fitted LWF for local electron-correlation methods was suggested. A very promising one is the so-called density-fitting approximation [146]. Exchange integral  $K$  is obtained in terms of two-center repulsion integrals  $J_{F_1 F_2}$  between two AO-like functions  $F_1(\mathbf{r})$  and  $F_2(\mathbf{r})$ , after expressing each product distribution as a linear combination of a suitable set of “fitting functions”  $F_n(\mathbf{r})$ .

In the problem of the four-index transformation from  $\{K^A\}$  to  $\{K\}$  advantage can be taken, as is customary in molecular calculations, of the fact that the same  $K^A$  is needed for many  $K$  integrals. When the involved LWF are sufficiently distant the approximate multipolar evaluation of  $K$  integrals is used. For an efficient use of this technique, a number of parameters must be accurately calibrated: the distance between WFs beyond which the multipolar technique substitutes the exact one; the value of the parameter defining the truncation of the AO expansion of WFs and PAOs, according to the value of the coefficient or of the distance of the AO from the LWF center. The last two aspects are interrelated: almost negligible tails at very large distance may give enormous high-order multipoles, leading to unphysical values of the interaction.

The possibility to eliminate the WFs’ tails may have a significant impact on the efficiency of LMP2 methods. For these methods the most expensive step is the evaluation and transformation of four-index two-electron integrals, where the computational cost is governed by the spatial extent of the AO support of the individual WFs. The details of the evaluation of these integrals can be found in [109].

To improve the efficiency of the local correlation methods in nonconducting crystals the technique for constructing compact (fitted) WFs in AO basis sets was suggested [157]. Nevertheless, the results are general and can also be applied to other cases where the LCAO expansion of WFs is a critical issue.

### 5.4.2 Fitted Wannier Functions for Periodic Local Correlation Methods

Although WFs are spatially localized, the localization region can be relatively large. As an illustration one can consider the case of diamond [157]. In the LCAO approximation, the WFs are represented by the AO expansion coefficients. The coefficients of the four translationally inequivalent WFs (which correspond to the four upper valence bands of the HF reference) larger (in absolute value) than a threshold of  $10^{-4}$  comprise the atomic functions centered in as much as 435(!) unit cells. Such a wide extent of WFs makes accurate calculations, in particular local MP2 calculations, for solids, computationally difficult.

The slow decay of WFs is often related to their mutual orthogonality, which gives rise to long-range oscillating tails, containing no physically relevant information. For quite sometime now, the possibility to avoid these tails by sacrificing orthogonality has been discussed. Many important results concerning the localization properties of WFs and nonorthogonal localized orbitals (NOLO) (following most of the authors, we do not use the term “Wannier functions” for nonorthogonal localized functions) were obtained for the one-dimensional (1D) case, [194–197]. It was shown that in the 1D case the spread of the NOLOs can be lower than that of the WFs and the term “ultralocalized” was introduced for NOLO [195]. The LCAO expansion of the WF  $W_{i0}(\mathbf{r})$  is defined as

$$W_i(\mathbf{r}) = \sum_{\mu \mathbf{R}} C_{\mu \mathbf{R}, i} \chi_{\mu}(\mathbf{r} - \mathbf{R}) \equiv \sum_{\mu} C_{\mu i} \chi_{\mu}(\mathbf{r}) \quad (5.102)$$

where  $\chi_{\mu}(\mathbf{r} - \mathbf{R})$  represents the atomic function centered in the  $\mathbf{R}$ th unit cell,  $C_{\mu \mathbf{R}, i}$  is the corresponding AO-WF coefficient and index  $\mu$  combines the indices  $\mu$  and  $\mathbf{R}$ . Equation (5.102) defines WFs for the reference unit cell. In [157] it was suggested to maximize the variational functional that defines the Löwdin population of the given localized function on a set of atoms surrounding the center of the localization:

$$I_i^{no} = \sum_{i \in S_i^{(loc)}} \left( C_{\mu i}^{(no-LW)} \right)^2 = \left( W_i^{(no)} | \hat{P}_{S_i^{(loc)}}^{(LW)} | W_i^{(no)} \right) \quad (5.103)$$

where  $C_{\mu i}^{(no-LW)}$  are the expansion coefficients of the NOLO  $W_i^{(no)}(\mathbf{r})$  over the Löwdin-orthogonalized atomic basis set functions  $\phi_{\mu}^{(LW)}(\mathbf{r})$

$$W_i^{(no)}(\mathbf{r}) = \sum_{\mu} C_{\mu i}^{(no-LW)} \phi_{\mu}^{(LW)}(\mathbf{r}) \quad (5.104)$$

$$\phi_{\mu}^{(LW)}(\mathbf{r}) = \sum_{\mu'} \left( S_{\mu' \mu}^{(AO)} \right)^{-1/2} \phi_{\mu'}(\mathbf{r}) \quad (5.105)$$

Here  $S_{\mu' \mu}^{(AO)}$  is the AO overlap matrix, and  $\hat{P}_{S_i^{(loc)}}^{(LW)}$  is an operator projecting onto the space of the Löwdin-orthogonalized AOs from the given set of atoms:

$$\hat{P}_{S_i^{(loc)}}^{(LW)} = \sum_{\mu \in S_i^{(loc)}} |\phi_{\mu}^{(LW)}\rangle \langle \phi_{\mu}^{(LW)}| \quad (5.106)$$

The set of atomic orbitals  $S_i^{(loc)}$  determines the region (or the set of atoms), the corresponding localized functions  $W_i^{(no)}(\mathbf{r})$  should concentrate within.

Maximization of the functional (5.103) with a constraint of normalization of the functions  $W_i^{(no)}(\mathbf{r})$  can be carried out by diagonalizing the matrix of the operator  $\hat{P}_{S_i^{(loc)}}^{(LW)}$  (5.106). The eigenvector of this matrix, corresponding to the highest eigenvalue, holds the coefficients of the expansion (5.104), providing the most localized NOLO in the sense of the functional (5.103). The basis for this matrix could be formed by the Bloch functions of the occupied bands, WFs or even atomic orbitals, projected onto the occupied space.

During generation of the nonorthogonal functions one should not lose the rank of the space spanned by these functions (*i.e.* the linear independency of the functions should be kept). For the crystals of sufficiently high symmetry the rank can be preserved automatically, if the basis used for the variational procedure is symmetrized [198]. The localized functions are basis functions of irreducible representations (irreps) of the site groups related to the centroids of these functions [13]. Thus, if the basis for the functional (5.103) is symmetrized according to these site group and irrep, the centering site of the localized function cannot change [13, 198]. So, when the localized functions are centered on an isolated symmetry point, the symmetrization of the basis keeps the functions linearly independent. Moreover, even if the centroid of the localized function is not an isolated symmetry point (lies on the symmetry axis or in the symmetry plane), but the symmetry of the crystal is still high enough, the rank still may be kept by just taking symmetry into account. Yet, in this case the latter is not guaranteed. If preservation of rank cannot be assured by applying symmetry, one may have to apply some additional constraints – *e.g.*, as suggested in [199], the constraint of the nonsingularity for the localized functions overlap matrix, or in [200], the constraint of freezing the centroids of the localized functions. However, the latter constraint might collide with the requirement of higher localization, if the centers of the functions are not fixed by the symmetry.

The variational procedure should be performed in the space of the first vectors of the corresponding irreps. In other words, only symmetry-unique localized functions are to be obtained variationally. The remaining functions can be generated by applying the appropriate symmetry operators [13, 198]. If there is more than one independent set of localized functions centered on the same site and transforming according to the same irrep, one can obtain all of them in the variational procedure either by taking the eigenfunctions of the diagonalized matrix corresponding to several of the highest eigenvalues instead of just one, or by performing independent procedures for their generation. In the latter case, the variational procedure should be run in the WF-basis, and only one out of several WFs with the considered symmetry, which are centered on the same site, should be included in this basis. The symmetry properties of the WFs and localized functions can be determined in high-symmetry cases without the actual construction of WFs, by analyzing the symmetry of the Bloch functions corresponding to the valence bands. The symmetry information on the NOLOs (the site groups of the WF centroids and the irreps of the site groups) can be extracted using the induced representation theory. Let the symmetry of the WFs be defined unambiguously by the symmetry of Bloch states forming the occupied crystalline orbitals. For example, as was seen in Chap. 3, the four upper valence-band

Bloch states in diamond-type crystals are connected with four WFs centered at the center of the atom–atom bond with the site-symmetry group  $D_{3d}$  and transforming over the one-dimensional  $a_{1g}$ -irrep of this group. The coset representatives in the decomposition of space group  $O_h^7$  in cosets over subgroup  $D_{3d}$  transform this WF into another three equivalent WFs directed along the interatomic bonds. In MgO crystal four upper valence bands, nondegenerated and triple degenerated, correspond to four WFs centered at the oxygen site (site symmetry group  $O_h$  coincides with the point group of a crystal) and transforming over irreps  $a_{1g}$  and  $t_{1u}$  of  $O_h$  group. This is the case when NOLOs different by symmetry are centered at the same atom.

In low-symmetry cases one needs to know also the centering points of the initial orthogonal symmetry-adapted WFs. Let instead of the diamond structure one consider ZnS (spalerite) structure. The centering of four WFs corresponding to four upper valence bands, is defined by symmetry as  $C_{3v}$ , *i.e.* WFs centers are at the atom–atom bond. The actual centering can not be found only from symmetry considerations. In this case, the additional information is necessary to fix the WFs centers. One possibility – to use the nonsymmetry-adapted WFs generated by CRYSTAL code [23] and *a posteriori* to apply the technique of Casassa *et al.* [201] to nonsymmetrized WFs. This technique is considered in the next section. If the WFs centers are not fixed the method under consideration can give highly localized, but linearly dependent functions, which of course are of no use.

In some special low-symmetry cases, when there are several independent WFs of the same symmetry (like  $s$ - and  $p_z$ -WFs of oxygen in rutile structure  $TiO_2$ ), the method also requires the orthogonal WFs themselves to use them as a basis for construction NOLOs. In other cases one can also use Bloch functions as such a basis.

Let the symmetry-adapted localized orthogonal WF be constructed and used furthermore in the post-Hartree–Fock calculations. In numerical local MP2 calculations the sum (5.102) has to be truncated according to some threshold. It is possible to make a truncation based on the magnitude of the calculated WFs coefficients in this sum. In effect, all contributions due to WF coefficients below some threshold could be disregarded. Unfortunately, only relatively loose thresholds can presently be afforded in practical calculations [109] and the numbers of translation vectors  $\mathbf{R}$  taken into account may become a critical parameter significantly influencing the accuracy of the calculation. For example, the four-index transformation of the two-electron integrals in the CRYSCOR computer code [117] uses tolerances for the LCAO coefficients of the WFs of  $10^{-2}$ – $10^{-3}$ . Such loose thresholds can hardly guarantee sufficient accuracy for reliable results, yet tighter thresholds render the calculations too expensive.

In order to treat the truncation of the WFs' tails in an improved way the fitting of WFs was suggested [157]. The localization criterion is introduced

$$I_i^{(fit)} = \int \left( \widetilde{W}_i(\mathbf{r}) - W_i(\mathbf{r}) \right)^2 d\mathbf{r} \quad (5.107)$$

where the function  $\widetilde{W}_i(\mathbf{r})$  is the truncated (fitted) localized function

$$\widetilde{W}_i(\mathbf{r}) = \sum_{\mu \in S_i^{(fit)}} C_{\mu i} \phi_{\mu}(\mathbf{r}) \quad (5.108)$$

The sum (5.108) differs from the infinite sum (5.102) because the summation is made over  $S_i^{(fit)}$  containing an incomplete set of atomic functions centered only on atoms,

which are in a way close to the centroid of the WF  $W_i(\mathbf{r})$ . The criterion (5.107)) is utilized to *fit* the WF spanned by the basis functions within  $S_i^{(fit)}$  (the WF-AO fit domain) in a least-squares sense with respect to the untruncated function. Hence, minimizing the functional (5.107) the fitted WFs are

$$\widetilde{W}_i^{(fit)}(\mathbf{r}) = \sum_{\mu \in S_i^{(fit)}} C_{\mu i}^{(fit)} \phi_{\mu}(\mathbf{r}) \quad (5.109)$$

with the fitted coefficients  $C_{\mu i}^{(fit)}$ , obtained by solving the linear equations

$$\sum_{\mu' \in S_i^{(fit)}} S_{\mu' \mu}^{(AO)} C_{\mu' i}^{(fit)} = \sum_{\mu'} S_{\mu' \mu}^{(AO)} C_{\mu' i} \quad (5.110)$$

The fitting according to (5.110) is formally equivalent to other fitting techniques like density fitting [146, 147], with the AOs from the WF-AO fit domain in the role of the auxiliary basis functions.

By successively adding coordination spheres of atoms and thus their atomic functions to the set  $S_i^{(fit)}$  and refitting the coefficients  $C_{\mu' i}^{(fit)}$  one can finally obtain the fitted WF  $\widetilde{W}_i^{(fit)}(\mathbf{r})$  that to a given tolerance, approximates the exact WF  $W_i(\mathbf{r})$ . Within a chosen tolerance the number of atoms contributing significantly to the fitted WFs  $\widetilde{W}_i^{(fit)}(\mathbf{r})$  is essentially smaller than that of the functions  $\widetilde{W}_i(\mathbf{r})$ .

The fitting procedure can be applied also to the NOLOs, once they are constructed. The localization-fitting process for the NOLOs is most efficient when the set of atomic orbitals and WF-AO fit domain  $S_i^{(fit)}$  at both stages are chosen to be the same. Indeed, small values of the fitting functional  $I_i^{(fit)}$  can be expected, if all the sites with a relatively large value of the NOLO are included in the corresponding WF-AO fit domain. Thus, it does not make sense to use domains  $S_i^{(fit)}$  smaller than  $S_i^{(loc)}$ , since the latter guarantees small values for localized functions only outside its region. On the other hand, if the value for the fitting functional within the chosen WF-AO fit domain is not sufficiently small, it is more efficient, when one does not just enlarge it (as in the case of WFs), but recalculates beforehand the reference NOLOs with the new set  $S_i^{(loc)}$  enlarged accordingly. Actually, only the LCAO coefficients of the NOLO (or WFs)  $C_{\mu i}$  can be refitted by minimizing the functional (5.107). The Löwdin coefficients cannot be modified by the fitting (5.110), since the corresponding AO overlap matrix involved is the identity matrix. This means that the Löwdin coefficients within the WF-AO fit domain are optimal with respect to the functional (5.107) providing its minimum. For orthogonal atomic-like basis sets (such as Löwdin-orthogonalized AOs), the fitting process just corresponds to the truncation of the WF coefficients according to the chosen WF-AO fit domain. Constructing the NOLO in the case of orthogonal basis sets might be more efficient, since the localization functional (5.103) addresses the coefficients relative to the orthogonalized basis-set functions directly. The efficiency of the fitting procedure for the localized functions depends on redundancies carried in the corresponding basis sets, which are large in the case of highly overlapping basis sets. Summarizing the above, the method for obtaining ultralocalized nonorthogonal fitted functions implies the following. Once the symmetry of the localized orbitals has been determined, for every symmetry-unique function the variational procedure

in the symmetrized basis according to the functional (5.103) is performed, followed by generating the fitted functions with limited support from the former by solving (5.110). The sets of the atomic orbitals  $S_i^{(loc)}$  and  $S_i^{(fit)}$  in these two steps are to be taken as the same. If the value of the fitting functional (5.107) does not drop below a predefined threshold, a new star of atoms is added and the process is repeated.

The atomic functions projected onto the orthogonal complement of the occupied space (PAOs), which represent in the framework of local correlation methods the virtual states (see Sect. 5.4.1) are also localized functions. Therefore, similar techniques could also be used to restrict the spatial extent of these PAOs. However, since PAOs are to be constructed by projecting out the space spanned by the *fitted* WFs or NO-LOs (rather than the untruncated parental WFs or NOLOs), one can anticipate that PAOs will automatically possess a limited support, determined basically by the WF AO fit domains.

The efficiency of the method suggested was demonstrated in diamond crystal local MP2 calculations [157]. Since in the present version of the CRYSCOR code [117] a possible nonorthogonality of the localized functions, representing the occupied manifold is not taken into account, the local MP2 energy in diamond has been calculated using only orthogonal WFs with and without fitting. The weak- and distant-pair distances were set to 2 Å. The threshold for PAOs coefficients was set to  $10^{-2}$ . Only the coefficients for the AOs from the first three stars of atoms were included in the transformation of the 4-index integrals (WF fitting was also performed within the first three stars of atoms). Local MP2 correlation energy and timings were then compared with the corresponding values of a reference calculation, which were obtained by employing quite a low screening threshold of  $5 \times 10^{-4}$  for the WF coefficients (smaller thresholds are hardly manageable, presently [109]). Evidently, the fitting of WF coefficients can improve the accuracy and/or reduce the computational cost of the local MP2 calculations for solids. The results of these calculations show: if fitted WFs are used, the estimate of the error in the calculated MP2 energy (the difference between the calculated and reference energies) becomes substantially smaller, while the CPU time of the calculation remains about the same.

### 5.4.3 Symmetry Exploitation in Local MP2 Method for Periodic Systems

In local MP2 calculations of solids it is important to exploit the point symmetry, in order to confine calculations to an irreducible subset; savings of computer time and storage can be substantial in a number of cases of importance. As was discussed in the preceding subsection, the WFs symmetry can be taken into account on the step of WFs generation using the theory of induced representations of space groups and symmetry information about the Bloch states involved in the WFs generation. However, there is another possibility – a symmetrization of a set of constructed LWF before starting the local MP2 calculations. A set of LWF is *a posteriori* symmetrized and symmetry-adapted localized WFs (SALWF) are constructed. A rapid account of this technique was given in [109], while a more detailed analysis can be found in [201].

SALWFs are partitioned into subsets ( $f$ ) belonging to a class  $b$ , each transforming into itself under the operators of a local symmetry point-subgroup  $F_f$  of the full point group  $F$ , while the operations of the associated left- or right-cosets transform subset  $f$  into another equivalent one in the same class. As an example in the diamond crystal

case ( $F = O_h$ ) subset  $f$  consists of one LWF centered in the middle of the atom–atom bond ( $F_f = D_{3d}$ ). The LWFs class consists of four LWFs describing the upper valence band of four subbands. Formally, the symmetrization and the localization procedures are in principle independent: for a chosen localization criteria the LWFs symmetrized before construction have to be close to those symmetrized *a posteriori* their construction. In fact, the real localization of electron density may be sufficiently complicated. In *a-posteriori* symmetrization the choice of  $F_f$  is generally not unique (in the simple case of diamond it was unique) and two possible cases may be mentioned: (i) The subsets are chosen so as to minimize the order of  $F_f$ ; (ii)  $F_f$  is chosen so that the representation of its elements in the SALWF basis set is maximally factorized according to the irreducible representations of  $F_f$ . Functions optimally localized under a given criterion may feature both properties (as is the case when a regular representation is possible), any one of them, or none of them [201]. For example, let us consider four nonsymmetrized LWFs defined by Bloch states of four upper valence bands in MgO crystal (the valence electron pairs related to the anions are supposed to be localized according to the Boys criterion [38]). In that situation, the localization criterion is just compatible with an  $sp^3$  hybridization but, as the local point-symmetry group of the atom is cubic and not tetrahedral, the set of orbitals is constrained to form a reducible representation of  $O_h$  with no privileged orientation. The LWFs fall into a situation not described by the previously mentioned cases. A similar behavior is displayed by “banana” orbitals in triple bonds, or core electrons in a variety of highly symmetric crystals.

For the scope of numerical applications, even in those cases where localization gives rise to definite symmetry properties (as in the diamond case), accurate symmetry equivalences are only reached under strong numerical conditions in the localization algorithm. This can be, in several cases, very computationally demanding and a more efficient shortcut to obtain accurate symmetry equivalence together with a good localization character is therefore desirable.

Due to the previously mentioned difficulties of an *a priori* prediction of what kind of symmetry behavior will be compatible with good localization properties under efficient criteria, in [201] an *a-posteriori* strategy was adopted based on a “chemical” analysis of the problem, which is made easier by the fact that WFs are expressed as a linear combination of atomic orbitals (AOs); it represents a compromise between the two criteria previously mentioned. Starting from a set of localized WFs, the main steps of the presented scheme are:

- (1) recognize if classes of symmetry-related single-WF subsets already exist;
- (2) classify the remaining WFs, if possible, into atomic or bond WFs, according to the Mulliken population analysis. The extension to periodic systems of Mulliken population analysis introduced for molecules is considered in Chap. 9. The electron density of LWF  $W_{i0}$  is partitioned into atomic populations  $Q_{AM}^i$ , assigned to different atoms in the primitive cells  $M$ . One can preclassify  $W_{i0}$  as
  - a) Atomic LWF: an atom  $AM$  exists for which  $Q_{AM} > 0.9$ . This category includes “core” LWFs, but also LWFs associated with valence AOs in anions of very ionic systems. “Lone-pair” or “hydrogen-bond” LWFs may also enter this category.
  - b) Bond LWF: two near-by atoms  $AM, BN$  exist such that  $Q_{AM}^i + Q_{BN}^i \geq 0.9$ , and the ratio  $Q_{AM}^i/Q_{BN}^i$  is comprised between 1 (pure covalency) and 1/4 (high ionicity).
  - c) Atypical LWF:  $W_{i0}$  does not enter the previous categories.

- (3) using the previous information recognize the subsets, the site-symmetry subgroups  $F_f$  and the irreducible representations to which they belong;
- (4) generate, and orthonormalize the new SALWFs.

A criterion based on a Mulliken analysis is adopted again to subdivide atomic LWFs associated to the same irreducible atom  $A$  into shell-subsets (without loss of generality,  $A$  can be assumed to be in reference 0 cell). The bond LWFs are the representatives of double and triple bonds, and are assigned to the  $(AO - BM)$ -subset. Thus, part of the LWFs, classified as SALWFs, only require numerical refinement, or the subset including all the atypical ones. All others are grouped in subsets  $S$ , either of a “shell” or of a “bond” type, each one comprising  $ns$  members.

Bond and atomic LWFs are characterized by one and two atomic centers, respectively. Using this information the subgroup  $G_f$  that leaves invariant the corresponding symmetry element (either a center or an axis in real space) is found. The irreducible representations of  $G_f$  are found and for each of them the representative matrices are first constructed and, then, used to build up the idempotent projector operators for the first row and the shift operators for all other rows. The details of this procedure can be found in [201, 202].

Finally, when all atomic and bond subsets have been symmetry adapted, they are orthonormalized. Orthonormalization is performed in two steps. Using a given net in reciprocal space, the nonorthogonal functions generated in the previously described steps are transformed into Bloch functions, orthonormalized using a Löwdin scheme in each  $\mathbf{k}$ -point of the net, and backtransformed into Wannier functions. This is accomplished using a straightforward modification of the Wannierization scheme reported in [203]. At this step, the resulting SALWFs are orthonormal just under Born–Von Karman cyclic conditions. If necessary, the functions can be corrected to satisfy accurate orthonormalization by integration over the whole real space. We discussed a method [201] for generating from a set of (generally nonsymmetric) localized Wannier functions (LWF), an equivalent set of orthonormal functions that are adapted not only to the translational, but also to the point symmetry of the crystalline structure, while maintaining good locality features. They are called therefore SALWFs (symmetry adapted localized Wannier functions). At variance with other methods based on the induced representations theory this method is largely based on a chemical analysis of the structure of LWFs: despite this somewhat empirical character, it performs very well with a variety of molecular and crystalline systems.

The effectiveness of this procedure was demonstrated [201] by way of examples, with reference to four test cases: the  $\text{CH}_3\text{Cl}$  molecule (with  $C_{3v}$  symmetry), linear polyacetylene, lithium bromide with the rocksalt structure (symmorphic space group  $O_h^5$ ) and crystalline silicon (nonsymmorphic space group  $O_h^7$ ). SALWFs generated appear well suited for use in the local correlation methods. In future, the symmetrized fitted LWFs can be used to have more a efficient computational procedure of LMP2 calculations.

Concluding the consideration of the modern electron-correlation methods for periodic systems we see that the first-principles LCAO post-HF methods for solids are essentially more difficult compared with those for the molecular systems. This is why until now the simpler semiempirical approaches have been popular for crystals. These approaches allow the intra-atomic and partly interatomic correlation effects to be taken into account by introduction of semiempirical parameters calibrated on the ba-

sis of first-principles calculations or experimental data. In many cases these methods give correct qualitative characteristics of the crystalline electronic structure that may be later corrected in the first-principles calculations.

The semiempirical LCAO methods for periodic systems are considered in the next chapter.

## Semiempirical LCAO Methods for Molecules and Periodic Systems

### 6.1 Extended Hückel and Mulliken–Rüdenberg Approximations

#### 6.1.1 Nonself-consistent Extended Hückel–Tight-binding Method

During the early days of molecular quantum chemistry, when computational power was minimal, the semiempirical LCAO methods were applied even for small molecules [204, 205]. Later, at the beginning of the 1970s, these approaches were extended to crystalline solids [206–208] and allowed calculations of their properties to be made in the period when the first-principles HF LCAO calculations for solids were practically unreliable. The limitations of the first-principles HF LCAO calculations are caused mainly by necessity of evaluation of multicenter two-electron integrals whose number grows proportionally as  $N^4$  ( $N$  is the number of AOs used). Therefore, in the quantum chemistry of large molecules and solids the semiempirical calculations continue to appear in large numbers in chemical literature. We refer the reader to the recently published book [102], Chap.5, where the corresponding bibliography of semiempirical methods for molecules can be found.

In this chapter we discuss the extension of LCAO semiempirical methods of molecular quantum chemistry to periodic systems and provide a comparison between semiempirical Hamiltonians for molecules and crystals.

The approximate LCAO methods of quantum chemistry can be divided on empirical (semiquantitative) and semiempirical grounds.

The *empirical (semiquantitative)* methods are based on a one-electron effective Hamiltonian and may be considered as partly intuitive: extended Hückel theory (EHT) for molecules [204] and its counterpart for periodic systems – the tight-binding (TB) approximation. As, in these methods, the effective Hamiltonian is postulated there is no necessity to make iterative (self-consistent) calculations. Some modifications of the EHT method introduce the self-consistent charge-configuration calculations of the effective Hamiltonian and are known as the method of Mulliken–Rüdenberg [209].

The *semiempirical* methods are based on the simplification of the HF LCAO Hamiltonian and require the iterative (self-consistent) density matrix calculations: complete and intermediate neglect of differential overlap (CNDO and INDO – approximations), neglect of diatomic differential overlap (NDDO) and others, using the neglect of differential overlap (NDO) approximation.

Both groups of methods use the valence-electron approximation, *i.e.* all core electrons are ignored. It is assumed that core electrons are sufficiently invariant to differing chemical environments so that changes in their orbitals as a function of environment are of no chemical consequence, energetic or otherwise. The valence atomic orbitals are represented by a so-called Slater-type orbital (STO). The mathematical form of a normalized STO (in atom-centered polar coordinates) is

$$\chi_{\mu}(\mathbf{r}) = R_{\mu}(r)Y_{lm}(\theta, \varphi) = N_{\mu}r^{n-1} \exp(-\zeta_{\mu}r)Y_{lm}(\theta, \varphi) \quad (6.1)$$

The radial part  $R_{\mu}(r)$  of STO  $\chi_{\mu}(\mathbf{r})$  depends on  $n$  (the principal quantum number for the valence orbital) and an orbital exponent  $\zeta_{\mu}$  that can be chosen according to a simple set of rules developed by Slater [210], (see Sect. 8.1.1), in EHT and TB methods or considered as semiempirical parameters. The angular parts are spherical harmonic functions  $Y_{lm}(\theta, \varphi)$  depending on the angular momentum quantum numbers  $l$  and  $m$  (in the majority of cases their real combinations  $Y_{lm}(\theta, \varphi) \pm Y_{l-m}(\theta, \varphi)$  are used, giving for  $l = 1, 2, 3$  the angular part of  $p, d, f$  atomic functions, respectively). STOs have a number of features that make them attractive. The orbital has the correct exponential decay with increasing  $r$ , the angular component is hydrogen-like, and the 1s orbital has, as it should, a cusp at the nucleus (*i.e.* is not smooth). More importantly, from a practical point of view, overlap integrals between two STOs as a function of interatomic distance are readily computed. In simple Hückel theory (SHT) all STOs in a molecule are supposed to be orthogonal, in EHT the AOs overlap matrix  $S$  is computed directly.

In EHT for molecules the MOs and the corresponding one-electron energies are found as the eigenfunctions and eigenvalues of the effective Hamiltonian  $H$ :

$$\det |H_{\mu\nu} - S_{\mu\nu}\epsilon_i| = 0 \quad (6.2)$$

The dimension of the matrices  $H$  and  $S$  is equal to the whole number of the atomic STOs.

The values for diagonal elements  $H_{\mu\mu}$  are taken as the negative of the average ionization potential for an electron in the appropriate valence orbital. Of course in many-electron atoms, the valence-shell ionization potential (VSIP) for the ground-state atomic term may not necessarily be the best choice for the atom in a molecule, so this term is best regarded as an adjustable parameter, although one with a clear, physical basis. VSIPs have been tabulated for most of the atoms in the periodic table [211, 212].

The nondiagonal elements (for the nearest neighbors known as resonance integrals) are more difficult to approximate. Wolfsberg and Helmholz [213] suggested the following convention:

$$H_{\mu\nu} = \frac{K}{2} (H_{\mu\mu} + H_{\nu\nu}) S_{\mu\nu} \quad (6.3)$$

where  $K$  is an empirical constant and  $S_{\mu\nu}$  is the overlap integral. Thus, the energy associated with the matrix element is proportional to the average of the VSIPs for the two orbitals  $\mu$  and  $\nu$  times the extent to which the two orbitals overlap in space (note that, by symmetry of angular parts the overlap between different valence STOs on the same atom is zero). Originally, the constant  $K$  was given a different value for matrix elements corresponding to  $\sigma$ - and  $\pi$ -type bonding interactions. In modern

EHT calculations, it is typically taken as 1.75 for *all* matrix elements, although it can still be viewed as an adjustable parameter when such adjustment is warranted.

Because the matrix elements do not depend on the final MOs in any way (unlike HF- theory), the process is not iterative, so it is very fast, even for very large molecules.

The very approximate nature of the resonance integrals in EHT makes it inaccurate for the calculation of the atomic positions in molecules so that use of EHT is best restricted to systems for which experimental geometries are available. For such cases EHT tends to be used today to generate qualitatively correct MOs in much the same fashion as it was used 50 years ago [102]. In the 21st century, such a molecular problem has become amenable to more accurate treatments (HF and post-HF methods, see Chapters 4 and 5), so the province of EHT is now primarily very large systems, like extended solids, where its speed makes it a practical option for understanding the band structure of bulk and surface states [214].

In the EHT method for solids, crystalline orbitals (4.55) are expanded over the Bloch sums (4.53) of valence AOs and the secular equation

$$\det |H_{\mu\nu}(\mathbf{k}) - S_{\mu\nu}(\mathbf{k})\epsilon_i(\mathbf{k})| = 0 \quad (6.4)$$

is solved where  $H_{\mu\nu}(\mathbf{k})$  and  $S_{\mu\nu}(\mathbf{k})$  are, respectively, the matrix elements of the effective one-electron Hamiltonian and of the overlap integrals between two LCAO Bloch sums expressed as

$$H_{\mu\nu}(\mathbf{k}) = \sum_{\mathbf{R}_n} \exp(i\mathbf{k}\mathbf{R}_n) H_{\mu\nu}(\mathbf{r} - \mathbf{R}_n), \quad S_{\mu\nu}(\mathbf{k}) = \sum_{\mathbf{R}_n} \exp(i\mathbf{k}\mathbf{R}_n) S_{\mu\nu}(\mathbf{r} - \mathbf{R}_n) \quad (6.5)$$

The difference between the matrix elements  $H_{\mu\nu}(\mathbf{k})$  (6.5) and  $F_{\mu\nu}(\mathbf{k})$  (4.56) is due to the difference between HF and EHT Hamiltonians: the former includes one-electron and two-electron parts and depends on the crystalline density matrix (4.65), the latter are assumed to be proportional to the overlap matrix elements. The explicit form of  $H_{\mu\nu}(\mathbf{r} - \mathbf{R}_n)$  is given as follows

$$H_{\mu\nu}(\mathbf{r} - \mathbf{R}_n) = \frac{1}{2} K_{\mu\nu} (H_{\mu\mu} + H_{\nu\nu}) S_{\mu\nu}(\mathbf{r} - \mathbf{R}_n) \quad (6.6)$$

where the proportionality constant  $K_{\mu\nu} = 1$  for  $\mu = \nu$  and otherwise  $K_{\mu\nu}$  is an empirically adjustable parameter,  $H_{\mu\nu}$  is the valence-state ionization potential (VSIP) of AO  $\chi_\mu$ . These matrix elements are fixed at the beginning of EHT calculations so that the secular equations (6.4) are solved independently for different wavevector  $\mathbf{k}$  values and the calculation does not require the self-consistency. Due to the translation symmetry the order of secular equation (6.4) is equal to the number of valence AOs per primitive cell. The field of lattice summations in matrix elements  $H_{\mu\nu}(\mathbf{k}), S_{\mu\nu}(\mathbf{k})$  depends on the model chosen. In the infinite-crystal model the summations are made up to the distance when the overlap integrals  $S_{\mu\nu}(\mathbf{r} - \mathbf{R}_n)$  become less than some threshhold. In the cyclic-cluster model these summations are made in such a way that the lattice summation is restricted by the cyclic-cluster translation vector. As was already mentioned the shape and size of the cyclic cluster chosen defines the  $\mathbf{k}$ -vectors set, for which the calculation is in fact made. As EHT is a nonself-consistent method (the matrix elements are calculated independently for different  $\mathbf{k}$ -vectors) the choice of one or another restriction for summation in the direct lattice is mainly

a conceptual point. The EHT approach to solids (known also as the tight-binding (TB) approximation) is applied in many cases as an interpolation method, to be used in connection with more accurate calculation schemes or experimental data [58]. As an example, we consider the EHT band structure of Si crystal, fitted in [214] to reproduce the experimental bandgap and optical properties. The lattice summation was taken over all atoms within the sixth-nearest neighbors. In order to reproduce optical properties it turned out that four proportionality constants ( $K_{ss}$ ,  $K_{sp\sigma}$ ,  $K_{pp\sigma}$  and  $K_{pp\pi}$ ) are required for each shell of neighbors resulting in 24 fitting parameters. Adding the ionization potentials  $I_s$ ,  $I_p$  and orbital exponents  $\zeta_s$ ,  $\zeta_p$  for the Slater-type AOs (which are also treated as fitting parameters), this amounts to a total 28 adjustable fitting parameters. These parameters have been determined by fitting to the pseudopotential band-structure calculations for the experimental value of the cubic lattice constant [215] and experimental data. The best-fit parameters are listed in Table 6.1.

**Table 6.1.** Fitted parameters for Si crystal, [214]

Si	Neighbors					
	1	2	3	4	5	6
$K_{ss}$	1.403	1.523	0.955	1.355	5.450	4.550
$K_{sp\sigma}$	1.409	1.931	2.095	0.375	2.485	0.000
$K_{pp\sigma}$	1.890	3.050	3.780	1.750	0.000	1.800
$K_{pp\pi}$	2.290	2.570	0.150	2.150	1.000	4.500

In fitting the bands, special weight has been given to the valence and conduction bands at  $\Gamma$ , the conduction bands at  $L$  and  $K$ , and the conduction-band minima at  $+0.85(2\pi/a_0)$  along the (001) directions, which may influence the optical properties. These band states are somewhat sensitive to the change in the individual values of the fitting parameters and special attention has been paid to their determination. The energy eigenvalues at high-symmetry points of the BZ (see Fig. 3.2) are compared to the Hartree–Fock LCAO calculation and experimental values in Table 6.2.

The energies in eV are measured relative to the top of the valence band with the symmetry  $\Gamma_{5+}$ . As is seen from Table 6.2 an excellent description of the valence and conduction bands has been achieved throughout the Brillouin zone. The main features of the bands are reproduced quite accurately. More specifically, the highest valence and lowest conduction bands run parallel along the  $\Lambda$ ,  $\Delta$ , and  $\Sigma$  lines and the indirect bandgap of Si, the  $\Delta$  minima of which lie at 85% of the way along the  $\Gamma$ – $X$  directions, has been exactly reproduced. It is seen from Table 6.1 that the fitted values of EHT parameters are essentially different compared to those used for molecules. The orbital exponent value  $\zeta_s = \zeta_p = 1.385$  found with Slater rules differs from the fitted values  $\zeta_s = 1.656$ ,  $\zeta_p = 1.728$ . The neutral Si atom ionization potentials  $I_s = 16.34$  eV,  $I_p = 8.15$  eV also differ from the corresponding fitted values 15.55 eV and 7.62 eV, respectively. Analyzing the data given in Table 6.1 one sees that the proportionality constant is not the same for  $2s$  and  $2p$  orbitals (its value, 1.75, is taken in molecular calculations) and essentially depends on the interatomic distance.

**Table 6.2.** EHT fitted, HF and experimental eigenvalues (in eV) for Si crystal at  $\Gamma$ , X, and L-points relative to the valence-band maxima

Level	Fitted	HF	Experimental
$\Gamma$	0.00	0.00	
$\Gamma$	-12.32	-12.36	-12.4, -12.5
$\Gamma$	3.43	3.43	3.45, 3.41
$\Gamma$	4.08	4.10	4.15
$L$	-10.82	-9.55	-9.3
$L$	-6.20	-6.96	-6.4, -6.8
$L$	-1.12	-1.23	-1.2
$L$	2.26	2.23	2.2, 2.3
$L$	4.43	4.34	3.9
$X$	-7.92	-7.69	
$X$	-2.95	-2.86	-2.5, -2.9
$X$	1.33	1.17	
$\Delta$	1.13	1.10	1.13
$K$	1.62	1.66	

The fitted EHT parameters were used in [214] for the EHT calculations to study the molecular oxygen chemisorption and hydrogen-terminated Si(001) ultrathin films. Even when using modern computer codes and facilities the first-principles calculations would be, in this case, very complicated as is seen from the examples given in Chap. 11. In the example considered the remarkable fit for Si crystal has been achieved within the EHT formalism by defining a rather large parameter basis set that resembled a typical Slater–Koster (tight-binding) parametrization. However, it is surprising that, to our knowledge, a systematic quantitative study on the accuracy attainable with the EHT when applied to different bulk materials has been attempted only recently [216]. It was shown how the simple EHT method can be easily parametrized in order to yield accurate band structures for bulk materials, while the resulting optimized atomic orbital basis sets present good transferability properties. The number of parameters involved is exceedingly small, typically ten or eleven per structural phase. A new EHT parametrization scheme was applied to almost fifty elemental and compound bulk phases. An orthonormal AO basis set was chosen for each inequivalent atom  $M$ . Generally, the basis involves rather extended radial wavefunctions, although any other type of basis set may be employed as well. In this work, the Hamiltonian matrix elements  $H_{\mu M, \nu N}$  were taken in the form

$$H_{\mu M, \nu N} = K_{EHT} (I_{\mu M} + I_{\nu N}) / 2 \quad (6.7)$$

where  $K_{EHT}$  is a constant traditionally set to a value of 1.75 and  $I_{\mu M}, I_{\nu N}$  are onsite energies of both elements  $M, N$ . From the above formula it follows that the strength of the Hamiltonian matrix elements is weighted by the mean value of the onsite energies, so that a shift in energy of these onsite parameters does not translate into a rigid shift in energy of the EHT-derived band structure. Therefore, and in order to avoid any arbitrariness in the origin of the energy scales, the Fermi level for transition

metals to  $-10$  eV was fixed and the top of the valence band for semiconductors at  $-13$  eV. It was then found that increasing  $K_{EHT}$  to 2.3 consistently provided better fits for all elements, although similar good fits may be obtained with  $K_{EHT} = 1.75$  if the Fermi level is lowered to around  $-20$  eV. A minimal *spd* basis set per element was employed, while each AO is described by a double Slater wavefunction. Apart from the onsite energies ( $I_s$ ,  $I_p$ , and  $I_d$ ), this leads to three parameters per  $l$  quantum number: the exponents  $\zeta_1$  and  $\zeta_2$  (with  $\zeta_1 < \zeta_2$ ), and the coefficient for the former,  $C_1$ . The second coefficient  $C_2$  is determined by imposing normalization of the wavefunction. For transition metals the optimization of the three AO parameters was found to be redundant for the  $s$  and  $p$  orbitals, and equally good fits could be obtained by fixing  $\zeta_2$  to a rather large value:  $\zeta_2 > 20.0$ . Since such a highly localized term gives a negligible contribution to the overlaps with neighboring orbitals, it was explicitly omitted, while allowing the coefficient  $C_1$  to take values smaller than 1.0 (*i.e.* the  $\zeta_2$  Slater orbital only contributes to the normalization of the wavefunction). For the  $d$  orbitals, on the contrary, it was found necessary to include the  $\zeta_2$  contribution. Hence, the transition-metal fits comprise 10 parameters per elemental phase. In order to improve the transferability of the EHT, the AO basis set of a given element simultaneously for different structural phases (*e.g.* Ti-fcc, -bcc, and -hex) has also been optimized, while the onsite energies have been treated as independent parameters for each phase. For the spin-polarized phases of Fe, Co, and Ni, the coefficient of the  $d$  orbitals was additionally varied independently for each spin, since the  $d$  bandwidths are larger for the spin minority bands than for the majority ones. The main difference from traditional TB schemes is clear – explicit definition of the AOs. This might look at first glance as a disadvantage, since it requires the calculation of the overlap matrix elements. However, the computational effort involved in constructing the actual overlap  $S(\mathbf{k})$  and Hamiltonian  $H(\mathbf{k})$  matrices is minimal (only two-center integrals plus the simple EHT formula are involved) and more importantly, for a fixed cutoff radius, it scales linearly with the number of orbitals in the unit cell. The explicit use of AOs can be regarded as advantageous, particularly in what concerns the transferability of the EHT parameters, since the dependence of the overlap terms  $S_{\mu M, \nu N}$  on the interatomic distance  $d_{MN}$  readily provides a natural scaling law that is not restricted to small variations of  $d_{MN}$ . A further advantage is the possibility to obtain the local density of states, while the traditional TB methods only provide real space-integrated quantities.

The empirically adjusted and consistent set of EHT valence orbital parameters for molecular calculations, based on the Hartree–Fock–Slater (see (4.23)) model of atoms, was recently suggested in [217] for all elements of the periodic table. The parametrization scheme uses individual values of the exchange parameter,  $\alpha$ , for each atom. Each value of  $\alpha$  was adjusted to reproduce the empirical value of the first ionization energy of the atom considered. The expectation values, energies and radial functions for all elements of the periodic table have been evaluated on the basis of the Hartree–Fock–Slater model and individual exchange parameters. A consistent set of Slater-type orbital single  $\zeta$  valence atomic orbital exponents and energies for all elements of the periodic table, suitable for orbital interaction analysis, was presented. These exponents were calculated by fitting the  $\langle r \rangle_{STO}$  moments to numerical empirically adjusted  $\langle r \rangle_{HFS}$  results. In future, these parameters may appear to be useful for TB method calculations of solids after some modifications.

The process in the EHT and TB methods does become iterative if VSIPs are not included in the set of fitted parameters but are adjusted as a function of partial atomic charge as described in the next subsection, since the partial atomic charge depends on the occupied orbitals. Such a scheme is applied for more ionic systems than those studied by the EHT method. The self-consistent one-electron Hamiltonian Mulliken–Rüdenberg calculation scheme is considered in the next subsection.

### 6.1.2 Iterative Mulliken–Rüdenberg Method for Crystals

The Rüdenberg's integrals approximations for molecules has been described in [209] and in more detail in [218]. This approximation was introduced by Rüdenberg [219] to simplify the calculation of two-electron four-center integrals

$$(\mu M, \nu N | \sigma P, \lambda L) = \int d\mathbf{r}_1 \int d\mathbf{r}_2 \chi_{\mu M}(\mathbf{r}_1) \chi_{\nu N}(\mathbf{r}_1) \frac{1}{r_{12}} \chi_{\sigma P}(\mathbf{r}_2) \chi_{\lambda L}(\mathbf{r}_2) \quad (6.8)$$

where  $\chi_{\mu M}(\mathbf{r})$  is the  $\mu$ th AO on the  $M$ th atom in a molecule. Let  $\chi_{1M}, \chi_{2M}, \dots$  be a complete set of orthogonal real orbitals on center  $M$  and analogously  $\chi_{1N}, \chi_{2N}, \dots, \chi_{1P}, \chi_{2P}, \dots$  and  $\chi_{1L}, \chi_{2L}, \dots$  on centers  $N, P$ , and  $L$ , respectively. If  $S_{\mu M, \nu N} = \int d\mathbf{r} \chi_{\mu M}(\mathbf{r}) \chi_{\nu N}(\mathbf{r})$  denotes the overlap integrals between the orbitals  $\chi_{\mu M}(\mathbf{r})$  and  $\chi_{\nu N}(\mathbf{r})$ , then we have the expansions

$$\chi_{\mu M}(\mathbf{r}_1) = \sum_{\omega} S_{\mu M, \omega N} \chi_{\omega N}(\mathbf{r}_1) \quad (6.9)$$

$$\chi_{\nu N}(\mathbf{r}_2) = \sum_{\omega} S_{\omega M, \nu N} \chi_{\omega M}(\mathbf{r}_2) \quad (6.10)$$

whence

$$\begin{aligned} \chi_{\mu M}(\mathbf{r}_1) \chi_{\nu N}(\mathbf{r}_2) &= \frac{1}{2} \sum_{\omega} [S_{\mu M, \omega N} \chi_{\nu N}(\mathbf{r}_1) \chi_{\omega N}(\mathbf{r}_2) \\ &\quad + S_{\nu N, \omega M} \chi_{\mu M}(\mathbf{r}_1) \chi_{\omega M}(\mathbf{r}_2)] \end{aligned} \quad (6.11)$$

Insertion of (6.11) and the analogous formula for the centers  $L, K$  in (6.8) expresses the four-center integral in terms of two-center Coulomb integrals and overlap integrals:

$$\begin{aligned} (\mu M, \nu N | \sigma P, \lambda L) &= \frac{1}{4} \sum_{\omega} \sum_{\omega'} [S_{\mu M, \omega N} S_{\sigma P, \omega' L} (\omega N, \nu N | \omega' L, \lambda L) \\ &\quad + S_{\mu M, \omega N} S_{\lambda L, \omega' P} (\omega N, \nu N | \sigma P, \omega' P) + S_{\nu N, \omega M} S_{\sigma P, \omega' L} (\mu M, \omega M | \omega' L, \nu L) \\ &\quad + S_{\nu N, \omega M} S_{\lambda L, \omega' P} (\mu M, \omega M | \sigma P, \omega' P)] \end{aligned} \quad (6.12)$$

In the Mulliken approximation [220] only the first term in expansion (6.12) is taken so that the one-electron distribution is approximated by

$$\chi_{\mu M}(\mathbf{r}_1) \chi_{\nu N}(\mathbf{r}_1) \cong \frac{1}{2} S_{\mu M, \nu N} [\chi_{\mu M}^2(\mathbf{r}_1) + \chi_{\nu N}^2(\mathbf{r}_1)] \quad (6.13)$$

Using expansions (6.9) and (6.10) for the two-electron distribution and the Mulliken approximation we obtain

$$\chi_{\mu M}(\mathbf{r}_1)\chi_{\nu N}(\mathbf{r}_2) \cong \frac{1}{2}S_{\mu M, \nu N}[\chi_{\mu M}(\mathbf{r}_1)\chi_{\mu M}(\mathbf{r}_2) + \chi_{\nu N}(\mathbf{r}_1)\chi_{\nu N}(\mathbf{r}_2)] \quad (6.14)$$

In the Mulliken approximation the HF operator can be written in the form [221]

$$\hat{F} = -\frac{\Delta}{2} + \sum_M \hat{V}_M \quad (6.15)$$

where

$$\hat{V}_M = \sum_{\mu}^M P_{\mu} [2(\dots | \chi_{\mu M} \chi_{\mu M}) - (\dots \chi_{\mu M} | \dots \chi_{\mu M})] - \frac{Z_M}{R_M} \quad (6.16)$$

The summation in (6.16) is made over AOs of atom  $M$ ,  $P_{\mu}$  is the Mulliken population of the  $\mu$ th AO, defined as

$$P_{\mu} = \sum_i^{occ} C_{i, \mu M}^2 + \sum_{N \neq M}^N \sum_{\nu}^{occ} \sum_i^{occ} C_{i, \mu M} C_{i, \nu N} S_{\mu M, \nu N} \quad (6.17)$$

The action of operator  $\hat{V}_M$  on the MO  $\varphi$  is defined by relations

$$(\dots | \chi_{\mu M} \chi_{\mu M})\varphi = (\varphi \varphi | \chi_{\mu M} \chi_{\mu M}) \quad (6.18)$$

$$(\dots \chi_{\mu M} | \dots \chi_{\mu M})\varphi = (\varphi \chi_{\mu M} | \varphi \chi_{\mu M}) \quad (6.19)$$

As in (6.8) the functions depending on coordinates of the first electron are up to the vertical line, those depending on coordinates of the second electron – after the vertical line.

As the valence-electron approximation is supposed to be introduced, the term  $Z_M/R_M$  in (6.16) means the electron interaction with the core of atom  $M$  in the point-charge approximation. As AO  $\chi_{\mu M}(\mathbf{r})$  can be considered as an eigenfunction of operator  $(-\frac{\Delta}{2} + \hat{V}_M)$  and introducing the point-charge approximation for  $Z_M/R_N (N \neq M)$ , we obtain the matrix elements of operator (6.15) in the form [222]

$$F_{\mu M, \mu M} = \varepsilon_{\mu M}(q_M) - \sum_{N \neq M} q_N (\chi_{\mu M} | \frac{1}{r_N} | \chi_{\mu M}) \quad (6.20)$$

$$F_{\mu M, \nu N} = S_{\mu M, \nu N} (\varepsilon_{\mu M}(q_M) + \varepsilon_{\nu N}(q_N)) - \frac{1}{2} S_{\mu M, \nu N} \sum_{L \neq M, N} q_L \left[ (\chi_{\mu M} | \frac{1}{r_L} | \chi_{\mu M}) + (\chi_{\nu N} | \frac{1}{r_L} | \chi_{\nu N}) \right] - T_{\mu M, \nu N} \quad (6.21)$$

In these expressions,  $\chi_{\mu M}$  is the  $\mu$ th atomic orbital on the  $M$ th atom;  $\varepsilon_{\mu M}(q_M)$  is the ionization potential of the  $\mu$ th valence orbital on the  $M$ th atom with charge  $q_M$ ;  $S_{\mu M, \nu N}$  and  $T_{\mu M, \nu N}$  are the overlap and kinetic energy integrals of the  $\mu$ th and  $\nu$ th orbitals on the  $M$ th and  $N$ th atom, respectively;  $(\chi_{\mu M} | \frac{1}{r_L} | \chi_{\mu M})$  is the core-attraction integral. The effective charge  $q_M$  is calculated using the Mulliken population analysis, *i.e.*  $q_M = \sum_{\mu} P_{\mu}$  where the AO population  $P_{\mu}$  is defined by (6.17).

The application of the Mulliken–Rüdenberg (MR) approximation to calculate the electronic structure not of the free molecule, but of a fragment of an ionic crystal (also

called a molecular cluster), requires the summation over an infinite number of lattice sites in terms corresponding to the interaction of the fragment atoms with those of the remaining crystal. For the  $N$ th atom in a binary crystal the field of ions surrounding the considered fragment can be calculated in the point-charge approximation using the formula

$$V^N = - \left( \frac{M_c}{a} + \sum_L \frac{sgn(q_L)}{R_{NL}} \right) |q_R| \quad (6.22)$$

Here  $M_c$  is the Madelung constant,  $a$  the nearest-neighbor distance in crystal,  $q_R$  the charge ascribed to the lattice ions beyond the fragment under consideration,  $L$  numbers atoms in the fragment considered.

Taking into account (6.22) one can write expressions (6.20) and (6.21) in the form

$$F_{\mu M, \mu M} = \varepsilon_{\mu M}(q_M) - \sum_{L \neq M} q_L (\chi_{\mu M} | \frac{1}{r_L} | \chi_{\mu M}) + V^M \quad (6.23)$$

$$\begin{aligned} F_{\mu M, \nu N} = & S_{\mu M, \nu N} (\varepsilon_{\mu M}(q_M) + \varepsilon_{\nu N}(q_N)) \\ & - \frac{1}{2} S_{\mu M, \nu N} \left\{ \sum_{L \neq M, N} q_L \left[ (\chi_{\mu M} | \frac{1}{r_L} | \chi_{\mu M}) + (\chi_{\nu N} | \frac{1}{r_L} | \chi_{\nu N}) \right] \right. \\ & \left. + V^M + V^N \right\} - T_{\mu M, \nu N} \end{aligned} \quad (6.24)$$

The MR approximation was extended to the periodic systems in [222, 223].

To describe the band structure of an infinite perfect crystal in the framework of the LCAO method one should calculate the matrix elements of operator (6.15) using the Bloch sums of atomic orbitals (AO), defined in (4.53):

$$\begin{aligned} \varphi_{\mu k}(\mathbf{r}) = & L^{-1/2} \sum_j \exp(i\mathbf{k}\mathbf{R}_j) \chi_{\mu j}(\mathbf{r} - \mathbf{R}_j) \\ \equiv & L^{-1/2} \sum_j \exp(i\mathbf{k}\mathbf{R}_j) \chi_{\mu j}(\mathbf{r}) \end{aligned} \quad (6.25)$$

Here,  $\mathbf{k}$  is the wavevector,  $\mu$  numbers the AOs in the unit cell,  $\varphi_{\mu k}(\mathbf{r})$  is the  $\mu$ th crystal orbital,  $\chi_{\mu j}(\mathbf{r})$  is the  $\mu$ th AO in the  $j$ th unit cell, and  $L$  the number of unit cells in the fundamental region of the crystal.

It is obvious that summation of core-attraction integrals over the whole lattice is very complicated. The values of these integrals decrease as  $1/R_{MN}$  with increasing distance, *i.e.* special methods are required to estimate their sums. As the values of core-attraction integrals approximate rapidly the value  $1/R$  when increasing the interatomic distance one can hope that the substitution of the Madelung energy for the sums of integrals would turn out to be a quite satisfactory approximation, at least for ionic crystals.

Using the Mulliken approximation in the three-center integrals, and the point-charge approximation for  $V_M$  it is shown in [222, 224] that the MR operator matrix elements for a periodic system are given by

$$\begin{aligned}
F_{\mu M, \nu N}(\mathbf{k}) = & \frac{1}{2} [2\varepsilon_\mu(q_M, n_M) - ME_M(q_M) + 2\varepsilon_\nu(q_N, n_N) - ME_N(q_N)] \\
& \cdot \sum_j \exp(i\mathbf{k}\mathbf{R}_j) S_{\mu M j, \nu N 0} + \frac{1}{2} (q_M + q_N) \sum_j \exp(i\mathbf{k}\mathbf{R}_j) S_{\mu M j, \nu N 0} \frac{1}{R_{M j, N 0}} \\
& - \sum_j \exp(i\mathbf{k}\mathbf{R}_j) T_{\mu M j, \nu N 0} - \delta_{MN} \delta_{\mu\nu} \varepsilon_\mu(q_M, n_M)
\end{aligned} \quad (6.26)$$

Here, the indices  $\mu M j$  denote the element of the  $\mu$ th AO on atom  $M$  from primitive unit cell  $j$ , defined by translation vector  $\mathbf{R}_j$ ;  $\varepsilon_\mu(q_M, n_M)$  is the ionization potential of the orbital on atom  $M$  with the atomic charge  $q_M$  and orbital population  $n_M$ ,  $S_{\mu M j, \nu N 0}$  and  $T_{\mu M j, \nu N 0}$  are overlap and kinetic energy integrals, respectively. The iteration procedure continues until self-consistent effective atomic charges  $q_M$  and electronic configuration  $n_M$  are obtained. The Madelung energy  $ME_M$  at the site of atom  $M$  is recalculated at each step of the iterative calculation. It is worth noting that the population-analysis scheme developed for molecules should be applied with caution to calculate the effective charges of atoms in crystals. Thus, according to the Mulliken population analysis that is widespread in molecular calculations, the contribution to the total atomic population is computed proportional to the atomic orbital overlap integrals. In the case of crystals the overlap integrals should be computed with the Bloch sums and, generally speaking, have some meaning other than the molecular ones. To avoid this difficulty Löwdin's population analysis [225] can be used [224] that is based on a symmetrically orthogonalized basis set and that has therefore no problems connected with the distribution of the overlap population.

In the cyclic-cluster model the matrix elements (6.26) should be modified, [222]. The AOs  $\chi_\mu(\mathbf{r})$  have to belong now not only to the atoms in the reference cell but to all the atoms included in the cyclic-cluster. Matrix elements (6.26) are calculated only for  $\mathbf{k} = 0$ , the summation over the crystal is changed by the summation over the cyclic-cluster atoms. For ionic systems the Madelung field of the surrounding crystal can be taken into account by subtracting from the Madelung energy at the site of an atom the part due to the interaction with atoms directly included in the cyclic cluster. To satisfy the PBC introduction for the cyclic cluster the overlap integrals have to satisfy the condition  $(\chi_{\mu M}(\mathbf{r} - \mathbf{R}_j + \mathbf{A})\chi_{\nu N}(\mathbf{r})) = S_{\mu M j, \nu N}$  where  $\mathbf{A}$  is the translation vector of the cyclic cluster as a whole (see Chap. 3).

The MR approximation was applied for electronic structure calculations of both perfect crystals (alkali halides [222], MgO and CaO [226], PbO [227], corundum [228]), point defects in solids ([229–234]) and surfaces [224].

The general analysis of Rüdenberg's approximation in the HF LCAO method for molecules [218] and solids [223] has shown that EHT and zero differential overlap (ZDO) approximations can be considered as particular cases of Rüdenberg's integral approximation. ZDO methods, considered in the next section, were applied to a wide class of molecules and solids, from purely covalent to purely ionic systems. Therefore, they are more flexible compared to the MR approximation, which is more appropriate for ionic systems.

## 6.2 Zero-differential Overlap Approximations for Molecules and Crystals

### 6.2.1 Zero-differential Overlap Approximations for Molecules

As was seen in Sec.6.1 in EHT the AO basis functions are only used for the calculation of overlap integrals (molecules) or lattice sums of overlap integrals (crystals). In the MR method kinetic energy integrals or their lattice sums are also included. These integrals in fact can be expressed through overlap integrals. All other contributions to the one-electron Hamiltonian matrix elements are based on empirical parameters.

As we have seen, EHT is a nonself-consistent method but the self-consistency over charge and configuration is included in the MR approximation. The *Ab-initio* HF SCF method requires the self-consistent calculation of the density matrix (see Chap. 4). This feature of the HF approach is maintained in the semiempirical methods, based on the zero differential overlap (ZDO) approximation. This approximation is used to reduce the number of multicenter integrals appearing in HF LCAO calculations.

In the ZDO approximation the differential overlap  $\chi_\mu(\mathbf{r}_1)\chi_\nu(\mathbf{r}_2)d\mathbf{r}_1d\mathbf{r}_2$  of valence AO basis functions is supposed to be zero for any  $\mu \neq \nu$  both for  $\mathbf{r}_1 = \mathbf{r}_2$  and  $\mathbf{r}_1 \neq \mathbf{r}_2$ . The ZDO approximation means that the AO basis is assumed to be orthogonal ( $S_{\mu\nu} = \int \chi_\mu(\mathbf{r})\chi_\nu(\mathbf{r})d\mathbf{r} = \delta_{\mu\nu}$ ). A recent review by Bredow and Jug [235] gives a brief summary of the basis features of ZDO semiempirical methods together with examples of their use. These authors are convinced that “the development of semiempirical methods and their extension to a growing number of research areas has been a continuous process over the last 4 decades and there is apparently no end to be seen”. This is demonstrated by the large number of semiempirical studies in organic, inorganic and physical chemistry, biochemistry, drug design, crystallography and surface science.

Depending on the level of the approximations used for other integrals ZDO methods differ. In the CNDO (complete neglect of differential overlap) method [205, 236] all two-electron integrals are approximated by Coulomb integrals according to

$$(\mu\nu|\lambda\sigma) = \int \chi_\mu(\mathbf{r}_1)\chi_\nu(\mathbf{r}_1) \frac{1}{r_{12}} \chi_\lambda(\mathbf{r}_2)\chi_\sigma(\mathbf{r}_2) d\mathbf{r}_1 d\mathbf{r}_2 = \delta_{\mu\nu}\delta_{\lambda\sigma}(\mu\mu|\lambda\lambda) \quad (6.27)$$

and only two-center electron-repulsion integrals  $(\mu\mu|\lambda\lambda) = \gamma_{MN}$  are retained ( $M$  and  $N$  are the atoms on which basis functions  $\chi_\mu(\mathbf{r})$  and  $\chi_\nu(\mathbf{r})$  reside, respectively). The independence of this integral on the angular part of AOs restores the AOs hybridization invariance of the original HF operator matrix elements, *i.e.* it is supposed that  $(S_M S_M|S_N S_N) = (P_M P_M|P_N P_N) = (P_M S_M|P_N S_N) = \gamma_{MN}$ . The two-center Coulomb integral  $\gamma_{MN}$  can either be computed explicitly from *s*-type STOs (6.1) or it can be treated as a parameter. The one-center Coulomb integral  $\gamma_M$  is parametrized using a so-called Pariser–Parr [237] approximation  $\gamma_M = I_M - A_M$ , where  $I_M$  and  $A_M$  are the atomic ionization potential and electron affinity, respectively. The parameter  $\gamma_M$  can be expressed with a commonly tabulated semiempirical parameter  $U_{\mu\mu}$  (the energy of interaction of electron-occupying AO  $\chi_\mu(\mathbf{r})$  with the core of atom  $M$ ):

$$U_{\mu\mu} = -I_\mu - (Z_\mu - 1)\gamma_M \quad (6.28)$$

$$U_{\mu\mu} = -0.5(I_\mu + A_\mu) - (Z_A - 1/2)\gamma_M \quad (6.29)$$

Equations (6.28) and (6.29) are used in CNDO/1 and CNDO/2 methods, respectively. For the two-center integral  $\gamma_{MN}$ , the Mataga–Nishimoto [238]

$$\gamma_{MN}(eV) = \frac{14.3986}{R_{AB} + \delta}, \quad \delta(eV) = \frac{14.3986}{(\gamma_{AA} + \gamma_{BB})^{1/2}} \quad (6.30)$$

or Ohno [239]

$$\gamma_{AB}(eV) = \frac{14.3986}{\sqrt{R_{AB} + \delta}} \quad (6.31)$$

formulas are adopted, where  $R_{AB}$ (Å) is the interatomic distance. At large distance,  $\gamma_{AB}$  in both cases goes to  $1/R_{AB}$ , as expected for widely separated charge clouds, while at short distances, it approaches the average of the two one-center parameters.

The one-electron terms for offdiagonal matrix elements are defined as

$$h_{\mu\nu} = \beta_{\mu\nu} = 0.5(\beta_M + \beta_N)S_{\mu\nu} \quad (6.32)$$

where  $S_{\mu\nu}$  is the overlap matrix element computed using Slater-type basis functions  $\chi_\mu(\mathbf{r})$  and  $\chi_\nu(\mathbf{r})$ , centered on atoms  $M$  and  $N$ , respectively; the  $\beta_M, \beta_N$  values are semiempirical parameters. Note that computation of the overlap is carried out for every combination of basis functions, even though in the secular equation  $FC = CE$  itself  $S$  is defined in ZDO approximation as  $S_{\mu\nu} = \delta_{\mu\nu}$ . There are, in effect, two different  $S$  matrices, one for each purpose. The  $\beta$  parameters are entirely analogous to the parameters  $\beta$  in EHT – they provide a measure of the strength of through-space interactions between atoms [240]. As  $\beta$  parameters are intended for completely general use it is not necessarily obvious how to assign them a numerical value, unlike the situation that obtains in EHT. Instead,  $\beta$  values for CNDO were originally adjusted to reproduce certain experimental quantities.

The diagonal  $F_{\mu\mu}$  and nondiagonal  $F_{\mu\nu}$  matrix elements in the CNDO approximation for molecules are defined by

$$F_{\mu\mu} = U_{\mu\mu} + (P_M - 1/2P_{\mu\mu})\gamma_M + \sum_{N \neq M} (P_N - Z_N)\gamma_{MN} \quad (6.33)$$

$$F_{\mu\mu'} = -0.5P_{\mu\mu'}\gamma_M \quad (6.34)$$

$$F_{\mu\nu} = \beta_{MN}S_{\mu\nu} - 0.5P_{\mu\nu}\gamma_{MN} \quad (6.35)$$

AOs  $\chi_\mu$  and  $\chi_{\mu'}$  in (6.34) are supposed to belong to the same atom  $M$ . In (6.34)  $Z_M$  is the atomic-core charge,  $P_{\mu\nu}$  are the density matrix elements in the LCAO approximation (see (4.37)),  $P_M = \sum_\mu^A P_{\mu\mu}$  is the electron population of atom  $M$ , the resonance integral  $\beta_{\mu\nu}$  is taken as  $\beta_{MN}$ , *i.e.* depends only on the atom type, but not on a particular orbital of this atom. The CNDO method represents a vast simplification of HF theory, reducing the number of two-electron integrals having nonzero values from formally  $N^4$  to  $N^2$ . Furthermore, these integrals are computed by trivial algebraic formulae, not by explicit integration, and between any pair of atoms all of the integrals have the same value irrespective of the atomic orbitals involved. Similarly, evaluation of one-electron integrals is also entirely avoided (excluding overlap integrals), with numerical values for those portions of the relevant matrix elements coming from easily

evaluated formulae. Historically, a number of minor modifications to the conventions outlined above were explored, and the different methods had names like CNDO/1, CNDO/2, CNDO/BW, *etc.* [205].

The computational simplifications inherent in the CNDO method are not without chemical cost, as might be expected. Like EHT, CNDO is quite incapable of accurately predicting good molecular structures. Furthermore, the electronic interactions on a single atom are not correctly reproduced due to the ZDO approximation for the different AOs of the same atom. In an attempt to overcome this deficiency of the CNDO scheme the intermediate neglect of differential overlap (INDO) approximation was introduced [241] to permit a more flexible handling of electron–electron interactions on the same center. In this case, the different values of one-center two-electron integrals are used for different AOs:  $(ss|ss) = G_{ss}$ ,  $(ss|pp) = G_{sp}$ ,  $(pp|pp) = G_{pp}$ ,  $(sp|sp) = L_{sp}$ . These integrals are in practice estimated from spectroscopic data. In the INDO scheme the valence bond angles are predicted with much greater accuracy than is the case for CNDO. Nevertheless, overall molecular geometries predicted from INDO tend to be rather poor. Preliminary efforts to address this problem have been reported only recently [242]. A careful parametrization of INDO for spectroscopic problems [243] was described in an INDO/S calculation scheme whose parametrization was later extended to most of the elements in the periodic table [244]. In a purely terminological sense one can make a distinction between the INDO semiempirical method and the INDO/S model [102]. The latter is a particular parametrization of the INDO method designed for spectroscopic applications. The MINDO/3 model [245], the third version of the modified INDO method, included some modifications: different orbital exponents were used for *s*- and *p*-orbital on the same atom, resonance integrals  $\beta_{MN}$  between two atoms were split into pairs corresponding to *s*–*s*, *s*–*p*, *p*–*p* orbital interactions, some empirical modifications to the nuclear repulsion energy were introduced. The MINDO/3 model allowed prediction of heats of formation with the mean absolute error of 11 kcal/mole, 0.7 eV for ionization potentials, 0.022 Å for bond lengths.

In both CNDO and INDO methods the two-center two-electron integral takes the value  $(\mu\mu|\nu\nu) = \beta_{MN}$ , irrespective of which orbitals on atoms *M* and *N* are considered.

The neglect of diatomic differential overlap (NDDO) method [236] is an improvement over the INDO approximation, since the ZDO approximation is applied only for orbital pairs centered at different atoms. Thus, all integrals  $(\mu\nu|\lambda\sigma)$  are retained provided  $\mu$  and  $\nu$  are on the same atomic center and  $\lambda$  and  $\sigma$  are on the same atomic center, but not necessarily the center hosting  $\mu$  and  $\nu$ . In principle, the NDDO approximation should describe long-range electrostatic interactions more accurately than INDO. Most modern semiempirical models (MNDO, AM1, PM3) are NDDO models.

The modified neglect of the diatomic overlap (MNDO) method [246] led to improved agreement with experiment. In the two-electron integrals calculation the continuous charge clouds were replaced with classical multipoles. Thus, an *ss* product was replaced with a point charge, an *sp* product was replaced with a classical dipole (represented by two point charges slightly displaced from the nucleus along the *p* orbital axis), and a *pp* product was replaced with a classical quadrupole (again represented by point charges). The magnitudes of the moments, being one-center in nature, are related to the parameterized integrals appearing in the INDO method. By adopting such a form for the integrals, their evaluation is made quite simple, and so too is

evaluation of their analytic derivatives with respect to nuclear motion. To complete the energy evaluation by the MNDO method, the nuclear repulsion energy is added to the SCF energy. The parameters of the MNDO model were optimized against a large test set of molecular properties (within the assumption of a valence orbital set comprised only of *s* and *p* orbitals).

In addition, a modified MNDO model explicitly adding electron-correlation effects (MNDOC) by second-order perturbation theory was described by Thiel [247]. By explicitly accounting for electron correlation in the theory, the parameters do not have to absorb the effects of its absence from HF theory in some sort of average way.

Later, two modifications of MNDO were introduced [102,235]. The most prominent of these are the Austin model 1 (AM1) by Dewar *et al.* [246] and the parametric method 3 (PM3) by Stewart [248]. In principle MNDO, AM1 and PM3 methods differ only in the parametrization and in the empirical function  $f_{MN}$  in the core–core repulsion

$$V_{nn} = \sum_{M>N} Z_M^* Z_N^* \gamma_{MN} + f_{MN} \quad (6.36)$$

where

$$f_{MN} = Z_M^* Z_N^* \gamma_{MN} (\exp(-\alpha_M R_{MN}) + \exp(-\alpha_N R_{MN}))$$

and  $Z^*$  is the effective core charge.

A variety of modifications of the original methods is now available. AM1 and PM3 have been extended for the treatment of transition-metal compounds by inclusion of *d* orbitals in the valence basis; the Green's function technique has been implemented in MNDO-type methods for the calculation of ionization potentials and electron affinities; a parameterized variational technique is used for the calculation of molecular polarizabilities and hyperpolarizabilities within the MNDO, AM1 and PM3 methods [235].

The most important modifications of the MNDO method are the use of effective core potentials for the inner orbitals and the inclusion of orthogonalization corrections in a way as was suggested and implemented a long time ago in the SINDO1 method [249] at first developed for organic compounds of first-row elements and later extended to the elements of the second and third row [250,251].

The most important feature of the SINDO1 method is that an orthogonalization transformation of the basis functions is taken into account explicitly in solving the HF LCAO equations. The one-electron integral matrix  $H$  is transformed to Löwdin symmetrically orthogonalized [225] AOs  $\chi^\lambda = S^{-1/2} \chi$

$$H^\lambda = S^{-1/2} H S^{-1/2} \quad (6.37)$$

Matrix  $S^{-1/2}$  can be expanded in a series

$$\begin{aligned} S &= I + \sigma \\ S^{-1/2} &= I - 1/2\sigma + 3/8\sigma^2 - \dots \end{aligned} \quad (6.38)$$

where  $I$  is the unit matrix and  $\sigma$  the remaining two-center overlap matrix. The expansion is truncated in such a way that only terms up to second order in the overlap are retained.

Another special feature of SINDO1 is the treatment of inner orbitals by a local pseudopotential introduced in [252]. Two-center one-electron integrals  $H_{\mu\nu}^\lambda$  are calculated by the following empirical formula:

$$H_{\mu\nu}^\lambda = L_{\mu\nu} + \Delta H_{\mu\nu}, \quad \mu \in M, \quad \nu \in N \quad (6.39)$$

Here,  $L$  is a correction to the Mulliken approximation for the kinetic energy, and  $\Delta H$  is entirely empirical and contains adjustable bond parameters. These are optimized in order to minimize the deviation from experiment for a set of reference compounds. Two sets of Slater-orbital exponents are used. One ( $\zeta^U$ ) for intra-atomic integrals, and the other ( $\zeta$ ) for interatomic integrals. Experimental heats of formation are calculated from binding energies  $E_B$ , which are corrected by the zero-point energies obtained from vibration analyses. This is theoretically more sound than in MNDO, AM1 and PM3, where binding energies are parameterized directly to reproduce experimental heats of formation without reference to zero-point energies.

Recently, a new version MSINDO was developed by substantial modifications in the SINDO1 formalism. The parameters are now available for the elements H, C–F, Na–Cl, Sc–Zn, and Ga–Br [253–256] for Li–B and K–Ca, [257].

In MSINDO the standard basis set for elements Al–Cl has been changed from  $\{3s, 3p\}$  to  $\{3s, 3p, 3d\}$  in order to account for hypervalent compounds [253]. For compounds containing Na and Mg an inclusion of  $3d$  functions was considered inconsistent, because these atoms already contain  $3p$  functions for polarization. Moreover, test calculations showed that the  $3d$  functions on these atoms had only insignificant effects on the molecular properties. As for SINDO1 the H basis set can be augmented with a  $2p$  shell for the treatment of hydrogen bonds. All Slater–Condon atomic parameters are calculated analytically for the one-center two-electron integrals and one-electron integrals  $U_{\mu\mu}$ . For the higher multipole terms, this differs from SINDO1, where these terms were taken from experimental spectra. The MSINDO procedure is more consistent since all parameters are derived at the same level of theory. To maintain rotational invariance a number of one-center hybrid integrals have to be included in the case of  $d$  functions [258]. This was already implemented in SINDO1 and was kept in MSINDO. The core integrals  $U_{3d}$  of second- and third-row elements were scaled by a screening potential  $K_{sc}$  in order to avoid unrealistically high populations for the  $3d$  shell:

$$U'_{3d} = (1 - K_{sc})U_{3d} \quad (6.40)$$

For second-row elements a fixed value of  $K_{sc} = 0.15$  is used. For third-row elements  $U_{3d}$ ,  $U_{4s}$  and  $U_{4p}$  were scaled with different screening potentials [256].

The most important change in MSINDO with respect to SINDO1 is a modification of the approximate Löwdin orthogonalization of the basis [253]. Only the first-order terms in overlap are retained in (6.38). In SINDO1 the expansion was to second order. If only first-order terms are taken into account, no transformation of the two-electron integrals is necessary. The one-electron integrals are transformed

$$\tilde{H}_{\mu\mu'}^\lambda = H_{\mu\mu'}^\lambda - f^M \frac{1}{2} \sum_{N \neq M} \sum_{\nu}^N (L_{\mu\nu'} S_{\nu\mu'} + S_{\mu\nu'} L_{\nu\mu'}) \quad (6.41)$$

The correction factor,  $f^M$ , accounts for the neglect of higher-order terms in the truncated expansion (6.38). Its value depends on the number of basis functions on atom  $M$ .  $f^M$  is 1 for an  $\{s\}$  basis, 0.75 for an  $\{s, p\}$  basis and 0.5 for an  $\{s, p, d\}$  basis.

We considered SINDO1-MSINDO methods in more detail as these methods were successfully applied in calculations of bulk solids and surfaces in the embedded and cyclic-cluster models (see Sect. 6.3). The role of long-range interactions in solids increases, compared to the case of molecules. In order to better describe long-range interactions, in particular at surfaces, dipole–monopole and dipole–dipole terms were added to the MSINDO formalism following an early suggestion by Voigt [259]. After modification of the formalism a complete reparameterization of all elements had to be performed. The new version, called MSINDO+, was tested for some cases where SINDO1 and MSINDO gave results in disagreement with experiment.

It should be noted that an analysis of some systematic errors of the ZDO approximation [260] allowed an improved semiempirical approach to be developed [261]. In this approach the Rüdenberg approximation is used for diatomic overlap densities appearing in Coulomb integrals, the Fock matrix is simplified such that its construction scales with  $N^2$  instead of  $N^4$  in *ab-initio* methods, if  $N$  is the dimension of the basis set. Thus, the one-electron and two-electron Coulomb parts of the Fock matrix are formulated explicitly in an atomic orbital (AO) basis, whereas the ZDO approximation is restricted to the two-electron exchange part. The complete two-electron Coulomb part of the Fock matrix is explicitly subjected to the Löwdin transformation. The proposed formalism is not necessarily an empirical one because, in principle, all matrix elements can be calculated exactly. Since only two-center integrals appear one can use a Slater instead of the Gaussian basis of *ab-initio* methods. However, if the formalism is restricted to the valence electrons as in normal semiempirical methods some parametrization is unavoidable. In this case, an additional pseudopotential accounting for the effects of core-valence orthogonality should be implemented. It may also be useful to absorb possible errors arising from the Rüdenberg approximation into the parametrization of the two-electron integrals.

Hybrid approaches combining *ab-initio* or DFT and semiempirical approaches have become popular. As an example, we can refer to LEDO (limited expansion of differential overlap) densities application to the density-functional theory of molecules [262]. This LEDO-DFT method should be well suited to the electronic-structure calculations of large molecules and in the authors' opinion its extension to Bloch states for periodic structures is straightforward. In the next sections we discuss the extension of CNDO and INDO methods to periodic structures – models of an infinite crystal and a cyclic cluster.

### 6.2.2 Complete and Intermediate Neglect of Differential Overlap for Crystals

The first applications of ZDO methods for extended systems refer to the electronic-structure calculations of regular polymer chains when the one-dimensional (1D) periodicity is taken into account. The corresponding modifications of molecular ZDO equations can be found in the literature: for the CNDO method in [263–266], for the INDO and MINDO methods in [267, 268], for the MNDO, PM3 and AM1 methods in [269–272].

The CNDO method extended to the two-dimensional (2D) periodicity case was applied in regular chemisorption studies of hydrogen and oxygen on a graphite surface [207, 273–275]. The equations of the CNDO method for three-dimensional (3D) solids

were given in [207, 273, 275–281]; the periodic MINDO method is considered in [282–284].

The main features of the CNDO and INDO approaches to periodic systems are similar to those used for molecules. A valence-electron approximation is adopted, which implies that only the valence electrons are in the bonding region and are polarized by the presence of neighboring atoms [277]. For periodic systems the LCAO approximation is based on use of the Bloch sums (4.53) of AOs  $\chi_{\mu n}(\mathbf{r}) = \chi_{\mu}(\mathbf{r} - \mathbf{R}_n)$  numbered by index  $\mu$  (labels all AOs in the reference primitive unit cell) and by the direct lattice translation vector  $\mathbf{R}_n$  ( $n = 0$  for the reference cell).

In the ZDO approximation AOs are supposed to be orthogonal both in the intracell and intercell overlap integrals

$$S_{\mu 0, \nu n} = \int \chi_{\mu 0}(\mathbf{r}) \chi_{\nu n}(\mathbf{r}) d\mathbf{r} = \delta_{0n} \delta_{\mu \nu} \quad (6.42)$$

The two-electron integrals are approximated by Coulomb integrals  $\gamma_{MN}^{0n}$ , calculated with  $s$  functions of the  $M$ th atom from reference cell and the  $N$ th atom from the cell  $n$ :

$$(\mu 0, \nu n | \lambda i, \sigma i') = \delta_{0n} \delta_{\mu \nu} \delta_{i i'} \delta_{\lambda \sigma} \gamma_{MN}^{0i} \quad (6.43)$$

The one-electron matrix elements  $H_{\mu 0, \nu n}$  are approximated by  $\beta_{MN} S_{0\mu, \nu n}$ , where the resonance integrals  $\beta_{MN}$  depend only on the type of atoms  $M$  and  $N$  to which the AOs  $\mu$  and  $\nu$  refer. In particular, in the CNDO/2 version of the CNDO method for the crystal the diagonal one-electron matrix elements are taken in the form

$$H_{\mu 0, \mu 0} = U_{\mu \mu} + Z_M \gamma_{MN}^{00} - \sum_{n, N} Z_N \gamma_{MN}^{0n} \quad (6.44)$$

The difference of (6.44) from its molecular analog is defined by the lattice summation over all atoms  $N$  (including  $M = N$ ) in the reference cell and in different unit cells of a crystal. In the model of an infinite crystal these lattice sums are infinite. All the simplifications mentioned are introduced in the Fock and overlap matrices (4.56) and HF LCAO equations (4.57) for periodic systems so that one obtains instead of (4.56) and (4.57):

$$S_{\mu \nu}^{ZDO}(\mathbf{k}) = \sum_n \delta_{0n} \delta_{\mu \nu} \exp(i\mathbf{k} \cdot \mathbf{R}_n) = \exp(i\mathbf{k} \cdot \mathbf{R}_0) \quad (6.45)$$

$$\sum_{\nu} \{ F_{\mu \nu}^{ZDO}(\mathbf{k}) \exp(i\mathbf{k} \cdot (\mathbf{R}_n - \mathbf{R}_0)) - E_i(\mathbf{k}) C_{i \mu}(\mathbf{k}) \} = 0 \quad (6.46)$$

Let  $\mathbf{R}_0$ , the lattice vector of the reference cell, correspond to the origin of the coordinate system. Then the core (H) and Fock (F) matrix elements have the following form within the CNDO formalism

$$\begin{aligned} H_{\mu \mu}(\mathbf{k}) &= U_{\mu \mu} + Z_M \gamma_{MM}^{00} - \sum_N \sum_{n=0}^{L-1} Z_N \gamma_{MN}^{0n} + \sum_{n=1}^{L-1} \beta_M^0 S_{\mu \mu}^{0n} \exp(i\mathbf{k} \cdot \mathbf{R}_n) \\ H_{\mu \nu} &= \sum_{n=0}^{L-1} \beta_{MN}^{00} S_{\mu \nu}^{0n} \exp(i\mathbf{k} \cdot \mathbf{R}_n) \end{aligned} \quad (6.47)$$

$$\begin{aligned}
F_{\mu\mu}(\mathbf{k}) &= H_{\mu\mu}(\mathbf{k}) + \frac{1}{L} \sum_{N,\nu} \sum_{n=0}^{L-1} \sum_{\mathbf{k}'} P_{\nu\nu}(\mathbf{k}') \gamma_{MN}^{0n} \\
&\quad - \frac{1}{2L} \sum_{n=0}^{L-1} \sum_{\mathbf{k}'} P_{\mu\mu}(\mathbf{k}') \gamma_{MN}^{0n} \exp(i(\mathbf{k} - \mathbf{k}') \mathbf{R}_n) \\
F_{\mu\nu}(\mathbf{k}) &= H_{\mu\nu}(\mathbf{k}) - \frac{1}{2L} \sum_{n=0}^{L-1} \sum_{\mathbf{k}'} P_{\mu\nu}(\mathbf{k}') \gamma_{MN}^{0n} \exp(i(\mathbf{k} - \mathbf{k}') \mathbf{R}_n)
\end{aligned} \tag{6.48}$$

As in the HF LCAO method the calculation of the wavevector of the  $\mathbf{k}$ -dependent density matrix

$$P_{\mu\nu}(\mathbf{k}) = 2 \sum_i^{\text{occ}} C_{i\mu}^*(\mathbf{k}) C_{i\nu}(\mathbf{k}) \tag{6.49}$$

requires the summation over occupied crystalline orbitals ( $i$ ) that are themselves defined as a linear combination of the basis atomic orbitals. The HF method allows both an all-electron calculation and a valence-electron approximation when the atomic cores pseudopotentials are introduced. In both cases the AOs are represented by GTO. In the CNDO method for crystals only the valence atomic orbitals are included and represented by a minimal Slater basis set. We return to the basis-sets consideration in Chap. 8.

Equations (6.47) and (6.48) contain an explicit  $\mathbf{k}$  dependence via the phase factors  $\exp(i\mathbf{k}\mathbf{R}_n)$  and an implicit  $\mathbf{k}$ -dependence via summations over  $\mathbf{k}'$ . Invoking the special  $\mathbf{k}$ -points theory (see Sect. 4.2.2) one need only use a small set of  $\mathbf{k}'$ -points to approximate the integral over BZ.

In (6.48) and (6.49),  $S_{\mu\nu}^{0n}$  and  $\gamma_{MN}^{0n}$  are the overlap and Coulomb integrals for atomic orbital  $\mu$  on atom  $M$  in the primitive unit cell 0 and atomic orbital  $\nu$  on atom  $N$  in the cell  $\mathbf{R}_n$ .  $U_{\mu\mu}$  describes the interaction of an electron with the atomic core of the atom  $M$  with the core charge  $Z_M$  (this is equal to the number of valence electrons of atom  $M$ ). The Coulomb integrals  $\gamma_{MN}$  and the bonding parameters  $\beta_{MN}$  are assumed to be orbitally independent.

It follows from (6.49) that in the CNDO approximation the nonlocal exchange is taken into account as nondiagonal elements of the Fock matrix contain nondiagonal elements  $P_{\mu\nu}(\mathbf{k}')$  of the density matrix. This means that lattice sums in this case are divergent, see Sect. 4.3.3. Indeed for sufficiently large  $\mathbf{R}_n$  the two-electron integrals  $\gamma_{MN}^{0m}$  in the exchange part of (6.48) may be approximated by  $1/|\mathbf{r}_M + \mathbf{r}_N - \mathbf{R}_n|$  where  $\mathbf{r}_M, \mathbf{r}_N$  are the vectors defining the positions of atoms  $M$  and  $N$  in the reference cell. Therefore, the convergence of the lattice sum over  $n$  is defined by the convergence of the lattice sum

$$S_j(\mathbf{k}) = \sum_n \frac{\exp(i(\mathbf{k} - \mathbf{k}_j) \mathbf{R}_n)}{|\mathbf{R}_n + \mathbf{r}_m - \mathbf{r}_N|} \tag{6.50}$$

The sum (6.50) can be calculated for  $\mathbf{k} \neq \mathbf{k}_j$ , for example, by the Ewald method. However, for  $\mathbf{k} = \mathbf{k}_j$  the series (6.50) appears to be divergent [95]. This divergence is the result of the general asymptotic properties of the approximate density matrix calculated by the summation over the special poits of BZ (see Sect. 4.3.3). The difficulties connected with the divergence of lattice sums in the exchange part have been resolved in CNDO calculations of solids by introduction of an interaction radius

for exchange [276, 277] or of distance-dependent modulating functions that weight certain Coulomb interaction terms [280]. Detailed studies of the HF LCAO density matrix properties (see Sect. 4.3.3) allow an interpolation procedure to be suggested for constructing an approximate density matrix for periodic systems, which ensures a balance between the direct lattice and BZ summations. Furthermore, this analysis is important for the cyclic-cluster ZDO calculations as it allows an additional parameter (exchange radius) introduction to be omitted (see Sect. 6.3).

The extension of INDO and MINDO semiempirical methods to periodic systems has no principal differences compared with the CNDO method. The advantage of these methods is the possibility to make spin-dependent calculations as is done in the UHF method.

The considered CNDO method for periodic systems formally corresponds to the model of an infinite crystal or its main region consisting of  $L$  primitive cells. This semiempirical scheme was also applied for the cyclic-cluster model of a crystal allowing the BZ summation to be removed from the two-electron part of matrix elements. In the next section we consider ZDO methods for the model of a cyclic cluster.

## 6.3 Zero-differential overlap Approximation in Cyclic-cluster Model

### 6.3.1 Symmetry of Cyclic-cluster Model of Perfect Crystal

In Sect. 4.2.1 we introduced supercell transformation (4.77) in the direct lattice allowing generation of special points of the BZ in the calculation of the one-electron density matrix of the perfect crystal. In this consideration, the perfect crystal was supposed to be infinite or represented by its main region. The latter was defined as a block on which opposite-sides periodic boundary conditions are imposed. The main region of a crystal can be called a cyclic cluster of huge size (in the shape of a parallelepiped with large edges) modeling the infinite crystal and maintaining its translation symmetry.

The idea to use relatively small cyclic clusters for comparative perfect-crystal and point-defect calculations appeared as an alternative to the molecular-cluster model in an attempt to handle explicitly the immediate environment of the chemisorbed atom on a crystalline surface [285] and the point defects in layered solids [286, 287] or in a bulk crystal [288, 289, 292, 293]. The cluster is formed by a manageable group of atoms around the defect and the difference between the molecular-cluster model (MCM) and the cyclic cluster model (CCM) is due to the choice of boundary conditions for the one-electron wavefunctions (MOs). Different notations of CCM appeared in the literature: molecular unit cell approach [288], small periodic cluster [286], large unit cell [289, 290]. We use here the cyclic cluster notation.

In MCM (as in molecules) MOs are supposed to be orthonormalized in the whole space; this condition is also fulfilled for the molecular clusters embedded by some or another means into the crystalline environment. Recent applications of the molecular-cluster model and MO calculations for materials design in the Hartree–Fock–Slater method are discussed in [291].

In the CCM model the periodic boundary conditions are introduced for MOs of a cluster having the shape of a supercell of a perfect crystal so that MOs are

orthonormal in the field of the cyclic cluster chosen. Postponing to Chap. 10 the more detailed discussion of molecular models of defective crystals we would like to note here the difference between the supercell model (SCM) and CCM for point defects. In the former, PBC are introduced for the main region of a crystal so that the point defect is periodically repeated over the crystalline lattice, in the latter the single point defect is considered. This means that CCM is conceptually a supercell-type approach but is technically more closely related to the simple MCM [294].

We discuss here the symmetry of CCM for perfect crystal [13, 295–299]. The symmetry of defective crystal in CCM is considered in Chap. 10.

To define a finite cyclic system, let us make a linear transformation of the primitive-lattice translation vectors

$$\mathbf{A}_j = \sum_i l_{ji} \mathbf{a}_j, \quad L = |\det l| \geq 1 \quad (6.51)$$

where the integer coefficients  $l_{ji}$  form the matrix  $l$ . The transformation (6.51) for  $L > 1$  determines a supercell (large unit cell) of the direct lattice. It may be chosen in the form of a parallelepiped with vectors  $\mathbf{A}_j$  as edges or in the form of the corresponding Wigner–Seitz unit cell.

The particular form of the matrix  $l$  in (6.51) defines the supercell shape and its volume (which is  $L$  times larger than that of a primitive unit cell) and the symmetry of the direct lattice based on the group  $T_{\mathbf{A}}$  of the translations

$$\mathbf{A}_n = \sum_{j=1}^3 n_j \mathbf{A}_j, \quad n_j \text{ are arbitrary integers} \quad (6.52)$$

The group  $T_{\mathbf{A}}$  is an invariant subgroup of  $T_{\mathbf{a}}$  (translation group of the infinite lattice with primitive translation vectors  $\mathbf{a}_i$ ) so that the cosets  $(E|\mathbf{a}^{(i)})T_{\mathbf{A}} (i = 1, 2, \dots, L)$  in the decomposition

$$T_{\mathbf{a}} = \sum_{i=1}^L (E|\mathbf{a}^{(i)})T_{\mathbf{A}} \quad (6.53)$$

form the factor group  $T_{\mathbf{a}}/T_{\mathbf{A}} = T^{(\mathbf{A})}$  of order  $L$ . The so-called inner translations of the supercell are assumed to be chosen as  $\mathbf{a}^{(i)}$  in (6.53).

Figure 6.1a shows the supercell of the plane hexagonal lattice of boron nitride, BN, formed by the diagonal  $l = \begin{pmatrix} 3 & 0 \\ 0 & 3 \end{pmatrix}$  matrix, with  $L = 9$ .

A cyclic cluster  $C^{(\mathbf{A})}$  is defined as a supercell with identical opposite faces, *i.e.* the periodic boundary conditions are introduced for the chosen supercell itself (not for the main region of a crystal!). In particular, in the supercell, shown on Fig. 6.1a, the atoms with the primed numbers are supposed to be identical with the atoms of the supercell, having the same unprimed numbers. This means that the translation of a supercell as a whole is equivalent to the zero translation.

The translation symmetry of  $C^{(\mathbf{A})}$  is characterized by a three-dimensional cyclic group  $\tilde{T}^{(\mathbf{A})}$  of order  $L$  with the elements  $(E|\mathbf{a}^{(i)})$  from (6.53) and multiplication law modulo  $T_{\mathbf{A}}$ . In our example, this group consists of 9 inner translations of the  $B_9N_9$  supercell, *i.e.* translations of the BN primitive unit cell, consisting of one formula unit. The group  $\tilde{T}^{(\mathbf{A})}$  is isomorphic to the factor group  $T^{(\mathbf{A})}$ .

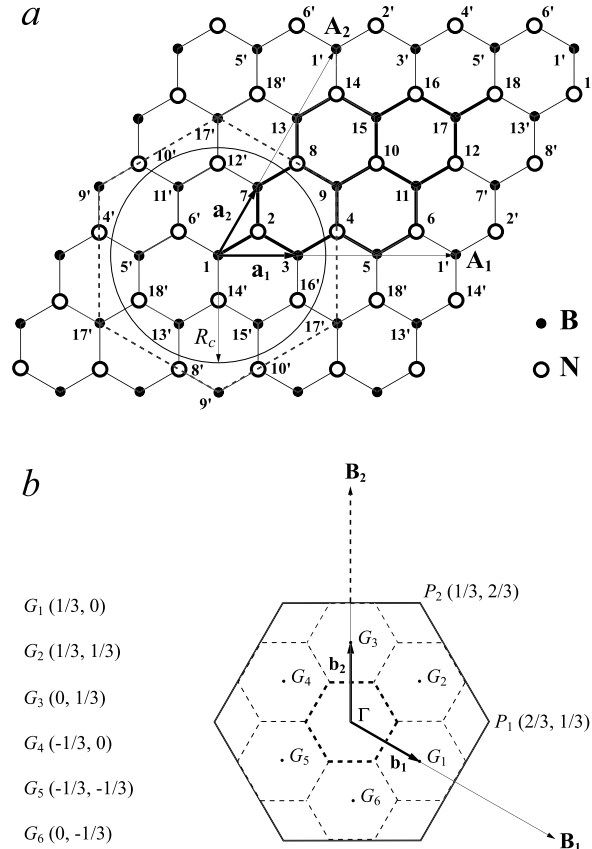


**Fig. 6.1.** Supercell (a) and small Brillouin zone (b) for hexagonal plane lattice of boron nitride BN. Atoms 1–18 belong to the supercell, the atoms with the primed numbers are supposed to be identical with the corresponding atoms, belonging to the supercell.

Let  $l^{(\mathbf{a})}(R)$  be the transformation matrix of the translation vectors  $\mathbf{a}_i$  under the point-symmetry operation  $R \in \mathbf{F}$

$$R\mathbf{a}_i = \sum_{i'} l_{i'i}^{(\mathbf{a})}(R) \mathbf{a}_{i'} \quad (6.54)$$

The corresponding transformation matrix for the translation vectors  $\mathbf{A}_j$  in (6.51) is

$$R\mathbf{A}_j = \sum_{j'} l_{j'j}^{(\mathbf{A})}(R) \mathbf{A}_{j'}, \quad l^{(\mathbf{A})}(R) = l^{-1} l^{(\mathbf{a})}(R) l \quad (6.55)$$

The operation  $(R'|\mathbf{v}' + \mathbf{a}_n) \in \mathbf{G}$  is compatible with the translation symmetry of the lattice composed of supercells, if the vectors  $R'\mathbf{A}_j$  are integer linear combinations of

the vectors  $\mathbf{A}_j$ , *i.e.* the matrix  $l^{(\mathbf{A})}(R')$  is integer. All these operations  $(R'|\mathbf{v}' + \mathbf{a}_n)$  form a group  $G' \subset G$ . The rotations  $R'$  form a point group  $F' \subset F$  of order  $n_{F'} \leq n_F$ . As

$$(R'|\mathbf{v}' + \mathbf{a}_n)(E|\mathbf{A}_j)(R'|\mathbf{v}' + \mathbf{a}_n)^{-1} = (E|R'\mathbf{A}_j) \quad (6.56)$$

the translation group  $T_A$  is an invariant subgroup of the group  $G'$ . The cosets in the decomposition

$$G' = \sum_{i=1}^L \sum_{s=1}^{n_{F'}} (R'_s|\mathbf{v}'_s + \mathbf{a}^{(i)}) T_A \quad (6.57)$$

form the factor group  $G^{(\mathbf{A})} = G'/T_A$  of the order  $n_{F'} L$ .

The coset representatives  $(R'_s|\mathbf{v}'_s + \mathbf{a}^{(i)})$  in (6.57) contain the inner translations  $\mathbf{a}^{(i)}$  of the supercell ( $i = 1, 2, \dots, L$ ) and rotational parts  $R' \in F'$  forming the point group of the space group  $G'$ .

Let us introduce a modified multiplication law modulo  $T_A$ , which does not distinguish between the translations of the group  $T_A$ . The set of  $n_{F'} L$  elements  $(R'_s|\mathbf{v}'_s + \mathbf{a}^{(i)})$  forms a group  $\tilde{G}^{(\mathbf{A})}$  (modulo  $T_A$ ), which is the symmetry group of the cyclic cluster  $C^{(\mathbf{A})}$ . The group  $\tilde{G}^{(\mathbf{A})}$  is isomorphic to the factor group  $G^{(\mathbf{A})}$ . Both groups  $(\tilde{G}^{(\mathbf{A})})$  and  $G^{(\mathbf{A})}$  are homomorphic images of the space group  $G'$ . The translation group  $T_A$  is the kernel of this homomorphism. If the space group  $G'$  coincides with the space group  $G$  the transformation (6.51) is called symmetric. In this case, the point symmetry of a cyclic cluster coincides with that of an infinite crystal. In our example, the cyclic cluster consisting of 9 primitive unit cells of hexagonal BN (see Fig. 6.1a) has the same point symmetry as the hexagonal BN in the one-layer model. The symmetric transformation (6.51) retains the point symmetry of the Bravais lattice, but it is compatible with a change of its type in the framework of the same crystalline system. As an example, one can consider the cyclic cluster defined by a crystallographic unit cell for face-centered cubic lattice (see Chap. 2) or the supercell of a hexagonal lattice, generated by the transformation with nondiagonal matrix  $l = \begin{pmatrix} 2 & 1 \\ -1 & 1 \end{pmatrix}$ , with  $L = 3$ . In the first case, the translation vectors of the cubic cluster of 4 primitive unit cells ( $l = \begin{pmatrix} -1 & 1 & 1 \\ 1 & -1 & 1 \\ 1 & 1 & -1 \end{pmatrix}$ ,  $L = 4$ ) form a simple cubic lattice. In the second case the lattice of supercells remains hexagonal. The nonsymmetric transformation (6.51) leads to a cyclic cluster with the point-symmetry group  $F'$  that is lower than that of an infinite crystal. The smallest possible cyclic cluster  $C^{(\mathbf{A})}$  is a primitive unit cell with the symmetry group  $\tilde{G}^{(\mathbf{a})}$  of the order  $n_F$  ( $\tilde{G}^{(\mathbf{a})} \leftrightarrow F$ ). The so-called main region of a crystal is also a cyclic cluster corresponding to the transformation (6.51) with very large  $L = N_1 N_2 N_3$ ; it is assumed that there are  $N_i$  primitive unit cells in direction  $\mathbf{a}_i$  ( $i = 1, 2, 3$ ) (where  $N_i$  is a very large number). When the cyclic boundary conditions are introduced for the main region of a crystal, the translation group  $T_A$  consists of translations  $\mathbf{A}_i = N_i \mathbf{a}_i$  ( $i = 1, 2, 3$ ), *i.e.* the transformation matrix  $l$  in (6.51) is assumed to be diagonal. Usually no attention is paid to the fact that the main region possesses the point symmetry of an infinite crystal only if the corresponding transformation (6.51) is symmetric. For example, the main region for a cubic crystal has to be defined with  $N_1 = N_2 = N_3$ . The space group  $G$  of the infinite

crystal may be obtained as a limit of the symmetry groups of a sequence of increasing cyclic systems.

As is seen, the symmetry operations in the cyclic-cluster symmetry group are defined with the modified multiplication law modulo  $T_A$ . These groups were named by Stewart [299] “the symmetry groups of unit cells in solids” and interpreted as a new type of group being intermediate between point-symmetry groups of molecules and space groups of infinite crystals. The irreducible representations of these groups are defined by those of space groups for the points of the BZ satisfying the condition  $\exp(i\mathbf{k}\mathbf{A}_j) = 1$  where  $\mathbf{A}_j$  are the translation vectors of the cyclic-cluster as a whole. These points are given by (4.84) for  $\mathbf{k} = \mathbf{0}$  and can be easily found. All the possible transformation matrices, given in Appendix A, can be used to generate the symmetric cyclic clusters of any of the 14 Bravais lattices. In the cyclic-cluster calculations both the point and inner translation symmetry can be taken into account [300].

The CCM model allows real-space calculations (formally corresponding to the BZ center for the infinite crystal composed of the supercells). From this point of view the cyclic cluster was termed a quasimolecular large unit cell [289] or a molecular unit cell [288].

The practical cyclic-cluster calculations for crystals were made by EHT, MR and different ZDO methods. In these calculations one has to take into account the multiplication law of the cyclic-cluster symmetry group. This requires the modifications (compared with molecules) of Fock matrix elements in the LCAO approximation. These modifications are considered in the next sections.

### 6.3.2 Semiempirical LCAO Methods in Cyclic-cluster Model

In cyclic-cluster calculations we return to the molecular level without the loss of the symmetry, replacing a whole crystal by one supercell (multiple of the primitive unit cell), applying to it PBC and embedding a cyclic cluster in the Madelung field of the surrounding crystal. Instead of the system of coupled LCAO equations (4.57) for different wavevectors in the BZ we have one equation to be solved in each iteration as in the case of molecules.

In EHT for crystals the one-electron Hamiltonian and overlap integrals matrix elements (6.4) and (6.5) depend on wavevector  $\mathbf{k}$  and are the sums over a direct lattice. The order  $M$  of the corresponding matrices  $H$  and  $S$  is equal to the number of AOs in the primitive unit cell.

In the CCM the supercell is introduced so that the order of the matrices in the secular equation (6.4) is equal to  $L \times M$ , where  $L$  is defined in (6.51) and means the number of primitive cells in a supercell. The calculation is made only for  $\mathbf{k} = \mathbf{0}$  so that instead of (6.4) we obtain the molecular-type secular equation

$$\det |H_{\mu\nu} - \varepsilon_i S_{\mu\nu}| = 0 \quad (6.58)$$

where  $\mu, \nu, i$  change from 1 to  $L \times M$ . The difference between the Hamiltonian and overlap matrices in (6.58) from the molecular analog (when the supercell atoms are taken as a free molecular cluster) is due to the introduction of PBC for the supercell chosen. Instead of lattice sums (6.5) we have now the matrix elements calculated for all  $L \times M$  AOs of a supercell. PBC are taken into account by modification of these matrix

elements. To show this modification let us consider a cyclic cluster  $B_9N_9$  of the one-layer model of hexagonal boron nitride  $BN_{\text{hex}}$ , see Fig. 6.1. The primitive unit cell in this case contains one formula unit BN, the cyclic cluster chosen is formed by threefold increase in both translation vectors of the primitive unit cell. The central cyclic cluster and the nearest translated atoms are shown in Fig. 6.1. The primed B and N atoms are not included in the cyclic cluster explicitly but are translation equivalent (with the supercell translation vectors) to the corresponding nonprimed atoms inside the cyclic cluster. As was shown in Sect. 6.3.1, due to PBC introduction the cyclic-cluster translations are multiplied *modulo* the translation group  $T_A$  of supercell as a whole (in our example this group consists of two supercell basic translations  $\mathbf{A}_1 = 3\mathbf{a}_1$ ,  $\mathbf{A}_2 = 3\mathbf{a}_2$  and all their combinations  $\mathbf{A}_n = \sum_{i=1}^2 n_i \mathbf{a}_i$  with integer coefficients  $n_i$ ). As a result the matrix elements of H and S matrices are modified. The interactions between atoms in the supercell and those outside are then used to replace their weaker analog within the supercell [285]. For example, boron atom 1 interacts with nitrogen atoms 14 and 6 in the supercell as with the nearest neighbors because in atomic pairs 14–14', 6–6' two atoms are connected by the translation vectors of a cyclic cluster as a whole (see Fig. 6.1). Thus, we have no more “central” and “boundary” atoms in the cyclic cluster – for all of them the interactions with the nearest, next-nearest and next-next-nearest neighbors are taken into account.

The cyclic cluster can be chosen in the form of the Wigner–Seitz unit cell (shown by the dotted line in Fig. 6.1 with the center at boron atom 1). A connection of the interaction range to this cells atoms was discussed in [301].

PBC introduction for the cyclic cluster chosen allows connection by of symmetry the MOs of the cyclic cluster with some COs of a whole crystal [297]. Let a perfect crystal be described in terms of supercells composed of  $L$  primitive unit cells. Correspondingly, the reduced (small) BZ of the supercell is a factor of  $L$  smaller than the original BZ of the primitive unit cell. If wavevectors in the original BZ are denoted by  $\mathbf{K}$  and wavevectors in the reduced (small) BZ by  $\mathbf{k}$ , a calculation at a single  $\mathbf{k}$ -point is equivalent to a calculation at a particular set of  $\mathbf{K}$ -points satisfying relation (4.84) determined by the translation vectors  $\mathbf{A}_n$  of the supercell chosen. This “folding back” of information was used to generate special points of BZ in the model of an infinite crystal, see Sect. 4.2.2 and also forms the basis of the cyclic-cluster model. When the whole crystal is replaced by a cyclic cluster, the  $\mathbf{k}' = \mathbf{0}$  approximation in the reduced BZ is made and (4.84) can be written in the form

$$\bar{\mathbf{K}}_t^{(0)} = \sum_j q_{tj} \mathbf{b}_j \quad (6.59)$$

where  $q_{tj}$  are integers,  $\mathbf{b}_j$  are translation vectors of a reduced BZ and  $\bar{\mathbf{K}}_t^{(0)}$  form the set of  $\mathbf{K}$ -points of the original BZ folding down onto the  $\mathbf{k} = \mathbf{0}$  point of a reduced BZ. Due to the relation  $(\mathbf{A}_i \mathbf{b}_j) = 2\pi\delta_{ij}$  between supercell translation vectors  $\mathbf{A}_i$ ,  $i = 1, 2, 3$  and small BZ translation vectors  $\mathbf{b}_j$ ,  $j = 1, 2, 3$ , (6.59) becomes equivalent to the condition

$$\exp(i\bar{\mathbf{K}}_t^{(0)} \mathbf{A}_j) = 1, \quad j = 1, 2, 3 \quad (6.60)$$

that has to be satisfied for those  $\mathbf{K}$ -points of the original BZ that fold down on  $\mathbf{k} = \mathbf{0}$  point of the reduced BZ.

In our example of a hexagonal lattice supercell with  $L = 9$  (Fig. 6.1b) the relation (6.60) is satisfied for three points of the plane hexagonal BZ,  $\Gamma(0, 0)$ ,  $2P(1/3, 1/3)$ ,

$6G(1/3, 0)$  (the integer numbers mean the number of rays in the stars, the coordinates of stars representatives from the irreducible part of the BZ are given in brackets). These points formally become equivalent to the  $\Gamma(\mathbf{k} = \mathbf{0})$  point of the primitive-cell BZ [289].

Therefore, the cyclic-cluster energy level degeneration differs from that which would be for the corresponding free cluster of the same atoms. In the latter case, the point symmetry of the cluster is  $C_{3v}$ , so that only the degeneracy of levels can be one or two (dimensions of irreps of point group  $C_{3v}$ ). In the former case, the degeneracy of MOs remains at 1, 2 only at the  $\Gamma$  point of the BZ. The one-electron states at  $P$  and  $G$  points are 2-, 4- and 6-times degenerate, respectively. It becomes clear when one takes into account that the space-group irrep dimension is the product of the dimension of the irrep of the wavevector point group ( $C_3$  for  $P$  point,  $C_1$  for  $G$  point) times the number of rays in wavevector star (2, 6 for  $P$  and  $G$  points, respectively, see Chap. 3). It is also necessary to take into account the time-inversion symmetry making additional degeneracy for  $\mathbf{k}$  and  $-\mathbf{k}$  values of the wavevector.

What happens when the cyclic cluster is increased? Depending on its shape and size different sets of  $\mathbf{k}$ -points are reproduced, but in the EHT matrix elements the number of interactions included (interaction radius) increases as the periodically reproduced atomic sites distance is defined by the translation vector of a cyclic cluster as a whole. It is important to reproduce in the cyclic-cluster calculations the states defining the bandgap. As the overlap matrix elements decay exponentially with the interatomic distance one obtains the convergence of results with increasing cyclic cluster. Of course, this convergence is slower the more diffuse are the AOs in the basis. From band-structure calculations it is known that for  $\text{BN}_{\text{hex}}$  in the one-layer model the top of the valence band and the bottom of the conduction band are at the point  $P$  of the BZ reproduced in the cyclic cluster considered.

We note that the symmetry connection of crystal and cyclic-cluster one-electron states is defined only by the supercell choice and therefore does not depend on the method used in the Hamiltonian matrix-elements calculations.

The EHT method is noniterative so that the results of CCM application depend only on the overlap interaction radius. The more complicated situation takes place in iterative Mulliken–Rüdenberg and self-consistent ZDO methods. In these methods for crystals, the atomic charges or the whole of the density matrix are calculated by summation over  $\mathbf{k}$  points in the BZ and recalculated at each iteration step. The direct lattice summations have to be made in the surviving integrals calculation before the iteration procedure. However, when the nonlocal exchange is taken into account (as is done in the ZDO methods) the balance between direct lattice and BZ summations has to be ensured. This balance is automatically ensured in cyclic-cluster calculations as was shown in Chap. 4. Therefore, in iterative MR and self-consistent ZDO methods the increase of the cyclic cluster ensures increasing accuracy in the direct lattice and BZ summation simultaneously. This advantage of CCM is in many cases underestimated.

In the MR method the matrix elements of a cyclic cluster are obtained from those for the crystal, taking  $\mathbf{k} = \mathbf{0}$  in (6.26). The modification of matrix elements due to PBC introduction has to be introduced in overlap and kinetic-energy integral calculation. The latter are expressed through overlap integrals so that there are no principal differences in the EHT and MR methods in the matrix-element modification, ensuring periodicity of the cluster chosen. The only difference is connected with the iterative

procedure of atomic charge and configuration self-consistency in the MR method, requiring the calculation of diagonal elements of the density matrix. In this calculation the summation over occupied MOs of the cyclic cluster is made that is equivalent to summation over those  $\mathbf{K}$ -points of the original BZ that satisfy relation (6.60). The diagonal elements of the MR method Hamiltonian are corrected by the point-charge (Madelung) field of the surrounding crystal acting on cyclic-cluster atoms, see (6.26). In fact, the embedded cyclic cluster is considered. For ionic systems such a correction of CCM is necessary both in the ZDO and SINDO methods [301, 302]. In CCM the iterative calculations the atomic charges are used at any step of the iterative procedure to recalculate the Madelung energy for all atoms of a cyclic cluster and at the next step the atomic charges are recalculated with the matrix elements corrected by a recalculated Madelung energy.

Within the  $\mathbf{k} = \mathbf{0}$  approximation the CNDO Hamiltonian for the supercell becomes

$$F_{\mu\mu}(\mathbf{0}) = U_{\mu\mu} + Z_M \gamma_{MM}^{00} + \sum_N \left( \frac{1}{L'} \sum_{\mathbf{k}'} P_N(\mathbf{k}') - Z_N \right) \sum_{n=0}^{L'-1} \gamma_{MN}^{0n} \\ + \sum_{n=0}^{L'-1} \beta_M^0 (S_{\mu\mu}^{0n} - \delta_{0n}) - \frac{1}{2L'} \sum_{n=0}^{L'-1} \sum_{\mathbf{k}'} P_{\mu\mu}(\mathbf{k}') \exp(-i\mathbf{k}'\mathbf{R}_n) \gamma_{MM}^{0n} \quad (6.61)$$

$$F_{\mu\nu}(\mathbf{0}) = \sum_{n=0}^{L'-1} \beta_{MN}^0 S_{\mu\nu}^{0n} - \frac{1}{2L'} \sum_{n=0}^{L'-1} \sum_{\mathbf{k}'} P_{\mu\nu}(\mathbf{k}') \exp(-i\mathbf{k}'\mathbf{R}_n) \gamma_{MN}^{0n} \quad (6.62)$$

where  $L'$  is the number of supercells in the main region of a crystal and  $\mathbf{k}'$ -summation is made over the reduced BZ.

A calculation performed solely at the  $\Gamma(\mathbf{k}' = \mathbf{0})$  point of the supercell BZ would become entirely equivalent to special  $\mathbf{K}$ -points (6.59) calculation if all the direct lattice summations were made over the whole crystal. However, in CCM the interaction range depends on the cyclic-cluster size. To determine the  $\mathbf{k}' = \mathbf{0}$  Fock matrix elements we need the full  $\mathbf{k}'$  dependence of the supercell density matrices  $P_{\mu\nu}(\mathbf{k}')$ , see (6.61) and (6.62). Meanwhile, each iteration in a cyclic-cluster calculation only provides the eigenvector coefficients  $C_{i\mu}(\mathbf{0})$  at  $\mathbf{k}' = \mathbf{0}$ , and hence only  $P_{\mu\nu}(\mathbf{0})$ . Therefore, it is necessary to relate the reduced BZ integrals over the fully  $\mathbf{k}'$ -dependent density matrices, namely  $\sum_{\mathbf{k}'} P_N(\mathbf{k}')$  and  $\sum_{\mathbf{k}'} P_{\mu\nu}(\mathbf{k}') \exp(-i\mathbf{k}'\mathbf{R}_n)$  to  $P_N(\mathbf{0})$  and  $P_{\mu\nu}(\mathbf{0})$ , respectively [280]. For sufficiently large supercells all the values of  $\mathbf{k}'$  in the reduced BZ will lie near  $\mathbf{k}' = \mathbf{0}$ , so that it should be valid to ignore the effect of the phase factor and use the fact that the reduced BZ is spanned by  $L$   $\mathbf{k}$ -points to obtain

$$\frac{1}{L'} \sum_{\mathbf{k}'} P_{\mu\nu} \exp(-i\mathbf{k}'\mathbf{R}_n) \rightarrow P_{\mu\nu}(\mathbf{0}) \quad (6.63)$$

Simple substitution of (6.63) into (6.61) and (6.62) would introduce divergent lattice sums of  $\gamma_{MN}^{0n}$  integrals. Therefore, a distance-dependent modulating function  $\omega(R_{MN}^{0n})$  was introduced [280] such that

$$\frac{1}{L'} \sum_{\mathbf{k}'} P_{\mu\nu}(\mathbf{k}') \exp(-i\mathbf{k}'\mathbf{R}_n) = \omega(R_{MN}^{0n}) P_{\mu\nu}(\mathbf{0}) \quad (6.64)$$

(orbital  $\mu$  on atom  $M$  is in cell 0 and orbital  $\nu$  is on atom  $N$  in cell  $n$ ).

To find an approximate form of this modulating function a tight-binding description of a one-dimensional chain of atoms possessing one atom per primitive unit cell and two orbitals per atom was studied [280]. The  $\text{sinc}^2(\frac{\pi}{a}R_{MN}^{0n})$  function found was simply extended to the three-dimensional cubic lattice case. Unfortunately, the form of this modulating function depends on the direct lattice of supercells and its extension to noncubic lattices is nontrivial.

In some cases the modulating function  $\omega(R_{MN}^{0n})$  is taken as the simple step function

$$\omega(R_{MN}^{0n}) = \begin{cases} 1 & \text{if } R_{MN}^{0n} \leq R_c \\ 0 & \text{if } R_{MN}^{0n} > R_c \end{cases} \quad (6.65)$$

where the exchange cutoff radius  $R_c$  in (6.65) was a variable parameter or taken intuitively to be about a half of the cyclic cluster smallest translation vector length. As was shown in Sect. 4.3.3, the modulating (weighting) function explicit form (4.157) can be found in the interpolation procedure for constructing an approximate density matrix. The modulating step function suggested in (4.157) is easily applied to any type of lattice and was incorporated into both HF and CNDO cyclic-cluster calculations [70]. It was shown that the exchange interaction range should be chosen such that the corresponding sphere of radius  $R_c$  differs only slightly from the Wigner–Seitz supercell, corresponding to the cyclic cluster. This gave a theoretical background to the former intuitive choice (6.65) of the exchange interaction radius  $R_c$ .

Cyclic-cluster CNDO Hamiltonian matrix elements may be written in the following form

$$\begin{aligned} F_{\mu\mu}(\mathbf{0}) = & U_{\mu\mu} + Z_M \gamma_{MM}^{00} + \sum_N \sum_{n=0}^{L'-1} \sum_{\nu \in N} (P_{\mu\mu}(\mathbf{0}) - Z_N) \gamma_{MN}^{0n} \\ & + \sum_{n=0}^{L'-1} \beta_M^0 S_{\mu\mu}^{0n} - \frac{1}{2} \sum_{n=0}^{L'-1} P_{\mu\mu}(\mathbf{0}) \omega(R_{MN}^{0n}) \gamma_{MM}^{0n} \end{aligned} \quad (6.66)$$

$$F_{\mu\nu}(\mathbf{0}) = \sum_{n=0}^{L'-1} \beta_{MN}^0 S_{\mu\nu}^{0n} - \frac{1}{2} \sum_{n=0}^{L'-1} P_{\mu\nu}(\mathbf{0}) \omega(R_{MN}^{0n}) \gamma_{MN}^{0n} \quad (6.67)$$

Comparing CCM Hamiltonian matrix elements (6.66) and (6.67) with those for a free molecule, Equations (6.33)–(6.35), one can see the differences. Equations (6.66) and (6.67) formally include summation over the main region of a crystal composed of the equivalent supercells. The lattice sums containing overlap integrals are truncated for a cyclic cluster in the CNDO method in the same way as is done in the EHT and MR methods. For the Coulomb interaction sums (third item in (6.66)) the Ewald method can be used to calculate the Madelung energy of a crystal surrounding the cyclic cluster. The modulating function  $\omega(R_{MN}^{0n})$  ensures the truncation of the diverging lattice sums appearing in the nonlocal exchange interactions (last items in (6.66) and (6.67)).

CCM has been implemented in various ZDO methods: CNDO-INDO [276, 277, 280, 303–310], MINDO/3 [311], MNDO [271], NDDO(AM1, PM3), [312]. All the semiempirical methods stand or fall by their parameter set. The ZDO methods parameter

sets suitable for molecular calculations will not necessarily be suitable for the solid state. The parametrization scheme may be dependent on the chemical bonding in the crystal (different sets of parameters are suitable for ionic and covalent crystals), introducing additional difficulties.

The main ZDO parameters for each orbital type are: the orbital exponent  $\zeta$  entering the radial part of Slater-type AOs, the diagonal matrix elements  $U_{\mu\mu}$  of the interaction of an electron occupying AO  $\chi_\mu$  with its own core expressed through electronegativity  $E_{neg}^M = -1/2(I_\mu + A_\mu)$  of this AO, the resonance integrals  $\beta$  depending only on the atom type. Additional parameters appear in the matrix elements of an interaction of an electron on the  $\mu$ th AO belonging to atom  $M$  with the core of another atom  $N$ , [313]:

$$V_{\mu N} = Z_N \left\{ \frac{1}{R_{MN}} + \left[ (\mu\mu|\nu\nu) - \frac{1}{R_{MN}} \right] \exp(-\alpha_N R_{MN}) \right\} \quad (6.68)$$

where  $R_{MN}$  is the distance between  $M$  and  $N$ ,  $Z_N$  is the core charge of atom  $N$ ,  $\alpha_N$  is an adjustable parameter characterizing the nonpoint nature of the atom  $N$  core. AOs  $\chi_\mu$  and  $\chi_\nu$  belong to atoms  $M$  and  $N$ , respectively, the two-center Coulomb integral  $(\mu\mu|\nu\nu)$  may be calculated with STOs or considered as  $\gamma_{MN}$  depending only on atoms types. The detailed discussion of parameter choice in CCM ZDO methods can be found for different types of crystalline solids: ionic crystals of alkali halides [300, 304, 314, 315] and simple oxides MgO, CaO [313], covalent and partly covalent semiconductors [276, 293, 310, 312, 316, 317], crystalline oxides with different structure [318], including high- $T_c$  superconductors [318].

In the next section we discuss MSINDO semiempirical and HF nonempirical methods implementation of CCM for the calculation of bulk properties of rutile crystal. The efficiency of the MSINDO method will be demonstrated that gives reasonable agreement with the results of HF calculations and at the same time is essentially simpler in practical realization.

### 6.3.3 Implementation of the Cyclic-cluster Model in MSINDO and Hartree–Fock LCAO Methods

The cyclic-cluster approach was implemented in the semiempirical SCF-MO method SINDO1 [319] and its recent modification MSINDO [301] and has been successfully applied for bulk and surface properties of oxides [302, 320].

The underlying strategy of the CCM implementation in MSINDO was to start from a molecular system and to introduce PBC in such a way that both local point symmetry and stoichiometry of the system are conserved. Within this approach the local environment of each cyclic-cluster atom is replaced by that of a fictitious cyclic arrangement. A cluster of  $n$  atoms in one dimension is treated in the same way as a cyclic arrangement of the same number of atoms on a ring. Two- and three-dimensional systems are treated as arrangements on a torus and a hypertorus, respectively. All interactions for each atom  $M$  are then calculated within an interaction region around that atom, corresponding to its Wigner–Seitz cell (WSC). For two-center integrals (overlap, nuclear attraction, electron repulsion) between the  $M$  atom of the interaction region and atoms at the boundaries of its WSC [301] weighting factors are used to retain the proper symmetry. In this approach, the cyclicity and summation

regions are the same and not dependent on integral thresholds as for periodic LCAO methods [23]. Long-range Coulomb interactions have been taken into account by additional finite point charge fields outside the cyclic cluster [302]. A scheme for the calculation of analytical gradients has been developed for structure optimization of cyclic clusters [301].

In MSINDO only two-center two-electron integrals of the form  $(\mu M \mu M | \nu N \nu N)$  are taken into account. Atomic orbitals  $\chi_\mu$  and  $\chi_\nu$  are taken as *s*-type functions. Therefore, these integrals have no angular dependence and an averaging over integrals between different atoms on the same radius around the considered atom causes no problems.

In MSINDO also two-center one-electron integrals are replaced by empirical formulas that do not contain any angular dependence, so that the two-center elements of the Fock matrix have the following form [249]:

$$F_{\mu\nu} = H_{\mu\nu} + P_{\mu\nu}(\mu\mu|\nu\nu) = \Delta H_{\mu\nu} + L_{\mu\nu} + P_{\mu\nu}(\mu\mu|\nu\nu) \quad (\mu \in M, \nu \in N) \quad (6.69)$$

with the two parametrized empirical functions

$$\begin{aligned} \Delta H_{\mu\nu} &= \frac{1}{4} (K_M + K_N) S_{\mu\nu} (f_M h_{\mu\mu} + f_N h_{\nu\nu}), \quad f_M = 1 - \exp(-\alpha_M R_{MN}) \\ L_{\mu\nu} &= -\frac{1}{2} (\zeta_\mu^2 + \zeta_\nu^2) \frac{S_{\mu\nu}(1 - S_{\mu\nu})}{1 + 1/2(\zeta_\mu + \zeta_\nu)R_{MN}} \end{aligned} \quad (6.70)$$

where  $\zeta_\mu, \zeta_\nu$  are orbital exponents,  $K_M, K_N$ , and  $\alpha_M$  are empirical parameters optimized for a given set of reference molecules. In CCM calculations these matrix elements remain unchanged when atom  $N$  is in the inner part of the interaction region of atom  $M$ . In the case that  $N$  is on the border of the interaction region around  $M$ , the contributions from all  $n_{MN'}$  atoms  $N'$  that are translationally equivalent to  $N$  and appear at the same radius are summed up into one matrix element with weighting coefficient [301]:

$$\begin{aligned} H_{\mu\nu} &= \sum_{N'}^{\text{equiv}} \omega_{MN'} H_{\mu\nu'}, \quad \nu' \in N \\ G_{\mu\nu} &= \sum_{N'}^{\text{equiv}} \omega_{MN'} (\mu\mu|\nu'\nu') \end{aligned} \quad (6.71)$$

The construction of the Fock matrix and the SCF procedure to obtain a converged density matrix of the cyclic system are essentially identical to the molecular case. The only extension is the inclusion of an external point charge field that is added to the diagonal terms of  $F$ . As the calculations for the cyclic clusters are performed in real space, no Bloch functions are used as the basis set. This strategy makes a direct comparison between calculations for free and cyclic clusters possible. Because of the quadratic increase of the number of two-center integrals with the number of cluster atoms a special technique can be used to reduce the computational effort [321]. This technique is based on the sorting of the interatomic distances because equal atom pairs with the same distance have identical integrals in a local coordinate system. With this technique the number of calculated integrals can be decreased by a factor of

1000 or more. All features available in the molecular version of MSINDO, for example, configuration interaction, geometry optimization, or vibration analysis, can also be used for the cyclic clusters. This also includes the treatment of charged systems that are generally difficult to treat with periodic methods.

Interactions of an ion  $M$  with ions  $N''$  at a distance beyond the borders of the WSC will decrease rapidly with increasing interatomic distance in covalent systems. This does not hold for ionic systems, since Coulomb-type interactions fall off slowly. If the ions  $N''$  are approximated as point charges with a net charge  $q$ , the Madelung potential due to these charges, which can be calculated by the Ewald summation technique as shown in [302], will modify the Fock matrix and the total energy in the following way

$$F^{MAD}(P) = F(P) + V^{MAD}(P) \quad (6.72)$$

$$E_{tot} = \frac{1}{2} \text{Tr} [P(H + F^{MAD})] + V_{NN} + E^{MAD} \quad (6.73)$$

Here  $F$  denotes the Fock matrix,  $F^{MAD}$  the Madelung-corrected Fock matrix,  $P$  the density matrix,  $H$  is the core Hamiltonian matrix,  $E_{tot}$  the total energy of the system and  $V_{NN}$  the nuclear repulsion term. The terms  $V^{MAD}(P)$  and  $E^{MAD}$  denote the Madelung correction of the Fock matrix and of the nuclear repulsion, respectively. Due to the application of the ZDO approximation in MSINDO,  $V^{MAD}(P)$  is a diagonal matrix,

$$V_{\mu M \mu M}^{MAD} = \Phi_{mD}(\bar{d}_M) - \sum_{N''} \omega_{MN''} \frac{q_{N''}}{|\bar{d}_M - \bar{d}_{N''}|} \quad (6.74)$$

$$E^{MAD} = \frac{1}{2} \sum_M Z_M^* \left[ \Phi_{mD}(\bar{d}_M) - \sum_{N''} \omega_{MN''} \frac{q_{N''}}{|\bar{d}_M - \bar{d}_{N''}|} \right] \quad (6.75)$$

$Z_M^*$  is the effective nuclear charge of atom  $M$ . The corrections are implemented in a self-consistent manner, since the net charges  $q_{N''}$  are calculated from the cluster density matrix  $P$  using a Löwdin population analysis. The electrostatic interactions of the ion  $M$  with the ions in its WSC must be subtracted from the Madelung potential  $\Phi_{mD}$ , because these interactions are already considered in the unmodified Fock matrix  $F(P)$ . To avoid double counting of interactions the factor 1/2 is introduced in (6.75).

It has to be mentioned that the simple procedure used in CCM MSINDO of an averaging of two-center integrals between the central atom of the interaction region and atoms at the boundaries of its WSC is not possible for *ab-initio* Hartree-Fock methods due to the presence of three- and four-center integrals.

The implementation of the CCM in the HF LCAO method is based on the use of the idempotency property of a one-electron density matrix (DM) of crystalline systems [100]. The underlying strategy in this case was to start from a periodic system and to make small modifications in the corresponding LCAO computer codes. It has to be mentioned that the CCM realization in PW basis seems to be impossible as the interaction region in this case can not be defined.

The idempotency of the DM is a consequence of the orthonormality of the one-electron Bloch functions that are the basis of the crystalline orbitals. In the CCM the DM has to be idempotent when a one-determinant wavefunction is used and convergence with cluster size is achieved. The infinite DM of a solid formally does not have this property, but the infinite solid itself is modeled by a very large cyclic cluster

describing the main region of the crystal when Born–von Karman PBC are introduced to ensure macroscopic periodicity of a crystal model. In Sect. 4.3.3 the CCM of the infinite crystal was deduced from the study of the approximate DM (4.164). The supercell corresponding to the cyclic cluster under consideration was taken as the Wigner–Seitz supercell; to have the proper point symmetry the weighting function (4.165) was introduced. Defining an atomic covalence as the sum of Wiberg indices for an atom in the cyclic cluster or all the other atoms of a crystal the relation (4.140) was obtained. This relation means that the atomic covalence in a cyclic cluster may be calculated as a lattice sum  $C_M^{(2)}$  of Wiberg indices and as an expression  $C_M^{(1)}$ , containing only those DM elements that refer to atom  $M$ :

$$\begin{aligned} \sum_M C_M^{(2)} &= \sum_M \sum_{M \neq N} \omega_N(\bar{R}_N) W_{MN}(\bar{R}_n) + \sum_M W_{MM}(0) = N_e^C \\ \sum_M C_M^{(1)} &= \sum_M \left( 2 \sum_{\mu \in M} P_{\mu\mu}^L(0) - W_{MM}(0) \right) = N_e \end{aligned} \quad (6.76)$$

where  $N_e^C, N_e$  is the number of electrons in the primitive unit cell. For each cyclic cluster there are certain weighting coefficients  $\omega_N(\bar{R}_N)$  of neighbor atoms in spheres around atom  $M$ . For the inner atoms of a cyclic cluster  $\omega_N = 1$ , while for border atoms  $\omega_N < 1$ .

Relation (6.76) provides a simple way to check the idempotency property of the DM. Therefore, it can be used to implement the CCM in HF LCAO calculations.

This implementation requires simple modifications in the property part of the CRYSTAL program [23]. A Löwdin population analysis is introduced for self-consistent DM and the bond-order sums are calculated for atoms of the crystal. The lattice summation in (6.76) is made over the same part of the lattice that has been used in the integrals calculation for the self-consistent procedure (the lattice summation field is defined by the most severe tolerance used in the two-electron exchange integrals calculation).

In order to receive results for a cyclic cluster, relation (6.76) is checked for different choices of tolerances in the integrals calculations and  $Q$  sets of wavevectors in the BZ, corresponding to those  $\mathbf{K}$ -sets that satisfy (6.60). The implementation of a cyclic cluster for perfect crystals is realized in most cases by using the primitive unit cell and taking into account that the *cyclicity field* of the DM is defined by the choice of  $Q$ . The implementation of the CCM in HF LCAO calculations is demonstrated for the rutile structure.

The tetragonal rutile structure belongs to space group  $P4_2/mnm(D_{4h}^{14})$  and contains two  $\text{TiO}_2$  units per cell. The two Ti atoms are located at the Wyckoff  $2a$  sites  $(0, 0, 0)$  and  $(1/2, 1/2, 1/2)$  with  $D_{2h}$  site symmetry, while the four O atoms are located at the  $4f$  sites  $\pm(u, u, 0)$  and  $\pm(u + 1/2, 1/2 - u, 1/2)$  with site symmetry  $C_{2v}$  (see Sect. 2.3.3). The primitive unit cell of rutile is illustrated in Fig. 6.2. Each Ti atom is surrounded by a slightly distorted octahedron of O atoms with two different Ti–O distances. In connection with the cyclic-cluster choice it is useful to label the atoms surrounding  $\text{Ti}_{(1)}$  and  $\text{O}_{(3)}$  in the primitive cell  $(000)$  by the translation vectors of the corresponding unit cells (see Fig. 6.2). From Fig. 6.2 it is seen that the inclusion of all nearest neighbors for a Ti atom requires at least a cyclic cluster with translation vectors  $\mathbf{a}_1(0, 0, a), \mathbf{a}_2(0, a, 0), 2\mathbf{a}_3(0, 0, 2c)$ . The smallest cyclic cluster

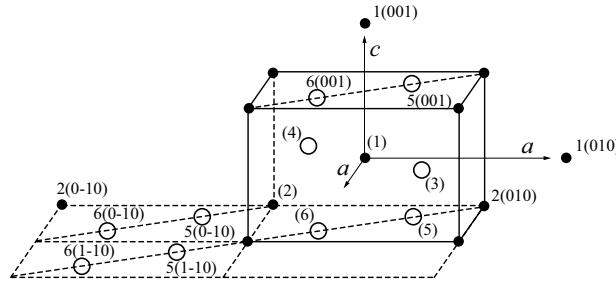


**Fig. 6.2.** Labeling of atoms in the rutile bulk unit cell; selected atoms of neighboring unit cells are also given

that contains the nearest neighbors to an O atom is formed by translation vectors  $2\mathbf{a}_1(2a, 0, 0), 2\mathbf{a}_2(0, 2a, 0), 2\mathbf{a}_3(0, 0, 2c)$ . For simple tetragonal lattices the symmetric supercells can be made in four different ways while maintaining tetragonal symmetry:

1. By simple extension of translation vectors ( $n_1\mathbf{a}_1, n_2\mathbf{a}_2, n_3\mathbf{a}_3$ ). The corresponding transformation matrix is given in Table 6.1 at the bottom of the first column.
2. By rotation of vectors  $\mathbf{a}_1$  and  $\mathbf{a}_2$  by  $45^\circ$  in their plane and extension of the vector. The transformation matrix is given in the second column of Table 6.1.
3. By changing from a simple to a body-centered tetragonal lattice. This can be achieved in two different ways. The corresponding transformation matrices are given in columns 3 and 4 of Table 6.3.

In Table 6.3 cyclic clusters representing the rutile bulk structure are given that are generated from the primitive bulk unit cell by applying the above-mentioned four types of LUC transformations. The cluster size was restricted to  $L = 24$  (144 atoms).

As it was noted in Sect. 6.3.2 CCM allows us to connect by symmetry the MOs of cyclic cluster with those COs of a whole crystal for which (6.60) is satisfied.

The BZ for the simple tetragonal lattice was shown in Fig. 3.7. The  $\mathbf{K}$  symmetry points and  $\mathbf{K}$ -points in symmetry lines (in units of the basic translation vectors of the reciprocal simple tetragonal lattice) are the following (for lines of symmetry the parameter  $p < 1$  has to be introduced). Symmetry points  $\Gamma(0, 0, 0)$ ,  $M(\frac{1}{2}, \frac{1}{2}, 0)$ ,  $Z(0, 0, \frac{1}{2})$ ,  $A(\frac{1}{2}, \frac{1}{2}, \frac{1}{2})$ ,  $2X(0, \frac{1}{2}, 0)$ ,  $2R(0, \frac{1}{2}, \frac{1}{2})$ ; symmetry lines  $\Gamma - X = \Delta(0, p, 0)$ ,  $\Gamma - M = \Sigma(p, p, 0)$ ,  $\Gamma - Z = \Lambda(0, 0, p)$ ,  $M - X = Y(p, \frac{1}{2}, 0)$ ,  $A - R = T(p, \frac{1}{2}, \frac{1}{2})$ ,  $Z - A = S(p, p, \frac{1}{2})$ ,  $M - A = V(\frac{1}{2}, \frac{1}{2}, p)$ ,  $Z - R = U(0, p, \frac{1}{2})$ ,  $X - R = W(0, \frac{1}{2}, p)$ ,  $\Gamma - A = \varepsilon(p, p, p)$ .

In Table 6.3 are given  $\mathbf{K}$ -point sets of the primitive cell BZ satisfying (6.60) and folding down on the  $\mathbf{k} = \mathbf{0}$  point of the reduced BZ. The interaction region in CCM may be defined by WSC around each atom of a cyclic cluster or by the number  $J$  of spheres of direct lattice translation vectors  $\mathbf{A}_n$  with smallest nonzero length, also given in Table 6.3.

To implement CCM into the HF LCAO calculations [100] the periodic crystalline-orbital program CRYSTAL95 [322] was used with the modifications [97] allow the DM idempotency (6.76) to be checked. In rutile  $\text{TiO}_2$  calculations the AO bases, lattice parameters and effective core potentials were taken to be the same as those used in [323] to calculate the optimized lattice parameters. In the CRYSTAL code

Table 6.3. Cyclic clusters used for the representation of the rutile bulk; special point (SP)-set, and its accuracy  $J$ 

$n_1$	$n_2$	CL <sup>a</sup> .1			CL <sup>a</sup> .2			CL <sup>a</sup> .3			CL <sup>a</sup> .4		
		cluster	SP-set	$J$	cluster	SP-set	$J$	cluster	SP-set	$J$	cluster	SP-set	$J$
1	1	C2.2		$\Gamma, Z$	C2.3		$\Gamma, A$	3	C4.4		$\Gamma, M, 2R$		4
1	2	C2.1	$\Gamma, M$	2	C4.2	$\Gamma, M, A, Z$	4	C4.3	$\Gamma, Z, 2V$	5	C8.4	$\Gamma, M, Z, A,$	8
2	1	C4.1	$\Gamma, M, 2X$	1	C8.2	$\Gamma, M, 2X,$ $4\Sigma(p = \frac{1}{4})$	1	C8.3	$\Gamma, M, 2X,$ $4S(p = \frac{1}{4})$	4	C16.4	$4W(p = \frac{1}{4})$	4
2	2	C8.1	$\Gamma, M, Z,$ $A, 2X, 2R$	4	C16.2	$\Gamma, M, Z,$ $A, 2X, 2R,$ $4\Sigma, 4S(p = \frac{1}{4})$	4	C16.3	$\Gamma, M, 2X, Z,$ $A, 2R,$ $8\varepsilon(p = \frac{1}{4})$	15		$\Gamma, M, 2X,$ $2V, 2A, 4W,$ $4S(p = \frac{1}{4}),$ $8(\frac{1}{4}, \frac{1}{4}, \frac{1}{3})$	19
2	3	C12.1	$\Gamma, M, 2X,$ $2A, 2V,$ $2W(p = \frac{1}{3})$	9	C24.2	$\Gamma, M, 2X,$ $2V, 2A, 4W,$ $4\Sigma(p = \frac{1}{3}), 8(\frac{1}{4}, \frac{1}{4}, \frac{1}{3})$	9	C24.3	$2V, 2A, 4W,$ $8(\frac{1}{4}, \frac{1}{4}, \frac{1}{6})$	19			
2	4	C16.1	$\Gamma, M, 2X,$ $Z, A, 2R, 2A,$ $2V, 4W(p = \frac{1}{4})$	10									

<sup>a</sup>  $L$  is the number of primitive unit cells in the large unit cell defining the cyclic cluster. The number  $m$  in CL.m defines the choice of the corresponding transformation matrix given at the bottom of each column.

[23] the lattice sums of the integrals are truncated when the integrals values are smaller than  $10^{-t_i}$ . The tolerances  $t_i (i = 1 - 5)$  define the accuracy of the lattice-sums calculation. The band-structure calculations using the primitive unit cell of the rutile, the tolerances  $t_1 = t_2 = t_3 = t_4 = 6, t_5 = 12$  (the latter is used for exchange interactions) and shrinking factor IS=6 (216  $\mathbf{k}$ -points of  $6 \times 6 \times 6$  Monkhorst-Pack special points in the BZ) ensure the converged results for the total energy per primitive cell, top of the valence band and Löwdin charge on the Ti-atom (-69.7758 a.u., -0.3028 a.u and  $q=1.73$ , respectively).

The cyclic-cluster calculations were performed using the SUPERCELL option of CRYSTAL95 and setting the shrinking factors IS to unity (corresponding to the  $\mathbf{k} = 0$  point in the BZ), defining the DM cyclicity region as the cyclic-cluster region itself. For the calculation of the total number of electrons per primitive cell (6.76) can be used. For each cyclic cluster there are certain weighting coefficients of neighbor atoms in spheres  $i$  around  $\text{Ti}(\omega_{\text{Ti}}(i))$  and  $\text{O}(\omega_{\text{O}}(i))$ . At the same time the above-mentioned tolerance  $t_5$  defines the interaction radius for the exchange-integral truncation. For the given structural parameters and basis sets this radius is 8.16 Å around a Ti atom and 7.84 Å around an O atom, respectively (for rutile  $\text{TiO}_2$  with the optimized structures parameters  $a=4.555$  Å,  $c=2.998$  Å,  $u=0.306$ ). The total number of electrons per unit cell  $N_e$  within the interaction radius calculated by summing bond orders over spheres  $i$ , containing a total number  $N(i)$  of atoms as given in the second line of Table 6.4. An analysis of Table 6.4 allows a cyclic cluster of relatively small size to be chosen in such a way that it still reproduces bulk properties with reasonable accuracy.

For the small-size clusters ( $L = 4, 8$ ) the imbalance of the cyclicity region and the interaction radius causes a huge difference between  $N_e^C$  and  $N_e^s$  as the sum of bond orders inside the interaction radius includes the neighboring cyclic clusters around the central cyclic cluster. The PBCs force atoms outside the central cyclic cluster to be equivalent to the corresponding atoms inside the cluster. At the same time the summation of bond orders inside a *cyclicity region* gives  $N_e^C$  values that are largely model-size independent, as the DM is calculated for the cyclic cluster under consideration.

From Table 6.4 one concludes also that even for the same size  $L$  of a cyclic cluster the difference of the calculated properties  $E_{\text{tot}}, \varepsilon_{\text{top}}$ , and atomic charges  $q$  strongly depends on the “compactness” of a cluster. The compactness is defined by the number of spheres  $i$  of neighboring atoms with  $\omega(i) = 1$  inside the cyclic cluster. This property of cyclic clusters is important as, for example, the more compact cluster C4.3 gives results closer to the band calculation limit than the larger but less compact cluster C8.2. In order to construct more compact clusters, the anisotropy of the rutile structure ( $a \approx 1.5c$ ) has to be taken into account.

Table 6.5 shows the effect of integral thresholds on the calculated properties of cyclic clusters.

For the cyclic cluster C12.1 the calculated properties are close to those for C16.3, but the difference  $N_e^s - N_e^C$  is much larger, 3.2, *i.e.* the DM is nonidempotent. It is well known that small changes of only the most severe integral threshold do not essentially affect the results [324]. Therefore, its decrease may restore the DM idempotency while the calculated properties are only slightly changed. It is demonstrated in Table 6.5 that by using  $t_5 = 9$  instead of 12, the difference  $N_e^s - N_e^C$  decreases drastically to 0.10 for the same cluster, C12.1. For C16.1 the influence of  $t_5$  is also small. For a

**Table 6.4.** Results of HF LCAO calculations of cyclic clusters for bulk rutile. Quality  $J$ , the difference of the total energy  $\Delta E$  and the energy of the valence band top  $\Delta\epsilon$  (a.u.) with respect to the largest cluster C216.1, total number of electrons per unit cell calculated with (6.76) within the corresponding cyclic cluster ( $N_e^C$ ) and within the interaction radius defined by the integral thresholds ( $N_e^S$ ), weighting coefficients of neighboring atoms in spheres  $i$  around Ti ( $\omega_{\text{Ti}}(i)$ ) and O ( $\omega_{\text{O}}(i)$ ), total number of atoms  $N(i)$  in sphere  $i$ , Löwdin charge  $q_{\text{Ti}}$  on Ti

Cluster	$J$	$\Delta E$	$\Delta\epsilon$	$N_e^C$	$N_e^S$	Spheres $i$													
						1	2	3	4	5	6	7	8	9	10				
						4	2	4	8	4	2	1	8	2	2	2	1	$q_{\text{Ti}}$	
CL4.1	1	-4.4041	-0.2856	63.91	245.80	$\frac{1}{2}$	1	0	1	$\frac{1}{2}$	0	$\frac{1}{2}$	1	1	$\frac{1}{2}$	0	1	0	1.97
CL4.2	4	-0.0302	-0.0136	63.85	199.57	1	1	$\frac{1}{2}$	$\frac{1}{2}$	$\frac{1}{2}$	1	1	1	$\frac{1}{2}$	$\frac{1}{2}$	0	$\frac{1}{2}$	0	1.60
CL4.3	5	-0.0138	-0.0134	63.89	185.90	1	1	$\frac{1}{2}$	$\frac{1}{2}$	$\frac{1}{2}$	1	1	1	$\frac{1}{2}$	$\frac{1}{2}$	1	1	0	1.60
CL4.4	4	-0.0248	-0.0170	63.73	248.79	1	1	$\frac{1}{2}$	$\frac{1}{2}$	$\frac{1}{2}$	1	1	1	$\frac{1}{2}$	$\frac{1}{2}$	1	1	$\frac{1}{2}$	1.68
CL8.1*	4	-0.0167	-0.0127	63.77	111.32	1	1	1	1	$\frac{1}{2}$	1	1	1	$\frac{1}{2}$	1	1	$\frac{1}{2}$	1	1.69
CL8.2	1	-4.4048	-0.2854	63.92	241.76	$\frac{1}{2}$	1	0	1	$\frac{1}{2}$	0	$\frac{1}{2}$	1	1	$\frac{1}{2}$	0	0	1	1.97
CL8.3	4	-0.0183	-0.0124	63.74	108.95	1	1	$\frac{1}{2}$	$\frac{1}{2}$	$\frac{1}{2}$	1	1	1	$\frac{1}{2}$	$\frac{1}{2}$	1	$\frac{1}{2}$	1	1.69
CL8.4	8	-0.0022	-0.0040	63.81	74.66	1	1	1	1	$\frac{1}{2}$	1	1	1	$\frac{1}{2}$	$\frac{1}{2}$	1	1	1	1.72
CL12.1	9	0.0014	-0.0001	63.77	70.17	1	1	1	1	1	1	1	1	1	1	1	1	1.73	
CL16.1	10	0.0010	-0.0003	63.79	67.04	1	1	1	1	1	1	1	1	1	1	1	1	1.73	
CL16.2	4	-0.0178	-0.0125	63.76	108.14	1	1	$\frac{1}{2}$	$\frac{1}{2}$	$\frac{1}{2}$	1	1	1	$\frac{1}{2}$	$\frac{1}{2}$	1	$\frac{1}{2}$	1	1.69
CL16.3	15	0.0018	-0.0002	63.83	63.86	1	1	1	1	1	1	1	1	1	1	1	1	1.73	
CL16.4	4	-0.0178	-0.0125	63.75	108.15	1	1	$\frac{1}{2}$	$\frac{1}{2}$	$\frac{1}{2}$	1	1	1	$\frac{1}{2}$	$\frac{1}{2}$	1	$\frac{1}{2}$	1	1.69
CL24.2	9	0.0014	-0.0001	63.78	66.94	1	1	1	1	1	1	1	1	1	1	1	1	1.73	
CL24.3	19	0.0005	-0.0006	63.80	63.80	1	1	1	1	1	1	1	1	1	1	1	1	1.73	
CL27.1*	9	0.0008	0.0005	63.79	66.93	1	1	1	1	1	1	1	1	1	1	1	1	1.73	
CL64.1*	18	0.0002	-0.0002	63.80	63.80	1	1	1	1	1	1	1	1	1	1	1	1	1.73	
CL216.1*	33	0.0000	0.0000	63.79	63.79	1	1	1	1	1	1	1	1	1	1	1	1	1.73	

\*Band calculations (the shrinking factors are 2, 3, 4, 6 for CL8.1, CL27.1, CL64.1, and CL216.1, respectively)

**Table 6.5.** Effect of integral thresholds on calculated properties of cyclic clusters CL12.1 and CL16.3; total energy  $E$  and top of valence band  $\epsilon$  (a.u.), Löwdin charge  $q_{Ti}$  of Ti, total number of electrons per unit cell calculated using (6.76) within the corresponding cyclic cluster ( $N_e^C$ ) and within the interaction radius defined by the integral thresholds ( $N_e^S$ )

Cluster	Integral thresholds	$E$	$\epsilon$	$q_{Ti}$	$N_e^C$	$N_e^S$
CL12.1	6 12	-69.7744	-0.3029	1.73	63.77	70.17
	6 9	-69.7747	-0.3032	1.73	63.81	64.01
	6 9 <sup>a</sup>	-69.7760	-0.3029	1.73	63.74	63.75
	6 8	-69.7746	-0.3034	1.73	63.75	63.94
	6 8 <sup>a</sup>	-69.7758	-0.3028	1.73	63.72	63.73
CL16.3	6 12	-69.7740	-0.3030	1.73	63.83	63.86
	6 12 <sup>a</sup>	-69.7758	-0.3029	1.73	63.83	63.83
	6 13	-69.7740	-0.3030	1.73	63.83	64.05
	6 13 <sup>a</sup>	-69.7758	-0.3029	1.73	63.79	63.79
band calculation <sup>b</sup>	6 12	-69.7758	-0.3028	1.73	63.79	63.79

<sup>a</sup>increased by a factor of 8 with shrinking factors  $s_1 = s_2 = s_3 = 2$

<sup>b</sup>primitive unit cell with shrinking factors  $s_1 = s_2 = s_3 = 6$

cyclic cluster that has been chosen properly, an increase of the cyclicity region has to give only small changes in the calculated results.

**Table 6.6.** MSINDO CCM results for bulk rutile; total energy per unit cell  $E_{tot}$  (a.u.), binding energy per unit  $E_B$  (kJ/mol), HOMO energy  $\epsilon_{top}$  (a.u.), atomic Löwdin charge on Ti  $q_{Ti}$ .

Cluster	$E_{tot}$	$E_B$	$\epsilon_{top}$	$q_{Ti}$
CL8.1	-70.2164	1880	-0.2947	1.74
CL12.1	-70.0959	1722	-0.2910	1.77
CL24.2	-70.3774	2092	-0.2898	1.77
CL32.2	-70.3428	2046	-0.2885	1.77

In CCM calculations of defective crystals such an increase of the cyclicity region allows investigation of the convergence of the results with cluster size. As is seen from Table 6.4, the  $k$ -sets accuracy  $J$  is important to reproduce the total energy. The cyclic-cluster increase without change of  $J$  (clusters C4.1 and C8.2 with  $J = 1$ , clusters C8.1, C16.1 and C16.4 with  $J = 4$ ) gives only small changes in total energy. The cyclic clusters C12.1 and C16.3 generate highly accurate SP-sets ( $J = 9$  and  $J = 15$ , respectively) and therefore the corresponding total energies are close to that of the infinite crystal. The same applies to the one-electron energy at the top of the valence band.

The idempotency of the DM in MSINDO cyclic-cluster calculations is guaranteed for all cases as the periodic boundary conditions were introduced into the molecular code. This was tested in [100] for the cyclic cluster C12.1 in two ways:

1. by calculating the difference  $C_M^{(1)} - C_M^{(2)}$  obtained with relation (6.76);
2. by directly calculating  $P^2 - 2P$  and summing the absolute values of the differences over all matrix elements,  $\Delta = \sum_{\mu\nu} |P_{\mu\nu}^2 - 2P_{\mu\nu}|$ .

By both ways of calculation it was clearly demonstrated that the MSINDO CCM density matrix is exactly idempotent. The differences of covalencies  $C_M^{(1)}$  and  $C_M^{(2)}$  as well as  $\Delta$  are in the same order of magnitude as the SCF threshold,  $10^{-8}$ . At the same time the symmetry of the crystalline system was correctly reproduced as checked by counting the degenerate one-electron levels in the oxygen 2s valence-band region and comparison with the results of a symmetry analysis. The symmetry of the cyclic cluster is different from the molecular cluster due to the presence of additional translation symmetry elements. Therefore, highly degenerate (8,4 degenerated) one-electron levels appear that are not present in any molecular model of rutile.

The calculated binding energies per unit cell  $E_B$ , HOMO orbital energies  $\varepsilon_{top}$ , and atomic Löwdin charges  $q$  for a number of cyclic clusters embedded in an infinite Madelung field, C8.1, C12.1, C24.2, and C32.2, are given in Table 6.6 [321].

The geometry of the four clusters has been optimized in terms of the three structural parameters  $c$ ,  $R_{\text{TiO}_{(5)}}$  and  $R_{\text{TiO}_{(3)}}$ . At low temperatures, the experimental references are  $c = 2.954$  Å,  $R_{\text{TiO}_{(5)}} = 1.946$  Å, and  $R_{\text{TiO}_{(3)}} = 1.976$  Å. For the largest cyclic cluster, C32.3, the corresponding MSINDO values are 2.96 Å, 1.90 Å, and 1.91 Å, which are in reasonable agreement with experiment. From Table 6.6 it can be seen that the convergence of  $E_{tot}$  is much slower than for the periodic HF calculations, see Table 6.3. On the other hand,  $\varepsilon_{top}$  and  $q_{\text{Ti}}$  show a similar convergence behavior. The MSINDO binding energies per  $\text{TiO}_2$  unit  $E_B$  vary between 1722 and 2096 kJ/mol and are close to the experimental value of 1900 kJ/mol. The calculated HOMO orbital energies for MSINDO (Table 6.6) and HF (Table 6.5) are similar. The MSINDO  $\varepsilon_{top}$  is only 0.6 eV less negative than the HF result.

The density matrix idempotency relations described here may be easily extended to the unrestricted Hartree–Fock (UHF) method when the orbitals for  $\alpha$  and  $\beta$  spins are treated independently.

As it is seen from the HF calculations of bulk rutile structure the CCM technique produces a good representation of the perfect crystal, which is essential for point-defect studies.

## Kohn–Sham LCAO Method for Periodic Systems

### 7.1 Foundations of the Density-functional Theory

#### 7.1.1 The Basic Formulation of the Density-functional Theory

Density-functional theory has its conceptual roots in the Thomas–Fermi model of a uniform electron gas [325, 326] and the Slater local exchange approximation [327]. A formalistic proof for the correctness of the Thomas–Fermi model was provided by Hohenberg–Kohn theorems, [328]. DFT has been very popular for calculations in solid-state physics since the 1970s. In many cases DFT with the local-density approximation and plane waves as basis functions gives quite satisfactory results, for solid-state calculations, in comparison to experimental data at relatively low computational costs when compared to other ways of solving the quantum-mechanical many-body problem.

It took a long time for quantum chemists to recognize the possible contribution of DFT. A possible explanation of this is that the molecule is a very different object to the solid as the electron density in a molecule is very far from uniform [329]. DFT was not considered accurate enough for calculations in molecular quantum chemistry until the 1990s, when the approximations used in the theory were greatly refined to better model the exchange and correlation interactions. DFT is now a leading method for electronic-structure calculations in both fields. In quantum chemistry of solids DFT LCAO calculations now have become popular especially with the use of so-called hybrid functionals including both HF and DFT exchange.

Traditional quantum chemistry starts from the electronic Schrödinger equation (SE) and attempts to solve it using increasingly more accurate approaches (Hartree–Fock and different post-Hartree–Fock methods, see Chapters 4 and 5). These approaches are based on the complicated many-electron wavefunction (and are therefore called wavefunction-based methods) and in these *ab-initio* methods no semiempirical parameters arise. Such an approach can be summarized by the following sequence [330]:  $V(\mathbf{r}) \xrightarrow{SE} \Psi(\mathbf{r}_1, \mathbf{r}_2, \dots, \mathbf{r}_N) \xrightarrow{\langle \Psi | \dots | \Psi \rangle}$  observables, *i.e.* one specifies the system by choosing potential  $V(\mathbf{r})$ , plugs it into the Schrödinger's equation, solves that equation for the wavefunction  $\Psi(\mathbf{r}_1, \mathbf{r}_2, \dots, \mathbf{r}_N)$ , and then calculates observables by taking the expectation values of operators with this wavefunction. One among the observables that are calculated in this way is the one-electron density

$$\rho(\mathbf{r}) = N \int d^3\mathbf{r}_2 \int d^3\mathbf{r}_3 \dots \int d^3\mathbf{r}_N \Psi^*(\mathbf{r}, \mathbf{r}_2, \dots, \mathbf{r}_N) \Psi(\mathbf{r}, \mathbf{r}_2, \dots, \mathbf{r}_N) \quad (7.1)$$

In DFT, the density (7.1) becomes the key variable: DFT can be summarized by the sequence

$$\rho(\mathbf{r}) \rightarrow \Psi(\mathbf{r}_1, \mathbf{r}_2, \dots, \mathbf{r}_N) \rightarrow V(\mathbf{r})$$

*i.e.* knowledge of  $\rho(\mathbf{r})$  implies knowledge of the wavefunction and the potential, and hence of all other observables. This also represents the fact that ultimately the electron density and not a wavefunction is the observable. Although this sequence describes the conceptual structure of DFT, it does not really represent what is done in actual applications of it and does not make explicit the use of many-body wavefunctions. Some chemists until now consider DFT as a containing “semiempirism” (not *ab-initio*) method but recognize that the small number of semiempirical parameters are used in DFT and these parameters are “universal to the whole chemistry” [329].

Two core elements of DFT are the Hohenberg–Kohn (HK) theorems [328,331] and the Kohn–Sham equations [332]. The former is mainly conceptual, but via the second the most common implementations of DFT have been done.

Whereas the many-electron wavefunction is dependent on  $3N$  variables, three spatial variables for each of the  $N$  electrons, the density is only a function of three variables and is a simpler quantity to deal with both conceptually and practically.

The literature on DFT and its applications is large. Some representative examples are the following: books [333–337], separate chapters of monographs [8, 10, 102] and review articles [330, 338–340].

We give here basic formulation of DFT and the Kohn–Sham method in the spirit of a “bird’s-eye view of DFT” [330], referring the reader for the mathematical details to the original papers. The original Hohenberg–Kohn (HK) theorems [328] held only for the ground state in the absence of a magnetic field, although they have since been generalized. The theorems can be extended to the time-dependent domain DFT (TDDFT), which can also be used to determine excited states [341]. Nevertheless, the inability of the DFT method to describe for molecular systems the spin and space degenerate states [342], as the diagonal element of the full density matrix is invariant with respect to all operations of the symmetry group, was proven.

The first HK theorem demonstrates the existence of a one-to-one mapping between the ground-state electron density (7.1) and the ground-state wavefunction of a many-particle system. The first Hohenberg–Kohn theorem is only an existence theorem, stating that the mapping exists, but does not provide any such exact mapping. It is in these mappings that approximations are made. Let us rewrite (4.7) for the many-electron function of the system in the form

$$H\Psi = [T + V + U]\Psi = \left[ -\frac{1}{2} \sum_{i=1}^N \Delta_i + \sum_{i=1}^N V(\mathbf{r}_i) + \sum_{i < j} U(\mathbf{r}_i, \mathbf{r}_j) \right] \Psi = E\Psi \quad (7.2)$$

where  $H$  is the electronic Hamiltonian,  $N$  is the number of electrons and  $U$  is the electron–electron interaction. The operators  $T$  and  $U$  are so-called universal operators as they are the same for any system, while  $V$  is system dependent (nonuniversal). The potential  $V$  is called the external potential. This may be not only that of nuclei but also for cases when the system is exposed to an external electrostatic or magnetic field.

We can write it as a sum of one-electron potentials  $\sum_{i=1}^N V(\mathbf{r}_i)$  but we do not know this potential in advance. The actual difference between a single-electron problem and the much more complicated many-electron problem just arises from the electron–electron interaction term  $U$ .

Hohenberg and Kohn proved [328] that the relation (7.1) can be reversed, *i.e.* to a given ground-state density  $\rho(\mathbf{r})$  it is in principle possible to calculate the corresponding ground-state wavefunction  $\Psi_0(\mathbf{r}_1, \mathbf{r}_2, \dots, \mathbf{r}_N)$ . This means that for a given ground-state density for some system we cannot have two different external potentials  $V$ . This means that the electron density  $\rho(\mathbf{r})$  defines all terms in the Hamiltonian (7.2) and therefore we can, in principle, determine the complete  $N$  electron wavefunction for the ground-state by only knowing the electron density. The HK theorem shows only that it is possible to calculate any ground-state property when the electron density is known but does not give the means to do it. Since the wavefunction is determined by the density, we can write it as  $\Psi_0 = \Psi_0[\rho]$ , which indicates that  $\Psi_0$  is a function of its  $N$  spatial variables, but a *functional* of  $\rho(\mathbf{r})$ . More generally, a functional  $F[n]$  can be defined as a rule for going from a function to a number, just as a function  $y = f(x)$  is a rule ( $f$ ) for going from a number ( $x$ ) to a number ( $y$ ). A simple example of a functional is the total number of electrons in a system  $N$

$$N = \int d^3\mathbf{r} \rho(\mathbf{r}) = N[\rho(\mathbf{r})] \quad (7.3)$$

which is a rule for obtaining the number  $N$ , given the function  $\rho(\mathbf{r})$ . Note that the name given to the argument of  $\rho$  is completely irrelevant, since the functional depends on the *function* itself, not on its variable. Hence we do not need to distinguish  $F[\rho(\mathbf{r})]$  from, e.g.,  $F[\rho(\mathbf{r}')]$ . Another important case is that in which the functional depends on a parameter, such as in

$$V_H[\rho(\mathbf{r})] = \int d^3\mathbf{r}' \frac{\rho(\mathbf{r}')}{|\mathbf{r} - \mathbf{r}'|} \quad (7.4)$$

that is a rule that for any value of the parameter  $\mathbf{r}$  associates a value  $V_H[\rho(\mathbf{r})]$  with the function  $\rho(\mathbf{r}')$ . This term is the so-called Hartree potential, introduced in (4.16) and is a potential of the Coulomb field created by all electrons of the system, with the electron in question included.

DFT explicitly recognizes that nonrelativistic Coulomb systems differ only by their external potential  $V(\mathbf{r})$ , and supplies a prescription for dealing with the universal operators  $T$  and  $U$  once and for all. This is done by promoting the electron density  $\rho(\mathbf{r})$  from just one of many observables to the status of the key variable, on which the calculation of all other observables can be based. In other words,  $\Psi_0$  is a unique functional of  $\rho$ , *i.e.*  $\Psi_0[\rho]$  and consequently all other ground-state observables  $O$  are also functionals of  $\rho$

$$\langle O \rangle[\rho] = \langle \Psi_0[\rho] | \hat{O} | \Psi_0[\rho] \rangle \quad (7.5)$$

From this it follows, in particular, that also the ground-state energy is a functional of  $\rho$

$$E_0 = E[\rho] = \langle \Psi_0[\rho] | T + V + U | \Psi_0[\rho] \rangle \quad (7.6)$$

where the contribution of the external potential can be written explicitly in terms of the density

$$V[\rho] = \int V(\mathbf{r})\rho(\mathbf{r})d^3\mathbf{r} \quad (7.7)$$

The functionals  $T[\rho]$  and  $U[\rho]$  are called universal functionals, while  $V[\rho]$  is obviously nonuniversal, as it depends on the system under study. Having specified a system, *i.e.*  $V$  is known, one then has to minimize the functional

$$E[\rho] = T[\rho] + U[\rho] + \int V(\mathbf{r})\rho(\mathbf{r})d^3\mathbf{r} \quad (7.8)$$

with respect to  $\rho(\mathbf{r})$ , assuming one has got reliable expressions for  $T[\rho]$  and  $U[\rho]$ . The second HK theorem proves that the ground-state density minimizes the total electronic energy of the system. It states that once the functional that relates the electron density with the total electronic energy is known, one may calculate it approximately by inserting approximate densities  $\rho'$ . Furthermore, just as for the variational method for wavefunctions, one may improve any actual calculation by minimizing the energy functional  $E[\rho']$ . A successful minimization of the energy functional will yield the ground-state density  $\rho_0$  and thus all other ground-state observables. A practical scheme for calculating ground-state properties from electron density was provided by the approach of Kohn and Sham [332] considered in the next section.

### 7.1.2 The Kohn–Sham Single-particle Equations

Within the framework of Kohn–Sham (KS) DFT, the intractable many-body problem of interacting electrons in a static external potential is reduced to a tractable problem of noninteracting electrons moving in an effective potential. The functional in (7.8) is written as a fictitious density functional of a noninteracting system

$$E_{eff}[\rho] = \langle \Psi_{eff}[\rho] | T_{eff} + V_{eff} | \Psi_{eff}[\rho] \rangle \quad (7.9)$$

where  $T_{eff}$  denotes the noninteracting electrons' kinetic energy and  $V_{eff}$  is an external effective potential in which the electrons are moving. It is assumed that the fictitious (model) system has the same energy as the real system. Obviously,  $\rho_{eff}(\mathbf{r}) = \rho(\mathbf{r})$  if  $V_{eff}$  is chosen to be

$$V_{eff} = V + U + (T - T_{eff}) \quad (7.10)$$

Thus, one can solve the so-called Kohn–Sham equations of this auxiliary noninteracting system with the effective Hamiltonian

$$H_{eff} = \sum_{i=1}^N \left[ -\frac{1}{2} \Delta_i + V_{eff}(\mathbf{r}_i) \right] = \sum_{i=1}^N h_{eff}(\mathbf{r}_i) \quad (7.11)$$

that yields the orbitals  $\varphi_i(\mathbf{r})$  that reproduce the density  $\rho(\mathbf{r})$  of the original many-electron system  $\rho(\mathbf{r}) = \rho_{eff}(\mathbf{r}) = \sum_{i=1}^N |\varphi_i(\mathbf{r})|^2$ . The effective single-electron potential  $V_{eff}(\mathbf{r})$  can be written as

$$V_{eff}(\mathbf{r}) = V + \int \frac{\rho_{eff}(\mathbf{r}')}{|\mathbf{r} - \mathbf{r}'|} d^3\mathbf{r}' + V_{XC}[\rho_{eff}(\mathbf{r})] \quad (7.12)$$

where the second term denotes the so-called Hartree term describing the electron–electron Coulomb repulsion, while the last term  $V_{XC}$  is called the exchange correlation

potential and includes all the many-electron interactions. Since the Hartree term and  $V_{XC}$  depend on  $\rho(\mathbf{r})$  that depends on the  $\varphi_i$ , which in turn depend on  $V_{eff}$ , the problem of solving the Kohn–Sham equation has to be done in a self-consistent (*i.e.* iterative) way. Usually, one starts with an initial guess for  $\rho(\mathbf{r})$ , then calculates the corresponding  $V_{eff}$  and solves the Kohn–Sham equations for the  $\varphi_i$ . From these one calculates a new density and starts again. This procedure is then repeated until convergence is reached.

There are only single-particle operators in (7.11). Therefore, the solution to the Schrödinger equation for a model system of noninteracting electrons can be written exactly as a single Slater determinant  $\Psi = |\varphi_1, \varphi_2, \dots, \varphi_N|$ , where the single-particle orbitals  $\varphi_i$  are determined as solutions of the single-particle equation

$$h_{eff}\varphi_i = \varepsilon_i\varphi_i \quad (7.13)$$

Furthermore,  $\rho(\mathbf{r}) = \sum_{i=1}^N |\varphi_i(\mathbf{r})|^2$ , where the summation runs over the  $N$  orbitals with the lowest eigenvalues  $\varepsilon_i$ .

The main problem is that we do not know the exact form of the effective potential  $V_{eff}$ , *i.e.* the so-called exchange-correlation energy and potential. There exist approximations to these (see Sections 7.1.3 and 7.1.4) that are good approximations in very many cases. On the other hand, by introducing an approximation in the Schrödinger equation for the model noninteracting particles, we do not know whether improved calculations (*e.g.*, using larger basis sets) also lead to improved results (compared with, *e.g.*, experiment or other calculations). The success of the Kohn–Sham approach is based on the assumption that it is possible to construct the model system of noninteracting particles moving in an effective external potential. Thus, it is indirectly assumed that for any ground-state density there exists an effective potential (the corresponding density matrix is called  $V$  representative). There exist (specifically constructed) examples where this is not the case, but in most practical applications, this represents no problem [8].

HK theorems and KS equations can be extended to the spin-polarized systems where the electron- density components  $\rho_\alpha(\mathbf{r}), \rho_\beta(\mathbf{r})$  for spin-up and spin-down orbitals differ *i.e.* the spin-density  $\rho^s(\mathbf{r}) = \rho_\alpha(\mathbf{r}) - \rho_\beta(\mathbf{r})$  is nonzero.

The result is that the total energy and any other ground-state properties become a functional not only of  $\rho(\mathbf{r})$  but also of spin-density  $\rho^s(\mathbf{r})$ , *i.e.*  $E_{eff} = E[\rho(\mathbf{r}), \rho^s(\mathbf{r})]$ . Spin-density-functional theory (SDFT) is a widely implemented and applied formalism of DFT.

Alternative DFT formulations that use other variables in addition to (or instead of) the spin densities are also useful [343].

The single-particle orbitals and complete  $N$ -electron wavefunctions in KS DFT belong to irreducible representations of the group for the symmetry operations of the system of interest (point-symmetry group for molecules and space-symmetry group for crystals). This means that we can consider each irreducible representation separately. For each of these, the variational principle will apply (since any state of a given irreducible representation will only contain contributions from exactly that irreducible representation). We can use this in generalizing the HK theorems that then apply for the energetically lowest state of each irreducible representation. This means that if we have the representations  $D^\alpha, D^\beta$  for a given system symmetry group then we can apply DFT in studying the energetically lowest state for the  $D^\alpha$  representation, that

for the  $D^\beta$  representation and so on, but not energetically higher ones of any of the representations.

Since 1990 there has been an enormous amount of comparison for molecules between DFT KS and HF (MO) theory. Such a comparison is easily extended to crystals when we consider CO instead of MO. The discussion of advantages and disadvantages of DFT compared to MO theory can be found for example, in [102] and is briefly reproduced here. The most fundamental difference between DFT and MO theory is the following: DFT optimizes an electron density, while MO theory optimizes a wavefunction. So, to determine a particular molecular property using DFT, we need to know how that property depends on the density, while to determine the same property using a wavefunction, we need to know the correct quantum-mechanical operator. As a simple example, consider the total energy of interelectronic repulsion. Even if we had the exact density for some system, we do not know the exact exchange-correlation energy functional, and thus we cannot compute the exact interelectronic repulsion. However, with the exact wavefunction it is a simple matter of evaluating the expectation value for the interelectronic repulsion operator to determine this energy. Thus, it is easy to become confused about whether there exists a KS “wavefunction”. Formally, the KS orbitals are pure mathematical constructs useful only in construction of the density. In practice, however, the shapes of KS orbitals tend to be remarkably similar to canonical HF MOs and they can be quite useful in qualitative analysis of chemical properties. If we think of the procedure by which they are generated, there are indeed a number of reasons to prefer KS orbitals to HF orbitals. For instance, all KS orbitals, occupied and virtual, are subject to the same external potential. HF orbitals, on the other hand, experience varying potentials, and, in particular, HF virtual orbitals experience the potential that would be felt by an extra electron being added to the molecule. As a result, HF virtual orbitals tend to be too high in energy and anomalously diffuse compared to KS virtual orbitals. This fact is especially important for crystalline solids and explains why HF bandgaps are overestimated compared to those in DFT and experiment. Unfortunately, for some choices of exchange-correlation potential DFT bandgaps are too small in comparison with the experimental data. In *exact* DFT, it can also be shown that the eigenvalue of the highest KS MO is the exact first ionization potential, *i.e.* there is a direct analogy to Koopmans’ theorem for this orbital – in practice, however, *approximate* functionals are quite poor at predicting IPs in this fashion without applying some sort of correction scheme, *e.g.* an empirical linear scaling of the eigenvalues.

The Slater determinant formed from the KS orbitals is the exact wavefunction for the fictitious *noninteracting* system having the same density as the real system. This KS Slater determinant has certain interesting properties by comparison to its HF analogs. It is an empirical fact that DFT is generally much more robust in dealing with open-shell systems where UHF methods show high spin contamination, *i.e.* incorporates some higher spin states (doublets are contaminated by quartets and sextets, while triplets are contaminated by pentets and heptets). The degree of spin contamination can be estimated by inspection of  $\langle S^2 \rangle$ , which should be 0.0 for a singlet, 0.75 for a doublet, 2.00 for a triplet, etc. Note, incidentally, that the expectation values of  $S^2$  are sensitive to the amount of HF exchange in the functional. A “pure” DFT functional nearly always shows very small spin contamination, and each added per cent of HF exchange tends to result in a corresponding percentage of the spin con-

tamination exhibited by the HF wavefunction. This behavior can make the hybrid HF-DFT functionals useful for open-shell systems (see Sect. 4.1.2).

The formal scaling behavior of DFT is, in principle, no worse than  $N^3$ , where  $N$  is the number of basis functions used to represent the KS orbitals. This is better than HF by a factor of  $N$ , and very substantially better than other methods that include electron correlation (see Chap. 5).

The most common methods for solving KS equations proceed by expanding the Kohn–Sham orbitals in a basis set. DFT has a clear advantage over HF in its ability to use basis functions that are not necessarily contracted Gaussians. The motivation for using contract GTOs is that arbitrary four-center two-electron integrals can be solved analytically. In the electronic-structure programs where DFT was added as a new feature to an existing HF code the representation of the density in the classical electron-repulsion operator is carried out using the KS orbital basis functions. Thus, the net effect is to create a four-index integral and these codes inevitably continue to use contracted GTOs as basis functions. In particular, such a scheme is used in the CRYSTAL code [23]. However, if the density is represented using an auxiliary basis set, or even represented numerically, other options are available for the KS orbital basis set, including Slater-type functions. The SIESTA density-functional code [344] for crystalline solids uses numerical AO basis instead of GTO. Slater-type orbitals (STO) enjoy the advantage that fewer of them are required (since they have the correct cusp behavior at the nuclei) and certain advantages associated with symmetry can more readily be taken, so they speed up calculations considerably. The Amsterdam density-functional code and its BAND version for solids [345] makes use of STO basis functions covering atomic numbers 1 to 118. Some information about the three mentioned computer LCAO codes for solids is given in Appendix C.

Another interesting possibility is the use of plane waves as basis sets in periodic infinite systems (crystalline solids) represented using periodic boundary conditions. While it takes an enormous number of plane waves to properly represent the decidedly aperiodic densities that are possible within the unit cells of interesting chemical systems, the necessary integrals are particularly simple to solve, and thus this approach has found wide use in solid-state physics.

Meanwhile, plane-wave basis use excludes the possibility of calculations with hybrid DFT-HF functionals.

### 7.1.3 Exchange and Correlation Functionals in the Local Density Approximation

The effective potential (7.10) includes the external potential and the effects of the Coulomb interactions between the electrons, *e.g.* the exchange and correlation interactions. In principle, it also includes the difference in kinetic energy between the fictitious noninteracting system and the real system. In practice, however, this difference is ignored in many modern functionals as the empirical parameters appear, which necessarily introduce some kinetic-energy correction if they are based on experiment [102].

Modeling the exchange and correlation interactions becomes difficult within KS DFT as the exact functionals for exchange and correlation are not known except for the homogeneous (uniform) electron gas. However, approximations exist that permit the calculation of real systems.

The simplest approximation is the local-density approximation (LDA), based upon the exact exchange energy for a uniform electron gas, which can be obtained from the Thomas–Fermi (TF) model, and from fits to the correlation energy for a uniform electron gas.

In the TF model it is suggested that the number of electrons is so large that the system could be treated using quantum-statistical arguments. The approximation in the TF model concerns the kinetic energy. For the homogeneous interaction-free electron gas the density is constant and the average kinetic energy per particle is  $\varepsilon_t^{hom} = Cn^{5/3}$ . The kinetic energy per unit volume in this model is  $n\varepsilon_t^{hom}$ . If the electron density varies sufficiently slowly in space  $T^{LDA} = \int d^3\mathbf{r}\varepsilon_t^{hom}(\rho(\mathbf{r}))$  may serve as a workable approximation for the kinetic-energy functional.

If this is combined with the expression for the nuclei–electron attractive potential and the electron–electron Hartree repulsive potential we have the TF expression for the energy of a homogeneous gas of electrons in a given external potential:

$$E_{TF}[\rho(\mathbf{r})] = C_F \int \rho^{5/3}(\mathbf{r}) d^3\mathbf{r} - \sum_j \frac{Z_j}{|\mathbf{r} - \mathbf{R}_j|} \rho(\mathbf{r}) + \frac{1}{2} \int \int \frac{\rho(\mathbf{r})\rho(\mathbf{r}')}{|\mathbf{r} - \mathbf{r}'|} d^3\mathbf{r} d^3\mathbf{r}' \quad (7.14)$$

The importance of this equation is not so much how well it is able to really describe the energy even of an atom, but that the energy is given completely in terms of the electron density  $\rho(\mathbf{r})$ .

This is an example of a density-functional for energy allowing us to map a density  $\rho(\mathbf{r})$  onto an energy  $E$  without any additional information required. Furthermore, the TF model employs the variational principle assuming that the ground state of the system is connected to the electron density for which the energy (7.14) is minimized under the constraint of  $N = \int d^3\mathbf{r}\rho(\mathbf{r})$ .

Before the KH theorems were proved it was not known either whether expressing the energy as a density-functional is physically justified or whether employing the variational principle on the density is really allowed [337].

Slater's approximation of HF exchange [346] is another example of exploiting the electron density as the central quantity. In this case, the nonlocal HF exchange energy is approximated by  $\alpha \cdot C \cdot \int \rho(\mathbf{r})^{4/3} d\mathbf{r}$ .

This approximate expression depends only on the local values of the electron density  $\rho(\mathbf{r})$  representing a density-functional for the exchange energy (in the TF model exchange and correlation effects are completely neglected). This formula was originally derived as an approximation to the HF exchange, without any reference to the density-functional theory but it is conceptually connected with this theory. The 4/3 power law for dependence of the exchange interaction on the electron density was also obtained from a completely different approach using the concept of the uniform electron gas [347]. Combined with the TF energy this approximation is known as the Thomas–Fermi–Dirac model having conceptual importance for DFT methods. In particular, it seems natural that the exchange–correlation energy  $E_{XC}$  is approximated by sum of the exchange  $E_X$  and correlation  $E_C$  energies.

In LDA for the exchange energy calculation the Dirac–Slater exchange energy is used

$$E_X[\rho] = C_X \int \rho^{4/3}(\mathbf{r}) d^3\mathbf{r} \quad (7.15)$$

or the more complicated suggested by Barth and Hedin [348].

For the correlation energy functional  $E_C[\rho(\mathbf{r})]$  the situation is more complicated since even for a homogeneous electron gas it is not known exactly. Early approximate expressions for correlation in homogeneous systems were based on applying the perturbation theory and were suggested by Barth and Hedin [348], Gunnarsson and Lundqvist [349]. With the advent of highly precise calculations of correlation energy for the electron liquid by Ceperley and Alder (CA) [350] the approximations for the correlation energy in a homogeneous system are made by parametrization of CA data for a free-electron gas. There are known parametrizations of Vosko–Wilk–Nisair [351], Perdew–Zunger [352] and Perdew–Wang [353]. The three latter parametrizations of the LDA are implemented in most standard DFT program packages (both for molecules and solids) and in many cases give almost identical results. On the other hand, the earlier parametrizations of the LDA, based on perturbation theory can deviate substantially and are better avoided.

The functional dependence of  $E_{XC}$  on the electron density is expressed as an interaction between the electron density and “an energy density”  $\varepsilon_{XC}$  that is dependent on the electron density

$$E_{XC}[\rho(\mathbf{r})] = \int \rho(\mathbf{r}) \varepsilon_{XC}[\rho(\mathbf{r})] d^3\mathbf{r} \quad (7.16)$$

The energy density  $\varepsilon_{XC}$  is treated as a sum of individual exchange and correlation contributions. Two different kinds of densities are involved [102]: the electron density is a per unit volume density, while the energy density is a per particle density. The LDA for  $E_{XC}$  formally consists in

$$E_{XC}^{LDA}[\rho(\mathbf{r})] = \int d^3\mathbf{r} [\varepsilon_X^{hom}[\rho(\mathbf{r})] + \varepsilon_C^{hom}[\rho(\mathbf{r})]] = \int d^3\mathbf{r} \varepsilon_{XC}^{hom}[\rho(\mathbf{r})] \quad (7.17)$$

The energy densities  $\varepsilon_X^{hom}$ ,  $\varepsilon_C^{hom}$  refer to a homogeneous system, *i.e.* the exchange-correlation energy is simply an integral over all space with the exchange-correlation energy density at each point assumed to be the same as in a homogeneous electron gas with that density. Nevertheless, LDA has proved amazingly successful, even when applied to systems that are quite different from the electron liquid that forms the reference system for the LDA.

In the local spin-density approximation (LSDA) the exchange-correlation energy can be written in terms of either of two spin densities  $\rho^\alpha(\mathbf{r})$  and  $\rho^\beta(\mathbf{r})$

$$\begin{aligned} E_{XC}^{LSDA}[\rho^\alpha(\mathbf{r}), \rho^\beta(\mathbf{r})] &= \int d^3\mathbf{r} \rho(\mathbf{r}) \varepsilon_{XC}^{hom}[\rho^\alpha(\mathbf{r}), \rho^\beta(\mathbf{r})] \\ &= \int d^3\mathbf{r} \rho(\mathbf{r}) [\varepsilon_X^{hom}[\rho^\alpha(\mathbf{r}), \rho^\beta(\mathbf{r})] + \varepsilon_C^{hom}[\rho^\alpha(\mathbf{r}), \rho^\beta(\mathbf{r})]] \end{aligned} \quad (7.18)$$

or the total density  $\rho(\mathbf{r})$  and the fractional spin polarization  $\zeta(\mathbf{r}) = (\rho^\alpha(\mathbf{r}) - \rho^\beta(\mathbf{r})) / \rho(\mathbf{r})$ .

For many decades the LDA has been applied in, *e.g.*, calculations of band structures and total energies in solid-state physics. The LDA provides surprisingly good results for metallic solids with delocalized electrons, *i.e.* those that most closely resemble the uniform electron gas (jellium). At the same time, there are well-known disadvantages of LDA for solids. LDA revealed systematic shortcomings in the description of systems with localized electrons and as a result the underestimation of

bond distances and overestimation of binding energies. LDA calculations as a rule give calculated bandgaps that are too small. In quantum chemistry of molecules LDA is much less popular because the local formulation of the energy expression does not account for the electronic redistribution in bonds. For well-localized electrons the nonexact cancellation of the self-energy part (self-interaction) of the Hartree term in the LDA exchange functional is important (in HF energy the self-energy part in the Hartree term is cancelled by the corresponding part of the exchange term). LDA fails to provide results that are accurate enough to permit a quantitative discussion of the chemical bond in molecules (so-called “chemical accuracy” requires calculations with an error of not more than about 1 kcal/mol per particle). LDA exploits knowledge of the density at point  $\rho(\mathbf{r})$ . The real systems, such as molecules and solids, are inhomogeneous (the electrons are exposed to spatially varying electric fields produced by the nuclei) and interacting (the electrons interact via the Coulomb interaction). The way density-functional theory, in the local-density approximation, deals with this inhomogeneous many-body problem is by decomposing it into two simpler (but still highly nontrivial) problems: the solution of a spatially uniform many-body problem (the homogeneous electron liquid) yields the uniform exchange-correlation energy, and the solution of a spatially inhomogeneous noninteracting problem (the inhomogeneous electron gas) yields the particle density. Both steps are connected by the local-density approximation, which shows how the exchange-correlation energy of the uniform interacting system enters the equations for the inhomogeneous noninteracting system.

We note that both the local density approximation and the local exchange approximation use only the diagonal part of the density matrix  $\rho(\mathbf{r}, \mathbf{r}')$ , *i.e.*  $\rho(\mathbf{r}) = \rho(\mathbf{r}, \mathbf{r})$ . However these approximations are different by their nature. In LDA the local density is used to include both the exchange and correlation of electrons, in the local exchange approximation to HF exchange the electron correlation is not taken into account at all.

The particular way in which the inhomogeneous many-body problem is decomposed, and the various possible improvements on the LDA, are behind the success of DFT in practical calculations, in particular, materials. The most important improvement of LDA is connected with the attempt to introduce a spatially varying density and include information on the rate of this variation in the functional. The corresponding functionals, known as semilocal functionals [330], are considered in the next section.

#### 7.1.4 Beyond the Local Density Approximation

The first successful extensions for the LDA were developed in the early 1980s when it was suggested to supplement the density  $\rho(\mathbf{r})$  at a particular point  $\mathbf{r}$  with information about the gradient of the electron density at this point in order to account for the nonhomogeneity of the true electron density [337]. LDA was interpreted as the first term of a Taylor expansion of the uniform density, the form of the functional was termed the gradient expansion approximation (GEA). It was expected to obtain better approximations of the exchange-correlation functional by extending the series with the next lowest term. In practice, the inclusion of low-order gradient corrections almost never improves on the LDA, and often even worsens it. The reason for this failure is that for GEA the exchange-correlation hole has lost many of the properties that

made the LDA whole physically meaningful [337]. Higher-order corrections, on the other hand, are exceedingly difficult to calculate, and little is known about them.

It was a major breakthrough when it was realized, in the early 1980s, that instead of power-series-like systematic gradient expansions one could experiment with more general functions of  $\rho(\mathbf{r})$  and  $\nabla\rho(\mathbf{r})$ , which need not proceed order by order. Such functionals, of the general form

$$E_{XC}^{GGA}[\rho_\alpha, \rho_\beta] = \int d^3\mathbf{r} f(\rho_\alpha, \rho_\beta, \nabla\rho_\alpha, \nabla\rho_\beta) \quad (7.19)$$

have become known as generalized-gradient approximations (GGAs), [355]. GGA functionals are the workhorses of current density-functional theory. Different GGAs differ in the choice of the function  $f(\rho, \nabla\rho)$ . Note that this makes different GGAs much more different from each other than the different parametrizations of the LDA: essentially there is only one correct expression for  $\varepsilon_{XC}^{hom}(\rho)$  and the various parametrizations of the LDA are merely different ways of writing it [330]. On the other hand, depending on the method of construction employed for obtaining  $f(\rho, \nabla\rho)$  one can obtain very different GGAs. In particular, GGAs used in molecular quantum chemistry typically proceed by fitting parameters to test sets of selected molecules. On the other hand, the GGAs used in physics tend to emphasize exact constraints on the density-functional for the exchange-correlation energy [357]. In this approach, the density-functional approximations are assigned to various rungs according to the number and kind of their local ingredients [357].

The lowest rung is the local spin-density approximation LSDA, the second rung is the generalized gradient approximation GGA (semilocal functionals). More accurate functionals of higher rungs can be called “beyond-GGA functionals” or nonlocal functionals. Third-rung Meta-GGA (MGGA) functionals depend, in addition to the density and its derivatives, also on the kinetic-energy density [362]. Fourth-rung hybrid functionals mix a fraction of the Hartree–Fock exchange into the DFT exchange functional (see Sect. 4.2). MGGA and hybrid functionals can be called orbital functionals because they are represented not only in terms of the electron density, but also contain parts represented in single-particle Kohn–Sham orbitals  $\varphi_i(\mathbf{r})$ . In MGGA functionals kinetic energy density  $\tau(\mathbf{r}) = 1/2\sum_i|\nabla\varphi_i(\mathbf{r})|^2$  is included. In hybrid functionals the nonlocal HF exchange energy is also orbital functional. Still another type of orbital functional is the self-interaction correction (SIC) (see Sect. 7.4). Higher-rung density-functionals are increasingly more complex.

The semiempirical functionals are fitted to selected data from experiment or from the *ab-initio* calculations. The higher the rung of the functional the larger is the number of parameters (functionals with as many as 21 fit parameters are popular in chemistry). Is DFT *ab-initio* or semiempirical? As was suggested in [357] it can fall in between as a nonempirical theory when the functionals are constructed without empirical fitting.

The best nonempirical functional for a given rung is constructed to satisfy as many exact theoretical constraints as possible while providing satisfactory numerical predictions for real systems [357]. Once a rung has been selected, there remains little choice about which constraints to satisfy (but greater freedom in how to satisfy them), [357]. Accuracy is expected to increase up the ladder of rungs as additional local ingredients enable the satisfaction of additional constraints. A short summary of

exact constraints on  $E_{XC}[\rho]$  can be found in [357]. In this paper some useful recommendations for users of DFT are also given. Users should not randomly mix and match functionals, but should use exchange and correlation pieces designed to work together, with their designer-recommended local parts. They should not shop indiscriminately for the functional that “works best”. Users should always say which functional they used, with its proper name and literature reference, and why they chose it. Statements like “we used density-functional theory” or “we used the generalized gradient approximation” are almost useless to a reader or listener who wants to reproduce the results.

Nowadays, the most popular (and most reliable) GGA functionals are PBE (denoting the functional proposed in 1996 by Perdew, Burke and Ernzerhof [356] in physics, and BLYP (denoting the combination of Becke’s 1988 exchange functional [358] with the 1988 correlation functional of Lee, Yang and Parr [359]) in chemistry. PWGGA denotes the GGA functional, suggested by Perdew and Wang [354, 355] and should be allowed to retire gradually. Many other GGA-type functionals are also available, and new ones continue to appear. The new meta-GGA (MGGA) functional TPSS (Tao–Perdew–Staroverov–Scuseria) [360] supersedes an older one the PKZB (Perdew–Kurth–Zupan–Blaha) functional [363]. The known functionals are modified as has been done recently for the PBE functional to improve its accuracy for thermodynamic and electronic properties of molecules [361, 362].

We close this subsection with more detailed consideration of the PBE functional [363]. It has two nonempirical derivations based on exact properties of the XC hole [364] and energy [356]. In discussion of the PBE functional we follow [365]. The exchange-correlation (XC) energy in the LSD approximation is given by

$$E_{XC}^{LSD}[\rho_\alpha, \rho_\beta] = \int d^3\mathbf{r} \rho(\mathbf{r}) [\varepsilon_X(\rho(\mathbf{r})) f(\zeta, \mathbf{r}) + \varepsilon_C(r_s(\mathbf{r}), \zeta(\mathbf{r}))] \quad (7.20)$$

where  $\zeta = \frac{\rho_\alpha - \rho_\beta}{\rho_\alpha + \rho_\beta}$  is the relative spin polarization and  $f(\zeta)$  is given by

$$f(\zeta) = \frac{1}{2} \left[ (1 + \zeta)^{4/3} + (1 - \zeta)^{4/3} \right] \quad (7.21)$$

The exchange energy per electron  $\varepsilon_X(\rho)$  of the unpolarized uniform electron gas of density  $\rho(\mathbf{r})$  depends on  $r_s = [\frac{3}{4\pi}\rho]^{1/3}$  as  $\varepsilon_X(\rho) = -\frac{C}{r_s}$  and the correlation energy  $\varepsilon_C$  per electron in a spin-polarized uniform electron gas depends on  $r_s$  and  $\zeta$  [354]. The PBE functional  $E_{XC}^{PBE}$  is a sum of PBE exchange  $E_X^{PBE}$  and PBE correlation  $E_C^{PBE}$  functionals. The exchange PBE functional is written in the form

$$E_X^{PBE}(\rho) = \int d^3\mathbf{r} \rho \varepsilon_X(\rho) F_X(s) \quad (7.22)$$

with

$$F_X(s) = 1 + k - \frac{k}{1 + \mu s^2/k} \quad (7.23)$$

and  $k = 0.804$ ,  $\mu = 0.21951$ . This functional is found from the exact spin-scaling relation

$$E_X[\rho_\alpha, \rho_\beta] = \frac{1}{2} E_X[2\rho_\alpha] + \frac{1}{2} E_X[2\rho_\beta] \quad (7.24)$$

The PBE correlation energy functional is

$$E_C^{PBE}[\rho_\alpha, \rho_\beta] = \int d^3\mathbf{r} \rho [\varepsilon_C(r_s, \zeta) + H(r_s, \zeta, t)] \quad (7.25)$$

where the nonlocal part  $H(r_s, \zeta, t)$  depends on the parameter  $t$  including the density gradient:

$$H = \gamma \Phi^3 \ln \left\{ 1 + \frac{\beta}{\gamma} t^2 \left[ \frac{1 + At^2}{1 + At^2 + A^2 t^4} \right] \right\} \quad (7.26)$$

where  $\beta = 0.066725$ ,  $\gamma = 0.03191$ , and

$$t = \left( \frac{\pi}{4} \right)^{1/2} \left( \frac{9\pi}{4} \right)^{1/6} \frac{s}{\Phi r_s^{1/2}} \quad (7.27)$$

$$s = \frac{|\nabla \rho|}{2(3\pi^2)^{1/3} \rho^{4/3}} = \frac{3}{2} \left( \frac{9}{4\pi} \right)^{1/3} |\nabla r_s| \quad (7.28)$$

$$\Phi(\zeta) = \frac{1}{2} \left[ (1 + \zeta)^{2/3} + (1 - \zeta)^{2/3} \right] \quad (7.29)$$

$$A = \left( \frac{\beta}{\gamma} \right) \frac{1}{\exp[-\varepsilon_C(r_s, \zeta)/\gamma \Phi^3] - 1} \quad (7.30)$$

The PBE GGA correctly reduces to LSD for uniform electron densities, its correlation component recovers the slowly varying ( $t \rightarrow 0$ ) and rapidly varying ( $t \rightarrow \infty$ ) limits of numerical GGA. Under uniform scaling ( $\rho(\mathbf{r}) \rightarrow \lambda^3 \rho(\lambda \mathbf{r})$ ), the PBE exchange energy scales like  $\lambda$  (as does the exact exchange functional) and the PBE correlation energy correctly scales to a constant as  $\lambda \rightarrow \infty$ . For small-amplitude density variations around a uniform density, LSD is a very good approximation. The PBE functional recovers this limit. The PBE functional satisfies the Lieb–Oxford bound [366]:

$$E_X^{PBE}[\rho_\alpha, \rho_\beta] \geq E_{XC}^{PBE}[\rho_\alpha, \rho_\beta] \geq 2.273 E_X^{LDA}[\rho] \quad (7.31)$$

A useful form to compare GGA functionals is to write

$$E_{XC}^{GGA}[\rho_\alpha, \rho_\beta] \approx \int d^3\mathbf{r} \rho \varepsilon_X(\rho) F_{XC}(r_s, \zeta, s) \quad (7.32)$$

where the enhancement factor  $F_{XC}(r_s, \zeta, s)$  over local exchange depends upon the local radius  $r_s$  ( $r_s \lesssim 1$  for core electrons and  $r_s \gtrsim 1$  for valence electrons), spin polarization  $\zeta$  and inhomogeneity  $s$ . The  $s$ -dependence of  $F_{XC}$  is the nonlocality of the GGA. We see that the nonempirical PBE functional best fulfils many of the physical and mathematical requirements of DFT. We will consider some applications of the PBE functional in LCAO calculations of crystals in Chapters 9–11. At the same time, there are some failures of the PBE functional essential for extended systems. For example, the exact exchange-correlation hole in crystals may display a diffuse long-range tail that is not properly captured by GGA (such a diffuse hole arises in the calculation of the surface energy of a metal). Neither LSD nor GGA describe correctly the long-range tail of the van der Waals interaction. Corrections of these failures might be possible by using orbital-dependent hybrid functionals considered in the next section.

### 7.1.5 The Pair Density. Orbital-dependent Exchange-correlation Functionals

Density-functional theory, even with rather crude approximations such as LDA and GGA, is often better than Hartree–Fock: LDA is remarkably accurate, for instance, for geometries and frequencies, and GGA has also made bond energies quite reliable. Therefore, “the aura of mystery” appeared around DFT (see discussion of this by Baerends and Gritsenko [367]). The simple truth is not that LDA/GGA is particularly good, but that Hartree–Fock is rather poor in the two-electron chemical-bond description. This becomes clear when one considers the statistical two-electron distribution, which is usually cast in terms of the exchange-correlation hole: the decrease in probability to find other electrons in the neighborhood of a reference electron, compared to the (unconditional) one-electron probability distribution [337].

The concept of electron density (7.1), which provides an answer to the question “how likely is it to find one electron of arbitrary spin within a particular volume element while all other electrons may be anywhere” can be extended to the probability of finding not one but a pair of two electrons with spins  $\sigma_1$  and  $\sigma_2$  simultaneously within two volume elements  $d\mathbf{r}_1$  and  $d\mathbf{r}_2$ , while the remaining  $N - 2$  electrons have arbitrary positions and spins. The quantity that contains this information is the pair-electron density  $\rho_2(\mathbf{x}_1, \mathbf{x}_2)$  which is defined as

$$\rho_2(\mathbf{x}_1, \mathbf{x}_2) = N(N - 1) \int \dots \int \Psi(\mathbf{x}_1, \dots, \mathbf{x}_N)^2 d\mathbf{x}_3 \dots d\mathbf{x}_N \quad (7.33)$$

The pair-electron density actually contains all the information about electron correlation. The pair density is a nonnegative quantity, symmetric in the coordinates and normalized to the total number of nondistinct electron pairs  $N(N - 1)$ . Obviously, if electrons would not interact, the probability of finding one electron at a particular point of coordinate-spin space would be completely independent of the position and spin of the second electron and it would be possible that both electrons are simultaneously found in the same volume element. In this case, pair density would reduce to a simple product of the individual probabilities, *i.e.*

$$\rho_2(\mathbf{x}_1, \mathbf{x}_2) = \frac{N - 1}{N} \rho(\mathbf{x}_1) \rho(\mathbf{x}_2) \quad (7.34)$$

The  $N(N - 1)$  factor enters because the particles are identical. From the antisymmetry of the many-electron wavefunction  $\Psi(\mathbf{x}_1, \dots, \mathbf{x}_N)$  it follows that  $\rho_2(\mathbf{x}_1, \mathbf{x}_2) = -\rho_2(\mathbf{x}_2, \mathbf{x}_1)$ , *i. e.* the probability of finding two electrons with the same spin at the same point in space is zero.

This effect is known as exchange or Fermi correlation and is a direct consequence of the Pauli principle. The Fermi hole is in no way connected to the charge of electrons and applies equally to neutral fermions. This kind of correlation is included in the HF approach due to the antisymmetry of the Slater determinant [337]. The electrostatic repulsion of electrons (the  $1/r_{12}$  term in the Hamiltonian) prevents the electrons from coming too close to each other and is known as Coulomb correlation. This effect is independent of the spin and is called simply electron correlation, and is completely neglected in the HF method.

The conditional probability  $\Omega(\mathbf{x}_1, \mathbf{x}_2) = \rho(\mathbf{x}_1, \mathbf{x}_2)/\rho(\mathbf{x}_1)$  defines the probability of finding any electron at position 2 in coordinate-spin space if there is one already known to be at position 1.

The exchange-correlation (xc) hole is defined as the difference between  $\Omega(\mathbf{x}_1, \mathbf{x}_2)$  and the uncorrelated probability of finding an electron at  $\mathbf{x}_2$ :

$$h_{xc}(\mathbf{x}_1, \mathbf{x}_2) = \frac{\rho_2(\mathbf{x}_1, \mathbf{x}_2)}{\rho(\mathbf{x}_1)} - \rho(\mathbf{x}_2) = \rho(\mathbf{x}_2)f(\mathbf{x}_1, \mathbf{x}_2) \quad (7.35)$$

and contains exactly the charge of one electron  $\int h_{xc}(\mathbf{x}_1, \mathbf{x}_2)d\mathbf{x}_2 = -1$ , [337]. The function  $f(\mathbf{x}_1, \mathbf{x}_2)$  is the correlation factor, being zero for the completely uncorrelated case.

The exchange-correlation hole describes the change in conditional probability caused by the correction for self-interaction, exchange and Coulomb correlation, compared to the completely uncorrelated situation. It can formally be split into the Fermi hole,  $h_x^{\sigma_1=\sigma_2}(\mathbf{r}_1, \mathbf{r}_2)$  and the Coulomb hole  $h_c^{\sigma_1, \sigma_2}(\mathbf{r}_1, \mathbf{r}_2)$

$$h_{xc}(\mathbf{x}_1, \mathbf{x}_2) = h_x^{\sigma_1=\sigma_2}(\mathbf{r}_1, \mathbf{r}_2) + h_c^{\sigma_1, \sigma_2}(\mathbf{r}_1, \mathbf{r}_2) \quad (7.36)$$

The exchange hole  $h_x$  applies only to electrons with the same spin, the correlation hole  $h_c$  has contributions for electrons of either spin and is the hole resulting from the  $1/r_{12}$  electrostatic interaction. This separation is convenient but only the total xc hole has a real physical meaning. In the HF method the Fermi hole is accounted for through the use of a single Slater determinant whereas the Coulomb hole is neglected. Like the total hole, the Fermi hole contains exactly the charge of one electron  $\int h_x(\mathbf{r}_1, \mathbf{r}_2)d\mathbf{r}_2 = -1$  and takes care of the self-interaction correction (SIC). The exchange hole  $h_x$  is negative everywhere  $h_x(\mathbf{r}_1, \mathbf{r}_2) < 0$  and its actual shape depends not only on the Fermi correlation factor but also on the density at  $\mathbf{r}_2$ . As a consequence,  $h_x$  is not spherically symmetric.

The Coulomb hole must be normalized to zero and this result is independent of the positions of electrons with  $\sigma' \neq \sigma: \int h_c(\mathbf{r}_1, \mathbf{r}_2)d\mathbf{r}_2 = 0$ .

The essential error of Hartree–Fock arises from the fact that in the HF model the exchange-correlation hole in a two-electron bond is not centered around the reference electron, but is too delocalized, having considerable amplitude on both atoms involved in the bond. The LDA and GGA models incorporate, simply by using an electron-centered hole, an important part of the effect of the interelectron Coulomb repulsion.

To improve the LDA and GGA models the orbital-dependent functionals are introduced. The introduction of orbital dependence, not only density and gradient dependence, into the functionals can be realized in different ways [330]. Hybrid HF-DFT functionals are the most popular beyond-GGA functionals. These functionals mix a fraction of HF exchange into the DFT exchange functional and use the DFT correlation part. But why is the exact HF exchange mixed with the approximate DFT exchange part? How can one find the weights of this mixing? May be it would be possible to use the exact HF exchange and rely on approximate functionals only for the part missing in the HF model, *i.e.* the electron correlation:  $E_{xc} = E_x^{HF} + E_c^{KS}$  (EXX – orbital-dependent exact exchange functional). The HF exchange is calculated using KS orbitals so that EXX energy will be slightly higher than the HF energy. The orbital-dependent exact-exchange (EXX) group of methods has received much attention in the literature. Two advantages of the EXX functional are often mentioned:

(a) the self-interaction correction is incorporated in this functional; (b) it is natural to break up the total problem of electron–electron interaction in the large (due to self-interaction correction) exchange part and the small correlation part. The hope is of course that it will be simpler to find an accurate density-functional for the small correlation energy.

A critique of the EXX method in DFT can be found, for example, in [337, 367]. It is clear that the EXX method does not offer any advantage over HF for energies. On the contrary, starting with EXX actually undermines the very basis of the success of DFT, which has been the breaking away from the quantum-chemistry paradigm of dividing up the full electron–electron interaction problem into two steps: first Hartree–Fock (or exchange only) and next the remaining correlation problem. That this is indeed the case is masked by the DFT terminology that still uses the names “exchange” (*e.g.*, Becke exchange, Perdew exchange) and “correlation” (*e.g.*, Perdew–Wang correlation, Lee–Yang–Parr (LYP) correlation). One should be aware that, while correlation is indeed much smaller than exchange in for instance (heavy) atoms, this is not true in the electron-pair bond. Both Hartree–Fock and the use of the exact-exchange functional in Kohn–Sham DFT are very deficient models for the description of chemical bonding. They both use a two-particle probability distribution that is wrong, as can be seen from the shape of the “hole” a reference electron creates around itself: the hole is not centered around the reference electron, but is delocalized over the atoms forming the bond. From this wrong hole shape one can understand the deficiencies of this model, such as too diffuse orbitals and density, hence wrong kinetic energy and electron–nuclear attraction energy. The true xc hole is substantially more localized around the reference electron. That is why rough localized model holes, like those of GGA, which approximate this total hole, are so successful.

This can be illustrated for the prototype electron-pair bond, the  $\text{H}_2$  molecule, at the equilibrium H–H distance [337, 367]: in the  $\text{H}_2$  case HF and EXX are identical. The Hartree–Fock (EXX) model is a poor zero-order approximation for the electron-pair bond. It is also extremely size inconsistent, in the sense that when we introduce a second H atom in the universe, remote from a given H atom, the HF/EXX model totally fails to deliver the sum of the energies of two H atoms. However, when we add the Coulomb hole (or correlation hole) to the Fermi (exchange) hole, we obtain a total hole that is localized at the nucleus where the reference electron is located. This will provide the right potential, and therefore the right density and kinetic energy. The localized hole does not require any knowledge of where the other H atom is located, it is the unphysical breaking up of this total hole into a delocalized exchange part and an equally delocalized Coulomb part that complicates the electron–electron interaction treatment and requires knowledge of the position of the second nucleus in order to build accurate holes. Actually, this example illustrates that the division in exchange and correlation holes creates one of the largest problems of DFT. The problem basically is that the total density  $\rho(\mathbf{r})$  around each H nucleus is identical at large H–H distances to that in a free H atom. However, the exchange and correlation energies in the stretched  $\text{H}_2$  are very different from those in two isolated H atoms. In particular, the correlation energy is zero in individual H atoms, in contrast to the strong left-right nondynamical correlation in the dissociating  $\text{H}_2$  molecule. It is virtually impossible to devise functionals that use only local information (local density and derivatives of the density) and still recognize the position of the other H atom and

build correctly the individual exchange and correlation holes, the shape of which is determined by the positions of the nuclei. The LDA and GGA total holes are localized around the reference electron, which is a definite advantage, the EXX approximation can not be regarded to be the next improvement beyond GGA. There are other possibilities of such an improvement: 1) to develop orbital-dependent functionals, which represent exchange and correlation simultaneously; 2) use HF-DFT exchange mixing.

The first possibility was realized recently in [367–370] where the virtual orbital-dependent xc functional  $E_{xc}^{BB}$  (BB, Buijse–Baerends) is suggested:

$$E_{xc}^{BB} [\{\varphi_j\}, \{\varphi_a\}] = -\frac{1}{2} \sum_i^M \sum_j^M \sqrt{w_i w_j} \int d\mathbf{r}_1 d\mathbf{r}_2 \frac{\varphi_i(\mathbf{r}_1) \varphi_i(\mathbf{r}_2) \varphi_j(\mathbf{r}_1) \varphi_j^*(\mathbf{r}_2)}{r_{12}} \quad (7.37)$$

and applied in calculations of hydrogen chains  $\text{H}_n$  and small molecules. Here  $w_i[\rho]$  is the xc orbital weight, which governs the involvement of the occupied/virtual orbital  $\varphi_i$  in the xc functional. It is important that the summation in (7.37) is made over  $M = N_{occ} + N_v$  orbitals where  $N_{occ}$  and  $N_v$  are the numbers of occupied and virtual KS orbitals. By giving weights to the virtual orbitals one can incorporate the effect of correlation. In [368] the functional form of  $w_i$  has been approximated with the Fermi-type distribution

$$w_i = \frac{2}{1 + \exp(f(\varepsilon_i - \varepsilon_F))} \quad (7.38)$$

where  $\varepsilon_i$  are the KS orbital energies and  $\varepsilon_F$  is the Fermi-level parameter. We do not consider the  $E_{xc}^{BB}$  functional in more detail as its possibilities for crystals are not well studied.

The second possibility of GGA improvement – mixing of HF and DFT exchange – is used in the well-known B3LYP, B3PW and PBE0 hybrid functionals. The performance of hybrid density-functionals (HDF) in solid-state chemistry is examined in a review [371] and many original publications. It is demonstrated that the HDF methods allow calculation of different properties of solids in good agreement with the experiment. We return to this point in Sect. 7.2. In Kohn–Sham density-functional theory, the exchange-correlation energy is rigorously given by

$$E_{xc} = \frac{1}{2} \int \rho(\mathbf{r}) \int \frac{h_{xc}(\mathbf{r}, \mathbf{r}')}{|\mathbf{r}' - \mathbf{r}|} d^3\mathbf{r}' d^3\mathbf{r} \quad (7.39)$$

$$h_{xc}(\mathbf{r}, \mathbf{r}') = \int_0^1 h_{xc}^\lambda(\mathbf{r}, \mathbf{r}') d\lambda \quad (7.40)$$

known as the “adiabatic connection” or “coupling strength integration”. In this most fundamental of DFT formulas,  $h_{xc}$  is an effective exchange-correlation hole, and  $\lambda$  is a coupling-strength parameter that switches on interelectronic  $1/r_{12}$  repulsion, subject to a fixed electronic density (achieved, in principle, by suitably adjusting the external potential as a function of  $\lambda$ ). The Kohn–Sham  $h_{xc}$  is therefore a coupling strength average of  $h_{xc}^\lambda$  as it evolves from  $\lambda = 0$  through  $\lambda = 1$  [372].

In an atom, the size of the hole is relatively insensitive to  $\lambda$  and remains of roughly atomic size. In a molecule, the changes in the character and size of the hole occur as  $\lambda$

varies from its noninteracting  $\lambda = 0$  to its fully interacting  $\lambda = 1$  limits. At  $\lambda = 0$  (pure exchange with no correlation whatsoever) delocalization of the hole over two or more centers is characteristic. Accurate DFTs must recognize this  $\lambda = 0$  nonlocality. As  $\lambda$  increases, the hole is localized by the long-range, nondynamical, left–right correlations that are absent in atoms but operative in molecules. At the fully interacting limit ( $\lambda = 1$ ), the hole has been localized to roughly atomic size. To incorporate the necessary nonlocality Becke [373] proposed so-called hybrid functionals

$$E_{xc}^{hyb} = E_{xc}^{KS} + a_{mix} (E_x^{HF} - E_x^{KS}) \quad (7.41)$$

The difference from the EXX functional is the following: the exact HF exchange  $E_x^{HF}$  is mixed with the DFT (LDA,GGA) exchange-correlation energy in hybrid functionals and with the DFT correlation energy in EXX functionals. The mixing parameter  $a_{mix}$  is used to patch an appropriate amount of HF exchange into the exchange-correlation energy. Even the simplest “half-half” hybrid functional ( $a_{mix} = 0.5$ ) greatly improves the calculated properties, compared with the pure DFT results. Becke developed the 3-parameter functional expressions known as B3PW and B3LYP hybrid functionals:

$$E_{xc}^{B3PW} = E_{xc}^{LSDA} + a (E_x^{HF} - E_x^{LSDA}) + b \Delta E_x^{Becke} + c \Delta E_x^{PW} \quad (7.42)$$

$$E_{xc}^{B3LYP} = E_{xc}^{LSDA} + a (E_x^{HF} - E_x^{LSDA}) + b \Delta E_x^{Becke} + c \Delta E_x^{LYP} \quad (7.43)$$

The B3PW functional (7.42) uses in  $E_{xc}$  the Becke [358] exchange and Perdew–Wang exchange-correlation [355], while in the B3LYP functional (7.43) the correlation part is that suggested by Lee–Yang–Parr [359]. The  $a, b, c$  parameters were optimized to fit the experimental data and do not depend on the molecule under consideration. It is clear that the choice of hybrid functionals is motivated by reasonable physical arguments. The term  $a (E_x^{HF} - E_x^{LSDA})$  replaces some electron-gas exchange with the exact exchange to capture the proper small- $\lambda$  limit in (7.39). The coefficient  $a$  reflects the rate of onset correlation as it increases from zero. The other terms allow optimum admixtures of exchange and correlation-type gradient corrections. These hybrid functionals are the simplest mixture of exact exchange, the LSDA for exchange-correlation, and gradient corrections of exchange and correlation type, that exactly recovers the uniform electron-gas limit. The B3LYP functional is the most popular in molecular quantum chemistry. Nevertheless, the correct amount of HF exchange included in any hybrid functional cannot be a constant over all species or even all geometries of a single species [374]. The rationale for mixing exact exchange with DFT approximation is discussed in [375]. The authors write the hybrid functional in the form

$$E_{xc} \cong E_{xc}^{KS} + \frac{1}{n} (E_x - E_x^{KS}) \quad (7.44)$$

where the optimum integer  $n$  can be found from the perturbation theory and  $n = 4$  for atomization energies of typical molecules. Such a formally parameter-free hybrid functional with a PBE exchange-correlation part is known as the PBE0 hybrid functional. The simplification of hybrid exchange-correlation functionals was suggested by Becke [372] based on simulation of delocalized exact exchange by local density-functionals. A simple model was introduced that detects exchange hole delocalization in molecules through a local variable related to kinetic-energy density.

Is it possible to use for extended systems (crystalline solids) the same hybrid functionals that are used in molecular DFT calculations? This problem is discussed in the next section.

## 7.2 Density-functional LCAO Methods for Solids

### 7.2.1 Implementation of Kohn–Sham LCAO Method in Crystals Calculations

Although the same fundamental theory underlies the density-functional approach in both solid-state physics and molecular quantum chemistry, and the same exchange-correlation functionals can be used in both disciplines (see Sect. 7.2.4), the detailed implementation is usually quite different [376]. First, this difference concerns the basis-set choice. Since the electronic charge density of an isolated molecule is necessarily localized in a finite region of space, the traditional quantum-chemical method is LCGTO (MOs are expanded in a basis of localized Gaussian-type orbitals, centered on the atomic nuclei). In contrast, the tradition in solid-state physics is to use plane waves (PW) as a basis set for expanding the one-particle Kohn–Sham wavefunctions (crystalline orbitals). These can be used in their pure form in the first-principles pseudopotential method [377] or modified near the atomic cores (augmented plane waves [378]). The all-electron (termed also full potential – FP) PW calculations are practically difficult as the core-states description requires a huge number of plane waves. The plane waves are a reasonable first approximation to conduction-band eigenfunctions and permit many formal simplifications and computational economies. Nevertheless, PW methods have the disadvantage that very localized or inhomogeneous systems may require excessive numbers of waves for their representation. This problem can be especially serious in surface calculations, where the requirement of periodicity in three dimensions leads to a model with slabs repeating periodically along the surface normal. If the space between the slabs is wide enough to make interactions between them negligible, the “lattice constant” normal to the surface has to be quite large and the corresponding reciprocal lattice vector quite short, resulting in a large number of plane waves within a given kinetic-energy cutoff and hence a relatively expensive calculation. This problem is discussed in Chap. 11 in more detail.

The distance between the slabs needs to be even larger if adsorbate molecules are to be added to the surface, since these molecules also should not interact across the space between the slabs. Localized-basis approaches to periodic systems do not suffer from this disadvantage. Very localized states, including core states if desired, can be represented by a suitable choice of atom-centered basis functions. The electronic charge density goes naturally to zero in regions of space where there are no atoms, and the lack of basis functions in such regions is not a problem unless a detailed description of energetic excitations, scattering states, or tunneling is required [376]. For surface modeling there is no need for periodicity normal to the surface; a single slab of sufficient finite thickness can be used, since these methods can be formulated equally easily for systems periodic in one, two or three dimensions. This facilitates the accurate treatment of molecule–surface interactions, especially when the molecules are relatively far from the surface. Also, if the basis functions are carefully constructed and optimized for the crystalline environment (we discuss this problem in Chap.

8) it is possible to represent the valence-electron eigenstates with a relatively small number of basis functions: just enough to accommodate all the electrons, plus a few more functions to give the Kohn–Sham orbitals sufficient variational freedom. Thus, only a few tens of basis functions per atom are typically needed, versus hundreds per atom in typical plane-wave approaches. The auxiliary basis sets needed to represent the charge density and, if desired, the exchange-correlation potential are also fairly modest in size. Once the basis set has been constructed and the required overlap and Hamiltonian matrices formed, the small (compared to plane wave) size of the basis can greatly reduce the computational cost of solving the Kohn–Sham equations.

Also, especially in systems with large unit cells, one can exploit sparsity in these matrices, since basis functions on distant centers will have negligible overlap and interaction (except for certain long-range Coulomb multipole interactions that can be summed according to Ewald’s convention or screened). Advanced techniques can be applied to calculate multicenter integrals in LCGTO methods for solids. For example, in the implementation of periodic boundary conditions in the MO LCAO program [379, 380] all terms contributing to the KS Hamiltonian are evaluated in real space, including the infinite Coulomb summations, which are calculated with the aid of the fast multipole method [381, 382]. In LCGTO methods with PBC the  $O(N)$  linear-scaling DFT calculations for large and complex systems are possible [379, 383]. For example, carbon nanostructures up to C540 were calculated [384] using DFT LCAO with the numerical atomic basis. Below, we present the basic formalism for DFT KS equations for periodic systems using a basis set of atomic orbitals. For more details of DFT LCAO methods the reader is referred to the original publications [376, 385–389].

The HF LCAO method for periodic systems was considered in Sections 4.1.5 and 4.1.6. We discuss here the KS LCAO method for crystals in comparison with the HF LCAO approach. The electronic energy of the crystal (per primitive cell) as calculated within the HF approximation ( $E_{HF}$ ) and DFT ( $E_{DFT}$ ) can be expressed in terms of the one-electron density matrix (DM) of the crystal defined as  $P(\mathbf{k})$  in terms of Bloch sums of AOs, (4.125) or as  $\rho(\mathbf{R}, \mathbf{R}')$  in coordinate space, (4.126). These expressions are:

$$E_{HF}[\rho] = E_0[\rho] + E_H[\rho] + E_X[\rho] \quad (7.45)$$

$$E_{DFT}[\rho] = E_0[\rho] + E_H[\rho] + E_{XC}[\rho] \quad (7.46)$$

where  $E_0[\rho]$  is defined as the expectation value of the one-electron operator  $\hat{h}(\mathbf{R})$

$$E_0[\rho] = \frac{1}{N} \int_{V_N} d^3 \mathbf{R} [\hat{h}(\mathbf{R}) \rho(\mathbf{R}, \mathbf{R}')]_{\mathbf{R}'=\mathbf{R}} \quad (7.47)$$

$E_H[\rho]$  is the Coulomb (Hartree) energy,

$$E_H[\rho] = \frac{1}{N} \int_{V_N} d^3 \mathbf{R} \int_{V_N} d^3 \mathbf{R}' \frac{\rho(\mathbf{R}, \mathbf{R}) \rho(\mathbf{R}', \mathbf{R}')}{|\mathbf{R} - \mathbf{R}'|} \quad (7.48)$$

$E_X[\rho]$  is the HF exchange energy,

$$E_X[\rho] = -\frac{1}{2N} \int_{V_N} d^3 \mathbf{R} \int_{V_N} d^3 \mathbf{R}' \frac{|\rho(\mathbf{R}, \mathbf{R}')|^2}{|\mathbf{R} - \mathbf{R}'|} \quad (7.49)$$

and  $E_{XC}[\rho]$  in (7.46) is the exchange-correlation energy functional of density  $\rho(\mathbf{R}, \mathbf{R}) = \rho(\mathbf{R})$  (different expressions for this functional depend on the DFT version and were discussed in Sect. 7.1). As in Sect. 4.3.1 the electron position vector  $\mathbf{R}$  is supposed to be written as the sum  $\mathbf{R} = \mathbf{r} + \mathbf{R}_n$ , where  $\mathbf{R}_n$  specifies the primitive cell and  $\mathbf{r}$  is the position vector of an electron within this primitive cell. The difference between the HF exchange energy  $E_X$  and DFT exchange-correlation energy  $E_{XC}$  is the following: the former depends on the total DM  $\rho(\mathbf{R}, \mathbf{R}')$ , the latter only on DM diagonal elements  $\rho(\mathbf{R})$ , *i.e.* electron density.

In the HF approximation and DFT, the crystal orbitals are solutions to the equations

$$\hat{F}(\mathbf{k})\varphi_i(\mathbf{k}) = \varepsilon_i(\mathbf{k})\varphi_i(\mathbf{k}) \quad (7.50)$$

where the one-electron operator  $\hat{F}(\mathbf{k})$  is either the HF operator,  $\hat{F}^{HF}(\mathbf{k})$

$$\hat{F}^{HF}(\mathbf{k}) = \hat{H}(\mathbf{k}) + \hat{J}(\mathbf{k}) + \hat{X}(\mathbf{k}) \quad (7.51)$$

or the Kohn–Sham operator  $\hat{F}^{KS}(\mathbf{k})$ ,

$$\hat{F}^{KS}(\mathbf{k}) = \hat{H}(\mathbf{k}) + \hat{J}(\mathbf{k}) + \hat{V}_{XC}(\mathbf{k}) \quad (7.52)$$

Here,  $\hat{H}(\mathbf{k})$  is a one-electron operator that describes the motion of an electron in the crystal and is equal to the sum of the kinetic-energy operator and the Coulomb interaction operator between the electron and fixed atomic nuclei and  $\hat{J}(\mathbf{k})$  and  $\hat{X}(\mathbf{k})$  are the Coulomb and exchange operators, respectively, which describe the interaction of the given electron with the other electrons of the crystal.

In the LCAO basis, both the Hartree–Fock and Kohn–Sham equations are the same (see (4.57)):

$$F(\mathbf{k})C(\mathbf{k}) = S(\mathbf{k})C(\mathbf{k})E(\mathbf{k}) \quad (7.53)$$

The HF and KS operators in the reciprocal space are represented by the Fock matrices  $F_{\mu\nu}^{HF}(\mathbf{k})$  and Kohn–Sham matrices  $F_{\mu\nu}^{KS}(\mathbf{k})$ , which are related to the matrices in the coordinate space by the relations

$$F_{\mu\nu}^{HF}(\mathbf{k}) = \sum_{\mathbf{R}_n} \exp(i\mathbf{k}\mathbf{R}_n) [h_{\mu\nu}(\mathbf{R}_n) + j_{\mu\nu}(\mathbf{R}_n) + x_{\mu\nu}(\mathbf{R}_n)] \quad (7.54)$$

$$F_{\mu\nu}^{KS}(\mathbf{k}) = \sum_{\mathbf{R}_n} \exp(i\mathbf{k}\mathbf{R}_n) [h_{\mu\nu}(\mathbf{R}_n) + j_{\mu\nu}(\mathbf{R}_n) + v_{\mu\nu}^{XC}(\mathbf{R}_n)] \quad (7.55)$$

where  $h_{\mu\nu}(\mathbf{R}_n)$ ,  $j_{\mu\nu}(\mathbf{R}_n)$  and  $x_{\mu\nu}(\mathbf{R}_n)$  are the one-electron, Coulomb, and exchange parts of the Fock matrix in the coordinate space, respectively (see (4.59)–(4.63)). In the DFT, instead of the nonlocal-exchange interaction matrix  $x_{\mu\nu}(\mathbf{R}_n)$ , the exchange-correlation matrix  $v_{\mu\nu}^{XC}(\mathbf{R}_n)$  is used, with different exchange-correlation functional approximations being employed in various versions of the DFT. In particular, in the local-density approximation (LDA), it is assumed that

$$\begin{aligned} v_{\mu\nu}^{XC}(\mathbf{R}_n) &= \int d^3\mathbf{R} \varphi_\mu(\mathbf{R}) v^{XC}(\mathbf{R}) \varphi_\nu(\mathbf{R} - \mathbf{R}_n) \\ v^{XC}(\mathbf{R}) &= \frac{\partial}{\partial \rho} \varepsilon[\rho(\mathbf{R})] \end{aligned} \quad (7.56)$$

The CO-LCAO calculations based on both the HF method and DFT allow one not only to make a comparison between the results obtained within these two approximations but also to employ a combination of these approximations used in hybrid HF-DFT methods. The HF self-consistent electron density of the crystal can be used to calculate correlation corrections to the total HF energy *a posteriori* [390]. In some cases it is useful to use the HF self-consistent density matrix to make the convergence of the DFT LCAO self-consistent procedure faster [23].

The extension of the existing HF-LCAO computer codes to DFT-LCAO ones allows a very direct comparison between these methods using the same code, the same basis set, and the same computational conditions. The modification of the HF LCAO code with PBC to perform DFT calculations is straightforward in principle. It is required only to delete the HF exchange and instead to evaluate the matrix elements of exchange-correlation operator, that is, to solve KS rather than HF equations in each iteration of the SCF procedure [389]. These modifications were made in the PBC HF codes Crystal95 [23] and Gaussian03 [107]. The main difficulty of this modification arises in the calculations of matrix elements of the exchange-correlation operator. Different approaches to this problem were suggested.

The principal merit of the HF LCAO scheme is the possibility to calculate the matrix elements of the Fock matrix analytically. This merit may be retained in the DFT LCAO calculation if the exchange-correlation potential is expanded in an auxiliary basis set of Gaussian-type functions, with even-tempered exponents. At each SCF iteration the auxiliary basis set is fitted to the actual analytic form of the exchange-correlation potential, which changes with the evolving charge density [391].

The numerical integration also can be used to calculate the matrix elements of the exchange-correlation potential. For the numerical integration, the atomic partition method proposed by Savin [392] and Becke [393] has been adopted and combined with Gauss–Legendre (radial) and Lebedev (angular) quadratures [394]. The Kohn–Sham LCAO periodic method based on numerical integration at each cycle of the self-consistent-field process is computationally more expensive than the periodic LCAO Hartree–Fock method that is almost fully analytical.

In conclusion of this section we give some comments concerning the meaning of the KS eigenvalues and orbitals [11]. Strictly speaking, the KS eigenvalues and eigenvectors do not have the physical meaning of one-electron energies and wavefunctions as in the HF theory. Also, the single-determinant many-electron wavefunction constructed out of the KS orbitals does not correspond to the exact wavefunction of the system of interacting electrons; it is merely a wavefunction of the corresponding fictitious noninteracting system. The HF eigenvalues for occupied and empty states are calculated with different potentials, but KS eigenvalues with the same. Therefore, one should be careful with the KS eigenvalues of the states lying above the “occupied” ones. For example, the energy gap between the uppermost valence and the lowermost conduction bands in a solid is strongly underestimated in the majority versions of DFT. Note that the gap is always overestimated in the HF theory. It can be shown that similarly to Koopman’s theorem in the HF theory, the ionization energy in the KS theory is given by the KS energy in the highest-occupied state. But this result cannot be applied to other occupied KS states since in the KS theory all states must be occupied sequentially from the bottom to the top: one cannot remove an electron below the highest-occupied state leaving a hole there.

As an advantage of the DFT LCAO method one can mention the possibility of linear scaling in calculations of complex molecules and crystals, considered in next next section.

### 7.2.2 Linear-scaling DFT LCAO Methods for Solids

The increase in computer power and the progress in the methodology have allowed the *ab-initio* calculations of increasingly more complex and larger systems with an increasing number of atoms  $N$  (for periodic systems  $N$  is the number of atoms in the primitive unit cell). In the HF LCAO and DFT PW methods the computer time and memory scales with  $N$  like  $N^{2-3}$  [377, 399]. inner only recently that two linear system-size scaling  $O(N)$  DFT LCAO methods for periodic systems were developed that resulted in general purpose, flexible DFT computer codes, [107, 344].

The *Siesta* (Spanish Initiative for Electronic Simulations with Thousands of Atoms) method [383, 384, 400] achieves linear scaling by the explicit use of localized Wannier-like functions and numerical pseudoatomic orbitals confined by a spherical infinite-potential wall [401]. As the restriction of the Siesta method we mention the difficulty of the all-electron calculations and use of only LDA/GGA exchange-correlation functionals.

The second DFT LCAO linear-scaling method by Scuseria and Kudin (SK method) [379] uses Gaussian atomic orbitals and a fast multipole method, which achieves not only linear-scaling with system size, but also very high accuracy in all infinite summations [397]. This approach allows both all-electron and pseudopotential calculations and can be applied also with hybrid HF-DFT exchange-correlation functionals.

The first step in the *Siesta* method calculation is the choice of pseudopotentials. In Chap. 8 we discuss in more detail the pseudopotentials used in periodic HF and KS LCAO calculations. The Siesta method relies on the use of strictly confined basis atomic orbitals, *i.e.* orbitals that are zero beyond a certain radius. This keeps the energy strictly variational, thus facilitating the test of the convergence with respect to the radius of confinement. In addition to the atomic valence orbitals polarization pseudoatomic orbitals are added to account for the deformation induced by bond formation. The different AO choices in HF and DFT LCAO calculations are discussed in Chap. 8. In calculations of silicon crystal it was shown [400] that the standard basis already offers quite well converged results, comparable to those used in practice in most plane-wave calculations. The study of the dependence of the lattice constant, bulk modulus and cohesive energy of bulk silicon on the range of the basis orbitals shows that a cutoff radius of 3 Å for both  $s$  and  $p$  orbitals already yields very well converged results.

Within the pseudopotential approximation, the standard KS one-electron Hamiltonian is written as

$$\hat{H} = \hat{T} + \sum_I \hat{V}_I^{loc} + \sum_I \hat{V}_I^{nonloc} + \hat{V}_H + \hat{V}_{xc} \quad (7.57)$$

where  $\hat{T}$  is the kinetic energy operator,  $I$  is an atom index,  $\hat{V}_H$  and  $\hat{V}_{xc}$  are the total Hartree and  $xc$  potentials. The pseudopotential operator is the sum of the local  $\hat{V}_I^{loc}$  and nonlocal  $\hat{V}_I^{nonloc}$  parts of the pseudopotential of atom  $I$ . The nonlocal part uses a different radial potential  $V_l(r)$  for each angular momentum  $l$  (see Chap. 8). In

order to eliminate the long range of  $V_I^{loc}$  it is screened with the potential  $V_I^{at}$ , created by an atomic electron density  $\rho_I^{at}$ , constructed by populating the basis functions with appropriate valence atomic charges. Notice that, since the atomic basis orbitals are zero beyond the cutoff radius  $r_I^c$ , the screened “neutral-atom” (NA) potential  $V_I^{NA} = V_I^{loc} + V_I^{nonloc}$  is also zero beyond this radius. Now, let  $\delta\rho(\mathbf{r})$  be the difference between the self-consistent electron density  $\rho(\mathbf{r})$  and the sum of atomic densities  $\rho^{at} = \sum_I \rho_I^{at}$ , and let  $\delta V^H(\mathbf{r})$  be the electrostatic potential generated by  $\delta\rho(\mathbf{r})$  that integrates to zero and is usually much smaller than  $\rho(\mathbf{r})$ . Then the total Hamiltonian may be rewritten as

$$\hat{H} = \hat{T} + \sum_I \hat{V}_I^{nonloc} + \delta V_H + V_{xc} \quad (7.58)$$

The matrix elements of the first two terms involve only two-center integrals that are calculated in reciprocal space and tabulated as a function of interatomic distance. The remaining terms involve potentials that are calculated on a three-dimensional real-space grid.

In the Brillouin sampling a supercell around the unit cell (and comprising the unit cell itself) is defined large enough to contain all the atoms whose basis orbitals are nonzero at any of the grid points of the unit cell, or that overlap with any of the basis orbitals in it. All the nonzero two-center integrals between the unit-cell basis orbitals and the supercell orbitals are calculated without any complex phase factors. Also calculated are the grid integrals between *all* the supercell basis orbitals  $\varphi_{\mu'}$  and  $\varphi_{\nu'}$  (primed indices run over all the supercell), but *within the unit cell only*. These integrals are accumulated in the corresponding matrix elements. Once all the real overlap and Hamiltonian matrix elements are calculated, they are multiplied, at every  $\mathbf{k}$  point, by the corresponding phase factors and accumulated by folding the supercell orbital to its unit-cell counterpart. The resulting  $N \times N$  complex eigenvalue problem, with  $N$  the number of orbitals in the unit cell, is then solved at every sampled  $\mathbf{k}$ -point, finding the Bloch-state expansion coefficients over AOs and the density at a grid point of the unit cell. The fineness of this grid is controlled by a  $\mathbf{k}$ -grid cutoff (see Sect. 4.2), a real-space radius that plays a role equivalent to the plane-wave cutoff of the real-space grid [89]. The origin of the  $\mathbf{k}$ -grid may be displaced from  $\mathbf{k} = \mathbf{0}$  in order to decrease the number of inequivalent  $\mathbf{k}$ -points (see Sect. 4.2.3). If the unit cell is large enough to allow a  $\Gamma$ -point-only calculation, the multiplication by phase factors is skipped and a single real-matrix eigenvalue problem is solved (in this case, the real matrix elements are accumulated directly in the first stage, if multiple overlaps occur).

To solve the KS equations in  $O(N)$  operations the localized, Wannier-like states are used as they are constrained by their own localization region. Each atom  $I$  is assigned a number of states equal to  $\text{int}(Z_I^{\text{core}}/2 + 1)$  so that, if doubly occupied, they can contain at least one excess electron (they can also become empty during the minimization of the energy functional). These states are confined to a sphere of radius  $R_c$  (common to all states) centered at nuclei  $I$ . Irrespective of whether the  $O(N)$  functional or the standard diagonalization is used, an outer self-consistency iteration is required, in which the density matrix is updated. Even when the code is strictly  $O(N)$ , the CPU time may increase faster if the number of iterations required to achieve the solution increases with  $N$ . In fact, it is a common experience that the required number of self-consistency iterations increases with the size of the system. This is mainly because of the “charge-sloshing” effect, in which small displacements

of charge from one side of the system to the other give rise to larger changes of the potential as the size increases. Fortunately, the localized character of the Wannier-like wavefunctions used in the  $O(N)$  method also helps to solve this problem, by limiting the charge sloshing. Figure 7.1 shows the essentially perfect  $O(N)$  behavior of the overall CPU time and memory in silicon supercells of 64, 512, 1000, 4096 and 8000 atoms calculations [400].

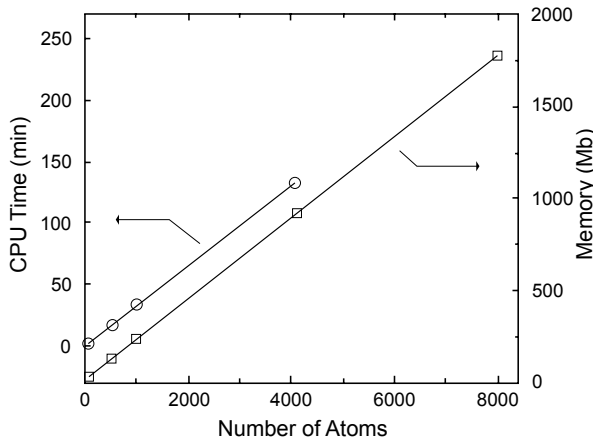


**Fig. 7.1.**  $O(N)$  behavior of the overall CPU time and memory in silicon supercell calculations [400]

The SIESTA method provides a very general scheme to perform a range of calculations from very fast to very accurate, depending on the needs and stage of the simulation, of all kinds of molecule, material and surface. It allows DFT simulations of more than a thousand atoms in modest PC workstations, and over a hundred thousand atoms in parallel platforms [400]. The numerous applications of the Siesta DFT LCAO method can be found on the Siesta code site [344]. These applications include nanotubes, surface phenomena and amorphous solids.

The *Scuseria-Kudin* method of  $O(N)$  scaling is due to the use of efficient direct lattice summation. The simulations of systems with periodic boundary conditions include the long-range Coulomb potential. To properly converge the resulting infinite Coulomb sum the Ewald summation method is adequate [71]. In this approach one part of the Coulomb contribution is computed in direct space and another in reciprocal space. The Ewald summation method yields  $O(N^{3/2})$  or  $O(N \log N)$  with the fast Fourier transform [382]. Alternatively, the infinite summation can be done using the periodic fast multipole method (FMM) [395,396], carried out entirely in direct space. The periodic FMM was extended to energy calculations for periodic systems with Gaussian charge distributions [382,397] and demonstrated  $O(N)$  scaling properties for the algorithm. In this particular situation, the FMM has certain advantages over the Ewald summation such as its universal applicability to systems periodic in one, two, and three dimensions. The FMM method was extended also to the analytic

calculation of the stress tensor whose components are required for energy optimization with respect to particle positions in the unit cell and the lattice dimensions [398]. The FMM partitions all pair interactions into near-field and far-field, and evaluates these contributions in CPU times that are approximately constant per particle, yielding an  $O(N)$  algorithm. In the FMM, the system under consideration is embedded in a hierarchy of  $8^n$  cubic boxes at the finest mesh level, where  $n$  specifies the total number of tiers [402, 403]. All charge distributions located in a given box are represented by multipole expansions about the center of the box. For highly accurate results, the near-field (NF) portion of the problem, which is defined by interactions inside a given box and neighboring boxes, is treated exactly. Interactions in the far-field (FF) are treated through multipole expansions. The distinctive characteristic of the FMM is that translation techniques allow these multipole expansions to interact at different mesh levels (depending on the distance between their centers) through an upward and downward pass of the tree hierarchy, yielding a method with effective linear-scaling.

In the Gaussian FMM (GFMM) implementation, a given interaction is included in the FF only if the number of boxes separating the edge of the boxes containing the two charge distributions is larger than the sum of the ranges of the distributions. For Gaussian functions, the range definition can be derived from the basic Coulomb integral between two  $s$ -type distributions as  $r = (2s)^{-1/2} \text{erfc}^{-1}(\varepsilon)$  where  $s$  is the exponent of the product Gaussian distribution,  $\text{erfc}^{-1}$  is the inverse of the complementary error function, and  $\varepsilon$  is the desired error in the approximation. The real number is rounded up to the nearest integer, thus guaranteeing an error smaller than  $\varepsilon$ . The electron–electron near-field (NF) interactions were treated exactly through six-dimensional analytic integration of Gaussian functions. The maximum  $l$  of a given multipole expansion was truncated to an effective value  $l_{\text{eff}}$  based on  $\varepsilon = k(a/R)^{l_{\text{eff}}}$ , where  $\varepsilon$  is the desired accuracy,  $a$  is a constant whose optimum value is 0.63, and  $k$  is adjusted such that  $l_{\text{eff}} = l_{\text{max}}$ , when  $R = 3$  boxes. This simple formula is straightforward, substantially improves the speed of the GFMM (which asymptotically scales as  $N$ ), and still yields very accurate results. This “very fast” approach is partially responsible for the good scaling properties of the GFMM used in the SK  $O(N)$  approach. The use of the GFMM for electrostatic interactions allows the infinite lattice sums to be computed exactly for systems of any periodicity. Calculations of energy derivatives with the FMM in periodic systems are similar to those in molecules.

In the SK DFT PBC implementation as much work as possible is done in real space. Consequently, all matrices are stored in real-space form and transformed into  $\mathbf{k}$  space only when needed. In the iterative part of the code, first the entire real-space Fock matrix  $F_{\mu\nu}^{\sigma R_n}$  is constructed, it is transformed into several  $\mathbf{k}$ -space matrices, which are diagonalized to obtain orbital coefficients and energies, and then the reciprocal-space density matrices are constructed. The latter are integrated by numerical means to yield the real-space density matrix that is used in the following SCF cycle. The gradient part of the code also deals with real-space quantities only. Overall,  $\mathbf{k}$ -space integration adds just a few extra steps to the PBC calculation when compared to the molecular case.

All the transformations between real and reciprocal spaces are computationally inexpensive and simple to implement. An extremely important feature of the SK direct-space Gaussian PBC method is that once the real-space matrices are available, the major cost of any additional  $\mathbf{k}$ -point calculation is just the transformation into

an orthonormal basis set plus the diagonalization. This is drastically different from the PW implementations where one computes the Fock matrix for each  $\mathbf{k}$  point separately. Even though the cost of such matrix formation may be considerably lower for PWs than for the real-space Fock matrix, the relatively low cost of additional  $\mathbf{k}$ -point calculations when using Gaussians permits denser  $\mathbf{k}$ -point meshes in reciprocal space even for systems of medium size. Furthermore, the derivatives of the band energies with respect to the  $\mathbf{k}$  vector are also rather straightforward to compute. Such information may be very useful in the Brillouin-zone integration for systems with complicated band structures. In order to reduce the number of SCF cycles, the direct inversion of the iterative subspace method (DIIS) developed by Pulay [404], has been used. DIIS requires formation of error matrices  $R = (FPS - SPF)$  ( $F, P, S$  are Fock, density and overlap matrices, respectively) for each SCF cycle. The matrix  $R$  approaches zero as the calculation proceeds toward convergence. During the DIIS procedure, one evaluates the inner products of the error matrices from different SCF cycles,  $B_{ij} = R_i R_j$  and uses these  $B_{ij}$  products to determine the DIIS mixing coefficients. A simple way to incorporate the DIIS procedure into a PBC code is to employ  $F, P$ , and  $S$  matrices just for one point in reciprocal space, for example the  $\Gamma$  ( $\mathbf{k} = \mathbf{0}$ ) point. For this point, the  $F, P$ , and  $S$  matrices are real, and all the DIIS steps are then the same as in the case of molecular calculations. The DIIS mixing coefficients, evaluated from matrices at  $\mathbf{k} = \mathbf{0}$ , are used to form the extrapolated real-space Fock matrix  $\tilde{F}_{\mu\nu}^{\mathbf{0}R_n}$  and Fock matrices in all  $\mathbf{k}$  points through the extrapolation of the real-space  $\tilde{F}_{\mu\nu}^{\mathbf{0}R_n}$  matrix.

In periodic calculations, large basis sets with diffuse functions may cause instabilities in the SCF procedure due to the limited accuracy of the Fock-matrix construction, and much more rarely due to the limited accuracy of the diagonalization. The usual prescription for restoring the stability of the SCF procedure is to project out the orbitals with small overlap eigenvalues from the basis set, which can be done during the orthonormalization. In order to transform GTOs to an orthonormal basis, one may employ symmetric orthogonalization and use the  $S^{-1/2}$  matrix. Another way to orthonormalize the basis set is called canonical orthogonalization and uses the matrix  $U = VS^{-1/2}$  ( $V$  is the eigenvector matrix of the overlap matrix  $S$ ). In calculations with PBC the instabilities arise mainly from numerical inaccuracies on the Hamiltonian-matrix formation rather than true linear dependences in the basis set [379]. Therefore, it is important in the SK method implemented in code [107], that kinetic and electrostatic contributions to the Fock matrix are evaluated exactly (the latter via FMM), while the DFT exchange-correlation quadrature is also carried out with high accuracy. Therefore, one might expect that the SCF instabilities would occur only for very small overlap matrix eigenvalues, somewhere in the  $10^{-6}$ – $10^{-7}$  range. Indeed, this is the behavior observed in all the calculations [379].

The key issue in PBC calculations seems to be the Hamiltonian matrix evaluation, which needs to be done to very high accuracy, especially in the infinite Coulomb sums. This goal is achieved by means of the GFMM without resorting to any truncation. There are three major contributions to the Fock-matrix formation: the kinetic-energy term, the electrostatic term, and the exchange-correlation contribution. In large systems, the kinetic-energy matrix is sparse, computed only once, and is therefore easy to deal with. The electrostatic part of our code uses the periodic FMM, so its scaling is very close to linear. The periodic exchange-correlation quadrature is a straightforward extension of the one used in molecular calculations whose linear-scaling has also

been demonstrated [405]. Furthermore, the analytic gradient code resembles the Fock-matrix formation, and, therefore, the force calculation also has  $O(N)$  computational cost. The density-matrix update is done in the conventional way, by diagonalizing the Kohn–Sham Hamiltonian matrix and constructing the density matrix from its eigenvectors. Although this procedure scales as  $O(N^3)$ , it has such a small scaling prefactor that the diagonalization cost for systems with up to a few thousand Gaussian basis functions is rather small compared to other steps in the PBC code.

For very large systems, the DIIS procedure uses sparse matrices and therefore its cost also becomes close to linear. In order to demonstrate the actual scaling properties of SK DFT PBC code [107], a series of calculations have been carried out for PPV (paraphenylenevinylene) with a different number of monomers in the unit cell [379]. The results of these LSDA calculations are presented in Table 7.1. The SCF took 10 cycles to converge the density to a rms deviation of  $10^{-8}$ . As is seen from Table 7.1 in the SCF part of the calculations, the CPU time required for the evaluation of electrostatic and exchange-correlation terms scales linearly for all practical purposes. On the other hand, the complex diagonalizations and the DIIS procedure scale as  $O(N^3)$ . The relative cost of all these  $O(N^3)$  steps is such that for the largest system in Table 7.1 (224 atoms, 1344 basis functions) the total CPU time is roughly similar to the CPU time required for the Fock-matrix formation.

**Table 7.1.** IBM Power3 CPU times (sec) for PPV LSDA/3-21G [379]

$(C_8H_6)_x, x$	1	2	4	8	16
No. atoms	14	28	56	112	224
No. basis 84	168	336	672	1344	
No. $k$ points	16	8	4	2	1
No. FMM levels	3	4	5	6	7
<b>Timings</b>					
Form $S^{-1}$ <sup>a</sup>	0.6	2.0	7	28	115
FMM, FF	1.3	2.5	5	10	20
FMM, NF	6.3	12.1	25	48	98
XC quad	13.0	26.4	54	109	223
DIIS	0.03	0.13	0.9	7.9	73
$\Gamma$ diag	0.04	0.21	1.3	9.9	78
Diag <sup>a</sup>	0.91	3.2	12.3	52	198
Total SCF	197	416	935	2342	7285
<b>Forces</b>					
FMM, FF	2.7	5.4	11	21	43
FMM, NF	28.4	57.4	115	232	446
XC quad	24.1	49.4	106	243	621
Total force	55	113	233	500	1123

<sup>a</sup>Timings reported include all  $k$  points

The references to the recent applications of the SK method implemented in the GAUSSIAN03 code [107] can be found on the site [406] and in original papers.

The important advantage of the Scuseria–Kudin implementation of the DFT LCAO  $O(N)$  method for solids is the possibility to use hybrid HF-DFT exchange-correlation functionals, including the recently developed screened Coulomb hybrid functional, discussed in the next subsection.

### 7.2.3 Heyd–Scuseria–Ernzerhof Screened Coulomb Hybrid Functional

In Sect. 7.1.5 we briefly discussed hybrid density-functionals, which contain a portion of HF exchange and are popular in molecular quantum chemistry since they provide higher accuracy than LDA and GGA functionals. The idea of hybrid functionals is related to the adiabatic connection method (ACM), (7.40), which connects the noninteracting KS reference system to the fully interacting real system. The ACM (hybrid) functionals (7.41) include the coefficient  $a_{mix}$  of mixing HF and KS exchange. Perdew and coworkers have also shown [375] that this mixing coefficient value can be fixed *a priori* ( $a_{mix} = 0.25$ ) taking into account that fourth-order perturbation theory is sufficient to get accurate numerical results for molecular systems. This leads to a family of adiabatic connection method functionals with the same number of adjustable parameters as their GGA’s constituents (ACM0 functionals, (7.44)). In particular the PBE0 variant gives results comparable to those of 3-parameter hybrids in B3LYP, whereas the modified mPW0PW functional gives results competitive with the B3LYP results [407]. The PBE0 hybrid functional [375] does not contain any adjustable parameter and proved to be successful in molecular calculations.

In solid-state calculations, however, the use of hybrid functionals is not a common practice because of the high computational cost that exact exchange involves. A recent alternative to conventional hybrid functionals is a screened exchange hybrid functional developed by Heyd, Scuseria, and Ernzerhof (HSE) [408, 409]. This functional uses a screened Coulomb potential for the exact exchange interaction, drastically reducing its computational cost, and providing results of similar quality to traditional hybrid functionals. It was demonstrated that the screened HF exchange (neglect of the computationally demanding long-range part of HF exchange) exhibits all physically relevant properties of the full HF exchange.

We discuss here the main features of the HSE hybrid functional and its application in solid-state LCAO calculations. The HSE functional for solids is much faster than regular hybrids and can be used in metals also.

The range of the exchange interaction in insulators decays exponentially as a function of the bandgap [410]. In metallic systems the decay is algebraic. To render the HF exchange tractable in extended systems, either the exchange interactions need to be truncated artificially or their spatial decay accelerated [409]. Various truncation schemes have been proposed to exploit the exponential decay in systems with sizable bandgaps [413–415]. Truncation schemes are very useful for systems with localized charge distributions where the HF exchange decays rapidly over distance. However these approaches fail to significantly decrease the computational effort in systems with small or no gaps. In delocalized systems truncation leads to severe convergence problems in the self-consistent-field (SCF) procedure as well as uncertainties

in the predicted energy of the system. The second option, accelerating the spatial decay, circumvents both of these problems but still neglects interactions that might be physically important. The HSE hybrid density-functional includes the spatial decay acceleration using a screened Coulomb potential and attempts to compensate for the neglected interactions.

A screened Coulomb potential is based on a splitting of the Coulomb operator into short-range (SR) and long-range (LR) components. The choice of splitting function is arbitrary as long as SR and LR components add up to the original Coulomb operator. HSE use the error function to accomplish this split since it leads to computational advantages in evaluating the short-range HF exchange integrals: the error function can be integrated analytically when using Gaussian basis functions. The following partitioning is used for the full  $1/r$  Coulomb potential:

$$\frac{1}{r} = \left( \frac{\text{erfc}(\omega r)}{r} \right)_{SR} + \left( \frac{\text{erf}(\omega r)}{r} \right)_{LR} \quad (7.59)$$

where the complementary error function  $\text{erfc}(\omega r) = 1 - \text{erf}(\omega r)$  and  $\omega$  is an adjustable parameter. For  $\omega = 0$ , the long-range term becomes zero and the short-range term is equivalent to the full Coulomb operator. The opposite is the case for  $\omega \rightarrow \infty$ . In the HSE approach the screened Coulomb potential is applied only to the exchange interaction. All other Coulomb interactions of the Hamiltonian, such as the Coulomb repulsion of the electrons, do not use a screened potential. The exchange energy in the PBE0 functional  $E_x^{\text{PBE0}} = a_{\text{mix}} E_x^{\text{HF}} + (1 - a_{\text{mix}}) E_x^{\text{PBE}} + E_c^{\text{PBE}}$  is split into short- and long-range components

$$E_x^{\text{PBE0}} = a_{\text{mix}} E_x^{\text{HF},SR}(\omega) + a_{\text{mix}} E_x^{\text{HF},LR}(\omega) + (1 - a_{\text{mix}}) E_x^{\text{PBE},SR}(\omega) + E_x^{\text{PBE},LR}(\omega) - a_{\text{mix}} E_x^{\text{PBE},LR}(\omega) \quad (7.60)$$

where  $\omega$  is an adjustable parameter governing the extent of short-range interactions. For the exchange-mixing parameter value  $a_{\text{mix}} = 0.25$  and  $\omega = 0$  (7.60) is equal to the exchange part of the PBE0 parameter-free functional. Numerical tests based on realistic  $\omega$  values ( $\omega \approx 0.15$ ) indicate that the HF and PBE long-range exchange contributions of this functional are rather small (just a few per cent), and that these terms tend to cancel each other [408].

Thus, if we neglect them and work under the assumption that this approximation may be compensated by other terms in the functional, one obtains a screened Coulomb potential hybrid density-functional of the form:

$$E_{xc}^{\omega \text{PBE}} = a_{\text{mix}} E_x^{\text{HF},SR}(\omega) + (1 - a_{\text{mix}}) E_x^{\text{PBE},SR}(\omega) + E_x^{\text{PBE},LR}(\omega) + E_c^{\text{PBE}} \quad (7.61)$$

where  $\omega$  is an adjustable parameter governing the extent of short-range interactions. The hybrid functional (7.61) is equivalent to PBE0 for  $\omega = 0$  and asymptotically reaches PBE for  $\omega \rightarrow \infty$ .

The short-range component of the HF exchange can be obtained by using the SR Coulomb potential when calculating the electron-repulsion integrals for the HF exchange energy:

$$(\mu\nu|\lambda\sigma)^{SR} = \int \int d\mathbf{r}_1 d\mathbf{r}_2 \varphi_\mu(\mathbf{r}_1) \varphi_\nu(\mathbf{r}_1) \frac{\text{erfc}(\omega r_{12})}{r_{12}} \varphi_\lambda(\mathbf{r}_2) \varphi_\sigma(\mathbf{r}_2) \quad (7.62)$$

over contracted Gaussian-type functions. For these calculations the algorithm of Gill and Pople [416] was modified [408] so that the evaluation of integrals (7.62) is only slightly more time consuming than the regular electron-repulsion integrals.

To calculate the screened Coulomb exchange PBE functional the exchange model hole  $J_x^{PBE}$  of the PBE functional constructed in a simple analytical form by Ernzerhof and Perdew [417] is used. The model hole reproduces the exchange energy density of the PBE approximation for exchange and accurately describes the change in the exchange hole upon the formation of single bonds. In the HSE functional this PBE exchange hole is screened by employing the short-range Coulomb potential from (7.59).

The PBE long-range exchange contribution is then defined as the difference of the exchange-hole-based PBE and the SR PBE exchange energy densities.

In the so-called revised HSE03 hybrid functional [409] the improvement was introduced in the calculation in the integration procedure of the PBE exchange hole. This modification made the calculations numerically more stable and ensures that the HSE03 hybrid functional for  $\omega = 0$  is closer to the PBE0 hybrid. The HSE03 (denoted also as  $E^{\omega PBE}$ ) functional was incorporated into the development version of the GAUSSIAN code [418]. It was demonstrated for molecular systems that the HSE03 hybrid functional delivers results (bond lengths, atomization energies, ionization potentials, electron affinities, enthalpies of formation, vibrational frequencies), that are comparable in accuracy to the nonempirical PBE0 hybrid functional [409, 411, 412].

The HSE03 hybrid functional was extended to periodic systems [409]. The calculations were made for 21 metallic, semiconducting and insulating solids. The examined properties included lattice constants, bulk moduli and bandgaps. The results obtained with HSE03 exhibit significantly smaller errors than pure DFT calculations.

The preliminary screening of the integrals is necessary to take advantage of the rapid decay of short-range exchange integrals for periodic systems [409]. Two different screening techniques are used. In the first technique (Schwarz screening) substituting the SR integrals in place of the  $1/r$  integrals yields an upper bound of the form

$$|(\mu\nu|\lambda\sigma)_{SR}| \leq \sqrt{(\mu\nu|\mu\nu)_{SR}} \sqrt{(\lambda\sigma|\lambda\sigma)_{SR}} \quad (7.63)$$

The  $(\mu\nu|\lambda\sigma)$  integrals are then evaluated for each batch of integrals and only batches with nonnegligible contributions are used in calculating the HF exchange. The SR screening integrals are evaluated by the same procedure as the SR exchange integrals.

The second – distance-based multipole screening technique – uses multipole moments introducing the following screening criterion

$$T_n = \sum_{M \in \mu\nu} \sum_{M \in \lambda\sigma} C_{\mu\nu}^{max} \frac{1}{r^{l+M_{\mu\nu}^{low}+M_{\lambda\sigma}^{low}}} C_{\lambda\sigma}^{max} \quad (7.64)$$

where  $T_n$  is an estimate for the contribution of a shell quartet and  $M$  is a multipole in the multipole expansion of a given shell pair.  $M_{ij}^{low}$  are the lowest-order multipoles that can contribute to the integral and  $C_{ij}^{max}$  are the maximum coefficients in each order of multipoles. Replacing the  $1/r$  potential with the  $erfc(\omega r)/r$  short-range potential yields

$$T_n^{SR} = \sum_{M \in \mu\nu} \sum_{M \in \lambda\sigma} C_{\mu\nu}^{max} \frac{erf(\omega r^{l+M_{\mu\nu}^{low}+M_{\lambda\sigma}^{low}})}{r^{l+M_{\mu\nu}^{low}+M_{\lambda\sigma}^{low}}} \quad (7.65)$$

This provides a distance-based upper bound for the SR exchange contribution of a given shell quartet.

The implementation of periodic boundary conditions relies on evaluating all terms of the Hamiltonian in real space [379]. The HF exchange is evaluated using replicated density matrices. All interactions within a certain radius from a central reference cell are calculated and the rest are neglected. This so-called near-field exchange (NFX) method [413] allows calculation of the HF exchange in time, scaling linearly with system size. It works reasonably well for insulating solids since the corresponding density matrix elements decay rapidly. In systems with smaller bandgaps, however, the spatial extent of nonnegligible contributions to the exchange energy is large. This large extent results in a large number of significant interactions. To render the computation tractable, the truncation radius must be decreased. Thus, significant interactions are neglected that leads to errors in the total energy of the system and introduces instabilities into the self-consistent field procedure.

Screened Coulomb hybrid functionals do not need to rely on the decay of the density matrix to allow calculations in extended systems [409]. The SR HF exchange interactions decay rapidly and without noticeable dependence on the bandgap of the system. The screening techniques do not rely on any truncation radius and provide much better control over the accuracy of a given calculation. In addition, the thresholds can be set very tightly, without resulting in extremely long calculations.

A series of benchmark calculations [409] on three-dimensional silicon (6-21G basis was used, see Chap. 8) demonstrates the effectiveness of the screening techniques. The time per SCF cycle was studied given as a function of the distance up to which exchange interactions were included in the calculation. As this radius grows, the number of replicated cells grows as  $O(N^3)$ . The PBE0 curve tracks this growth since regular HF exchange has a large spatial extent. The relatively small bandgap of silicon (1.9 eV in this calculation) is insufficient for density matrix elements to decay noticeably. HSE, on the other hand, only shows a modest increase in CPU time as the system becomes larger. Beyond 10 Å, the CPU time only increases due to the time spent on screening. The HSE calculation of the total energy converges very rapidly and only cells up to 10 Å from the reference cell contribute to the exchange energy. PBE0, by comparison, converges significantly slower. Thus, HSE not only reduces the CPU time drastically, but also decreases the memory requirements of a given calculation since fewer replicated density matrices need to be stored in memory. In practice, HSE calculations can be performed with the same amount of memory as pure DFT calculations, whereas traditional hybrid methods have larger memory demands. Given the fast decay of the SR HF exchange interactions and the high screening efficiency, the HSE hybrid functional was efficiently applied to a variety of three-dimensional solids. We mention only some of these applications: 1) 21 metallic, semiconducting and insulating solids [409]; 2) semiconductor set of 40 solids, containing 13 group IIA-VI systems, 6 group IIB-VI systems, 17 group III-V systems, and 4 group IV systems [419]; 3) the zinc-blende and rocksalt phases of platinum nitride [420] and platinum monoxide [421]; 4) lattice defects and magnetic ordering in plutonium oxides  $\text{PuO}_2$  and  $\text{Pu}_2\text{O}_3$  [422]; 5) carbon nanotubes [423]; 6) actinide oxides  $\text{UO}_2$ ,  $\text{PuO}_2$  and  $\text{Pu}_2\text{O}_3$  [424]. It was demonstrated that the screened Coulomb hybrid density-functional HSE not only reduces the amounts of memory and CPU time needed, when compared to its parent functional PBE0, but it is also at least as accurate as the latter for structural, optical

and magnetic properties of solids. The PBE0 functional and other hybrid functionals are transferred from molecules to solids. The possibility of such a transfer we discuss in the next section.

#### 7.2.4 Are Molecular Exchange-correlation Functionals Transferable to Crystals?

The question in the title of this subsection arises due to the well-known fact that the properties of crystals are quite often different from those of molecular systems. The difference is particularly evident for ionic and semi-ionic solids, in which the long-range electrostatic forces provide a strong localizing field for the electronic states that is not present in molecules. In this situation the shortcomings of standard LDA and GGA functionals, linked to the missing electronic self-interaction, are likely to be most severe [371]. This explains why the electronic-structure calculations in molecular quantum chemistry and solid-state physics were for a long time developing along two independent lines. While in the molecular quantum chemistry the wavefunction-based approaches (HF and post-HF) in the LCAO approximation were mainly used, in solid-state physics DFT-based methods with plane wave (PW) basis were popular. These two standard approaches were for a long time poorly transferable between the two fields [371]: early DFT functionals underperform post-HF techniques in reproducing the known properties of small molecules, while the extension of accurate post-HF methods to solid-state systems is difficult or has prohibitive computational expense.

The formulation of hybrid HF/DFT exchange-correlation functionals and their extension to periodic systems changed the situation; the combined HF-DFT approach has adequate accuracy for most needs in both quantum chemistry of molecules and solids, retaining a tractable computational cost and even allowing the system-size linear-scaling. One appealing feature of this approach is that it can readily exploit the progress and tools available to the quantum chemists for calculating the HF exchange, as it was demonstrated in Sections 7.2.2 and 7.2.3.

For molecules, the first hybrid functionals have been coded into GAUSSIAN94 in the MO LCAO approximation traditional for molecules. The DFT PW computer codes, existing for solids, can be modified to include HF method and hybrid exchange-correlation functionals [425]. However, the practical realization of HF method was made in LCAO approximation. The application of hybrid functionals to crystalline compounds (described under periodic boundary conditions (PBC)) was not possible until the late 1990s, when they were coded in CRYSTAL98 [426]. Numerous solid-state studies have been performed with molecular hybrid functionals, providing valuable experience on their accuracy and applicability. In the review article [371] the results are summarized of publications in which hybrid exchange functionals have been applied under PBC to represent crystalline solids. The list of later publications can be found on the site <http://www.crystal.unito.it>. The next step in the HF/DFT extension to solids was made by Scuseria and coworkers who coded the HF/DFT method with PBC in GAUSSIAN03 code [107] and included a linear-scaling hybrid exchange-correlation HSE functional.

The extension of HF-DFT methods to the crystalline solids encounters difficulties [371]. In molecular chemistry, very accurate thermochemical and structural data exist for a selection of simple species. These data have been effectively used to define

representative sets against which to measure the results of calculations. The availability of these representative sets has enabled the *empirical* derivation of hybrid DFT functionals for molecules (for example, B3LYP and B3PW functionals). Comparison to experiment in the solid state is often indirect: most reliable experimental results on crystalline solids are not directly related to the equilibrium structure, energy and electronic density (as for molecules), but to the response of the solid to a perturbation, for instance to elastic distortions or to external electromagnetic fields. As an additional complexity, some fundamental electronic properties of solids cannot be measured directly; bandgaps, for instance, can be readily calculated as edge-to-edge differences between specific filled and unfilled bands, but they cannot be measured directly. What experiments furnish are absorption edges and activation energies corresponding to processes that are often speculative. As another example, magnetic coupling constants can be neither measured nor calculated directly. Their extraction from calculations requires a mapping onto a phenomenological model of some sort, which by its very nature is inexact, while comparisons are made with indirect quantities such as disorder-transition temperatures, which in turn have to be expressed in terms of the phenomenological model.

The second difficulty is the lack for solids of a reference theoretical method. Post-HF techniques in molecular quantum chemistry can yield results with a controlled degree of accuracy. In the absence of experimental data, the results obtained with different DFT functionals could be compared against those calculated with the reference computational technique. Recent developments in wavefunction methods for solid-state systems (Chap. 5), GW perturbation theory [427], and quantum Monte Carlo (QMC) [428] are promising for future work, but at present they still suffer from a limited applicability.

In most solids, HF/DFT calculations with the CRYSTAL code [23] the B3LYP hybrid functional was used with the standard molecular formulation (with the mixing parameter  $a_{mix}=0.2$ ) and its results graded against a set of other Hamiltonians (HF, LDA, PWGGA, PBE). In some calculations of oxides the different mixing parameter values were used [429–432]. These studies point to the need specific formulations of the hybrid functionals for solids, in particular systematic investigations on the effect of changing the mixing parameter. Such a systematic investigation on the effect of changing the mixing parameter from 0% to 100% was performed [371] for perovskite-structured transition-metal oxides  $\text{AMO}_3$  (including ferroelectric materials  $\text{BaTiO}_3$  and  $\text{KNbO}_3$ ), rocksalt-structured oxides and fluorides and open-shell defects in these matrices. All these systems share the fact that standard DFT calculations, in either LDA or GGA formulations, fail to reproduce with sufficient accuracy the correct electronic ground-state and/or the structural and electronic properties of the material. Several observables have been examined (structural parameters, elastic constants and bulk moduli, phonon spectra, bandgaps, thermochemical data, point defects and surfaces, magnetic ordering). We refer the reader to the review article [371] for comments on each observable separately. The details of the LCAO basis and an auxiliary Gaussians for exchange-correlation calculation choice are given in [371]. The truncation thresholds and BZ summation parameters are also given, ensuring convergence of the total energies to within 0.1 meV. As an example of observables calculations we show in Table 7.2 some results obtained in [371] for structural properties (lattice constants and bulk moduli) of cubic perovskites. The first line of the Table gives the

**Table 7.2.** Equilibrium lattice parameter  $a$  (Å) and bulk modulus  $B$  (GPa) for cubic perovskites, as a function of  $a_{mix}$  parameter ( $a_{mix}=0.2$ , 0.4, 0.6, 0.8, 1.0) in the DFT and hybrid B3LYP functional ([371])

Solid		LDA	PW	BLYP	B3LYP	0.2	0.4	0.6	0.8	1.0	HF	Expt
CaTiO <sub>3</sub>	<i>a</i>	3.817	3.884	3.921	3.885	3.890	3.863	3.840	3.820	3.802	3.870	3.84
	<i>B</i>	213.8	187.2	175.8	194.6	193.0	208.9	223.2	236.5	248.5	218.0	
SrTiO <sub>3</sub>	<i>a</i>	3.888	3.960	4.001	3.959	3.965	3.935	3.909	3.887	3.867	3.937	3.90
	<i>B</i>	207.7	176.8	163.3	185.0	183.2	201.1	217.2	232.0	245.6	212.3	179
BaTiO <sub>3</sub>	<i>a</i>	3.953	4.024	4.072	4.033	4.039	4.011	3.987	3.966	3.947	4.020	4.01
	<i>B</i>	204.7	177.8	162.5	181.6	179.8	195.4	209.7	222.9	235.0	203.9	195
CaZrO <sub>3</sub>	<i>a</i>	4.084	4.149	4.186	4.155	4.160	4.137	4.117	4.098	4.081	4.150	4.02
	<i>B</i>	187.8	167.4	157.9	170.1	168.9	178.9	188.1	196.7	205.0	181.4	
SrZrO <sub>3</sub>	<i>a</i>	4.133	4.203	4.244	4.208	4.214	4.187	4.164	4.143	4.124	4.197	4.15
	<i>B</i>	179.4	157.3	147.5	161.4	160.1	171.7	182.0	191.9	201.1	176.1	
BaZrO <sub>3</sub>	<i>a</i>	4.167	4.235	4.282	4.249	4.255	4.232	4.212	4.193	4.175	4.250	4.19
	<i>B</i>	180.3	166.0	154.6	166.9	165.5	175.4	184.8	193.5	201.7	176.5	
NaNbO <sub>3</sub>	<i>a</i>	3.960	4.018	4.051	4.008	4.013	3.980	3.951	3.927	3.905	3.962	3.94
	<i>B</i>	203.7	178.0	168.3	188.2	186.6	205.4	222.9	238.7	235.1	226.7	
KNbO <sub>3</sub>	<i>a</i>	3.996	4.063	4.103	4.057	4.063	4.028	3.998	3.972	3.949	4.013	4.01
	<i>B</i>	197.4	172.1	158.9	182.5	181.0	200.5	218.8	235.6	251.0	221.5	
KTaO <sub>3</sub>	<i>a</i>	3.938	3.992	4.018	3.978	3.982	3.951	3.923	3.900	3.881	3.941	
	<i>B</i>	144.7	146.4	155.4	156.6	156.8	164.8	176.0	187.7	208.5	189.8	

exchange-correlation functional type. For the HF-DFT hybrid functional both the standard molecular B3LYP functional and the BLYP exchange-correlation functional with a fraction  $a_{mix}$  of HF exchange (the numerical values of  $a_{mix}$  are given in the first line of Table 7.2) were used. For comparison, the available experimental data are given in the last column of this table. The following trends can be observed from the results given in Table 7.2. The lattice constant  $a$  increases systematically on increasing the mixing parameter  $a_{mix}$  and has a variation of approximately 3% in the series  $0 < a_{mix} < 1$ . The bulk modulus also increases with increasing  $a_{mix}$ , with a change for most materials of about 80% between  $a_{mix} = 0$  and  $a_{mix} = 1$ . Increasing the percentage of the HF exchange in the functional, therefore, makes the structure more compact and harder, and one may expect this feature to influence the behavior of the material towards structural distortions.

The lattice constant and bulk modulus are the ground-state properties defined by the total energy and its derivatives. The measured bandgap is defined by the excitation energies and its calculation includes the eigenvalues corresponding to the bottom of the conduction band. Nevertheless, recent calculations with hybrid functionals show that the observed bandgaps are reliably reproduced in a wide variety of materials. As an example, we give in Table 7.3 the results of B3LYP LCAO bandgap calculations [433] in comparison with the experimental data.

To establish the reliability of the hybrid functional the different types of materials have been studied: semiconductors (diamond and GaAs), semi-ionic oxides ( $\text{ZnO}$ ,  $\text{Al}_2\text{O}_3$ ,  $\text{TiO}_2$ ), sulfides ( $\text{FeS}_2$ ,  $\text{ZnS}$ ), an ionic oxide  $\text{MgO}$  and the transition-metal oxides ( $\text{MnO}$ ,  $\text{NiO}$ ). For each system the AO basis sets were developed and full structural optimization of the cell and internal coordinates was performed [433]. Typically, the optimized structural parameters are within  $\pm 2\%$  of the experimental values. The bandgaps were determined from the band structure of the optimized system as the difference in the converged eigenvalues. As is seen from Table 7.3 even the molecular version of the B3LYP exchange correlation functional is capable of reproducing bandgaps for a wide variety of materials in good agreement with the experimental

**Table 7.3.** A comparison of observed bandgaps with those calculated using the B3LYP functional for a wide range of materials (all values are given in eV) [433]

Material	Expt	B3LYP
Diamond	5.5	5.8
GaAs	1.4	1.5
ZnO	3.4	3.2
$\text{Al}_2\text{O}_3$	9.0	8.5
$\text{Cr}_2\text{O}_3$	3.3	3.4
$\text{MgO}$	7.8	7.3
$\text{MnO}$	3.6	3.8
$\text{NiO}$	3.8	3.9
$\text{TiO}_2$	3.0	3.4
$\text{FeS}_2$	1.0	2.0
$\text{ZnS}$	3.7	3.5

data (the latter even measured under well-controlled conditions are reliable to about 5%, [433]). This agreement is at least as good as that obtained with more sophisticated correlated calculations or perturbation theories.

The latter studies confirmed the efficiency of HF/DFT approach for solids and also use of the HSE hybrid functional. In [419] a set of 40 semiconductors was chosen based on the following criteria: all considered systems were both closed shell and of simple or binary composition; the majority of them have simple zincblende or rocksalt structures but also several systems with wurtzite structure were included. In addition, the availability of experimental data for lattice constants (and to a lesser extent bandgaps) was an important factor (the references to the experimental data can be found in [419]). These criteria led to the semiconductor/40 (SC/40) set of 40 solids containing 13 group IIA-VI systems, 6 group IIB-VI systems, 17 group III-V systems, and 4 group IV systems.

Table 7.4 contains a full list of all compounds and the calculated lattice constants and bandgaps. Based on the results of previous calculation with the HSE screened hybrid functional [409] the short-range – long-range splitting parameter was chosen as system independent and equal to 0.15, the PBE0 functional mixing parameter was taken to be 0.25. The results in Table 7.4 are given for the LSDA, PBE, meta-GGA TPSS (Tao–Perdew–Staroverov–Scuseria, [360]) and HSE hybrid functionals. All calculations employed the PBC option of the GAUSSIAN03 code, total energies are accurate to  $10^{-6}$  a.u. All basis sets used are modified molecular Gaussian basis sets (all diffuse basis functions with exponents below 0.12 were removed). The modification of the atomic basis sets for solids is discussed in Chap. 8 in more detail. For 31 of 40 systems the inclusion of relativistic effects in the pseudopotential was examined. In Chap. 8 we discuss relativistic pseudopotentials in more detail. Table 7.4 gives in comparison with the experimental data the calculated lattice constants and bandgaps for 40 semiconductors (with optical bandgaps ranging from 0.2 to 7.2 eV). The comparison of results is given for three nonhybrid (LSDA, PBE and TPSS) functionals and hybrid HSE functional. Table 7.5 contains the error statistics for predicting lattice constants  $a$  (in Å) and bandgaps (in eV).

As is seen from Table 7.2.4 LSDA underestimates lattice constants in nearly all cases, while PBE and TPSS always overestimate them. The screened hybrid functional HSE reduces the overestimation of PBE (on which it is based) drastically, leading to the best predictions overall. The 20% accuracy improvement of HSE over LSDA is noteworthy since LSDA is the most widely used method for lattice optimizations in solids. In addition, the overestimation of lattice constants by using the pseudopotentials (instead of all-electron calculations) is partly responsible for the observed errors with HSE. It is possible to expect that all-electron calculations yield even better results with HSE while the underestimation exhibited by LSDA would only be exaggerated. Bandgaps calculated with all three nonhybrid density-functionals are severely underestimated (mean absolute errors are about 1 eV, see Table 7.5), in extreme cases such as MgO, by as much as 2.88 eV. In addition, several small-bandgap systems (Ge, GaSb, InN, InAs, and InSb) are predicted to be quasimetallic. All bandgaps correspond to lattices optimized with the respective functional. The HSE hybrid functional yields a drastically reduced mean absolute error of only 0.26 eV and predicts even small-bandgap systems correctly. The HSE errors for bandgaps are comparable to those obtained with the GW approximation [434]. However, these calculations do not

**Table 7.4.** Lattice constants (Å) and bandgaps (eV) for the set of 40 simple and binary semiconductors ([419]), a–spalerite structure, c–wurtzite structure

Solid	Lattice constants					Bandgaps					
	LSDA	PBE	TPSS	HSE	Expt.	LSDA	PBE	TPSS	HSE	Expt.	
C	3.537	3.579	3.579	3.553	3.567	4.23	4.17	4.21	5.49	5.48	
Si	5.410	5.479	5.466	5.444	5.430	0.59	0.75	0.82	1.28	1.17	
Ge	5.634	5.776	5.744	5.701	5.658	0.00	0.00	0.00	0.56	0.74	
SiC	4.355	4.404	4.394	4.372	4.358	1.40	1.46	1.42	2.39	2.42	
BN	3.584	3.629	3.629	3.603	3.616	4.45	4.51	4.52	5.98	6.22	
BP	4.509	4.567	4.566	4.543	4.538	1.31	1.41	1.45	2.16	2.40	
BAs	4.750	4.829	4.821	4.794	4.777	1.16	1.27	1.29	1.92	1.46	
BSb	5.201	5.291	5.280	5.251	n/a	0.80	0.88	0.81	1.37	n/a	
AlN	(a)	3.112	3.153	3.147	3.127	3.111	4.9	4.95	5.01	6.45	6.13
	(c)	4.974	5.045	5.028	5.000	4.981					
AlP		5.436	5.508	5.497	5.472	5.463	1.60	1.83	1.90	2.52	2.51
AlAs		5.639	5.733	5.713	5.691	5.661	1.40	1.62	1.71	2.24	2.23
AlSb		6.079	6.188	6.172	6.146	6.136	1.29	1.40	1.63	1.99	1.68
GaN	(a)	3.167	3.233	3.224	3.198	3.189	2.09	1.70	1.73	3.21	3.50
	(c)	5.165	5.272	5.244	5.204	5.185					
$\beta$ – GaN		4.476	4.569	4.552	4.518	4.523	1.93	1.55	1.56	3.03	3.30
GaP		5.418	5.534	5.522	5.484	5.451	1.59	1.71	1.98	2.47	2.35
GaAs		5.626	5.771	5.745	5.705	5.648	0.43	0.19	0.52	1.21	1.52
GaSb		6.043	6.208	6.183	6.140	6.096	0.09	0.00	0.08	0.72	0.73
InN	(a)	3.523	3.599	3.589	3.555	3.537	0.02	0.01	0.00	0.71	0.69
	(c)	5.684	5.807	5.765	5.729	5.704					
InP		5.839	5.970	5.961	5.909	5.869	0.83	0.68	0.90	1.64	1.42
InAs		6.038	6.195	6.170	6.120	6.058	0.00	0.00	0.00	0.39	0.41
InSb		6.430	6.608	6.585	6.535	6.479	0.00	0.00	0.00	0.29	0.23
ZnS		5.319	5.467	5.465	5.432	5.409	2.25	2.16	2.39	3.42	3.66
ZnSe		5.588	5.751	5.736	5.707	5.668	1.21	1.19	1.48	2.32	2.70
ZnTe		6.017	6.195	6.174	6.150	6.089	1.28	1.14	1.45	2.19	2.38
CdS		5.776	5.934	5.944	5.896	5.818	1.01	1.11	1.34	2.14	2.55
CdSe		6.025	6.210	6.195	6.152	6.052	0.34	0.48	0.73	1.39	1.90
CdTe		6.422	6.626	6.610	6.568	6.480	0.61	0.62	0.88	1.52	1.92
MgO		4.178	4.268	4.247	4.218	4.207	4.92	4.34	4.56	6.50	7.22
MgS		5.618	5.721	5.719	5.681	5.622	3.54	3.57	3.88	4.78	5.4
MgSe		5.417	5.532	5.520	5.499	5.40	1.70	1.76	2.07	2.62	2.47
MgTe		6.381	6.517	6.517	6.478	6.42	2.74	2.68	3.12	3.74	3.6
CaS		5.572	5.715	5.710	5.698	5.689	2.16	2.56	2.69	3.59	n/a
CaSe		5.799	5.962	5.955	5.946	5.916	1.74	2.11	2.23	3.02	n/a
CaTe		6.209	6.387	6.386	6.381	6.348	1.25	1.60	1.72	2.37	n/a

to be continued

Solid	LSDA	PBE	TPSS	HSE	Expt.	LSDA	PBE	TPSS	HSE	Expt.
SrS	5.926	6.066	6.052	6.037	5.99	2.27	2.68	2.79	3.59	n/a
SrSe	6.151	6.306	6.290	6.282	6.234	1.89	2.26	2.37	3.09	n/a
SrTe	6.543	6.714	6.703	6.701	6.64	1.51	1.89	2.00	2.57	n/a
BaS	6.303	6.436	6.433	6.413	6.389	2.05	2.44	2.61	3.28	3.88
BaSe	6.517	6.671	6.659	6.649	6.595	1.76	2.12	2.26	2.87	3.58
BaTe	6.897	7.062	7.062	7.051	7.007	1.49	1.87	2.01	2.50	3.08

**Table 7.5.** Lattice constant  $a$  ( in Å) and bandgap (in eV) error statistics for the set of 40 simple and binary semiconductors( [419])

		LSDA	PBE	TPSS	HSE
Mean error	a	-0.046	0.076	0.063	0.035
	bandgap	-1.14	-1.13	-0.98	-0.17
Mean absolute error	a	0.047	0.076	0.063	0.037
	bandgap	1.14	1.13	0.98	0.26
Root-mean-square error	a	0.058	0.084	0.071	0.044
	bandgap	1.24	1.25	1.12	0.34
Maximum positive deviation	a	0.017	0.158	0.143	0.100
	bandgap	...	...	...	0.32
Maximum negative deviation	a	0.139	...	...	-0.014
	bandgap	-2.30	-2.88	-2.66	-0.72

include any excitonic or quasiparticle effects. While these effects are small for some systems, they can be nonnegligible for others. Some systems in the SC/40 test set exhibit significant spin-orbit coupling effects that can split the bandgap by 1 eV, for example ZnTe. For these systems, the comparison is made to the weighted average of the split experimental bandgap, but a better description of the systems is highly desirable. As follows from [419] the computational effort involved in HSE calculations presents only a modest increase (a factor of less than 2) over pure DFT calculations giving a vast improvement in accuracy.

Concludig the discussion of hybrid functionals we stress that the HSE functional is universally applicable and does not contain any system-dependent parameter. It yields excellent results, in molecules and solids, for many different properties. In contrast to other methods, HSE can be employed for both structural and electronic properties; HSE provides a unique and powerful alternative for the study of large complex systems, such as chemisorption at surfaces and three-dimensional impurities in semiconductors. These fields of HSE functional applications await future study.

In the next subsection we consider two orbital-dependent exchange-correlation functionals used for solids with the strong electron correlation. These functionals are used mainly with non-LCAO (PW, LMTO) basis and from this point of view are not quantum-chemical approaches. Therefore, we discuss them only briefly.

### 7.2.5 Density-functional Methods for Strongly Correlated Systems: SIC DFT and DFT+U Approaches

DFT (LDA, GGA approximations) have a great predictive power for solids only as long as one is treating electronic states extended over the whole system, so that electrons can be considered completely delocalized [151]. In the case of  $3d$ -states in transition-metal atoms and  $4f$ -states in rare-earth atoms and their compounds the metal-atom electrons partially preserve their atomic-like (localized) nature. The Coulomb correlations between localized electrons are strong, so that DFT results in many cases are in disagreement with experiment. A well-known example of such a disagreement is represented by some insulating transition-metal oxides, which LDA predicts to be metallic. The DFT methods are in serious trouble for the strongly correlated electrons as these methods describe noninteracting electrons moving in an effective self-consistent mean field. For the strongly correlated molecular systems post-HF methods in the LCAO approximation are traditionally applied (see Chap. 5). In solids with strong correlations approaches based on LDA (GGA) approximations are applied as a starting point and additional terms intended to treat strong Coulomb correlations between electrons are introduced. As a rule, the LCAO approximation is not used in these approaches. More traditional for solid-state physics localized muffin tin orbitals (LMTO) or augmented plane waves (APW) are popular in the calculations of strongly correlated systems. Various methods have been developed to extend the DFT approach to the strongly correlated systems. The best suited for strongly correlated systems is the so-called GW approximation, which is formally the first term in the perturbation expansion of the self-energy operator in powers of the screened Coulomb interaction (we return to the Coulomb-screening problem later). The reader can find the detailed description of GW method in the review article by Aryasetiawan [435] and other publications. The GW approximation is computationally very heavy and some simpler methods were proposed. Two of these methods (self-interaction corrected (SIC) DFT and DFT + U) are briefly discussed in this subsection.

The HF operator for a system of  $N$  electrons includes Coulomb  $\hat{J}_j\psi_i(\mathbf{x}_1) = \int \frac{|\psi_i(\mathbf{x}_2)|^2}{|\mathbf{r}_2 - \mathbf{r}_1|} d\mathbf{x}_2 \psi_i(\mathbf{x}_1)$  and exchange  $\hat{K}_j\psi_i(\mathbf{x}_1) = \int \frac{\psi_i^*(\mathbf{x}_2)\psi_i(\mathbf{x}_2)}{|\mathbf{r}_2 - \mathbf{r}_1|} d\mathbf{x}_2 \psi_j(\mathbf{x}_1)$  operators (here,  $\psi_i(\mathbf{x})$  are spin-orbitals and  $\mathbf{x} = \mathbf{r}, \sigma$  – the space  $\mathbf{r}$  and spin  $\sigma$  coordinates). From the definitions of these operators it follows that  $\hat{J}_i\psi_i = \hat{K}_i\psi_i$ . Without this identity the HF operator would have been orbital dependent  $\hat{F} = \hat{H} + \sum_{j \neq i}^N (\hat{J}_j - \hat{K}_j)$ ,

i.e. we would have different HF operators for different orbitals. By including the  $i = j$  term we obtain the same HF operator for all orbitals and allow the electron to interact with itself, in the Coulomb part and also in the exchange part. But these two self-interaction terms cancel. The HF approximation uses the exact expression of the exchange energy, but omits the correlation energy, and the resulting effective potential is nonlocal (it depends on the electron-density matrix  $\rho(\mathbf{r}, \mathbf{r}')$ ). The DFT (LDA, GGA approaches) uses an approximate local form of the exchange-correlation energy and the Kohn–Sham effective potential is local (depends on the electron density  $\rho(\mathbf{r}, \mathbf{r}) = \rho(\mathbf{r})$ ). In particular, the LDA is exact for a completely uniform system of noninteracting particles, and thus is self-interaction-free in this limit. In other versions of DFT the approximate exchange-correlation energy functionals are used so that the self-interaction terms may not cancel. The self-interaction-corrected (SIC)

DFT functionals must fulfill the equations, which describe their values in the limit of a single-electron system (hydrogen atom, for example) with density  $\rho_\sigma(\mathbf{r})$ , where  $\sigma$  may be  $\alpha$ ,  $\int \rho_\alpha(\mathbf{r}) = 1$ , and  $\rho_\beta(\mathbf{r}) = 0$ , [440]. The first equation

$$E_J[\rho] + E_X[\rho_\alpha, 0] = 0 \quad (7.66)$$

expresses that a single electron does not interact with itself, *i.e.* the self-repulsion energy (Hartree energy)  $E_J[\rho]$  is canceled by the self-exchange energy covered by the exchange functional  $E_X[\rho]$ . The second equation

$$E_c[\rho_\sigma, 0] = 0 \quad (7.67)$$

clarifies that a single electron does not possess any correlation energy (self-correlation is zero). The next two equations

$$v_J([\rho]; \mathbf{r}) + v_x^\sigma([\rho_\sigma, 0]; \mathbf{r}) = \text{const} \quad (7.68)$$

$$v_c^\sigma([\rho_\sigma, 0]; \mathbf{r}) = 0 \quad (7.69)$$

make sure that the single electron moves under the influence of the external potential  $v(\mathbf{r})$  rather than the Coulomb potential  $v_J$ , the exchange potential  $v_x$  or the correlation potential  $v_c$ . An approximate exchange-correlation functional may violate all or some of the equations (7.66)–(7.69) and, therefore, has to be corrected. The common LDAs, GGAs or Meta-GGAs have a remaining self-interaction error in their exchange part [436]. This self-interaction error is particularly critical for localized one-electron states in molecules and crystals. The delocalized electrons move fast, thus experiencing mainly the LDA (LSDA) mean-field potential; this is why LDA methods are so fruitful for metals. The localized electrons reside on each atomic site for so long that the surroundings must respond to their presence [437]. Therefore, the LDA theory problems are the most severe in systems where the electrons tend to be localized and strongly interacting (strongly correlated systems). As was already noted, the well-known examples of such systems are the crystalline transition-metal oxides (with localized  $d$ -electron states) and rare earth elements and compounds (with localized  $f$ -electrons). These systems exhibit phenomena associated with strong correlation effects (metal–insulator transitions, high temperature superconductivity, *etc.*). The already discussed hybrid DFT methods are most popular both in molecules and solids. The hybrid exchange-correlation functionals include HF exchange with some mixing coefficient and in this way partly compensate the self-interaction error. Other possibilities of DFT extension to the strongly correlated systems are known: the self-interaction-corrected (SIC) DFT method by Perdew–Zunger [352] (PZ-SIC approach) and the LDA+U method by Anisimov–Zaanen–Anderson [153]. The SIC-LSDA and LDA+U methods are described in many publications and applied to different molecules and solids. We refer the reader to reviews [438–441].

Let the many-electron system consist of  $N = N_\alpha + N_\beta$  electrons, where  $N_\alpha$  and  $N_\beta$  are the number of electrons with spin  $\alpha$  and spin  $\beta$ , respectively. The total density of electrons with spin  $\sigma$  is a sum of orbital densities  $\rho_{i\sigma}(\mathbf{r}) = |\psi_{i\sigma}(\mathbf{r})|^2$ . The total density of the  $N$ -electron system is  $\rho(\mathbf{r}) = \sum_{\sigma} \sum_{i=1}^{N_\sigma} \rho_{i\sigma}(\mathbf{r})$ . In the KS method the energy of a many-electron system is expressed as

$$E^{KS}[\rho_\alpha, \rho_\beta] = \sum_{\sigma=\alpha, \beta} \sum_{i=1}^{N_\sigma} \langle \psi_{i\sigma} | -\frac{1}{2} \Delta | \psi_{i\sigma} \rangle + \int \rho(\mathbf{r}) v(\mathbf{r}) d\mathbf{r} + J[\rho] + E_{xc}[\rho_\alpha, \rho_\beta] \quad (7.70)$$

The first two terms in (7.70) are the kinetic energy of a system of noninteracting electrons and the interaction between the electron density  $\rho(\mathbf{r})$  and external potential  $v(\mathbf{r})$ . The Hartree energy  $J[\rho] = \frac{1}{2} \int \int \frac{\rho(\mathbf{r})\rho(\mathbf{r}')}{|\mathbf{r}-\mathbf{r}'|} d\mathbf{r} d\mathbf{r}'$  is the Coulomb interaction of an electron density with itself,  $E_{xc}$  is the exchange-correlation density-functional. The SIC corrected density-functional

$$E^{SIC\ KS} = E^{KS} - \sum_{\sigma=\alpha, \beta} \sum_{i=1}^{N_\sigma} (J[\rho_{i\sigma}] + E_{xc}[\rho_{i\sigma}, 0]) = E^{KS} + E^{SIC} \quad (7.71)$$

includes the self-interaction correction  $E^{SIC}$  for all occupied spin-orbitals, which eliminates all spurious self-interaction terms orbital by orbital. In the SIC-DFT we have  $E_c[\rho_\alpha, 0] = 0$  and  $E_x[\rho_\alpha, 0] = -E_J[\rho]$ , *i.e.* an approximate exchange-correlation functional fulfills the exact conditions (7.67)–(7.68). The energy of equation (7.71) must be made stationary with regard to a mixing of occupied with occupied and occupied with virtual orbitals, which is accomplished by solving self-consistent KS equations for the SIC-DFT method. The SIC method gives significant improvements over the LSDA (SGGA) results [438], but there are also significant difficulties in applying the method. The SIC exchange-correlation potential becomes orbital dependent, and since the KS orbitals thereby are not solutions to the exact same Hamiltonian, one can not in general be sure that the orbitals become orthogonal. Due to the mixing of occupied orbitals in the SCF-SIC-DFT procedure, the energy functional is no longer invariant with regard to unitary transformations of the orbitals. To circumvent these problems the Optimized Potential Method was suggested [151, 339] allowing the local single-particle potential in the scheme that is both self-interaction free and orbital independent to be found. The simplest approximate implementation of the SIC-DFT method in molecular codes is the SIC correction applied after a self-consistent KS calculation is done [442]. The references to other SIC DFT method applications for molecules can be found in [443], where the SIC-DFT method was implemented self-consistently using a direct minimization approach. This approach was applied to calculate ionization potentials and electron affinities of atoms and small molecules [444]. It was concluded that this method works for molecules worse than for atoms, in particular it significantly overcorrects the one-electron energy for the highest-occupied MO.

In condensed matter studies the SIC DFT calculations have been extensively used. A review of solid-state SIC DFT techniques can be found in [438, 445, 446]. The well-known most serious failure of LSDA is an underestimation of energy gaps for semiconductors and insulators and the suppression of magnetic ordering for antiferromagnetic insulators. For transition-metal monoxide insulators with the sodium chloride structure (MnO, CoO, FeO, and NiO) the relative positions of transition-metal  $d$  bands and oxygen  $p$  bands are important to clarify whether they are Mott–Hubbard insulators or charge-transfer insulators. In Mott–Hubbard insulators the occupied bands of transition-metal atoms appear at higher energy than the occupied  $p$  bands of oxygen atoms, while the relative positions are reversed in charge-transfer insulators. The lowest-unoccupied band is, in both cases, transition-metal  $d$  states. In the LSDA, the transition-metal  $d$  bands appear at higher energy than oxygen  $p$  bands and therefore

they were considered as Mott–Hubbard-type materials. Such LSDA results do not agree with those by experiments and with the cluster calculations including correlation effects by the configuration interaction (CI) method. It was shown that the SIC removes unphysical self-interaction for occupied orbitals and decreases their energies [438,447]. As in the case of molecules, the application of the LSDA SIC to solids has severe problems. Since the LSDA SIC energy functional is not invariant under the unitary transformation of the occupied orbitals one can construct many solutions in the LSDA SIC. If one chooses delocalized Bloch orbitals, the orbital charge densities vanish in the infinite-volume limit so that the SIC energy is exactly zero for such orbitals. But the localized Wannier orbitals constructed from Bloch orbitals have finite SIC energies. In many calculations for solids, the SIC was adapted to the localized orbitals, which are selected under some physical assumption. The criterion to choose these orbitals was carefully examined in [447], trying both solutions with localized and extended oxygen  $2p$  orbitals. In solutions of types 1 (LSDA) and 2 all valence-state orbitals were extended or localized, respectively. In the solution of type 3 the transition-metal  $d$ -orbitals were localized and the oxygen  $p$ -orbitals were Bloch-type functions from the SIC potentials. In Table 7.6 are given bandgaps and magnetic moments of transition-metal monoxides for all the three types of LDA-SIC solution. The LDA+U results are discussed later. The type-1 solution is just the LSD result where all orbitals are extended, narrow  $d$ -bands appear at higher energy than the oxygen  $p$ -bands for all compounds. The bandgap of MnO is about 30% of the experimental value, there is no gap for other compounds. For the type 2 solution the transition-metal orbitals are more localized than those of oxygen  $p$ -orbitals so that the SIC potentials are larger in transition-metal  $d$  orbitals and the energies of  $d$  orbitals are pulled down significantly. The  $d$ - and  $p$ -bands become strongly hybridized, in good agreement with the observed results. As is seen from Table 7.6, the energy gaps are overestimated but the magnetic moments are well estimated. In type-3 solutions the transition-metal  $d$ -orbitals are localized and the oxygen  $p$ -orbitals are Bloch-type functions free from the SIC potential, so that the  $p$ -orbitals energies do not shift from the position of the LSDA results. On the contrary, the transition-metal  $d$ -orbitals energies are pulled down below those of the oxygen  $p$ -orbitals. Therefore, the highest-occupied band has the character of the oxygen  $p$ -band and the lowest-unoccupied band keeps mainly a character of the transition-metal  $d$ -orbitals. Then, the transition-metal monoxides are the charge-transfer type. As is seen from Table 7.6 the LDA-SIC values of the bandgaps and magnetic moments are in good agreement with the experiment. Unfortunately, the hybridization of  $p$ - and  $d$ -bands for occupied states, which appeared in the type-2 solution, is not reproduced in the type-3 solution. At the same time the type-2 solution overestimates the bandgaps. It was cleared up [438] that this overestimation is due to the overestimate in LSDA-SIC the Coulomb repulsion  $U$  of localized  $d$ -electron states in the solid (the SIC splits the occupied and unoccupied  $d$ -bands by the Coulomb repulsion  $U$  or slightly less than that). In condensed systems, the electron–electron Coulomb interaction is screened and the Coulomb repulsion should be much reduced. The “bare” (HF) value of the Coulomb interaction parameter  $U$  is 15–20 eV, while the screening in a solid to a much smaller value 8 eV or less [438]. This means that the LSDA-SIC functional form should be reformulated to include this screening. This is confirmed by investigations of  $f$ -electron bands in rare-earth element compounds [437].

Table 7.6. Bandgaps and magnetic moments of transition-metal monoxides in SiC LSDA, [447] and LSDA+U, [439] calculations

Compound	Bandgap (eV)						Magnetic moment ( $\mu_B$ )					
	Type 1 (LSD)	Type 2	Type 3	Type +U	Expt.	Type 1 (LSD)	Type 2	Type 3	Type LSD	Type +U	expt.	
MnO	1.1	6.5	3.4	3.5	3.6–3.8	4.5	4.7	4.7	1.67	4.79,4.58		
FeO	0.0	6.1	3.4	3.2	2.4	3.2	3.7	3.6	3.62	3.32		
CoO	0.0	5.3	2.7	3.2	2.4	2.0	2.7	2.6	2.63	3.35,3.38		
NiO	0.0	5.6	2.8	3.1	4.0,4.3	0.7	1.7	1.5	1.59	1.77,1.64,1.93		

The unscreened nature of Coulomb interaction is a serious problem of the Hartree–Fock approximation also – due to the neglect of screening, the HF energy gap values are a factor of 2–3 larger than the experimental values. A combination of the LDA and HF-type approximation called the LDA+U method was proposed [153]. The DFT+U solution can be obtained either at the LDA or GGA levels, giving rise to what have been called the LDA+U and the GGA+U formulations, respectively. In this approach the contribution of the interaction to U is added to the LDA energy. Instead of the energy-dependent interaction the averaged static Coulomb interaction between localized orbitals is used. This approach can be viewed as a way of connecting the theory of strongly correlated systems, which is based on such models, with the *ab initio* electronic-structure calculation methods like the HF method [151]. In contrast to the GW approximation, where the screened Coulomb interaction is used in the form of a nonlocal energy-dependent operator, in the DFT+U method a set of site-centered atomic-type orbitals is introduced and the Coulomb interaction is present only between electrons on such orbitals. This can be called the “orbital-restricted” solution because the DFT-potential is the same for all orbitals (for example, for all five 3d-orbitals of a transition-metal ion). The DFT+U method can reproduce the splitting of *d*- (or *f*-) bands into occupied lower and unoccupied upper bands, which was the main problem of LDA. This leads to the possibility of investigating the influence of correlation effects on structural properties, such as Jahn–Teller distortions. The orbital dependence of the DFT+U potential allows one to treat orbital and charge ordering in transition-metal compounds, which is very important for modern materials with anomalous magnetic and electronic properties.

In the LDA+U method electrons are separated into two subsystems: localized *d*- or *f*-electrons for which Coulomb *d*–*d* (*f*–*f*) interaction is taken into account by a term  $\frac{1}{2}U \sum_{i \neq j} n_i n_j$  ( $n_i$  are *d*- or *f*-orbital occupancies) as in a mean-field (HF) approximation and delocalized *s*, *p*-electrons that could be described by using an orbital-independent one-electron LDA potential.

In the LDA+U method the total Coulomb-interaction energy expression  $E = UN(N-1)/2(N = \sum_i n_i)$  is subtracted from the LDA total energy and the orbital-dependent Coulomb-interaction energy is added:

$$E^{LDA+U} = E^{LDA} - UN(N-1)/2 + \frac{1}{2}U \sum_{i \neq j} n_i n_j \quad (7.72)$$

The orbital energies  $\varepsilon$  are derivatives of (7.72) with respect to the orbital occupations

$$\varepsilon_i = \frac{\partial E}{\partial n_i} = \varepsilon_{LDA} + U\left(\frac{1}{2} - n_i\right) \quad (7.73)$$

This simple formula shifts the LDA orbital energy by  $-U/2$  for occupied orbitals ( $n_i = 1$ ) and by  $+U/2$  for unoccupied orbitals ( $n_i = 0$ ). A similar formula is found for the orbital-dependent potential ( $V_i(\mathbf{r}) = \frac{\delta E[\rho]}{\delta \rho_i(\mathbf{r})}$ ) where a variation is taken not on the total charge density  $\rho(\mathbf{r})$  but on the charge density of a particular *i*th orbital  $\rho_i(\mathbf{r})$ )

$$V_i(\mathbf{r}) = V_{LDA}(\mathbf{r}) + U\left(\frac{1}{2} - n_i\right) \quad (7.74)$$

Such an approach introduces, in fact, the self-interaction correction for these orbitals. Therefore DFT+U and DFT+U methods give close results in many cases.

The LDA+U orbital-dependent potential (7.74) gives the energy separation between the upper valence and lower conduction bands equal to the Coulomb parameter  $U$ , thus reproducing qualitatively the correct physics for Mott–Hubbard insulators. To construct a calculation in the LDA+U scheme one needs to define an orbital basis set and to take into account properly the direct and exchange Coulomb interactions inside a partially filled  $d$ -( $f$ -) electron subsystem [439]. To realize the LDA+U method one needs the identification of regions in a space where the atomic characteristics of the electronic states have largely survived (“atomic spheres”). The most straightforward would be to use an atomic-orbital-type basis set such as LMTO [448].

As is seen from Table 7.6 the SIC LSDA (type-3) and LSDA+U calculations give close results both for bandgaps and magnetic moments in transition-metal crystalline oxides. In both cases the agreement with the experiment appears to be essentially better than in pure DFT LSDA calculations.

The deficiency of the DFT+U method is the necessity to define explicitly the set of localized orbitals for interacting electrons. While for rare-earth and transition-metal ions the good approximation is to use atomic-type  $f$ - or  $d$ -orbitals and LMTO basis, for more extended systems like, for example, semiconductors, some more complicated Wannier-type orbitals are needed. Furthermore, the DFT+U method does not necessarily provide a reliable way of treating the  $U$  term, while, in a sense, all the important effects of strong correlation are defined by this term. Another problem of this method is that the estimate of  $U$  may depend on the choice of the basis [449]. Different choices of local orbitals such as the LMTO and LCAO give different  $U$  because the definition of the orbital becomes ambiguous whenever there is strong hybridization. In this situation the  $U$  value fitted to experimental data can also be used. Recently, [450] the DFT+U method was implemented in the computer code VASP [451], which uses the pseudopotential description for core electrons (see Chap. 8) and plane waves as the basis in the Bloch-functions calculations. Use of this modified code allows the systematic DFT+U study of correlation effects in different solids. In particular, application of DFT+U method for transition-metal sulfides yielded improved predictions for volume, magnetic moment, exchange splitting and bandgap [450]. In these calculations the dependence of results on the  $U$  parameter is studied. It was shown that the observed width of the semiconducting gap is reached at  $U=5$  eV in the LDA+U method and  $U=3$  eV in the GGA+U method. The comparative DFT study with B3LYP (LCAO basis) and GGA+U (PW basis) of electronic-structure and magnetic coupling in  $\text{FeSbO}_4$  crystal [452] allows the differences due to the different choice of exchange-correlation functional and basis to be estimated. In Table 7.7 we give the electronic bandgap values obtained in [452].

These results correspond to the experimentally found antiferromagnetic ordering of Fe ions in two dimensions. Such an ordering is correctly reproduced giving for the B3LYP functional the magnetic coupling constant value  $-21$  K (experimental value is  $-25$  K). From experimental studies,  $\text{FeSbO}_4$  is known to be a charge-transfer semiconductor (with an  $\text{O}2p$ - $\text{Fe}3d$  bandgap), with an activation energy of  $0.75$  eV for  $n$ -type conduction. This value represents a lower limit for the bandgap, as is the energy required to excite electrons from the donor levels to the conduction band. In DFT+U calculations the parameter  $U_{\text{eff}}$  is defined as the difference  $U-J$  ( $J$  is

**Table 7.7.** Electronic bandgap values (in eV) in  $\text{FeSbO}_4$  crystal, obtained for the antiferromagnetic solutions using different methods\*, [452]

LCAO	Bandgap	Plane Waves	Bandgap
GGA(BLYP)	0.2	GGA(PW91)	0.2
B3LYP	3.0	GGA+U ( $U_{eff} = 4\text{eV}$ )	1.6
HF	12.8	GGA+U ( $U_{eff} = 9\text{eV}$ )	1.7

\*Experimental value is estimated as being greater than 0.75 eV  
(see explanations to this table in the text)

a parameter representing the screened exchange energy, being almost constant at 1 eV). It was concluded [452] that the bandgap and the relative positions of the bands are affected in similar ways by the inclusion of 20% Hartree–Fock exchange and by the GGA+U correction with  $U_{eff} = 4$  eV. In particular, the occupied Fe-3d levels shift down in the valence-band region for both methods, in comparison with the GGA solutions. However, increasing the HF exchange up to 100% and using higher values of  $U_{eff}$  do not have equivalent effects on the band structure, due to the local character of the GGA+U correction.

As a main conclusion of these calculations we note the consistency between B3LYP and GGA+U results. *This means that LCAO calculations with hybrid functionals can play the same role in quantum chemistry of solids as DFT+U and SIC DFT calculations in solid-state physics.*

Recent LDA+U calculations were made on different solids:  $\text{ZnX}$  ( $\text{X}=\text{O, S, Se, Te}$ ), [453],  $\text{NiO}$  [454] and other transition-metal oxides ( $\text{Cu}_2\text{O}$  [455],  $\text{ReO}_2$  [456],  $\text{TiO}_2$  [457]). The results of these calculations confirm the efficiency of the DFT+U approach for strongly correlated systems. We hope that future LCAO calculations with the hybrid exchange-correlation functionals will discover the same efficiency.

This chapter concludes Part I (Theory) of our book. In Part II (Applications) we consider the applications in the quantum chemistry of solids of the theoretical methods described in Part I.

## **Part II**

---

### **Applications**

---

## Basis Sets and Pseudopotentials in Periodic LCAO Calculations

### 8.1 Basis Sets in the Electron-structure Calculations of Crystals

#### 8.1.1 Plane Waves and Atomic-like Basis Sets. Slater-type Functions

The choice of the basis set is of particular importance when treating periodic systems where a large variety of chemical bonding can be found. The following three approaches to the basis-set choice define three types of methods of the electronic-structure calculations in crystals [10]: atomic-sphere (AS) methods, plane-wave (PW) methods, localized atomic-like orbitals (LCAO) methods. Each method has its advantages and disadvantages.

The basic idea of AS methods is to divide the electronic-structure problem, providing efficient representation of atomic-like features that are rapidly varying near each nucleus and smoothly varying functions between atoms [10]. The smooth functions are augmented near each nucleus by solving the Schrödinger equation in the sphere at each energy and matching to the outer wave function. The resulting APW (augmented plane waves) or KKR (Kohn–Korringa–Rostoker) methods are powerful but require solution of nonlinear equations. The linear modifications of AS methods (LAPW, LMTO) use the familiar form of a secular equation involving a Hamiltonian and overlap matrix. The full-potential linear methods (FPLAPW) provide the most precise solutions of the Kohn–Sham equations.

The simpler PW methods are the most popular in the Kohn–Sham periodic-systems calculations. Plane waves are an orthonormal complete set; any function belonging to the class of continuous normalizable functions can be expanded with arbitrary precision in such a basis set. Using the Bloch theorem the single-electron wavefunction  $\varphi_i(\mathbf{r})$  can be written as a product of a wave-like part and a cell-periodic part  $\varphi_{i\mathbf{k}} = \exp(i\mathbf{k}\mathbf{r})u_i(\mathbf{r})$  (see Chap. 3). Due to its periodicity in a direct lattice  $u_i(\mathbf{r})$  can be expanded as a set of plane waves  $u_i(\mathbf{r}) = \sum_{\mathbf{B}} C_{i\mathbf{B}} \exp(i\mathbf{B}\mathbf{r})$ , where  $\mathbf{B}$  is the reciprocal lattice vector. Thus, in the PW basis the single-electron wavefunction can be written as a linear combination of plane waves

$$\varphi_{i\mathbf{k}}(\mathbf{r}) = \sum_{\mathbf{B}} C_{i\mathbf{B}} \exp(i(\mathbf{k} + \mathbf{B})\mathbf{r}) \quad (8.1)$$

The number of basis functions used is controlled by the largest wavevector in the expansion (8.1). This is equivalent to imposing a cutoff on the kinetic energy as the kinetic energy of an electron with wavevector  $(\mathbf{k} + \mathbf{B})$  is given by  $\frac{|\mathbf{k} + \mathbf{B}|^2}{2}$ . Thus, the size of the PW basis set is defined by the so-called cutoff energy, *i.e.* the kinetic energy for the largest reciprocal lattice vector included in the PW basis. The Kohn–Sham equations take on a very simple form using plane waves [377]

$$\left\{ \sum_{\mathbf{B}'} \left( \frac{1}{2} |\mathbf{k} + \mathbf{B}|^2 \delta_{\mathbf{B}\mathbf{B}'} + V_{eN}(\mathbf{B} - \mathbf{B}') + V_{ee}(\mathbf{B} - \mathbf{B}') \right. \right. \\ \left. \left. + V_{XC}(\mathbf{B} - \mathbf{B}') \right) \right\} C_{i,\mathbf{k}+\mathbf{B}'} = C_{i,\mathbf{k}+\mathbf{B}} \varepsilon_{i\mathbf{k}} \quad (8.2)$$

where  $V_{eN}(\mathbf{B} - \mathbf{B}')$ ,  $V_{ee}(\mathbf{B} - \mathbf{B}')$ , and  $V_{XC}(\mathbf{B} - \mathbf{B}')$  are the Fourier transforms of the electronic–nuclei, electron–electron Coulomb, and exchange–correlation potentials.

The PW basis set is universal, in the sense that it does not depend on the positions of the atoms in the unit cell, nor on their nature [458]. One does not have to construct a new basis set for every atom in the periodic table nor modify them in different materials, as is the case with localized atomic-like functions and the basis can be made better (and more expensive) or worse (and cheaper) by varying a single parameter – the number of plane waves defined by the cutoff energy value. This characteristic is particularly valuable in the molecular-dynamics calculations, where nuclear positions are constantly changing. It is relatively easy to compute forces on atoms. Finally, plane-wave calculations do not suffer from the basis-set superposition error (BSSE) considered later. In practice, one must use a finite set of plane waves, and this in fact means that well-localized core electrons cannot be described in this manner. One must either augment the basis set with additional functions (as in linear combination of augmented plane waves scheme), or use pseudopotentials to describe the core states. Both AS and PW methods, developed in solid-state physics are used to solve Kohn–Sham equations. We refer the reader to recently published books for the detailed description of these methods [9–11].

In the quantum chemistry of solids the LCAO methods are preferable [458]. These methods are more flexible as they allow both Hartree–Fock and Kohn–Sham equations to be solved, are applicable in the correlated wavefunction approaches (post-Hartree–Fock methods, see Chap. 5) and in Kohn–Sham theory based on hybrid exchange–correlation functionals (see Chap. 7). In comparison with plane waves, the use of all-electron LCAO calculations allows us to describe accurately electronic distributions both in the valence and the core region with a limited number of basis functions. The local nature of the basis allows a treatment both of finite systems and of systems with periodic boundary conditions in one, two or three dimensions. This has an advantage over plane-wave calculations of molecules, polymers or surfaces that work by imposing artificial periodicity: the calculation must be done on, *e.g.* a three-dimensional array of molecules with a sufficiently large distance between them (the molecule is placed at the center of a periodic supercell). LCAO total energies can be made very precise (*i.e.* reliable to many places of decimals) since all integrals can be done analytically (in practice, this is only true for Hartree–Fock calculations; density-functional theory LCAO calculations require a numerical integration of the exchange–correlation potential that reduces the attainable precision). Having an “atomic-like” basis facil-

tates population analyses, the computation of properties such as projected densities of states, and “pre-SCF alteration of orbital occupation” making the convergence of SCF calculations faster. As was already noted the LCAO basis allows easy comparison of the results obtained for molecules and solids at the same precision level of calculations.

The molecular basis set atomic-like orbitals can be considered as a starting point to generate atomic basis sets to be used in crystalline compounds. Therefore, we begin with the molecular basis-sets description.

In molecular quantum chemistry two types of atomic-like basis sets are used: Slater-type orbitals (STO) and Gaussian-type orbitals (GTO). In fact, it is not really correct to call them “orbitals”. They are better described as basis-set functions, since they are Slater-type or Gaussian-type functions used to approximate the shapes of the orbitals defined as one-electron wavefunctions. Using the acronyms accepted in solid-state theory it would be possible even call LCAO methods for crystals to “all-electron or full potential linear combination of Slater (Gaussian)-type functions – FP LS(G)TF method” [458], compare with the acronym FP LAPW (full potential linear combination of augmented plane waves).

The mathematical form of the normalized primitive Slater-type function (STF) in atom-centered polar coordinates is

$$\chi_{nlm}^{STF}(\mathbf{r}) = N_{nl}(\zeta) r^{n-1} \exp(-\zeta r) Y_{lm}(\theta, \varphi) = R_{nl}(r) Y_{lm}(\theta, \varphi) \quad (8.3)$$

where  $\zeta$  is an orbital exponent,  $n$  is the principal quantum number,  $Y_{lm}(\theta, \varphi)$  are the spherical harmonics, depending on the angular momentum quantum numbers  $l$  and  $m$ . STF have a number of features that make them attractive, see Sect. 6.1.1. We note the difference between Slater-type orbitals (8.3) and Slater orbitals introduced by Slater [210] and used in semiempirical LCAO methods, see Chap. 6. The radial part of the Slater orbitals  $R_{nl}^*(r)$  depends on two parameters: the effective quantum number  $n^*$  and screening parameter constant  $s$ . The values of these parameters are given by the following rules:

(1)  $n^*$  is assigned by the following table, in terms of the real principal quantum number  $n$ : for  $n = 1, 2, 3, 4, 5, 6 - n^* = 1, 2, 3, 3.7, 4.0, 4.2$ .

(2) For determining  $(Z - s)$ , the electrons are divided into the following groups, each having a different screening constant:  $1s; 2s, 2p; 3s, 3p; 3d; 4s, 4p; 4d; 4f; 5s, 5p; 5d$ ; etc. That is, the  $s$  and  $p$  of a given  $n$  are grouped together but the  $d$  and  $f$  are separated. The shells are considered to be arranged from inside out in the order named.

(3) The screening constant  $s$  is formed, for any group of electrons, from the following contributions: (a) Nothing from any shell outside the one considered, (b) an amount 0.35 from each other electron in the group considered (except in the  $1s$  group, where 0.30 is used instead).

(c) If the shell considered is an  $s, p$  shell, an amount 0.85 from each electron with total quantum number less by one, and an amount 1.00 from each electron still further in; but if the shell is a  $d$  or  $f$ , an amount 1.00 from every electron inside it. As an example, we take the carbon atom C,  $Z = 6$ . Here, we have two  $1s$  electrons, four  $2s, 2p$  electrons. For the effective nuclear charge,  $Z - s$ , we have  $1s : 6 - 0.30 = 5.70; 2s, p : 6 - 3(0.35) - 2(0.85) = 3.25$ . As a second example, we take the iron atom Fe,  $Z = 26$ . There are two  $1s$ , eight  $(2s, p)$ , eight  $(3s, p)$ , six  $(3d)$ , two  $(4s)$ . The effective nuclear charges are:  $1s : 26 - 0.30 = 25.70; 2s, p :$

$26 - 7(0.35) - 2(0.85) = 21.85$ ;  $3s, p : 26 - 7(0.35) - 8(0.85) - 2(1.00) = 14.75$ ;  $3d : 26 - 5(0.35) - 18(1.00) = 6.25$ ;  $4s : 26 - 1(0.35) - 14(0.85) - 10(1.00) = 3.75$ . These simple rules give approximate Slater analytic atomic wavefunctions for all the atoms and ions.

The Slater orbitals can be written in the form (8.3) with the orbital exponent  $\zeta = \frac{Z-s}{n^*}$  and  $n = n^*$ .

The Slater-type functions (STF) with the radial part in the form (8.3) and integer  $n$  can be used as the basis functions in Hartree–Fock–Roothaan calculations of atomic wavefunctions. The radial dependence of the atomic orbitals is an expansion in the radial Slater-type basis functions  $\varphi_{lmp}$  whose indices are  $l$ , running over  $s, p, d, f, \dots$  symmetries, and  $p$  counting serially over basis-set members for a given symmetry:

$$\varphi_{lmi} = \sum_p C_{lmp} R_{lp}(\mathbf{r}) Y_{lm}(\theta, \varphi) \quad (8.4)$$

The radial expansion is independent of  $m$ ; all electrons with a given  $l, i$  have the same radial dependence. The orbital angular dependence  $Y_{lm}(\theta, \varphi)$  is a normalized spherical harmonic. The expansion coefficients  $C_{lmp}$  of the  $i$ th orbital, for the occupied atomic orbitals, are tabulated for elements with  $Z=1–54$  in [65] and with  $Z=55–92$  in [459]. Relatively few primitive STOs are needed to closely approximate HF solutions of atoms (the latter are known as the contracted Slater-type orbitals). For example, six  $s$ -functions and four  $p$ -functions are enough to give seven-figure accuracy in total energy for the ground states of the first-row atoms. In Table 8.1 we give the results of Hartree–Fock–Roothaan carbon atom ground-state calculations. The one-electron energies  $\epsilon$  of occupied  $1s$ ,  $2s$  and  $2p$  AOs and the corresponding primitive STFs orbital exponents  $\zeta$  and coefficients  $C_{lmp}$  are shown. The STF basis set for the carbon atom can be denoted as  $6s\text{-}6s4p$ , meaning that the core  $1s$  AO is represented by six  $s$ -orbitals and the valence  $2s$ - and  $2p$ -orbitals are represented by six  $s$ - and four  $p$ -orbitals, respectively.

The Slater-type orbitals were the first to be used in the molecular quantum chemistry semiempirical calculations. Unfortunately, such functions are not suitable for fast calculations of multicenter integrals in *ab-initio* calculations. Gaussian-type functions (GTFs) were introduced to remedy the difficulties. GTFs are used in basis sets in practically all modern codes for LCAO calculations of molecules. We know two exclusions

**Table 8.1.** HF SCF occupied atomic orbitals for the ground state of a carbon atom given as linear combinations of  $s$  and  $p$  STOs [65]. The one-electron energies are given in a.u.

$s$		$1s : C$	$2s : C$	$p$		$2p : C$		
basis	$\zeta$	$\epsilon$	-11.32554	-0.70563	basis	$\zeta$	$\epsilon$	-0.43335
$1s$	5.43599	0.93262	-0.20814	$2p$	0.98073		0.28241	
$1s$	9.48256	0.06931	-0.01071	$2p$	1.44361		0.54697	
$2s$	1.05749	0.00083	0.08099	$2p$	2.60051		0.23195	
$2s$	1.52427	-0.00176	0.75045	$2p$	6.51003		0.0.1025	
$2s$	2.68435	0.00559	0.33549					
$2s$	4.20096	0.00382	-0.14765					

from this rule – KS LCAO codes SIESTA [344] and ADF [345]. The SIESTA code uses a numerical AO basis set, the ADF code uses Slater-type basis set orbitals (see Appendix C). In the next section we consider the GTF used in molecular quantum chemistry.

### 8.1.2 Molecular Basis Sets of Gaussian-type Functions

A primitive Gaussian-type function can be written in a local Cartesian coordinate system in the form

$$\chi^{GTF} = x^l y^m z^n \exp(-\alpha r^2) \quad (8.5)$$

where  $\alpha$  is the orbital exponent, and the  $l, m, n$  are not quantum numbers but simply integral exponents of Cartesian coordinates. Gaussian primitives (8.5) can be factorized into their Cartesian components, *i.e.*  $\chi^{GTF} = \chi_x^{GTF} \chi_y^{GTF} \chi_z^{GTF}$ , where each Cartesian component has the form (introducing an origin such that the Gaussian is located at position  $A$ ),

$$\chi_x^{GTF} = (x - x_A) \exp(-\alpha(x - x_A)^2) \quad (8.6)$$

This simplifies considerably the calculation of integrals. If we write the exponential part of an STF,  $\exp(-\alpha r)$  in Cartesian components we get  $\exp(-\alpha\sqrt{x^2 + y^2 + z^2})$  that is not so separable. Note that the absence of the STO pre-exponential factor  $r^{n-1}$  restricts single Gaussian primitives to approximating only  $1s$ ,  $2p$ ,  $3d$  *etc.* orbitals and not, *e.g.*  $2s$ ,  $3p$ ,  $4d$ , *etc.* However, combinations of Gaussians are able to approximate correct nodal properties of atomic orbitals if the primitives are included with different signs. The sum of exponents of Cartesian coordinates  $L = l+m+n$  is used analogously to the angular-momentum quantum number for atoms to mark Gaussian primitives as  $s$ -type ( $L = 0$ ),  $p$ -type ( $L = 1$ ),  $d$ -type ( $L = 2$ ),  $f$ -type ( $L = 3$ ) *etc.* From six  $3d$  GTFs ( $x^2, xy, xz, yz, y^2, z^2$ ) there are only five linearly independent and orthogonal atomic  $d$ -orbitals being linear combinations of Cartesian Gaussians ( $3z^2 - r^2, xz, yz, x^2 - y^2, xy$ ), the sixth combination  $x^2 + y^2 + z^2 = r^2$  is Gaussian primitive of  $s$ -type.

It is clear that the behavior of a Gaussian is qualitatively wrong both at the nuclei and in the long-distance limit for a Hamiltonian with point-charge nuclei and Coulomb interaction. From this point of view STFs would be preferable.

In so-called Pople basis sets, the basis functions are made to look more like Slater-type functions by representing each STF  $\chi^{STF}$  as a linear combination of Gaussian primitives:

$$\chi^{STF} = \sum_{i=1}^N C_i \chi_i^{GTF} \quad (8.7)$$

where  $C_i$  is a fixed coefficient and  $N$  is the number of Gaussian primitives used to represent the Slater-type basis function. The sums (8.7) are known as the contracted Gaussian basis set. Linear combinations of Gaussian primitives allow the representation of the electron density close to the nucleus to be improved. Recall that STF has a cusp at the nucleus, while GTF does not. By taking linear combinations of Gaussian primitives, the cusplike behavior is better reproduced.

The Gaussian basis set can also be used without any connection with the Slater-type orbitals: HF equations solutions for atoms are reached by Roothaan's expansion

method with Gaussian-type functions as was done with STFs (see Sect. 8.1.1). The details of both procedures – Gaussian expansion of Slater-type orbitals and atomic SCF calculations with Gaussian-type basis – are well known in molecular quantum chemistry [460]. It was found that GTF expansions require inclusion of more primitives than STF expansions for the same accuracy in the total and one-electron SCF energies for atoms. For example, in the case of the carbon atom the inclusion of 10 *s*-type primitive GTFs and 6 *p*-type primitive GTFs is necessary ( $10s - 10s6p$ ) to obtain only six-figure accuracy in the total energy (in the STF case seven-figure accuracy was obtained for 6 and 4 STF *s*-type and *p*-type primitives, respectively).

In molecular quantum chemistry Gaussian-type basis functions are expanded as a linear combination (contraction) of individually normalized Gaussian primitives  $g_j(\mathbf{r})$  characterized by the same center and angular quantum numbers but with different exponents

$$\chi_i(\mathbf{r}) = \sum_{j=1}^N d_j g_j(\mathbf{r}), \quad g_j(\mathbf{r}) = g(\mathbf{r}; \alpha, l, m) = N_{lm}(\alpha) r^l Y_{lm}(\theta, \phi) \exp(-\alpha_j r^2) \quad (8.8)$$

where  $N$  is the length of the contraction, the  $\alpha_j$  are the contraction exponents, the  $d_j$  are contraction coefficients. Gaussian primitives can be written in terms of real spherical harmonics including a normalization constant.

If accurate solutions for an atom are desired, they can be obtained to any desired accuracy in practice by expanding the “core” basis functions in a sufficiently large number of Gaussians to ensure their correct behavior. Furthermore, properties related to the behavior of the wavefunction near nuclei can often be predicted correctly, even without an accurately “censed” wavefunction [461]. In most molecular applications the asymptotic behavior of the density far from the nuclei is considered much more important than the nuclear cusp [458]. The molecular wavefunction for a bound state must fall off exponentially with distance, whenever the Hamiltonian contains Coulomb electrostatic interaction between particles. However, even though an STFs basis would, in principle, be capable of providing such a correct exponential decay, this occurs in practice only when the smallest exponent in the basis set is  $\zeta_{min} = \sqrt{2I_{min}}$ , where  $I_{min}$  is the first ionization potential. Such a restriction on the range of exponent values, while acceptable for atomic SCF calculations, is far too restrictive for molecular and solid-state work. Some of these formal limitations have thus turned out to be of relatively little importance in practice.

By proper choice of the  $N$ ,  $\alpha_j$ , and  $d_j$  in the contraction (8.8) the “contracted Gaussians” may be made to assume any functional form consistent with the primitive functions used. One may therefore choose the exponents of the primitives and the contraction coefficients so as to lead to basis functions with desired properties, such as reasonable cusp-like behavior at the nucleus (*e.g.* approximate Slater functions or HF atomic orbitals). Integrals involving such basis functions reduce to sums of integrals involving the Gaussian primitives. Even though many primitive integrals may need to be calculated for each basis function integral, the basis function integrals will be rapidly calculated provided the method of calculating primitive integrals is fast, and the number of orbital coefficients in the wavefunction will have been considerably reduced. The exponents and contraction coefficients are normally chosen on the basis of relatively cheap atomic SCF calculations so as to give basis functions suitable for

describing exact Hartree–Fock atomic orbitals. An approximate atomic basis function, whose shape is suitable for physical and chemical reasons, is thus expanded in a set of primitive Gaussians, whose mathematical properties are attractive from a computational point of view. Note that the physical motivation for this procedure is that, while many primitive Gaussian functions may be required to provide an acceptable representation of an atomic orbital, the relative weights of many of these primitives are almost unchanged when the atoms are formed into molecules or crystals. The relative weights of the primitives can therefore be fixed from a previous calculation and only the overall scale factor for this contracted Gaussian function need be determined in the extended calculation. It is clear that contraction will in general significantly reduce the number of basis functions.

For molecular basis sets of Gaussian-type functions (GTF) general acronyms and notations are used that are well known in molecular quantum chemistry.

A *Minimal-basis sets* are constructed by using one Slater-type orbital basis function of each type occupied in the separated atoms that comprise a molecule. If at least one *p*-type, *d*-type or *f*-type orbital is occupied in the atom, then the complete set (3 *p*-type, 5 *d*-type, 7 *f*-type) of functions must be included in the basis set. The simplest of these basis sets is that designated *STO-3G*, an acronym for *Slater-type-orbitals* simulated by 3 primitive Gaussians added together. The coefficients of the Gaussian functions are adjusted to give as good a fit as possible to the Slater orbitals. To illustrate this, let us consider a 1s Slater-type orbital radial part  $\exp(-\zeta r)$  (for  $\zeta = 1.0$  it is an exact hydrogen atom atomic orbital). A plot of this STO function is given in Fig. 8.1b, taken from [458]. A plot of Gaussian-type orbitals  $\exp(-\zeta r^2)$  for different orbital exponents is shown in Fig. 8.1a. Note the cusp at the origin for the Slater-type orbital while the Gaussian-type orbital has no cusp at the origin. In addition, the shape of the Gaussian-type orbital is different due to the squared distance that appears in its exponent. In Fig. 8.1a are shown individually three 1s-Gaussian primitives with orbital exponents 0.1098, 0.4058 and 2.2277. When the Gaussian primitives are combined using the coefficients 0.4446, 0.5353 and 0.1543, a new STO-3G function is produced, which is shown in Fig. 8.1b. It is seen that the new basis function resembles the Slater-type orbital much more closely than any of the single Gaussian-type orbitals. The only slight variation is observed near the cusp. The new basis function, because it consists of Gaussian primitive functions, does not have a cusp. However, the overall shape even close to the nucleus is very much like the Slater-type orbital.

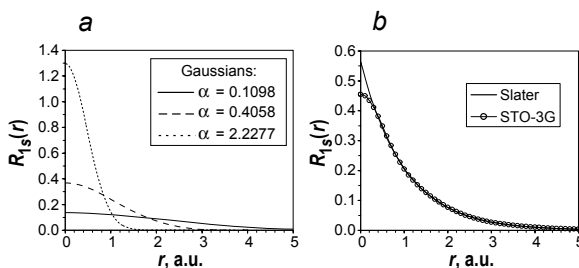


Fig. 8.1. 1s orbitals, [458]: (a) Gaussian; (b) Slater and fitted STO-3G

Only one best fit to a given type of Slater orbital is possible for a given number of Gaussian functions. Hence, all STO-3G basis sets for any row of the periodic table are the same, except for the exponents of the Gaussian functions. The exponents are expressed as scale factors, the squares of which are used as multipliers of the adjusted exponents in the original best-fit Gaussian functions. In this way, the ratios of exponents remain the same while the effective exponent of each orbital can be varied, [458]. The STO-3G basis set, and other minimal basis sets, usually do reasonably well at reproducing geometries of only simple organic molecules. The minimal basis sets do not allow alteration of the basis orbitals in response to a changing molecular environment and therefore make comparison between charged and uncharged species unreliable. Anisotropic environments are another problem for minimal basis sets [458].

Because the core electrons of an atom are less affected by the chemical environment than the valence electrons, the core electrons can be treated with a minimal basis set while the valence electrons are treated with a larger basis set. This is known as a *split-valence basis set*. In these bases, the AOs are split into two parts: an inner, compact orbital and an outer, more diffuse one. The coefficients of these two kinds of orbitals can be varied independently during construction of the MOs. Thus, the size of the AO can be varied between the limits set by the inner and outer functions. Basis sets that similarly split the core orbitals are called double zeta, DZ (implying two different exponents) or triple zeta, TZ (implying three different exponents). For example, the 3-21G notation of split valence basis set means that the core orbitals are represented by three Gaussians, whereas the inner and outer valence orbitals consist of two and one Gaussians, respectively. If we were to name bases consistently, of course, this one would be labeled STO-3-21G, but the STO is customarily omitted from all split-valence descriptors. Two other split-valence bases are the 6-31G and the 6-311G. Both have six Gaussian cores. The 6-311G is a triply split basis, with an inner orbital represented by three Gaussians, and middle and outer orbitals represented as single Gaussians. The triple split improves the description of the outer valence region.

Further improvement of the basis set is achieved including *polarization functions* in the basis set. For example, this is done by adding *d*-orbitals to the basis of all atoms having no *d*-electrons. For typical organic compounds these are not used in bond formation, as are the *d*-orbitals of transition metals. They are used to allow a shift of the center of an orbital away from the position of the nucleus. For example, a *p*-orbital on carbon can be polarized away from the nucleus by mixing into it a *d*-orbital of lower symmetry. One obvious place where this can improve results is in the modeling of small rings; compounds of second-row elements also are more accurately described by the inclusion of polarization. The presence of polarization functions is indicated in the Pople notation by appending an asterisk to the set designator. Thus, 3-21G\* implies the previously described split valence basis with polarization added. Typically, six *d*-functions ( $x^2$ ,  $y^2$ ,  $z^2$ ,  $xy$ ,  $xz$ , and  $yz$ ), equivalent to five *d*-orbitals and one *s*, are used (for computational convenience). Most programs can also use five real *d*-orbitals. An alternative description of this kind of basis is DZP: double zeta, polarization. A second asterisk, as in the 6-31G\*\* basis set, implies the addition of a set of *p*-orbitals to each hydrogen to provide for their polarization. Again, an alternative notation exists: DZ2P(double zeta 2 polarization). An asterisk in parentheses signals that polarization functions are added only to second-row elements. Another alternative to the asterisk for specifying polarization functions is (*d*), placed after the G.

To provide more accurate descriptions of anions, or neutral molecules with unshared pairs, basis sets may be augmented with so-called *diffuse functions*. These are intended to improve the basis set at large distances from the nuclei, thus better describing the barely bound electrons of anions. Processes that involve changes in the number of unshared pairs, such as protonation, are better modeled if diffuse functions are included.

The augmentation takes the form of a single set of very diffuse (exponents from 0.1 to 0.01) *s* and *p* orbitals. The presence of diffuse functions is symbolized by the addition of a plus sign, +, to the basis set designator: 6-31+G. (Since these are *s*- and *p*-orbitals, the symbol goes before the G.)

Again, a second + implies diffuse functions added to hydrogens; however, little improvement in results is noted for this addition unless the system under investigation includes hydride ions.

All of the codes for molecular *ab-initio* calculations offer at least one set of diffuse functions. Still more extensive basis sets exist, and are described by more complicated notation.

Let us summarize the notations used for molecular GTO basis sets. Basis sets denoted by the general nomenclature N-M1G or N-M11G, where N and M are integers, are called Pople basis sets. The first, N-M1G, is a split-valence double-zeta basis set while the second, N-M11G is a split-valence triple-zeta basis set. The integers N and M in the basis set name give the number of Gaussian primitives used. For example, in the split-valence double-zeta basis set 6-31G for a carbon atom, the first number (N=6) represents the number of Gaussian primitives used to construct the core orbital basis function (the 1s function). The second two numbers (M=3 and 1) represent the valence orbitals, 2s, 2s', 2p(3) and 2p'(3). The first number after the dash in the basis set name (3 in this case) indicates the number of Gaussian primitives used to construct the 2s and 2p(3) basis functions. The second number after the dash (1 in this case) gives the number of Gaussian primitives used to construct the 2s' and 2p'(3) basis functions. There are two common methods for designating that polarization functions are included in a basis set. The first method is to use \* or \*\* after the Pople basis set name; for example, 6-31G\* or 6-31G\*\*. The single \* means that one set of *d*-type polarization functions is added to each nonhydrogen atom in the molecule. The double \*\* means that one set of *d*-type polarization functions is added to nonhydrogens and one set of *p*-type polarization functions is added to hydrogens. The second method for including polarization functions in the basis-set designation is more general. It is indicated by the notation (l1,l2) following the Pople basis-set name; for example, 6-31G(*d*) or 6-31G(*d,p*). The first label indicates the polarization functions added to nonhydrogen atoms in the molecule. The notations 6-31G(*d*) and 631G(*d,p*) mean that one set of *d*-type polarization functions is added to all nonhydrogens. The notation 6-31 l(2df) means that two sets of *d*-type and one set of *f*-type polarization functions are added to nonhydrogens. The second label in the notation (l1,l2) indicates the polarization functions added to hydrogen atoms. The basis set 6-31G(*d*) has no polarization functions added to hydrogen, while the basis set 6-31G(*d,p*) has one set of *p*-type polarization functions added to hydrogen atoms. The basis set 6-31 1G(2df, 2pd) has two sets of *p*-type and one set of *d*-type polarization functions added to hydrogen atoms. The use of diffuse functions in a Pople basis set is indicated by the notation + or ++. The + notation, as in 6-31+G(*d*), means that one set of *sp*-type

diffuse basis functions is added to nonhydrogen atoms (4 diffuse basis functions per atom). The ++ notation, as in 6-31++G(d), means that one set of *sp*-type diffuse functions is added to each nonhydrogen atom and one *s*-type diffuse function is added to hydrogen atoms.

In Table 8.2 we give a list of basis sets of orbitals that are commonly used in modern MO calculations. The H and C atomic orbitals that are included are listed. The first set contains “Gaussian-like orbitals”. Outside of the STO-3G basis set, most Gaussian basis sets are “split-valence”, which means that they use different numbers of Gaussian functions to describe core and valence atomic orbitals. Thus, a 6-31G basis set uses 6 Gaussians for the core orbitals, and two sets of Gaussians for the valence orbitals, one with 3 Gaussians and another with one. Adding more Gaussians allows more flexibility in the basis set so as to give a better approximation of the true orbitals. Therefore, although some of the basis sets incorporate the same AOs, the larger ones provide a much better description of them. For each basis set, polarization (\*), and diffuse functions (+) can also be added, which add flexibility into the basis set.

**Table 8.2.** The basis sets and orbitals they include

Basis	AOs on C*	AOs on H
STO-3G	1s, 2s, 2p <sub>x</sub> , 2p <sub>y</sub> 2p <sub>z</sub>	1s
3-21G*	1s, 2s, 2p, 3s, 3p	1s, 2s
3-21+G*	1s, 2s, 2p, 3s, 3p, 4s, 4p	1s, 2s
6-31G	1s, 2s, 2p, 3s, 3p	1s, 2s
6-31G*	1s, 2s, 2p, 3s, 3p, 3d	1s, 2s
6-31G**	1s, 2s, 2p, 3s, 3p, 3d	1s, 2s, 2p
6-31+G*	1s, 2s, 2p, 3s, 3p, 3d, 4s, 4p	1s, 2s
6-311G*	1s, 2s, 2p, 3s, 3p, 3d, 4s, 4p	1s, 2s, 3s
6-11++G(2df, 2pd)	1s, 2s, 2p, 3s, 3p, 3d, 4s, 4p, 4d, 4f	1s, 2s, 2p, 3s, 3p, 3d, 4s

Alternate basis sets that are commonly used are the Dunning correlation-consistent polarized valence X zeta basis sets, denoted cc-pVXZ, see Table 8.3. Dunning pointed out that basis sets optimized at the Hartree–Fock level might not be ideal for correlated computations [462]. The “correlation consistent” basis sets are optimized using correlated wavefunctions and cc-pVXZ means a Dunning correlation-consistent, polarized valence, X-zeta basis; X=D,T,Q,5,6,7. In particular, the cc-pVDZ for C atom

**Table 8.3.** Correlation-consistent polarized valence X zeta (XZ) basis sets

Basis	AOs on C	AOs on H
cc-pVDZ	1s, 2s, 2p, 3s, 3p, 3d	1s, 2s, 2p
cc-pVTZ	1s, 2s, 2p, 3s, 3p, 3d, 4s, 4p, 4d, 4f	1s, 2s, 2p, 3s, 3p, 3d
cc-pVQZ	1s, 2s, 2p, 3s, 3p, 3d, 4s, 4p, 4d, 4f, 5s, 5p, 5d, 5f, 5g	1s, 2s, 2p, 3s, 3p, 3d, 4s, 4p, 4d, 4f
cc-pV6Z	total of 7s, 6p, 5d, 4f, 3g, 2h, <i>i</i>	

consists of  $3s2p1d$ , cc-pVTZ would be  $4s3p2d1f$ , cc-pVQZ would be  $5s4p3d2f1g$  (see Table 8.3). The advantage of these is that increasing basis-set size is systematic. In fact, if energies are calculated with the cc-pVDZ, cc-pVTZ and cc-pVQZ basis sets, then there is an analytical function that can be used to extrapolate to cc-pVmZ (the complete basis-set limit). Unfortunately, cc-pVQZ calculations are not commonly doable. Moreover, cc-VXZ functions are more difficult to integrate than the Gaussian functions and these calculations take longer even for comparably sized basis sets. Dunning basis sets already contain polarization functions, but they can be augmented with diffuse functions.

The EMSL (the environmental molecular sciences laboratory) [463] library supplies a wide selection of atomic basis sets optimized for molecules. This library allows extraction of Gaussian basis sets, and any related effective core potentials (the effective core potentials are considered in the next sections), from the Molecular Science Research Center's Basis Set Library. A user may request the basis set be formatted appropriately for a wide variety of popular molecular electronic-structure packages. In addition to the exponents and contraction coefficients that define the basis set, the user can obtain descriptive data that include the overall philosophy behind the basis literature citations, the angular momentum composition of the basis and many other pieces of information.

Molecular AO basis sets can formally be used in periodic LCAO calculations but their adequacy must be carefully checked [23]. We discuss in the next section the modification of molecular basis sets to the study of crystals.

### 8.1.3 Molecular Basis Sets Adaptation for Periodic Systems

In the periodic systems the basis sets are chosen in such a way that they satisfy the Bloch theorem. Let a finite number  $m_A$  of contracted GTFs be attributed to the atom  $A$  with coordinate  $\mathbf{r}_A$  in the reference unit cell. The same GTFs are then formally associated with all translationally equivalent atoms in the crystal occupying positions  $\mathbf{r}_A + \mathbf{a}_n$  ( $\mathbf{a}_n$  is the direct lattice translation vector). For the crystal main region of  $N$  primitive unit cells there are  $N \sum_A m_A$  Gaussian-type Bloch functions (GTBF) constructed according to

$$\chi_{\mathbf{k}i}(\mathbf{r}) = \frac{1}{\sqrt{N}} \sum_{\mathbf{a}_n} \exp(i\mathbf{k}\mathbf{a}_n) \chi_i(\mathbf{r} - \mathbf{r}_A - \mathbf{a}_n) \quad (8.9)$$

The total number  $M$  of GTBFs equals  $M = \sum_A m_A$  where the summation is made over atoms of the reference cell. Thus, in solids the basis-set functions are modulated over the infinite lattice: any attempt to use large uncontracted molecular or atomic basis sets, with very diffuse functions can result in the wasting of computational resources [23]. Therefore exponents and contraction coefficients in the molecular and periodic systems are generally rather different, and with some exceptions, such as molecular crystals and certain covalent solids, molecular basis sets are not directly transferable to the study of crystalline solids. As in the case of molecules, basis functions in solids are grouped into shells. In general, a shell contains all functions characterized by the same  $n$  and  $l$  quantum numbers (e.g. all the different  $d$ -functions in a  $3d$  shell); this allows the partitioning of the total charge density into “shell charge

distributions" and is useful in the selection of bielectronic integrals and in the evaluation of long-range interactions. A feature of the contraction schemes originally used in the basis sets of the Pople type (and often useful in calculations with the CRYSTAL code [23]) is the additional grouping of basis functions with only the same principle quantum number into shells; *e.g.* a  $2sp$  shell, in which both  $2s$  and  $2p$  functions have the same set of exponents  $\alpha_j$  but different contraction coefficients  $d_j$ . For STF this is illustrated by Table 8.1. This procedure reduces the number of auxiliary functions to be calculated in the evaluation of electron integrals. Note that if the basis set is restricted to  $s$ ,  $p$  and  $d$  basis functions only  $sp$  shells may be formed in this way. In certain circumstances it may actually represent an important constraint on the form of the basis functions. For relatively small calculations where the time and storage limitations are not an important factor, some consideration should be given to describing the  $s$  and  $p$  functions with separate sets of exponents. Most standard molecular codes use what is known as a segmented contraction scheme, in which the transformation from the larger primitive set to the smaller contracted set is restricted in such a way that each Gaussian primitive  $g_j(\mathbf{r})$  contributes to exactly one contracted GTF. In contrast, the general contraction scheme makes no such assumptions, and allows each Gaussian primitive to contribute to several contracted GTFs. A considerable advantage of the general scheme is that the contracted GTFs reproduce exactly the desired combinations of primitive functions. For example, if an atomic SCF calculation is used to define the contraction coefficients in a general contraction, the resulting minimal basis will reproduce the SCF energy obtained in the primitive basis. This is not the case with segmented contractions. There are other advantages with a general contraction: for example, it is possible to contract inner-shell orbitals to single functions with no error in the atomic energy, making calculations on heavy elements much easier. Another advantage is a conceptual one: using a general contraction, it is possible to perform calculations in which the one-particle space is a set of atomic orbitals, a true LCAO scheme, rather than being a segmented grouping of a somewhat arbitrary expansion basis. The MOs or COs can then be analyzed very simply, just as for the original qualitative MO LCAO or CO LCAO approach, but in terms of "exact AOs" rather than relatively crude approximations to them.

We describe here in more detail some computational aspects of GTFs use in the CRYSTAL code [23], following [458]. The important reason for the usefulness of a Gaussian basis set is embodied in the Gaussian product theorem (GPT), which in its simplest form states that the product of two primitive Gaussian functions with exponents  $\alpha$  and  $\beta$ , located at centers  $\mathbf{A}$  and  $\mathbf{B}$ , is itself a primitive Gaussian with exponent  $\gamma = \alpha + \beta$ , multiplied by a constant factor  $F$ , located at a point  $\mathbf{C}$  along the line segment  $\mathbf{A} - \mathbf{B}$ , where  $\mathbf{C} = \frac{\alpha\mathbf{A} + \beta\mathbf{B}}{\gamma}$  and  $F = \exp\left(-\frac{\alpha\beta}{\gamma}(\mathbf{A} - \mathbf{B})^2\right)$ .

The product of two polynomial GTF, of degree  $\mu$  and  $\nu$  and located at points  $\mathbf{A}$  and  $\mathbf{B}$  is therefore another polynomial GTF located at  $\mathbf{C}$  of degree  $\mu + \nu$  in  $x_C$ ,  $y_C$  and  $z_C$ , which can be expressed as a short expansion of one-center Gaussians:

$$\chi_{A_x}(x)\chi_{B_x}(x) = \sum_{i=0}^{\mu+\nu} C_i^{\mu+\nu} \varphi_{Ci}(x - x_C) \quad (8.10)$$

where  $\varphi_{Ci}(x) = x^i \exp(-\alpha_p(x - x_c)^2)$  and  $x_c = \frac{\alpha x_A + \beta x_B}{\alpha + \beta}$ .

The product of two Gaussians that are functions of the coordinates of the same electron is referred to as an overlap distribution, and all the integrals that must be calculated involve at least one such overlap distribution. The most important consequence of the GPT is that all four-center two-electron integrals can be expressed in terms of two-center quantities. CRYSTAL code actually uses a common and more efficient approach for the evaluation of integrals over Gaussian basis functions, in which Hermite Gaussian functions (HGFs) are used instead of the usual Cartesian Gaussians in the re-expansion (8.10). Hermite Gaussians are defined as derivatives of an *s*-type Gaussian:

$$A(\xi) = H_i(\xi) \exp(-\alpha_p(x - x_p)^2) = (-1)^i \frac{d^i}{d\xi^i} \exp(-\xi^2) \quad (8.11)$$

where  $H_i(\xi)$  is a polynomial of order  $i$ , and  $\xi = \alpha_p^{1/2}(x - x_p)$ . The set of HGFs spans the same space as the expansion functions in (8.10) and as a consequence they can be used for expanding the basis function products:

$$\chi_{Ax}(x)\chi_{Bx}(x) = \sum_{i=0}^{l_A+l_B} C_i^{l_A+l_B} A_i(\xi) \quad (8.12)$$

where the expansion coefficients must now be redefined. Because of the natural relations between Hermite polynomials and Gaussians, the necessary two-center integrals can be evaluated with very high efficiency. Basis functions with higher quantum numbers can be generated through repeated differentiation of an *s*-type Gaussian. Even though the four-center bielectronic integrals can be written in terms of two-center quantities, the cost of evaluating them still scales nominally as  $N^4$ , where  $N$  is the number of functions in the expansion. This scaling must be reduced in order to treat large systems. One way of doing this that is used in CRYSTAL is the method of *prescreening* where, rather than attempting to calculate the integrals more efficiently, one seeks, where possible, to avoid their evaluation altogether. The expression for an integral over primitive Gaussians can be formally written as

$$(ab|cd) = S_{ab}S_{cd}T_{abcd} \quad (8.13)$$

where  $S_{ab}$  is a radial overlap between functions  $\chi_a$  and  $\chi_b$ , and  $T_{abcd}$  is a slowly varying angular factor. In many situations the product  $S_{ab}S_{cd}$  thus constitutes a good estimate of the magnitude of the integral whose product is used as an estimate in screening out small integrals. In order to estimate these overlaps quickly, a single, normalized *s*-type Gaussian called an adjoined Gaussian is associated with each shell, whose exponent  $\alpha$  is the smallest of the exponents in the shell contraction. This function thus reproduces approximately the absolute value of the corresponding AOs at intermediate and long range. The adjoined Gaussian is used in fast algorithms for estimating overlaps on the basis of which integrals are either evaluated exactly, approximately, or not at all. The level of approximation is user-definable through a set of tolerances given in the input. Such algorithms, and a consideration of the crystalline symmetry, mean that the integrals part of CRYSTAL code scales at between  $N$  and  $N^2$ , depending on the size of the system. The most unpleasant scaling in this code is thus the SCF part that, since it involves diagonalization of the Fock matrix, scales as approximately  $N^3$ . It requires

a special consideration of the role of diffuse basis-set functions in crystalline systems. Very diffuse functions can yield numerical instabilities and risk of linear-dependent catastrophes [458]. Furthermore, due to the truncation criteria of the infinite sums, based on the overlap, decreasing the exponents of the primitive Gaussians the number of integrals to be calculated increases very rapidly. Too extended basis sets are not needed in periodic calculations because the complete basis-set limit is reached quicker than in molecular calculations. Furthermore, the risk of linear dependence problems increases. The choice of the AO basis set is a compromise between accuracy and costs. As the accuracy must be the main goal of *ab-initio* calculations, the good-quality basis sets should always be used in spite of their computational cost to avoid producing meaningless numbers.

The choice of the basis set (BS) is one of the critical points, due to the large variety of chemical bonding that can be found in a periodic system. For example, carbon can be involved in covalent bonds (polyacetylene, diamond) as well as in strongly ionic situations ( $\text{Be}_2\text{C}$ , where the Mulliken charge of carbon is close to  $-4$ ). Some general principles of the basis-set choice for periodic systems are formulated [23, 458] and we briefly reproduce them here. Much experience gained in the molecular computational chemistry can be used in the selection of basis sets for studies of crystalline solids. However, the molecular quantum chemists do not, in general, optimize basis sets by varying the exponents or contraction coefficients to minimize the energy. Rather, there is a hierarchy of basis sets with perceived qualities, and for a difficult problem where accuracy is important, one would use a “good-quality” standard basis set from a library without modification. In crystalline systems by contrast, basis-set optimization is usually necessary, essentially for two reasons. First, there is a much larger variety of binding than in molecules and basis sets are thus less transferable. Secondly, hierarchical libraries of basis sets comparable to those available for molecules do not really exist for solids. For certain types of compounds, such as molecular crystals or many covalent materials, the molecular sets can sometimes be used largely unmodified, but this has to be done carefully. However, for strongly ionic crystals and metals the basis sets, particularly the valence states, need to be redefined completely. In essentially all cases, the core states may be described using the solutions of atomic calculations, as even in the presence of strong crystal fields the core states are barely perturbed and may be described by the linear variation parameters in the SCF calculation.

Redefining basis sets in this way is obviously time consuming and even more obviously rather boring, and so over recent years various workers involved with the CRYSTAL code have contributed to an effort to develop libraries of basis sets to be made available on the Internet. The URL of the official site is: [www.crystal.unito.it/Basis sets /Ptable.html](http://www.crystal.unito.it/Basis%20sets/Ptable.html). We recommend to the reader to use the information given on this site. The site shows a periodic table. Clicking on the symbol for the required element will reveal a text file containing various different basis sets that may have been used in different materials containing that element type. Accompanying each basis set is a list of authors, a list of materials where the set has been used, references to publications and hints on optimization where relevant. This table is obviously not complete (in particular lanthanides and actinides are not practically represented as the calculations with *f*-electrons are not included even in the CRYSTAL06 code). Additional information can be found on the site of Cambridge basis set library: [www.tcm.phy.cam.ac.uk/~mdt26/crystal.html](http://www.tcm.phy.cam.ac.uk/~mdt26/crystal.html).

We follow [458] in discussion of optimization strategies for the basis sets given in the libraries mentioned and also the adaptation of molecular bases for various types of solids. First, a number of general principles are given that should be taken into account when choosing a basis set for a periodic system.

The *diffuse basis functions* are used in atoms and molecules to describe the tails of the wavefunction, which are poorly described by the long-range decay of the Gaussian function. In periodic systems the cost of HF/DFT calculations can more essentially increase when the diffuse basis functions are included (in the silicon and diamond crystals, for example, the number of bielectronic integrals, can increase by a factor of 10 simply by changing the exponent of the most diffuse single Gaussian from 0.168 to 0.078 (Si) and from 0.296 to 0.176 (C), [458]. Fortunately, in crystalline compounds in contrast to molecules, particular in nonmetallic systems, the large overlap between neighbors in all directions drastically reduces the contribution of low-exponent Gaussians to the wavefunction. This has the consequence that a small “split-valence” basis set such as 6-21G is closer to the Hartree–Fock limit in crystals than in molecules.

The *number of primitives* is an important feature of the basis set. A typical basis set for all electron calculations includes “core functions” with higher exponents and a relatively large number of primitives – these will have a large weight in the expansion of the core states. The “valence functions” with a large weight in the outer orbitals will have lower exponents and contractions of only a very few primitives. It is possible to get away with putting a lot of primitives in the core since core states have very little overlap with neighboring atoms. The use of many primitives in the valence shells would add significantly to the cost of a calculation, but in many cases it is necessary.

There are several ways to improve a basis set [458]: 1) reoptimize the more diffuse exponents (and contraction coefficients if necessary; 2) decontract *i.e.* convert the more diffuse contractions into single Gaussian primitives; 3) convert *sp* functions into separate *s* and *p* functions; 4) add polarization functions if not already present; 5) add more primitives (watch out for linear dependence problems); 6) use a better starting point for the basis set. Optimization in this sense means varying an appropriate subset of the basis-set parameters until the energy is minimized. In principle, this is a reasonably complex multidimensional minimization, but there are various standard shell scripts available. Two of them can be downloaded from the Internet sites: BILLY code [www.tcm.phy.cam.ac.uk/~mdt26/downloads/billy.tar.gz](http://www.tcm.phy.cam.ac.uk/~mdt26/downloads/billy.tar.gz)) and LoptCG code ([www.crystal.unito.it/LoptCG/LoptCG.html](http://www.crystal.unito.it/LoptCG/LoptCG.html)).

The adequacy of the starting molecular basis sets depends on the type of crystalline compound.

To describe *covalent crystals* the small molecular split-valence basis sets can be used with confidence and essentially without modification. It is enough to reoptimize the exponent of the most diffuse shell, which produces a slightly improved basis, while reducing the cost of the calculation. That said, 6-21G\* is not really all that good and a larger better basis set with more variation freedom is quite easy to make for these cases (see web libraries).

For *fully-ionic* crystals (like alkali halides, LiH or MgO) with an almost completely empty cation valence shell it often proves convenient to use a basis set containing only “core” functions plus an additional *sp* shell with a relatively high exponent. It is usually difficult, and often impossible, to optimize the exponents of functions that only have appreciable weight in almost empty orbitals. Anions present a different

problem. Reference to isolated ion solutions is possible only for halides, because in such cases the ions are stable even at the Hartree–Fock level. For other anions, which are stabilized by the crystalline field, the basis set must be redesigned with reference to the crystalline environment. Consider, for example, the optimization of the oxygen basis set in  $\text{Li}_2\text{O}$  [458]. The difficulty is to allow the valence distribution to relax in the presence of two more electrons. We can begin from a standard STO-6G basis set, *i.e.* six contracted primitive Gaussians for the  $1s$  shell, and six more to describe the  $2sp$  shell. First, two more Gaussians were introduced into the  $1s$  contraction, in order to improve the virial coefficient and total energy. The two outer Gaussians of the valence  $sp$  shell were then removed from the contraction and allowed to vary independently. The exponents of the two outer independent Gaussians and the coefficients of the four contracted ones were optimized in  $\text{Li}_2\text{O}$ . The best outer exponents of the ion were found to be 0.45 and 0.15 and are therefore considerably more diffuse than the neutral isolated atom, where the best exponents are 0.54 and 0.24. The rest of the oxygen valence shell is unchanged with respect to the atomic situation. The introduction of  $d$  functions in the oxygen basis set gives only a minor improvement in the energy, with a population of 0.02 electrons/atom/cell ( $d$  functions may be important in the calculation of certain properties, however). Thus, for anions, reoptimization of the most diffuse valence shells is mandatory when starting from a standard basis set.

The majority of crystals can be classified as *semi-ionic* (with chemical bonding being intermediate between covalent and purely ionic limits). For such crystals the adequacy of selected basis sets must be carefully tested as is discussed in [458], for example, for semi-ionic compounds  $\text{SiO}_2$  (quartz) and  $\text{Al}_2\text{O}_3$  (corundum). The exponents of the outer shell for the two cations (Si and Al) used in molecular calculations prove to be too diffuse. For the Si atom in quartz, reoptimization in the bulk gives  $\alpha = 0.15$  (instead of the molecular value 0.09). Corundum is more ionic than quartz, and in this case it is better to eliminate the most diffuse valence shell of Al, and to use two Gaussians of the inner valence shells as independent functions ( $\alpha = 0.94$  and  $\alpha = 0.3$ , respectively).

For *metals* very diffuse Gaussians are required to reproduce the nearly uniform density so that it was often stated that the plane waves are a more appropriate basis for these systems. It is generally impossible to optimize atomic-like basis set in Hartree–Fock calculations of metallic systems. However, Gaussian DFT studies indicate that GTFs are able to provide a reliable and efficient description of simple metallic systems (see, for example, metallic lithium calculations [464]). Thus, the effects of basis set and Hamiltonian were separated.

UHF and hybrid DFT calculations for strongly correlated *transition-element magnetic compounds* require the reasonably good basis sets for the transition elements. These are not that widely available even to molecular quantum chemists since most of the effort in developing molecular GTF basis sets has been for first- and second-row atoms. One reason for this may be that molecules containing transition metal atoms tend to be very badly described at the Hartree–Fock level. Molecular bonds tend to have a fairly high degree of “covalency” and the existence of partially-occupied  $d$  states leads to a great many nearly degenerate levels, and thus to a large “static correlation” (*i.e.* the weight of the HF determinant in a CI expansion would be small, and a multideterminant treatment is more appropriate). Basis sets to describe the correlation using quantum chemistry correlated wavefunction techniques need to be

much richer than those for systems well described at the HF level since they need to treat all of the unoccupied levels. It may seem surprising that single-determinant HF could be so successful in periodic crystalline magnetic insulators containing transition elements, but this is an important characteristic of these ionic materials. The highly symmetric environment and long-range Coulomb forces tend to separate the orbitals into well-defined subsets with a significant gap between occupied and unoccupied states. Hence, the ground state of NiO (for example) is rather well described by a single determinant. In this sense, a strongly correlated magnetic insulator is in many ways a “simpler system” than many molecules. The success of UHF calculations in these materials (and also hybrid DFT schemes) is now well known. We consider some examples of such calculations in Chap. 9. Molecular GTF basis sets for transition elements have been reoptimized in the solid state and are available on the Torino and Cambridge Gaussian basis set library web sites referred to earlier.

In the final part of this section we shall discuss a rather serious problem, associated with Gaussian basis sets – basis-set superposition error (BSSE). A common response to this problem is to ignore it, since it will go away in the limit of a complete basis but to achieve this limit one needs calculations that are seldom performed. The problem of BSSE is a simple one: in a system comprising interacting fragments A and B, the fact that in practice the basis sets on A and B are incomplete means that the fragment energy of A will necessarily be improved by the basis functions on B, irrespective of whether there is any genuine binding interaction in the compound system or not. The improvement in the fragment energies will lower the energy of the combined system giving a spurious increase in the binding energy. It is often stated that BSSE is an effect that one needs to worry about only in calculations on very weakly interacting systems. This is not really true [458]. BSSE is an ever-present phenomenon and accurate calculations should always include an investigation of BSSE. Examples of areas in which one should be particularly worried are the study of the binding energy of molecules adsorbed on surfaces (see, for example [465] for an interesting discussion) or the calculation of defect-formation energies.

The approach most commonly taken to estimate the effect of BSSE is the counterpoise correction of Boys [466]: the separated fragment energies are computed not in the individual fragment basis sets, but in the total basis set for the system including “ghost functions” for the fragment that is not present. These energies are then used to define a counterpoise-corrected (CPC) interaction energy, which by comparison with perturbation theory, has been shown to converge to the BSSE-free correct value [467].

Linear dependencies of Gaussian-type orbital basis sets employed in the framework of the HF SCF method for periodic structures, which occur when diffuse basis functions are included in a basis set in an uncontrolled manner, were investigated [468]. The basis sets constructed avoid numerical linear dependences and were optimized for a number of periodic structures. The numerical AO basis sets for solids were generated in [469] by confining atoms within spheres and smoothing the orbitals so that the first and second derivatives go to zero at the boundary. This forms small atomic-like basis sets that can be applied to solid-state problems and are efficient for treating large systems.

We considered the basis sets for all-electron calculations in which all the core electrons are involved explicitly. Both in molecular and solid-state quantum chemistry the core states can be treated implicitly as creating an effective core potential (pseudopo-

tential). The pseudopotential approximation becomes the most efficient for crystalline compounds of heavy elements. Simultaneously, the relativistic effects on the electronic structure play an important role. In the next sections we consider nonrelativistic and relativistic pseudopotentials used in modern LCAO calculations of periodic systems. The choice of the corresponding valence basis sets is also discussed.

## 8.2 Nonrelativistic Effective Core Potentials and Valence Basis Sets

### 8.2.1 Effective Core Potentials: Theoretical Grounds

It is well established from chemical experience that most chemical properties of molecules and solids are determined by the valence electrons of the constituent atoms. The core states are weakly affected by changes in chemical bonding. The effect of core electrons is principally to shield the nuclear charges and to provide an effective potential for the valence electrons. The main reason for the limited role of the core electrons is the spatial separation of the core and valence shells that originates from the comparatively strong binding of the core electrons to the nucleus. This effect is illustrated in Fig. 8.2, [470], where the radial orbitals of the oxygen atom are plotted. The spatial separation of the  $1s$  core state from the valence  $2s$ ,  $2p$  states and

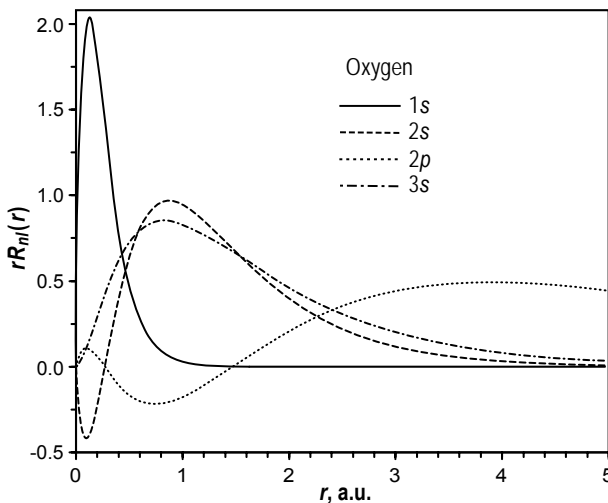


**Fig. 8.2.** Radial orbitals of oxygen atom in the ground state, [470]

unoccupied (excited)  $3s$  state is seen. The HF eigenvalues of  $1s$ ,  $2s$  and  $2p$  states (for the ground state of free oxygen atom) are  $-20.6687$  a.u.,  $-1.2443$  a.u.,  $-0.6319$  a.u., respectively [65], *i.e.* the valence and core eigenvalues differ by an order of magnitude. The precise decomposition of electrons into core and valence becomes more difficult

when the spatial and/or energetic separation between two shells breaks down. This is, for instance, the case for the  $3d$  transition metal elements, for which the most weakly bound  $4s$ -state is not well separated from the  $3d$ -states and the latter are not well separated from  $3s$ ,  $3p$  states (for example, in the case of Ti atom, HF one-electron energies are  $-0.2208$  a.u. ( $4s$ ),  $-0.4407$  a.u. ( $3d$ ),  $-1.7952$  a.u. ( $3p$ ),  $-2.8735$  a.u. ( $3s$ ), [65]). As a result, the overlap of the  $3d$ -orbitals (and even  $3s$ ,  $3p$  orbitals) with the orbitals from neighboring atoms is too large to be ignored. In this situation large core and small core effective potentials can be introduced; the former differs from the latter by exclusion of the  $3s$ ,  $3p$  electrons from the core.

The idea behind effective core potentials (ECPs), also called pseudopotentials (PP), is to treat the core electrons as creating effective averaged potentials rather than actual particles. Effective core potentials are based on the frozen-core approximation and serve to represent the potential generated by core electrons, also incorporating relativistic effects. ECP application can introduce significant computational efficiencies as it allows formulation of a theoretical method for dealing only with the valence electrons, while retaining the accuracy of all-electron methods. Fock, Veselov and Petrashen were the first to formulate the approach for treating a subset of the electrons, such as the valence electrons, in the field of the remaining electrons. They considered the special case of atoms with two valence electrons outside a closed shell [101].

As we already noted, the pseudopotentials are essentially mandatory in plane-wave calculations of solids since the core orbitals have very sharp features in the region close to the nucleus and too many plane waves would be required to expand them if they were included. In atomic-like basis-set calculations pseudopotentials are formally not mandatory and have different characteristics from those designed for plane waves since localized basis functions actually have necessary sharp features in the core region. Nevertheless, ECP methods are also used in LCAO calculations of molecules and solids since the difficulty of the standard LCAO methods rises rapidly with the number of electrons. If the CPU time in LCAO calculations were dominated by the integrals calculation, PP introduction would not give very much since the number of integrals is controlled by more diffuse functions that overlap strongly with neighboring atoms. These diffuse functions are introduced mainly to describe the change of atomic valence states. However, the use of ECP will decrease the number of coefficients in the one-electron wavefunctions and might give significant savings in the SCF part. It is also quite easy to incorporate relativistic effects into pseudopotentials, which is increasingly important for heavy atoms. All electron relativistic calculations are very expensive and in many cases are practically difficult.

The parameters and the underlying basis set of so-called energy-consistent ECPs can be adjusted in accordance with representative experimental data, not only for the ground state, but also for excited states, electron affinities, ionization potentials and so on. Being of semiempirical origin, they can perform remarkably well for a given system, but their transferability to other environments can be poorer than that of shape-consistent ECPs. So-called shape-consistent ECPs (known in computational condensed matter as the norm conserving ECPs) are rather easy to derive and contain no adjustable parameters, *i.e.* these are *ab-initio* ECPs. The construction of shape-consistent ECPs for molecules is based on the original proposal of Christiansen *et al.* [471] where shape consistency was introduced. Simultaneously, norm conserving ECP were introduced in computational condensed-matter physics by Hamann *et al.*

[472]. This example demonstrates practically independent development of ECPs for molecules and crystals when for the same ECP property different terms are used. The work by Phillips and Kleinman (PK) [473] is an important step in the ECP applications for solids. PK developed the pseudopotential formalism as a rigorous formulation of the earlier “empirical potential” approach. They showed that ECP that has the plane-wave pseudo wavefunctions as its eigenstates could be derived from the all-electron potential and the core-state wavefunctions and energies. Thus a nonempirical approach to finding ECP was introduced.

The PK pseudopotential shortcomings are well known [474]: it depends explicitly on the one-electron eigenvalue and outside the core region the normalized pseudo orbital (PO) is proportional but not equal to the true orbital. Typically, generation of a pseudopotential proceeds as follows. First, a cutoff distance  $r_c$  for the core is chosen (in the case of our example, the oxygen atom,  $r_c$  can be taken as 0.5 a.u., see Fig. 8.2). In a PP approach all radial  $R_{nl}(r)$  orbitals of the valence shell must be nodeless, as for each  $l$  all lower-lying states have to be projected out by the PP. In the case of oxygen, for instance, the  $2s$ -PO must be nodeless. An example of such a nodeless  $R_{nl}(r)$  that, nevertheless, agrees with the corresponding true AO in the relevant part of space, is shown in Fig. 8.3a.

It is, however, impossible to produce two (or more) nodeless orbitals in the same energy range with only a single spherical PP, as for fixed PP only the angular momentum term can generate differences. Since PP replaces the potential of a nucleus and the core electrons, it is spherically symmetric and each angular momentum  $l$  can be treated separately, which leads to nonlocal  $l$ -dependent PP  $V_l(r)$ . Consequently, the total atomic PP usually consists of several components, one for each angular momentum present in the valence space. The PP dependence upon  $l$  means that, in general, PP is a nonlocal operator, that can be written in semilocal (SL) form

$$\hat{V}^{PS} = \sum_{lm} |Y_{lm}(\theta, \varphi)\rangle V_l(r) \langle Y_{lm}^*(\theta, \varphi)| \quad (8.14)$$

where  $Y_{lm}(\theta, \varphi)$  are spherical harmonics and  $V_l(r)$  is the pseudopotential for the  $l$ th angular-momentum component. This is termed semilocal because it is nonlocal in the angular variables, but local in the radial variable: when operating on a function  $f(r, \theta', \varphi')$ ,  $\hat{V}^{PS}$  has the effect [10]

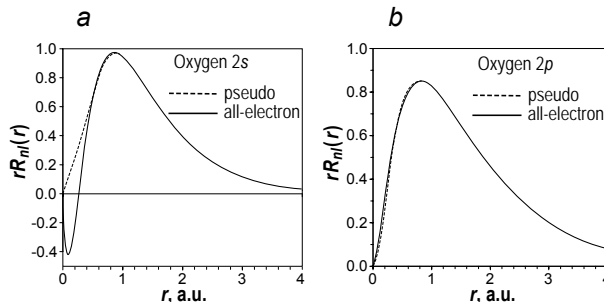


**Fig. 8.3.** Radial pseudo- versus all-electron orbitals of oxygen: (a) 2s (b) 2p [470]

$$[\hat{V}^{PS} f]_{r,\theta,\varphi} = \sum_{lm} Y_{lm}(\theta, \varphi) V_l(r) \int d(\cos \theta') d\varphi' Y_{lm}(\theta', \varphi') f(r, \theta', \varphi') \quad (8.15)$$

All the PP information is in the radial functions  $V_l(r)$ . (We note that the HF exchange operator is fully nonlocal both in the angular and in the radial variables.) To generate PP an all-electron calculation (HF or DFT) of a free atom is performed. The DFT PP Hamiltonian includes the local (Hartree and exchange-correlation) and semilocal (PP) parts; the HF PP Hamiltonian includes local (Hartree), nonlocal (exchange) and semilocal (PP) parts. The set of PP parameters is chosen to accurately reproduce the eigenvalues and eigenfunctions of valence states. Clearly, in the region of space in which most of the electronic norm is concentrated both orbitals must be very close, if not identical. On the other hand, the form of the valence orbitals in the core region, where the core electrons are moving, is less relevant. Otherwise, the core states themselves would play a more important role. In the core region one can thus allow the pseudo-orbital (PO) to differ from the all-electron orbital (AO) without losing too much accuracy [470].

The calculations of real systems (for example, color centers in ionic crystals, [475]) were made based on the model potential of Abarenkov and Heine [476]:

$$V_M = \begin{cases} V_{val}(r) - \sum_{lm} |Y_{lm}\rangle A_l(E) \langle Y_{lm}|, & r < r_c \\ -\frac{Z}{r} + V_{val}(r), & r > r_c \end{cases} \quad (8.16)$$

where  $V_{val}$  is the Coulomb and exchange potential due to the valence electrons,  $Z$  is the valence charge, and  $A_l(E)$  is a constant (in space) function of energy  $E$  chosen to make the PO logarithmic derivative equal that of the true eigenfunction at several atomic eigenvalues. To a high degree of accuracy  $A_l(E)$  may be linearized:  $A_l(E) = A_l + B_l E$ .

A giant step forward in pseudopotentials was taken by Hamann *et al.* [472], who introduced norm conserving pseudopotentials (NCCP). NCCP for angular momentum  $l$  is chosen so that

(1) the resulting atomic valence PO agrees with the corresponding all-electron (AE) AO for all  $r$  larger than some  $l$ -dependent cutoff (core) radius

$$R_{nl}^{PS}(r) = R_{nl}^{AE}(r) \quad (8.17)$$

(2) the norm of the orbital is conserved,

$$\int_0^{r_{c,l}} |R_{nl}^{PS}(r)|^2 dr = \int_0^{r_{c,l}} |R_{nl}^{ae}(r)|^2 dr \quad (8.18)$$

(3) The logarithmic derivatives of the true and pseudowavefunctions and their first energy derivatives agree for  $r > r_c$ .

Condition 1 automatically implies that the real and pseudovalence eigenvalues agree for a chosen “prototype” configuration, as the eigenvalue determines the asymptotic decay of the orbitals.

Properties (2) and (3) are crucial for the pseudopotential to have optimum transferability among a variety of chemical environments [470].

The PP concept has been motivated by the inertness of the atomic core states in binding so that the ionic core of the atom provides a fixed potential in which the

valence electrons are moving, independently of the system (atom, molecule or solid) that is considered. However, in polyatomic systems the valence states undergo obvious modifications compared to the atomic valence orbitals, even if the polyatomic core potential is given by a simple linear superposition of atomic core potentials. Most notably, the eigenenergies change when packing atoms together, which leads to bonding and antibonding states in molecules and to energy bands in solids. Thus, while PPs are designed to reproduce the valence AOs of some chosen atomic reference configuration (usually the ground state), it is not clear *a priori* that they will have the same property for all kinds of polyatomic systems and for other atomic configurations. Consequently, one has to make sure that the PP is *transferable* from its atomic reference state to the actually interesting environment. To check the transferability of PP one has to analyze the sensitivity of the agreement between atomic POs and AOs to the specific eigenenergy in the single-particle equation. One finds that the variation of the logarithmic derivative  $R_{nl}^{PS}(r)/R_{nl}^{ae}(r)$  with the single-particle energy is determined by the norm contained in the sphere between the origin and  $r$ . This is true in particular in the neighborhood of one of the actual atomic eigenvalues  $\varepsilon_{nl}$ , *i.e.* for a bound atomic eigenstate. Thus, as soon as normconservation is ensured, the POs exactly reproduce the energy dependence of the logarithmic derivative of the AOs for  $r > r_{c,l}$ . Consequently, one expects the POs to react as the AOs when the valence states experience some energy shift in a polyatomic environment – provided the underlying PPs are normconserving. This argument supporting the transferability of PPs emphasizes the importance of normconservation in a very explicit way. In practice, it is, nevertheless, always recommended to check the transferability explicitly by examination of some suitable atomic excitation process and of the binding properties of simple molecular or crystalline systems [470]. In the next section we consider pseudopotentials used in modern periodic calculations.

### 8.2.2 Gaussian Form of Effective Core Potentials and Valence Basis Sets in Periodic LCAO Calculations

The form of ECP used in the condensed-matter applications depends on the basis chosen – PW or LCAO. The numeric pseudopotentials in plane-wave calculations must be used with the density functional that was employed to generate them from a reference atomic state. This is a natural and logical choice whenever one of the plane-wave DFT codes is used. In PW calculations the valence functions are expanded in Fourier components, and the cost of the calculation scales as a power of the number of Fourier components needed in the calculation. One goal of PP is to create POs that are as smooth as possible and yet are accurate. In PW calculations maximizing smoothness is to minimize the range of Fourier space needed to describe the valence properties to a given accuracy [10]. Normconserving PPs achieve the goal of accuracy, usually at some sacrifice of smoothness. A different approach by Vanderbilt, known as “ultrasoft pseudopotentials” (US) [477] reaches the goal of accurate PW calculations by a transformation that re-expresses the problem in terms of a smooth function and an auxiliary function around each core that represents the rapidly varying part of the density. The generation code for Vanderbilt US pseudopotentials and their library can be found on site <http://www.physics.rutgers.edu/~dhv/uspp>.

*Ab-initio* pseudopotentials for PW calculations of solids can be generated also by the fhiPP package [478], see also site <http://www.fhi-berlin.mpg.de/th/fhiimd/>.

The numerical AO-based DFT code SIESTA [344] employs the same numeric pseudopotentials as plane-wave-based codes. An alternative approach is used in the Slater-orbital-based DFT code ADF [345], where so-called core functions are introduced. They represent the core-electron charge distribution, but are not variational degrees of freedom and serve as fixed core charges that generate the potential experienced by valence electrons [479].

In molecular quantum chemistry Gaussian-function-based computations, effective core potentials were originally derived from a reference calculation of a single atom within the nonrelativistic Hartree–Fock or relativistic Dirac–Fock (see Sect. 8.3) approximations, or from some method including electron correlations (CI, for instance). A review of these methods, as well as a general theory of ECPs is provided in [480,481].

In this section we discuss those effective core potentials and the corresponding valence basis sets that are used for Gaussian-function-based LCAO periodic computations implemented in the computer codes CRYSTAL [23] and GAUSSIAN [107].

The ECP general form is a sum of a Coulomb term, a local term and a semilocal term

$$V_{PS}(r) = C + V_{loc} + V_{sl} = -\frac{Z_N}{r} + \sum_{k=1}^M r^{n_k} C_k \exp(-\alpha_k r^2) + \sum_{l=0}^3 \left[ \sum_{k=1}^{M_l} r^{n_{kl}-2} C_{kl} \exp(-\alpha_{kl} r^2) \right] \hat{P}_l \quad (8.19)$$

where  $Z_N$  in a Coulomb term is the effective nuclear charge (total nuclear charge minus the number of electrons represented by ECP). The local term is a sum of products of polynomial and Gaussian radial functions. A semilocal term is a sum of products of polynomial radial functions, Gaussian radial functions and angular-momentum projection operators  $\hat{P}_l$ . Therefore, to specify semilocal ECP one needs to include a collection of triplets (coefficient, power of  $r$  and exponent) for each term in each angular momentum of ECP.

Hay and Wadt (HW) ECP [483] are of the general form (8.19). The procedure employed for generation of ECPs includes the following sequence of steps: 1) the “core” orbitals to be replaced and the remaining “valence” orbitals are defined. This step defines whether the small-core (the outermost core electrons are explicitly treated along with the valence electrons) or a large-core HW pseudopotential is generated; 2) the true numerical valence orbitals are obtained from self-consistent nonrelativistic Hartree–Fock (or relativistic Dirac–Fock) calculations for  $l = 0, 1, \dots, L$ , where  $L$ , in general, is one greater than the highest angular-momentum quantum number of any core orbital; 3) smooth, nodeless pseudo-orbitals (PO) are derived from the true Hartree–Fock (Dirac–Fock) orbitals in a manner so that PO behave as closely as possible to HF orbitals in the outer, valence region of the atom; 4) numerical effective core potentials  $V_l^{PS}$  are derived for each  $l$  by demanding that PO is a solution in the field of  $V_l$  with the same orbital energy  $\varepsilon$  as the Hartree–Fock (Dirac–Fock) orbital; 5) the numerical potentials are fit in analytic form with Gaussian functions, the total potential is represented as (8.19); 6) the numerical POs are also fit with Gaussian functions to obtain basis sets for molecular or periodic calculations. In the case of large-core ECP the primitive Gaussian bases  $(3s2p5d)$ ,  $(3s3p4d)$  and  $(3s3p3d)$  are tabulated for the first, second, and third transition series atoms, respectively. The

figures in brackets mean the number of primitive of Gaussians in  $ns$ ,  $np$  and  $(n-1)d$  contracted AOs for  $n = 4, 5, 6$ . In the case of small-core ECP  $(n-1)s, (n-1)p$  contracted AOs are added and given as the linear combinations of primitive Gaussians. Hay-Wadt ECPs and valence-electron basis sets are also generated for main-group elements: large core – for Na to Xe, and Cs to Bi, small core – for K, Ca, Rb, Sr, Cs, Ba.

The other known ECP and valence-electron basis sets were generated using the procedure, described for Hay-Wadt ECP generation. Durand-Barthelat large-core semilocal ECP [484] and corresponding valence-electron basis sets are generated for  $3d$ -transition elements and the main-group elements Li to Kr.

Compact one- and two-Gaussian expansions for the components of the effective potentials of atoms in the first two rows are presented by Stevens-Basch-Krauss [485]. Later, the list of ECP was extended to the third-, fourth- and fifth-row atoms [486] and includes relativistic ECP (RECP). The pseudo-orbital basis-set expansions for the first two rows of atoms consist of four Gaussian primitives using a common set of exponents for the  $s$  and  $p$  functions. Analytic SBK RECP are generated in order to reproduce POs and eigenvalues as closely as possible. The semilocal SBK ECP are given by

$$r^2 V_l(r) = \sum_k A_{lk} r^{n_{l,k}} \exp(-B_{l,k} r^2) \quad (8.20)$$

The potentials and basis sets have been used to calculate the equilibrium structures and spectroscopic properties of several molecules. The results compare extremely favorably with the corresponding all-electron calculations.

Stuttgart-Dresden (SD)ECP (formerly Stoll and Preuss ECP) are under constant development [487]. SD semilocal ECPs are written in the form

$$V_{sl} = \sum_{l=0}^3 \left[ \sum_{k=1}^{\mu_k} r^{n_{kl}-2} C_{kl} \exp(-\alpha_k r^2) \right] \hat{P}_l \quad (8.21)$$

Note the different convention for the factor  $r^{n_{kl}-2}$  compared to (8.19). The database of SD ECP include relativistic ECP (RECP) generated by solving the relativistic Dirac-Fock equation for atoms. Improved SD pseudopotentials exist for many of the main-group elements, and the pseudopotentials are also available for  $5d$  and other heavier elements. The most recent ECP parameters, optimized valence-electron basis sets, a list of references and guidelines for the choice of the pseudopotentials can be found at site <http://www.theochem.uni-stuttgart.de>. SD ECP can be used in periodic LCAO CRYSTAL and GAUSSIAN codes [23, 107].

Pseudopotentials are also used as embedding potentials when some special region of a covalently bonded solid or very large molecule is modeled by a modest-size cluster. The embedding pseudopotentials are considered in the next section.

### 8.2.3 Separable Embedding Potential

As was noted in the preceding section the use of atomic pseudopotentials (or effective core potentials-ECPs) considerably simplifies the quantum-mechanical description of polyatomic systems (molecules and crystals) as the much more localized and chemically inert core electrons are simulated by ECP introduction. The choice of the norm

conserving and transferable ECPs ensures that the valence states are reproduced in the majority of cases as accurately as would be done in all-electron calculations.

The second important application of pseudopotentials is connected with the so-called embedded-cluster model. This model is applied when one is interested in the electronic structure and properties of some small region of a large system such as a localized point defect in a solid, an adsorbed molecule on a solid surface or an active site in a very large biological molecule. In such a case one may model the region of interest by cutting a modest-sized but finite cluster out of the larger system and performing the calculation on it. For ionic solids the surrounding crystal can be modeled by the system of point charges. More difficult is the case when the environment is a covalently bonded system and the boundary between the cluster and environment passes through chemical bonds (covalent or partly covalent). In this case, the distant and nearest parts of an environment should be treated separately [488]. In the distant part, only the electrostatic potential representing the ionic component of an environment should be retained. The nearest part, corresponding to the “broken or dangling bonds”, needs special consideration. Each atom of the cluster boundary surface has unsaturated “dangling bonds” that cause spurious effects unless saturated in some way, usually by adding a hydrogen or pseudoatoms there [489]. This is better than leaving the dangling bond but clearly the termination is still imperfect in the sense that the bond to the attached atom is different from the bond to whatever atom is situated there in the real system [488]. Use of the embedding potentials (EP) to saturate dangling bonds of the cluster gives a cluster surface bond identical to that in the real large system.

Recently introduced new separable potentials [488, 490] have several kinds of applications: 1) when some special region of a covalently bonded solid or very large molecule is modeled by a modest-sized cluster, each dangling bond at the cluster surface can be saturated in a way that exactly reproduces the bond in the complete system; 2) a similar approach can be used at the matching surface in an embedding scheme for calculations on the same type of systems; 3) application to atomic effective core potentials where the new potential operator avoids the possibility of “ghost” states that sometimes plague the widely used pseudopotentials.

The important property of the introduced embedding potential is its separability. Let the nonlocal operator  $\hat{V}(\mathbf{r})$  depend on the space variable  $\mathbf{r}$  only and be represented by the integral operator  $\hat{V}$ :

$$\hat{V}\psi(\mathbf{r}) = \int v(\mathbf{r}, \mathbf{r}')\psi(\mathbf{r}')d\mathbf{r}' \quad (8.22)$$

with the kernel  $v(\mathbf{r}, \mathbf{r}')$ . Expanding the kernel in both arguments with the complete orthonormal set of functions  $\varphi_i(\mathbf{r}) (i = 1, 2, 3, \dots)$  the following representation of the potential can be obtained:

$$\hat{V} = \sum_{i,j=1}^{\infty} |\varphi_i\rangle V_{ij} \langle \varphi_j| \quad (8.23)$$

where  $V_{ij}$  is the infinite Hermitian matrix. If this matrix has a finite rank  $k$ , then only  $k$  of its eigenvalues are not equal to zero and the corresponding potential has the form

$$\hat{V}_{sep} = \sum_{i=1}^k |\chi_i\rangle \mu_i \langle \chi_i| \quad (8.24)$$

where  $\chi_i(\mathbf{r})$  and  $\mu_i$  are eigenfunctions and eigenvalues of the potential. Equation (8.24) defines the separable potential as a finite sum of single-state projectors ( $|\chi_i\rangle\langle\chi_i|$ ) with constant weights  $\mu_i$ . A separable operator is an operator with a finite-dimensional functional space for its range. If one employs another orthonormal basis set  $\varphi_i(i = 1, 2, \dots, k)$  that spans the same functional space as the set  $\chi_i(\mathbf{r})(i = 1, 2, \dots, k)$ , the separable potential will have the nondiagonal form

$$\hat{V}_{sep} = \sum_{i,j=1}^k |\varphi_i\rangle V_{ij} \langle\varphi_j| \quad (8.25)$$

but with finite sum over  $i, j$ . The difference between the separable potential and the potential of the general form is that the separable potential with a suitable choice of the basis could be transformed to the form (8.24) or (8.25) and the potential of the general form could not.

As an example of separable potentials we mention the semilocal ECP, see (8.14), which have a form similar to (8.24), but where  $\mu_i = V_i(r)$  are functions of the radial variable. These semilocal potentials are separable only in the angular variables (in which these potentials are nonlocal) as the separability is the property of nonlocal potentials.

Separable nonlocal ECPs were extensively studied [474, 491–494]. The nonlocal separable potentials application is complicated by the problem of “ghost states” [495] *i.e.* extra bound states with levels, under the reference atomic eigenenergy. For semilocal ECPs, used in modern computer LCAO codes, this problem does not occur [493], for the embedding potential this problem has to be taken into account.

Let us consider a Hamiltonian  $\hat{H}_0$  with eigenfunctions  $\Psi_i^0$  and eigenvalues  $E_i^0$ . Suppose we have an arbitrary set of orthonormal functions  $\Psi_p$  and an arbitrary set of real numbers  $E_p(p = 1, \dots, n)$ . The aim is to develop another Hamiltonian

$$\hat{H}_{sep} = \hat{H}_0 + \hat{V}_{sep} \quad (8.26)$$

with separable potential  $\hat{V}_{sep}$  so that  $n$  eigenfunctions and eigenvalues of  $\hat{H}_{sep}$  are exactly  $\Psi_p$  and  $E_p$ , whereas all other eigenvalues  $E_i, i > n$  of  $\hat{H}_{sep}$  are equal to eigenvalues of  $\hat{H}_0$ .

Of course, eigenfunctions  $\Psi_i, (i > n)$  of  $\hat{H}_{sep}$  will differ from eigenfunctions  $\Psi_i^0$  of  $\hat{H}_0$  because the former are orthogonal to  $\Psi_p, (p \leq n)$  and the latter to  $\Psi_p^0$ .

The transformation  $\hat{H}_0$  into  $\hat{H}_{sep}$  could be done in two steps.

In the first step the similarity transformation  $\hat{H}' = \hat{U}\hat{H}_0\hat{U}^\dagger$  with a unitary operator  $\hat{U}$  is made, which changes the eigenfunctions and leaves eigenvalues unchanged. To find the desired similarity transformation the following auxiliary problem is considered: a unitary operator  $\hat{U}$  is found that transforms one set of orthonormal functions  $\Psi_p^0$  into another set of orthonormal functions  $\Psi_p$ :

$$\hat{U}\Psi_p^0 = \alpha_p \Psi_p, \quad |\alpha_p| = 1, \quad p = 1, 2, \dots, n \quad (8.27)$$

and there is no linear dependence among functions  $\Psi_p^0$  and  $\Psi_p$ , *i.e.* the dimension of functional space spanned by both sets of functions together is equal to  $2n$ . The operator  $\hat{U}$  is taken in the form  $\hat{U} = \hat{I} - \hat{R}$  and  $\hat{R} = \sum_{p,q=1}^n |\chi_p\rangle T_{pq} \langle\chi_q|$  is a separable

operator with the smallest possible dimension. Dropping the mathematical details given in [488], we write the explicit form of the operator  $\hat{R}$ :

$$\hat{R} = \sum_{p,q=1}^n |\Psi_p^0 - \alpha_p \Psi_p\rangle \{Q^{-1}\}_{pq} \langle \Psi_q^0 - \alpha_q \Psi_q| \quad (8.28)$$

where  $\chi_p = \Psi_p^0 - \alpha_p \Psi_p$  and  $Q_{pq} = \langle \chi_p | \Psi_q^0 \rangle = \delta_{pq} - \alpha_p^* \langle \Psi_p | \Psi_q^0 \rangle$ . The second step is the energy-shift transformation that changes specified eigenvalues only:

$$\begin{aligned} \hat{H}_{sep} &= \hat{H}' + \sum_{p=1}^n |\Psi_p\rangle (E_p - E_p^0) \langle \Psi_p| \\ &= \hat{U} \hat{H}_0 \hat{U}^\dagger + \sum_{p=1}^n |\Psi_p\rangle (E_p - E_p^0) \langle \Psi_p| \end{aligned} \quad (8.29)$$

Hence the potential  $\hat{V}_{sep}$  can be written as

$$\hat{V}_{sep} = \hat{H}_{sep} - \hat{H}_0 = \hat{R} \hat{H}_0 \hat{R}^\dagger - \hat{R} \hat{H}_0 - \hat{H}_0 \hat{R}^\dagger + \sum_{p=1}^n |\Psi_p\rangle (E_p - E_p^0) \langle \Psi_p| \quad (8.30)$$

This potential is separable with dimension  $n$ , *i.e.* can be represented in the form

$$\hat{V}_{sep} = \sum_{i,j}^{3n} |f_i\rangle V_{ij} \langle f_j| \quad (8.31)$$

where the expression for  $V_{ij}$  can be found from expressions of  $\hat{R} \hat{H}_0$ ,  $\hat{H}_0 \hat{R}^\dagger$  and  $\hat{R} \hat{H}_0 \hat{R}^\dagger$ . Although all equations were developed for arbitrary phase factors  $\alpha_p$ , in applications the real orbitals are used. For the sake of simplicity all the phase factors  $\alpha_p$  can be selected to be real, which makes the separable potential real as well. The signs of  $\Psi_p$  and  $\Psi_p^0$  are selected so that  $\langle \Psi_p | \Psi_p^0 \rangle \geq 0$  and all  $\alpha_p = -1$  to make  $\hat{V}_{sep} \rightarrow 0$  when  $G \rightarrow G^0$  ( $G$  is a collection of  $\Psi_p, E_p, p = 1, 2, \dots$ , and  $G^0$  is a similar collection of  $\Psi_p^0, E_p^0$ ).

The separable embedding potential (8.31) was applied to model the single chemical bond between the atom  $A$  of the cluster and the atom  $B$  of the cluster environment [488]. To simulate the effect of the cluster environment the atom  $B$  is replaced by a pseudoatom  $B_{PS}$  at the same position as the actual atom  $B$ . The influence of the pseudoatom on the cluster is described by the potential that was assumed to have the following form:

$$\hat{V}_{psat} = \hat{V}_H + \hat{V}_{sl} + \hat{V}_{sep} \quad (8.32)$$

Here,  $\hat{V}_H = -1/r$  is the hydrogen potential (in a.u.), responsible for the asymptotic behavior of the potential,  $\hat{V}_{sl}$  is a semilocal potential

$$\hat{V}_{sl} = \sum_{lm} V_l(r) |Y_{lm}\rangle \langle Y_{lm}| \quad (8.33)$$

and  $\hat{V}_{sep}$  is a case  $n = 1$  separable potential (8.31) defined by the Hamiltonian  $\hat{H}_0$ , the energy  $E_1^0$  and the wavefunction  $\Psi_1^0$  of this Hamiltonian ground state, and by the

energy  $E_1$  and the wavefunction  $\Psi_1$  of the operator  $\hat{H}_0 + \hat{V}_{sl}$ . As  $\hat{H}_0$  was taken the following

$$\hat{H}_0 = -\frac{1}{2}\Delta + \hat{V}_H + \hat{V}_{sl} \quad (8.34)$$

where  $\hat{V}_{sl}$  is selected so as to reproduce the spectrum of the excited states of the atom  $B$  similarly to what is usually done in the calculation of the effective atomic core potentials. The wavefunction  $\Psi_1^0$  of the ground state of this Hamiltonian is a spherically symmetrical  $1s$  function and it is not at all a directed hybrid orbital of the atom  $B$  that makes the single bond with the atom  $A$ . The separable potential  $\hat{V}_{sep}$  being added to  $\hat{H}_0$  will change the ground-state wavefunction  $\Psi_1^0$  for function  $\Psi_1$  without changing the excited-state spectrum. Therefore,  $\Psi_1$  should be considered as a hybrid orbital of the atom  $B$  that is not known. However, the bond orbital  $\varphi_{bond}$  can be found. The new localization criterion was proposed to calculate the localized on bond  $A - B$  orbital  $\varphi_{bond}$ . This criterion is based on the maximization of the single-orbital contribution to the Wiberg index  $W_{AB}$  defined by (4.137). The one-electron density matrix is calculated in the bases of AOs orthogonalized according to Löwdin procedure [225]. This bond orbital depends on  $\Psi_1$  implicitly and in [488] a method to calculate  $\varphi_{bond}$  and its effective energy  $E_{bond}$  was developed.

The transferability of the separable embedding potential used seems very likely as the developed method of pseudopotential calculation results in the one-center potential (all the components of this potential, including  $\hat{V}_{sep}$ , are centered on the atom  $B$ ). This is demonstrated by use of the proposed separable potential (8.32) for the pseudosilicon atom that is to substitute the  $-\text{SiH}_3$  radical in  $\text{X-SiH}_3$  molecules ( $\text{X}$  was taken to be H, F, Cl, Br, and I). In all these molecules the hydrogen or halogen constitute the single chemical bond with Si. This bond is broken when the radical  $-\text{SiH}_3$  is removed and it could be saturated with the pseudosilicon atom so that the original five-atom molecule would be replaced by the diatomic molecule  $\text{X-Si}_{ps}$ . The angles between bonds in  $\text{SiH}_3\text{X}$  molecules vary only a little and the perfect tetrahedron angle was used for all molecules. The Si–H bond length in these molecules is also approximately equal to that in the  $\text{SiH}_4$  molecule, and silicon–halogen bond length varies considerably (the experimental values for silicon–halogen bond lengths were taken from diatomic Si–Hal molecules). The potential (8.32) was generated for the pseudosilicon atom to make the bond in the two-electron diatomic molecule  $\text{H-Si}_{ps}$  the same as the single chemical bond H–Si in the  $\text{SiH}_4$  molecule, this potential is centered at the Si atom.

The potential-generation procedure consists of several stages. In the first stage the all-electron HF calculations on the  $\text{SiH}_4$  molecule were performed. The canonical HF orbitals, orbital energies, and the total density matrix were obtained in the GTO basis. In the second stage, the noncanonical HF orbital  $\varphi_{bond}$  localized on the selected Si–H bond was calculated using the Wiberg index for the localization criteria. The maximum localizing functional value obtained was 0.965, which is close enough to the maximum possible value 1 for the single covalent bond. In the third stage, the semilocal potential  $\hat{V}_{sl}$  was generated so that the excited energy levels of the equation

$$\left(-\frac{1}{2}\Delta - \frac{1}{r} + \hat{V}_{sl}\right)\psi_{nlm}^0(\mathbf{r}) = E_{nl}^0\psi_{nlm}^0 \quad (8.35)$$

coincide with unoccupied energy levels of the neutral silicon atom ( $E_{2s}^0 = E(\text{Si})_{4s}$ ,  $E_{2p}^0 = E(\text{Si})_{4p}$ ,  $E_{3d}^0 = E(\text{Si})_{3d}$  and so on). No adjustment was done for the  $E_{1s}^0$  energy level and it could be quite different from  $E(\text{Si})_{3s}$ . In the fourth and final stage, the function  $\Psi_1$  and the energy  $E_1$  were determined, and the pseudosilicon potential was obtained. The obtained potential of the pseudosilicon atom was used to calculate the diatomic molecules  $\text{X}-\text{Si}_{\text{ps}}$  ( $\text{X} = \text{F}, \text{Cl}, \text{Br}, \text{I}$ ). The properties of the bond and the state of the halogen atom in the diatomic molecule could be compared with those in the real five-atom molecule. This comparison will show whether the same pseudosilicon potential could be used in all considered molecules, *i.e.*, whether the generated pseudosilicon potential is transferable. The dipole moment of the bond was chosen for the bond property, and the atomic charge for the halogen property. For the diatomic molecule the dipole moment of the bond is the dipole moment of the molecule itself. However, for the five-atom molecule the dipole moment of the particular bond is not defined *a priori*. To make the comparison possible several assumptions were used that are natural enough. It was assumed that the dipole moment of every five-atom molecule  $\text{SiH}_3\text{X}$  is the sum of the dipole moment of the  $\text{X}-\text{Si}$  bond and the dipole moment of the  $\text{SiH}_3$  radical. Next, it was assumed that the dipole moment of the  $(\text{SiH}_3)$  radical is the same in all five molecules. The latter assumption can be considered as the “frozen bond” approximation, *i.e.* the neglect of the radical polarization when the  $\text{X}-\text{Si}$  bond is changing. Other details of the dipole-moment calculations can be found in [488]. To improve the agreement of the calculated dipole moments with the experimental data one  $d$ -orbital was added to the GTO 6-311G basis of silicon and halogen atoms.

In Tables 8.4 and 8.5 the dipole moments and Mulliken atomic charges found in the all-electron HF calculations are compared with those obtained with the use of a pseudosilicon atom and a hydrogen atom to saturate the bond. The disagreement between experimental and HF data is explained by the neglect of the correlation effects, and in the case of a  $\text{SiH}_3\text{I}$  molecule the neglect of relativistic effects. The analysis of Table 8.4 allows us to conclude that the pseudosilicon potential generated for one molecule ( $\text{SiH}_4$ ) to represent the  $\text{SiH}_3$  radical could be employed in calculations of other molecules ( $\text{SiH}_3\text{X}$ ,  $\text{X} = \text{F}, \text{Cl}, \text{Br}, \text{I}$ ) with the same radical.

From Table 8.5 it follows that the correlation between charges calculated with different methods is similar to that for the dipole moments. However, it should be remembered that atomic charges are not physically observable quantities and they strongly depend on their definition and on the basis employed in calculations.

Approximations to the exact (in the Hartree–Fock approximation) separable embedding potential were introduced in [490] that enable one to incorporate this potential into existing molecular calculation packages. The test calculations on the  $(\text{CH}_3)_2\text{O}$  molecule were performed that showed good accuracy of the potential.

So far, the formulation of pseudopotentials has been strictly nonrelativistic, so that the issue of heavy elements still remains to be addressed. In the next section we consider relativistic pseudopotentials.

**Table 8.4.** The dipole moments (a.u) [488]

	Theor.1 <sup>a</sup>	Theor.2 <sup>b</sup>	Theor.3 <sup>c</sup>	Expt.
SiH <sub>3</sub> F	1.226	0.555	0.527	0.511
SiH <sub>3</sub> Cl	0.899	0.644	0.631	0.515
SiH <sub>3</sub> Br	0.267	0.502	0.533	0.519
SiH <sub>3</sub> I	0.257	0.536	0.560	

<sup>a</sup>The bond is saturated with the hydrogen  
<sup>b</sup>The bond is saturated with the pseudosilicon  
<sup>c</sup>All-electron Hartree–Fock calculations

**Table 8.5.** The charge on atom A, A= H, F, Cl, Br, I, [488]

	Theor.1 <sup>a</sup>	Theor.2 <sup>b</sup>	Theor.3 <sup>c</sup>
SiH <sub>4</sub>	0.000	-0.157	-0.149
SiH <sub>3</sub> F	-0.380	-0.523	-0.687
SiH <sub>3</sub> Cl	-0.278	-0.398	-0.416
SiH <sub>3</sub> Br	-0.032	-0.035	-0.040
SiH <sub>3</sub> I	-0.097	-0.263	-0.352

<sup>a</sup>The bond is saturated with the hydrogen  
<sup>b</sup>The bond is saturated with the pseudosilicon  
<sup>c</sup>All-electron Hartree–Fock calculations

### 8.3 Relativistic Effective Core Potentials and Valence Basis Sets

#### 8.3.1 Relativistic Electronic Structure Theory: Dirac–Hartree–Fock and Dirac–Kohn–Sham Methods for Molecules

Heavy-element systems are involved in many important chemical and physical phenomena. However, they still present difficulties to theoretical study, especially in the case of solids containing atoms of heavy elements (with the nuclear charge  $Z \geq 50$ ). In this short description of relativistic electronic-structure theory for molecular systems we follow [496] and add a more detailed explanation of the Dirac–Kohn–Sham (DKS) method. For a long time the relativistic effects underlying in heavy atoms had not been regarded as such an important effect for chemical properties because the relativistic effects appear primarily in the core atomic region. However, now the importance of the relativistic effects, which play essential and vital roles in the total natures of electronic structures for heavy-element molecular and periodic systems, is recognized [496].

To treat the relativistic effect theoretically, the Dirac Hamiltonian should be applied instead of the nonrelativistic Schrödinger Hamiltonian. The Dirac one-particle Hamiltonian has the form

$$\hat{h}_D = c\boldsymbol{\alpha} \cdot \hat{\mathbf{p}} + (\beta - 1)c^2 + V(\mathbf{r}) \quad (8.36)$$

where  $c$  is the speed of light,  $V(\mathbf{r})$  is the external potential, and  $\hat{\mathbf{p}} = -i\nabla$  is the momentum operator. The  $4 \times 4$  Dirac matrices  $\alpha$  and  $\beta$  in (8.36) are given by

$$\alpha^t = \begin{pmatrix} 0_2 & \sigma_t \\ \sigma_t & 0_2 \end{pmatrix}, \quad t = (x, y, z), \quad \beta = \begin{pmatrix} I_2 & 0_2 \\ 0_2 & -I_2 \end{pmatrix} \quad (8.37)$$

with a  $2 \times 2$  Pauli spin matrix,  $\sigma_t$

$$\sigma_x = \begin{pmatrix} 0 & 1 \\ 1 & 0 \end{pmatrix}, \quad \sigma_y = \begin{pmatrix} 0 & -i \\ i & 0 \end{pmatrix}, \quad \sigma_z = \begin{pmatrix} 1 & 0 \\ 0 & -1 \end{pmatrix} \quad (8.38)$$

Here,  $0_2$ ,  $I_2$  are zero and identity  $2 \times 2$  matrices.

The free-particle Dirac Hamiltonian provides a physical structure that the eigenvalue spectrum  $\{E_k\}$  consists of two parts. The states of the higher-energy spectrum, where  $E_k \geq +mc^2$  are called the positive-energy states, and comprises states corresponding to those found in the nonrelativistic theory. The second branch of the eigenvalue spectrum consists of states with energy less than  $-mc^2$  and in a second-quantized theory they can be interpreted as states of positrons, and are called the negative-energy states.

To apply the Dirac theory to the many-particle system the one-particle Dirac operator (8.36) is augmented by the Coulomb or Coulomb–Breit operator as the two-particle term,  $g_{ij}$ , to produce the Dirac–Coulomb (DC) or Dirac–Coulomb–Breit (DCB) Hamiltonian derived from the quantum electrodynamics [496–498]:

$$g_{ij} = \begin{cases} g_{ij}^c = \frac{1}{r_{ij}}, & \mathbf{r}_{ij} = \mathbf{r}_i - \mathbf{r}_j, \quad r_{ij} = |\mathbf{r}_{ij}| \\ g_{ij}^{CB} & \end{cases} \quad (8.39)$$

where

$$g_{ij}^{CB} = \frac{1}{r_{ij}} - \frac{1}{2} \left( \frac{(\alpha_i \alpha_j)}{r_{ij}} + \frac{(\alpha_i \mathbf{r}_{ij})(\alpha_j \mathbf{r}_{ij})}{r_{ij}^3} \right) \quad (8.40)$$

By applying the independent particle approximation to many-particle relativistic DC or DCB Hamiltonians, one obtains the four-component Dirac–Hartree–Fock (DHF) method with large- and small-component spinors treated explicitly.

The DHF wavefunction  $\Psi$  is given as the Slater determinant with  $N_e$  one-particle spinors  $(\psi_i(\mathbf{r}), i = 1, \dots, N_e)$ , where  $N_e$  represents the number of electrons. The one-particle spinor  $\psi_i(\mathbf{r})$  is the four-component vector whose components are the scalar wavefunctions,

$$\psi_i = \begin{pmatrix} \psi_i^{2L} \\ \psi_i^{2S} \end{pmatrix} = \begin{pmatrix} \psi_{1i}^L \\ \psi_{2i}^L \\ \psi_{3i}^S \\ \psi_{4i}^S \end{pmatrix} \quad (8.41)$$

The two-component electron functions  $\psi_i^{2L}$  and  $\psi_i^{2S}$  are called the large-component and small-component spinors, respectively, which are expanded in the basis spinors  $\chi^L$  and  $\chi^S$ .

The matrix DHF-LCAO equation for closed-shell systems is given as,

$$\mathbf{FC} = \mathbf{SCE} \quad (8.42)$$

where  $\mathbf{C}$  is a matrix of molecular spinor coefficients,  $\mathbf{E}$  is a diagonal spinor(orbital) energy matrix,  $\mathbf{S}$  is an overlap matrix,

$$\mathbf{S}_{\mu\nu} = \begin{pmatrix} \langle \chi_{\mu}^L | \chi_{\nu}^L \rangle & 0 \\ 0 & \langle \chi_{\mu}^S | \chi_{\nu}^S \rangle \end{pmatrix} \quad (8.43)$$

and the Fock matrix  $\mathbf{F}$  is given by

$$\mathbf{F}_{\mu\nu} = \begin{pmatrix} \mathbf{V}_{\mu\nu}^{LL} + \mathbf{J}_{\mu\nu}^{LL} - \mathbf{K}_{\mu\nu}^{LL} & c\mathbf{P}_{\mu\nu}^{LS} - \mathbf{K}_{\mu\nu}^{LS} \\ c\mathbf{P}_{\mu\nu}^{SL} - \mathbf{K}_{\mu\nu}^{SL} & \mathbf{V}_{\mu\nu}^{SS} + \mathbf{J}_{\mu\nu}^{SS} - \mathbf{K}_{\mu\nu}^{SS} - 2c^2\mathbf{S}_{\mu\nu}^{SS} \end{pmatrix} \quad (8.44)$$

The matrices  $\mathbf{\Pi}_{\mu\nu}^{X\bar{X}}$ ,  $\mathbf{V}_{\mu\nu}^{XX}$ ,  $\mathbf{J}_{\mu\nu}^{XX}$ , and  $\mathbf{K}_{\mu\nu}^{XX}$  ( $X, Y = L$  or  $S$ ,  $\bar{L} = S$  and  $\bar{S} = L$ ) are the kinetic-energy integral, the nuclear-attraction integral and the Coulomb integral, respectively, defined by,

$$\mathbf{\Pi}_{\mu\nu}^{X\bar{X}} = \langle \chi_{\mu}^X | \boldsymbol{\sigma} \mathbf{p} | \chi_{\nu}^{\bar{X}} \rangle \quad (8.45)$$

$$\mathbf{V}_{\mu\nu}^{X\bar{X}} = \langle \chi_{\mu}^X | V^{nuc} | \chi_{\nu}^{\bar{X}} \rangle \quad (8.46)$$

$$\mathbf{J}_{\mu\nu}^{XX} = \sum_{Y=L,S} \sum_{\lambda\sigma} \mathbf{P}_{\lambda\sigma}^{YY} (\chi_{\mu}^{2X} \chi_{\nu}^{2X} | \chi_{\lambda}^{2Y} \chi_{\sigma}^{2Y} ) \quad (8.47)$$

and

$$\mathbf{K}_{\mu\nu}^{XY} = \sum_{\lambda\sigma} \mathbf{P}_{\lambda\sigma}^{XY} (\chi_{\mu}^{2X} \chi_{\nu}^{2X} | \chi_{\lambda}^{2Y} \chi_{\sigma}^{2Y} ) \quad (8.48)$$

The density matrix  $\mathbf{P}_{\lambda\sigma}^{XY}$  is calculated as,

$$\mathbf{P}_{\lambda\sigma}^{XY} = \sum_i^{occ} C_{i\lambda}^X C_{i\sigma}^{Y*} \quad (8.49)$$

where the negative-energy states are ignored. Even applying the four-component single-configuration (SCF) approximation, Dirac–Hartree–Fock–Breit(DHFB) or DHF methods , to calculation of heavy-atom molecules (followed by transformation of two-electron integrals to the basis of molecular spinors) is not always an easy task because a very large set of primitive atomic basis functions can be required for such all-electron four-component SCF calculations.

In the high- $Z$  case the effects of relativity can be just as important as those of electron correlation, making it necessary to develop efficient methods for the simultaneous treatment of correlation and relativity [499]. Such a treatment can be made in the framework of post-DHF methods (very complicated in the practical realization) or relativistic DFT theory.

Although the DFT method has been extensively applied to nonrelativistic calculations, the four-component DFT approaches have only recently appeared (see the book [335] and the review [499] and references therein). Relativistic versions of the Kohn–Sham equations have been developed based on the relativistic extension of the Hohenberg–Kohn theory [500].

The one-electron effective Hamiltonian for the Dirac–Kohn–Sham (DKS) method, as a relativistic extension of the conventional KS approach, takes the form,

$$\hat{h}_{DKS} = \hat{h}_D + \mathbf{V}_H + \mathbf{V}_{XC} + \beta \boldsymbol{\sigma} \frac{\delta E_{XC}[\rho, \mathbf{m}]}{\delta \mathbf{m}(\mathbf{r})} \quad (8.50)$$

where  $\hat{h}_D$  is the one-electron Dirac operator (8.36),  $\mathbf{V}_H = \int \frac{\rho(\mathbf{r}')}{|\mathbf{r}-\mathbf{r}'|} d\mathbf{r}'$  is the Hartree potential, defined by the electron-charge spin density  $\rho(\mathbf{r})$ . In contrast to the non-relativistic theory the relativistic exchange-correlation potential consists of the spin-independent part (the functional derivative of the exchange-correlation energy functional with respect to total density  $\frac{\delta E_{XC}}{\delta \rho}$ ) and the spin-dependent part  $\beta \boldsymbol{\sigma} \frac{\delta E_{XC}}{\delta \mathbf{m}(\mathbf{r})}$ , where  $\mathbf{m}(\mathbf{r})$  is the spin magnetization vector [501]. The latter is defined as  $\mathbf{m}(\mathbf{r}) = \sum_i^{occ} \psi_i^* \boldsymbol{\sigma} \psi_i$ , where  $\psi_i$  are two-component spinors  $\psi_i = \begin{pmatrix} \psi_{i\alpha} \\ \psi_{i\beta} \end{pmatrix}$  and  $\boldsymbol{\sigma} = (\sigma_x, \sigma_y, \sigma_z)$  is the vector of the Pauli spin matrices. In the so-called “collinear approach” the vector  $\mathbf{m}(\mathbf{r})$  is projected on the  $z$ -axis to define the spin density  $s(\mathbf{r}) = m_S(\mathbf{r}) = \sum_i^{occ} \psi_i^* \boldsymbol{\sigma} \psi_i = \sum_i^{occ} (\psi_{i\alpha}^* \psi_{i\alpha} - \psi_{i\beta}^* \psi_{i\beta})$ . The total density is given by

$$\rho(\mathbf{r}) = \sum_i^{occ} \psi_i^* \psi_i = \sum_i^{occ} (\psi_{i\alpha}^* \psi_{i\alpha} + \psi_{i\beta}^* \psi_{i\beta}) \quad (8.51)$$

where positron states are excluded by employing the so-called no-sea approximation. The DKS equation is then the matrix pseudoeigenvalue equation by introducing basis set expansion as,

$$\hat{\mathbf{h}}^{DKS} \mathbf{C} = \mathbf{S} \mathbf{C} \mathbf{E} \quad (8.52)$$

where  $\hat{\mathbf{h}}^{DKS}$  takes the form of a Fock matrix

$$\mathbf{h}_{\mu\nu}^{DKS} = \begin{pmatrix} \mathbf{V}_{\mu\nu}^{LL} + \mathbf{J}_{\mu\nu}^{LL} - \mathbf{V}_{(XC)\mu\nu}^{LL} & c \boldsymbol{\Pi}_{\mu\nu}^{LS} \\ c \boldsymbol{\Pi}_{\mu\nu}^{SL} & \mathbf{V}_{\mu\nu}^{SS} + \mathbf{J}_{\mu\nu}^{SS} - \mathbf{V}_{(XC)\mu\nu}^{SS} - 2c^2 \mathbf{S}_{\mu\nu}^{SS} \end{pmatrix} \quad (8.53)$$

In (8.53)  $\mathbf{V}_{(XC)\mu\nu}^{XX}$  is the exchange-correlation potential defined by,

$$\mathbf{V}_{(XC)\mu\nu}^{XX} = \langle \chi_\mu^X | \frac{\delta E_{XC}}{\delta \rho} + \frac{\delta E_{XC}}{\delta \mathbf{m}(\mathbf{r})} | \chi_\nu^X \rangle \quad (8.54)$$

During the last decade, good progress was attained in four-component techniques for molecules (see [496, 502, 503] and references therein) that allowed one to reduce efforts in calculation and transformation of two-electron matrix elements with small components of four-component molecular spinors. The straightforward DHF and DKS methods with the four-component spinors were implemented in several *ab-initio* MO LCAO programs: MOLFDIR, [504], DIRAC, [505], BERTHA, [506]. However, fully relativistic DFT calculations on molecules containing more than one or two heavy atoms are not yet routine. The efficient computational scheme for the Gaussian-based fully relativistic DHF and DKS methods is proposed in [496] and applied to hydrides MH and dimers M<sub>2</sub> (M=Cu, Ag, Au).

As the fully relativistic (four-component) calculations demand severe computational efforts, several quasirelativistic (two-component) approximations have been proposed in which only large components are treated explicitly. The approaches with perturbative treatment of relativistic effects [507] have also been developed in which a nonrelativistic wavefunction is used as reference. The Breit–Pauli (BP) approximation uses the perturbation theory up to the  $(p/mc)^2$  term and gives reasonable results in the first-order perturbation calculation. Unfortunately, this method cannot be used in

variational treatment. One of the shortcomings of the BP approach is that the expansion in  $(p/mc)^2$  diverges in the case where the electronic momentum is too large, for example, for a Coulomb-like potential [496]. The zeroth-order regular approximation (ZORA), [509], can avoid this disadvantage by expanding in  $E/(2mc^2 - V)$  up to first order. The ZORA Hamiltonian is variationally stable. However, the Hamiltonian obtained by a higher-order expansion has to be treated perturbatively, similarly to the BP Hamiltonian.

Two recently developed quasirelativistic approaches are considered in [496]. In particular, in the RESC method (the relativistic scheme by eliminating small components) the Hamiltonian is separated into the spin-averaged (scalar relativistic, which can be called the one-component approximation) and spin-dependent parts. The RESC approach has several advantages. It is variationally stable. This method can easily be implemented in various nonrelativistic *ab-initio* programs, and the relativistic effect is considered on the same footing with the electron-correlation effect. RESC has been applied to various systems in ground and excited states. As the energy gradient of the RESC method is also available it is possible to study the chemical reaction in the heavy-element systems (as an example, the ionization of OsO<sub>4</sub> is considered in [496]).

While accurate relativistic (both four- and two-component) calculations of simple heavy-atom molecules can be performed on modern computers the relativistic calculations of periodic systems are made mainly using relativistic effective core potential (RECP). We consider these potentials in the next section.

### 8.3.2 Relativistic Effective Core Potentials

The two-component RECP approximation was suggested originally by Lee *et al.* [508] and is widely used in molecular calculations (see [487, 510, 511]). There are several reasons for using RECPs in calculations of complicated heavy-atom molecules, molecular clusters and periodic solids. As the nonrelativistic ECP approaches, the RECP approaches allow one to exclude the large number of chemically inactive electrons from calculations and treat explicitly only valence and outermost core electrons. The oscillations of the valence spinors are usually smoothed in heavy-atom cores simultaneously with exclusion of small components from the explicit treatment (quasirelativistic approximation). As a result, the number of primitive basis functions can be essentially reduced; this is especially important for calculation and transformation of two-electron integrals when studying many-atomic systems with very heavy elements including lanthanides and actinides. The RECP method is based on a well-developed earlier nonrelativistic technique of pseudopotential calculations; however, effective scalar-relativistic and spin-orbit interaction effects are taken into account by means of the RECP operator. Post-DHF correlation calculations with RECPs are performed in a natural way in the basis of spin-orbitals (and not of spinors as in all-electron four-component relativistic calculations) even for the cases when the Dirac–Coulomb–Breit(DCB) Hamiltonian is used [512]. Note, however, that the DCB technique with the separated spin-averaged and spin-dependent terms also has been developed [513], but it can be efficiently applied only in the cases when spin-dependent effects can be neglected both for valence and for core shells. In the RECP method, the interactions with the excluded inner core shells (spinors!) are described by spin-dependent potentials, whereas the explicitly treated valence and outer core shells can

be described by spin-orbitals. This means that some “soft” way of accounting for the core-valence orthogonality constraints is applied in the latter case [514]. Meanwhile, the strict core-valence orthogonality can be retrieved after the RECP calculation by using the restoration procedures described below. The use of the spin-orbitals allows one to reduce dramatically the expenses at the stage of correlation calculation. Thus, many complications of the DC or DCB calculations are avoided when employing RECPs.

When core electrons of a heavy atom do not play an active role, the effective Hamiltonian with RECP can be presented in the form

$$\mathbf{H}^{\text{Ef}} = \sum_{i_v} [\mathbf{h}^{\text{Schr}}(i_v) + \mathbf{U}^{\text{Ef}}(i_v)] + \sum_{i_v > j_v} \frac{1}{r_{i_v j_v}} \quad (8.55)$$

This Hamiltonian is written only for a valence subspace of electrons that are treated explicitly and denoted by indices  $i_v$  and  $j_v$  (large-core approximation). As in the case of nonrelativistic pseudopotentials, this subspace is often extended by inclusion of some outermost core shells for better accuracy (small-core approximation) but below we consider them as the valence shells if these outermost core and valence shells are not treated using different approximations. In (8.55),  $\mathbf{h}^{\text{Schr}}$  is the one-electron Schrödinger Hamiltonian

$$\mathbf{h}^{\text{Schr}} = -\frac{1}{2} \nabla^2 - \frac{Z_{ic}}{r} \quad (8.56)$$

where  $Z_{ic}$  is the charge of the nucleus decreased by the number of inner-core electrons.  $\mathbf{U}^{\text{Ef}}$  in (8.55) is an RECP (relativistic pseudopotential) operator that is usually written in the radially local (semilocal) [510] or separable [515] approximations when the valence pseudospinors are smoothed in the heavy-atom cores. In LCAO calculations of heavy-atom molecules among the radially local RECPs, the shape-consistent (or normconserving) RECP approaches [510] are employed and “energy-consistent” pseudopotentials by the Stuttgart–Dresden–Cologne group are also actively used [487, 511, 516]. The latter are now applied also in LCAO calculations of periodic systems with modified valence basis sets (see Sect. 8.3.5). To generate “energy-consistent” RECP the direct adjustment of two-component pseudopotentials is made (scalar-relativistic + spin-orbit potentials) to atomic total energy valence spectra. The latter is derived from the four-component multiconfiguration DHF all-electron atomic calculations based on the DCB Hamiltonian. The “energy-consistent” RECPs are now tabulated for all the elements of periodic table at the site [www.theochem.uni-stuttgart.de](http://www.theochem.uni-stuttgart.de). The adjustment of the pseudopotential parameters has been done in fully numerical atomic calculations, valence basis sets have been generated *a posteriori* via energy optimization. The complete set of potentials includes one-component (nonrelativistic and scalar-relativistic) effective-core potentials (ECP), spin-orbit (SO) and core-polarization potentials (CPP); only the one-component ECPs are listed in full. The “energy-consistent” pseudopotentials are under continuous development and extension [516, 517] and the corresponding Gaussian basis sets are published [518–520].

In plane-wave calculations of solids and in molecular dynamics, the separable pseudopotentials [93, 492, 515] are more popular now because they provide linear scaling of computational effort with the basis-set size in contrast to the radially local RECPs. Moreover, the nonlocal Huzinaga-type “*ab-initio* model potentials” [521–523] conserving the nodal structure for the valence spinors are often applied. Contrary to the

four-component wavefunction used in DC(B) calculations, the pseudowavefunction in the RECP case can be both two- and one-component. The RECP operator simulates, in particular, interactions of the explicitly treated electrons with those that are excluded from the RECP calculations. The use of the effective Hamiltonian (8.55) instead of all-electron four-component Hamiltonians leads to the question about its accuracy. It was shown both theoretically and in calculations, see [514], that the typical accuracy of the radially local RECPs is within  $1000\text{--}3000\text{ cm}^{-1}$  for transition energies between low-lying states though otherwise is sometimes stated, [481, 482].

In a series of papers [482, 514, 524, 525] a generalized RECP(GRECP) approach was developed that involves both radially local, separable and Huzinaga-type potentials as its components. Additionally, the GRECP operator can include terms of other types, known as “self-consistent” and two-electron “term-splitting” corrections [514], which are important particularly for economical (but precise!) treatment of transition metals, lanthanides and actinides. With these terms, the accuracy provided by GRECPs can be even higher than the accuracy of the “frozen-core” approximation (employing the same number of explicitly treated electrons) because they can account for relaxation of explicitly excluded (inner core) electrons [514]. In contrast to other RECP methods, GRECP employs the idea of separating the space around a heavy atom into three regions: inner core, outer core and valence, which are first treated by employing different approximations for each. It allows one to attain practically any desired accuracy for compounds of lanthanides, actinides, and superheavy elements as well, while requiring moderate computational efforts since the overall accuracy is limited in practice by possibilities of correlation methods.

### 8.3.3 One-center Restoration of Electronic Structure in the Core Region

It should be noted that calculation of such properties as spin-dependent electronic densities near nuclei, hyperfine constants, chemical shifts, *etc.* with the help of the two-component pseudospinors smoothed in cores is impossible. However, the above properties (and the majority of other “core-type” properties of practical interest that are described by the operators heavily concentrated within inner cores or on nuclei) are mainly determined by the electronic densities of the valence and outer core shells near to, or on, nuclei. The valence shells can be open or easily perturbed by external fields, chemical bonding, *etc.*, whereas outer-core shells are noticeably polarized (relaxed) in contrast to the inner-core shells. Therefore, accurate calculation of electronic structure in the valence and outer-core region is of primary interest for such properties. The electronic densities evaluated from the two-component pseudowavefunction very accurately reproduce the corresponding all-electron four-component densities in the valence and outer-core regions not only for the state used in the RECP generation but also for other states that differ by excitations of valence electrons. In the inner-core region, the pseudospinors are smoothed, so that the electronic density with the pseudowavefunction is not correct. When operators describing properties of interest are heavily concentrated near or on nuclei, their mean values are strongly affected by the wavefunction in the inner region. The proper shapes of the valence four-component spinors must, therefore, be restored in atomic core regions after performing the RECP calculation. The applicability of the above two-step algorithm for calculation of wavefunctions of systems containing heavy atoms is a consequence of

the fact that the valence and core electrons may be considered as two subsystems, interaction between which is described mainly by some integrated properties of these subsystems. The methods for consequent calculation of the valence and core parts of electronic structure give a way to combine the relative simplicity and accessibility both of RECP calculations in Gaussian basis set and of relativistic finite-difference one-center calculations inside a sphere with the atomic core radius. In 1959, a non-relativistic procedure of restoration of the orbitals from smoothed Phillips–Kleinman pseudo-orbitals was proposed [473] based on the orthogonalization of the latter to the original atomic core orbitals. In 1985, Pacios and Christiansen [526] suggested a modified orthogonalization scheme in the case of shape-consistent pseudospinors. At the same time, a simple procedure of “nonvariational” one-center restoration (NOCR) employing the idea of generation of equivalent basis sets in four-component DHF and two-component RECP/SCF calculations was proposed by Titov and first applied in the calculations of the PbF molecule. Later, the two-step RECP/NOCR calculations of the hyperfine structure constants and other properties were performed for the XF molecules and radicals, X=Pb,Yb,Ba [527–531], the TIF [532] and PbO [533, 534] molecules, and the molecular ion  $\text{HI}^+$ , [535]. In 1994, a similar procedure was used by Blöchl inside the augmentation regions [536] in solids to construct the transformation operator between pseudo-orbitals and original orbitals in his projector augmented-wave (PAW) method.

The NOCR scheme consists of the following steps [537]:

- Generation of *equivalent* basis sets of one-center four-component spinors  $\begin{pmatrix} f_{nlj}(r)\chi_{ljm} \\ g_{nlj}(r)\chi_{2j-l,jm} \end{pmatrix}$  and smoothed two-component pseudospinors  $\tilde{f}_{nlj}(r)\chi_{ljm}$  in finite-difference all-electron Dirac–Fock(–Breit) and RECP/SCF calculations of the same configurations of a considered atom and its ions. The  $\chi_{ljm}$  is the two-component spin-angular function, the  $f_{nlj}(r)$  and  $g_{nlj}(r)$  are the radial parts of the large and small components of Dirac spinors, respectively. The nucleus is usually modeled by a Fermi-charge distribution within a sphere. The all-electron four-component and two-component calculations are employed to generate two equivalent numerical basis sets used at the restoration. These sets, describing mainly the atomic core region, are generated independently of the basis set used for the RECP calculations.
- The molecular *pseudospinorbitals* from the RECP calculation are then expanded in the basis set of one-center two-component atomic *pseudospinors* (for  $r \leq R_{\text{nocr}}$ , where  $R_{\text{nocr}}$  is the radius of restoration that should be sufficiently large for calculating core properties with the required accuracy),

$$\tilde{\phi}_p(\mathbf{x}) \approx \sum_{l=0}^{L_{\text{max}}} \sum_{j=|l-1/2|}^{|l+1/2|} \sum_{n,m} c_{nljm}^p \tilde{f}_{nlj}(r) \omega_{ljm} , \quad (8.57)$$

where  $\mathbf{x}$  denotes spatial and spin variables

- Finally, the atomic two-component pseudospinors in the basis set are replaced by equivalent four-component spinors and the expansion coefficients from (8.57) are preserved:

$$\phi_p(\mathbf{x}) \approx \sum_{l=0}^{L_{\max}} \sum_{j=|l-1/2|}^{|l+1/2|} \sum_{n,m} c_{nljm}^p \begin{pmatrix} f_{nlj}(r) \omega_{ljm} \\ g_{nlj}(r) \omega_{2j-l,jm} \end{pmatrix}. \quad (8.58)$$

The four-component spinors constructed in this way are orthogonal to the inner-core spinors of the atom, because the atomic basis functions used in (8.58) are generated with the inner-core shells treated as “frozen”.

### 8.3.4 Basis Sets for Relativistic Calculations of Molecules

The fully relativistic (four-component) LCAO calculations of molecular systems use contracted Gaussian-type spinors as the basis: two scalar wavefunctions within a two-component basis spinor are multiplied by a common expansion coefficient, for dimensions  $n$  of both the large and small components the total number of variational parameters (the scalar expansion coefficients) is equal to  $2n$  [496]. In the relativistic correlated calculations the atomic basis sets should be optimized in the atomic correlated calculations. As Almlöf and Taylor showed [538], atomic basis sets optimized to describe correlations in atoms also describe correlation effects in molecules very well. The two main types of basis sets are used in correlation calculations of molecules: basis of atomic natural orbitals (ANO) suggested by Almlöf and Taylor [538]; correlation-consistent (CC) basis set suggested by Dunning [462].

Atomic natural orbitals  $\{\psi_p\}$  are obtained by unitary transformation of some set of orthonormal basis functions  $\{\phi_p\}$ . Natural orbitals diagonalize density matrix  $D_{ij}$  for some state (or group of the states) of the atom or its ions:

$$\rho(\mathbf{r}, \mathbf{r}') = \sum_{p,q} D_{pq} \phi_p^\dagger(\mathbf{r}) \phi_q(\mathbf{r}') = \sum_p n_p \psi_p^\dagger(\mathbf{r}) \psi_p(\mathbf{r}') \quad (8.59)$$

where  $n_p$  are *occupation numbers*. Only those  $\{\psi_p\}$  are selected in the ANO basis set for which  $n_p$  is greater than some threshold:  $n_p \geq n^{thr}$ ;  $n^{thr} \sim 10^{-3} - 10^{-5}$ .

Unlike the ANO scheme, the different number of primitive Gaussian functions are used in each basis set in the CC approach. Exponents of the polarization-correlation functions are optimized in correlation calculations of the atomic terms to provide the lowest possible total energy. It turns out that basis functions can be separated in groups and every function in each group lowers the total energy approximately by the same amount. Correlation-consistency means that whole groups of functions are added to the basis set, not just separate functions.

Both ANO and CC schemes have a number of advantages, *i.e.* the ANO basis set is relatively easy to construct and the smaller ANO basis is just a subset of the larger one. Advantages of the CC basis are the smaller number of the primitive functions and a natural criterion for estimation of the completeness of the basis set. The following disadvantages can be emphasized for CC and ANO basis sets:

- for *heavy atoms* with many electrons, the number of ANO and CC functions becomes too large to obtain satisfactory accuracy in transition energies and properties. Even for the light Ne atom, ANO basis sets obtained in correlation CI-SD calculation are [3s 2p 1d] with  $n^{thr} \sim 10^{-3}$  and [5s 4p 3d 2f 1g] for  $n^{thr} \sim 10^{-5}$ ;
- “occupation number-optimized” (ANO) or “energy-optimized” (CC) basis sets do not take into account special features of one or another property and do not reflect properly the state of the “atom-in-molecule”;

- the incompleteness of atomic basis sets with the change of internuclear distance leads to basis-set superposition error (BSSE). This error is usually corrected by a “counterpoise” correction [539] that is calculated rather arbitrarily (it depends, in particular, on the atomic state used for its calculation) for ANO and CC basis sets.

The generalization of the correlation-consistent scheme of the basis-set generation was suggested, see [524] and references therein, which allows one to control effectively the quality of the basis set in different space regions depending on the property of interest. Practically all properties can be divided into two groups: (1) “valence” properties, which are determined by the wavefunction in the valence region, like dissociation energy or transition energies and (2) “core” properties, which are described by operators heavily concentrated near the nuclei of the heavy atom, like the hyperfine structure. The calculations of the different kind of properties require, in principle, different optimization criteria for basis sets. The generalized correlation (GC) basis set is constructed in the following stages:

- 1 Generation of the trial spin-orbitals, two-component spinors or four-component spinors in the atomic SCF calculation with *numerical functions*. Functions are obtained in SCF calculations of the atom and its ions, thus trial functions are localized in valence or outer-core regions.
- 2 Criterion of choice of the optimal function is the *maximization* of some functional that depends on total energies of the states and transition energies between them. The energies of the states are obtained in some correlation calculation of the group of the states that describe an “atom-in-molecule” in the best way. The choice of the energetic functional is the key element of the GC-basis generation.
- 3 The resulting sets of functions are approximated by Gaussian functions with the same exponents for each  $l$  (or pair of  $lj$ ) by the least square fit.

A commonly used choice of the functional is:

$$\mathcal{F}_c(\Delta E_1, \dots, \Delta E_M) = \frac{1}{M} \sum_i^M \Delta E_i \quad (8.60)$$

Here,  $\mathcal{F}_c$  is the change in the average energy for some considered group of the lowest-lying terms.

The functional used in the GC generation scheme can be chosen as follows:

$$\mathcal{F}_v(\Delta E_1, \dots, \Delta E_M) = \max_{i>j}^M |\Delta E_i - \Delta E_j| \quad (8.61)$$

where  $M$  is the number of atomic terms,  $\Delta E_i \geq 0$  is the lowering of the total energy of the  $i$ th term in comparison to calculation without the given function. Thus,  $\mathcal{F}_v$  presents the maximal change in transition energies. (Some other versions of the functional on changes of transition energies can also be used but their results are not very different.)

Functional  $\mathcal{F}_c$  is reasonable to use for generation of the GC basis for “core” properties, while  $\mathcal{F}_v$  can be used when one is interested in “valence” properties. When only valence electrons are correlated, any functional can be used since the function giving the maximal change in total energy, as a rule, also provides the maximal change in

transition energies in this case. In a universal scheme, both of the above functionals can be applied together when  $\mathcal{F}_c$  is used in the first step to select the most important correlation functions and then,  $\mathcal{F}_v$  is used (see also [540] for a variational justification of the suggested functionals). If the effect of atomic polarization is important the GC basis can be augmented by diffuse polarization functions, whose exponents are optimized in the SCF calculation of an atom in an electric field. The valence basis sets, used in relativistic molecular calculations, have to be in correspondence with RECP used in the basis set optimization. As was already mentioned the basis sets corresponding to the “energy-consistent” RECP can be found on the site [www.theochem.uni-stuttgart.de](http://www.theochem.uni-stuttgart.de). Highly accurate relativistic Gaussian basis sets are developed for the 103 elements from H to Lr [544]. Orbital exponents are optimized by minimizing the atomic self-consistent field (SCF) energy with the scalar relativistic approximation. The basis sets are designed to have equal quality and to be appropriate for the incorporation of relativistic effects. The basis-set performance was tested by calculations on prototypical molecules, hydrides, and dimers of copper, silver, and gold using SCF, MP theory, and the single and double coupled-cluster methods. Spectroscopic constants and dissociation energies are reported for the ground state of hydrides, which agree well with the experimental data (the mean absolute error relative to the experiment in dissociation energy, equilibrium bond length and harmonic frequency is 0.09eV, 0.003 Å, and 2  $cm^{-1}$ , respectively). The optimized Slater-type basis sets for elements 1–118 are developed in [545]. The exponents of the Slater-type functions are optimized for the use in scalar-relativistic zero-order regular approximation (ZORA). These basis sets are used in DFT code ADF [345] for calculations of molecules and solids. The use of RECP and valence basis sets for periodic systems is considered in the next section.

### 8.3.5 Relativistic LCAO Methods for Periodic Systems

The influence of relativistic effects on the structural and electronic properties of the crystals with heavy elements is well known [541].

One important effect is the strong relativistic contraction of  $s$  and  $p$  orbitals due to the non-negligible probability to find them close to the nucleus; in turn  $d$  and  $f$  orbitals are stretched due to indirect relativistic effects. This largely affects the interatomic distances, the cohesive energies, the one-electron energies, *etc.* This effect can be partly handled within the scalar relativistic (SR) calculation, neglecting spin-orbit interaction. Another important relativistic effect is due to the spin-orbit coupling, which plays an essential role in the magnetic properties of solids [546]. The spin-orbit coupling requires more elaborate treatment beyond the SR calculations, *i.e.* the two- or four-component relativistic calculations.

The four-component DHF LCAO equations for 1D-, 2D- and 3D-periodic systems were at first presented by Ladik [547]. The resulting somewhat complicated generalized matrix eigenvalue equation for solids is described (for details we refer the reader to [547]). It was also shown for 1D and 2D systems how MP2 methods could be applied in their relativistic form. With the help of these, on the one hand, the total energy per unit cell (including correlation effects) can be computed. On the other hand, the relativistic band structure can also be corrected for correlation. Note that the symmetry of crystalline orbitals changes, compared with the nonrelativistic case, as the symmetry of the DHF Hamiltonian is described by double space groups. Finally,

a scheme is proposed in which most of the electrons are treated in the standard way (Dirac–Hartree–Fock equations with only Coulomb interactions and calculation of all the other terms with the aid of first-order perturbation theory), while for the core electrons of large- $Z$  atoms or ions, the generalized relativistic HF equations are used. Therefore, one applies the solutions of the generalized relativistic HF equations for the construction of the relativistic Slater determinant in the case of core electrons, while for the rest of the electrons the one-electron functions are obtained from the standard Dirac–Hartree–Fock equations. Unfortunately, the application of this fully relativistic theory (involving four-component spinors built in terms of a large and small component) is practically too difficult not only for solids but even for molecular systems (this application is limited to small-size molecules).

As was noted in the preceding sections the relativistic calculations of molecular systems are made in quasirelativistic (two-component) approximations based on Hamiltonians operating on the large component only. Between different alternatives to decouple large and small components for molecules and solids the Douglas–Kroll–Hess (DKS) approach [548, 549] is the most popular as this approach is variationally stable (and therefore can be incorporated into SCF calculations) and allows its accuracy to be improved [550]. In the DKS approach the decoupling of large and small components of the Dirac Hamiltonian is made through a sequence of unitary transformations

$$H_m = U_m U_{m-1} \cdots U_1 U_0 H_D U_0^\dagger U_1^\dagger \cdots U_{m-1}^\dagger U_m^\dagger \quad (8.62)$$

Each transformation  $U_n$  is chosen in such a way that the offdiagonal blocks of the Dirac Hamiltonian are zero to a given order in the potential. The decoupled, block-diagonal transformed Hamiltonian

$$H_n = \begin{pmatrix} H_{DKH_n}^L & O(V^n) \\ O(V^n) & H_{DKH_n}^S \end{pmatrix} \quad (8.63)$$

The large-component block,  $H_{DKH_n}^L$  is the two-component effective Hamiltonian to be included in the electronic-structure calculation. The order  $n$  of transformation can be systematically increased to improve the accuracy of transformation. Two classes of operators are involved in the construction of the  $DKH_n$  Hamiltonian: a function of the square of the momentum  $f(P^2)$ ,  $\mathbf{p} = -i\nabla$  and those involving the potential  $V, (\sigma\mathbf{p})V(\sigma\mathbf{p})$ , where  $\sigma$  are the Pauli spin-matrices [550]. The explicit form of  $H_{DKH_n}$  up to fifth order was derived in [551, 552]. The DKH approach leads to a two-component formalism, which is separable in a spin-averaged (spin-free) and spin-dependent part. In the scalar-relativistic (SR) approximation the spin-dependent part is ignored. The DKH transformation for the one-electron operators in scalar-relativistic HF LCAO calculations with periodic boundary conditions is used in [553] and implemented in CRYSTAL88 code. The fact that scalar-relativistic effects are short range was made use of so that the electrostatic potential calculated by the Ewald method was not relativistically corrected. The results of SR HF LCAO calculations [553] of silver halides  $\text{AgX}$  ( $\text{X}=\text{F}, \text{Cl}, \text{Br}$ ) with the fcc  $\text{NaCl}$  structure are presented in Table 8.6.

The reoptimized uncontracted correlation corrected basis sets were used. The diffuse exponents ( $< 0.04$ ) in the basis set for  $\text{Ag}$  were discarded. The results given in Table 8.6 demonstrate the influence of scalar-relativistic effects in the  $\text{AgX}$  crystals

**Table 8.6.** Scalar-relativistic effects in AgX (X=F, Cl, Br) crystals, [553]

Property	AgF	AgCl	AgBr	Ag
Lattice parameter (Å)	5.175 (5.191)	5.937 (5.990)	6.207 (6.260)	4.456 (4.546)
Binding energy (kJmol <sup>-1</sup> )	-371.2 (-407.5)	-385.9 (-417.7)	-333.4 (-362.8)	-53.0 (-39.4)
Bulk modulus (kbar)	459 (460)	306 (297)	273 (259)	298 (322)

properties (the results of nonrelativistic HF LCAO calculations are given in brackets, the binding energy is given with reference to the HF ground-state energies of the free atoms). It is seen that lattice parameters show small relativistic effects – they decrease (up to 2% for Ag) as compared to the nonrelativistic values. The binding energies demonstrate a remarkable bond destabilization (up to 8.9% for AgF and 34.5% for Ag as compared to the nonrelativistic values). Bulk moduli change up to 7.5% (for Ag). Though scalar-relativistic effects of silver compounds are expected to be relatively small (compared with the compounds of heavier elements), remarkable changes of the HF binding energy and of the bulk modulus are observed. We note that in the relativistic HF calculations the correlation effects are not included explicitly in the Hamiltonian (the correlation correction is included only in AO basis sets). In Table 8.7 properties of AgCl crystal are compared at various levels of theory. Table 8.7 demonstrates good agreement for the lattice parameter and bulk modulus between HF calculations with RECP (Hay–Wadt RECP is used) and the scalar (one-component) relativistic HF DKH approach. Slight differences are seen for the binding energy.

**Table 8.7.** Crystal properties of fcc AgCl at various levels of theory [553]

Method	Total energy (a.u.)	Lattice const. (Å)	Binding energy (kJ mol <sup>-1</sup> )	Bulk modulus (kbar)
Nonrel. HF	-5656.601	5.990	-417.7	297
Rel. HF	-5771.344	5.937	-385.9	306
HF RECP	-159.709	5.943	-376.5	307
DFT ECP	-160.870	5.610	-514.6	560
Exper.	–	5.510	-519.8	535

We noted that it is necessary to simultaneously include the relativistic and correlation effects in the Hamiltonian. Such inclusion for periodic systems is usually made in the relativistic DFT approaches.

The fully relativistic LCAO method for solids, based on the DKS scheme in the LDA approximation was represented in [541]. The basis set consists of the numerical-type orbitals constructed by solving the DKS equations for atoms. This choice of basis set allows the spurious mixing of negative-energy states known as variational collapse to be overcome. Furthermore, the basis functions transform smoothly to those in the nonrelativistic limit if one increases the speed of light gradually in a hypothetical way.

This is also an important feature to avoid the variational collapse. The proposed approach was applied to Au and InSb crystals. The basis functions were chosen so that they have enough variational flexibility: not only were used AOs of neutral atoms but also those of positive ions  $\text{Au}^+$ ,  $\text{Au}^{2+}$ ,  $\text{Au}^{3+}$ ,  $\text{In}^{2+}$ ,  $\text{Sb}^{2+}$ . In the comparison for Au the results of scalar- and two-component relativistic calculations (lattice constant and bulk modulus) indicates that the spin-orbit coupling plays a minor role in the structural properties of Au. The comparison of results of the relativistic calculations with those of the nonrelativistic calculations shows that the lattice constant is overestimated by 5% and the bulk modulus is underestimated by 35% in nonrelativistic calculations. This strongly shows the importance of the inclusion of the relativistic effects in the study of the structural properties of Au. In contrast with the case of Au, the results of nonrelativistic calculations of InSb are not so poor; the error in the lattice constant is 1% and the error in the bulk modulus is 10%. This should be due to the fact that In and Sb are not so heavy that the relativistic effects do not play an important role in studying the structural properties of InSb.

The implementation of scalar relativity in an all-electron LDA linear combinations of the Gaussian-type orbitals (LC-GTO) method for solids was reported by Boettger [542] and applied for crystalline Au with a fcc lattice. This initial implementation was later extended to include spin-orbit coupling terms, produced in the second-order DKH transformation. The GTO Au atomic basis set of  $19s14p10d5f$  primitive GTOs was derived from scalar-relativistic (SR) and nonrelativistic (NR) calculations of paramagnetic atom. These calculations show that bulk and one-electron properties obtained by the LCGTO method, are very close to those obtained with all-electron, scalar-relativistic DFT techniques using other basis sets (LAPW or LMTO SR methods). The efficiency of the LCGTO approximation in relativistic calculations of solids was demonstrated also in the calculations of equilibrium volumes and bulk moduli for the light actinides Th through Pu [555]. It is concluded that two independent (both scalar and quasirelativistic) electronic-structure DFT methods with the different choice of basis set (LCGTO and LAPW) are in good agreement with each other. Table 8.8 shows this agreement for fcc Th and Pu metals giving numerical values of the equilibrium volume  $V$  (a.u) and the bulk modulus  $B$  (GPa), for comparison also results of FPLMTO calculations are given. The agreement between LCGTO and FPLAPW results is important, keeping in mind the primary advantage of LCAO methods over other existing DFT approaches (FLAPW, FLMTO)- *the possibility of LCAO methods to treat both molecular and periodic systems and in this way to bridge the gap between quantum chemistry and solid-state physics.*

Comparison of the nonrelativistic and scalar-relativistic results for fcc Au reveals the large impact that relativity has on the lattice constant (6%) and bulk modulus (57%) [542]. The most important qualitative change in the band structure of fcc Au is the more than 2-eV lowering of the  $s$ -band relative to the bottom of  $d$ -bands. In addition, the overall width of the  $d$ -bands is increased by more than 15% due to a relativistic delocalization of the  $d$ -states. The spin-orbit coupling included LCGTO DFT-GGA calculations were made for fluorite structure actinide oxides  $\text{MO}_2$  ( $\text{M}=\text{Th}, \text{U}, \text{Pu}$ ) and their clean and hydroxylated surfaces, [556], magnetic ordering in fcc Pu [557] and bulk properties of fcc Pb [558].

In the calculations using nonrelativistic LCAO codes for solids the relativistic effects are included implicitly in RECPs and basis sets. In the relativistic calculations

**Table 8.8.** Equilibrium volume  $V$  (a.u) and bulk modulus  $B$  (GPa) for Th and Pu with FP-LMTO, LCGTO and FPLAPW calculations, using DFT LDA and GGA Hamiltonians, with and without spin-orbit (SO) effects included [555]. Experimental data for fcc Th:  $V=221.7$  a.u.,  $B=58$  GPa

		fcc Th				fcc Pu			
		LDA	+SO	GGA	+SO	LDA	+SO	GGA	+SO
FPLMTO	$V$	-	182.1	-	199.9	109.2	-	119.2	-
	$B$	82.6	61.5	-	-	214	-	143	-
LCGTO	$V$	200.5	199.3	216.9	214.8	111.5	125.7	121.2	141.4
	$B$	64.8	71.7	58.8	63.4	218	124	170	97
FPLAPW	$V$	199.7	204.1	219.3	218.1	111.9	120.2	122.3	133.4
	$B$	61.0	78.6	56.7	73.1	194	143	153	121

of periodic systems RECPs of the Stuttgart-Köln group (energy-consistent RECPs) are often applied. These RECPs (and the corresponding basis sets) are obtained in the relativistic DHF atomic calculations and are tabulated as the linear combination of GTFs, see [www.theochem.uni-stuttgart.de](http://www.theochem.uni-stuttgart.de). As was noted in Sect. 8.1, the basis sets generated for molecular calculations have to be adapted for the periodic systems calculations. As an example we mention the valence basis sets for lanthanide 4f-in-core relativistic pseudopotentials, adapted for crystal orbital *ab-initio* calculations [559]. The crystalline calibration calculations were made for  $\text{Ln}_2\text{O}_3$  ( $\text{Ln}=\text{La-Pm}$ ) crystals with hexagonal space group  $P3m1$  and one formula unit per cell. The calibration within the HF and DFT schemes was made using the CRYSTAL03 code [23]. To verify these basis sets the calculated geometries and cohesive energies were compared with experimental data. The valence basis sets adapted for crystal calculations restore the calculated cohesive energy of  $\text{Ln}_2\text{O}_3$  ( $\text{Ln} = \text{La-Nd}$ ) to more than 88% of the experimental data within the *a-posteriori* HF correlation scheme in combination with gradient-corrected functionals. Good agreement has also been found between the conventional DFT results and the experimental cohesive energy with a deviation of only a few per cent.

The implementation of the LCGTO relativistic two-component DKH approximation in a fully self-consistent all-electron DFT approach for molecules (this implementation requires changes to be made in the Hamiltonian [550]), allows the RECP results (when the nonrelativistic calculations are made with the use of relativistic pseudopotentials) to be compared with those obtained in scalar-relativistic and two-component relativistic calculations. Such a comparison was made in [560] for the bond dissociation energy in the  $\text{UF}_6$  molecule, obtained from the relative energies of the fragments ( $\text{UF}_6 = \text{UF}_5 + \text{F}$ ), corrected for zero-point energy and spin-orbit interaction. The small-core RECP PBE0 and B3LYP calculations give the bond-dissociation energy as 68.34 and 69.59 kcal/mole, respectively, all-electron two-component relativistic PBE0 and B3LYP calculations – the values 68.94 and 70.39 kcal/mole, while the experimental values are given between 69.5 and 73 kcal/mole. Note that the large-core RECP result is off by more than 50% so that to obtain a good agreement with experiment one needs to work with a hybrid density functional and small-core RECP.

This conclusion was taken into account in RECP calculations of crystals. RECP hybrid DFT calculations were made for PtO crystal [421]. For Pt, 60 core electrons  $[\text{Kr}]4d^{10}4f^{14}$  were replaced with the small-core relativistic Stuttgart–Dresden effective core potentials RECPs. A valence basis set was optimized for Pt considering  $5s$ ,  $5p$ ,  $5d$ ,  $6s$ , and  $6p$  orbitals. This basis set circumvents numerical linear dependencies in periodic calculations and it is of similar quality to the Stuttgart basis set for most practical applications. Benchmark calculations in PtO using the 6-31G(d), the 6-311G(d), and 8-411G(d) basis sets for oxygen showed that these three bases yielded similar results. RECPs of the Stuttgart group were also applied in periodic hybrid DFT calculations of  $\text{PuO}_2$ ,  $\text{Pu}_2\text{O}_3$  [422], PtN [420],  $\text{UO}_2$  [543].

The molecular calculations [550, 560] allow us to conclude that the DKH approximation in combination with hybrid DFT functionals provides a reliable tool for the prediction of structural and thermochemical properties of molecules.

The all-electron DFT LCAO approach with Gaussian basis sets was extended to scalar-relativistic calculations of periodic systems [561]. The approach is based on a third-order DKH approximation, and similar to the molecular case, requires only a modification of the one-electron Hamiltonian. The effective core Hamiltonian is obtained by applying the DKH transformation to the nuclear–electron potential  $V_N$ . Considering that relativistic effects are dominated by the short-range part of the Coulomb interaction, it is proposed to replace the nuclear–electron Coulomb operator used to build the DKH Hamiltonian by a short-range Coulomb operator

$$V^\zeta(\mathbf{r}) = -\frac{Z}{r} \text{erfc}(\zeta r) \quad (8.64)$$

where the complimentary error function screens the long-range tail of the potential. The use of the complimentary error function simplifies the calculation of the matrix elements between GTOs, but in general, any screening function could be employed. The correct nonrelativistic long-range behavior of the Coulomb operator is retained if the core Hamiltonian is defined as

$$H_{\text{core}} = H_{\text{DKHn}}^\zeta - V_N^\zeta + V_N \quad (8.65)$$

where the supraindex stands for quantities involving the short-range potential given by (8.64). The parameter  $\zeta$  switches from a Hamiltonian where only the free-particle (averaged) kinetic energy is relativistically corrected ( $\zeta \rightarrow \infty$ ), to the full-range DKHn Hamiltonian ( $\zeta = 0$ ). In this way, the relativistic term  $H_{\text{DKHn}}^\zeta - V_N^\zeta$  for periodic systems can be evaluated using  $V_N^\zeta$  and  $\mathbf{p}V_N^\zeta\mathbf{p}$  obtained by adding contributions from a finite number of cells in direct space. It should be pointed out that the summation of  $V_N^\zeta$  and  $\mathbf{p}V_N^\zeta\mathbf{p}$  for  $\zeta = 0$  diverges. The divergent term can be removed from the summation by adding a uniform charge-canceling background, as is usually done in Ewald-type summations. For the relativistic term  $H_{\text{DKHn}}^\zeta - V_N^\zeta$  the contribution from the uniform background is exactly zero, since the DKH transformation does not change a uniform potential. The choice of  $\zeta$  only affects the relativistic correction to the core Hamiltonian, while the nonrelativistic electrostatic contributions are entirely done using FMM, see Chap. 7. The tests on bulk systems by changing the value of  $\zeta$  from 0.05 a.u. to 0.5 a.u., showed that the lattice constants, bulk moduli, and bandgaps are rather insensitive to  $\zeta$  in this range [561], ( $\zeta = 0.1$  has been chosen in the discussed

calculations). In this approach, relativistic effects are included through the nucleus–electron interaction, while the electron–electron, Coulomb, the portion of Hartree–Fock exchange, and DFT exchange–correlation potential remain nonrelativistic. Such a strategy has been successfully employed for molecules and solids earlier.

The benchmark scalar-relativistic calculations [561] were made for the bulk metals (Pd, Ag, Pt and Au) and the large bandgap semiconductors AgF and AgCl. It was shown that scalar-relativistic effects reduce the lattice constant by 0.06–0.10 Å for the 4d metals (Pd and Ag), and by 0.14–0.22 Å for the 5d metals (Pt and Au). For the 4d metals, scalar-relativistic effects increase the calculated bulk moduli by 20–40 GPa, while for the 5d metals this increase is between 60 GPa and 100 GPa. For both AgF and AgCl crystals scalar-relativistic effects decrease the energy gap – by 1.0 eV for AgF and 0.9 eV for AgCl.

The DKH approach allows relativistic all-electron DFT calculations to be performed using the traditional LDA and GGA approximations, as well as meta-GGA and hybrid density functionals. Slater-type basis sets were used in the relativistic DFT calculations, based on the ZORA Hamiltonian and applied for heavy metals and their surfaces [562, 563].

Concluding this chapter we note that the relativistic correlated calculations of solids are mainly made in the DFT scheme. The post-DHF methods for solids wait their further development and implementation in computer codes for periodic systems.

## LCAO Calculations of Perfect-crystal Properties

In the next three chapters we illustrate the possibilities of LCAO methods in the calculations of different crystalline-solid properties.

We do not discuss here the electron–phonon and isotope effects on the optical spectra of solids. In [564, 565] these effects were studied in the framework of the tight-binding (TB) LCAO approach for several semiconductors with diamond and zincblende structure. The results reproduce the overall trend of the available experimental data for the bandgap as a function of temperature, as well as give correctly the mass dependence of the bandgap.

The TB approach represents a conceptual bridge between *ab-initio* simulations and model-potential ones. In particular, the coupling of TB with the molecular dynamics (MD) generates the TBMD method as a valuable tool for atomic-scale materials modeling [566]. A description of the TB method can be found, for example, in [6, 567].

In this chapter the perfect-crystal properties are considered: the analysis of chemical bonding on the basis of population analysis, the one-electron properties and properties, defined by the total energy and its derivatives and the magnetic ordering in crystals.

In Chap. 10 we discuss the models of crystals with point defects and calculation of their properties by LCAO methods.

In Chap. 11 the possibilities of LCAO methods in surface modeling are illustrated by numerous results of recent LCAO calculations.

We refer the reader to the very informative review article [568], where it is possible to find many illustrations of *ab-initio* simulation possibilities in the area of solid-state chemistry, physics, materials and surface science, and catalysis. This publication is especially useful as an introductory overview for the reader who is not acquainted with solid-state simulation. All the examples discussed in [568] have been generated with the CRYSTAL code and implemented by the authors and collaborators. CRYSTAL was the first periodic *ab-initio* code to be distributed to the scientific community beginning in 1989. Now, several *ab-initio* LCAO codes are available to users (see Appendix C), but the CRYSTAL code remains the most user-friendly and fast-developing code being applied now in more than 200 research groups in the world.

## 9.1 Theoretical Analysis of Chemical Bonding in Crystals

### 9.1.1 Local Properties of Electronic Structure in LCAO HF and DFT Methods for Crystals and Post-HF Methods for Molecules

Crystals, like molecules, are made up of atoms interacting with one another, which gives rise to electronic-density localization along bonds (covalent solids), around atomic nuclei (ionic crystals), or to the more complex and most widespread pattern of electronic-density distribution. Considered in Chap. 4, the density matrix of molecules and crystals in the LCAO approximation permits one to derive the local characteristics of the electronic structure employed usually when describing chemical bonding in molecules or crystals (the electronic configuration of an atom, atomic charges  $Q_A$ , atomic bond orders  $W_{AB}$  and covalency  $C_A$ , and the total and free atomic valences). In molecular quantum chemistry such calculations are known as population analysis. In molecular theory the local electronic-structure characteristics were introduced at first for the orthogonal atomic basis used in semiempirical ZDO calculations (see Chap. 6), with subsequent generalization to the case of a nonorthogonal basis employed in nonempirical HF and DFT calculations [96, 569, 570]. The first attempts at a theoretical determination of local electronic-structure characteristics of periodic systems were made later: for the orthogonal basis set used in semiempirical versions of the HF method in [571, 572] and for the nonorthogonal AO basis – in [573, 574]. Note that determination of local characteristics of electronic structure by traditional methods of solid-state physics, which make use, as a rule, of the plane-wave basis, requires special projection techniques (see Sect. 9.1.4), involving additional approximations to calculate electronic-density-matrix elements in an atomic basis.

The local properties of the electronic structure of a periodic system are defined by the density matrix  $\rho(\mathbf{R}, \mathbf{R}')$ , see (4.91); the electron position vectors  $\mathbf{R}$  and  $\mathbf{R}'$  vary within the basic domain of a crystal consisting of  $N$  primitive unit cells. For a one-determinant wavefunction the density matrix can be expressed through Bloch-type spin orbitals  $\psi_{i\mathbf{k}}^\sigma(\mathbf{R})(\sigma = \alpha, \beta)$ :

$$\rho(\mathbf{R}, \mathbf{R}') = \rho^\alpha(\mathbf{R}, \mathbf{R}') + \rho^\beta(\mathbf{R}, \mathbf{R}') = \sum_{\sigma} \sum_i^{\text{occ}} \sum_{\mathbf{k}} \psi_{i\mathbf{k}}^\sigma(\mathbf{R}) \psi_{i\mathbf{k}}^{\sigma*}(\mathbf{R}') \quad (9.1)$$

In the LCAO approximation

$$\psi_{i\mathbf{k}}^\sigma(\mathbf{R}) = \sum_{\mu} C_{i\mu\mathbf{k}}^\sigma \chi_{\mu\mathbf{k}}(\mathbf{R}) \quad (9.2)$$

$$\chi_{\mu\mathbf{k}}(\mathbf{R}) = \frac{1}{\sqrt{N}} \sum_n \exp(i\mathbf{k}\mathbf{R}_n) \chi_{\mu}(\mathbf{R} - \mathbf{R}_A - \mathbf{R}_n) \quad (9.3)$$

where  $\chi_{\mu}(\mathbf{R} - \mathbf{R}_A - \mathbf{R}_n) = \chi_{\mu}^{An}(\mathbf{R})$  is the atomic orbital centered on atom  $A$  in the primitive unit cell with a translation vector  $\mathbf{R}_n$ . In the basis of Bloch sums  $\chi_{\mu\mathbf{k}}(\mathbf{R})$  the overlap matrix  $S_{\mu\nu}(\mathbf{k})$  and density matrix  $P_{\mu\nu}(\mathbf{k})$  are introduced:

$$S_{\mu\nu}(\mathbf{k}) = \sum_n \exp(i\mathbf{k}\mathbf{R}_n) \int \chi_{\mu}^*(\mathbf{R} - \mathbf{R}_A) \chi_{\nu}(\mathbf{R} - \mathbf{R}_B - \mathbf{R}_n) d\mathbf{R} \quad (9.4)$$

$$P_{\mu\nu}^{\sigma}(\mathbf{k}) = \sum_i^{occ} C_{i\mu\mathbf{k}}^{\sigma*} C_{i\mu\mathbf{k}}^{\sigma} \quad (9.5)$$

The expansion coefficients  $C_{i\mu\mathbf{k}}^{\sigma}$  are calculated by solving the matrix equation of the CO LCAO method for crystals, see (4.67):

$$F^{\sigma}(\mathbf{k})C^{\sigma}(\mathbf{k}) = S(\mathbf{k})C^{\sigma}(\mathbf{k})E^{\sigma}(\mathbf{k}) \quad (9.6)$$

In (9.6)  $F^{\sigma}(\mathbf{k})$  is the matrix of the Hartree–Fock (HF) or Kohn–Sham (KS) operator. The former operator includes a nonlocal exchange part, depending on the density matrix  $\rho(\mathbf{R}, \mathbf{R}')$ , whereas the latter operator involves the electron density  $\rho(\mathbf{R}) = \rho(\mathbf{R}, \mathbf{R})$ , that is, it depends only on the diagonal elements of the density matrix, see Chapters 4 and 7.

In view of the translational symmetry of a crystal, one can introduce density normalization per primitive unit cell containing  $n$  electrons:

$$Sp(PS) = \frac{1}{N} \sum_{\mathbf{k}} \sum_{\mu} [P(\mathbf{k})S(\mathbf{k})]_{\mu\mu} = \sum_{\mu} (PS)_{\mu\mu}^{A0, A0} = n \quad (9.7)$$

The Mulliken population analysis may be extended to crystalline solids [573, 574, 576] giving the following definitions for an electronic population  $N_{A0}$  on an atom, atomic charge  $Q_{A0}$ , bond order  $W_{A0, Bn}$ , covalency  $C_{A0}$ , and the total valency  $V_{A0}$  ( $A0, Bn$  mean atom  $A$  in the reference unit cell and atom  $B$  in the unit cell with a translation vector  $\mathbf{R}_n$ ):

$$N_{A0} = \sum_{\mu \in A0} P_{\mu\mu}^{A0, A0} + \sum_{B \notin A0} R_{A0, B0} + \sum_{n \neq 0} \sum_{B} R_{A0, Bn} \quad (9.8)$$

where the overlap population is defined as

$$R_{A0, Bn} = \sum_{\mu \in A0} \sum_{\nu \in Bn} P_{\mu\nu}^{A0, Bn} S_{\nu\mu}^{Bn, A0} \quad (9.9)$$

and the atomic charge as

$$Q_{A0} = Z_{A0} - N_{A0} \quad (9.10)$$

In (9.10)  $Z_{A0}$  is the nuclear charge for the all-electron calculation or the core charge if the pseudopotential approximation is used. The bond order and covalency are

$$W_{A0, B0} = \sum_{\mu \in A0} \sum_{\nu \in Bn} \left[ (PS)_{\mu\nu}^{A0, Bn} (PS)_{\nu\mu}^{Bn, A0} + (P^s S)_{\nu\mu}^{A0, Bn} (P^s S)_{\nu\mu}^{Bn, A0} \right] \quad (9.11)$$

$$C_{A0} = \sum_{B \neq A0} W_{A0, B0} + \sum_{n \neq 0} \sum_{Bn} W_{A0, Bn} = 2N_{A0} - W_{A0, A0} \quad (9.12)$$

In (9.11),  $P = P^{\alpha} + P^{\beta}$  and  $P^s = P^{\alpha} - P^{\beta}$ . In deriving (9.12) the idempotency relation for the density matrix in the nonorthogonal AO basis  $(PS)^2 = 2(PS) - (P^s S)^2$  was used (see (4.130)). Equations 9.11 and 9.12 are applied in unrestricted HF (UHF) or spin-polarized (SP)KS calculations. For the closed-shell case (RHF and KS calculations)  $P^{\alpha} = P^{\beta}$  and  $P^s = 0$ .

The definition of the total valency of the atom accounting for both the ionic (electrovalence) and covalent (covalence) components of chemical bonding was suggested

in [571] for molecular systems and extended to crystalline solids in [572]. The atomic total valence is of the form

$$V_{AO} = \frac{1}{2} \left( C_{AO} + \sqrt{C_{AO}^2 + 4Q_{AO}^2} \right) \quad (9.13)$$

To study the influence of the correlation effects on the local properties of electronic-structure DFT or post-HF methods can be used. If the KS equations are solved the definitions (9.8)–(9.13) of local properties include the correlated density matrix and therefore take into account the correlation effects.

We note that there are no rigorous quantum-mechanical definitions for the local characteristics of the electronic structure. The definitions given above require the LCAO approximation, and the numerical results depend on the choice of atomic basis. In attempting to separate an atomic subsystem or a molecular subsystem in systems with a strong coupling, we should refuse to describe this subsystem by using pure states, which leads to considerable conceptual and computational problems. For example, an atomic subsystem in a molecular system, as a rule, cannot be assigned a certain integral number of the electrons involved (the calculated atomic electronic population (9.8) is noninteger), which implies that this subsystem should be represented by an ensemble of states matched by different numbers of electrons. However, an approach exists that gets around the above difficulties. This approach rests on the analysis of reduced density matrices (as a rule, these are the first-order and second-order matrices) of a system as a whole, and the separation of a particular subsystem is generally based on some geometric criteria. This makes it possible to considerably simplify computations, but leads to some arbitrariness in the choice of the definitions for local characteristics of the electronic structure.

This arbitrariness most clearly manifests itself in going beyond the scope of the HF approximation, as evidenced by a wide variety of definitions for molecular systems available in the literature for valences and bond orders in the case of post-Hartree–Fock methods for molecular systems [570, 578–580]. In post-HF methods local characteristics of molecular electronic structure are usually defined in terms of the first-order density matrix and in this sense there is no conceptual difference between HF and post-HF approaches [577]. It is convenient to introduce natural (molecular) spin orbitals (NSOs), *i.e.* those that diagonalise the one-particle density matrix. The first-order density matrix in the most general case represents some ensemble of one-electron states described by NSOs

$$\rho = \sum_{i=1}^{2n} \lambda_i |\psi_i\rangle\langle\psi_i| \quad (9.14)$$

where  $\lambda_i$  are the NSO occupation numbers so that  $\sum_{i=1}^{2n} \lambda_i = N$ ,  $\lambda_i \geq 0$  for all  $i = 1, 2, \dots, 2n$  and the characteristic feature of the HF case is that exactly  $N$  weights  $\lambda_i$  in this expansion are equal to 1 (due to the normalization condition, the remaining  $(2n - N)$  should be equal to 0). Here,  $N$  is the total number of electrons. In geometric terms, this property of the HF density matrix means that it is a projector on the subspace of occupied NSO or, equivalently, that the  $N$ -electron state is described by a single-determinant wavefunction. In any post-HF method, based on the wavefunction formalism, the coefficients in expansion (9.14) satisfy the representability conditions:

$0 \leq \lambda_i \leq 1$ . Some of these coefficients can be close to 1 (strongly occupied NSO) and some close to 0 (weakly occupied NSO), but in any case the post-HF density matrix loses its property  $\rho^2 = \rho$ . Turning to the basis of natural orbitals (NOs) results in the appearance of two spin components of the density matrix,  $\rho^\alpha$  and  $\rho^\beta$ . For RHF, ROHF, and UHF cases, these spin components are idempotent, being projectors on the subspace of the full MO space spanned by the occupied  $\sigma$ -MOs ( $\sigma = \alpha, \beta$ ). The density operator is the Hermitian positive-semidefinite operator with a spur equal to the number of electrons. At the same time, in general, this operator does not possess any other specific properties such as, for example, idempotency. After the convolution over the spin variables, the density operator breaks down into two components whose matrix representation in the basis set of atomic orbitals (AOs) has the form

$$\hat{\rho}^\sigma \chi_\mu = \sum_{\nu=1}^n \chi_\nu (P^\sigma S)_{\nu\mu} \quad (9.15)$$

where  $S$  is the AO overlap matrix, and the matrix elements of the  $P^\sigma$  matrix are related to the occupation numbers and the coefficients  $C_{i\mu}^\sigma$  in the expansion of the spatial parts of natural spin orbitals in the AO basis set through the expressions

$$P_{\mu\nu}^\sigma = \sum_{i=1}^n C_{i\mu}^\sigma \lambda_i^\sigma (C_{\nu i}^\sigma)^* \quad (9.16)$$

In principle, it is not difficult to define the  $\sigma$ -occupancy of the atomic subspace (subspace spanned by AOs of atom A). To this end it is sufficient to calculate

$$N_A^\sigma = Sp [\hat{\rho}^\sigma \hat{\rho}_A] \quad (9.17)$$

where  $\hat{\rho}_A$  is the projector on the subspace of atom A. This value gives us a certain measure of immersion of atom A subspace into the subspace of  $\sigma$ -occupied NOs. Such a definition, however, is not satisfactory because due to the nonorthogonality of the AO basis the sum of occupancies will be greater than the total number of electrons. A reasonable approach consists of turning to the so-called biorthogonal basis  $\tilde{\chi}_\mu$  and introducing the atomic projector as

$$\hat{\rho}_A = \sum_{\mu \in A} |\chi_\mu\rangle \langle \tilde{\chi}_\mu| \quad (9.18)$$

where  $\tilde{\chi} = \chi S^{-1}$  and  $\langle \chi_\mu | \tilde{\chi}_\mu \rangle = \delta_{\mu\nu}$ . Operator (9.18) is idempotent and Hermitian.

Let the atomic basis set be well localized on atoms (or the atomic fragments under consideration) and be orthonormal. The unit operator can be expanded as

$$\hat{I} = \sum_A \hat{\rho}_A \quad (9.19)$$

This operator has a unit matrix with respect to the AO basis set and can be used as the right identity in manipulations in AO basis. In particular,

$$Sp \hat{\rho}^\sigma = \sum_A Sp \hat{\rho}^\sigma \hat{\rho}_A = N^\sigma \quad (9.20)$$

With such definitions, the total electron occupancy of atom  $A$  is calculated as

$$N_A = N_A^\alpha + N_A^\beta = \sum_{\sigma} \text{Sp} \hat{\rho}^{\sigma} \hat{\rho}_A = \sum_{\sigma} \sum_{\mu \in A} (P^{\sigma} S)_{\mu\mu} \quad (9.21)$$

In order to determine the two-center bond order, it is reasonable to attempt to obtain the expansion similar to (9.20), but for the squares of the density-operator components. Unfortunately, in the general case, the spur of the density operator squared  $\text{Sp}(\hat{\rho}^2) = \sum_{\sigma} \text{Sp}(\hat{\rho}^{\sigma})^2$  depends on both the AO basis set and the computational technique and can be treated as a certain characteristic of a system only with the very large basis sets and full configuration interaction. Furthermore, even in this limiting case, the physical meaning of the given characteristic is not quite clear. However, instead of the  $\sigma$ -components of the density operator, it is possible to consider their combinations  $\hat{\rho}^{\alpha+\beta} = \hat{\rho}^{\alpha} + \hat{\rho}^{\beta}$  and  $\hat{\rho}^{\alpha-\beta} = \hat{\rho}^{\alpha} - \hat{\rho}^{\beta}$  that are referred to as the total electron and spin density operators, respectively, and to examine the contributions to the squares of these operators. Both approaches are consistent with each other and with the standard analysis within the Hartree–Fock approximation for occupied shells when one uses the expansion of the doubled sum of the density-operator  $\sigma$ -components squared

$$\sum_{\sigma} \text{Sp}(\hat{\rho}^{\sigma})^2 = \sum_{\sigma} \sum_{A,B} \text{Sp} \hat{\rho}^{\sigma} \hat{\rho}_A \hat{\rho}^{\sigma} \hat{\rho}^B = \sum_{\sigma} \sum_{A,B} \sum_{\substack{\mu \in A \\ \nu \in B}} (P^{\sigma} S)_{\mu\nu} (P^{\sigma} S)_{\nu\mu} \quad (9.22)$$

The quantities

$$W_{AB} = 2 \sum_{\sigma} \sum_{\substack{\mu \in A \\ \nu \in B}} (P^{\sigma} S)_{\mu\nu} (P^{\sigma} S)_{\nu\mu} \quad (9.23)$$

at  $B \neq A$  can be interpreted as certain characteristics of bond  $A - B$  order. Their sum

$$C_A = \sum_{B \neq A} W_{AB} \quad (9.24)$$

may be treated as the covalence of  $A$  atom. The one-center terms  $F_A = W_{AA}$  in (9.23) are termed the free (nonrealized) valence of atom  $A$ .

The results obtained in post-HF methods for solids refer mainly to the energy of the ground state but do not provide the correlated density matrix. The latter is calculated for solids in the one-determinant approximation. The density matrix calculated for crystals in RHF or ROHF one-determinant methods describes the many-electron state with the fixed total spin (zero in RHF or defined by the maximal possible spin projection in ROHF). Meanwhile, the UHF one-determinant approximation formally corresponds to the mixture of many-electron states with the different total spin allowed for the fixed total spin projection. Therefore, one can expect that the UHF approach partly takes into account the electron correlation. In particular, of interest is the question to what extent UHF method may account for correlation effects on the chemical bonding in transition-metal oxides. An answer to this question can be obtained in the framework of the *molecular-crystalline approach*, proposed in [577] to evaluate the correlation corrections in the study of chemical bonding in crystals.

Conceptually, the method is as follows. The local characteristics of a crystal electronic structure are calculated within the periodic model by the Hartree–Fock method

to choose the molecular cluster that adequately describes the local features of the electronic structure. In the majority of cases, the number of atoms comprising this cluster is appreciably less than the number of atoms contained in the clusters simulating one-electron states in a crystal. At the next stage of the advanced approach, the chosen cluster is calculated in the framework of the multiconfigurational approximation using the molecular programs providing the expansion of wavefunctions into determinants. Then, by applying the UHF method to the calculations of the cluster and the crystal, one can obtain the one-determinant solutions, which correspond to the generalized valence bonds. Simple rearrangements of the multiconfigurational cluster function permit one to explicitly separate the obtained valence bonds in its expansion. If these valence bonds turn out to be dominant in the expansion, then, in order to construct the many-electron function of a crystal, it is sufficient to replace the cluster valence bonds by the crystal valence bonds. Thus, the constructed wavefunction explicitly includes the electron-correlation effects. By convoluting the many-particle density matrix into two- and one-particle density matrices, it is possible to calculate the local characteristics of chemical bonding in a crystal by the known formulas.

In Sect. 9.1.3 we discuss the results of such an approach for application to the  $\text{Ti}_2\text{O}_3$  crystal with the open-shell configuration  $d^1$  of the  $\text{Ti}^{3+}$  ion. It is common knowledge that the electron correlation can play an important role in compounds of transition metals with an unfilled  $d$  electronic shell. The density-functional method (LDA or GGA), which has been widely employed for these crystals, often appears to be unsatisfactory because of an incorrect description of the self-interaction, see Chap. 7.

### 9.1.2 Chemical Bonding in Cyclic-cluster Model: Local Properties of Composite Crystalline Oxides

The above formalism for calculation of local electronic-structure characteristics of crystals was at first applied in the cyclic-cluster CNDO semiempirical calculations [571] of composite crystalline oxides with the metal atom oxidized to various degrees. In chemistry the oxidation state is a measure of the degree of oxidation of an atom in a chemical compound. It is the hypothetical charge that an atom would have if all bonds to atoms of different elements were 100% ionic. Metal oxidation states are positive and denoted by I, II, III for oxidation states one, two, three, respectively. It should be remembered that the oxidation state of an atom does not represent the “real” charge on that atom: this is particularly true of high oxidation states, where the ionization energies required to produce a multiply positive ion are far greater than the energies available in chemical reactions. The assignment of electrons between atoms in calculating an oxidation state is purely a formalism, albeit a useful one for the understanding of many chemical reactions. It was shown [306] that it is the full atomic valence (9.13) that correlates and in many cases is numerically close to the oxidation state. Usually, composite oxides of heavy-metal atoms crystallize in structures with low-symmetry space groups and contain many atoms in their unit cell. Due to the large atomic (or ionic) radii of the metallic atoms these compounds have both nontypical metal–oxygen bond lengths and atomic coordination numbers. As a rule, the constituent heavy-metal elements exhibit a different oxidation state. The

variable valence of the metal atoms makes the formation of oxides with a different chemical compositions (simple, composite and miscellaneous oxides) possible. The simple oxides contain metal atoms with constant valence (for example,  $\text{Cu}_2\text{O}$ ,  $\text{La}_2\text{O}_3$  etc.). However in miscellaneous oxides the metal atoms of the same chemical elements occur in the different oxidation states (for example,  $\text{Fe}_3\text{O}_4$ ,  $\text{Cu}_4\text{O}_3$ ). The heavy-metal oxides may lose or acquire oxygen atoms forming a defective crystalline structure and nonstoichiometric compounds.

Unlike light-metal oxides, the investigation of the electronic structure of crystalline heavy-metal oxides is a difficult task because of their composite crystal structure. Thus, it is necessary to use approximations both for the crystal-structure description and for the choice of one-electron Hamiltonian.

It is necessary to investigate the electronic structure of defect-containing metal oxides to understand their physical and chemical properties. However, the first step of such an investigation is connected with the calculation of the electronic structure of perfect nondefective crystal. The analysis of ionic and covalent components of the chemical bonding in perfect crystal allows one to propose realistic models describing the defects in these compounds.

The calculations of local properties of metal-oxide electronic structure [571, 581–583] were made in the cyclic-cluster model, in the CNDO approximation. As in the CNDO approximation AOs are supposed to be orthogonalized by the Löwdin procedure (see Chap. 6), the definitions of local properties given in Sect. 9.1.1 for nonorthogonal basis, have to be modified. In particular, the overlap population (9.9) becomes zero in the CNDO approximation, so that the electronic population is defined only by diagonal density matrix elements  $P_{\mu\mu}^{A0, A0}$ . In (9.6) and in the bond-order definition (9.11) the overlap matrix has to be replaced by an identity matrix. The matrix elements of the cyclic-cluster Hamiltonian are given by (6.61), (6.62) and depend on the semiempirical one-center parameters  $\beta_M$ ,  $U_{\mu\mu}$ ,  $\gamma_{MM}$  and two-center Coulomb integrals  $\gamma_{MN}$ . The one-center parameters for the light elements with  $s$  and  $p$  valence electrons have been taken from [584], where these parameters were calibrated for molecular calculations. The one-center parameters for copper, lead, nickel and lanthanum atoms were calibrated so that the results of the electronic-structure calculations correlate well with the experimental data for the simple oxides of these elements. The Coulomb integrals  $\gamma_{MN}$  were estimated from the one-center  $\gamma_{MM}$  and  $\gamma_{NN}$  Coulomb integrals using Ohno's approximation [239]. The numerical values of the bonding parameters  $\beta_{MN}$  are connected with the choice of the atomic basis functions. As the double-dzeta atomic functions of the neutral atoms were used the bonding parameters  $\beta_M$  for the light elements were recalibrated as their values in [584] correspond to Slater single-dzeta atomic functions. The bonding parameter  $\beta_{MN}$  was taken to be equal to  $\sqrt{\beta_{MM}\beta_{NN}}$  as is done in many molecular calculations. The numerical values of CNDO parameters of atoms are given in Table 9.1. The details of their choice for actual atoms can be found in [571]. The crystal structures of the considered composite metal oxides are given in Table 9.2 (the references to the corresponding experimental data can be found in [571]). The calculated atomic charges and full atomic valencies are given in Table 9.3 for nonequivalent (not connected by the symmetry transformations) atoms, both with variable valence ( $\text{Cu}, \text{Pb}, \text{Ni}$ ) and constant valence (oxygen and metal atoms  $\text{Me}$  in different oxidation states).

**Table 9.1.** CNDO semiempirical parameters of atoms used in crystalline metal oxides calculations (in eV)

Element	$\gamma_{MM}$	$U_{ss}$	$U_{pp}$	$U_{dd}$	$\beta_M$
Li	3.47	-4.99			-1.8
O	13.63	-101.31	-84.287		-17.0
K	3.70	-4.15			-1.8
Cu	17.20	-162.23		-171.46	-8.4,-14.6
Sr	3.75	-9.43			-1.8
Y	8.50	-20.80		-22.80	-5.8
Ba	4.20	-10.30			-1.8
La	7.30	-15.08		-19.08	-5.0
Pb	4.30	-26.30	-21.500		-7.7
Ni	17.00	-140.90		-149.00	-5.0,-10.0

For comparison the crystallographic valencies in copper–oxide compounds, calculated for the experimental bond lengths, are given in brackets.

The crystallographic valence (CV) of the  $i$ th atom in a crystal is defined as the sum

$$\tilde{V}_i = \sum_j B_{ij} \quad (9.25)$$

where the summation is performed over all the atoms with charge opposite in sign to that of the  $i$ th atom and  $B_{ij}$  is the so-called bond valence of the  $i$ th and  $j$ th atoms. It has been found that in acid–base networks the bond valence  $B_{ij}$  correlates well with the bond length  $R_{ij}$  and can be approximated by the inverse power or logarithmic function,

$$B_{ij} = (R_{ij}/R_0)^{-N} \quad (9.26)$$

$$B_{ij} = \exp \left[ -\frac{R_{ij} - R_0}{B} \right] \quad (9.27)$$

The fitted constants  $N$ ,  $R_0$  and  $B$  depend only on the nature of the bonded atoms ( $i, j$ ) and are given in the literature [585, 586] or may be calculated by the computer code VALENCE [587] designed to calculate bond valences from bond lengths and *vice versa*. This code allows also calculation of bond–valence sums and average bond lengths, and can determine bond–valence parameters from the bonding environments of different cations.

The numerical values of parameters  $N$ ,  $R_0$  and  $B$  are usually found by fitting the crystallographic valence  $\tilde{V}_i$  to the mean value of the stoichiometric atomic valence in the row of the simplest crystals containing the  $i$ th atom. One has to be careful in interpreting the bond–valence sums. The drawbacks of the CV definition are evident:

1. only the central part of the typical valence–bond length curve may be approximated by (9.26) and (9.27);
2. the real interaction between two atoms in a crystal depends not only on the interatomic distance between atoms, but also on the covalent or ionic character of the formed chemical bonding (in some cases this is taken into account by introducing

**Table 9.2.** The crystal structure of metal oxides ( $Z$  is the number of formula units in the unit cell)

Compound	Space group	$Z$	Cu,Pb,Ni	Me	O
$\text{Cu}_2\text{O}$	$Pm\bar{3}m$	2	4b		2a
$\text{YCuO}_2$	$R\bar{3}m$	3	3a	3b	6c
$\text{LaCuO}_2$	$R\bar{3}m$	3	3a	3b	6c
$\text{CuO}$	$C2/c$	4	4c	4e	
$\text{NiO}$	$R\bar{3}m$	3	3a		3b
$\text{Cu}_4\text{O}_3$	$I4_1/adm$	4	8c,8d		4a,8e
$\text{Li}_2\text{CuO}_2$	$Immm$	2	2b	4j	4i
$\text{SrCuO}_2$	$Cmcm$	4	4c	4c	4c,4c
$\text{Sr}_2\text{CuO}_3$	$Immm$	2	2d	4f	2a,4f
$\text{MgCu}_2\text{O}_3$	$Pmmm$	2	4e	2a	2b,4e
$\text{Y}_2\text{Cu}_2\text{O}_5$	$Pn2_1a$	4	4a,4a	4a,4a	4a,4a,4a,4a,4a
$\text{NaCuO}_2$	$P\bar{1}$	1	1a	1h	2i
$\text{KCuO}_2$	$Cmcm$	4	4c	4c	8f
$\text{LaCuO}_3$	$R\bar{3}c$	6	6b	6a	18e
$\text{La}_2\text{O}_3$	$P\bar{3}m1$	3		6d	3a,6d
$\text{La}_2\text{CuO}_4$ orth					
$\text{La}_2\text{NiO}_4$ orth	$Cmca$	4	4a	8f	8e,8f
$\text{La}_2\text{CuO}_4$ tetr					
$\text{La}_2\text{NiO}_4$ tetr	$I4/mmm$	1	1a	2e	2c,2e
$\text{YBa}_2\text{Cu}_3\text{O}_6$	$P4/mmm$	1	1a,2g	Y:1d Ba:2h	4i,2g
$\text{YBa}_2\text{Cu}_3\text{O}_7$	$Pmmm$	1	1a,2q	Y:1h Ba:2t	1e,2s,2r,2q
$\alpha\text{-PbO}$	$P4/mnm$	2	2c		2a
$\beta\text{-PbO}$	$Pbcm$	4	4d		4d
$\alpha\text{-PbO}_2$	$Pbcn$	2	4c		8d
$\beta\text{-PbO}_2$	$P4/mnm$	4	2a		4f
$\text{Pb}_2\text{O}_3$	$P2_1/a$	4	4e,4e		4e,4e,4e
$\text{Pb}_3\text{O}_4$	$P4_2/mbc$	4	4d,8h		8g,8h

additionally the dependence of the fitting parameters on the oxidation states of bonded atoms).

Nevertheless, the crystallographic valence has a number of practical applications, in particular in the determination of crystal structures or identifying elements that cannot be distinguished by X-ray diffraction. The fitting parameters values for CV given in Table 9.3 were taken from [588].

It can be seen that the CVs of atoms correlate on the whole with their full atomic valence  $V$  and oxidation state in the compounds considered. However, the dispersion of CV values is large for an atom with the same oxidation state in different crystals. For example, the CV of the oxygen atom appears to be in the interval 1.5 to 2.6. The CV approach was used by some authors to find the copper oxidation states in high-temperature superconductors [585]. However, as a rule, these compounds have

**Table 9.3.** Atomic charges and full atomic valencies in crystalline metal oxides\*

Crystal	Atomic charges			Full atomic valencies				
	Cu, Pb, Ni	O1	O2	Me	Cu, Pb, Ni	O1	O2	Me
Cu <sub>2</sub> O	0.97	-1.94			1.03 (1.29)	2.00 (2.58)		
YC <sub>u</sub> O <sub>2</sub>	0.99	-1.59		2.18	1.08	2.03	3.06	
LaCuO <sub>2</sub>	0.97	-1.73		2.49	1.02 (1.25)	2.01 (2.16)	3.03 (3.07)	
CuO	1.60	-1.60			2.18 (2.04)	2.01 (2.04)		
NiO	1.87	-1.87			2.00	2.00		
Cu <sub>4</sub> O <sub>3</sub>	0.96	1.57	-1.72	-1.56	1.02 (1.25)	2.11 (1.99)	2.00 (2.15)	2.01 (2.17)
Li <sub>2</sub> CuO <sub>2</sub>	1.43	-1.71		0.99	1.92 (1.84)	1.99 (1.99)	1.00	
SrCuO <sub>2</sub>	1.43	-1.60		-1.74	1.90 (2.01)	1.98 (2.08)	2.00 (1.80)	1.99 (1.87)
Sr <sub>2</sub> CuO <sub>3</sub>	1.38	-1.84			1.99 (1.90)	1.81 (1.82)	1.99 (2.16)	1.97 (1.96)
MgCu <sub>2</sub> O <sub>3</sub>	1.31	-1.49			1.98	1.72 (2.01)	2.01 (1.98)	2.00
Y <sub>2</sub> Cu <sub>2</sub> O <sub>5</sub>	1.59	1.67	-1.20	-1.32	1.68 2.25	2.29 2.09	2.06 3.13	
			-1.58	-1.32	1.67		2.02 2.06	3.14
			-1.18				2.10	
NaCuO <sub>2</sub>	1.89	-1.44			0.99 (2.52)	2.56 (1.91)	2.01 (1.29)	
KCuO <sub>2</sub>	2.08	-1.54			0.99 (2.50)	2.73 (1.73)	2.00 (0.95)	
LaCuO <sub>3</sub>	2.19	-1.54			2.45 (2.96)	2.82 (1.90)	2.02 (2.75)	
La <sub>2</sub> O <sub>3</sub>			-1.68, -1.60		2.43		2.01 2.03	3.02 3.03
La <sub>2</sub> CuO <sub>4</sub> orth	1.56		-1.52, -1.54		2.28	2.18 (2.38)	2.00 (2.19)	1.98 (1.67)
La <sub>2</sub> NiO <sub>4</sub> orth	1.86		-1.76, -1.65		2.45	2.01	2.00	3.00
La <sub>2</sub> CuO <sub>4</sub> tetr	1.70		-1.61, -1.63		2.39	2.38 (2.45)	2.01 (2.28)	1.98 (1.46)
La <sub>2</sub> NiO <sub>4</sub> tetr	1.88		-1.76, -1.67		2.48	2.01	2.00	3.00
YBa <sub>2</sub> Cu <sub>3</sub> O <sub>6</sub>					Y:2.44	1.00 (1.42)	2.00 (1.94)	3.03
Cu–O chains	0.97		-1.97			2.12 (2.12)	2.01 (2.13)	(2.89)
Cu–O planes	1.57		-1.65					
YBa <sub>2</sub> Cu <sub>3</sub> O <sub>7</sub>					Y:2.44	2.66 (2.21)	1.99 (1.87)	3.03 (2.00)
Cu–O chains	2.04		-1.78, -1.64					
Cu–O planes	1.52		-1.74, -1.51			2.06 (2.13)	2.01 (2.03)	1.99 (2.03)

to be continued

Crystal	Atomic charges				Full atomic valencies			
	Cu, Pb, Ni	O1	O2	Me	Cu, Pb, Ni	O1	O2	Me
$\alpha$ -PbO	0.91	-0.91			2.38		2.21	
$\beta$ -PbO	0.88	-0.88			2.41		2.21	
$\alpha$ -PbO <sub>2</sub>	2.78	-1.39			3.95		2.04	
$\beta$ -PbO <sub>2</sub>	2.80	-1.40			3.95		2.05	
Pb <sub>2</sub> O <sub>3</sub>	0.94	2.80	-1.11, -1.24		2.32	3.94	2.11	2.07
			-1.38				2.06	
Pb <sub>3</sub> O <sub>4</sub>	0.74	3.09	-1.05, -1.24		2.34	3.97	2.10	2.09

\*Cu, Pb, Ni – atoms with variable valence; oxygen and Me (I,II,III) – atoms with constant valence; crystallographic atomic valencies are given in brackets.

nonstoichiometric composition, which introduces some uncertainty into their crystal-structure interpretation.

The experimental Cu–O distance in the orthorhombic modification of La<sub>2</sub>CuO<sub>4</sub>, see Fig. 2.13, is larger than in the tetragonal one. The corresponding CV of copper is less in the orthorhombic modification. This tendency is reproduced by the calculated full valence values. However, in both La<sub>2</sub>CuO<sub>4</sub> modifications the copper CV values are larger than two (stoichiometric value) while the full valences are closer to this value. The crystal valence of copper atoms also changes when the oxygen vacancies concentrate on the O<sub>1</sub> site (oxygen in chains) in YBa<sub>2</sub>Cu<sub>3</sub>O<sub>7</sub>, (see Fig. 2.15), and change the composition to YBa<sub>2</sub>Cu<sub>3</sub>O<sub>6</sub>, and symmetry from orthorhombic to tetragonal. In YBa<sub>2</sub>Cu<sub>3</sub>O<sub>7</sub> both Cu<sub>1</sub> copper atoms in chains and Cu<sub>2</sub> copper atoms in planes have CV values larger than that in CuO crystal (see Table 9.3) and the CV of the Cu<sub>1</sub> atom is somewhat larger. The absence of oxygens on the O<sub>1</sub> site destroys the chain structure of Cu<sub>1</sub> atoms that become linearly coordinated by two oxygen atoms in YBa<sub>2</sub>Cu<sub>3</sub>O<sub>6</sub>, and have a CV value close to that of Cu I copper. The five-coordinated Cu<sub>2</sub> atom has a crystal valence close to that of Cu II (see Table 9.3). The calculation of not only the full valencies but also other local properties of electronic structure gives more detailed information about the chemical bonding in crystals of metal oxides.

As is seen from Table 9.3, the copper atomic charge  $Q_{Cu}$  is close to +1 in the Cu I oxide compounds. This means that the Cu I–O bonding is essentially ionic. The calculated 4s population of copper atoms appears to be near zero so that the copper atomic configuration in Cu I oxide crystals is close to 3d<sup>10</sup>. The results for Cu II-containing copper oxide compounds indicate that Cu II–O bonding is more covalent compared to Cu I–O bonding; the copper atomic charge in Cu II oxide compounds lies between 1.38 and 1.70 so that the copper atomic configuration appears to be between 3d<sup>9.6</sup> and 3d<sup>9.3</sup>. The Cu III atomic charge is close to +2 (see Table 9.3); calculated atomic populations correspond to a 3d<sup>9</sup> configuration. Thus, there are no Cu<sup>3+</sup> ions in cuprates, although these compounds do contain Cu III atoms, which lose two electrons to form an ionic bond with oxygen and supply one electron to form the covalent bonds. Calculated atomic charges on alkali and alkali-earth metal atoms (Me) are close to the number of their valence electrons, so that these metal atoms are present as Me<sup>+</sup> and Me<sup>2+</sup> ions, respectively. As shown in Table 9.3 the calculated charge of the rare-earth atoms Y and La are close to +3.

In Table 9.3 the results suggest that the absolute value of the atomic charge in plumbic oxides  $\text{PbO}_2$  are larger than those in plumbous oxides  $\text{PbO}$ . However, all the lead–oxygen crystals are very far from purely ionic compounds.

The nonequivalent metal atoms in the miscellaneous oxides  $\text{Cu}_4\text{O}_3$ ,  $\text{Pb}_2\text{O}_3$ ,  $\text{Pb}_3\text{O}_4$  have different atomic charges, and the charge values are close to those in either higher ( $\text{CuO}$ ,  $\text{PbO}_2$ ) or lower ( $\text{Cu}_2\text{O}$ ,  $\text{PbO}$ ) oxides.

We see that the calculated atomic-charge values agree qualitatively with those expected from the chemical point of view. On the other hand, the electronic-charge distribution calculated by other approaches (more traditional for solid-state physics) appears to be unrealistic: for example, it was found in an LAPW calculation of the  $\text{Cu}_2\text{O}$  crystal [589] that the atomic charges (estimated by the density integration inside the atomic spheres) are positive for both atoms:  $Q_{\text{Cu}} = 2.05$  and  $Q_{\text{O}} = 0.40$ . LCAO calculations of the electron density and direct integration over a spherical region near atomic cores [590] also do not allow one to distinguish the atomic charges on atoms with different oxidation states (the numerical values for the copper atomic charge in  $\text{Cu}_2\text{O}$  and  $\text{CuO}$  crystals are practically the same :+0.58 and +0.48, respectively). These examples demonstrate the advantage of quantum-chemical LCAO calculations of the local electronic-structure properties to describe reasonably both the valence and charge states of metal atoms in crystals. This conclusion is important for the study of new complicated crystalline structures, synthesized experimentally. As an example, we refer to the high- $T_c$  superconductors. It is well known that a small variation of the composition or the way in which the material is prepared may essentially change the superconducting properties. Evidently this is connected with a change of the electronic structure of the superconductor.

In [582] the comparative theoretical analysis of chemical bonding was made in two pairs of copper oxide compounds : (a) orthorhombic and tetragonal modifications of  $\text{La}_2\text{CuO}_4$  (the latter modification has a structure similar to that of the superconductor  $\text{La}_{2-x}\text{Sr}_x\text{CuO}_4$ ) and (b) nonsuperconducting tetragonal  $\text{YBa}_2\text{Cu}_3\text{O}_6$  and superconducting orthorhombic  $\text{YBa}_2\text{Cu}_3\text{O}_7$  crystals. In accordance with the results of previous band-structure calculation, it was found that  $\text{La}_2\text{CuO}_4$ , and  $\text{YBa}_2\text{Cu}_3\text{O}_7$  are metallic with small values of the density of states at the Fermi level, but  $\text{YBa}_2\text{Cu}_3\text{O}_6$  is a semiconductor with a forbidden energy gap of 2.5 eV. It was also found that the density of states for the  $\text{YBa}_2\text{Cu}_3\text{O}_7$  crystal contains  $3d$  Cu I (copper in chains) peak around 13 eV below Fermi level, but in the case of  $\text{YBa}_2\text{Cu}_3\text{O}_6$  this peak was absent. An analysis of chemical bonding in high- $T_c$  superconductors and related nonsuperconductor crystals shows changes that take place in the local electronic structure of these substances. As seen in Table 9.3 the charge distribution around the copper atom in the orthorhombic modification of the  $\text{La}_2\text{CuO}_4$  crystal is practically the same as in the  $\text{CuO}$  crystal. Contrary to this, in the tetragonal modification of  $\text{La}_2\text{CuO}_4$  the copper atomic valence exceeds the ordinary Cu II valence in copper oxide compounds. The calculated atomic charge on the copper atoms in  $\text{La}_2\text{CuO}_4$  crystals correlates well with that from it ab-initio Hartree–Fock cluster calculation (1.79e) [591]. If we consider the following defect-formation process, the substitution of La III by Sr II atoms, or the addition of oxygen atoms (for example,  $\text{La}_2\text{CuO}_{4.13}$  compound exists) it still further increases the copper valence in  $\text{La}_2\text{CuO}_4$ . A comparison of the atomic charges and bond orders in  $\text{YBa}_2\text{Cu}_3\text{O}_6$  and  $\text{YBa}_2\text{Cu}_3\text{O}_7$  crystals shows that electron-density distributions are practically identical in Cu–O planes, see Table 9.3.

The main changes in the chemical bonding take place in Cu–O chains. The results in Table 9.3 show that the charge state of Cu I atoms (in Cu–O chains) in  $\text{YBa}_2\text{Cu}_3\text{O}_6$  crystal is close to the state of copper atoms in Cu I oxides, but that in  $\text{YBa}_2\text{Cu}_3\text{O}_7$  they are close to copper atoms in Cu III oxides.

The analysis of calculated bond orders shows that there is no peroxide bonding in copper oxygen superconducting materials. It was also shown by atom–atom potential modeling that even additional oxygen atoms in  $\text{La}_2\text{CuO}_{4+x}$  do not cause the formation of peroxide bonds.

One of the questions to be considered is the role of the tetragonal–orthorhombic transition in superconductor materials. To analyze the changes in the electronic structure that are connected with the tetragonal–orthorhombic transition the  $\text{YBa}_2\text{Cu}_3\text{O}_7$  crystal with an oxygen vacancy was considered. The composition of this phase is  $\text{YBa}_2\text{Cu}_3\text{O}_6$ , but the lattice parameters and space symmetry are the same as those in the  $\text{YBa}_2\text{Cu}_3\text{O}_7$  crystal. It was found [571] that differences in atomic charges between perfect  $\text{YBa}_2\text{Cu}_3\text{O}_6$  and orthorhombic  $\text{YBa}_2\text{Cu}_3\text{O}_6$  do not exceed 0.05. These results show the strong correlation between Cu III (though not  $\text{Cu}^{3+}$ ) atoms presence and high- $T_c$  superconductivity in copper oxides.

The correlating bonding and structure in Cu II and Ni II mixed oxides is a matter of high interest. The comparative study of the chemical bonding in  $\text{NiO}$ – $\text{CuO}$  and  $\text{La}_2\text{NiO}_4$ – $\text{La}_2\text{CuO}_4$  crystals was made in [582, 583].  $\text{NiO}$  crystals were calculated in rhombohedral structure, corresponding to nonmetallic antiferromagnetic phase of this crystal. Analysis of local properties of electronic structure of crystals containing a Ni II–O bond with those containing Cu II–O bond, allows us to conclude that the former is more ionic than the latter (see Table 9.3). The increase of ionicity degree in the Ni II–O bonding with respect to Cu II–O bonding is understood in terms of the mutual position of the oxygen  $2p$  and metal  $3d$  subbands that lie nearly in the same energy interval for Cu, whereas the  $3d$  Ni subband lies approximatively 2 eV above the center of gravity of the oxygen  $2p$  level.

The ionic part of the Ni II–O bonding is the same for  $\text{NiO}$  and  $\text{La}_2\text{NiO}_4$  (see Table 9.3). As regards the Cu II–O bonding, the data obtained for  $\text{La}_2\text{CuO}_4$  as compared to  $\text{CuO}$  and other Cu II mixed oxides such as  $\text{Sr}_2\text{CuO}_3$ ,  $\text{Sr}_2\text{CuO}_2$ ,  $\text{Li}_2\text{CuO}_2$ , atomic charges that are found in the range 1.4 to 1.6, point to a rather high ionic part of the Cu II–O bonding. Comparing the full atomic valence for Ni II and Cu II (Table 9.3) evidences a striking feature: the quantum-chemical value of the valence fits perfectly the formal oxidation state of Ni, namely (II), whereas for Cu, the quantum-chemical valence is larger than the oxidation state, with an enhancement for  $\text{La}_2\text{CuO}_4$ , ( $V_{\text{Cu}} = 2.38$ ). Such a data is likely to depend on an increase of the covalence of the Cu II–O bonding, as compared to the corresponding Ni II–O bonding.

As regards the problem of the true meaning of the (II) valence in tetragonal  $\text{La}_2\text{NiO}_4$ , quantum-chemical data cannot be considered as contradictory to the occurrence of some Ni II–Ni III oxidation coupled with the presence of interstitial oxygen, which is rather usual for air-prepared polycrystalline  $\text{La}_2\text{NiO}_4$ .

From the data of Table 9.3, one can get an insight into the anisotropy of the M II–O bonding in  $\text{La}_2\text{MO}_4$ , *i.e.* the electronic anisotropy in the  $\text{MO}_6$  octahedra (see Fig. 2.13), in terms of the two following features:

(i) The Ni II–O bonding in  $\text{La}_2\text{NiO}_4$  does not exhibit any significant anisotropic trend: the covalence is rather low and equally distributed in the equatorial plane and

the apical direction. Consequently, the nature of the Ni II–O bonding in the  $\text{NiO}_6$  octahedra is nearly unchanged when going from the binary oxide  $\text{NiO}$  to the composite oxide  $\text{La}_2\text{NiO}_4$ .

(ii) The increase of the covalent bond order of the Cu II–O bonding, as compared to the Ni II–O one, concerns the Cu II–O inplane bonds: such Cu–O equatorial bonds are very similar to the Cu II–O bonding in the binary oxide  $\text{CuO}$ . Conversely, the Cu–O apical bonds are slightly covalent and look like the corresponding Ni–O apical bonds in the  $\text{NiO}_6$  octahedra of  $\text{La}_2\text{NiO}_4$  and  $\text{NiO}$ , as well. The strong ionic character of the Cu–O apical bonds in  $\text{La}_2\text{CuO}_4$  results in an unusual overall increase of the atomic charge of Cu (Table 9.3), when compared to  $\text{CuO}$  and other Cu II mixed oxides. The absence of any significant anisotropic covalent effect of the Ni–O bonding in  $\text{La}_2\text{NiO}_4$  found in calculations, fully agrees with the conclusions of magnetization density studies, which point to an equal population of  $d_{x^2-y^2}$  and  $d_{z^2}$  orbitals and no significant covalence in the M–O plane [592]. Moreover, as also stated in [592], the covalent effect to be found in the apical direction of the octahedra is likely to be due not to Ni II but to La III, in terms of a “hybridization between the La 5d and O 2p bands”. This is consistent with the lowering of the atomic charge of the apical oxygen, as compared to the equatorial one, modeled in  $\text{La}_2\text{NiO}_4$  (Table 9.3); such a lowering cannot depend on an increase of the covalent effect of the Ni II–O bonding in the apical direction, but more likely it can be ascribed to the covalent character of the La III–O bonding (Table 9.3).

From the main differences in the Ni II–O and Cu II–O bonding emphasized above, it is possible to clear up the problem of the actual nature of the anisotropic effects in the Ni II and Cu II octahedral oxygen coordination in  $\text{La}_2\text{MO}_4$  oxides ( $\text{M} = \text{Cu, Ni}$ ), namely to appreciate the mutual electronic and geometric or steric contributions. In this respect, Ni II and Cu II behave in a completely different way:

(i) The electronic contribution to the overall anisotropy of the  $\text{NiO}_6$  octahedra in  $\text{La}_2\text{NiO}_4$  is nearly absent ( $4\text{Ni} - \text{O}_{\text{eq}}$ : 1.934 Å,  $2\text{Ni} - \text{O}_{\text{ap}}$ : 2.243 Å) [593]). This means that the tetragonal distortion of the  $\text{NiO}_6$  octahedra largely depends on steric effects originating in the impossibility to match properly the usual La–O and Ni–O bond lengths: 2.57 and 2.06 Å, respectively, when building the structure of  $\text{La}_2\text{NiO}_4$ , as proposed in [594].

(ii) The electronic contribution of Cu II in terms of a significant covalent effect of the Cu II–O inplane bonding, results in a cooperative shortening/lengthening of the Cu–O<sub>eq</sub> and Cu–O<sub>ap</sub> bonds, respectively: 4 Cu–O<sub>eq</sub>: 1.904 Å, 2 Cu–O<sub>ap</sub>: 2.397 Å. The enhancement of the tetragonal distortion of the  $\text{CuO}_6$  octahedra results from adding the electronic contribution of Cu II to the typical steric effect of the  $\text{La}_2\text{CuO}_4$ .

Finally, the quantum-chemical data, as used to compare the anisotropy of the M II–O bonding in the M II octahedral oxygen coordination of  $\text{La}_2\text{MO}_4$  oxides ( $\text{M} = \text{Ni, Cu}$ ), allow the following two features to be emphasized:

(i) The so-called Jahn–Teller effect of the  $d^9$  Cu II must be understood in terms of an anisotropy of bonding, namely a strong covalent character of the Cu II–O inplane bonding that no longer exists in the Cu II–O apical bonding. Such an anisotropic covalent bonding character cannot be found in the high-spin  $d^8$  Ni II: as a consequence, the occurrence of a distortion of the  $\text{NiO}_6$  octahedra is related to the steric effects of the geometric structure in question: the rocksalt structure of  $\text{NiO}$  permits only a very

slight distortion of the octahedra, as the structure of  $\text{La}_2\text{NiO}_4$  results in significant steric constraints on the octahedra.

(ii) The overall anisotropy of the  $\text{MO}_6$  octahedra in the  $\text{La}_2\text{MO}_4$  oxides ( $\text{M} = \text{Ni}, \text{Cu}$ ) cannot be fully understood in terms of the typical  $\text{M II}-\text{O}$  bonding properties. The role of  $\text{La III}-\text{O}$  bonding can be held as crucial in enhancing the covalent character of the apical oxygen and consequently increasing the tetragonal distortion of the  $\text{MO}_6$  octahedra. This is clear from the data obtained for  $\text{La}_2\text{NiO}_4$ .

Thus, anisotropy of the  $\text{NiO}_6$  octahedra can be assumed to originate from geometric contributions. Conversely, the anisotropy of the  $\text{Cu II}-\text{O}$  bonding, in terms of a significant covalency of the  $\text{Cu II}-\text{O}$  inplane bonding, is unambiguously settled. More generally, each increase of the covalency effect of inplane bonding in  $\text{MO}_6$  octahedra, results in a corresponding lengthening of the apical  $\text{M}-\text{O}$  bonding. Such an effect, which was previously well evidenced for the anisotropic electronic configurations of some so-called exotic cations such as low-spin  $\text{Ni}^{3+}$  or low-spin  $\text{Cu}^{3+}$  is presently being investigated in  $\text{Ni I}-\text{O}$  and  $\text{Cu I}-\text{O}$  bonding of the structures of the reduced phases  $\text{LaNiO}_2$  and  $\text{LaSrNiO}_3$  [595].

The use of local electronic-structure properties conception in the chemical-bonding analysis was demonstrated also in *ab-initio* calculations of crystalline metal oxides, discussed in the next section using the example of titanium oxides.

### 9.1.3 Chemical Bonding in Titanium Oxides: Periodic and Molecular-crystalline Approaches

As demonstrated above by the results of semiempirical calculations of metal oxides, the full valence of the metal atom, defined according to (9.13), correlates with the metal oxidation state. Such a conclusion was confirmed later in *ab-initio* HF calculations [574] of titanium oxides. Although the quadrivalent state (oxidation state IV) of the titanium atom is the most stable, the existence of oxygen compounds of titanium in formal oxidation states of III and II, as well as of a series of nonstoichiometric compounds was established. Table 9.4 presents the space-group symbol, the number of formula units in the cell, and the shortest  $\text{Ti}-\text{Ti}$  and  $\text{Ti}-\text{O}$  experimental distances for  $\text{TiO}$  in hexagonal structure,  $\text{Ti}_2\text{O}_3$  in corundum structure and  $\text{TiO}_2$  (in the rutile (r), anatase (a), and brookite (b) modifications).

**Table 9.4.** Crystal structure of titanium oxides: space group, number of formula units per cell  $Z$ , and nearest interatomic distances (in Å)

Structure data	$\text{TiO}(\text{hex})$	$\text{Ti}_2\text{O}_3$	$\text{TiO}_2(\text{r})$	$\text{TiO}_2(\text{a})$	$\text{TiO}_2(\text{b})$
Group	$P\bar{6}m2$	$R\bar{3}c$	$P4_2/mnm$	$I4_1/amd$	$Pbca$
$Z$	2	2	2	2	8
$R_{\text{Ti}-\text{Ti}}$	3.03 3.24	2.58 2.99	3.00 3.55	3.10 3.76	2.95 3.06
$R_{\text{Ti}-\text{O}}$	2.38 3.86	2.02 2.07	1.95 1.97	1.94 1.99	1.86 1.92

The titanium oxides are of considerable technological interest, so different theoretical studies of electronic and atomic structure and properties have been performed both for  $\text{TiO}_2$  [100,323,596,597] and  $\text{Ti}_2\text{O}_3$  [598,599] crystals. We are not aware of the existence of the electronic-structure calculations of  $\text{TiO}$ . The available publications focus attention primarily on description of the band structure and phase stability of titanium oxides and restrict the discussion of the nature of chemical bonding in these compounds to an analysis of Mulliken atomic charges and overlap populations.

The chemical bonding in titanium oxides was studied in more detail in [574,575, 577,600]. The calculations are made by HF-LCAO and DFT-LCAO methods, incorporated in the computer code CRYSTAL [23]. The core electrons of Ti and O atoms are described by Durand–Barthelat [484] pseudopotentials and the atomic basis sets were taken from [323], where the outer exponents of the Gaussians were fitted to reproduce the parameters of rutile structure. For the structural parameters those calculated in [323,598] were taken. The sufficiently good accuracy of the calculations was ensured by the following choice of input computational parameters: 1. The good-quality set of the threshold parameters controlling the accuracy of the bielectronic series in RHF and UHF calculations ( $10^{-6}, 10^{-6}, 10^{-6}, 10^{-6}, 10^{-12}$ ). 2. The reasonably accurate tolerances controlling the DFT calculations of density, potential, and grid weight ( $10^{-9}, 10^{-9}, 10^{-14}$ ). 3. The values  $10^{-6}$  and  $10^{-5}$  a.u. for the convergence thresholds of eigenvalues and total energy, respectively. 4. For the sampling  $\mathbf{k}$ -point net of the integration in the reciprocal space Monkhorst–Pack set with shrinking factors  $s_1 = s_2 = s_3 = 6$  was used.

Table 9.5 presents local electronic-structure characteristics of the titanium oxides obtained by the RHF method, namely, the Ti  $d$ -orbital populations  $P_d$  and atom charges  $Q_{\text{Ti}}$ , as well as the atomic valences  $V_A$ . Also given are the local characteristics calculated in a nonorthogonal atomic basis and a basis orthogonalized according to Löwdin. As follows from a comparison of the results obtained from population analyses by Mulliken and Löwdin, the Löwdin analysis shows the chemical bonding in the crystals under study to be largely covalent, with the total valences of the titanium and oxygen atoms differing substantially from the expected stoichiometric values.

**Table 9.5.** Local electronic-structure characteristics of titanium oxides in the restricted Hartree–Fock method

Crystal	Mulliken				Löwdin			
	$P_d$	$Q_{\text{Ti}}$	$V_{\text{Ti}}$	$V_{\text{O}}$	$P_d$	$Q_{\text{Ti}}$	$V_{\text{Ti}}$	$V_{\text{O}}$
$\text{TiO}(\text{hex})$	2.38	1.62	2.14	2.04	2.70	1.27	2.30	2.15
$\text{Ti}_2\text{O}_3$	1.82	2.26	3.61	2.05	2.50	1.43	3.98	2.30
$\text{TiO}_2(\text{r})$	1.46	2.66	3.94	2.08	2.18	1.73	4.18	2.36
$\text{TiO}_2(\text{a})$	1.47	2.65	3.98	2.08	2.19	1.72	4.23	2.36
$\text{TiO}_2(\text{b})$	1.49	2.63	3.97	2.09	2.21	1.70	4.23	2.38

It was shown [602] that the calculations made using a valence-atomic basis without polarizing functions in the Löwdin population analysis agree better with the expected values of atomic valencies. The population analysis by Mulliken made in a nonorthogonal basis was found to be less sensitive to the inclusion of polarizing functions into the

calculation. The results obtained with the restricted and unrestricted HF methods for  $\text{TiO}_2$  in formal titanium configuration  $d^0$  do not differ practically from one another. The results of a calculation of the local properties of the three  $\text{TiO}_2$  modifications show them to be only weakly sensitive to structural changes.

**Table 9.6.** Local properties of chemical bonding in titanium oxide crystals in the restricted and unrestricted HF methods: titanium  $d$ -orbital populations  $P_d$ , atomic charges  $Q_A$ , covalencies  $C_A$ , atomic valences  $V_A$ , and bond-orders  $W_{AB}$  for nearest-neighbor atoms\*

Local properties	TiO (hex)		Ti <sub>2</sub> O <sub>3</sub>		TiO <sub>2</sub> (r)
	RHF	UHF	RHF	UHF	
$P_d$	2.38	2.34	1.82	1.77	1.46
$Q_{\text{Ti}}$	1.63	1.67	2.26	2.32	2.66
$C_{\text{Ti}}$	0.90	0.69	2.19	1.23	2.15
$V_{\text{Ti}}$	2.14	2.05	3.61	3.01	3.94
$Q_{\text{O}}$	-1.63	-1.67	-1.51	-1.55	-1.33
$C_{\text{O}}$	0.74	0.66	0.94	0.88	1.24
$V_{\text{O}}$	2.04	2.03	2.05	2.05	2.08
$W_{\text{Ti-Ti}}$	0.03	0.01	0.89	0.03	0.01
	0.00	0.00	0.00	0.01	0.01
$W_{\text{Ti-O}}$	0.11	0.10	0.20	0.19	0.36
	0.00	0.00	0.21	0.19	0.30

\*For the  $\text{TiO}_2$  crystal, the RHF and UHF results coincide.

As seen from Table 9.6 the largest difference between the calculations made in the RHF and UHF approximations was found for  $\text{Ti}_2\text{O}_3$  in corundum structure, see Fig. 2.19, with a formal titanium atom configuration  $d^1$ , where one can expect substantial spin-polarization and correlation effects. In the  $\text{Ti}_2\text{O}_3$  case the RHF method predicts a high bond order between titanium atoms, which, in its turn, results in an overestimated titanium valence. This pattern of chemical bonding is not borne out by experiments. As follows from Table 9.6, an increase in the degree of Ti oxidation from II to IV gives rise to an increase in the charge on the titanium atom, but the relative ionicity and the absolute value of the charge on the oxygen atom decrease. UHF calculations show that, in all the above insulator oxygen compounds of titanium, there is no strong covalent interaction among the Ti atoms.

An appreciable role in transition-metal compounds is played by electron-correlation effects, which may be taken into account in periodic DFT calculations or within the framework of multiconfigurational methods employing the cluster model of the crystal. In particular, of interest is the question to what extent the single-determinant UHF method (applied in the periodic LCAO calculations of solids) may account for the correlation effects. In the general case only a qualitative answer to this question is possible. The comparison of the whole set of local properties for rutile  $\text{TiO}_2$  and corundum  $\text{Ti}_2\text{O}_3$  structures as seen from results of calculations [575, 577, 600] demonstrates the different role of correlation effects on the chemical bonding in these two solids. In Tables 9.7 and 9.8 results are given for RHF, UHF, KS (Kohn-Sham Hamil-

tonian with BLYP exchange-correlation functional – nonspin-polarized) and KSS (the same KS Hamiltonian with inclusion of spin polarization). Also given are results for hybrid spinless and spin-dependent schemes using HF exchange and LYP correlation in the Hamiltonian (HB and HBS, respectively).

As follows from the results of the calculations, the effects of electronic correlation on local properties of the electronic structure of two crystals under consideration have both similarities and differences. Their explanation can be given if the peculiarities of the structure are taken into account. In both crystals the essentially covalent Ti–

**Table 9.7.** DFT and HF results for rutile  $\text{TiO}_2$  crystal (Mulliken population analysis)

Method	$E$ (a.u.)	$Q_A$	$C_A$	$V_A$	$W_{\text{Ti}-\text{O}1}$	$W_{\text{Ti}-\text{O}2}$
RHF	−69.776	2.66	2.15	3.94	0.36	0.30
		−1.33	1.24	2.08		
UHF						
$S_Z = 0$	−69.776	2.66	2.15	3.94	0.36	0.30
		−1.33	1.24	2.08		
$S_Z = 1$	−69.491	2.80	1.99	3.97	0.32	0.26
		−1.40	1.11	2.07		
KS (BLYP)	−71.348	1.88	3.18	4.06	0.50	0.43
		−0.94	1.85	2.25		
KSS (BLYP)						
$S_Z = 0$	−71.351	1.88	3.18	4.06	0.50	0.43
		−0.94	1.85	2.24		
$S_Z = 1$	−71.481	2.24	2.73	3.99	0.43	0.39
		−1.12	1.60	2.17		
HB (LYP)	−70.834	2.64	2.17	3.94	0.36	0.30
		−1.32	1.25	2.09		
HBS (LYP)						
$S_Z = 0$	−70.834	2.64	2.17	3.94	0.36	0.30
		−1.32	1.25	2.09		
$S_Z = 1$	−70.554	2.80	1.99	3.97	0.32	0.27
		−1.40	1.11	2.07		

O interaction takes place as the two spheres of the Ti atom's nearest neighbors are formed by oxygen atoms: 1. In  $\text{TiO}_2$  the Ti atom is surrounded by four oxygens at 1.95 Å and the next two oxygens at 1.97 Å *i.e.* oxygens form a distorted octahedron, see Fig. 2.11. 2. In  $\text{Ti}_2\text{O}_3$  crystal six oxygens are grouped into two triangles (with close Ti–O distance 2.02 and 2.07 Å, respectively), see Fig. 9.1. The Ti–Ti atoms' configuration in two crystals is different: 1. In  $\text{TiO}_2$  crystal there are two Ti atoms at distance 2.99 Å as a third neighbor of the Ti atom. In  $\text{Ti}_2\text{O}_3$  crystal each Ti atom interacts with only one Ti atom at the distance 2.58 Å, being smaller than that in  $\text{TiO}_2$  crystal. The results, given in Tables 9.7 and 9.8, may be explained when only the three first neighbors of the Ti atom are considered (from the analysis of calculated bond orders, it follows that the interactions with more distant atoms are sufficiently weak). From Tables 9.7 and 9.8 it is seen that both HF and KS calculations demonstrate the essential role of covalence in both crystals due to Ti–O interactions. When comparing atomic charges  $Q_{\text{Ti}}$  for the same calculational scheme, one finds that the Ti–O bonding

**Table 9.8.** DFT and HF results for  $\text{Ti}_2\text{O}_3$  crystal in corundum structure (Mulliken population analysis)

Method	$E$ (a.u.)	$Q_A$	$C_A$	$V_A$	$W_{\text{Ti}-\text{Ti}}$	$W_{\text{Ti}-\text{O}1}$	$W_{\text{Ti}-\text{O}2}$
RHF	-108.029 -1.51	2.26 0.94	2.20 2.05	3.61	0.87	0.20	0.21
UHF							
$S_z = 0$	-108.362 -1.54	2.32 0.88	1.23 2.05	3.01	0.03	0.19	0.19
$S_z = 1$	-107.902 -1.49	2.24 0.96	2.37 2.05	3.72	0.49	0.20	0.20
KS (BLYP)	-110.682 -1.10	1.65 1.63	3.47 2.18	4.13	0.34	0.35	0.30
KSS (BLYP)							
$S_z = 0$	-110.702 -1.13	1.69 1.60	3.11 2.18	3.85	0.10	0.33	0.30
$S_z = 1$	-110.744 -1.12	1.68 1.56	3.04 2.15	3.79	0.19	0.33	0.28
HB (LYP)	-109.672 -1.50	2.24 0.96	2.22 2.05	3.61	0.86	0.20	0.21
HBS (LYP)							
$S_z = 0$	-110.027 -1.54	2.31 0.90	1.25 2.05	3.01	0.03	0.19	0.20
$S_z = 1$	-109.588 -1.49	2.24 0.97	2.41 2.05	3.74	0.51	0.20	0.20

in  $\text{TiO}_2$  crystal is partly more ionic. For  $\text{TiO}_2$  crystal the  $\text{Ti}-\text{Ti}$  interaction is weak (the corresponding bond orders  $W_{\text{Ti}-\text{Ti}}$  are in the range of values 0.01–0.02 for all calculation schemes and are not given in Table 9.7). For  $\text{Ti}_2\text{O}_3$  crystal the results of calculations depend on the spin correlation: 1. In the RHF method bond order  $W_{\text{Ti}-\text{Ti}}$  appears to be large (0.87) and does not practically change in hybrid HF-KS calculations (HB) without spin; 2. For spin projection  $S_z = 0$  (antiferromagnetic case),  $W_{\text{Ti}-\text{Ti}}$  is close to zero in UHF, KSS, and HBS calculations, which means that spin-correlation effects are mainly important when the  $\text{Ti}-\text{Ti}$  interaction is considered; 3. For spin projection  $S_z = 1$  (ferromagnetic case), not only spin correlation but also the Coulomb one influences  $W_{\text{Ti}-\text{Ti}}$ : UHF value  $W_{\text{Ti}-\text{Ti}} = 0.49$  decreases to  $W_{\text{Ti}-\text{Ti}} = 0.19$  in KSS calculation. It is seen also that in UHF and Becke exchange Hamiltonians spin correlation is described in a different manner: the  $W_{\text{Ti}-\text{Ti}}$  value decreases from 0.49 (UHF) to 0.19 (KSS). Analyzing the total energy  $E$  per unit cell, one can draw interesting conclusions from Tables 9.7 and 9.8.

In  $\text{TiO}_2$  crystal: 1. Spin-correlation effects are small for  $S_z = 0$  (antiferromagnetic ordering practically does not change  $E$ , as seen from a comparison of the RHF-UHF, KS-KSS, and HB-HBS results). 2. The energy of the ferromagnetic state ( $S_z = 1$ ) is higher than for the antiferromagnetic state ( $S_z = 0$ ) for UHF and HBS calculations. It again shows the difference between HF and Becke approximations for exchange. This difference is due to the nonlocal exchange in the HF Hamiltonian (the one-electron

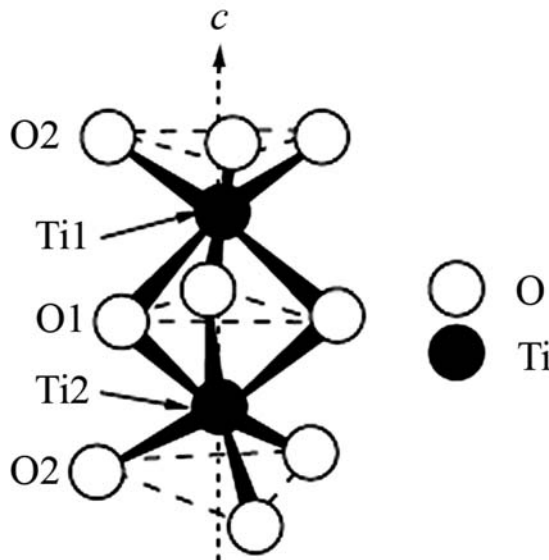


**Fig. 9.1.** Geometric structure of  $[\text{Ti}_2\text{O}_9^{12-}]$  cluster, modeling  $\text{Ti}_2\text{O}_3$  crystal in corundum structure

density matrix offdiagonal elements are not taken into account in DFT approximation for exchange).

In  $\text{Ti}_2\text{O}_3$  crystal the same difference in the total energy for  $S_z = 0$  and  $S_z = 1$  cases was found: In HF and HBS calculations, antiferromagnetic ordering gives an energy gain compared with the diamagnetic picture (compare in Table 9.8 the total energy for  $S_z = 0$  and  $S_z = 1$  in UHF and HBS calculations); however, Becke exchange gives the opposite order of the total energies (compare  $S_z = 0$  and  $S_z = 1$  for KSS calculations). As for covalencies of oxygen atoms and  $W_{\text{Ti}-\text{O}}$ , one can draw from Tables 9.7 and 9.8 the following conclusions: 1. Only spin correlation of  $\text{Ti}$  atoms gives small changes for these properties of electronic structure in both crystals (compare in Tables 9.7 and 9.8 RHF-UHF, KS-KSS, and HB-HBS results). 2. Inclusion of Coulomb correlation with Becke exchange gives a more covalent picture of chemical bonding (compare the results for RHF and KS calculations), but only the correlation correction gives small changes of the covalence of chemical bonding (compare the results for RHF and HB calculations).

As was demonstrated in [571], the full valence of the metal atom, calculated for different metal oxides according to definition (9.13), correlates with the oxidation state in the semiempirical calculations, implicitly taking into account the correlation effects (see Chap. 6). In  $\text{TiO}_2$  and  $\text{Ti}_2\text{O}_3$  crystals the  $\text{Ti}$  atom oxidation state should be +4 and +3, respectively. The calculated total valence  $V_{\text{Ti}}$  is close to oxidation state 4 for all calculations of  $\text{TiO}_2$  (see Table 9.7) but strongly depends on the spin-correlation description for  $\text{Ti}_2\text{O}_3$  (see Table 9.8). The calculated total valence  $V_{\text{O}}$  appears to be close to a reasonable value, 2.0, in all cases.

For rutile  $\text{TiO}_2$  the LCAO results for Mulliken charges and the Ti–O overlap population can be compared with those found in DFT-PW calculations [601] after projecting the eigenstates onto a localized basis set of atomic pseudo-orbitals. In KS-LCAO calculations,  $Q_{\text{Ti}} = 1.88$  and overlap populations of Ti–O bonds are 0.11 and 0.10 for nearest and next-nearest oxygens, respectively. In PW calculations [20],  $Q_{\text{Ti}} = 1.46$ , and the overlap populations are 0.35 and 0.43, respectively. This comparison shows that the calculated local properties' numerical values depend on the choice of basis set used in calculations (LCAO or PW sets). Moreover, in PW calculations the procedure of projection is used to receive atomic orbitals (see Sect. 9.1.5), which is not necessary in LCAO calculations.

From the discussion of the results obtained it follows that the spin-correlation effects are described in an essentially different manner in HF and DFT calculations for  $\text{Ti}_2\text{O}_3$  crystal and as a result give different descriptions of Ti–Ti interaction: in the HF method, this interaction is weak (for energetically more favorable antiferromagnetic ordering); in the DFT method, the ferromagnetic ordering appears to be more favorable and Ti–Ti interaction remains essential.

It seems reasonable to use post-HF descriptions of spin-correlation effects other than that used in HF and DFT methods. For this, one can perform, say, UHF and CASSCF electronic-structure calculations of reasonably selected clusters of the crystal under consideration to get single-determinant UHF and multiconfigurational CASSCF wavefunctions. Then, expanding UHF  $\beta$ -MOs over an  $\alpha$  set and inserting these expansions in the UHF determinant, we obtain a certain multiconfigurational wavefunction that is, in general, a mixture of different spin states. Annihilation of the highest-spin contaminants leads to the multiconfigurational wavefunction that should be compared with the CASSCF one. If these functions are similar, that is, in both functions the same determinants are dominating, then one can state that the UHF method accounts for part of the Coulomb-correlation effects. Estimation of relevant energies may give an impression of what part of the correlation energy (in comparison with the CASSCF method) is obtained on the UHF level. Then, all qualitative conclusions concerning a cluster may be directly applied to the corresponding crystal. In particular, if local molecular characteristics (such as atomic charges, bond orders, valences, and covalences) of a cluster are notably affected by correlation effects and UHF cluster calculation reproduces this tendency, then the UHF calculation of a crystal should certainly display the same tendency.

There exists one simple but important case where more detailed analysis is possible. Indeed, let us consider a molecular system (cluster) with a nondegenerate singlet ground state that can be described by a MCSCF wavefunction with dominating contribution of only two configurations:

$$\Psi_{MCSCF} = C_1 \det | \dots \varphi_h \alpha \varphi_h \beta | + C_2 \det | \dots \varphi_l \alpha \varphi_l \beta | \quad (9.28)$$

With the aid of a nondegenerate (nonorthogonal) transformation (for the standard case  $C_1 > 0$  and  $C_2 < 0$ ) generalized valence bond orbitals may be constructed:

$$\varphi_a = \sqrt{\frac{1}{2}} \left\{ \sqrt{C_1} \varphi_h + \sqrt{|C_2|} \varphi_l \right\} \quad (9.29)$$

$$\varphi_b = \sqrt{\frac{1}{2}} \left\{ \sqrt{C_1} \varphi_h - \sqrt{|C_2|} \varphi_l \right\} \quad (9.30)$$

Simple algebraic manipulations lead to the conclusion that

$$\Psi_{MCSCF} \simeq \Phi_{ab} + \Phi_{ba} \quad (9.31)$$

where

$$\Phi_{ab} = \det | \dots \varphi_a \alpha \varphi_b \beta | \quad (9.32)$$

and

$$\Phi_{ba} = \det | \dots \varphi_b \alpha \varphi_a \beta | \quad (9.33)$$

are typical single-determinant UHF configurations. These determinants correspond to zero projection of the total spin but are not, in general,  $S^2$  eigenfunctions. Their symmetrical combination gives the initial singlet wavefunction (9.28) whereas the antisymmetrical combination gives the related triplet state. In general, the nondiagonal matrix element  $\langle \Phi_{ab} | \hat{H} | \Phi_{ab} \rangle$  differs from zero and its absolute value may serve as a certain measure of the UHF method's capability to account for Coulomb- correlation effects. Indeed, if this matrix element is small (in absolute value) then singlet and triplet states are energetically close and the UHF method for a singlet state accounts for about the same part of the correlation effects as the MCSCF one with wavefunction (9.28).

Calculations of the lowest singlet and triplet states of cluster  $[\text{Ti}_2\text{O}_9^{12-}]$ , see Fig. 9.1, were performed by UHF and CASSCF methods using the GAMESS program set for molecular calculations [35]. The cluster includes two nearest Ti atoms and their nearest oxygen neighbors. The initial MOs for this cluster were obtained by the RHF method with  $C_{3h}$  as the point-symmetry group. The active space of the CASSCF method involved five highest occupied and three lowest virtual MOs (active space  $[2a'2a''2e']^{10}$ ). From Table 9.9 it is seen that the cluster chosen reasonably reproduces the Ti atom's local properties compared with periodic calculations for  $S_z = 0$  (see Table 9.8). In UHF calculations,  $Q_{\text{Ti}} = 2.22$  (cluster model),  $Q_{\text{Ti}} = 2.32$  (periodic model),  $C_{\text{Ti}} = 1.37$  (cluster model), and  $C_{\text{Ti}} = 1.23$  (periodic model). It turned out that the singlet state of the cluster under consideration is described by two configurational wavefunctions.

$$0.8[\varphi_h^2 \varphi_l^0] - 0.6[\varphi_h^0 \varphi_l^2] \quad (9.34)$$

whereas the related triplet state with  $S_Z = 1$  is reasonably described by a single determinant.

The comparison of the total energies for the cluster shows (see Table 9.9) that the UHF calculation reproduces well the small difference of the CASSCF energies for the total spin values  $S = 0$  and  $S = 1$ . Moreover, as seen from Table 9.9, the UHF calculation describes correctly the influence of the correlation effects on the Ti-Ti bond-order value. Indeed, in RHF calculations this bond order constitutes 0.88, whereas in UHF calculations the bond-order values are 0.03 for  $S_z = 0$  and 0.01 for  $S_z = 1$ , in full accordance with CASSCF calculations (0.09 for  $S = 0$  and 0.01 for  $S = 1$ ). At the same time, the Ti atomic charges are practically not affected by the method used.

Calculations of the electronic structure of crystals  $\text{TiO}_2$  and  $\text{Ti}_2\text{O}_3$  and corresponding cluster show that numerical results for local properties of the electronic structure of crystals (atomic charges, covalences, free and total valences, and bond

**Table 9.9.** Energies and local characteristics of electronic structure of molecular cluster  $[\text{Ti}_2\text{O}_9]^{12-}$  in UHF and MCSCF calculations

Characteristics of electronic structure	UHF		MCSCF	
	$S_z = 0$	$S_z = 1$	$S_z = 0$	$S_z = 1$
$E$ (a.u.)	-137.874	-137.867	-137.913	-137.904
$Q_{\text{Ti}}$	2.22	2.28	2.11	2.12
$Q_{\text{O}1}$	-1.68	-1.68	-1.63	-1.64
$Q_{\text{O}2}$	-1.90	-1.90	-1.89	-1.89
$W_{\text{Ti}-\text{Ti}}$	0.03	0.01	0.09	0.01
$W_{\text{Ti}-\text{O}1}$	0.17	0.17	0.19	0.20
$W_{\text{Ti}-\text{O}2}$	0.27	0.27	0.31	0.32
$C_{\text{Ti}}$	1.37	1.34	1.62	1.56
$C_{\text{O}1}$	0.63	0.62	0.70	0.71
$C_{\text{O}2}$	0.21	0.21	0.23	0.24
$V_{\text{Ti}}$	3.01	3.02	3.07	3.04
$V_{\text{O}1}$	2.02	2.02	2.02	2.03
$V_{\text{O}2}$	2.01	2.01	2.01	2.01

orders) depend on (a) Choice of basis for calculation (LCAO, PW); (b) Choice of Hamiltonian (RHF, UHF, DFT); (c) Choice of population analysis (POPAN) scheme (Löwdin, Mulliken). The effects of electron correlation on local properties may be estimated using (a) periodic and cluster DFT and hybrid HF–DFT calculations in the periodic model; (b) post-HF calculations in the molecular cluster model; (c) the results of (a) and (b) agree when the appropriate cluster choice is made and the same basis and population analysis are used.

To minimize the essential dependence of results on the basis-set choice and POPAN, it is reasonable to generate Wannier-type atomic functions that are orthogonal and localized on atomic sites. These functions can be generated from Bloch-type functions (after relevant symmetry analysis), see Chap. 3. In the next section it is shown that the results of POPAN with use of Wannier-type atomic functions weakly depend on the basis choice in Bloch function LCAO calculations.

#### 9.1.4 Wannier-type Atomic Functions and Chemical Bonding in Crystals

As we have seen above chemical bonding in crystals (as well as in molecules) is analyzed in terms of the local properties of the electronic structure, obtained from the one-electron density matrix, written in a localized basis. Since local properties of electronic structure are essential ingredients of a number of theories and models (for example, the numerical values of atomic charges are used in the atom–atom potentials of the shell model), their estimation is of great importance. Traditionally, the same AO basis is used both in LCAO SCF calculations and in the local properties definition, as was noted above. However, this approach is not always reliable, since the results of the population analyses are often strongly dependent on an inclusion of diffuse orbitals into the basis (useful for the electronic-structure calculations) and on the scheme chosen for the population analysis.

As discussed in Chap. 3 the variational method of localized functions generation allows development of an approach of the chemical-bonding analysis, which is much less basis-set dependent than the conventional approaches. The population analysis in this case is done using the density matrix given in the minimal valence basis of Wannier-type atomic orbitals (WTAOs) – Wannier functions centered on atoms and having the behavior of atomic-valence states in the cores of atoms [47, 603, 604]. WTAOs are analogous to atomic functions in form and by symmetry but, in contrast to the initial LCAO basis, they are directly connected with the calculated electronic band structure and the Bloch states involved. WTAOs are constructed from the occupied and some vacant Bloch states, chosen so that they assure the maximal localization for the corresponding WTAOs (see Chap. 3). The summary of the results of WTAO application for the calculations of local properties of the electronic structure of periodic systems is given in [605].

WTAOs are defined as the Wannier functions that are constructed from a set of specially chosen occupied and vacant bands and have a definite symmetry (they are centered on atoms and transform via irreducible representations (irreps) of the corresponding site groups). Thus, the index  $t$  in (3.114) may be substituted by several indices –  $i, j, a, \beta, \mu$  – that reflect the symmetry properties of the WTAOs –  $W_{ija}^{\beta\mu}(\mathbf{r} - \mathbf{a}_n)$ : the index  $a$  marks the symmetrically nonequivalent atoms, the index  $j$  runs through the set of symmetrically equivalent atoms of the type  $a$ ; the Wyckoff positions of these atoms  $\mathbf{q}_a$  are characterized by their site groups, whose irreps are labeled by the index  $\beta$ , the index  $i$  numbers the basis functions of the irrep  $\beta$  and the index  $\mu$  discriminates between the independent sets of the functions transforming according to the same irrep  $\beta$ . The requirement for WTAOs to have fixed symmetry properties implies additional restrictions on the matrices  $U(\mathbf{k})$  in (3.112). These restrictions can be completely taken into account by using, instead of canonical Bloch orbitals, their linear combinations, symmetrized according to the desired irreps of the site-symmetry groups of atoms [47].

WTAOs were generated by the variational method [604], which allows both orthogonal  $W_{ija}^{\beta\mu}(\mathbf{r} - \mathbf{a}_n)$  and nonorthogonal  $V_{ija}^{\beta\mu}(\mathbf{r} - \mathbf{a}_n)$  sets of symmetry adapted WTAOs to be obtained. In this method the functional

$$I_{\beta\alpha} = \int \omega_{\beta\alpha} \left| V_{11a}^{(\beta,1)}(\mathbf{r}) \right|^2 d\mathbf{r} \quad (9.35)$$

with the weight function:

$$\omega_{\beta\alpha} = (\pi r_{\beta\alpha}^2)^{-3/2} \exp \left( -\frac{(\mathbf{r} - \mathbf{q}_a)^2}{2r_{\beta\alpha}^2} \right) \quad (9.36)$$

is maximized ( $r_{\beta\alpha}^2$  is a parameter, for which a value of 1 Å was used). The orthogonal WTAOs  $W_{ija}^{\beta\mu}(\mathbf{r} - \mathbf{a}_n)$  are obtained from the nonorthogonal ones  $V_{ija}^{\beta\mu}(\mathbf{r} - \mathbf{a}_n)$  via Löwdin's procedure:

$$\mathbf{W} = \mathbf{V} \left( S^{(V)} \right)^{-1/2} \quad (9.37)$$

where  $S^{(V)}$  is the overlap matrix of nonorthogonal WFs  $V_{ija}^{\beta\mu}(\mathbf{r} - \mathbf{a}_n)$ , and  $\mathbf{W}$  and  $\mathbf{V}$  are row vectors constituted by the sets of the orthogonal and nonorthogonal WFs, correspondingly. The orthogonalization procedure can be performed either in the direct or reciprocal space. The latter is computationally faster.

Before constructing the minimal basis of WTAOs one should choose the energy bands whose states are to be used in the process of the WTAOs generation. For each of the WTAOs a band or a group of bands is chosen according to the following criteria: the band states should be compatible with the corresponding WTAOs by symmetry, in the context of the induced representations (indreps) theory, see Chap. 3, and provide the maximal localization for them. Hereafter, we mark such bands by the type of the WTAOs corresponding to them (*e.g.*  $s$ -band of the oxygen atom: the  $s$ -WTAOs centered on oxygen and constructed from the states of this band appear to be the most localized comparing to those constructed from any other states). After the desired bands for all the WTAOs are chosen the final WTAOs are constructed using the states from this group of bands. When the WTAOs (orthogonal or nonorthogonal) are found, the density matrix is calculated in the localized basis of these functions. The local properties are expressed via the matrix elements of this matrix.

WTAOs' analog of Mulliken population analysis is made using nonorthogonal WTAOs.

Let us now consider WTAOs  $V_{\nu A}(\mathbf{r} - \mathbf{a}_n)$  ( $\nu$ -th WTAO of atom  $A$  in the  $n$ th cell) as the linear combinations of Bloch functions:

$$V_{\nu A}(\mathbf{r} - \mathbf{a}_n) = \sum_{\tau \mathbf{k}} b_{\tau \mathbf{k}, \nu A n} \varphi_{\tau \mathbf{k}}(\mathbf{r}), \quad \text{or} \quad \mathbf{V} = \varphi b, \varphi = \mathbf{V} b^{-1} \quad (9.38)$$

where Bloch functions  $\varphi_{\tau \mathbf{k}}(\mathbf{r})$  are given in LCAO or PW basis. The density matrix in the corresponding basis  $\rho^{(V)}$  can be written in the following way:

$$\rho^{(V)} = 2\bar{b}^{-1}\bar{b} \quad (9.39)$$

where  $\bar{b}$  is the truncated matrix  $b$  with rows corresponding only to the occupied states.

For the orthogonalized WTAOs:

$$W_{\nu A}(\mathbf{r} - \mathbf{a}_n) = \sum_{\tau \mathbf{k}} d_{\tau \mathbf{k}, \nu A n} \varphi_{\tau \mathbf{k}}(\mathbf{r}), \quad \text{or} \quad \mathbf{W} = \varphi d, \varphi = \mathbf{V} d f^\dagger \quad (9.40)$$

the density matrix  $\rho^{(V)}$  is given by

$$\rho^{(V)} = 2\bar{d}^\dagger\bar{d} \quad (9.41)$$

The electronic population  $N_{A n}$  of an atom  $A$  in the  $n$ th primitive cell and an order of the bond  $W_{A 0, B n}$  between an atom  $A$  of the reference cell and an atom  $A'$  in the  $n$ th cell can be obtained from the density matrix (9.41):

$$N_{A n} = N_{A 0} = \sum_{\nu} \rho_{\nu \nu}^{A 0, A 0} \quad (9.42)$$

$$W_{A 0, B n} = \sum_{\mu \nu} \rho_{\mu \nu}^{A 0, B n} \rho_{\nu \mu}^{B n, A 0} \quad (9.43)$$

Using these quantities one can obtain the atomic charge  $Q_A$  (9.10) of an atom  $A$ , the covalence  $C_A$  (9.12) and total valence  $V_A$  (9.13) of this atom.

To demonstrate the efficiency of WTAO use for chemical-bonding analysis, we consider at first the cubic crystals with the perovskite structure [603]. The LCAO

approximation in the HF and DFT methods was used to calculate the band structure and the Bloch functions of bulk  $\text{SrTiO}_3$  (STO),  $\text{BaTiO}_3$  (BTO),  $\text{PbTiO}_3$  (PTO) and  $\text{LaMnO}_3$  (LMO) crystals. The Hay–Wadt pseudopotentials [483] were adopted: small-core for Ti, Sr, Ba, La and Mn atoms, large-core for Pb atoms. The oxygen atoms were included with the all-electron basis set. The optimized Gaussian-type atomic basis was taken from [606], where the same pseudopotentials were used. The basis optimization made it possible to obtain the lattice constant, bulk modulus and elastic constants of the considered crystals that were in good agreement with the experimental data. For the exchange-correlation functional the hybrid HF-DFT form (B3PW) was used, as it reproduces, for optimized basis sets, optical band gaps close to the experimental values [606].

The Monkhorst–Pack [14] mesh of  $4 \times 4 \times 4 = 64$   $\mathbf{k}$ -points, used in the calculations, corresponds to a cyclic model with 64 primitive unit cells in the direct lattice, see Chap. 3. An increase of this number in the band-structure calculations up to  $8 \times 8 \times 8 = 512$  does not lead to any significant changes in the values of the one-electron energies.

The cubic structure of perovskite-like  $\text{ABO}_3$  compounds is characterized by the primitive cubic lattice with the  $O_h^1$  ( $Pm\bar{3}m$ ) space group, see Sect. 2.3.2. The A-atoms and B-atoms occupy the Wyckoff positions a (0,0,0) and b (0.5,0.5,0.5), correspondingly, with the site group  $O_h$ . The oxygen atoms occupy c (0.5,0.5,0) positions, site group  $D_{4h}$ . The minimal atomic-like basis for the crystals under consideration consists of  $s$ - and  $p$ -type functions of the oxygen atoms,  $s$ - and  $d$ -type functions of the Ti atoms and  $s$ - and  $p$ -type functions of Sr, Ba and Pb in STO, BTO, PTO, or  $s$ - and  $d$ -type functions of La and Mn in LMO. So these are the types of WTAOs to be used in the population analysis for the compounds under consideration. Table 9.10 lists the symmetries of these functions.

**Table 9.10.** The symmetry properties of the WTAOs of the minimal valence basis for STO, BTO, PTO and LMO crystals

Atom	Function's type	Symmetry
Sr, Ba, Pb	$s$	$(a, a_{1g})$
	$p$	$(a, t_{1u})$
La	$s$	$(a, a_{1g})$
	$d$	$(a, t_{2g}) + (a, e_g)$
Ti, Mn	$s$	$(b, a_{1g})$
	$d$	$(b, t_{2g}) + (b, e_g)$
O	$s$	$(c, a_{1g})$
	$p$	$(c, a_{2u}) + (c, e_u)$

Once the types of WTAOs are determined one should find the energy-bands states corresponding to these WTAOs. First, the bands to be chosen should be symmetry compatible with the corresponding WTAOs (see [604] for details). Secondly, the WTAOs constructed from the Bloch states of the chosen bands should be principally the most localized WTAOs of the corresponding type. The analysis of the electronic structure of STO and BTO has shown (excluding the semicore states from consideration) that the oxygen  $s$ - and  $p$ -bands and the Sr (Ba) atom  $p$ -bands form 15 upper

valence bands states, see also next section. The Ti atom *d*-states form the five lowest conduction bands, while the Sr (Ba) and the Ti atom *s*-states are located among vacant conduction-band states very high in energy. In the case of PTO the difference in the location of the bands is that the Pb atom *s*-band is one of the valence bands and the Pb atom *p*-bands are vacant and lie high in the conduction band. This agrees with the results of DFT LDA calculations [607].

Unlike STO, BTO and PTO, the electronic structure of cubic LMO is metallic both in HF and DFT calculations (a nonzero bandgap in LMO appears only if an orthorhombic structure with four formula units in the primitive cell is considered). The *s*- and *p*-bands of the oxygen atoms are occupied. As in STO and BTO the *s*-bands of the metal atoms are located at high energies. But the *d*-bands of both metal atoms are located in the region of the Fermi energy. These bands are partly occupied and partly vacant, which is caused by the metallic nature of the calculated electronic structure.

The WTAOs that are used in the population analysis are built from the space of all the chosen bands taken together. The density matrix is then calculated using the coefficients connecting the orthogonal or nonorthogonal WTAOs and the occupied Bloch states.

In Table 9.11 the atomic charges for STO, BTO, PTO, correspondingly, calculated by the WTAOs technique, and using the traditional Mulliken population-analysis scheme are compared.

**Table 9.11.** Atomic charges in cubic ATiO<sub>3</sub> (A=Sr,Ba,Pb)

Method of electronic-structure calculation	Population-analysis scheme	Atomic charges,  e		
		Sr	Ti	O
HF	nonorthogonal WTAO	2.00	3.20	-1.73
	Orthogonal WTAO	2.00	3.13	-1.71
	Mulliken	1.92	2.76	-1.56
DFT	nonorthogonal WTAO	2.00	2.68	-1.56
	Orthogonal WTAO	2.00	2.63	-1.54
	Mulliken	1.87	2.35	-1.40
HF	nonorthogonal WTAO	2.00	3.19	-1.73
	Orthogonal WTAO	2.00	3.16	-1.72
	Mulliken	1.86	2.82	-1.56
DFT	nonorthogonal WTAO	2.00	2.65	-1.55
	Orthogonal WTAO	2.01	2.60	-1.54
	Mulliken	1.80	2.37	-1.39
HF	nonorthogonal WTAO	1.99	3.27	-1.75
	Orthogonal WTAO	1.89	3.14	-1.68
	Mulliken	1.59	2.79	-1.46
DFT	nonorthogonal WTAO	1.99	2.72	-1.57
	Orthogonal WTAO	1.93	2.64	-1.52
	Mulliken	1.34	2.34	-1.23

The Mulliken atomic charges coincide with those given in [606]. The results of the WTAO population analysis in these three crystals show the following: 1. The results of population analysis performed on orthogonal and nonorthogonal WTAOs are close. 2. The fully ionic charge +2 for the Sr, Ba or Pb atoms remains practically the same for both methods of the electronic-structure calculation – Hartree–Fock and DFT. The only exception is the orthogonal WTAOs analysis in PTO, but even in this case the charge is very close to +2. The reason for such a high ionicity is related to the high-energy location of the *s*-bands of the Sr and Ba atoms and the *p*-bands of Pb atom, which leads to a negligible contribution of the corresponding WTAOs to the covalence of these atoms. The switch from the HF calculations to DFT practically does not affect the location of high-lying vacant bands of the Sr, Ba and Pb atoms and, therefore, no covalence for these atoms appears. On the contrary, the traditional Mulliken analysis displays some covalence for these atoms, which increases in the case of DFT calculations. This is especially noticeable in a PTO crystal. 3. The Ti and O atom charges differ from the purely ionic ones (indicating a partial covalence of the Ti and O atoms). For these atoms the covalence is higher in the DFT calculations than in the HF ones. This correlates with the decrease of the bandgaps in DFT calculations compared to the HF ones (in DFT calculations the *d*-bands of the Ti atom shift down and become closer to the valence oxygen bands). As a result, mixing of the vacant states of the Ti atom *d*-bands with the oxygen WTAOs increases, generating the larger values of the covalence for these atoms. 4. The results of the WTAO analysis demonstrate a mixed (ionic-covalent) character of chemical bonding in  $\text{ABO}_3$  crystals. However, the ionicity, calculated by the WTAOs method, appears to be larger than that obtained in the traditional Mulliken population analysis. 5. The values of atomic charges in all the three considered perovskite-type crystals are close.

The values of some other local characteristics of the electronic structure of STO, BTO, PTO – bond orders, covalences and full valences of atoms – are listed in Table 9.12. These values correspond to nonorthogonal WTAOs analysis. The results given in Table 9.12 allow the following to be concluded. 1. The numerical values of the local characteristics of the electronic structure of the cubic STO, BTO, PTO are very close. 2. The covalence in these crystals appears only in the nearest-neighbor Ti–O bonds (all the other bonds manifest almost no covalence both in HF and DFT calculations). Each Ti atom has six bonds of this type, and each oxygen atom two bonds. In DFT calculations the value of the bond order is larger than in HF ones. 3. Both in the DFT and HF calculations the values of the total calculated valence of the metal atoms practically coincide with the values of the oxidation state used by chemists for these compounds.

The population analysis is not entirely correct for metallic crystals, because they are characterized by a special metallic type of bonding. But since the nonconducting state in LMO arises already within small distortions from the cubic structure, a formal population analysis performed on the cubic structure can show some tendencies in the local properties. Their values for the cubic LMO obtained with the help of the orthogonal WTAOs in HF calculations are given in Table 9.13.

Analyzing these values one can conclude the following. 1. Some of the results are principally different from those of STO, BTO and PTO. These are a nonzero covalence of the A (La) atom, a nonzero La–O bond order, the calculated valence of the B (Mn) atom is different from the expected one. Probable reasons for these results

**Table 9.12.** Atomic charges in cubic ATiO<sub>3</sub> (A=Sr,Ba,Pb)

Method of electronic-structure calculation	Order of Ti–O bond	Covalence			Full valence			
		Sr	Ti	O	Sr	Ti	O	
HF	0.24	0.00	1.47	0.51	2.00	4.01	2.01	
	0.36	0.00	2.28	0.82	2.00	4.06	2.02	
DFT		Ba	Ti	O	Ba	Ti	O	
		0.24	0.00	1.46	0.51	2.00	4.01	2.01
HF	0.37	0.01	2.33	0.83	2.01	4.06	2.02	
		Pb	Ti	O	Pb	Ti	O	
DFT		0.22	0.02	1.35	0.47	2.00	4.01	2.01
		0.35	0.04	2.23	0.80	2.02	4.06	2.02

**Table 9.13.** Local properties of electronic structure of cubic LaMnO<sub>3</sub>

Atomic charges			Bond orders		Covalence			Full valence		
La	Mn	O	La–O	Mn–O	La	Mn	O	La	Mn	O
2.48	2.09	-1.53	0.08	0.16	1.00	2.48	0.80	3.04	3.68	1.98

are connected with the metallic nature of the considered crystal in cubic structure and with the difference of the LMO crystal from STO, BTO or PTO. 2. On the other hand, the value of the La atomic charge is relatively close to the fully ionic one +3. Besides, the calculated valences of the La and oxygen atoms are similar to those obtained in STO, BTO and PTO crystals. This indicates the similarity between these crystals and LMO, manifested in spite of the metallic nature of the latter. 3. The largest value of a bond order in LMO corresponds to the nearest-neighbor Mn–O bond. This correlates with the interatomic charge distribution in STO, BTO and PTO. The difference is in the value of the bond order – in LMO this bond order is smaller, while the covalence (which is, actually, the sum of all the bond orders) of the Mn atoms practically coincides with that of the Ti atoms in the other three considered crystals. This is, apparently, a consequence of the metallic nature of LMO, which leads to smearing of the nearest-neighbor Mn–O bond charge over the other bonds. Finally, we note that the local properties for STO, BTO and PTO not that close to each other might be obtained if noncubic low-temperature phases are studied. It is especially important to consider the orthorhombic phase of LMO since in this phase LMO is no longer metallic.

WTAO population analysis can be made also using the Bloch functions found in the calculations with plane-wave basis (as was noted, the majority of modern computer codes for periodic systems calculations use this basis and the DFT Hamiltonian).

The results of chemical-bonding analysis for crystal MgO, performed via the conventional and WF schemes of population analysis, were compared in [608]. The MgO crystal is a good testing system for studying the accuracy of such methods, since on the one hand, the nature of chemical bonding in it is well known to be ionic, and on the other hand, some of the methods give contradictory results of chemical-bonding analysis in this crystal (see below and [601, 609]).

The electronic structure for the MgO crystal was calculated in [608] both in the LCAO approximation and in the PW basis. In both cases the calculations were done by the density-functional theory (DFT) method in the local density approximation (LDA). The Monkhorst–Pack set of special points of BZ, which allows a convergence to be obtained (relating to extended special-points sets) in the calculations of electronic structure, was used in both cases. For the LCAO calculations the Durand–Barthelat pseudopotential [484] was used. In the case of the PW calculations the normconserving pseudopotential and a PW kinetic energy cutoff of 300 eV were used.

For construction of the WTAOs the delta-functions were used as the weight functions in the variational functional (9.35). In this case, the variational procedure is equivalent to projecting the delta-functions onto the space of the states of chosen energy bands and demands a very low computational effort.

In both types of calculations the *s*- and *p*-bands of oxygen atoms form the four valence bands. The *s*-band of the Mg in the case of the LCAO basis is the highest possible (twelfth) conduction band. For the PW calculations, the lower 32 conduction bands were examined. This analysis showed that the *s*-band of the Mg atom in PW calculations is also located among high-energy conduction bands. If one considers more than 32 conduction bands, the location of the *s*-band of the Mg atom can only increase, which would not affect the results of the population analysis.

The calculations [608] showed that the WTAOs, corresponding to the LCAO and PW bases are essentially different in their form. This distinction is probably caused mainly by the difference in the structure of the bases used for the LCAO and PW calculations. All the WTAOs, excluding the *s*-WTAO of the Mg atom in the PW calculations, are well localized. The poor localization of the latter is probably due to considering only 32 lower bands, while the actual *s*-band of the Mg atom might lie higher in the energy than the examined ones. Anyway, the difference in the WTAOs' form and localization level does not affect the results of WTAO-based population analysis for MgO.

The atomic charges and covalences, calculated within the conventional approaches and WTAOs method, are given in Table 9.14.

**Table 9.14.** Calculated atomic charges and covalencies in MgO

Basis	Population analysis	Charge on Mg atom	Atomic covalence	
			Mg	O
LCAO	Mulliken	1.93	0.15	0.30
	Löwdin	1.54	0.88	1.13
PW	Mulliken	1.06	1.63	1.65
	Löwdin	0.90	1.90	1.89
LCAO	Nonorthogonal WTAOs	2.00	0.00	0.00
	Orthogonal WTAOs	1.97	0.05	0.05
PW	Nonorthogonal WTAOs	2.00	0.00	0.05
	Orthogonal WTAOs	1.93	0.13	0.14

The spilling parameter for the projection procedure (see Sect. 9.1.6) in the PW calculations was  $2.5 \times 10^{-3}$ . It is seen from this table that among the traditional schemes, only the Mulliken analysis performed for the LCAO calculations exhibits a

more or less ionic picture of chemical bonding in MgO. All the other conventional methods give the results corresponding to the mixed ionic-covalent type of bonding, which is actually quite unnatural for MgO. Besides, for the traditional methods the values of the atomic charges and covalences are significantly different depending on the calculation scheme and the type of basis.

On the contrary, the method based on orthogonal or nonorthogonal WTAOs correctly demonstrates the ionic nature of chemical bonding in MgO crystal whatever basis is used for the electronic-structure calculations. The values obtained within the different types of basis are close and correspond to the practically pure ionic character of bonding in this crystal. Though the LDA band-structure calculations for the MgO crystal in LCAO and PW bases give different values for the total energy and bandgap width and the forms of corresponding WTAOs are quite dissimilar, nevertheless, the results of population analysis performed in the basis of WTAOs are practically the same. This is a consequence of a high-energy location of the *s*-band of the Mg atom in both types of calculations.

### 9.1.5 The Localized Wannier Functions for Valence Bands: Chemical Bonding in Crystalline Oxides

The approach to the analysis of the chemical bonding in crystals discussed above is based on the population-analysis procedure, applied in the basis of AOs or WTAOs. In the second approach [63] the Wannier functions are generated using the Bloch functions of only the upper valence bands (see Chap. 3), so that the number  $N_{WF}$  of WFs per primitive cell is equal to the number of valence bands under consideration. For metal oxides, considered in this section, the upper valence energy bands are formed by  $2s$  and  $2p$  states of oxygen atoms. Therefore, the number of WFs per cell  $N_{WF} = 4N_f N_O$  ( $N_f$  is the number of formula units per cell,  $N_O$  is the number of oxygen atoms in the formula unit). In particular,  $N_{WF} = 4, 24, 48$  for MgO, Al<sub>2</sub>O<sub>3</sub> and AlPO<sub>4</sub> crystals with one, two and three formula units per cell, respectively. This approach provides the additional numerical characteristics of chemical bonding, which complement the population analysis in periodic systems.

Any of the WFs in the reference cell is given in the AO basis set (used in the Bloch-functions calculation) as

$$W_i(\mathbf{r} - \mathbf{g}) = W_i(\mathbf{r}) = \sum_{\mu=1}^M \sum_{\mathbf{g}'} C_{\mu i}^{\mathbf{g}'} \chi_{\mu}(\mathbf{r} - \mathbf{A}_{\mu} - \mathbf{g}') \quad (9.44)$$

where the orthonormality condition  $\langle W_i^{\mathbf{g}} | W_i^{\mathbf{g}'} \rangle = \delta_{\mathbf{g}\mathbf{g}'}$  holds for the periodic images  $W_i(\mathbf{r} - \mathbf{g})$  of the reference cell WF. The coefficients  $C_{\mu i}^{\mathbf{g}'}$  in (9.44) are related to the coefficients  $C_{\mu i}(\mathbf{k})$  in the Bloch functions of  $M$  valence bands by the relation

$$C_{\mu i}(\mathbf{k}_j) = \sum_{\mathbf{g}'} \exp(-i\mathbf{k}_j \mathbf{g}') C_{\mu i}^{\mathbf{g}'} \quad (9.45)$$

In these relations  $\mu = 1, 2, \dots, M$  numbers AOs in the primitive cell,  $\mathbf{g}$  is the direct lattice translation vector,  $i = 1, 2, \dots, N_{WF}$  numbers the valence bands and WFs and  $\mathbf{k}_j (j = 1, 2, \dots, L)$  are defined by the size of cyclic system  $L$  used for the summation

over BZ (see Chap. 3). WFs are characterized in terms of their Mulliken atomic populations by

$$q_{A,i}^g = \sum_{\mu \in A} \sum_{\nu, g'} C_{\mu,i}^g C_{\nu i}^{g+g'} S_{\mu\nu}^{g'} \quad (9.46)$$

where the first sum runs over the AOs  $\mu$  centered on atom  $A$  and the second one over all the AOs  $\nu$  and cells  $g'$ . The atomic populations (9.46) are normalized to one *i.e.*, they satisfy the condition  $\sum_{A,g} q_{A,i}^g = 1$ . These populations are used to describe

the localization properties of WFs, as  $q_{A,i}^g$  gives the fraction of the electron density of WF  $W_i(\mathbf{r})$  assigned to atom  $A$  in cell  $g$ . The range of WF  $W_i(\mathbf{r})$  localization is defined by nonzero values of (9.46) in spheres of atoms around the localization center of WF. The latter (centroid position) is defined by

$$\bar{r}_i = \int \mathbf{r} |W_i(\mathbf{r})|^2 d\mathbf{r} = \sum_s \bar{x}_{si} \bar{e}_s, \bar{x}_{si} = \int x_s |W_i(\mathbf{r})|^2 d\mathbf{r} \quad (9.47)$$

The centroid positions are used in the definition of the second-order central moment tensor,  $\tau_{i,lm}$  of the electron density associated to WF  $W_i(\mathbf{r})$ :

$$\tau_{i,lm} = \int d\mathbf{r} |W_i(\mathbf{r})|^2 (r_l - r_{i,l})(r_m - r_{i,m}) \quad (9.48)$$

where  $\mathbf{r} = (r_1, r_2, r_3)$  and  $\mathbf{r}_i = (r_{i1}, r_{i2}, r_{i3})$ . Tensor (9.48) contains useful information on the shape and spatial extent of the WFs. Centroid position  $\mathbf{r}_i$  of the WF  $W_i(\mathbf{r})$  also determines the so-called polarization fraction for  $W_i(\mathbf{r})$ :

$$P_i = \left| 2 \frac{(\mathbf{r}_i - \mathbf{r}_A)(\mathbf{r}_B - \mathbf{r}_A)}{|\mathbf{r}_B - \mathbf{r}_A|^2} - 1 \right|, \quad (0 \leq P_i \leq 1) \quad (9.49)$$

which is proposed to estimate the degree of ionicity and covalency of the chemical bonding between atoms  $A$  and  $B$  ( $\mathbf{r}_A$  and  $\mathbf{r}_B$  are their position vectors). This parameter takes the value  $P_i = 1$  for a pure ionic bond and  $P_i = 0$  for a pure covalent bond.  $A$  and  $B$  atoms are supposed to give the two largest contributions of the Mulliken atomic population to the WF  $W_i(\mathbf{r})$ .

These indices were used to analyze the chemical bonding in semiconductors [610] and metal oxides [63], based on HF LCAO calculations. In Table 9.15 the results for metal oxides are presented. In this table  $N_f$ ,  $N_{WF}$  and  $N_c$  are the number of formula units in the primitive cell, the number of valence-WFs in the primitive cell and the coordination number of the oxygen atom. According to the point symmetry at the O position, the four WFs can be equivalent, as in the case of MgO and MnO, or split into 2, 3, or 4 sets; the number of equivalent WFs in each set is indicated in the  $N_{eq}$  column. In those systems where crossings occur between the valence and the most diffuse semicore bands (the transition-metal oxides MnO and ZnO and CaSO<sub>4</sub>) the cation  $d$  and the Ca 2p bands, respectively, have also been included within the active subspace. In MnO, where only the ferromagnetic spin polarized solution was considered,  $\alpha$  and  $\beta$  subspaces are localized independently (the former conventionally containing the five Mn  $d$  states), [63]. In the right part of the table some features of the oxygen-WFs are provided:  $N_{eq}$  is the number of equivalent oxygen-WFs in the set;  $q_1, q_2$  and  $q_3$  are the three largest Mulliken atomic populations (the number of

equivalent contributions is given in brackets!). The Or column indicates whether the second-order moment tensor principal axis is oriented along the bond axis (*y*) or not (*n*), and the last column classifies the WFs as *covalent bond* (cv), *ionic* (io), or *lone-pair* (lp). The degree of localization of the oxygen WFs is estimated in terms of the

**Table 9.15.** Characterization of the oxides through their symmetry and WF features [63] (explanations are given in text)

System	Space group	N <sub>f</sub>	N <sub>WF</sub>	N <sub>c</sub>	N <sub>eq</sub>	q <sub>1</sub>	q <sub>2</sub>	q <sub>3</sub>	Or	Class
MgO	<i>Fm3m</i>	1	4	6	4	0.991	0.005(2)	0.004	<i>n</i>	io
MnO- $\alpha$	<i>Fm3m</i>	1	9	6	4	1.005	-0.001(4)	—	<i>n</i>	io
MnO- $\beta$	—		4		4	0.969	0.016(2)	0.005	<i>n</i>	io
ZnO	<i>P6<sub>3</sub>mc</i>	2	18	4	1	0.929	0.065(3)	0.002	<i>y</i>	cv
					3	0.927	0.065(3)	0.003	<i>y</i>	cv
Al <sub>2</sub> O <sub>3</sub>	<i>R3c</i>	2	24	4	2	0.964	0.043	0.004	<i>y</i>	cv
					2	0.942	0.060	0.003	<i>y</i>	cv
SiO <sub>2</sub>	<i>P3<sub>2</sub>11</i>	3	24	2	1	0.957	0.022	0.020	<i>n</i>	lp
					1	0.947	0.029	0.026	<i>n</i>	lp
					1	0.815	0.167	0.017	<i>y</i>	cv
					1	0.812	0.171	0.017	<i>y</i>	cv
AlPO <sub>4</sub>	<i>P3<sub>1</sub>21</i>	3	48	2	1	0.965	0.030	0.006	<i>n</i>	lp
					1	0.952	0.031	0.021	<i>n</i>	lp
					1	0.910	0.070	0.023	<i>y</i>	cv
					1	0.821	0.173	0.006	<i>y</i>	cv
CaSO <sub>4</sub>	<i>P6<sub>2</sub>22</i>	3	48	1	3	0.958	0.039	0.004	<i>n</i>	lp
					1	0.711	0.296	0.001	<i>y</i>	cv

Mulliken atomic populations (9.46), attributed to oxygen and its neighboring atoms. These data are summarized in columns q<sub>1</sub>, q<sub>2</sub>, and q<sub>3</sub> of Table 9.15. It turns out that, in all cases, most of the electron density is localized on the oxygen atom, q<sub>1</sub> ranging from 0.71 (CaSO<sub>4</sub>) to 1.01 (MnO). The value of the second atomic contribution is never larger than 0.30 (CaSO<sub>4</sub>); in most cases, however, it is of the order of 0.05. The third largest atomic population is much smaller and never exceeds 0.03 (SiO<sub>2</sub>).

The Or column provides information as to whether the principal axis connected to the largest eigenvalue of the second-order moment tensor is oriented along the bond axis or not. The bond axis of an O-WF is defined as the line joining the oxygen and the atom that brings the second largest contribution to the total population. For ease of discussion, one can try to use the two kinds of information (q<sub>i</sub> and Or indices) to classify (with a certain degree of arbitrariness) the O-WFs bonds as covalent bond (cv), lone-pair (lp), or ionic (io). In particular, it is considered as cv, a WF oriented along the bond direction, (orientation criterion); alternatively, a WF can be classified as cv, when q<sub>1</sub> < 0.95 and q<sub>2</sub> > 0.05 (population criterion), where q<sub>1</sub> and q<sub>2</sub> are the two largest contributions to the total population (see Table 9.15). A non-cv-WF is classified as io or lp when the coordination number of O is larger or smaller than 4 (the number of WFs formally attributable to oxygen), respectively. As is shown in [63], io and lp WFs do have quite different characteristics. The two criteria provide a very

consistent classification, the only exception being the most localized O-WFs of  $\text{Al}_2\text{O}_3$ , classified as cv or not according to the first or second criteria, respectively. Indeed in this case, both types of WFs are of the same chemical nature and quantitative differences are probably due to geometrical constraints. The orientation criterion seems to be the most appropriate and has been adopted (see last column of Table 9.15). This classification allows various trends to be traced with respect to the nature of the O-WFs along the series of compounds, as was done in [63]. In particular, it turns out that WFs give quite a complete picture of the chemical nature of the X–O bond, indicating that the covalent character increases according to the following sequence with respect to X:  $\text{Mg} < \text{Mn} < \text{Al} < \text{Zn} < \text{Si} < \text{P} < \text{S}$ . This order coincides with the cation Pauling electronegativities and demonstrates the atomic nature dependence of the chemical bonding in crystals.

This approach was applied also in [611] in the comparative study of chemical bonding in  $\text{SrTiO}_3$  and  $\text{SrZrO}_3$  crystals. The results of these calculations are discussed in the next section in the consideration of the projection technique for population analysis in crystals.

The numerical values of the indices dependence on the basis-set choice requires additional investigation. It is evident that use of Löwdin atomic populations instead of Mulliken ones can change the localization of WFs, especially in the case when diffuse AOs are included in the basis set. From this point of view the WTAOs use is preferable. As was demonstrated above, the numerical values of local properties are close in Mulliken and Löwdin population analysis made with WTAOs.

In the approach [63] WFs are generated directly from Bloch valence states without any preliminary symmetry analysis. In this case one obtains WFs that have the centroid positions in the vicinities of some points of the direct lattice of the crystal occupied by atoms or being midpoint between the pairs of symmetry-equivalent atoms (for the oxides listed in Table 9.15, these points are near oxygen atom positions). The noncontradictory chemical interpretation of the WFs obtained is difficult due to the absence of the symmetry analysis. Indeed, it is difficult to explain the appearance in  $\text{MgO}$  crystal (see Table 9.15) of four equivalent WFs corresponding to the tetrahedral  $sp^3$  hybridization, while the oxygen atom is octahedrally coordinated.

The improvements of this theory were suggested in [612]. The importance of the symmetry analysis in the procedure of the generation of maximally LOs in crystals was shown. It was suggested that the numerical parameters of the LOs corresponding to the valence energy bands of the crystal can be used in the theory of chemical bonding only if these functions form bases of irreducible representations of site-symmetry groups of atoms and bonds in crystals. The background of LOs symmetry analysis is the theory of band representations (BRs) of space groups, considered in Chap. 3. This analysis is applicable both to nonorthogonal atomic-like localized orbitals, centered on the atoms, and to localized Wannier orbitals (LWOs), *i.e.* to an orthonormal set of LOs. BRs of space groups are used to identify possible LOs symmetry from the symmetry of the canonical (Bloch) orbitals of the calculated energy bands or to establish the fact that the construction of LOs from the canonical orbitals chosen is impossible for the reasons of symmetry. In the general case, the LWOs are centered on some center  $\mathbf{q}$  and transform according to some representation  $\text{Re}$  (in the general case reducible) of the site-symmetry group  $L_{\mathbf{q}}$  of this center. Let us represent these functions as linear combinations of the LWOs  $\widetilde{W}_j^{(\beta)}$  transforming according to IRs  $\beta$

of the site group  $L_{\mathbf{q}}$ ,

$$W_i(\mathbf{r}) = \sum_{\beta,j} \alpha_{\beta,j,i} \widetilde{W}_j^{(\beta)}(\mathbf{r}), \quad \alpha^T \alpha = E \quad (9.50)$$

The transformation, with the help of the matrix  $\alpha$ , is orthogonal as it relates to two orthonormal bases in the space of the representation  $\text{Re}$  ( $E$  is the unit matrix). Inserting (9.50) in (9.47), one obtains

$$\bar{x}_{si} = \sum_{\beta\beta'jj'} D_{\beta j, \beta' j'}^{(s)} \alpha_{\beta j, i}^* \alpha_{\beta' j', i} \quad (9.51)$$

where the number of independent values  $D_{\beta j, \beta' j'}^{(s)} = \langle \widetilde{W}_j^{(\beta)}(\mathbf{r}) | x_s | \widetilde{W}_{j'}^{(\beta')}(\mathbf{r}) \rangle$  is equal to the number of irreducible components of the vector representation contained in the symmetric square  $\{Re \times Re^*\}^+$  of the representation  $\text{Re}$  [13]. If  $W_i(\mathbf{r})$  coincide with their irreducible components ( $\alpha_{\beta j, i} = \delta_{\beta j, i}$ ), then  $\mathbf{r}_i = 0$  for centrosymmetric site groups  $L_{\mathbf{q}}$  as all  $D_{\beta j, \beta' j'}^{(s)} = 0$  ( $\bar{x}_{si} = 0$ ). In the general case, as seen from (9.51),  $\mathbf{r}_i \neq 0$  and their lengths and orientations depend on the value of the coefficients  $\alpha_{\beta j, i}$ . Being functions of the centroid position, the polarization fractions  $P_i$  (9.49) also depend on the value of the coefficients  $\alpha_{\beta j, i}$ . It is obvious that *in the general case one can not attribute to the centroid of a LWO some physical meaning*. But a particular choice of LOs can attach to the centroid a common sense useful in the theory of chemical bonding.

LWOs  $W_A(\mathbf{r})$  sited on atoms describe lone pairs or a purely ionic bonding ( $P_i = 1$ ). LWOs  $W_B(\mathbf{r})$  sited on interatomic bonds mean the presence of a covalent component of the chemical bonding ( $0 < P_i < 1$ ), the degree of covalence being determined by the value of the polarization fraction  $P_i$  that takes the form

$$P_i = \left| 2 \frac{d_i - d_A}{d_B - d_A} - 1 \right| \quad (9.52)$$

where  $d_A$ ,  $d_B$ , and  $d_i$  are positions of atoms  $A$ ,  $B$ , and the centroid of the LWO  $W_i(\mathbf{r})$  on the bond line  $A - B$  counted off some arbitrary point on it. In the latter case, the BR associated with the valence bands of the crystal has to include the BR induced from some IR  $\beta$  of the site-symmetry group  $L_{\mathbf{q}_b}$  of the bond. The value  $P_i = 0$  corresponds to a pure covalent bond. Note that this BR is a composite one. Indeed, the group  $L_{\mathbf{q}_b}$  is a subgroup of the site group  $L_{\mathbf{q}_A}$  of the atom  $A$  (and of the site group  $L_{\mathbf{q}_B}$  of the atom  $B$ ) lying on the bond. The IR  $\beta$  induces in the groups  $L_{\mathbf{q}_A}$  some reducible representation that, in its turn, induces in the space group  $G$  a composite BR [13]. There is an exception when a middle point of the bond is a symmetry point. In this case, the IR of the site group of this point induces in the space group  $G$  a simple BR. This situation takes place, for example, in the Si crystal where the IR  $a_{1g}$  of the site group  $D_{3d}$  of the middle point of the bond Si-Si (Wyckoff position c) induces in the space group  $O_h^7$  of the crystal the BR with  $\mathbf{q}$ -basis consisting of the canonical Bloch states of the four-sheeted upper valence band. This LWO describes the purely covalent bond ( $P = 0$ ).

In [612] the following procedure was suggested to describe the chemical bonding in crystals by analyzing only occupied valence states in the basis of LOs.

As the first step a symmetry analysis of valence band states is carried out. The purpose of this analysis is to find the  $\mathbf{q}$ -basis indices of the band representation (BR) corresponding to the valence states of the crystal. These indices can consist of: (a1) the irreducible representations (IRs) of the site groups of the bonds (including those of symmetry points on the bond lines, if there are any); (a2) the IRs of site groups of atoms. If a composite BR has several variants to be represented as a sum of simpler ones, the preference has to be given to the BRs induced from site groups of bonds. This symmetry analysis allows the centroid positions (on atoms or on bonds) of the LOs, generated from the Bloch functions of the valence states, to be found. The numerical characteristics of only these symmetry-defined LOs are suggested to give a noncontradictory unambiguous interpretation of chemical bonding in crystals. It was proposed in [612] to introduce not only the centroids position, but also the other numerical characteristics of the chemical bond related to the centroids position:

1) Contributions  $Q_i^{(A)}$  and  $Q_i^{(B)}$  to charges on atoms  $A$  and  $B$  related to the LO  $W_i(\mathbf{r})$

$$Q_i^{(A)} = 2 \frac{d_i - d_B}{d_B - d_A}, \quad Q_i^{(B)} = 2 \frac{d_A - d_i}{d_B - d_A}, \quad -2 \leq Q_i^{(A)}, Q_i^{(B)} \leq 0 \quad (9.53)$$

An electron charge  $Q_i^{(A)} + Q_i^{(B)} = -2$  associated with the fully occupied LO is partitioned between atoms  $A$  and  $B$  and is inversely proportional to the distances between the centroid position and the atoms.

2) The degree of ionicity  $I_i$  of the bond  $A - B$  related to the LO  $W_i(\mathbf{r})$ ,

$$I_i = \left| \frac{2d_i - d_A - d_B}{d_B - d_A} \right| = \frac{1}{2} \left| Q_i^{(A)} - Q_i^{(B)} \right|, \quad 0 \leq I_i \leq 1 \quad (9.54)$$

The degree of covalency  $K_i$  of the bond A–B related to the LO  $W_i(\mathbf{r})$ ,

$$K_i = 1 - \left| \frac{2d_i - d_A - d_B}{d_B - d_A} \right| = 1 - \frac{1}{2} \left| Q_i^{(A)} - Q_i^{(B)} \right|, \quad 0 \leq K_i \leq 1 \quad (9.55)$$

Ionicity  $I_i$  coincides with the polarization fraction (9.52).

For pure ionic bonding  $Q_i^{(A)} = -2, Q_i^{(B)} = 0$  (or vice versa),  $K = 0, I = 1$ . For pure covalent bonding  $Q_i^{(A)} = Q_i^{(B)} = -1, K = 1, I = 0$ . The definitions (9.52)–(9.55) are introduced in such a way that the LWO centroid position defines the characteristics of chemical bonding. In fact, the details of the electron density distribution have to be included, as is done in the definition (9.48) of the second-order central moment tensor.

In the second step of the chemical-bonding analysis the space  $\Omega$  of the states of all the valence energy bands is projected on the spaces  $\Omega_i$  of IR of the site-symmetry groups related to the components of the BR in the  $\mathbf{q}$ -basis established above.

The third step is the generation from the canonical Bloch valence states maximally localized orbitals in the spaces  $\Omega_i$  by any known procedure.

The fourth step consists of calculation of numerical characteristics of the chemical bonding on the base of these LOs. This calculation includes both the characteristics, defined by the centroids positions, and those depending on the details of the electron density distribution.

As follows from the theory of BR, the LOs obtained without any preliminary symmetry analysis, are in fact to be bases of some representations (in the general case reducible) of site-symmetry groups of the Wyckoff positions of atoms and bonds, the preference has to be given also to BRs induced from site groups of bonds. In this case, steps 2 and 3 have to be replaced by: (2a) Generation maximally LOs in the space of the canonical Bloch valence states by any known procedure. (3a) A proper symmetrization of generated LOs according to the results of the symmetry analysis of step 1.

We shall illustrate the discussed procedure using the example of the  $\text{SrZrO}_3$  crystal with the cubic perovskite structure. In Table 9.16 band representations of space group  $O_h^1$  induced by those atomic states that take part in the valence band formation are given. Each line of this table defines the connection of the  $\mathbf{q}$ -basis for site-symmetry groups  $O_h(\text{Sr}), D_{4h}(\text{O})$  with the  $\mathbf{k}$ -basis at the symmetry points of BZ, see also Sect. 3.3.

**Table 9.16.** Band representations of upper valence bands in the  $\text{SrZrO}_3$  crystal induced from Sr 4p-, O 2s- and O 2p-atomlike states

Atom states	$\mathbf{q}$ -basis	$\Gamma$	$R$	$M$	$X$
Sr 4p	(b, $t_{1u}$ )	4 <sup>-</sup>	5 <sup>+</sup>	2 <sup>-</sup> 5 <sup>-</sup>	1 <sup>+5+</sup>
O 2s	(d, $a_{1g}$ )	1 <sup>+3<sup>+</sup></sup>	4 <sup>-</sup>	1 <sup>+5-</sup>	1 <sup>+2<sup>+3-</sup></sup>
O 2p <sub>z</sub>	(d, $a_{2u}$ )	4 <sup>-</sup>	1 <sup>+3<sup>+</sup></sup>	1 <sup>+2<sup>+3-</sup></sup>	1 <sup>+5-</sup>
O 2p <sub>x,y</sub>	(d, $e_u$ )	4 <sup>-5-</sup>	4 <sup>+5<sup>+</sup></sup>	3 <sup>+4<sup>+5<sup>±</sup></sup></sup>	3 <sup>-4<sup>-5<sup>±</sup></sup></sup>

To include the electron-correlation effects on the chemical bonding, the calculations of  $\text{SrZrO}_3$  crystal [612, 613] were performed by the DFT LCAO method with the CRYSTAL03 code [23] and the PBE exchange-correlation potential used in [614] for the geometry optimization in the generalized gradient approximation (GGA). For the Sr and Zr atoms, the Hay–Wadt pseudopotentials [483] in the small-core approximation were used. In this case, the 4s, 4p, and 5s states of the Sr atom in the  $4s^24p^65s^2$  configuration and the 4s, 4p, 4d, and 5s states of the Zr atom in the  $4s^24p^64d^25s^2$  configuration were treated as valence states. The basis functions were taken as the atomic functions of the Sr atom from [606] and the 8-411G \* functions obtained for the Zr atom in [615] with optimization of the 5sp, 6sp, and 5d outer orbitals for the  $\text{ZrO}_2$  crystal with experimental geometric parameters. For the oxygen atom, the full-electron basis set [606] describing the oxygen atom in the  $1s^22s^22p^4$  configuration was used. The Monkhorst–Pack  $8 \times 8 \times 8$  set of special points was used in the BZ sampling. The lower valence bands are composed of Sr 4p- and O 2s-states (six sheets), whereas the upper valence band is produced mainly by the O 2p-atomic orbitals (nine sheets), see Fig. 9.2. The symmetry of all these valence-band states and the atomic nature of the projected density of states is the same both in these DFT-LCAO and in former DFT-PW calculations [616]. The iterative procedure implemented in CRYSTAL03 code was applied to generate LOs using crystal orbitals of these 15 occupied bands. The Bloch functions for the  $\Gamma$  point of the BZ are taken as the starting LOs. As a result, the iterative procedure gives 15 LOs. Three of them are centered on the Sr

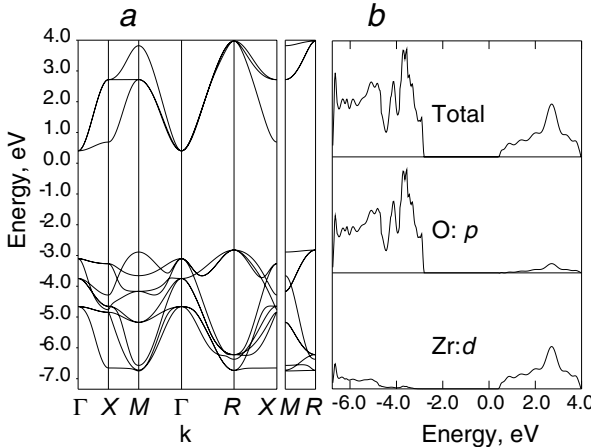


**Fig. 9.2.** Electronic structure of  $\text{SrZrO}_3$  crystal: (a) band structure; (b) total and projected DOS. LCAO DFT calculations [613]

atom and are connected with Sr atom  $4p$ -states. The remaining 12 LOs are connected with the three symmetry-equivalent oxygen atoms in the crystal, four LOs with the centroid positions near each oxygen atom. To analyze the nature of chemical bonding with these LOs, the information about the symmetry of the band states induced from Sr  $4p$ -, O  $2s$ -, and O  $2p$ -states forming two upper valence bands given in Table 9.16 is used. It is seen that these states form a basis of composite BR described in  $\mathbf{q}$ -basis by the symbol

$$(b, t_{1u}) + (d, a_{1g} + a_{2u} + e_u) \quad (9.56)$$

Therefore, four LWOs  $W_i(\mathbf{r})$  with the centroid positions near each oxygen atom form a basis of a four-dimensional representation  $a_{1g} + a_{2u} + e_u$  of the site group  $D_{4h}$  of the oxygen atom. Let us denote LOs that are the basis functions of these IRs as follows:  $\widetilde{W}_1(\mathbf{r}) = \widetilde{W}_1^{(d, e_u)}(\mathbf{r})$ ,  $\widetilde{W}_2(\mathbf{r}) = \widetilde{W}_2^{(d, e_u)}(\mathbf{r})$ ,  $\widetilde{W}_3(\mathbf{r}) = \widetilde{W}_3^{(d, a_{2u})}(\mathbf{r})$ ,  $\widetilde{W}_4(\mathbf{r}) = \widetilde{W}_4^{(d, a_{1g})}(\mathbf{r})$ . Then, instead of (9.50), one has

$$W_i(\mathbf{r}) = \sum_{j=1}^4 \alpha_{ji} \widetilde{W}_j(\mathbf{r}), \quad i = 1, 2, 3, 4 \quad (9.57)$$

The starting LWOs of the computer code [23] result in  $W_i(\mathbf{r})$  (9.57) with some definite values of the coefficients  $\alpha_{ji}$ . In this case,  $Re = e_u + a_{2u} + a_{1g}$ , the representation  $\{Re \times Re^*\}^{(+)} = 3a_{1g} + b_{1g} + b_{2g} + e_g + e_u + a_{2u}$  contains only one times two irreducible components of the vector representation  $(e_u + a_{2u})$ , *i.e.* there are only two independent parameters in (9.51),

$$\bar{r}_i = \sum_{s=1}^3 \bar{x}_{si} \bar{e}_s, \quad \bar{x}_{si} = D_s \alpha_{4i} \alpha_{si} \quad (9.58)$$

where

$$D_1 = 2\langle \widetilde{W}_4(\mathbf{r}) | x_1 | \widetilde{W}_1(\mathbf{r}) \rangle = D_2 = 2\langle \widetilde{W}_4(\mathbf{r}) | x_2 | \widetilde{W}_2(\mathbf{r}) \rangle, \quad D_3 = 2\langle \widetilde{W}_4(\mathbf{r}) | x_3 | \widetilde{W}_3(\mathbf{r}) \rangle \quad (9.59)$$

In Table 9.17 the Cartesian coordinates  $\bar{x}_{si}$  of centroid positions and the polarization fractions  $P_i$  for LWOs  $W_i(\mathbf{r})$  evaluated by the computer code [23] are given. It is evident (see (9.58)) that the other choice of the starting LWOs can, in principle, give other centroid positions and other values of  $P_i$ . Let us note that the BR ( $d, a_{1g} + a_{2u}$ ) is

**Table 9.17.** Centroids positions ( $x_{1i}, x_{2i}, x_{3i}$ ), in a.u., and polarization fractions  $p_i$  for functions  $W_i(\mathbf{r})$  in the  $\text{SrZrO}_3$  crystal localized according to the Wannier–Boys mixed scheme [63]

$W_i$	$x_{1i}$	$x_{2i}$	$x_{3i}$	$p_i$
$W_1$	-0.039	0.465	-0.002	0.999
$W_2$	0.465	-0.039	-0.002	0.999
$W_3$	-0.211	-0.211	0.774	0.610
$W_4$	-0.215	-0.215	-0.769	0.612

a composite one. The points on the line binding Zr and O atoms (Wyckoff position e) have the site-symmetry  $C_{4v}$ . The IR  $a_1$  of this group induces in the group  $D_{4h}$  (the site symmetry group of the oxygen atom) the representation  $a_{1g} + a_{2u} : a_1(C_{4v}) \uparrow D_{4h} = a_{1g} + a_{2u}(D_{4h})$ . Therefore, instead of (9.56) one can write another symbol in  $\mathbf{q}$ -basis

$$(b, t_{1u}) + (d, e_u) + (e, a_1) \quad (9.60)$$

for the same BR corresponding to the 15-sheeted band chosen. Note that the IR  $a_1$  of  $C_{4v}$  induces also the representation  $a_{1g} + e_g + t_{1u}$  of the site group  $O_h$  of the Zr atom – the second atom on the bond line Zr–O:  $a_1(C_{4v}) \uparrow O_h = a_{1g} + e_u + t_{1u}(O_h)$ . Thus, one can attribute one more symbol in the  $\mathbf{q}$ -basis to the BR corresponding to the same 15-sheeted energy band,

$$(b, t_{1u}) + (d, e_u) + (a, a_{1g} + e_g + t_{1u}) \quad (9.61)$$

It is seen that the part  $(b, t_{1u}) + (d, e_u)$  is common for three symbols (9.56)–(9.60)–(9.61) of the BR under consideration. They correspond to LWOs, localized on Sr and oxygen atoms. The rest of the BR is given in three different ways by its labels (9.56)–(9.60)–(9.61). The symmetry considerations show that it is possible to generate from the states of valence bands of the  $\text{SrZrO}_3$  crystal the LWOs centered on zirconium and on oxygen atoms. These LWOs form the bases of reducible representations of the site groups of Zr and O atoms,  $a_{1g} + e_g + t_{1u}$  of  $O_h$  and  $a_{1g} + a_{2u}$  of  $D_{4h}$ , respectively. Linear combinations of functions of any of these bases are equivalent from the group-theoretical point of view, but will give *different* values for the numerical characteristics of chemical bonding (9.52)–(9.55). However, there is only *one* possibility to reconcile these two bases. Both bases are induced from the same IR  $a_1$  of the common subgroup  $C_{4v}$  (the site group of the Wyckoff position e on the bond line Zr–O) of the groups  $O_h$  and  $D_{4h}$ .

The BR with  $\mathbf{q}$ -basis (9.60) corresponds to a particular choice of the linear combinations of  $\widetilde{W}_j(\mathbf{r})$  (9.57): two of them are transformed according to the IR

$e_u$  of the site group ( $D_{4h}$ ) of the oxygen atom, the linear combination  $\widetilde{W}_+^{(e,a_1)} = \frac{1}{\sqrt{2}} (\widetilde{W}^{(d,a_{1g})} + \widetilde{W}^{(d,a_{2u})})$  of two others engenders the LWO sited on the bond line Zr–O and transforming according to IR  $a_1$  of the symmetry group  $C_{4v}$  of the bond. This LWO induces another one  $\widetilde{W}_-^{(e,a_1)} = \frac{1}{\sqrt{2}} (\widetilde{W}^{(d,a_{1g})} - \widetilde{W}^{(d,a_{2u})})$  centered on the Zr–O bonding line but at the other side of the same oxygen atom. On the whole, the number of LWOs per unit cell remains the same. These functions describe the covalent bonding of the oxygen atom with its two neighboring Zr atoms. The numerical value of covalency can be evaluated from the centroid positions of these LWOs counted off the oxygen atom.

To find the centroid positions of the LWOs  $\widetilde{W}_i(\mathbf{r})$  it is sufficient to symmetrize the LWOs  $\widetilde{W}_i(\mathbf{r})$  calculated without symmetry by the usual group-theoretical methods. Instead of extracting the LWO s themselves from the results of computer code [23] application it was done in [612] by using the relation (9.58) with the normality condition and the orthogonality of the matrix  $\alpha$  in (9.58) connecting the symmetrized LWOs and those found in the direct calculations. This matrix was found in numerical form and analyzed in [612]. It was found that LWOs  $W_i(\mathbf{r}), i = 1, 2$  almost coincide with  $\widetilde{W}_i^{(d,e_u)}(\mathbf{r})$  although they have a noticeable admixture of LWO  $\widetilde{W}^{(d,a_{1g})}(\mathbf{r})$ . LWOs  $W_i(\mathbf{r}), i = 3, 4$  are formed essentially by  $\widetilde{W}^{(d,a_{2u})}(\mathbf{r})$  and  $\widetilde{W}^{(d,a_{1g})}(\mathbf{r})$  although they have a noticeable admixture of LWO  $\widetilde{W}^{(d,e_u)}(\mathbf{r})$ . Using (9.59), one obtains  $\langle \widetilde{W}^{(d,a_g)}(\mathbf{r}) | x_3 | \widetilde{W}^{(d,a_{2u})}(\mathbf{r}) \rangle = 0.912$ . The centroid positions relative to oxygen atoms for the LWOs  $\widetilde{W}_i(\mathbf{r}) (i = 1, 2, 3, 4)$ ,  $\mathbf{r} - \mathbf{r}_0 = 0$  and the corresponding polarization fraction  $P_i = 1$  for all four LWOs. In particular, for  $\widetilde{W}_1^{(d,e_u)}(\mathbf{r})$  and  $\widetilde{W}_2^{(d,e_u)}(\mathbf{r})$ ,  $P = 1$ . They describe lone pairs on the oxygen atom in the crystal. But for the linear combinations  $\widetilde{W}_\pm^{(e,a_1)}(\mathbf{r})$  (the IR  $a_1$  of the site group  $C_{4v}$  of the Wyckoff position e on the bond line Zr–O),  $\mathbf{r}_\pm - \mathbf{r}_0 = \pm 0.912e_3$  (in a.u.) and the polarization fractions  $P_\pm = 0.54$ . These LWOs describe the partly covalent binding of atoms O and Zr in the crystal  $\text{SrZrO}_3$ . The other numerical characteristics (9.53) and (9.54) of this bond are:  $Q^{(\text{O})} = -1.54$ ,  $Q^{(\text{Zr})} = -0.46$ ,  $I_{\text{O-Zr}} = 0.54$ ,  $K_{\text{O-Zr}} = 0.46$ . Taking into account the choice of valence and semicore electrons, atomic cores have the charges: +6(O), +8(Sr), +4(Zr). According to the  $q$ -basis index of the BR (9.60) the electron structure of the crystal can be represented by 15 LWOs per primitive cell, every orbital being occupied by two electrons:

1. Three orbitals  $\widetilde{W}^{(b,t_{1u})}(\mathbf{r})$  of symmetry  $t_{1u}$  ( $p$ -type) are localized on Sr (site group  $O_h$ ) and bring to it the charge -6. Finally, atom Sr has in the crystal the charge +2=8-6 rigorously. This value is close to that found by population analysis with WTAOs.
2. Six orbitals  $\widetilde{W}^{(d,e_u)}(\mathbf{r})$  of symmetry  $e_u$  ( $p_x, p_y$ -type) are localized on O atoms (site group  $D_{4h}$ , three atoms per primitive cell) and bring to every atom the charge -4.
3. Six orbitals  $\widetilde{W}^{(e,a_1)}(\mathbf{r})$  of symmetry  $a_1$  ( $sp_z$ -type) are localized on the bonding line O–Zr (site group  $C_{4v}$ , six bonding lines per primitive cell). The charge -2 associated with every orbital is partitioned between oxygen (-1.54) and zirconium (-0.46) atoms. As there are two bonds for the oxygen atom, its charge in the crystal is -1.08 ( $=+6-4-1.54 \times 2$ ). Equally for the zirconium atom, one has +1.24 ( $=+4-0.46 \times 6$ ; 6 bonds for Zr). The traditional Mulliken population analysis gives values -1.29 and

+2.02, the projection techniques -1.14 and +1.63, WTAO population analysis gives more ionic charges -1.67 +3.00, [611].

Using the symmetry analysis in MgO crystal [612] for the Bloch states of the four upper valence bands one obtains the  $\mathbf{q}$ -basis of symmetry

$$(a, a_{1g} + t_{1u}) \quad (9.62)$$

with the oxygen atom in the Wyckoff position a. Electronic states of these energy bands are originated certainly from  $2s, 2p$ -O atomic states. The points on the bond line of the atoms Mg and O (Wyckoff position e) have the symmetry  $C_{4v}$ . Even the one-dimensional IR  $a_1$  of this group induces in the group  $O_h$  the six-dimensional representation  $a_1(C_{4v}) \uparrow O_h = a_{1g} + e_g + t_{1u}(O_h)$ . This means that there exists no LWO centered on this bond that could generate a four-sheeted upper valence energy band in the MgO crystal. One can say the same about the LWOs centered on the Wyckoff position f (x,x,x) with site group  $C_{3v}$ : they could engender an eight-sheeted energy band.

Therefore, there is no other alternative but (9.62) for the BR corresponding to valence bands in the MgO crystal. For a reasonable interpretation of bonding in the crystal only the functions  $\widetilde{W}_1(\mathbf{r}) = \widetilde{W}^{(a,a_{1g})}(\mathbf{r})$ ,  $\widetilde{W}_i(\mathbf{r}) = \widetilde{W}_1^{(a,t_{1u})}(\mathbf{r})$ ,  $i = 2, 3, 4$  are suited. They are centered on an oxygen atom and  $\mathbf{r}_i = \mathbf{r}_O$ ,  $Q_i^{(O)} = -2$ ,  $I_i = P_i = 1$ ,  $K_i = 0$  ( $i = 1, 2, 3, 4$ ). The centroid positions and the values of other numerical characteristics of chemical bonding are not changed evidently for any linear combination of the functions  $\widetilde{W}_i(\mathbf{r})$ ,  $i = 1, 2, 3, 4$  in the space of IR  $t_{1u}$ . The charges on atoms are: +2(Mg), -2(O) strongly. Such a picture of chemical bonding in MgO crystal corresponds to the accepted one for this ionic system. Nevertheless, it is necessary to introduce such numerical characteristics of LWOs that could describe the small covalent part of Mg-O bonding and relative change of this part in the row MgO–CaO–SrO–BaO.

This discussion demonstrates the importance of the symmetry analysis in the procedure of the generation of LWOs in crystals. The theory of space group BR gives a powerful tool to determine the centroid positions of LWOs.

(1) If this centroid is at the symmetry point in the direct lattice, its position is defined exactly by the BR theory. If this position is occupied by an atom, the corresponding LWO describes an ionic bond or a lone pair. This is the case for the MgO crystal and the LWOs  $\widetilde{W}_1^{(d,e_u)}$  and  $\widetilde{W}_2^{(d,e_u)}$  in the SrZrO<sub>3</sub> crystal. If it is a middle point between two atoms, the corresponding LWO describes a pure covalent bond. This is the well-known example of the Si crystal.

(2) If the centroid is located on a symmetry line (possible site groups are  $C_{6v}, C_{4v}, C_{3v}, C_{2v}, C_6, C_4, C_3, C_2$ ), its exact position cannot be defined by the BR theory, and numerical calculations are necessary. The corresponding LWO describes a two-atom partly covalent bond. This is the case of the LWO  $\widetilde{W}^{(e,a_1)}$  (site group  $C_{4v}$ ) in the SrZrO<sub>3</sub> crystal with the following numerical characteristics of the bond:

$$I_{O-Zr} = P_{O-Zr} = 0.54, K_{O-Zr} = 0.46, Q^{(O)} = -1.54, Q^{(Zr)} = -0.46$$

(3) If the centroid is located at a symmetry plane (possible site group is  $C_s$ ), its exact position cannot be defined by the BR theory, and numerical calculations are also necessary. The corresponding LWO describes a three-(and more)-atom bond.

As we saw in the example of  $\text{SrZrO}_3$  crystal the absolute atomic-charge values differ in the different approaches to their calculation. Do different approaches (including those based on PW calculations) reproduce correctly at least the relative changes in the chemical bonding in crystals with analogous structure? This point is discussed in the next section.

### 9.1.6 Projection Technique for Population Analysis of Atomic Orbitals. Comparison of Different Methods of the Chemical-bonding Description in Crystals

At present, the electronic structure of crystals, for the most part, has been calculated using the density-functional theory in a plane-wave (PW) basis set. The one-electron Bloch functions (crystal orbitals) calculated in the PW basis set are delocalized over the crystal and do not allow one to calculate the local characteristics of the electronic structure. As a consequence, the functions of the minimal valence basis set for atoms in the crystal should be constructed from the aforementioned Bloch functions. There exist several approaches to this problem. The most consistent approach was considered above and is associated with the variational method for constructing the Wannier-type atomic orbitals (WTAO) localized at atoms with the use of the calculated Bloch functions. Another two approaches use the so-called projection technique to connect the calculated in PW basis Bloch states with the atomic-like orbitals of the minimal basis set.

The first approach (A) consists in using the technique for projecting the Bloch functions calculated in the PW basis set onto atomic orbitals of the minimal valence basis set for free atoms [617, 618]. Within this procedure the atomic-like functions are generated using the pseudopotentials chosen for the PW band structure calculations. Such functions are neither orthonormal nor complete in the sense of spanning the space of the occupied states. To measure how completely the localized atomic orbitals represent the eigenstates a so-called spilling parameter is introduced, which varies between one and zero. If the spilling parameter is nonzero a special projection procedure is needed to correctly define the density-operator for the incomplete basis of atomic-like functions. Since this constructed localized basis is not orthogonal, as in the case of LCAO calculations both Mulliken and Löwdin schemes may be used.

The second approach (B), proposed for constructing quasiamionic minimal basis orbitals (QUAMBO) in [609] is also closely related to the projection technique (being in fact a projection reverse to the first one): the projection of a given minimal atomic basis is made on the Bloch states obtained in the PW calculations. This method can be regarded as a sort of localization procedure, and it describes the electronic structure of periodic solids in terms of localized quasiamionic minimal basis orbitals (QUAMBO).

Both variants of the projection technique were used for calculations of the local characteristics in the bulk of crystals [601, 609, 618] and, in a number of cases, led to results that are rather difficult to explain from the chemical standpoint. For example, the calculated charge of Mg atom in the ionic crystal  $\text{MgO}$  equals 0.76 [601]. Note that the construction of the WTAOs from the Bloch functions obtained in the PW basis set permitted almost ionic charges at atoms in the  $\text{MgO}$  crystal to be derived, see Table 9.14. However, it should also be noted that comparison of the data available

in the literature on different characteristics obtained by the projection technique is complicated because the crystal orbitals are calculated with different variants of the DFT method, different pseudopotentials for excluding the core electrons from consideration, different atomic basis sets, etc. In order to interpret the results obtained by the projection technique, it is necessary to perform a comparative analysis of the density matrices (in the atomic orbital basis set) determined by the two aforementioned projection variants. In [619] such an analysis is carried out for the first time, and a simplified version of technique B was proposed to avoid cumbersome calculations of a large number of vacant crystal orbitals. Thus, in both variants A and B of the projection technique when the atomic orbital set for free atoms or free ions is assumed to be known, the population analysis can be carried out without invoking vacant crystal orbitals. We refer the reader for the mathematical details of this analysis to the publications [611, 619]. Here, we discuss only the numerical results, obtained in these studies for the local properties of electronic structure of crystals in both projection techniques and compare them with those obtained in traditional AO and WTAO Mulliken population analysis, including Bloch functions of vacant states. The comparison is also made with the results obtained with localized Wannier functions, generated only for the valence bands by method [63].

In Table 9.18 we give the local properties of electronic structure (atomic charges  $Q_A$ , covalencies  $C_A$ , bond orders  $W_{AB}$  and overlap populations  $R_{AB}$ ) calculated by projection techniques A and B for the crystals with different nature of chemical bonding: Si, SiC, GaAs, MgO, cubic BN, and  $\text{TiO}_2$  with a rutile structure,  $R_0$  is the nearest-neighbor distance, given in Å.

**Table 9.18.** Local properties of electronic structure in projection technique, [619]

Crystal	$R_0$	$Q_A$		$C_A$		spl ( $10^{-3}$ )		$W_{AB}$		$R_{AB}$	
		A	B	A	B	A	B	A	B	A	B
MgO	2.107	1.609	1.607	0.630	0.632	1.4	1.1	0.112	0.113	0.095	0.096
BN	1.565	0.681	0.715	3.292	3.263	3.7	3.0	0.804	0.800	0.709	0.700
$\text{TiO}_2$	1.951	1.730	1.739	3.474	3.459	2.2	1.4	0.552	0.550	0.305	0.302
Si	2.364	0.000	0.000	3.823	3.801	9.6	6.5	0.894	0.889	0.756	0.744
SiC	1.901	1.260	1.284	3.497	3.472	8.9	5.3	0.831	0.827	0.760	0.751
GaAs	2.451	0.361	0.380	3.231	3.202	1.8	1.8	0.768	0.765	0.636	0.629

The crystal orbitals were calculated by the DFT method in the plane-wave basis set with the CASTEP code [377] in the GGA density functional. A set of special points  $\mathbf{k}$  in the Brillouin zone for all the crystals was generated by the supercell method (see Chap. 3) with a  $5 \times 5 \times 5$  diagonal symmetric extension, which corresponds to 125 points. In all cases, the pseudopotentials were represented by the normconserving optimized atomic pseudopotentials [621], which were also used to calculate the atomic potentials of free atoms. In the framework of both techniques (A, B), the population analysis was performed in the minimal atomic basis set; *i.e.* the basis set involved only occupied or partially occupied atomic orbitals of free atoms. It is well known that the inclusion of diffuse vacant atomic orbitals in the basis set can substantially change the results of the population analysis. For example, if the Mg 2p vacant atomic orbitals are included in the basis set, the charge calculated by technique A for the Mg

atom in the MgO crystal decreases from 1.61 to 1.06. Consequently, the inclusion of the Mg  $2p$  functions leads to a considerable decrease in the ionic component of the bonding and, correspondingly, to an increase in the covalence of atoms. Chemically, it is difficult to explain this high covalency of the bonding in the MgO crystal.

The spilling parameter  $spl$  values are also given in Table 9.18, which characterize the accuracy of the projection of occupied crystal orbitals onto the space of the atomic orbitals (technique A) and the accuracy of the projection of atomic orbitals onto the Bloch functions (technique B).

The atomic charges obtained by technique A can be compared with those calculated in [601] with the use of a similar method. The atomic charges and the spilling parameters presented in [601] are considerably smaller than those in the calculation discussed. In our opinion, the main factor responsible for this disagreement is the difference between the atomic basis sets that are used for the projection. This assumption is confirmed by the following fact noted in [601]. The removal of the Si  $d$  vacant orbital from the atomic basis set leads to an increase in the charge at the Si atom in the SiC crystal from 0.66 to 1.25 and an increase in the spilling parameter from  $2 \times 10^{-3}$  to  $9 \times 10^{-3}$ . It follows from Table 9.18 that, in calculations in the minimal basis set (without the Si  $d$  function), these quantities are equal to  $1.26 \times 10^{-3}$  and  $8.9 \times 10^{-3}$ , respectively, which agrees well with the results obtained in [601] (without the Si  $d$  function). It is evident that an increase in the size of the basis sets should result in a decrease in the spilling factor in method A, because this is accompanied by an increase in the space of the atomic orbitals onto which the occupied crystal orbitals are projected. However, we believe that it is incorrect to decrease the spilling parameter in the population analysis of the atomic orbitals by increasing the atomic basis sets, as was actually done in [601]. For example, if the basis set of the atomic orbitals is increased to a complete set, the spilling coefficient can be reduced to zero; however, the population analysis of the atomic orbitals in this basis set loses all physical meaning.

For the purely covalent cubic Si crystal, the results obtained by technique B can be compared with the data reported in [609], for Si–Si bond order  $W_{AB} = 0.885$  and the Mulliken overlap population is  $R_{AB} = 0.756$ . As can be seen from Table 9.18, the results obtained by technique B ( $W_{AB} = 0.889$ ,  $R_{AB} = 0.744$ ) are very close to those given in [609]. The insignificant differences can be associated with the use of different variants of the DFT method in the plane-wave basis set. Note that technique B used in [619] is a simpler modified variant of the method proposed in [609] and does not deal with the vacant Bloch states.

It can be seen from Table 9.18 that the data calculated by the techniques A and B are in good agreement. It should only be noted that the ionic component of the bonding ( $Q_A$ ) in technique B is somewhat larger than the analogous component in technique A. Correspondingly, the covalent component ( $C_A$ ,  $W_{AB}$ ,  $R_{AB}$ ) is somewhat smaller in technique B. Moreover, the spilling parameters in technique B are regularly smaller in magnitude.

In Table 9.19 we compare the local characteristics of the electronic structure determined for the  $\text{TiO}_2$  crystal with the use of the projection technique and those obtained in an earlier study [623], in which the Wannier-type atomic functions of the minimal valence basis set of titanium and oxygen atoms were constructed by the variational method. In [623], the Bloch functions were calculated by the DFT method

**Table 9.19.** Local characteristics of the electronic structure of the  $\text{TiO}_2$  (rutile) crystal\*

Method	$Q_{\text{Ti}}$	$C_{\text{Ti}}$	$W_{\text{Ti}-\text{O}}$	$V_{\text{Ti}}$
A	1.79	3.36	0.51	4.13
B	1.80	3.34	0.51	4.12
LCAOM	1.78	3.30	0.52	4.08
LCAOL	1.04	4.29	0.66	4.52
WTAOM	1.98	3.16	0.51	4.11
WTAOL	1.92	3.23	0.52	4.12

\*LCAOM(L) – traditional Mulliken (Löwdin) population analysis with basis set used in LCAO calculations; WTAOM(L) – Mulliken (Löwdin) population analysis with WTAO basis set

in the LCAO approximation with the CRYSTAL code [23] and the atomic pseudopotentials taken from [484]. It follows from Table 9.19 that the local characteristics of the electronic structure of the  $\text{TiO}_2$  crystal are close for two projection variants (techniques A, B) and differ only slightly from the results of the Mulliken (not Löwdin!) population analysis performed in the basis set of the atomic orbitals at the LCAO level. It is seen that the traditional Löwdin population analysis with the initial LCAO basis set containing diffuse atomic functions leads to an overestimated covalence of chemical bonding.

When analyzing the populations in the WTAO basis set, the Löwdin orthogonalization of the basis set leads to insignificant differences as compared to the results of the Mulliken population analysis (due to the localized character of the Wannier-type atomic functions). The Löwdin atomic charges and the atomic covalences correspond to a somewhat lower degree of ionicity. An important conclusion can be drawn from comparison of WTAO results with those obtained in the projection technique: despite the use of substantially different basis sets for calculating the crystal orbitals (plane waves in the projection technique, LCAO in the WTAO method), the local characteristics of the rutile electronic structure obtained within the two approaches are in good agreement. Meanwhile, the results of traditional population analysis differ from those obtained by the projection technique (see Table 9.19). This difference is demonstrated also in Table 9.20, where for  $\text{SrTiO}_3$  and  $\text{SrZrO}_3$  crystals the results of traditional Mulliken population analysis are compared with those obtained by the projection technique (both crystals were taken in cubic perovskite structure with the space group  $Pm\bar{3}m$ ).

The results, given in Table 9.20, were obtained by the DFT PBE method in LCAO and PW calculations (the details of the LCAO basis set and other parameters choice can be found in [611]). In the projection technique the atomic orbitals were numerically calculated for occupied states of free atoms using the same pseudopotentials as in the PW band-structure computations. As can be seen in Table 9.20, the results of projection-techniques application, unlike the traditional population analysis, exhibit the correct trends in the chemical-bonding change when the Ti atom is replaced by the Zr atom in the same structure (the experimental lattice constants were used for both cases). The population analysis based on the projection technique shows that ionicity of chemical bonds M–O (M= Ti, Zr) in  $\text{SrZrO}_3$  is larger than in  $\text{SrTiO}_3$ . This is in agreement with the experimental data on the bandgaps in  $\text{SrTiO}_3$  (3.2

**Table 9.20.** Local properties of electronic structure of  $\text{SrMO}_3$  crystals (M=Ti, Zr) in Mulliken population analysis, projection techniques and WTAO population analysis [611]

Quantity	Mulliken		Projection A		Projection B		WTAO	
	LCAO		PW		PW		LCAO	
	$\text{SrTiO}_3$	$\text{SrZrO}_3$	$\text{SrTiO}_3$	$\text{SrZrO}_3$	$\text{SrTiO}_3$	$\text{SrZrO}_3$	$\text{SrTiO}_3$	$\text{SrZrO}_3$
$Q(\text{Sr})$	1.85	1.85	1.83	1.80	1.83	1.80	2.00	2.00
$Q(\text{M})$	2.24	2.02	1.46	1.63	1.46	1.63	2.54	3.00
$Q(\text{O})$	-1.36	-1.29	-1.09	-1.14	-1.09	-1.14	-1.51	-1.67
$W_{\text{Sr}-\text{O}}$	0.036	0.033	0.025	0.026	0.026	0.027	0.00	0.00
$W_{\text{M}-\text{O}}$	0.461	0.496	0.626	0.607	0.663	0.606	0.389	0.269

eV) and  $\text{SrZrO}_3$  (5.9 eV) and the relative Pauling electronegativities of Ti (1.4) and Zr (1.2) atoms. Both variants of the projection approach give very close results for the local properties of electronic structure, possibly because the projection method A produces almost orthogonal crystalline orbitals. From Table 9.20 one can conclude that the traditional Mulliken population analysis within the framework of LCAO calculations does not correctly reproduce the relative ionicity of chemical bonding in  $\text{SrTiO}_3$  and  $\text{SrZrO}_3$  crystals, while the WTAO-based populations and projection-techniques application allows one to reflect properly the more ionic nature of  $\text{SrZrO}_3$  in comparison with  $\text{SrTiO}_3$ .

Table 9.21 gives the localization indices of Wannier functions in  $\text{SrTiO}_3$  and  $\text{SrZrO}_3$  crystals calculated for the valence bands by the method used in [63].

**Table 9.21.** Localization indices of localized Wannier functions in  $\text{SrTiO}_3$  and  $\text{SrZrO}_3$  crystals [611]

Crystal	LWF $W_i(\mathbf{r})$	$\lambda_i$	$p_i$	$q_O$	$q_{Os}$	$q_{Op_x}$	$q_{Op_y}$	$q_{Op_z}$
$\text{SrTiO}_3$	a ( $i=1$ )	1.145	0.978	0.934	0.191	0.731	0.011	0.002
	b ( $i=2$ )	1.145	0.978	0.934	0.191	0.011	0.731	0.002
	c ( $i=3$ )	1.252	0.627	0.890	0.311	0.064	0.064	0.453
	d ( $i=4$ )	1.230	0.670	0.890	0.296	0.117	0.117	0.373
$\text{SrZrO}_3$	e ( $i=1$ )	1.183	0.999	0.918	0.136	0.005	0.778	0.000
	f ( $i=2$ )	1.183	0.999	0.918	0.136	0.778	0.005	0.000
	g ( $i=3$ )	1.302	0.610	0.870	0.343	0.064	0.064	0.403
	h ( $i=4$ )	1.300	0.610	0.870	0.341	0.066	0.066	0.400

Localized Wannier functions (LWFs) have been calculated for three upper valence bands in  $\text{SrTiO}_3$  and  $\text{SrZrO}_3$ , represented mainly by O 2p, Sr 4p, and O 2s atomic states (in the case of  $\text{SrZrO}_3$  the last two bands overlap considerably). A total of 15 crystalline orbitals have been used to generate, correspondingly, 15 LWFs per primitive unit cell: in both crystals under consideration, three oxygen atoms occupy the same Wyckoff positions, and four LWFs can be attributed to each oxygen atom. It was found by calculations with CRYSTAL03 code [23] that the centroids of four functions are positioned near the center of one oxygen (at distances of about 0.3 Å).

Table 9.21 presents the following localization indices: the Mulliken population of LWF (9.46)  $q_O$  due to the oxygen atom and corresponding contributions from  $2s$  and  $2p$ -oxygen functions. The atomic delocalization index of LWF

$$\lambda_i = \left[ \sum_A \sum_g (q_{Ai}^g)^2 \right]^{-1} \quad (9.63)$$

is a measure of the extent of the LWF in terms of the number of “contributing” atoms. This index is close to 1.0 for much localized LWF, and it is  $> 1.0$  for more diffuse LWFs. The polarization fraction, (9.49) for all LWFs is also given.

Figure 9.3 presents the fragment of crystal containing four primitive unit cells to show the axes orientation: the oxygen atom is positioned in the center and the two nearest Ti or Zr atoms lie on the  $z$ -axis.

The counter density maps of the obtained LWFs are shown in Fig. 9.4.

As is well seen from Fig. 9.4 and Table 9.21 (functions a, b and e, f) two of the four LWFs for each crystal are perpendicularly oriented toward the M–O–M line and lie along  $x$ - (Fig. 9.4, a and e) and  $y$ - (Fig. 9.4, b and f) axes, respectively.

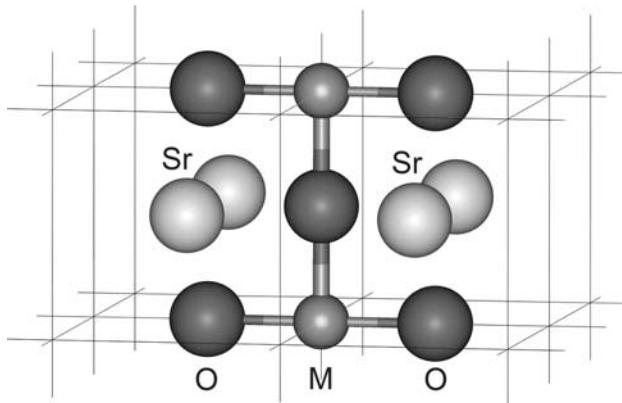


**Fig. 9.3.** Local environment of oxygen atom in cubic perovskites  $\text{SrMO}_3$  ( $\text{M} = \text{Ti}, \text{Zr}$ ).

The polarization fractions of LWFs a, b for  $\text{SrTiO}_3$  and e, f for  $\text{SrZrO}_3$  are very close to 1.0; *i.e.*, these LWFs practically represent the electron lone pairs of oxygen ions  $\text{O}^{2-}$  with a predominant contribution of oxygen  $2p_x$ - and  $2p_y$ -orbitals. Two other LWFs (see Fig. 9.4 c, d, g and h) are directed along the  $z$ -axis. As can be seen from the populations (Table 9.21), they closely correspond to hybrid  $sp_z$  orbitals of oxygens. The polarization fractions are substantially less than 1.0 for these two orbitals, revealing the rather strong covalent character of Ti (Zr)–O bonds in both crystals (these covalency effects are well known for transition-metal–oxygen compounds). Thus, localized Wannier functions, generated with the inclusion of only the valence-band states, appear to be a useful tool in analyzing the electronic distribution and

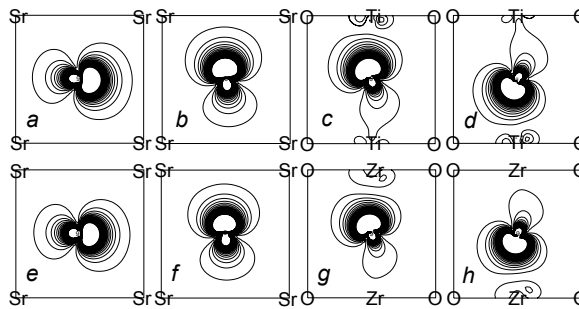


**Fig. 9.4.** Localized orbitals for oxygen atom in cubic  $\text{SrTiO}_3$  (a,b,c,d) and  $\text{SrZrO}_3$  (e,f,g,h). Functions a,b,e,f in Sr-plane; functions c,d,g,h in MO plane (M= Ti, Zr)

chemical bonds in solids. It should be noted that the LWFs obtained are not entirely symmetry-agreed: they do not transform via the representations of the oxygen atom site-symmetry group under the point-symmetry operations because there is no explicit symmetry constraints in the localization procedure [63]. Further symmetrization of WTAOs is desirable to correlate the results with those qualitatively known in quantum chemistry. This symmetrization procedure was discussed in Sect. 9.1.5 and allows the LWFs centered on oxygen atoms and transforming over  $e_u$  and  $a_{1u}$  irreducible representations of the oxygen site-symmetry group  $D_{4h}$  to be obtained. The symmetrization of LWF is considered in general form in [109].

Concluding this section we note that the projection technique with PW calculations gives reasonable results for local properties of electronic structure, close to those obtained in LCAO calculations after using WTAO population analysis. In general, WTAO results correspond to the more ionic bonding. The useful information about the atomic nature of the band states is obtained in the PW calculations of solids from the orbital and site decompositions of the densities of states (DOS). As an example, we refer to the DFT PW calculations [620] of transparent conductive oxides  $\text{In}_4\text{Sn}_3\text{O}_{12}$  and  $\text{In}_5\text{SnSbO}_{12}$  – complicated rhombohedral structures with 19 atoms in the primitive unit cell. It was found by DOS analysis that the tops of the valence states of both materials are formed by oxygen  $2p$  states, whereas the bottom of the conduction bands are due primarily to the Sn  $5s$  electrons. For such crystals LCAO calculations with *a posteriori* WTAO generation or the projection technique application would be very cumbersome.

The analysis of DOS and other one-electron properties of crystals in the LCAO calculations is discussed in the next section.

## 9.2 Electron Properties of Crystals in LCAO Methods

### 9.2.1 One-electron Properties: Band Structure, Density of States, Electron Momentum Density

The local properties of chemical bonding in crystals considered above are defined by the electron-density distribution in real space described by a one-electron density

matrix (DM), see (4.125)-(4.127). The latter is calculated self-consistently for the finite set of  $L$  discrete  $\mathbf{k}$ -points in BZ and corresponds to the cyclic cluster of  $L$ -primitive unit cells modeling the infinite crystal:

$$\rho_{\mu\nu}(\mathbf{R}_n) = \frac{1}{L} \sum_{i=1}^M \sum_{j=1}^L \exp(-i\mathbf{k}\mathbf{R}_n) C_{i\mu}(\mathbf{k}_j) C_{i\nu}^*(\mathbf{k}_j) n_i(\mathbf{k}_j) \quad (9.64)$$

The total number of bands  $M$  in (9.64) equals the number of AOs associated with the primitive unit cell. The one-electron energy levels form energy bands consisting of  $L$  levels in each band. Therefore, each energy band can allocate  $2 \times L$  electrons; if in the unit cell there are  $n$  electrons, and the bands do not cross, the lowest  $n/2$  bands are occupied and are separated from the empty bands. In this case the occupation numbers in (9.64) are  $n_i = 2, 0$  for the occupied and empty bands, respectively (insulators and semiconductors). However, if  $n$  is odd, or if the valence and conduction bands cross, more than  $n/2$  bands are partially occupied (metal).

The eigenvalue spectrum of an infinite periodic system does not consist of discrete energy levels as the wavevector  $\mathbf{k}$  changes continuously along the chosen direction of the BZ. The DM of an infinite crystal is written in the form where the summation over the discrete  $\mathbf{k}$ -vectors of the BZ is replaced by the integration over the BZ. In the LCAO approximation written for the cyclic-cluster (4.126) for DM in the coordinate space is replaced by

$$\begin{aligned} \rho_{\mu\nu}(\mathbf{R}_n) &= \sum_{i=1}^M \rho_{\mu\nu}^{(i)}(\mathbf{R}_n) \\ &= \frac{1}{V_{BZ}} \sum_{i=1}^M \int_{BZ} \exp(-i\mathbf{k}\mathbf{R}_n) C_{i\mu}(\mathbf{k}) C_{i\nu}^*(\mathbf{k}) (\varepsilon_F - \varepsilon_i(\mathbf{k})) d\mathbf{k} \end{aligned} \quad (9.65)$$

where  $\rho_{\mu\nu}^{(i)}(\mathbf{R}_n)$  is the contribution of the  $i$ th energy band.

For the infinite crystal at each cycle of the SCF process, an energy  $\varepsilon_F$  (the Fermi energy) must be determined, such that the number of one-electron levels with energy below  $\varepsilon_F$  is equal to the number of electrons (or, in other words, the number of filled bands below  $\varepsilon_F$  is equal to half the number of electrons in the unit cell). The Fermi surface is the surface in reciprocal space that satisfies the condition  $\varepsilon_i(\mathbf{k}) = \varepsilon_F$ . By limiting the integration over the BZ to states with energy below  $\varepsilon_F$ , a Heaviside step function  $\theta(\varepsilon_F - \varepsilon)$  excludes the empty states from the summation over the energy bands. In fact, the band structure of the infinite crystal is obtained after the cyclic-cluster self-consistent calculation by the interpolation of the one-electron energy levels considered as continuous functions  $\varepsilon(\mathbf{k})$  of the wavevector. The band structure of solids is an important feature, defining their optical, electrostatic and thermal properties. Both the electron charge distribution and the band structure are defined by the self-consistent DM of a crystal.

As we have seen, two binary oxides – MgO in sodium chloride structure and TiO<sub>2</sub> in rutile structure (see Chap. 2 for descriptions of these structures) – differ significantly in the character of chemical bonding, which is due to the electron-density distribution being much different in them. We discuss now the differences in the band structures of these crystals.

The electronic structures of both compounds have been well studied experimentally. The experimental data show that the MgO crystal is a wide-bandgap insulator ( $E_g = 7.8$  eV); titanium dioxide  $\text{TiO}_2$  in the rutile structure is a semiconductor with an experimental bandgap of approximately 3 eV. These differences are reproduced in the band structure of these two binary oxides, calculated in [623] by HF and LDA LCAO methods and shown in Figures 9.5 and 9.6, respectively. The details of the AO basis-set choice and BZ summation can be found in [623].

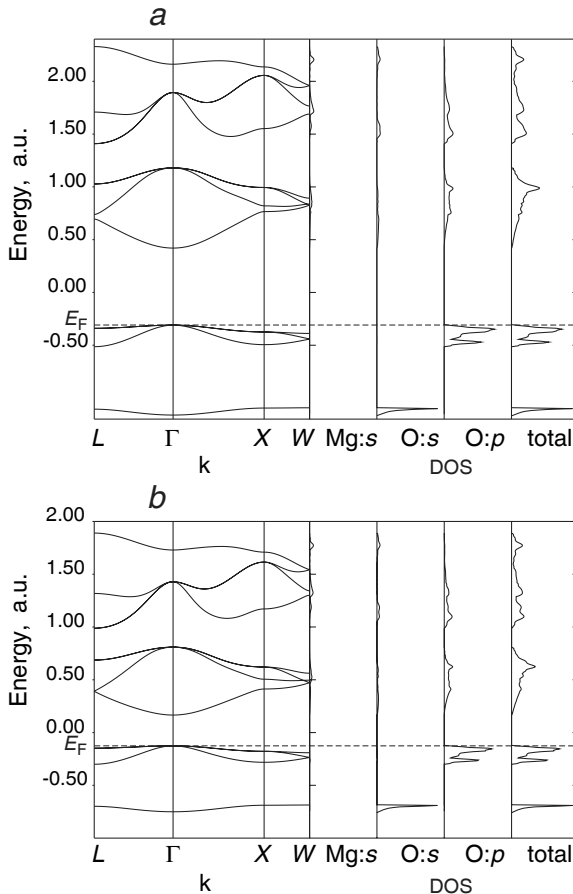


**Fig. 9.5.** Band structure and DOS of MgO crystal, [623]: (a) HF LCAO method; (b) DFT(LDA) LCAO method

In MgO (in accordance with the results of other calculations), the two highest valence bands are the oxygen  $s$ - and  $p$ -like bands, respectively, whereas the conduction bands are more complicated. The upper valence bands in  $\text{TiO}_2$  are also oxygen  $s$ -

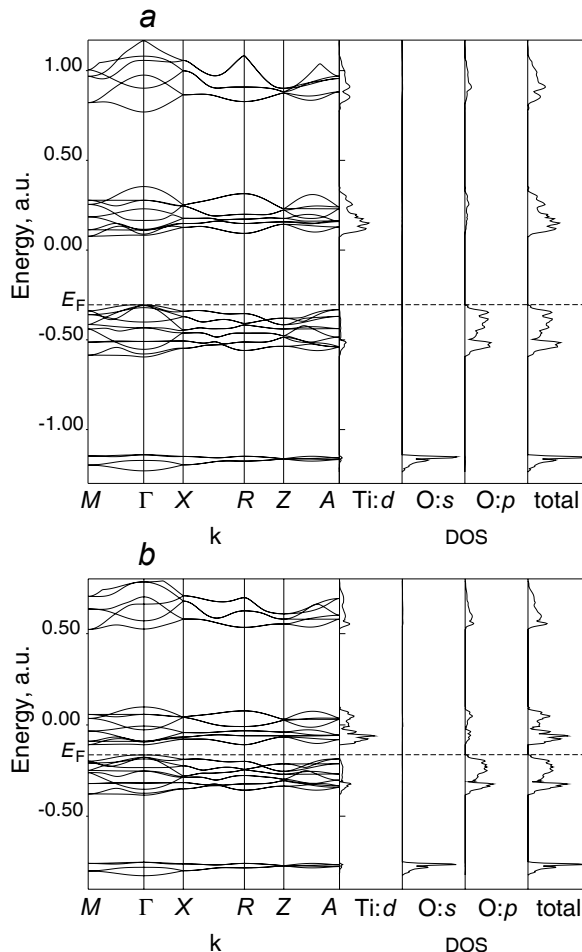


**Fig. 9.6.** Band structure and DOS of rutile  $\text{TiO}_2$  crystal, [623]: (a) HF LCAO method; (b) DFT(LDA) LCAO method

and  $p$ -like bands; however, they consist of 4 and 12 sheets, respectively, because the primitive cell of titanium oxide contains four oxygen atoms.

The lowest conduction band in  $\text{TiO}_2$  consists of 10 branches formed by  $3d$ -states of two titanium atoms and is noticeably separated in energy from the upper conduction bands. The symmetry of the one-electron states can be found using the BR theory of space groups and data on the crystalline structures (see Chap. 3).

Evidently the symmetry of band states does not depend on the basis choice for the calculation (LCAO or PW); the change of basis set can only make changes in the relative positions of one-electron energy levels.

An important parameter in the band theory of solids is the Fermi-level energy (see Figures 9.5 and 9.6), the top of the available electron energy levels at low temperatures. The position of the Fermi level in relation to the conduction band is a crucial factor in determining electrical and thermal properties of solids. The Fermi energy is the analog of the highest-occupied MO energy (HOMO) in molecules. The LUMO (the lowest unoccupied MO) energy in molecules corresponds to the conduction-band bottom in solids. The HOMO-LUMO energy interval in a solid is called the forbidden energy gap or simply bandgap.

Depending on the translation symmetry of the corresponding Bloch states the gap may be direct or indirect. In HF and LDA calculations of both crystals under consideration the bandgap is direct, *i.e.* the one-electron energies at the top of the valence band and the bottom of the conduction band belong to the same  $\Gamma$ -point of the BZ (this result agrees both with the experiment and other band-structure calculations). It is seen that the HF bandgap in both crystals is essentially overestimated and decreases in LDA calculations mainly due to the lowering of the conduction-band bottom energy (see Chap. 7). The influence of the correlation effects on the valence-band states is smaller.

It is also seen that the oxygen  $2p$  bandwidth in  $\text{MgO}$  is smaller than that in  $\text{TiO}_2$ . The bandwidth is a measure of dispersion in the  $\mathbf{k}$ -space and depends on the magnitude and the range of interactions within the crystal: for the more covalent rutile crystal the oxygen-oxygen interactions are stronger. The core bands of both crystals (not shown on the figures) are separated by a large energy gap from the valence bands and are completely flat due to the high localization of core states near the atomic nuclei.

The Fermi energy of a crystal with  $n$  electrons in the primitive unit cell is defined from the condition

$$n = 2 \sum_{i=1}^M \int_{-\infty}^{\varepsilon_F} \frac{1}{V_B} \int_{BZ} \theta(\varepsilon - \varepsilon_i(\mathbf{k})) d\mathbf{k} = \int_{-\infty}^{\varepsilon_F} n(\varepsilon) d\varepsilon = \sum_i \int_{-\infty}^{\varepsilon_F} n_i(\varepsilon) d\varepsilon \quad (9.66)$$

where  $n(\varepsilon)$  is the total density of states (DOS) per unit energy. DOS is an important quantity calculated for crystals. The total DOS can be expressed as the sum of contributions  $n_i(\varepsilon)$  from individual energy bands, see (9.66). The total DOS definition is independent of the basis set choice (PW or LCAO); the product  $n_i(\varepsilon) d\varepsilon$  defines the number of states with energy in the interval  $d\varepsilon$ . Each energy band spans a limited energy interval between the minimal and maximal one-electron energies  $\varepsilon_{\min}$ ,  $\varepsilon_{\max}$  so that  $\int_{\varepsilon_{\min}}^{\varepsilon_{\max}} n(\varepsilon) d\varepsilon$  gives DOS in the corresponding energy interval.

The connection between the electronic structure of a crystal and the one-electron states of the constituent atoms is given by the projected density of states (PDOS), associated with the separate AOs, their shells or individual atoms.

Let us rewrite the total DOS as

$$n(\varepsilon) = \sum_{i=1}^M n_i(\varepsilon) = \frac{1}{V_B} \sum_{i=1}^M \int_{BZ} f^i(\mathbf{k}) \delta(\varepsilon - \varepsilon_i(\mathbf{k})) d\mathbf{k} \quad (9.67)$$

The weighting function  $f^{(i)}(\mathbf{k})$  in (9.67) chosen as

$$f^{(i)}(\mathbf{k}) = C_{i\mu}(\mathbf{k}) C_{i\nu}^*(\mathbf{k}) \exp(-i\mathbf{k}\mathbf{R}_n) \quad (9.68)$$

defines PDOS associated with AO  $\mu$  in the reference cell and AO  $\nu$  in the cell with the translation vector  $\mathbf{R}_n$ . After summation over band index  $i$  and integration up to  $\varepsilon_F$  PDOS (9.68) gives the density matrix elements (9.65).

According to Mulliken population analysis, the DOS projected onto a given set of AOs  $\{\lambda\}$  (belonging to the given shell or to the whole atom), is defined by the weight function

$$f_{\{\lambda\}}^{(i)}(\mathbf{k}) = \sum_{\mu \in \{\lambda\}} \sum_{\nu} C_{i\mu}(\mathbf{k}) C_{i\nu}^*(\mathbf{k}) S_{\mu\nu}(\mathbf{k}) \quad (9.69)$$

where the overlap integral  $S_{\mu\nu}(\mathbf{k})$  is defined by (4.123).

Let the set  $\{\lambda\}$  consist of one AO from the reference cell. The summation of (9.69) over the direct lattice translations  $\mathbf{R}_n$  and integration over BZ gives the orbital DOS

$$n_{\mu}(\varepsilon) = \frac{1}{V_{BZ}} \sum_i \sum_{\nu} \int_{\mathbf{R}_n BZ} C_{i\mu}(\mathbf{k}) C_{i\nu}^*(\mathbf{k}) \exp(i\mathbf{k}\mathbf{R}_n) S_{\mu\nu}(\mathbf{k}) \delta(\varepsilon - \varepsilon_i(\mathbf{k})) d\mathbf{k} \quad (9.70)$$

The DOS of an atom  $A$   $n_A(\varepsilon)$  and the total DOS  $n_{tot}(\varepsilon)$  are calculated from the orbital DOS:

$$n_A(\varepsilon) = \sum_{\mu \in A} n_{\mu}(\varepsilon); n_{tot}(\varepsilon) = \sum_A n_A(\varepsilon) \quad (9.71)$$

The total DOS and PDOS give rich information on the chemical structure of a system, connecting the calculated band structure with the atomic states. We demonstrate this by considering total and projected DOS for binary oxides MgO, TiO<sub>2</sub> and ternary oxides SrTiO<sub>3</sub> and SrZrO<sub>3</sub> with cubic perovskite structure (see Figures 9.5–9.8).

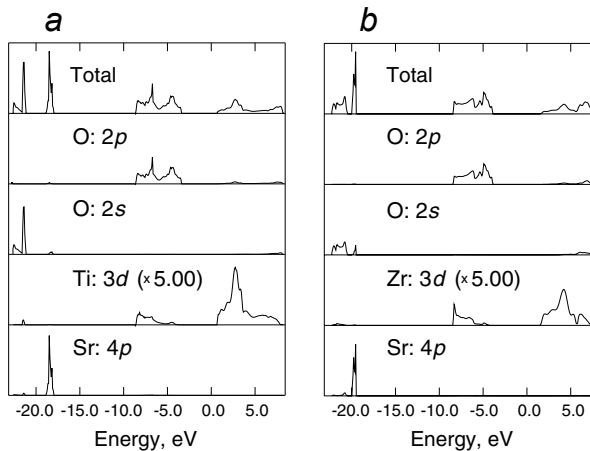
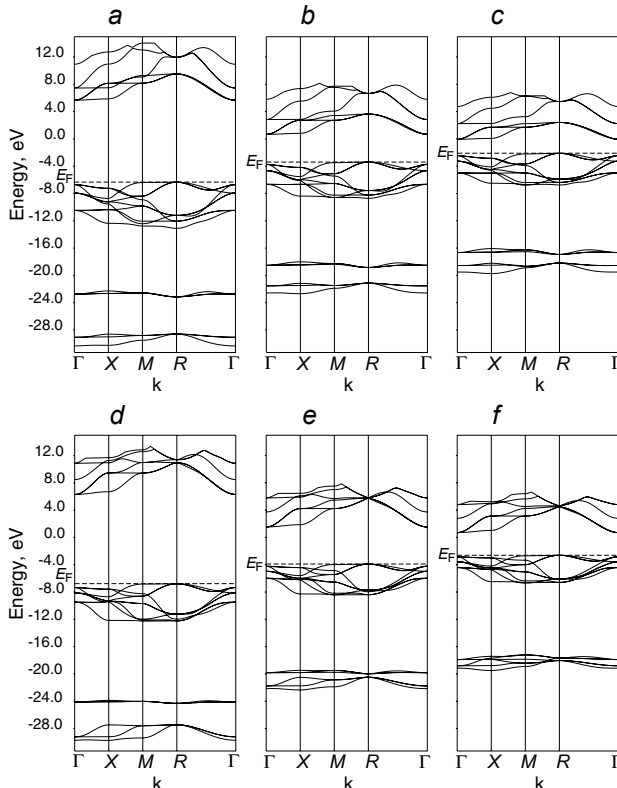


Fig. 9.7. Full and partial DOS in (a) SrTiO<sub>3</sub> and (b) SrZrO<sub>3</sub> crystals

The analysis of total and partial DOS demonstrates that in all the oxides under consideration the upper valence band is predominantly formed by the O 2p states. It



**Fig. 9.8.** Band structure of cubic crystals: (a), (b), (c)–SrTiO<sub>3</sub>, (d), (e), (f)–SrZrO<sub>3</sub>. HF LCAO method–(a), (d); hybrid HF-DFT(PBE0) LCAO method–(b), (e); DFT(PBE) LCAO method–(c), (f).

can also be seen that Mg 3s, Ti 3d and Zr 4d states make the dominant contribution to the bottom of the conduction band.

As is seen from Fig. 9.8, the inclusion of correlation effects moves the valence and conduction bands to the higher and lower energies, respectively, which decreases the bandgap. In more ionic strontium zirconate the energy bands are narrower than in less-ionic strontium titanate.

The ground-state electron-charge density in a crystal can be expressed as

$$\rho(\mathbf{r}) = \sum_{\mu\nu} \sum_{\mathbf{R}_n} \sum_{\mathbf{R}_m} \rho_{\mu\nu}(\mathbf{R}_n - \mathbf{R}_m) \chi_{\mu}(\mathbf{r} - \mathbf{R}_n) \chi_{\nu}(\mathbf{r} - \mathbf{R}_m) \quad (9.72)$$

and reproduces the essential features of the electron-density distribution near atomic nuclei and along interatomic bonds. For each  $\mathbf{r}$  the sums over  $\mathbf{R}_n$  and  $\mathbf{R}_m$  are restricted to those direct lattice vectors such that the value of  $\chi_{\mu}(\mathbf{r} - \mathbf{R}_n)$  and  $\chi_{\nu}(\mathbf{r} - \mathbf{R}_m)$  are nonnegligible.

The total electron-density maps provide a pictorial representation of the total electronic distribution and are obtained by calculation of the charge density in a grid of points belonging to some planes. More useful information is obtained by considering difference maps, given as a difference between the crystal electron-density and a “reference” electron density. The latter is a superposition of atomic or ionic charge distributions.

Fig. 9.9 shows the total and difference maps for  $\text{Cu}_2\text{O}$  crystal, obtained in HF LCAO calculations [622].

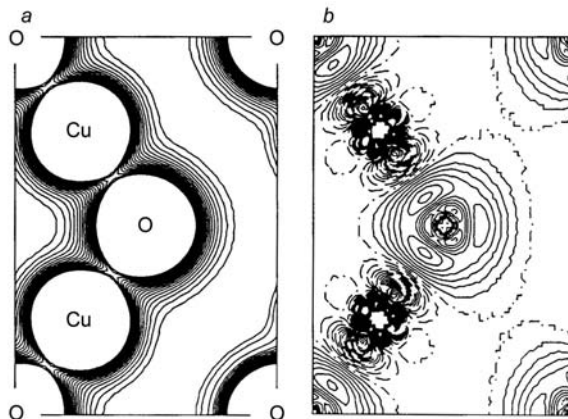


**Fig. 9.9.** Electron-density maps obtained for  $\text{Cu}_2\text{O}$  on a (110) plane, [622]. (a) Total electron density. (b) Density difference maps, bulk minus neutral atom superposition. Values corresponding to neighboring isodensity lines differ by  $0.01 \text{ e/Bohr}^3$ . The full and broken curves in (b) indicate density increase and decrease, respectively.

Two important quantities that require an integration involving  $\rho(\mathbf{r})$  are the electrostatic potential and the electric field, [324]. In particular, maps of the electrostatic potential created by electrons and nuclei at a crystal surface may be useful for gathering information about reaction paths and active sites of electrophilic or nucleophilic chemical processes at the surface. As concerns the electric field, it may be of interest to calculate the electric-field gradient at the location of nuclei with a nonzero nuclear quadrupole moment, since comparison with experimental data is possible in such cases.

Three functions may be computed that have the same information content but different use in the discussion of theoretical and experimental results [23]: the electron momentum density itself (EMD)  $\rho(\mathbf{p})$ ; the Compton profile (CP) function  $J(\mathbf{p})$ ; the autocorrelation function, or reciprocal space form factor,  $B(\mathbf{r})$ .

Let  $\chi_\mu(\mathbf{p})$  be defined as the Fourier transform of AO  $\chi_\mu(\mathbf{r})$  belonging to atom A

$$\chi_\mu(\mathbf{p}) = \int \exp(i\mathbf{p}\mathbf{r}) \chi_\mu(\mathbf{r}) d\mathbf{r} \quad (9.73)$$

and  $s_\mu$  is the fractional coordinate of atom A in the reference cell.

EMD is defined as the diagonal element of the six-dimensional Fourier transform of the one-electron density matrix from coordinate to momentum space:

$$\rho(\mathbf{p}) = \sum_{\mu\nu} \sum_{\mathbf{R}_n} \rho_{\mu\nu}(\mathbf{R}_n) \exp(-i\mathbf{p}(\mathbf{R}_n + \mathbf{s}_\mu - \mathbf{s}_\nu)) \chi_\mu(\mathbf{p}) \chi_\nu(\mathbf{p}) \quad (9.74)$$

The Compton profile function is obtained by 2D integration of the EMD over a plane through and perpendicular to the direction

$$J(\mathbf{p}) = \int \rho(\mathbf{p} + \mathbf{p}'_\perp) d\mathbf{p}'_\perp \quad (9.75)$$

after indicating with  $\mathbf{p}'_\perp$  the general vector perpendicular to  $\mathbf{p}$ .

It is customary to make reference to CPs as functions of a single variable  $p$ , with reference to a particular direction  $\langle hkl \rangle$  identified by a vector  $\mathbf{e} = (h\mathbf{a}_1 + k\mathbf{a}_2 + l\mathbf{a}_3)/|h\mathbf{a}_1 + k\mathbf{a}_2 + l\mathbf{a}_3|$ . We have

$$J_{\langle hkl \rangle}(p) = J(p\mathbf{e}) \quad (9.76)$$

The function  $J_{\langle hkl \rangle}(p)$  is referred to as directional CPs. The weighted average of the directional CPs over all directions is the average CP. In the so-called impulse approximation,  $J_{\langle hkl \rangle}(p)$  may be related to the experimental CPs, after correction for the effect of limited resolution [23].

Once the directional CPs are available, the numerical evaluation of the corresponding autocorrelation function, or reciprocal-space form factor,  $B(\mathbf{r})$  is given by the 1D Fourier transform:

$$B_{\langle hkl \rangle}(\mathbf{r}) = \frac{1}{\pi} \int_{-\infty}^{\infty} J_{\langle hkl \rangle}(p) \exp(i\mathbf{p}\mathbf{r}) dp \quad (9.77)$$

The structural and electronic properties of  $\text{Cu}_2\text{O}$  have been studied in [622] using the HF LCAO method and *a posteriori* density-functional corrections. The electronic structure and bonding in  $\text{Cu}_2\text{O}$  were analyzed and compared with  $X$ -ray photoelectron spectroscopy spectra, showing a good agreement for the valence-band states. The Fourier transform of the ground-state charge density of a crystalline system provides the  $X$ -ray structure factors of the crystal, which can be determined experimentally by  $X$ -ray diffraction. To check the quality of the calculated electron density in  $\text{Cu}_2\text{O}$  crystal, structure factors have been calculated in [622], showing a good agreement with the available experimental data, see Table 9.22.

### 9.2.2 Magnetic Structure of Metal Oxides in LCAO Methods: Magnetic Phases of $\text{LaMnO}_3$ and $\text{ScMnO}_3$ Crystals

The crystalline transition metal oxides  $\text{TiO}_2$ ,  $\text{SrTiO}_3$ ,  $\text{SrZrO}_3$  considered above are classified as  $d^0$  insulators with quite wide bandgap, being diamagnetic with no unpaired electrons. This means that these crystals have no inherent magnetization, but when subjected to an external field develop magnetization that is opposite to the field (the transition atom spins tend to be oriented in the direction opposite to the field).

**Table 9.22.** Structure factors for Cu<sub>2</sub>O calculated with the periodic HF LCAO method, [622]. Experimental values are obtained from X-ray data

<i>hkl</i>	<i>F</i> <sub>calc</sub>	<i>F</i> <sub>expt</sub>
110	13.52	12.42
111	94.78	93.70
200	79.48	78.98
211	9.10	8.53
220	84.34	82.52
222	61.07	59.40
310	6.94	6.56
311	69.22	67.49
330	4.63	4.71
331	55.57	53.78
332	4.39	4.24
333	46.86	45.42
400	65.05	63.09
411	4.80	4.71
420	49.72	48.06
422	53.90	52.18

As we saw in the preceding subsection, the bandgap in  $d^0$  insulators is between a filled band of bonding orbitals, with predominately oxygen  $2p$  atomic character, and an empty metal  $d$  band of antibonding orbitals.

The transition-metal oxides with  $d^n$  ions (such as NiO, Cr<sub>2</sub>O<sub>3</sub>, LaMnO<sub>3</sub>) form a class of compounds with the localized “impurity-like”  $d$ -levels [624]. These systems are known as Mott–Hubbard or magnetic insulators (exhibit magnetic order in the absence of an external field); their magnetic properties indicate the unpaired electrons expected for the appropriate  $d^n$  open-shell configuration.  $d - d$  transitions in these crystals appear due to the crystal-field splitting and give rise to optical absorptions, with only quite weak perturbations from those expected for isolated  $d^n$  ions. These oxides have narrow upper valence bands (1–2 eV), because of small overlap between the metal  $d$  and oxygen  $2p$  orbitals, so that their local electronic structure can be described in terms of atomic-like states. The fully ionic O<sup>2-</sup> configuration is not exactly the state of an oxygen atom in a crystal, and O<sup>-</sup> mobile and correlated configuration (oxygen holes with  $2p^5$  configuration) has to be included. The weak interactions between magnetic moments of  $d^n$ -ions give rise to magnetic ordering (most commonly antiferromagnetic at low temperatures). At the same time, these compounds are good insulators with bandgaps that may be as large as those in some  $d^0$  compounds. Like the latter, however, the magnetic insulators are susceptible to nonstoichiometry, and this may give rise to semiconductive properties and strong optical absorptions. For example, NiO is green and highly insulating when pure, but easily takes up excess oxygen to become black and semiconducting.

The magnetic insulators have an the extraordinary range of structures and properties [625] and provide an excellent case study in quantum chemistry of solids. The existence of a magnetic ground state is a many-body effect caused by correlated electron–electron interactions. The need for the inclusion of electron-correlation ef-

fects has limited the majority of applications to solids by DFT methods. We noted in Chap. 7 that due to the strong Coulomb correlations DFT methods are in serious trouble for systems with localized electrons as these methods overestimate delocalization of the electron density due to nonexact cancelation of the electron self-interaction. DFT results in many cases are in disagreement with experiment. For example, when the LDA is used to describe the magnetically ordered insulating ground states of NiO, a nonmagnetic metallic state is obtained [626]. Initially, this was thought to be a failure of the one-electron approximation itself, meaning that such highly correlated systems could not be described using band theory. It is now apparent that this is not the case [627]: the failure of DFT was due to its approximate treatment of the exchange interaction. Analyzing different approaches, introducing better descriptions of the onsite exchange interactions we concluded in Chap. 7 that LCAO calculations with hybrid DFT functionals can play the same role in quantum chemistry of solids as DFT+U and SIC DFT calculations (with PW and LMTO basis) in solid-state physics. This is demonstrated by the results of recent numerous LCAO (UHF and hybrid DFT) calculations of the properties of magnetic insulators [568].

The magnetic properties of different oxides have been investigated in the LCAO approximation: MO (M=Ni, Mn), [628],  $M_2O_3$  (M=Cr, Fe), [629, 630],  $Mn_3O_4$ , [631],  $CuGeO_3$ ,  $Ag_2Cu_2O_3$ , [632], high- $T_c$  superconductor parent compounds  $A_2CuO_2X_2$  ( $A=Ca, Sr$ ,  $X=F, Cl$ ), [633]. The main parameter used to quantify the magnetic properties is the exchange coupling constant between the paramagnetic centers with total spins  $S_i$  and  $S_j$  that is defined through the phenomenological Heisenberg–Ising Hamiltonian with total spin operators  $\hat{S}$ :

$$\hat{H} = - \sum_{i>j} J'_{ij} \hat{S}_i \hat{S}_j = - \sum_{i \neq j} J_{ij} \hat{S}_i \hat{S}_j \quad (9.78)$$

The interactions are generally assumed to be limited to nearest neighbors, but the range of interactions can be extended beyond the nearest neighbors (we refer the reader to Chap. 7 in [9] for a detailed discussion of magnetic behavior of solids and the Heisenberg–Ising model). The comparison of calculated exchange coupling constants with those obtained experimentally is, however, not straightforward since experimental data are in most cases obtained from a fitting of the magnetic susceptibility to the expression obtained using a model that includes simplifying assumptions [632]. The latter are adopted to reduce the number of fitting parameters. In this situation the use of theoretical methods to estimate the exchange coupling constants becomes a valuable tool for the experimentalists.

We discuss here in more detail the recent applications of LCAO methods to the  $LaMnO_3$  and  $ScMnO_3$  crystals, two representatives of the rare-earth manganese oxides,  $RMnO_3$  ( $R=La, Sc$ ). The structures of these two crystals were described in Chap. 2.  $LaMnO_3$  crystal has the orthorhombic perovskite structure, found in  $RMnO_3$  with a large ionic radius of rare-earth element  $R$  ( $R= La, Pr, Nd, Sm, Eu, Gd, and Tb$ ).  $ScMnO_3$  crystal has hexagonal structure found in  $RMnO_3$  oxides containing the rare-earth elements with a small ionic radius ( $R= Ho, Er, Tm, Yb, Lu, and Y$ ). We note that some of the hexagonal manganites can also form in the orthorhombic structure depending on the heat treatment.

Perovskite materials display a wide variety of fundamental properties, from magnetism to ferroelectricity, from colossal magnetoresistance to half-metallicity; they

are used in a number of important technological applications, such as transducers and memories. They also show electronic and structural peculiarities including orbital and charge ordering, formation of local moments, and Jahn–Teller distortions. Such a richness of properties, combined with their relatively simple structure, makes them ideal materials for investigating the general principles that govern these properties. Unlike the recently extensively studied perovskite manganites, the hexagonal  $\text{RMnO}_3$  compounds have a ferroelectric transition at very high temperature (*e.g.* 900 K for  $\text{YMnO}_3$ ), and an antiferromagnetic transition at a much lower temperature (*e.g.*, 570 K for  $\text{YMnO}_{3.7}$ ). Such compounds are known as ferroelectromagnets.

There exists a series of  $\text{LaMnO}_3$  bulk electronic-structure calculations, using a number of first-principles methods *e.g.* UHF LCAO [634, 635], LDA+U PW [636], and relativistic FPGLA LAPW [637]. LCAO studies with hybrid DFT functionals [638, 639] provided a most reliable description of the electronic and magnetic structure of  $\text{LaMnO}_3$ . These studies deal with the energetics of the ferromagnetic (FM) and antiferromagnetic (AF) phases. The experiments show that below 750 K the cubic perovskite phase of  $\text{LaMnO}_3$  with a lattice constant of  $a_0 = 3.95 \text{ \AA}$  is transformed into the orthorhombic phase (four formula units per unit cell). Below  $T_N = 140 \text{ K}$  (Neel temperature) the A-type AF configuration (AAF) is the lowest in energy. This corresponds to the ferromagnetic-coupling in the basal *ab* (*xy*) plane combined with antiferromagnetic coupling in the *c* (*z*)-direction in the *Pbnm* setting, see Fig. 9.10.

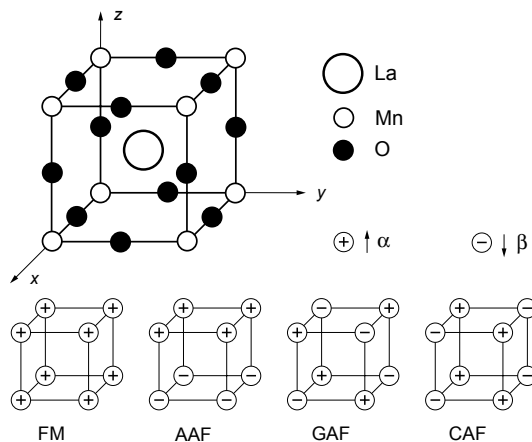


**Fig. 9.10.** Magnetic ordering in  $\text{LaMnO}_3$  crystal. FM—ferromagnetic ordering, AAF, GAF, CAF—antiferromagnetic orderings.

Also, FM, GAF and CAF magnetic states exist: FM corresponds to a fully ferromagnetic material, in GAF all the spins are antiferromagnetically coupled to their nearest neighbors, and in a CAF cell the spins are antiferromagnetically coupled in the basal plane and ferromagnetically between the planes (along the *c*-axis). In the DFT LCAO calculations [639] Becke three-parameter hybrid functional (B3PW) was

applied, [373], which uses in the exchange part the mixture of the Fock (20%) and Becke's (80%) exchange, whereas in the correlation part the Perdew–Wang (PWGGA) nonlocal correlation functional is employed. As was demonstrated in [606], the B3PW functional gives the best description of the atomic and electronic structures, as well as elastic properties of several  $\text{ABO}_3$  perovskite materials. In some cases, for a comparison the B3LYP hybrid functional was also used (the exchange part is the same as in the B3PW functional and the correlation is the Lee–Yang–Parr nonlocal functional). For comparison, the DFT PW calculations with the PW91 GGA nonlocal functional were made in [639]. As was noted earlier DFT PW calculations with hybrid functionals are not implemented in modern computer codes.

The relative smallness of the total energy differences between different magnetic phases requires a high numerical accuracy in the direct-lattice and Brillouin-zone summations. Therefore, in [639] the cutoff threshold parameters of the CRYSTAL code for Coulomb and exchange integrals evaluation have been set to 7, 7, 7, 7, and 14, respectively. The integration BZ has been carried out on the Monkhorst–Pack grid of shrinking factor 8 (its increase up to 16 gave only a small change in the total energy per unit cell).

The self-consistent procedure was considered as converged when the total energy in the two successive steps differs by less than  $10^{-6}$  a.u. In order to check how the results depend on the basis-set (BS) choice, B3LYP and B3PW LCAO calculations were performed for the cubic  $\text{LaMnO}_3$  with one formula unit per primitive cell with the experimental lattice constant of 3.95 Å. Five different BS (BS1–BS5) were used, including the BS optimized both in all electron (AE) and pseudopotential calculations (large- and small-core Hay–Wadt pseudopotentials were taken for La and Mn atoms). The details of BS optimization and choice are given in [639]. The total energies for the cubic structure (with the five atom primitive unit cell) obtained in nonspin-polarized and spin-polarized B3PW calculations were compared with different magnetic ordering of four  $d$  electrons on the  $\text{Mn}^{3+}$  ion (the  $d$ -levels are split in the cubic field into  $t_{2g}$  and  $e_g$  levels, the latter are higher in energy than the former): total spin projection  $S_z = 2$  (four electrons occupy  $t_{2g}$  and  $e_g$  levels),  $S_z = 1$  (three  $\alpha$  electrons and one  $\beta$  electron occupy the  $t_{2g}$  level), and  $S_z = 0$  (two  $\alpha$  electrons and two  $\beta$  electrons occupy the  $t_{2g}$  level). The calculated self-consistent Mn atom magnetic moment is close to 0, 2 and 4 for the three cases under consideration. Since the number of electrons per cell depends on the basis used (AE or without core electrons), the absolute values of these energies are quite different. The basis optimization for the same BS choice results in a lower energy for the same spin projection. It was shown that the order of relative energies for different magnetic configurations is the same for all BS chosen and even the absolute values of energy differences are close. Independently of the BS choice the lowest total energy per cell corresponds to the maximal spin projection  $S_z = 2$ , *i.e.* for the  $\text{Mn}^{3+}$  ion in a crystal the Hund rule holds and the lowest energy corresponds to the maximal spin. This result demonstrates that the magnetic behavior of insulators can usually be discussed in terms of the physics that applies to isolated atoms or ions that have a magnetic moment. The Mulliken atomic charges remain practically the same for different magnetic orderings, provided the BS is fixed. At the same time, their absolute values show the BS dependence for the same spin projection value. The relative energies of different magnetic orderings reveal the same sign in PW DFT and LCAO calculations (the lowest energy corresponds to  $S_z = 2$ ). The Bader atomic

charges, calculated in the PW DFT method, compared with the Mulliken charges, are much smaller and also show a weak dependence on the magnetic ordering.

To study the magnetic ordering in  $\text{LaMnO}_3$ , the so-called broken symmetry approach was adopted [638]. It allows one to deduce the magnitude of the magnetic coupling data making spin-polarized calculations for different magnetic orderings of transition-metal atoms.  $\text{LaMnO}_3$  is stabilized at moderate temperatures in the orthorhombic structure comprising four formula units, space group  $D_{2h}^{16}$  (in  $Pbnm$  and  $Pnma$  settings the largest orthorhombic lattice translation vector is directed along the  $z$  or  $y$  axis, respectively; in what follows, the  $Pbnm$  setting is chosen). The real structure can be viewed as a distorted cubic perovskite structure with a quadrupled tetragonal unit cell ( $a_p\sqrt{2}, a_p\sqrt{2}, 2a_p$ ) where  $a_p$  is the lattice parameter of the cubic perovskite structure. This tetragonal cell is slightly distorted in the real orthorhombic structure. The calculations on the tetragonal model (both in LCAO and PW basis), *i.e.* four formula units without the structural distortion have shown that  $\text{LaMnO}_3$  is metallic in all magnetic states and the ground state is FM. This contradicts the experimental data, for both the energy gap ( $\text{LaMnO}_3$  is believed to be a spin-controlled Mott–Hubbard insulator with the lowest-energy  $d$ – $d$  transitions around 2 eV [640]) and magnetic AAF ordering in the ground state below 140 K. The results obtained in [639] for cubic  $\text{LaMnO}_3$  with the primitive cell of five atoms explain this fact: the tetragonal structure remains in fact cubic, with the tetragonal supercell; since in the primitive unit cell the FM configuration corresponds to the metallic ground state, the same is true for the undistorted tetragonal structure. However, when the orthorhombic atomic distortions are taken into account, the AAF structure turns out to be the ground state, in agreement with experiment.

This is seen from results given in Table 9.23, [639], where the relative energies of different magnetic phases are presented (the energy for the FM phase is taken as zero energy). The calculations were made for orthorhombic structure with the structural parameters from a neutron-diffraction study [641]. Magnetic moments  $\mu$  on the Mn atom and magnetic and coupling constants  $J_{ab}$  and  $J_c$  are also presented there.

The Ising model Hamiltonian

$$H = -J_{ab} \sum_{ij} S_{zi} S_{zj} - J_c \sum_{kl} S_{zk} S_{zl} \quad (9.79)$$

was used, where  $J_{ab}$  and  $J_c$  are exchange integrals (magnetic coupling constants) between nearest neighbors in the basal plane ( $xy$ ) and between nearest neighbors along the  $c$ -axis, respectively,  $S_{zi}$  stands for the  $z$ -component of the total spin on the magnetic center  $i$ , and  $(ij)$  and  $(kl)$  indicate summation over intraplane and interplane nearest magnetic centers, respectively. Due to two different possible choices of the Ising Hamiltonian presentation, we stress that in (9.79) that the form of (9.78) is used that contains double summation over each pair of centers and gives positive values for  $J_{ab}$  and negative for  $J_c$ . The latter must be taken into account in a comparison with the experimental data obtained by fitting to the Ising Hamiltonian. In particular, experimental  $J_{ab}$  and  $J_c$  values [641] have to be multiplied by a factor of 2 for the Hamiltonian (9.79).

A set of equations relating the energy differences for the FM, AAF, GAF and CAF configurations with the magnetic coupling constants sought for was used:

$$E(\text{FM}) - E(\text{AAF}) = E(\text{CAF}) - E(\text{GAF}) = -32J_c \quad (9.80)$$

**Table 9.23.** The energy (in meV per unit cell) of the different magnetic phases for orthorhombic LaMnO<sub>3</sub> for the experimental structure [641]. The energy of the FM configuration is taken as zero energy. Magnetic moments  $\mu$  on the Mn atom in  $\mu_B$ , magnetic coupling constants  $J_{ab}$  and  $J_c$  in meV. Experimental data:  $\mu = 3.87$  for AAF [632],  $J_c = -1.2$ ,  $J_{ab} = 1.6$  [640]

Method/basis set	AAF	GAF	CAF	$J_c$	$J_{ab}$
UHF(BS1) <sup>a</sup>	-4.8	—	55.6	—	—
B3LYP(BS1) <sup>b</sup>	-33.0	3.80	112.0	3.72	120.0
UHF(BS2) <sup>c</sup>	-8.0	—	48.0	—	56.0
B3LYP(BS2) <sup>b</sup>	-33.0	3.78	84.0	3.71	101.0
UHF(BS3) <sup>d</sup>	-5.2	3.96	51.2	—	55.9
Fock-50(BS3) <sup>d</sup>	-12.2	3.89	89.22	—	93.64
B3LYP(BS3) <sup>d</sup>	-32.2	3.80	114.0	—	121.5
B3LYP(BS4) <sup>b</sup>	-32.0	3.81	103.0	3.73	117.0
B3LYP(BS5) <sup>b</sup>	-30.0	3.82	106.0	3.74	117.0
B3PW(BS5) <sup>b</sup>	-19.0	3.86	153.0	3.75	152.0
GGAPW91(BS5) <sup>b</sup>	-40.0	3.71	248.0	3.58	234.0
(GGA-PW) <sup>b</sup>	-59.0	3.55	189.0	3.35	224.0
(LAPW) <sup>e</sup>	-72.0	—	96.0	—	136.0
(LMTO) <sup>f</sup>	-62.0	3.46	243.0	3.21	—
FLMTO(GGA) <sup>g</sup>	-98.8	—	142.8	—	167.2
(LDA+U) <sup>h</sup>	-34.0	—	170.0	—	—
					-1.06
					2.66

<sup>a</sup> Reference [635], <sup>b</sup> Reference [639], <sup>c</sup> Reference [634], <sup>d</sup> Reference [638], <sup>e</sup> Reference [642],

<sup>f</sup> Reference [643], <sup>g</sup> Reference [644], <sup>h</sup> Reference [645].

$$E(\text{FM}) - E(\text{CAF}) = E(\text{AAF}) - E(\text{GAF}) = -64J_{ab} \quad (9.81)$$

Again, to avoid misunderstanding, (9.80) and (9.81) are written for a quadruple cell, corresponding to four formula units. For calculating the coupling constants both (9.80) and (9.81) were used and an averaging was performed. Unfortunately,  $E(\text{CAF})$  is not always presented in the published results (see Table 9.23). The calculated magnetic coupling constants are compared with the experimental data in the last two columns of Table 9.23. This table demonstrates how the calculated magnetic coupling constants depend on the Hamiltonian choice (LDA, UHF, hybrid) and the BS choice (LCAO, PW, LAPW).

These results can be briefly summarized as follows. Independently from the BS and Hamiltonian used, all calculations mentioned in Table 9.23 correctly reproduce the sign of the experimental exchange integrals and their relative values ( $|J_{ab}| > |J_c|$ ). In all UHF and hybrid (B3LYP, B3PW) calculations the exchange integrals agree better with the experimental data than in DFT calculations. We explain this by the incorporation of the Fock exchange into UHF and the hybrid methods. For example, if we fix the AO basis as BS3 and analyze a series of the UHF (pure Fock exchange), Fock-50 (50% of Fock exchange) and B3LYP (20% of Fock exchange included), the coupling constants  $J_{ab}$  and  $J_c$  in this series are getting closer to the experimental values. The effect of the correlation part is smaller (compare B3LYP and B3PW results for BS5). The lack of Fock exchange in LCAO GGA and GGA-PW calculations leads to overestimated values of both magnetic coupling constants. This overestimate is

well observed also in previous LAPW, FLMTO, and LDA+U calculations. Therefore, in agreement with the conclusions, made by other researchers it is demonstrated that when calculating the experimentally observable magnetic coupling constants, the nonlocal exchange plays an important role. Such hybrid DFT or UHF calculations are practically possible only for the LCAO BS. These results confirm again the conclusion [632] that the CRYSTAL code is a valuable tool for the study of magnetic properties for open-shell transition-metal compounds. The optical gap for the AAF orthorhombic phase was also calculated in [639]. The B3PW LCAO gives 2.9 eV and 4 eV for the Mn  $d$ - $d$  and O $2p$ -Mn $d$  transitions, in good agreement with the experiment [640], whereas the DFT PW gap of 0.6 eV is an underestimate typical for the DFT. These results, in line with those in [638], demonstrate that it is a combination of the nonlocal exchange with correlation effects realized in the hybrid functionals that considerably narrows the gap between calculated and experimental magnetic coupling constants. This questions the generally accepted idea that DFT is better suited than UHF and related methods for the study of transition-metal oxides, in particular, LaMnO<sub>3</sub>. The surface calculations of this crystal made in [639] we discuss in Chap. 11.

We noted that the hexagonal manganites RMnO<sub>3</sub> (R = Sc, Y, Ho–Lu) are an interesting group of compounds because of their unusual combination of electric and magnetic properties. At low temperatures, they show coexistence of ferroelectric and magnetic orderings. ScMnO<sub>3</sub> plays a prominent role in the series of hexagonal manganites. It has the smallest distance between magnetic Mn<sup>3+</sup> centers along the  $c$ -direction and has the highest Neel temperature. Below the temperature 1220 K its structure belongs to space group  $P6_3cm$  [646]. The Mn<sup>3+</sup> ions are surrounded by five oxygen ions that form a distorted trigonal bipyramidal, see Fig. 2.18. In this environment the  $^5D$  state of Mn<sup>3+</sup> with  $3d^4$  occupancy splits into three states. The magnetic moment of the Mn<sup>3+</sup> ions in ScMnO<sub>3</sub> has been measured as  $4.11 \mu_B$ . Its Neel temperature is 130 K [647], much higher than that of YMnO<sub>3</sub> (71 K), [648]. The assignment of the strong optical absorption band at about 1.6 eV for hexagonal manganites is a matter of debate [649]. From local spin-density approximation (LSDA) and LSDA+U calculations of YMnO<sub>3</sub> [650] this band was interpreted as an interatomic charge-transfer transition from O  $2p$  to Mn  $3d$  orbitals. In another theoretical study of YMnO<sub>3</sub> based on LSDA and LSDA+U [651], it was found that the states near the top of the valence band have predominantly Mn  $3d_{x^2-y^2}$  character, while the lowest-unoccupied subband has Mn  $3d_{z^2}$  character. The  $d$ -band centers of the occupied and empty bands are separated by 2.0 eV. The latter theoretical result is in agreement with a careful analysis of experimental spectra [649] that revealed that the band at 1.6 eV is due to an intra-atomic  $3d - 3d$  transition in the Mn<sup>3+</sup> ions. The O( $2p$ ) $\rightarrow$ Mn( $3d$ ) charge-transfer transition in LaMnO<sub>3</sub> and related compounds occurs at 3.1 eV or higher. Later experiments on ScMnO<sub>3</sub> [652] were interpreted differently, partly based on previous LSDA calculations. In particular, the strong band in ScMnO<sub>3</sub> (at 1.57 eV), ErMnO<sub>3</sub> (1.59 eV), and YMnO<sub>3</sub> (1.61 eV) was considered now as a charge-transfer band. In this context we have to point out that LSDA values for bandgaps are usually much too small. In [638] a charge-transfer transition in LaMnO<sub>3</sub> was found at 2.3 eV with B3LYP and at 4.0 eV with Fock35 (35 per cents of the HF exchange in the hybrid functional) functionals. Considering that one-particle energies obtained by band-structure calculations do not describe local  $d$ - $d$  transitions, the agreement between LSDA charge-transfer and the experimentally determined band may be fortuitous.

The LCAO calculations [653] with the computer code CRYSTAL03, [23] is the first attempt to establish the electronic and magnetic structure of the low-temperature phase of  $\text{ScMnO}_3$  from first principles. The solid phase was modeled with three-dimensional periodic supercells of stoichiometry  $\text{Sc}_6\text{Mn}_6\text{O}_{18}$ . Three different Hamiltonians were used: UHF, hybrid HF-DFT (B3LYP) and DFT (BLYP). In a previous study of magnetic coupling in  $\text{CuGeO}_3$  [632] the same Hamiltonians had been compared and it was found that the hybrid HF-DFT B3LYP Hamiltonian gives the most accurate values for the magnetic coupling constant  $J$ . Optimized basis functions were used for Mn and O as obtained in [639]. The valence basis of Sc was optimized for  $\text{Sc}_2\text{O}_3$  bulk crystal, Sc atom inner ( $1s$   $2s$ ) electrons were described with the Hay-Wadt small-core effective core potential. The  $\text{Sc}_6\text{Mn}_6\text{O}_{18}$  cell contains two hexagonal atomic planes. Three magnetic phases were considered: ferromagnetic (FM) when the four unpaired electrons of each of six Mn ions have parallel spins; two antiferromagnetic (AFc and AFa). In the AFc phase the spins of the Mn ions in different atomic planes along the  $c$ -direction are antiparallel, while all spins are parallel in the same plane (between two planes, the Mn–Mn distance is about 5.8 Å, while it is only 3.4 Å in the plane). In the AFa state each plane contains two types of Mn with antiparallel spin in a ratio of 1:2. The local spin arrangements are shown in Fig. 9.11.

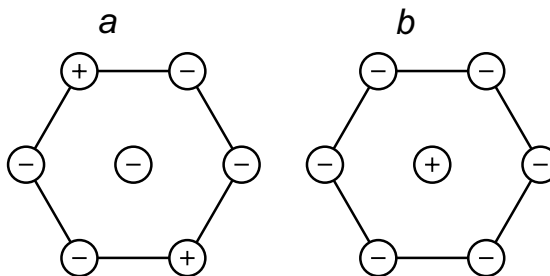


**Fig. 9.11.** Two local spin configurations in the AFa state in a hexagonal plane; in case (a) the central spin-down Mn ion is surrounded by 4 spin-down and 2 spin-up Mn ions, in (b) the central spin-up Mn ion is surrounded by 6 spin-down Mn ions.

This is a simplification of the real situation in  $\text{ScMnO}_3$  where the Mn spins are not collinear [647]: the projections of neighboring Mn spins in the same plane are in fact rotated by  $120^\circ$ .

If the FM state and the AFc state are compared, the two neighbors along the  $c$ -direction in the planes above and below each magnetic center have different spin. It was found that the corresponding interplane coupling constant  $J_c \leq 0.2$  meV for all three Hamiltonians under consideration, *i.e.* the magnetic coupling between Mn ions of different planes is negligible. The results of the calculation of intraplane coupling constant are given in Table 9.24. The magnetic coupling constants of  $\text{ScMnO}_3$  have

**Table 9.24.** Energy difference (eV) between the AF and the FM states of  $\text{ScMnO}_3$ , estimated magnetic coupling constant (meV), Mulliken charges  $q$  (a.u.), magnetic moment of Mn ions ( $\mu_B$ ) obtained with three different Hamiltonians [653]

Hamiltonian		$J_a$	$Q_{\text{sc}}$	$Q_{\text{Mn}}$	$Q_{\text{O}}$	eff
UHF <sup>a</sup>	-0.163	4.1	+2.3	+2.4	-1.5	4.0
B3LYP <sup>a</sup>	-0.555	13.9	+1.9	+2.0	-1.37	3.7
B3LYP <sup>b</sup>	-0.449	11.2	+1.9	+2.0	-1.3	3.8
BLYP <sup>a</sup>	-0.925	23.1	+1.87	+1.9	-1.2	3.5
Exper.		5.5–7.0 <sup>c</sup>				4.11 <sup>d</sup>

<sup>a</sup> with fixed structural parameters from experiment [654]

<sup>b</sup> with fully optimized in [653] structures

<sup>c</sup> estimated from a comparison with  $\text{YMnO}_3$  (the Neel temperature 70 K and  $J_a = 3.8$  meV)

<sup>d</sup> Reference [648]

not yet been measured at the time of calculations [653]. The simplest assumption is a linear relation between  $J$  and the Neel temperature  $T_N$  [655]. It is then possible to estimate  $J_a$  of  $\text{ScMnO}_3$  from the coupling constant of the isostructural compound  $\text{YMnO}_3$  (3.0–3.8 meV, [655]). With  $T_N = 130$  K for  $\text{ScMnO}_3$  and  $T_N = 71$  K for  $\text{YMnO}_3$  [648] one obtains  $J_a = 5.5$ –7.0 meV. In Table 9.24 the calculated coupling constants are compared to this crude estimate. The UHF method gives  $J_a = 4.1$  meV, which is slightly smaller than the estimated value. When electron correlation is taken into account with B3LYP, a much larger value ( $J_a = 13.9$  meV) is obtained. But also the description of electron exchange has a substantial effect on the magnetic structure. The BLYP method, which has no contributions from exact HF exchange, gives the largest coupling constant,  $J_a = 23.1$  meV. The same ordering of magnetic coupling constants obtained with these methods has been obtained in studies of  $\text{CuGeO}_3$  [632], where the B3LYP result favorably agreed with the measured value. Since for  $\text{ScMnO}_3$  the deviation from the estimated crude value is substantial with B3LYP, it is likely that the linear extrapolation scheme is inadequate. But before any conclusion was drawn the effect of changes in the local structure on the calculated coupling constant was investigated. A full optimization of hexagonal lattice parameters and fractional coordinates of  $\text{ScMnO}_3$  was performed with B3LYP for both the FM and the AFa states, [653]. The energy difference between these two states is reduced by 20% (compared with that obtained for the experimental structure) and  $J_a$  accordingly decreases to 11.2 meV. Since this value is still considerably larger than the estimated one the above statement about the inaccuracy of the linear interpolation scheme holds. In Table 9.24 there are also compared the calculated self-consistent magnetic moments  $\mu_{\text{eff}}$  with the experimental value  $4.11 \mu_B$  [648]. The obtained values range from  $3.5 \mu_B$  (BLYP) to  $4.0 \mu_B$  (UHF) and are thus in agreement with experiment. The small change from  $3.7 \mu_B$  to  $3.8 \mu_B$  due to optimization at the B3LYP level indicates that the local atomic structure has a small effect on this property. Atomic charges were calculated based on the Mulliken population analysis. Table 9.24 shows that the ionicity is reduced in the series from UHF to BLYP. The oxygen and manganese charges range from -1.2 to -1.5 and +1.9 to +2.4, respectively, indicating substantial covalent contributions to the bonding. These values do not essentially differ from those (-1.6 to -1.8 and +1.5 to +1.8), obtained in the  $\text{LaMnO}_3$  calculations [639]. The

PDOS calculated for  $\text{ScMnO}_3$  with B3LYP for the fully optimized structure of the AFa state shows the following. The highest-occupied states between  $-0.5$  eV and 0 eV (the Fermi level is taken as the zero energy), and the lowest-unoccupied bands between  $3.3$  eV and  $4.5$  eV consist of a mixture of O( $2p$ ) and Mn( $3d$ ) orbitals. Sc orbitals only contribute to higher unoccupied states above  $5$  eV. In agreement with experimental estimates [649], the interband transition at  $3.3$  eV with B3LYP was found. On the basis of the calculated PDOS the excitation is neither a pure  $d-d$  nor a charge-transfer transition, rather it represents an intermediate situation.

As is seen from Table 9.24 the structure-parameter optimization influences the results of the electronic-structure calculations. Such an optimization also allows the calculation of the such important properties of solids as the cohesive energy, relative stability of phases with different structure, bulk moduli, elastic constants. LCAO calculations of these total energy related properties are considered in the next section.

## 9.3 Total Energy and Related Observables in LCAO Methods for Solids

### 9.3.1 Equilibrium Structure and Cohesive Energy

The theoretical determination of the equilibrium structure of molecules and periodic systems and their cohesive energy is of primary importance in quantum chemistry of molecules and solids.

In the molecular systems, the parameters that must be optimized are the nuclear coordinates. Such an optimization requires the numerical or analytic calculation of forces – the total energy derivatives with respect to nuclear coordinates. The methodology for calculating analytic first derivatives at the HF (SCF) LCAO level of theory was suggested by Pulay [656]. Extensions of the HF derivatives to density-functional theory methods were straightforward. Derivatives of correlated (post-HF) energies followed a number of years after the SCF derivatives [657]. Analytical gradients have become a standard tool for the optimization of molecular structures and are implemented in modern molecular electronic-structure codes. Calculations with the structure optimization are now possible on molecules with hundreds of atoms, and energy derivatives provide an enormous amount of information about the potential-energy surface at very little additional cost. Analytic derivatives with respect to geometrical parameters are used not only for the structure optimization but also for exploring potential-energy surfaces and the study of transition states and following reaction paths.

Such molecular properties as vibrational frequencies, IR and Raman intensities, NMR shielding constants, *etc.*, can be formulated in terms of second and higher derivatives with respect to geometry and applied fields. Such calculations are now practical and routine using analytic derivatives at the SCF level and a few correlated methods, [657].

In periodic systems, the cell dimensions are a set of optimized structure parameters additional to nuclear coordinates in the primitive unit cell. Nowadays, the majority of solid-state codes compute the total energy with KS PW methods. In KS PW calculations the analytical gradients of total energy for nuclear coordinates and cell-parameter optimization are implemented in computer codes and widely used in the

electronic-structure calculations of crystals [377]. The more complicated task is the analytical gradients theory in LCAO methods for periodic systems. The total energy  $E$  of the crystal (per primitive cell) is the sum of electron energy  $E_e$  and nuclear repulsion energy  $E_N$  :  $E = E_e + E_N$ . The electron energy  $E_e$  as calculated within the HF LCAO approximation can be expressed in terms of the one-electron density matrix and includes the direct lattice sums, see (7.46). In the KS LCAO method only the electron-density is involved in the Hamiltonian, see (7.47).

The analytical gradients in HF and MP2 LCAO calculations were applied for a long time only for one-periodic (1D) systems [658, 659]. The efficient method of analytic energy-gradient calculation in the KS LCAO method for periodic systems with one-, two- and three-dimensional periodicity was presented only recently in [82] and implemented in the code GAUSSIAN03 [107]. A real space approach is used, where all the summations are performed in direct space. Energy derivatives with respect to geometrical parameters (atomic forces and stress tensor) are computed analytically to high accuracy using techniques based on the fast multipole method (see Chap. 7). This allows for the accurate lattice parameters and nuclear-coordinate optimization and evaluation of vibrational frequencies using finite differences of analytic forces. The extension of this technique to the hybrid HF-DFT LCAO Hamiltonians allowed optimization of the structure of different solids in good agreement with experiment (as was demonstrated in Chap. 7).

Simultaneously, progress has been achieved to implement analytical HF gradients in the LCAO code CRYSTAL [23, 660]. The formulas for analytic total-energy gradients with respect to nuclear coordinates in periodic systems were presented in [661, 662] and illustrated in test calculations. It was demonstrated that an efficient nuclear-coordinates optimization of large systems with any periodicity can be performed. Later, the theory of analytical HF gradients with respect to the cell parameter for three-periodic systems was presented [663], so that full structure optimization with the help of analytical gradients is now possible. It is important to note that the CRYSTAL code is based on the Ewald method in three dimensions, so that computing analytical gradients with respect to the cell parameter requires various additional derivatives that were not yet available with the implementation of nuclear gradients, and this has been documented in great detail in [663]. The one- and two-dimensional cases are again different because different potentials are used in a real-space approach. The article [664] complements [663] by analytical HF gradients with respect to cell parameters for systems periodic in one and two dimensions. The implementations mentioned include the cases of spin-restricted and unrestricted polarization.

We intentionally do not give here the mathematical details of the approaches allowing implementation of analytical gradients in the calculations of periodic systems (for these details readers are referred to the cited publications and references therein). We note that such an implementation is essentially more complicated than in the case of molecular systems and requires high accuracy in the total-energy calculation. One can find the detailed analysis of the accuracy in gradients calculations on numerical examples in [660, 661, 663]. The comparison of the numerical and analytical derivatives values can also be found. In what follows we turn to the results obtained for the equilibrium structure and cohesion energy in the crystalline metal oxides. The LCAO calculations discussed were made with the CRYSTAL code and use of HF, KS and hybrid Hamiltonians.

The cohesive (binding) energy  $E_{coh}$  is defined as the energy required to dissociate a solid into noninteracting atomic species  $A$  with energies  $E_A$

$$E_{coh} = \sum_A E_A - E_{solid} \quad (9.82)$$

In this definition,  $E_{coh}$  is positive for any thermodynamically stable crystal. The summation is made over the atoms included in the primitive unit cell,  $E_{solid}$  is the total energy per primitive cell. Calculated values of the cohesive energy are compared with experimental results that can be obtained by measuring the latent heat of sublimation at various low temperatures, and extrapolating to zero Kelvin.

The binding-energy definition depends on what the constituent parts are considered to be: reference can be made to the ions in ionic crystals or to the molecules for molecular crystals. The expression “lattice energy” is also in use either as a synonym of cohesive energy or to denote the energy difference relative to the free ions or molecules [568]. In the calculations of  $E_{coh}$  we are interested not in the total energy of a system as such, but rather in energy differences that might be as small as a few kcal/mol. It is with respect to this scale of energy that the overall accuracy of a calculation must be verified. The molecular codes now allow an accuracy of 1 kcal/mol for thermochemical data, which is still far from being attained in solid-state chemistry, although attention to the quantitative aspects of the calculation is increasing rapidly, [568]. The different computational aspects of the ground-state total-energy evaluation for crystals are considered in [665]. In particular, some sources of errors in the total-energy calculations are analyzed: 1) the choice of Hamiltonian (HF, DFT, HF+ *a-posteriori* correlation correction, description of the core electrons by one or other pseudopotential); 2) the use of a finite variational basis; 3) the numerical approximations, introduced in the solution of LCAO equations (truncations of infinite lattice sums, reciprocal-space integration). In the evaluation of the cohesive energy, partially different basis sets for the valence or semicore states need to be used for the atoms or ions and the bulk crystal. The bulk basis set can be improved by the addition of polarization functions, which do not contribute to the energy of atoms and ions in the gas phase because of AO orthogonality, but they can be important in the expansion of the bulk wavefunction. The atomic function tails become unnecessary in the description of the crystalline orbitals. Moreover, the use of diffuse AOs is normally to be avoided (see Chap. 8). Thus, separate optimizations of basis set for the bulk and the isolated atoms are necessary, *i.e.* not equal, but variationally-equivalent basis sets are to be used. The handling of these problems in the cohesive-energy calculation is illustrated in [568] and the general influence of the Hamiltonian choice on the calculated cohesive energy is discussed. An important aspect of the comparison between the calculated and experimental cohesive energy is related to the difference between the definition of cohesive energy and the crystal-formation energy that is reported in thermodynamic tables, the main point probably being that quantum-mechanical calculations refer to the static limit ( $T = 0$  K and frozen nuclei), whereas experiments refer to some finite temperature. In fact, the comparison is never straightforward, and the original experimental datum is linked to the calculated cohesive-energy values through a chain of thermodynamic transformations. As an example, the Born–Haber cycle for the formation of a crystal has to be considered (see below).

A general feature of the HF LCAO method is the underestimation of the cohesive energy (the error varies between -20% and -45% for the series of compounds considered in [568]). DFT calculations of  $E_{coh}$  allow one to recover part of the contributions that are disregarded with HF, at about the same computational cost. LDA even tends to overestimate the cohesive energy, whereas GGA and B3LYP results are closer to the experimental measurements. At any rate, the performance of none of the Hamiltonians used is fully satisfactory, and the correct answer is always somewhere in between the two extremes represented by HF and LDA, but LDA results are generally improved when gradient corrections are included. Properly correlated wavefunctions perform better than HF and DFT methods: the binding energies for the incremental scheme and local MP2 methods (see Chap. 5) agree better with the experimental data.

**Table 9.25.** The equilibrium structure and cohesive energy for rutile  $\text{TiO}_2$  ([666]). Lattice parameters are given in Å, cohesive energy in eV

Observable	HF (AE)*	HF(PP)*	HF+correlation	Experiment
$a$	4.559	4.555	4.548	4.592
$c$	3.027	3.024	2.993	2.958
$u$	0.3048	0.3061	0.3046	0.3048
$E_{coh}$	13.95	15.99	19.35	20.00

\*Reference [596]

As an example, we give in Table 9.25 the results obtained for equilibrium structure and cohesive energy in rutile  $\text{TiO}_2$  by different LCAO methods [666]. For the correlation calculations in [666] an incremental scheme was used, one-, two- and three-atom clusters in a large slab of Madelung point charges were included in the CCSD calculations. For the Ti ions nearest to the cluster atoms  $\text{Ti}^{4+}$  pseudopotentials were used instead of the bare point charges, in order to simulate the Pauli repulsion on the  $\text{O}^{2-}$  electrons of the inner cluster. The cohesive energy was calculated including zero-point vibrations (see Sect. 9.3.3). As is seen from Table 9.25 the electron correlation for  $\text{TiO}_2$  crystal does not influence the equilibrium structure parameters in a major way but is important for the cohesive energy.

In Table 9.26, a summary of the results from a selection of experimental and recent *ab-initio* studies of the structural parameters of rutile is presented, see [597]. Early LCAO-HF and PW-LDA studies of rutile yielded lattice parameters to within 2% of experiment. More recent studies that have taken advantage of improvements in the theoretical techniques and available computing power to perform calculations with improved treatments of exchange and correlation (DFT calculations based on the GGA) and higher numerical accuracy improved basis sets have yielded results consistent with those from the earlier work.

Generally speaking, all the *ab-initio* studies of rutile have yielded structural parameters to within a few per cent of experiment. In particular, LCAO methods give results with the same accuracy as PW methods.

**Table 9.26.** The theoretical and experimental structural parameters for rutile (in Å), numbers in parentheses indicate the percent deviation from low-temperature neutron-diffraction experiments. The references to the theoretical and experimental data, given in this table, can be found in [597]. SC,LC mean small-core and large-core pseudopotentials, AE –all electron calculations

Method	<i>a</i>	<i>c</i>	<i>u</i>
PW-LDA SC	4.555 (-0.70)	2.922 (-1.08)	0.304 (-0.33)
PW-LDA SC	4.528 (-1.29)	2.918 (-1.21)	0.303 (-0.66)
PW-LDA SC	4.567 (-0.44)	2.932 (-0.74)	0.305 (0.00)
PW-LDA LC	4.536 (-1.11)	2.915 (-1.32)	0.304 (-0.33)
PW-LDA LC	4.653 (1.44)	2.966 (0.41)	0.305 (0.00)
PW-LDA LC	4.603 (0.35)	2.976 (0.74)	0.304 (-0.33)
PW-LDA LC	4.638 (1.11)	2.923 (-1.05)	0.305 (0.00)
PW-GGA LC	4.624 (0.81)	2.992 (1.29)	0.305 (0.00)
PW-GGA LC	4.690 (2.25)	2.990 (1.22)	0.306 (0.33)
OLCAO-LD AE	4.622 (0.77)	2.983 (0.99)	0.304 (-0.33)
LCAO-HF LC	4.555 (-0.70)	2.998 (1.49)	0.306 (0.33)
LCAO-HF AE	4.560 (-0.59)	3.022 (2.30)	0.305 (0.00)
LCAO-HF AE	4.529 (-1.26)	3.088 (4.54)	0.305 (0.00)
LCAO-HF AE	4.548 (-0.85)	2.993 (1.32)	0.305 (0.00)
LCAO-LDA AE	4.529 (-1.26)	2.942 (-0.41)	0.304 (-0.33)
X ray 298 K	4.594 (0.15)	2.958 (0.14)	0.305 (0.00)
Neutron 295 K	4.593 (0.13)	2.959 (0.17)	0.305 (0.00)
Neutron 15 K	4.587	2.954	0.305

Table 9.27 shows the results of binding-energy HF LCAO calculations [598] in corundum-like  $M_2O_3$  oxides ( $M=Ti,V,Cr,Fe,Co,Ni$ ). The *a-posteriori* DFT correlation correction of total energy was added in the UHF LCAO AE calculations with numerical optimization of corundum structure parameters.

**Table 9.27.** Calculated and experimental binding energies (eV) of corundum-like oxides [598]

Oxides	UHF	UHF+corr	Experiment
$Al_2O_3$	-23.64	-30.08	-32.14
$Ti_2O_3$	-21.41	-28.05	-33.45
$V_2O_3$	-19.28	-26.23	-31.21
$Cr_2O_3$	-18.10	-25.08	-28.05
$Fe_2O_3$	-17.46	-22.00	-25.17
$Co_2O_3$	-19.80	-24.90	—
$Ni_2O_3$	-17.41	-22.74	—

The atomic energies of Al, Ti, V, Cr, Co, Ni and oxygen were derived by using the basis sets adopted for solid oxides, but supplemented by two more diffuse

shells, the exponents of which were optimized. The binding energy is computed as the difference between the total crystal energy per formula unit (for the most stable antiferromagnetic configuration) and the energies of the constituent isolated atoms. For comparison, experimental binding energies are also given. These were obtained by applying a suitable Born–Haber thermochemical cycle of type

$$E_{coh}(expt) = \sum_i [H_{a,i}^0 + (H_i^{298} - H_i^0)] + \Delta_f H^{298} - (H^{298} - H^0) - E_{vib}^0 \quad (9.83)$$

Here, the sum is extended to all chemical elements in the formula unit. The formation enthalpy  $\Delta_f H^{298}$  of  $\text{Me}_2\text{O}_3$  compounds, sublimation (Me) and dissociation ( $\text{O}_2$ ) enthalpies  $H_{a,i}^0$  and heating enthalpies  $H_i^{298} - H_i^0$  for all chemical species involved were taken from [667]. The zero-point vibrational energies  $E_{vib}^0$  of all oxides were estimated by the Debye model, using an isotropic approximation for the mean acoustic-wave velocity derived from the bulk modulus in order to obtain the Debye temperature.

Table 9.27 shows that the general trend of experimental data (from  $\text{Al}_2\text{O}_3$  to  $\text{Fe}_2\text{O}_3$ ) is simulated correctly by theoretical binding energies, with deviations of the order of  $-30\%$  for UHF energies, which are reduced to  $-12\%$  by including the DFT-based correction for electron correlation. A secondary feature of the experimental data is not reproduced by the calculated results: the peculiar stabilization energy of  $\text{Ti}_2\text{O}_3$  with respect to other oxides. Also,  $\text{V}_2\text{O}_3$  seems to be affected by a larger error than the average. This is consistent with the difficulties found in achieving SCF convergence to stable insulating states for these two oxides: oxides of early-row transition metals, with their very diffuse  $d$  orbitals and tendency to metal states, are harder to simulate by HF methods than those of end-row metals. As we have seen in Sect. 9.1 the UHF calculations of  $\text{Ti}_2\text{O}_3$  reproduce the electron-correlation effects on the local properties of chemical bonding. It appears that *a-posteriori* correction of UHF total energy is not enough to reproduce the correlation effects on the binding energy, *i.e.* self-consistent hybrid HF-DFT calculations are required.

In the next section we consider the LCAO calculations of other total-energy-related observables.

### 9.3.2 Bulk Modulus, Elastic Constants and Phase Stability of Solids: LCAO ab-initio Calculations

We considered above the calculation of observables requiring the first-order derivatives of the total energy. For the equilibrium structure of crystal (equilibrium nuclear coordinates and unit-cell parameters) the total-energy derivatives with respect to nuclear coordinates  $\mathbf{r}$  and lattice parameters  $\mathbf{a}_i$  equal zero at constant temperature  $T$ :  $\left(\frac{\partial E}{\partial \mathbf{r}_i}\right)_T = 0$ ,  $\left(\frac{\partial E}{\partial \mathbf{a}_i}\right)_T = 0$ .

An important variable is pressure as under pressure interatomic distances in crystals show larger variations than those induced by temperature. At constant temperature  $T$  pressure  $P$  is related to the rate of energy change with the unit-cell volume  $V$  by relation  $P = -\left(\frac{\partial E}{\partial V}\right)_T$ , including the first-order derivative of total energy with respect to the cell volume. Such observables as the bulk modulus, the elastic and force constants depend on the second-order derivatives of the total energy.

The bulk modulus  $B$  measures the response of a crystal to *isotropic* lattice expansion or compression and can be related to the second-order derivative of the total

energy with respect to the volume,  $V$ , evaluated at the equilibrium volume  $V_0$ :

$$B = -V \left( \frac{\partial P}{\partial V} \right)_T = -V \left( \frac{\partial^2 E}{\partial V^2} \right)_{V_0} \quad (9.84)$$

The *anisotropic* response of a crystal to a mechanical force can be described by the elastic constants,  $C_{ij}$ , which are defined as the second derivatives of the total energy with respect to the components  $\varepsilon_i$  and  $\varepsilon_j$  of the strain tensor,  $\varepsilon$ :

$$C_{ij} = \left( \frac{\partial^2 E}{\partial \varepsilon_i \partial \varepsilon_j} \right)_{eq} \quad (9.85)$$

The strain-tensor components  $\varepsilon_{ij} = \frac{1}{2} \left( \frac{\partial u_i}{\partial x_j} + \frac{\partial u_j}{\partial x_i} \right)$  are first-order derivatives of the displacements  $u$ . The elastic constants provide a full description of the mechanical properties of crystalline materials. The bulk modulus is related to the elastic tensor. In the case of a cubic system, where only three independent components of the elastic tensor differ from zero,  $B$  can be obtained from  $C_{11}$  and  $C_{12}$  as  $\frac{1}{3} (C_{11} + 2C_{12})$ . Table 9.28 shows the results of the HF LCAO optimization of the  $\text{Cu}_2\text{O}$  crystal structure with the all-electron basis set [622]. These results show the feature noted above of the HF method – an overestimation of the lattice size, mainly due to the neglect of electronic correlation. The *a-posteriori* inclusion of the electronic correlation considerably improves the results of the structure optimization.

**Table 9.28.** Calculated lattice constant  $a$  (Å), interatomic distances (Å), bulk modulus (GPa) and elastic constants (GPa) for  $\text{Cu}_2\text{O}$  [622]

	HF	HF+LYP	Expt.
$a$	4.435	4.277	4.2696
Cu–O	1.920	1.852	1.849
Cu–Cu	3.136	3.025	3.012
$B$	100	93	112
$C_{11}$	118	103	116 – 126
$C_{12}$	90	88	105 – 108
$C_{44}$	59	65	11 – 13

The isotropic variation of the volume of the cubic unit cell was used also to evaluate the bulk modulus. The calculated bulk modulus is in good agreement with the available experimental data. The three independent components of the elastic tensor were derived numerically from the changes in energy obtained by applying adequate deformations to the unit cell. Good agreement has been obtained for the  $C_{11}$  and  $C_{12}$  elastic constants, while there is definite disagreement for  $C_{44}$ . This disagreement is certainly to be attributed to the lack of precision of these methods to estimate small values of the elastic constants. Good-quality calculations of the elastic constants would require a larger accuracy, in contrast to those properties like the cell parameters.

Various possible structures of a crystal and the associated relative energies can be determined experimentally as a function of pressure. This structure evolution as

a function of pressure can involve one (polymorphism) or several (solid-state reaction driven by pressure) types of systems. For example, CaO crystal phase transition  $\text{CaO}(\text{B}_1) \rightleftharpoons \text{CaO}(\text{B}_2)$  includes two polymorphic phases  $\text{B}_1$  (fcc lattice, Ca atom is six-fold coordinated) and  $\text{B}_2$  (sc lattice, Ca atom is eightfold coordinated). The decomposition reaction of  $\text{MgAl}_2\text{O}_4$  spinel into its oxide components  $\text{MgAl}_2\text{O}_4 \rightleftharpoons \text{MgO} + \text{Al}_2\text{O}_3$  includes three types of system. The knowledge of pressure enables investigation of phase stability and transitions, [568]. In fact, enthalpy is immediately obtained from the total energy by  $H = E + PV$  at  $T = 0$  K, where any transformation of a pure substance tends to be isotropic, phase stability can be related to the enthalpy and a phase transition occurs at those points in the phase diagram where two phases have equal enthalpy. From the computational point of view, it is possible to explore a range of crystalline volumes by isometric lattice deformations and obtain the corresponding values of pressure and, consequently, of enthalpy. It is intended that nuclei are allowed to relax to their equilibrium geometry after every lattice deformation.

The theoretical study of phase transitions is made as follows. For each crystal phase, the total energy  $E$  is computed at a number of unit-cell volumes  $V$ ; at each volume, the structure parameters (nuclear coordinates and lattice parameters) that minimize  $E$  are determined. An analytical representation of  $E$  vs.  $V$  is obtained by using a polynomial expression or the Murnaghan equation of state (or any other fitting function). The Murnaghan function, by far the most universally adopted, is as follows:

$$E(V) = E_0 + B_0 V_0 \left[ \frac{1}{B'(B' - 1)} \left( \frac{V_0}{V} \right)^{B' - 1} + \frac{V}{B' V_0} - \frac{1}{B' - 1} \right] \quad (9.86)$$

The four fitting parameters are  $V_0$  (equilibrium volume),  $B_0$  (zero-pressure bulk modulus) and  $B'$  (pressure derivative of the bulk modulus  $B$  at  $P = 0$ ), and  $E_0$  (equilibrium energy). From the  $P(V) = -\frac{\partial E}{\partial V}$  relationship, we get

$$V(P) = V_0 \left( \frac{B'}{B_0} P + 1 \right)^{-\frac{1}{B'}} \quad (9.87)$$

Inserting (9.87) in (9.86), one obtains the analytic  $E$  vs.  $P$  dependence; by adding the  $PV$  term, the enthalpy as a function of pressure is obtained:

$$H(P) = E + PV = E_0 + \frac{B_0 V_0}{B' - 1} \left[ \left( \frac{B'}{B_0} P + 1 \right)^{1 - \frac{1}{B'}} - 1 \right] \quad (9.88)$$

At  $T=0$  K, the transition pressure,  $P_t$ , corresponds to the point where all the systems have the same enthalpy:

$$\Delta H(P_t) = 0 \quad (9.89)$$

This equation is solved numerically yielding the transition or the decomposition pressure. Knowing this pressure, the equation of state followed by the system during the process can be deduced.

A rough estimate of the transition pressure,  $P_{t'}$ , can be obtained just from the knowledge of the equilibrium values ( $E_0$  and  $V_0$ ) for each phase. At  $T=0$  K, the enthalpy as a function of pressure can be evaluated as follows:

$$H(P) = H_0 + \int_0^P dH = E_0 + \int_0^P VdP \quad (9.90)$$

Using this relation, (9.89) becomes

$$\Delta H(P_t) = \Delta E_0 + \int_0^{P_t} \Delta V dP = 0 \quad (9.91)$$

If the pressure dependence of  $\Delta V$  is negligible, one obtains

$$P_t \cong P'_t = -\Delta E_0 / \Delta V_0 \quad (9.92)$$

For fitting of one or multiphase transitions MULFAS (multiphase transition analysis program) by Llunell can be used. The information about this program can be found at the site [www.crystal.unito.it](http://www.crystal.unito.it) in tutorials (phase transitions) directory. An input file for this program contains the volume and total energy data of one phase obtained by using an external quantum-mechanical or shell-model program.

The first-principles all-electron LCAO calculations of the crystal structures, bulk moduli, and relative stabilities of seven  $\text{TiO}_2$  polymorphs (anatase, rutile, columbite, baddeleyite, cotunnite, pyrite, and fluorite structures) have been carried out in [597]. From the optimal crystal structures obtained with the Hartree–Fock theory at various pressures, the bulk modulus and phase-transition pressures of various high-pressure polymorphs have been derived at the athermal limit. In most cases, the calculated unit-cell data agree to within 2% of the corresponding experimental determination. In Table 9.29 the calculated bulk moduli of the various phases of  $\text{TiO}_2$  are given and compared with the existing experimental data. The calculated bulk moduli are within 10% of the most reliable experimental results. It was shown in [597] that the com-

**Table 9.29.** The bulk moduli (GPa) of various phases of  $\text{TiO}_2$  compound [597]

Method	Rutile $P4_2/mnm$ $Z=2$	Anatase $I4/amd$ $Z=2$	Columbite $Pbcn$ $Z=4$	Baddeleyite $P2_1/c$ $Z=4$	Pyrite $Pa\bar{3}$ $Z=4$	Fluorite $Fm\bar{3}m$ $Z=1$	Cotunnite $Pnma$ $Z=4$
LCAO-HF	$239 \pm 10$	$202 \pm 10$	$264 \pm 10$	$300 \pm 10$	$318 \pm 10$	$331 \pm 10$	$380 \pm 10$
LCAO-LDA	$241 \pm 10$	$195 \pm 10$	—	—	$273 \pm 10$	$308 \pm 10$	—
PW-LDA	243	194	247	249	—	282	—
experiment	$211 \pm 7$	$178 \pm 1$	$253 \pm 4$	$304 \pm 6$	—	—	$431 \pm 10$

puted anatase–columbite, rutile–columbite, columbite–baddeleyite, and baddeleyite–cotunnite phase transitions appear in the same order as observed in experiments, and the transition pressures agree semiquantitatively with those measured. The pyrite and fluorite structures are predicted to be less stable than other polymorphs at pressures below 70 GPa, in agreement with experiments.

The detailed LCAO calculations for bulk properties and the electronic structure of the cubic phase of  $\text{SrTiO}_3$  (STO),  $\text{BaTiO}_3$  (BTO), and  $\text{PbTiO}_3$  (PTO) perovskite

crystals with optimization of basis set (BS) are presented in [606]. The results given in Table 9.30 are obtained using it ab-initio Hartree–Fock (HF) and density-functional theory (DFT) with Hay–Wadt pseudopotentials. A number of different exchange-correlation functionals including hybrid (B3PW and B3LYP) exchange techniques are used. Results, obtained for seven types of Hamiltonians, are compared in Table 9.30 with available experimental data. On average, the disagreement between the lattice constants computed using hybrid HF-DFT functionals and experimental values for all three perovskites is less than 0.5%.

The bulk moduli were calculated in two ways – as the total energy second derivatives (9.84),  $B_1$  and using the elastic constants,  $B_2$ . The results for both ways of bulk-moduli evaluation differ by no more than 10–15%. Especially good agreement with the experimental data has been achieved for hybrid functionals. With the polarization orbitals added to the BS of oxygen atom, the calculated optical bandgaps are 3.57, 3.42 and 2.87 eV for STO, BTO and PTO respectively, in very good agreement with experimental data.

**Table 9.30.** The optimized lattice constants  $a$  (Å), bulk moduli  $B$  (GPa) and elastic constants  $C_{ij}$  (in  $10^{11}$  dyn/cm $^2$ ) for perovskites SrTiO<sub>3</sub> (STO), BaTiO<sub>3</sub>(BTO), PbTiO<sub>3</sub>(TO), [606]

Method	LDA	PWGGA	PBE	BLYP	P3PW	B3LYP	HF	Exper.
STO								
$a$	3.86	3.95	3.94	3.98	3.90	3.94	3.92	3.89
$C_{11}$	42.10	31.29	31.93	29.07	31.60	32.83	41.7	31.72
$C_{12}$	12.21	9.80	9.75	9.39	9.27	10.57	7.11	10.25
$C_{44}$	13.32	11.34	11.30	11.09	12.01	12.46	10.5	12.35
$B_1$	222	170	171	159	167	180	186	174
$B_2$	214	167	169	164	177	177	219	179
BTO								
$a$	3.96	4.03	4.03	4.08	4.01	4.04	4.01	4.00
$C_{11}$	35.81	30.11	31.04	28.22	31.12	29.75	30.1	20.60
$C_{12}$	11.52	10.35	10.72	10.78	11.87	11.57	13.46	14.00
$C_{44}$	14.98	13.22	13.98	12.24	14.85	14.54	17.34	12.60
$B_1$	196	169	175	166	183	176	190	162
$B_2$	204	175	180	154	188	172	194	195
PTO								
$a$	3.93	3.96	3.96	4.02	3.93	3.96	3.94	3.97
$C_{11}$	45.03	32.47	34.25	23.03	43.04	34.42	39.83	22.9
$C_{12}$	26.14	15.81	15.52	9.93	24.95	18.08	16.90	10.1
$C_{44}$	11.28	10.69	10.96	8.25	10.93	10.35	17.20	10.0
$B_1$	324	213	217	143	310	235	245	144
$B_2$	321	246	252	140	279	242	299	

We note that the results given in Table 9.30, were obtained with the BS optimization (the details of this optimization can be found in [606]). In our opinion, it is this optimization that allowed good agreement of calculated and experimental data to be obtained.

Strontium zirconate  $\text{SrZrO}_3$  is of interest because of possible applications in fuel cells, hydrogen gas sensors and steam electrolysis. The powder neutron-diffraction data suggest the following sequence of phase transitions in  $\text{SrZrO}_3$ : from the orthorhombic  $Pbnm$  to the orthorhombic  $Cmcm$  at 970 K, to the tetragonal  $I4/mcm$  at 1100 K and lastly, to the cubic



at 1400 K [668]. The first *ab-initio* DFT PBE calculations for all four phases of  $\text{SrZrO}_3$  using both PW and LCAO basis sets are presented in [614]. The structural parameter optimization was performed using DFT PBE-PW calculations and good agreement with experimental data was obtained. LCAO PBE calculations were made both for the experimental and optimized structures. Table 9.31 shows the calculated relative energies (per formula unit) of four  $\text{SrZrO}_3$  polymorphs.

**Table 9.31.** Calculated relative energies (eV per formula unit) of  $\text{SrZrO}_3$  polymorphs [614]

phase	Structure parameters		
	Exper.		Optimized
	LCAO	LCAO	PW
$Pm\bar{3}m$	0.000	0.000	0.000
$I4/mcm$	-0.040	0.002	0.004
$Cmcm$	-0.177	-0.252	-0.235
$Pbnm$	-0.241	-0.303	-0.274

It is seen from Table 9.31 that both LCAO and PW results agree with the experimental sequence of the  $\text{SrZrO}_3$  phases: the most stable turn out to be two orthorhombic phases, whereas the tetragonal and cubic high temperature phases are close in energy.

The sequence of phase transitions in  $\text{ABO}_3$ -type oxides with the temperature increase could be described in terms of the nearest  $\text{BO}_6$  octahedral tilts/rotations [668]. In the  $\text{SrZrO}_3$  case, the orthorhombic structure with three rotations is changed by two rotations for  $Cmcm$  and finally by one rotaton for the tetragonal structure. The combination of three rotations produces the lowest-energy structure. The electrostatic energy is lowest for the lowest symmetry because of the inherent instability of the ideal corner-shared octahedral network. To compensate the loss in Madelung energy, the repulsive energy should also be lowered, in order to achieve the equilibrium. Thermal expansion or entropy is the driving force for the octahedral tilts.

### 9.3.3 Lattice Dynamics and LCAO Calculations of Vibrational Frequencies

The second-order derivatives of the energy with respect to the nuclear coordinates are involved in lattice dynamics, in particular, in the calculation of vibrational (phonon) spectra. We shall begin from the molecular case, [669]. The decoupling of the nuclear from the electronic motion is made in the adiabatic approximation (see Chap. 4).

Let  $u_i$  represents a displacement of the  $i$ th cartesian coordinate from its equilibrium value ( $i = 1, 2, \dots, 3N$ ), where  $N$  is the number of nuclei in a molecule, and  $q_i = \sqrt{M_i}u_i$  are the generalized coordinate ( $M_i$  is the mass of the atom associated with the  $i$ th coordinate) and its derivative with respect to time  $\dot{q}_i = p_i$ . In the harmonic approximation the classical vibrational Hamiltonian of a polyatomic molecule becomes

$$H = T + V = \frac{1}{2} \left( \sum_i M_i \dot{u}_i^2 + \sum_{ij} H_{ij} U_j \right) + V_0 = \frac{1}{2} (\langle p|p \rangle + \langle q|W|q \rangle) + V_0 \quad (9.93)$$

Here  $V_0$  is the electron energy for the equilibrium atomic coordinates, and  $H_{ij}$  are the Hessian matrix elements

$$H_{ij} = \frac{1}{2} \left[ \frac{\partial^2 V}{\partial u_i \partial u_j} \right]_0 \quad (9.94)$$

evaluated at equilibrium. The relation  $W_{ij} = \frac{H_{ij}}{\sqrt{M_i M_j}}$  defines the elements of the weighted Hessian.

The eigenvalues  $\varkappa_j$  of the Hermitian matrix  $W$  are the generalized force constants. The Hamiltonian (9.93) then can be factorized into  $3N$  one-dimensional harmonic Hamiltonians

$$H = \sum_{\nu} h_{\nu} = \sum_{\nu} \frac{1}{2} (P_{\nu}^2 + \omega_{\nu}^2 Q_{\nu}^2) \quad (9.95)$$

Thus each of the  $3N - 6$  vibrational modes can be interpreted as a collective oscillatory movement with frequency  $\omega_{\nu} = \sqrt{\varkappa_{\nu}}/2\pi$  and the problem of calculating vibrational spectra reduces to the diagonalization of matrix  $W$  to find the set of eigenvalues  $\varkappa_j$ .

For periodic systems, the translation invariance of the potential energy and Hessian matrix should be used. The generalized coordinates obey the Bloch theorem and are written in the form

$$q_i(\mathbf{k}) = N \sum_{\mathbf{g}} \exp(-i\mathbf{k}\mathbf{g}) q_i^{\mathbf{g}} \quad (9.96)$$

The vibrational problem is block-factorized into a set of problems (one for each  $\mathbf{k}$  point in BZ) of dimension  $3N - 6$  where  $N$  is the number of atoms in the primitive unit cell.

The  $\mathbf{k}$ -block of the  $\mathbf{k}$ -factorized  $W$  matrix takes the form

$$W_{ij}(\mathbf{k}) = \sum_{\mathbf{g}} \exp(i\mathbf{k}\mathbf{g}) \frac{H_{ij}^{\mathbf{0}\mathbf{g}}}{\sqrt{M_i M_j}} \quad (9.97)$$

where  $H_{ij}^{\mathbf{0}\mathbf{g}}$  is the second derivative of potential energy at equilibrium with respect to atom  $i$  in the reference cell  $\mathbf{0}$  and atom  $j$  in cell  $\mathbf{g}$ . The number of equations (9.97) to be solved equals the number of  $\mathbf{k}$ -points in the BZ, *i.e.* is infinite for the infinite crystal. In practice, the calculations of phonon frequencies are made for a finite number of  $\mathbf{k}$ -points and the interpolation is used to obtain so-called phonon branches  $\omega_1(\mathbf{k}), \dots, \omega_i(\mathbf{k}), \dots, \omega_{3N}(\mathbf{k})$  (like one-electron energies are obtained in SCF calculations for a finite set of  $\mathbf{k}$ -points and then interpolated to form the electron-energy bands). The relationship between phonon frequencies  $\omega$  and wavevector  $\mathbf{k}$  determines the phonon dispersion.

Comparing the vibrational branches and electronic bands calculations we note that in the former case the equations for different  $\mathbf{k}$  values are solved independently while in the latter case the self-consistent calculation is necessary due to the BZ summation in the HF or KS Hamiltonian (see Chapters 4 and 7). Once the phonon dispersion in a crystal is known, thermodynamic functions can be calculated on the basis of statistical mechanics equations. As an example, the Helmholtz free energy,  $F$ , can be obtained as:

$$\langle F \rangle = \sum_{i\mathbf{k}} \left\{ \frac{1}{2} \hbar \omega_{i\mathbf{k}} + k_B T \ln \left[ 1 - \exp \left( -\frac{\hbar \omega_{i\mathbf{k}}}{k_B T} \right) \right] \right\} \quad (9.98)$$

where the sum is extended to all lattice vibrations,  $\omega_{i\mathbf{k}}$ , and  $k_B$  is the Boltzmann's constant. Another way of computing thermodynamic functions is based on the use of the phonon density of states. The evolution of the crystal structure as a function of temperature and pressure can also be simulated by minimizing  $G = F + pV$ . The procedure requires a sequence of geometry optimizations, and lattice-vibration calculations [568].

Lattice vibrations can be measured experimentally by means of classical vibration spectroscopic techniques (infrared and Raman) or neutron inelastic scattering. However, only the latter technique allows one to measure the full spectrum in a range of  $\mathbf{k}$  vectors, whereas with infrared and Raman spectroscopy, only lattice vibrations at  $\Gamma(\mathbf{k} = \mathbf{0})$  are usually detected (the second-order spectra, corresponding to nonzero wavevector  $\mathbf{k} \neq \mathbf{0}$  are demanding). The calculations of the vibrational frequencies only at  $\Gamma$  point require the solution of only one equation

$$\det |W(0)| = 0, \quad W_{ij}(0) = \sum_{\mathbf{g}} \frac{H_{ij}^{\mathbf{0}\mathbf{g}}}{\sqrt{M_i M_j}} \quad (9.99)$$

To analyze the symmetry of phonon states the method of induced reps of space groups can be used [13]. The procedure of analysis of the phonon symmetry is the following. First, for the space group  $G$  of a given crystal the simple induced reps are generated (see Chap. 3). Second, using the simple induced reps together with the compatibility relations and arranging atoms in the primitive cell over the Wyckoff positions one can determine the symmetry of the phonons. Only those of the induced reps that are induced by the irreps of the site-symmetry groups according to which the components of the vectors of the local atomic displacements transform are used. The total dimension  $n$  of the induced rep (called the mechanical representation) equals  $3N$  ( $N$  is the number of atoms in the primitive cell).

As an example, Table 9.32 shows the phonon symmetry in rutile  $\text{TiO}_2$  crystal. The results given are easily obtained from the simple induced reps of the space group  $D_{4h}^{14}$  (see Table 4.5 in [13]) and the atomic arrangement in rutile  $\text{TiO}_2$  (see Chap. 2).

There is a one-to-one correspondence between irreps of crystal point group  $D_{4h}$  and irreps of the space group at  $\Gamma$  point:  $A_{1g,u} - 1^\pm, A_{2g,u} - 3^\pm, B_{1g,u} - 2^\pm, B_{2g,u} - 4^\pm, E_{g,u} - 5^\pm$ . The atomic displacements of six atoms in the primitive cell generate the 18-dimensional reducible representation, which contains three acoustic modes and 15 optical modes ( $A_{1g} + A_{2g} + A_{2u} + B_{1g} + 2B_{1u} + B_{2g} + E_g + 3E_u$ ). Three acoustic modes have zero frequency at the  $\Gamma$  point and are associated with the translation of the entire crystal along any direction in space. These branches are called *acoustic* modes as the corresponding vibrations behave as acoustic waves. The translation of

**Table 9.32.** Phonon symmetry in rutile  $\text{TiO}_2$  crystal with space group  $D_{4h}^{14}$ 

$q$ -basis		$k$ -basis					
$G_q$	Rep. of $G_q$	$\Gamma$	M	Z	A	X	R
Ti(2a)	$b_{1u}(z)$	$2^-, 3^-$	$2^-, 3^-$	1	1	1	$1^-$
(000)	$b_{2u}(x - y)$	$5^-$	$5^-$	3	3	2	$1^-$
$D_{2h}$	$b_{3u}(x + y)$	$5^-$	$5^-$	4	4	2	$1^-$
O(4f)	$a_1(x + y)$	$1^+, 4^+, 5^-$	$1^+, 4^+, 5^-$	1,4	1,4	2,2	$1^+, 1^-$
( $xx0$ )	$b_2(x - y)$	$2^+, 3^+, 5^-$	$2^+, 3^+, 5^-$	2,3	2,3	2,2	$1^+ 1^-$
$C_{2v}$	$b_1(z)$	$2^-, 3^-, 5^+$	$2^-, 3^-, 5^+$	1,3	1,3	1,1	$1^+ 1^-$

the entire crystal along the  $z$ -axis corresponds to irrep  $3^- (A_{2u})$  at  $\Gamma$  point, translation in the plane  $xy - 5^- (E_u)$ .

Both acoustic modes are polar and split into transverse  $A_{2u}$  (TO) and longitudinal  $E_u$  (LO) with different frequencies due to macroscopic electric field. All other branches show finite nonzero frequencies at  $\Gamma$  and are known as optical modes, because they correspond to unit-cell dipole moment oscillations that can interact with an electromagnetic radiation.

In the model of a finite crystal the rotation of the entire crystal around the  $z$ - and  $xy$ -axis corresponds to the irreps  $3^+$  and  $5^+$ , respectively, including the displacements of only oxygen atoms, see Table 9.32. As seen from Table 9.32, the phonons of even symmetry ( $1^+, 2^+, 3^+, 4^+, 5^+$ ) are connected only with the oxygen-atom displacements. Due to the different atomic masses of oxygen and titanium atoms, the corresponding lines can appear in different parts of the vibrational spectra, making its interpretation easier. The knowledge of phonon symmetry is useful in the analysis of infrared and Raman spectra of solids as the symmetries of active phonons in these spectra are governed by selection rules following from the symmetry restrictions imposed on the transitions matrix elements [13]. Using the symmetry of the phonons found one can establish which vibrational modes are active in the first- and second-order infrared and Raman spectra.

The calculation of phonon frequencies of the crystalline structure is one of the fundamental subjects when considering the phase stability, phase transitions, and thermodynamics of crystalline materials. The approaches of *ab-initio* calculations fall into two classes: the *linear response* method [670] and the *direct* method, see [671] and references therein.

In the first approach, the dynamical matrix is expressed in terms of the inverse dielectric matrix describing the response of the valence electron-density to a periodic lattice perturbation. For a number of systems the linear-response approach is difficult, since the dielectric matrix must be calculated in terms of the electronic eigenfunctions and eigenvalues of the perfect crystal.

There are two variants of the direct method. In the frozen-phonon approach the phonon energy is calculated as a function of the displacement amplitude in terms of the difference in the energies of the distorted and ideal lattices. This approach is restricted to phonons whose wavelength is compatible with the periodic boundary conditions applied to the supercell used in the calculations. Another approach of the direct method uses the forces  $\left(\frac{\partial E}{\partial u_i}\right)_{eq}$  calculated in the total-energy calculations, derives

from them the values of the force-constant matrices and hence the dynamical matrix and phonon-dispersion curves. The majority of calculations were performed based on DFT PW method, for example to study phonons in the rutile structure, [672]. The calculation of the vibrational frequencies of crystals was implemented in the LCAO CRYSTAL06 code (see [www.crystal.unito.it](http://www.crystal.unito.it)) and applied to different oxides: quartz  $\text{SiO}_2$  [669], corundum  $\text{Al}_2\text{O}_3$  [673], calcite  $\text{CaCO}_3$  [674].

In the LCAO approximation frequencies at  $\Gamma$  are evaluated in the direct method in the same way as for molecules [669]: a set SCF calculations of the unit cell are performed at the equilibrium geometry and incrementing each of the nuclear coordinates in turn by  $u$  (use of symmetry can reduce the number of the required calculations). Second-order energy derivatives are evaluated numerically. Obtaining frequencies at wavevector symmetry points different from  $\Gamma$  would imply the construction of appropriate supercells (see Chap. 3). These supercells are chosen in the same way as was discussed in the electronic-structure calculations due to the one-to one correspondence between the supercell choice and the set of  $\mathbf{k}$ -points equivalent to the  $\Gamma$  point in the reduced BZ. A finite range of interaction in the lattice sum (9.99) is assumed, usually inside the supercell chosen (compare with the cyclic-cluster model in the electronic-structure calculations). In the case of ionic compounds, long-range Coulomb effects due to coherent displacement of the crystal nuclei are neglected, as a consequence of imposing the periodic boundary conditions [669]. Therefore,  $W_{ij}(0)$  needs to be corrected for obtaining the longitudinal optical (LO) modes [675]. For this reason, in some cases only transverse optical (TO) parts of the phonon spectrum are calculated as is done in the combined DFT PW-DFT LCAO lattice dynamics study of  $\text{TiO}_2$  rutile [676]. The phonon frequencies computed in [676] for optimized crystal structure are reported in Table 9.33 and compared with experimental data.

The LDA frequencies are in excellent agreement with the experimental frequencies, especially if compared with the frequencies measured at low temperature ( $T \sim 4$  K), when these data are available. The deviation between the LDA and experimental frequencies is  $\sim 13 \text{ cm}^{-1}$  at most, and is often much smaller than that. For instance, the deviation drops to no more than  $\sim 2 \text{ cm}^{-1}$  for the two stiffest modes,  $B_{2g}$  and  $A_{1g}$ , and it remains small also for several of the softer modes. Both PBE and PW91 results are much less satisfactory. With the exception of the  $B_{1g}$  mode, the GGA functionals systematically underestimate the LDA and measured frequencies. It is found in [676] that this discrepancy between LDA and GGA results is mostly due to the difference in the equilibrium lattice parameters at zero pressure predicted by the functionals. The LDA frequency is the highest because LDA predicts the smallest equilibrium volume, and the PBE equilibrium volume is large enough to lead to an imaginary frequency.

All the results discussed were obtained within the plane-wave pseudopotential implementation of DFT. For all functionals, calculations were repeated for the equilibrium geometries, bulk moduli, and energy profiles along the ferroelectric TO  $A_{2u}$  mode with the all-electron LCAO scheme. Apart from slight quantitative differences, in all cases the all-electron LCAO calculations agree well with the plane-wave, pseudopotential results, confirming their independence of the particular numerical scheme used to implement DFT. We note that the hybrid HF-DFT LCAO calculations could in principle give better agreement with experimental data for phonon frequencies of rutile as was shown in the B3LYP LCAO calculations of the vibrational spectrum

**Table 9.33.** Calculated and measured frequencies (in  $\text{cm}^{-1}$ ) relative to the  $\Gamma$ -point of bulk  $\text{TiO}_2$  rutile ([676]).\*

Mode	PBE	PW91	LDA	Neutrons	IR and Raman	
Raman						
$B_{2g}$	774.3	780.9	824.7	825		827
$A_{1g}$	565.9	572.0	611.6	610		612 (611)
$E_g$ (2)	429.2	434.2	463.2	445		447 (455)
$B_{1g}$	154.2	151.7	137.0	142		143 (143)
Silent						
$A_{2g}$	423.6	425.4	421.7	not found		—
$B_{2u}$	357.5	363.4	393.0	406		—
$B_{1u}$	79.2	99.2	104.0	113		—
Infrared						
$E_u$ (TO)	468.6	472.0	488.4	494		500
$E_u$ (TO)	353.5	357.1	383.9	not found		388
$E_u$ (TO)	124.0	127.4	191.4	189		183
$A_{2u}$ (TO)	186.3	47.1	154.4	173 (142)		167 (144)

\*The double degeneracy of the  $E_g$  mode is indicated by the label (2). The references to the experimental neutron-scattering and the infrared (IR) and Raman data are given in [676]. When available, the low-temperature ( $T \sim 4$  K) experimental frequencies are reported in brackets

of calcite  $\text{CaCO}_3$ , [674]. In this case the mean absolute error is less than  $12 \text{ cm}^{-1}$  (frequencies range from  $100$  to  $1600 \text{ cm}^{-1}$ ).

As we have seen in this chapter, the HF and DFT LCAO methods, implemented in the computer code CRYSTAL, present efficient computational schemes for the study of different properties of periodic systems. Real-solid properties in many cases depend on the point defects, destroying the translational symmetry. In the next chapter we discuss the models used for defective crystals study and give examples of the LCAO calculations of defective crystals.

## Modeling and LCAO Calculations of Point Defects in Crystals

### 10.1 Symmetry and Models of Defective Crystals

#### 10.1.1 Point Defects in Solids and Their Models

The theory of perfect crystalline solids explains those bulk properties of crystals that do not depend on boundary effects and other defects of the structure. However, real solids do not demonstrate translational symmetry. Boundaries and other regions of disruption of translational symmetry called defects are always present. Many practical applications of solids are based on the use of the properties caused by defects. By varying the defect structure of solids it is possible to change their physical and chemical properties in such a way that the defective crystals find useful applications. As an example, we mention  $\text{TiO}_2$  crystal that has been successfully applied as a semiconductor photocatalyst with high oxidizing power and high resistance to photo- and chemical corrosion. However, the relatively large bandgap ( 3 eV) does not permit efficient absorption of visible light and hence prevents  $\text{TiO}_2$  from being used in large-scale environmental applications. Chemical doping of  $\text{TiO}_2$  allows the bandgap to be reduced. The theoretical study of the doped  $\text{TiO}_2$  helps to solve the important problem: how to best manipulate the gap while maintaining the beneficial photocatalytic properties [677].

The defects in solids can be classified according to the dimensions of the region of translation symmetry disruption. When one or a few nearest host crystal sites are disturbed, we speak of *point* (zero-dimensional) defects, called also *local defects*. Also known are *extended defects* that introduce structural imperfections in lattice directions - *linear* (one-dimensional) defects or in the lattice planes (*planar* or two-dimensional defects). The surface of a crystal and dislocations are the important examples of two-dimensional and linear defects, respectively.

The point defects, in turn, are classified as *native* (intrinsic) and *substitution* defects. The intrinsic point defects appear as a *vacancy* (the absence of an atom in a crystal lattice position) or as an *interstitial* defect (the presence of the host crystal atom in an interstitial position). The host crystal atoms can be substituted for another atom of a different chemical species at a regular lattice site or at the interstitial position (impurity center or *substitution* defect). The point defects can also be classified as neutral and charged relative to the host crystal lattice. The perturbation of a solid by

the charged point defect includes the short-range (local) and long-range (Coulomb) parts. The former is reproduced in the calculations of the sufficiently small fragments of the defective crystal, the calculation of the latter requires special methods, taking into account the polarization of the surrounding crystal by the point defect.

In what follows we consider, as examples, LCAO calculations of different types of point defects in oxides: native point defects – interstitial oxygen atom in  $\text{MgO}$  crystal and neutral oxygen vacancy (F-center) in corundum  $\text{Al}_2\text{O}_3$  and  $\text{SrTiO}_3$  crystals; substitution defects (vanadium-doped rutile  $\text{TiO}_2$  crystal, iron impurity in  $\text{SrTiO}_3$  crystal). The calculations of the charged point defects are demonstrated by a charged oxygen vacancy ( $\text{F}^+$  center) in corundum  $\text{Al}_2\text{O}_3$  crystal.

For low defect concentration it becomes appropriate to model a single point defect in an environment of the remaining solid. In such a model the translation symmetry is completely absent so that the crystal with a single point defect can be seen as a gigantic molecule. However, in the case of a solid solution the single-defect model is not appropriate as the stoichiometry change is introduced by regular substitution of the host-crystal atoms by those of other chemical species. In this case the periodic point-defect model is more appropriate. As an example, we discuss in Sect. 10.3 the modeling of  $\text{Ba}_x\text{Sr}_{1-x}\text{TiO}_3$  solid solutions.

The calculational methods of quantum chemistry are widely applied to the point defects in solids. This application is made after the choice of one of the existing defective crystal models, (see Fig. 10.1).

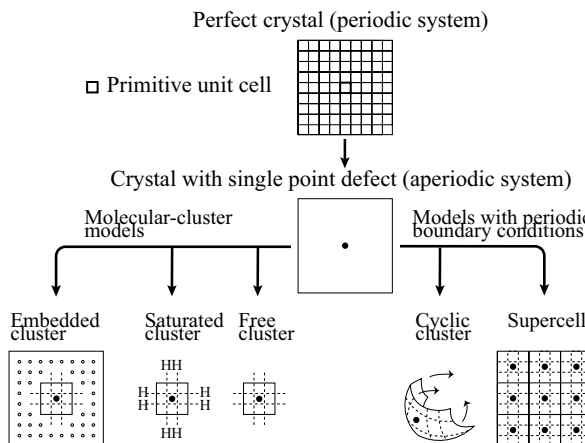


Fig. 10.1. Defective crystal models

If a single point defect is introduced into an otherwise perfect crystal, the translational symmetry is, in principle, lost completely (see Fig. 10.1), and equations should be solved for all atoms of the solid, *i.e.* for the aperiodic system [294]. Obviously, the application of some kind of simplified model is desirable. In many cases the electronic states of defects in a crystal are localized in some relatively small region. The degree of this localization depends on the nature of the defect and of the host crystal. The local

nature of a single point defect allows a smaller piece of a crystal to be taken (called *a cluster*) but its size must be chosen in such a way that there is at least one shell of atoms between the defect zone and the cluster surface that remains undisturbed. The obvious way is to separate the part of the crystal perturbed by the defect from the still crystalline background, and treat only the former in an explicit manner. On the one hand, the need for economizing calls for a model consisting of as few atoms as possible. On the other, the explicitly treated part of the crystal should, in principle, extend far enough for the effect of the defect to become negligible [294]. This means, up to the point where the amplitude of the localized wavefunctions, the deviations of charge density and of host-atom positions relative to the unperturbed case become close to zero. In practice, this is assumed to be for a group of atoms around the defect (cluster). The three criteria above are almost never satisfied to a necessary degree with clusters that can be squeezed into the computer. Therefore, at least some kind of convergence test in all three respects is proper.

The electronic structure of the molecular cluster can be calculated using any of the methods developed for the molecules. However, the problem arises at the molecular cluster surface, *i.e.* with the representation of the rest of the crystal. As is shown schematically in Fig. 10.1, there are different possibilities for this representation. In *molecular-cluster* models the group of atoms chosen is embedded into the crystalline environment (*embedded-cluster* model) or the cluster surface atoms are saturated by hydrogen or other species atoms (*saturated-cluster* model). In the most crude model the free cluster (neutral or charged) is chosen.

The models with periodic boundary conditions (*the supercell* and *the cyclic-cluster* models) allow calculation of the one-electron states of perfect and defective crystals at the same level of approximation. The supercell model (SCM) and cyclic-cluster model (CCM) have both similarities and discrepancies. One similarity is that in both models not a standard primitive unit cell but an *extended* unit cell (supercell or large unit cell) is considered. The discrepancy is that the periodic boundary conditions in the SCM are introduced for the infinite crystal or its main region, but in the CCM model – for the extended unit cell itself.

The calculation schemes usually used for point defect include: 1. the choice of the *model* of the defective crystal; 2. the choice of the *Hamiltonian* (Hartree–Fock, DFT or hybrid, semiempirical); 3. the choice of the *basis* for the one-electron Bloch functions decomposition – linear combination of atomic orbitals (LCAO) or plane waves (PW).

SCM is used as a rule for the neutral-point-defects calculations (for the charged point defects the field of periodically repeated charge has to be suppressed in one or another way). The molecular- and cyclic-cluster models are more universal as they can be applied both for the neutral and charged point defects.

In the SCM the calculations with HF or hybrid Hamiltonians are made in the LCAO approximation, DFT Hamiltonians are used both in the LCAO and PW representations. CCM can be practically realized with the semiempirical LCAO Hamiltonians.

In SCM we let the defects be situated periodically and try to make the separation between defects as large as possible. If the extended unit cell is large enough the defects are separated by large distances and do not affect each other's electron structure so that the results of the application of SCM and CCM models become close. The bandwidth of defect states depends primarily on the degree of overlap of the functions

describing the defect electron states from different supercells and decreases rapidly with increasing defect period. Therefore, this bandwidth can be used as the criterion of the convergence of the SCM results to those of CCM. The cyclic-cluster model is conceptually a supercell-type approach but is technically more closely related to the simple molecular-cluster model. SCM introduces the artificial point-defect periodicity, CCM describes the single point defect.

All the approaches to the theoretical description of defective crystals use information about the symmetry of the system or its model. As mentioned above, a single defect embedded in a crystal disrupts the translational symmetry of a perfect crystal so that it may be considered as a gigantic molecule with a point-symmetry group inherent to molecules. There are two cases: an *atomic type* point defect, which occupies one point of a crystal lattice or an interstitial position and can be a substitutional impurity, vacancy or interstitial atom; and a *molecular type* point defect, which occupies several atomic or interstitial points of a crystal lattice and can be composed of an impurity molecule or a cluster of several vacancies at neighboring lattice points. In the first case the symmetry group of the defect crystal is fully determined by the site symmetry of the point  $q$  where the atomic defect appears. In a crystal with a symmorphic space group the atomic defect may occupy the position  $q$  with the symmetry of the crystal class or one of its subgroups. In nonsymmorphic crystals the point group of the crystal with a single point defect of atomic type is always a subgroup of the crystal class. In a crystal with point defects of molecular type the center of the impurity molecule is situated at a point with some site symmetry. A molecular defect has its own point symmetry so that the point symmetry of the whole system is determined by the common elements of two groups: the point group of the isolated molecule and the site-symmetry group of the site where the impurity molecule is situated. However, it is necessary to also take into account the orientation of the impurity molecule with respect to the crystal symmetry axes.

It can be assumed that when a point defect appears the configuration of the crystal matrix around the defect does not change (the model of a rigid lattice). In reality, this assumption is approximately correct only for some point defects and as a rule only for the ground electron state. Excitation of the defect electrons causes significant reconstruction of the defect's surroundings so that the point symmetry of the entire system may change. In many calculations, the distortion of the crystal lattice by a defect is at first neglected. Then, this distortion is taken into account with approximate wavefunctions obtained for the rigid-lattice model. Therefore, initially, the symmetry is approximated in the framework of the rigid-lattice model. The knowledge of the actual symmetry of a crystal with a point defect is necessary for correct understanding of all its properties: the symmetry determines the selection rules for optical transitions in the defect, the symmetry and the splitting of local energy levels in external fields, the features of EPR and NMR spectra, *etc.*

To understand the nature of a point defect in a crystal and the degree of its influence on the properties of the crystal matrix it is necessary to relate the local energy levels of the defect to the energy-band structure of the perfect crystal. But these two systems (crystal with defect and perfect crystal) have different symmetries and the classification of electron states is made according to irreps of either a point group (for a crystal with a single defect) or a space group (for a perfect crystal).

In the molecular-cluster model it is rather easy to establish the relationship between energy levels and one-electron states of a molecular cluster with and without a point defect. The symmetries of both systems are described either by the same point group or by a point group that is a subgroup of the other (in the case of a molecular-type defect). Hence, in the cluster model the relationship between the classification schemes of electron energy levels and states of perfect and imperfect crystals is simple. But the relationship between the cluster electron energy structure and that of a perfect crystal is much more complicated. In the models using PBC the application of the site-symmetry approach is quite useful [13]. The single-defect localized electron states of a given energy level span the space of an irrep of defect point-symmetry group  $F_D$ . The band states of a perfect crystal are classified according to irreps of the space group  $G$ . It is useful to determine which band and localized states are allowed by symmetry to mix (e.g., for calculating the electron structure from atomic basis functions). We consider the appearance of a point defect as a perturbation of a perfect crystal. According to perturbation theory, only states with the same symmetry may interact with one another. The common symmetry group of both systems is  $F_D \subset G$ . Let  $\beta$  be an irrep of  $F_D$  that describes one of the defect states. To establish the possibility of its mixing with the perfect crystal states of symmetry  $D^{(*\mathbf{k}\gamma)}$  it is sufficient to know whether the restriction  $D^{(*\mathbf{k}\gamma)} \downarrow F_D$  contains the irrep  $\beta$ . If the state of symmetry  $D^{(*\mathbf{k}_0\gamma)}$  does not contain the state of symmetry  $\beta$ , then the contribution of the states with  $\mathbf{k}$  near  $\mathbf{k}_0$  is small according to the perturbation theory, although it is not equal to zero due to the symmetry. As an example, let us consider the  $s$ -states of an impurity at a cation site (Wyckoff position  $a$ , site group  $D_{2h}$   $s$ -state has symmetry  $a_g$ ) or at an anion site (Wyckoff position  $f$ , site group  $C_{2v}$ ,  $s$ -state has symmetry  $a_1$ ) in rutile  $\text{TiO}_2$ . From band calculations we know the symmetry of states on the boundaries of the forbidden gap in a rutile  $\text{TiO}_2$  crystal (see Chap. 9):  $\Gamma_1^+$  (the bottom of the lowest conduction band) and  $\Gamma_3^+$  (the top of the highest valence band). From the table of induced representations of the space group  $D_{4h}^{14}$  we find  $\Gamma_1^+ \downarrow D_{2h}^{(a)} = a_g$ ;  $\Gamma_3^+ \downarrow D_{2h}^{(a)} = b_{1g}$ , i.e. the  $s$ -states of an impurity may mix with the states of the bottom of the lowest conduction band, but not with the states of the top of the uppermost valence band. The anion site is at the Wyckoff position  $f$  ( $F_f = C_{2v}$ ). We get  $\Gamma_1^+ \downarrow C_{2v}^{(f)} = a_1$ ;  $\Gamma_3^+ \downarrow C_{2v}^{(f)} = b_2$ , i.e. the  $s$ -states of an impurity at an anion site may mix with the states of the bottom of the lowest conduction band but not with the states of the top of the uppermost valence band. From this consideration it follows that the defect local levels due to the  $s$ -states of the impurity both at Ti and O sites split from the conduction-band bottom. Such information is useful for the study of doping influence on the rutile crystal bulk properties.

In the next sections we consider in more detail the defective-crystal models mentioned above.

### 10.1.2 Symmetry of Supercell Model of Defective Crystals

The recent trends in the theory of the point defects in solids and of the crystalline surfaces, formally aperiodic systems, are connected with the widespread application of periodic boundary conditions (PBC) and computer codes developed for the perfect crystals, see [568, 678, 679] and references therein. This allows one to use the same numerical schemes both for the host and defective crystal to study changes induced

by a point defect or surface: additional local energy levels in the optical gap, lattice relaxation around defects, *etc*. As was noted above, in the theory of point defects two models with PBC are used: the supercell model (SCM) and the cyclic-cluster model (CCM).

The application of the supercell model to the defective crystals requires consideration of periodic systems with a sufficiently large number of atoms in the unit cell. The possibilities of the supercell model extend if the full symmetry of the object is taken into consideration. It was demonstrated [681–683] that the study of the symmetry of a crystal with a periodic defect permits, in some cases, investigation of the dependence of the results of electronic-structure calculations on the period of a defect by only changing the symmetry of the system without any augmentation of the supercell. The symmetry of the crystal with a periodic defect is determined by the site symmetry of the defect in the crystal and by the symmetry of the host-crystal matrix. Let a point defect (impurity atom or molecule, one or a few vacancies) occupy a position  $\mathbf{q}$  in a perfect crystal with a space group  $G$  (crystal class  $F$ ). A site-symmetry group of the defect in the crystal  $S_D$  consists of common elements of two groups: of the symmetry group  $S_D^{(0)}$  of the defect itself and the site-symmetry group  $S_q$  of the position  $\mathbf{q}$  in the crystal occupied by the defect. The group  $S_D$  depends on the mutual orientation of the symmetry elements of the groups  $S_D^{(0)}$  and  $S_q$ .

Let us consider now a periodic structure that arises in the supercell model when the embedded defect is periodically repeated and occupies in this structure some position  $\mathbf{Q}$  with site-symmetry group  $S_Q = S_D$ . The symmetry of the obtained periodic structure is characterized by some space group  $G_D$ . One seeks for all the possible space groups  $G_D = T_A F_D$  of the defective crystal for a given host crystal (space group  $G$ ) and for a given point defect in the crystal (point group  $S_D$ ). Here, translation group  $T_A$  includes translations  $\mathbf{A}$  of the supercell. Some symmetry operations disappear when one goes from the space group  $G$  to the space group  $G_D$ . Therefore, the group  $G_D$  has to be a subgroup of  $G_D \subseteq G$  with a crystal class satisfying the condition  $S_D \subseteq F_D \subseteq F$ . The possible space groups  $G_D$  of the crystal class  $F_D$  are those that have the group  $S_D$  as a site-symmetry subgroup. In this way, one obtains the list of space groups  $G_D$  that may describe the symmetry of the supercell model of a defective crystal for a given site symmetry  $S_D$  of the embedded defect and space group  $G$  of a host crystal.

In the framework of the same space group  $G_D$  the periodical structures may differ by the length of supercell basic translation vectors  $\mathbf{A}_1, \mathbf{A}_2, \mathbf{A}_3$  for the same type of Bravais lattice. These vectors have a definite orientation with respect to the symmetry elements of the group  $G_D$ , and sometimes there is a definite relation between their lengths. In addition, they have to be integer linear combinations, see (4.77), of basic translation vectors of the host perfect crystal. This combination defines the transformation matrix  $l$  with the determinant  $L$  (the number of primitive unit cells in the supercell). As was noted, this transformation is called a symmetric one if the point symmetry of the Bravais lattice of supercells is the same as that of the host-crystal Bravais lattice, see Chap. 4. Use of the symmetric transformation for the supercell generation allows the point symmetry of the defective crystal in the supercell model to be maintained as high as possible. These conditions determine the matrix  $l$ , *i.e.* the translational subgroup  $T_A$  of the symmetry group  $G_D$ . Finally, it is necessary to verify whether the obtained group  $G_D$  is a subgroup of the symmetry group of the

host crystal. This condition assures that all the atoms of the system transform into themselves under the operations of the group  $G_D$ . If  $\tilde{G}_D \subset G$ , then  $G_D = \tilde{G}_D$ ; if  $G_D \not\subset G$ , then the group  $\tilde{G}_D$  has to be excluded from the list of the possible groups  $G_D$ .

Finally, the generation of the possible space groups with a periodical defect in the supercell model consists of the following steps [683]:

(i) determination of the site group  $S_D$  of the defect in the crystal; (ii) determination of the crystal classes satisfying the condition  $S_D \subseteq F_D \subseteq F$ ; (iii) determination in the space groups of these classes those that have the site-symmetry subgroups  $S_D$ ; (iv) generation of the matrix  $l$  and the supercell translation vectors  $\mathbf{A}_i$  by symmetric transformation of the host crystal basic translations; (v) verification of the condition  $G_D \subseteq G$ .

The groups  $G_D$  of a supercell model with one point defect for a supercell are isomorphic, they belong to the crystal class  $F_D = S_D$  with all the types of crystal lattices possible for this crystal class. The point symmetry of the cyclic-cluster coincides for the host crystal – with the point-symmetry group  $F$ , for the defective crystal – with the point-symmetry group  $S_D$ .

Let us consider some examples. In MgO crystal the supercells, containing 8, 16 and 32 atoms (S8, S16, S32), are obtained by a linear symmetric transformation of the fcc lattice basic translation vectors with matrices

$$l^{(4)} = \begin{pmatrix} 1 & 1 & -1 \\ 1 & -1 & 1 \\ -1 & 1 & 1 \end{pmatrix}, \quad l^{(8)} = \begin{pmatrix} 2 & 0 & 0 \\ 0 & 2 & 0 \\ 0 & 0 & 2 \end{pmatrix}, \quad l^{(16)} = \begin{pmatrix} 3 & -1 & -1 \\ -1 & 3 & -1 \\ -1 & -1 & 3 \end{pmatrix}$$

Superscript  $(n)$  in  $l^{(n)}$  denotes the number of primitive unit cells in the supercell. The supercell translation vectors for  $\mathbf{A}_1$ ,  $\mathbf{A}_2$ , and  $\mathbf{A}_3$  for  $l^{(4)}$ ,  $l^{(8)}$ ,  $l^{(16)}$  correspond to simple cubic, face-centered-cubic, and body-centered-cubic lattices, respectively. The host crystals, consisting of the corresponding supercells, have the symmetry of cubic space groups  $O_h^1$ ,  $O_h^5$ , and  $O_h^9$ , respectively. For the isoelectronic Be, Ca impurities in the Mg site the site-symmetry group coincides with the point-symmetry group of the host crystal, *i.e.* the space groups of the defective crystals are the same as for the host crystal. The Li impurity atom is displaced from the Mg site along the fourth order symmetry axis (the Li atom site symmetry is  $C_{4v}$ ). As a result, the space groups of the defective crystal are now tetragonal –  $C_{4v}^{(1)}$ ,  $C_{4v}^{(9)}$ , and  $C_{4v}^{(9)}$ , respectively (the face-centered lattice is absent in the tetragonal system).

An additional neutral interstitial oxygen  $O_i$  atom as a point defect in MgO crystal can have several configurations. In three of these (called  $v$ ,  $f$ , and  $e$ ) the oxygen atom is at the volume, face, or edge centers, respectively, of the cubic unit cell. Fig. 10.2 shows volume-(a), face-(b) centered configurations and a (110)-oriented dumbbell (see below) configuration (c). The point symmetry of the  $v$ ,  $f$  and  $e$  configurations is  $T_d$ ,  $D_{2h}$ , and  $C_{4v}$ , respectively. The space groups for MgO with these centers in the supercell model depend on the supercell chosen and they are given in Table 10.1. The other three configurations  $vd$ ,  $fd$ , and  $ed$  are so-called dumbbell-shaped defects formed when the  $O_i$  is moved towards a nearest-neighbor  $O^{2-}$  lattice anion along  $\langle 111 \rangle$ ,  $\langle 110 \rangle$ , or  $\langle 001 \rangle$  directions, respectively, the lattice anion being simultaneously displaced from its site along the same direction. The center of the dumbbell is at the lattice site, and the point symmetry of these defects is  $D_{3d}$ ,  $D_{2h}$ , and  $D_{4h}$ , respectively. The space

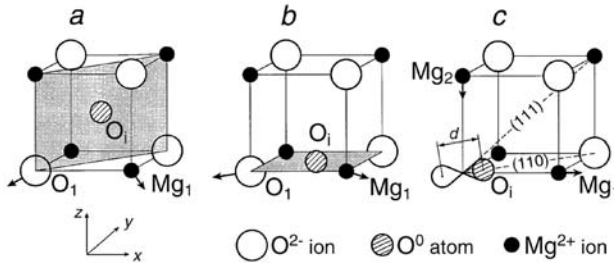


Fig. 10.2. Configurations of the interstitial oxygen atom in MgO

groups of MgO containing these defects are given in the last three lines of Table 10.1. The results of Table 10.1 were obtained using the list of subgroups of the space groups given on the Internet site [www.cryst.ehu.es](http://www.cryst.ehu.es). For example, the supercell transformation with the matrix  $l^{(4)}$  changes the host-crystal space group from  $O_h^5$  to  $O_h^1$ . Choosing from the list of subgroups of space group  $O_h^1$  those symmorphic subgroups that refer to the crystal class  $T_d$  (point symmetry of the  $v$  configuration), we obtain directly the result given in the third column of Table 10.1.

Table 10.1. Space-group symmetry for the supercell model of an oxygen-atom interstitial  $O_i$  in MgO crystal [682]

Center	F <sub>D</sub>	Supercells		
		$l^{(4)}$	$l^{(8)}$	$l^{(16)}$
$v$	$T_d$	$T_d^1(215)$	$T_d^2(216)$	$T_d^3(217)$
$f$	$D_{2h}$	$D_{2h}^{19}(65)$	$D_{2h}^{25}(71)$	$D_{2h}^{25}(71)$
$e$	$C_{4v}$	$C_{4v}^1(99)$	$C_{4v}^9(107)$	$C_{4v}^9(107)$
$vd$	$D_{3d}$	$D_{3d}^5(166)$	$D_{3d}^5(166)$	$D_{3d}^5(166)$
$fd$	$D_{2h}$	$D_{2h}^{19}(65)$	$D_{2h}^{25}(71)$	$D_{2h}^{23}(69)$
$ed$	$D_{4h}$	$D_{4h}^1(123)$	$D_{4h}^{17}(139)$	$D_{4h}^{17}(139)$

The next example – the impurity atom on the Ti site of rutile structure with the space group  $D_{4h}^{14}$ . There are two titanium atoms in the primitive unit cell, occupying the two-site Wyckoff position  $a$  with coordinates  $(000)$  and  $(\frac{1}{2} \frac{1}{2} \frac{1}{2})$ . An impurity atom replaces a Ti atom with the site symmetry  $D_{2h}$ . Therefore, the space group of the defective crystal belongs to the crystal class  $D_{2h}$ . Four possible symmetric supercell transformations for the space group  $D_{4h}^{14}$  are given in Table 6.3. The first of them maintains the simple tetragonal lattice of the host crystal, the other three transform it to the body-centered tetragonal lattice. Respectively, the possible symmetry groups of the defective crystal are the following:  $D_{2h}^1$ ,  $D_{2h}^{19}$ ,  $D_{2h}^{23}$ ,  $D_{2h}^{25}$ .

In the Ti atom site-symmetry group two of three second-order axes are directed along the diagonals of the square, see Chap. 2. In the standard setting of the space groups with  $D_{2h}$  point symmetry all the three second-order axes are directed along the Cartesian coordinate axes. This difference must be taken into account [683].

The point symmetry of the cyclic-cluster model coincides with point groups  $F$  and  $F_D$  for the host and defective crystal.

### 10.1.3 Supercell and Cyclic-cluster Models of Neutral and Charged Point Defects

In the point-defect calculations there are two criteria to be met: the model used for solving the quantum-mechanical problem has to describe sufficiently well both (i) the extended crystalline states and (ii) the localized states of a single point defect. The CCM can be defined from the two points of view: it can be regarded either as the application of the Born– von Karman cyclic boundary conditions directly to the large unit cell (supercell), or as the band-structure calculation on SCM with (A) applying the  $\mathbf{k} = \mathbf{0}$  approximation, and (B) neglecting interactions beyond the Wigner–Seitz cell corresponding to the supercell chosen. The SCM have no restrictions like A and B and thus CCM could be considered as a special approximation to the SCM.

The economic approach to a single-point-defect study in a model with PBC consists of three stages [680].

*In stage 1* the band-structure calculation of a perfect crystal is performed, in order to fix the shape and size of the supercell that reasonably models the host crystal, *i.e.* when the above-described condition (i) is met. These calculations are made using a primitive unit cell and  $\mathbf{k}$ -sampling in the usual (primitive) BZ.

The one-to-one correspondence was demonstrated between a fixed  $\mathbf{k}$ -mesh and the supercell in a real space, see Equations (4.77), (4.80) and (4.84). Due to the one-to-one correspondence between  $\mathbf{k}$ -point sampling and the supercell size in a real space it is possible to find such a  $\mathbf{k}$ -mesh that ensures a compromise between its size and a reasonable reproduction of the total- and one-electron energies, as well as the electron-density distribution in the host crystal. At this stage, the  $\mathbf{k}$ -point sets satisfying (4.84) are used.

*In stage 2* the calculations are made for a defective crystal using SCM, in order to check the above-described criterion (ii). It is reasonable to begin from the smallest supercell, chosen at stage 1, *i.e.* corresponding to the converged results of the band calculations. The supercell shape should be such as to exploit the point symmetry of the defect as far as possible. In the particular case of the cubic  $\text{SrTiO}_3$  crystal cubic supercell of 80 atoms ( $L = 2 \times 2 \times 2$ , the diagonal matrix  $\mathbf{l}$  in transformation (4.77) is taken) may be used for a perfect crystal in the HF calculations but larger supercells are necessary in the DFT-PWGGA calculations [680]. When estimating the defect–defect interaction from the calculated defect bandwidth in the second stage, one makes a decision about the need for a further increase of the supercell. In particular, the Fe impurity at the Ti site bandwidth in the HF calculations still changes when the supercell is increased from 80 to 160 atoms [680]. This means that the local states induced by the point defect are sufficiently well localized only in the larger, 160-atom supercell [680]. That is, in stage 2 the comparison of supercell results for different  $\mathbf{k}$ -meshes allows us to decide if it is necessary to further increase a supercell, in order

to surpass artificial defect–defect interaction. When energies at  $\mathbf{k} = \mathbf{0}$  and nonzero  $\mathbf{k}$  supercell calculations turn out to be close, this means that the corresponding cyclic cluster is appropriate for the single-point-defect study as CCM corresponds to the  $\Gamma$  point only consideration for the supercell chosen.

*In the most time-consuming stage 3* the CCM is used (*i.e.* the band-structure calculations for the chosen supercell are performed only at  $\mathbf{k} = \mathbf{0}$ ) for the determination of the equilibrium geometry, *i.e.* relaxation of the crystalline lattice around the point defect and calculation of other defective crystal properties.

As is seen, the approach described combines both supercell and cyclic-cluster models of the defective crystal and differs from the traditional supercell calculations by an attempt to exclude in stage 3 the spurious point-defect periodicity. This exclusion allows us formally to escape periodic repeating of the crystalline lattice relaxation around the point defect. Furthermore, the different charge states of the point defect could be also considered in stage 3 without principal difficulties since in CCM the charge is not periodically repeated over the lattice.

The defect-formation energy is an important property of the defective crystal. The formation energy  $\Delta E_f$  of a neutral defect in CCM is given by

$$\Delta E_f = E_d - E_B + E_R - E_A \quad (10.1)$$

where  $E_B$  is the bulk-crystal total energy,  $E_d$  is the total energy of the cyclic cluster with the point defect,  $E_A$  and  $E_R$  the energies of the added and removed species, respectively. The bulk crystal energy  $E_B = LE^{(0)}$ , where  $L$  is the number of primitive cells in the cyclic cluster and  $E^{(0)}$  is the energy per primitive cell. As an example, for ionic MgO crystal the formation energy of X substitution impurities (X=Ca, Be substitutes Mg atom), [684], can be given in terms of the isolated atoms or isolated ions

$$\Delta E_X^L = E_{\text{MgO}-\text{X}} - LE_{\text{MgO}}^{(0)} + E_{\text{Mg}^{2+}} - E_{\text{X}^{2+}} \quad (10.2)$$

$$\Delta E_X^L = E_{\text{MgO}-\text{X}} - LE_{\text{MgO}}^{(0)} + E_{\text{Mg}} - E_{\text{X}} \quad (10.3)$$

When the relaxation is taken into account (shifting of some nuclei around a defect from a reference bulk-crystal situation) the total energy  $E_d$  is corrected by the relaxation energy  $E_{\text{rel}}$ .

The oxygen-removal energy for MgO crystal  $\Delta E_f$  (formation energy of neutral oxygen vacancy, also called an F center) is defined as the energy of the system, containing the F center, plus the energy of an isolated oxygen atom minus the energy of the perfect crystal [685]. In the LCAO approximation the energies of added or removed atoms are calculated in the same numerical scheme that is used for the bulk and defective crystal calculation (the atomic basis is used that is appropriate for a free atom, see Chap. 9). In PW calculations the energy of the isolated atom is obtained by calculations on a number of periodic systems, containing one atom per increasing supercells, and the final size of the supercell is taken large enough to ensure that the interaction between atoms introduces a sufficiently small error (this error was 0.01 eV in calculations [685]). Within the supercell approach,  $\Delta E_f$  should tend to a well-defined limit with increasing supercell size. For a defect to be considered as single, sufficiently large supercells must be adopted to avoid spurious interactions among neighboring defects.

In the SCM (CCM) models two finite energies are compared when determining the defect-formation energy: they are the total energies per unit supercell of the two crystals (perfect and defective). In view of the large energies involved, it is important that the same cell be used for the perfect and defective crystals to ensure cancellation of errors.

As an example, we consider the convergence of the LCAO HF AE supercell calculations of Ca and Ba atom substitution in bulk MgO, the details of the computational scheme used can be found in [684]. In Table 10.2 the substitution energies are given as a function of the supercell size for nonrelaxed and relaxed defective lattice. The supercells of 8, 16 and 32 atoms correspond to the host crystal fcc lattice vector transformations, giving simple, face-centered and body-centered cubic lattices of supercells with  $L=4$ , 8, 16 (8, 16 and 32 atoms), respectively (see Sect. 10.1.2). Table 10.2 shows that in an unrelaxed lattice the increasing of the supercell from 8 to 32 atoms changes the defect-formation energy from 0.11 eV (Ca substitution) and 0.02 eV (Be substitution). It is also seen that for the largest supercell the Ca substitutional energy reduces from 7.09 eV to 6.43 eV when the first star of neighbors (six O ions) is allowed to relax; a further energy gain of 0.19 eV is obtained after allowing the second neighbors (12 Mg ions) to relax, the total relaxation energy, 0.84 eV, being substantial. In the case of the Be substitution, the relaxation energy, 0.27 eV, is considerably smaller. In the Be case the displacements are smaller and in the opposite direction to those for the Ca substitution, but the pattern is otherwise qualitatively similar. Thus, quite small unit cells appear to be able to describe the effect of electronic rearrangement. In contrast, Table 10.2 indicates that nuclear-positional relaxation is much more long ranged, at least for fully ionic compounds such as MgO.

**Table 10.2.** Ca and Be HF substitutional energies  $\Delta E_f$  (in eV) in MgO as a function of the size of the supercell.  $M$  is the number of atoms in the supercell,  $\Delta R$  is the variation (in Å) of the distance between the defect and its first (6O) and second (12Mg) [684]

$M$	Ca			Be		
	$\Delta E_f$	$\Delta R$		$\Delta E_f$	$\Delta R$	
		First(6O)	Second(12Mg)		First(6O)	Second(12Mg)
8	7.20	—	—	-3.81	—	—
16	7.12	—	—	-3.80	—	—
32	7.09	—	—	-3.83	—	—
16	6.56	0.073	—	-3.93	-0.044	—
32	6.43	0.084	—	-4.00	-0.053	—
32	6.25	0.097	0.031	-4.10	-0.070	-0.022

The dependence of the defect-calculation results on the supercell size in MgO was obtained for oxygen atom removal energies in DFT PW calculations [685]: increasing of the supercell from 8 to 64 atoms changed the defect-formation energy from 10.656 eV to 10.568 eV in unrelaxed lattice and from 10.553 eV to 10.547 eV for the relaxed lattice. In this case, the effect of relaxation appeared to be completely negligible.

The convergence of the results with the supercell size is strongly dependent on the point-defect nature. Ca and Be substitutions of Mg atom in MgO are examples

of isoelectronic substitution, giving small impurity-atom displacement from the substituted atom site. However, in the case of the MO : X point defect (M=Mg, Ca, Sr; X = H, Li, Na, K) this displacement becomes large due the difference between the host and substitution atoms. The difference in the number of valence electrons in M and X atoms (two and one, respectively) is called hole trapping. Ionizing radiation produces a variety of trapped hole centers in metal oxides, both alkaline-earth oxides and perovskite-type compounds.

As a result of the impurity-atom displacement the point defect in MgO has axial symmetry along one of the fourth-order symmetry axes of the cubic lattice. This lowering of the crystalline symmetry from cubic to tetragonal generates a dipole moment within the cell. A long-range dipolar defect–defect interaction then originates among defects in neighboring cells, and larger supercells are needed to obtain the converged results. As an example, the defect formation energy of the MgO : Li center in UHF calculations (for the Li only relaxation taken into account) changes with the supercell increase are the following [568]:4.82 eV(8), 4.99eV(16), 5.06eV(32), 5.10eV(64). Here, the number of atoms in the supercell is given in brackets. When all the atoms in the supercell are allowed to relax, the defect-formation energy changes (in the calculations of the largest supercell of 64 atoms) from 5.43 eV (unrelaxed) to 4.15 eV (fully relaxed). The comparison with the data given in Table 10.2, demonstrates that for the hole-trapping center the convergence is slower than for isoelectronic substitution and the geometry optimization plays a crucial role for the hole-trapping center: the difference in the defect-formation energy for fully relaxed and nonrelaxed largest supercells is 0.84 eV (Ca substitution), 0.27 eV (Be substitution) and 1.28 eV for the hole-trapping center. The atomic relaxations themselves are especially large for the Li atom (about 0.3 Å). It was found [568] that in the fully relaxed case, the convergence of the defect-formation energy is much faster (0.03 eV in going from a supercell of 8 atoms to one of 64 atoms) that shows that structural relaxation is an effective mechanism to screen and minimize long-range electrostatic interactions induced by the dipolar nature of the defect center.

When the alkali-metal ion replaces an alkaline-earth cation, it relaxes from the perfect lattice position toward the oxygen ion (O2) along the axial direction, which brings a formal +2 charge; the electron hole localizes at the opposite oxygen (O1), which in turn relaxes away from the X monovalent ion. However, this relaxation is periodically repeated, and it would be desirable to compare its role for the supercell calculations at the center and symmetry points of the BZ.

The supercell calculations give important information concerning the charge redistribution in the defective crystal. In particular, the UHF electronic structure of the trapped-hole defect MgO : [Li]<sup>0</sup> indicates the localization of the unpaired electron at the O1 atom [568]. However, the degree of localization is quantified by the spin moment of O1 and changes significantly when different Hamiltonians are considered: the spin moment decreases from 0.98 at the UHF level, to 0.41 for B3LYP, to about 0.1 with other DFT Hamiltonians [568]. The different degree of localization produced by DFT methods has important consequences for the atomic relaxation. Magnetic coupling constants determined by EPR and ENDOR techniques permit a direct comparison with experimental data to be made. In the particular case of the Li defect, the agreement is reasonable for the UHF result, where the hole is localized at O1. For

the other Hamiltonians, the disagreement increases in parallel with the delocalization of the hole [568].

In PW calculations of defective crystals the use of PBC is the only possibility in the model choice. Apart from the problem of getting rid of interactions between defects by considering sufficiently large cells or by introducing corrections by averaging over the sampled  $\mathbf{k}$ -points [686], the supercell technique seems to provide a natural “universal” reference for the neutral point defects in crystals: the two structures that are compared satisfy the same boundary conditions, and the two wavefunctions (or density matrices) differ only in the vicinity of the defect in each supercell [687]. This is, however, no longer true when charged defects are considered. The artificial long-range Coulomb interactions between the periodic charged defect images introduce the divergence in the energy. The problem of the neutrality of the periodic array of charged defects is solved by superimposing a neutralizing charge uniformly spread in each supercell (a uniform, neutralizing “jellium” background charge is introduced to restore the electroneutrality of the unit cell).

It is also necessary to correct the defect-formation energy using an estimate of the dielectric response of the host system to the periodic ensemble of neutralized defects. While the self-energy of this charge becomes vanishingly small with increasing supercell size, this is not true for its interaction with the host crystal. Polarization of the crystalline medium by the local charge could be taken into account by allowing full relaxation of nuclear positions with very large supercell sizes. This is impossible in practice, and the corresponding finite contribution to the stabilization of the defect must be evaluated separately. With “reasonable” supercell sizes, it is necessary to correct for the interaction between charged defects. This correction can be performed classically, using the experimental  $\epsilon$  static dielectric constant [688]. However, using the experimental  $\epsilon$  value makes the model inconsistent, not only because of the semi-empirical character of this assumption, but also because use of the static dielectric constant would imply full relaxation of electrons and nuclei in the field of the defect charge, while use of the optical dielectric constant would require that no nuclear relaxation takes place [687]. To calculate the charged point defect formation energy in SCM some other correction schemes are suggested, [689–692]. These schemes were applied for the supercell calculations of point defects in semiconductors: tetrahedral – Si [690], diamond [693], InP [692], SiC [691] and hexagonal –AlN [694], GaN [695].

LCAO calculations of the charged point defects in metal oxides are made mainly in the molecular-cluster model, considered in the next section. As we already noted PW molecular-cluster calculations are impossible as use of the PW basis requires the periodicity of the structure under consideration.

#### 10.1.4 Molecular-cluster Models of Defective Solids

The molecular-cluster model (MCM) of the defective crystal is the simplest and most direct approach. As was already noted, MCM is obtained by cutting out in the crystal some fraction of atoms consisting of the point defect and several spheres of nearest neighbors, followed by an embedding of this cluster into the field of the surrounding crystal and (or) by saturating with the pseudoatoms the dangling bonds on the cluster surface. The embedding pseudopotential can also be used (see Sect. 8.2.3).

The main attractive features of a cluster model are the following: the simplicity of the mathematical formulation; the possibility of direct transfer of computational

schemes, worked out in quantum chemistry of molecules; and applicability to almost all types of solids and point defects in them. A reasonable choice of cluster is possible when well-localized point defects are considered [696].

There are well-known [294] difficulties of the cluster model connected with changes of host-crystal symmetry, pseudoatom choice at the cluster boundaries and the necessity to consider nonstoichiometric (charged) clusters. The validity of the results obtained within the cluster approach is often questionable due to some serious drawbacks: the strong unpredictable influence of the cluster shape and size on the results of calculations; the difficulties arising when relating the cluster one-electron energy levels with the band energies of the perfect crystal; and the appearance of “pseudosurface” states in the one-electron energy spectrum of the cluster. The appearance of the “pseudosurface” states is accompanied by the unrealistic distortion of electronic density on the cluster boundaries and can lead to artefactual resonances between the “pseudosurface” and the point defect one-electron states.

In order to make the cluster model more realistic, a large number of embedding schemes have been developed. Most of them are oriented on special types of crystal (ionic, simple covalent) or are based on the use of special approximations in the Hamiltonian operator (local exchange, tight-binding approximations). The other group of cluster models is based on adding the effective-potential operator (the embedding operator) to the unperturbed-cluster Hartree–Fock operator, giving the proper one-electron solution for the perfect crystal. When the cluster shape and size are chosen, this embedding operator can be determined and used in the following perturbed-cluster calculations. This so-called embedded-cluster approach is sufficiently general and can be applied to different types of solids.

The only characteristic that to a certain extent depends on the nature of the solid and local center in it is the minimal appropriate cluster size. This size is limited by the extent of localization of one-electron states in the perturbed and nonperturbed solid. At the same time the extent of the defect-potential localization is not so critical if the cluster is chosen in such a way that the long-range polarization outside the cluster can be taken into account.

The use of *localized orbitals* for the cluster calculation is an efficient approach for defective crystals. To connect the perfect crystal localized orbitals and molecular cluster one-electron states the molecular cluster having the shape of a supercell was considered [699]. Such a cluster differs from the cyclic cluster by the absence of PBC introduction for the one-electron states. Evidently, the molecular cluster chosen is neutral and stoichiometric but its point symmetry can be lower than that of the cyclic cluster. Let the localized orthogonal crystalline orbitals (Wannier functions) be defined for the infinite crystal composed of supercells. The corresponding BZ is  $L$ -times reduced (the supercell is supposed to consist of  $L$  primitive unit cells). The Wannier functions  $W_n(\mathbf{r} - \mathbf{A}_i)$  are now introduced for the supercells with the translation vectors and satisfy the following equation:

$$\hat{H}W_n(\mathbf{r} - \mathbf{A}_i) = \sum_{\mathbf{A}_l} \varepsilon_n(\mathbf{A}_l - \mathbf{A}_i) \quad (10.4)$$

Here,  $\hat{H}$  is the one-electron Hamiltonian of the crystal,

$$\varepsilon_n(\mathbf{A}_l) = \frac{1}{\sqrt{N}} \sum_{\mathbf{k}'} E_n(\mathbf{k}') \exp(i\mathbf{k}\mathbf{A}_l) \quad (10.5)$$

are the Fourier coefficients of the energy  $E_n(\mathbf{k}')$  of the  $n$ th band. The range of  $\mathbf{k}'$  summation, numbering of energy bands and the coefficients  $\varepsilon_n(\mathbf{A}_l)$  in (10.5) correspond to the supercell chosen,  $N$  is the number of supercells in the macrocrystal. Let  $E_n^{\min}, E_n^{\max}$  be the minimum and maximum values of the energy in the  $n$ th band. Introducing  $\Delta E_n = \frac{1}{2} (E_n^{\max} - E_n^{\min})$  and  $E_n = E_n^{\min} + \Delta E_n$  we get

$$\begin{aligned} \frac{1}{N} \left| \sum_{\mathbf{k}'} (E_n(\mathbf{k}') - E_n) \exp(i\mathbf{k}' \cdot \mathbf{A}_l) \right| &\leq \\ \leq \frac{1}{N} \cdot N \cdot \max \{ |E_n(\mathbf{k}') - E_n| \exp(i\mathbf{k}' \cdot \mathbf{A}_l) \} &\leq \\ \leq \max \{ |E_n(\mathbf{k}') - E_n^{\min} - \Delta E_n| \} &\leq \Delta E_n \end{aligned}$$

The inequality obtained

$$\frac{1}{N} \left| \sum_{\mathbf{k}'} (E_n(\mathbf{k}') - E_n) \exp(i\mathbf{k}' \cdot \mathbf{A}_l) \right| \leq \Delta E_n \quad (10.6)$$

is fulfilled for any choice of the supercell, defining the translation vectors  $\mathbf{A}_l$ , the range of  $\mathbf{k}'$  summation and the band numbering. For any choice of the supercell  $\sum_{\mathbf{k}'} \exp(i\mathbf{k}' \cdot \mathbf{A}_l) = N \cdot \delta_{\mathbf{A}_l, \mathbf{0}}$ . Using (10.6) we have the relation

$$|\varepsilon(\mathbf{A}_l) - E_n \delta_{\mathbf{A}_l, \mathbf{0}}| \leq \Delta E_n \quad (10.7)$$

that can be rewritten as

$$|\varepsilon(\mathbf{0}) - E_n| \leq \Delta E_n, \quad |\varepsilon(\mathbf{A}_l)| \leq \Delta E_n \quad (10.8)$$

Hence

$$\begin{aligned} \varepsilon(\mathbf{A}_l) &\rightarrow 0, \quad \varepsilon(\mathbf{0}) \rightarrow E_n \\ \Delta E_n &\rightarrow 0 \end{aligned} \quad (10.9)$$

On increasing the size of the supercell one can approach the limits in (10.9) as closely as desired. When the size of the supercell increases, the number of energy bands in some fixed energy interval  $\Delta E$  increases proportionally, and the width  $\Delta E_n$  of the  $n$ th band decreases. From (10.8) it follows that the narrower the energy bands of the perfect crystal (in the usual band numbering for the primitive cell), the smaller will be the unit cell for which one can neglect on the right side of (10.4) all the terms with  $\mathbf{A}_l \neq \mathbf{A}_i$  and consider the approximate equation

$$\hat{H} \widetilde{W}(\mathbf{r} - \mathbf{A}_i) = \varepsilon_n(0) \widetilde{W}(\mathbf{r} - \mathbf{A}_i) \quad (10.10)$$

This equation is written for the Wannier function of the  $i$ th supercell. Due to (10.9)  $\varepsilon_n(0)$  can be considered as the average energy of the  $n$ th band (in the supercell classification of crystalline states). In fact, (10.10) corresponds to the molecular cluster having the shape of the supercell. The Bloch functions of the macrocrystal can be constructed from the cluster one-electron states:

$$\Psi_n(\mathbf{k}, \mathbf{r}) = \frac{1}{N} \sum_{\mathbf{R}_l} \exp(i\mathbf{k}\mathbf{R}_l) \widetilde{W}(\mathbf{r} - \mathbf{A}_l) \quad (10.11)$$

This consideration is the foundation of the approach originally called “the cyclically embedded cluster” model [697]: the crystal is divided into the sets of regions chosen in the shape of a Wigner–Seitz supercell of the perfect crystal. The central region  $A$  contains the defect with its surrounding, the other regions together form the rest of the crystal. We refer the reader to [697] for the mathematical details of this approach. We note only that in the limit when the region  $A$  is the whole crystal this model gives the traditional HF LCAO equations for a defective crystal considered as a large molecule. In the other limit, when the defect potential is equal to zero, the cyclic cluster of the perfect crystal is obtained. The cyclically embedded cluster model is relatively simple in implementation and has been used for point defects in ionic [698] and covalent [697] crystals. The drawback of the model is that it does not take into account the polarization of the crystal by the perturbative potential of the defect.

The consideration above using a Wannier function for the supercell shows that the molecular-cluster model is more appropriate for the solids with the relatively narrow (1–3 eV) upper valence bands and sufficiently large energy gap. For ionic insulating crystals these conditions are fulfilled and the convergence of the results with increasing cluster size is rapid. The results of recent molecular-cluster calculations [432] confirmed these conclusions made about thirty years before [699]. As an example, we mention the localized orbitals approach used to introduce the embedded-cluster model of  $\alpha$ -quartz [700]. The localized orbitals are constructed by applying various localization methods to canonical HF orbitals calculated for a succession of finite molecular clusters of increased size with appropriate boundary conditions. The calculated orbitals span the same occupied Fock space as the canonical HF solutions, but have the advantage of reflecting the true chemical nature of the bonding in the system.

In strongly ionic systems, where coupling between the cluster and the background is mainly by classical Coulomb interactions, the long-range forces from the background can be accounted for by a Madelung term. A higher level of approximation applies a shell model for the environment, *i.e.* places a set of ions with rigid positive cores and polarizable, negatively charged shells around the cluster. The parameters of this shell model can be determined, *e.g.*, from self-consistent calculations on model systems. The charges in the embedding point charge model or in the shell model must be determined self-consistently with charges in the cluster [294]. Except for ionic solids, the interaction between the cluster and the background is quantum mechanical in nature, *i.e.* the electronic equation is to be solved.

A rigorous mathematical basis for the separation of cluster and background is provided by Green-function (GF) techniques. There are essentially two possible ways: the perturbed-crystal and the perturbed-cluster approaches. In the former approach it is assumed that the defect introduces a perturbation relative to the perfect crystal, localized to the cluster. If the GF of the perfect crystal is known in any localized basis representation, and the matrix elements of the perturbation can be constructed, the GF of the perturbed crystal can be calculated [294]. The perturbed-crystal approach looks conceptually like the cleanest and most sophisticated solution as far as the description of the crystalline background is concerned. The problems arise more with the cluster. The perturbation should be constructed self-consistently and at the same

level as the crystal potential. The perfect-crystal problem can easily be solved on a plane-wave basis but then the solutions must be transformed into Wannier functions in order to construct the perturbation. Alternatively, a localized basis set can be used for the perfect crystal in the first place. The perturbed-crystal model is most often used in metals where the screening effect of electrons is strong and the extent of atomic displacements is smaller.

The perturbed-cluster approach [701, 702] is formulated in the LCAO approximation and is based on the following sequence of steps, [703]: a) subdivide the entire defect system into a molecular cluster (C), containing the defect, and an external region (D), the indented crystal; b) calculate the wavefunction for the molecular cluster in the field of the indented crystal; c) correct the cluster solution in order to allow for the propagation of the wavefunction into the indented crystal while generating the density matrix of the defect system. Steps “b” and “c” are repeated to self-consistency. The corrective terms in step “c” are evaluated by assuming that the density of states projected onto the indented crystal is the same as in the perfect host crystal (fundamental approximation).

With respect to standard molecular-cluster techniques, this approach has some attractive features: explicit reference is made to the HF LCAO periodic solution for the unperturbed (or perfect) host crystal. In particular, the self-embedding-consistent condition is satisfied, that is, in the absence of defects, the electronic structure in the cluster region coincides with that of the perfect host crystal; there is no need to saturate dangling bonds; the geometric constraints and the Madelung field of the environment are automatically included. With respect to the supercell technique, this approach does not present the problem of interaction between defects in different supercells, allows a more flexible definition of the cluster subspace, and permits the study of charged defects. The perturbed-cluster approach is implemented in the computer code EMBED01 [703] and applied in the calculations of the point defects both in the bulk crystal, [704] and on the surface [705]. The difficulties of this approach are connected with the lattice-relaxation calculations.

Concluding this section we compare the results obtained in the supercell and perturbed-cluster HF LCAO treatment for the cation vacancy in MgO [706]. The supercells with 16, 32 and 64 atoms have been considered. The perturbed-cluster was chosen so that the most important effects of electronic rearrangement and ionic relaxation occur within the cluster, *i.e.* the cluster included sufficiently large number of oxygen ions, which are the most polarizable species (perturbed-clusters of 7, 13 and 25 atoms were considered). For the largest supercell (64 atoms) and the largest perturbed-cluster (25 atoms) the cation-vacancy-formation energy was obtained (in eV) as 1.58 (1.48) and 1.29 (1.19), respectively. In brackets are given the formation energies after relaxation of first-neighbor oxygens; this relaxation is close in both models – 0.36 a.u and 0.37 a.u for the supercell and perturbed-cluster, respectively. This agreement can be called close.

The majority of the point-defect calculations are now made with the use of the supercell model as it allows use of the computer codes developed for the perfect-crystals calculations. The examples of supercell LCAO calculations of some point defects in the metal oxides are given in the next sections.

## 10.2 Point Defects in Binary Oxides

### 10.2.1 Oxygen Interstitials in Magnesium Oxide: Supercell LCAO Calculations

Calculations on interstitial oxygen atoms  $O_i$  in MgO crystal are of interest because of the possibility of their formation as a primary product during radiation damage.

Irradiation of alkali halides (MX) leads to the formation of primary pairs of Frenkel defects, namely F centers (electrons trapped at anion vacancies) and interstitial atoms  $X^0$ . The latter are chemically active and immediately form diatomic molecular-type defects  $X_2^-$  (H centers), each of which is centered on one anion lattice site.

However, much less is known about interstitial defects in MgO crystals. The efficient creation of F centers under irradiation is known and means that complementary interstitial  $O_i$  atoms should also be formed. However, the volume change due to irradiation of MgO is surprisingly small, in contrast to that accompanying the formation of H centers in alkali halides. A diffusion-controlled process related to  $O_i$  defects was experimentally observed and characterized by an activation energy of 1.6 eV. This was ascribed to the destruction of some complexes. Therefore, the theoretical study of the stability and configuration of oxygen-atom interstitials in MgO is of importance in trying to understand radiation damage of this

important ceramic material.

We discuss here the results of all-electron HF and semiempirical valence-electron CNDO LCAO calculations of oxygen interstitials in MgO crystal [682]. The supercells of 8, 16 and 32 atoms (S8, S16, S32, see Sect. 10.1.2) were taken in HF calculations, in CNDO calculations the larger supercells were taken to study the convergence of the results obtained. The different configurations for the interstitial oxygen atom were considered, corresponding to an oxygen atom at the volume ( $v$ ), face( $f$ ) and edge ( $e$ ) centers, respectively, see Fig. 10.2. The dumbbell-shaped configurations  $vd$ ,  $fd$ ,  $ed$  are formed when the interstitial oxygen atom  $O_i$  is moved toward the nearest-neighbor  $O^{2-}$  lattice anion along  $\langle 111 \rangle$ ,  $\langle 110 \rangle$  and  $\langle 001 \rangle$  directions, respectively. The lattice oxygen anion is simultaneously displaced from its site along the same direction, the center of the dumbbell formed is at the lattice site. To settle the question of an adequate size for the supercell, the calculations for  $v$ ,  $f$ , and  $e$  configurations are made for supercells containing 9, 17, and 33 atoms. The defect energy levels in the bandgap are observed to change between the 9-atom and 33-atom supercells, although the influence of supercell size on the charge distribution is relatively small. In HF LCAO calculations the size of the supercell is limited by the computational facilities available. Therefore, the convergence of the properties of these defects was investigated also by means of the semiempirical complete neglect of differential overlap (CNDO) approximation, using a code, written by Tupitsyn [707] for the CNDO band calculations. In the CNDO approximations it was possible to use supercells containing 65, 129, and 257 atoms, obtained by enlarging all three smaller supercell translation vectors by a factor of two. It was found that both the charge distribution and the defect levels in the bandgap for the larger supercells were close to those obtained for the 33-atom supercell.

HF and CNDO calculations were done to investigate convergence with respect to supercell size. All basis atoms, except those involved in a defect, occupy lattice sites. The CNDO results show that the defect-formation energy changes by only 0.3%

on increasing the supercell size from 33 to 257 atoms. The HF energies generally change by less than 0.03% on increasing the supercell from 17 to 33 atoms. This suggests that the variations observed in the CNDO energies may be due more to inherent approximations in the method than to defect interactions and that a 33-atom supercell is definitely sufficient. If we were only interested in the energy of the unrelaxed crystal then an S8 supercell, containing eight primitive unit cells, would in fact be adequate. However, the number of shells of atoms around the defect that may be relaxed is dependent upon the size of the supercell, and the 33-atom supercell is the smallest that can be used to obtain quantitatively accurate results.

In Table 10.3 is given the optimized distance between the two dumbbell atoms calculated by both the HF and CNDO methods. The labels S16, S64, and S128 are used for supercells containing 16, 64, and 128 primitive unit cells, respectively.  $q$  is the charge on each of the two oxygen atoms in the dumbbell configuration and  $d$  is the optimized distance between the two O atoms in the dumbbell.  $\Delta E_d$  is the energy change on forming the dumbbell from an interstitial in the rigid lattice.

**Table 10.3.** Results of HF and CNDO calculations for O atom interstitials in MgO (only the dumbbell oxygen atoms are relaxed), [682]

Configuration	Supercell	$d(\text{\AA})$	$q(e)$	$-\Delta E_d$
<i>ed</i>	S16 (HF)	1.310	-1.160	—
	S16 (CNDO)	1.280	-0.944	32.6
	S64 (CNDO)	1.280	-0.944	32.6
	S128 (CNDO)	1.282	-0.944	32.6
<i>vd</i>	S16 (HF)	1.355	-1.070	—
	S16 (CNDO)	1.394	-0.918	7.9
	S64 (CNDO)	1.392	-0.917	7.9
	S128 (CNDO)	1.393	-0.917	7.8
<i>fd</i>	S16 (HF)	1.372	-1.033	—
	S16 (CNDO)	1.369	-0.929	3.2
	S64 (CNDO)	1.366	-0.928	3.2
	S128 (CNDO)	1.369	-0.928	3.3

The charge  $q$  on each of the two ions in the dumbbell is close to -1, negative charge on the dumbbell in excess of -2 is being made up by a slight deficit on the next-nearest ions. The optimized HF values for  $d$  are close to those found for a 17-atom supercell using the full-potential linear muffin-tin orbital (FPLMTO) method [708]. The optimized  $d$  values in the CNDO approximation are also close to those obtained using the HF and LMTO methods. Since the CNDO method is semiempirical these calculations were performed with all atoms except the added interstitial, or the two dumbbell atoms, fixed on their normal lattice sites. In the HF calculation,  $d$  was first optimized for a crystal with all except the defect atoms on perfect lattice sites. The charges on the two dumbbell atoms are again close to -1 and the values of  $d$  and  $q$  (the charge on each of the dumbbell atoms) in Table 10.3 are from these calculations. The optimum relaxed positions of the near-neighbor ions were then determined iteratively, and finally the value of  $\Delta E_d$  was reoptimized.

The values of  $d$  and  $q$  with the relaxed positions are in Table 10.4 together with the energy changes that accompany the formation of a dumbbell from the corresponding interstitial ( $ed$  from  $e$ , and so forth) and the further energy changes associated with relaxation of near neighbors.  $\Delta E_d$  is the difference between the total energy of the unrelaxed crystal in the dumbbell configuration and that for the unrelaxed crystal with the added O atom in the interstitial site,  $\Delta E_{rel}$  is the further energy change (in eV) accompanying the relaxation of near neighbors.

**Table 10.4.** Results of HF calculations of interstitial oxygen in MgO using S16 supercell, [682].

Type of dumbbell	$d$ (Å)	$q(e)$	$-\Delta E_d$ (eV)	$-\Delta E_{rel}$ (eV)	Relaxations $\delta$ (Å)
$ed$	1.319	21.001	28.88	0.12	$\delta_{Mg_1} = 0.241$ $\delta_{Mg_2} = 0.051$ $\delta_{Mg_2} = 0.051$ $\delta_O = 0.0245$ $\delta_O = 0.1030$
$vd$	1.383	21.049	15.94	0.27	$\delta_{Mg} = 0.077$ $\delta_O = 0.1057$
$fd$	1.324	21.010	7.15	2.59	$\delta_{Mg_1} = 0.152$ $\delta_{Mg_2} = -0.010$ $\delta_O = 0.0997$

Subscripts 1,2 mean nearest- and next-nearest atoms (of that species) to the dumbbell, see Fig. 10.2c. For  $ed$ ,  $\delta O_{\parallel}$  is the displacement parallel to the axis of the dumbbell and  $\delta O_{\perp}$  the displacement perpendicular to the axis of the dumbbell. In each case all the atoms of a symmetry-related set that lies wholly within the supercell were allowed to relax.

The importance of supercell size is shown, for example, by the calculations for  $vd$  where for S8, only the six nearest-neighbor Mg atoms may be relaxed because the nearest O atoms lie on the supercell boundary. This may be why comparable FPLMTO calculations [708] for S8 found the  $vd$  defect to be slightly more stable than  $fd$ , whereas in HF calculations the reverse is true (Table 10.4). The decrease in energy  $\Delta E_d$  on forming a dumbbell in a perfect lattice from a  $v$ ,  $f$ , or  $e$ -centered interstitial O atom (calculated as the difference between the HF total energies for the two configurations) is largest (28.9 eV) for the  $ed$  center and smallest for the  $fd$  center (7.1 eV). The former result is to be expected because of the greater overlap in the  $e$  configuration. The CNDO results for  $\Delta E_d$  agree with the HF results only qualitatively, but they serve to confirm convergence with increasing size of supercell, which was the reason for doing the calculations. The further energy gain on the relaxation of near neighbors,  $-\Delta E_{rel}$ , was found to be small compared to that on forming the dumbbells, which evidently provides a very effective mechanism for reducing charge overlap.

The optimized displacements are given in Table 10.4 and these are seen not to exceed 0.1–0.2 Å. With respect to the most stable  $fd$  relaxed dumbbell configuration the  $vd$  and  $ed$  configurations are less favorable by 1.31 and 1.86 eV, respectively. So O atoms formed in MgO during radiation damage will become trapped in face-

centered dumbbell configurations. The excitation of this configuration to the relaxed face-centered interstitial requires an energy of 2.12 eV, which would therefore be the activation energy for diffusion of  $fd$ . This energy may be compared with: 1.45 eV the activation energy for oxygen-atom diffusion calculated by the supercell FPLMTO approach [708]; the 1.6 eV for some diffusion-controlled process involving interstitial oxygen atom that has been observed experimentally in MgO.

### 10.2.2 Neutral and Charged Oxygen Vacancy in $\text{Al}_2\text{O}_3$ Crystal: Supercell and Cyclic-cluster Calculations

Aluminum oxide ( $\alpha\text{-Al}_2\text{O}_3$ , corundum) has a large number of technological applications. Due to its hardness, its chemical and mechanical stability at high temperatures and its electronic properties as a widegap insulator it is used for the fabrication of abrasives, as a carrier for thin metal films in heterogeneous catalysis and in optical and electronic devices.

The structural and electronic properties of  $\alpha\text{-Al}_2\text{O}_3$  are altered by defects such as oxygen vacancies, which can be formed as a result of the bombardment of the oxide with high-energy particles. Neutral oxygen vacancies (F centers) and positively charged oxygen vacancies ( $\text{F}^+$  centers) in aluminum oxide have been investigated in a number of experimental and theoretical studies. Experimental and theoretical results agree that the two electrons of the F center are localized and remain in the vacancy vicinity indicating a singlet ground state. Despite numerous investigations, the defect-formation energies of the F center,  $E_f(\text{F})$ , and the  $\text{F}^+$  center,  $E_f(\text{F}^+)$ , are rarely given in the literature. To our knowledge, no experimental data are available up to now.

In [709] supercell calculations based on the orthogonalized linear combination of atomic orbitals (OLCAO) method within the local density approximation (LDA) were performed. In this case, the oxygen vacancy was modeled by removing one oxygen atom from the cell. They obtained a defect-formation energy of  $E_f(\text{F}) = 38.36$  eV for the neutral oxygen vacancy without relaxation of the geometry. When the four nearest-neighbor aluminum and 12 next-nearest-neighbor oxygen atoms around the vacancy (see Fig. 2.19) were allowed to relax the defect-formation energy decreased to  $E_f(\text{F}) = 5.83$  eV. This corresponds to a relaxation energy of  $E_{rel} = 32.53$  eV. The distance of the neighboring aluminum atoms to the vacancy increased by about 16% and the distance of the oxygen neighbors by about 8% with respect to the unrelaxed structure. Similar values were obtained for the  $\text{F}^+$  center. The defect-formation energy for the F center was calculated with respect to an isolated neutral O atom, see (10.1), using the difference of the total energy of the supercell with and without vacancy, and adding the energy of the free oxygen atom  $E_O$ .

In [710] a 65-atom molecular cluster is used that was treated semiempirically at the INDO level and embedded in the electrostatic field generated by multipoles. To model the F and  $\text{F}^+$  centers in corundum additional 2s and 2p Slater-type atomic orbitals were placed in the vacancy after removing one O atom. The relaxation of the four aluminum atoms nearest to the vacancy resulted in an outward displacement by 2–3% and 5–6% for the F and  $\text{F}^+$  center, respectively. From the 12 next-nearest oxygen atoms only two were allowed to relax. In contrast to the results of [709] the two oxygen atoms moved toward the vacancy by about –2.2% and –4.6% for the F and  $\text{F}^+$  center, respectively. Defect-formation energies were not calculated.

The neutral oxygen vacancy was investigated in [711] by supercell-DFT calculations within the generalized gradient approximation (GGA) using a plane-wave basis and ultrasoft Vanderbilt pseudopotentials. The calculated defect-formation energy is  $E_f(F) = 7.13$  eV and  $E_f(F) = 7.08$  eV for the F center without and with the relaxation of the nearest aluminum and next-nearest oxygen atoms, at the oxygen-rich limit. As a reference for the calculation of the defect-formation energy  $E_O = 0.5E_{O_2}$  was taken instead of a free oxygen atom energy  $E_O$ . The aluminum atoms show an inward relaxation of  $-1.5\%$ , the positions of the oxygen atoms are almost unchanged ( $-0.1\%$ ).

The intrinsic defects in  $\alpha\text{-Al}_2\text{O}_3$  were also studied in [712] by the supercell DFT PW method (the supercell contained up to 120 atoms). The relaxation of the four nearest aluminum atoms, 12 next-nearest oxygen atoms and two next-next-nearest aluminum atoms around the neutral and positively charged oxygen vacancy was taken into account. The results given in [712] show an average inward relaxation of the nearest Al for the neutral oxygen vacancy of about  $-1.5\%$  and a slight inward relaxation of the next-nearest O atoms by  $-0.4\%$ . For the single positively charged oxygen vacancy they find an outward relaxation of the nearest Al atoms of  $4.6\%$ . The oxygen atoms relax by  $-1.4\%$  toward the vacancy. The defect-formation energy of the neutral oxygen vacancy  $E_f(F) = 13$  eV was calculated at the oxygen-rich limit.

It is seen that the results of the different theoretical simulations of oxygen vacancies in corundum are contradictory. An attempt to resolve this contradiction was made in [713] where the energies of the formation of an F center and an  $\text{F}^+$  center were calculated and relaxation effects were investigated with a combination of HF, DFT and semiempirical methods in the framework of supercell and cyclic-cluster models. All supercell LCAO calculations were made using the CRYSTAL code [23], the details of the basis and computational parameters choice can be found in [713]. The semiempirical cyclic-cluster calculations were made using the MSINDO code developed in the Hannover theoretical chemistry research group [256], see Chap. 6. The cyclic cluster was embedded in an infinite field of point charges using the Ewald summation technique [714]. The charges for the embedding can either be calculated self-consistently from the atoms of the cyclic cluster using a Lowdin population analysis at each SCF cycle or can be kept fixed at the values of the perfect crystal.

The scheme of the SCM model realization, discussed in Sect. 10.1.3, requires in stage 1 the calculations of the perfect crystal. The perfect corundum crystal has a rhombohedral structure with the space group  $\bar{R}\bar{3}c(D_{3d}^6$ , see Chap. 2). The oxygen atoms form a hexagonal close-packed structure, the aluminum atoms occupy  $2/3$  of the octahedral vacancies so that all Al atoms have the same environment. Every O atom has two neighboring Al atoms at a distance of  $r_1 = 1.86$  Å and two others at a distance of  $r_2 = 1.97$  Å. The primitive rhombohedral unit cell consists of two  $\text{Al}_2\text{O}_3$  formula units with experimental lattice parameters  $a = 5.128$  Å and  $\alpha = 55.333^\circ$ .

Using the transformation of basic rhombohedral lattice translation vectors with the matrix

$$l = \begin{pmatrix} 2n_1 & n_1 & 0 \\ -n_1 & n_1 & 0 \\ 0 & 2n_1 & n_2 \end{pmatrix}, \quad L = 3n_1^2 n_2 \quad (10.12)$$

one obtains the hexagonal setting of the corundum structure. Its unit cell ( $n_1 = n_2 = 1$ ) consists of  $L=3$  primitive unit cells. The lattice parameters in this

hexagonal setting are  $a = 4.763 \text{ \AA}$  and  $c = 13.003 \text{ \AA}$ . Furthermore, corundum has two internal structure parameters  $u_{\text{Al}} = 0.352$  and  $u_{\text{O}} = 0.306$ , which define the Al and O positions, respectively (see Sect. 2.3.5). The experimental heat of atomization is  $\Delta_a H_0 = 31.60 \text{ eV/Al}_2\text{O}_3$ . This has been obtained by the experimental heat of formation of the solid ( $\Delta_f H_0(\text{Al}_2\text{O}_3) = -17.22 \text{ eV}$ ) and the heats of formation of the corresponding atoms in the gas phase ( $\Delta_f H_0(\text{Al}) = 3.35 \text{ eV}$ ,  $\Delta_f H_0(\text{O}) = 2.56 \text{ eV}$ ).

As was noted in Sect. 10.1.3, the first stage of supercell-cyclic-cluster calculations of the defective crystal consists of the band-structure calculations of the perfect crystal to choose the supercell for its modeling. Table 10.5 shows the results for the HF and DFT LCAO band calculations of the perfect  $\text{Al}_2\text{O}_3$ .

**Table 10.5.** HF and DFT cohesive energies  $E^{\text{HF}}$  and  $E^{\text{DFT}}$  (eV/ $\text{Al}_2\text{O}_3$ ) obtained from band calculations using different sets  $(s_1 s_2 s_3)$  of  $\mathbf{k}$ -points, [713]\*

Unit cell	$(s_1 s_2 s_3)$	$L$	$N_{\text{efficient}}$	$E^{\text{HF}}$	$E^{\text{DFT}}$
rhombohedral	(222)	8	$\text{Al}_{16}\text{O}_{24}$	21.47	29.70
	(333)	27	$\text{Al}_{108}\text{O}_{162}$	21.50	29.72
hexagonal	(111)	3	$\text{Al}_{12}\text{O}_{18}$	—	29.84
	(221)	12	$\text{Al}_{48}\text{O}_{72}$	21.49	29.70
	(331)	27	$\text{Al}_{108}\text{O}_{162}$	21.50	29.71
	(662)	216	$\text{Al}_{432}\text{O}_{1296}$	21.50	29.72

\*  $E_{\text{exp}} = 31.60 \text{ eV}$

The geometrical parameters were fixed to the experimental values. The cohesive energy per formula unit was calculated as the difference between the total energy per  $\text{Al}_2\text{O}_3$  unit in the crystal and the sum of the energies of the corresponding free atoms. The calculations were made using Monkhorst–Pack sets  $(s_1, s_2, s_3)$  of  $\mathbf{k}$  points, which correspond to supercells of  $L$ -primitive unit cells consisting of  $N_{\text{efficient}}$  atoms.  $E_{\text{coh}}$  calculated corresponds to the experimental heat of atomization  $\Delta_a H_0$  except for the zero-point energy that is neglected in the calculation of  $E_{\text{coh}}$ . The energies of the free Al and O atoms were obtained by increasing the basis sets successively with diffuse sp-functions until the energies of the free atoms were converged, see Chap. 8. The HF cohesive energy of  $21.50 \text{ eV/Al}_2\text{O}_3$  is too low by  $10.10 \text{ eV/Al}_2\text{O}_3$  compared with the experimental value of  $31.60 \text{ eV/Al}_2\text{O}_3$ . This discrepancy is mainly due to the missing correlation and the incompleteness of the basis set [715].

The DFT results, using the PWGGA-PWGGA exchange-correlation functional ( $29.72 \text{ eV/Al}_2\text{O}_3$ ), are closer to the experiment. But the cohesive energy is still underestimated by about  $1.88 \text{ eV/Al}_2\text{O}_3$ . The bandgap  $E_g = 6.28 \text{ eV}$  from DFT calculation is about  $0.4 \text{ eV}$  larger than the value obtained in [712] but still too small compared with the experimental range of the bandgap between  $8.5$  and  $9.9 \text{ eV}$ . The bandgap of  $17.51 \text{ eV}$  calculated at the HF level is much too high in line with experience.

The results of the cyclic-cluster MSINDO calculations are shown in Table 10.6.

Since the CCM does not involve a summation over the reciprocal space the size of the cyclic cluster was increased in direct space to obtain convergence for the cohesive energy. Each cluster was embedded in an infinite Madelung field of

**Table 10.6.** Cohesive energies  $E^{\text{MSINDO}}$  (eV/Al<sub>2</sub>O<sub>3</sub>) for cyclic-cluster MSINDO calculations using different cyclic clusters, [713].

Cluster	$L$	$n_1$	$n_2$	$E^{\text{MSINDO}}$
Al <sub>12</sub> O <sub>18</sub>	3	1	1	35.45
Al <sub>48</sub> O <sub>72</sub>	12	2	1	31.17
Al <sub>96</sub> O <sub>144</sub>	24	2	2	31.17
Al <sub>108</sub> O <sub>162</sub>	27	3	1	31.09
Al <sub>192</sub> O <sub>288</sub>	48	4	1	31.09

point charges. Again, the geometry was fixed to the experimental values to enable the comparison with the results of the supercell calculations. The MSINDO-optimized lattice parameters ( $a = 4.779$  Å,  $c = 13.074$  Å), internal structure parameters ( $u_{\text{Al}} = 0.354$ ,  $u_{\text{O}} = 0.301$ ) and the cohesive energy ( $E_{\text{coh}} = 31.16$  eV/Al<sub>2</sub>O<sub>3</sub>) [714] of the perfect  $\alpha$ -Al<sub>2</sub>O<sub>3</sub> are in very good agreement with the experimental data. A bandgap of  $E_g = 10.9$  eV was obtained by a  $25 \times 21$  configuration interaction (CI) calculation for the defect-free Al<sub>192</sub>O<sub>288</sub> cluster. This value is at least 1 eV above the experimentally observed range of the bandgap of the perfect crystal but there are no forbidden transitions, which is an indication of a direct bandgap, in agreement with the generally accepted opinion. The valence-band maximum (VBM) consists of O 2p orbitals, while the conduction band minimum (CBM) consists mainly of Al 3s orbitals in agreement with other theoretical [712] and experimental results. The cohesive energies for the experimental geometry of  $\alpha$ -Al<sub>2</sub>O<sub>3</sub> given in Table 10.6 show a fast convergence with increasing cluster size. Already the energy value of the Al<sub>48</sub>O<sub>72</sub> cluster that corresponds to  $L = 12$  primitive unit cells is, with 31.17 eV/Al<sub>2</sub>O<sub>3</sub>, close to the calculated limit of 31.09 eV/Al<sub>2</sub>O<sub>3</sub>. Therefore, the experimental value of 31.60 eV/Al<sub>2</sub>O<sub>3</sub> is reproduced with a deviation of about 0.50 eV/Al<sub>2</sub>O<sub>3</sub>.

In stage 2 (the supercell calculation of a defective crystal, see Sect. 10.1.3), for the simulation of the F center in  $\alpha$ -Al<sub>2</sub>O<sub>3</sub> a supercell was created by using the transformation matrix (10.12) with  $n_1 = 2$  and  $n_2 = 1$  ( $L=12$ ). One oxygen atom was removed from the supercell and the defect-formation energy for the F center was calculated for different  $\mathbf{k}$ -point grids ( $s_1 s_2 s_3$ ) keeping the geometry fixed to the experimental values. For the calculation of the defect-formation energy  $E_{\text{O}} = 0.5E_{\text{O}_2}$  was used. Table 10.7 shows the results using the HF and the DFT (PWGGA-PWGGA) approach.

**Table 10.7.** HF and DFT defect-formation energies  $E^{\text{HF}}(\text{F})$  and  $E^{\text{DFT}}(\text{F})$  (eV) for the neutral oxygen vacancy in Al<sub>2</sub>O<sub>3</sub> obtained from supercell calculations using different sets ( $s_1, s_2, s_3$ ) of  $\mathbf{k}$ -points, [713].

$(s_1, s_2, s_3)$	$E^{\text{HF}}(\text{F})$	$E^{\text{DFT}}(\text{F})$
(1 1 1)	16.55	13.08
(2 2 2)	16.38	12.92
(3 3 3)	16.38	12.24
PW-DFT GGA [712]		

The defect-formation energy shows fast convergence with the increase of the number of sampling  $\mathbf{k}$  points. Already the  $(2 \times 2 \times 2)$  grid gives the converged HF energy of  $E_f^{HF}(F) = 16.38$  eV. For the DFT calculations the same set of  $\mathbf{k}$  points was used to yield a defect-formation energy of  $E_f^{DFT}(F) = 12.92$  eV, which is about 3.46 eV lower than the HF result.

In stage 3 relaxation effects were included in the simulation of the F and the F<sup>+</sup> centers in  $\alpha$ -Al<sub>2</sub>O<sub>3</sub> using the MSINDO cyclic-cluster calculations (Table 10.8).

**Table 10.8.** Cyclic-cluster MSINDO defect-formation energies  $E^{\text{MSINDO}}(F)$  and  $E^{\text{MSINDO}}(F^+)$  (eV), distances  $r_1$  and  $r_2$  (Å) of nearest-neighbor (NN) and next-nearest neighbor (NNN) atoms from the defect and changes of the distances  $\Delta r$  (%) for the unrelaxed and relaxed F and F<sup>+</sup> center in Al<sub>2</sub>O<sub>3</sub> using the Al<sub>192</sub>O<sub>288</sub> cyclic cluster, [713]

	Unrelaxed	Relaxed (NN+NNN)
F center	$E^{\text{MSINDO}}(F) = 12.32$ , $r_1 = 1.86$ , $r_2 = 1.97$	$E^{\text{MSINDO}}(F) = 11.81$ , $r_1 = 1.872$ ( $\Delta r = 0.5$ ), $r_2 = 2.053$ ( $\Delta r = 4.0$ )
F <sup>+</sup> center	$E^{\text{MSINDO}}(F^+) = 12.22$ , $r_1 = 1.86$ , $r_2 = 1.97$	$E^{\text{MSINDO}}(F^+) = 10.33$ , $r_1 = 1.971$ ( $\Delta r = 6.0$ ), $r_2 = 2.089$ ( $\Delta r = 6.0$ )

The Al<sub>192</sub>O<sub>288</sub> cyclic cluster ( $n_1 = 4$ ,  $n_2 = 1$ ,  $L=48$ ) was chosen for the simulations. One oxygen atom was removed from the cyclic cluster to create the F center, keeping the system neutral. To model the F<sup>+</sup> center the charge of the system was set to +1 after removing one oxygen atom. In both cases the cyclic cluster was embedded in the Madelung field of the perfect crystal. The charges for this embedding were the Löwdin charges calculated from the simulation of the corresponding perfect cyclic cluster. In contrast to the standard supercell model of a periodic point defect, no artificial neutralizing background and additional charge corrections are needed in the cyclic-cluster model as the point defect is not periodically repeated. The four nearest-neighbor (NN) aluminum atoms and the 16 next-nearest-neighbor (NNN) oxygen atoms close to the vacancy were allowed to relax using a quasi-Newton method until the residual forces had converged to less than 0.02 eV/Å. The rest of the cyclic cluster was fixed in the experimental geometry. The defect-formation energy of the F<sup>+</sup> center was calculated using as the reference a single oxygen atom energy  $E_{O'} = 0.5E_{O_2}$  as in the case of the neutral oxygen vacancy. Additionally, one electron is removed from the cluster to create a positive charge and the chemical potential of the electron  $\mu_e$  is assumed to be zero, different from the models of the charged defects where the electron is assumed to remain in the lattice. The CCM value for the defect-formation energy of the unrelaxed F center  $E_f^{\text{MSINDO}}(F) = 12.32$  eV is close to the DFT supercell value of  $E_f^{DFT}(F) = 12.92$  eV and the 13 eV obtained in [712], despite substantial differences in the defect-level positions above the VBM. The latter are 8.1 eV for MSINDO, 4.9 eV for DFT supercell calculation and 2.3 eV as obtained in [712]. The SCM calculation using the HF method gives a larger defect-formation energy ( $E_f^{HF}(F) = 16.38$  eV). The defect-formation energy of 7.13 eV calculated

in [711] is considerably lower than the values obtained in [713]. The defect-formation energy of  $E_f(F) = 38.36$  eV calculated in [709] was obtained using the total energy of the oxygen atom. If one uses the same reference [709] and not  $1/2E_{O_2}$  one finds a defect-formation energy of 15.06 eV for the MSINDO cyclic-cluster simulation of the unrelaxed vacancy.

An absorption band of about 6 eV has been assigned experimentally to the F center, indicating a location of a doubly occupied defect level roughly 3 eV above the VBM. The corresponding excitation energies are 1.8 eV and 8.8 eV for DFT and HF calculations [713], respectively. The defect level obtained using the MSINDO-CCM method consists mainly of Al 3s orbitals of the aluminum atoms next to the vacancy. Using a  $40 \times 30$  CI the first allowed excitation was found to occur at 3.1 eV for the relaxed structure. Therefore, the excitation energy is underestimated by about 3.0 eV. In comparison the excitation energy in [712] is 3.52 eV which is also too small.

Concerning the relaxation, the CCM simulations of the F center show that the NN Al atoms increase their distance from the vacancy by 1% to 4% which agrees well with the corresponding data of 2% to 6% of [710]. The value from [709] is larger (16%) but the NN Al atoms also show a movement away from the vacancy. This is reasonable, since the NN Al atoms are positively charged and should therefore repel each other. Under these circumstances the inward relaxation to the vacancy (1.5%) of the aluminum neighbors found in [711, 712] is difficult to understand. Their choice of pseudopotentials and of basis set, restriction only by  $\Gamma$  point in BZ might be the reason for the discrepancy. Table 10.7 shows that a Monkhorst–Pack net of at least (222) must be used for the defective supercell to reach convergence with respect to the energy. Using only the  $\Gamma$  point might also influence the relaxation.

Considering the NNN O atoms, an average relaxation of  $-0.4\%$  toward the vacancy and the total relaxation energy  $E_{rel} = 0.51$  eV was found in the LCAO calculations [713] of the F center. This agrees well with the values  $-0.1\%$  and  $-0.4\%$  of [711, 712] indicating that the positions of the oxygen atoms are almost unchanged. An inward relaxation was also found in [710]. In contrast to these results, a large outward relaxation of 8% and  $E_{rel} = 32.53$  eV were found in [709]. The value of 32.53 eV for the relaxation energy appears to be much too high, because this value is larger than the experimental heat of formation for the  $\alpha$ -Al<sub>2</sub>O<sub>3</sub> (31.60 eV).

A singly occupied defect level occurs in the bandgap in the case of the F<sup>+</sup> center. The results of the CCM calculations for the F<sup>+</sup> center (Table 10.8) indicate a larger relaxation of the NN Al atoms (6.0%) and of the NNN oxygen atoms (-1.2%) compared to the values obtained for the neutral oxygen vacancy. This is reasonable, since the aluminum atoms repel each other more strongly due to the missing electron in the vacancy. In consequence, the relaxation energy ( $E_{rel} = 1.90$  eV) is also larger than the corresponding value for the F center. This trend is confirmed by results found in DFT PW calculations [712]: an outward relaxation of 4.6% for the Al neighbors and an inward relaxation of -1.4% of the oxygen atoms close to the vacancy, which agrees well with the MSINDO CCM results. The movements found in semiempirical LCAO calculations [710] are slightly larger (5–6% for the Al atoms, -4.6% for the oxygen atoms) but they also confirm the tendency.

The defect-formation energy of the F<sup>+</sup> center is smaller than that of the F center in both the relaxed and the unrelaxed structures using  $\mu_e = 0$  for the chemical potential of the electrons. This agrees qualitatively with the results of [712] when compared to

their values at  $\mathbf{k} = \mathbf{0}$ . It was noted that no experimental data for the defect-formation energy are available in the literature for the F and  $\text{F}^+$  center in  $\alpha\text{-Al}_2\text{O}_3$ . The detailed consideration of the results of application of different models and calculation schemes to F and  $\text{F}^+$  centers in corundum demonstrate that LCAO methods reproduce well the results of PW calculations for the neutral defect. Furthermore, the LCAO methods are more appropriate for the charged-defect modeling as the artificial defect-periodicity is escaped in the LCAO cyclic-cluster approach.

### 10.2.3 Supercell Modeling of Metal-doped Rutile $\text{TiO}_2$

Titanium dioxide ( $\text{TiO}_2$ ) is a wide-bandgap material useful in many practical applications (electrochemistry, sun lotions, nanostructured electrodes). The electronic structure of  $\text{TiO}_2$  can be strongly influenced by  $3d$  transition-metal dopants that introduce local electronic levels into the bulk energy bandgap and thus shift the absorption edge to the visible region.

The effects of metal doping on the properties of  $\text{TiO}_2$  have been a frequent topic of experimental investigation. In particular, according to a systematic study on the photoreactivity and absorption spectra of  $\text{TiO}_2$  doped with 21 different metals [716] the energy level and d-electron configuration of the dopants were found to govern the photoelectrochemical process in  $\text{TiO}_2$ . The resonance photoemission study [717] was applied to investigate the nature of bandgap states in V-doped  $\text{TiO}_2$  in rutile structure.

The computer simulation has been employed to clarify in detail impurity-doping effects. A molecular-cluster approach was extensively adopted, see references in [718]. These cluster calculations have never led to unifying conclusions regarding the effects of doping on the electronic states due to the influence of dangling bonds.

The supercell approach demonstrated its capacity to deal with metal-doped  $\text{TiO}_2$  defective crystals in DFT FPLAPW supercell electronic-structure calculations [718, 719]. It was found that when  $\text{TiO}_2$  is doped with V, Cr, Mn, Fe or Co, an electron-occupied localized level in the bandgap occurs and the electrons are localized around each dopant. As the atomic number of the dopant increases the localized level shifts to the lower energy. The energy of the localized level due to Co is sufficiently low to lie at the top of the valence band, while the other metals produce midgap states. In contrast, the electrons from the Ni dopant are somewhat delocalized, thus significantly contributing to the formation of the valence band with the O  $2p$  and Ti  $3d$  electrons. These conclusions were made in [718] on the basis of the DFT FPLAPW calculations on a relatively small supercell consisting of four primitive unit cells stacked along the  $b$ - and  $c$ -axis of the simple tetragonal lattice. The experimental values of the lattice constants  $a=b=4.594 \text{ \AA}$ ,  $c=2.959 \text{ \AA}$  were taken, so that the translation vectors lengths  $a$ ,  $b$ ,  $c$  of the orthorhombic supercell equal  $4.594 \text{ \AA}$ ,  $9.188 \text{ \AA}$  and  $5.918 \text{ \AA}$ , respectively. Such a choice of supercell is not optimal as the defect–defect distance  $R_{d-d}$  is not the same along the three supercell translation vectors and the defect–defect interaction corresponds in fact to the smallest distance  $R_{d-d} = 4.594 \text{ \AA}$  (the length of the primitive tetragonal unit cell translation in the perfect rutile crystal).

As in the FPLAPW method the further increasing of the supercell is sufficiently difficult that the dependence of the results on the supercell size was not studied in [718]. Such a study was made in semiempirical cyclic-cluster calculations of Li and

Cl, Br impurities in  $\text{TiO}_2$  [720, 721] without preliminary symmetry analysis of the cyclic clusters chosen. Such an analysis was made in [683] and allowed the convergence of the supercell UHF LCAO calculations of V-doped rutile with the supercell size to be investigated. This first nonempirical supercell LCAO calculation of the defective rutile crystal is discussed here in more detail.

The impurity vanadium atom substitutes for a titanium atom introducing an unpaired electron in the unit cell. The symmetry of the supercell model is described by any of four orthorhombic space groups  $D_{2h}^1, D_{2h}^{19}, D_{2h}^{23}, D_{2h}^{25}$ . Analyzing the period of the defect for the same supercell size (given  $L$ -value) in these groups it was found that for rutile structure the best choice would be  $D_{2h}^{25}$  corresponding to the symmetric transformation of the simple tetragonal lattice translation vectors with matrix ( $n_1, n_2, n_3$  - integers,  $n_1 \neq n_2$ ):

$$l = \begin{pmatrix} -n_1 & -n_2 & n_3 \\ n_1 & n_2 & n_3 \\ n_2 & n_1 & -n_3 \end{pmatrix}, \quad L = 2(n_1^2 - n_2^2) n_3 \quad (10.13)$$

The space group  $D_{2h}^{25}$  corresponds to the body-centered orthorhombic lattice of supercells with the translation vectors of equal length in all three translation directions. This means that the point-defect period is also the same in these directions (equidistant configuration of defects). This choice of defective crystal space group ensures the largest defect period for a chosen supercell size (fixed value of  $L$ ).

The UHF LCAO calculations of V-doped rutile were made using the CRYSTAL code [23] and Durand–Barthelat pseudopotentials [484]. The atomic basis functions of Ti and O atoms were taken from [323] that were fitted to reproduce the band structure and bonding properties of perfect rutile crystal. The vanadium atom functions were found by fitting these properties of  $\text{VO}_2$  crystal in the rutile modification. The accuracy of the calculation was ensured by the choice of the computational parameters of the CRYSTAL code ensuring a good accuracy of the bielectronic series, the convergence thresholds of the eigenvalues and total energy and  $\mathbf{k}$ -point sampling in BZ.

Table 10.9 shows the results obtained for the supercells of increasing size. The Monkhorst–Pack shrinking factor was taken to be 6 for supercells with  $L=2, 4, 6$  and 4 for supercells with  $L=10, 14$ . Table 10.9 gives the integers  $n_1, n_2, n_3$  defined according to (10.13) the supercell of the defective crystal consisting of  $L$  primitive unit cells and corresponding doping per cent, the number of atoms  $N_A$  and atomic basis functions  $N_B$  in the supercell, vanadium–vanadium distance  $R_{d-d}$  (defect period) in the supercell model. The convergence of the absolute value of the one-electron energy  $E_d$  occupied by the unpaired electron is seen. It appears that already the supercell for  $L=6$  is enough to reproduce the vanadium atom charge  $Q_V$ , covalence  $C_V$  (the sum of the bond orders of the impurity atom with all the crystal atoms) and spin-density  $N_V^{\alpha-\beta}$ . Using the calculated  $Q_V$  and  $C_V$  the total valence  $V_{tot} = 0.5(C_V + \sqrt{4Q_V^2 + C_V^2})$  is 3.88, *i.e.* the impurity atom is in oxidation state IV, and the calculated spin density corresponds to the fifth vanadium electron not taking part in the chemical bonding. This result is in accordance with the experimentally found [717] ESR signal for V-doped rutile.

The Fermi energy  $E_F$  in the perfect rutile  $\text{TiO}_2$  ( $E_F = -0.3029$  a.u.) was calculated using the same pseudopotential and basis functions of titanium and oxygen atoms

**Table 10.9.** The convergence of the results of the unrestricted Hartree–Fock LCAO calculations [683] of the V-doped rutile (defective-crystal space group  $D_{2h}^{25} = Imm\bar{m}$ ;  $L = 2(n_1^2 - n_2^2)n_3$ )<sup>\*</sup>

$(n_1, n_2, n_3)$	(1,0,1)	(1,0,2)	(2,1,1)	(3,2,1)	(4,3,1)
$L$	2	4	6	10	14
doping (%)	0.25	0.125	0.083	0.050	0.036
$N_A$	12	24	36	60	84
$N_B$	120	240	360	600	840
$R_{d-d}$ (Å)	5.45	7.53	10.62	16.69	22.97
$E_d$ (a.u.)	-0.2955	-0.2991	-0.3004	-0.3012	-0.3016
$Q_V$	2.761	2.760	2.759	2.759	2.759
$C_V$	1.921	1.924	1.927	1.927	1.927
$N_V^{\alpha-\beta}$	1.115	1.114	1.099	1.099	1.099

\* The supercell transformation matrix  $l = \begin{pmatrix} -n_1 & -n_2 & n_3 \\ n_1 & n_2 & n_3 \\ n_2 & n_1 & -n_3 \end{pmatrix}$

that were used for the defective-crystal calculation. Thus, the V-atom impurity level (occupied by an electron) is relatively close to the perfect-crystal valence-band edge ( $\Delta E = -0.3016 + 0.3029 = 0.0013$  a.u. or 0.04 eV). Experimental data [717] predict larger values of  $\Delta E$  (0.03 a.u. or 0.81 eV). The difference may be explained both by the necessity to take into account the atomic relaxation around the impurity atom and experimental ambiguity in the assignment of the gap states to electrons localized on the V dopant. Bearing in mind the energy gap of 3.0 eV for the perfect crystal and midgap position of the localized level in FPLAPW calculations [718] for V-doped rutile, we conclude that both LCAO (0.04 eV) and FPLAPW (1.5 eV) results for the defect-level position in the bandgap differ from the experimental estimation (0.81 eV).

Table 10.9 shows that the increase of the supercell size moves the defect energy level closer to the valence-band edge. Therefore, DFT FPLAPW-correlated calculations with the larger supercells would make the agreement with the experimental data better. When using HF LCAO approach for the calculations it is important to estimate the possible influence of the electron correlation on the obtained results. We have seen that the highest-occupied level position moves to higher energies when the correlation is taken into account and this movement may appear different for the perfect and defective crystal, so that the defect-level position in the bandgap also changes. This requires further study.

Nevertheless, the calculation [683] demonstrates: (1) the efficiency of the more detailed symmetry analysis for the supercell choice when the periodic defect calculations are made in the complicated crystalline structures with the symmetry of a nonsymmorphic space group and noncubic lattice; (2) the reality of the supercell model for the nonempirical LCAO calculations of the point defects in such a complicated crystalline structure as a rutile structure; 3) higher efficiency of LCAO basis compared with LAPW basis in the supercell calculations of defective crystals. Moreover, the supercell model allows the dependence of the electronic properties of doped crys-

tals on the doping level to be investigated. In the next section we consider supercell calculations of defective crystals with perovskite structure.

## 10.3 Point Defects in Perovskites

### 10.3.1 Oxygen Vacancy in $\text{SrTiO}_3$

Ternary  $\text{ABO}_3$  perovskite materials have numerous technological applications as these materials display a wide range of useful physical and chemical properties. They are important as catalysts, as ceramics, ferroelectrics, superconductors, as materials for fuel cells, fusion reactors, and optical and piezoelectric devices.

The properties of perovskite materials are heavily dominated by their oxygen content, as well as by donor- and acceptor-type impurities. An essential contribution to the knowledge of the structural and electronic properties of point defects in these materials comes from theoretical approaches. The results of large-scale computer semiempirical and first-principles modeling of point defects, polarons and perovskite solid solutions can be found in [722], focusing mostly on  $\text{KNbO}_3$  and  $\text{KTaO}_3$ .

First-principles calculations of formation energies of point defects were made on  $\text{BaTiO}_3$  [723, 724] and  $\text{NaNbO}_3$  [725] crystals. Among the various fundamentally and technologically important oxides,  $\text{SrTiO}_3$  is a simple structural prototype for many perovskites, in which the detailed investigation of native and dopant defects can lay the theoretical groundwork that can be applied to structurally and chemically more complex perovskite materials [726].

The Green-function method appeared to be very useful for displaying the chemical trends in defect energy levels [727, 728]. However, the calculation of other defective-crystal properties (defect-formation energy, lattice relaxation, local-states localization) requires approaches based on molecular cluster or supercell models. Only recently have these models been used in the first-principles calculations to study point defects in  $\text{SrTiO}_3$ .

The supercell calculations are made mostly by the DFT PW method [726, 729]. The comparative PW (supercell) and LCAO (cluster and supercell) calculations are known for the oxygen vacancy in  $\text{SrTiO}_3$  crystal [730–732].

Oxygen vacancies in  $\text{SrTiO}_3$  act as effective donors and are important defects in  $\text{SrTiO}_3$ . Theoretical simulation of defective  $\text{SrTiO}_3$  is very important since modern scanning transmission electron microscopy (STEM) and reflection high-energy electron diffraction (RHEED) combined with atomic-scale electron-energy-loss spectroscopy (EELS) are able to detect the presence of even single impurities and vacancies in  $\text{SrTiO}_3$ . A deliberate deviation of oxygen content from the ideal stoichiometry of perovskites, is relevant for their numerous high-tech applications as sensors, fuel cells, microelectronic devices. At low oxygen partial pressure, the electrical conductivity of  $\text{SrTiO}_3$  perovskite is controlled by both the concentration and mobility of oxygen vacancies, which act as effective donors; therefore, this material becomes n-type conductive. Increasing the partial pressure reduces the carrier concentration, and at high pressures the conductivity goes through a minimum: the material becomes p-type [733, 734]. Consequent thermal reduction of oxygen in single-crystalline strontium titanate results in the insulator-to-metal transition, up to a possible superconducting state, accompanied by intensive formation of vacancies and their high

density within the skin region [735]. Oxygen vacancies play a noticeable role in the structural transformations in bulk  $\text{SrTiO}_3$ , which possesses two relevant structures: the tetragonal antiferrodistortive (AFD) phase, and the cubic phase [726]. The latter (Fig. 10.3a) is stable at 105 K, whereas AFD (slightly distorted cubic phase) is stable at lower temperatures.

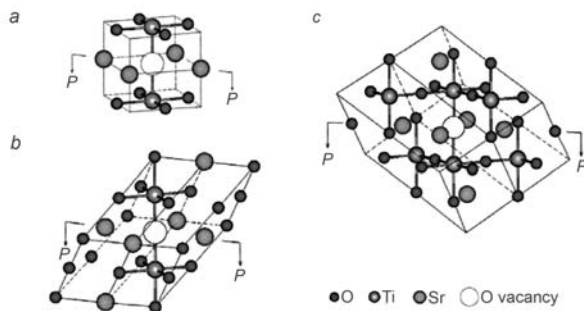


**Fig. 10.3.** Three types of equidistant crystalline cells with a centered O vacancy for the cubic phase of  $\text{SrTiO}_3$  perovskite: (a) simple cubic (sc); (b) face-centered cubic (fcc); (c) body-centered cubic (bcc). Sticks between the oxygen and titanium ions indicate the partly covalent bonds between them. To construct the difference electron-density plots, each cell is sectioned along the Ti–O–Ti axis by the plane PP

When simulating a single point defect, the main problem is to understand changes induced by it in the atomic and electronic structure of a host crystal. A perfect  $\text{SrTiO}_3$  crystal has a mixed ionic-covalent nature of the chemical bonding, which is not in complete conformity with the formal charges on  $\text{Sr}^{2+}$ ,  $\text{Ti}^{4+}$ , and  $\text{O}^{2-}$  ions, see Chap. 9. The formalism of Wannier functions applied for the determination of effective charges and bond populations in several perovskite crystals [736] calculated previously using the density-functional theory (DFT) method [606] gives the atomic charge of +2.55 on titanium and -1.55 on oxygen, whereas the Ti–O bond order is 0.35; only the charge on Sr (+1.95) is close to the nominal ionic value +2, confirming that strontium is ionically bonded in  $\text{SrTiO}_3$ . Partly covalent chemical bonding makes the simulations of the structural defects in strontium titanate rather complicated, even in a cubic phase.

The simplest native defect may be described in terms of either a neutral oxygen vacancy (single O atom removed from the lattice site) or neutral F center (the oxygen ion  $\text{O}^{2-}$  vacancy trapped 2 electrons remaining in a host crystal).

Theoretical studies mainly predict equal contributions of the  $3d$  orbitals of the two nearest titanium ions (Fig. 10.3) into the wavefunction of the F center [729, 730, 734]. According to DFT calculations on a cubic phase of  $\text{SrTiO}_3$  perovskite [730], the Mulliken electron charge of 1.1–1.3 is localized in the neutral O vacancy (depending on the supercell size), and 0.6–0.8 are equally divided by the two nearest Ti ions if we consider the F center. This result does not confirm the formal conclusions that the F center is supposed to have released both electrons, whereas the nearest titanium

ions change their valence from  $\text{Ti}^{4+}$  to  $\text{Ti}^{3+}$ . The position of the F center level in the optical bandgap of  $\text{SrTiO}_3$  is also not completely clear: it is an open question as to whether it lies well below the conduction-band bottom or close to it. The latter is supported by the indirect experimental study on the conductivity of  $\text{SrTiO}_3$  ceramics, suggesting that the F center is a rather shallow defect [737].

Supercell *ab-initio* calculations on the  $\text{SrTiO}_3$  give the values of the formation energy for O vacancy within the range of 6.5–8.5 eV [726, 729, 730, 734], whereas in cluster models [738], removal of an O atom from the lattice has a higher energy cost ( $> 9$  eV). However, this value cannot be directly measured experimentally. Conductivity in  $\text{SrTiO}_3$  at low partial oxygen pressures depends on the mobility of O vacancies [737]. Experiments performed at high temperatures suggest an energy barrier of 0.86 eV for the F center diffusion in bulk, whereas semiempirical pair-potential calculations on migration on the empty O vacancy result in the barrier of 0.76 eV [739].

In [732] the results of both LCAO (made with the CRYSTAL code [23]) and PW (made with the VASP code [740]) DFT calculations on the F center in a cubic phase of  $\text{SrTiO}_3$  perovskite are analyzed, combining the advantages of LCAO and plane-wave formalisms. The lattice structural relaxation around an oxygen vacancy was optimized for supercells of different shapes and sizes. This is important as DFT PW calculations [726] show the strong dependence of the results on the supercell size (it was concluded that at least a  $4 \times 4 \times 4$  supercell of 320 atoms is needed to describe the structural parameters of an oxygen vacancy accurately). In [732] the supercells were obtained by a consequent equidistant extension of crystalline lattice vectors (Fig. 10.3) increasing the supercell size from 80- up to 320-atom cells, in order to eliminate the interaction of periodically repeated point defects and to reach the limit of a single F defect. These supercells are described by transformation matrices

$$\begin{pmatrix} n & 0 & 0 \\ 0 & n & 0 \\ 0 & 0 & n \end{pmatrix}, \quad \begin{pmatrix} 0 & n & n \\ n & 0 & n \\ n & n & 0 \end{pmatrix}, \quad \begin{pmatrix} -n & n & n \\ n & -n & n \\ n & n & -n \end{pmatrix} \quad (10.14)$$

where  $n$  is varied between 2 and 4. The corresponding equidistant supercells form *sc*, *fcc* and *bcc* lattices (cases a), b) and c) in Fig. 10.3, respectively). The ratio of volumes for the supercells extended from the primitive unit cell using matrices (10.14) with the same  $n$  is

$$V_{bcc} = 2V_{fcc} = 4V_{sc} \quad (10.15)$$

Supercells with extensions  $3 \times 3 \times 3$  (135 atoms) and  $4 \times 4 \times 4$  (320 atoms) form a simple cubic lattice (Fig. 10.3a). In turn, supercells with the fcc extensions  $2\sqrt{2} \times 2\sqrt{2} \times 2\sqrt{2}$  (80 atoms) and  $3\sqrt{2} \times 3\sqrt{2} \times 3\sqrt{2}$  (270 atoms) are rhombohedral with a  $60^\circ$  angle between the lattice vectors, see Fig. 10.3b. Lastly, for a 160-atom rhombohedral bcc supercell (extension  $2\sqrt{3} \times 2\sqrt{3} \times 2\sqrt{3}$ ), the angle is  $109.47^\circ$ . For all three types of equidistant cells shown in Fig. 10.3, their shapes correlate with the orientation of the  $-\text{Ti}-\text{O}-\text{Ti}-$  axis, it may be: (i) the rotation axis joining the centers of opposite faces (Fig. 10.3a), (ii) the diagonal joining the opposite apices of the rhombohedron (Fig. 10.3b), and (iii) the axis joining the centers of opposite rhombohedron edges (Fig. 10.3c).

The computational details (the optimization of LCAO basis and choice of cutoff energy in PW calculations,  $\mathbf{k}$ -meshes used for BZ integration, choice of pseudopotentials) can be found in [732]. The advantage of PW calculations is that the complete

optimization of lattice relaxation upon vacancy creation, even for large supercells, can be performed much faster than in LCAO calculations. Geometry optimizations in PW calculations have been carried out with an accuracy of  $10^{-3}$  eV in the total energy. The electronic structure of defective  $\text{SrTiO}_3$  perovskite calculated with both the CRYSTAL and VASP codes has been studied for the diamagnetic closed electronic shell (singlet) state, since no lower state was found employing spin-polarized calculations [730].

The basic properties of a perfect cubic  $\text{SrTiO}_3$  crystal (lattice constant, bulk modulus, elastic constants) were obtained in reasonable agreement with experiment in LCAO calculations. The best agreement with experimental results for the energy gap was obtained for the hybrid HF-DFT technique (B3PW), see Chap. 9. Further improvement of the calculated optical gap was achieved by adding the d polarization orbital into the oxygen basis set: at the  $\Gamma$  point of BZ the calculated gap 3.65 eV is close to the experiment, 3.25 eV for the indirect bandgap. In DFT (PW91) PW calculations the structural parameters were again found to be quite reasonable but the optical bandgap of 2.59 eV is an evident underestimate, typical for the DFT method.

The F center was modeled by removing an oxygen atom in the supercell (see Fig. 10.3). For estimation of the formation energy  $E_f(F)$  of the F center the energy for the spin-polarized isolated oxygen atom ( $^3P$  state) was taken and (10.1) was used. A similar approach for the determination of  $E_f(F)$  was used in [734]. In an alternative approach [726, 729] the formation energies of the O vacancy were expressed via chemical potentials of O, Sr, and Ti atoms. However, the range of  $E_f(F)$  calculated using both approaches for supercells of different shapes and sizes is not so large as to give a preference to one of them.

Table 10.10 shows the dependence of the vacancy-formation energy in  $\text{SrTiO}_3$  bulk on both supercell shape and size, which is accompanied by the large contribution coming from the lattice relaxation upon vacancy formation. The formation energy is reduced considerably (by 1.5–2.0 eV) when the positions of all atoms in the supercells are fully optimized. This demonstrates that the relaxation of even 14 nearest ions (neighboring Ti, O, and Sr coordination spheres directly shown in Fig. 10.3a) might be somewhat insufficient, and the inclusion of next-nearest coordination spheres is necessary, see Table 10.11.

**Table 10.10.** Dependence of the nearest distance between F centers ( $d_{\text{F-F}}$ ), formation energy of a single oxygen vacancy  $E_f(F)$ , and energy barrier  $E_{\text{diff}}(F)$  of its (011) diffusion on both shape and size of supercell used for PW calculations, [732]

Supercell	Extension	Type of lattice	$d_{\text{F-F}}$ (Å)	$E_f(F)$ (eV)		$E_{\text{diff}}(F)$ (eV)
				unrelaxed	relaxed	
S80	$2\sqrt{2} \times 2\sqrt{2} \times 2\sqrt{2}$	<i>fcc</i>	11.04	9.00	7.73	0.41
S135	$3 \times 3 \times 3$	<i>scc</i>	11.71	9.17	7.89	0.35
S160	$2\sqrt{3} \times 2\sqrt{3} \times 2\sqrt{3}$	<i>bcc</i>	13.52	8.98	7.35	0.50
S270	$3\sqrt{2} \times 3\sqrt{2} \times 3\sqrt{2}$	<i>fcc</i>	16.56	8.98	7.17	0.38

The lattice relaxation around the defect is periodically repeated in the supercell model, thus affecting the calculated total energy per cell: the larger the supercell,

**Table 10.11.** Dependence of lattice relaxation for the nearest equivalent atoms around a single F center in a cubic  $\text{SrTiO}_3$  crystal on shape and size of supercells in PW calculations [732]. Relative radial shifts from unrelaxed positions (%)\* are given

Nearest atoms	Distance (in units of $a$ )	Number of equiv. atoms	S80	S135	S160	S270	S320
Ti	$1/2$	2	7.21	7.16	7.08	8.28	7.76
O	$\sqrt{2}/2$	8	-7.59	-7.92	-7.98	-7.43	-7.79
Sr	$\sqrt{2}/2$	4	3.51	3.48	3.45	3.42	3.94
O	1.0	4	3.16	2.98	2.49	2.87	3.56
O	1.0	2	-1.72	-1.56	-1.67	-1.05	-1.28

\*Positive shift corresponds to expansion of the atomic coordinate sphere, whereas negative sign means its compression

the smaller this artifact. The numerical results given in Tables 10.10 and 10.11 are obtained in PW calculations, as complete optimization of the lattice relaxation in the large supercells is extremely time consuming in the LCAO calculations.

The calculated defect-formation energies mainly decrease with the increase of the supercell size, but they also depend on the shape of the supercell (compare the corresponding values for fcc 80-atom and sc 135-atom cells). To calculate the energy barrier  $E_{\text{diff}}(F)$  for oxygen-vacancy diffusion a jump of the O atom from the eight possible sites nearest to the F center (Fig. 10.3a) toward the vacancy is considered. The saddle point energy has been estimated by fixing a hopping O atom at the middle of the Sr–Ti–Sr triangle (Fig. 10.3a) crossed by the oxygen migration trajectory, which has been found to be nonlinear, while the rest of the lattice has been allowed to relax to the minimum of the total energy. The  $E_{\text{diff}}(F)$  (Table 10.10) is sensitive to both the shape and size of the  $\text{SrTiO}_3$  supercell; moreover, for optimized rhombohedral *fcc* and *bcc* supercells (Fig. 10.3, b and c), the migration trajectories are not completely equivalent. Nevertheless, migration energies mainly decrease with increase of the supercell size. The sensitivity of the calculated lattice relaxation around the defect to both supercell shape and size is also clearly seen in Table 10.11. For the same type of superlattice (*sc*, *fcc*, or *bcc*), expansion of the first coordination sphere (two Ti ions) is larger, whereas compression of the second sphere (eight O ions) is smaller with increasing size of the supercell. However, the convergence of the lattice relaxation is complex, and a very low concentration of F centers should be used to achieve it. For instance, fcc supercells are stretched along the  $z$ -axis and are compressed in the  $xy$ -plane (Fig. 10.3b). This causes the larger  $z$ -shifts of Ti ions nearest to the O vacancy in 80- and 270-atomic *fcc* supercells, as compared with 135- and 320-atomic cubic supercells (Table 10.11), whereas  $xy$ -shifts of the nearest O and Sr ions are smaller in the former case. Nevertheless, the range of  $\delta R$  for equivalently shifted atoms in equidistant supercells of different shapes and sizes is small enough ( $\leq 1.0\%$ ) to suggest the stabilization of a single O vacancy in a cubic  $\text{SrTiO}_3$  crystal when using large equidistant supercells containing 270 and 320 atoms.

When trying to use the LCAO basis for partial optimization of the total energy for the same supercells, a markedly smaller expansion of the first coordination sphere involving the two nearest titanium ions as compared with complete optimization in

PW calculations (1.5–2% vs. 7–8%) was obtained. The same is true for the next-nearest coordination spheres.

While use of the PW basis is more efficient for optimization of the lattice relaxation around a vacancy, the LCAO basis possesses a noticeable advantage when describing the electronic properties of defective crystals. To gain deeper insight into the defective  $\text{SrTiO}_3$  bulk from LCAO calculations on different supercells in [732] the electron density due to O-vacancy formation was analyzed. Redistribution of the electron density due to O-vacancy formation is shown in Fig. 10.4(a and b) as calculated for the equidistant fcc supercells with different extensions.

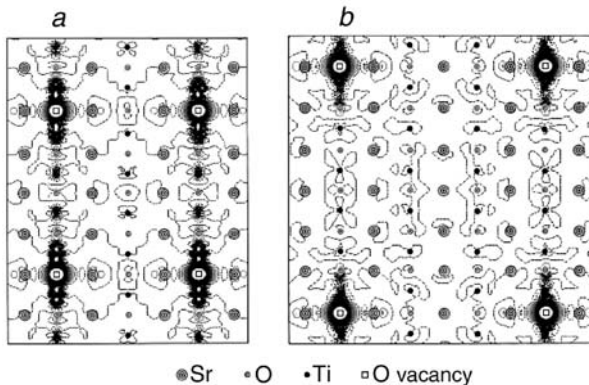


**Fig. 10.4.** Two-dimensional (2D) difference electron-density maps (the total density in the perfect  $\text{SrTiO}_3$  bulk minus the sum of electron densities of both isolated oxygen atoms and defective  $\text{SrTiO}_3$ ) projected onto the (110) section plane PP for 80-atom (a) and 270-atom (b) fcc supercells containing a single oxygen vacancy [732]. Dash-dot isolines correspond to the zero level. Solid and dashed isolines describe positive and negative values of electron density, respectively. The isodensity increment is  $0.002 \text{ e}/\text{\AA}^{-3}$ .

In both plots, the Mulliken electron charge (1.1–1.3 e) is localized within a neutral O vacancy; in other words, 0.6–0.8 e is equally divided by the two Ti ions nearest to the neutral F center and mainly localized on their  $3d_{z^2}$  orbitals, making the largest contribution to the defect bands shown in Fig. 10.5(a and b). Figure 10.4 clearly demonstrates the effect of size of the *fcc*-type supercell (80 atoms and 270 atoms) on localization of the charge redistribution. For the 80-atom supercell, mutual interaction of the neighboring O vacancies is clearly seen, especially along the  $-\text{Ti}-\text{O}-\text{Ti}-$  axes, whereas for the 270-atom supercell, the more-or-less visible redistribution of the electron density is limited by a region of 1.5–2.0 lattice constants around a vacancy, in the *z*-direction.

From Fig. 10.5 it is seen that the defect-band dispersion becomes very small for a 270-atom supercell demonstrating decreasing the defect–defect interaction. The latter is also manifested in LCAO calculations through the finite defect bandwidth. As noted earlier, a pure DFT (PW91) functional strongly underestimates the bandgap. As is seen from Table 10.12 (the results of LCAO calculations are given), the F-center

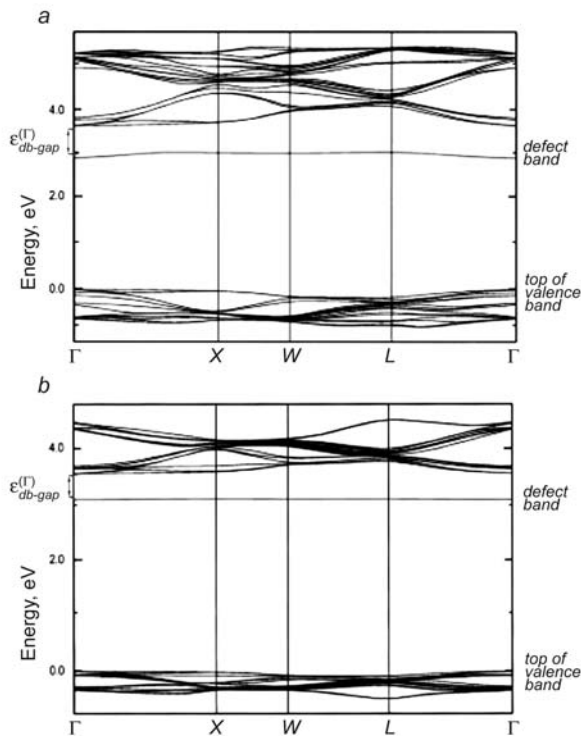


**Fig. 10.5.** Band structure of unrelaxed SrTiO<sub>3</sub> crystal with a single F center per fcc supercell containing either 80 atoms (a) or 270 atoms (b), [732]. Energy bands corresponding to the F center are split off the conduction bands. Their depth (gap) is shown relative to the bottom of the conduction band at the  $\Gamma$  point

energy level, remaining in the bandgap, approaches the conduction-band bottom, moving from 0.69 eV for the 80-atom supercell (with a bandwidth of 0.15 eV), down to 0.57 eV (0.08 eV) for 160 atoms, and finally reaching the optical ionization energy of 0.49 eV (almost neglecting the dispersion of 0.02–0.03 eV) for supercells of 270 and 320 atoms where the distance between the nearest defects is close to four lattice constants.

The results presented in Table 10.12 confirm that the 135-atom supercell is not big enough to reduce defect–defect interactions; its dispersion  $\delta\varepsilon$  is even larger than for an 80-atom supercell with a different shape, *i.e.*  $\delta\varepsilon$  is sensitive to both the shape and size of the equidistant supercell, similar to other properties described before. At the same time, the defect band for the 270-atom supercell (Fig. 10.5b) is almost a straight

**Table 10.12.** Dependence of the F-center energy-level position with respect to the conduction-band bottom of unrelaxed  $\text{SrTiO}_3$  crystal with periodically distributed oxygen vacancies ( $\epsilon$ ), its dispersion ( $\delta\epsilon$ ) and distance between the nearest F centers ( $d_{\text{F-F}}$ ) as a function of the supercell size used in LCAO B3PW calculations [732] with  $2 \times 2 \times 2$   $\mathbf{k}$ -mesh\*

Supercell	Extension	Type of lattice	$d_{\text{F-F}}$ (Å)	$\epsilon$	$\delta\epsilon$
S80	$2\sqrt{2} \times 2\sqrt{2} \times 2\sqrt{2}$	<i>fcc</i>	11.04	0.69	0.15
S135	$3 \times 3 \times 3$	<i>scc</i>	11.71	0.72	0.23
S160	$2\sqrt{3} \times 2\sqrt{3} \times 2\sqrt{3}$	<i>bcc</i>	13.52	0.57	0.09
S270	$3\sqrt{2} \times 3\sqrt{2} \times 3\sqrt{2}$	<i>fcc</i>	16.56	0.49	0.02
S320	$4 \times 4 \times 4$	<i>sc</i>	15.61	0.49	0.03

\*The defect-level position is calculated at the  $\Gamma$  point of the BZ

line. Table 10.12 clearly shows that the use of both supercells of 270 and 320 atoms practically eliminates the interaction between periodically distributed point defects.

The calculations [732] clearly demonstrate the advantage of combining DFT PW and DFT LCAO calculations. The former is necessary for the complete optimization of both lattice relaxation upon vacancy creation (especially for large supercells) and its migration, whereas the latter allows one to study in more detail the electronic structure for both unrelaxed and relaxed lattices. Such a combined study of the oxygen vacancy in  $\text{SrTiO}_3$  crystal shows that achieving the convergence with the supercell increases up to 270–320 atoms, the defect–defect interaction becomes negligible, thus approaching a realistic model of a single F center. A similar conclusion follows from the study of the Fe impurities in  $\text{SrTiO}_3$ , considered in next section.

### 10.3.2 Supercell Model of Fe-doped $\text{SrTiO}_3$

The properties of transition-metal impurities, especially iron, in  $\text{ABO}_3$  perovskite ferroelectrics are of considerable interest due to their photochromic, photorefractive and other applications.

There were several theoretical calculations for ion impurities substituting for B atoms. Molecular-cluster calculations were made to study charged point defects in  $\text{SrTiO}_3$ – $3d^3$  ions  $\text{Cr}^{3+}$ ,  $\text{Mn}^{4+}$ ,  $\text{Fe}^{5+}$  [741] and  $\text{Fe}^{3+}$ ,  $\text{Fe}^{4+}$ ,  $\text{Fe}^{5+}$  ions [742–744]. The formal charges used in designations of impurity ions mean the metal-atom oxidation state. As was already noted the calculated charges on transition-metal atoms in perovskites differ essentially from the formal charges due to strong covalent interaction with oxygen atoms. Bearing in mind that in perfect  $\text{SrTiO}_3$  crystal  $\text{Ti}^{4+}$  means the titanium-atom oxidation state 4,  $\text{Fe}^{3+}$ ,  $\text{Fe}^{4+}$ ,  $\text{Fe}^{5+}$  ions can be considered as impurity centers with charges  $-1$ ,  $0$ ,  $+1$ , respectively. The supercell calculations are known for Fe impurities in  $\text{KNbO}_3$  [745] in the LDA+U approximation, Li-doped  $\text{KTaO}_3$  (semiempirical INDO simulations [746] and comparative DFT, PW and INDO calculations [747]).

The supercell DFT PW calculations of different donor and acceptor centers in  $\text{SrTiO}_3$  [748] demonstrated the dependence of the formation energy on doping levels in the bulk crystal. In the majority of calculations cited no lattice relaxation around the impurity was studied, the calculated density of states depends on the parameters, used in the LDA+U or INDO approximations for the Hamiltonian.

A combination of first-principles supercell HF and DFT calculations that include lattice relaxations have been used in [680] to investigate the energy levels of neutral  $\text{Fe}^{4+}$  substitution on the Ti site. Here we consider these calculations in more detail. A consistent supercell–cyclic-cluster approach was applied for defective solids (see Sect. 10.1.3) with a focus on a detailed treatment of lattice relaxation around a single defect.

For a perfect crystal results of periodic HF and DFT calculations based on LCAO approximation are compared. Despite the fact that the supercell approach is widely used in defect calculations, very little attention is paid to the supercell shape and size optimization and the effect of periodically repeated defect interaction. Following the method accepted for the above-considered supercell calculations of native point defects (interstitial oxygen in  $\text{MgO}$ , F center in  $\text{Al}_2\text{O}_3$  and  $\text{SrTiO}_3$ ) a study of the convergence of results to the limit of a single defect is one of the main emphases of the calculations [680] on Fe-doped  $\text{SrTiO}_3$ . The transformation matrices for the supercells used are given in (10.14) in general form and define the equidistant supercells, forming sc, fcc and bcc lattices. In the footnote to Table 10.13 actual transformation matrices used in Fe-doped  $\text{SrTiO}_3$  calculations are given [680].

For the perfect crystal the special  $\mathbf{k}_q$  points sets corresponding to these supercells satisfy the Chadi–Cohen condition, see (4.83):

$$\sum_{\mathbf{k}_q} W_q \sum_{|\mathbf{A}_j|=R_m} \exp(i\mathbf{k}_q \cdot \mathbf{A}_j) = 0, \quad m = 0, 1, 2, 3, \dots \quad (10.16)$$

where the second sum is over lattice vectors of the same length equal with the  $m$ th neighbor distance  $R_m$ , the first sum is over a set of these special  $\mathbf{k}_q$  points, and  $W_q$  are weighting factors equal to the number of rays in their stars. The larger the number  $m$ , the better is the electronic-density approximation for the perfect crystal. The numbers  $M$  ( $m = 0, 1, 2, \dots$ ), defined according to (10.16) the accuracies of the corresponding sets, are given in Table 10.13.

The *ab-initio* periodic restricted and unrestricted HF (RHF,UHF) calculations were performed for perfect and defective  $\text{SrTiO}_3$  crystals, respectively, using the CRYSTAL computer code [23]. This code has the option to perform both HF and DFT calculations on equal grounds, for a large number of implicitly or *a posteriori* used exchange-correlation functionals that permits one to analyze directly the relevant electron-correlation effects keeping other computational conditions the same. The same LCAO basis set was used in the HF and DFT (PWGGA) calculations. Large-core Durand–Barthelat [484] for Ti and O atoms and Hay–Wadt small-core pseudopotentials [483] for Sr atoms were used. The impurity iron atoms were treated as all-electron atoms. The “standard” basis for Ti and O was taken from previous  $\text{TiO}_2$  LCAO calculations [574] whereas that for Fe and Sr from [629] and the CRYSTAL code site [23], respectively. The outer Ti, Fe and oxygen O basis functions were reoptimized. To characterize the chemical bonding and covalency effects for both defective and perfect crystals, a standard Mulliken population analysis was used for the effective atomic charges  $q$  and other local properties of electronic-structure – bond orders, atomic covalencies and full valencies (these local properties of electronic structure are defined in Sect. 9.1.1).

Since the lattice-relaxation calculations around a point defect was one of the aims, the band-structure calculations with the lattice constant  $a$  optimization were made

**Table 10.13.** Convergence of results for pure  $\text{SrTiO}_3$  ( $a=3.905$  Å) obtained for pure HF (a) and DFT-PWGGA (b) LCAO band calculations corresponding to cyclic clusters of an increasing size [680]. All energies in eV, total energies are presented with respect to the reference point of 80 a.u.=2176.80 eV.  $q$  and  $V$  are effective atomic charges and valencies (in  $e$ ), respectively.  $R_M$  and  $M$  are explained in the text

Supercell	Matrix	$M$	$R_M$ (Å)	$E_{\text{tot}}$ (eV)	$V$	$C$	$q(\text{Ti})$	$q(\text{O})$	$q(\text{Sr})$	$V(\text{Ti})$	$V(\text{O})$	$V(\text{Sr})$
a) HF LCAO calculations												
S8, <i>sc</i>	<i>A</i>	4	7.81	-24.288	-6.838	3.393	2.39	21.41	1.84	3.94	2.07	2.01
S16, <i>fcc</i>	<i>B</i>	7	11.04	-24.818	-6.895	3.766	2.54	21.46	1.84	3.97	2.06	2.01
S32, <i>bcc</i>	<i>C</i>	11	13.53	-24.873	-6.906	3.725	2.54	21.46	1.84	3.98	2.06	2.01
S64, <i>sc</i>	<i>D</i>	14	15.62	-24.873	-6.906	3.720	2.54	21.46	1.84	3.98	2.06	2.01
S108, <i>bcc</i>	<i>E</i>	24	20.29	-24.883	-6.895	3.744	2.54	21.46	1.84	3.98	2.06	2.01
b) DFT-PWGGA LCAO calculations												
S8, <i>sc</i>	<i>A</i>	4	7.81	-73.059	-4.647	4.367	3.43	21.74	1.79	3.98	2.06	2.04
S16, <i>fcc</i>	<i>B</i>	7	11.04	-73.024	-2.735	2.169	2.82	21.51	1.71	3.97	2.09	2.04
S32, <i>bcc</i>	<i>C</i>	11	13.53	-70.874	-2.737	1.219	2.55	21.42	1.70	3.99	2.11	2.04
S64, <i>sc</i>	<i>D</i>	14	15.62	-66.101	-2.414	0.027	1.69	21.13	1.70	4.12	2.18	2.04
S108, <i>bcc</i>	<i>E</i>	24	20.29	-66.134	-2.443	-1.025	1.69	21.13	1.70	4.12	2.18	2.04

Transformation matrices

$$A = \begin{pmatrix} 2 & 0 & 0 \\ 0 & 2 & 0 \\ 0 & 0 & 2 \end{pmatrix}, \quad B = \begin{pmatrix} 2 & 2 & 0 \\ 2 & 0 & 2 \\ 0 & 2 & 2 \end{pmatrix}, \quad C = \begin{pmatrix} 2 & 2 & -2 \\ 2 & -2 & 2 \\ -2 & 2 & 2 \end{pmatrix}, \quad D = \begin{pmatrix} 4 & 0 & 0 \\ 0 & 4 & 0 \\ 0 & 0 & 4 \end{pmatrix}, \quad E = \begin{pmatrix} 3 & 3 & -3 \\ -3 & 3 & 3 \end{pmatrix}$$

for the perfect crystal. The values obtained were  $a=3.92$ , 3.84, and 3.92 Å, for HF, HF-PWGGA and DFT-PWGGA, respectively. The experimental value is  $a_0=3.905$  Å. The bulk modulii are  $B=222$ , 242, and 195 GPa, respectively, to be compared with the experimental value (extrapolated to 0 K)  $B=180$  GPa. That is, pure HF gives an error of 0.5% only for the lattice constant, and by 20% overestimates the bulk modulus. Its *a posteriori* electron-correlation correction, HF-PWGGA, gives too small  $a$  value, and  $B$  even larger than the pure HF. Use of an optimized basis set results in  $a=3.93$ , 3.85, and 3.93 Å for HF, HF-PWGGA, and DFT-PWGGA, respectively. The relevant bulk moduli are  $B=220$ , 249, and 191 GPa, respectively. That is, the basis optimization only slightly affected the calculated  $a$  and  $B$  values.

Tables 10.13a and b demonstrate the effect of the cyclic-cluster increase for both HF and DFT-PWGGA methods, respectively. The main calculated properties are: the total energy  $E_{\text{tot}}$  (per primitive unit cell), one-electron band-edge energies of the valence-band top and conduction-band bottom  $\varepsilon_v$  and  $\varepsilon_c$ , Mulliken effective atomic charges  $q$  and full atomic valencies  $V$ . As is seen, the result convergence, as the supercell size increases, is quite different for the HF and DFT. We explain the much slower DFT convergence by a more covalent calculated electron-charge distribution, as compared to the HF case. For both methods, the convergence of local properties of the electronic structure is faster than that for the total and one-electron energies.

Based on the results of Table 10.13 the conclusion can be drawn that in the HF LCAO calculations of a perfect crystal, the electronic structure is reasonably well

reproduced by the supercell of 80 atoms ( $L=16$ ). This is confirmed by the band-structure analysis. The results of the standard band-structure calculations for the  $\text{SrTiO}_3$  primitive unit cell with Monkhorst–Pack  $\mathbf{k}$  set  $6 \times 6 \times 6$  and the cyclic cluster of 80 atoms (only at the  $\Gamma$  point of the BZ) are very similar. It appears that the most important features of the electronic structure of a perfect crystal (valence- and conduction- bandwidths, local properties of electronic structure) are well reproduced by the cyclic cluster of 80 atoms. The corresponding one-electron energies do not practically change along all the symmetry directions in the narrowed BZ for supercell band calculations.

Analysis of the difference electron-density plots, calculated for the band and the 80-atom cyclic-cluster calculations confirms that the latter well reproduces the electron-density distribution in a perfect crystal. Lastly, the total and projected density of states for a perfect crystal show that the upper valence band consists of O  $2p$  atomic orbitals with admixture of Ti  $3d$  orbitals, whereas the Sr states contribute mainly to the energies close to the conduction-band bottom, in agreement with previous studies.

However, as follows from Table 10.13, very accurate modeling of pure  $\text{SrTiO}_3$  by means of DFT-PWGGA needs use of cyclic clusters as large as 320 atoms ( $L=64$ ). This conclusion agrees with the results of DFT PW supercell calculations on  $\text{SrTiO}_3$  discussed in the preceding subsection.

Table 10.13 has shown that an increase of the cyclic cluster from S16 to S32 does not change the HF-calculated top of the valence band. However, the calculated width of the defect impurity band  $E_W$  found using a standard Monkhorst–Pack set  $6 \times 6 \times 6$  for three different supercells (Table 10.14) demonstrates clearly a considerable dispersion of defect energies across the supercell BZ.

**Table 10.14.** The width of the Fe impurity band  $E_W$  calculated for the relevant supercells

Supercell	Number of atoms	Fe–Fe distance (Å)	$E_W$ (eV)
S8	40	7.81	1.42
S16	80	11.04	0.23
S32	160	13.53	0.14

Indeed, the  $E_W$  decreases rapidly, from 1.42 eV (S8) down to 0.23 eV (S16), and further down to 0.14 eV (S32), when the Fe–Fe distance increases only by a factor of about 2, from 7.81 to 13.53 Å, since an overlap of the impurity atomic functions decreases exponentially. This is why only S32 (160-atom cyclic cluster) is suitable for a careful modeling of the single Fe impurity and lattice relaxation around it. This is in contrast to many previous supercell calculations of defects in perovskites where S8 supercells were often used without any convergence analysis.

Mulliken effective charges calculated for ions at different positions in supercells modeling pure and Fe-doped  $\text{SrTiO}_3$  are summarized in Table 10.15.

Table 10.15 demonstrates that the standard band-structure calculation and the S64 cyclic cluster give essentially identical charges. The more so, charges of the same ions in a 320-atom supercell are the same, irrespective of the ion position inside the cyclic cluster. Next, in the defective-crystal calculations, say, for the S32 cyclic

**Table 10.15.** Effective charges  $q$  of ions obtained in the HF band-structure calculations with a Monkhorst–Pack  $k$ -set  $6 \times 6 \times 6$  and different cyclic clusters modeling perfect and defective  $\text{SrTiO}_3$ . The lengths in the first column are lattice constants of the relevant supercells the distances  $R$  given above the effective charges are calculated with respect to the supercell coordinate origin where the Fe ion is placed

$R$ (Å)	0.00	1.95	3.38	3.90	4.37	5.52	5.86	6.48	6.76	7.04	7.81
Lattice const.(Å)	$q(\text{Fe})$	$q(\text{O})$	$q(\text{Sr})$	$q(\text{Ti})$	$q(\text{O})$	$q(\text{Ti})$	$q(\text{O})$	$q(\text{Sr})$	$q(\text{Ti})$	$q(\text{O})$	$q(\text{Ti})$
3.90 (band struct.)		-1.458	1.837	2.538							
15.62 (S64) (perfect cryst.)		-1.459	1.837	2.540	-1.459	2.540	-1.459	1.837	2.540	-1.459	2.540
7.81 (S8)	2.583	-1.464	1.835	2.406							
11.04 (S16)	2.571	-1.464	1.840	2.536	-1.460	2.543					
13.53 (S32)	2.570	-1.464	1.838	2.534	-1.458	2.540	-1.459	1.837	2.540		
15.62 (S64)	2.570	-1.463	1.838	2.534	-1.458	2.540	-1.459	1.837	2.540	-1.459	2.539

cluster, the effective charges of atoms close to its boundary are the same as in the perfect crystal. This confirms that the chosen cyclic cluster is large enough.

The S32-UHF supercell calculations for the zero-spin and high-spin ( $S=2$ ) states show that the latter is much lower in energy (by 5.4 eV) (after lattice relaxation). In the perovskite crystalline field a fivefold degenerate  $\text{Fe } 3d$  state splits into  $e_g$  and  $t_{2g}$  states (see Fig. 10.6) separated by 2.1 eV (for an undistorted lattice).

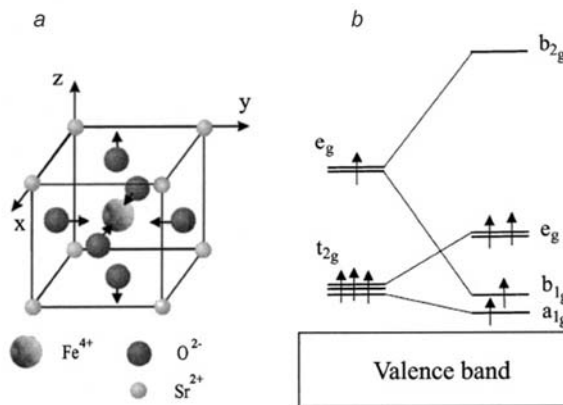


**Fig. 10.6.** (a) Schematic view of the Fe impurity with asymmetric  $e_g$  relaxation of the six nearest O atoms. (b) The relevant energy levels before and after relaxation

In the high spin state with  $S=2$  the upper level is occupied by one  $\alpha$  electron and three other  $\alpha$  electrons occupy  $t_{2g}$  states. As is well known in this case an  $E_g \otimes E_g$  Jahn–Teller effect takes place. This means that an orbital degeneracy is lifted by an asymmetrical displacement of six O ions, as shown in Fig. 10.6: four equatorial O

atoms lying in the  $xy$ -plane relax towards the impurity, whereas the two other O atoms relax outwards along the  $z$  axis. This results in two nondegenerate levels close to the valence-band top: the  $e_g$  level at 0.5 eV above the band edge, and a virtual nondegenerate  $b_{2g}$  level lying much higher (Table 10.16).

**Table 10.16.** Positions of one-electron Fe levels (in eV) with respect to the valence-band top calculated by means of HF method for S16 (80 atoms) and S32 (160 atoms) cyclic clusters with and without lattice relaxation

Cyclic cluster	Before relaxation		After relaxation			
	$t_{2g}$	$e_g$	$a_{1g}$	$b_{1g}$	$e_g$	$b_{2g}$
80 atoms	0.36	2.31	0.02	0.03	0.5	5.4
160 atoms	0.25	2.50	0.02	0.05	0.5	5.0

If we assume that  $x$ ,  $y$ ,  $z$  displacements have equal magnitudes, pure HF and HF-PWGGA calculations with the “standard” basis set give practically the same magnitude of the six O displacements  $\delta = 0.04$  Å, a quite flat minimum and an energy gain of 1.40 eV. This means that we have a combination of the Jahn–Teller and breathing modes of surrounding O-atom displacements. With the optimized basis set a slightly smaller energy gain 1.33 eV was obtained. It was checked also whether the magnitudes of the O-atom displacements along the  $x$ ,  $y$  and the  $z$  axes could be different and indeed a small additional energy gain, down to 1.42 eV for the following asymmetrical displacements in the latter case was found: 0.028 Å along the  $x,y$  axis and  $-0.052$  Å along the  $z$  axis, *i.e.* outward displacements of two O atoms are twice larger than those for four equatorial O atoms. Note that UHF calculation effectively incorporates the spin-dependent electron-correlation effects during the self-consistent loops and thus gives nearly the same results as HF with *a posteriori* (nonself-consistent) corrections for electron correlations. The total valence of the iron impurity  $V_{\text{Fe}}=3.3$  correlates much better with the  $\text{Fe}^{4+}$  model than with the calculated Mulliken effective charge of +2.59. These effective charges  $q$  of atoms collected in Table 10.17 demonstrate considerable covalency effects, well known for  $\text{ABO}_3$  perovskites.

**Table 10.17.** The effective Mulliken charges of atoms  $q$  and bond orders  $W$  (in  $e$ ) for S32 HF cyclic cluster with unrelaxed and relaxed lattices

$\text{SrTiO}_3$	$q(\text{Ti})$	$q(\text{O}_{x,y})$	$q(\text{O}_z)$	$W(\text{Ti–O}_x)$	$W(\text{Ti–O}_z)$
Pure	2.540	-1.459	-1.459	0.375	0.375
Fe-doped	$q(\text{Fe})$	$q(\text{O}_{x,y})$	$q(\text{O}_z)$	$W(\text{Fe–O}_x)$	$W(\text{Fe–O}_z)$
Unrelaxed	2.570	-1.464	-1.464	0.164	0.164
Relaxed	2.594	-1.440	-1.534	0.235	0.154

In particular, in pure  $\text{SrTiO}_3$  the effective charges are  $q(\text{Ti})=+2.54$ ,  $q(\text{Sr})=+1.84$ , and  $q(\text{O})=-1.46$ . The  $\text{Ti}-\text{O}$  bond order in a pure crystal is 0.375. When the two O atoms are displaced outwards from the Fe impurity along the  $z$  axis and thus approach the nearest Ti atoms, the  $\text{Ti}-\text{O}$  bond order increases to 0.489. The combination of a large lattice relaxation energy and relatively small O displacements is not surprising in the light of a considerable covalent bonding between the unpaired iron electrons occupying  $\text{Fe } 3d$  orbitals and  $2p$  orbitals of four equatorial oxygen ions: the  $\text{Fe}-\text{O}_{x,y}$  bond orders (Table 10.17) increase upon mutual approach of these atoms from 0.164 to 0.235.

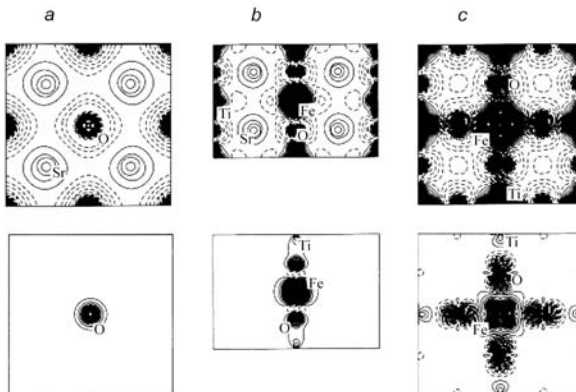


**Fig. 10.7.** (a) The electronic-density plots for the (010) cross section of Fe and nearest ions in  $\text{SrTiO}_3$  as calculated by means of the HF method for the cyclic cluster of 160 atoms. Isodensity curves are drawn from  $20.8$  to  $0.8 \text{ e a.u.}^{-3}$  with an increment of  $0.0022 \text{ e a.u.}^{-3}$ , b) the same as (a) for the (001) section, (c) the same for the (110) section. Left panels are HF difference electron densities, right panels are spin densities.

Analysis of the total electron-density and spin-density distribution (Fig. 10.7) shows that in the HF calculation four unpaired electrons are well localized on the Fe ion.

Lastly, a comparison of the band structures for the cyclic cluster containing the Fe impurity with that for a pure crystal clearly demonstrates that the Fe impurity induces additional energy levels below the valence band (in the region around  $-20 \text{ eV}$ ) and above the valence band, at around  $-2 \text{ eV}$ . These bands have practically no dispersion over the BZ, which demonstrates that the defect is almost isolated from its periodic images.

Any method is not completely universal, and the approach described also has its limitations. In particular, it does not work when incorporation of the lattice relaxation qualitatively changes the electron localization (*e.g.*, for free electron and hole polarons). On the other hand, it could be very efficient for many impurities in insulators characterized by high symmetry and when calculating forces is computationally expensive.

It was demonstrated that the size of the cyclic cluster large enough for a correct reproduction of the perfect crystal depends on the particular quantum-mechanical method; for  $\text{SrTiO}_3$  this means 80-atom cyclic clusters for the HF but 320 atoms for the DFT-PWGGA. In the HF defect calculations for the single  $\text{Fe}^+$  impurity the cyclic cluster should not be smaller than 160 atoms. This is in contrast with many previous supercell calculations on perovskites where supercells as small as S8 were used without convergence analysis.

It was already mentioned in Chap. 9 that the HF method typically overestimates the optical gap, whereas DFT underestimates it. This can affect the electronic-density distribution (chemical-bond covalency) and defect-level positions within the gap (even determined with respect to the valence-band top). In this respect, the hybrid HF-DFT methods widely used in the molecular chemistry, *e.g.*, B3LYP, seem to be more promising tools.

The calculations [680] have demonstrated the strong covalent bonding between unpaired electrons of Fe impurity and four nearest O ions relaxed towards an impurity. The positions of Fe energy levels in a  $\text{SrTiO}_3$  gap are very sensitive to the lattice relaxation that was neglected in previous studies. The predicted positions of the Fe energy levels with respect to the valence-band top could be checked by means of UPS spectroscopy whereas the local lattice relaxation around iron and its spin state was checked by means of EXAFS. The results of the calculations under consideration are important since the single  $\text{Fe}^{4+}$  ions were not detected by ESR (only  $\text{Fe}^{4+}$ -O vacancy complexes were experimentally studied) and their optical absorption bands at 2.1 and 2.8 eV [749] are tentative. Note that the high-spin state of  $\text{Fe}^{4+}$  impurity predicted in *ab-initio* calculations contradicts previous semiempirical and nonself-consistent calculations ( $X_\alpha - \text{FeO}_6$  cluster calculation [742] and tight-binding calculation [743]). On the other hand, a high spin state is indirectly supported by its observation for host Fe ions in  $\text{SrFeO}_3$  perovskite.

We conclude this chapter by discussion of the supercell use for the solid-solution modeling. In this case the supercells of different size allow different percentages of doping in solid solution to be modeled.

### 10.3.3 Modeling of Solid Solutions of $\text{La}_c\text{Sr}_{1-c}\text{MnO}_3$

One of the extensively studied perovskite-type materials,  $\text{La}_c\text{Sr}_{1-c}\text{MnO}_3$  (LSM), is of special interest due to numerous applications, particularly as the cathode for solid oxide fuel cells [750].

LSM was investigated both theoretically [751, 752] and experimentally [753] with a focus on the chemical-bonding nature, magnetic properties, metal-insulator transitions, structural transformations and surface properties.

Numerous efforts were undertaken to study the phase transformations and phase stability in LSM in a wide range of solid solutions. These materials exhibit a complicated dependence of the properties on the concentration of the Sr dopant and oxygen nonstoichiometry. Nowadays, it is well recognized that the dielectric, piezoelectric and other LSM properties are entirely related to the phase equilibrium and the phase separation that occurs under different thermodynamic conditions.

In what follows we discuss the results of *ab-initio* supercell studies of the relative stability of different LSM phases [754]. To perform the *ab-initio* calculations the program packages WIEN-2k [378] and CRYSTAL-03 [23] were used.

The spin-polarized DFT FP LAPW and LCAO electronic and atomic-structure calculations [754] use the exchange-correlation PBE functional.

The basis set of augmented plane waves combined with local orbitals (APW+lo) is used in the WIEN-2k code for solving the Kohn–Sham equations. In this method the unit-cell volume is divided into two regions: (I) nonoverlapping atomic spheres centered at the atomic sites and (II) an interstitial region. In the two types of regions different basis sets are used. Inside atomic sphere  $i$  of radius  $R_i$ , where electrons behave as they were in a free atom, a linear combination of radial functions times spherical harmonics is used. In the interstitial region between these atomic spheres, where the electrons are more or less “free,” a plane-wave expansion is used. On the sphere boundary the wavefunctions of both regions are matched by a value. The APW+lo basis set has a significantly smaller size than the basis set in the LAPW method and thus the computational time is drastically reduced. Nevertheless, these two schemes converge practically to identical results. The convergence of the method is controlled by a cutoff parameter  $R_{mt}K_{max}$ , where  $R_{mt}$  is the smallest atomic sphere radius in the unit cell and  $K_{max}$  is the magnitude of the largest  $\mathbf{k}$ -vector in the reciprocal space. To improve the convergence of the calculations it is necessary to increase this product. A reasonably large  $R_{mt}$  can significantly reduce the computational time. A value of  $R_{mt} = 1.7$  a.u. was chosen and a plane-wave cutoff  $R_{mt}K_{max} = 9$ .

The calculations [754] are performed for the high-temperature cubic phase of  $\text{LaMnO}_3$  (LMO)-based crystals doped with Sr, substituting for La atoms in different fractions. This substitution results in a charge-compensating hole formation. The formation of other defects like oxygen or metal vacancies is neglected.

To model the  $\text{LaMnO}_3$  doped by Sr (LSM), a  $2 \times 2 \times 2$  supercell is used, which consists of eight primitive unit cells and thus contains 40 atoms. The WIEN-2k code generates the  $\mathbf{k}$ -mesh in the irreducible wedge of the Brillouin zone (BZ) on a special-point grid that is used in a modified tetrahedron integration scheme (500  $\mathbf{k}$ -points were used). The accuracy in total-energy calculations was  $10^{-4}$  Ry. Different configurations of Sr atoms substituting for La atoms allow ordered LSM solid solutions to be modeled. In particular,  $\text{La}_{0.875}\text{Sr}_{0.125}\text{MnO}_3$  is typically used in fuel cells and thus is the subject of detailed thermodynamic study. The calculations are carried out for the ferromagnetic spin alignment (all Mn spins in the supercells are oriented in parallel), which results in a metallic character of the resistivity [753]. However, the resistivity of this phase is larger by three orders of magnitude than that of a typical metal. This is confirmed by FP LAPW band-structure calculations: a very small density of states (DOS) in the vicinity of the Fermi level is observed. The model used is in agreement with the calculations [752] where the ferromagnetic state was revealed for layers of a cubic  $\text{La}_{0.7}\text{Sr}_{0.3}\text{MnO}_3$ .

In [754] DFT B3LYP LCAO calculations for  $\text{La}_c\text{Sr}_{(1-c)}\text{MnO}_3$  mixed crystals ( $c = 0, 0.125, 0.5, 1.0$ ) were performed, see Fig. 10.8. La, Sr and Mn core electrons were described by Hay–Wadt small-core (HWSC) pseudopotentials [483]. For the oxygen atoms an all-electron 8-411(1d)G basis was taken from previous  $\text{MnO}$  calculations [628], performed with basis-set (BS) optimization. For La, Mn and Sr ions BSs 411(1d)G, 411(311d)G and 311(1d)G were taken from  $\text{La}_2\text{CuO}_4$  [755] calculations, the CRYSTAL web site [23] and  $\text{SrTiO}_3$  calculations [606], respectively.

To achieve a high numerical accuracy in the lattice and in the BZ summations, the cutoff threshold parameters of the CRYSTAL03 code for Coulomb and exchange

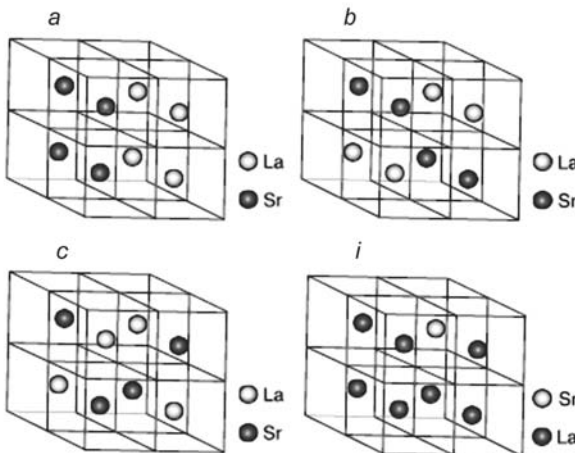


**Fig. 10.8.** Four structures used in calculations of  $\text{La}_c\text{Sr}_{1-c}\text{MnO}_3$

integrals evaluation to 7, 7, 7, 7 and 14, respectively, were taken. The integration over the BZ has been carried out on the Monkhorst–Pack grid of shrinking factor 8 (its increase up to 16 gave only a small change in the total energy per unit cell). The self-consistent procedure was considered as converged when the total energy in the two successive steps differs by less than  $10^{-6}$  a.u.

As the first step, B3LYP spin-polarized LCAO calculations for the cubic  $\text{LaMnO}_3$  and  $\text{SrMnO}_3$  (with one formula unit per primitive cell) are performed, using the maximal spin projection  $S_z = 2$  for four  $d$ -electrons of the  $\text{Mn}^{3+}$  ion. As we have seen in Chap. 9, such a spin projection ensures the lowest total energy compared with  $S_z = 0, 1$ . The optimized cubic lattice constants are  $a=3.967 \text{ \AA}$  and  $a=3.840 \text{ \AA}$  for  $\text{LaMnO}_3$  and  $\text{SrMnO}_3$ , respectively. These values are in a reasonable agreement with the experimental lattice constants  $a=3.947 \text{ \AA}$  and  $a=3.846 \text{ \AA}$ , respectively. The two optimized cubic lattice constants for  $\text{LaMnO}_3$  and  $\text{SrMnO}_3$  were used for calculating the lattice constants of their solid solutions according to Vegard's law (linear dependence of the lattice parameters on the composition). As follows from the WIEN-2k calculations, this is fulfilled quite well in this system.

To predict the relative stability of different phases, which might appear in the quasibinary phase diagram of LSM solid solutions in a wide range of dopant concentrations, the statistical thermodynamic approach combined with the *ab-initio* calculations was used. Such an approach has been successfully applied to different systems (see, *e.g.*, [756–758] and references therein).

The standard periodic *ab-initio* approach could be used only for ground-state energy calculations and ordered structures and thus does not allow prediction of thermodynamic stability of these phases as the temperature grows. This forces the problem to be reformulated so as to permit the extraction of the necessary energy parameters from the calculations for the ordered phases, and to apply these parameters to the study of the disordered or partly ordered solid solutions, in order to get information on the thermodynamic behavior of LSM solid solutions. From the exper-

imental data [759] it follows that in these solid solutions Sr atoms substitute for La at all atomic fractions,  $0 < c < 1$ . Therefore, it is possible to consider the LSM solid solution as formed by La and Sr atom arrays occupying the sites of a simple cubic lattice immersed in the external field of the remaining lattice of Mn and O ions. The thermodynamics of such solid solutions can be formulated in terms of the effective interatomic mixing potential, which describes the interaction of La and Sr atoms embedded into the field of the remaining lattice. The study is based on the calculation of the relative stabilities of different ordered LSM cubic phases.

Figure 10.8 illustrates four phases: three of them (a, b, c) correspond to  $c = 0.5$ , the last one (i) with  $c = 7/8$  corresponds to 12.5% Sr-doped  $\text{LaMnO}_3$ . The remaining phases in Table 10.18 are the same as those used in  $\text{Ba}_c\text{Sr}_{(1-c)}\text{O}_3$  calculations [756].

**Table 10.18.** Total energies  $E_{\text{tot}}$  per  $2 \times 2 \times 2$  cell, for  $\text{La}_c\text{Sr}_{1-c}\text{MnO}_3$  compositions and equilibrium lattice parameters  $a_{\text{eq}}$  for different structures, see [754] and Fig. 10.8.

Structure	$c$	WIEN-2k		Crystal-03	
		$E_{\text{tot}}$ (Ry)	$a_{\text{eq}}$ (Å)	$E_{\text{tot}}$ (Ry)	$a_{\text{eq}}$ (Å)
a	0.5	-115574.4034	3.881	-5771.8383	3.903
b	0.5	-115574.4248	3.881	-5771.8688	3.903
c	0.5	-115574.4178	3.879	-5771.8812	3.903
d	0.25	-94302.8877	3.862		
e	0.75	-136845.8880	3.901		
f	0.25	-94302.8725	3.865		
g	0.75	-136845.8763	3.901		
h	0.125	-83667.1051	3.855(3.828)*		
i	0.875	-147481.5822	3.914	-5776.8921	3.951
$\text{LaMnO}_3$		-158117.2795	3.921(3.947)*	-5778.3816	3.967
$\text{SrMnO}_3$		-73031.3269	3.848(3.806)*	-5764.9568	3.840

\*For the references to these experimental data see in [754].

In the concentration wave (CW) theory [760] the distribution of atoms A in a binary A–B alloy is described by a single occupancy probability function  $n(\mathbf{r})$ . This is the probability to find the atom A (La) at the site  $\mathbf{r}$  of the crystalline lattice. The configurational part of the free energy of solid-solution formation (per atom) includes the internal formation energy  $\Delta U$ , the function  $n(\mathbf{r})$ , a concentration of particles La(A), the effective interatomic potentials between La atoms (A) and Sr atoms (B), for details see [754].

To find the internal formation energies, which are differences between total energies of superstructures and the reference-state energy, the energy of a heterogeneous mixture,  $c\text{LaMnO}_3 + (1-c)\text{SrMnO}_3$ , has been chosen for the reference state. This energy is calculated as the sum of weighted (according to the atomic fractions) total energies of the two pure limiting phases,  $\text{LaMnO}_3$  and  $\text{SrMnO}_3$ . From *ab-initio* calculations the total energies  $E_{\text{tot}}$  and equilibrium lattice constant for all superstructures are obtained, Table 10.18. The internal formation energies for ordered phases (Table 10.19) are calculated by the definition

$$\Delta U = E_{tot} - \left( cE_{tot}^{\text{LaMnO}_3} + (1 - c)E_{tot}^{\text{SrMnO}_3} \right) \quad (10.17)$$

**Table 10.19.** Formation energies of different superstructures (in eV per atom on La/Sr sublattice) as calculated by means of the WIEN-2k (FPLAPW) and CRYSTAL-03 (LCAO) codes, [754]

Configuration	FPLAPW	LCAO
a	0.170	0.288
b	0.207	0.339
c	0.195	0.360
i	0.080	0.320

All these energies calculated using two very different DFT methods (FPLAPW and LCAO) are negative, *i.e.* the formation of these ordered phases is energetically favorable with respect to their decomposition at  $T = 0$  K into a heterogeneous mixture of  $\text{LaMnO}_3$  and  $\text{SrMnO}_3$  phases. It is easy to see from Table 10.18 that at the stoichiometric composition  $c=1/2$  the ordered phases a, b, c (which have different local impurity arrangements in the supercell) are energetically more favorable than other phases. Also, these three phases differ slightly between themselves in the formation energies.

The absolute values for formation energies, given in Table 10.19, are larger in LCAO calculations than those from FPLAPW calculations, especially for the “i” configuration. In order to check this point, additional LCAO calculations were performed using two different hybrid exchange-correlation functionals (B3LYP and B3PW) and optimized lattice constants in all four configurations. However, the results are very close to those obtained by using Vegard’s law. Therefore, the only reason for the energy discrepancy is the use of different computational schemes. However the use of two different methods allows more reliable information to be obtained. In this particular case, both methods give qualitatively similar results. Using these formation energies it is possible to calculate the temperature evolution of the long-range order (LRO) parameters of the superlattices. The LRO parameters characterize the atomic ordering in sublattices of the  $\text{ABO}_3$ -type perovskite. Their values were taken to be equal to unity (which corresponds to completely ordered phases at stoichiometric compositions). The concentration was taken to be equal to the stoichiometric compositions of the corresponding phases. Finally, the free energy of formation of the phase  $\text{La}_{0.875}\text{Sr}_{0.125}\text{MnO}_3$  was calculated (we refer the reader to [754] for details).

The calculations of LSM solid solution considered here demonstrate the efficiency of use of thermodynamic formalism based on combination of the *ab-initio* electronic-structure calculations as developed in [754, 756–758]. The main feature of this approach is the treatment of ordered superstructures presenting the La-Sr sublattice immersed in the field of the remaining lattice formed by Mn and O atoms. The total-energy calculations allow the formation energies of these superstructures for different compositions to be found and their competition at  $T = 0$  K to be analyzed. These calculations for a series of ordered structures permit extraction of the key energy parameters – the

Fourier transforms of the mixing potential and thus the free energy for temperature induced partly disordered structures to be determined. Using the 12.5% Sr-doped  $\text{LaMnO}_3$  a thermodynamic analysis was performed [754]. It was predicted, in particular, that disordering of this phase with respect to the decomposition into the heterogeneous mixture of  $\text{LaMnO}_3$  and  $\text{SrMnO}_3$  can occur only at temperatures above the melting point. This is in contrast to a similar study of isostructural  $\text{Ba}_c\text{Sr}_{(1-c)}\text{TiO}_3$  solid solution where below a certain temperature Ba impurities in  $\text{SrTiO}_3$  tend to form  $\text{BaTiO}_3$  nanoclusters.

In this chapter we have seen that in modern quantum chemistry of solids the first-principles periodic calculations are successfully extended to formally aperiodic systems – defective crystals and solid solutions. In the next chapter we consider the application of periodic models in the calculations of crystalline surfaces and adsorption.

## Surface Modeling in LCAO Calculations of Metal Oxides

### 11.1 Diperiodic Space Groups and Slab Models of Surfaces

#### 11.1.1 Diperiodic (Layer) Space Groups

To model the electronic structure of surface states of crystals three basic approaches are used: the cluster, slab (single and periodic), and semi-infinite crystal models. The latter is the most exact because it takes into account all the atoms of the crystal with a surface.

A *semi-infinite crystal* is a three-dimensional (3D) object. Its symmetry group contains, in addition to translations in the surface plane, only the rotations and mirror reflections that keep the atoms in the planes parallel to the surface. Only 17 such groups exist. Formally, these groups are isomorphic with diperiodic space groups in two dimensions. They are called *plane groups*.

In the *molecular-cluster* approach a crystal with a surface is modeled by a finite system consisting of the atoms on the surface and of some atomic planes nearest to it. The diperiodicity of the surface is not taken into account. The symmetry of such a model is described by one of the crystallographic point groups.

In the *single-slab* model a crystal with a surface is approximated by a slab of finite thickness. The symmetry group of this model allows the existence of symmetry operations that move the atoms out of the plane of the layer but bring them into positions occupied by other atoms of the slab. These are space diperiodic groups in three dimensions. They are also called the layer groups. We denote them by DG. These groups also describe the symmetry of thin films. In layered crystals the interaction between the nearest layers is usually weaker than that between nearest atoms in the same layer plane. Therefore, the slab model is a convenient approximation for such crystals. Layer groups describe the symmetry of this model. Diperiodic (layer) groups are the symmetry groups of three-dimensional (3D) objects with two-dimensional (2D) periodicity.

In plane-wave calculations the *periodic (repeated) slab* model is used. In this model the slab is periodically repeated along the normal to the slab surface plane. This repeating of the slab restores the 3D periodicity of the surface model. The symmetry group of the periodic slab is a space group (Chap. 2) – three-dimensional group with three-dimensional translations.

The layer groups DG belong to the so-called subperiodic groups. The latter include 7 frieze groups (two-dimensional groups with one-dimensional translations), 75 rod groups (three-dimensional groups with one-dimensional translations), and 80 layer groups (three-dimensional groups with two-dimensional translations). The information presented about the subperiodic groups in [761] is in the same format and consists of the same content as that provided in [19] for space groups G.

In [761] a relationship is considered between space and subperiodic groups: given a crystal of a specific space-group symmetry and a plane transecting the crystal, one can enquire as to what is the layer subgroup of the space group that leaves this plane invariant. The physical motivation for answering this question is clear as this problem arises, for example, in the surface modeling by a single slab. The information about subperiodic groups is followed in [761] by the scanning tables in which the layer symmetries of sectional planes are tabulated for all crystallographic orientations and for all positions (locations) of these planes. These tables also contain explicitly the orbits of these planes (an orbit is defined as a set of planes connected by the symmetry operations) and implicitly, via the so-called “scanning groups”, information about the rod symmetries of straight lines that penetrate through the crystal. Rod groups are used for studying polymers, nanotubes, quantum wells.

Diperiodic group DG contains a subgroup of two-dimensional translations  $T^{(2)}$  with elements  $(E|\mathbf{a}_n)$ , where

$$\mathbf{a}_n = n_1 \mathbf{a}_1 + n_2 \mathbf{a}_2 \quad (11.1)$$

is an arbitrary translation vector of the plane lattice, and  $\mathbf{a}_1, \mathbf{a}_2$  are unit cell (primitive) translation vectors. The ends of all vectors  $\mathbf{a}_n$  beginning at some origin  $O$  form a two-dimensional Bravais lattice. The point-symmetry group  $F_{DG}$  of this lattice must satisfy the following requirements: symmetry axes of order  $n$  (with  $n > 2$ ) must be perpendicular to the plane of vectors  $\mathbf{a}_1, \mathbf{a}_2$  (layer plane), reflection planes must be either perpendicular or parallel to this plane. These requirements restrict the number of possible two-dimensional lattices. The two-dimensional lattice of a layer group is also a two-dimensional lattice of a plane group (two-dimensional groups with two-dimensional translations). There exist five plane lattices, distributed over four crystal systems: oblique, rectangular (2 lattices – primitive and centered), square and hexagonal.

The point symmetry of the oblique, rectangular, square and hexagonal systems is given by  $C_2$ ,  $C_{2v}$ ,  $C_{4v}$  and  $C_{6v}$  point groups, respectively. Note that in a plane lattice the inversion at the origin of the coordinate system is equivalent to the rotation through the second-order axis normal to the plane. Screw axes in layer groups may be only the second-order axes lying in the layer plane. Improper translations in operations of reflection in glide planes (parallel or perpendicular to the layer plane) must be oriented along the layer plane.

One can find the information about subperiodic groups on the Bilbao Crystallographic server [16]. These groups are specified by their number as given in [761] or by the international symbols. The international symbol of layer group DG contains, first, the information about the plane Bravais lattice type: P (primitive) or C (centered). Then the information about symmetry elements is given. The screw axes (of second order) have the subscript 1. The reflection planes are denoted as follows: m (mirror planes), n, a, b (glide planes, depending on the direction of the improper translations).

The subperiodic groups are described by means of a crystallographic coordinate system consisting of a crystallographic origin, denoted by  $O$ , and a crystallographic basis. The conventional basis vectors for the three-dimensional layer groups are labeled  $\mathbf{a}$ ,  $\mathbf{b}$ , and  $\mathbf{c}$ . Unlike space groups, not all basis vectors of the crystallographic basis are lattice vectors (for primitive lattices vectors  $\mathbf{a}$  and  $\mathbf{b}$  coincide with the primitive translations  $\mathbf{a}_1$ ,  $\mathbf{a}_2$ ). Like space groups, the crystallographic coordinate system is used to define the symmetry operations and the Wyckoff positions. The symmetry operations are defined with respect to the directions of both lattice  $\mathbf{a}$ ,  $\mathbf{b}$  and nonlattice  $\mathbf{c}$  basis vectors. A Wyckoff position, denoted by a coordinate triplet  $(x, y, z)$  for the three-dimensional layer groups, is defined in the crystallographic coordinate system by  $O + \mathbf{r}$ , where  $\mathbf{r} = x\mathbf{a} + y\mathbf{b} + z\mathbf{c}$ .

Like space groups, the term setting will refer to the assignment of the labels  $\mathbf{a}$ ,  $\mathbf{b}$ , and  $\mathbf{c}$  (and the corresponding directions [100], [010] and [001], respectively) to the basis vectors of the crystallographic basis. In the standard setting, those basis vectors that are also lattice vectors are labeled for layer groups with their two-dimensional lattice by  $\mathbf{a}$  and  $\mathbf{b}$ . The Wyckoff positions for the 80-layer groups can be found in [16, 761]. Note that the setting of the layer groups for rectangular lattices may be chosen different for the same group (symbols  $P211$  or  $P121$  refer to the same group in two different settings) but at the same time  $P112$  and  $P211$  denote different layer groups. In the first group the axis of second order (oriented along the  $z$ -axis) is perpendicular to the layer plane, in the second it lies in the layer plane  $xy$  and is directed along the  $x$ -direction. In the first case, the second-order axis is oriented along the plane translation lattice vector, in the second case along the nonlattice vector. Respectively, the Wyckoff positions for both groups are different, see [16].

Any element of the layer group may be written as  $(R_i|\mathbf{v}_i + \mathbf{a}_n)$ , where  $\mathbf{a}_n$  and  $\mathbf{v}_i$  are lattice and improper translations,  $i=1,2$ .

Let  $\mathbf{a}_3$  be a vector that does not lie in the layer plane. A set of elements  $(E|\mathbf{n}_3\mathbf{a}_3)$  forms a group  $T_3$  of one-dimensional translations. Consider the elements

$$(R_i|\mathbf{v}_i + \mathbf{a}_n)(E|\mathbf{n}_3\mathbf{a}_3), \quad (R_i|\mathbf{v}_i + \mathbf{a}_n) \in \text{DG}, i = 1, 2, \quad (E|\mathbf{n}_3\mathbf{a}_3) \in T_3 \quad (11.2)$$

The set (11.2) of symmetry operations contains a group of three-dimensional translations  $(E|\mathbf{a}_n + \mathbf{n}_3\mathbf{a}_3) \in T$ . The set (11.2) is some space group provided the translational symmetry (the group  $T$ ) is compatible with the point symmetry  $F_{\text{DG}}$  of the layer group DG. This condition is fulfilled if the vector  $\mathbf{a}_3$  is chosen perpendicular to the layer plane. Indeed, the translations  $(E|\mathbf{a}_n) \in T^{(2)} \subset T$  are compatible with  $F_{\text{FD}}$  as they are the elements of DG. The compatibility of the translations  $(E|\mathbf{n}_3\mathbf{a}_3) \in T_3$  with point group  $F_{\text{FD}}$  follows from the fact that the rotations (proper and improper) from DG transform the layer into itself and, therefore, the vector perpendicular to the layer is transformed into a vector also perpendicular to the layer. Thus, the set of elements (11.2) forms one of the three-periodic space groups  $G$ . Moreover, the translational group  $T_3$  is invariant in  $G$ : with the translation  $(E|\mathbf{a}_3)$  it contains also the translation  $(E|R_i\mathbf{a}_3)$  for any  $R_i$  from (11.2). Therefore, the group  $G$  may be expressed as a semidirect product

$$G = T_3 \wedge \text{DG} \quad (11.3)$$

and be decomposed into cosets with respect to  $T_3$

$$G = \sum_i (R_i | \mathbf{v}_i + \mathbf{a}_n) T_3, \quad (R_i | \mathbf{v}_i + \mathbf{a}_n) \in DG, i = 1, 2 \quad (11.4)$$

Thus, subperiodic layer group DG is isomorphic to factor group  $G/T_3$ . A relationship between factor groups of space groups and subperiodic groups is studied in [762, 763].

Table 11.1 gives correspondence  $DG \leftrightarrow G/T_3$  between three-dimensional diperiodic (DG) and three-periodic (G) space groups. This correspondence was at first given by Wood [764] in the setting that differs for rectangular diperiodic groups from that given in Table 11.1 (the setting in this Table corresponds to the standard setting of [761]). The layer and rod groups isomorphic to factor groups of space groups (the corresponding space groups are called reducible space groups) have been tabulated [763].

**Table 11.1.** Correspondence between three-dimensional two-periodic (DG) and three-periodic (G) space groups ( $DG \leftrightarrow G/T_3$ ), [761].

DG	G	DG	G	DG	G
<u>1</u> $P1$	$C_1^1$ 1	28 $Pm2_1b$	$C_{2v}^2$ 26	55 $P4mm$	$C_{4v}^1$ 99
2 $P\bar{1}$	$C_i^1$ 2	29 $Pb2_1m$	$C_{2v}^2$ 26	56 $P4bm$	$C_{4v}^2$ 100
<u>3</u> $P112$	$C_2^1$ 3	30 $Pb2b$	$C_{2v}^3$ 27	57 $P\bar{4}2m$	$D_{2d}^1$ 111
4 $P11m$	$C_s^1$ 6	31 $Pm2a$	$C_{2v}^4$ 28	58 $P\bar{4}2_1m$	$D_{2d}^3$ 113
5 $P11a$	$C_s^2$ 7	32 $Pm2_1n$	$C_{2v}^5$ 31	59 $P\bar{4}m2$	$D_{2d}^5$ 115
6 $P112/m$	$C_{2h}^1$ 10	33 $Pb2_1a$	$C_{2v}^5$ 29	60 $P\bar{4}b2$	$D_{2d}^2$ 117
7 $P112/a$	$C_{2h}^4$ 13	34 $Pb2n$	$C_{2v}^6$ 30	61 $P4/mmm$	$D_{4h}^1$ 123
8 $P211$	$C_2^1$ 3	35 $Cm2m$	$C_{2v}^{14}$ 38	62 $P4/nbm$	$D_{4h}^3$ 125
9 $P2_111$	$C_2^2$ 4	36 $Cm2a$	$C_{2v}^{15}$ 39	63 $P4/mbm$	$D_{4h}^5$ 127
10 $C211$	$C_2^3$ 5	37 $Pmmm$	$D_{2h}^1$ 47	64 $P4/nmm$	$D_{4h}^7$ 129
<u>11</u> $Pm11$	$C_s^1$ 6	38 $Pmaa$	$D_{2h}^3$ 49	<u>65</u> $P3$	$C_3^1$ 143
<u>12</u> $Pb11$	$C_2^2$ 7	39 $Pban$	$D_{2h}^4$ 50	66 $P\bar{3}$	$C_{3i}^1$ 147
<u>13</u> $Cm11$	$C_3^3$ 8	40 $Pmam$	$D_{2h}^5$ 51	67 $P312$	$D_3^1$ 149
14 $P2/m11$	$C_{2h}^1$ 10	41 $Pmma$	$D_{2h}^5$ 51	68 $P321$	$D_3^2$ 150
15 $P2_1/m11$	$C_{2h}^2$ 11	42 $Pman$	$D_{2h}^7$ 53	69 $P3m1$	$C_{3v}^1$ 156
16 $P2/b11$	$C_{2h}^4$ 13	43 $Pbaa$	$D_{2h}^8$ 54	70 $P31m$	$C_{3v}^2$ 157
17 $P2_1/b11$	$C_{2h}^5$ 14	44 $Pbam$	$D_{2h}^9$ 55	71 $P\bar{3}12/m$	$D_{3d}^1$ 162
18 $C2/m11$	$C_{2h}^3$ 12	45 $Pbma$	$D_{2h}^{11}$ 57	72 $P\bar{3}2/m1$	$D_{3d}^3$ 164
19 $P222$	$D_2^1$ 16	46 $Pmmn$	$D_{2h}^{13}$ 59	<u>73</u> $P6$	$C_6^1$ 168
20 $P2_122$	$D_2^2$ 17	47 $Cmmm$	$D_{2h}^{19}$ 65	74 $P\bar{6}$	$C_{3h}^1$ 174
21 $P2_12_12$	$D_2^3$ 18	48 $Cmma$	$D_{2h}^{21}$ 67	75 $P6/m$	$C_{6h}^1$ 175
22 $C222$	$D_2^6$ 21	49 $P4$	$C_4^1$ 75	76 $P622$	$D_6^1$ 177
23 $Pmm2$	$C_{2v}^1$ 25	50 $P\bar{4}$	$S_4^1$ 81	77 $P6mm$	$C_{6v}^1$ 183
24 $Pma2$	$C_{2v}^4$ 28	51 $P4/m$	$C_{4h}^1$ 83	78 $P\bar{6}m2$	$D_{3h}^1$ 187
25 $Pba2$	$C_{2v}^8$ 32	52 $P4/n$	$C_{4h}^3$ 85	79 $P\bar{6}2m$	$D_{3h}^3$ 189
26 $Cmm2$	$C_{2v}^{11}$ 35	53 $P422$	$D_4^1$ 89	80 $P6/mmm$	$D_{6h}^1$ 191
27 $Pm2m$	$C_{2v}^1$ 25	54 $P42_12$	$D_4^2$ 90		

The numbers of 17 plane groups are underlined.

For some layer groups of oblique and rectangular crystal systems (DG 1, 2, 8–18) the vector  $\mathbf{a}_3$  may be inclined to the layer plane.

In the cases when a space group  $G$  may be represented as a semidirect product (11.3)) in two different manners it generates two nonisomorphic layer groups. For example, the layer groups  $P112$  and  $P211$  are related to one space group  $P2(C_2^1)$  with two different settings (the second-order axis is oriented along the  $z$ - and  $x$ -directions, respectively). The space group  $P2/b$  ( $C_{2h}^4$ ) generates two layer groups  $P112/a$  and  $P2/b11$ . In the first group the rotation axis is perpendicular to the layer and the layer plane itself is a glide plane with an improper translation on a half-period along the  $x$ -direction. In the second group the rotation axis is directed along the  $x$ -axis; the glide reflection plane is perpendicular to the layer (and to the rotation axis) and reflection in this plane is followed by improper translation on the half-period along the  $y$  direction. The latter corresponds to the space group, with a nonconventional setting.

A particular case of layer groups is that of the so-called plane groups mentioned above. Formally, they are the symmetry groups of diperiodic systems in two dimensions. They correspond to the layer groups that do not contain the rotation axes lying in the layer plane and the reflection planes coinciding with the layer plane. Semi-infinite crystals with plane diperiodic surfaces have plane groups as the groups of symmetry.

The Wigner–Seitz (WS) cell for an arbitrary group  $DG$  is a right prism with a directrix lying in the layer plane. The projection of the Wigner–Seitz (WS) cell on the layer plane is a polygon constructed from the basis vectors  $\mathbf{a}_1$  and  $\mathbf{a}_2$  [13]. The WS cell of the corresponding triperiodic group  $G$  is derived by construction of additional planes perpendicular to the vectors  $\mathbf{a}_3$  (and perhaps to their integer combinations with the vectors  $\mathbf{a}_1$  and  $\mathbf{a}_2$ ) and passing through their midpoints. Thus, the WS of the group  $G$  is a part of that for the corresponding group  $DG$ .

The site-symmetry groups of Wyckoff positions for the majority of positions belonging to both WS cells (of  $G$  and of  $DG$ ) are identical since they are determined by the same set of symmetry operations. The only exception may be for the points on the sides of the group  $G$  cell that are absent in that of the group  $DG$ . The existence of translational symmetry in the third dimension in the group  $G$  may give rise to additional symmetry operations in site-symmetry groups for these points in the group  $G$  with respect to  $DG$ . The part of the WS cell of the layer group  $DG$  that has no common points with the cell of the corresponding group  $G$  contains the points of general position and the points with site symmetry defined by vertical planes and rotation axes. These types of site symmetry are already represented in the common part of the cells for  $G$  and  $DG$ . Therefore, the set of points with different types of site symmetry in the group  $G$  is larger than that in the group  $DG$ . Thus, the points of different types of site symmetry (Wyckoff positions) in  $DG$  may be specified by the same roman letters as in the corresponding groups  $G$  [16]. In layer groups the inversion center and the points of intersection of vertical and horizontal symmetry elements may be situated only in the layer plane. This means that the symmetry points of the Wigner–Seitz cell for a layer group  $DG$  may appear only in its intersection with the layer plane. An example illustrating the Wyckoff positions connection in space group  $C_{2h}^5$  and layer DG 18, is given in [13].

It can be shown that all the irreps of DG are contained in the irreps of the related space group G. The simple connection between the irreps of G and DG may be established using (11.3), *i.e.* isomorphism  $DG \leftrightarrow G/T_3$ : every irrep of DG is related to a definite irrep of G (of the same dimension). In these irreps of G all the elements of the coset  $(R_i|\mathbf{v}_i + \mathbf{a}_n)T_3$  are mapped by the same matrix. In particular, all the translations in  $T_3$  (coset  $(E|\mathbf{0})T_3$ ) are mapped by unit matrices. We refer the reader to Chap. 6 in [13] for details. The same approach can be used to connect irreps of space group G with those of subperiodic rod group RD  $\leftrightarrow G/T^{(2)}$  ( $T^{(2)}$  is the two-dimensional group of translations in a plane that does not contain the one-dimensional translations of a rod group), [765]. The two-dimensional plane groups and the corresponding layer groups are isomorphic (see Table 11.1) and therefore have the same sets of irreps. The theory of induced reps described in Chap. 3 for triperiodic space groups G may be easily applied to diperiodic groups DG. The tables of simple induced reps of DG may be directly constructed by using this theory [13]. The induced reps of layer groups are useful when analyzing electron-density localization on a crystal surface. Such analysis is important in the study of chemisorption of atoms and molecules.

In order to understand the principal features of the origin of surface states it is important to know how the energy bands of a crystal look in terms of the diperiodic specification. The comparison of bulk and surface states according to the symmetry is based on the relation between the irreps of the corresponding tri- and diperiodic groups G and DG. The bulk states are specified by the wavevector  $\mathbf{k}^{(3)}$  in the three-dimensional BZ (BZ-3) for the group G. The surface states are classified by  $\mathbf{k}^{(2)}$  in the two-dimensional BZ (BZ-2) of the layer (plane) group DG. The choice of the translation vectors  $\mathbf{a}_1$  and  $\mathbf{a}_2$  in the surface plane defines its orientation relative to the primitive translation vectors  $\mathbf{a}_i^{(3)} (i = 1, 2, 3)$  of the corresponding space group G. The surface is identified by three integers  $(hkl)$  – Miller indices, specifying the atomic planes in the crystal by means of the components of a vector perpendicular to that plane. Planes perpendicular to crystallographic axes  $X, Y, Z$  are indicated  $(h00), (0k0)$  and  $(00l)$ , respectively. In particular, the planes closest to the origin are identified with indices  $(100), (010)$  and  $(001)$ . Planes parallel to one of the three axes  $X, Y, Z$  are indicated  $(0kl), (h0l)$  and  $(hk0)$ , respectively. When the surface reconstruction effects (change of the surface plane translational symmetry with respect to that of the perfect crystal) may be neglected, the symmetry group DG of a crystal with a surface is a subgroup of the bulk crystal group G. However, the BZ-2 depends on the indices of the surface plane.

Consider, for example, crystals with face-centered cubic Bravais lattices. For the  $(001), (110)$  and  $(111)$  sections the plane lattices are square, rectangular and hexagonal, respectively. The basic translation vectors of the direct and reciprocal lattices for these three cases are given in Table 11.2 ( $\mathbf{a}_1$  and  $\mathbf{a}_2$  are given in units  $a/2$ ,  $\mathbf{B}_i$  in units  $2\pi/a$ , where  $a$  is the cubic lattice parameter). Note that for a cubic lattice the planes  $(100), (010)$  and  $(001)$  are equivalent. The equivalence takes place also for  $(110), (101)$ , and  $(011)$  planes. We see that the vectors  $\mathbf{B}_i (i = 1, 2)$  are now not the translation vectors of the three-dimensional reciprocal lattice. Therefore, the boundaries of BZ-2 do not coincide with those of BZ-3.

Figure 11.1 shows the Brillouin zones corresponding to the surface  $(001), (110)$  and  $(111)$  inscribed in the three-dimensional Brillouin zone for a face-centered cubic lattice.

**Table 11.2.** Vectors of basis translations for three sections of a face-centered cubic Bravais lattice

Surface translation vectors	(001)	(110)	(111)
$\mathbf{a}_1$	110	-110	1-10
$\mathbf{a}_2$	1-10	002	10-1
$\mathbf{B}_1$	110	-110	2/3, -4/3, 2/3
$\mathbf{B}_2$	1-10	001	2/3, 2/3, -4/3

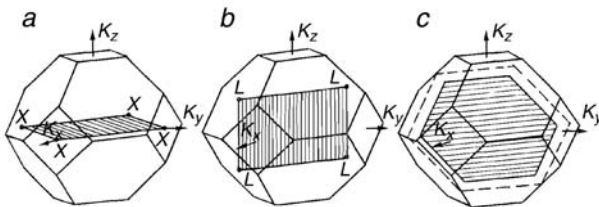


**Fig. 11.1.** Brillouin zones for a face-centered cubic lattice and surfaces (a) (001), (b) (110), (c) (111)

Note that some nonequivalent points of BZ-3 become equivalent in BZ-2 (for example, the points  $X$  for the surface (001) and the points  $L$  for the (110) surface). Some points of BZ-2 have higher symmetry than in BZ-3 (for example, the vertices of BZ-2 for the (111) surface). These properties of BZ-2 arise because the unit-cell vectors in the two-dimensional reciprocal space  $\mathbf{B}_i$  are not the lattice vectors of the three-dimensional reciprocal lattice.

To obtain the crystal energy band structure in terms of a diperiodic specification it is necessary to represent the dispersion law  $E = E_n(\mathbf{k}^{(3)})$  in the form

$$E_n^s(\mathbf{k}_\parallel^s) = E_n(\mathbf{k}_\parallel^s + \mathbf{k}_\perp - \mathbf{B}_n) \quad (11.5)$$

where  $\mathbf{k}_\parallel^s$  is a projection of the three-dimensional wavevector  $\mathbf{k}^{(3)}$  onto the surface and  $\mathbf{k}_\perp$  is its component perpendicular to the surface. The vector  $\mathbf{B}_n$  is assumed to be chosen so that the wavevector  $\mathbf{k}_\parallel^s = \mathbf{k}_\parallel + \mathbf{B}_n$  takes values in the limits of BZ-2. In the projection of the energy bands of the three-dimensional crystal on the two-dimensional Brillouin zone forbidden energy lacunas can appear. When the surface is taken into account, a band of surface states appears inside the energy lacuna. These surface states are analogous to the local energy levels of point defects that appear in the forbidden energy gap of a perfect crystal. The energy levels of surface states may arise in the continuous energy spectrum of a bulk three-dimensional perfect crystal. These are the so-called resonance surface states. They are analogous to the point defect states in the spectrum of bulk-crystal states.

In the next sections we describe the slab models of the surface and illustrate the choice of the slab by examples of metal oxides with sodium chloride, rutile and cubic perovskite structures.

### 11.1.2 Oxide-surface Types and Stability

Oxides are very common in nature and play a fundamental role in corrosion, friction, electronic devices and superconductivity. The study of the properties of oxide surfaces has an interdisciplinary nature, being included in several fields of research – not only solid-state chemistry and physics, but also electrochemistry, catalysis, electronics and even geophysics and geology. Nowadays, nanostructured surfaces are used as substrates for growing artificial structures, for example, to make quantum wires or size-controlled clusters.

The present understanding of oxide surfaces in the light of experimental and theoretical studies is summarized in books and review articles, see for example, [766–768]. Computer simulation plays an important role in the surface study and in recent decades has become an important tool for investigations of structural, electronic and catalytic properties of surfaces. Computer simulation of surfaces is based on two key issues – model of the surface and the Hamiltonian used for the chosen model. Methodological developments and the rapid improvement of computer hardware have enabled theorists to work with systems of increasing complexity and apply *ab-initio* (HF, DFT and hybrid) Hamiltonians in the surface calculations. Thereby, it is possible not only to reproduce experimental findings with increasing accuracy, but it is also possible to help in the prediction and interpretation of experimental results. As for models there were already mentioned both finite (molecular cluster and cyclic cluster), and infinite (semi-infinite crystal and slab) models. The model of a semiinfinite crystal is the most appropriate, because it takes into account an infinite number of atoms in the crystal below the surface. Slab and cluster models are, nevertheless, more popular, since they are more feasible from the computational point of view. The cyclic-cluster model is intermediate between the slab and molecular-cluster models. It takes into account the translational symmetry of the surface but considers only a finite number of interatomic interactions within a strictly defined region [320, 770].

The surface modeling is connected with the basic concepts, introduced by Tasker [772] in a discussion of the stability of surfaces of ionic or partly ionic crystals. According to classical electrostatic criteria, the stability of a compound surface depends on the characteristics of the charge distribution in the structural unit that repeats itself in the direction perpendicular to the surface. The surface can be studied by considering the crystal as a stack of atomic planes. Each plane consists of sublattices of nonequivalent atoms, a sum over each sublattice on each plane gives the total electrostatic potential. For perpendicular distances  $z$  greater than a few interionic spacings, the contribution from a planar sublattice reduces to the particularly simple form

$$V(z) = \frac{2\pi}{S} qz \quad (11.6)$$

where  $S$  is the area of the unit cell in the plane and  $q$  is the planar sublattice charge. This expression is identical to the potential due to an infinite charged plane of charge density  $\rho = \frac{q}{S}$ ; the field  $E = \frac{2\pi}{S} q$  due to the charged plane is constant. Since  $V(z)$  and  $E$  do not diminish with increasing distance  $z$  the electrostatic sum must be over the whole crystal as stacks of planes unless cancellation of these terms occurs. Although the potential  $V(z)$  becomes infinite at infinite distances from the plane, it should be noted that when the crystal is constructed as a neutral block the infinities cancel and the potential becomes constant at large distances. In fact, it becomes zero in all

cases except where there is a dipole moment perpendicular to the surface. Similarly the field  $E$  cancels to zero outside a neutral crystal block, irrespective of the stacking sequence.

The repeat unit of a stack of planes is introduced when analyzing the distribution of the bulk structure atoms over the atomic planes in the direction  $z$  normal to the surface. This distribution depends on the oxide bulk structure and Miller index, defining the surface. The three different possible stacking sequences define three types of surfaces.

As a simplest case of the *type-1 surface* we consider the (001) surface of MgO crystal (Fig. 11.2).

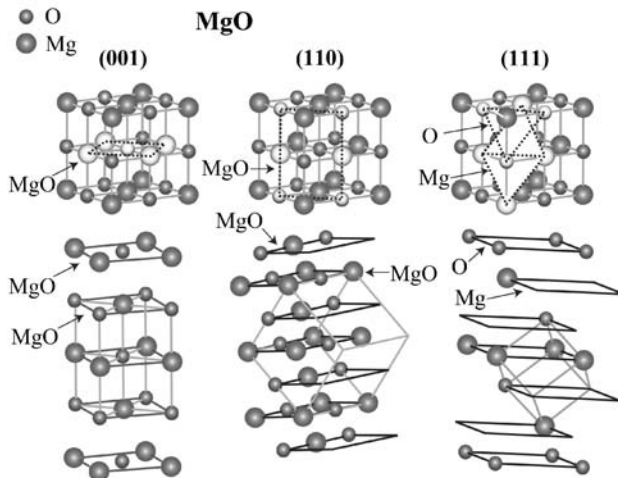


Fig. 11.2. Stacking of atomic planes for MgO surfaces

The neutral bulk unit cell consists of two atoms (Mg and O) and both of them occupy the same atomic plane. Each atomic plane has overall zero charge since it consists of both anions and cations in stoichiometric ratio. The potential  $V(z)$  cancels on each plane since the contributions of the sublattices are equal and opposite. Additional planes in the surface of the crystal make no contribution to the energy of ions in the bulk of crystal, and the lattice sums required for the Madelung energy at any ion site need include only a few planes either side of that site. It is seen from Fig. 11.2, that the (110) surface of MgO crystal refers also to type 1.

When a stacking sequence consists of charged planes, there are two possible cases. In the first case the repeat unit has no dipolar moment perpendicular to the surface (*type-2 surface*), in the second case the stack of charged planes has a nonzero dipole moment along the  $z$ -direction (*type-3 surface*).

For the type-2 surface each plane contributes a term in the potential  $V(z)$ , but a sum over the planes in repeat units cancels the potential to zero. Addition of extra neutral repeat units at the type-2 surface of the crystal cannot therefore affect the energy of ions in the bulk, and again the Madelung sums for the potential at any ion

site are rapidly convergent. The (110) surface of the  $\text{TiO}_2$  rutile structure (Fig. 11.3) is an example of a type-2 surface.

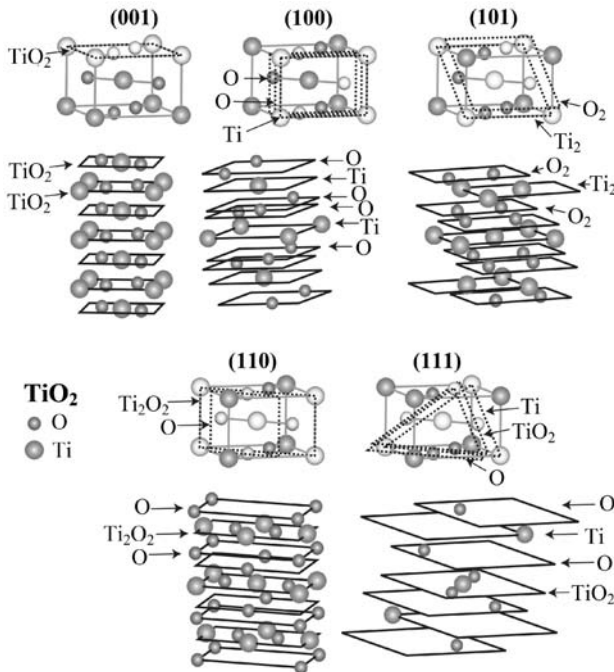


**Fig. 11.3.** Stacking of atomic planes for rutile  $\text{TiO}_2$  surfaces

Indeed, the bulk crystal unit  $\text{Ti}_2\text{O}_4$  atoms are distributed over three planes with the surface unit cells consisting of one oxygen atom (two planes) or  $\text{Ti}_2\text{O}_2$  units (one plane). The atomic planes in this repeating unit are charged ( $q = -2$  for oxygen planes and  $q = +4$  for  $\text{Ti}_2\text{O}_2$  planes). However, the stacking of planes with the repeat unit as  $\text{O}-\text{Ti}_2\text{O}_2-\text{O}$  allows one to obtain zero as its dipole moment along the  $z$ -direction. Two other terminations ( $\text{O}-\text{O}-\text{Ti}_2\text{O}_2$  and  $\text{Ti}_2\text{O}_2-\text{O}-\text{O}$ ) give the repeat unit that bears a nonzero dipole moment. This example demonstrates that the surface orientation only is not always sufficient to refer the surface to the one of three types, especially when various terminations may be produced. The atomic  $\text{TiO}_2$  planes in the repeat unit of the (001) surface of rutile (Fig. 11.3) are also charged ( $q = -2$ ), but the dipole moment of any stack of an integer number of such planes is again zero (type-2 surface). The repeat units for (100) and (101) type-2 surfaces have also zero dipole moment ( $\text{O}$ - and  $\text{O}_2$ -terminated repeat units of 6 and 3 atomic planes, respectively, can be chosen).

For the majority of cases of the oxide surfaces the stacking sequence of charged planes has a dipole moment perpendicular to the surface. In particular, the stacks of

alternately charged planes form the repeat unit for (111) surface of MgO (Fig. 11.2), (101) surface of TiO<sub>2</sub> (Fig. 11.3).

Table 11.3 gives the formal plane charges in the stack of different surfaces in the cubic perovskite ABO<sub>3</sub> crystal with one formula unit in the primitive unit cell. The bulk atoms distribution over atomic planes is shown on Fig. 11.4.

**Table 11.3.** Formal and calculated (in brackets) atomic planes charges of ABO<sub>3</sub> cubic perovskite

Surface	(001)		(110)		(111)	
Termination	AO	BO <sub>2</sub>	ABO	O <sub>2</sub>	AO <sub>3</sub>	B
A <sup>I</sup> B <sup>V</sup> O <sub>3</sub> (KNbO <sub>3</sub> )	-1		+1	+4	-4	-5
A <sup>II</sup> B <sup>IV</sup> O <sub>3</sub> (SrTiO <sub>3</sub> )	0(+0.27)		0(-0.27)	+4	-4	-4
A <sup>III</sup> Bi <sup>II</sup> O <sub>3</sub> (LaMnO <sub>3</sub> )	+1(+0.95)	-1(-0.95)		+4	-4	-3

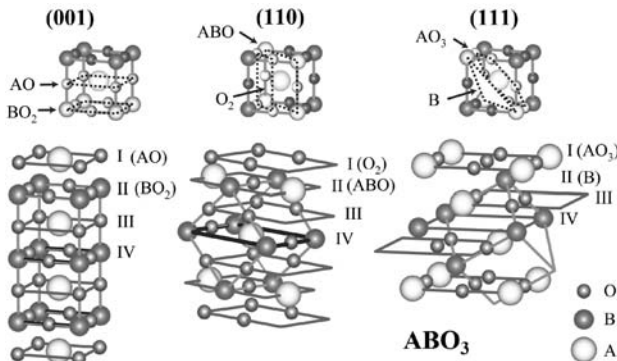


**Fig. 11.4.** Stacking of atomic planes for cubic perovskite ABO<sub>3</sub> surfaces

All the surfaces in cubic perovskite structure are type-3 surfaces being stacks of alternately charged planes. It is less obvious in the case of the (001) surface in A<sup>II</sup>B<sup>IV</sup>O<sub>3</sub> as the repeat unit consists of neutral atomic planes (see below). It is also seen that the charge of the atomic plane depends both on the oxidation states of A and B atoms (the sum of oxidation states is in all cases 6) and Miller indexes of the surface.

For the stacking sequence of alternately charged planes (producing a dipole moment perpendicular to the surface) the two-plane repeat unit produces a potential at large distances whose magnitude is given by

$$V = 2\pi|q|\frac{a}{S} \quad (11.7)$$

where  $a$  is the interplanar spacing. Addition of an extra neutral repeat unit of two planes on the surface of the crystal will affect the energy of ions an infinite distance

below the surface. Consequently, the Madelung sum cannot be truncated and must include contributions from every plane out to the surface. The potential at any ion site never reaches a constant bulk value, the energy of a neutral pair of ions never reaches the usual cohesion energy and the surface energy is infinite [772]. The stacking of planes for rutile (100), (101) and (111) type-3 surfaces is more complicated as it can not be named as the stacking sequence of alternatively charged planes.

The classification of the surfaces by Tasker is based on the formal ionicities (oxidation states) of metal atoms. As we already noted, the oxidation state and calculated atomic charges are close only in purely ionic compounds (MgO, for example). As we have seen in Chap. 9, the transition-metal atoms charges differ essentially from the oxidation states due to the covalence part of the chemical bonding with oxygen atom.

In Table 11.3 are given in brackets the atomic planes charges for (001) surface in  $\text{SrTiO}_3$  and  $\text{LaMnO}_3$  crystals calculated for the bulk crystals with the use of Wannier-type atomic functions in the population analysis, see Chap. 9 and reference [736]. As the Ti–O bond in  $\text{SrTiO}_3$  presents a non-negligible part of covalent character the actual charges of atomic planes  $\text{SrO}$  and  $\text{TiO}_2$  are nonzero. This means that  $\text{SrTiO}_3$  (001) should be considered as a polar (type-3) surface.

Type-1 or -2 surfaces have a zero dipole moment in their repeat unit and are thus potentially stable. By contrast, polar type-3 surfaces have a diverging electrostatic surface energy due to the presence of a nonzero dipole moment not only on the outer layers, but on all the repeat units throughout the material, [768]. An electrostatic instability of type-3 surfaces results from the presence of that macroscopic dipole. Type-3 surfaces can be stabilized when the macroscopic field is removed by surface reconstruction, absorption of charged specks and so on. The modification of the surface electronic structure due to the reconstruction introduces compensating charges in the outer planes, stabilizing the surface structure. The absorption of charged specks is also a very effective mechanism to achieve the stabilization of polar orientations. Indeed, polar orientations are generally much more reactive than cleavage planes [768].

The classification of surfaces considered above was introduced for ionic or semi-ionic metal oxides. In covalent solids, the creation of a surface requires cutting covalent bonds, which means that dangling bonds would be present at the surface. The saturation of dangling bonds by chemisorption is important, for example, in silicates. When a surface is cut out from the bulk, unstable Si–O radicals at the surface react readily with water to give a fully hydroxylated surface with hydrophilic character [568].

Tasker's classification of surfaces allows some qualitative conclusions to be made about the surface stability. The quantitative calculations of the surface formation energy in slab models are considered in the next sections.

### 11.1.3 Single- and Periodic-slab Models of $\text{MgO}$ and $\text{TiO}_2$ Surfaces

As was seen above in the slab model the surface plane is supposed to be fixed by its orientation (by the set of Miller indices) relative to the bulk structure and its symmetry elements. All the atoms of the bulk primitive unit cell are distributed within one or several atomic planes with the same 2D-translation periodicity, see Figures 11.2–11.4. Let these planes of atoms form a layer, being stoichiometric and neutral as by definition it contains all the atoms of the bulk primitive unit cell. Depending on the host-crystal structure the one-layer single slab can have zero (types-1 and type-2 surfaces) or nonzero (type-3 surfaces) dipole moment along the normal

to the surface plane. To ensure the zero dipole moment in the type-3 surface modeling the nonstoichiometric slabs can be used.

Figure 11.3 shows that for the type-3 (111) surface of rutile  $\text{TiO}_2$  structure O- or  $\text{TiO}_2$ -terminated layer of the smallest thickness consists of 5 atomic planes: O–Ti–O– $\text{TiO}_2$ –O or  $\text{TiO}_2$ –O–Ti–O– $\text{TiO}_2$ , respectively.

For the cubic perovskite  $\text{ABO}_3$  (001) surface the nonstoichiometric slabs with AO or  $\text{BO}_2$  terminations can be introduced. Figure 11.4 shows a AO-terminated slab, consisting of 7 atomic planes – 4 AO planes and 3  $\text{BO}_2$  planes. As is seen from Fig. 11.4, the slab termination is different for different surfaces.

The symmetry of the single slab corresponds to one of 80 diperiodic (layer) space groups. Fig. 11.5 shows a 3-layer single-slab model of (001) surface of  $\text{MgO}$  crystal (each layer consists of one atomic plane). The symmetry group of this slab DG61 ( $P4/mmm$ ) belongs to a square system.

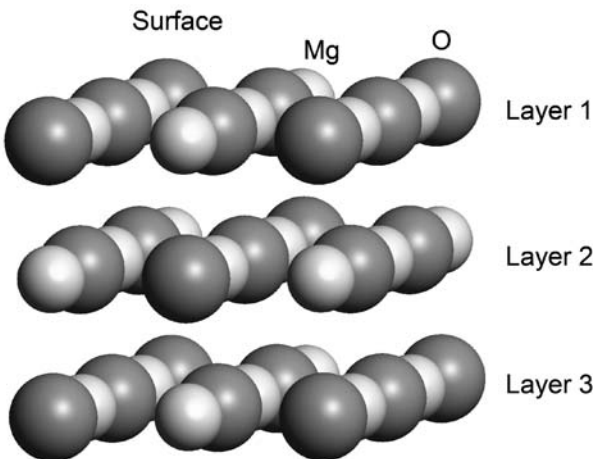
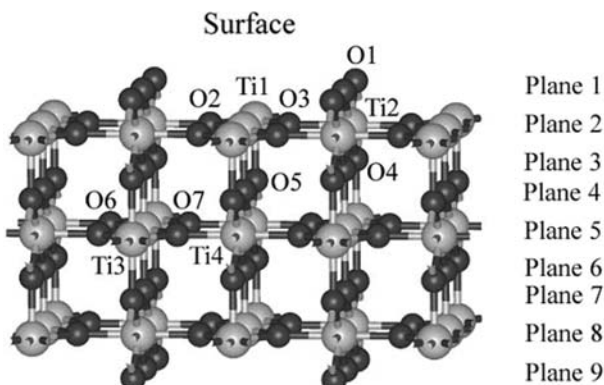


Fig. 11.5. 3-layer (3-plane) slab for  $\text{MgO}$  (001) surface

Figure 11.6 shows a 3-layer single slab of (110) rutile  $\text{TiO}_2$ . In this case each layer consists of 3 atomic planes. In particular, the upper layer includes an oxygen plane (O1 atoms), a  $\text{Ti}_2\text{O}_2$  plane ( $\text{Ti}_1, \text{Ti}_2, \text{O}_2, \text{O}_3$  atoms) and an oxygen plane (O4 atoms). Oxygen atoms O5 belong to the next O– $\text{Ti}_2\text{O}_2$ –O layer. The symmetry group of this slab is DG37 ( $Pmmm$ ).

In the multislab model (periodically repeated slab) the 3D periodicity is restored: slab of  $n$  layers ( $nL$ -slab) is supposed to be periodically repeated along the normal to the surface (let the translation vector of a single slab be  $\mathbf{c}$ ). Figures 11.7 and 11.8 show the periodic 3-layer slabs, modeling  $\text{MgO}$  (001) and  $\text{TiO}_2$  (110) surfaces, respectively. The corresponding space symmetry groups can be found from Table 11.1: G123( $D_{4h}^1$ ) and G47( $D_{2h}^1$ ), for  $\text{MgO}$  and  $\text{TiO}_2$  3-layer slabs, respectively.

In 3D-slab calculations the results depend not only on the number of layers in the slab (slab thickness), but also on the separation between periodically repeated



**Fig. 11.6.** 3-layer (9-plane) slab for rutile  $\text{TiO}_2$  (110) surface

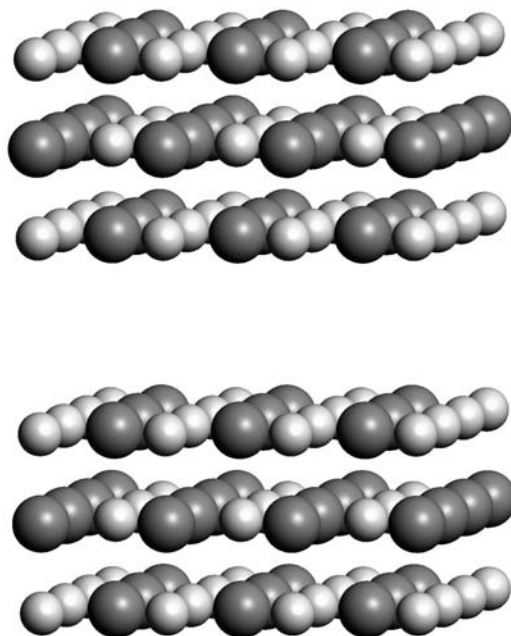


**Fig. 11.7.** Periodic slab model of (001)  $\text{MgO}$  surface

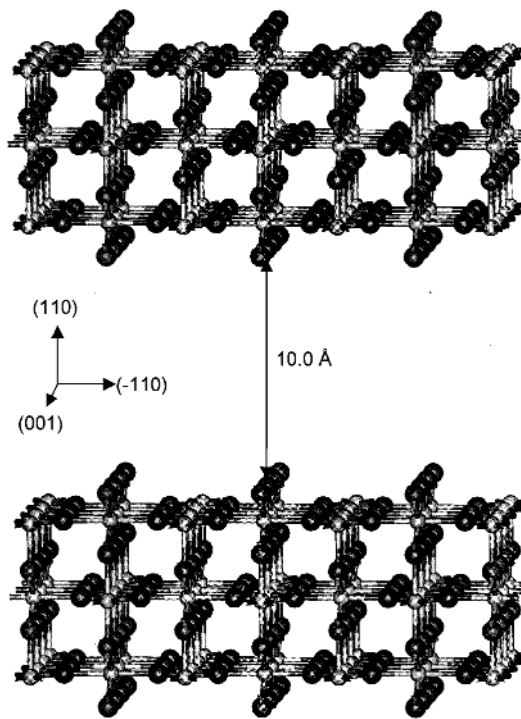


**Fig. 11.8.** Periodic slab model of rutile  $\text{TiO}_2$  (110) surface

slabs defined both by the slab thickness and the length of the translation vector along the normal to the surface. The interslab distance (vacuum gap) is equal to the difference between the length of translation vector  $\mathbf{c}$  and the vertical distance between the top atoms of one slab and the nearest repeated one, *i.e.* the difference between the translation vector  $\mathbf{c}$  and the single slab thickness (see Figures 11.7 and 11.8).

The symmetry of the 3D-slab model is given by one of the 3D space groups  $G$  (see Table 11.1) and may depend on the slab thickness, *i.e.* number of layers in the slab and its termination. As is seen from Fig. 11.1, for  $\text{MgO}$  crystal (001) surface slabs of an odd number of atomic planes have inversion symmetry (relative to the central atomic plane) but slabs of an even number of atomic planes have no inversion symmetry. For the cubic perovskite  $\text{ABO}_3$  (001) surface the stoichiometric slabs ( $\text{AO}-\text{BO}_2-\text{AO}-\text{BO}_2-$ ) consist of an even number of atomic planes and have no inversion symmetry. But the nonstoichiometric  $\text{AO}$ - or  $\text{BO}_2$ -terminated slabs have inversion symmetry relative to the central  $\text{AO}$  or  $\text{BO}_2$  planes, respectively.

Note that the space-symmetry group of a periodic slab differs from the space group of the host crystal. As an example, we consider  $\text{MgO}$  crystal with symmetry of space group  $O_h^5$ . The single-slab model refers to a square lattice and has the symmetry of

DG 61 ( $P4/mmm$ ) or DG 51 ( $P4mm$ ) for slabs of odd and even number of planes, respectively (see Figures 11.2 and 11.5). As is seen from Table 11.1, the periodic slab model in these cases has the symmetry of  $D_{4h}^1$  (G123) or  $C_{4v}^1$  (G99) space groups, respectively.

One of the goals of slab-model studies is to investigate the dependence of the calculated surface energy on the dimensionality of the slab model and on the Hamiltonian applied. The surface energy  $E_s^n$  per unity of surface area for an  $n$ -layer slab is defined by the relation

$$E_s^n = \lim_{n, W \rightarrow \infty} \frac{1}{2S} [E(n, W) - nE_b] \quad (11.8)$$

where  $E(n, W)$  is the total energy in a 3D-slab calculation of an  $n$ -layer slab with the vacuum gap  $W$  and  $E_b$  is the total energy of primitive unit cell in a separate bulk calculation. In the 2D-slab model  $W$  is infinite, *i.e.*  $E(n, \infty)$  is the  $n$ -layer single slab energy  $E(n)$ . In (11.8)  $S$  is the surface area per repeating 2D-unit cell, the factor  $1/2$  accounts for the existence of two limiting surfaces.  $E_s^n$  is the energy per unit area required to form the surface from the bulk, and it is intrinsically a positive quantity.

The value of surface energy is very dependent not only on  $E(n, W)$  but also on the bulk total energy  $E_b$  used in (11.8). In (11.8) total energies from 3D ( $E(n, W)$ ) or 2D ( $E(n, \infty)$ ) systems are used, creating a problem of equivalent accuracy in periodic codes for 3D and 2D systems. Boettger pointed out [773] that any difference between  $E_b$  and the change in  $E(n, w)$  with slab thickness will cause the calculated surface energy to diverge linearly with  $n$ . Thus, increasing the slab thickness must sooner or later lead to unacceptable results because the bulk energy from a separate calculation will never exactly equal the slope of the slab energy versus  $n$ , [774]. To avoid the divergence problem, it was suggested [773], for each slab thickness  $n$ , pick as the bulk energy  $E_b$  the differential increase in the slab total energy upon addition of one layer of material:

$$E_s^n = \lim_{n, W \rightarrow \infty} \frac{1}{2S} [E(n, W) - n(E(n, W) - E(n - 1, W))] \quad (11.9)$$

In this expression,  $E_b$  has been replaced by  $(E(n, W) - E(n - 1, W))$ . This relation has the merit of using only slab-related quantities, making no reference to separately calculated bulk energies.

The surface formation-energy calculations impose two strong requirements to the accuracy of calculated energies: (1) numerical precision, and (2) computational consistency. While the first condition may be relatively easily satisfied by increasing the computational thresholds, the second one can lead to considerable problems due to inevitable approximations that are inherent to all quantum-mechanical computation techniques [679]. The surface modeling of real interest lies in a semi-infinite crystal *i.e.* the calculation of the surface energy limit when  $n$  and  $W$  tend to infinity. However, one could not *a priori* guarantee the convergence to definite limit in (11.8). So, the existence of such a limit is the obligatory condition for the possibility to obtain the correct value of  $E_s$  using slab models.

Use of different surface models (2D- and 3D-slabs) and basis sets in HF (LCAO) and DFT (PW) calculations makes it difficult to understand the origin of differences in calculated results that may be due both to the model applied and to the features of the calculation scheme chosen (basis set, integral approximations, Brillouin-zone sampling, and so on).

The first attempt to compare 2D- and 3D-slab models within the same calculation scheme was made in [775] for HF LCAO studies of the surface properties of  $\text{BaTiO}_3$  in the cubic perovskite structure. The authors of [775] concluded that results for periodic 3D-slabs are systematically affected by the interactions among repeated images, and possibly the fictitious field imposed by periodic boundary conditions.

In the LCAO approximation (for HF, KS and hybrid HF-DFT Hamiltonians) the systems periodic in 2 (2D-slabs) and 3 dimensions (3D-crystals) can be treated on an equal footing. The LCAO package CRYSTAL [23] gives the unique possibility to compare results of 2D- and 3D-slab models when the LCAO basis set is used. Such a comparison was made in [776] for the (001) surface of  $\text{MgO}$  crystal and in [777] for the (110) surface of rutile  $\text{TiO}_2$ .

We discuss here the results for  $\text{MgO}$  crystal. In [776] the experimental value  $4.21 \text{ \AA}$  of the *fcc* lattice constant for the bulk crystal was adopted in slab calculations. As was already noted, the square unit cell of one layer is stoichiometric as it consists of one Mg and one O atoms lying in one (001) plane (see Fig. 11.5). The calculations were made for single slabs of one to twenty atomic layers in a truncated-bulk geometry without relaxing the positions of atoms. The converged surface energy value was obtained for the single slab of 5 layers. The dependence of 3D-slab calculations results on the vacuum gap was investigated via calculating the 5-layer 3D-slabs with gaps up to  $42 \text{ \AA}$ . The symmetry of slabs depends both on the 2D or 3D periodicity and on the evenness of the number  $n$  of atomic layers. For 3-D slabs the tetragonal space groups G 123 ( $P4/mmm$ ) and G 99 ( $P4mm$ ) with tetragonal lattice constant  $a' = a/2 = 2.977 \text{ \AA}$  were used for odd and even  $n$ , respectively. The translation vector  $\mathbf{c}$  was varied in the calculations.

Table 11.4 shows the convergence of results for the single slab (2D)  $\text{MgO}$  (001) surface model depending on the slab thickness.

**Table 11.4.** Convergence of results for the  $\text{MgO}$  (001) single slabs depending on the 2D slab thickness ( $E_s$  – surface energy in  $\text{J/m}^2$ ,  $E_F$  – Fermi energy in  $\text{H}$ ), [776]

Number of layers, $n$	HF		DFT (default ABS)		DFT (extra ABS)	
	$E_s$	$E_F$	$E_s$	$E_F$	$E_s$	$E_F$
1	1.4571	-0.3293	1.5516	-0.1035	1.5506	-0.1075
2	1.4689	-0.3397	1.5766	-0.1082	1.5344	-0.1226
3	1.4678	-0.3403	1.5341	-0.1217	1.5335	-0.1217
4	1.4678	-0.3407	1.5630	-0.1140	1.5339	-0.1208
5	1.4678	-0.3409	1.5341	-0.1204	1.5336	-0.1203
6	1.4678	-0.3410	1.5554	-0.1157	1.5337	-0.1199
9	1.4678	-0.3413	1.5342	-0.1193	1.5337	-0.1193
12	1.4678	-0.3414	1.5460	-0.1171	1.5338	-0.1190
15	1.4678	-0.3415	1.5345	-0.1188	1.5338	-0.1189
20	1.4678	-0.3415	1.5417	-0.1175	1.5338	-0.1187

To eliminate the results dependence on Brillouin-zone sampling the dense Monkhorst–Pack  $\mathbf{k}$ -point mesh was used. For primitive unit cells the  $12 \times 12 \times 12$  and  $12 \times 12$  special-point sets have been taken for bulk and slab calculations, respectively. In the case of 3D-slabs the number of points in the third  $\mathbf{k}$ -direction depends on the chosen value of the  $\mathbf{c}$  translation vector in direct space. The latter was chosen to provide a similar size in all directions of the corresponding cyclic model of the crystal (the crystal is composed of equidistant supercells). The increasing of the 3D unit cell in direct space for producing the 2D supercell was accompanied by the corresponding reduction in the  $\mathbf{k}$ -points mesh in the reciprocal space.

The same all-electron basis sets have been used both in HF and DFT calculations to allow the direct comparison of obtained energies. The choice of high precision tolerances for the Gaussian overlap criteria in truncation of Coulomb and exchange series ensured the high numerical accuracy required for the evaluation of the corresponding surface energy. In DFT calculations the exchange and correlation were treated in PWGGA approximation. In the CRYSTAL code the periodic DFT version in a basis of local Gaussian-type functions is implemented to avoid the numerical integration. This auxiliary basis set (ABS) is used for fitting the exchange-correlation potential. In DFT computations two types of ABS were used: (1) ABS1—even tempered basis set of 12  $s$ -type Gaussian-type functions, and (2) the basis proposed with extra  $p$ ,  $d$ ,  $f$ , and  $g$ -functions ABS-2.

Table 11.4 shows the fast convergence of 2D periodic results for surface energy with increasing number of layers. Three to five MgO layers are sufficient to obtain the converged values of the HF surface energy for unrelaxed slabs, in agreement with the results of other calculations, [778]. The convergence of the Fermi-level energy (highest-occupied one-electron energy level for the slab) is much slower. The limiting value seems to be reached just at  $n = 20$ . As seen from Table 11.4, the use of extended ABS2 (for the fitting of the exchange-correlation potential) proved to be necessary for obtaining the convergence of the surface energies. The DFT values of surface energy exhibit a similar fast convergence with the slab thickness as HF values, and the difference between HF and DFT surface energy does not exceed 5%. However, the initial part of  $E_s^n$  for  $n = 3$  has a different sign of slope for these two methods. The DFT result, which corresponds to decreasing of  $E_s^n$  with  $n$ , seems to be more physically reliable.

There is no large discrepancy between HF and DFT atomic charges, although the latter exhibit a slightly more covalent character [776].

The numerical value of Fermi energy  $E_F$  may be used for approximate estimation (according to the Koopmans' theorem) of the surface ionization potential that defines the adsorption energies. Due to the correlation effects the DFT Fermi energy  $E_F$  differs essentially from that in HF calculations. Table 11.4 shows that  $E_F$  is inside the valence band of a perfect crystal, *i.e.* the resonance surface states are predicted both in HF and DFT single-slab calculations.

Taking into account the convergence of results obtained for 2D slabs, only the 5-layer 3D models have been calculated in [776]. The results are given in Table 11.5. Table 11.5 shows that the 3D-slab with vacuum gap 6–8 Å gives the converged (001) surface energy of ionic MgO crystal. The DFT values of  $E_s^n$  exhibit a similar fast convergence as HF ones and the difference between them is small. The convergence of the surface energy with the single-slab thickness is slower for rutile  $\text{TiO}_2$  due to

**Table 11.5.** Convergence of the results for the periodically repeated 3D MgO (001) unrelaxed slab depending on the vacuum gap for 5-layer models (primitive 2D cell), [776], ( $E_s$  – surface energy in  $\text{J}/\text{m}^2$ ,  $E_F$  – Fermi energy in a.u.)

Cell dimensions, Å	Gap	C	k-point set	HF		DFT	
				$E_s$	$E_F$	$E_s$	$E_F$
∞	∞		12 12	1.468	-0.3409	1.532	-0.1202
2.105	10.525		12 12 4	5.365	-0.2458	4.8937	-0.0486
4.210	12.630		12 12 3	1.503	-0.3181	1.555	-0.1164
6.315	14.735		12 12 3	1.468	-0.3215	1.533	-0.1170
8.420	16.840		12 12 2	1.468	-0.3239	1.533	-0.1174
12.630	21.050		12 12 2	1.468	-0.3273	1.533	-0.1180
21.050	29.470		12 12 1	1.468	-0.3312	1.533	-0.1186
42.100	50.520		12 12 1	1.468	-0.3352	1.532	-0.1193

the partly covalent Ti–O interaction. Table 11.6 demonstrates the convergence of the surface energy in all-electron HF LCAO single-slab calculations [777] of the (110) surface of rutile  $\text{TiO}_2$ .

**Table 11.6.** Convergence of the results for single-slab (2D) model of (110) rutile  $\text{TiO}_2$  surface, [777], ( $E_s$  – surface energy,  $E_F$  – Fermi energy)

No. of atomic planes (layers)	No. of Ti planes	Total energy (a.u)	$E_s$ ( $\text{J}/\text{m}^2$ )	$E_F$ (a.u)
Perfect crystal	–	-1996.8016	–	-0.3077
9	3	-5990.211	2.193	-0.4171
15	5	-9983.815	2.183	-0.4235
21	7	-13977.418	2.183	-0.4237
27	9	-17971.021	2.183	-0.4237

It follows from Table 11.6 that surface energy is sufficiently well reproduced for the 5 layers (15 atomic planes) slab, in accordance with the results of HF all-electron calculations [779].

As in the case of MgO crystal the convergence of the Fermi energy with slab thickness is much slower than that of surface energy (see the last column of Table 11.6). Calculations of 3D-slabs for rutile  $\text{TiO}_2$  [777] show that the periodic supercells in the plane with extensions  $2c \times 2a\sqrt{2}$  and  $2c \times a\sqrt{2}$  give the same surface energies for the vacuum gap values 41 Å and 15 Å, respectively.

The LCAO approximation allows comparison of the electron-charge distribution in the bulk crystal and on the surface. The application of Wannier functions for this comparison can be found in [781], where the Boys localization criteria was applied and only the valence-band states were included for WFs generation (for bulk crystals such an approach is discussed in Chap. 9). As was seen in Chap. 9 for bulk crystals, the population analysis using Wannier-type atomic orbitals (WTAO) gives more adequate

results for charge distribution than traditional Mulliken population analysis or the projection techniques applied in PW calculations.

The WTAOs for systems with 2D periodicity were generated in [780] for the first time and used for the surface charge distribution analysis in a single-slab model of (001)MgO and (110)TiO<sub>2</sub>. First, WFs of the bulk crystal, corresponding to valence bands, were used as a tool allowing one to estimate the values for the slab parameters needed to adequately model the surface electronic structure. Secondly, a minimal valence basis of WTAOs, which are the Wannier functions, generated from occupied and vacant Bloch states and centered on atoms, were used for the analysis of chemical bonding at the surfaces under study. HF LCAO calculations were performed for 3-layer single slabs of (001)MgO (3 atomic planes) and rutile (110) TiO<sub>2</sub> (9 atomic planes), see Figures 11.5 and 11.6.

For construction of the WTAOs for the minimal valence basis, the corresponding energy bands are to be chosen. The *s*- and *p*-bands of oxygen atoms form the higher valence bands in both slabs considered. In the case of the TiO<sub>2</sub> slab, the *d*-bands of the titanium atoms are the lower conduction bands, while the *s*-bands of the metal atoms in both slabs are located among vacant states high in energy. The latter makes the contribution of *s*-WTAOs of the metal atoms into the covalence of these atoms negligible.

One can estimate the slab thickness needed for surface modeling by a preliminary qualitative analysis of the behavior of WFs, corresponding to valence bands of a bulk crystal. Indeed, the offdiagonal elements of the density matrix of a bulk crystal fall off with distance as the Wannier functions of valence bands or faster (exponentially in the case of insulators), see Chap. 4. Thus, beyond a sufficiently large domain of the crystal (basic domain) the values of Wannier functions, assigned to the central unit cell of the domain, are negligible. Consequently, truncation of the rest of the crystal and imposition of the periodical boundary conditions on the domain-edge atoms, practically do not affect the electron-density distribution inside the domain chosen. The basic domain of the crystal corresponds to a special set of *k*-points, which provides a convergence of the calculation results relative to the extension of this set.

A similar ideology can be used for the slab model. Let us consider the slab as consisting of the finite number of atomic planes. Let, at the surface planes of the slab chosen, the numerical values of bulk valence-band WFs be close to zero. The corresponding number of atomic planes determines the minimal thickness of a slab for the studied surface, which can be expected to provide the convergence of the results relative to increasing its thickness. However, the convergence might not occur for the chosen thickness of the slab due to an absence of periodical boundary conditions at the slab surface. But, if the slab WFs, localized in its central part, are close to the bulk ones and the localization of the slab WFs, centered near the slab edge, is to a certain extent the same as in the bulk crystal, the electron density in the middle part of the slab do not differ much from the bulk electron density, and would not change when the thickness of the slab is increased. Thus, the analysis of bulk WFs can help in estimating the slab thickness, which allows the bulk-like results in the central planes of the slab to be obtained and thus corresponds to more or less adequate surface modeling. Still, this is only a qualitative and estimative analysis.

Let us illustrate the aforesaid by the results obtained for MgO and TiO<sub>2</sub> crystals. In [780] it is shown that Wannier functions for the valence bands of the bulk MgO

crystal calculated along the [001] direction are practically completely localized inside a domain containing just three (001) atomic planes. Furthermore, according to calculations the difference between these WFs and the WFs generated for the slab and centered on the plane 2 (see Fig. 11.5), is negligible. This means that the 3-plane slab is sufficient for modeling the (001)-surface properties of MgO. As we demonstrated above, this consideration is, in principal, confirmed by thorough calculations of MgO slabs with a varied thickness – the surface energy and other characteristics converge at the 3-plane slab.

In the case of TiO<sub>2</sub> the bulk WFs does not fit into the 9 atomic planes shown in Fig. 11.6. As a result, the WFs, calculated from the slab states and localized in the “central” region of the slab, are different from the corresponding bulk WFs. Consequently, 9 planes are not sufficient for correct modeling of the TiO<sub>2</sub> crystalline surface. This result correlates with the results given in Table 11.6.

As seen from Table 11.7A the values of atomic charges for the MgO slab correspond to the purely ionic type of chemical bonding both at the surface and inside the slab. The charges in the slab model practically coincide with the bulk ones. The results, obtained by the WTAOs method and according to the traditional Mulliken and Löwdin schemes, are nearly the same.

**Table 11.7.** Atomic charges for the single MgO 3-plane (001)-surface and TiO<sub>2</sub> 9-plane (110) surface slabs and bulk crystals, [780], (NWTAO is nonorthogonal WTAO, OWTAO is orthogonal WTAO)

A) MgO crystal

Atoms	Atomic charges,  e			
	NWTAOs	OWTAOs	Mulliken	Löwdin
O1, Surface	-1.98	-1.96	-1.96	-1.83
Mg1, Surface	2.00	1.97	1.96	1.83
O2	-1.99	-1.96	-1.97	-1.82
Mg2	1.97	1.95	1.97	1.82
O Bulk	-2.00	-1.98	-1.98	-1.82

B) TiO<sub>2</sub> crystal

Planes	Atoms	Atomic charges,  e			
		NWTAOs	OWTAOs	Mulliken	Löwdin
1	O1, surface	-1.33	-1.30	-1.13	-0.88
2	Ti1, surface	2.99	2.87	2.62	1.84
	Ti2	2.86	2.79	2.54	1.63
	O2,3, surface	-1.48	-1.44	-1.35	-0.86
3	O4	-1.57	-1.51	-1.38	-0.91
4	O5	-1.54	-1.45	-1.28	-0.82
5	Ti3	3.06	2.95	2.66	1.72
	Ti4	3.01	2.93	2.65	1.73
	O6,7	-1.50	-1.46	-1.33	-0.87
Bulk	Ti	2.76	2.70	2.66	1.72
	O	-1.38	-1.35	-1.33	-0.86

For the  $\text{TiO}_2$  slab the Mulliken and Löwdin population analyses give contradictory results. Particularly, as noted in Table 11.7B, the values of atomic charges at the surface planes of the slab, calculated according to the Mulliken scheme, are smaller in magnitude than those inside the slab. This corresponds to a lower ionicity at the crystalline surface compared to the bulk. An opposite tendency is demonstrated in the Löwdin analysis, where the surface charges are larger or the same as in the bulk. Besides, the absolute values of the charges obtained according to the two traditional schemes are quite different from each other. Table 11.7B shows that the analysis performed by the orthogonal and nonorthogonal WTAOs gives approximately the same results. They show the tendency of decreasing the ionicity level at the surface, which is similar to the results of the traditional Mulliken analysis.

Let us consider the values of atomic charges, obtained for the central planes of the slab (planes 3–7 on Fig. 11.6). Due to the symmetry of the slab the planes 6 and 7 are equivalent to the planes 4 and 3, respectively. As noted above, a nine-plane slab is not sufficient to model the  $\text{TiO}_2$  surface, as the electron density at the central planes of the slab is different from that of the bulk crystal. However, the values of atomic charges calculated according to both the Mulliken and Löwdin schemes practically coincide with the bulk ones (Table 11.7B). In contrast to these results, the population analysis based on WTAOs reproduces this slab-bulk misfit: the values for the charges of atoms of the inner planes in the slab and the bulk crystal differ noticeably.

When analyzing the Ti–O bond orders, which are given in Table 11.8, one can conclude the following.

The values, obtained by the two traditional schemes, can be hardly interpreted. Some of the bonds have the same orders in both schemes ( $\text{Ti1–O5}$ ,  $\text{Ti2–O1}$ ,  $\text{Ti3–O4}$ ,  $\text{Ti4–O5}$ ), while the others are essentially different ( $\text{Ti1–O2}$ ,  $\text{Ti2–O2}$ ,  $\text{Ti3–O6}$ ,  $\text{Ti4–O6}$ ), see Fig. 11.6. As to the results obtained by orthogonal and nonorthogonal WTAOs, they are close for all the bonds under consideration.

Every oxygen atom (excluding the atoms O1) has two neighboring titanium atoms at a distance of 3.687 a.u. and one at 3.727 a.u. (three-coordinated atoms). The O1 atoms are two-coordinated and have the neighbors only at 3.687 a.u. The titanium atoms are six-coordinated ( $\text{Ti2}$ ,  $\text{Ti3}$ ,  $\text{Ti4}$ ) or five-coordinated ( $\text{Ti1}$ ) and have four neighboring oxygen atoms at 3.687 a.u. and two or one – at 3.727 a.u., respectively. Only for some of the atoms ( $\text{Ti2}$ ,  $\text{O2}$ ,  $\text{Ti4}$ ) do the Mulliken and Löwdin schemes allow the larger orders for the shorter bonds (among the nearest-neighbor Ti–O bonds) to be obtained. For other atoms the values of the shorter bonds orders are approximately of the same magnitude as the longer ones (O6) or even significantly smaller (Ti3, O4, O5), which is unreal from the chemical point of view. The WTAOs method for all the atoms gives the expected tendency – the shorter is a bond, the larger is the value of the corresponding bond order. Also, WTAOs analysis gives the noticeably larger values for the insurface bonds. This agrees with the decreased values of the atomic charges at the surface relative to those at the inner part of the slab.

The results of the calculations of atomic covalences are presented in Table 11.9. Again, the Mulliken and Löwdin methods demonstrate contradictory and obscure bulk–surface tendencies. For some atoms the values of the covalences, calculated according to the Mulliken scheme are close to the Löwdin ones, for the other they differ significantly. Thus, these coincidences of the Mulliken and Löwdin results can be regarded as casual. And since the nine-plane slab does not provide the bulk-like electron

**Table 11.8.** Orders of the bonds between the near-neighbour Ti and O atoms in the single  $\text{TiO}_2$  nine-plane (110)-surface slab and bulk crystal (NWTAO is nonorthogonal WTAO, OWTAO is orthogonal WTAO,  $d$  is a distance between neighbor atoms, s denotes in-surface atom), [780].

Atom	Neighbor atoms			Bond orders			
	Atom	$N$	$d$	NWTAO	OWTAO	Mulliken	Löwdin
O1	Ti2, s	2	3.687	0.54	0.55	0.80	0.79
	Ti1	4	3.687	0.37	0.39	0.42	0.62
	O5	1	3.727	0.17	0.25	0.62	0.63
Ti2	O1, s	2	3.687	0.54	0.55	0.80	0.79
	O4	2	3.687	0.27	0.29	0.47	0.50
	O2,3	2	3.727	0.11	0.13	0.17	0.40
O2,3	Ti1, s	2	3.687	0.37	0.39	0.42	0.62
	Ti2	1	3.727	0.11	0.13	0.17	0.40
O4	Ti2	2	3.687	0.27	0.29	0.47	0.50
	Ti3	1	3.727	0.17	0.21	0.52	0.54
O5	Ti4	2	3.687	0.30	0.32	0.52	0.54
	Ti1	1	3.727	0.17	0.25	0.62	0.63
Ti3	O6,7	4	3.687	0.31	0.32	0.34	0.54
	O4	2	3.727	0.17	0.21	0.52	0.54
Ti4	O5	4	3.687	0.30	0.32	0.52	0.54
	O6,7	2	3.727	0.22	0.23	0.34	0.53
O6,7	Ti3	2	3.687	0.31	0.32	0.34	0.54
	Ti4	1	3.727	0.22	0.23	0.34	0.53

**Table 11.9.** Atomic covalences for the single  $\text{TiO}_2$  nine-plane (110)-surface slab and bulk crystal, [780], (NWTAO is nonorthogonal WTAO, OWTAO is orthogonal WTAO)

Planes	Atoms	Atomic covalences			
		NWTAOs	OWTAOs	Mulliken	Löwdin
1	O1, surface	1.20	1.24	1.86	1.88
2	Ti1, surface	1.74	1.91	2.44	3.35
	Ti2	1.92	2.03	2.36	3.02
	O2,3, surface	0.95	1.02	1.28	2.01
3	O4	0.80	0.90	1.76	1.95
4	O5	0.85	0.99	1.92	2.07
5	Ti3	1.64	1.82	2.49	3.47
	Ti4	1.73	1.85	2.87	3.45
	O6,7	0.92	0.99	1.27	2.03
Bulk	Ti	2.06	2.16	2.15	3.46
	O	1.11	1.17	1.24	2.04

density in the middle of the slab, the correspondence between the values for the covalences of the bulk and slab atoms, obtained by the traditional population analysis schemes, also cannot be considered as reliable.

The WTAOs method, in its turn, allows one to obtain the values of atomic covalences in the slab, which can be physically interpreted. First, the values calculated with the orthogonal and nonorthogonal WTAOs are alike. Secondly, the inslab atoms have a covalence different from the bulk one. This result can be expected due to an insufficient thickness of the nine-plane slab for the  $\text{TiO}_2$  (110) surface modeling.

And last but not least, the results of the WTAOs population analysis clearly show the increase of the covalence at the surface of the slab when compared to the inslab values. The surface atom O1 has the maximal covalence among all the oxygen atoms of the slab. This effect is even sharper if it is remembered that this atom is only two-coordinated, while the others are three-coordinated. The large value of the covalence is also observed for the surface atoms O2/O3, but it is not as pronounced as for the atom O1. The atom Ti1, which can be regarded as a surface atom, has a smaller covalence than the atom Ti2, but taking into account that the former is only five-coordinated, one can conclude that the effect of higher covalence at the surface is valid for this atom as well.

The values of local characteristics of the slab electronic structure, differing from the bulk one, may indicate the possibility of significant structural relaxation of the studied  $\text{TiO}_2$  slab. This relaxation would involve insurface and intraslab atoms, since the  $\text{TiO}_2$  nine-plane slab at its inner planes does not reproduce the bulk electronic structure. Taking into account the results of the WTAO population analysis, one can assume that the atoms would shift so that the length of the bonds would increase or decrease to compensate the excessive or deficient values of the covalence, respectively. These considerations correlate with the studies of the geometry optimization in  $\text{TiO}_2$  slabs [782].

## 11.2 Surface LCAO Calculations on $\text{TiO}_2$ and $\text{SnO}_2$

### 11.2.1 Cluster Models of (110) $\text{TiO}_2$

Titanium dioxide (in rutile and anatase structures) is the most investigated crystalline system in the surface science of metal oxides. The review article [783] summarizes the results of experimental and theoretical studies of titanium dioxide (bulk and surface) made up to 2002 inclusive. The information about calculations of the surface reconstruction, surface defects and growth of metals on  $\text{TiO}_2$  is also included. The results of the later theoretical studies of rutile surfaces can be found in [784–795] and references therein. In the majority of the calculations the slab model was used for the study of periodic surface structures.

Here, we consider the molecular- and cyclic-cluster models of (110)  $\text{TiO}_2$ , following [770], where the connection between the slab and cluster models was considered by performing a symmetry analysis of the crystalline surface.

The cyclic-cluster (CC) model of the surface is connected to the slab-2D-supercell approach, but it is different due to the different introduction of cyclic boundary conditions (CBC). In the slab-supercell approach, these conditions are, in fact, introduced for a very large system, *e.g.*, for the main region of the 2D periodic plane lattice, so

that band-theory methods can be used in the slab calculations. In the CC model, the CBC are introduced for the cluster itself, so that the model turns out to be finite. The convergence of the results to the slab values must be investigated by increasing the CC. However, the CC approach offers evident advantages: (a) the spurious boundary effects of molecular clusters are absent; (b) the periodicity of adsorbed species or of defects is excluded because the CC is a finite system; (c) there is a one-to-one symmetry correspondence between the electronic states of the 2D CC and the band states of the corresponding slab model.

The CC model was applied in semiempirical calculations [796] of the adsorption geometry for organic adsorbates on a rutile (110) surface. The INDO parametrization scheme was modified to reproduce the experimental results for geometries of carbon- and nitrogen-containing molecules. The CC representing the rutile (110) surface consists of 120 atoms. It includes two layers of  $5 \times 2$  2D unit cells with six atoms in each 2D unit cell. It is seen from Fig. 11.6, that 2D primitive unit cells form a plane rectangular lattice with parameters  $c$  and  $a$  ( $a, c$  are the tetragonal lattice parameters of the bulk crystal).

The molecular-cluster (MC) model is extremely popular in surface simulations because of its simplicity and flexibility and the possibility of its use in the standard techniques of molecular quantum chemistry [320, 769]. It is also possible to study defects or adsorption reactions in the limit of low coverage. In the MC approach, a crystal with a surface is modeled by a finite (molecular) system consisting of atoms on the surface and of some atomic planes nearest to it. The 2D periodicity of the surface is disregarded so that the symmetry of such a model is described by one of the crystallographic point groups. In adsorption studies, the adsorbed species are included in the cluster-adsorbate systems. An MC is cut out of the slab to simulate a portion of the surface so that spurious effects arise that are related to the limited cluster size and to the presence of the boundary. To eliminate these effects, the dangling bonds are saturated either by hydrogen atoms or pseudoatoms or the whole cluster is placed in an external field simulating the influence of the bulk crystal [769].

In the MC model, the results critically depend on the choice of the cluster size, stoichiometry, and shape. Nevertheless, the MC model can provide useful information if the cluster is properly chosen and the influence of its size is investigated. A number of general rules were suggested in [770, 771] for the generation of an MC suitable for surface simulations based on the connection between the MC and the slab model. These rules have been intuitively applied in different studies, in most cases without explicitly considering the relationship between periodic and molecular models. The following rules allow artefacts of MC surface models to be minimized: (a) the clusters correctly reflect the stoichiometry of the bulk crystal and are electroneutral; (b) atoms on the crystal surface should be equivalent to those on the cluster surface except for corners and edges; (c) the average coordination of all cluster atoms is as close as possible to that of atoms on the crystal surface; (d) as many symmetry elements of the crystal surface as possible are retained in the cluster; and (e) an extension to rule (a) is that each layer of the cluster should have the stoichiometry of the crystal.

In fact, such principles of the MC choice ensure the simulation of the crystal surface as closely as possible and are directly connected with the 2D periodic slab model. By using 2D unit cells as basic units of the model clusters, it is possible to increase the cluster size in a systematic way and, thereby, to study the convergence behavior

of calculated surface properties. As examples of MC model applications to surface studies using some of the above-mentioned rules, calculations of MgO, TiO<sub>2</sub> (rutile, anatase structures), and Cr<sub>2</sub>O<sub>3</sub> (corundum structure) surfaces and adsorption of small molecules on them can be considered, see [770] and references therein. However, it is also possible to find examples in the literature where these rules have not been applied and, in part, unphysical results were obtained.

In MgO and NaCl crystals, the MCs were chosen [797] so that they simulated the 2D supercell of the surface and included several layers of the bulk crystal. For these crystals, the stoichiometry of the chosen MC was ensured by this choice.

For more complicated systems, *e.g.*, TiO<sub>2</sub> structures, the stoichiometry of the MC is only ensured when several additional oxygen atoms are added. There are two principle ways to add these additional atoms. They can be placed on the regular surface around the cluster. This is denoted as type A in Figures 11.9 and 11.10. In some cases, this procedure leads to clusters that do not correspond to rules (d) and (e). Another possibility is to place the additional atoms for saturation at irregular positions of the crystalline lattice so that rules (d) and (e) will be fulfilled. Examples of this second type (B) of cluster generation are presented in Figures 11.9 and 11.10.

If all layers of a multilayer cluster have the same stoichiometry, artificial polarization, which can affect the calculated surface properties, is reduced. To study the effect of the distribution of saturation atoms on the calculated properties of crystalline surfaces, the rutile (110) surface has been selected for the MSINDO calculations [770]. The water adsorption in the molecular and dissociated form was modeled on clusters of Ti<sub>5</sub>O<sub>10</sub>, Ti<sub>9</sub>O<sub>18</sub>, Ti<sub>14</sub>O<sub>28</sub>, and Ti<sub>18</sub>O<sub>36</sub> (Fig. 11.9) chosen according to the rules given above. Nevertheless, even if these rules are applied, several different types of clusters can be constructed. Two types of possible cluster models were used. In type-A clusters additional oxygen atoms, necessary to ensure total stoichiometry (shaded in Fig. 11.9), were placed at regular lattice positions. In type-B clusters additional oxygen atoms were placed at nonlattice positions to maximize the symmetry of the clusters and to reduce polarization, as discussed in the previous section.

**Table 11.10.** MSINDO adsorption energies (kJ/mol) for water adsorption on rutile (110) (relaxed cluster calculations), [770]

Cluster	Type A		Type B	
	molecular	dissociative	molecular	dissociative
Ti <sub>5</sub> O <sub>10</sub>	51	39	70	201
Ti <sub>9</sub> O <sub>18</sub>	139	-24	94	107
Ti <sub>14</sub> O <sub>28</sub>	66	8	92	143
Ti <sub>18</sub> O <sub>36</sub>	157	192	129	162
Ti <sub>49</sub> O <sub>98</sub>	120	151	119	157

The adsorption energies calculated with these small cluster models are presented in Table 11.10. The geometries of the clusters were optimized within the symmetry of the rutile structure. In model B, there are one or two more degrees of freedom for oxygen atoms in nonlattice positions.

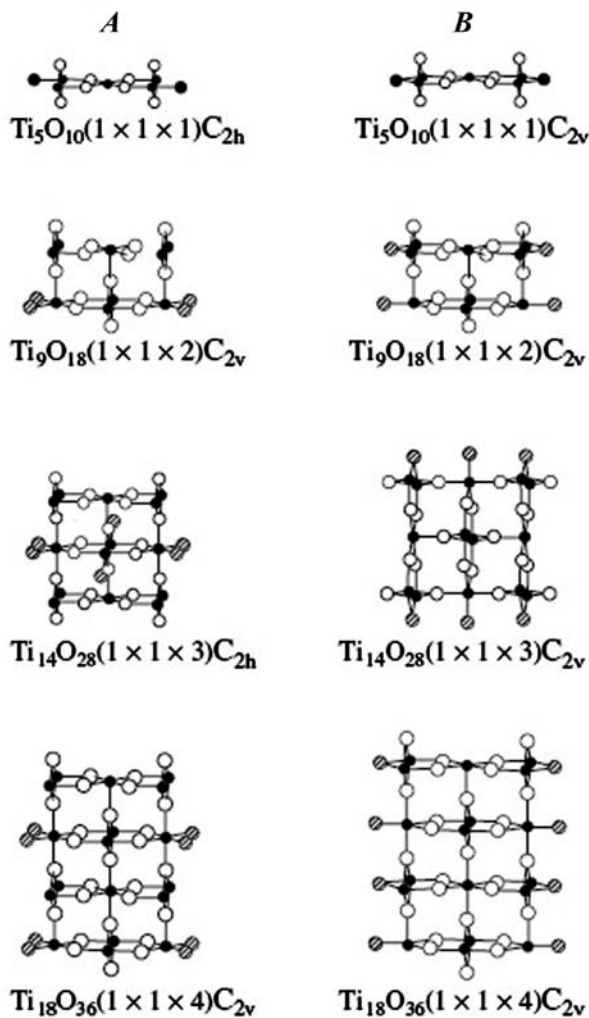


**Fig. 11.9.** Rutile (110) surface of size  $1 \times 1$ : 1–4 layer clusters of types A and B, [770]. Black, white and shaded spheres label Ti, O and additional O atoms.

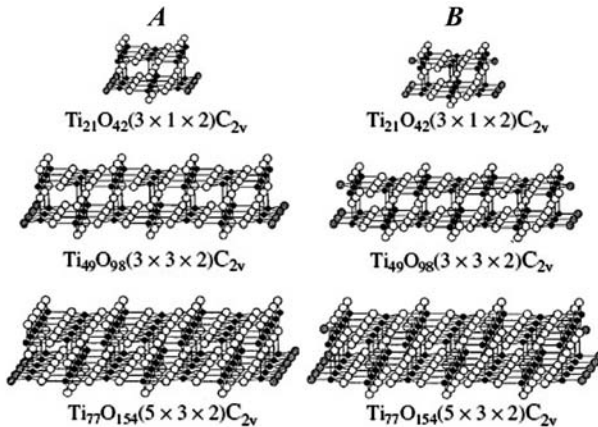


**Fig. 11.10.** Rutile (110) surfaces of size  $3 \times 1$ ,  $3 \times 3$  and  $5 \times 3$ : two-layer clusters of types A and B, [770]. The labels of atoms are the same as in Fig. 11.9.

For the cluster–water systems, the Cartesian coordinates of all water atoms, the two surface atoms close to the oxygen atom, and the hydrogen atom of water are optimized. The adsorption energy is calculated as the difference in the total energies of the  $\text{TiO}_2$  cluster and the cluster+ $\text{H}_2\text{O}$  system. Therefore, positive values indicate stabilization. A comparison is made with the results of the calculations on a much larger cluster,  $\text{Ti}_{49}\text{O}_{98}$  (Fig. 11.10), which is a better representation of the surface.

From Table 11.10, it can be seen that the different distribution of additional oxygen atoms in clusters A and B has a substantial influence on the calculated adsorption energies. The variation of adsorption energy with an increasing number of layers is significantly reduced if model B is considered. Even for rather small systems, the adsorption energies are relatively close to that of the largest cluster,  $\text{Ti}_{49}\text{O}_{98}$ . The most important difference between the two models is that only for model B is the dissociative adsorption always more stable than that of the molecular form. The relative stability of the two forms of water on the rutile (110) surface is still a matter of debate (see the next section). At the moment, we only focus on the convergence of results obtained for clusters with increasing sizes.

A comparison of models A and B of the largest cluster ( $\text{Ti}_{49}\text{O}_{98}$ ) shows that the influence of additional atoms is negligible due to their large distance from the adsorption position. This indicates that, in this case, it is the description of the local environment near the adsorption site rather than the effect of the global polarization of the cluster that is responsible for the differences observed for the smaller clusters. Thus, the numerical results for the adsorption behavior of rutile (110) towards water with different clusters demonstrate that convergence to the methodological limit is significantly improved if the criteria mentioned above are taken into account.

Since the underlying considerations are of a general nature, they can also be applied to cluster models of surfaces in other systems. In any case, only the comparison of the results of both slab and cluster models application allow those results of calcu-

lations that can be taken as confident to be extracted. In the next section we consider this point returning to the water adsorption on the (110) surface of rutile.

### 11.2.2 Adsorption of Water on the $\text{TiO}_2$ (Rutile) (110) Surface: Comparison of Periodic LCAO-PW and Embedded-cluster LCAO Calculations

The adsorption of water on  $\text{TiO}_2$  surfaces has been extensively investigated using both experimental and theoretical methods, see [790] and references therein. Nevertheless, the adsorption of  $\text{H}_2\text{O}$  on the  $\text{TiO}_2$  (110) surface is still a matter of controversy. From experiments, it has been proposed that  $\text{H}_2\text{O}$  adsorbs mainly associatively and dissociates at defect sites, see [798] and references therein. If dissociation does occur, it is only at low coverages (< 15%) that may be associated with surface defects. In contrast, most DFT 3D periodic calculations with the plane-wave (PW) basis predict dissociation at all coverages or an equivalent amount of dissociative and associative mechanisms. In contrast, Hartree–Fock (HF) embedded-cluster calculations with an atomic (Gaussian) basis set [801] predict that the associative mechanism should be favored due to overestimation of H-bonding in the dissociated configuration by DFT-PW studies.

The first two-periodic all-electron HF LCAO calculations of the rutile relaxed surfaces, made in [779], gave atomic displacements of surface atoms that did not differ significantly from the later results of DFT-PW investigations. Further periodic LCAO studies of  $\text{TiO}_2$  bare surfaces have been made in [777, 799, 800]. For studies of  $\text{H}_2\text{O}$  adsorption on  $\text{TiO}_2$  the single-slab periodic HF-LCAO and DFT-LCAO methods were first applied in [790] and compared with PW-DFT results to test various methods with cyclic- and embedded-cluster calculations and resolve discrepancies between the methods.

In the discussion of numerical results of this study we use the following labels for atoms of the (110) $\text{TiO}_2$  shown on Fig. 11.6:  $\text{Ti}1$ ,  $\text{Ti}2\text{-Ti}_{5\text{f}}$ ,  $\text{Ti}_{6\text{f}}$  (five- and sixfold coordinated titanium atoms),  $\text{O}1$ ,  $\text{O}2\text{-O}_{\text{br}}$ ,  $\text{O}_{3\text{f}}$  (bridging and threefold coordinated oxygen atoms).

Both in 2D (single-slab) LCAO and 3D (periodic-slab) PW calculations the same 3-layer (9 atomic planes) slab was used with the fixed positions of the middle-layer atoms. Both associative (molecular) and dissociative water monolayer adsorption has been investigated.

DFT-PW calculations were performed on different  $\text{H}_2\text{O}-\text{TiO}_2$  structures to determine which one corresponds to the most stable arrangement on the rutile (110) surface. To this end, a 3D-supercell consisting of  $1 \times 1$  or  $2 \times 1$  surface unit cells was used to model the (110) surface geometry. The smallest surface unit cell was chosen for bare-surface calculations, having dimensions of  $|\mathbf{c}|$  (2.959 Å) and  $\sqrt{2}|\mathbf{a}|$  (6.497 Å) in the (001) and (−110) directions, respectively, where  $\mathbf{a}$  and  $\mathbf{c}$  are translation vectors for the bulk rutile unit cell. This surface unit cell is doubled in the (001) direction for the hydroxylated or hydrated surfaces. The calculations were performed for 3-layer slabs with a total cell thickness  $\approx 19$  Å, *i.e.* slab thickness + vacuum gap 10 Å. A model with the fixed atomic positions of the central layer is assumed to be more appropriate to the real 2D surface relaxation because real crystals are not thin films and the bulk crystal structure probably exists a few atomic layers beneath the mineral

surface. Use of the constrained central layer was also accompanied by imposition of the inversion symmetry. This symmetry saves computational time and minimizes any possible dipole moment of the slab.

Adsorption was simulated with a pair of  $\text{H}_2\text{O}$  molecules (one at each side of the 3-layer  $\text{TiO}_2$  slab) using a  $2 \times 1$  unit cell. The use of one  $\text{H}_2\text{O}$  molecule on each side allows a cell with inversion symmetry to be used and creates a system with zero dipole moment associated with the slab.

In a PW study of water *associative adsorption* (with structure optimization) it was found that the lowest energy corresponds to the following structure: the water O is directly bonded to the five-coordinate  $\text{Ti}_{5\text{f}}^-$  atom, a single H-bond between an H in  $\text{H}_2\text{O}$  and a bridging oxygen atom ( $\text{O}_{\text{br}}$ ) and the torsion angle  $\text{H} - \text{O} - \text{H} \cdots \text{O}_{\text{br}}$   $117^\circ$ , see Fig. 11.11. In the structure with an angle of  $180^\circ$  all atoms of the water molecule and bridging oxygen are in the same plane, but this structure appears to be less favorable.

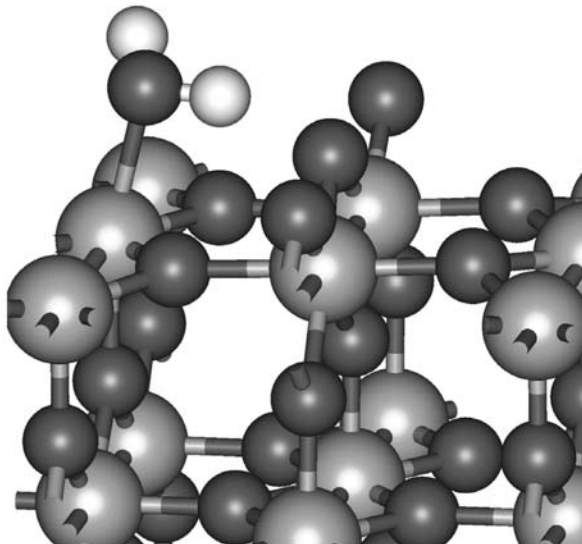


**Fig. 11.11.** Associative (molecular) adsorption at half-monolayer coverage

The *dissociative adsorption* of  $\text{H}_2\text{O}$  onto the (110) surface was modeled assuming that one H atom was bonded to the  $\text{O}_{\text{br}}$  next to the Ti atom with a terminal OH group. (Note that this Ti atom was originally 5-coordinated on the bare (110) surface.) Due to the half-monolayer configuration, the neighboring OH groups can be adsorbed either in a zigzag geometry or inline. In the latter case, there exists the possibility of H-bonding between neighboring bridging and terminal OH groups:  $\text{O}_{\text{br}} - \text{H} \cdots \text{O}_{\text{ter}} - \text{H}$ . Consequently, the inline configuration only was considered because this H-bonding should lower the adsorption energy. As in the case of molecular  $\text{H}_2\text{O}$  adsorption,

there are two possible OH orientations: inplane, with torsion angle  $\text{H} - \text{O} \cdots \text{H} - \text{O}$  equal to  $180^\circ$  (structure 1, Fig. 11.12) and a conformation with smaller torsion angle (structure 2, Fig. 11.13).

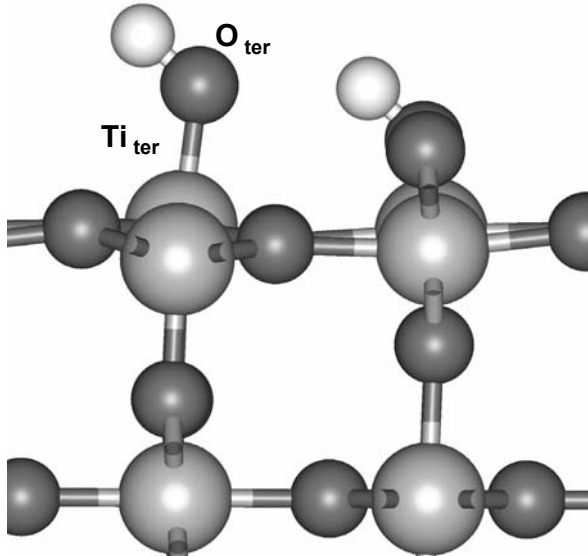


**Fig. 11.12.** Dissociative adsorption, half-monolayer coverage: structure 1, view in (001) direction

Energy minimizations of the corresponding slabs led to similar adsorption energies for both structures, which were lower than the corresponding associative values for 1/2 monolayer coverage by  $\approx 3\text{--}5$  kcal/mol. Thus, these results are in accordance with previous DFT simulations for half-monolayer coverage that predict  $\text{H}_2\text{O}$  dissociation on the rutile (110) surface.

A different conclusion was obtained from calculations on models corresponding to full-monolayer coverages. The distinct feature of these structures, in contrast to other cases, is the nearly equivalent displacements of the Ti and O atoms on the surface Ti layer such that they lie in one plane. Also, it is interesting to note that the overall arrangement of H and O atoms in the (110) surface is similar in both associative and dissociative adsorption. The obtained binding energies are stronger for associative adsorption on both the 3- and 5-layer slabs. This size of difference (3.6 kcal/ $\text{H}_2\text{O}$  molecule) in favor of associative adsorption was not obtained in previous DFT calculations.

In Table 11.11, the adsorption energies, obtained in PW calculations, are compared with those obtained in LCAO HF and DFT calculations for the structures, optimized

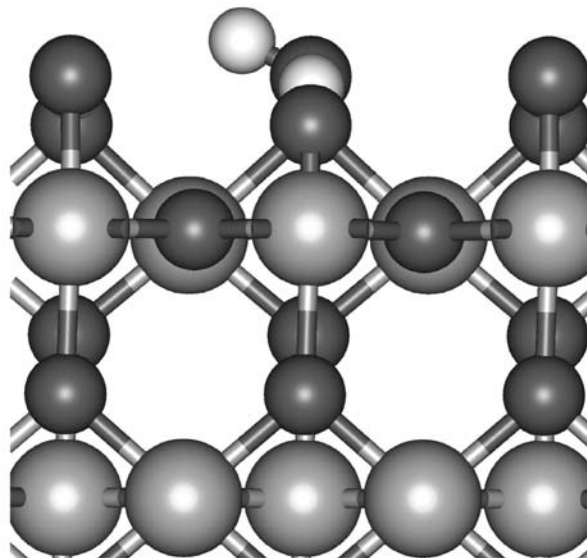


**Fig. 11.13.** Dissociative adsorption, half-monolayer coverage: structure 2, view in (1-10) direction

in PW DFT calculations. The computational details of both PW and LCAO calculations are given in [790].

In Table 11.12  $n$  Ti-L designates the number of Ti planes in the slab model, DB ECP means Durand–Barthelat effective core potential for Ti atoms, [484]. As can be seen, the HF method using both all-electron and ECP bases gives the dissociative adsorption energies that are about 2 to 3 kcal/mole more favorable than those for associative adsorption. The DFT method results in the opposite picture: associative adsorption energies exceed the dissociative values by approximately 5 kcal/mole both for the 3 and 5 Ti-layer slabs.

The basis-set superposition error was estimated for ECP 3 Ti-layer hydroxylated slabs and it appears to be 6.4 kcal/mole per water molecule. The  $\text{TiO}_2$  slabs with the dissociated and molecular form of  $\text{H}_2\text{O}$  have been calculated using exactly the same basis sets in all cases, so the large value of BSSE influences the absolute values of  $\Delta E$  only, but not the relative energy of water dissociation on the  $\text{TiO}_2$  surface. Taking into account the value of BSSE, the absolute values of the obtained LCAO water-adsorption energies seem to lie in the interval of 25–35 kcal/mole that is slightly greater than the corresponding PW results.

The  $z$ -shifts of positions of the surface atoms on  $\text{TiO}_2$  slabs obtained by LCAO methods are given in Table 11.12.

The optimized geometry of a bare  $\text{TiO}_2$  surface and of hydroxylated (hydrated) slabs exhibits qualitatively the same relaxations in LCAO calculations as were found in PW calculations. But there are some quantitative differences between the results of the DFT-PW, DFT-LCAO, and HF-LCAO approximations. It appears that the

**Table 11.11.** Calculated (without zero-point correction) at monolayer coverage and experimental adsorption energies (per one water molecule) for  $\text{H}_2\text{O}/\text{TiO}_2(110)$  (kcal/mol), [790].

Method	Molecular adsorption	Dissociative adsorption
PW:DFT-GGA-PW91, 340 eV; 3 Ti-L	-24.9	-23.0
PW:DFT-GGA-PW91, 340 eV; 3 Ti-L (Monkhorst-Pack $\mathbf{k}$ -point set 3 3 1)	-24.7	-22.7
PW:DFT-GGA-PW91, 1000 eV; 3 Ti-L (Monkhorst-Pack $\mathbf{k}$ -point set 3 3 1)	-25.2	-24.6
PW:DFT-GGA-PW91, 340 eV; 5 Ti-L	-22.0	-18.4
PW:DFT-GGA-BP88, 1000 eV <sup>a</sup>	-18.9	-24.9
PW:DFT-GGA-PW91, 750 eV <sup>b</sup>	-22.8	-21.0
LCAO:HF, DB ECP; 3 Ti-L	-35.63	-37.27
LCAO:HF, DB ECP; 3 Ti-L, with equal basis on all species (for BSSE)	-28.25	-28.91
LCAO:HF, all-electron; 3 Ti-L	-28.32	-31.39
LCAO:DFT-GGA-PW91, DB ECP; 3 Ti-L	-40.74	-36.42
LCAO:DFT-GGA-PW91, DB ECP; 5 Ti-L	-35.15	-30.20
Experiment <sup>c</sup>	-(14-24)	-

<sup>a</sup> [809]<sup>b</sup> [803]<sup>c</sup> [798]**Table 11.12.**  $z$ -shifts ( $\text{\AA}$ ) of Ti and O atoms on the bare surface of (110) rutile 3 Ti-layer models obtained by LCAO calculations, [790]

Method $\rightarrow$ Atom type (symbol) $\downarrow$	HF, all-electron	HF, DB ECP	DFT, DB ECP	HF, all-electr. [779]	Exp. [804]
Sixfold coordinated surface Ti ( $\text{Ti}_{6f}$ )	0.13	0.15	0.19	0.09	$0.12 \pm 0.05$
Fivefold coordinated surface Ti ( $\text{Ti}_{5f}$ )	-0.12	-0.12	-0.09	-0.15	$-0.16 \pm 0.05$
Bridging surface oxygen ( $\text{O}_{\text{br}}$ )	-0.07	-0.07	0.01	-0.14	$-0.27 \pm 0.08$
Threefold coordinated surface oxygens ( $\text{O}_{3f}$ )	0.15	0.14	0.21	0.07	$0.05/0.16 \pm 0.08$
Oxygen underneath $\text{O}_{\text{br}}$ ( $\text{O}_{\text{uO}}$ )	-0.02	-0.02	-0.01	-0.07	$0.05 \pm 0.08$
Oxygen underneath $\text{Ti}_{5f}$ in the middle Ti-layer ( $\text{O}_{\text{uTi}}$ )	-0.01	0.01	0.03	-0.02	$0.00 \pm 0.08$

Kohn–Sham Hamiltonian (both on the PW and LCAO basis) produces the larger expansion of the slabs towards the vacuum, making them thicker and thus affects the vertical displacements of atoms to be more positive relative to HF and experimental values. The same effect was found for hydroxylated and hydrated species: horizontal and vertical distortions of top-surface oxygens and titaniums from their bulk positions are substantially larger for DFT-LCAO than for HF-LCAO. Also, the DFT method leads to more flexible hydroxyl groups on hydroxylated surfaces and as a consequence, to shorter H-bonds between them.

The LCAO basis gives the possibility to calculate atomic charges in a more direct way than the PW basis. It was found in [790] that the values of Mulliken charges lie in a reasonable region and reflect the partially covalent nature of chemical bonds in titanium oxides, although the HF method gives absolute values about 25% larger than the DFT method. The deviations of atomic charges on the surface of unhydroxylated slabs from their bulk values, generally, were less than 0.1 e both for Ti and O atoms, except the charge on the bridging oxygen obtained in DFT calculations that was reduced by more than 0.2 e. It is interesting to note that oxygen charges in hydroxylated and hydrated slabs become less negative in the order:  $|q(O_{br})| > |q(O_{3f})| > |q(O_{H_2O})|$ , which is correlated with the acidity of the corresponding hydroxyls.

Tables 11.11 and 11.12 demonstrate the relatively large dependence of the calculated water-adsorption energies on the nature of the quantum-mechanical approximation (HF or DFT) and type of basis set (PW or LCAO) within the same periodic-slab model. It should be noted that the results for the equivalent 2D and 3D slab models coincide if the sufficiently large vacuum gap for 3D model is used, see Sect. 11.1.3. Nevertheless, we can conclude that the Kohn–Sham Hamiltonian using both PW and LCAO basis sets gives the order of the adsorption energy that is in better agreement with the experimental observations. However, the relaxation of the surface atoms seems to be more appropriate to experimental data [804] in the case of the HF calculations.

The long-term goal of research [790] was to model the interface of  $TiO_2$  and bulk water, so solvation forces will need to be included to predict adsorption energies and surface structures. Solvation forces are difficult to include in periodic DFT calculations because a large number of  $H_2O$  molecules must be included in layers between rutile slabs to simulate bulk water. On the other hand, the HF embedded-cluster approach in the program CECILIA [801] can include H-bonding to  $H_2O$  molecules not directly bonded to the surface and long-range solvation via a dielectric continuum half-space representing bulk water. The embedded-cluster approach is one obvious way to develop a force field for the  $Ti$ – $O$ – $H$  system representing the real  $TiO_2$ – $H_2O$  interface [791], so consistency between this approach and the results of periodic calculations would be a useful step toward reliable molecular-dynamics simulations of the larger-scale rutile–water system.

Embedded-cluster calculations have been made for comparison with periodic studies using the model developed in [801]. This model utilizes a three-level interaction approach and takes into account the long-range forces properly. The central stoichiometric part of the cluster is treated by the *ab-initio* LCAO method using pseudopotential cores of extra Ti atoms to saturate the dangling bonds of the outermost oxygen atoms. A large stoichiometric grid of point charges represents the surrounding ions, and a special array of point charges distributed on a closed surface around the cluster

is constructed to reproduce the remainder of the long-range Coulomb interactions (*i.e.* the Madelung potential of the bulk crystal at the surface). The neutrality condition is satisfied separately for the stoichiometric part of the cluster and lattice array of ions plus extra pseudopotential cores.

Embedded-cluster calculations were carried out on stoichiometric clusters of different size:  $\text{Ti}_7\text{O}_{14}$ ,  $\text{Ti}_{13}\text{O}_{26}$  and  $\text{Ti}_{17}\text{O}_{34}$  (the largest cluster is shown in Figures 11.14 and 11.15).

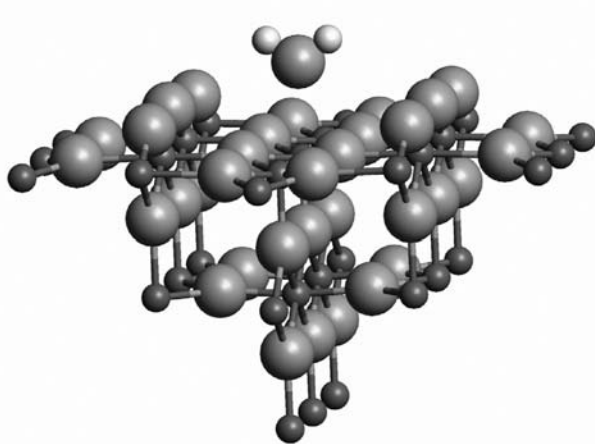


**Fig. 11.14.** Embedded-cluster results for the HF geometry of  $\text{Ti}_{17}\text{O}_{34} - \text{H}_2\text{O}$ : associative adsorption, [790]. Small-sized balls represent the Ti pseudopotential cores

In the  $\text{Ti}_7\text{O}_{14}$  and  $\text{Ti}_{13}\text{O}_{26} - \text{H}_2\text{O}$  clusters only one Ti, one bridging O and the  $\text{H}_2\text{O}$  atoms were allowed to relax during energy minimization. In contrast, the additional 4 oxygen atoms (nearest to the central Ti) were free to move in the  $\text{Ti}_{17}\text{O}_{34} - \text{H}_2\text{O}$  cluster. The larger cluster and greater surface relaxation were considered necessary to adequately describe the possible H-bonding arrangements of associatively and dissociatively adsorbed  $\text{H}_2\text{O}$  on the  $\text{TiO}_2$  (110) surface. About 1000 full-point charges (*i.e.* +4 and -2) from the 4 Ti-layer slab and up to 310 partial charges fitted to the Madelung potential of the rest of the crystal were introduced to represent the electrostatics of the bulk  $\text{TiO}_2$ . The positions of cluster atoms and lattice ions were chosen in accordance with the experimentally determined surface relaxation [804]. For embedded-cluster HF LCAO calculations the Hay–Wadt LANL1 or LANL2 [483] pseudopotentials for Ti atoms and SBK [485] pseudopotential on O atoms and corresponding basis sets have been used. In the case of LANL1, the 3s and 3p electrons of the Ti atom are included in the atomic core, whereas in the case of LANL2 the corresponding orbitals are treated as semicore states. For the pseudopotential cores of Ti atoms saturating the dangling bonds, only the semicore basis functions were included in the case of the LANL2 pseudopotential, whereas in the case of the LANL1

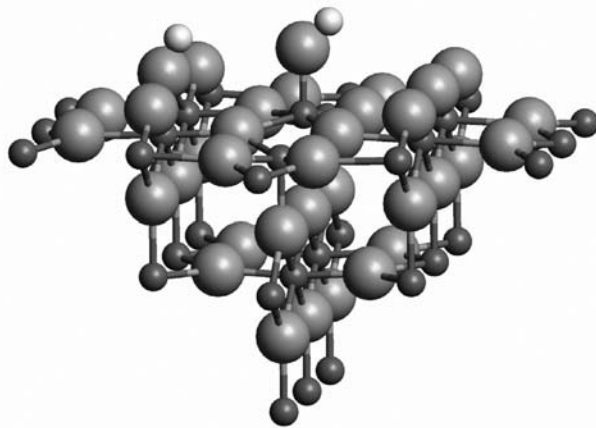


**Fig. 11.15.** Embedded-cluster results for the HF geometry of  $\text{Ti}_{17}\text{O}_{34} - \text{H}_2\text{O}$ : dissociative adsorption, [790]. Small-sized balls represent the Ti pseudopotential cores

pseudopotential the basis functions were not included. This trick provides the same net charge on the extra pseudopotential Ti cores as on the lattice ions.

**Table 11.13.** Embedded-cluster results (without BSSE), [790] and experimental adsorption energies for  $\text{H}_2\text{O}/\text{TiO}_2$  (110) (kJ/mol)

Method	Cluster	Molecular adsorption	Dissociative adsorption	Reference
LCAO:HF,LANL1	$\text{Ti}_{17}\text{O}_{34}$	-94 <sup>a</sup>	-48 <sup>a</sup>	[790]
LCAO:HF,LANL2	$\text{Ti}_{13}\text{O}_{26}$	-158	-90	[790]
LCAO:HF,LANL1	$\text{Ti}_7\text{O}_{14}$	-137 <sup>b</sup>	-31 <sup>b</sup>	[805]
LCAO:B3LYP,LANL1	$\text{Ti}_7\text{O}_{14}$	-146	-95	[805]
Experiment		-(59–100)		[798]

<sup>a</sup>Estimated BSSE is about 35 kJ/mol.

<sup>b</sup>Estimated BSSE is about 29 kJ/mol.

The embedded-cluster results for water-adsorption energies are given in Table 11.13. This table demonstrates the dependence of the embedded-cluster results on the cluster size, basis set and Hamiltonian used. When the size of the cluster is increased, the energy difference between the associative and dissociative adsorption mechanisms decreases.

The results for embedded-cluster calculations are different from that for the periodic models. Adsorption energies of a water molecule in the cluster case were much more favorable for the associative mechanism (Table 11.13), which is in better agreement with experimental observations. The predicted adsorption energies for the asso-

ciative mechanisms are higher than the measured values. There is no significant difference between the optimized geometry for water adsorption in  $\text{Ti}_{13}\text{O}_{26}$  and  $\text{Ti}_{17}\text{O}_{34}$ , the structures of the largest one are shown in Figures 11.14 and 11.15. No evidence of H-bond interactions was found in either the dissociative or associative adsorption structures in contrast to periodic PW and LCAO calculations. Bridging oxygen atoms in the cluster model appear to exhibit less relaxation than in periodic slabs.

The reason for such divergence between the periodic and cluster approaches is not entirely clear. The most probable reason is the differences in symmetry and boundary conditions: the absence of periodic boundary conditions may lead to artificial rigidity of the Ti–O bonds. Also, assigning of formal charges to lattice ions may overestimate the Madelung potential of the bulk crystal in the cluster model. On the other hand, the 3- and 5-layer periodic models apparently overestimate the surface relaxation and the thicker-slab models are needed for improved quantities.

The results obtained in [790] correspond well with the experimental observation that the probability of  $\text{H}_2\text{O}$  dissociation is increased with decreasing coverage. One explanation of this change in mechanism with coverage is that  $\text{H}_2\text{O}$  molecules can readily align to provide the maximum H-bonding interaction in associatively adsorbed structures. At low coverages, H-bonding energies are not as significant as at higher coverages, so the additional energy of forming stronger Ti–OH bonds (as compared to Ti– $\text{OH}_2$  bonds) outweighs the H-bonding term and dissociation may dominate.

Applying the different *ab-initio* quantum-mechanical approximations (DFT-PW, DFT-LCAO or HF-LCAO) within the periodic models produces qualitatively close results, but disagreement may exist in reproducing the difference between close values if this difference is about several kcal/mole. In particular, the DFT-LCAO method gives the order of the associative and dissociative water adsorption energy that is in better agreement with the experimental observations. Additional investigations of H-bonding between water molecules and oxygen atoms on the  $\text{TiO}_2$  surface using both DFT and HF methods should be made to resolve the disagreement between the periodic and embedded-cluster calculations.

The additional information about the water adsorption mechanism can be obtained in calculations of the oxides with the same bulk structure but different metal atom. The results of water adsorption on  $\text{SnO}_2$  surfaces is discussed in the next section.

### 11.2.3 Single-slab LCAO Calculations of Bare and Hydroxylated $\text{SnO}_2$ Surfaces

Cassiterite ( $\text{SnO}_2$  in rutile structure)-based materials are extensively studied due to their gas-sensing properties. The theoretical modeling of the surface processes plays an important role in this research.

The first-principles methods have made an increasingly significant contribution to understanding the nature of clean  $\text{SnO}_2$  surfaces [806–808] and the interaction of these surfaces with adsorbed water [809–811], methanol [812], CO [813, 814], and  $\text{O}_2$  [815] molecules. Many of these calculations use the DFT PW periodic-slab model. The LCAO single-slab approach has been successfully applied for investigation of cassiterite [806, 812–815]. A review of both PW and LCAO studies of adsorption on the perfect and reduced surfaces of metal oxides can be found in [784].

We discuss here the results of LCAO calculations [816] based on both plain DFT PBE and hybrid B3LYP Hamiltonians to investigate the surface relaxation and adsorption of water molecules on the stoichiometric (110) and (100)  $\text{SnO}_2$  surfaces. The aims of this study can be summarized as follows: (1) comparison of the plain DFT functionals with the B3LYP hybrid functional for the surface modeling; (2) analysis of the energetic and structural adsorption properties of the stoichiometric (110) and (100)  $\text{SnO}_2$  surfaces (the latter was not studied before); and (3) finding the difference in the adsorption of water on (110) and (100) surfaces.

Table 11.14 gives the comparison of calculated and experimental structure parameters ( $a, c, u$ ), valence band (VB) width and bandgap (BG) for bulk  $\text{SnO}_2$  in rutile structure. As can be seen in Table 11.14, the LCAO-calculated values are in reason-

**Table 11.14.** Calculated equilibrium crystallographic parameters, valence-band width, and bandgap for the bulk rutile  $\text{SnO}_2$  crystal, [816]

Parameter	Experi- ment	LCAO DFT calc. [816] <sup>a</sup>		LCAO DFT calc.		PW DFT calc.	
		B3LYP	PBE	B3LYP [815]	LDA [817]	PW91 [807]	PW91 [818]
$a$ (Å)	4.737	4.690	4.745	4.718	4.714	4.778	4.731
$c$ (Å)	3.186	3.147	3.185	3.187	3.241	3.232	3.157
$c/a$	0.673	0.671	0.671	0.675	0.688	0.676	0.667
$u$	0.306	0.307	0.307	0.307	0.307	0.306	0.306
VB width (eV)	7.5–9.0 [820]	8.56	8.24	9.0	–	–	6.5
BG (eV)	3.6 [821]	4.03	1.56	3.30	–	–	1.15

<sup>a</sup>Calculated Fermi-energy level: –4.73 eV (B3LYP) and –4.01 eV (PBE). Experimental estimation: –4.35 eV [819]

able agreement with the experimental data and the results of DFT PW computations. The B3LYP form of GGA slightly underestimates the cell dimensions, whereas the PBE functional gives values that are closer to the experimental data. The minor discrepancies between the results of B3LYP calculations [816] and [815] may be due to the different form of pseudopotentials (Hay–Wadt in the first case and Durand–Barthelat in the second case) taken. The theoretical valence-band (VB) width (of 8.56 eV using B3LYP and 8.24 eV using PBE) agrees well with the experimental data [821] of 7.5–9.0 eV. As expected, the B3LYP method gives the bandgap (BG) of 4.0 eV that is close to the experimental value of 3.6 eV [821]. The differences between the various PW-DFT calculations reported in Table 11.14 are obviously due to the computational details (choice of pseudopotentials, cutoff energy, and others). In all cases, the plain DFT methods produce a bandgap that is about 2 to 3 times narrower than the experimental value. The valence-band density of electronic states (DOS) in bulk crystal calculated using the B3LYP functional [816] shows the well-known fact that oxygen  $p$ -states give the main contribution to the VB DOS, whereas the tin  $s$ - and  $p$ -states form the bottom of the conduction band.

From the results of PW-DFT periodic slab calculations [807], the cassiterite (110) and (100) type-2 surfaces are the most stable of the low-index faces and, hence, they should be the dominant crystallite arrangement of  $\text{SnO}_2$ .

To check this by the single-slab approach LCAO calculations of the stoichiometric slabs (consisting of a whole number of  $\text{SnO}_2$  formula units) have been used for surface modeling [816]. As in the rutile  $\text{TiO}_2$  case the distribution of the bulk unit cell six atoms over atomic planes depends on the surface chosen: (110) O– $\text{Sn}_2\text{O}_2$ –O; (100) O–Sn–O–O–Sn–O (see Fig. 11.3). The bridging oxygen atoms  $\text{O}_{\text{br}}$  terminate both surfaces; two bonds connect them with the sixfold Sn ( $\text{Sn}_{6\text{f}}$ ) atoms on the rutile structure surfaces. There are fivefold tin atoms ( $\text{Sn}_{5\text{f}}$ ) with one unsaturated bond and threefold oxygens ( $\text{O}_s$ ) in the atomic plane next to  $\text{O}_{\text{br}}$ , see Sect. 11.2.2 and Fig. 11.6. The positions of all the atoms in slabs were allowed to relax at a fixed dimension of the 2D surface unit cell that was taken from the bulk optimization result. The surface energy was calculated using (11.8) for three- and five-layer slabs for a (110) surface (9 and 15 atomic planes), and two- and 2.5-layer (12 and 15 atomic planes) slabs for a (100) surface to check the convergence of the surface energy with  $n$  in the DFT PBE LCAO calculations. The influence of the basis-set superposition error (BSSE) on the calculated values has also been estimated. For this purpose, three extra atomic layers of ghost atoms have been added on each side of the relaxed slabs and the total energy was recalculated.

**Table 11.15.** Calculated energy per unit area of the (110) and (100) surfaces of  $\text{SnO}_2$  crystal, [816]

Sur- face	cell	$\mathbf{k}$ -set	Number of atomic planes / $\text{Sn}_2\text{O}_4$ layers	Surface energy ( $\text{J}/\text{m}^2$ )			
				PBE		B3LYP	Ref.data
				unrelaxed	relaxed	relaxed	relaxed
110	$1 \times 1$	$6 \times 3$	9/3	1.70	1.29	1.40	1.45 [818]
			15/5	1.69	1.26 (1.14) <sup>a</sup>		1.04 [807] <sup>b</sup>
100	$1 \times 1$	$6 \times 4$	12/2	1.74	1.37	1.48	–
			15/2.5	1.73	1.37 (1.26) <sup>a</sup>		1.14 [807] <sup>b</sup>

<sup>a</sup>BSSE-corrected values are given in parentheses.

<sup>b</sup>5–6  $\text{Sn}_2\text{O}_4$ -layers have been used in [807] for estimation of the surface energy.

The obtained surface energies are given in Table 11.15. Table 11.15 demonstrates that for both DFT PBE LCAO and hybrid B3LYP LCAO methods a (110) surface is more stable than a (100) surface, in accordance with PW-DFT calculations [807]. Comparing the surface energies in Table 11.15 before relaxation, we see that they are approximately the same for both surfaces. So, apparently, it is relaxation that provides the larger relative stability of the (110) surface. The B3LYP surface energies are larger than the corresponding PBE values by about  $0.1 \text{ J}/\text{m}^2$ . On the other hand, the BSSE correction reduces the surface energies by about  $0.1 \text{ J}/\text{m}^2$ , making them closer to the PW result [807]. However, it should be noted that the difference between (110) and (100) surface energies is smaller using the B3LYP functional.

In Table 11.16 we compare the bandwidths for the different surface models; the calculated Fermi energy is also included.

**Table 11.16.** Widths of electronic bands and Fermi energy (eV) for bulk  $\text{SnO}_2$  and for the different surface models (B3LYP results; AH – associatively hydroxylated, DH – dissociatively hydroxylated), [816]

Band	Bulk	Surfaces					
		(110)			(100)		
		clean	AH	AD	clean	AH	AD
VB width	8.56	9.24	8.45	8.56	8.34	8.23	8.61
BG	4.04	3.14	4.22	4.29	4.07	4.45	4.54
$E_{\text{Fermi}}$	-4.73	-8.38	-7.22	-8.11	-9.24	-7.07	-7.39

Table 11.16 shows that a clean (110) surface has a wider VB and a narrower BG than a clean (100) surface. This fact can be attributed to the difference in distribution of the electronic states corresponding to bridging oxygens on these two surfaces. It is known that just the bridging oxygens primarily contribute to the density of electronic states at the top of the VB. The LCAO calculations confirm this conclusion. We compare the obtained total DOS of the valence band for bulk, (110), and (100) surfaces in Fig. 11.16.

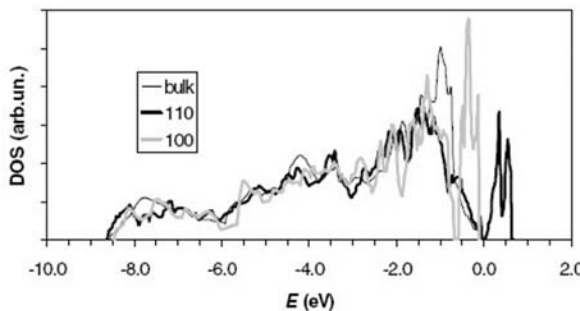


**Fig. 11.16.** Total valence-band DOS of bulk  $\text{SnO}_2$  crystal (fine line), its (110) (bold dark line) and (100) (bold gray line) surfaces calculated using the B3LYP functional (see text for explanation of energy scale)

Here, and in all figures below, the zero energy is taken at the Fermi level of the bulk crystal and all curves were shifted in such a way that the centers of O 1s bands coincide. All DOS values have been calculated per  $\text{Sn}_2\text{O}_4$  formula unit in the solid phase to permit comparison on an equal scale. It is clearly seen in Fig. 11.16 that the new  $\text{O}_{\text{br}}$  subband appears in the surface systems at the top of the bulk VB.

In the case of a (110) surface the broadening of the DOS distribution towards the BG is wider and the separation of the  $\text{O}_{\text{br}}$  subband from the bulk VB is more prominent than those in the case of a (100) surface. This fact indicates [784] that the basicity of  $\text{O}_{\text{br}}$  is larger on a (110) surface than on a (100) surface.

Vertical displacements of the surface atoms relative to their positions in the bulk structure are reported in Tables 11.17 and 11.18.

**Table 11.17.** Vertical displacements ( $\text{\AA}$ ) and atomic charges<sup>a</sup> ( $e$ ) on the  $\text{SnO}_2$  (110) surface (5  $\text{Sn}_2\text{O}_4$ -layer slab results using LCAO DFT (B3LYP calculations; AH – associatively hydroxylated, DH – dissociatively hydroxylated), [816]

Atom <sup>b</sup>	Bare surface		AH surface		DH surface	
	$z$ -shift <sup>c</sup>	charge	$z$ -shift	charge	$z$ -shift	charge
$\text{Sn}_{6\text{f}}$ , 6-fold surface tin	0.21 (0.22)	1.91	0.10	1.97	-0.05	1.96
$\text{Sn}_{5\text{f}}$ , 5-fold surface tin	-0.12 (-0.11)	1.76	-0.06	2.00	0.04	1.99
$\text{O}_{\text{br}}$ , bridging oxygen	0.05 (0.09)	-0.91	0.05	-1.01	0.02	-0.79
$\text{O}_{\text{s}}$ , 3-fold surface oxygen	0.14 (0.18)	-0.93	0.04	-1.02	-0.01	-1.03
$\text{O}_{\text{u6f}}$ , subbridging oxygen	0.04 (0.07)	-1.03	0.03	-1.03	-0.02	-1.04
$\text{O}_{\text{u5f}}$ , oxygen underneath $\text{Sn}_{5\text{f}}$	-0.04 (-0.04)	-0.93	-0.01	-1.04	0.02	-1.03
$\text{O}_{\text{term}}$ , oxygen in terminal hydroxyl or water oxygen	-	-	-	-0.66	-	-0.84
$\text{H}_{\text{term}}$ , hydrogen at $\text{O}_{\text{term}}$ or corresponding water hydrogen	-	-	-	0.35	-	0.34
$\text{H}_{\text{br}}$ , hydrogen at $\text{O}_{\text{br}}$ or corresponding water hydrogen	-	-	-	0.39	-	0.38

<sup>a</sup>Charges in the bulk  $\text{SnO}_2$ :  $q(\text{Sn}) = 2.12$ ,  $q(\text{O}) = -1.06$ ; charges in the isolated water molecule:  $q(\text{O}) = -0.62$ ,  $q(\text{H}) = 0.31$ .

<sup>b</sup>For atom indexing see text.

<sup>c</sup>DFT result of [807] is given in parentheses.

As expected, the top-surface atoms have the largest displacements. However, there is a qualitative difference between the two surfaces under consideration. Namely, in the case of a (110) surface the shifts of  $\text{Sn}_{5\text{f}}$  (inward) and  $\text{Sn}_{6\text{f}}$  together with  $\text{O}_{\text{s}}$  (upward) are the most noticeable, while in the case of a (100) surface only the bridging oxygen has a marked positive displacement. In spite of the different calculation methods used, the agreement of these LCAO values with the PW data from [807] is excellent.

The Mulliken population analysis has been applied for the calculation of the atomic charges that are also included in Tables 11.17 and 11.18. The noticeable reduction of the absolute charges for the top surface atoms is seen. This effect is relatively larger for a (100) surface than for a (110) surface. Thus, the charge of  $\text{Sn}_{5\text{f}}$  decreases by

**Table 11.18.** Vertical displacements ( $\text{\AA}$ ) and atomic charges ( $e$ ) on the  $\text{SnO}_2$  (100) surface (5  $\text{Sn}_2\text{O}_4$ -layer slab results using LCAO DFT (B3LYP calculations)<sup>a</sup>, [816]

Atom	Bare surface		AH surface		DH surface	
	$z$ -shift <sup>c</sup>	charge	$z$ -shift	charge	$z$ -shift	charge
$\text{Sn}_{5f}$ , surface 5-fold tin	0.03 (0.05)	1.67	0.02	1.95	-0.01	1.97
$\text{Sn}_{6f}$ , surface 6-fold tin	0.00	2.07	0.00	2.10	-0.01	2.11
$\text{O}_{\text{br}}$ , bridging oxygen	0.13 (0.18)	-0.83	0.05	-1.03	0.00	-0.81
$\text{O}_s$ , 3-fold surface oxygen	0.07 (0.09)	-0.94	0.04	-1.02	-0.02	-1.05
$\text{O}_{u5f}$ , oxygen underneath $\text{Sn}_{5f}$	-0.02	-0.95	-0.01	-1.04	0.01	-1.03
$\text{O}_{u6f}$ , oxygen underneath $\text{Sn}_{6f}$	0.00	-1.05	0.00	-1.06	-0.01	-1.06
$\text{O}_{\text{term}}$ , oxygen in terminal hydroxyl or water oxygen	-	-	-	-0.65	-	-0.85
$\text{H}_{\text{term}}$ , hydrogen at $\text{O}_{\text{term}}$ or corresponding water hydrogen	-	-	-	0.35	-	0.32
$\text{H}_{\text{br}}$ , hydrogen at $\text{O}_{\text{br}}$ or corresponding water hydrogen	-	-	-	0.40	-	0.40

<sup>a</sup>See footnotes to Table 11.17.

0.36 on a (110) surface, while on a (100) surface it decreases by 0.45 relative to the tin charge in the bulk crystal.

No such significant charge reduction was found in the case of rutile  $\text{TiO}_2$  [790] for the surface Ti atoms. The  $\text{O}_{\text{br}}$  charge on a (110) surface is more negative than that on a (100) surface (-0.91 vs. -0.83). This correlates with the conclusion about the larger basicity of the bridging oxygen on the (110) surface.

The results of LCAO calculations of the bare surface slabs validate the admitted approach (including single-slab model, LCAO basis, and BSSE correction) and indicate that the use of hybrid functionals to describe  $\text{SnO}_2$  surfaces provides more reasonable results.

PW-DFT calculations [811] predicted a significant difference in the structure of adsorbed  $\text{H}_2\text{O}$  on (110)  $\text{TiO}_2$  (rutile) and  $\text{SnO}_2$  surfaces, where the dissociative adsorption was favored on  $\text{SnO}_2$  vs. associative adsorption on  $\text{TiO}_2$ . The difference in  $\text{H}_2\text{O}$  behavior on the surface was attributed [811] to the larger 2D unit-cell parameters of  $\text{SnO}_2$  compared to those of  $\text{TiO}_2$  ( $a = 3.186 \text{ \AA}$ ,  $b = 6.699 \text{ \AA}$  vs.  $a = 2.959 \text{ \AA}$ ,  $b = 6.497 \text{ \AA}$ , respectively). The larger unit-cell dimensions caused H-bonding among the adsorbed  $\text{H}_2\text{O}$  molecules on the surface to be less energetically important on  $\text{SnO}_2$  than on  $\text{TiO}_2$ .

It was pointed out in [784] that molecular adsorption on an oxide surface can be understood as an acid-base process. From this point of view, the more covalent character of the Sn–O bonds compared to the corresponding Ti–O bonds might be the second factor that enforces the dissociation of water on the  $\text{SnO}_2$  surface. In fact, the electronegativity of tin (1.8) is markedly greater than the electronegativity of titanium (1.4). The significant reduction of the top surface  $\text{Sn}_{5f}$  charges (see Tables

11.17 and 11.18) correlates with the higher electronegativity of tin. As a result, the hydrated  $\text{Sn}_{5f}$  ion perhaps is a stronger Brønsted acid than the hydrated  $\text{Ti}_{5f}$  ion on the rutile surfaces. The water hydrolysis can obviously be promoted further by the larger basicity of the bridging oxygens (see discussion below).

To check the validity of the computational scheme used for describing the hydrogen bonds, a preliminary calculation of the water-water interactions has been made [816]. Full geometry optimization has been made for the isolated water dimer starting with the well-known most favorable relative orientation of the water molecules. The values of 30 kJ/mol using PBE and 26 kJ/mol using B3LYP for the H-bond energy (without zero-point correction and BSSE correction) have been obtained. This is not bad compared to the corresponding MP2 value, 25 kJ/mol. The optimal geometry is also very close to the MP2 result: the O–O distance is 2.86 Å, 2.88 Å, and 2.91 Å for PBE, B3LYP, and MP2 calculations, respectively. On the other hand, this example shows that the energy difference of the order of 5 kJ/mol per H-bond is within the error bounds of the usual DFT calculations. It also gives evidence that the B3LYP functional can produce more correct values for H-bonded systems.

A single-slab LCAO approach was firstly used in [816] for modeling the water adsorption on  $\text{SnO}_2$  surfaces. A doubled (in the  $x$  direction) 2D unit cell was used to model the water adsorption on both surfaces. The Monkhorst–Pack  $3 \times 3$  and  $3 \times 4$  sets of special  $\mathbf{k}$ -points were taken for the Brillouin-zone sampling in (110) and (100) slabs, respectively. Up to fifteen atomic planes were included in both types of  $\text{SnO}_2$  slabs for the adsorption-energy calculation. Two water molecules were placed on each side of the slab to simulate the full-monolayer coverage. Inversion symmetry was imposed on all systems containing water molecules to ensure the equivalence of both slab sides. The optimization of all atomic positions in the slabs has been made. The contribution of BSSE to the calculated adsorption energies has been estimated using the PBE functional. As in the case of the surface-energy calculation, the ghost atoms have been added to represent the water molecules above the optimized slabs and the total energy was recalculated. The energy of the isolated water molecule has also been recalculated with the 10–15 ghost atoms originated from the corresponding  $\text{SnO}_2$  surfaces. The resulting BSSE is approximately independent of the surface kind and reaches 18 kJ/mol of adsorbed water (see Table 11.19).

Although this is a noticeable contribution, it decreases all calculated adsorption energies by almost the same value, and does not influence the relative stability of associative and dissociative adsorption forms. The obtained adsorption energies for the (110) surface (Table 11.19) satisfactorily agree with the former periodic-slab PW-DFT calculations [810, 811].

In simulations [816] the water molecules initially were placed above the fivefold tin. During the optimization both (on each side) water molecules spontaneously dissociated in the case of PBE calculations, whereas a stable associative structure has been obtained in the case of the B3LYP functional (Fig. 11.17a).

Hence, in contrast to previous DFT calculations the hybrid HF-DFT functional leads to stable molecular adsorption on this surface. Starting with the broken water molecules, a stable dissociated structure has been obtained where hydroxyls were attached to fivefold tin and protons were bonded to the bridging oxygens (Fig. 11.17b). The energy of the hydrolyzed structure is lower by about 35 kJ/mol than the energy of the molecular structure (see Table 11.19). It is difficult to compare directly these

**Table 11.19.** Ab-initio adsorption energies per water molecule for H<sub>2</sub>O monolayer on SnO<sub>2</sub> surfaces (*N/M* – Number of atomic planes/Sn<sub>2</sub>O<sub>4</sub> layers), [816]

Surface	Cell	<b>k</b> -set	<i>N/M</i>	Method	Adsorption energy (kJ/mol)	
					associative	dissociative
110	2×1	3×3	15/5	LCAO DFT (PBE)	<i>unstable</i>	-179.7 (-162) <sup>a</sup>
				LCAO DFT (B3LYP)		-143.2 -176.6
				PW DFT (PW91) [810]	<i>unstable</i>	-165.0
				PW DFT (PW91) [811]	<i>unstable</i>	-170.8
100	2×1	3×4	15/2.5	LCAO DFT (PBE)	-130.2 (-112) <sup>a</sup>	-147.0 (-129) <sup>a</sup>
				LCAO DFT (B3LYP)	-116.86	-145.0

<sup>a</sup>BSSE-corrected values are given in parentheses for LCAO DFT (PBE) calculations.

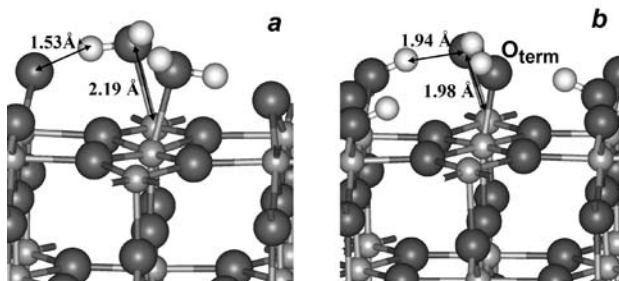


**Fig. 11.17.** Optimized monolayer structure for the water molecules adsorbed on a (110) SnO<sub>2</sub> surface obtained using the B3LYP functional, [816]: a) stable structure for molecular adsorption; b) stable structure for dissociative adsorption. Large dark gray balls are O atoms; light gray balls are Sn atoms; small white balls are H atoms.

adsorption energies of water on SnO<sub>2</sub> with those on TiO<sub>2</sub> [790] due to the different methods used; however, the adsorption on a (110) surface of cassiterite seems to be more exothermic by approximately 30 kJ/mol than the adsorption on a (110) surface of TiO<sub>2</sub>. This conclusion is in accordance with the DFT result of [809], where it is found that the dissociative configuration gives an adsorption energy of 134 kJ/mol for SnO<sub>2</sub>(110) and 104 kJ/mol for TiO<sub>2</sub>(110). In [809] it has been roughly estimated that the experimental adsorption energy on SnO<sub>2</sub>(110) should be about 110 kJ/mol. The data in Table 11.19 show that most of the theoretical values are 50% larger than the proposed estimation.

Both resulting geometries are stabilized by the H-bonds between water hydrogen and bridging oxygen in the associative case (Fig. 11.17a) and bridging hydrogen and oxygen of the terminal hydroxyl in the dissociative case (Fig. 11.17b). It should

be noted that the PBE functional produces shorter hydrogen bonds than the B3LYP functional. In contrast to the (110)  $\text{TiO}_2$  surface, there is no sufficiently strong interaction between the neighboring water molecules on the (110)  $\text{SnO}_2$  surface. The distance  $\text{Ow-Ow}$  between the water oxygens is 3.1 Å and 3.4 Å on  $\text{TiO}_2$  and on  $\text{SnO}_2$ (110) surfaces, respectively. This is in accordance with the results of Lindan [811], who pointed out the role of intermolecular interactions in the stabilizing of the molecular adsorption on the (110)  $\text{TiO}_2$  surface. On the other hand, the H-bond between water hydrogen and bridging oxygen proves to be very short, 1.53 Å, indicating the large basicity of  $\text{O}_{\text{br}}$ . Moreover, H-bonds, which could be hypothetically obtained with the PBE functional for molecular adsorption on a (110) surface, should be even shorter than those using the B3LYP functional, as occurs in all other cases with the real H-bonds. This can be the main reason why the molecular adsorption becomes unstable using the PBE variant of DFT. Also, this example shows that particular approximations influence the details of the calculated potential energy surface for the water–oxide interactions.

Taking into account the fact that the B3LYP approximation gives the better values of energy and bond distances for the H-bonded systems, it can be supposed that hybrid HF-DFT functionals can produce the more correct data for the water adsorption as well. This could be important not only in the case of  $\text{SnO}_2$  but also for other materials: applying the hybrid functionals may lead to the greater stability of molecular forms adsorbed on the oxide surfaces than predicted by plain DFT techniques.

Whereas many groups have studied the water adsorption on  $\text{TiO}_2$  surfaces, there have been few experimental water-adsorption studies for  $\text{SnO}_2$ . In [822] thermal desorption spectroscopy and ultraviolet photoemission spectroscopy have been used to investigate perfect and defective surfaces of  $\text{SnO}_2$ . In this study it was suggested that the amount of dissociation was about 10–15% on the stoichiometric (110) surface and the dissociation increased to 35% on the defective surface. Although additional experimental and theoretical work may be needed to confirm these conclusions, these data at least show that the molecular form of water can be stable on the cassiterite (110) surface, which is in accordance with B3LYP results under consideration.

The DOS for both types of water adsorption on a (110) surface are displayed in Fig. 11.18.

In the molecular adsorption case, depicted in Fig. 11.18a, the  $\text{O}_{\text{br}}$  subband tightly adjoins the bulk VB states, and a new  $\text{O}_w$  subband (corresponding to the water electronic states) was formed at the bottom of the VB. For comparison, the clear surface DOS projected to bridging oxygen states is also plotted in Fig. 11.18. In the dissociative case, Fig. 11.18b, the  $\text{O}_{\text{br}}$  subband almost completely disappeared and three new peaks originated from electronic states of the terminal hydroxyl group. One of these peaks is very sharp and is prominently separated from the top of the VB. As in the case of the (110) surface, two different initial states were chosen for the (100) surface. In the first, the water molecules were placed near the fivefold tin. The optimization did not change considerably the positions of water molecules using both PBE and B3LYP functionals (Fig. 11.19a).

Thus, the molecular form of adsorption is obviously stable on the (100) surface. The relative positions of fivefold tin and bridging oxygen favor the formation of H-bonds between the water hydrogen and bridging surface oxygen (Fig. 11.19a), although these bonds are not so short as in the (110) case. A stable structure for the

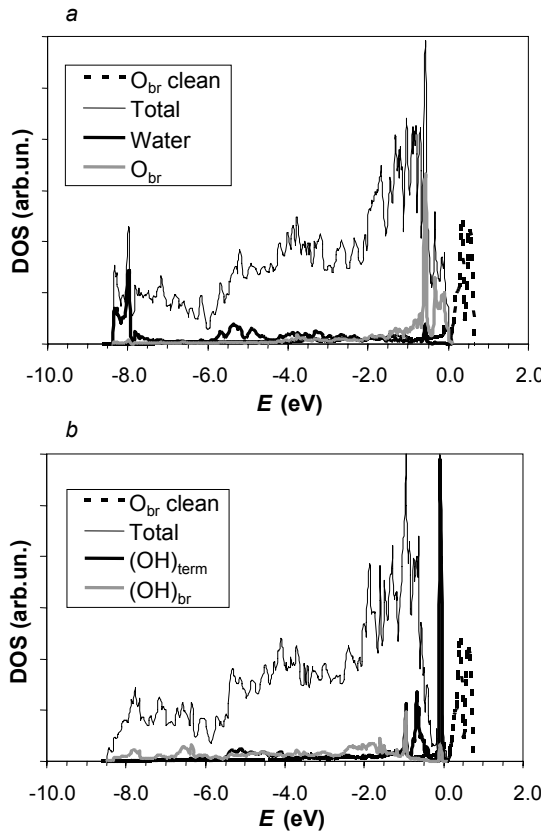


**Fig. 11.18.** Total and O-projected valence-band DOS in the hydroxylated (110) SnO<sub>2</sub> surface systems (see text for explanation of energy scale), [816]. a) Molecular adsorption: total DOS (fine line), projection onto the water states (bold dark line), projection onto the  $O_{br}$  states (bold gray line); b) dissociative adsorption: total DOS (fine line), projection onto the  $(OH)_{term}$  states (bold dark line), projection onto the  $(OH)_{br}$  states (bold gray line). The projection onto the  $O_{br}$  states in the clean (110) surface is shown by a dotted line.

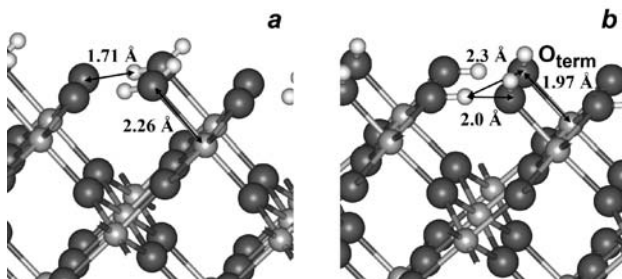


**Fig. 11.19.** Optimized monolayer structure for the water molecules adsorbed on a (100)  $\text{SnO}_2$  surface obtained using the B3LYP functional, [816]: a) stable structure for molecular adsorption; b) stable structure for dissociative adsorption. Large dark gray balls are O atoms, light gray balls are Sn atoms; small white balls are H atoms.

dissociative adsorption (Fig. 11.19b) was obtained from another initial state with the broken water molecules. There are no straight-line H-bonds in this structure. Nevertheless, as in the case of the (110) surface, the dissociative adsorption is more favorable (by about 30 kJ/mol) for the (100)  $\text{SnO}_2$  surface. The absolute value of the adsorption energy on a (100) surface is lower than that on a (110) surface. This is in accordance with the PW-DFT investigation of Bandura et al. [791].

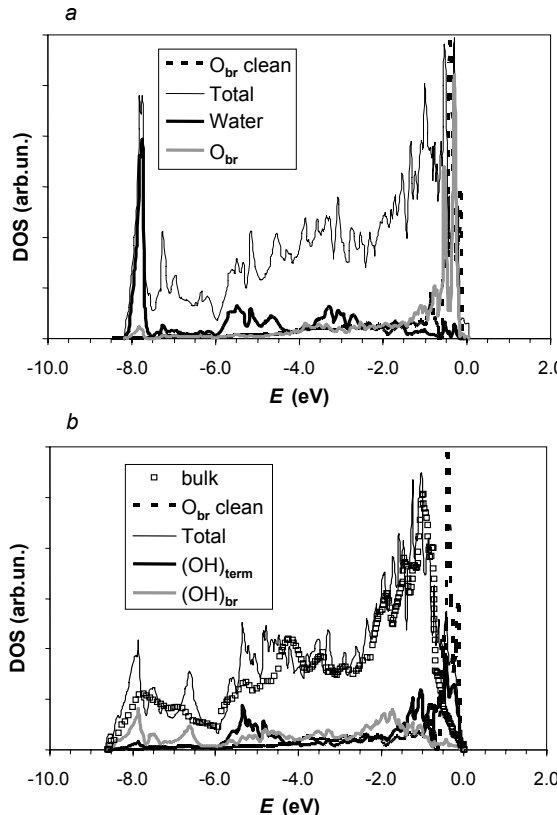
As may be expected, the atomic displacements for the hydroxylated surfaces are much smaller (especially for the dissociative adsorption) than those in the case of the bare surfaces (Tables 11.17 and 11.18), due to saturation of the vacant coordination places for the surface tin up to the total coordination number 6. Data in Tables 11.17 and 11.18 show that oxygen charges in the hydroxyl groups are noticeably less negative than charges on the other surface oxygens. The hydrogen charges were arranged in the order  $q(\text{H}_{\text{br}}) > q(\text{H}_{\text{term}}) > q(\text{H}_{\text{H}_2\text{O}})$ , which correlates with the relative acidity of the corresponding O–H bonds [823].

Figure 11.20 reports the DOS distributions for hydroxylated (100) surfaces. The DOS for the associative adsorption (Fig. 11.20a) differs from that for the clean (100) surface mainly by the presence of the  $\text{O}_w$  subband at the bottom of the VB.

The difference between the DOS for the slab dissociatively adsorbing water (Fig. 11.20b) and the DOS for the clean (100) surface is less significant than that in the (110) case. The terminal OH states also contribute to the top of the VB, but corresponding peaks are not as sharp as for the hydroxylated (110) surface. Except for the narrow zone at the top of the VB, the total DOS in the last case resembles the total DOS for the bulk crystal, which is also plotted in Fig. 11.20b for comparison.

Comparing the results for the clean and hydroxylated surfaces, one can conclude that a (110) surface exhibits stronger hydrophilic properties than a (100) surface due both to the more favorable geometrical structure and the more basic nature of the bridging oxygen.

The discussion above demonstrates that use of the hybrid HF-DFT approach allowed new results for the clean and hydroxylated oxide surfaces compared with plain DFT techniques to be obtained. The comparison of plain DFT functionals with the HF-DFT B3LYP hybrid functional shows interesting differences, which could be im-



**Fig. 11.20.** Total and O-projected valence-band DOS in the hydroxylated (100)  $\text{SnO}_2$  surface systems. a) Molecular adsorption; b) dissociative adsorption. (The sense of line types and energy scale are the same as in Fig. 11.19.) The projection onto the  $\text{O}_{br}$  states for the clean (100) surface is shown by the dotted lines, and the total bulk DOS is shown in b) by open circles.

portant not only in the case of  $\text{SnO}_2$  but also for other materials: in contrast to DFT plane-wave calculations (spontaneous dissociation), an associated adsorption of the water molecules becomes possible not only in the case of the (100) surface but also at the most stable (110) surface judging by the hybrid functional. This fact is probably due to the shortening of the H-bonds by the plain DFT methods.

LCAO HF-DFT investigation, as well as previous plane-wave calculations, shows that water dissociation on  $\text{SnO}_2$  surfaces is more favorable than on the similar  $\text{TiO}_2$  surfaces. Not only may the geometrical factors favor the hydrolysis of water on cassi-

terite surfaces but also the more covalent nature of Sn–O bonds and the larger basicity of bridging oxygens in SnO<sub>2</sub> comparably to TiO<sub>2</sub>.

One can conclude that the arrangement of H-bonds between the hydroxyl hydrogens and surface oxygens, as well as between the water molecules themselves, plays an important role in stabilizing the water adsorption on the metal-oxide surfaces. Thus, one of the reasons why the absolute value of adsorption energy on a (100) surface is lower than that on a (110) surface is the relative positions of oxygen and tin atoms being less profitable for the H-bond formation.

The general agreement between the results of calculations using the different bases (LCAO and PW) or the different slab models (2D and 3D) justifies the validity of the various *ab-initio* methods to study the molecular adsorption on the crystalline surfaces. However, the BSSE correction may be needed to obtain more precise absolute adsorption energies within the LCAO calculations.

In the next section we consider the surface modeling in cubic perovskites.

## 11.3 Slab Models of SrTiO<sub>3</sub>, SrZrO<sub>3</sub> and LaMnO<sub>3</sub> Surfaces

### 11.3.1 Hybrid HF-DFT Comparative Study of SrZrO<sub>3</sub> and SrTiO<sub>3</sub> (001) Surface Properties

A variety of practical applications of perovskite systems ABO<sub>3</sub> (the piezoelectrical and electro-optical devices, fuel cells, microelectrodes) have stimulated experimental and theoretical investigations of their surfaces.

Neither experimental nor theoretical investigations of the (001) surface structure of SrZrO<sub>3</sub> are known. However, a large number of experimental studies of SrTiO<sub>3</sub> (001) surfaces have been reported, see [824, 825] and references therein. In some of these investigations the reconstructed surfaces have been observed. A reconstruction of the SrTiO<sub>3</sub> surface mostly relates to surface defects, *e.g.*, oxygen vacancies that can be created by annealing in O<sub>2</sub> atmosphere at high temperature [826]. At the same time, the relaxation of a perfect titanate surface (no oxygen vacancies) has been experimentally observed and investigated [827]. This confirms the fact that perovskite surfaces with regular stoichiometry can be stable in some conditions. The displacements of atoms for the surface relaxation have been found in [827] by medium-energy ion scattering (MEIS) method. Charlton *et al.* [828] have used room-temperature surface X-ray diffraction (SXRD) to investigate the 300 K structure of SrTiO<sub>3</sub>(001) with 78% terminated TiO<sub>2</sub> and 22% terminated SrO. For the TiO<sub>2</sub> surface, there is good agreement with MEIS data in the position of the top-layer Ti, with both techniques pointing to an essentially bulk-terminated position. The data in [828] indicated that a lateral ferroelectric distortion is absent at 300 K on both terminations, consistent with some theoretical calculations [829]. However, a reflection high-energy electron diffraction (RHEED) study of the SrTiO<sub>3</sub> (001) surface structure in a temperature region from 300 down to 5 K [830] gave evidence for a surface phase transition of a soft-mode type, promoted by the surface symmetry.

The properties of the SrTiO<sub>3</sub> (001) surface have been examined in many quantum-mechanical studies [824, 829, 831–833, 836, 837]. Calculations of (001) surfaces of BaTiO<sub>3</sub>, PbTiO<sub>3</sub>, [775, 838–841] and defective (001) and (110) SrTiO<sub>3</sub> surfaces

[842,843] have also been made. A large number of cited calculations of surface properties of the strontium titanate are based on density-functional theory (DFT) and plane-wave basis (PW) set. In DFT LDA simulations [829] of the surface relaxation it has been found that relaxations account for 0.18 eV of the surface energy per surface unit cell, compiling around 15% of the total surface energy ( $1.36 \text{ J/m}^2$ ). Examining slabs with different surface terminations, the authors conclude that the bandgap (BG) for the  $\text{SrO}$  surface almost does not change with respect to the bulk value, and no ingap state occurs. For the  $\text{TiO}_2$  surface, there is a substantial reduction of the BG. However, there are also no deep-gap surface states, in accord with experimental reports. It should be noted that the LDA approach utilized in [829] (as well as the generalized-gradient approximation, GGA) tends to underestimate the BG and leads to a substantial discrepancy between calculated (1.85 eV) and experimental (3.30 eV) BG for the bulk  $\text{SrTiO}_3$ .

In [833,836] the results of GGA calculations for  $\text{SrTiO}_3$  surface systems are reported. In general, the data obtained in these studies do not differ considerably from LDA results except for the values reported in [836] for atomic displacements that seem to be on the order of a half of the values reported by all other DFT studies and may be attributed to some systematic error. Again, no midgap surface state for either  $\text{TiO}_2$ - or  $\text{SrO}$ -terminated surfaces was found in the band structure, [836]. However, a clear small peak appears below the energy gap in the electronic density of states (DOS) of the  $\text{TiO}_2$ -terminated surface, which has a tendency to move into the midgap. In [833] the electron redistribution in the surface layers has been analyzed using charge-density decomposition based on the Bader criteria [844]. The authors concluded that relatively strong hybridization between the Ti and O atoms leads to a noticeable charge transfer in the  $\text{SrTiO}_3$  surface systems. This enhanced charge transfer correlates with the strength of the surface relaxation.

In [824,831,832] HF and DFT LCAO calculations of (001)  $\text{SrTiO}_3$  surface employing a number of different exchange-correlation functionals have been performed. Prior to investigation of the surface properties, these authors tested the different quantum-mechanical methods on some bulk characteristics such as the lattice constant, bulk modulus, and BG. They obtained the best agreement between theoretical and experimental data for the hybrid HF-DFT B3PW method. The surface structure, surface energies, and electronic properties of the  $\text{SrTiO}_3$  (001) surface has been calculated by different HF and DFT LCAO methods. It was concluded that it is very difficult to choose a method reproducing all properties equally well, but hybrid HF-DFT techniques B3PW and B3LYP turned out to be the most reasonable.

In [845] the comparison has been made between the calculated relaxed structures of the  $\text{SrTiO}_3$  surface obtained in various DFT PW studies and the data of several experimental investigations. Good agreement was found between the most theoretical studies, whereas the accordance of theoretical data with the available experimental results proved to be low. This fact can be explained by the poor agreement between the different experimental studies themselves [829,831]. It was suggested in [828] that a possible reason for this discrepancy is the influence of soft vibrational modes, which are thought [799] to give rise to a  $0.2\text{\AA}$  – disagreement between 0 K theory and 300 K experiment for  $\text{TiO}_2$  (110). Whatever the origin of the discrepancy, it presumably affects the  $\text{TiO}_2$ -terminated surface and the second-layer atoms on both surface types of  $\text{SrTiO}_3$  crystal.

We discuss here in more detail the results of a hybrid HF-DFT LCAO comparative study of cubic SrZrO<sub>3</sub> and SrTiO<sub>3</sub> (001) surface properties in the single-slab model [825]. As known from [824], the consideration of systems with 7–8 atomic layers is sufficient to reproduce the essential surface properties of cubic perovskites. Three different slab models have been used in [825]. The first (I) and the second (II) ones consist of 7 crystalline planes (either SrO- or MO<sub>2</sub>-terminated, respectively) being symmetrical with respect to the central mirror plane but nonstoichiometric (see Fig. 11.4). The central layer is composed of MO<sub>2</sub> (M = Ti, Zr) units in the model I and SrO units in the model II. Both models I and II have been applied for studying the surface properties of titanates by *ab-initio* calculations [832]. The asymmetric model III is stoichiometric and includes 4 SrO and 4 MO<sub>2</sub> atomic planes. Accordingly, it is terminated by a SrO plane on one side and by a MO<sub>2</sub> plane on the other side and there is no central atomic layer. The model III has been included in the simulation to investigate the influence of the stoichiometry-violation in the symmetrical models I and II on the calculated surface properties. For all slabs a 1 × 1 surface unit cell has been taken. For the 2D translations in slabs the experimental bulk lattice constants of SrZrO<sub>3</sub> (4.154 Å) and SrTiO<sub>3</sub> (3.900 Å) were used that does not differ significantly from DFT B3PW LCAO theoretical values (4.165 Å and 3.910 Å respectively).

In Table 11.20 are presented the results obtained for charge distribution and atomic relaxations for models I and II (Mulliken atomic charges and vertical atomic displacements are given). The displacements in the normal to the surface direction are given with respect to atomic positions in the unrelaxed bulk structure. The negative displacements correspond to the relaxation inwards, towards the bulk, while the positive ones relax outwards, *i.e.* to the vacuum side. It should be noted that the positions of atoms in the central plane exactly fit the corresponding bulk sites and can not relax due to the imposed mirror symmetry. There are no such restrictions for the model III. However, the absolute atomic displacements cannot be calculated unambiguously in this case due to uncertainty in the zero-level choice when the relaxed and unrelaxed structures are superimposed. This problem may be overcome by fixing the positions of the two middle layers at the bulk geometry. The model III does not satisfy this condition, so the corresponding absolute atomic displacements have not been calculated in model III.

The obtained displacement  $d$  values for the SrTiO<sub>3</sub> practically coincide with the shifts from calculations [831] where almost the same LCAO procedure has been used. Calculated vertical shifts for the upper Sr atoms are noticeably greater than the shifts of other atoms in both models I and II, though they are negative in the first and positive in the second case. Also, for SrZrO<sub>3</sub> they are larger than for SrTiO<sub>3</sub>. Displacements of other atoms are very similar on SrZrO<sub>3</sub> and SrTiO<sub>3</sub> surfaces, except the inward shift of the top oxygen atom on the ZrO<sub>2</sub> surface that is much greater than the shift of the corresponding oxygen atom on TiO<sub>2</sub> surface. The X-ray diffraction data [828] for SrTiO<sub>3</sub> (001) surface are presented in the last column of Table 11.20. Note that the experimental values correspond to 300 K whereas, the theoretical values correspond formally to 0 K. As well as in other *ab-initio* investigations, the satisfactory agreement between the theory and experiment was found only for the displacements of the top Sr atoms in the model I. The comparison of calculated and measured displacements for the deeper atoms in SrTiO<sub>3</sub> slabs is difficult as the experimental data reveals large errors. Furthermore, in these slab simulations, as in most other

**Table 11.20.** Mulliken charges<sup>1</sup>  $q$  ( $|e|$ ) and vertical atomic displacements  $d$  ( $\text{\AA}$ ) for the SrO- and  $\text{TiO}_2$ -terminated slabs models (I and II, respectively)

Mo-del	La- yer	SrZrO <sub>3</sub>			SrTiO <sub>3</sub>				
		Ion	$q$	$d$	Ion	$q$	$d$	$d_{\text{calc}}^2$	$d_{\text{exper}}^3$
I	1	Sr	1.86	-0.304	Sr	1.85	-0.185	-0.220	-0.25 $\pm$ 0.07
		O	-1.50	0.035	O	-1.52	0.036	0.004	-0.3 $\pm$ 0.4
	2	Zr	2.17	0.083	Ti	2.36	0.075	0.046	-0.24 $\pm$ 0.07
		$\text{O}_2$	-1.38	0.027	$\text{O}_2$	-1.45	0.040	0.000	-0.4 $\pm$ 0.7
	3	Sr	1.88	-0.058	Sr	1.87	-0.031	-0.046	0.02 $\pm$ 0.04
		O	-1.36	0.006	O	-1.43	0.009	-0.004	0.1 $\pm$ 0.2
	4	Zr	2.13	-	Ti	2.36	-	-	-
		$\text{O}_2$	-1.35	-	$\text{O}_2$	-1.42	-	-	-
II	1	Zr	2.16	-0.092	Ti	2.29	-0.084	-0.131	0.00 $\pm$ 0.03
		$\text{O}_2$	-1.26	-0.097	$\text{O}_2$	-1.30	-0.005	-0.062	-0.5 $\pm$ 0.3
	2	Sr	1.86	0.159	Sr	1.85	0.140	0.097	-0.01 $\pm$ 0.01
		O	-1.27	0.025	O	-1.36	0.020	-0.019	0.2 $\pm$ 0.1
	3	Zr	2.12	-0.014	Ti	2.35	-0.010	-0.027	-
		$\text{O}_2$	-1.31	-0.008	$\text{O}_2$	-1.38	0.002	-0.019	-
	4	Sr	1.87	-	Sr	1.87	-	-	-
		O	-1.33	-	O	-1.40	-	-	-

<sup>1</sup>Bulk charges: SrZrO<sub>3</sub>:  $q(\text{Sr}) = 1.88$ ,  $q(\text{Zr}) = 2.12$ ,  $q(\text{O}) = -1.33$ ; SrTiO<sub>3</sub>:  $q(\text{Sr}) = 1.87$ ,  $q(\text{Ti}) = 2.53$ ,  $q(\text{O}) = -1.47$ .

<sup>2</sup> Experimental data [828] for SrTiO<sub>3</sub> at 300 K.

<sup>3</sup> Results of DFT PW calculations [829] using the optimized lattice constant  $a = 3.86 \text{ \AA}$ .

studies, the cubic bulk unit cell is used to generate the surface unit cell and the corresponding symmetry (in the surface plane) is kept fixed; whereas the unit cell must be doubled and symmetry should be lowered to tetrahedral for reproducing of the ferroelectric distortions. Most certainly, the surface phase transition can also take place in the case of zirconate due to the existence of the lower-symmetrical orthorhombic modification at room temperature. Table 11.20 also presents the results of a previous LDA PW simulation [829] for SrTiO<sub>3</sub>. LCAO displacements satisfactory correlate with the data of PW calculations.

The Mulliken atomic charges are also given in Table 11.20. These quantities can be used for analysis of the electron redistribution in the surface layers, which may be important for adsorption of another species on the surface. Table 11.20 clearly shows that the Sr atomic charge is close to the bulk one and exhibits insensitivity to the kind of M atom, type of termination and number of layers. On the contrary, calculated Ti and Zr charges give evidence of considerable covalency of M–O bonds in both crystals. It can also be seen that deviations of the surface oxygen charges from their bulk values are relatively large and exhibit the opposite sign for the two types of surface termination. The calculated Mulliken charges are very similar to the charges obtained in [833] via the Bader density decomposition.

When using models I and II the surface energy  $E_s$  can be determined as a sum of two parts,  $E_s = E^{\text{unrel}} + E^{\text{rel}}(T)$ . The first term  $E^{\text{unrel}}$  is equal to one half of the energy for crystal cleavage into SrO- and MO<sub>2</sub>-terminated slabs. It can be written as

$$E^{unrel} = \frac{1}{4S} [E_{slab}^{unrel}(\text{SrO}) + E_{slab}^{unrel}(\text{MO}_2) - 7E_{bulk}] \quad (11.10)$$

where  $E_{slab}^{unrel}(\text{SrO})$  and  $E_{slab}^{unrel}(\text{MO}_2)$  are the energies for unrelaxed SrO- and MO<sub>2</sub>-terminated slabs,  $E_{bulk}$  is a bulk energy per primitive cell, and  $S$  is the area of the 2D cell. The second term is the relaxation energy for SrO- or MO<sub>2</sub>-terminated slabs and is computed as a difference between the relaxed and unrelaxed slab energies:

$$E^{rel} = \frac{1}{2S} [E_{slab}^{rel}(T) - E_{slab}^{unrel}(T)] \quad (11.11)$$

where  $T = \text{SrO}$  or  $\text{MO}_2$ .

The surface energy of model III (stoichiometric slab) equals the difference between the energy of the slab and the quadruple energy of bulk primitive cell divided by  $2S$ . The results for surface energy are summarized in Table 11.21.

**Table 11.21.** The calculated surface energies  $E_s$  (J/m<sup>2</sup>) and bandgaps BG (eV)

Quantity	Relaxed			Unrelaxed		Bulk
	I	II	(I+II)/2	III	(I+II)/2	
SrZrO <sub>3</sub>						
$E_s$	1.01	1.26	1.14	1.13	1.41	1.42
BG	4.84	4.61	—	4.56	—	3.94
SrTiO <sub>3</sub>						
$E_s$	1.20	1.29	1.25 (1.36) <sup>2</sup>	1.24	1.46 (1.55) <sup>2</sup>	1.46
BG	3.68 (1.86) <sup>2</sup>	2.76 (1.13) <sup>2</sup>	—	2.48	—	2.63 (1.85) <sup>2</sup>

<sup>1</sup>Experimental BG in bulk crystals: 5.9 eV for SrZrO<sub>3</sub> [835], and 3.3 eV for SrTiO<sub>3</sub> [834].

<sup>2</sup>The results of DFT PW calculations [829] are given for comparison in parentheses.

For both crystals  $E_s$  for SrO termination is slightly less than that for MO<sub>2</sub> termination. It is important that the surface energies averaged over models I and II are very close to  $E_s$  for the model III (this is valid both for relaxed and unrelaxed systems). The obtained values show that the surface energy of SrZrO<sub>3</sub> is smaller than the surface energy of SrTiO<sub>3</sub> crystal. The calculated value for the surface energy of SrTiO<sub>3</sub> (1.24–1.25 J/m<sup>2</sup>, see Table 11.21) agrees satisfactorily with the value calculated in [829] using the DFT PW framework (1.36 J/m<sup>2</sup>).

In Table 11.21 the calculated bandgaps (BG) for slabs are compared. It is clearly seen that in all cases the BG for SrZrO<sub>3</sub> systems is wider. This agrees with the larger ionicity of SrZrO<sub>3</sub> in comparison with SrTiO<sub>3</sub>. One can notice that in the case of SrTiO<sub>3</sub> the BG for the model I is markedly greater than that for models II and III. The substantial reduction of BG for the TiO<sub>2</sub> surface relative to the bulk value is due to an extended shoulder in the valence-band electronic DOS (see below). The same picture has been found in DFT PW calculations [829], in spite of the fact that the LDA gaps are half of others (see Table 11.21).

In all figures below the zero energy is taken at the Fermi level of the bulk crystal (SrZrO<sub>3</sub> or SrTiO<sub>3</sub>) and all curves were shifted so that the centers of O 1s bands

coincide. Also, the DOS values have been reduced to one oxygen atom to ensure the same scale for bulk crystal and different slabs.

In Fig. 11.21 the total oxygen DOS for the surface model III and bulk crystal are compared. The bulk and slab VB have similar shapes and widths except the small areas at the top and bottom that reflect the surface contributions.

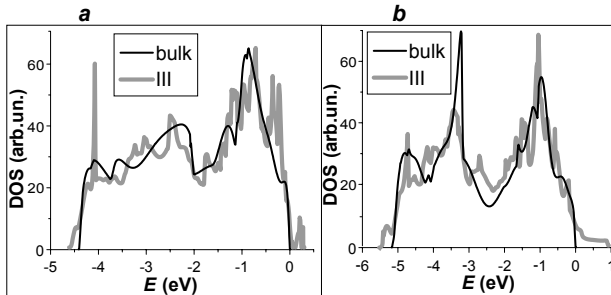


**Fig. 11.21.** Oxygen-projected VB DOS for bulk crystal and for surface model III (a –  $\text{SrZrO}_3$ ; b –  $\text{SrTiO}_3$ )

These contributions are resolved in Fig. 11.22 where the DOS projected to the surface oxygens is plotted. Figures 11.22a and b demonstrate that the oxygen DOS distribution for  $\text{SrO}$  and  $\text{TiO}_2$  terminations are qualitatively different, whereas the distinctions between the model types (I and III or II and III) are less significant.

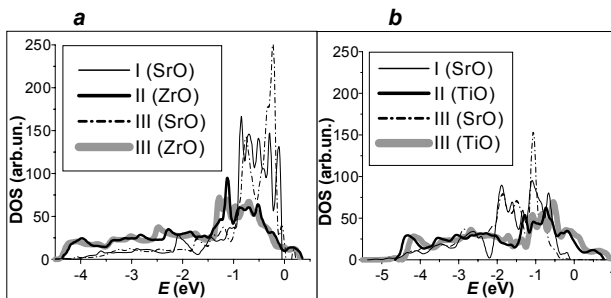


**Fig. 11.22.** Projected VB DOS for oxygen atom in the first surface layer for all three models (a –  $\text{SrZrO}_3$ ; b –  $\text{SrTiO}_3$ ). For the model III the first oxygen projection corresponds to the  $\text{SrO}$ -side and the second to the  $\text{MO}_2$ -side

It is clearly seen in Fig. 11.22 that the new O-subbands appear in the slabs at the top of the bulk VB. The corresponding peaks for the oxygen on an  $\text{SrO}$ -terminated  $\text{SrZrO}_3$  surface (in models I and III) are significantly higher than the peaks for oxygen on  $\text{ZrO}_2$ -terminated surfaces. Also, the charge of the O atom in the first layer in  $\text{SrO}$ -terminated slab of a  $\text{SrZrO}_3$  crystal is noticeably lower than its bulk value (1.50 vs.

1.33 in Table 11.20). This can be explained by the larger ionicity of the M–O bond in the zirconate than in the titanate.

These features allow one to expect that a (001) SrO-terminated surface can accumulate the excess negative charge in the case of SrZrO<sub>3</sub> crystal and it should be more basic in nature than a SrO-terminated surface of SrTiO<sub>3</sub> crystal. In the case of SrTiO<sub>3</sub> slabs the corresponding oxygen contribution to SrO surface states is lower, whereas the new surface states originated from the TiO<sub>2</sub> termination form a low but extended shoulder that is alike in models II and III. The indicated shoulder reduces the bulk BG noticeably (see Table 11.21). This means that electronic shells on the TiO<sub>2</sub>-terminated SrTiO<sub>3</sub> surface are more polarizable than electronic shells on the other surface types regarded. The similarities of the results obtained for the surface energy and DOS from the surface models I and II on the one hand, and from the model III on the other hand confirm the weak interaction between the opposite slab faces if its thickness is sufficiently large, resulting in the mutual independence of two types of termination (SrO and MO<sub>2</sub>) in the surface models of perovskites considered.

One can conclude that disagreement between the theory and experiment for the vertical displacements of the SrTiO<sub>3</sub> surface atoms does not depend on the actual (LCAO hybrid HF-DFT or PW DFT) *ab-initio* method used. The dependence on the slab model and thickness may also be excluded from the possible reasons. Most probably, this discrepancy can be explained by the possible surface phase transition or surface reconstruction under the experimental conditions. The *ab-initio* calculations using the extended tetragonal surface unit cell can resolve the indicated contradiction. The values obtained show that relaxation of the top surface atoms is more prominent in the case of SrZrO<sub>3</sub> than in the case of SrTiO<sub>3</sub>, and the corresponding surface energy for zirconate is lower by about 0.1 J/m<sup>2</sup>. This fact may be attributed to the larger ionicity of SrZrO<sub>3</sub> bulk crystal in comparison with SrTiO<sub>3</sub> bulk crystal. The results under consideration give evidence that the SrO surface of a SrZrO<sub>3</sub> crystal is more basic than the SrO surface of a SrTiO<sub>3</sub> crystal. Based on this conclusion one can suppose, for example, a stronger interaction of oxygen atoms on the SrO surface with the H atoms of the adsorbed water molecules (with possible water ionization) occurs in the case of zirconate than in the case of titanate.

### 11.3.2 F Center on the SrTiO<sub>3</sub> (001) Surface

In Sect. 10.3.1 we considered the calculations of the oxygen vacancy in a bulk SrTiO<sub>3</sub> crystal (bulk F centers). The atomic and electronic structure of surface F centers is practically unknown.

Only a few theoretical papers deal with the analysis of the F centers on the TiO<sub>2</sub>-terminated SrTiO<sub>3</sub>(001) surface: one of them is based on semiempirical INDO calculations [846] and another one on GGA and LDA+U slab calculations [847]. In both papers, the structure of the F centers was studied for very high defect concentrations as the small 2D supercells were used. It has been demonstrated above in the bulk F center calculations that the results for low defect concentrations might be significantly different from those corresponding to the infinite dilution limit. Moreover, it is very likely that in the calculations [846] both lattice relaxation and vacancy-formation energies are not converged to the infinite dilution limit and no surface defect-migration energies were presented.

In [848] the surface F centers on the  $\text{TiO}_2$ -terminated unreconstructed (001) $\text{SrTiO}_3$  surface are studied in more detail by the DFT method. A stoichiometric slab containing six atomic  $\text{TiO}_2$  and  $\text{SrO}$  planes (6 bulk unit cells, *i.e.* 30 atoms) has been chosen as a material model. The surface F center was studied for 2D supercells  $2 \times 2$ (120 atoms) and  $3 \times 3$ (270 atoms). The formation energy for relaxed (unrelaxed) surface oxygen vacancies was found to be 6.22 eV (8.86 eV) and 5.94 eV (8.81 eV) for 120-atom and 270-atom supercells, respectively. Again, one must be aware of the fact that the present values might not be completely converged to the infinite-dilution limit. This surface vacancy-formation energy could be compared to the 7.73 eV and 7.17 eV formation energies for the relaxed F centers in the bulk, calculated for the bulk supercells  $n\sqrt{2} \times n\sqrt{2} \times n\sqrt{2}$ ,  $n = 2, 3$ , with similar interdefect distances along the  $z$  axis. The conclusion could be drawn that the defect-formation energy on the  $\text{TiO}_2$ -terminated surface is considerably smaller than in the bulk; it is roughly reduced by 1.5 eV or 20–25%. This is similar to what has been obtained for other oxides and it is due to the reduced coordination at the surface, [850]. The following relaxation of the atoms nearest to the vacancy and in the Ti–O–Ti surface chain is reported in [848]. The Ti and O nearest neighbors of the vacancy are displaced by  $7\%a_0$  and  $4\%a_0$ , respectively ( $a_0$  is the parameter of bulk cubic lattice). The former displacements exceed by a factor of two those in the bulk and result from the half-coordination sphere left when the surface is formed. Unlike the bulk, where atoms move towards and outwards from the O vacancy, on the surface the direction of atomic displacements is more complicated.

A well-pronounced strong anisotropy in the atomic displacements along the  $\text{Ti} - \text{V}_\text{O} - \text{Ti}$  axis was clearly observed. Atomic displacements in the smaller supercell show a nonmonotonic decay with the distance from the vacancy that is caused by the interference effects on the border of the nearest supercells and demonstrates that this supercell is not big enough to avoid defect–defect interactions on the surface. The calculated activation energy for defect migration for the two supercells of 120 and 270 atoms is 0.19 and 0.11 eV, respectively. This demonstrates that (i) an increase of the distance between defects reduces the migration energy (due to the reduced repulsion energy between periodically distributed defects), and (ii) compared to the bulk migration, the defect-migration energy on the perovskite surface is largely reduced.

This is in line with the calculations of the F-center migration on the  $\text{MgO}$  surface where the activation energy obtained was also considerably smaller than in the bulk [850]. In addition, high vacancy mobility makes the surface reconstruction easier to see in the experiments. The difference electronic density map for the surface F center on the  $2 \times 2 \times 3$  slab shows that the electronic density around it is more delocalized than that corresponding to the bulk F center. The calculated Bader effective charges of the two nearest Ti atoms give an electronic density increase of 0.4  $e$  per atom, whereas the rest of the missing O charge is spread in the vicinity of the vacancy. Finally, the defect ionization energy of the surface F center is almost half that in the bulk (0.25 eV vs. 0.49 eV). Its dispersion is still not negligible (0.14 eV), being comparable with that for the bulk  $2\sqrt{2} \times 2\sqrt{2} \times 2\sqrt{2}$  supercell (0.15 eV). The single bulk F center in  $\text{SrTiO}_3$  is a small-radius defect. The surface F center is predicted to be more delocalized than that in the bulk. This is in agreement with previous findings for ionic oxides such as  $\text{MgO}$ , [850] or  $\text{Al}_2\text{O}_3$  [849] and results from the reduced Madelung potential and atomic coordination at the surface.

The oxygen vacancies on the SrTiO<sub>3</sub> (001) surface essentially change its properties and they have to be taken into account when adsorption modeling. Unfortunately, the surface-defect calculations in the slab model are complicated due to the delocalized nature of the surface oxygen vacancy electron states. Such a study requires both sufficiently thick slabs (in modeling the surface) and large 2D supercells (in modeling the single vacancy on the surface).

While the theoretical study of the atomic and electronic structure of titanate surfaces is active, for manganites such a study began only in 2004, as is seen in the next section.

### 11.3.3 Slab Models of LaMnO<sub>3</sub> Surfaces

Of primary interest for fuel-cell applications are the LaMnO<sub>3</sub> (LMO) surface properties, *e.g.* the optimal positions for oxygen adsorption, its surface transport properties, as well as the charge-transfer behavior. In fuel-cell applications, the operational temperature is so high ( $T > 800$  K) that the LMO unit cell is cubic and thus Jahn–Teller (JT) lattice deformation around Mn ions and related magnetic and orbital orderings no longer take place.

The first *ab-initio* calculation of cubic LaMnO<sub>3</sub> surface properties [851] has been made by the HF LCAO method for (110) LMO surface in the single-slab model. The extension of these calculations to the (001) LMO surface was made in [852]. The bulk cubic unit cell atoms are distributed over atomic planes (normal to the surface direction) in the following way: for the (110) surface – O<sub>2</sub>–LaMnO–O<sub>2</sub>–LaMnO · · · ; for the (001) surface – LaO–MnO<sub>2</sub>–LaO–MnO<sub>2</sub> · · · (see Fig. 11.4). In both cases the surfaces are polar.

In LMO (110) surface calculations [851] the O<sub>2</sub>-terminated slab consisting of seven planes was taken, *i.e.* four O<sub>2</sub> planes and three LaMnO planes. Such a symmetrical slab is nonstoichiometric, *i.e.* it does not consist of an integer number of formula units. To restore the stoichiometry of the 7-plane slab, one oxygen atom has been removed from both O<sub>2</sub>-planes terminating the slab, *i.e.* the slab of three bulk primitive unit cells with periodically repeated surface oxygen vacancies was used. Such an approach is justified since it is well known that the polar surfaces are stabilized by surface defects and surface-atom relaxation. The surface energy  $E_s$  (per surface unit cell) for such a slab equals:

$$E_s = \frac{1}{2} (E_O^{slab} - 3E_{bulk}) \quad (11.12)$$

where  $E_O^{slab}$  and  $E_{bulk}$  are the total energies for the O-terminated slab and bulk unit cells, respectively. On the other hand, the defectless surfaces could be modeled using nonstoichiometric slabs: O<sub>2</sub>-terminated or LaMnO-terminated. In this case the surface energy  $E_s$  could be calculated as the average:

$$E_s = \frac{1}{4} (E_{O_2}^{slab} + E_{LMO}^{slab} - 7E_{bulk}) \quad (11.13)$$

where  $E_{O_2}^{slab}$  and  $E_{LMO}^{slab}$  are the total energies of the slabs with O<sub>2</sub> and LaMnO terminations, respectively.

The comparison of energies for the stoichiometric and nonstoichiometric 7-plane slabs permits conclusions to be drawn on the role of surface oxygen vacancies in

surface stabilization. The O-terminated slab consists of three Mn-containing planes, each Mn atom is supposed to have oxidation state +3, *i.e.* 4 valence electrons are localized on  $\text{Mn}^{3+}$  ions. The UHF LCAO calculations have been performed for both the FM (the number of  $\alpha - \beta$  electrons is  $3 \times 4 = 12$ ) and the AFM ( $\alpha - \beta = 4$  electrons) states. Since the SCF calculations of these slabs are extremely slow and timeconsuming, to a first approximation, the relaxed surface geometry optimized by means of the classical shell model [853] based on atom–atom potentials has been used. Since one of the two surface O atoms (per 2D unit cell) is removed, the remaining atoms reveal displacements not only perpendicularly to the surface, but also inplane.

In slab calculations [852] the displacements in the first two top planes were taken into account, which are considerably larger than those in deeper planes. Similar to the bulk calculations, the FM stoichiometric (110) slab for the O termination turns out to be energetically more favorable than AFM, by 0.9 eV per Mn. The calculated O-terminated surface energy is 3.5 eV for the unrelaxed slab and 0.7 eV for the relaxed one, *i.e.* the relaxation energy (per surface unit cell) is 2.8 eV.

**Table 11.22.** The effective atomic charges  $Q(|e|)$  in four unrelaxed top layers of the LMO (110) surface, both stoichiometric O-terminated ( $Q_1$ ), and nonstoichiometric  $\text{O}_2$ - and  $\text{LaMnO}$ -terminated ( $Q_2$  and  $Q_3$ ), as well as the relevant deviations of plane charges,  $\Delta Q(|e|)$  from those in the bulk ( $Q(\text{La})=2.56$ ;  $Q(\text{Mn})=2.09$ ;  $Q(\text{O})=-1.55$ )

Plane	Atom	$Q_1$	$\Delta Q_1$	$Q_2$	$\Delta Q_2$	$Q_3$	$\Delta Q_3$
I	O	-1.16	0.39	-0.77	1.56	-1.86(O) 1.73 (La) 1.83 (Mn)	-1.40
II	La	2.45	-0.06	2.52	-0.06	-1.67 (O)	-0.24
	Mn	2.19		2.10			
	O	-1.60		-1.58			
III	O	-1.66	-0.16	-1.58	-0.06	-1.69 (O) 2.56 (La) 2.40 (Mn)	0.17
	O	-1.60		-1.58			
IV	La	2.54	-0.35	2.55	0.18	-1.63 (O)	-0.16
	Mn	1.87		2.31			
	O	-1.66		-1.58			

Table 11.22 shows the effective atomic charges  $Q$  of slab atoms and the deviation of the plane charges  $\Delta Q$  (per unit cell) from those calculated with the bulk atomic charges. For example, in the plane II for the O-terminated stoichiometric surface the effective charge of the La deviates from that in the bulk by  $2.45 e - 2.56 e = -0.11 e$ . The effective charges of Mn and O deviate from those in the bulk by  $0.1 e$  and  $-0.05 e$ , respectively. That is, the  $\text{LaMnO}$  plane's charge deviates from that in the bulk by  $-0.06 e$ . This value characterizes the charge redistribution in near-surface planes compared to the bulk. For stoichiometric surfaces the sum of  $\Delta Q$  over all planes is zero. Thus, the effective charge of a surface O atom is considerably reduced with respect to that in the bulk. The charges of both metal atoms in the second plane are slightly more positive, which is almost compensated by the charge of a more negative

O atom. Charges of the two O atoms in the third plane are close to those in the bulk. Surprisingly, in the central, fourth plane, the Mn charge turns out to be considerably (by 0.22  $e$ ) less positive than in the bulk. This is enhanced by the same trend for the O atoms, which results in a considerable ( $-0.35\text{ }e$ ) effective charge of the central plane with respect to the bulk.

The calculation for the surface energy for the 7-plane nonstoichiometric slabs, obtained using (11.13), gives  $E_s=6.8\text{ eV}$ , *i.e.* about a factor of two larger than the surface energy of the stoichiometric slab. This demonstrates that oxygen vacancies strongly stabilize the polar (110) surface. The charge distribution for the nonstoichiometric O<sub>2</sub><sup>-</sup> and LaMnO-terminated surfaces is summarized in Table 11.22. As one can see, the effective charge of Mn in the central plane of the O<sub>2</sub>-terminated surface with respect to the bulk value is  $-0.22\text{ }e$ , *i.e.* the same in absolute value but with the opposite sign to that on the O-terminated surface. The two surface O atoms share nearly the same charge as a single O atom possesses on the stoichiometric surface. Other planes are only slightly perturbed. Since the O<sub>2</sub>- and LaMnO-terminated surfaces complement each other, their total charges (with respect to those in the bulk) are expected to be equal in magnitude but of the opposite signs, which indeed takes place.

Calculations for the asymmetric, 8-plane stoichiometric LaO $\cdots$ MnO<sub>2</sub> slab show that the surface energy is larger by 1 eV than that for the stoichiometric 7-plane slab with surface vacancies. This means that the surface vacancies serve as a better stabilizing factor than the charge redistribution near the surface compensating for the macroscopic dipole moment. From the relevant charge redistribution one can see that both surfaces of this 8-plane slab, the O<sub>2</sub>- and LaMnO-terminated ones, are charged strongly positively with respect to the bulk charges, whereas the internal planes are charged mostly slightly negatively.

The LMO (001) surface was modeled in [852] by similar symmetric 7-plane slabs with two kinds of terminations (LaO $\cdots$ LaO and MnO<sub>2</sub> $\cdots$ MnO<sub>2</sub>) and an 8-plane LaO $\cdots$ MnO<sub>2</sub> slab. The former is nonstoichiometric, the latter is stoichiometric (four bulk unit cells per surface unit cell). Unlike the (110) O-terminated surface, it is not easy to make the 7-plane (001) slab stoichiometric through introduction of surface vacancies. If we count the formal ionic charges, La<sup>3+</sup>, Mn<sup>3+</sup>, O<sup>2-</sup>, these two slabs have the total charges of 1  $e$  (LaO) and  $-1\text{ }e$  (MnO<sub>2</sub>). In the SCF calculations, slabs are assumed to be neutral by definition, which results in the electronic-density redistribution between atoms in different planes.

The calculated defectless surface energy for the (001) using (11.13) equals 2.04 eV. This is smaller by a factor of 3 than that for a similar nonstoichiometric (110) surface.

Analysis of the charge redistribution for the LaO- and MnO<sub>2</sub>-terminated (001) surfaces shows that the largest charge perturbation with respect to the bulk charges is observed for the top and bottom planes, similarly to the (110) case. The deviations of the effective atomic charges starting the second plane are quite small, of the order of 0.1–0.2  $e$ . These two surface terminations are complementary, which is why the total charges of the LaO- and MnO<sub>2</sub>-terminated slabs are equal in absolute values and have opposite signs of  $-1\text{ }e$  and  $1\text{ }e$ , respectively. As to the use of the asymmetric, stoichiometric 8-plane slab LaO $\cdots$ MnO<sub>2</sub>, its main problem was believed to arise due to the macroscopic polarization caused by a dipole moment perpendicular to the surface as a consequence of the alternating oppositely charged ( $1\text{ }e$ ,  $-1\text{ }e$ ) planes.

However, as was demonstrated for the  $\text{SrTiO}_3$  (110) polar surface [854], the charge redistribution near the surface is able to cancel the macroscopic surface polarization. For this, the absolute value of the effective charge of the top plane should be smaller than that in the slab center. As was found in [852], the effective charge of the fourth  $\text{MnO}_2$ -plane of the 8-plane slab is  $-0.86\text{ e}$ , whereas that of the top  $\text{LaO}$ -plane  $0.37\text{ e}$ , *i.e.* the condition is fulfilled and the (001) plane is stable. The same is true for the 8-plane (110) slab. For the 8-plane (001) slab only the top and bottom planes of a slab are considerably perturbed as compared to the bulk charges, charges in all the other planes are only slightly modified. The effective charges of the  $\text{LaO}$  and  $\text{MnO}_2$  (top and bottom) planes are close in magnitude and opposite in sign. The relevant surface energy calculated using (11.2) turns out to be as small as  $1.02\text{ eV}/\text{cell}$  for the FM state. This means that the (001) surface is stable and energetically favorable. The (0 0 1) surface energy in the AFM state is formally even lower,  $0.83\text{ eV}$ . However, the relevant total energies for the bulk unit cell (per formula unit) and the slab in the AFM state are higher (by  $0.22$  and  $0.56\text{ eV}$ , respectively) than the FM states.

The LCAO single-slab calculations [852] of the electronic structure of the polar  $\text{LnMnO}_3$  (001) and (110) surfaces clearly demonstrate that the stoichiometric slabs have considerably lower energies than the nonstoichiometric ones. It should be stressed that the structural oxygen vacancies are energetically required and hence are essential elements of the (110) polar surface structure. Their formation makes the (110) slabs stoichiometric and energetically more favorable than the stoichiometric slabs stabilized by the near-surface electronic density redistribution necessary to compensate the macroscopic dipole moment perpendicular to the asymmetric  $\text{LaO} \cdots \text{MnO}_2$  surfaces.

The comparative DFT B3PW LCAO (single-slab) and GGA PW (periodic-slab) calculations of  $\text{LaMnO}_3$  (001) and (110) surfaces in slab models has been made in [855], we refer the reader to this publication for details of the calculations. It is important that the B3PW LCAO and GGA PW calculations for the  $\text{LaMnO}_3$  surfaces show reasonable agreement for atomic displacements, effective charges (in the PW calculations, Bader analysis was used), and surface energies. The effective charges of surface atoms markedly depend on the surface relaxation and less on the particular (FM or AAF) magnetic configuration. The HF-based conclusion (see discussion above) that the polar (001) surface is energetically more favorable than the (110) one was confirmed. This conclusion is important for the modeling of surface adsorption and  $\text{LaMnO}_3$  reactivity. The surface relaxation energy is typically of the order of  $1\text{--}1.5\text{ eV}$  (per square unit  $a^2$ , where  $a$  is the cubic lattice parameter) *i.e.* much larger than the tiny difference between various magnetic structures. Moreover, the calculated surface energy for the slab built from orthorhombic unit cells is close to and even slightly larger than that for the cubic unit cells. These two facts justify the use in surface and adsorption modeling of slabs built from the cubic cells. This is a very important observation since the detailed adsorption and migration modeling, *e.g.*, for surface O atoms at moderate coverages that is relevant for fuel-cell applications, is very time consuming even for the smallest slab thicknesses.

*The discussion of LMO surface modeling concludes Part II (Applications) of this book. We tried to demonstrate, via numerous examples, the efficiency of modern quantum-chemical approaches to calculate the properties of crystalline solids – bulk and defective crystals, surfaces and adsorption.*

The list of computer programs used in LCAO (both *ab-initio* and semiempirical) calculations of periodic systems is given in Appendix C.

## A

---

### Matrices of the Symmetrical Supercell Transformations of 14 Three-dimensional Bravais Lattices

#### A.1. The triclinic crystal system

(i)  $l(P,P)$  is an arbitrary integer matrix.

#### A.2. The monoclinic crystal system

$$(i) \quad l(P,P) = \begin{pmatrix} n_1 & n_5 & 0 \\ n_4 & n_2 & 0 \\ 0 & 0 & n_3 \end{pmatrix}, \quad L = (n_1 n_2 - n_4 n_5) n_3; \quad (A.1)$$

$$(ii) \quad l(A,P) = \begin{pmatrix} n_1 & n_5 & 0 \\ n_4 & n_2 & -n_3 \\ n_4 & n_2 & n_3 \end{pmatrix}, \quad L = 2(n_1 n_2 - n_4 n_5) n_3;$$

$$(iii) \quad l(P,A) = \begin{pmatrix} n_1 & n_4 & n_4 \\ n_5 & n_2 & n_2 \\ 0 & -n_3 & n_3 \end{pmatrix}, \quad L = 2(n_1 n_2 - n_4 n_5) n_3;$$

$$(iv) \quad l(A,A) = \begin{pmatrix} n_1 & n_5 & n_5 \\ n_4 & n_2 + n_3 & n_2 - n_3 \\ n_4 & n_2 - n_3 & n_2 + n_3 \end{pmatrix}, \quad L = 4(n_1 n_2 - n_4 n_5) n_3;$$

#### A.3. The hexagonal crystal system

$$(i) \quad l^{(1)}(P,P) = \begin{pmatrix} n_1 & 0 & 0 \\ 0 & n_1 & 0 \\ 0 & 0 & n_2 \end{pmatrix}, \quad L = n_1^2 n_2; \quad (A.2)$$

$$(ii) \quad l^{(2)}(P,P) = \begin{pmatrix} n_1 & -n_1 & 0 \\ n_1 & 2n_1 & 0 \\ 0 & 0 & n_2 \end{pmatrix}, \quad L = 3n_1^2 n_2;$$

#### A.4. The rhombohedral crystal system

$$(i) \quad l(R,R) = \begin{pmatrix} n_1 + n_2 & n_2 & n_2 \\ n_2 & n_1 + n_2 & n_2 \\ n_2 & n_2 & n_1 + n_2 \end{pmatrix}, \quad L = n_1^2(n_1 + 3n_2);$$

A.5. The orthorhombic crystal system

(i)  $l(P,P)$  coincides with (A.1);

$$(ii) \quad l(C,P) = \begin{pmatrix} n_1 & -n_2 & 0 \\ n_1 & n_2 & 0 \\ 0 & 0 & n_3 \end{pmatrix}, \quad L = 2n_1n_2n_3;$$

$$(iii) \quad l(F,P) = \begin{pmatrix} 0 & n_2 & n_3 \\ n_1 & 0 & n_3 \\ n_1 & n_2 & 0 \end{pmatrix}, \quad L = 2n_1n_2n_3;$$

$$(iv) \quad l(I,P) = \begin{pmatrix} -n_1 & n_2 & n_3 \\ n_1 & -n_2 & n_3 \\ n_1 & n_2 & -n_3 \end{pmatrix}, \quad L = 4n_1n_2n_3;$$

$$(v) \quad l(P,C) = \begin{pmatrix} n_1 & n_1 & 0 \\ -n_2 & n_2 & 0 \\ 0 & 0 & n_3 \end{pmatrix}, \quad L = 2n_1n_2n_3;$$

$$(vi) \quad l(C,C) = \begin{pmatrix} n_1 & n_2 & 0 \\ n_2 & n_1 & 0 \\ 0 & 0 & n_3 \end{pmatrix}, \quad L = (n_1^2 - n_2^2)n_3;$$

$$(vii) \quad l(A,C) = \begin{pmatrix} n_1 & n_1 & 0 \\ -n_2 & n_2 & -n_3 \\ -n_2 & n_2 & n_3 \end{pmatrix}, \quad L = 4n_1n_2n_3;$$

$$(viii) \quad l(F,C) = \begin{pmatrix} -n_2 & n_2 & n_3 \\ n_1 & n_1 & n_3 \\ n_1 - n_2 & n_1 + n_2 & 0 \end{pmatrix}, \quad L = 4n_1n_2n_3;$$

$$(ix) \quad l(I,C) = \begin{pmatrix} -n_1 & -n_2 & n_3 \\ n_1 & n_2 & n_3 \\ n_2 & n_1 & -n_3 \end{pmatrix}, \quad L = 2(n_1^2 - n_2^2)n_3;$$

$$(x) \quad l(P,F) = \begin{pmatrix} -n_1 & n_1 & n_1 \\ n_2 & -n_2 & n_2 \\ n_3 & n_3 & -n_3 \end{pmatrix}, \quad L = 4n_1n_2n_3;$$

$$(xi) \quad l(C,F) = \begin{pmatrix} -n_1 & n_1 & n_2 \\ -n_2 & n_2 & n_1 \\ n_3 & n_3 & -n_3 \end{pmatrix}, \quad L = 2(n_1^2 - n_2^2)n_3;$$

$$(xii) \quad l(F,F) = \frac{1}{2} \begin{pmatrix} n_2 + n_3 & -n_2 + n_3 & n_2 - n_3 \\ -n_1 + n_3 & n_1 + n_3 & n_1 - n_3 \\ -n_1 + n_2 & n_1 - n_2 & n_1 + n_2 \end{pmatrix}, \quad \begin{array}{l} L = n_1n_2n_3; \\ n_1, n_2, n_3 \text{ are of} \\ \text{the same parity;} \end{array}$$

$$(xiii) \quad l(I,F) = \begin{pmatrix} n_1 + n_2 + n_3 & -n_3 & -n_2 \\ -n_3 & n_1 + n_2 + n_3 & -n_1 \\ -n_2 & -n_1 & n_1 + n_2 + n_3 \end{pmatrix}, \quad L = 2[(n_1 + n_2 + n_3)(n_1n_2 + n_2n_3 + n_3n_1) - n_1n_2n_3];$$

$$(xiv) \quad l(P,I) = \begin{pmatrix} 0 & n_1 & n_1 \\ n_2 & 0 & n_2 \\ n_3 & n_3 & 0 \end{pmatrix}, \quad L = 2n_1n_2n_3;$$

$$(xv) \quad l(C,I) = \begin{pmatrix} -n_2 & n_1 & n_1 - n_2 \\ n_2 & n_1 & n_1 + n_2 \\ n_3 & n_3 & 0 \end{pmatrix}, \quad L = 4n_1n_2n_3;$$

$$(xvi) l(F,I) = \begin{pmatrix} n_2 + n_3 & n_3 & n_2 \\ n_3 & n_1 + n_3 & n_1 \\ n_2 & n_1 & n_1 + n_2 \end{pmatrix}, \quad L = 4n_1 n_2 n_3;$$

$$(xvii) l(I,I) = \frac{1}{2} \begin{pmatrix} n_2 + n_3 & -n_1 + n_3 & -n_1 + n_2 \\ -n_2 + n_3 & n_1 + n_3 & n_1 - n_2 \\ n_2 - n_3 & n_1 - n_3 & n_1 + n_2 \end{pmatrix}, \quad \begin{array}{l} L = n_1 n_2 n_3; \\ n_1, n_2, n_3 \text{ are of} \\ \text{the same parity;} \end{array}$$

A.6. The tetragonal crystal system

(i)  $l^{(1)}(P,P)$  coincides with (A.2);

$$(ii) l^{(2)}(P,P) = \begin{pmatrix} n_1 & -n_1 & 0 \\ n_1 & n_1 & 0 \\ 0 & 0 & n_2 \end{pmatrix}, \quad L = 2n_1^2 n_2;$$

$$(iii) l^{(1)}(I,P) = \begin{pmatrix} 0 & n_1 & n_2 \\ n_1 & n_2 & 0 \\ n_1 & n_1 & 0 \end{pmatrix}, \quad L = 2n_1^2 n_2;$$

$$(iv) l^{(2)}(I,P) = \begin{pmatrix} -n_1 & n_1 & n_2 \\ n_1 & -n_1 & n_2 \\ n_1 & n - 1 & -n_2 \end{pmatrix}, \quad L = 4n_1^2 n_2;$$

$$(v) l^{(1)}(P,I) = \begin{pmatrix} 0 & n_1 & n_1 \\ n_1 & 0 & n_1 \\ n_2 & n_2 & 0 \end{pmatrix}, \quad L = 2n_1^2 n_2;$$

$$(vi) l^{(2)}(P,I) = \begin{pmatrix} -n_1 & n_1 & 0 \\ n_1 & n_1 & 2n_1 \\ n_2 & n_2 & 0 \end{pmatrix}, \quad L = 4n_1^2 n_2;$$

$$(vii) l^{(1)}(I,I) = \begin{pmatrix} n_1 + n_2 & n_2 & n_1 \\ n_2 & n_1 + n_2 & n_1 \\ n_1 & n_1 & 2n_1 \end{pmatrix} \quad L = 4n_1^2 n_2;$$

$$(viii) l^{(2)}(I,I) = \frac{1}{2} \begin{pmatrix} n_1 + n_2 & -n_1 + n_2 & 0 \\ -n_1 + n_2 & n_1 + n_2 & 0 \\ n_1 - n_2 & n_1 - n_2 & 2n_1 \end{pmatrix} \quad \begin{array}{l} L = n_1^2 n_2; \\ n_1, n_2 \text{ are of} \\ \text{the same parity;} \end{array}$$

A.7. The cubic crystal system

$$(i) l(P,P) = l(F,F) = l(I,I) = \begin{pmatrix} n & 0 & 0 \\ 0 & n & 0 \\ 0 & 0 & n \end{pmatrix}, \quad L = n^3;$$

$$(ii) l(F,P) = l(P,I) = \begin{pmatrix} 0 & n & n \\ n & 0 & n \\ n & n & 0 \end{pmatrix}, \quad L = 2n^3;$$

$$(iii) l(I,P) = l(P,F) = \begin{pmatrix} -n & n & n \\ n & -n & n \\ n & n & -n \end{pmatrix}, \quad L = 4n^3;$$

$$(iv) l(I,F) = \begin{pmatrix} 3n & -n & -n \\ -n & 3n & -n \\ -n & -n & 3n \end{pmatrix}, \quad L = 16n^3;$$

$$(v) l(F,I) = \begin{pmatrix} 2n & n & n \\ n & 2n & n \\ n & n & 2n \end{pmatrix}, \quad L = 4n^3.$$

## B

---

### Reciprocal Matrices of the Symmetric Supercell Transformations of the Three Cubic Bravais Lattices

$$Q_1 = \begin{pmatrix} 1 & 0 & 0 \\ 0 & 1 & 0 \\ 0 & 0 & 1 \end{pmatrix} \quad Q_2 = \begin{pmatrix} -1 & 1 & 1 \\ 1 & -1 & 1 \\ 1 & 1 & -1 \end{pmatrix} \quad Q_3 = \begin{pmatrix} 0 & 1 & 1 \\ 1 & 0 & 1 \\ 1 & 1 & 0 \end{pmatrix}$$
$$Q_4 = \begin{pmatrix} 2 & 1 & 1 \\ 1 & 2 & 1 \\ 1 & 1 & 2 \end{pmatrix} \quad Q_5 = \begin{pmatrix} 3 & -1 & -1 \\ -1 & 3 & -1 \\ -1 & -1 & 3 \end{pmatrix}$$

## C

---

# Computer Programs for Periodic Calculations in Basis of Localized Orbitals

The information about computer programs applied in molecular quantum chemistry and materials science can be found on different Internet sites [856–858]. In particular, on site [856] on-line links are given to the appropriate information. The majority of the existing computer codes for calculations of periodic systems can be divided into two main groups: LO codes using a basis set of localized orbitals (LO) and PW(APW) codes using plane waves (PW) or augmented plane waves (APW) as a basis set. The only exclusion is the hybrid Gaussian LO and PW (GPW) DFT code QI-UCKSTEP/CP2K [859]. The sites mentioned include references to both LO and PW codes. The information about periodic codes using LO or PW bases can also be found in [568, 860]. Here, we restrict ourselves only to brief information about computer codes for periodic LO calculations (see Table C.1). The indication of the corresponding homepage and references on the publications are given in the last two columns of Table C.1. Both ab-initio (HF,DFT (LDA,GGA), hybrid HF-DFT, time-dependent DFT (TDFT)) and semi-empirical (SE) codes are included in the list. The codes listed allow all-electron (AE) calculations (also termed full potential-FP) or valence-only ones with the use of pseudopotential (PP) for core electrons or both. For the localized basis we use the acronyms GTO (Gaussian-type orbitals), STO (Slater-type orbitals) and NTO (numerical type orbitals). In particular, *f*-GTO and *f*-polarization-GTO mean the possibility to make full GTO calculations for *f*-elements or the simple extension of Gaussian basis-sets to include *f*-polarization basis-functions, respectively. In the remaining cases only *s*, *p* and *d* orbitals can be used in the basis set. The geometry optimization can be made over the atomic coordinates only (GO) or including both the lattice parameters optimization (full GO). Some codes allow linear scaling ( $O(N)$ ) with the basis-set size and molecular-dynamics (MD) calculations. The semiempirical codes can allow the band structure calculations for nonzero wave vectors (BAND) or the cyclic-cluster model (CCM) without the BZ summation can be used. The CRYSTAL suite remains the mostly advanced and developing LCAO periodic program, compared to other codes listed in Table C.1. We refer the reader to the calculations of metal-organic frameworks (MOF), [872] as a case study showing that the CRYSTAL program allows reliable *ab-initio* prediction of materials properties of complex systems to be made. Note that from January 1st, 2007, CRYSTAL03 will not be supported any more.

**Table C.1.** List of periodic computer programs using localized orbitals basis

No	Program	Description	Web site	Refs
1	CRYSTAL03	HF;DFT (LDA,GGA); Hybrid HF-DFT; AE; PP; GTO; GO	<a href="http://www.crystal.unito.it">www.crystal.unito.it</a> <a href="http://www.cse.clrc.ac.uk/cmg">www.cse.clrc.ac.uk/cmg</a>	[568,860–863]
2	CRYSTAL06	+ <i>f</i> -polarization-GTO, full GO, vibrational frequencies	<a href="http://www.crystal.unito.it/home.html">www.crystal.unito.it/home.html</a>	
3	CRYSCOR	+ MP2 correlation	<a href="http://www.crystal.unito.it">www.crystal.unito.it</a>	[201]
4	GAUSSIAN03	HF;DFT (LDA,GGA); PHF; Hybrid HF-DFT; AE; PP; <i>f</i> -GTO; GO;O(N)	<a href="http://www.gaussian.com">www.gaussian.com</a>	[379]
5	ADF2006 (BAND)	DFT (LDA,GGA); Hybrid HF-DFT; TD-DFT; AE; STO;	<a href="http://www.scm.com/Doc/Doc2006.01">/www.scm.com/Doc/Doc2006.01</a>	[864]
6	SIESTA	DFT (LDA,GGA);PP; NTO; GO; MD ;O(N)	<a href="http://www.uam.es/departamentos/ciencias/fismateriac/siesta">www.uam.es/departamentos/ciencias/fismateriac/siesta</a>	[400]
7	AIMPRO	DFT(LDA,GGA); PP; LGTO	<a href="http://newton/ex.ac.uk/research">http://newton/ex.ac.uk/research</a>	[555]
8	SEQUEST	DFT (LDA, GGA);PP; GTO;O(N);GO	<a href="http://dft.sandia.gov/Quest">http://dft.sandia.gov/Quest</a>	[865]
9	DMOL3	DFT (LDA, GGA);AE; NTO; GO	<a href="http://people.web.psi.ch/delley/dmol3.html">http://people.web.psi.ch/delley/dmol3.html</a>	[866]
10	FPLO	DFT (LSDA,LSDA+U); AE; LO;	<a href="http://www.fplo.de">www.fplo.de</a>	[867]
11	PLATO	DFT (LDA); NTO;GO	<a href="http://www-staff.lboro.ac.uk/masdk/plato.html">www-staff.lboro.ac.uk/masdk/plato.html</a>	[868]
12	QUICKSTEP/ CP2K	DFT(LDA,GGA); PP;GTO/PW	<a href="http://cp2k.berlios.de">http://cp2k.berlios.de</a>	[859]
13	CNDO 4.0	SE,BAND,GE	<a href="http://www.wgc.chem.psu.edu/valera/cndo/manual.html">www.wgc.chem.psu.edu/valera/cndo/manual.html</a>	[869]
14	MOPAC2002	SE,BAND,GE	<a href="http://www.cachesoftware.com/mopac">www.cachesoftware.com/mopac</a>	[312,870]
15	MSINDO	SE,CCM,STO,GO,MD	<a href="http://www.theochem.uni-hannover.de/Bredow/MSINDO">www.theochem.uni-hannover.de/Bredow/MSINDO</a>	[256]
16	SOLID2000	SE,CCM,QR-INDO, STO,GO	<a href="http://www.stech.sk/stechsoft/htm">www.stech.sk/stechsoft/htm</a>	[307]
17	SYM-SYM	SE,CCM,INDO,GO	<a href="http://www.cmmmp.ucl.ac.uk/lev/recearc4/node8.html">www.cmmmp.ucl.ac.uk/lev/recearc4/node8.html</a>	[871]

The reader can also find useful such codes as XCrysDen( [873], GULP( [875] and BAND-GUI( [345].

*XCrysDen* program can be used as a graphical user interface (GUI) for the CRYSTAL95/98/03/06 programs. The advantage of the GUI is its rendering possibility, which yields graphical feedback to the user. Every manipulation of the structure is visualized immediately and to enhance the usefulness of XCrySDen even further, an UNDO/REDO option is available, which makes every false move recoverable. Several graphical procedures make the manipulation of the atomic structures easier, while other graphical functions are suitable for checking the geometry of the structure. This program uses the ease of a GUI and the flexibility of manual editing and allows the user to view and edit the input scripts for the CRYSTAL programs on request. Immediately after the manual editing is completed the program visualizes the result. We refer the reader for details to the program description [874].

*GULP* is a program for performing a variety of types of simulation on materials using boundary conditions of 0D (molecules and clusters), 1D (polymers), 2D (surfaces, slabs and grain boundaries), or 3D (periodic solids). The focus of the code is on analytical solutions, through the use of lattice dynamics, where possible, rather than on molecular dynamics. A variety of force fields can be used within GULP spanning the shell model for ionic materials, molecular mechanics for organic systems, and the embedded-atom model for metals. Analytic derivatives are included up to at least second order for most force fields, and to third order for many.

*ADF2006.01* is the first ADF release containing a graphical user interface for the BAND program. BAND input also enables inexperienced ADF-BAND users to easily create BAND jobs. You can use BAND input to define your periodic structure (geometry), and to set details of your BAND job using an easy-to-use graphical user interface. BAND input will generate the complete job script for you. This script takes care of running BAND. You can also use BAND input to run these script files on your local machine in the background.

---

## References

1. R. Dronkowski, *Computational Chemistry of Solid State Materials. A Guide for Materials Scientists, Chemists, Physicists and Others* (Wiley-VCH, Weinheim, 2005)
2. C.M. Quinn, *An Introduction to Quantum Chemistry of Solids* (Clarendon Press, Oxford, 1973)
3. A.A. Levin, *Solid State Quantum Chemistry* (McGraw-Hill, New York, 1977)
4. *Ab-initio Calculations of the Properties of Crystalline Materials*, ed. C. Pisani, Lecture Notes in Chemistry **67** (Springer Verlag, Berlin, 1996)
5. P. Fulde, *Electron Correlations in Molecules and Solids*, 3rd edn. Springer Series in Solid State Sciences 100 (Springer, Berlin Heidelberg New York, 1995)
6. W. Harrison, *Electronic Structure and Properties of Solids: Physics of the Chemical Bond*, 2nd edn. (Dover, New York, 1989)
7. R. Hoffmann, *Solids and Surfaces: A Chemist View on Bonding in Extended Structures* (Weinheim VCH, 1988)
8. M. Springborg, *Methods of Electronic Structure Calculations* (Wiley, 2000)
9. E. Kahiras, *Atomic and Electronic Structure of Solids* (Cambridge University Press, Cambridge, 2003)
10. R. Martin, *Electronic Structure. Basic Theory and Practical Methods* (Cambridge University Press, Cambridge, 2004)
11. L. Kantorovich, *Quantum Theory of the Solid State* (Kluwer Academic Publishers, Dordrecht, 2004)
12. K. Ohno, R. Esfarjani, Y. Kawazoe, *Computational Materials Science*, Springer Series in Solid State Sciences, **129** (Springer, Berlin Heidelberg New York, 1999)
13. R.A. Evarestov, V.P. Smirnov, *Site Symmetry in Crystals: Theory and Applications*, 2nd edn. Springer Series in Solid State Sciences, **108** (Springer, Berlin Heidelberg New York, 1997 )
14. R.L. Flurry, *Symmetry Groups. Theory and Chemical Applications* (Prentice-Hall, Englewood Cliffs, NJ, 1980)
15. P.W.M. Jacobs, *Group Theory with Applications in Chemical Physics* (Cambridge University Press, New York, 2005)
16. *Bilbao Crystallographic Server*, <http://www.cryst.ehu.es/>
17. A.P. Cracknell, B.L. Davies, S.C. Miller, W.F. Love, *Kronecker Product Tables, 1 General Introduction and Tables of Irreducible Representations of Space Groups* (IFI/Plenum, New York-Washington-London, 1979)
18. M.I. Petrashen, E.D. Trifonov, *Applications of Group Theory in Quantum Mechanics* (M.I.T. Press, Massachusetts, 1969)

19. *International Tables for Crystallography*, ed. T.Hahn, **A** Space-group symmetry (Reidel, Dordrecht, 1983 )
20. <http://cst-www.nrl.navy.mil/lattice/>
21. <http://cst-www.nrl.navy.mil/lattice/others.html>
22. Inorganic Crystal Structure Database (ICSD), <http://www.fiz-informationsdienste.de/en/DB/icsd/>
23. V.R. Saunders, R. Dovesi, C. Roetti, R. Orlando, C.M.Zicovich-Wilson, N.M.Harrison, CRYSTAL-2003 Users Manual, University of Torino, Torino, 2003; <http://www.crystal.unito.it>
24. Richard J.D. Tilley, *Crystals and Crystal Structures* (Wiley, 2006)
25. A. Munoz, J.A. Alonso, M.J. Martinez-Lope, M.T. Casais, J.L. Martinez, M.T. Fernandez-Diaz, *Phys. Rev. B* **62**, 6498 (2000)
26. John Z.H. Zhang, *Theory and Application of Quantum Molecular Dynamics* (World Scientific Publishing Co., Singapore, 1999)
27. G.L. Bir, G.E. Pikus, *Symmetry and Strain-induced Effects in Semiconductors* (Wiley, New York, 1972)
28. C. Zicovich-Wilson, R. Dovesi, *Int. J. Quantum Chem.* **67**, 299 (1998)
29. C. Zicovich-Wilson, R. Dovesi, *Int. J. Quantum Chem.* **67**, 311 (1998)
30. C.J. Bradley, A.P. Cracknell, *The Mathematical Theory of Symmetry in Solids* (Clarendon, Oxford, 1972)
31. O.V. Kovalev, *Representations of the Crystallographic Space Groups: Irreducible Representations, Induced Representations and Corepresentations*, 2nd edn. ed. by H.T. Stokes, D.M. Hatch (Gordon and Breach, Philadelphia, PA 1993)
32. I. Shur, *J.F.Math.* **139**, 155 (1911)
33. G.Ya. Lyubarskii, *The Application of Group Theory in Physics* (Pergamon, Oxford, 1960)
34. C.Herring, *J. Franklin Inst.* **233**, 525 (1942)
35. M.W. Schmidt, K.K. Baldridge, J.A. Boatz, S.T. Elbert, M.S. Gordon, J.H. Jensen, S. Koseki, N. Matsunaga, K.A. Nguyen, S. Su, T.L. Windus, M. Dupuis, J.A.J.Jr. Montgomery, *J. Comput. Chem.* **14**, 1347 (1993)
36. C. Edmiston, K. Ruedenberg, *Rev. Mod. Phys.* **35**, 457 (1963)
37. J. Pipek, P.G. Mezey, *J. Chem. Phys.* **90**, 4916 (1989)
38. S.F. Boys, *Rev. Mod. Phys.* **32**, 296 (1960)
39. J. Zak, *Phys. Rev. B* **23**, 2824 (1981)
40. H. Bacry, L. Michel, J. Zak, *Lect. Notes Phys.* **313**, 291 (Springer, Berlin, Heidelberg, 1988)
41. M. Schütz, G. Hetzer, H.-J. Werner, *J. Chem. Phys.* **111**, 5691 (1999)
42. V.P. Smirnov, D.E. Usvyat, *Phys. Rev. B* **64**, 245108 (2001)
43. G. Wannier, *Phys. Rev.* **52**, 191 (1937)
44. W. Kohn, *Phys. Rev.* **115**, 809 (1959)
45. J. Des Cloizeaux, *Phys. Rev.* **135**, A698 (1964)
46. N. Marzari, D. Vanderbilt, *Phys. Rev. B* **56**, 12847 (1997)
47. V.P. Smirnov, R.A. Evarestov, D.E. Usvyat, *Int. J. Quantum. Chem.* **88**, 642 (2002)
48. B. Sporkmann, H. Bross, *Phys. Rev. B* **49**, 10869 (1994)
49. A. Shukla, M. Dolg, P. Fulde, H. Stoll, *Phys. Rev. B* **60**, 5211 (1999)
50. S. Goedecker, *Rev. Mod. Phys.* **71**, 1085 (1999)
51. I. Souza, R.M. Martin, N. Marzari, X. Zhao, D. Vanderbilt, *Phys. Rev. B* **62**, 15505 (2000)
52. P.Y. Yu, M. Cardona, *Fundamentals of Semiconductors. Physics and Materials Properties*, 3rd rev. and enlarged edn. (Springer, Berlin, Heidelberg, 2005)
53. C.M. Zicovich-Wilson, R. Dovesi, V.R. Saunders, *J. Chem. Phys.* **115**, 9708 (2001)
54. I. Mayer, G. Rather, S. Suhai, *Chem. Phys. Lett.* **293**, 81 (1998)

55. R.A. Evarestov, V.P. Smirnov, phys. stat. sol. (b) **180**, 411 (1993)
56. J. Des Cloizeaux, Phys. Rev. **129**, 554 (1963)
57. W. Kohn, Phys. Rev. B, **7**, 4388 (1973)
58. J.C. Slater, G.F. Koster, Phys. Rev. **94**, 1498 (1954)
59. V.P. Smirnov, D.E. Usvyat, Phys. Rev. B **59**, 9695 (1999)
60. N. Marzari, D. Vanderbilt, in *First-Principles Calculations for Ferroelectrics*, ed. R.E. Cohen, AIP Conf. Proc. No 436 (AIP, Woodbury, 1998), p.146
61. I. Souza, N. Marzari, D. Vanderbilt, Phys. Rev. B **65**, 035109 (2001)
62. <http://www.wannier-transport.org>
63. C.M. Zicovich-Wilson, A. Bert, C. Roetti, R. Dovesi, V.R. Saunders J. Chem. Phys. **116**, 1120 (2002)
64. A. Bert, M. Llunell, R. Dovesi, C.M. Zicovich-Wilson, Phys. Chem. Chem. Phys. **5**, 5319 (2003)
65. E. Clementi, C. Roetti, *Roothaan–Hartree–Fock Atomic Functions*, in Atomic Data and Nuclear Data Tables, **14**, 177 (1974)
66. C.C.J. Roothaan, Rev. Mod. Phys. **23**, 69 (1951)
67. C.C.J. Roothaan, Rev. Mod. Phys. **32**, 179 (1960)
68. J.A. Pople, R.K. Nesbet, J. Chem. Phys. **22**, 571 (1954)
69. E. Apra, Lecture Notes in Chem. **67**, 101 (1996)
70. R.A. Evarestov, I.I. Tupitsyn, Phys. Solid State **44**, 1656 (2002)
71. P.P. Ewald, Ann. Phys. **64**, 253 (1921)
72. A.B. Kunz, Phys. Rev. B **6**, 606 (1972)
73. J.J. Ladik, Phys. Rep. **313**, 171 (1999)
74. J.-M. Andre, L. Gouverneur, G. Leroy, Int. J. Quantum Chem. **1**, 427, 451 (1967)
75. C. Pisani, R. Dovesi, Int. J. Quantum Chem. **17**, 501, 517 (1980)
76. R. Dovesi, C. Pisani, C. Roetti, P.Dellarole, Phys. Rev. B **24**, 4170 (1981)
77. R. Dovesi, M. Causa, G. Angonoa, Phys. Rev. B **24**, 4177 (1981)
78. M. Causa, Lecture Notes in Chem. **67**, 91 (1996)
79. C. Pisani, U. Birkenheuer, Comp. Phys. Commun. **96**, 221 (1996)
80. <http://www.crystal.unito.it>
81. <http://www.cse.clrc.ac.uk>
82. K.N. Kudin, G.E. Scuseria, Phys. Rev. B **61**, 16440 (2000)
83. R. Imrota, K.N. Kudin, G.E. Scuseria, V. Barone, J. Am. Chem. Soc **124**, 113 (2002)
84. N.W. Ashcroft, N.D. Mermin, *Solid State Physics* (Cole, London, 1976)
85. M.F. Guest, V.R. Saunders, Mol. Phys. **28**, 819 (1974)
86. R.A. Evarestov, V.P. Smirnov, J. Phys.: Condens. Matter **9**, 3023 (1997)
87. R.A. Evarestov, V.P. Smirnov, phys. stat. sol. (b) **119**, 9 (1983)
88. D. J. Chadi, M.L. Cohen, Phys. Rev. B **8**, 5747 (1973)
89. J. Moreno, J.M. Soler, Phys. Rev. B **46**, 13891 (1992)
90. H.J. Monkhorst, J.D. Pack, Phys. Rev. B **13**, 5188 (1976)
91. R.A. Evarestov, V.P. Smirnov, Phys. Rev. B **70**, 233101 (2004)
92. A. Baldereschi, Phys. Rev. B **7**, 5212 (1973)
93. D. Vanderbilt, Phys. Rev. B **41**, 7892 (1990)
94. M. Causa, R. Dovesi, C. Roetti, Phys. Rev. B **43**, 11937 (1991)
95. R.A. Evarestov, V.A. Lovchikov, I.I. Tupitsin, phys. stat. sol. (b) **117**, 417 (1983)
96. K.B. Wiberg, Tetrahedron **24**, 1083 (1968)
97. V.A. Veryazov, A.V. Leko, R.A. Evarestov Phys. Solid State **41**, 1286 (1999)
98. R.A. Evarestov, I.I. Tupitsyn, Russ. J. Phys. Chem. **74**, S363 (2000)
99. C. Pisani, E. Apra, M. Causa, Int. J. Quantum Chem. **38**, 419 (1990)
100. T. Bredow, R.A. Evarestov, K. Jug, phys. stat. sol. (b) **222**, 495 (2000)
101. V. Fock, M. Vesselow, M. Petrashen, Zh. Exsp. Theor. Fiz. **10**, 723 (1940)

102. C.J. Cramer, *Essentials of Computational Chemistry*, 2nd edn. (Wiley, New York, 2004).
103. M.J. Wong, L. Radom, *J. Phys. Chem.* **99**, 8582 (1995)
104. C. Moller, M.S. Plesett, *Phys. Rev.* **46**, 618 (1934)
105. Per-Olov Löwdin, *Int. J. Quantum Chem.* **55**, 77 (1995)
106. P. Knowles, M. Schütz, H.-J. Werner, in *Modern Methods and Algorithms of Quantum Chemistry*, Proceedings, 2nd edn. ed. by J. Grotendorst, John von Neumann Institute for Computing, Julich, NIC Series, **3**, 97 (2000)
107. Gaussian 03, Revision C.02, M.J. Frisch, G.W. Trucks, H.B. Schlegel, G.E. Scuseria, M.A. Robb, J.R. Cheeseman, J.A. Montgomery Jr., T. Vreven, K.N. Kudin, J.C. Burant, J.M. Millam, S.S. Iyengar, J. Tomasi, V. Barone, B. Mennucci, M. Cossi, G. Scalmani, N. Rega, G.A. Petersson, H. Nakatsuji, M. Hada, M. Ehara, K. Toyota, R. Fukuda, J. Hasegawa, M. Ishida, T. Nakajima, Y. Honda, O. Kitao, H. Nakai, M. Klene, X. Li, J.E. Knox, H.P. Hratchian, J.B. Cross, V. Bakken, C. Adamo, J. Jaramillo, R. Gomperts, R.E. Stratmann, O. Yazyev, A.J. Austin, R. Cammi, C. Pomelli, J.W. Ochterski, P.Y. Ayala, K. Morokuma, G.A. Voth, P. Salvador, J.J. Dannenberg, V.G. Zakrzewski, S. Dapprich, A.D. Daniels, M.C. Strain, O. Farkas, D.K. Malick, A.D. Rabuck, K. Raghavachari, J.B. Foresman, J.V. Ortiz, Q. Cui, A.G. Baboul, S. Clifford, J. Cioslowski, B.B. Stefanov, G. Liu, A. Liashenko, P. Piskorz, I. Komaromi, R.L. Martin, D.J. Fox, T. Keith, M.A. Al-Laham, C.Y. Peng, A. Nanayakkara, M. Challacombe, P.M.W. Gill, B. Johnson, W. Chen, M.W. Wong, C. Gonzalez, and J.A. Pople, Gaussian, Inc., Wallingford CT, 2004, <http://www.gaussian.com/citation.htm>
108. <http://www.eecs.harvard.edu/~mdw/proj/old/jaguar/release.html>
109. C. Pisani, M. Busso, G. Capecci, S. Casassa, R. Dovesi, L. Maschio, C. Zicovich-Wilson, M. Schutz, *J. Chem. Phys.* **122**, 094113 (2005)
110. P. Fulde, *Adv. Phys.* **51**, 909 (2002)
111. H. Stoll, *Chem. Phys. Lett.* **191**, 548 (1992)
112. A. Shukla, M. Dolg, P. Fulde, H. Stoll, *Phys. Rev. B* **60**, 5211 (1999)
113. B. Paulus, *Chem. Phys. Lett.* **371**, 7 (2003)
114. P. Fulde, H. Stoll, *Found. Physics* **30**, 2049 (2000)
115. K.N. Kudin, G.E. Scuseria, *J. Chem. Phys.* **113**, 7779 (2000)
116. <http://www.molpro.net>
117. <http://www.theochem.unito.it/lcc2004/cryscor.pdf>
118. B.O. Roos, *Acc. Chem. Res.* **32**, 137 (1999)
119. <http://www.emsl.pnl.gov/docs/nwchem/>
120. J. Cizek, *J. Chem. Phys.* **45**, 4256 (1966)
121. T.D. Crawford, J. Stanton, *Int. J. Quantum Chem.* **70**, 601 (1998)
122. K. Raghavachari, G.W. Trucks, J.A. Pople, M. Head-Gordon, *Chem. Phys. Lett.* **157**, 479 (1989)
123. K.L. Bak, A. Halkier, P. Jorgensen, J. Olsen, T. Helgaker, W. Klopper, *J. Mol. Structure (Theochem)* **567–568**, 375 (2001)
124. K. Hald, A. Halkier, P. Jorgensen, S. Horiani, S. Hättig, L. Helgaker, *J. Chem. Phys.* **118**, 2985 (2003)
125. M. Kallay, J. Gauss, *J. Chem. Phys.* **120**, 6841 (2004)
126. Y. He, D. Cremer, *Mol. Phys.* **98**, 1415 (2000)
127. M.S. Lee, P.E. Masien, M. Head-Gordon, *J. Chem. Phys.* **112**, 3592 (2000)
128. C. Hampel, H.-J. Werner, *J. Chem. Phys.* **104**, 6286 (1996)
129. P.Y. Ayala, G.E. Scuseria, *J. Chem. Phys.* **110** 3660 (1999)
130. P. Pulay, S. Sacho, *Theor. Chim. Acta* **69**, 357 (1986)
131. M. Schütz, G. Hetzer, H.-J. Werner, *J. Chem. Phys.* **111**, 5691 (1999)
132. P. Knowles, M. Schutz, H.-J. Werner, in *Modern Methods and Algorithms of Quantum Chemistry*, Proceedings, 2nd edn., ed. by J. Grotendorst, John von Neumann Institute for Computing, Jeulich, NIC Series, **3**, 97 (2000).

133. M.Schütz, J. Chem. Phys. **114**, 661 (2001)  
134. M.Schütz, J. Chem. Phys. **116**, 8772 (2002)  
135. S.Goedecker, G.Scuseria, Comput. Sci. Eng., **5**(4), 14 (2003)  
136. S. Saebo, P. Pulay, J. Chem. Phys. **86**, 914 (1987)  
137. M. Haser, J. Almlöf, J. Chem. Phys. **96**, 489 (1992)  
138. P. Constans, G.E. Scuseria, Collect. Czech. Chem. Commun. **68**, 357 (2003)  
139. M. Schütz, H-J. Werner, R. Lindh, F.R. Manby, J. Chem. Phys. **121**, 737 (2004)  
140. A. Hesselmann, G. Jansen, M.Schütz J. Chem. Phys. **122**, 014103 (2005)  
141. M. Schütz, G. Rauhut, H.-J. Werner, J. Phys. Chem. A **102**, 5997 (1998)  
142. M. Schütz, Phys. Chem. Chem. Phys. **4**, 3941 (2002)  
143. G.E. Scuseria, P.Y. Ayala, J. Chem. Phys. **111**, 8330 (1999)  
144. J.W. Boughton, P.Pulay, J. Comput. Chem. **14**, 736 (1993)  
145. G. Hetzer, P. Pulay, H-J. Werner, Chem. Phys. Lett. **290**, 143 (1998)  
146. H-J. Werner, F.R. Manby, P.J. Knowles, J. Chem. Phys. **118**, 8149 (2003)  
147. M.Schütz, F.R. Manby, Phys. Chem. Chem. Phys. **5**, 3349 (2003)  
148. F. Weigend, M. Häser, Theor. Chim. Acta **97**, 331 (1997)  
149. M. Schütz, J. Chem. Phys. **113**, 9986 (2000)  
150. W. Heitler, F. London, Z. Phys. **44**, 455 (1927)  
151. *Strong Coulomb Correlations in Electronic Structure Calculations. Beyond the Local Density Approximation*, ed. by Vladimir I.Anisimov (Gordon and Breach Sci. Publ., Amsterdam, 2000)  
152. J.P. Perdew, A. Zunger, Phys. Rev. B **23**, 5048 (1991)  
153. V.I. Anisimov, J. Zaanen, O.K. Andersen, Phys. Rev. B **44**, 943 (1991)  
154. C. Pisani, J. Molec. Structure (Theochem) **621**, 141 (2003)  
155. C.M. Zicovich-Wilson, R. Dovesi, Chem. Phys. Lett. **277**, 227 (1997)  
156. <http://www.theochem.unito.it/lcc2004/>  
157. D.E. Usvyat, M. Schütz, Theor. Chem. Acc. **114**, 276 (2005)  
158. A. Shukla, M. Dolg, H. Stoll, P. Fulde, Phys. Rev. B **57**, 1471 (1998)  
159. B. Paulus, P. Fulde, H. Stoll, Phys.Rev B **51**, 10572 (1995)  
160. B. Paulus, Physics Reports **428**, 1 (2006)  
161. W.Kutzelnigg, in: *Methods of Electronic Structure Theory*, ed. by H.F. SchaeferIII (Plenum, New York, 1977), pp.129  
162. H. Stoll, B. Paulus, P. Fulde, J. Chem. Phys. **123**, 144108 (2005)  
163. B. Paulus, P. Fulde, H. Stoll, Phys. Rev. B **54**, 2556 (1996)  
164. M. Albrecht, B. Paulus, H. Stoll, Phys. Rev. B **56**, 7339 (1997)  
165. K. Doll, M. Dolg, P. Fulde, H. Stoll, Phys. Rev. B **52**, 4842 (1995)  
166. K. Doll, M. Dolg, H. Stoll, Phys. Rev. B **54**, 13529 (1996)  
167. K. Doll, M. Dolg, P. Fulde, H. Stoll, Phys. Rev. B **55**, 10282 (1997)  
168. K. Doll, H. Stoll, Phys. Rev. B **57**, 4327 (1998)  
169. K. Rosciszewski, K. Doll, B. Paulus, P. Fulde, H. Stoll, Phys. Rev. B **57**, 14667 (1998)  
170. K. Rosciszewski, B. Paulus, P. Fulde, H. Stoll, Phys. Rev. B **60**, 7905 (1999)  
171. K. Rosciszewski, B. Paulus, P. Fulde, H. Stoll, Phys. Rev. B **62**, 5482 (2000)  
172. B. Paulus, K. Rosciszewski, N.Gaston, P. Schwerdtfeger, H. Stoll, Phys. Rev. B **70**, 165106 (2004)  
173. N. Gaston, B. Paulus, K. Rosciszewski, P. Schwerdtfeger, H. Stoll, Phys. Rev. B **74**, 094102 (2006)  
174. S. Kalvoda, M. Dolg, H.-J. Flad, P. Fulde, H. Stoll, Phys. Rev. B **57**, 2127 (1998)  
175. E. Voloshina, B. Paulus, Theor. Chem. Acc. **114**, 259 (2005)  
176. J. Gräfenstein, H. Stoll, P. Fulde, Chem. Phys. Lett. **215**, 611 (1993)  
177. J. Gräfenstein, H. Stoll, P. Fulde, Phys. Rev. B **55**, 13588 (1997)  
178. M. Albrecht, P. Reinhardt, J.-P. Malrieu, Theor. Chem. Acc. **100**, 241 (1998)  
179. A. Abdurahman, M. Albrecht, A. Shukla, M. Dolg, J. Chem. Phys. **110**, 8819 (1999)

180. M. Albrecht, P. Fulde, H. Stoll, Chem. Phys. Lett. **319**, 355 (2000)  
181. A. Shukla, M. Dolg, P. Fulde, H. Stoll, Phys. Rev. B **57**, 1471 (1998)  
182. R. Orlando, R. Dovesi, C. Roetti, V.R. Saunders, J. Phys: Condens. Matter **2**, 7769 (1990)  
183. P. Fulde, Theor. Chem. Acc. **114**, 255 (2005)  
184. J.Q. Sun, R.J. Bartlett, J. Chem. Phys. **104**, 8553 (1996)  
185. P.Y. Ayala, K.N. Kudin, G.E. Scuseria, J. Chem. Phys. **115**, 9698 (2001)  
186. J. Almlöf, Chem. Phys. Lett. **181**, 319 (1991)  
187. M. Haser, Theor. Chim. Acta **87**, 147 (1993)  
188. R. Pino, G.E. Scuseria, J. Chem. Phys. **121**, 2553 (2004)  
189. P.Y. Ayala, G.E. Scuseria, Chem. Phys. Lett. **322**, 213 (2000)  
190. A. Zunger, A. Katzir, A. Halperin, Phys. Rev. B **13**, 5560 (1976)  
191. K. Kobayashi, T. Sano, Y. I'Haya, Chem. Phys. Lett. **219**, 53 (1994)  
192. C. Pisani, G. Capecci, S. Casassa, L. Maschio, Mol. Phys. **103**, 2527 (2005)  
193. W. Boughton, P. Pulay, J. Comput. Chem. **14**, 736 (1993)  
194. W. Kohn, Phys. Rev. **115**, 809 (1959)  
195. P.W. Anderson, Phys. Rev. Lett. **21**, 13 (1968)  
196. P. Zeiner, R. Dirl, B.L. Davies, Phys. Rev. B **58**, 7681 (1998)  
197. L. He, D. Vanderbilt, Phys. Rev. Lett. **86**, 5341 (2001)  
198. R.A. Evarestov, D.E. Usvyat, V.P. Smirnov, Phys. Solid State **45**, 2072 (2003)  
199. S. Lui, J.M. Perez-Jorda, W. Yang, J. Chem. Phys. **112**, 1634 (2000)  
200. H. Feng, J. Bian, L. Li, W. Yang, J. Chem. Phys. **120**, 9458 (2004)  
201. S. Casassa, C.M. Zicovich-Wilson, C. Pisani, Theor. Chem. Acc. **116**, 726 (2006)  
202. C.M. Zicovich-Wilson, R. Dovesi, Int. J. Quantum Chem. **67**, 299 (1998)  
203. C.M. Zicovich-Wilson, R. Dovesi, V.R. Saunders, J. Chem. Phys. **115**, 9708 (2001)  
204. R. Hoffmann, J. Chem. Phys. **39**, 1397 (1963)  
205. J.A. Pople, D.L. Beveridge, *Approximate Molecular Orbital Theory* (McGraw-Hill, N.Y., 1970)  
206. E.B. Moore, C.M. Carlson, Phys. Rev. B **4**, 2063 (1971)  
207. R. Dovesi, C. Pisani, F. Ricca, C. Roetti, Chem. Phys. Lett. **39**, 103 (1976)  
208. A.R. Leach, *Molecular Modelling: Principles and Applications*, 2nd edn. ( Pearson Education EMA, 2001)  
209. R. Canadine, I. Hiller, J. Chem. Phys. **50**, 2985 (1969)  
210. J.C. Slater, Phys. Rev. **36**, 57 (1930)  
211. J. Hinze, H.H. Jaffe, J. Am. Chem. Soc. **84**, 540 (1962)  
212. L.C. Cusachs, J.W. Reinolds, D. Barnard, J. Chem. Phys. **44**, 835 (1966)  
213. M. Wolfsberg, L.J. Helmholz, J. Chem. Phys. **20**, 837 (1952)  
214. M. Nishida, Phys. Rev. B **58**, 7103 (1998)  
215. J.R. Chelikowsky, M.L. Cohen, Phys. Rev. B **10**, 5095 (1974)  
216. J. Cerda, F. Soria, Phys. Rev. B **61**, 7965 (2000)  
217. A. Herman, Modeling Simul. Mater. Sci. Eng. **12**, 21 (2004)  
218. W. Koch, B. Frey, J.F.S. Ruiz, T. Scior, Z. Naturforsch. **58a**, 756 (2003)  
219. K. Ruedenberg, J. Chem. Phys. **19**, 1433 (1951)  
220. R.S. Mulliken, J. Chim. Phys. **46**, 500, 521 (1949)  
221. R. Fenske, K. Caulton, D. Radtke, C. Sweeney, Inorg. Chem. **5**, 951 (1966)  
222. R.A. Evarestov, A.N. Ermoshkin, phys. stat. sol. (b) **86**, 47 (1978)  
223. W. Koch, B. Frey, J.F.S. Ruiz, T. Scior, Z. Naturforsch. **58a**, 785 (2003)  
224. A.N. Ermoshkin, E.A. Kotomin, A.L. Shluger, J. Phys. C: Solid State Phys. **15**, 847 (1982)  
225. P.O. Löwdin, J. Chem. Phys. **18**, 365 (1950)  
226. A.N. Ermoshkin, E.A. Kotomin, R.A. Evarestov, phys. stat. sol. (b) **72**, 787 (1975)

227. G.A. Bordovskii, M.L. Gordeev, A.N. Ermoshkin, R.A. Evarestov, phys. stat. sol. (b) **111**, K123 (1982)
228. R.A. Evarestov, A.N. Ermoshkin, V.A. Lovchikov, phys. stat. sol. (b) **99**, 387 (1980)
229. A.N. Ermoshkin, R.A. Evarestov, Optica i Spectroskopija **35**, 786 (1973)
230. A.N. Ermoshkin, R.A. Evarestov, phys. stat. sol. (b) **66**, 687 (1974)
231. A.N. Ermoshkin, R.A. Evarestov, E.A. Kotomin, phys. stat. sol. (b) **73**, 81 (1976)
232. R.A. Evarestov, A.N. Ermoshkin, Optica i Spectroskopija **40**, 610 (1976)
233. R.A. Evarestov, A.N. Ermoshkin, E.A. Kotomin, phys. stat. sol. (b) **73**, 483 (1976)
234. A.N. Ermoshkin, E.A. Kotomin, R.A. Evarestov, phys. stat. sol. (b) **103**, 581 (1981)
235. T. Bredow, K. Jug, Theor. Chem. Acc. **113**, 1 (2005)
236. J.A. Pople, D.P. Santry, G.A. Segal, J. Chem. Phys. **43**, S129 (1965)
237. R. Pariser, G.R. Parr, J. Chem. Phys. **21**, 466, 767 (1953)
238. N. Mataga, K. Nishimoto, Z. Phys. Chem. **13**, 140 (1957)
239. K. Ohno, Adv. Quantum Chem. **3**, 240 (1967)
240. M.G. Veselov, M.M. Mestechkin, Theor. Exp. Chem. **6**, 471 (1973)
241. J.A. Pople, D.L. Beveridge, P.A. Dobosh, J. Chem. Phys. **47**, 2026 (1967)
242. Da Motta Neto, M.C. Zerner Int. J. Quantum Chem. **81**, 187 (2001)
243. J.E. Ridley, M.C. Zerner, Theor. Chim. Acta **32**, 111 (1973)
244. M. Kotzian, N. Rosch, M.C. Zerner, Theor. Chim. Acta **81**, 201 (1992)
245. R.C. Bingham, M.J.S. Dewar, D.H. Lo, J. Am. Chem. Soc. **97**, 1285, 1307 (1975)
246. M.J.S. Dewar, E.G. Zoebisch, E.F. Healey, J.J.P. Stewart, J. Am. Chem. Soc. **107**, 3902 (1985)
247. W. Thiel, J. Am. Chem. Soc. **103**, 1413, 1421 (1981)
248. J.J.P. Stewart, J. Comput. Chem. **10**, 209 (1989)
249. D.N. Nanda, K. Jug, Theor. Chim. Acta **57**, 95 (1980)
250. K. Jug, R. Iffert, J. Schulz, Int. J. Quantum Chem. **32**, 265 (1987)
251. J. Li, P. Correa de Mello, K. Jug, J. Comput. Chem. **13**, 85 (1992)
252. M.C. Zerner, Mol. Phys. **23**, 963 (1972)
253. B. Ahlsweide, K. Jug, J. Comput. Chem. **20**, 563 (1999)
254. B. Ahlsweide, K. Jug, J. Comput. Chem. **20**, 572 (1999)
255. K. Jug, G. Geudtner, T. Homann, J. Comput. Chem. **21**, 974 (2000)
256. T. Bredow, G. Geudtner, K. Jug, J. Comput. Chem. **22**, 861 (2001)
257. T. Bredow, K. Jug, in *Encyclopedia of Computational Chemistry (online edition)*, eds. P. Schleyer, N.L. Allinger, T. Clark, J. Gasteiger, P.A. Kollman, H.F. Schaefer III, P.R. Schreiner (Wiley, Chichester, 2004)
258. J. Schultz, R. Iffert, K. Jug, Int. J. Quantum Chem. **27**, 461 (1985)
259. B. Voigt, Theor. Chim. Acta **31**, 289 (1973)
260. C. Kollmar, M.C. Böhm, Theor. Chim. Acta **92**, 13 (1995)
261. C. Kollmar, Chem. Phys. Lett. **269**, 215 (1997)
262. C. Kollmar, B.A. Hess, Mol. Phys. **100**, 1945 (2002)
263. H. Fujita, A. Imamura, J. Chem. Phys. **53**, 4555 (1970)
264. S. O'Shea, D.P. Santry, J. Chem. Phys. **54**, 2667 (1971)
265. K. Mororuma, J. Chem. Phys. **54**, 962 (1971)
266. B.J. McAloon, P.G. Perkins, J. Chem. Soc. Faraday Trans.II **68**, 1121, 1833 (1972)
267. D.L. Beveridge, I. Jano, J. Ladik, J. Chem. Phys. **56**, 4744 (1972)
268. M.C. Böhm, Theor. Chim. Acta **62**, 351, 373 (1983)
269. M.J.S. Dewar, K.M. Merz Jr, Organometallics **5**, 1494 (1986)
270. J.J.P. Stewart, New Polym. Mater. **1**, 53 (1987)
271. J. Chandrasekhar, P.K. Das, J. Phys. Chem. B **96**, 679 (1992)
272. L.Y.A. Davila, M.J. Caldas, J. Comput. Chem. **23**, 1135 (2002)
273. F. Ricca, J. Phys. (Paris) **38**, Suppl.C-4, 173 (1977)
274. R. Dovesi, C. Pisani, F. Ricca, C. Roetti, Surf. Sci. **75**, 316 (1978)

275. R. Dovesi, C. Pisani, F. Ricca, C. Roetti, *J. Chem. Phys.* **65**, 3075, 4116 (1976)
276. R.A. Evarestov, V.A. Lovchikov, *phys. stat. sol. (b)* **79**, 743 (1977)
277. A.H. Harker, F.P. Larkins, *J. Phys. C: Solid State Phys.* **12**, 2487 (1979)
278. R. Dovesi, C. Pisani, C. Roetti, *Surf. Sci.* **103**, 482 (1981)
279. P.G. Perkins, A.K. Marwaha, J.J.P. Stewart, *Theor. Chim. Acta* **57**, 1 (1980)
280. P.V. Smith, J.E. Szymanski, J.A.D. Matthew, *J. Phys.: Solid State Phys.* **18**, 3157 (1985)
281. R.Ramirez, M.C. Böhm, *Int. J. Quantum Chem.* **34**, 47 (1988)
282. R. Dovesi, C. Pisani, C. Roetti, J.M. Ricart, F.Illas, *Surf. Sci.* **148**, 225 (1984)
283. B.I. Craig, P.V. Smith, *Surf. Sci.* **210**, 468 (1989)
284. J.D. Weibel, D. Yaron, *J. Chem. Phys.* **116**, 6846 (2002)
285. A.J. Bennett, B. McCarroll, R.P. Messmer, *Phys. Rev. B* **3**, 1397 (1971)
286. A. Zunger, *J.Phys. C: Solid State Phys.* **7**, 76 (1974)
287. A. Zunger, *J. Chem. Phys.* **62**, 1861 (1975)
288. R.P. Messmer, G.D. Watkins in *Radiation Damage and Defects in Semiconductors*, N16, p.255, Institute of Physics, London (1973)
289. A.M. Dobrotvorskii, R.A. Evarestov, *phys. stat. sol. (b)* **66**, 83 (1974)
290. R.A. Evarestov, M.I. Petrashev, E.M. Ledovskaya, *phys. stat. sol. (b)* **76**, 377 (1976)
291. *Hartree-Fock-Slater Method for Materials Science. The DV-X Alpha Method for Design and Characterization of Materials*, eds. H.Adachi, T.Mukoyama, J. Kawai, in Springer Series in Materials Science, vol. **84**, (Springer, Berlin, Heidelberg, New York, 2006)
292. U.Lindefeldt, *J. Phys. C: Solid State Phys.* **11**, 85 (1978)
293. P. Deak, L. Snyder, *Phys. Rev. B* **36**, 9619 (1987)
294. P. Deak, *phys. stat. sol. (b)* **217**, 9 (2000)
295. R.A. Evarestov, M.I. Petrashev, E.M. Ledovskaya, *phys. stat. sol. (b)* **68**, 453 (1975)
296. V.A. Koptzik, R.A. Evarestov, *Kristallographia* **25**, 5 (1980)
297. R.A. Evarestov, A.V. Leko, V.P. Smirnov, *phys. stat. sol. (b)* **128**, 275 (1985)
298. P.G. Perkins, J.J.P. Stewart, *J. Chem. Soc. Faraday II* **76**, 520, 534 (1980)
299. J.J.P. Stewart, *J. Comput. Chem.* **19**, 168 (1998)
300. R.A. Evarestov, V.A. Lovchikov, *phys. stat. sol. (b)* **93**, 469 (1979)
301. T. Bredow, G.Geudtner, K. Jug, *Int. J. Quantum Chem.* **22**, 89 (2001)
302. F. Janetzko, T. Bredow, K. Jug, *J. Chem. Phys.* **116**, 8994 (2002)
303. P. Deak, *Phys. Lett. A* **83**, 39 (1981)
304. A.L. Shluger, E.A. Kotomin, *phys. stat. sol. (b)* **108**, 673 (1981)
305. R.A. Evarestov, V.A. Veryazov, *phys. stat. sol. (b)* **157**, 281 (1990)
306. R.A. Evarestov, V.A. Veryazov, *Rev. Solid State Sci.* **5**, 415 (1991)
307. J. Noga, P. Banacky, S. Biskupic, R. Boca, P. Pelikan, M. Svrcek, A. Zajac, *Int. J. Quantum Chem.* **20**, 253 (1999)
308. P. Pelikan, J. Noga, S. Biskupic, *J. Solid State Chem.* **174**, 233 (2003)
309. E. Stefanovich, E. Shidlovskaya, A. Schluger, *phys. stat. sol. (b)* **160**, 529 (1990)
310. S.S. Moliver, *Phys. Solid State* **42**, 673 (2000)
311. A.O. Litinskii, I.P. Zakharov, *J. Struct. Chem.* **27**, 517 (1986)
312. J.J.P. Stewart, *J. Molec. Struct. (Theochem)* **556**, 59 (2000)
313. A. Schluger, *Theor. Chim. Acta* **66**, 355 (1985)
314. A.H. Harker, F.P. Larkins, *J. Phys. C: Solid State Phys.* **12**, 2509 (1979)
315. E.A. Kotomin, A.L. Shluger, *phys. stat. sol. (b)* **109**, 75 (1982)
316. A.H. Harker, F.P. Larkins, *J. Phys. C: Solid State Phys.* **12**, 2497 (1979)
317. P.V. Smith, J.E. Szymanski, J.A.D. Matthew, *phys. stat. sol. (b)* **136**, 261 (1986)
318. R.A. Evarestov, V.A. Veryazov, *phys. stat. sol. (b)* **158**, 201 (1990)
319. A. Porreda, V.A. Lovchikov, K. Jug in *NATO ASI Series B Cluster Models for Surface and Bulk Phenomena*, eds. G. Pacchioni, P.S. Bagus, F. Parmigiani, Plenum New York, 1992, **283**, p.641

320. K. Jug, T. Bredow, *J. Comput. Chem.* **25**, 1551 (2004)
321. K. Jug, T. Bredow in *Methods and Techniques in Computational Chemistry, METECC-95*, ed. E. Clementi, p. 89, STEF, Calgary (1995)
322. R. Dovesi, V.R. Saunders, C. Roetti, N.M. Harrison, R. Orlando, E. Apra, *Crystal95 User's Manual*, Universita di Torino, Torino (1996)
323. B. Silvi, N. Fouranti, R. Nada, C.R. Catlow, *J. Phys. Chem. Solids* **52**, 1005 (1991)
324. C. Pisani, R. Dovesi, C. Roetti, *Hartree-Fock ab-initio Treatment of Crystalline Systems*, Lecture Notes in Chemistry **48**, Springer-Verlag, Berlin (1988)
325. L.H. Thomas, *Proc. Camb. Philos. Soc.* **23**, 542 (1927)
326. E. Fermi, *Z. Phys.* **48**, 73 (1928)
327. J.C. Slater, *Phys. Rev.* **91**, 528 (1953)
328. P. Hohenberg, W. Kohn, *Phys. Rev.* **136**, B864 (1964)
329. N.C. Handy, *Molec. Phys.* **102**, 2399 (2004)
330. K. Capelle, *A Birds-eye View of Density Functional Theory*, <http://arXiv.org/archive/cond-mat/0211443v4>
331. W. Kohn, *Rev. Mod. Phys.* **71**, 1253 (1998)
332. W. Kohn, L.J. Sham, *Phys. Rev.* **140**, A1133 (1965)
333. R.M. Dreizler, E.K.U. Gross, *Density Functional Theory* (Springer, Berlin, 1990).
334. N.H. March, *Electron Density Theory of Atoms and Molecules* (Academic Press, London, 1992).
335. H. Eschrig, *The Fundamentals of Density Functional Theory* (Teubner, Leipzig, 1996).
336. *Density Functional Theory: Recent Progress and New Directions*, eds. J.F. Dobson, G. Vignale, M.P. Das (Plenum, New York, 1998)
337. W. Koch, M.C. Holthausen, *A Chemist's Guide to Density Functional Theory*, 2nd edn. (John Wiley, New York, 2002).
338. R.O. Jones, O. Gunnarsson, *Rev. Mod. Phys.* **61**, 689 (1989)
339. R. Neumann, *Molec. Phys.* **87**, 1 (1996)
340. J.P. Perdew, S. Kurth, *Lecture Notes in Phys.* **620**, 1 (2003)
341. K. Burke, J. Werschnik, E.K.U. Gross, *J. Chem. Phys.* **123**, 062206 (2005)
342. I.G. Kaplan, *Intermolecular Interactions. Physical Picture, Computational Methods and Model Potentials*, (Wiley, 2006).
343. K. Capelle, V.L. Libero, *Int. J. Quantum Chem.* **105**, 679 (2005)
344. <http://www.uam.es/departamentos/ciencias/fismateriac/siesta/>
345. <http://www.scm.com/Doc/Doc2006.01>
346. J.C. Slater, *Phys. Rev.* **81**, 385 (1951)
347. P.A.M. Dirac, *Proc. Camb. Philos. Soc.* **26**, 376 (1930)
348. U. von Barth, L. Hedin, *J. Phys. C: Condens. Matter* **5**, 1629 (1972)
349. O. Gunnarsson, B.I. Lundqvist, *Phys. Rev. B* **13**, 4274 (1976)
350. D.M. Ceperley, B.J. Alder, *Phys. Rev. Lett.* **45**, 566 (1980)
351. S.J. Vosko, L. Wilk, M. Nussair, *Can. J. Phys.* **1980**, 1200 (1980)
352. J.P. Perdew, A. Zunger, *Phys. Rev. B* **23**, 5048 (1981)
353. J.P. Perdew, Y. Wang, *Phys. Rev. B* **40**, 3389 (1989)
354. J.P. Perdew, A. Zunger, *Phys. Rev. B* **45**, 13244 (1992)
355. J.P. Perdew, A. Zunger, *Phys. Rev. B* **33**, 8800 (1986)
356. J.P. Perdew, K. Burke, M. Ernzerhof, *Phys. Rev. Lett.* **77**, 3865 (1996)
357. J.P. Perdew, A. Ruzsinszky, J. Tao, V.N. Staroverov, G.E. Scuseria, G.I. Csonka, *J. Chem. Phys.* **123**, 062201 (2005)
358. A.D. Becke, *Phys. Rev. A* **38**, 3098 (1988)
359. C. Lee, W. Wang, R.G. Parr, *Phys. Rev. B* **37**, 785 (1988)
360. J. Tao, J.P. Perdew, V.N. Staroverov, G.E. Scuseria, *Phys. Rev. Lett.* **91**, 146401 (2003)
361. Xin Xu, W.A. Goddard III, *J. Chem. Phys.* **121**, 4068 (2004)
362. J. Tao, J.P. Perdew, V.N. Staroverov, G.E. Scuseria, *Phys. Rev. B* **69**, 075102 (2004)

363. J.P. Perdew, S. Kurth, A. Zupan, P. Blaha, Phys. Rev. Lett. **82**, 2544 (1999)
364. J.P. Perdew, K. Burke, Y. Wang, Phys. Rev. B **54**, 16533 (1996)
365. P. Ziesche, S. Kurth, J.P. Perdew, Comput. Mater. Sci. **11**, 122 (1998)
366. E.H. Lieb, S. Oxford, Int. J. Quantum Chem. **19**, 427 (1981)
367. E.J. Baerends, O.V. Gritsenko, J. Chem. Phys. **123**, 062202 (2005)
368. M. Gruning, O.V. Gritsenko, E.J. Baerends, J. Chem. Phys. **118**, 7183 (2003)
369. E.J. Baerends, Phys. Rev. Lett. **87**, 133004 (2001)
370. M.A. Buijse, E.J. Baerends, Molec. Phys. **100**, 401 (2002)
371. F. Cora, M. Alfredsson, G. Mallia, D. Midlemmiss, W.C. Mackrodt, R. Dovesi, R. Orlando, Struct. and Bond. **113**, 171 (2004)
372. A.D. Becke, J. Chem. Phys. **112**, 4020 (2000)
373. A.D. Becke, J. Chem. Phys. **98**, 1372, 5468 (1993)
374. O.V. Gritsenko, P.R. T.Schipper, E.J. Baerends, Int. J. Quantum Chem. Symp. **30**, 1375 (1996)
375. J.P. Perdew, M. Ernzerhof, K. Burke, J. Chem. Phys. **105**, 9982 (1996)
376. J.E. Jaffe, A.C. Hess, J. Chem. Phys. **105**, 10983 (1996)
377. M.C. Payne, M.P. Teller, D.C. Allan, J.A. Arias, J.D. Joannopoulos, Rev. Mod. Phys. **64**, 1045 (1992)
378. <http://www.wien2k.at>
379. K.N. Kudin, G.E. Scuseria, Phys. Rev. B **61**, 16440 (2000)
380. V.N. Staroverov, G.E. Scuseria, J. Tao, J.P. Perdew, Phys. Rev. B **69**, 075102 (2004)
381. L. Greengard, V. Rokhlin, J. Comput. Phys. **73**, 325 (1987)
382. K.N. Kudin, G.E. Scuseria, Chem. Phys. Lett. **289**, 611 (1998)
383. E. Artacho, D. Sanchez-Portal, P. Ordejon, A. Garcia, J.M. Soler, phys. stat. sol. (b) **215**, 809 (1999)
384. P. Ordejon, E. Artacho, J.M. Soler, Phys. Rev. B **53**, R10441 (1996)
385. J.R. Chelikowsky, S.G. Louie, Phys. Rev. B **29**, 3470 (1987)
386. G. Velde, E.J. Baerends, Phys. Rev. B **44**, 7888 (1991)
387. P.J. Feibelman, Phys. Rev. B **44**, 3916 (1991)
388. G. Seifert, D. Porezug, Th. Frauenheim, Int. J. Quantum Chem. **58**, 185 (1996)
389. M. Towler, A. Zupan, M. Causa, Comput. Phys. Commun. **98**, 181 (1996)
390. A. Lichanot, M. Merawa, M. Causa, Chem. Phys. Lett. **246**, 263 (1995)
391. A. Zupan, M. Causa, Int. J. Quantum Chem. **56**, 337 (1995)
392. A. Savin, Int. J. Quantum Chem. **S22**, 457 (1988)
393. A.D. Becke, J. Chem. Phys. **96**, 2155 (1992)
394. M. Causa, Lecture Notes in Chem. **48**, 91 (1996)
395. F. Figueirido, R.M. Levy, R. Zhou, B. Berne, J. Chem. Phys. **106**, 9835 (1997)
396. M. Challacombe, C. White, M. Head-Gordon, J. Chem. Phys. **107**, 1013 (1997)
397. K.N. Kudin, G.E. Scuseria, J. Chem. Phys. **121**, 2886 (2004)
398. K.N. Kudin, G.E. Scuseria, Phys. Rev. B **61**, 5141 (2000)
399. D.L. Strout, G.E. Scuseria, J. Chem. Phys. **102**, 8448 (1995)
400. J.M. Soler, E. Artacho, J.D. Gale, A. Garcia, J. Junquera, P. Ordejon, D. Sanchez-Portal, J. Phys.: Condens. Matter **14**, 2745 (2002)
401. E. Anglada, J.M. Soler, J. Junquera, E. Artacho, Phys. Rev. B **66**, 205101 (2002)
402. M.C. Strain, G.E. Scuseria, M.J. Frisch, Science **271**, 51 (1996)
403. J.C. Burant, M.C. Strain, G.E. Scuseria, M.J. Frisch, Chem. Phys. Lett. **258**, 45 (1998)
404. P. Pulay, J. Comput. Chem. **3**, 556 (1982)
405. R.E. Stratmann, G.E. Scuseria, M.J. Frisch, 257 **257**, 213 (1996)
406. [http://www.gaussian.com/g\\_people/gus.htm](http://www.gaussian.com/g_people/gus.htm)
407. C. Adamo, V. Barone, J. Chem. Phys. **110**, 6158 (1999)
408. J. Heyd, G.E. Scuseria, M. Ernzerhof, J. Chem. Phys. **118**, 8207 (2003)
409. J. Heyd, G.E. Scuseria, J. Chem. Phys. **120**, 7274 (2004)

410. W. Kohn, *Int. J. Quantum Chem.* **56**, 229 (1995)
411. J.P. Perdew, M. Ernzerhof, K. Burke, *J. Chem. Phys.* **105**, 9982 (1996)
412. M. Ernzerhof, G.E. Scuseria, *J. Chem. Phys.* **110**, 5029 (1999)
413. J.C. Burant, G.E. Scuseria, M.J. Frisch, *J. Chem. Phys.* **105**, 8969 (1996)
414. E. Schwegler, M. Challacombe, *J. Chem. Phys.* **105**, 2726 (1996)
415. C. Ochsenfeld, C.A. White, M. Head-Gordon, *J. Chem. Phys.* **109**, 1163 (1998)
416. M.W. Gill, J.A. Pople, *Int. J. Quantum Chem.* **40**, 753 (1991)
417. M. Ernzerhof, J.P. Perdew, *J. Chem. Phys.* **109**, 3313 (1998)
418. GAUSSIAN Development Version, Revision B.07, M.J. Frisch, G.W. Trucks, H.B. Schlegel, G.E. Scuseria, M.A. Robb, J.R. Cheeseman, J.A. Montgomery Jr., T. Vreven, K.N. Kudin, J.C. Burant, J.M. Millam, S.S. Iyengar, J. Tomasi, V. Barone, B. Mennucci, M. Cossi, G. Scalmani, N. Rega, G.A. Petersson, H. Nakatsuji, M. Hada, M. Ehara, K. Toyota, R. Fukuda, J. Hasegawa, M. Ishida, T. Nakajima, Y. Honda, O. Kitao, H. Nakai, M. Klene, X. Li, J.E. Knox, H.P. Hratchian, J.B. Cross, V. Bakken, C. Adamo, J. Jaramillo, R. Gomperts, R.E. Stratmann, O. Yazyev, A.J. Austin, R. Cammi, C. Pomelli, J.W. Ochterski, P.Y. Ayala, K. Morokuma, G.A. Voth, P. Salvador, J.J. Dannenberg, V.G. Zakrzewski, S. Dapprich, A.D. Daniels, M.C. Strain, O. Farkas, D.K. Malick, A.D. Rabuck, K. Raghavachari, J.B. Foresman, J.V. Ortiz, Q. Cui, A.G. Baboul, S. Clifford, J. Cioslowski, B.B. Stefanov, G. Liu, A. Liashenko, P. Piskorz, I. Komaromi, R.L. Martin, D.J. Fox, T. Keith, M.A. Al-Laham, C.Y. Peng, A. Nanayakkara, M. Challacombe, P.M.W. Gill, B. Johnson, W. Chen, M.W. Wong, C. Gonzalez, and J.A. Pople, Gaussian Inc., Pittsburgh, PA, 2003
419. J. Heyd, J.E. Peralta, G.E. Scuseria, R.L. Martin, *J. Chem. Phys.* **123**, 174101 (2005)
420. J. Uddin, G.E. Scuseria, *Phys. Rev. B* **72**, 035101 (2005)
421. J. Uddin, J.E. Peralta, G.E. Scuseria, *Phys. Rev. B* **71**, 155112 (2005)
422. I.D. Prodan, G.E. Scuseria, J.A. Sordo, K.N. Kudin, R.L. Martin, *J. Chem. Phys.* **123**, 014703 (2005)
423. V. Barone, J.E. Peralta, J. Uddin, G.E. Scuseria, *J. Chem. Phys.* **124**, 024709 (2006)
424. I.D. Prodan, G.E. Scuseria, R.L. Martin, *Phys. Rev. B* **73**, 045104 (2006)
425. J. Paier, R. Hirschl, M. Marsman, G. Kresse, *J. Chem. Phys.* **122**, 234102 (2005)
426. V.R. Saunders, R. Dovesi, C. Roetti, M. Causa, N.M. Harrison, R. Orlando, C.M. Zicovich-Wilson, Crystal98 User's Manual, University of Torino, Torino (1998)
427. M.S. Hybertsen, S.G. Louie, *Phys. Rev. Lett.* **55**, 1418 (1985)
428. M.C. Foulkes, L. Mitas, R. Needs, G. Rajagopal, *Rev. Mod. Phys.* **73**, 33 (2001)
429. T. Bredow, A.R. Gerson, *Phys. Rev. B* **61**, 5194 (2000)
430. I. Moreira, F. Illas, R.L. Martin, *Phys. Rev. B* **65**, 155102 (2002)
431. W.C. Mackrodt, D.S. Middlemiss, T.G. Owens, *Phys. Rev. B* **69**, 115119 (2004)
432. F. Illas, R.L. Martin, *J. Chem. Phys.* **108**, 2519 (1998)
433. J. Muscat, A. Wander, N.M. Harrison, *Chem. Phys. Lett.* **342**, 397 (2001)
434. W.G. Aulbur, L. Johnsson, J.W. Wilkins, *Solid State Phys.* **54**, 1 (2000)
435. F. Aryasetiawan, in Strong Coulomb Correlations in Electronic Structure Calculations, ed. V.I. Anisimov, p.1 (Gordon and Breach, Singapore, 2000 )
436. J.P. Perdew, S. Kurth, A. Zupan, P. Blaha, *Phys. Rev. Lett.* **82**, 544 (1999)
437. L. Petit, A. Svane, Z. Szotek, W.M. Temmerman, *Phys. Rev. B* **72**, 205118 (2005)
438. T. Fujiwara, M. Arai, Y. Ishii, in Strong Coulomb Correlations in Electronic Structure Calculations, ed. V.I. Anisimov, p.167 (Gordon and Breach, Singapore, 2000 )
439. V.I. Anisimov, A.I. Lichtenstein, in Strong Coulomb Correlations in Electronic Structure Calculations, ed. V.I. Anisimov, p.97 (Gordon and Breach, Singapore, 2000 )
440. V. Polo, E. Kraka, D.Cremer, *Molec. Phys.* **100**, 1771 (2002)
441. D.Cremer, *Molec. Phys.* **99**, 1899 (2001)
442. G.I. Csonka, B.J. Johnson, *Theor. Chem. Acc.* **99**, 158 (1998)
443. O.A. Vydrov, G.E. Scuseria, *J. Chem. Phys.* **121**, 8187 (2004)

444. O.A. Vydrov, G.E. Scuseria, *J. Chem. Phys.* **122**, 184107 (2005)
445. A. Svane, W.M. Temmerman, Z. Szotek, J. Laegsgaard, H. Winter, *Int. J. Quantum Chem.* **77**, 799 (2000)
446. A. Flipetti, N.A. Spaldin, *Phys. Rev. B* **67**, 125109 (2003)
447. M. Arai, T. Fujiwara, *Phys. Rev. B* **51**, 1477 (1995)
448. O.K. Anderson, *Phys. Rev. B* **12**, 3060 (1975)
449. M. Imada, A. Fujimori, Y. Tokura, *Rev. Mod. Phys.* **70**, 1040 (1998)
450. A. Rohrbach, J. Hafner, G. Kresse, *J. Phys. C: Condens. Matter* **15**, 979 (2003)
451. G. Kresse, J. Furthmüller, *Comput. Mater. Sci.* **6**, 15 (1996)
452. G. Ricardo, F. Cora, A.A. Sokol, N.H. de Leeuw, C.R.A. Catlow, *Phys. Rev. B* **73**, 035116 (2006)
453. S.ZN. Karazhanov, P. Ravindran, A. Kjekhus, H. Fjellvag, U. Grossner, B.G. Svensson, *J. Cryst. Growth* **287**, 162 (2006)
454. A.G. Eguiluz, O.D. Restrepo, B.C. Larson, J.Z. Tischler, P. Zschack, G.E. Jellison, *J. Phys. Chem. Solids* **66**, 2281 (2005)
455. R. Laskowskii, P. Blaha, K. Schwarz, *Phys. Rev. B* **67**, 075102 (2003)
456. A.L. Ivanovskii, T.I. Chupakhina, V.G. Zubkov, A.P. Tyutyunnik, V.N. Krasilnikov, G.V. Bazuev, S.V. Okatov, A.I. Lichtenstein, *Phys. Lett. A* **348**, 66 (2005)
457. Y. Wang, D.J. Doren, *Solid State Commun.* **136**, 142 (2005)
458. M. Towler, *An introductory guide to Gaussian basis sets in solid state electronic structure calculations*, <http://www.crystal.unito.it/tutojan2004/tutorials/index.html>
459. A.D. McLean, R.S. McLean, *Roothaan-Hartree-Fock atomic wave functions (Slater basis-set expansions for Z=55-92)*, *Atomic Data and Nuclear Data Tables*, **26**, 197 (1981)
460. S. Huzinaga, *J. Chem. Phys.* **42**, 1293 (1965)
461. M. Challacombe, J. Cioslowsky, *J. Chem. Phys.* **100**, 464 (1994)
462. T.H. Dunning, *J. Chem. Phys.* **90**, 1007 (1989)
463. <http://www.emsl.pnl.gov/forms/basisform.html>
464. K. Doll, N.M. Harrison, V.R. Saunders, *J. Phys.: Condens. Matter* **11**, 5007 (1999)
465. J. Sauer, P. Ugliengo, E. Garrone, V.R. Saunders, *Chem. Rev.* **94**, 2095 (1994)
466. S.F. Boys, F. Bernardi, *Molec. Phys.* **19**, 553 (1970)
467. M. Gutowski, J.G. G.M van der Rijdt, J.H van Lenthe, F.B. van Duijneveldt, *J. Chem. Phys.* **98**, 4728 (1993)
468. A. Grunreich, B.A. Hess, *Theor. Chem. Acc.* **100**, 253 (1998)
469. S.D. Kenny, A.P. Horsfield, H. Fujitami, *Phys. Rev. B* **62**, 4899 (2000)
470. <http://www.physik.uni-frankfurt.de/~engel/ncpp.html>
471. A.P. Christiansen, Y.S. Lee, K.S. Pitzer, *J. Chem. Phys.* **71**, 4445 (1970)
472. D.R. Hamann, M. Schlüter, C. Chiang, *Phys. Rev. Lett.* **43**, 1494 (1979)
473. J.C. Phillips, L. Kleinman, *Phys. Rev.* **116**, 287 (1959)
474. L. Kleinman, D.M. Bylander, *Phys. Rev. Lett.* **48**, 1425 (1982)
475. M.I. Petrushen, I.V. Abarenkov, A.A. Berezin, R.A. Evarestov, *phys. stat. sol. (b)* **40**, 9, 433 (1970)
476. I.V. Abarenkov, V. Heine, *Philos. Mag.* **12**, 529 (1965)
477. D. Vanderbilt, *Phys. Rev. B* **41**, 7892 (1990)
478. M. Fuchs, M. Scheffer, *Comput. Phys. Commun.* **119**, 67 (1999)
479. A. Alkauskas, A. Baratoff, C. Bruder, *J. Phys. Chem. A* **108**, 6863 (2004)
480. M. Krauss, W.J. Stevens, *Ann. Rev. Phys. Chem.* **35**, 357 (1984)
481. M. Dolg, in *Modern Methods and Algorithms of Quantum Chemistry*, ed. J. Grotendorst, NIC Series, **1**, 479 (2000), **3**, 507 (2000), online <http://www.fz-juelich.de/nic-series/NIC-Series-e.html>
482. A.V. Titov, N.S. Mosyagin, [arXiv.org/physics/0008239](http://arXiv.org/physics/0008239) (2000)
483. P.J. Hay, W.R. Wadt, *J. Chem. Phys.* **52**, 270, 284, 299 (1985)

484. P. Durand, J.C. Barthelat, *Theor. Chim. Acta* **38**, 283 (1975)
485. W.J. Stevens, H. Basch, M. Krauss, *J. Chem. Phys.* **81**, 6026 (1984)
486. W.J. Stevens, M. Krauss, H. Basch, P.J. Jasic, *Can. J. Phys.* **70**, 612 (1992)
487. H. Stoll, B. Metz, M. Dolg, *J. Comput. Chem.* **23**, 767 (2002)
488. I.V. Abarenkov, I.I. Tupitsyn, *J. Chem. Phys.* **115**, 1650 (2004)
489. *Electronic Properties of Solids Using Cluster Methods*,  
eds. T.A. Kaplan, S.D. Mahanti, (Plenum Press, New York London, 1994)
490. I.V. Abarenkov, I.M. Antonova, *Int. J. Quantum Chem.* **100**, 649 (2004)
491. S. Goedecker, K. Maschke, *Phys. Rev. B* **42**, 8858 (1990)
492. P.E. Blochl, *Phys. Rev. B* **41**, 5414 (1999)
493. X. Gonze, R. Stumpf, M. Scheffer, *Phys. Rev. B* **44**, 8503 (1991)
494. A. Khein, *Phys. Rev. B* **51**, 16608 (1995)
495. X. Gonze, P. Käckell, M. Scheffer, *Phys. Rev. B* **41**, 12264 (1990)
496. T. Nakajima, T. Yanai, K. Hirao, *J. Comput. Chem.* **23**, 847 (2002)
497. *Relativistic Electronic Structure Theory, Part I, Fundamentals*,  
ed. P. Schwerdtfeger, vol. **11** of *Theoretical and Computational Chemistry* (Elsevier, Amsterdam, 2002)
498. *Relativistic Electronic Structure Theory, Part II, Applications*,  
ed. P. Schwerdtfeger, vol. **14** of *Theoretical and Computational Chemistry* (Elsevier, Amsterdam, 2004)
499. T. Saué, T. Helgaker, *J. Comput. Chem.* **23**, 814 (2002)
500. A.K. Rajagopal, J. Callaway, *Phys. Rev. B* **7**, 1912 (1973)
501. C. van Wullen, *J. Comput. Chem.* **23**, 779 (2002)
502. K.G. Dyall, *J. Comput. Chem.* **23**, 786 (2002)
503. L. Visscher, *J. Comput. Chem.* **23**, 759 (2002)
504. L. Visscher, O. Visser, H. Aerts, H. Merenga, W.C. Nieuwport, *Comput. Phys. Commun.* **81**, 120 (1994)
505. T. Saué, K. Fargi, T. Helgaker, O. Gropen, *Molec. Phys.* **91**, 937 (1997)
506. I.P. Grant, H.M. Quiney, *Int. J. Quantum Chem.* **80**, 283 (2000)
507. W. Kutzelnigg, *Z. Phys. D* **15**, 27 (1990)
508. Y.S. Lee, W.C. Ermler, K.S. Pitzer, *J. Chem. Phys.* **67**, 5861 (1977)
509. E. Lenthe, E.J. Baerends, J.G. Snijders, *J. Chem. Phys.* **99**, 4597 (1993)
510. W.C. Ermler, R.B. Ross, P.A. Christiansen, *Adv. Quantum Chem.* **19**, 139 (1988)
511. P. Schwerdtfeger, in *Theoretical Chemistry and Physics of Heavy and Superheavy elements*, eds. U. Kaldor, S. Wilson (Kluwer, Dordrecht, 2003)
512. A.N. Petrov, N.S. Mosyagin, A.V. Titov, I.I. Tupitsyn, *J. Phys. B* **37**, 4621 (2004)
513. K.G. Dyall, *J. Chem. Phys.* **100**, 2118 (1994)
514. A.V. Titov, N.S. Mosyagin, *Int. J. Quantum Chem.* **71**, 359 (1999)
515. G. Treurich, N.A. Hill, *Phys. Rev. B* **64**, 073106 (2001)
516. D. Figgen, G. Rauhut, M. Dolg, H. Stoll, *Chem. Phys.* **311**, 227 (2005)
517. M. Dolg, *Theor. Chem. Acc.* **114**, 297 (2005)
518. K.A. Peterson, C. Puzzarini, *Theor. Chem. Acc.* **114**, 283 (2005)
519. X. Cao, M. Dolg, *J. Mol. Struct. (Theochem)* **673**, 203 (2004)
520. X. Cao, M. Dolg, H. Stoll, *J. Chem. Phys.* **118**, 487 (2003)
521. V. Bonifacic, S. Huzinaga, *J. Chem. Phys.* **60**, 2779 (1974)
522. S. Katsuki, S. Huzinaga, *Chem. Phys. Lett.* **152**, 203 (1988)
523. L. Seijo, Z. Barandiaran in *Relativistic Electronic Structure Theory, Part II, Applications*, ed. P. Schwerdtfeger, vol. **14** of *Theoretical and Computational Chemistry* (Elsevier, Amsterdam, 2004), p.417
524. N.S. Mosyagin, A.V. Titov, E. Eliav, U. Kaldor, *J. Chem. Phys.* **115**, 2007 (2001)
525. N.S. Mosyagin, A.V. Titov, *J. Chem. Phys.* **122**, 234106 (2005)
526. L.F. Pacios, P.A. Christiansen, *J. Chem. Phys.* **82**, 2664 (1985)

527. M.G. Kozlov, V.I. Fomichev, Y.Y. Dmitriev, L.N. Labzovsky, A.V. Titov, *J. Phys. B* **20**, 4939 (1987)
528. Y.Y. Dmitriev, Y.G. Khait, M.G. Kozlov, L.N. Labzovsky, A.O. Mitrushenkov, A.V. Titov, *Phys. Lett. A* **167**, 280 (1992)
529. A.V. Titov, N.S. Mosyagin, V.F. Ezhov, *Phys. Rev. Lett.* **77**, 5346 (1996)
530. N.S. Mosyagin, M.G. Kozlov, A.V. Titov, *J. Phys. B* **31**, L763 (1998)
531. M.G. Kozlov, A.V. Titov, N.S. Mosyagin, P.V. Souschko, *Phys. Rev. A* **56**, R3326 (1997)
532. A.N. Petrov, N.S. Mosyagin, T.A. Isaev, A.V. Titov, V.F. Ezhov, E. Eliav, U. Kaldor, *Phys. Rev. Lett.* **88**, 073001 (2002)
533. T.A. Isaev, A.N. Petrov, N.S. Mosyagin, A.V. Titov, E. Eliav, U. Kaldor, *Phys. Rev. A* **69**, R03050 (2004)
534. A.N. Petrov, A.V. Titov, T.A. Isaev, N.S. Mosyagin, D.P. DeMolle, *Phys. Rev. A* **72**, 022505 (2005)
535. T.A. Isaev, N.S. Mosyagin, A.N. Petrov, A.V. Titov, *Phys. Rev. Lett.* **95**, 163004 (2005)
536. P.E. Blöchl, *Phys. Rev. B* **50**, 17953 (1994)
537. A.V. Titov, N.S. Mosyagin, A.N. Petrov, T.A. Isaev, *Int. J. Quantum Chem.* **104**, 223 (2005)
538. J. Almlöf, P.R. Taylor, *J. Chem. Phys.* **86**, 4070 (1987)
539. B. Liu, A.D. McLean, *J. Chem. Phys.* **91**, 2348 (1989)
540. A.V. Titov, *Int. J. Quantum Chem.* **45**, 7 (1993)
541. S. Suzuki, K. Nakao, *J. Phys. Soc. Jpn.* **68**, 1982 (1999)
542. J.C. Boettger, *Phys. Rev. B* **57**, 8743 (1998)
543. K. Kudin, G.E. Scuseria, R.L. Martin, *Phys. Rev. Lett.* **89**, 266402 (2002)
544. T. Tsuchiya, M. Abe, T. Nakajama, K. Hirao, *J. Chem. Phys.* **115**, 4463 (2001)
545. E. van Lenthe, E.J. Baerends, *J. Comput. Chem.* **24**, 1142 (2003)
546. J.C. Boettger, *Eur. Phys. J.* **36**, 15 (2003)
547. J.J. Ladik, *J. Mol. Struct. (Theochem)* **391**, 1 (1997)
548. M. Douglas, N.M. Kroll, *Ann. Phys.* **82**, 89 (1974)
549. B.A. Hess, *Phys. Rev. A* **33**, 3742 (1986)
550. J.E. Peralta, G.E. Scuseria, *J. Chem. Phys.* **120**, 5875 (2004)
551. T. Nakajima, K. Hirao, *J. Chem. Phys.* **113**, 7786 (2000)
552. A. Wolf, M. Reiher, B.A. Hess, *J. Chem. Phys.* **117**, 9215 (2002)
553. N.J.M. Geipel, B.A. Hess, *Chem. Phys. Lett.* **273**, 62 (1997)
554. J.C. Boettger, *Phys. Rev. B* **57**, 8743 (1998)
555. M.D. Jones, J.C. Boettger, R.C. Albers, D.J. Singh, *Phys. Rev. B* **61**, 4644 (2000)
556. J.C. Boettger, A.K. Ray, *Int. J. Quantum Chem.* **90**, 1470 (2002)
557. J.C. Boettger, *Int. J. Quantum Chem.* **95**, 380 (2003)
558. J.C. Boettger, *Int. J. Quantum Chem.* **100**, 845 (2004)
559. J.Yang, M. Dolg, *Theor. Chem. Acc.* **113**, 212 (2005)
560. E.R. Batista, R.L. Martin, P.J. Hay, *J. Chem. Phys.* **121**, 2144 (2004)
561. J.E. Paralta, J. Uddin, G.E. Scuseria, *J. Chem. Phys.* **122**, 084108 (2005)
562. P.H.T. Phillipsen, E. van Lenthe, J.G. Snijders, E.J. Baerends, *Phys. Rev. B* **56**, 13556 (2000)
563. P.H.T. Phillipsen, E.J. Baerends, *Phys. Rev. B* **61**, 1773 (2000)
564. D.Olguin, M. Cardona, A. Cantarero, *Solid State Commun.* **122**, 575 (2002)
565. M. Cardona, M.L. Thewalt, *Rev. Mod. Phys.* **77**, 1173 (2005)
566. L. Colombo, *La Rivista del Nuovo Cimento* **28**, 1 (2005)
567. C.M. Goringe, D.R. Bowler, E. Hernandez, *Rep. Progr. Phys.* **60**, 1447 (1997)
568. R. Dovesi, B. Civalleri, R. Orlando, C. Roetti, V.R. Saunders, *Rev. Comput. Chem.* **21**, 1 (2005)
569. S.G. Semenov, *Vestnik LGU*, **N16**, 119 (1973)

570. I. Mayer, Int. J. Quantum Chem. **29**, 73 (1986)
571. R.A. Evarestov, V.A. Veryazov, Theor. Chim. Acta **81**, 95 (1991)
572. R.A. Evarestov, V.A. Veryazov, Rev. Solid State Sci. **5**, 415 (1991)
573. R.C. Bochicchio, H.F. Reale, J.A. Medrano, Phys. Rev. B **40**, 7186 (1989)
574. V.A. Veryazov, A.V. Leko, R.A. Evarestov, Phys. Solid State **41**, 1286 (1999)
575. R.A. Evarestov, A.I. Panin, Int. J. Quantum Chem. **88**, 472 (2002)
576. R.C. Bochicchio, H.F. Reale, J. Phys. B **26**, 4871 (1993)
577. R.A. Evarestov, A.I. Panin, Phys. Solid State **42**, 59 (2000)
578. R.C. Bochicchio, Theochem **429**, 229 (1998)
579. R.C. Bochicchio, L.Lain, A. Torre, J. Comput. Chem. **24**, 1902 (2003)
580. R.C. Bochicchio, L.Lain, A. Torre, Chem. Phys. Lett. **374**, 567 (2003)
581. R.A. Evarestov, V.A. Veryazov, phys. stat. sol. (b) **157**, 281, **158**, 201 (1990)
582. J. Choisnet, R.A. Evarestov, I.I. Tupitsyn, V.A. Veryazov, phys. stat. sol. (b) **179**, 441 (1993)
583. R.A. Evarestov, I.I. Tupitsyn, V.A. Veryazov, Int. J. Quantum Chem. **52**, 295 (1994)
584. J. Sichel, M.A. Whitehead, Theor. Chim. Acta **11**, 220 (1968)
585. I.D. Brown, J. Solid State Chem. **82**, 122 (1989)
586. I.D. Brown, J. Chem. Educat. **77**, 1070 (2000)
587. I.D. Brown, J. Appl. Crystallogr. **29**, 479 (1996)
588. I.D. Brown, in *Structure and Bonding in Crystals*, eds. M.O. Keffe, A. Navrotsky, vol. **2**, 1 (Academic Press, New York, 1981)
589. P. Marksteiner, P. Blaha, K. Schwarz, Z. Phys. B: Condens. Matter **64**, 119 (1986)
590. W.Y. Ching, Y.N. Xu, K.W. Wong, Phys. Rev. B **40**, 7684 (1989)
591. P. Saalfrank, M.A. Abdel-Raouf, J. Ladik, R.F. Wood, Phys. Rev. B **41**, 8824 (1990)
592. G.H. Hander, P.J. Brown, J. Spalek, J.M. Monig, Phys. Rev. B **40**, 4463 (1989)
593. J. Choisnet, J.M. Bassat, H. Pilliere, P. Odier, M. Leblanc, Solid State Commun. **66**, 1245 (1988)
594. I.D. Brown, Acta Crystallogr. B **48**, 553 (1992)
595. M. Crespin, C. Landorn, P. Odier, J.M. Bassat, P. Mouron, J. Choisnet, J. Solid State Chem. **100**, 281 (1992)
596. P. Reinhardt, B.A. Hess, M. Causa, Int. J. Quantum Chem. **58**, 297 (1996)
597. J. Muscat, V. Swamy, N.M. Harrison, Phys. Rev. B **65**, 224112 (2002)
598. M.Catti, C. Sandrone, R. Dovesi, Phys. Rev. B **55**, 16122 (1997)
599. M.Catti, G. Sandrone, Faraday Disc. **106**, 189 (1997)
600. R.A. Evarestov, A.I. Panin, phys. stat. sol. (b) **214**, R5 (1999)
601. M.D. Segall, R. Stah, C.J. Pickard, M.C. Payne, Phys. Rev. B **52**, 1005 (1996)
602. R.A. Evarestov, A.V. Leko, V.A. Veryazov, phys. stat. sol. (b) **203**, R3 (1997)
603. R.A. Evarestov, D.E. Usvyat, V.P. Smirnov, Solid State Commun. **127**, 423 (2003)
604. R.A. Evarestov, D.E. Usvyat, V.P. Smirnov, Phys. Solid State **45**, 459 (2003)
605. R.A. Evarestov, V.P. Smirnov, D.E. Usvyat, Theor. Chem. Acc. **114**, 19 (2005)
606. S. Piskinov, E. Heifets, R. Eglitis, G. Borstel, Comput. Mater. Sci. **29**, 165 (2004)
607. M. Veithen, X. Gonze, M. Chosez, Phys. Rev. B **66**, 235113 (2002)
608. R.A. Evarestov, V.P. Smirnov, I.I. Tupitsyn, D.E. Usvyat, Int. J. Quantum Chem. **104**, 110 (2005)
609. W.C. Lu, C.Z. Wang, T.L. Chan, K. Ruedenberg, K.M. Ho, Phys. Rev. B **70**, 041101 (2004).
610. A. Bert, M. Llunell, R. Dovesi, C.M. Zicovich-Wilson, Phys. Chem. Chem. Phys. **5**, 5319 (2003)
611. R.A. Evarestov, I.I. Tupitsyn, A.V. Bandura, V.E. Alexandrov, Int. J. Quantum Chem. **106**, 2191 (2006)
612. V.P. Smirnov, R.A. Evarestov, Phys. Rev. B **72**, 075138 (2005)
613. R.A. Evarestov, A.V. Bandura, V.E. Alexandrov, Phys. Solid State **47**, 2248 (2005)

614. R.A. Evarestov, A.V. Bandura, V.E. Alexandrov, E.A. Kotomin, phys. stat. sol. (b) **242**, R11 (2005)
615. S. Gennard, F. Cora, C.R.A. Catlow, J. Phys. Chem. B **103**, 10158 (1999)
616. E. Mete, R. Shattaf, S. Ellialtioglu, Phys. Rev. B **68**, 035119 (2003)
617. D.Sanchez-Portal, E. Artacho, J.M. Soler, Solid State Commun. **95**, 685 (1995)
618. D.Sanchez-Portal, E. Artacho, J.M. Soler, J. Phys.: Condens. Matter **8**, 3859 (1995)
619. I.I. Tupitsyn, R.A. Evarestov, V.P. Smirnov, Phys. Solid State **47**, 1837 (2005)
620. C.Y. Ren, S.H. Chiou, J. Choisnet, J. Appl. Phys. **99**, 23706 (2006)
621. J.S. Lin, A. Quteish, M.C. Payne, V. Heine, Phys. Rev. B **47**, 4174 (1993)
622. E. Ruiz, S. Alvarez, P. Alemany, Phys. Rev. B **56**, 7189 (1997)
623. R.A. Evarestov, D.E. Usyyat, V.P. Smirnov, Phys. Solid State **45**, 2072 (2003)
624. P.A. Cox, *Transition Metal Oxides* (Carendon Press, Oxford, 1992)
625. C.N.R. Rao, B. Raveau, *Transition Metal Oxides* (VCH Publishers, New York, 1995)
626. W.E. Pickett, Rev. Mod. Phys. **61**, 433 (1989)
627. N.M. Harrison, V.R. Saunders, R. Dovesi, W.C. Mackrodt, A.S. Alexandrov, C.N.R. Rao, J.N. Murrell, R.L. Johnston, D.E. Logan, Philos. Trans. Roy. Soc. London A **356**, 75 (1998)
628. M.D. Towler, N.L. Allan, N.M. Harrison, V.R. Saunders, W.C. Mackrodt, E. Apra, Phys. Rev. B **50**, 5041 (1994)
629. M. Catti, G. Valerio, R. Dovesi, Phys. Rev. B **51**, 7441 (1995)
630. M. Catti, G. Sandrone, G. Valerio, R. Dovesi, J. Phys. Chem. Solids **57**, 1735 (1996)
631. A. Chartier, P. D'Arco, R. Dovesi, V.R. Saunders, Phys. Rev. B **60**, 14042 (1999)
632. E. Ruiz, M. Llunell, P. Alemany, J. Solid State Chem. **176**, 400 (2003)
633. I.D.P.R. Moreira, R. Dovesi, Phys. Rev. B **67**, 134513 (2003)
634. Y.-S. Su, T.A. Kaplan, S.D. Mahanti, J.F. Harrison, Phys. Rev. B **61**, 1324 (2000)
635. M. Nicastro, C.H. Patterson, Phys. Rev. B **65**, 205111 (2002)
636. G. Trimarchi, N. Binggeli, Phys. Rev. B **71**, 035101 (2005)
637. P. Pavindra, A. Kjekshus, H. Fjellvag, A. Delin, O. Eriksson, Phys. Rev. B **65**, 064445 (2002)
638. D. Munoz, N.M. Harrison, F. Illas, Phys. Rev. B **69**, 085115 (2004)
639. R.A. Evarestov, E.A. Kotomin, Yu. A. Mastrikov, D. Gryaznov, E. Heifets, J. Maier, Phys. Rev. B **72**, 124411 (2005)
640. N.N. Kovaleva, A.V. Boris, C. Bernhard, A. Kulakov, A. Pimenov, A.M. Balbashov, G. Khaliullin, B. Keimer, Phys. Rev. Lett. **93**, 147204 (2004)
641. F. Moussa, M. Hennion, J. Rodriguez-Carvajal, H. Moudden, L. Pinsard, A. Revcolevschi, Phys. Rev. B **54**, 15149 (1996)
642. N. Hamada, H. Sawada, I. Solovyev, K. Terakura, Physica **B237**-**238**, 11 (1997)
643. R. Lorenz, R. Hafner, D. Spisak, J. Hafner, J. Magn. Reson., Ser. A **226**-**230**, 889 (2001)
644. P. Ravindran, A. Kjekshus, H. Fjellvag, A. Delin, O. Eriksson, Phys. Rev. B **65**, 064445 (2002)
645. T. Saitoh, A.E. Boquet, T. Mizokawa, H. Namatame, A. Fujimori, M. Abbate, Y. Takeda, M. Takano, Phys. Rev. B **51**, 13942 (1995)
646. TH. Lonkai, D.G. Tomuta, U. Amann, J. Ihringer, R.W.A. Hendrikx, D.M. Tobbens, J.A. Mydosh, Phys. Rev. B **69**, 134108 (2004)
647. M. Fiebig, D. Frolich, K. Kohn, St. Leute, T.H. Lottermoser, V.V. Pavlov, R.V. Pisarev, Phys. Rev. Lett. **84**, 5620 (2000)
648. D.G. Tomuta, S. Ramakrishnan, G.J. Nieuwenhuys, J.A. Mydosh, J. Phys.: Condens. Matter **13**, 4543 (2001)
649. C. Degenhardt, M. Fiebig, D. Frolich, TH. Lottermoser, R.V. Pisarev, Appl. Phys. B **73**, 139 (2001)
650. M.C. Qian, J. Dong, Q. Cheng, Phys. Lett. A **270**, 96 (2000)

651. J.E. Medvedeva, V.I. Anisimov, M.A. Korotin, O.N. Mryasov, A.J. Freeman, *J. Phys.: Condens. Matter* **12**, 4947 (2000)
652. A.M. Kalashnikova, R.V. Pisarev, *JETP Lett.* **78**, 3 (2003)
653. T. Bredow, K. Jug, R.A. Evarestov, *phys. stat. sol. (b)* **243**, R10 (2006)
654. M. Bieringer, J.E. Greedan, *J. Solid State Chem.* **143**, 132 (1999)
655. J. Park, J.-G. Park, G.S. Jeon, H.Y. Choi, C. Lee, W. To, R. Bewley, K.A. McEwen, T.G. Perring, *Phys. Rev. B* **68**, 104426 (2003).
656. P. Pulay, *Mol. Phys.* **17**, 197 (1969)
657. H.B. Schlegel, *Theor. Chem. Acc.* **103**, 294 (2000)
658. S. Hirata, H. Tori, M. Tatsumi, *Phys. Rev. B* **57**, 11994 (1998)
659. D.Jacquemin, J.M. Andre, B. Champagne, *J. Chem. Phys.* **111**, 5306, 5324 (1999)
660. B. Civalleri, Ph.D'Arco, R. Orlando, V.R. Saunders, R. Dovesi, *Chem. Phys. Lett.* **348**, 131 (2001)
661. K. Doll, V.R. Saunders, N.M. Harrison, *Int. J. Quantum Chem.* **82**, 1 (2001)
662. K. Doll, *Comput. Phys. Commun.* **137**, 74 (2001)
663. K. Doll, R. Dovesi, R. Orlando, *Theor. Chem. Acc.* **112**, 394 (2004)
664. K. Doll, R. Dovesi, R. Orlando, *Theor. Chem. Acc.*, published online, (2005)
665. R. Dovesi, *Lecture Notes in Chem.* **67**, 179 (1996)
666. K. Rosciszewski, K. Doll, B. Paulus, P. Fulde, *Phys. Rev. B* **57**, 14667 (1998)
667. *Handbook of Chemistry and Physics*, ed. R.C. Weast, CRC, Boca Raton, FL (1987)
668. B.J. Kennedy, C.J. Howard, B.C. Chakoumakos, *Phys. Rev. B* **59**, 4023 (1999)
669. F. Pascale, C.M. Zicovich-Wilson, F. Lopez, B. Civalleri, R. Orlando, R. Dovesi, *J. Comput. Chem.* **25**, 888 (2004)
670. S. Baroni, S. de Gironcoli, A. Dal Corso, P. Giannozzi, *Rev. Mod. Phys.* **73**, 515 (2001)
671. K. Parlinski, Z.Q. Li, Y. Kawazoe, *Phys. Rev. Lett.* **78**, 4063 (1997)
672. P. Sikora, *J. Phys. Chem. Solids* **66**, 1069 (2005)
673. B. Montanari, B. Civalleri, C.M. Zicovich-Wilson, R. Dovesi, *Int. J. Quantum Chem.* **106**, 1703 (2006)
674. M. Principe, F. Pascale, C.M. Zicovich-Wilson, V.R. Saunders, R. Orlando, R. Dovesi, *Phys. Chem. Miner.* **31**, 559 (2004)
675. P. Umari, A. Pasquarello, A. Dal Corso, *Phys. Rev. B* **63**, 094305 (2001)
676. B. Montanari, N.M. Harrison, *Chem. Phys. Lett.* **364**, 528 (2002)
677. S. Na-Phattalung, M.F. Smith, K. Kim, M.H. Du, S.H. Wei, S.B. Zhang, S. Limpijum-nong, *Phys. Rev. B* **73**, 125205 (2006)
678. R.A. Evarestov, in *Computational Materials Science*, NATO Science Series III, **187**, 122 (2003)
679. R.A. Evarestov, *phys. stat. sol. (a)* **202**, 235 (2005)
680. R.A. Evarestov, S. Piskunov, E.A. Kotomin, G. Borstel, *Phys. Rev. B* **67**, 064101 (2003)
681. R.A. Evarestov, V.P. Smirnov, *phys. stat. sol. (b)* **201**, 75 (1997)
682. R.A. Evarestov, P.W.M. Jacobs, A.V. Leko, *Phys. Rev. B* **54**, 8969 (1996)
683. R.A. Evarestov, V.P. Smirnov, *phys. stat. sol. (b)* **215**, 949 (1999)
684. C. Freyria-Fava, R. Dovesi, V.R. Saunders, M. Leslie, C. Roetti, *J. Phys.: Condens. Matter* **5**, 4793 (1993)
685. L.N. Kantorovich, J.M. Holender, M.J. Gillan, *Surf. Sci.* **343**, 221 (1995)
686. C.W.M. Castelone, S. Mirb, *Phys. Rev. B* **70**, 175202 (2004)
687. C. Pisani, *Phase Trans.* **52**, 123 (1994)
688. M. Leslie, M.J. Gillan, *J. Phys. C: Solid State Phys.* **18**, 973 (1985)
689. G. Makov, M.C. Payne, *Phys. Rev. B* **51**, 4014 (1995)
690. J. Lento, J.L. Mozos, R.M. Nieminen, *J. Phys.: Condens. Matter* **14**, 2637 (2002)
691. U. Gerstmann, P. Deak, R. Rurrali, B. Aradi, TH. Frauenheim, H. Overhof, *Physica B* **340-342**, 190 (2003)
692. C.W.M. Castleton, A. Hoglund, S. Mirbt, *Phys. Rev. B* **73**, 035215 (2006)

693. J. Shim, E.Lee, Y. Lee, R.M. Niemenen, Phys. Rev. B **71**, 035206 (2005)
694. J.M. Vail, D.Schindel, A. Yang, O. Penner, R. Pandy, S.H. Jiang, M. Blanco, A. Costales, J. Phys. C: Condens. Matter **16**, 3371 (2004)
695. A. Gulans, R.A. Evarestov, I. Tale, phys. stat. sol. (c) **2**, 507 (2005)
696. C. Sousa, Coen de Graaf, F. Illas, Phys. Rev. B **62**, 10013 (2000)
697. R.A. Evarestov, A.R. Sokolov, A.V. Leko, V.A. Veryazov, J. Phys.: Condens. Matter **1**, 6611 (1989)
698. B.T. Plachenov, A.R. Sokolov, R.A. Evarestov, Fiz. Tverdogo Tela **28**, 867 (1986)
699. A.V. Bandura, R.A. Evarestov, phys. stat. sol. (b) **64**, 635 (1974)
700. O. Daniliv, L. Kantorovich, J. Phys. C:Condens. Matter **16**, 7233 (2004)
701. C. Pisani, F. Cora, R. Nada, S. Casassa, Comp. Phys. Commun. **82**, 139 (1994)
702. C. Pisani, U. Birkenheuer, Comp. Phys. Commun. **96**, 221 (1996)
703. C.Pisani, U. Birkenheuer, C. Casassa, F. Cora, EMBED01 User's Manual, University of Torino, Torino (1999)
704. V. Sulimov, S. Casassa, C. Pisani, J. Garapon, B. Poumelle, Modeling Simul. Mater. Sci. Eng. **8**, 763 (2000)
705. E. Scorza, U. Birkenheuer, C. Pisani, J. Chem. Phys. **107**, 9645 (1997)
706. C. Pisani, F. Cora, R. Dovesi, R. Orlando, J. Elect. Spectrosc. Relat. Phenom. **69**, 1 (1994)
707. <http://wgc.chem.pu.ru/~valera/cndo/manual.html>
708. T. Brudevoll, E.A. Kotomin, N.E. Christensen, Phys. Rev. B **53**, 7731 (1996)
709. Y.N. Hu, Z.Q. Gu, X.F. Zhong, W.Y. Ching, Phys. Rev. B **56**, 7277 (1997)
710. A. Stashans, E. Kotomin, J.L. Calais, Phys. Rev. B **49**, 14854 (1994)
711. I. Tanaka, K. Tatsumi, M. Nakano, H. Adachi, J. Am. Ceram. Soc. **85**, 68 (2002)
712. K. Matsunaga, T. Tanaka, T. Yamamoto, Y. Ikuhara, Phys. Rev. B **68**, 085110 (2003)
713. F. Janetzko, R.A. Evarestov, T. Bredow, K. Jug, phys. stat. sol. (b) **241**, 1032 (2004)
714. F. Janetzko, T. Bredow, K. Jug, J. Chem. Phys. **116**, 8994 (2002)
715. M. Catti, G. Valerio, R. Dovesi, M. Causa, Phys. Rev. B **49**, 14179 (1994)
716. W. Choi, A. Termin, M.R. Hoffmann, J. Phys. Chem. **98**, 13669 (1994)
717. D.Morris, R. Dixon, F.H. Jones, Y. Dou, R. Egddell, S.W. Downes, G. Beamson, Phys. Rev. B **55**, 16083 (1997)
718. T. Umebayashi, T. Yamaki, H. Itoh, K. Asai, J. Phys. Chem. Solids **63**, 1909 (2002)
719. L.A. Errico, G. Fabricius, M. Renteria, Z. Naturforsch. **55**, 267 (2000)
720. A. Stashans, S. Llunell, R. Bergstrom, A. Hagfeldt, S. Lundquist, Phys. Rev. B **53**, 159 (1996)
721. A. Stashans, S. Llunell, R.W. Grimes, J. Phys. Chem. Solids **57**, 1293 (1996)
722. R.I. Eglitis, E.A. Kotomin, G. Borstel, Defects Diffus. Forum **226-228**, 169 (2004), online at <http://www.scientific.net>
723. H. Donnerberg, A. Birkholz, J. Phys.: Condens. Matter **12**, 8239 (2000)
724. H. Moriwake, Int. J. Quantum Chem. **99**, 824 (2004)
725. A. Shigemi, T. Wada, Jpn. J. Appl. Phys. **43B**, 6793 (2004)
726. J.P. Buban, H. Iddir, S. Ogut, Phys. Rev. B **69**, R180102 (2004)
727. S.A. Prosandeyev, A.V. Fisenko, A.I. Riabchinski, I.A. Osipenko, I.P. Raevski, N. Sa- fontsera, J. Phys.: Condens. Matter **8**, 6705 (1996)
728. J. Robertson, J. Appl. Phys. **93**, 1054 (2003)
729. T. Tanaka, K. Matsunaga, Y. Ikuhara, T. Yamamoto, Phys. Rev. B **68**, 205213 (2003)
730. J. Carrasco, F. Illas, N. Lopez, E.A. Kotomin, Yu. F. Zhukovskii, S. Piskunov, J. Maier, K. Hermansson, phys. stat. sol. (c) **2**, 153 (2005)
731. D.Ricci, G. Bano, G. Paccioni, F. Illas, Phys. Rev. B **68**, 224105 (2003)
732. R.A. Evarestov, E.A. Kotomin, Yu. F. Zhukovskii, Int. J. Quantum Chem. **106**, 2173 (2006)
733. P.A. Cox, *Transition Metal Oxides*; Clarendon Press, Oxford, UK (1995)

734. R. Astala, P.D. Bristowe, *Simul. Mater. Sci. Eng.* **9**, 415 (2001)
735. K. Szot, W. Speier, R. Carius, U. Zastrow, W. Beyer, *Phys. Rev. Lett.* **88**, 075508 (2002)
736. D.E. Usvyat, R.A. Evarestov, V.P. Smirnov, *Int. J. Quantum Chem.* **100**, 352 (2004)
737. R. Moos, K.H. Saerdtl, *J. Am. Ceram. Soc.* **80**, 2549 (1997)
738. D.Ricci, G. Bano, G. Pachchioni, F. Illas, *Phys. Rev. B* **68**, 224105 (2003)
739. J. Crawford, P.W.M. Jacobs, *Solid State Chem.* **144**, 423 (1999)
740. G. Kresse, J. Hafner, *VASP Guide*, University of Vienna, Austria, 2003
741. M.G. Brik, *J. Phys. Chem. Solids* **67**, 856 (2006)
742. F.M. Michel-Calendini, K.A. Muller, *Solid State Commun.* **40**, 255 (1981)
743. M.O. Selme, P. Pecheur, G. Toussaint, *J. Phys. C: Solid State Phys.* **17**, 5185 (1984)
744. H. Donnerberg, *Phys. Rev. B* **50**, 9053 (1994)
745. A.V. Postnikov, A.I. Poteryaev, G. Borstel, *Ferroelectrics* **206–207**, 69 (1998)
746. R.I. Eglitis, A.V. Postnikov, G. Borstel, *phys. stat. sol. (b)* **209**, 187 (1998)
747. I.I. Tupitsyn, A. Deineka, V.A. Trepakov, L. Jastrabik, S.E. Kapphan, *Phys. Rev. B* **64**, 195111 (2001)
748. R.K. Astala, P.D. Bristowe, *Model. Simul. Mater. Sci. Eng.* **12**, 79 (2004)
749. R. Waser, T. Bieger, J. Maier, *Solid State Commun.* **76**, 1077 (1990)
750. J. Fleig, K.D. Kreuer, J. Maier, in *Handbook of Advanced Ceramics*, Elsevier, Singapore, 2003, p.57
751. G. Banach, W.M. Temmerman, *Phys. Rev. B* **69**, 054427 (2004)
752. H. Zenia, G.A. Gehring, G. Banach, W.M. Temmerman, *Phys. Rev. B* **71**, 024416 (2005)
753. J. Geck, P. Wochner, D.Bruns, B. Buchner, U. Gebhardt, S. Kiele, P. Reutler, A. Revcolevschi, *Phys. Rev. B* **69**, 104413 (2004)
754. D.Fuks, L. Bakaleinikov, E.A. Kotomin, J. Felsteiner, A. Gordon, R.A. Evarestov, D. Gryaznov, J. Maier, *Solid State Ion.* **177**, 217 (2006)
755. J.K. Perry, J. Tahir-Kheli, W.A. Goddard III, *Phys. Rev. B* **63**, 144510 (2001)
756. D.Fuks, S. Dorfman, S. Piskunov, E.A. Kotomin, *Phys. Rev. B* **71**, 014111 (2005)
757. D.Fuks, S. Dorfman, E.A. Kotomin, Yu. Zhukovskii, A.M. Stoneham, *Phys. Rev. Lett.* **85**, 4333 (2000)
758. D.Fuks, S. Dorfman, J. Felsteiner, L. Bakaleinikov, A. Gordon, E.A. Kotomin, *Solid State Ion.* **173**, 107 (2004)
759. L. Rormark, S. Stolen, K. Wik, T. Grande, *J. Solid State Chem.* **163**, 186 (2002)
760. A.G. Kchachaturyan, *Theory of Structural Transformations in Solids*, Wiley, New York, 1983
761. *International Tables for Crystallography, volume E, Subperiodic Groups*, eds. V. Kopsky, D.B. Litvin (Kluwer Academic Publishers, Dordrecht/Boston/London, 2002)
762. V. Kopsky, *Acta Cryst. A* **45**, 805, 816 (1989)
763. V. Kopsky, *Acta Cryst. A* **56**, 370 (2000)
764. E.A. Wood, *Bell Telephone Tech. J.* **43**, 541 (1964)
765. V.P. Smirnov, P. Tronc, *Phys. Solid State* **48**, 1295 (2006)
766. C. Noguera, *Physics and Chemistry at Oxide Surfaces*, Cambridge University Press (1996)
767. C. Noguera, *J. Phys.: Condens. Matter* **12**, R367 (2000)
768. F. Finocchi, F. Bottin, C. Noguera, in *Computational Materials Science*, eds. C.R.A. Catlow, E.A. Kotomin, IOS Press, 2003, p.196
769. T. Bredow, G. Geudtner, K. Jug, *J. Chem. Phys.* **105**, 6395 (1996)
770. R.A. Evarestov, T. Bredow, K. Jug, *Phys. Solid State* **43**, 1774 (2001)
771. T. Bredow, K. Jug, *Chem. Phys. Lett.* **223**, 89 (1994)
772. P.W. Tasker, *J. Phys. C: Solid State Phys.* **12**, p (1979)
773. J.C. Boettger, *Phys. Rev. B* **49**, 16798 (1994)

774. V. Fiorentini, M.J. Methfesse, *J. Phys.: Condens. Matter* **8**, 6525 (1996)
775. L. Fu, E. Yaschenko, L. Resta, *Phys. Rev. B* **60**, 2697 (1999)
776. R.A. Evarestov, A.V. Bandura, *Int. J. Quantum Chem.* **100**, 452 (2004)
777. R.A. Evarestov, A.V. Bandura, *Int. J. Quantum Chem.* **96**, 282 (2002)
778. L.N. Kantorovich, M.J. Gilan, *Surf. Sci.* **374**, 373 (1997)
779. P. Reinhardt, B. Hess, *Phys. Rev. B* **50**, 12015 (1994)
780. R.A. Evarestov, V.P. Smirnov, D.E. Usvyat, *Int. J. Quantum Chem.* **104**, 102 (2005)
781. G. Fernandes-Cata, L.G. Alvarez, R. Dovesi, C.M. Zicovich-Wilson, *J. Phys. Chem. B* **106**, 7316 (2004)
782. S.P. Bates, G. Kresse, M.G. Gillan, *Surf. Sci.* **385**, 386 (1997)
783. U. Diebold, *Surf. Sci. Rep.* **48**, 53 (2003)
784. M. Calatayud, B. Mguig, C. Minot, *Surf. Sci.* **526**, 297 (2003)
785. M. Calatayud, A. Markovits, M. Menetrey, B. Mguig, C. Minot, *Catal. Today* **85**, 125 (2003)
786. M. Menetrey, A. Markovits, C. Minot, G. Pacchioni, *J. Phys. Chem. B* **108**, 12858 (2004)
787. C. Noguera, F. Finocci, J. Goniakowski, *J. Phys.: Condens. Matter* **16**, S2509 (2004)
788. T. Bredow, L. Giordano, F. Cinquini, G. Pacchioni, *Phys. Rev. B* **70**, 035419 (2004)
789. M. Calatayud, C. Minot, *Surf. Sci.* **552**, 169 (2004)
790. A.V. Bandura, D.G. Sykes, V. Shapovalov, T.N. Truong, J.D. Kubicki, R.A. Evarestov, *J. Phys. Chem. B* **108**, 7844 (2004)
791. A.V. Bandura, J.O. Sofo, J.D. Kubicki, *J. Phys. Chem. B* **110**, 8386 (2006)
792. S.J. Thompson, S.P. Lewis, *Phys. Rev. B* **73**, 073403 (2006)
793. K.J. Hameeuw, G. Cantele, D. Ninno, F. Trani, G. Iadonisi, *J. Chem. Phys.* **124**, 024708 (2006)
794. M.L. Sushko, A.Yu. Gal, A.L. Shluger, *J. Phys. Chem. B* **110**, 4853 (2006)
795. G.U. von Oertzen, A.R. Gerson, *Int. J. Quantum Chem.* **106**, 2054 (2006)
796. P. Persson, A. Stashans, R. Bergstrom, S. Lunell, *Int. J. Quantum Chem.* **70**, 1055 (1998)
797. K. Jug, G. Geudtner, *J. Mol. Cat. A* **119**, 143 (1997)
798. T. Brinkley, M. Dietrich, T. Engel, P. Farral, G. Gantner, A. Schafer, A. Szuchmacher, *Surf. Sci.* **395**, 292 (1998)
799. N.M. Harrison, X.G. Wang, J. Muskat, M. Scheffer, *Faraday Discuss.* **114**, 305 (1999)
800. J. Leconte, A. Markovits, M.K. Skalli, C. Minot, A. Belmajdoub, *Surf. Sci.* **497**, 194 (2002)
801. E.V. Stefanovich, T.N. Truong, *J. Phys. Chem. B* **102**, 3018 (1998)
802. J. Goniakowski, M.J. Lindan, *Surf. Sci.* **350**, 145 (1996)
803. P.J.D. Lindan, N.M. Harrison, J.M. Holender, M.J. Gillan, *Phys. Rev. Lett.* **80**, 762 (1998)
804. G. Charlton, P.B. Howes, C.L. Nickin, P. Steadman, J.S.G. Taylor, C.A. Muryn, S.P. Harte, J. Mercer, R. McGrath, D. Norman, T.S. Turner, G. Thornton, *Phys. Rev. Lett.* **78**, 495 (1997)
805. E.V. Stefanovich, T.N. Truong, *Chem. Phys. Lett.* **299**, 623 (1999)
806. T.T. Rantala, T.S. Rantala, V. Lannto, *Surf. Sci.* **420**, 103 (1999)
807. J. Oviedo, M.J. Gillan, *Surf. Sci.* **463**, 93 (2000)
808. I. Manassidis, J. Goniakowski, L.N. Kantorovich, M.J. Gillan, *Surf. Sci.* **339**, 258 (1995)
809. J. Goniakowski, M.J. Gillan, *Surf. Sci.* **350**, 145 (1996)
810. S.P. Bates, *Surf. Sci.* **512**, 29 (2002).
811. P.J.D. Lindan, *Chem. Phys. Lett.* **328**, 325 (2000)
812. M. Calatayud, J. Andrus, A. Beltrn, *Surf. Sci.* **430**, 213 (1999)
813. F. Ciriaco, L. Cassidei, M. Cacciatore, G. Petrella, *Chem. Phys.* **303**, 55 (2004)
814. M. Melle-Franco, G. Pacchioni, *Surf. Sci.* **461**, 54 (2000)

815. F.R. Sensato, R. Custodio, M. Calatayud, A. Beltron, J. Andrus, J.R. Sambrano, E. Longo, *Surf. Sci.* **511**, 408 (2002)
816. R.A. Evarestov, A.V. Bandura, E.V. Proskurov, *phys. stat. sol. (b)* **243**, 1823 (2006)
817. A.V. Postnikov, P. Entel, P. Ordejon, *Phase Trans.* **75**, 143 (2002)
818. Y. Yamaguchi, K. Tabata, T. Yashima, *J. Mol. Struct. (Theochem)* **714**, 221 (2005)
819. H. Szuber, G. Czempik, R. Larciprete, B. Adamowicz, *Sens. Actuators B Chem.* **70**, 177 (2000)
820. J.M. Thelin, R. Sporken, J. Darville, R. Caudano, J.M. Gilles, R.L. Johnson, *Phys. Rev. B* **42**, 11914 (1990).
821. A.L. Dawar, J.C. Joshi, *J. Mater. Sci.* **19**, 1 (1984)
822. V.A. Gercher, D.F. Cox, *Surf. Sci.* **322**, 177 (1995)
823. T. Hiemstra, H. Yong, W.H. van Riemsdijk, *Langmuir* **15**, 5942 (1999)
824. S. Piskunov, E.A. Kotomin, E. Heifets, J. Maier, R.I. Eglitis, G. Borstel, *Surf. Sci.* **575**, 75 (2005)
825. R.A. Evarestov, A.V. Bandura, V.E. Alexandrov, *phys. stat. sol. (b)* **246**, 1013 (2006)
826. N. Erdman, K.R. Poeppelmeier, M. Asta, O. Warschkow, D.E. Ellis, L.D. Marks, *Nature* **419**, 55 (2002)
827. A. Ikeda, T. Nishimura, T. Morishita, Y. Kido, *Surf. Sci.* **433–435**, 520 (1999).
828. G. Charlton, S. Brennan, C.A. Muryn, R. McGrath, D. Norman, T.S. Turner, G. Thornton, *Surf. Sci.* **457**, L376 (2000).
829. J. Padilla, D. Vanderbilt, *Surf. Sci.* **418**, 64 (1998)
830. N.V. Krainyukova, V.V. Butskii, *Surf. Sci.* **454**, 628 (2000)
831. E. Heifets, R.I. Eglitis, E.A. Kotomin, J. Maier, G. Borstel, *Phys. Rev. B* **64**, 235417 (2001)
832. E. Heifets, R.I. Eglitis, E.A. Kotomin, J. Maier, G. Borstel, *Surf. Sci.* **513**, 211 (2002)
833. A. Asthagiri, D.S. Sholl, *Phys. Rev. B* **73**, 125432 (2006)
834. K. van Benthem, C. Elsässer, *J. Appl. Phys.* **90**, 6156 (2001)
835. Y.S. Lee, J.S. Lee, T.W. Noh, D.Y. Byun, K.S. Yoo, K. Yamaura, E.T. Muromachi, *Phys. Rev. B* **67**, 113101 (2003).
836. Z.Q. Li, J.L. Zhu, C.Q. Wu, Z. Tang, Y. Kawazoe, *Phys. Rev. B* **58**, 8075 (1998)
837. S. Kimura, J. Yamauchi, M. Tsukada, S. Watanabe, *Phys. Rev. B* **51**, 11049 (1995)
838. Yu. F. Zhukovskii, S. Piskunov, E.A. Kotomin, O. Sychev, G. Borstel, *Microelectr. Eng.* **81**, 467 (2005)
839. S. Piskunov, E.A. Kotomin, E. Heifets, *Microelectr. Eng.* **81**, 472 (2005)
840. S. de Lazaro, E. Longo, J.R. Sambrano, A. Bertran, *Surf. Sci.* **552**, 149 (2004)
841. X.Y. Hue, C.L. Wang, W.L. Zhong, *Surf. Sci.* **550**, 73 (2004)
842. G. Borstel, R.I. Eglitis, E.A. Kotomin, E. Heifets, *phys. stat. sol.(b)* **236**, 253 (2003)
843. N. Erdman, L.D. Marks, *Surf. Sci.* **526**, 107 (2003)
844. R. Bader, *Atoms in Molecules: A Quantum Theory*, Oxford University Press, New York, 1990
845. A. Asthagiri, D.S. Sholl, *J. Chem. Phys.* **116**, 9914 (2002)
846. A. Stashans, F. Erazo, J. Ortiz, P. Valverde, *Philos. Mag. B* **81**, 1977 (2001)
847. Z. Fang, K. Terakura, *Surf. Sci.* **470**, L75 (2000)
848. J. Carrasco, F. Illas, N. Lopez, E.A. Kotomin, Yu. F. Zhukovskii, R.A. Evarestov, Yu. A. Mastrikov, S. Piskunov, J. Maier, *Phys. Rev. B* **73**, 064106 (2006)
849. J. Carrasco, J.R.B. Gomes, F. Illas, *Phys. Rev. B* **69**, 064116 (2004)
850. P. Mori-Sanchez, J.M. Recio, B. Silvi, C. Sousa, A.M. Pendas, V. Luana, F. Illas, *Phys. Rev. B* **66**, 075103 (2002)
851. R.A. Evarestov, E.A. Kotomin, E. Heifets, J. Maier, G. Borstel, *Solid State Commun.* **127**, 367 (2003)
852. R.A. Evarestov, E.A. Kotomin, D. Fuks, J. Felsteiner, J. Maier, *Appl. Surf. Sci.* **238**, 457 (2004)

853. E. Heifets, E.A. Kotomin, J. Maier, *Phys. Chem. Chem. Phys.* **5**, 4180 (2003)  
854. F. Bottin, F. Finocchi, C. Noguera, *Phys. Rev. B* **68**, 035418 (2003)  
855. R.A. Evarestov, E.A. Kotomin, Yu. A. Mastrikov, D.Gryaznov, E. Heifets, J. Maier, *Phys. Rev. B* **72**, 214411 (2005)  
856. <http://www.supercomputing.it/software.php?cat=11>  
857. <http://www.msg.ku.edu/msg/MGM/links/comp.html>  
858. <http://www.redbrick.dcu.ie/noel/linux4chemistry>  
859. J.V. Vondele, M. Crack, F. Mohamed, M. Parrinello, T. Chassaing, J. Hutter, *Comp. Phys. Commun.* **167**, 103 (2005)  
860. C. Pisani, J. Mol. Struct.(Theochem), **463**, 125 (1999)  
861. R. Orlando, R. Dovesi, P. Ugliengo, C. Roetti, V.R. Saunders, *Int. J. Inorg. Mater.* **1**, 147 (1999)  
862. R. Dovesi, R. Orlando, C. Roetti, C. Pisani, V.R. Saunders, *phys. stat. sol. (b)* **217**, 63 (2000)  
863. C. Pisani, R. Dovesi, C. Roetti, M. Causa, R. Orlando, S. Casassa, V.R. Saunders, *Int. J. Quantum Chem.* **77**, 1032 (2000)  
864. G.Te Velde, F.M. Bickelhaupt, E.J. Baerends, C.F. Guerra, S.J.A. VAN Gisbergen, J.G. Snijders, T. Ziegler, *J. Comput. Chem.* **22**, 931 (2001)  
865. A.E. Mattson, P.A. Schultz, M.P. Desjarlais, T.R. Mattsson, K. Leung, *Model. Simul. Mater. Sci. Eng.* **13**, R1 (2005)  
866. B. Delley, *J. Chem. Phys.* **113**, 7756 (2000)  
867. H. Eschrig, K. Koepernik, I.Chaplygin, *J. Solid State Chem.* **176**, 482 (2003)  
868. S.D. Kenny, A.P. Horsfield, H. Fujitani, *Phys. Rev. B* **62**, 4899 (2000)  
869. R.A. Evarestov, I.I. Tupitsyn, V.A. Veryazov, *Int. J. Quantum Chem.* **52**, 295 (2004)  
870. J.J.P. Stewart, *J. Mol. Mod.* **10**, 155 (2004)  
871. L. Kantorovich, A. Stashans, E. Kotomin, P.W.M. Jacobs, *Int. J. Quantum Chem.* **52**, 1177 (1994)  
872. B. Civalleri, F. Napoli, Y. Noel, C. Roetti, R. Dovesi, *Cryst. Eng. Commun.* **8**, 364 (2006), see online [www.rsc.org/crystengcomm](http://www.rsc.org/crystengcomm)  
873. <http://www.ccr.jussieu.fr/ccr/Documentation/Calcul/XCRYSDEN/Documentation.html>  
874. A. Kokalj, *Comput. Mater. Sci.* **28**, 155 (2003)  
875. <http://www.ivec.org/GULP/>

---

# Index

Adiabatic approximation 105

Band representation 78

-  $\text{SrZrO}_3$  crystal 84

-  $\text{MgO}$  and  $\text{Si}$  crystals 84

Basic translation vectors 11

Basis sets in molecular calculations

- localized atomic-like orbitals

- Gaussian-basis notations 290

- Gaussian-type orbitals 285

- Slater-type orbitals 283, 285

- correlation-consistent basis 291

- minimal-basis set 287

- polarization functions 288

Basis sets in periodic calculations

- localized atomic-like orbitals 283

- Gaussian-type basis 294

- basis set superposition error 297

- molecular-basis adaptation 291

- plane waves 281

Boundless crystal 10

Bravais lattice 11

- 2D (plane) 460

- base-centered 12

- body-centered 12

- cubic 14

- face-centered 12

- hexagonal 14

- monoclinic 12

- orthorhombic 13

- parameters 12

- point symmetry 11

- primitive 12

- tetragonal 14

- triclinic 12, 14

- type 12

Brillouin zone

- special points 126

- Monkhorst–Pack 129

- cubic crystals 128

- modified Monkhorst–Pack 130

- supercell generation 127

- symmetry line 57

- symmetry point 57

Bulk crystals

- Compton profile

-  $\text{Cu}_2\text{O}$  383

- band structure

-  $\text{MgO}$ ,  $\text{TiO}_2$  377

- bulk moduli, elastic constants

-  $\text{SrTiO}_3$ ,  $\text{BaTiO}_3$ ,  $\text{PbTiO}_3$  402

- bulk modulus

-  $\text{Cu}_2\text{O}$  399

-  $\text{TiO}_2$  phases 401

- cohesive energy

-  $\text{TiO}_2$  396

- corundum-like oxides 397

- cyclic cluster model

-  $\text{Al}_2\text{O}_3$  431

- density of states

-  $\text{SrTiO}_3$ ,  $\text{SrZrO}_3$  380

- projected density of states 379

- electron-density maps

-  $\text{Cu}_2\text{O}$  382

- electron-momentum density

-  $\text{Cu}_2\text{O}$  383

- magnetic structure

-  $\text{LaMnO}_3$  385, 388

-  $\text{ScMnO}_3$  391

- phonon symmetry

-  $\text{TiO}_2$  405

- polymorphs

- $\text{SrZrO}_3$  403
- structure parameters
  - $\text{SnO}_2$  (110) 496
  - $\text{TiO}_2$  396
- supercell model
  - $\text{SrTiOO}_3$  446
- total energy
  - cohesive energy 394
- vibrational frequencies
  - $\text{TiO}_2$  407
  - calculation 404

#### Chemical bonding in crystals

- Wannier functions for valence bands
  - crystalline oxides 358
- localized orbitals
  - local electronic structure properties 363
- Wannier-type atomic functions
  - $\text{PbTiO}_3$  354
  - $\text{SrTiO}_3, \text{BaTiO}_3$  353
  - local properties of electronic structure 351
- bulk crystal
  - $\text{TiO}_2, \text{TiO}_2, \text{Ti}_2\text{O}_3$  342, 344, 347
- crystallographic valence
  - crystalline oxides 335
- cyclic cluster
  - crystalline oxides 334, 335
  - $\text{Cu}_4\text{O}_3, \text{Pb}_2\text{O}_3, \text{Pb}_3\text{O}_4$  339
  - $\text{La}_2\text{CuO}_4, \text{La}_2\text{NiO}_4$  341
  - $\text{YBa}_2\text{Cu}_3\text{O}_7$  340
- density matrix
  - LCAO 328
  - natural orbitals 330, 332
- electron correlation
  - molecular-crystalline approach 332
  - $\text{Ti}_2\text{O}_3$  349
- local properties of electronic structure
  - atomic population 329
  - bond order, covalency 329
  - total atomic valency 330
- localized orbitals
  - $\text{MgO}$  368
  - $\text{SrZrO}_3$  364, 368
- population analysis
  - projection technique 369
- projection technique
  - Si, SiC, GaAs,  $\text{MgO}$ ,  $\text{TiO}_2$  370
  - $\text{SrTiO}_3$ ,  $\text{SrZrO}_3$  372, 374

#### Computer programs for LCAO calculations

527

Conventional unit cell 15

#### Crystal structure

- cubic
  - zincblende 31
  - antifluorite 31
  - cesium chloride 32
  - diamond 29
  - fluorite 31
  - perovskite 33
  - rocksalt 30
- database 27
- description 26
- hexagonal
  - $\text{ScMnO}_3$  45
  - graphite 43
  - wurtzite  $\text{ZnS}$  45
- orthorhombic
  - $\text{LaMnO}_3$  38
- rhombohedral
  - $\alpha\text{Al}_2\text{O}_3$ , corundum 46
- tetragonal
  - $\text{La}_2\text{CuO}_4$  37
  - $\text{YBa}_2\text{Cu}_3\text{O}_7$  41
  - anatase 36
  - rutile 35
- type 26

#### Crystal system

- cubic 12
- hexagonal 12
- monoclinic 12
- orthorhombic 12
- rhombohedral 12
- syngony 11, 12
- tetragonal 12
- triclinic 12

#### Crystallographic point groups

- Schönflies notation 15
- international notation 15

#### Density matrix

- crystal 133
- LCAO approximation 137
- approximate 140
- properties 133, 135
- cyclic cluster
  - properties 136
- molecule 107

#### Density-functional theory (molecules)

- Thomas-Fermi model 231

#### Density-functional theory (crystals)

- LCAO approximation 250

- HSE screened Coulomb hybrid functional 259
  - HSE03 hybrid functional 261
  - Kohn–Sham equations 252
  - linear-scaling method 253, 256
  - screened Coulomb hybrid functional 262
  - exchange-correlation functionals 264
  - LDA+U method 275
  - SIC-LSDA method 271
- Density-functional theory(molecules)
- Hohenberg–Kohn theorems 232
  - Kohn–Sham equations 234, 237
  - generalized-gradient approximation GGA
  - PBE functional 243
  - exchange-correlation functionals 242
  - local spin density approximation LSDA 239
  - local density approximation LDA
    - exchange-correlation functionals 239
  - orbital-dependent exchange-correlation functionals 244
  - hybrid functionals 246, 248
- Effective core potentials
- relativistic 314
  - basis sets 318
  - generalized 316
  - periodic systems 320
- Effective core potentials
- nonrelativistic
    - Hay–Wadt potentials 304
    - energy-consistent 300
    - generation 301
    - norm-conserving 302
    - pseudo wavefunctions 298
    - valence basis-sets 302
    - separable embedding potentials 305
  - relativistic
    - Stevens–Basch–Krauss potentials 304
    - Stuttgart-Dresden potentials 304
- Electron correlation
- crystals
  - Laplace-MP2 174, 177
  - embedded cluster 168
  - local MP2 method 180, 184
  - local electron-correlation methods 164, 166
  - method of increments 166, 170, 173
  - molecules
- CI-method 151
  - CISDT-method 153
  - MCSCF-method 153
  - coupled cluster-method 154
  - local electron-correlation methods 158, 162
  - perturbation theory 155
  - spin correlation 148
- Equivalent points of space 8
- Group 7
- diperiodic (layer) 460
  - plane 460
  - point 7
  - space 7
  - superperiodic 460
  - translation 7
- Hartree–Fock method 107
- Coulomb operator 107
  - LCAO approximation
    - crystals 121, 122
    - cyclic cluster 117
    - molecules 115
    - UHF
      - crystals 123
      - cyclic cluster 222
    - exchange operator 108
    - local exchange approximation 109
    - restricted RHF 112
    - restricted for open shells ROHF 114
    - self-consistent calculation 108
    - symmetry of Fockian 109
    - unrestricted UHF 114
- Induced representations
- of point group 67
  - correlation table 69
  - of space group
    - $\mathbf{k}$ -basis 74
    - $\mathbf{q}$ -basis 72
    - composite 76
    - simple 76
    - tables 78
- Irreducible representations 7
- of space group
    - full representation 60
    - small(allowed) representation 60
  - of translation group
    - $\mathbf{k}$  vector 51
    - Bloch functions 52
    - Brillouin zone 52

- Layer group
  - Brillouin zone 464
  - element 461
  - irreducible representations 464
  - setting 461
  - site-symmetry 463
  - table 462
- LCAO and PW basis
  - Wannier-type atomic functions
  - MgO 357
- Local properties of electronic structure
  - molecules
  - Wiberg index 140
  - atomic covalence 140
- Localized orbitals
  - crystalline 86, 88, 89
  - for valence bands 94
  - molecular 70
  - generation 71
- Molecular cluster 10
- Monoatomic crystal 11
- Orbits of points 8
  - crystallographic 22
  - in a crystal 9
  - in a molecule 8
- Point defects in solids
  - classification 409
  - cyclic-cluster model
    - $F^+$  center in  $Al_2O_3$  433
    - F center in  $Al_2O_3$  432, 434
    - formation energy 418
  - models
    - cyclic cluster 411
    - cyclically-embedded cluster 424
    - molecular cluster 410
    - supercell 412
  - molecular-cluster model
    - realization 422
  - perturbed-cluster model
    - MgO 425
  - supercell model
    - realization 417, 420
    - F center in  $SrTiO_3$  441, 443
    - Fe-impurity in  $SrTiO_3$  445, 448, 449
    - $SrTiO_3$ ,  $BaTiO_3$  438
    - oxygen vacancy in  $SrTiO_3$  439
    - vanadium-doped  $TiO_2$  436
    - $TiO_2$  416
    - F center in  $Al_2O_3$  431
- MgO crystal 415, 419
- binary oxides 426
- charged defects 421
- convergence 423
- interstitial oxygen in MgO 428
- oxygen vacancy in  $Al_2O_3$  429
- symmetry 414, 415
- Primitive unit cell 11
- Projective representations
  - characters 64
  - factor system 62
  - of point group 62
- Reference unit cell 11
- Relativistic theory
  - molecules
    - Dirac–Hartree–Fock method 310, 311
    - Dirac–Kohn–Sham method 313
- Semiempirical LCAO methods 193
  - crystals
    - cyclic cluster 212, 215, 217
    - CNDO 209
    - Mulliken–Rüdenberg 201
    - extended Hückel 195
  - molecules
    - CNDO 203, 205
    - INDO 205
    - MNDO 206
    - MSINDO 206
    - Mulliken–Rüdenberg 199, 201
    - PM3 206
    - extended Hückel 194, 196
  - cyclic cluster
    - CNDO 218
    - INDO 220
    - MSINDO 221
- Site-symmetry group 8, 22
  - oriented 25
- Solid solutions
  - supercell model
    - $La_cSr_{1-c}MnO_3$  453, 455
- Space group 17
  - 1D 17
  - 2D 17
  - 3D 17
  - designations 18
  - elements 17
  - nonsymmorphic 18
  - plane 17
  - symmorphic 18
  - table 18

- Supercell
  - for centered lattices 16
  - transformation 16
  - symmetrical 124, 521
- Surfaces of crystals
  - (001)
    - MgO 471
    - cubic perovskites 473
  - (110)
    - $TiO_2$  471
  - surface energy
    - $TiO_2$  (110) 477
    - MgO (001) 475, 476
    - slab model 474
  - $SnO_2$ (110)
    - atomic charges 499
  - BSSE
    - $SnO_2$  (110) 497
  - atomic charges
    - $LaMnO_3$  (001) 516
  - bare surface (001)
    - $SrTiO_3$ ,  $SrZrO_3$  507, 509
  - cyclic cluster
    - $TiO_2$  (110) 482
  - density of states
    - $SrTiO_3$ ,  $SrZrO_3$  (001) 512
  - models
    - molecular cluster 459
    - periodic slab (supercell) 459
    - semi-infinite crystal 459
    - single slab 459
  - molecular cluster
    - $TiO_2$  (110) 483
    - $TiO_2$  (110) 484
  - slab
    - $SnO_2$  (110) 496
  - surface F center
    - $SrTiO_3$  (001) 513
  - surface energy
    - $LaMnO_3$  (001) 515, 517
    - $SnO_2$ (110) 497
    - $SrTiO_3$ ,  $SrZrO_3$  (001) 511
  - water adsorption
- $SnO_2$ (100) 505
- $SnO_2$ (110) 501, 503
- $TiO_2$  (110) 484, 488, 490, 492, 493
- Surfaces types
  - type-1
    - MgO 466, 467
  - type-2
    - $TiO_2$  (110) 468
  - type-3
    - $SrTiO_3$ ,  $LaMnO_3$  469, 470
- Symmetry elements 7
- Symmetry operations 7
- Symmetry properties 48
  - of crystalline orbitals 49
  - of molecular orbitals 49
  - of the Hamiltonian 48
  - time-reversal transformation 50
- Translation
  - improper or fractional 17
  - proper 17
- Wannier function 87, 90
  - local MP2 method 185
  - surface
    - slab model 478
    - surface
      - MgO (001) 479
      - $TiO_2$  (110) 480
    - Wannier type atomic orbitals 96
  - generation 91, 92, 94
    - variational method 97
    - comparison of methods 95
    - variational method 99, 101
  - symmetry
    - local MP2 method 189
- Wavevector
  - little group 60
  - point-symmetry group 57
  - star 58
- Wyckoff positions
  - notation 22
  - parameter-dependent 22
  - parameter-free 22